Saint-Petersburg State University
Saint-Petersburg Branch of the EurAsian Geophysical Society

Proceedings of the 10th International Conference

PROBLEMS OF GEOCOSMOS

Saint-Petersburg

2014

Saint-Petersburg State University
Saint-Petersburg Branch of the EurAsian Geophysical Society

Proceedings of the 10th International Conference

PROBLEMS OF GEOCOSMOS

St. Petersburg, Petrodvorets

October 06-10, 2014

Editors: V. N. Troyan, N. Yu. Bobrov, A. A. Kosterov, A. A. Samsonov,
N. A. Smirnova, and T. B. Yanovskaya

Saint-Petersburg

2014

Editors: V. N. Troyan, N. Yu. Bobrov, A. A. Kosterov, A. A. Samsonov, N. A. Smirnova and T. B. Yanovskaya. Proceedings of the 10th International Conference “Problems of Geocosmos”. – SPb., 2014 – 436 p.

ISBN 978-5-9651-0878-7

C O N T E N T S

CONDUCTIVITY OF THE EARTH

PALEOMAGNETISM AND ROCK MAGNETISM

SEISMO-ELECTROMAGNETIC PHENOMENA

SEISMOLOGY

SOLAR-TERRESTRIAL PHYSICS

ELABORATION OF A COMPLEX ALGORITHM OF NEURAL NETWORK SOLUTION OF THE INVERSE PROBLEM OF ELECTRICAL PROSPECTING BASED ON DATA CLASSIFICATION*

S.A. Dolenko[1], I.V. Isaev[1], I.E. Obornev[2],
E.A. Obornev[2], I.G. Persiantsev[1], M.I. Shimelevich[2]

[1]D.V. Skobeltsyn Institute of Nuclear Physics, M.V.Lomonosov Moscow State University, Moscow, Russia, e-mail: dolenko@srd.sinp.msu.ru;
[2]S.Ordjonikidze Russian State Geological Prospecting University, Moscow, Russia

Abstract. The inverse problem (IP) of electrical prospecting is a complicated high-dimensional ill-posed problem with a well-known instability. To describe the sought distribution of the electrical conductivity, different parameterization schemes are used. The most general scheme uses the values of conductivity in the nodes of a pre-defined grid, with further interpolation between nodes. More specific schemes may assume presence of certain geological structures. Transfer from the solution of the IP within general scheme to its much more stable solution within one of specific schemes in a narrower class of geoelectric sections causes the necessity of prior classification of the studied data pattern, resulting in the selection of the most appropriate parameterization scheme. In their previous studies, the authors considered the solution of the IP of magnetotelluric sounding (MTS) using artificial neural networks (ANN) (perceptrons). Also, it was demonstrated that the described classification problem can be successfully solved by ANN with average rate of correct determination of the parameterization scheme exceeding 97%. Since then, the authors have elaborated a novel method of ANN-based solution of the MTS IP within scheme G_0, based on simultaneous determination of a group of several parameters at once. In this study, the developed method has been extended to other parameterization schemes. It is demonstrated that group determination of parameters is an effective method for ANN solution of the MTS IP for any parameterization scheme. In future studies, it is planned to test the complex algorithm combining classification and IP solution within partial classes of geoelectrical sections against the general approach within the most general parameterization scheme G_0.

INTRODUCTION

The inverse problem (IP) of electrical prospecting is the problem of determining the distribution of electrical conductivity (EC) in the thickness of earth by the values of electromagnetic field observed on its surface. The distribution of the EC is described by a finite number of parameters using some parameterization scheme. Usually the parameters represent the EC in a number of discrete points of the area, with subsequent interpolation between the points providing the continuous EC distribution. Some parameterization schemes also assume presence of certain geological structures within the studied area; then some of the parameters may describe the geometrical dimensions of these structures.

It is well known that the IP of electrical prospecting is a complicated high-dimensional ill-posed problem (Zhdanov, 2002). The number of observed values of electromagnetic fields is about 10^3-10^4, and the distribution is usually described by several hundred parameters even in the 2D case. Transfer from the most general parameterization scheme using only a pre-defined spatial grid to specific parameterization schemes assuming presence of certain structures allows reducing the number of parameters; it may increase the stability of the IP and convert the general problem incorrect by Hadamard to several partial problems correct by Tikhonov. However, a solution of the IP may be only as good as close is the selected parameterization scheme to actual structure of the area. To apply this approach, the following tasks should be accomplished:

1) Elaboration of general parameterization scheme and several specific parameterization schemes;
2) Elaboration of a classification method capable to choose the most appropriate parameterization scheme by the observed values, without solving the IP for all the schemes;
3) Implementation of a technology of IP solution working within the general scheme;
4) Testing adaptability of the IP solution technology to specific parameterization schemes.

* This study was supported by the grant of Russian Scientific Foundation (project no.14-11-00579).

If all these tasks are accomplished successfully, then it would be possible to claim elaboration of a complex IP solution algorithm based on data classification/ Within this algorithm, first the classification method would be applied to select the most appropriate parameterization scheme, and then the IP solution technology would be used based on this scheme.

In this paper, we report accomplishment of the four listed tasks for a specific type of electrical prospecting – magnetotelluric sounding (MTS) with the help of artificial neural networks (ANN). For MTS, the electromagnetic waves used for sounding are induced by ionosphere sources and may be assumed to be plane waves. The details of the studied case, the obtained results and the perspective of elaboration of the complex algorithm are discussed.

PARAMETERIZATION SCHEMES

The considered case is a two-dimensional case, for which the MTS IP is a coefficient IP for the Helmholtz equation (Zhdanov, p. 214) with 6500+ observed field values.

One general parameterization scheme and six specific schemes assuming presence of layers with different types of conductivity were considered (Fig. 1, 2).

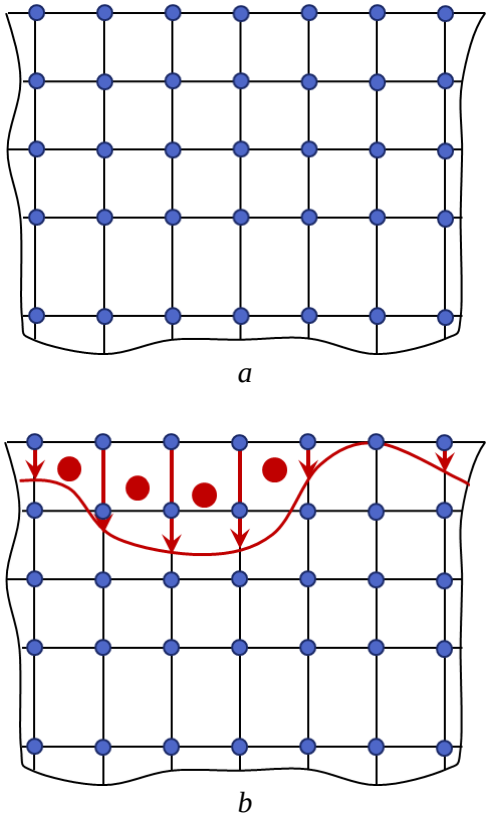

Fig. 1. Parameter setting for parameterization schemes G_0 (a) and G_1^C, G_1^I (b).

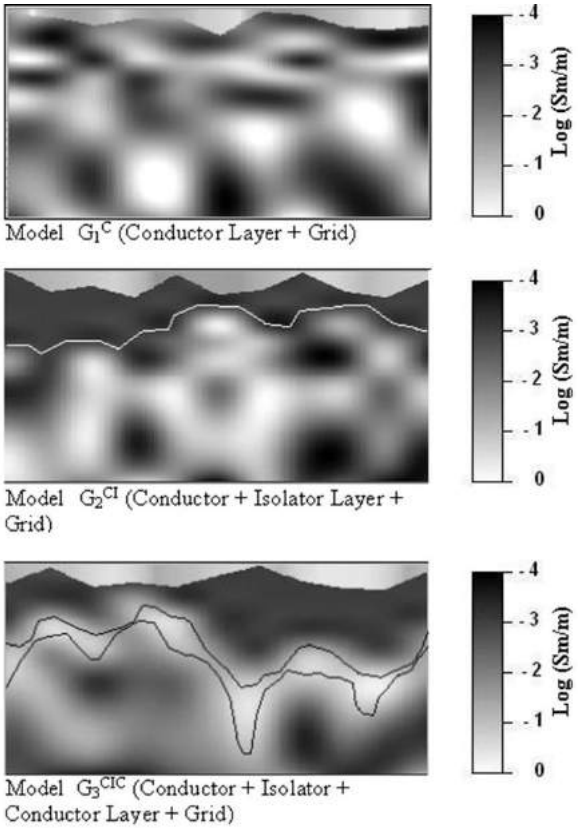

Fig. 2. Sample EC distributions for parameterization schemes G_1^C, G_2^{CI}, G_3^{CIC}.

Scheme G_0 (macro-grid, MG) is a structure present in all models. The parameters in G_0 are the values of electrical conductivity in fixed nodes of MG, which may change in the wide range $10^{-4} < \sigma_{i,j} < 1$ Sm/m (Fig. 1, a, blue dots). The MG is interpolated by a 2D spline for numeric solution of the direct problem. This parameterization scheme is described in more detail in (Dolenko et al, 2013).

The rest six schemes assume explicit presence of one, two or three conducting or dielectric layers with alternating properties (G_1^C, G_2^{CI}, G_3^{CIC}, G_1^I, G_2^{IC}, G_3^{ICI}). In all the models, index C denotes conductor with the range of specific electrical conductivity $10^{-2} < \sigma_j^{(L)} < 1$ Sm/m, while index I denotes isolator with the values of specific electrical conductivity in the range $10^{-4} < \sigma_j^{(L)} < 10^{-2}$ Sm/m. Fig. 1, b illustrates the principle of parameter setting for schemes G_1^C and G_1^I. The MG constructed similar to MG of scheme G_0, is partially overlapped in its upper part by the layer. The blocks of this layer are not rectangle; the EC distribution is set by its values in the centers of blocks (red circles) and by the values of layer thickness at the edges of the grid (red arrows).

It should be separately noted that the dimensionality of this problem is very high. The number of input features of the IP (observed field values) was N_I =4 field components × 13 frequencies × 126 pickets = 6552, and the number of output features was N_O = 336 parameters for scheme G_0 and N_O = 233 parameters for all the other six schemes.

CLASSIFICATION

In their previous study (Dolenko et al., 2008), the authors solved the classification problem by artificial neural networks (ANN). Within this approach, the vector of the observed data is fed to the inputs of an ANN. The ANN has several outputs, each corresponding to one of the considered classes (parameterization schemes). The distribution of amplitudes at the outputs of the classifier can be used to estimate the certainty of the classifier answer, and to make the decision about applicability of specific models for the IP solution. The decision is made using a pre-set threshold. If the highest amplitude among the outputs of the classifier exceeds the threshold value, then the classified sample is assigned to the class to which this output corresponds (this may be a correct or a wrong answer). If the highest amplitude is less than the threshold, then it is accepted that the classifier refused to recognize this sample. This is a standard technique for applying NN to solve classification problems.

As an alternative classification method to NN classification, the method of K nearest neighbors (K-NN) has been considered in the following implementation. For a studied sample, the belonging of which should be determined, K samples of the training data set are found that are nearest to it in the space of input features (K nearest neighbors). If it turns out that more than half of the nearest neighbors belong to the same class, then the studied sample is considered to be attributed by the method to the same class; otherwise it is considered that the method failed to give an answer (recognition refusal).

The Table presents the results obtained by different classification methods – single perceptron, hierarchical neural classifiers with fixed and with adaptively defined structure, probabilistic neural network, and k-NN with one nearest neighbor. The presented statistics are correct recognition rates (green), false recognition rates (pink) and refusal rates (yellow), averaged over all seven classes, and for the class with the worst result. The detailed description of these results can be found in (Dolenko et al., 2008).

Table. Comparison of classification results obtained by different methods.
HNC – hierarchical neural classifier, PNN – probabilistic neural network, 1-NN – 1 nearest neighbour.

Method	Perceptron	Fixed HNC	Adaptive HNC	PNN	1-NN
Threshold	0.7	0.1	0.7	0.9	-
% correct average	96.78	97.49	97.43	78.94	87.78
% wrong average	2.71	2.48	2.03	5.52	12.22
% refusals average	0.50	0.03	0.54	15.54	-
% correct worst	95.20	95.84	92.68	18.80	42.68
% wrong worst	3.96	4.16	6.52	33.36	57.32
% refusals worst	0.84	0.00	0.80	47.84	-

One should stress a very important peculiarity of the considered classification problem. It is mediated by the IP, i.e. the classes are determined by the distribution of the conductivity in the space of parameters, while the data for the solution of the classification problem are the values of the observed fields. Due to the incorrectness of the IP mentioned above, solvability of the classification problem with required precision was not guaranteed, and the complexity of recognition could turn out to be different for different classes. However, the results of classification turned out to be very good in these circumstances, reaching nearly 97.5% on the average for the hierarchical classifiers, and more than 95% for the worst class. So we can consider the classification task to be accomplished to an extent sufficient to move to the next task.

IP SOLUTION WITH PARAMETER GROUPING FOR GENERAL SCHEME G_0

There are several possible approaches to the ANN solution of multi-parameter inverse problems:

1) Solution of a separate single-output IP with construction of a separate ANN for each of the determined parameters (*autonomous determination*). This is the most universal approach, used most often.

2) Solution of a single IP with *simultaneous determination* of all the sought-for parameters. This approach requires construction of a single ANN with the number of outputs N_O equal to the full number of the determined parameters. The efficiency of this approach rapidly degrades with increase of N_O.

3) Aggregation of parameters into groups with simultaneous determination of the parameters (by construction of a single ANN) within each group (*group determination*). The method of aggregation is governed by the physical sense of the determined parameters and by their known interrelations. This approach was investigated in (Dolenko et al, 2013), where an improvement in the IP solution quality has been demonstrated.

4) *Sequential determination* of parameters. Within this approach, at the first stage the values of those parameters for which this problem is solved with acceptable precision, are determined independently of each other or simultaneously. At the subsequent stages, the values of these parameters obtained by applying the ANN of the first stage are fed to the inputs of the ANN of the next stage, together with the values of the input features. This approach was investigated in (Isaev and Dolenko, 2014), where it has been demonstrated that in some cases it may also have positive effect on the IP solution precision.

Among all these approaches, the best results for scheme G_0 were demonstrated by group determination. So it was selected as the main IP solution algorithm.

As the initial input data dimensionality is very large (N_I=6552), prior two-step selection of significant input features was performed for each of the parameters using ANN weight analysis. Note that if such selection is performed properly, the computational cost of the ANN solution is reduced, and the quality of the IP solution is increased (Dolenko et al., 2009). The number of significant input features for various parameters ranged from 16 to 94. For group determination, each ANN was fed with all the input features significant at least for one of the determined output parameters. Depending on the size of the group and on the intersection of the sets of significant input features, the total number of input features for group determination of parameters ranged from 32 to 940.

In all experiments (except some special cases) the problem was solved by a perceptron with three hidden layers having 24, 16, and 8 neurons, linear activation function in the output layer, and logistic activation function in all the other layers. Training was stopped 500 epochs after the minimal value of the mean squared error on the test set of data has been reached.

To assess the quality of problem solution, the multiple determination coefficient R^2 (R squared), equal to 1 for exact approximation of the studied dependence with a model, and 0 for the trivial model-average, was used in this study. To reduce the dependence of the results on random factors, each ANN was trained five times, with different sets of initial weights, and the results were averaged.

Note that group determination turned out to be efficient in reducing IP solution error only then the aggregated parameters (whose values were determined together) corresponded to the blocks lying just one above another, in a single vertical, for the reasons discussed in detail in (Dolenko et al, 2013). So the considered parameters correspond to EC in the points along vertical grid edge (blue dots in Fig. 1, a).

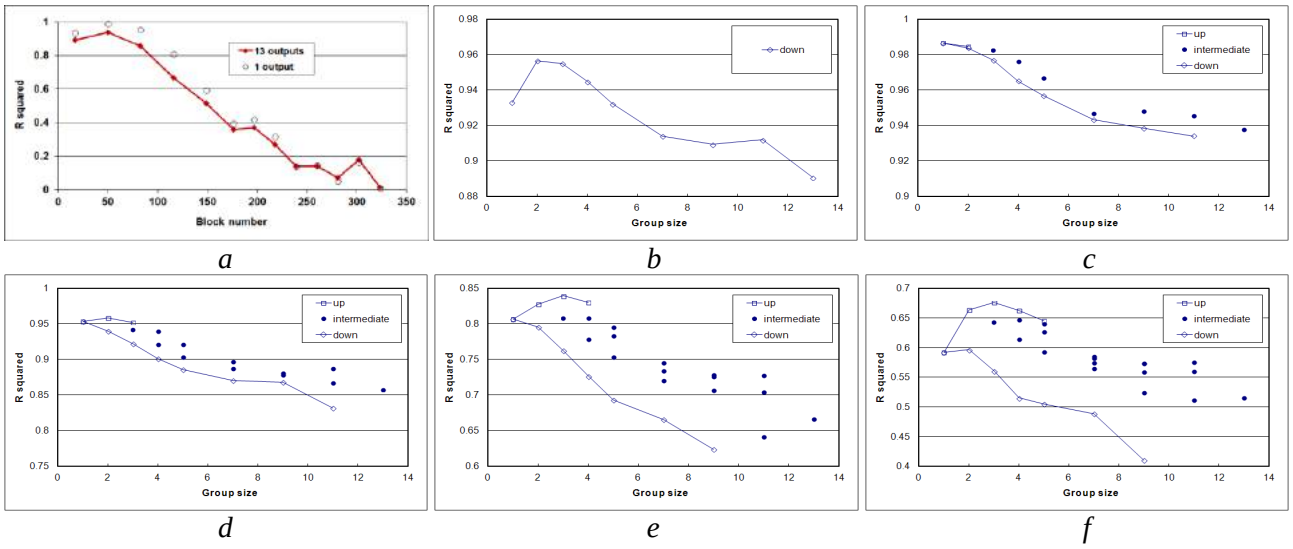

Fig. 3. IP solution quality, scheme G_0: a – autonomous determination (open circles) and simultaneous determination (line), b-f – group determination for grid layers 1-5 respectively, for various group positions, versus group size. Layers 1-5 describe upper 3.5 km of the section.

Fig. 3 displays the quality of IP solution for autonomous and simultaneous determination (*a*) and for group determination with vertical grouping (*b-f*) for the five uppermost layers (total thickness 3.5 km). Different points at the diagrams for the same group size correspond to various positions of the parameter grouping window. Specially marked (with open signs and curves) are the values for window shifted up or down to maximum possible extent. Points for Group size = 1 correspond to autonomous determination.

The following facts attract attention.

1) For the uppermost block (Fig. 3, b), the quality of the group solution of the IP is increased as compared with that of autonomous determination, if the group includes up to 4 output features. However, the best result is achieved for group size Sg=2.

2) For the second layer block (Fig. 3, c), for which the problem solution quality in autonomous mode is the best one (Fig. 3, a), group determination always gives worse results.

3) For deeper occurring blocks, the situation depends on the position of parameter grouping window. If the window is shifted up (towards parameters that are better determined in autonomous mode), group determination improves the results; if the window is shifted down, the group determination usually makes the results worse.

In the whole, we see that group determination of parameters, when properly used, can improve the IP solution quality for scheme G_0. Now we need to check the applicability of this approach for other schemes of parameterization.

IP SOLUTION WITH PARAMETER GROUPING FOR SCHEMES G_1^C AND G_1^I

Fig. 4 displays the quality of IP solution for scheme G_1^C, for autonomous determination (*a*) and for group determination with vertical grouping (*b-f*) for the layers 3-7. Points for Group size = 1 correspond to autonomous determination. Fig. 4 is similar to Fig. 3 except for the following.

As described above, scheme G_1^C assumes presence of a sub-surface layer with variable thickness (Fig. 1, b). So the leftmost parameter in Fig. 4, a describes thickness of the sub-surface layer (red arrow in Fig. 1, b) just above the vertical grid edge corresponding to the grouped parameters describing EC in the points along vertical grid edge (blue dots in Fig. 1, b). The second and third parameters from the left in Fig. 4, a describe EC in the centers of the two adjacent sub-surface blocks (red circles in Fig. 1, b) lying just above this vertical grid edge. Now, the sub-surface layer fully overlaps Layer 1 of the grid (that is why the value of R^2 for this layer is close to zero) and partially overlaps Layer 2. So the grouping effect is studied and demonstrated for Layers 3-7.

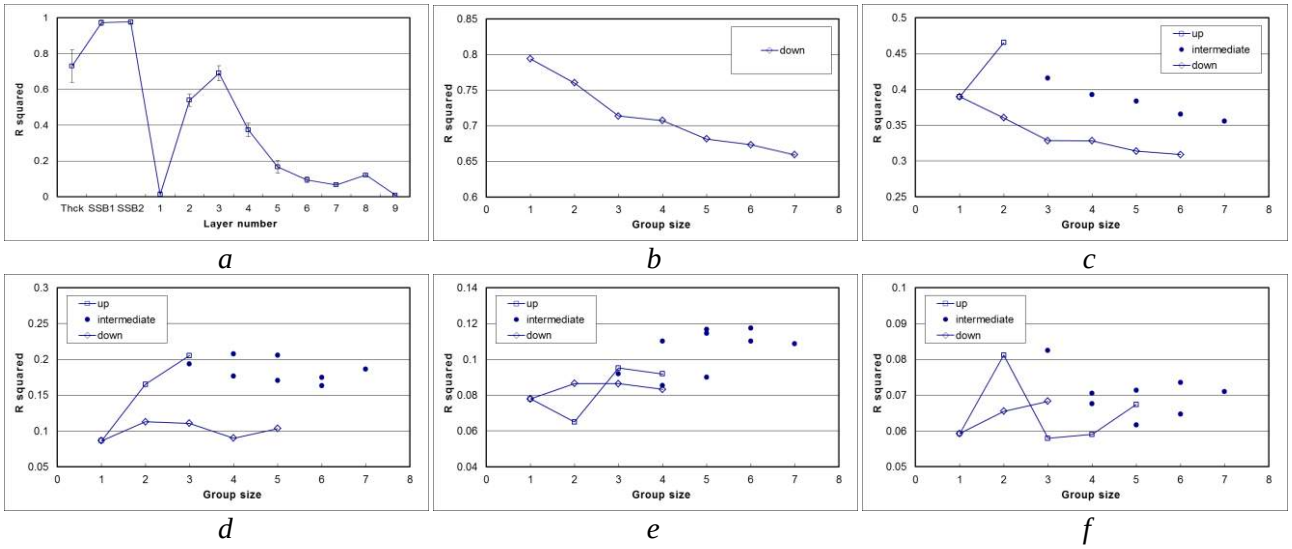

Fig. 4. IP solution quality, scheme G_1^C: a – autonomous determination, b-f – group determination for grid layers 3-7 respectively, for various group positions, versus group size. Three leftmost parameters (a) describe: Thck – sub-surface layer thickness, SSB1 and SSB2 – EC of two blocks in the sub-surface layer.

Fig. 5 displays the quality of IP solution for scheme G_1^I, for autonomous determination (*a*) and for group determination with vertical grouping (*b-f*) for the layers 3-7. Points for Group size = 1 correspond to autonomous determination. Fig. 5 is similar to Fig. 4 starting from Layer 3.

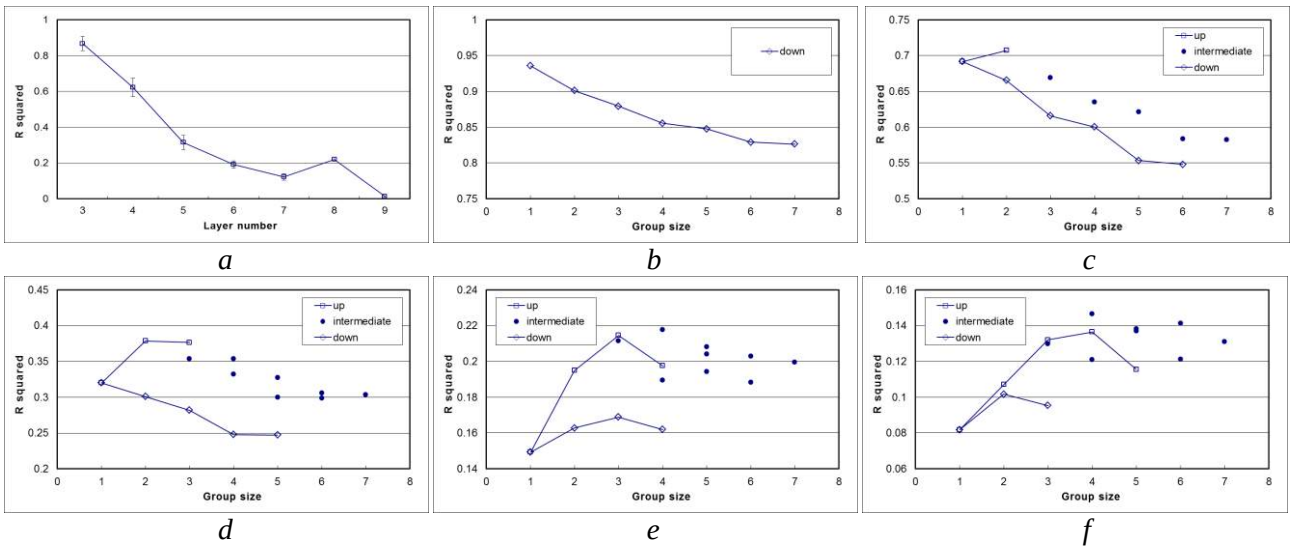

Fig. 5. IP solution quality, scheme G_1^I: a – autonomous determination, b-f – group determination for grid layers 3-7 respectively, for various group positions, versus group size.

It can be seen from Fig. 4 and Fig. 5 that the positive effect of group determination of parameters is confirmed. One can conclude that this effect is a general property of ANN solving multi-parameter inverse problems, and therefore it can be used for other schemes of parameterization.

CONCLUSION

In this study it has been demonstrated that all the main parts needed to create a complex algorithm for ANN solution of MTS IP based on data classification have been elaborated and tested. Namely, (a) various parameterization schemes, (b) a classification algorithm able to distinguish the most appropriate scheme by the observed field values, and (c) an advanced algorithm of IP solution based on ANN with group determination of parameters, efficient with various parameterization schemes, are available.

Future studies should include putting all these parts together and testing of the complex algorithm against the approach with no classification within the most general parameterization scheme G_0.

ACKNOWLEDGEMENT

The authors thank A.G. Guzhva for writing the ANN software which was used to conduct this study.

REFERENCES

Dolenko, S.A., E.A. Obornev, I.G. Persiantsev, M.I. Shimelevich (2008), Use of adaptive neural network based algorithms of data classification in the solution of the inverse problem of electrical prospecting, *In: 9th International Conference "Pattern Recognition and Image Analysis: New Information Technologies" (PRIA-9-2008): Conference Proceedings*, Nizhni Novgorod, 1, 100-103.

Dolenko, S., A. Guzhva, E. Obornev, I. Persiantsev, M. Shimelevich (2009), Comparison of adaptive algorithms for significant feature selection in neural network based solution of the inverse problem of electrical prospecting, Lecture Notes in Computer Science (LNCS), 5769, 397-405.

Dolenko, S., I. Isaev, E. Obornev, I. Persiantsev, and M. Shimelevich (2013), Study of influence of parameter grouping on the error of neural network solution of the inverse problem of electrical prospecting, *Communications in Computer and Information Science (CCIS)*, 383, 81-90. DOI 10.1007/978-3-642-41013-0_9.

Isaev, I.V. and S.A. Dolenko (2014), Improving the accuracy of neural network solution of the inverse problem of electrical prospecting by sequential determination of parameters: verification on model data, *In: Proc.10th Intl. Conf. "Problems of Geocosmos" (Oct.06-10, 2014, St. Petersburg, Russia)*, Saint Petersburg State University, Russia, in press.

Zhdanov, M.S. (2002), *Geophysical inverse theory and regularization problems.* 609 pp., Elsevier, Amsterdam, New-York, Tokyo.

IMPROVING THE ACCURACY OF NEURAL NETWORK SOLUTION OF THE INVERSE PROBLEM OF ELECTRICAL PROSPECTING BY SEQUENTIAL DETERMINATION OF PARAMETERS: VERIFICATION ON MODEL DATA*

Isaev I.V., Dolenko S.A.

D.V.Skobeltsyn Institute of Nuclear Physics, M.V.Lomonosov Moscow State University, Moscow, Russia, e-mail: isaev_igor@mail.ru

Abstract. The inverse problem (IP) of electrical prospecting is a problem of construction of the distribution of electrical conductivity (EC) in an underground area by the components of electromagnetic fields measured on its surface. The sought distribution in its most general form is described by parameters – the values of EC at the nodes of a pre-defined spatial grid, with subsequent interpolation of values between nodes. To describe the distribution adequately, the number of such parameters must be sufficiently large, reaching several hundred even in the two-dimensional case. In their previous studies, the authors considered the solution of the IP of magnetotelluric sounding (MTS) using artificial neural networks (perceptrons). First, the solution of the multi-parameter MTS IP with N determined parameters was performed by its division into N single-parameter problems. Later it was shown that introducing information about EC of higher-lying blocks to the input of the neural network allows increasing the precision of the solution in a number of cases. In this study, the observed effect was verified in computational experiment on artificial model data specified explicitly as complex polynomial dependences of the "observed values" (dependent variables) on the "parameters" (independent variables).

INTRODUCTION

The inverse problem of magnetotelluric sounding (MTS IP) is the problem of reconstruction of the distribution in the thickness of the earth by the values of the components of electromagnetic fields measured at its surface. In the two-dimensional case it is a coefficient IP for the Helmholtz equation (Zhdanov, p. 214). The problems of such type are incorrect, non-linear, and neither an analytical nor a direct numerical solution are known for such problems. Besides that, the necessity of detailed description of geological sections causes high dimensionality of the problem, as by input, as by output, thus additionally complicating its solution.

The traditional method of solving such problems is the method of residual minimization, based on repeated solution of the direct problem. This determines the inherent shortcomings of this method: high computational cost, low operation speed, necessity of pointing out the first approximation; when this method is used, the role of an expert is high. One of the methods free of many shortcomings inherent for traditional methods of IP solving, is the use of artificial neural networks (ANN). The method of ANN use considered in this study is the straightforward solution of the inverse problem by the ANN, when the components of the fields are fed to the inputs of the network, and the outputs provide estimation for one or several parameters describing the distribution of the EC.

APPROACHES TO THE ANN SOLUTION OF MULTI-PARAMETER INVERSE PROBLEMS

There are several possible approaches to the ANN solution of multi-parameter inverse problems:

1) Solution of a separate single-output IP with construction of a separate ANN for each of the determined parameters (*autonomous determination*). This is the most universal approach, and it is used most often.

2) Solution of a single IP with *simultaneous determination* of all the sought-for parameters. This approach requires construction of a single ANN with the number of outputs N_o equal to the full number of the determined parameters. The efficiency of this approach rapidly degrades with increase of N_o.

3) Aggregation of parameters into groups with simultaneous determination of the parameters (by construction of a single ANN) within each group (*group determination*). The method of aggregation is

* This study was supported by the grant of Russian Scientific Foundation (project no.14-11-00579).

governed by the physical sense of the determined parameters and by their known interrelations. This approach was investigated in (Dolenko et al, 2013a), where an improvement in the IP solution quality has been demonstrated.

4) *Sequential determination* of parameters. Within this approach, at the first stage the values of those parameters for which this problem is solved with acceptable precision, are determined independently of each other or simultaneously. At the subsequent stages, the values of these parameters obtained by applying the ANN of the first stage are fed to the inputs of the ANN of the next stage, together with the values of the input features.

Consideration of the sequential determination of parameters has been started by the authors elsewhere (Dolenko et al, 2013b). The purpose of the present study was determination of the reason of the observed positive effect of sequential determination of parameters in IP solution. Is it determined by the properties of a specific problem or is it a fundamental property of ANN as a method of IP solution?

INITIAL DATA AND PROBLEM STATEMENT

The study was performed on model data obtained as the result of numerical solution of the direct 2D problem of MTS.

When this problem is solved, the components Ex, Ey, Hx, Hy of induced electromagnetic fields at various frequencies and in different points at the Earth's surface are calculated by the distribution of EC in the thickness of the earth (across the section).

The calculation depends to a significant degree on the parameterization scheme, i.e. on the method of description of the EC distribution in the sub-surface area. The data used in this study were obtained for the most general parameterization scheme G_0 (Fig. 1), where the distribution is described by the values of EC in the upper right corners of blocks arranged in layers, with subsequent interpolation among the blocks. The data array consisted of 30,000 samples obtained for random combinations of EC of different blocks in the range from 10^{-4} to 1 Sm/m.

			Column	1	2	3	4	5	6	7	8	9	10	11	12	13	14	15	16	17	18	19	20	21	22	23	24	25	26	27	28	29	30	31	32	
Layer	H	Z	Y=	35	25	17	12	6	5	5	5	5	5	5	5	5	5	5	5	5	5	5	5	5	5	5	5	5	5	6	12	17	25	35	km	
1	0.5	0.5		1	2	3	4	5	6	7	8	9	10	11	12	13	14	15	16	17	18	19	20	21	22	23	24	25	26	27	28	29	30	31	32	33	
2	0.5	1		34	35	36	37	38	39	40	41	42	43	44	45	46	47	48	49	50	51	52	53	54	55	56	57	58	59	60	61	62	63	64	65	66	
3	0.5	1.5		67	68	69	70	71	72	73	74	75	76	77	78	79	80	81	82	83	84	85	86	87	88	89	90	91	92	93	94	95	96	97	98	99	
4	1	2.5		100	101	102	103	104	105	106	107	108	109	110	111	112	113	114	115	116	117	118	119	120	121	122	123	124	125	126	127	128	129	130	131	132	
5	1	3.5		133	134	135	136	137	138	139	140	141	142	143	144	145	146	147	148	149	150	151	152	153	154	155	156	157	158	159	160	161	162	163	164	165	
6	1.5	5		166	167	168	169	170	171	172	173	174	175	176	177	178	179	180	181	182	183	184	185	186													
7	2.5	7.5	334	187	188	189	190	191	192	193	194	195	196	197	198	199	200	201	202	203	204	205	206	207												335
8	2.5	10		208	209	210	211	212	213	214	215	216	217	218	219	220	221	222	223	224	225	226	227	228													
9	3	13		229	230	231	232	233	234	235	236	237	238	239	240	241	242	243	244	245	246	247	248	249													
10	4	17		250	251	252	253	254	255	256	257	258	259	260	261	262	263	264	265	266	267	268	269	270													
11	5.5	23		271	272	273	274	275	276	277	278	279	280	281	282	283	284	285	286	287	288	289	290	291													
12	7.5	30		292	293	294	295	296	297	298	299	300	301	302	303	304	305	306	307	308	309	310	311	312													
13	km	km		313	314	315	316	317	318	319	320	321	322	323	324	325	326	327	328	329	330	331	332	333													
				336																																

Fig. 1. Medium parameterization scheme "G_0". The calculation is performed within the area limited by the borders. Inside each block, its number is specified. The first column shows the layer numbers, the first line – the column numbers. The most interesting area is the central area of the section marked with thick frames: layers 1 to 13, columns 5 to 28. Parameters 334-336 specify border conditions for calculations. H is the thickness of a layer, Z is the depth of the bottom of a layer, Y is the horizontal size of a block; all parameters in km. The marked blocks were used in the investigations of the present study.

The described data array was used for the solution of the IP – determination of the values of EC (N_O = 336 parameters, Fig. 1) by the values of the fields (N_I =4 field components × 13 frequencies × 126 pickets = 6552 input features).

The solution of this IP is connected with significant difficulties caused by large dimensionality of input and output data.

THE RESULTS OF NEURAL NETWORK SOLUTION OF THE MTS IP

The problem solution was studied for the parameters corresponding to the conductivity of the blocks marked grey in Fig. 1 (the central column no.16). For each of these parameters, the statistic index of precision of its determination (the multiple determination coefficient, R^2) was compared for the following approaches:

- Autonomous determination;
- The best result obtained by group determination (Dolenko et al., 2013a);
- *Aprioristic* sequential determination, when the ANN is fed by the exact values of the EC of higher-lying blocks (to estimate the best result possible for sequential determination);
- *Recursive* sequential determination, when the ANN is fed with the EC values for all the higher-lying blocks, obtained by applying ANNs trained with the same version of sequential determination at the preceding stages.

As the initial input data dimensionality is very large (N_I=6552), prior two-step selection of significant input features was performed for each of the parameters using ANN weight analysis. Note that if such selection is performed properly, the computational cost of the ANN solution is reduced, and the quality of the IP solution is increased (Dolenko et al., 2009). The number of significant input features for various parameters ranged from 16 to 94. For group determination, each ANN was fed with all the input features significant at least for one of the determined output parameters. Depending on the size of the group and on the intersection of the sets of significant input features, the total number of input features for group determination of parameters ranged from 32 to 940. For sequential parameter determination, the ANN was fed only with features significant for the parameter being determined, plus the values of the EC of the higher-lying blocks.

In all experiments (except some special cases) the problem was solved by a perceptron with three hidden layers having 24, 16, and 8 neurons, linear activation function in the output layer, and logistic activation function in all the other layers. Training was stopped 500 epochs after the minimal value of the mean squared error on the test set of data has been reached.

To assess the quality of problem solution, the multiple determination coefficient R^2 (R squared), equal to 1 for exact approximation of the studied dependence with a model, and 0 for the trivial model-average, was used in this study.

To reduce the dependence of the results on random factors, each ANN was trained five times, with different sets of initial weights, and the results were averaged.

In this series of computational experiments, during sequential determination, the ANN inputs were fed with the EC values only for single blocks situated exactly above the block whose EC is determined, i.e. for blocks from column no.16, marked grey in Fig. 1.

Fig. 2 (A) displays the dependence of the multiple determination coefficient R^2 on block number for different methods of parameter determination. The results were averaged over ANN realizations with different sets of initial weights; the standard deviation of the R^2 value does not exceed 0.01, and it is not shown. For clearness, Fig. 2 (B) displays the change of the R^2 value for different methods of parameter determination as compared to autonomous determination.

Analysis of Fig. 2 allows one to draw the following conclusions:

1) Recursive sequential determination nearly always allows improving the result compared to autonomous determination, but the gained improvement is always less than for the best variant of group determination of parameters.

2) Aprioristic sequential determination in most of the cases gives several fold more significant gain against autonomous determination than the recursive one. Unfortunately, aprioristic determination cannot be used in practice, when the exact solution of the IP for the above-lying parameters is unknown. The difference between the results of application of aprioristic and recursive approaches is caused by errors in IP solution for the above-lying blocks. This means that if it would be possible to elaborate a method of more precise solution of the IP in autonomous determination mode, then the gain obtained with recursive determination may increase.

3) The quality of the IP solution with autonomous determination of parameters, as a rule, decreases with depth; this is caused by shielding of lower-lying blocks with upper-lying ones. Exceptions to this rule are mainly observed near the borders of the section (blocks 50 and 302) and when section discretization is changed (blocks 149-176). Deviations from the rules of items 1) and 2) are also mainly observed for those blocks, for which the monotonous character of the dependence of IP solution quality on depth for autonomous determination is violated.

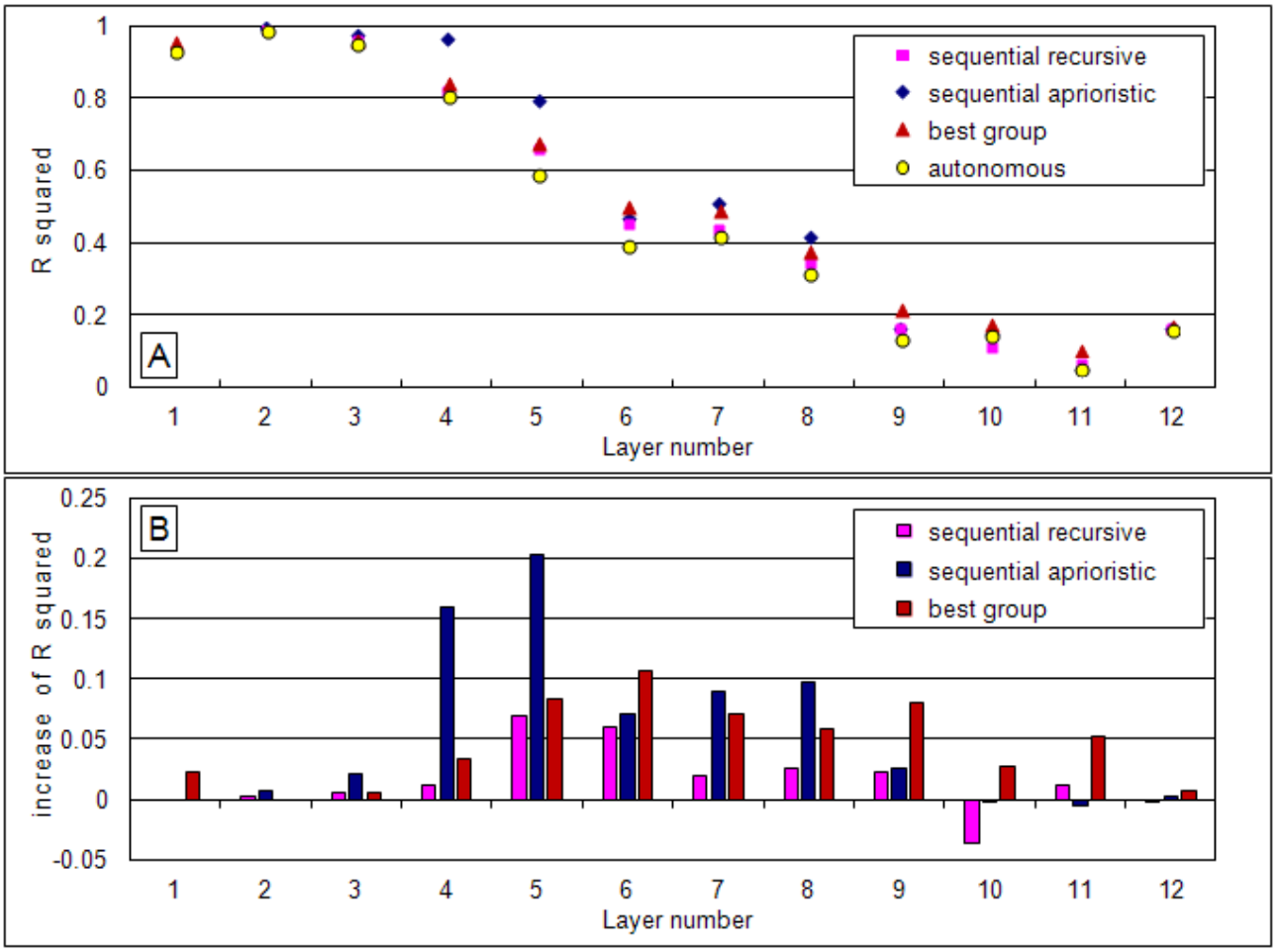

Fig. 2. The results of ANN solution of MTS IP.
A – Dependence of solution quality on layer number and on the method of parameter determination.
B – Change in R^2 for different methods of parameter determination in respect to autonomous determination.

TEST OF THE EFFECT OF SEQUENTIAL PARAMETER DETERMINATION ON ARTIFICIAL MODEL DATA DEFINED EXPLICITLY

Consider an artificial model inverse problem (Fig. 3) with five input features x_i, each of which depends on all the five determined parameters y_j.

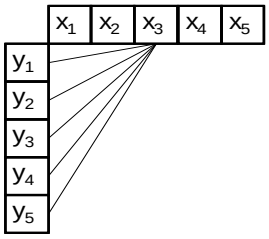

Fig. 3. A scheme of the considered artificial model problem.

Let us define an inverse problem with the help of a simple polynomial model with coefficients a_{ij}, b_{ij}, c_{ijk}, d_{ij}, e_i:

$$x_i \sim \sum_{j=1}^{5} a_{ij} \cdot y_j^{\,3} + \sum_{j=1}^{5} b_{ij} \cdot y_j^{\,2} + \sum_{j=1}^{4} \sum_{k=j+1}^{5} c_{ijk} \cdot y_j \cdot y_k + \sum_{j=1}^{5} d_{ij} \cdot y_j + e_i \qquad (1)$$

Monotonous decrease in the precision of IP solution in autonomous mode (Fig. 4) will be provided by the dependence of the coefficients on conventional "distance" from the input to the output (Fig. 3). In this study, they will be inverse proportional to the square of the "distance":

$$a_{ij} \sim b_{ij} \sim d_{ij} \sim \frac{1}{i^2 + j^2} \qquad c_{ijk} \sim \frac{a_{ij} + a_{ik}}{2} \qquad e_i \sim \sum_{j=1}^{5} a_{ij} \tag{2}$$

The values of the determined parameters y_i are random numbers from the range from 0 to 1. The corresponding values of the "observed" variables x_i are calculated by formula (1). Then the ANN is trained to reconstruct the values of y_j by the values of x_i, i.e. to solve the inverse problem.

The ANN used to solve this artificial model problem was a perceptron with three hidden layers consisting of 16, 12 and 8 neurons. The training set included 3000 samples. All the other training parameters were identical to those described above for the MTS IP.

Fig. 4 presents the results of ANN solution of the artificial model IP with sequential determination of parameters.

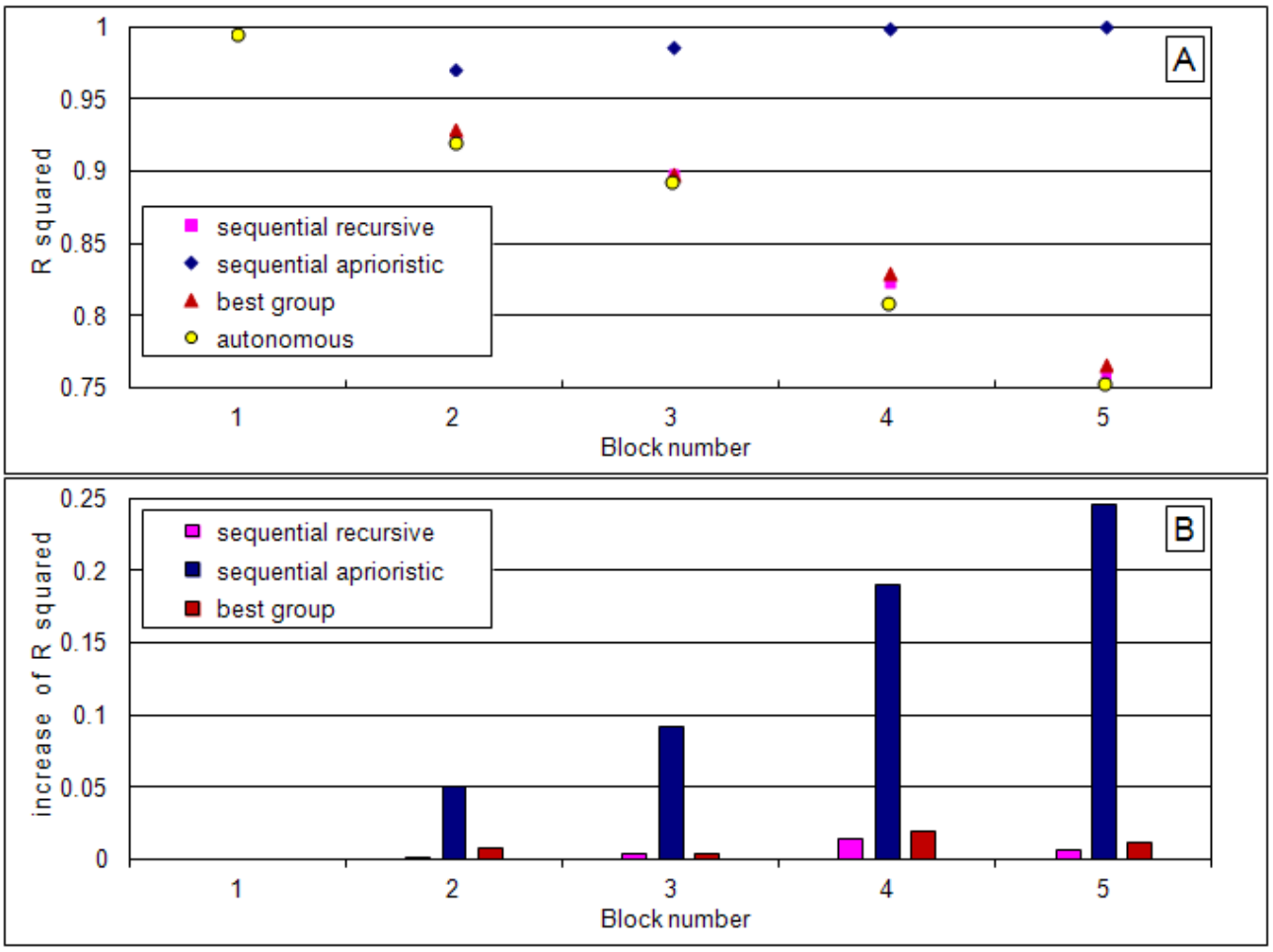

Fig. 4. The results of ANN solution of artificial model IP.
A – Dependence of solution quality on block number and on the method of parameter determination.
B – Change in R^2 for different methods of parameter determination in respect to autonomous determination.

We can see that the situation in Fig. 4 is much similar to that obtained above for the MTS IP (Fig. 2). So we can claim that the observed effect of sequential parameter determination is connected not with the properties of a specific problem, but with the properties of the multi-layer perceptron as an algorithm of data processing. The only condition that must be obeyed to apply sequential parameter determination is to sort the parameters in descending order by the value of efficiency of autonomous determination. Then sequential determination should be performed in this order.

However, large difference in the results of aprioristic and recursive determination is an evidence of relatively low stability of the method against low results of autonomous determination. As can be seen from Fig. 2 and Fig. 4, the severity of this problem may depend on the specific IP. Investigation into this issue should be the subject of a future study.

DISCUSSION

Introduction of additional features to the input of an ANN causes two contradictory effects.

From one side, these additional features carry new information about the object (in this case – about the conductivity of the upper-lying blocks that shield the studied one). If the ANN will be capable to use this information, the quality of problem solution should increase.

From the other side, introduction of a significant number of additional input features with the number of samples in the training set remaining constant leads to degradation of the ratio of the number of samples and the number of input features. As a rule, this causes reduction of ANN training efficiency and degradation of problem solution quality.

The final result depends on the relative contribution of these two processes. If it turns out that addition of new features does not bring enough new information, or if this information cannot be used by the ANN during training, then the result usually degrades. In particular, use of sequential determination in this situation does not lead to the desired result.

Note that for the specific problem studied here (MTS IP), the situation is hampered by the fact that the introduced features are of completely another nature (values of EC of the upper-lying blocks) than that of the features of the initial set (amplitudes of electromagnetic fields). This means that for efficient use of both types of features the ANN needs to construct simultaneously two strongly different non-linear mappings of the value sets of the input features to the value set of the determined parameter. The severity of this problem may be different for different kinds of IP.

CONCLUSION

The main results of this study are the following.

Existence of positive effect of sequential parameter determination for ANN solution of multi-parameter inverse problems has been confirmed.

It has been demonstrated that this effect is connected with fundamental properties of neural networks and not with the properties of data. Therefore, this method may be also used to solve other multi-parameter inverse problems.

It has been supposed that the method may turn unstable in respect to rapid degradation of the efficiency of autonomous determination of parameters. This issue needs further investigation.

ACKNOWLEDGEMENT

The authors express their gratitude to E.A. Obornev and M.I. Shimelevich, who elaborated the parameterization scheme G_0, and provided the model MTS data used in the first part of this study. Also, the authors would like to thank A.G. Guzhva for writing the ANN software which was used to conduct this study.

REFERENCES

Dolenko, S., A. Guzhva, E. Obornev, I. Persiantsev, M. Shimelevich (2009), Comparison of adaptive algorithms for significant feature selection in neural network based solution of the inverse problem of electrical prospecting, Lecture Notes in Computer Science (LNCS), 5769, 397-405.

Dolenko, S., I. Isaev, E. Obornev, I. Persiantsev, and M. Shimelevich (2013a), Study of influence of parameter grouping on the error of neural network solution of the inverse problem of electrical prospecting, *Communications in Computer and Information Science (CCIS)*, 383, 81-90.

Dolenko, S.A., I.V. Isaev, E.A. Obornev, I.G. Persiantsev, and M.I. Shimelevich (2013b), Investigation of efficiency of sequential parameter determination in neural network solution of electrical prospecting inverse problem, *in: Proc. XV All-Russian Scientific and Technical Conference "Neuroinformatics-2013" (Moscow, Russia, January 2013)*, NRNU MEPhI, Moscow, 2, 215–225. (In Russian.)

Zhdanov, M.S. (2002), *Geophysical inverse theory and regularization problems.* 609 pp., Elsevier, Amsterdam, New-York, Tokyo.

TWO-DIMENSIONAL INVESTIGATION OF THE EARTH CRUST SUBSURFACE LAYER BY METHOD OF INTERNAL SLIDING CONTACT

V.E. Kolesnikov[1], A.A. Skorokhodov[1]

[1]Geological Institute of the Kola Science Center of Russian Academy of Sciences, 184209 Apatity, Russia, e-mail: vk51@list.ru

Abstract. Method of internal sliding contact (MISC) is a DC investigation method of Earth crust subsurface, which combines elements of profiling and sounding. Variation of distance between current electrode A and receiver electrode M allows the carrying on the investigations of this kind. Media sounding is conducted when the signal on receiver electrodes is registered and AM distance is varied. The electrode array movement along a profile permits to carry on profile investigations.The variation of AM distance is realized using the multi-electrode array. Electric current is injected to the ground through current dipole AB, and multi-channel digital receiver system records the signal from the ground. The MISC modeling and data processing was done by using ZondRes2D software that was designed by A.E. Kaminskiy. The software permits to carry on 2D-interpretation (2D-inversion) of the DC resistivity and IP data taking into consideration topography and prior information. The efficiency of MISC was investigated by physical modelling in a tank installation. MISC field research equipment includes AB current dipole and receiver system: receiver lines, switch, AD-converter and mobile PC that registers the digital signal and saves the data obtained to HDD. Method of internal sliding contact may be useful in structural research and in search of ore bodies.

Introduction

Method of internal sliding contact (MISC) is a DC method of investigation of Earth crust subsurface which combines elements of profiling and sounding. It is known that registration of DC signal on receiver electrodes with variation of distance between current electrode A and receiver electrode N gives information about media properties variation to depth (sounding). Moving of fixed electrode distance array along a profile permits to carry out investigations on earth-air surface (profiling). Thus simultaneous Earth crust survey along a profile and depth investigation on each point of the profile allows to conduct two-dimensional research of geoelectric cross-section subsurface layer.

Two-dimensional investigations of Earth crust subsurface using multi-electrode arrays were conducted at the first time in 1970-1980s. Manual and automatic switch multi-electrode survey systems are described in the works [Barker, 1981; Dahlin, 1989]. Further development of research technique is described in proceedings [Griffiths, D.H., Barker, R.D., 1993; Bobachev et al., 1996]. Summary overview of development of the method is presented in publication [Dahlin, 2001]. Method of internal sliding contact was designed by A.A. Zhamaletdinov. Features and application of the method are described in publications [Zhamaletdinov et al., 1976; Zhamaletdinov et al., 1995].

Field research technique

Practical MISC geological media investigations are conducted with variation of distance between A and M electrodes in multi-electrode electrical profiling array. The array is current dipole AB and receiver array that includes N electrode and some M electrodes on different distances from N electrode. Electric current is injected to the ground through the current dipole; signal is registered by multi-channel receiver system.

Field research equipment which applied in Geological Institute if KSC RAS includes current dipole and receiver system. Generator injects low-frequency pulse current to the ground through the AB current dipole. Signal is registered on multi-channel system that connected with receiver electrode array. The system includes switch, AD-converter and field PC that registers the signal and saves the data to HDD.

Fig.1. MISC field equipment for investigations by DC resistivity and IP methods (GI KSC RAS)

MISC data interpretation technique

The one of the means of MISC field data processing and numerical modeling of research process is ZondRes2D software that is designed by A.E. Kaminskiy. The software permits to carry on 2D-interpretation (2D-inversion) of the DC resistivity and IP data taking into consideration topography and prior information.

Observed data interpretation by means of ZondRes2D is multi-stage process. Full interpretation process can be divided to three stages: data input, data interpretation, data output.

At the stage of data input some actions are performed:

1) data file creation;
2) interpretation model mesh construction;
3) prior information input;
4) inversion parameters input;

Observed data file contains information about electrode relative coordinates, apparent resistivity values, registered signal values related to the current value, apparent polarizability values if IP measurements were conducted, weight values for each measurement. The file can also contain the topography and media reference model data.

Interpretation model is divided to horizontal layers according to array geometry. Lower model boundary fits the maximum depth of investigation. Number of layers is equal to number of AM distances of array. First layer thickness is the depth of investigation on minimal AM distance. Thickness of the rest layers is increased so that the sum of all layer thicknesses will be equal to maximum depth of investigation.

Prior information input is well-logging and lithology data addition.

Inversion parameters are inversion algorithm, iterative process stop criteria, smoothing. The parameters are entered immediately before inversion process start.

The second stage, or interpretation stage, begins from calculation of apparent resistivity values on each point of profile over the model. This is forward problem solution. This solution is followed by calculation of difference between observed and model apparent resistivity values (misfit), correction of model according to misfit values, new calculation of model apparent resistivity. The iterative process continues until the misfit value required to all the profile is reached.

If the inversion results don't correspond to the prior information, it is necessary to correct the inversion parameters. If the inversion process doesn't bring to required misfit value, or the misfit value is decreased very slowly, inversion parameters should also be corrected.

If the inversion results are in accordance to all requirements, they are imaged as a resistivity cross-section; also they can be saved to HDD as ZondRes2D special file or exported to external software data file such as text file and Microsoft Excel file.

Numerical modeling process also contains of several stages. At the first stage it is necessary to create data file that contains information about all electrode positions over a model medium. At the second stage the model mesh is constructed. To create the mesh it is necessary to enter horizontal and vertical relative coordinates of mesh nodes, and also to note whether a node is matched a coordinate of any electrode on profile. After the mesh construction the matrix of cell resistivity values is entered. The last stage is forward problem solution.

It should be noted that the model can be constructed by two ways: addition the model information to the data file or creation the model immediately in software window.

One of the main field data interpretation problems is non-linear electrode arrangement on terrain and, as a consequence, distortions in array geometry. Distortions in geometric factor values are a cause of apparent resistivity or polarizability calculation mistakes. In order to solve this problem the ZondRes2D opportunity to appoint the weight values to observed data is used. Observed geometric factor values are calculated from registered electrode absolute coordinates, and then the residual between theoretical and observed values for each measurement is calculated. The reverse value of the residual is appointed to each measurement as a weight value.

Other problem is inversion process parameters selection. This problem is solved by multiple conduction of test inversion process with different algorithms until the required misfit value is reached. Also, knowingly false values should be deleted from observed data.

Physical and mathematical modeling of MISC investigations

During the ZondRes2D preparation for field data interpretation, its opportunities testing and adapting were conducted in the context of MISC investigation. The data of MISC physical modeling in test layout were used as test data. The layout is an electrolyte-filled tank with models of structural geological objects. This layout was used to prepare the electrical prospecting equipment EMAK-1 to field investigations and to study the MISC investigation efficiency in search of conductive objects and structural mapping.

Fig.2. Installation for physical modeling and testing of DC resistivity and IP multi-electrode survey systems

During the physical modeling four models were created – three models of conductive steeply dipping dike on different depths, and one model of two steeply dipping dikes on some distance between them. Physical models was created by means of metal plates buried to the tank. Models of single dikes were constructed to determine the maximum depth of investigation with the array. The

aim of construction two dikes model was to determine an opportunity of their separate allocation on resistivity cross-section.

The studying MISC array is not symmetrical, therefore the location of conductivity or resistivity anomalies related to structural elements differs from elements' true location. To compensate the distortions caused by array dissymmetry, profile observations in «two traverses» should be conducted: «forward traverse», in which the array moves from relative start of profile to relative finish, and «reverse traverse», in which the array moves from relative finish of profile to relative start.

Observations over the physical model medium were conducted only in «forward traverse», that was a cause a mistake in horizontal localization of structural element. The mistake evaluation was not conducted because precise horizontal localization wasn't aim of physical modeling.

Results of interpretation for two models, in which the structural elements is localized, by means of ZondRes2D software are presented.

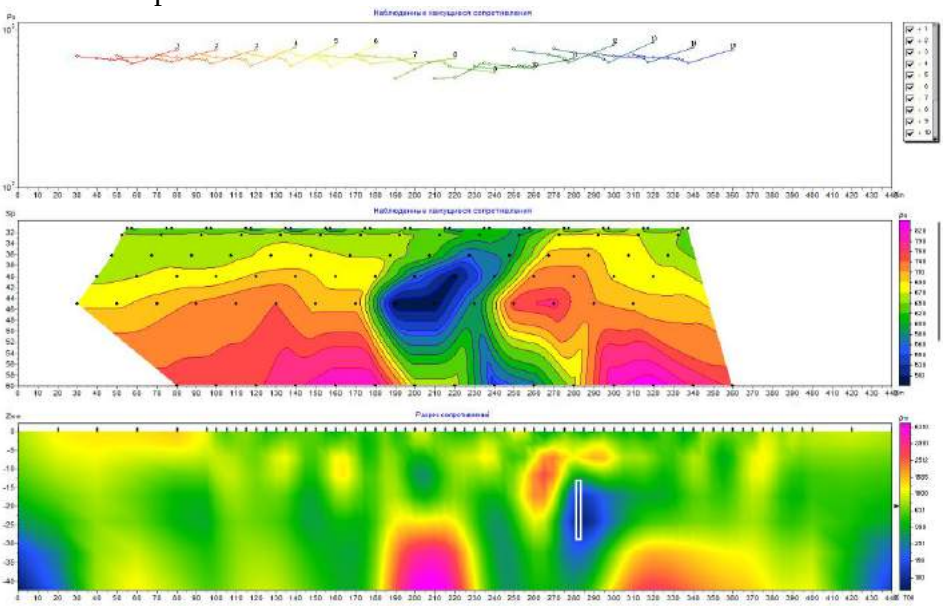

Fig.3. Model of steeply dipping dike, depth to top 1 cm. ZondRes2D interpretation results. Upper part – observed apparent resistivity plot, medium part – calculated apparent resistivity pseudosection, lower part – interpretation model resistivity cross-section. Structural element is marked as a white stripe.

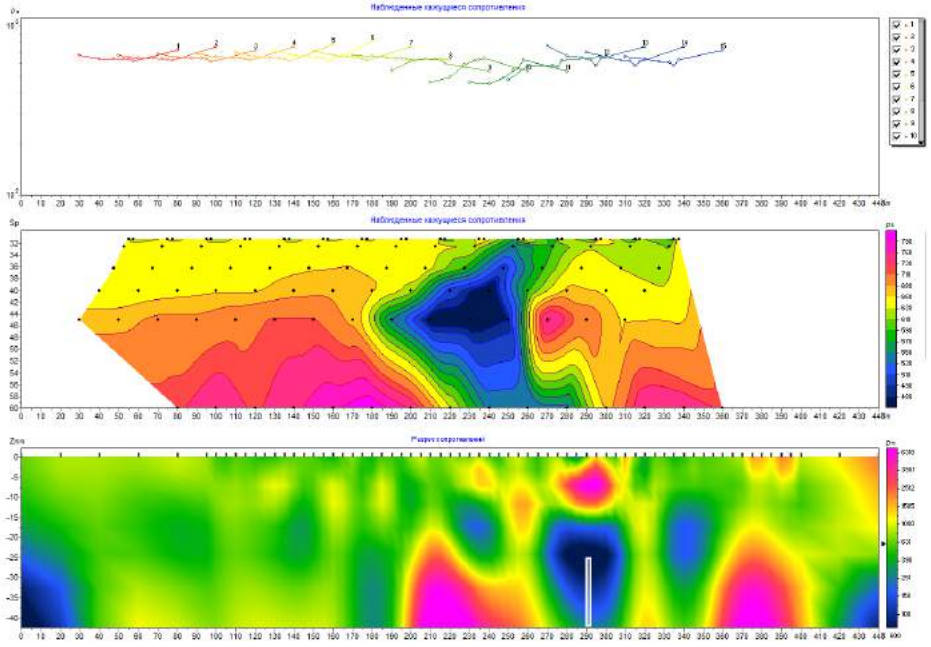

Fig.4. Model of steeply dipping dike, depth to top 2.5 cm. ZondRes2D interpretation results.

Structural elements in other two models were not localized. Depth of model dike 4.5 cm is larger than the maximum depth of investigation. Two model dikes on distance 2.5 cm were not separated and formed an uniform conductivity anomaly.

In addition to physical modeling material, numerical modeling by means of ZondRes2D for «two traverses» was conducted. Two models were created. Parameters of the models were matched to physical models. Also one additional model of two conductive dikes was created, with distance between dikes that larger than distance between two dikes in physical model. Background resistivity was 700 Ohm.m, elements' resistivity was 50 Ohm.m.

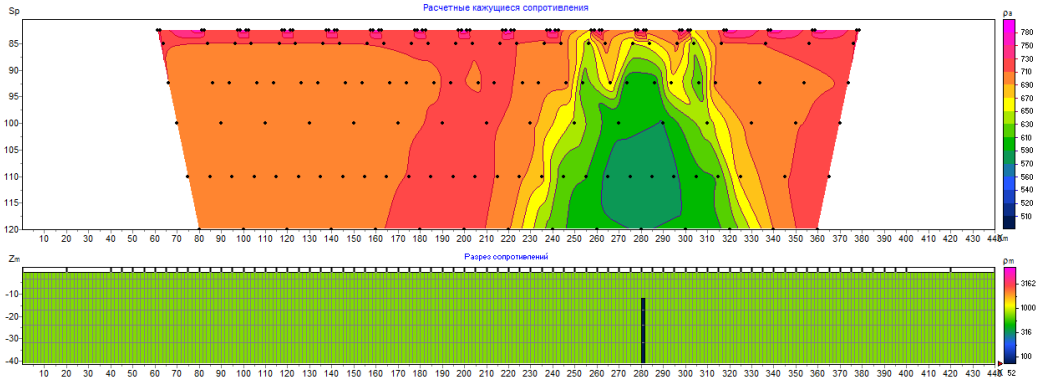

Fig.5. Forward problem solving results in ZondRes2D for model of steeply dipping dike, depth to top 1 cm. Upper part – calculated apparent resistivity pseudosection, lower part – model geoelectric cross-section.

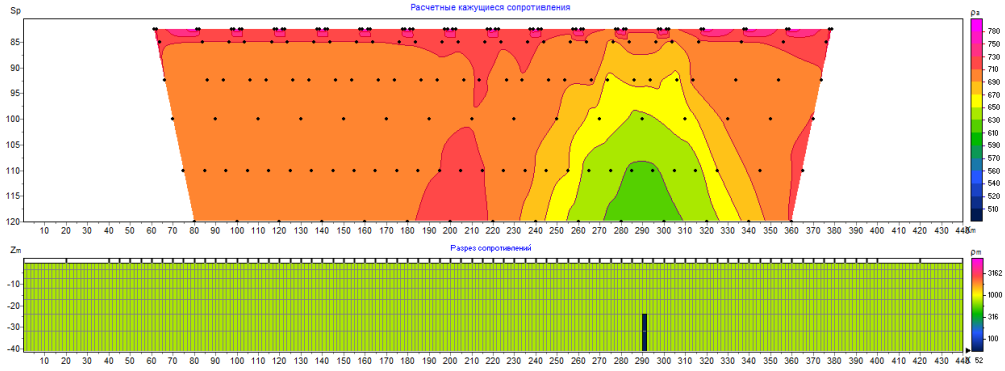

Fig.6. Forward problem solving results in ZondRes2D for model of steeply dipping dike, depth to top 2.5 cm.

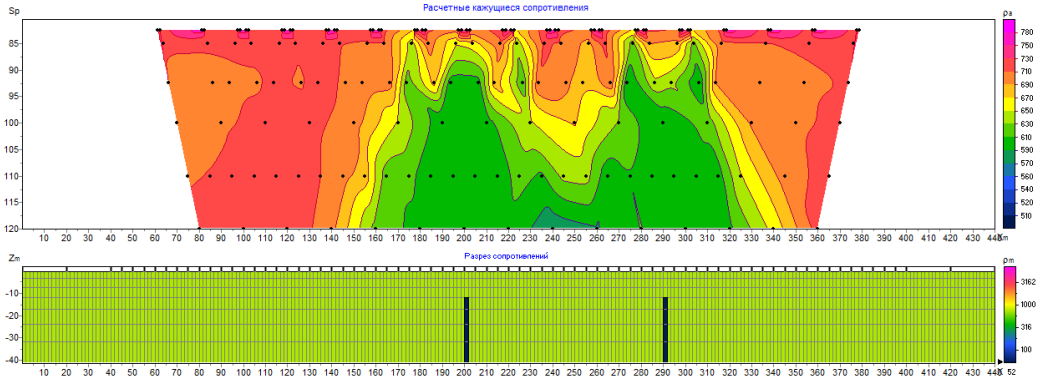

Fig.7. Forward problem solving results in ZondRes2D for model of two steeply dipping dikes, depth to top 1 cm, distance between the dikes 9 cm.

Field data interpretation results

MISC investigations were carried out during the field excursion research in the north part of Pechenga structure as a part of investigation works complex to search of homologues of Archaean section of Kola Superdeep Borehole on earth-air surface.

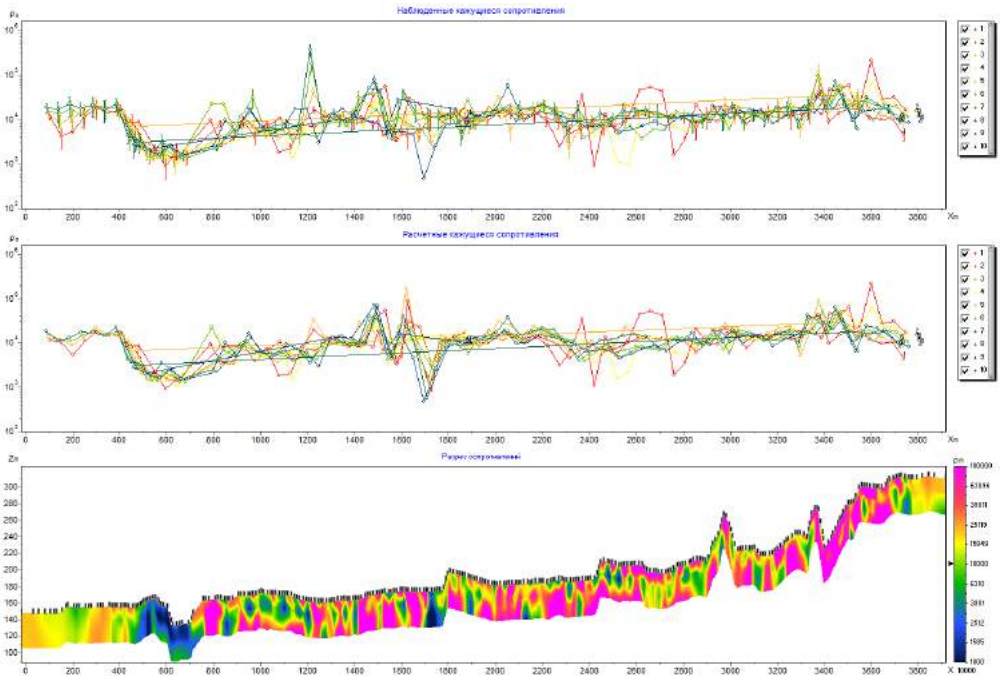

Fig.8. Field data interpretation results in ZondRes2D for MISC investigations in Pechenga area.

Conclusions

Combination of elements of profiling and sounding in the method of internal sliding contact permits to carry on two-dimensional investigation of Earth crust subsurface layer. This investigation allows to identify borders of structural geological elements and to localize the elements to depth, that is useful in structural research.

Also, two-dimensional Earth crust subsurface studies with MISC array are less time-consuming than the same investigations with other DC resistivity method arrays.

ZondRes2D software is useful for interpretation and modeling of two-dimensional investigations of Earth crust subsurface with MISC array or with other arrays. However, work with this software requires thorough analysis of the data observed and operator's active participation in interpretation process.

Gratitude

Authors of this paper express a great appreciation and gratitude to Organizing Committee of the conference «Problems of Geocosmos» for opportunity given to submit the results of investigations, to participants of the Conference for discussion and criticism, and to scientific advisors Abdulkhay A. Zhamaletdinov and Aleksandr N. Shevtsov for overall aid and support and wise direction of research carrying out.

References

Glaznev V.N., Dyakov S.N., Raevskiy A.B., Tokarev A.D. (2004). *Geophysical methods (Field geophysical surveys manual)*, 66 pp., MSTU press, Murmansk.

Balkov, E.V., Panin, G.L., Mainshtein, Yu.A., Mainshtein, A.K., Beloborodov, V.A. (2010) Electrotomography: equipment, technique and using experience. [Electronic resource] www.nemfis.ru, 1-2.

Kaminskiy, A.E. (2010), ZondRes2D. Two-dimensional DC resistivity and IP methods interpretation software. *Zond geophysical software*, Saint-Petersburg, 3, 18-62.

Zhamaletdinov A.A., Ronning J.S. & Vinogradov (1995), Electrical profiling by the MISC and Slingram methods in the Pechenga-Pasvik area. *Norges Geologiske Undersokelse*, Special publication 7, 333-338.

Skorokhodov, A.A. (2007) Using of multi-functional electrical prospecting equipment EMAK-1 in DC resistivity method. *Book of abstracts of X International scientific conference, Apatity, April 5-6, 2007. Vol. 3.*, 126 pp., Kola Branch of PetrSU Press, Apatity.

TWO-DIMENSIONAL NUMERICAL MODELING OF MV AND MT PARAMETERS ON THE VYBORG- SUOYARVI PROFILE

A.A. Kovtun, I.L. Vardaniants, N.I. Uspenski
St. Petersburg University, St. Petersburg, 198504, Russia, e-mail: aakovtun@mail.ru

Abstract. Data of numerous soundings on the Vyborg-Suoyarvi profile made it possible to obtain the magnetovariational (MV) and magnetotelluric (MT) parameters distribution and approximately estimate resistivity distribution on this profile till the depth 200-300 km. Using 2D numerical modeling there has been built the MT and MV parameters distribution on the profile within the period range $1\text{-}10^4$ s. There were revealed regions not corresponding with the experimental data at the South-East piece of the profile which points to the more complicated structure of this piece of the profile and indicates the necessity of supplemental soundings at this part. The work was performed according to the RFFI grant N 013-05-00-786.

1. History

We begun to investigate geoelectrical structure of the Ladoga-Bothnia zone (LBZ) long-living fractures located at the joining zone of two different-age Karelian and Svekofennian geoblocks in 70-th years. The interest to this region has been arise owing to the results of magnetovariational (MV) investigations performed in 1970-th years by I.I. Rokityansky at the northern coast of the Ladoga Lake and magnetotelluric (MT) soundings carried out by Physics Institute of Leningrad State University and Leningrad Mining Institute at the south part of Ladoga Lake. These works made it possible to draw the conclusion on the increased crust conductivity of this region. The approximate estimation showed that crust conductance at the southern coast of Ladoga Lake reaches to 2000 Sm and conductance of the abnormal zone section is $2\cdot10^8$ Sm·m (Kovtun A.A., 1989).

The interest to this conductive region is supported by the absence of clear indication on its tectonic origin. Some of geophysics find hear features of subductive zone, the others – of the rift one. It stimulated the beginning of MT and MV investigation of this region. At that time there have been performed about 20 MV soundings on the periods $1\text{-}10^3$ s by the Leningrad Mining Institute (Vasin N.D., 1988) on the profile directed from the LBZ center to Suoyarvi and intersecting the joint zone between LBZ and Karelian geoblock; the sounding sites were set with the step 10 km. We have performed near these sites audio MT (AMT) soundings within the range 10^{-3}-0.1 s which allowed us to investigate the geoelectrical section beginning with some first km. The data of both investigations gave the material for building in 1990 year the first geoelectrical model of LBZ (Kovtun A.A., et al., 1990).

This model has been compared with the seismic data of N.K. Bulin showing the splintered character of the central part of the abnormal zone which makes it impossible to define hear the location of A and K seismic boundaries (Bulin N.K., 1975).

These peculiarities of the seismic model showed that it is necessary to define the more detailed picture of the conductivity depth distribution at the adjoined to LBZ blocks – the central Karelian block on the North and the Vyborg block on the South. For this purpose in the 90-th years we carried out on the Suoyarvi-Vyborg profile MT-soundings within the extended range $10^{-3}\text{-}10^4$ s. Only one site was located within the abnormal zone, the rest – at the adjoining with the LBZ blocks. The location of all soundings carried out till the end of 1990-th years is shown on the fig. 1. Using of the additional material allowed to prove that with the moving from the abnormal zone the structure of the crust become approximately homogeneous-layered one (Kovtun A.A. et al., 1998). Never the less obtained data don't allow to draw the conclusion on the tectonic origin of the abnormal zone.

During the last years there has been obtained new seismic data at the southern Karelia territory. The seismic model of the upper 60 km of the studied profile is given on the fig. 2*a*. The authors of the model draw the conclusion on the rift origin of abnormal zone (Berzin R.G. et al., 2004, Isanina E.V. et al., 2004). It made us to return to the analysis of the AMT-MT data with the aim to understand what geoelectrical peculiarity may give the reason for such a conclusion. This problem has been considered in our work (Kovtun A.A. et al., 2012) where the last model of LBZ section has been presented.

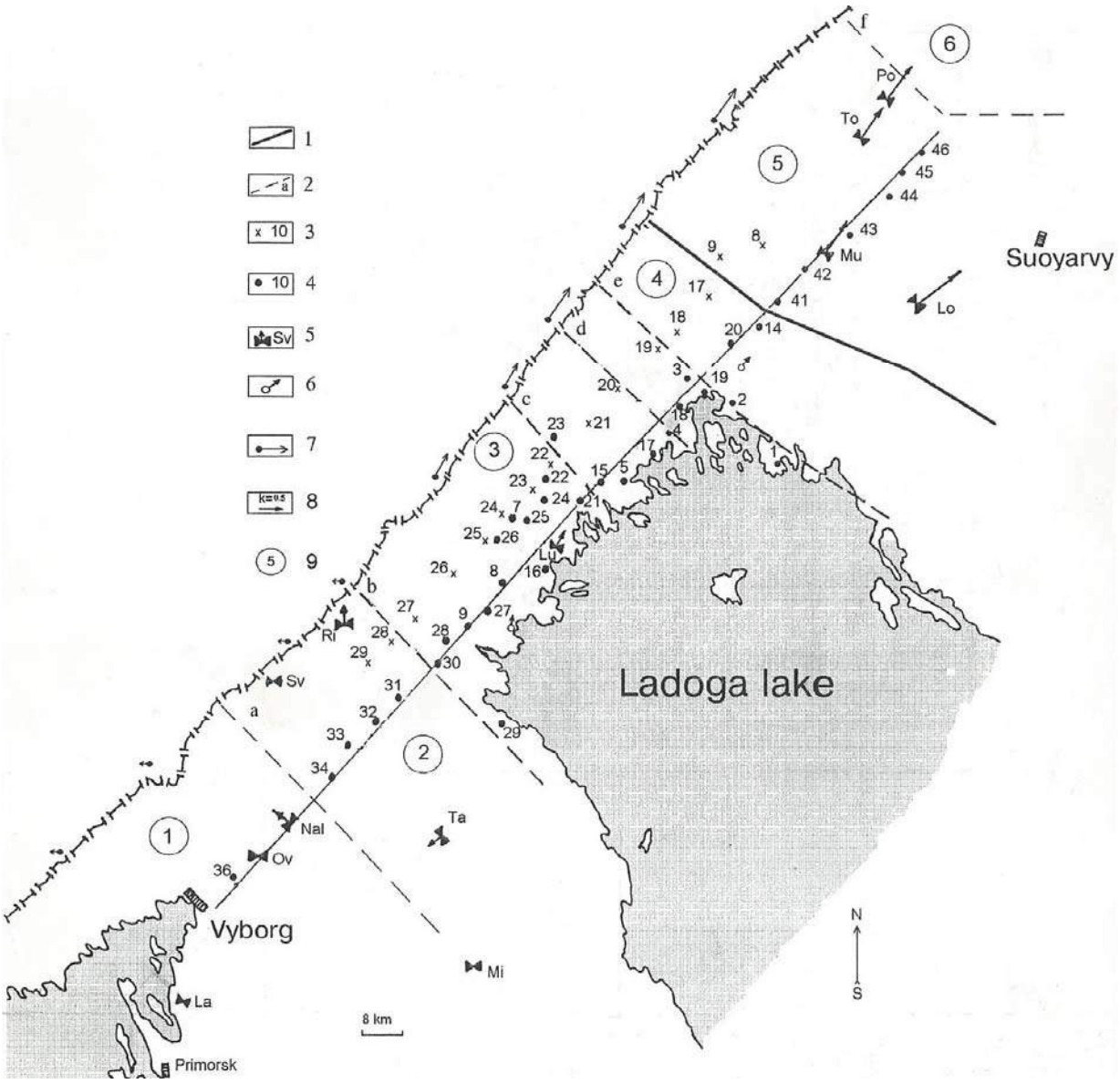

Fig. 1. The location of AMT-MT soundings sites on the Suoyarvi-Vyborg profile.
1 – Yanisyarvinsky inter-megablock fracture; 2 – inter-block fractures; 3 – MT sounding sites by N.D. Vasin; 4 – AMT sounding sites; 5 – AMT-MT sounding sites by SPb University; 6 – MV soundings sites by I.I. Rokityansky; 7 – MVsoundings sites on the Finland territory; 8 – Vise vectors (with the value 0.5); 9 – the blocks: Vyborgsky (1), Vuoksinsky (2), Lakhdenpokhsky (3), Yanisyarvinsky (4), Yalonvarsky (5), Gimolsky (6).

2. Let us dwell on the building of the last model

In all cases of building models we used the quasi-2D approximation. The reason for such approach is the behaviour of the MV parameters within the large periods (T > 1000 s) range. As is shown on the fig. 1, at the North and at the South of the abnormal zone the inductive Vise-vectors are directed from the conductive body approximately under the same angle (about 45^o) to the meridian.

On the first step of the investigation we carried out the express-interpretation of the obtained MTS data with quasi-2D approximation. The methodic of the proposed express-analysis is based on the following statements. After processing of the MT sounding data we receive impedance tensor Z in the coordinate system connected with the observation axes x and y:

$$Z = \begin{vmatrix} Zxx & Zxy \\ Zxy & Zyy \end{vmatrix} \qquad (1)$$

In case of arbitrary medium the tensor may be reduced to two non-diagonal impedance values which are radicals of the characteristic equation of the impedance tensor determinant:

$$Z_{\mp} = \frac{Z_{xy} - Z_{yx}}{2} \pm \sqrt{\frac{(Z_{xy} - Z_{yx})^2}{4} - (Z_{xx}Z_{yy} - Z_{xy}Z_{yx})} \qquad (2)$$

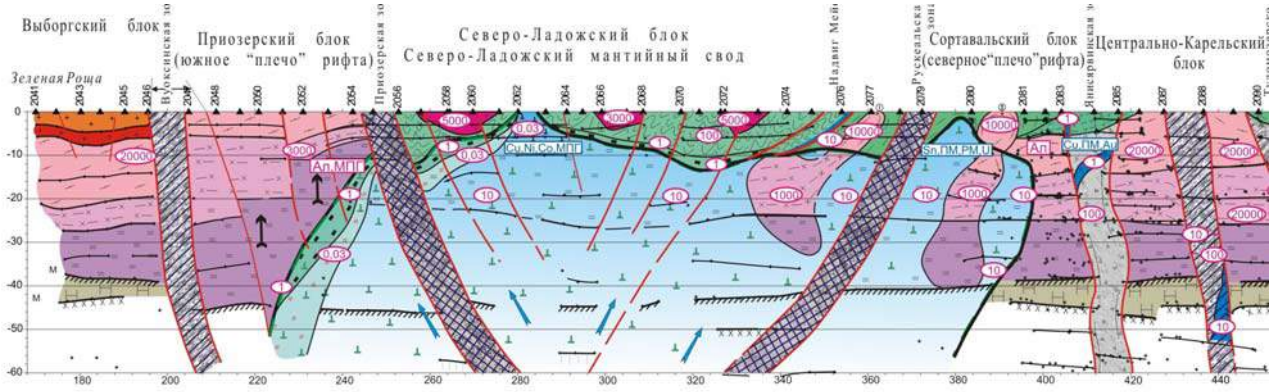

Fig.2. The geological-geophysical section on the profile Zelenaya Roshcha –Spasskaya Guba by the Isanina E.V., Krupnova N.A., Sharov N.V., 2004.

In case of 2D medium parameters $Z_{\mp}$ named Egger's impedances transfer to the maximal and minimal impedances corresponding to the maximal and minimal values of the Z_{xy} polar diagram on the *x y* plane. As we have shown on the whole territory of the East-European platform and on the Baltic Shield the difference between the values of $Z_{\mp}$ and maximal and minimal impedances is rather small even in case of 3D medium if the value of $skew = \left|\frac{Z_{xx} + Z_{yy}}{Z_{xy} - Z_{yx}}\right|$ characterizing dimensionality of the medium does not exceed one. So it is possible to receive the information on the medium by the analysis of the maximal and minimal values of impedance which allow to connect the impedance polar diagram main directions with the directions of the structure axes.

In order to avoid the large mistakes using the results of 1D interpretation of maximal and minimal sounding curves it is necessary to divide them beforehand into "longitudinal" and "transversal" ones. For this purpose it is possible to use the geologic-geophysics information on the region or analysis of the behavior of the frequency characteristics of the impedance anomalies for main directions of the polar diagram (Kovtun A.A., 1989). But the more simple way to divide the curves is the following: the "longitudinal" curves must lay close to the global MV curve within the period range T > 1000 s. 1D interpretation of these curves satisfactorily reflects the resistivity distribution at large depths. However it must be noted, that in case of presence of contact between the conductive and non-conductive regions, there arises near the contact the grate divergence between the "longitudinal" and "transversal" curves (as in case of "coastal effect"). In this case it is advisable to interpret the effective curve. As the numerical modeling shows this curve is close to the local-normal one over the non-conductive medium. The chosen quasi-2D "longitudinal" curves are interpreted together with the four first data of global curve obtained by Sq-variations and the results are used for building the 2D section. In most cases the discrepancy between the experimental impedance values and values calculated for the model built using the longitudinal curves does not exceed 5%. On the first step of the investigations when we don't have sufficient data on the territory of the abnormal zone such an approach to the analysis of the MT data is the most effective. It has been tested on the large number of the theoretical models and always gave the satisfactory result.

This approach to the interpretation of the MT data allows estimate with minimal errors the geological structure at the large depths. The sites where none of curves goes near to the global one are under the influence of the 3D non-homogeneity and must be excluded from the consideration. Further on there is

necessary to carry out in such regions the additional area soundings and to perform 3D interpretation which will require data on the area exceeding the abnormal zone.

On the fig. 3 there are shown the typical apparent resistivity sounding curves for the Karelian and Svekofennian geoblocks and for LBZ, used for building the quasi-2D geoelectrical section. All of them come rather well to the global curve. In most cases there were chosen the minimal curves, in some sites – the effective ones.

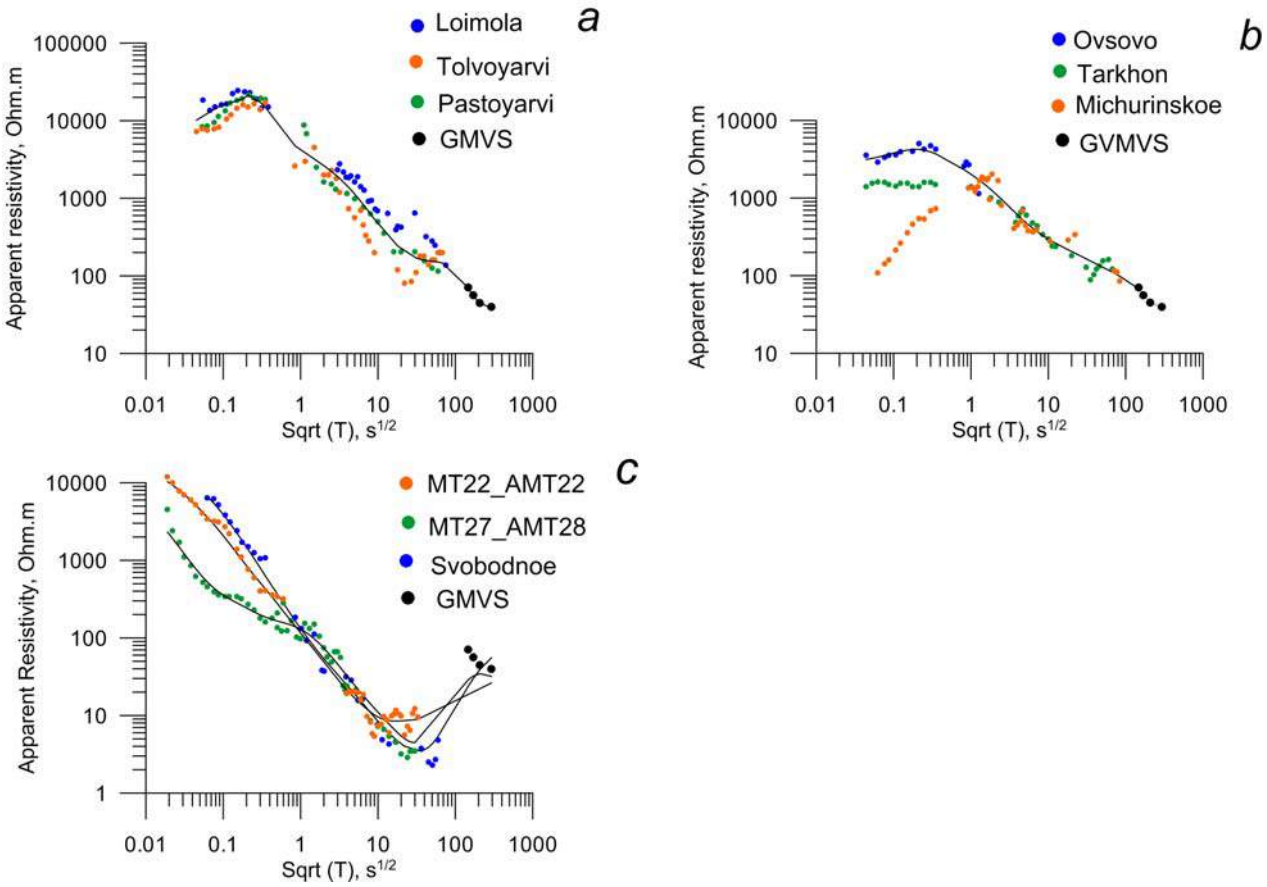

Fig. 3. The "longitudinal" soundings curves at the different pieces of the profile; *a* – at Yalonvarsky block, *b* – at Vyborgsky block, used for building the "normal" section on the Karelian and Svecofennian geoblocks; *c* – at the piece from the Yanisyarvinsky till Vuoksinsky fracture (LBZ).

Let' note that within the central abnormal part (fig. 3*c*) the "longitudinal" curves go noticeably lower then the global points and the combined interpretation can give increased value of the resistivity at the large depths. In order to obtain the true resistivity there is necessary to increase the duration of soundings at least for a month which at presence is practically impossible.

On the fig. 4 there is presented the improved model of the resistivity distribution on the Vyborg-Suoyarvi profile. This model differs from the previous one by the presence of new AMT data obtained in sites located within the central part of the abnormal region which made it possible to study the complicated character of the upper part of anomaly structure till the depth 20 km. The comparison of the built LBZ model with the geological-geophysical section (fig. 2) carried out in work (Kovtun A.A., 2012) did not allow to draw the conclusion on the character of the tectonic processes at the borders of the blocks.

In order to estimate the validity of the built model there has been performed numerical comparison of MV and MT parameters of built model with the experimental data. The most interesting was to compare the MV parameters, because these data were not used for building the model.

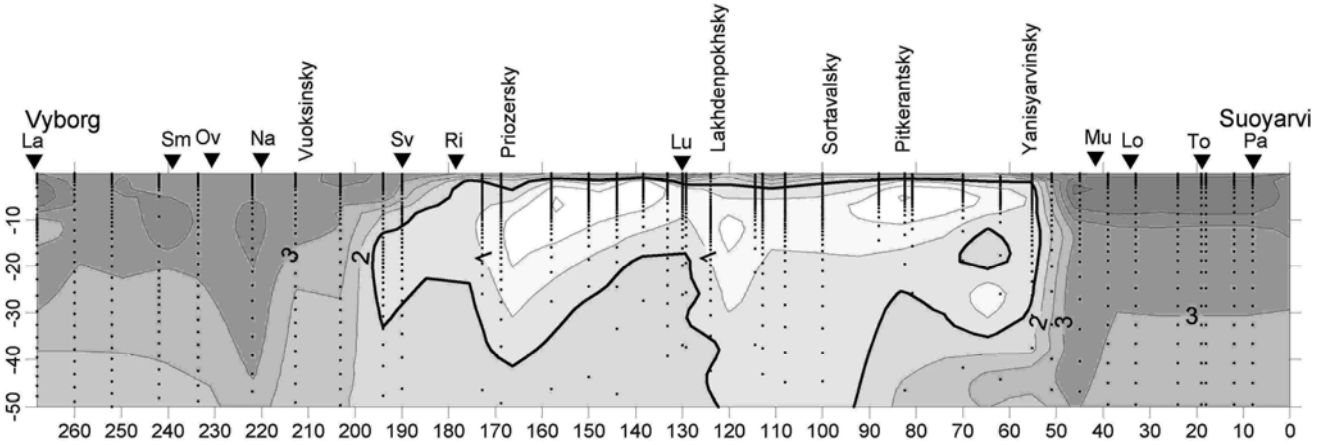

Fig. 4. The new model of the resistivity distribution on the Vyborg-Suoyarvi profile.The bold line borders the region with the resistivity less 30 Ohm.m.

3. The testing of the new model

The numerical modeling was performed using the program by I.L. Vardaniants. The upper part of the section till 100 km was described by the 2D medium corresponding to the result of interpretation. The lower part was the layered medium corresponding to the normal section of the Svecofennian Shield.

As it was already noted, in case of E-polarization the impedance behavior is in good agreement with the experimental values within the period range 0.1-10^3 s. Let's pay the main attention to the MV parameters. On the fig. 5 there are shown the frequency characteristics of the Vise vectors at the model sites where we had the experimental data: Lumivaara (130 km), Pastoyarvi (8 km), Tolvoyarvi (34 km), Rintala and Svobodnoe (190 km), Tarkhon and Michurinskoe (230 km).

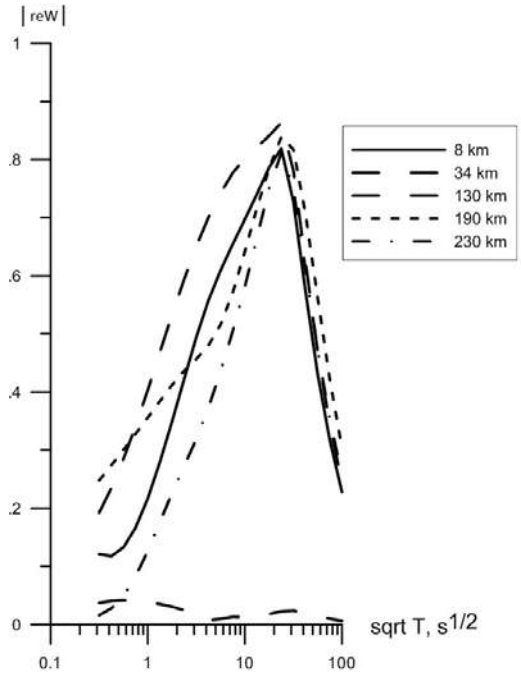

Fig. 5. The frequency characteristics of the Vise vectors at the model sites.

There can be noted following peculiarities. The maximums of the frequency characteristics of MV parameters fall on the same period T_{max} =600 s. The change of the Vise vector direction according the calculations takes place at the piece 110-150 km. Hear the Vise vector is small and cannot be define experimentally. It is in good agreement with the MV data at Lumivaara (130 km).The good agreement with

the experimental data can be seen also in sites Pastoyarvi and Tolvoyarvi. But calculated maximal values of Vise vectors fall on the period 600 s, while the experimental ones – on 1000-1600 s. It points that in the model the abnormal body has the increasing resistivity. The reason of this divergence is that in some sites the effective curves have been taken instead of the minimal ones. The most important difference between the model and experiment is that at the southern part of the profile the calculated Vise vector values noticeably exceed the experimental values. At the part of LBZ at the sites Rintala, Svobodnoe, Tarkhon, Michurnskoe the Vise vector values till T=1000 s don't exceed 0.1-0.3, while according to calculations they must be the same as in northern part. Such a divergence may be explained by the insufficient information on the southern part of the territory.

The comparison showed that the built model is not the last one. We may expect that the additional material that will be obtained within the frame of grant RFBR N 013-05-00-786 and developed 2D combined interpretation of MT and MV data (Varentsov Iv.M., 2002) will allow to improve the model.

References

Bulin N.K. (1975), The Earth Crust of the Upper Mantle between the Finnish Bay and the Onega Lake. *The Earth Crust of the Continents and Inner Seas*. Moscow, p. 152-161.

Berzin R.G., Andryushchenko Yu.N., Zamozhnaya N.G., et al. (2004), *The Deep Structure and Seismicity of the Karelia Region and its Framing* / Under the redaction of Sharov N.V. Petrozavodsk: Karelian Scientist Center of RAN, p. 35-56.

Isanina E.V., Krupnova N.A., Sharov N.V. (2004), Seismological investigations MOVZ at the South of Karelia. *The Deep Structure and Seismicity of the Karelia Region and its Framing*/ Under the redaction of Sharov N.V. Petrozavodsk: Karelian Scientist Center of RAN, p. 60-69.

Kovtun A.A. (1989), *The Crust and Upper Mantle structure at the North-West of the East-European Platform by Magnetotelluric Soundings Data*, LGU, Leningrad, USSR, 284 pp.

Kovtun A.A., Vasin N.D., Popov M.K., et al. (1990), The Model of the Ladoga-Bothnia Zone by the Data of MT and AMT Sounding. *Izvestia AN SSSR, Fizika Zemli*, N 9, p. 64-70.

Kovtun A.A., Vagin S.A., Vardaniants I.L., et al. (1998), The Crust and Mantle Structure on the Suoyarvi-Vyborg Profile by the Magnetotelluric Data. *Vestnik SPbGU*, Ser. 4, Vypusk 4, p. 25-34.

Kovtun A.A., Vardaniants I.L., Uspensky I.N. (2011), Comparison of Seismic and Geoelectric Models for the Ladoga-Bothnia anomalous zone. *Problems of geophysics*, Issue 44, p.124-132.

Rokityansky I.I., Vasin N.D., Golod M.I. et al. (1979), Electroconductivity Anomaly at the South of Karelia, in: *Geofiz. Sbornik Academy of Science of USSR*, Kiev, USSR, Vypusk 89, p. 35-36.

Varentsov Iv. M. (2002), The General Approach to the Magnetotelluric Data Inversion in a Piecewise-Continuous Medium. *Izvestia RAN, Fizika Zemli*, N 11, p. 11-32.

Vasin N.D. (1988), Geoelectric Characteristic of the South-Western Karelia Section. *Zapiski of Mining Institute*, V. 113, pp. 57-63.

THE PECULIARITY OF THE LADOGA-BOTHNIA ZONE AT THE NORTH-WESTERN PIECE OF THE VYBORG-SUOYARVI PROFILE

A.A. Kovtun[1], I.L. Vardaniants[1], N.I.Uspenski[1], and LADOGA-WG

[1]St. Petersburg University, St.Petersburg, 198504, Russia, e-mail: aakovtun@mail.ru

Abstract. For the purpose of the more precise definition of the Ladoga-Bothnia zone (LBZ) structure at the piece from the Yanisyarvinsky fracture till the Pitkeranta fracture there has been performed according to RFFI grant № 13-05-00786 the MT-MV soundings within the period range 0.01-4000 s with the step 5-7 km. At present there is performed the express-analysis of the obtained data which allowed to find out a number of peculiarities in the structure of the abnormal zone. By the MV data there were built the frequency characteristics which made it possible to reveal, besides the large anomaly with the maximum at all sites on the period 1000-3000 s, a number of small anomalies on periods 0.01-100 s. The presence of the small anomalies is confirmed by the 1D interpretation of the longitudinal MT curves. By the longitudinal curves there was estimated the location of the upper edge of the conductive bodies. Using the known relation between the conductance G and T_{max} ($G=3T_{max}10^5$ Sm·m) there were approximately estimated parameters of the conductive bodies. It must be noted that G value, corresponding to the maximal period of the MV anomaly, practically coincides with its value obtained earlier on the Southern part of LBZ (A.A. Kovtun, 1989), which points to the presence of the electrical contact between the conductive objects of the abnormal zone. Further on we suppose to perform the 2D inversion of MV-MT data.

In 2013 the MV and MT studies of the Ladoga-Bothnia Zone (LBZ) were extended by the collaborative effort of MSU, IPE RAS and SPbSU. The main purpose of these investigations is using the already obtained material to extend limits of previous interpretation and proceed to 2D and 3D approaches on the base of modern synchronous MT/MV soundings in combination of broad-band and long-period ranges. New 5-component observations have been carried out in 2013 by Nord-West ltd and in 2014 by Moscow State University. Viborg-Suoyarvi-2 profile across the Karelian Isthmus includes now 21 sites: 13 for MT/MV observations with Phoenix MTU-5 and LEMI-417M and 8 for deep (3-day) MT/MV observations with LEMI-417M.

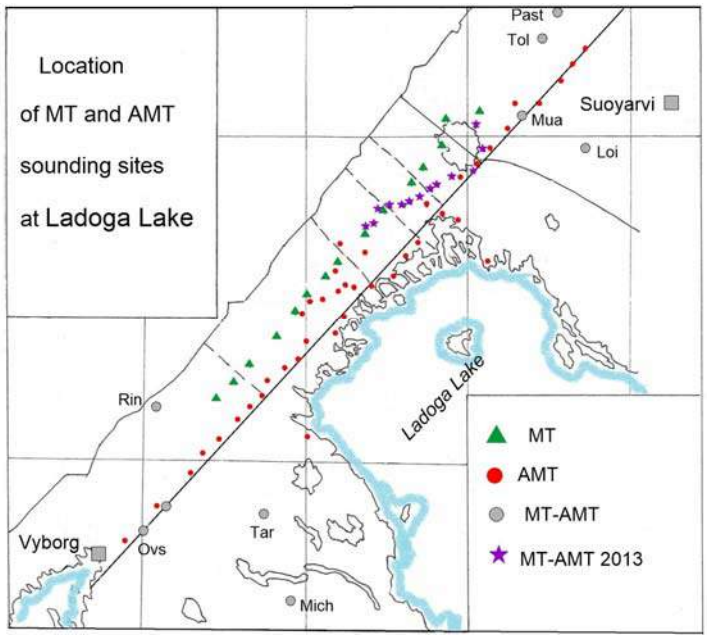

Fig.1. Scheme of the sounding sites location.

At present there is fully accomplished the processing of the MT and MV data obtained in 13 sites at the Northern piece of the Vyborg-Suoyarvi profile within the 10^{-2} – 10^{3} s. The location of these new sites is shown on the fig. 1. The soundings sites are placed with the step 5-7 km on the piece from the Pitkeranta-Yanisyarvinsky fracture (the right wing of the LBZ) and successfully complemented the previous data at the Vyborg-Suoyarvi profile. Unfortunately the insufficient length of the recorders (2-3 days) does not allow to obtain the certain data within the range of the daily variations which are necessary in order to build the LBZ model on the depths exceeding 50 km. Before we accumulate the necessary material for 2D – 3D interpretation it is advisable to carry out the quasi-2D interpretation using the express-analysis technique used for building the previous LBZ model (Kovtun A.A, Vardaniants I.L., Uspenski N.I., 2011). This model is presented on the fig.5a.

On the fig. 2 there are shown the maximal, minimal and effective sounding curves at these sites. Practically in all sites the maximal and minimal curves strongly divergence. The maximal curves at all periods go noticeably higher the global curve and the minimal curves may come to the global curve only at the periods exceeding the daily variations. It made it difficult to choose the "longitudinal" curves. The most near to the global curve are the effective curves, and further on these curves will be used for building this piece of the quasi-2D LBZ model, but this decision requires the additional grounds.

On the fig.3 there is presented the MV parameters behavior depending on $T^{1/2}$ in all sites. As the MV parameter there has been used the real part of the Shmucker vector ReW. It was shown (Kovtun A.A. et al., 2007), that on the Fennoscandian Shield territory this parameter practically coincides on the value and direction with the previous used Vise-vector. Earlier we have no MV data within the small periods range and now we for the first time obtained the MV parameter behavior within the period range 0.01-3600 s. There was reviled the complicated structure of LBZ. Besides the maximum in the frequency characteristic at 1600 s there can be seen the maximums at smallest periods which may be interpreted as the presence of the small conductive bodies within the upper part of the section.

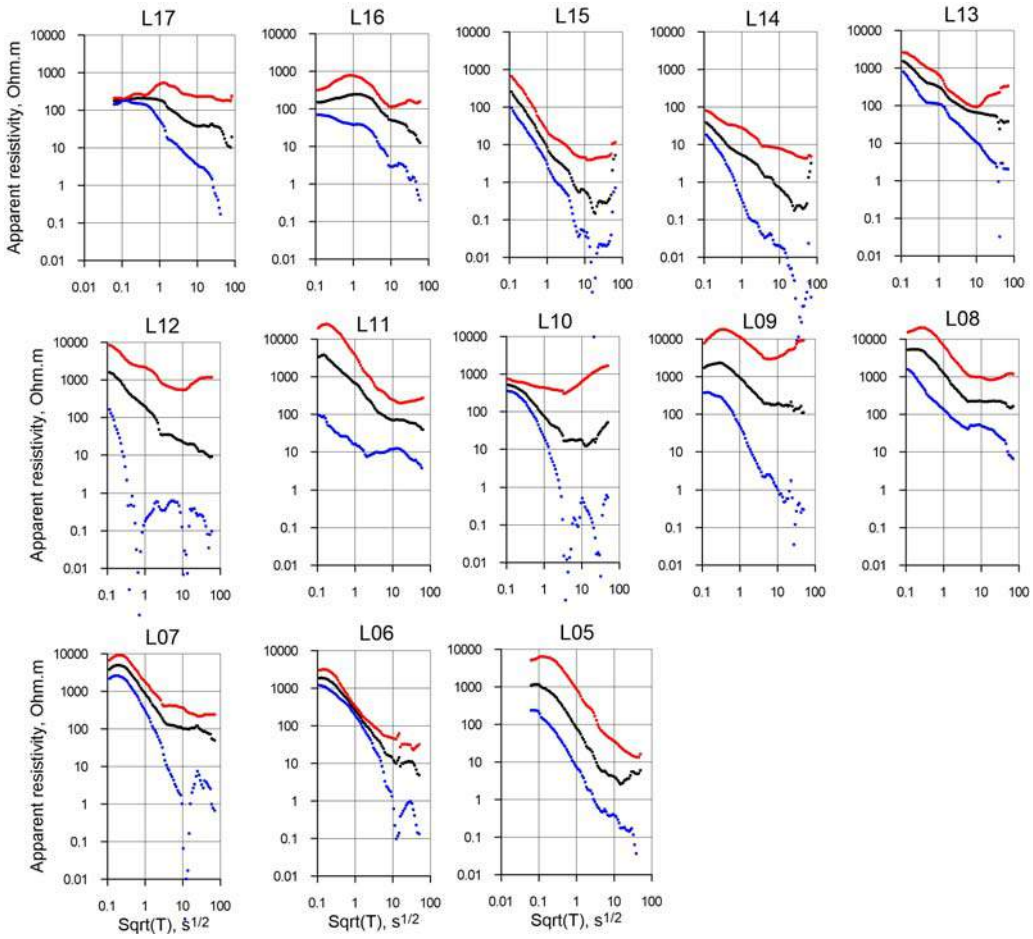

Fig. 2. Maximal, minimal and effective sounding curves at sites MT 2013.

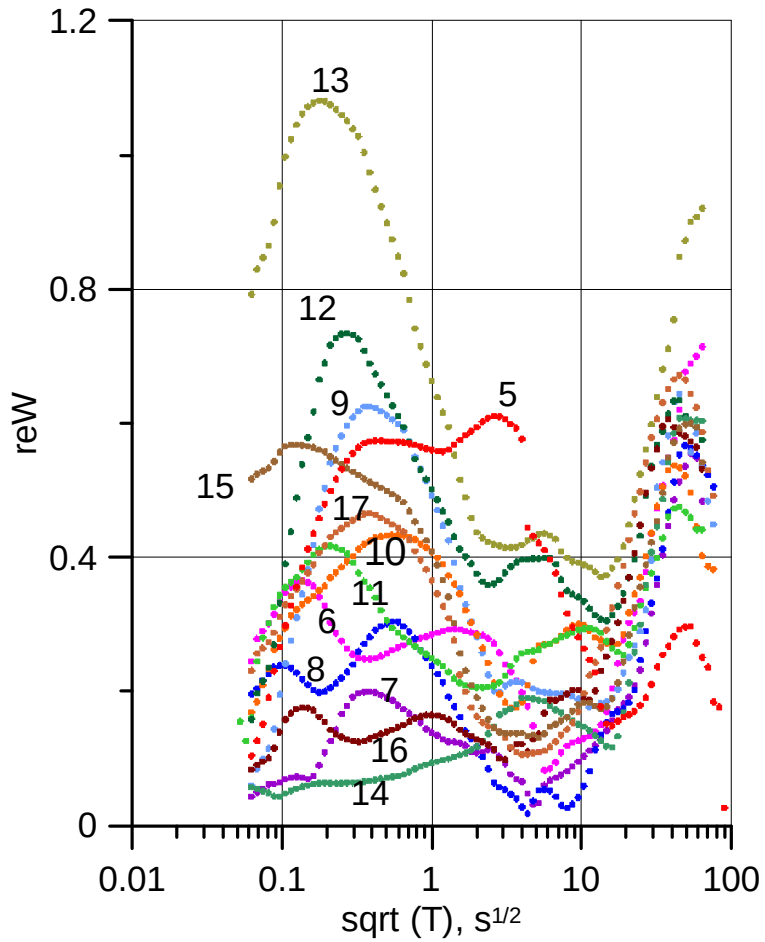

Fig. 3.The behavior of real part of *W* on the period at sites 2013.

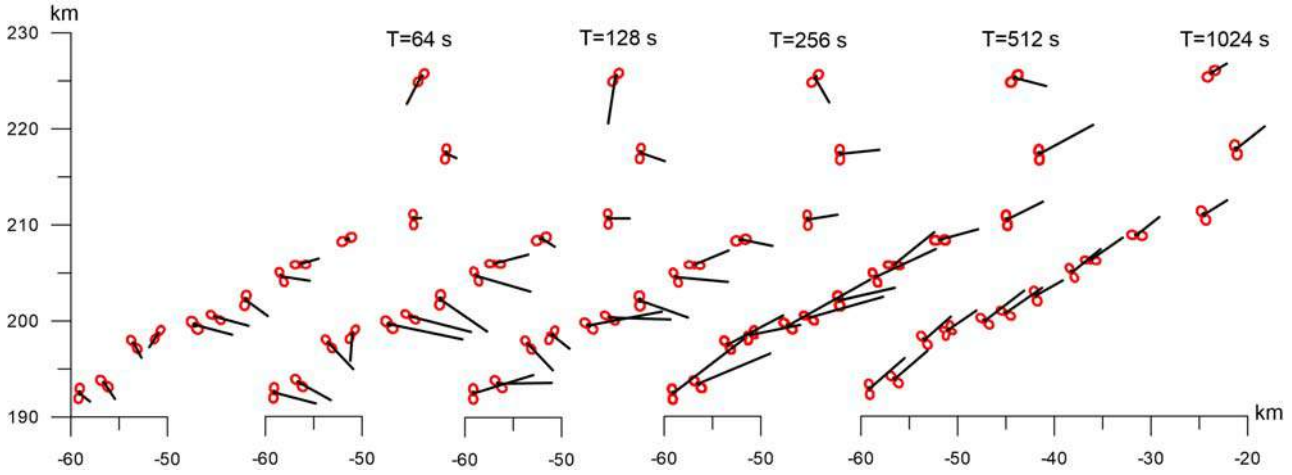

Fig. 4. The behavior of the Vise vectors in sites 2013 depending on period.

Using the approximate dependence between the period where the frequency characteristic achieve maximum and the conductance of the transversal section $G=3T_{max}10^5$ Sm·m, there is possible to roughly estimate the conductance of the transversal section of the bodies. The conductance of the transversal section of these bodies more then 10^4 times exceeds the transversal section conductance of the whole LBZ (which is

about $2 \cdot 10^8$ Sm.m). As can be seen from the fig.3, maximum of this anomaly corresponds to maximum real part of *W* on the period 1600s-2000s. The presence of the small conductive bodies must be seen also in behavior of the "longitudinal" sounding curves.

The behavior of the Vise vectors direction on the profile is shown on the fig.4. The direction of vectors differs a little from site to site, but beginning with the period 500 s they become directed under 45° to the meridian which may speak for the two-dimensionality of LBZ within the large periods range.

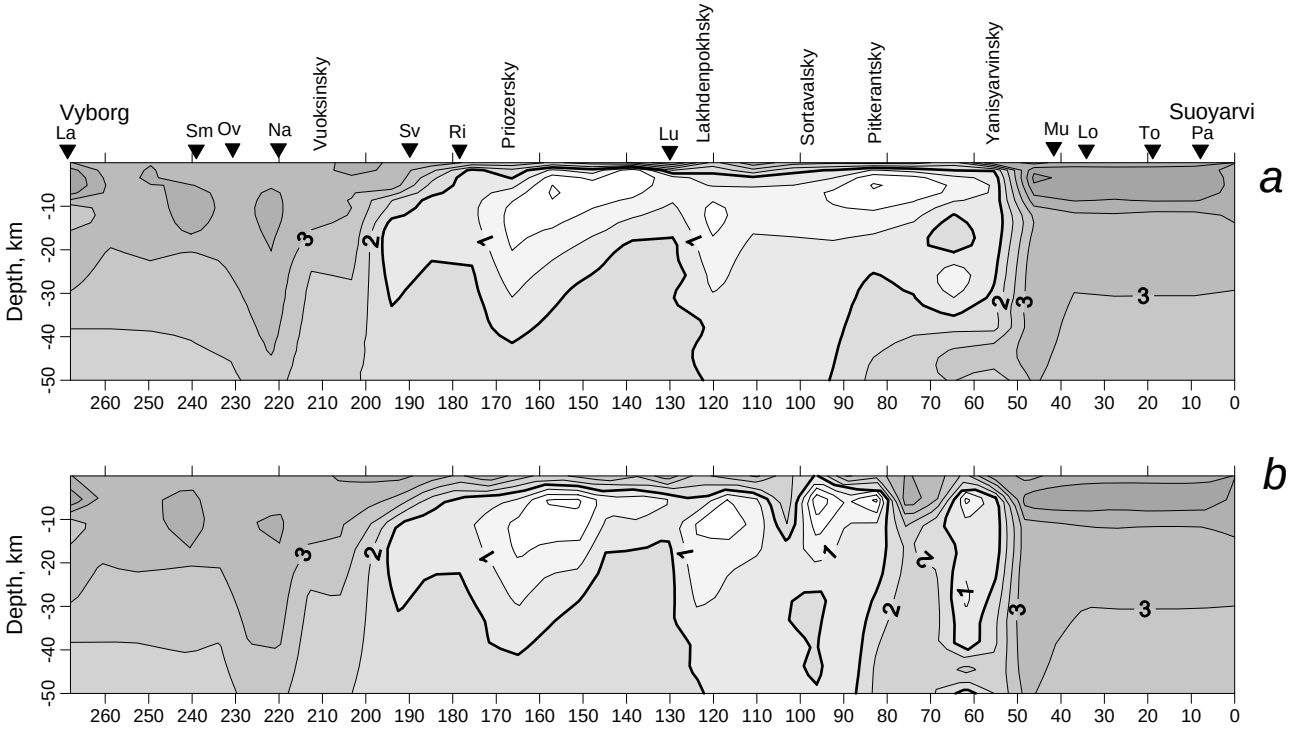

Fig. 5. Comparison of the LBZ models: old (*a*) and new (*b*); the isolines are – log ρ, ρ Ohm.m

On the fig.5*b* there is shown the improved version of the LBZ model taking into account new data obtained on the piece from 50-th till 100-th km of the profile. New data gave the new ideas on the northern part of LBZ structure. Hear has been revieled the Yanisyarvinsky Fracture zone with the conductivity 30 Ohm.m till the 50 km depth (the region with the resistivity less then 30 Ohm.m is marked by the bold line). This conductive zone is separated from the LBZ by approximately 15 km zone of the increased resistivity. In the previous model (fig.5*a*) these conductive zones practically interflow. Let's note that we interpreted new curves together with the global MV curve which allow us to increase the depth of model.

On the fig. 6 there is shown the behavior of the real part of Shmucker vector *W* for the old model (*a*) and new model including the additional points (*b*). There can be seen that the additional data decrease a little the real part of *W* even in points far removed from the new sites. In the sites near the Yanisyarvinsky fracture zone (Loimola, 8 km and Pastoyarvi, 35 km) the location of the *ReW* maximal values remain 600 s as in old model. At the same time, as the old so the new experimental data note that the main maximum of the frequency characteristic of the *reW* lies within the interval 1500-1600 s. It may signify that the real resistivity of the abnormal region is noticeably lower than in model. May be the minimal curves must be taken for interpretation instead the effective ones. In this case we must use the global curve beginning with D_{st} variations.

For the further investigation of the anomaly structure at the large depth it is necessary to carry out the prolonged soundings, till 10- 20 days, in order to obtain the curves which can be combine with the global curve in the region of D_{st} variations. At this stage of investigations we can roughly verify this supposition by the three times decreasing the fracture zones resistivity in the model on the fig. 5 *b*. This procedure gave the shift of the frequency characteristics of real part of *W* from 600 s to 1600 s. In case when it is difficult to choose the "longitudinal" curves this technique of building the quasi-2D model may lead to mistakes but the proposed method of the verification of the model using the MV data allows to exclude its. The most perspective in these cases is using the program of the 2D combine interpretation of MV and MT data.

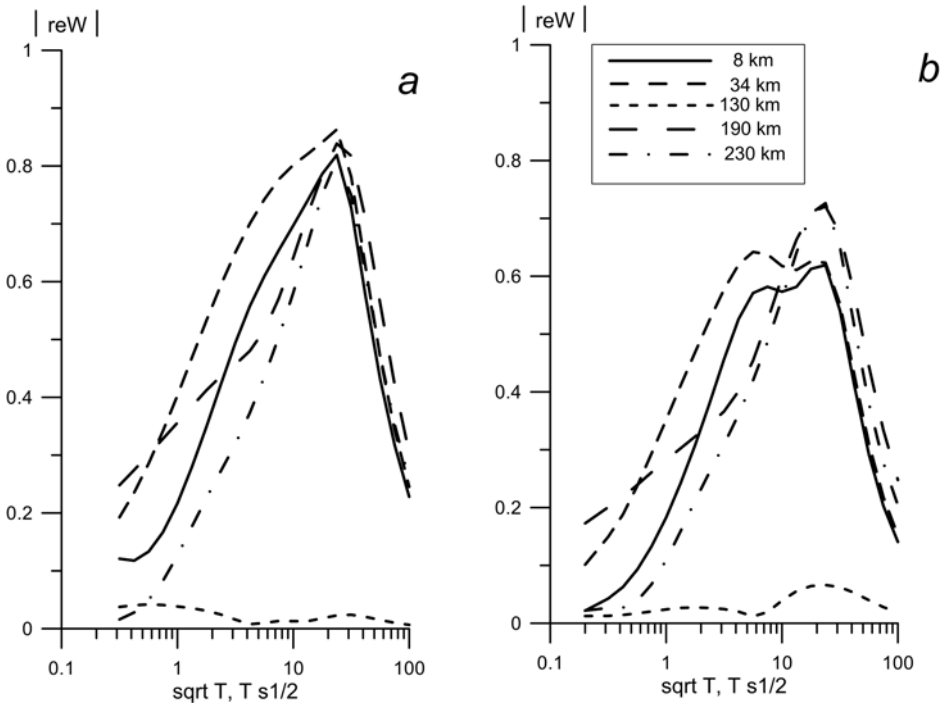

Fig. 6. The behavior of the real part of W on the period in the old (*a*) and new (*b*) models including the additional data (*b*) in the different points of the profile.

The works were supported by the grant RFBR No 013-05-00-786. We may expect that the additional material that will be obtained within the frame of grant RFFI and developed 2D-3D combined interpretation of MT and MV data will allow to decide this problem. Already the first experimental data obtained in 2013 year gave some corrections of the model.

References

Kovtun A.A. (1989), The Crust and Upper Mantle structure at the North-West of the East-European Platform by Magnetotelluric Soundings Data, LGU, Leningrad, USSR, 284 pp.

Kovtun A.A., Vardaniants I.L., Legen'kova N.P. (2007), Influence of the Crust Electroconductivity Anomalies on the Behavior of the Magnetotelluric Field on the Fennoscandinavian Shield, Problems of geophysics, Issue 40, p.24-43.

Kovtun A.A., Vardaniants I.L., Uspensky I.N. (2011), Comparison of Seismic and Geoelectric Models for the Ladoga-Bothnia anomalous zone, Problems of geophysics, Issue 44, p.124-132.

APPLICATION OF THE RADIOHOLOGRAPHIC METHOD FOR SEARCHING OF ORE BODIES

V.A. Lubchich

Polar Geophysical Institute, Apatity, 184209, Russia, e-mail: lubchich@yandex.ru

Abstract. The radioholographic method is destined for quick visualization of geoelectric heterogeneities in the earth's crust. The areal measurement of amplitudes and phases of electromagnetic field components is used for the holographic reconstruction of medium, anomaly areas with high electrical conductivity are localized in the earth's crust by using the holographic reconstruction. The report deal with the application of the radioholographic method for searching of ore bodies on the mount Loipishnjun in the Monchegorsk ore region. The result of holographic visualization of geoelectric heterogeneities are in good agreement with the geological structure of this site, where rich sulfide ore zones have been discovered by drilling wells.

Modern magnetometers with exact synchronization of measured signal to the Universal Time (UT) by using GPS satellite navigation systems allow observing distribution of amplitude and phase characteristics of magnetic field. As a result, magnetic field values observed on the earth's surface might be processed by the radioholographic method for localization of anomalous conductive areas in the earth's crust. Indeed, superposition of two fields is measured on the earth's surface when electromagnetic sounding is carried out. The primary field is field from the artificial source of electromagnetic waves. The secondary field is field from currents induced in anomalous conductive zones. In terms of holography primary field may be considered as the reference wave, the secondary field - as the object wave.

The holographic reconstruction of magnetic field in lower half-space is calculated by the formula [Tereshchenko, 1987]:

$$\boldsymbol{H}_{\boldsymbol{H}}(\rho,z)=\frac{1}{2\pi}\int_{\Sigma} d\rho'\boldsymbol{H}(\rho',z')\frac{\partial}{\partial z}\frac{exp(-ik\sqrt{|\rho-\rho'|^2+(z-z')^2})}{\sqrt{|\rho-\rho'|^2+(z-z')^2}} \qquad (1),$$

where $\boldsymbol{H}$ – magnetic field observed on the earth's surface, $k=\sqrt{i\omega\mu\sigma}$ - wave number for lower half-space, ω - circular frequency of electromagnetic wave, σ - electrical conductivity, μ - magnetic permeability, ρ, ρ' - horizontal projections of radius-vectors, z, z' – vertical coordinates of points of reconstruction and observation of magnetic field, i – the imaginary unit. The integration is taken along the plane of signal registration Σ.

However, only in the high frequency limit the holographic reconstruction of magnetic field allows localizing sources of anomalous fields in the earth's crust [Stone, 1981]. In general the holographic reconstruction $\boldsymbol{H}_{\boldsymbol{H}}$ is associated with the unknown function of anomalous field sources $\boldsymbol{j}_{\boldsymbol{m}}$ by the integral equation:

$$\boldsymbol{H}_{\boldsymbol{H}}(\boldsymbol{r})=\boldsymbol{H}_0(\boldsymbol{r})+2i\int_V dV\boldsymbol{j}_m(\boldsymbol{r}')\,ImG(\boldsymbol{r},\boldsymbol{r}') \qquad (2),$$

where $\boldsymbol{H}_0$ – normal magnetic field, $\boldsymbol{j}_{\boldsymbol{m}}$ - density of fictitious magnetic current, *ImG* - imaginary part of the green's function, the integration is taken over the volume *V* of lower half-space. Grid approximation of the integral equation (2) gives the system of linear equations for unknown values of function of anomalous field sources $\boldsymbol{j}_{\boldsymbol{m}}$ in grid nodes.

Researchers of the Polar Geophysical Institute have carried out experimental work on the Loypishnjun site in the Monchegorsk ore region on the Kola Peninsula to verify the effectiveness of the radioholographic method for localization of ore bodies. The Loypishnjun site is located in the South-Eastern part of the Monchetundra mountain massif. The Monchetundra massif is intrusion of basic rocks. Epigenetic sulfide copper-nickel ore bodies are formed in tectonic zones of intrusive massifs in the Monchegorsk ore region [Sholohnev, Poljakov et al., 1998]. Content of sulfides in these ore bodies can reach up to 50-60 %. Vein-type mineralization of ore bodies is often observed. As a result, these ore bodies are anomalous areas with high electrical conductivity. Such ore bodies have been discovered by drilling wells at the Loypishnjun site.

Square grid of observation points was divided at the Loypishnjun site. Linear size of the experimental site was 350×400 meters, size of grid cell was 50 meters. Total number of observation points was equal to 72.

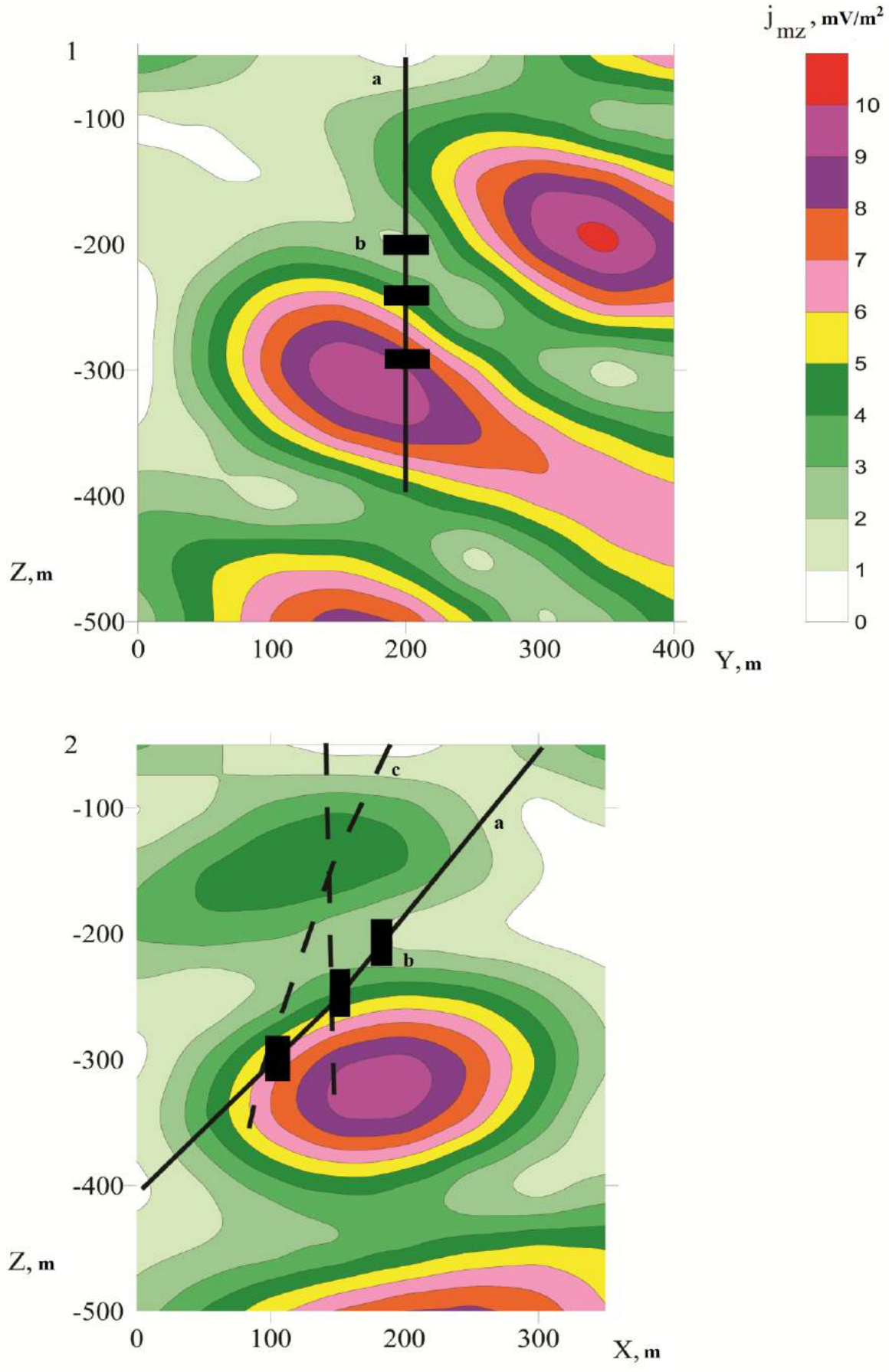

Fig. 1 Contour maps of amplitude of the vertical magnetic current component j_{mz} for two orthogonal sections of the earth's crust: 1 - X = 200 m, 2 - Y = 200 m. Labels on the figure: a - projection of the well, b – intervals of ore mineralization, c – tectonic faults.

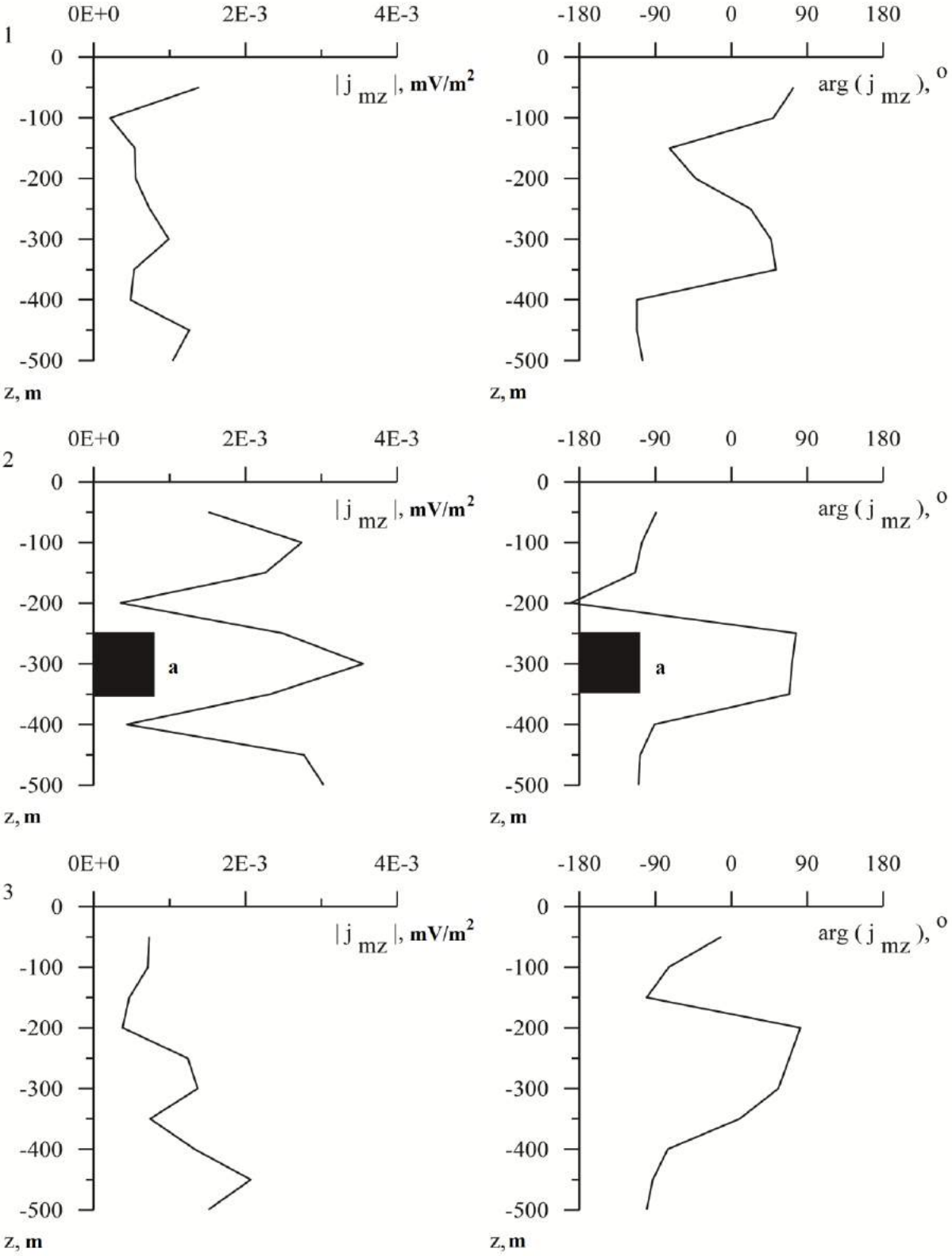

Fig. 2 Graphs of amplitude and phase of the vertical magnetic current component j_{mz} in points with coordinates: 1 - X = 0 m, Y = 100 m; 2 - X = 200 m, Y = 100 m; 3 - X = 350 m, Y = 100 m. The label on the figure: a – the location of the anomalous area.

Three orthogonal components of the magnetic field were measured by the modern magnetometer with exact synchronization of signal to the Universal Time (UT). The source of electromagnetic field was square ungrounded loop with side length of 50 meters. The loop was located 200 meters from the edge of the experimental site. The frequency of harmonic signal generated in the loop was equal to 136 Hz. Current in

the loop reached up to 3 A. The harmonic signal generated in the loop was recorded in the digital system of data registration with exact synchronization of signal to the Universal Time (UT). This experimental technique allowed us to determine not only amplitude of magnetic field, but also phase shift between the measured component of magnetic field and the current in the generator loop.

The lower half-space under the experimental site was broken to depth of 500 meters by cubic grid. Length of cube edge was equal to 50 meters. Using magnetic field values measured on the Earth's surface, the holographic reconstruction $\boldsymbol{H}_{\boldsymbol{H}}$ of magnetic field was calculated in grid nodes by the formula (1). Values of normal field $\boldsymbol{H}_0$ also were calculated in these grid nodes. As a result of the grid approximation, the integral equation (2) was converted to system of linear equations for unknown values of fictitious magnetic current density $\boldsymbol{j}_{\boldsymbol{m}}$ in these grid nodes. Solving this system of linear equations, distribution of sources of anomalous electromagnetic fields in the crust was obtained. These areas with high electrical conductivity might be associated with local ore bodies.

Due to inductive nature of eddy currents induced in the earth's crust by ungrounded horizontal loop, vertical component j_{mz} dominates in the magnetic current. Figure 1 shows contour maps of amplitude of the vertical magnetic current component j_{mz} for two orthogonal sections of the earth's crust Y = 200 m and X = 200 m. The figure shows, that the anomalous zone in range of X = +150...+250 m, Y = +100...+250 m and Z = -350...-250 m is clearly localized in the lower half-space.

This area is displayed also on phase graphs of the source function $\boldsymbol{j}_{\boldsymbol{m}}$. Figure 2 shows graphs of amplitude and phase of the vertical magnetic current component j_{mz} in points with coordinates X = 0 m, Y = 100 m; X = 200 m, Y = 100 m and X = 350 m, Y = 100 m. Graphs for the middle point show, that the anomalous zone is marked by maximum amplitude of the magnetic current at the depth of 300 meters and sharp jumps of phase by 180 degrees. At the same time, additional maxima at depths of 100 and 500 meters are not marked by such jumps of phase. This fact demonstrates, that usage of phase characteristics of the source function $\boldsymbol{j}_{\boldsymbol{m}}$ in addition to amplitude characteristics is necessary for correct interpretation of the holographic reconstruction of heterogeneities in the earth's crust. Influence of the anomalous area is observed also at boundary points, where jumps of phase occur approximately at same depths as in the central point. However, these jumps of phase have diffuse form and they correspond to weak maxima of amplitude.

The drilling profile was located along the cross section Y = 200 m of the experimental site. The well C-1720 discovered ore zones with rich content of sulfides at depth intervals 218-219 m, 265-270 m, 360-365 m. Depth intervals are measured along the well. Length of the well was equal 502.7 meters. Discovered ore zones are controlled by system of tectonic faults, this situation is typical for the epigenetic type of mineralization. The figure 1 shows, that the anomalous area with high electrical conductivity detected by the radioholographic method is somewhat away from projection of the well. But depth of the anomalous zone, in general, is accorded with the location of ore zones at intervals 265-270 m and 360-365 m. In addition, the location of the anomalous area is correlated with sub-vertical tectonic fault, which controls the ore zone at depth interval 265-270 m. Therefore, this ore zone may be continued to depth of about 300-350 meters.

Thus, we can conclude. The radioholographic method is destined for quick visualization of geoelectric heterogeneities in the earth's crust. The areal measurement of amplitudes and phases of magnetic field components is used for the holographic reconstruction. Anomaly areas with high electrical conductivity are localized in the earth's crust by using the holographic reconstruction. These anomalies may be associated with ore zones.

Joint analysis of amplitude and phase characteristics of the magnetic current function $\boldsymbol{j}_{\boldsymbol{m}}$ is required for correct interpretation of the holographic reconstruction of heterogeneities in the earth's crust. This procedure provides rejection of false anomalies.

Utilization of modern magnetometers with exact synchronization of measured signals to the Universal Time (UT) by using GPS satellite navigation systems allows organizing effective areal observations of amplitude and phase characteristics of magnetic field components on the earth's surface. The holographic reconstruction of distribution of anomalous conductive areas in the earth's crust may be produced by using the result of surface observations.

References.

Stone W.R. (1981), The inverse medium (or inhomogeneous medium remote probing) problem and a closed-form inverse scattering solution to the medium synthesis problem, *Radio Science*, 16(6), 1029-1035.

Tereshchenko E.D. (1987), *The radioholographic method of investigation of ionospheric heterogeneities*, 99 pp., Apatity (in Russian language).

Sholohnev V.V., Poljakov I.V. et al. (1998), *Report on results of prospecting for copper-nickel sulfide ore and other minerals in the contact zone of Monchepluton and Monchetundra massif in 1994-98 (the Loypishnjun site)*, Monchegorsk (in Russian language).

SYNCHRONOUS MAGNETOTELLURIC SOUNDING WITH NON-UNIFORM SOURCE FIELD EXCITATION

V.V. Plotkin

Institute of Petroleum Geology and Geophysics SB RAS, Novosibirsk, 630090, Russia, e-mail: PlotkinVV@ipgg.sbras.ru

Abstract. At interpretation of magnetotelluric sounding (MTS) data, it is considered usually that the medium is excited by a vertically incident plane wave. However near auroral zones and sources of primary field, is quite real that this electromagnetic field is non-uniform along a terrestrial surface. In this study, synchronous data processing is carried out in the assumption that medium is excited by non-uniform primary field with a prevailing spatial harmonic. For verification of this assumption and determination of parameters of the spatial harmonic, it is used the angular spatial filtration of the wave field and the directional diagram calculation. The maximum of the directional diagram corresponds to an azimuth of the wave vector of the field prevailing spatial harmonic. Optimization methods are applied to the subsequent definition of the wave vector components using bimodal decomposition of the electromagnetic field. Amplitudes of modes and various responses of the media depending on the temporary period can be defined using data of the synchronous registration of electromagnetic field components in three or more points. In simple situations, there is an opportunity not to register electric field components. Testing of offered algorithm is executed using data of the BEAR project which confirms reliability of this approach.

At interpretation of magnetotelluric sounding (MTS) data, it is considered usually that the medium is excited by a vertically incident plane wave. However near auroral zones and sources of primary field, is quite real that this electromagnetic field is non-uniform along a terrestrial surface. Using synchronous registration of field components in three or more points, it is possible to apply algorithms of a spatial filtration for data processing and the bimodal electromagnetic field decomposition can be used for interpretation of these data.

The electromagnetic field generally consists of two modes. It can be expressed (Plotkin et al., 2010) through their scalar potentials (the time multiplier $\sim e^{i\omega t}$ is omitted, OX and OY axes of the Cartesian system of coordinates are located on the medium surface, the OZ axis is directed deep into medium on a normal to this surface):

$$E_x = \frac{\partial E^{(e)}}{\partial x} + \frac{\partial E^{(m)}}{\partial y}, \quad E_y = \frac{\partial E^{(e)}}{\partial y} - \frac{\partial E^{(m)}}{\partial x}, \quad E_z^{(m)} = 0, \quad E_z^{(e)} \neq 0,$$
$$H_x = \frac{\partial H^{(m)}}{\partial x} + \frac{\partial H^{(e)}}{\partial y}, \quad H_y = \frac{\partial H^{(m)}}{\partial y} - \frac{\partial H^{(e)}}{\partial x}, \quad H_z^{(e)} = 0, \quad H_z^{(m)} \neq 0. \tag{1}$$

Potentials of electric $E^{(m,e)}(x,y,z)$ and magnetic $H^{(m,e)}(x,y,z)$ fields belong to the TE-mode (index m) and to the TM-mode (index e). If fields of both modes are presented by only one spatial $\exp(ik_x x + ik_y y)$ harmonic, on a surface of horizontally layered medium relations are carried out:

$$\frac{dH_z^{(m)}}{dz} + \frac{k_1 H_z^{(m)}}{R^{(m)}} = 0, \quad H_{x,y}^{(m)} = ik_{x,y} H^{(m)}, \quad E_{x,y}^{(m)} = \pm ik_{y,x} E^{(m)},$$
$$\frac{dE_z^{(e)}}{dz} + \frac{k_1 E_z^{(e)}}{R^{(e)}} = 0, \quad E_{x,y}^{(e)} = ik_{x,y} E^{(e)}, \quad H_{x,y}^{(e)} = \pm ik_{y,x} H^{(e)}. \tag{2}$$

Here σ_n, h_n, $n = 1, \cdots, N$ are characteristics of a geoelectric section, $k_n = \sqrt{k_x^2 + k_y^2 + i\mu_0\omega\sigma_n}$, and the normalized impedance relations for modes have an appearance (Zhdanov, 1986):

$$R^{(m)} = cth\left\{k_1 h_1 + arcth\left[\frac{k_1}{k_2} cth\left(k_2 h_2 + \ldots arcth\frac{k_{N-1}}{k_N}\right)\right]\right\}, \tag{3}$$

$$R^{(e)} = cth\left\{k_1 h_1 + arcth\left[\frac{k_1\sigma_2}{k_2\sigma_1} cth\left(k_2 h_2 + \ldots arcth\frac{k_{N-1}\sigma_N}{k_N\sigma_{N-1}}\right)\right]\right\}.$$

Expressions for vertical field components and their derivatives can be taken from the equations: $div\,\mathbf{E} = 0$, $(rot\,\mathbf{E})_z = -i\omega\mu_0 H_z$, $div\,\mathbf{H} = 0$, $(rot\,\mathbf{H})_z = \sigma_1 E_z$, considering properties of modes:

$$\sigma_1 E_z^{(e)} = ik_x H_y^{(e)} - ik_y H_x^{(e)}, \quad -\frac{dE_z^{(e)}}{dz} = ik_x E_x^{(e)} + ik_y E_y^{(e)},$$
$$k_x H_x^{(e)} + k_y H_y^{(e)} = 0, \quad k_y E_x^{(e)} - k_x E_y^{(e)} = 0, \qquad (4)$$
$$i\omega\mu_0 H_z^{(m)} = ik_y E_x^{(m)} - ik_x E_y^{(m)}, \quad -\frac{dH_z^{(m)}}{dz} = ik_x H_x^{(m)} + ik_y H_y^{(m)},$$
$$k_x E_x^{(m)} + k_y E_y^{(m)} = 0, \quad k_y H_x^{(m)} - k_x H_y^{(m)} = 0.$$

Substitution (4) in (2) gives expressions for the mode impedances and the reciprocal tippers:

$$Z_{xy}^{(m)} = \frac{E_x^{(m)}}{H_y^{(m)}} = Z_0^{(m)}, \quad Z_{yx} = \frac{E_y^{(m)}}{H_x^{(m)}} = -Z_0^{(m)}, \quad Z_0^{(m)} = \frac{i\omega\mu_0 R^{(m)}}{k_1},$$
$$Z_{xy}^{(e)} = \frac{E_x^{(e)}}{H_y^{(e)}} = Z_0^{(e)}, \quad Z_{yx} = \frac{E_y^{(e)}}{H_x^{(e)}} = -Z_0^{(e)}, \quad Z_0^{(e)} = \frac{k_1}{\sigma_1 R^{(e)}}, \qquad (5)$$
$$T_{x,y}^{(m)} = \frac{H_{x,y}^{(m)}}{H_z^{(m)}} = \frac{k_1}{ik_0 R^{(m)}}\frac{k_{x,y}}{k_0} = T_0^{(m)}\frac{k_{x,y}}{k_0}, \quad T_0^{(m)} = \frac{k_1}{ik_0 R^{(m)}},$$
$$T_{x,y}^{(e)} = \frac{E_{x,y}^{(e)}}{E_z^{(e)}} = \frac{k_1}{ik_0 R^{(e)}}\frac{k_{x,y}}{k_0} = T_0^{(e)}\frac{k_{x,y}}{k_0}, \quad T_0^{(e)} = \frac{k_1}{ik_0 R^{(e)}}, \quad k_0 = \sqrt{k_x^2 + k_y^2}.$$

Considering (1)-(5), now it is possible to write down bimodal representation of the field spatial harmonic in the point with coordinates x_j, y_j on the surface of the horizontally layered medium:

$$H_{x,y}(x_j, y_j) = \left(H_{m0} n_{x,y} \pm H_{e0} n_{y,x}\right) e^{i\left(k_x x_j + k_y y_j\right)}, \quad H_z(x_j, y_j) = \frac{H_{m0}}{T_0^{(m)}} e^{i\left(k_x x_j + k_y y_j\right)},$$
$$E_{x,y}(x_j, y_j) = \left(E_{e0} n_{x,y} \pm E_{m0} n_{y,x}\right) e^{i\left(k_x x_j + k_y y_j\right)}, \quad E_z(x_j, y_j) = \frac{E_{e0}}{T_0^{(e)}} e^{i\left(k_x x_j + k_y y_j\right)}, \qquad (6)$$
$$Z_0^{(m,e)} = \frac{E_{m0,e0}}{H_{m0,e0}}, \quad Z_0^{(m)} = \frac{\omega\mu_0}{k_0 T_0^{(m)}} = \frac{i\omega\mu_0 R^{(m)}}{k_1}, \quad Z_0^{(e)} = \frac{ik_0}{\sigma_1} T_0^{(e)} = \frac{k_1}{\sigma_1 R^{(e)}},$$

where $n_{x,y} = \frac{k_{x,y}}{k_0}$, and $H_{m0}, H_{e0}, E_{m0}, E_{e0}$ are the mode amplitudes. Using data of synchronous registration various components of laterally non-uniform electromagnetic field in several points, the mode impedance and reciprocal tipper dependences on the temporary period can be defined from (6). Further by means of inversion of these dependences it is possible to receive characteristics of a geoelectric section.

Representation (6) is fair for horizontally layered medium excited by non-uniform primary field with one prevailing spatial harmonic. There is a question of possibility of its use in practice of MTS. The spatial harmonic spectrum of the field can be found by the inverse Fourier transform using data of synchronous registration various components in several points of the polygon:

$$f(k_x, k_y) = \sum_j F(x_j, y_j) e^{-i\left(k_x x_j + k_y y_j\right)}, \qquad (7)$$

where $F(x_j, y_j)$, $f(k_x, k_y)$ are any of a component of a field and amplitude of its spatial harmonic respectively. The number of points and the sizes of the polygon are defined by spatial structure of a registered electromagnetic field. In MTS practice, data recording is usually carried out by consecutive transfer of the equipment on profile points. It is based on representation of primary field by vertically incident plane wave and is often realized in practice. In more difficult situations, synchronous field registration by the minimum quantity of points becomes the following step which is necessary for performance of field spatial filtration (7). In particular, according to three points it is possible to count the directional pattern characterizing azimuthal dependence of spatial harmonic amplitudes of electromagnetic field modes registered:

$$\Phi_H^{(m,e)}(\alpha, s) = \left| \sum_j \left(H_x(x_j, y_j) n_{x,y} \pm H_y(x_j, y_j) n_{y,x} \right) e^{-is(n_x \cos\alpha_j + n_y \sin\alpha_j)} \right|,$$

$$\Phi_E^{(e,m)}(\alpha, s) = \left| \sum_j \left(E_x(x_j, y_j) n_{x,y} \pm E_y(x_j, y_j) n_{y,x} \right) e^{-is(n_x \cos\alpha_j + n_y \sin\alpha_j)} \right|, \qquad (8)$$

$$\cos\alpha_j = \frac{x_j}{d_j}, \quad \sin\alpha_j = \frac{y_j}{d_j}, \quad n_x = \frac{k_x}{k_0} = \cos\alpha, \quad n_y = \frac{k_y}{k_0} = \sin\alpha,$$

$$d_j = \sqrt{x_j^2 + y_j^2}, \quad s = k_0 L \approx k_0 d_j,$$

where s is the parameter depending on the a priori value k_0 assumed and the characteristic size of the polygon $L \approx d_j$ which should be chosen taking into account the Nyquist theorem ($2\pi / k_0 > 2L$). The maximum of the directional patterns (8) in fact close to results of the inverse Fourier transform (7), corresponds to azimuths α of a wave vector.

Representation (6) is received for a case of horizontally layered medium which in a real situation can be 3D non-uniform. Lateral medium heterogeneities as secondary sources of the field make an additional contribution to field components registered on the surface. Unlike contribution of regular boundaries of the layered medium their contribution is not identical on different points of the polygon and can be considered as errors. With use of formulas (6) and synchronous registration data there is an opportunity to define average characteristics of the medium that is a normal geoelectric section.

It is important to consider that a conductivity of the atmosphere is very small. In this case the induction excitation of the electromagnetic field TE-mode in the medium is realized. The TM-mode arises with lateral conductivity not uniformity. So, galvanic distortions of magnetotelluric curves are caused by influence of near-surface inhomogeneities. For elimination of such distortions the field of TM-mode should be excluded, TE-mode selection is necessary. From this point of view representation (6) is also suitable.

To find the unknown values entering representation (6) it is possible to apply optimization methods, finding their values that are most suitable to synchronous component data in several points. For definition of wave numbers and mode amplitudes it is possible to use the following functionals:

$$\Phi_1(k_x, k_y, H_{m0}, H_{e0}) = \sum_j \left| H_x(x_j, y_j) - \left(H_{m0} n_x + H_{e0} n_y \right) e^{i\left(k_x x_j + k_y y_j\right)} \right|^2 + \sum_j \left| H_y(x_j, y_j) - \left(H_{m0} n_y - H_{e0} n_x \right) e^{i\left(k_x x_j + k_y y_j\right)} \right|^2, \qquad (9)$$

$$\Phi_2(k_x, k_y, E_{m0}, E_{e0}) = \sum_j \left| E_x(x_j, y_j) - \left(E_{e0} n_x + E_{m0} n_y \right) e^{i\left(k_x x_j + k_y y_j\right)} \right|^2 + \sum_j \left| E_y(x_j, y_j) - \left(E_{e0} n_y - E_{m0} n_x \right) e^{i\left(k_x x_j + k_y y_j\right)} \right|^2. \qquad (10)$$

At minimization of functionals (9)-(10) as initial values of wave vector azimuths it is possible to use their values received by means of (8). Initial values of mode amplitudes get out as component values on one of points. For functional (9) it is possible to consider also that a magnetic field of TM-mode $H_{e0} \to 0$ on an medium surface.

The mode impedances, their phases and apparent resistivities are calculated:

$$Z_0^{(m)} = \frac{E_{m0}}{H_{m0}} = \frac{i\omega\mu_0 R^{(m)}}{k_1}, \quad Z_0^{(e)} = \frac{E_{e0}}{H_{e0}} = \frac{k_1}{\sigma_1 R^{(e)}},$$

$$\rho_k^{(m)} = \frac{\left|Z_0^{(m)}\right|^2}{\omega\mu_0} = \frac{\left|R^{(m)}\right|^2 \omega\mu_0}{\sqrt{k_0^4 + (\omega\mu_0\sigma_1)^2}}, \quad \phi^{(m)} = \arctan Z_0^{(m)}, \tag{11}$$

$$\rho_k^{(e)} = \frac{\left|Z_0^{(e)}\right|^2}{\omega\mu_0} = \frac{\sqrt{k_0^4 + (\omega\mu_0\sigma_1)^2}}{\left|R^{(e)}\right|^2 \omega\mu_0\sigma_1^2}, \quad \phi^{(e)} = \arctan Z_0^{(e)}.$$

Dependences of apparent resistivities and phases on the temporary period can be inverted in characteristics of a normal geoelectric section. It should be noted that formulas (11) for TM-mode are fair only in case of its external excitation by primary source. Dependences of mode apparent resistivities on the temporary period at $\omega \to 0$ could be a sign of external excitation. As seen from (11), there is $\rho_k^{(e)}(\omega) \sim \omega^{-1} \to \infty$ and $\rho_k^{(m)}(\omega) \sim \omega \to 0$ in this case. Because of the small atmosphere conductivity the external excitation of TM-mode isn't realized by MTS. The magnetic field of TM-mode isn't enough $|H_{e0}| << |H_{m0}|$. It is very difficult to find $Z_0^{(e)}$. In practice it is better to use formulas (11) only for TE-mode as the TM-mode in most cases arises in medium owing to lateral conductivity inhomogeneities.

In simple situations when medium is close to horizontally layered, representation of a field by one TE-mode is fair. Thus it is possible to do without registration electric field components.

The described processing synchronous registration data was applied to the model of surface inhomogeneities (Plotkin and Gubin, 2014) presented in Fig. 1. It was considered horizontally layered medium covered with thin layer of 10 m thick of lateral inhomogeneous conductivity. The polygon sizes L

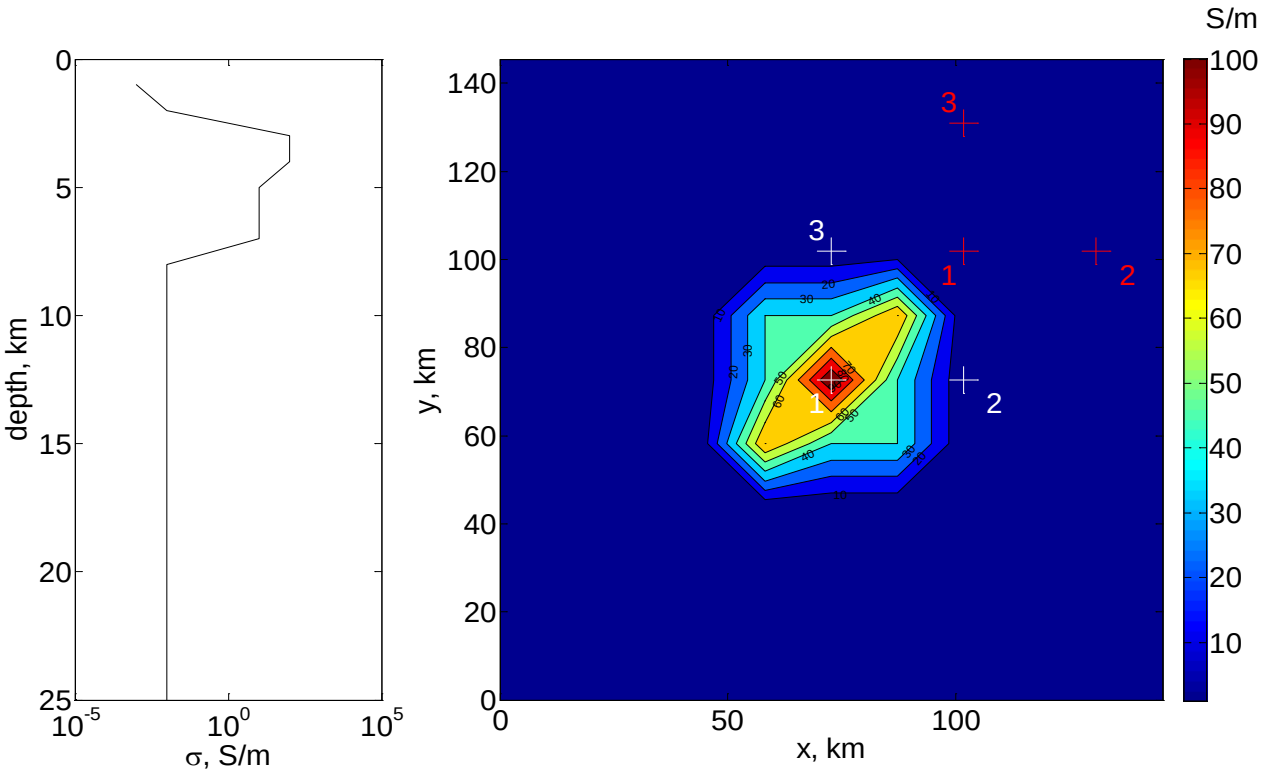

Fig. 1. Geoelectric section and map of surface inhomogeneities. Cross-marks showed points of synchronous sounding.

on coordinate axes are equal 160 km. Excitation of the medium was carried out by the first spatial harmonic of TE-mode with $k_x = k_y = 2\pi / L = 0.0393$ 1/km. Points of sounding are visible in Fig. 1. Data processing only on TE-mode was carried out. Results of numerical modeling are shown in Fig. 2 by different curves. "Experimental" (input distorted) curves of synchronous sounding for considered model computed by method (Plotkin and Gubin, 2014) are displayed for two field polarization by points (ρ_{yx}) and circles (ρ_{xy}). The undistorted curves (ρ_L, dashed) calculated on analytical formulas (Zhdanov, 1986) for the horizontally layered medium with local characteristics of the section in point of sounding.

On input values of electromagnetic field components in points was imposed "experimental" normally distributed noise ~ by 1%. Data more than 300 sessions were so imitated. During processing the "experimental" data obtained, wave vector components k_x, k_y were restored reliably, amplitudes of TE-mode are determined and their impedances and apparent resistances are calculated. In Fig. 2 solid curves with points (ρ_{TE}) displayed results of described synchronous data processing.

As seen in Fig. 2, in point 1 over the center of surface heterogeneity noticeable galvanic distortions of magnetotelluric curves (blue) on the periods more than 100 s are observed. The effect practically vanishes in all remote points (red crosses in Fig. 1). It is important that on the periods more than 100 s, close coincidence of undistorted curves (dashed) with curves (solid with points) received according to synchronous data of three points is observed. Thus, as a result of synchronous data processing by the described algorithm it is possible to eliminate galvanic distortions in points.

Offered algorithm was applied to the data of the BEAR project on Baltic Shield in 1998. Three points (Fig. 3) with synchronous registration five electromagnetic field components (sample period is 2 s) were selected. The data of 324 sliding sessions lasting 10 hours with shifting on 1 hour were used for averaging results. In each session temporary spectra of variations of three components of a geomagnetic field and two horizontal component of electric field were calculated. Received amplitudes for 50 temporary periods in the range from 4 to 36000 s, evenly distributed on a logarithmic scale, were basic data for the subsequent processing by described algorithm.

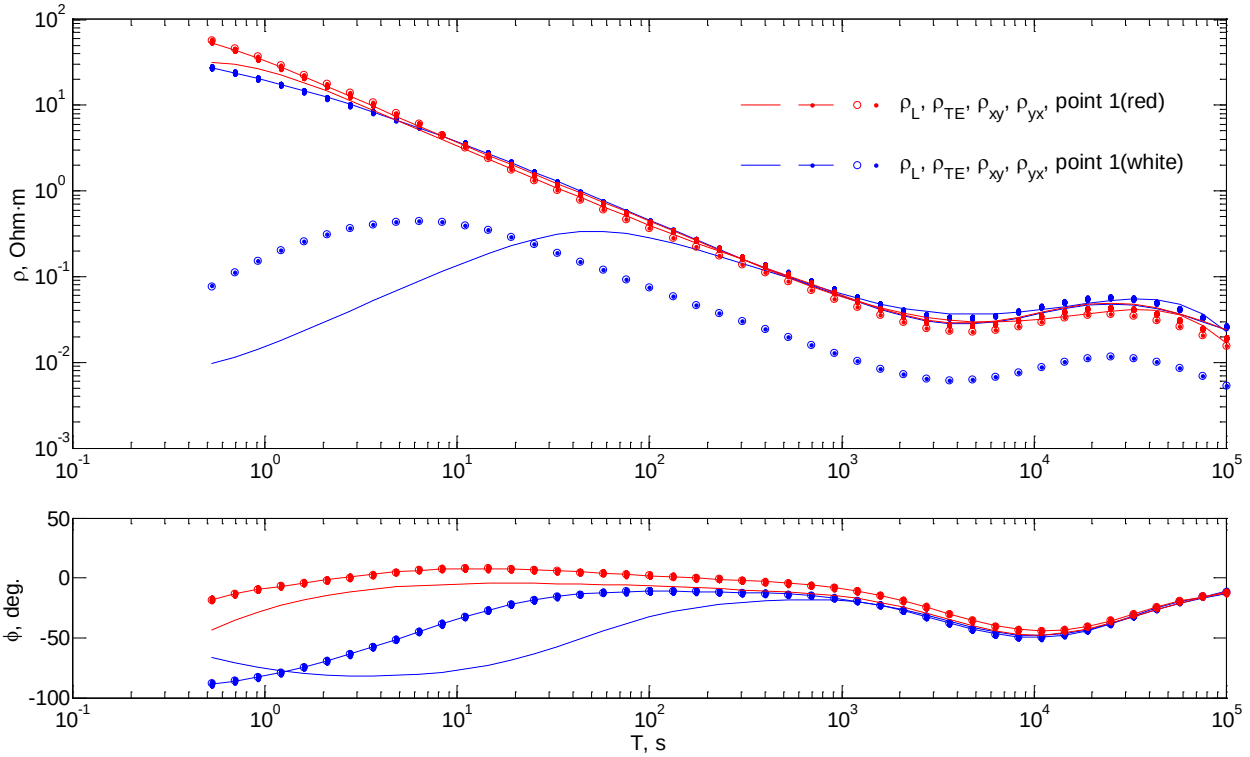

Fig. 2. Dependences of apparent resistivities and impedance phases on the temporary period for points 1. Color of curves corresponds to arrangements of points in Fig. 1.

All values of wave vector components found in each of sessions by functional Φ_1 minimization on data of three points on variations horizontal magnetic field are shown in Fig. 4. Values of wave vector components received by electric field data (minimization of Φ_2) have a similar view. For further processing, sessions

were selected only where defined in both ways wave vectors are identical approximately in the given narrow corridor. Besides, amplitudes of magnetic field modes in these sessions meet a condition $|H_{m0}| > |H_{e0}|$. In Fig. 5, the selected data on wave vectors are shown. Impedances of TE-mode, their phases and apparent resistivities were calculated on formulas (11). Results are presented in Fig. 6 and 7.

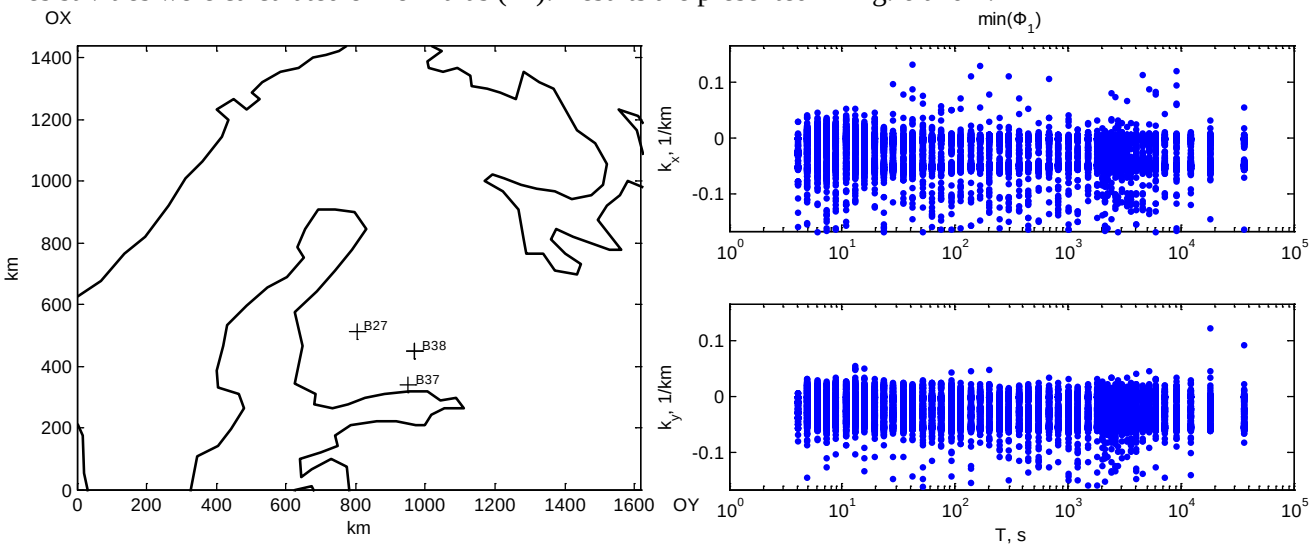

Fig. 3. Locations of three points of the BEAR project (crosses), which data are used for testing.
Fig. 4. Wave vectors defined by magnetic field data in all 324 sessions depending on the temporary period.

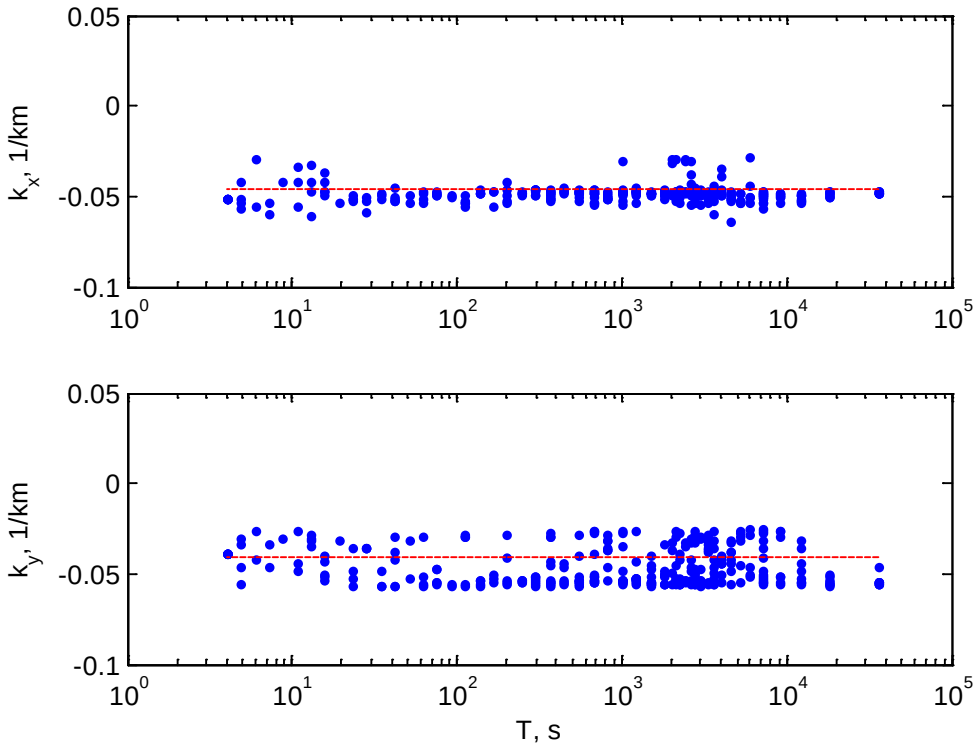

Fig. 5. Wave vector components depending on the temporary period in the sessions selected for search of parameters of a geoelectric section. Red dashed lines are given values of k_x, k_y.

Conclusions

Synchronous data of three points are processed in the assumption that medium is excited by non-uniform primary field with a prevailing spatial harmonic. At first, the angular spatial filtration of the wave field is carried out. The directional diagram maximum corresponds to the wave vector of prevailing spatial harmonic. Bimodal electromagnetic field decompositions and optimization methods are applied to the subsequent definition of the wave vector components and mode amplitudes. Processing by the described algorithm allow to eliminate galvanic distortions in points.

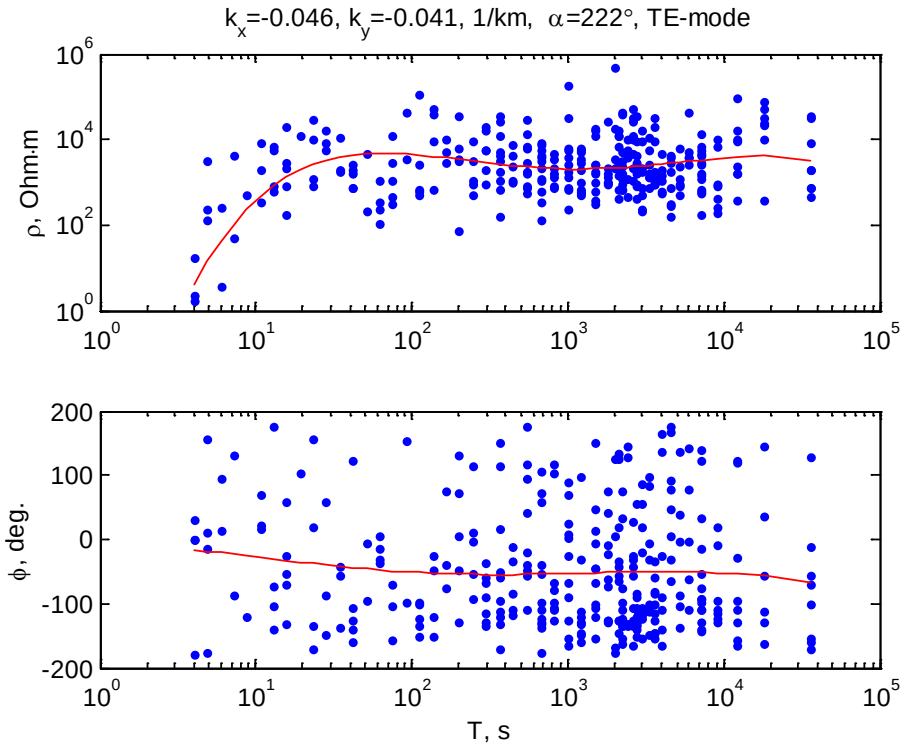

Fig. 6. Apparent resistivities and impedance phases of TE-mode depending on the temporary period (blue points) in the sessions selected with given wave vector component and its azimuth in narrow corridor (Fig. 5). Red solid lines gave polynomial fit.

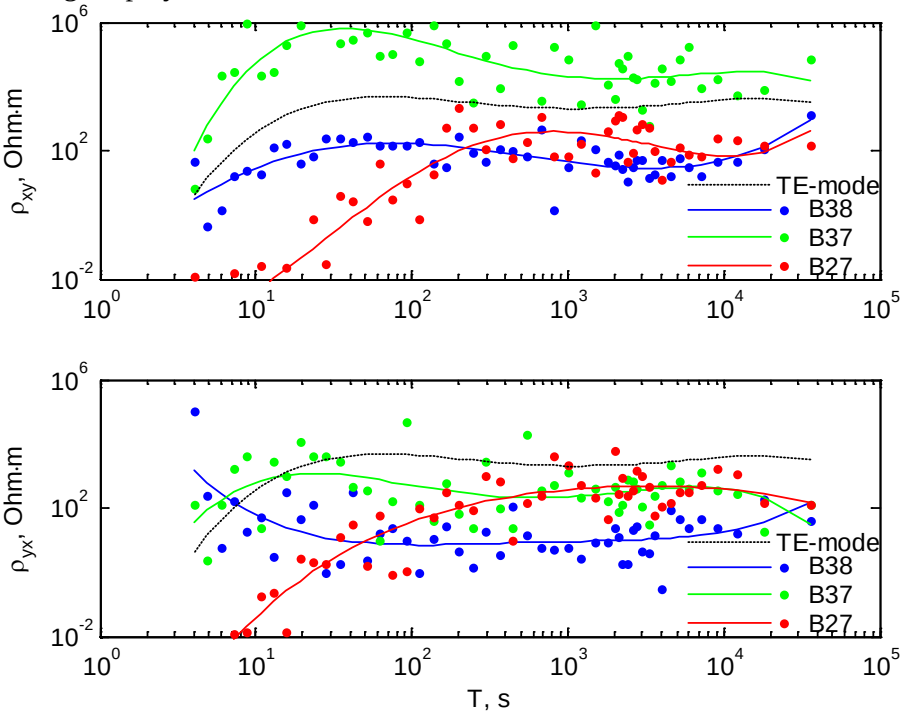

Fig. 7. Apparent resistivities depending on the temporary period calculated by standard technique (color of marks and lines correspond to points) and by offer method for TE-mode according to synchronous data of three points (black dashed lines, $k_x = -0.0461$, $k_y = -0.041$ 1/km).

References

Plotkin, V.V., A.Ya. Belinskaya and P.A. Gavrysh (2010), Lateral lithospheric conductivity patterns, from European synchronous observatory data, *Russian Geology and Geophysics*, 51, 808–813.

Plotkin, V.V. and D.I. Gubin (2014), Near-surface inhomogeneities over horizontally layered section: implication in the magnetotelluric sounding, *Russian Geology and Geophysics*, 55.

Zhdanov, M.S. (1986), *Electrical prospecting*, Moscow, Nedra, 316 pp.

CORRELATION PROPERTIES OF SECULAR VARIATION FORECAST

I.M. Demina, S.S. Bricheva

St. Petersburg Branch of N.V. Pushkov Institute of Terrestrial Magnetism, Ionosphere, and Radiowave Propagation (SPbF IZMIRAN), St.-Petersburg, 199034, Universitetskaya 5, Russia
e-mail: dim@izmiran.spb.ru, svebrich@gmail.com

Abstract. In this work, statistical and correlation properties of secular variation (SV), SV forecast (*SVf*) and SV forecast error (*ErrSVf*) are compared. Spatial structure of SV components was calculated from the IGRF11 coefficients. The SV forecast was reconstructed from the IGRF3-10 coefficients. We calculate statistical and correlation characteristics both for the globe and six separate regions. Four of these regions were selected at the high latitudes and one of them includes Russia and adjacent waters. Two other regions are located near the equator and one of them includes the so-called Brazilian Geomagnetic Anomaly. The maximum of the *ErrSVf* was obtained for Russia and adjoining near-equatorial region. Three correlation coefficients for the spatial distribution of *SV* and *SVf* were calculated. The first one is the correlation coefficient of SV_i and SV_{i-1} for two consequent periods; the second one is the correlation coefficient of SV_i and SVf_i for the same period; and the final one is the correlation coefficient of SVf_i and SV_{i-1}. The latter correlation coefficient proved to be the maximum. The *SVf* and *SV* for the same period correlate well only when high correlation between SV_i and SV_{i-1} is observed. It means that the *SVf* reproduces a spatial structure of *SV* of previous epoch independent of the forecast method used. The existence of a large and long-term anomaly produces a high correlation of sequential periods, and the correlation coefficient between the SV forecast and SV for the same period is greater than 0.9. The spatial distribution of the *ErrSVf* is characterized by an existence of independent processes occurring in the liquid core, and single anomalies of small scales. However, even if one can identify an individual flow in the liquid core, study of its parameters changes does not let us to improve the forecast accuracy, since the origin of these flows is not well determined. We propose that the topographic heterogeneity of the core-mantle boundary which presently is a subject of active study could play an important role in these processes.

Introduction

The variability of the spatial structure of the Earth's main magnetic field leads to a request for the qualitative forecast of geomagnetic secular variation (SV) from geological exploration, navigation and other geologic and geophysical tasks. Nowadays the 11th generation coefficients (IGRF11) are widely used in different geophysical studies as a mathematical description of the geomagnetic field spatial structure. This model represents the sets of spherical harmonic expansion coefficients of geomagnetic field components up to the order 13 with the 5 years interval. Each following generation of coefficients is developed by group of scientists taking into account all data from magnetic observatories, repeat stations and satellites. However for calculations between epochs the coefficients are interpolated linearly that, owing to the complexity of spatial structure of SV, can lead to errors.

At the same time, with the acceptance of a new generation of coefficients for the current epoch a SV forecast for the next 5 years is developed. The methods of SV forecast are constantly improved, but authors of the IGRF model allow for the possibility of forecast error up to 20 nT/year. The systematic decrease of the geomagnetic field intensity and the resulting decrease of the protection against cosmic rays stimulate the interest to the long-term SV forecasting. As long as the increase of the forecast accuracy, especially of the declination (D), is an important problem it is the subject of many studies.

Despite the significant progress, the question about the long-term SV forecasting still remains open. As the geomagnetic field is generated in the liquid core of the Earth, its changes in time have to be connected with processes taking place there. Nowadays the mechanism causing SV remains uncertain. Owing to the complexity of a problem of magnetohydrodynamic description of the geodynamo, only numerical solutions [Hulot et al., 2010, Kuang et al., 2009] with the assumptions, allowing to simplify the problem, exist. But these models cannot be used for the SV forecasting, because they describe a field on the Earth surface only at a qualitative level.

The main objective of this work is to estimate the accuracy of the SV forecast for Russia and adjacent waters region and to compare it with the world data and with the data for regions with various spatial structure of SV.

Method and data used

In this work statistical and correlation properties of SV, SV forecast and SV forecast error for the territory of Russia are obtained and compared with other regions of the globe. For this purpose, five more regions were chosen. Four of these regions were selected at the high latitudes and one of them includes Russia and adjacent waters. Two other regions include the near-equatorial region and one of them includes the so-called Brazilian Geomagnetic Anomaly (Fig.1). The choice of these regions was caused by features of the SV spatial structure.

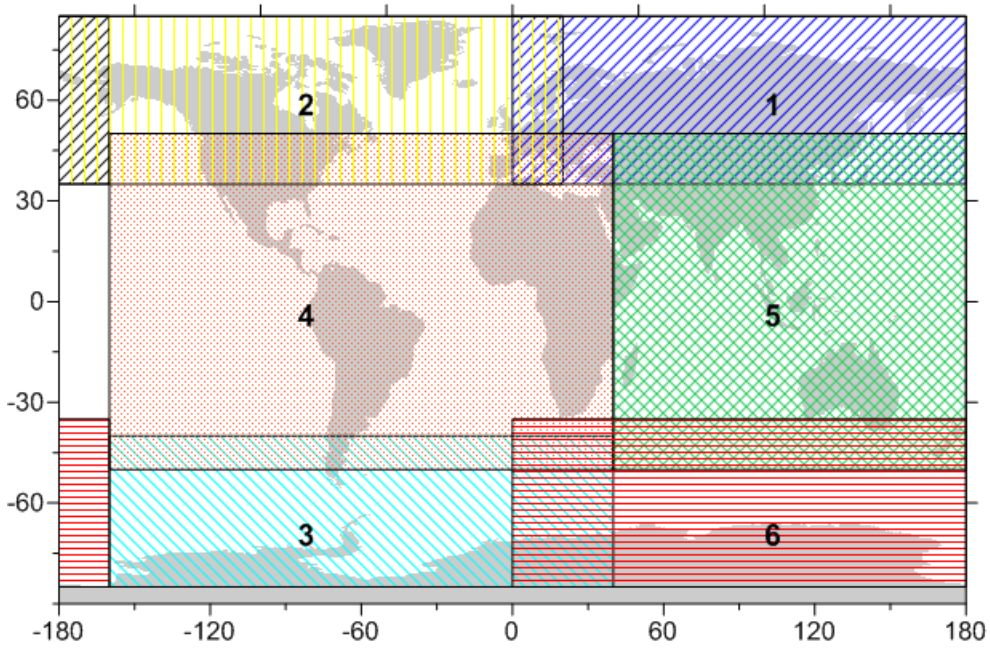

Fig. 1 Division of the Earth surface into the study areas. Digits are the region numbers. Different hatching corresponds to different regions. The hatching of areas where the regions crossed is overlapped.

The region 1 includes Russia and adjacent waters. The region 2 is characterized by a lack of large stable foci, but it includes the North magnetic Pole. The region 3 is similar to the region 1 by the spatial structure of SV and by closeness to the magnetic pole. The region 4 includes the so-called Brazilian Geomagnetic Anomaly; the region 5 contains foci of variable shape and small size and the region 6 includes the South magnetic Pole.

Fig. 1 shows the division of the Earth surface into the study regions. The spherical harmonic decomposition with IGRF11 coefficients was used for calculations of the spatial structure of field components. All geomagnetic components for the region 1 (including Russia) in the range of 1900-2010 and the SV's for consecutive epochs were found from these coefficients. SV of declination (D) was calculated in minutes. Each generation contained coefficients of the SV forecast. Out of these coefficients, we restored the spatial structure of SV forecast components for region 1 («SV forecast»). We can calculate the modified SV, which reflects real changes of geomagnetic field between corresponding epochs, using IGRF11 coefficients («SV IGRF»). The difference between real and predicted SV defines the forecast error for the corresponding epoch («SV forecast error») and allows us to evaluate the properties of the spatial distribution of this error. Results are shown in Fig. 2 for vertical component Z and declination D.

The distribution and the form of forecast anomalies mimic the structure of real SV for the previous epoch.

Correlation characteristics of SV component spatial distribution

The correlation coefficient between the spatial distribution of SV and the SV forecast has been calculated for different year pairs, for all components, during the 1980-2010 epochs. Results are shown in the Table 1. For Z and H components, the correlation coefficient between spatial structure of SV forecast and real SV of the previous epoch has the greatest value.

In the region 4 (including the Brazilian Geomagnetic Anomaly) the existence of a large anomaly produces high correlation of SV of consecutive epochs, but in this case the correlation between SV forecast and SV of the previous epoch dominates as well. The region 3 is an exception of this rule; here the correlation between the real SV and the SV forecast is higher than the correlation with the previous epoch.

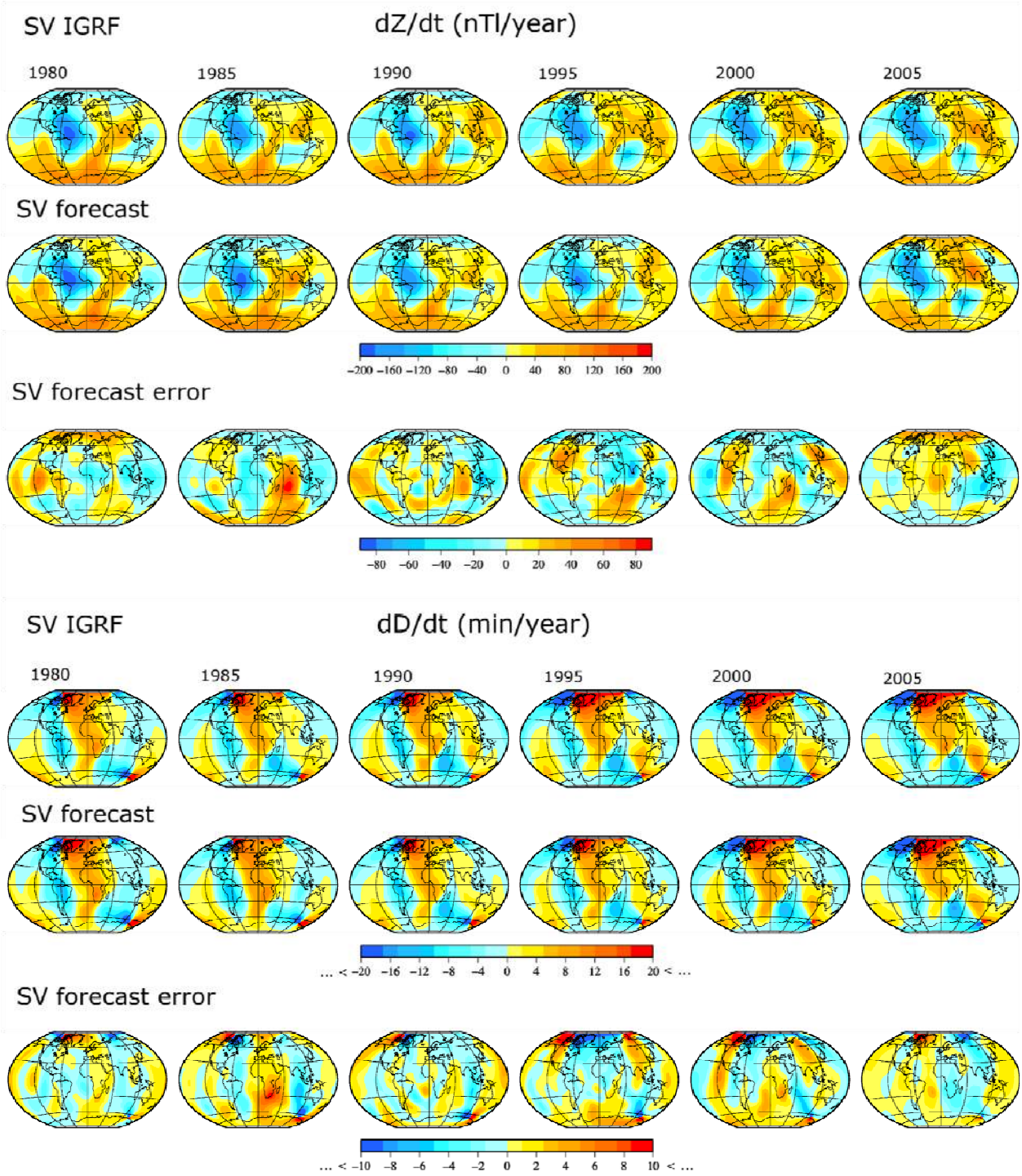

Fig. 2 Comparison of real SV, SV forecast and forecast error for vertical geomagnetic component (Z) and declination (D).

Table 1. Correlation coefficients between SV and SV forecast for three geomagnetic components.

dZ/dt

SV IGRF \ SV forecast	1975	1980	1985	1990	1995	2000	2005	2010	SV IGRF
1980	0.54	**0.56**	0.96						
1985		0.91	**0.97**	0.98					
1990			0.95	**0.94**	0.95				
1995				0.57	**0.51**	0.78			
2000					0.43	**0.17**	0.92		
2005						0.78	**0.63**	0.96	

SV IGRF

dH/dt

SV IGRF \ SV forecast	1975	1980	1985	1990	1995	2000	2005	2010	SV IGRF
1980	0.60	**0.82**	0.95						
1985		0.74	**0.79**	0.96					
1990			0.93	**0.92**	0.95				
1995				0.63	**0.65**	0.83			
2000					0.72	**0.53**	0.86		
2005						0.84	**0.71**	0.99	

SV IGRF

dD/dt

SV IGRF \ SV forecast	1975	1980	1985	1990	1995	2000	2005	2010	SV IGRF
1980	0.83	**0.34**	0.98						
1985		0.87	**0.92**	0.94					
1990			0.95	**0.95**	0.93				
1995				0.94	**0.97**	0.99			
2000					0.95	**0.92**	0.95		
2005						0.99	**0.96**	0.99	

SV IGRF

For declination D, a difference takes place related primarily to the magnetic poles. As seen in Fig. 2, the maximum forecast error of dD/dt is concentrated in the North magnetic Pole region, but a non-negligible error extends over all considered territory as a «wide strip». It produces the observed extreme values of the forecast error, up to 40' per year, in the north Russia and the adjacent waters. At the same time near the South magnetic Pole the error forms a compact area, and a value and sign of the forecast error change from epoch to epoch.

Statistical characteristics of SV component spatial distribution

To estimate how an existence of a stable focus at SV spatial structure influences the statistical and correlation characteristics of the SV forecast, we calculated average values, standard deviations and extreme values. The statistical characteristics of the forecast error (for dZ/dt and dD/dt) obtained for each of study regions are shown in Fig. 3. As one can see, in all parameters, except the average, the SV forecast error of Z component for the region 5 stands apart. The average value for regions 1 and 3 was predicted worst of all

parameters during different epochs. For the region 4 the average value of forecast error varies around zero, as it is for poles and for the region 5.

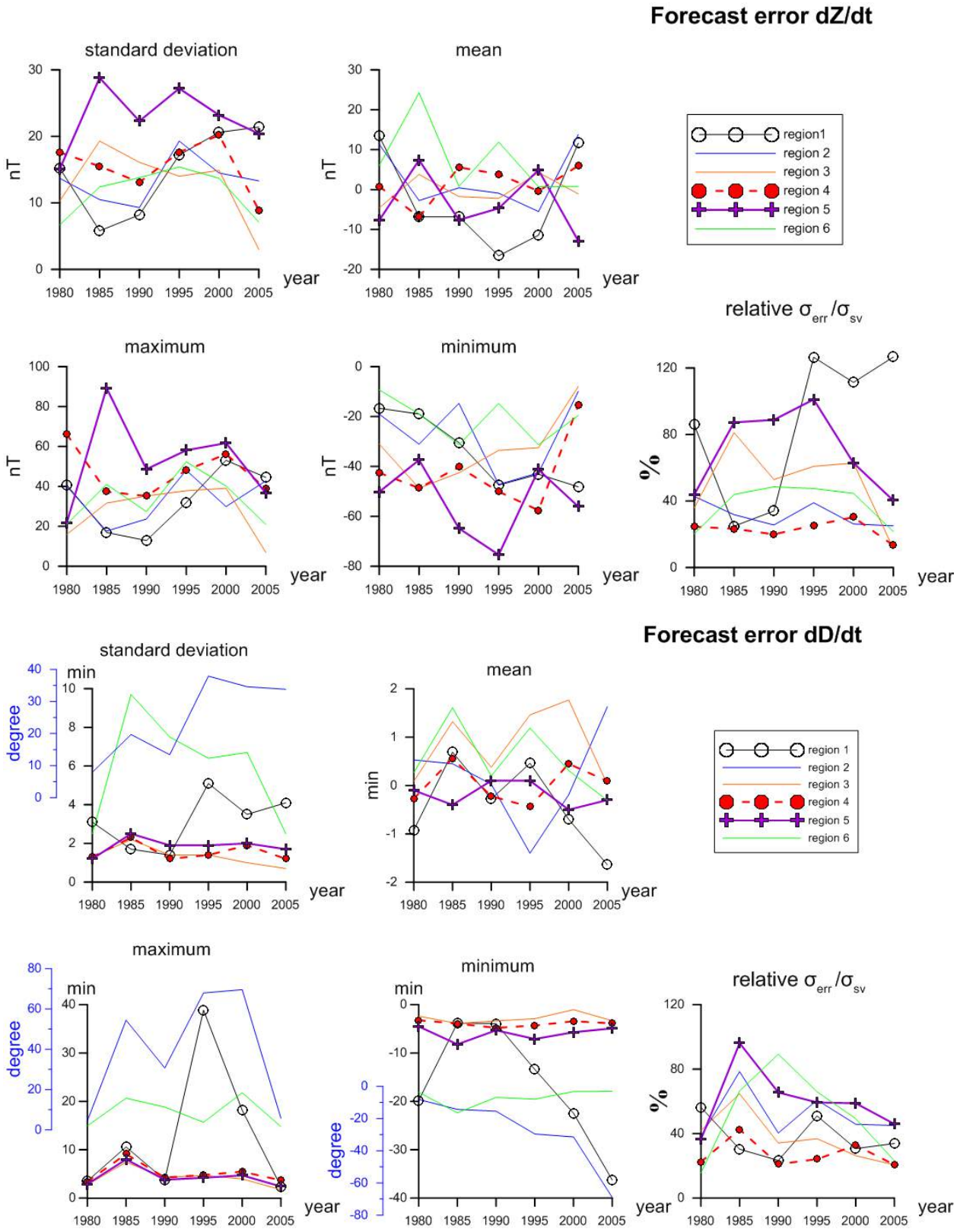

Fig. 3 The average characteristics of SV forecast error spatial structure for Z and D components for all regions.

In terms of the standard deviation of an error (σ_{err}), the existence of large anomaly does not provide any advantage in the accuracy of forecast. As one see from Fig. 3, the standard deviation of the error obtained for the region 4, is comparable with the respective values for the regions 2, 3 and 6. The maximum

σ_{err} is obtained for the region 5. It should be noted that σ_{err} for the region 1 has the minimum values only for the 1985 - 1995 epochs, and since 2000 it approaches a maximum. Since the standard deviation of SV (σ_{SV}) for the region 4 is determined by the powerful Brazilian anomaly, the ratio σ_{err}/σ_{sv} for this region is minimum, but it remains comparable with the similar value for the polar regions 2 and 6. The value of therelative error for the region 1, including territory of Russia, is particularly large (except for the epochs 1985 and 1990), it reaches 126%. The Brazilian anomaly region also shows some extreme values.

A similar result is obtained for the SV forecast for H component. The existence of a large SV anomaly does not give any advantage in terms of the accuracy of SV forecast for D component as well.

Conclusions

Despite an improvement of SV forecast methods, the SV spatial structure correlates best with the SV of the previous epoch. The change of SV anomalies is predicted with the largest error for two regions: the region including the territory of Russia and adjacent waters, and the near-equatorial region in east hemisphere. The SV spatial structure in these regions is characterized by short-lived foci of variable shape and small size. The existence of a large anomaly in the SV spatial structure reduces only the level of forecast error of the average value and the ratio σ_{err}/σ_{sv}.

For the region 1 including territory of Russia and adjacent waters the standard deviation of SV forecast error (σ_{err}) is comparable with the SV standard deviation (σ_{sv}), and during certain epochs even exceeds it. The extreme values of the forecast error for D component during certain epochs exceed ±40′ per year. The spatial structuring of the forecast error suggests that the observed SV is an integrated result of independent change of parameters of certain currents of different scale in the liquid core of the Earth.

The increase in the SV prediction accuracy at this stage can only be achieved by a correction of forecast coefficients between epochs from IGRF generations based on magnetic observatories data and repeat stations data at intervals not more than 2 years.

We propose that the topographic heterogeneity of the core-mantle boundary which presently remains a subject of discussion could play an important role in the formation of the SV spatial structure.

References

Hulot G., Lhuillier F., Aubert J. (2010), Earth's dynamo limit of predictability, *Geophys. Res. Lett.*, 37, L06305.

Kuang W., Tangborn A., Wei Z., Sabaka T. (2009), Constraining a numerical geodynamo model with 100 years of surface observations, *Geophys. J. Int.*, 179, 1458–1468.

EFFECT OF HETEROGENEITIES IN THE LOWER MANTLE STRUCTURE ON THE FORMATION OF SOME SECULAR VARIATION FOCI

I.M. Demina, S.S. Bricheva, Yu.G. Farafonova

St. Petersburg Branch of N.V. Pushkov Institute of Terrestrial Magnetism, Ionosphere, and Radiowave Propagation (SPbF IZMIRAN), St.-Petersburg, 199034, Universitetskaya 5, Russia, e-mail: dim@izmiran.spb.ru

Abstract. In this paper we consider a region which is at different times characterized by well-known foci of the main magnetic field of the Earth (MGMF) secular variation: Europe and the Caspian. Previously, on the basis of a macro model of MGMF sources the impact of the parameters changes for the different scale sources on the secular variation spatial structure was studied. The formation and decay of the considered secular variation foci proved to be due to the parameters change of two particular sources of the third order of smallness, located at the core-mantle boundary. This effect was also observed in the records of all nearby magnetic observatories. The reasons underlying this change of the sources parameters however remained unclear. In this work we compare visible trajectories of these sources to different models of the lower mantle structure, based on seismic tomography data. As a result, we obtain that density and temperature heterogeneities of the lower mantle have the decisive influence on the change of sources parameters. This result coincides with that obtained earlier for the Caribbean region.

Introduction

The local foci in spatial distribution of the secular variation (SV) components of the main geomagnetic field (MGMF) are primarily generated by changes in the core-mantle boundary flow structure. Previously, we investigated the degree of influence of different scale sources on SV using a macro model of MGMF sources developed by us [Demina et al., 2008b]. Results of this study as well as an analysis of the spatial structure of SV forecast error [Demina and Bricheva, 2014] show that SV anomalies can be considered as an integral result of change of several sources, including those with a magnetic moment three orders of magnitude less than the magnetic moment of the main dipole. However, in some cases, the influence of sources of such scale can be identified in the SV spatial structure. The question about the reasons of these changes is still open. Previously we considered as possible influencing factors the heterogeneity of the lower mantle structure and the topography of the core-mantle boundary [Demina and Soldatov, 2012, Demina, 2014].

Formulation of the problem and the data used

In this work we consider the area including the well-known SV foci: Europe and the Caspian. Demina et al. [2008a] have shown how the change of parameters of two sources of the third order of smallness located at the core-mantle boundary can be traced in the records of all surrounding magnetic observatories. Since the size of SV anomalies created by sources of the third order of smallness is significantly less than the size of anomalies created by large-scale sources, to estimate the influence of the former it is necessary to detect their contribution to SV. For this purpose we calculated the SV components depending on the large-scale sources and subtracted the obtained result from the SV components calculated from the IGRF model. The residuals can then be compared with SV depending on the selected sources of the third order. So one can estimate an influence of each of them on the SV structure in different epochs and compare with changes of corresponding magnetic parameters. Then, using a 3D model of the lower mantle structure, one can estimate the extent of its influence on these changes, as it has been done for the Caribbean region [Demina and Soldatov, 2012, Demina, 2014].

Results

For the comparison, we have selected two sources with the magnetic moment of the 3rd order of smallness with respect to the main dipole. For the sake of definiteness, we have arbitrarily numbered them 17^{th} and 18^{th} for eastern and western one, respectively. SV anomalies generated by these sources are located in the area of well-known SV foci. For the selected area we calculate SV components for the period 1900-2010 from the coefficients of IGRF. Then we calculate the total contribution to SV from large-scale sources,

for which the size of the anomalies produced by them is much larger than area considered. The difference between SV-IGRF and SV of large-scale sources represents a total contribution of small-scale sources, including the two that we explore and compare. The spatial structure of Z - components of SV in these three variants for a number of epochs is shown in Fig. 1. A contribution from the changing parameters of the two selected sources is superimposed on the spatial structure of SV differences.

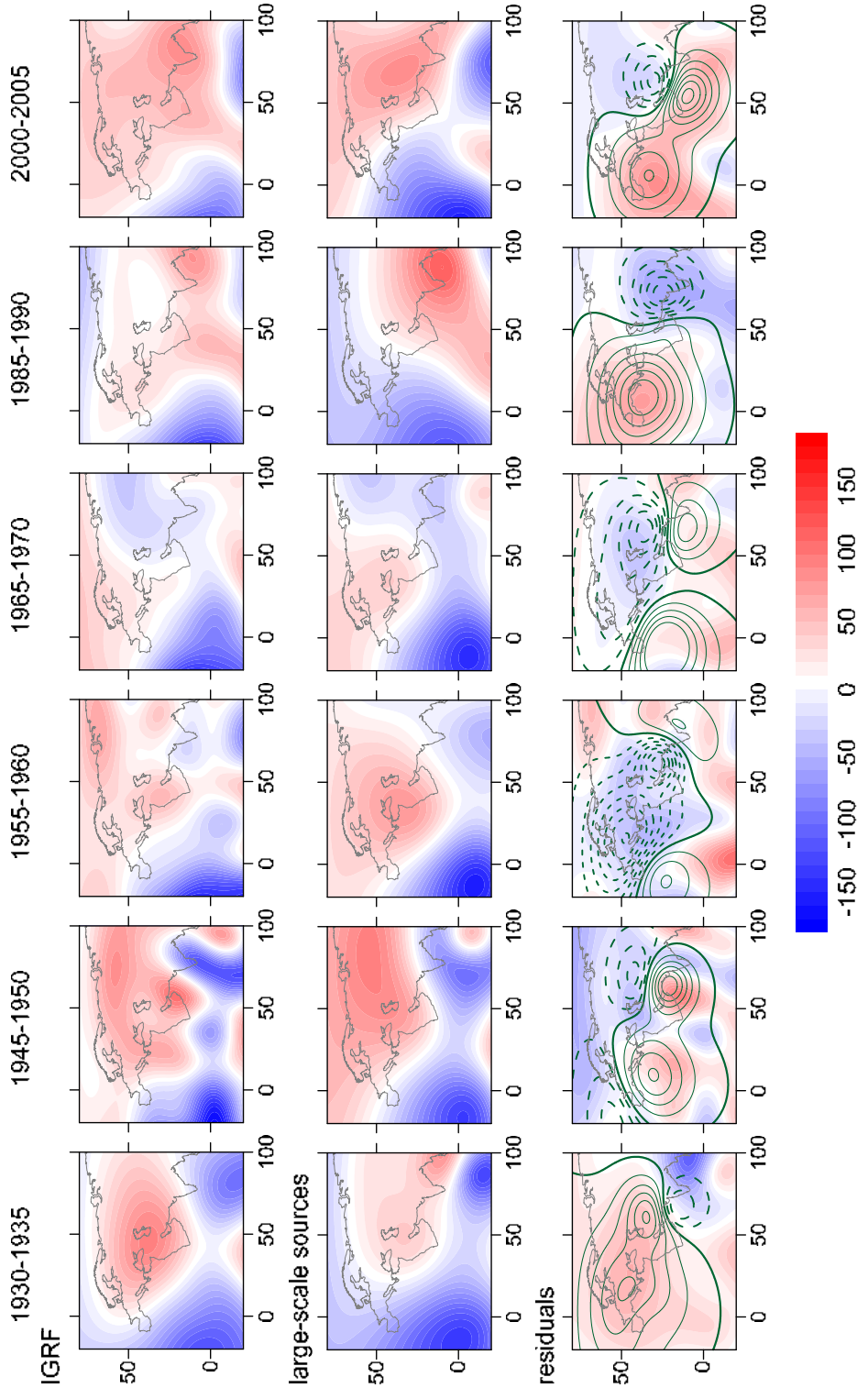

Fig. 1 A comparison of the difference between SV-IGRF and SV of large-scale sources with the SV of 17 and 18 sources. Isolines on the residual charts are traced with 5 nT spacing, the positive values are shown by solid lines, the negative values are shown by dashed lines, the bold solid line denotes zero value.

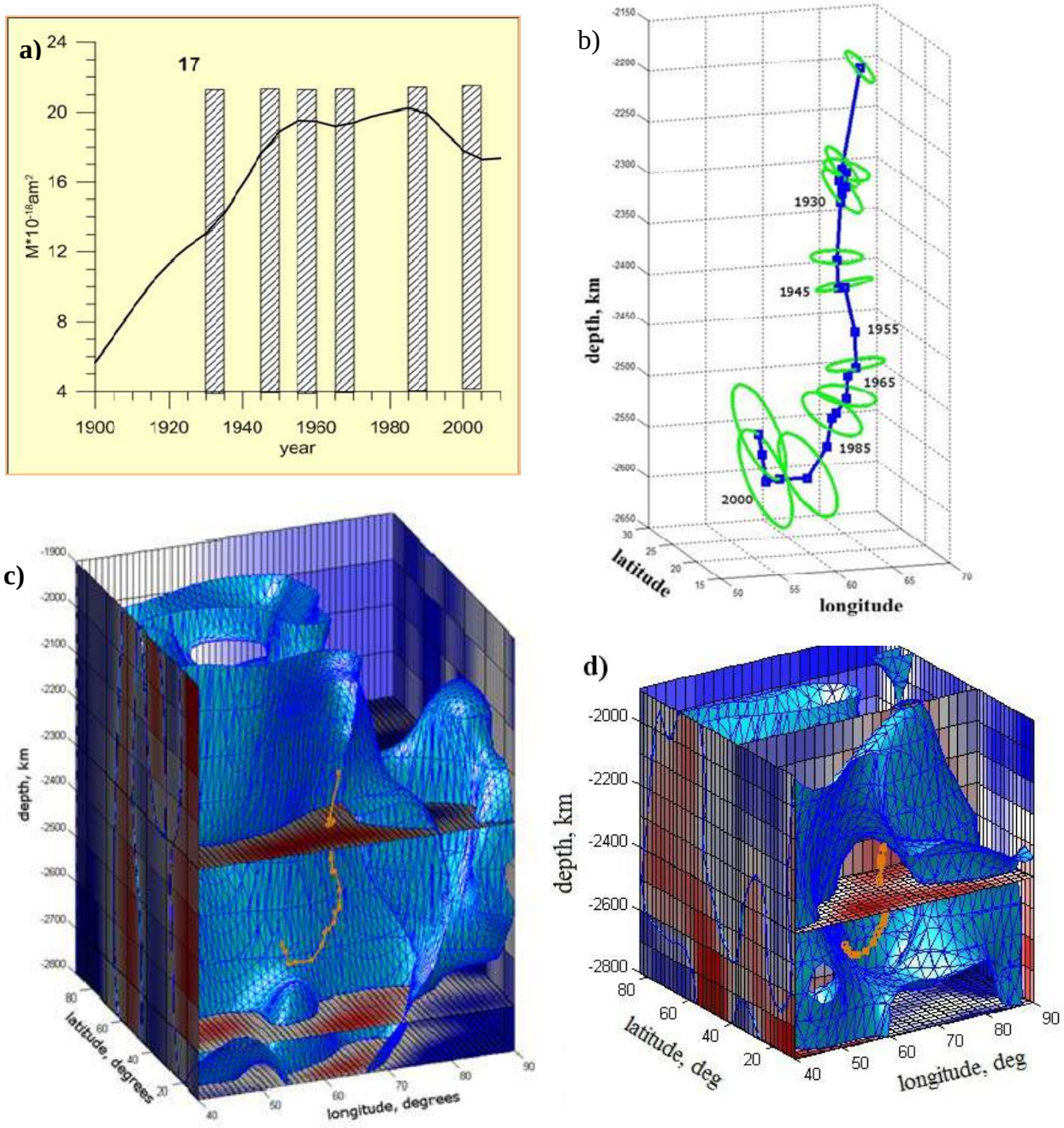

Fig. 2 Change of the 17th source parameters and a comparison with the lower mantle structure.
a) – change of the magnetic moment, time intervals presented in Fig. 1 are marked by hatching. b) – the 3-D trajectory of source, orientation of the magnetic moment vector is perpendicular to the circles plane. c) and d) – the 3-D presentation of velocity heterogeneities of the mantle and the trajectory of source. The areas of lower velocities are shown in red, the areas of higher velocities in blue, zero surfaces are shown by light blue color, the source trajectory is shown by light brown color. (c) is the S20 model of mantle structure [Ritsema et al., 2004] and (d) is the SAW24 model [Megnin and Romanowicz, 2000].

Changes in the magnetic moment magnitude for the 17th source and its trajectory are shown in Fig. 2 and for the 18th source in Fig. 3. Circles, modeling the source geometry are superimposed on the tracks; some points are omitted for the sake of clarity. Orientation of the circles reflects a direction of the magnetic moment vector. Two models, S20 [Ritsema et al., 2004] and SAW24 [Megnin and Romanowicz, 2000], were selected for comparison with the lower mantle structure. Figs. 2c, d and 3c, d, show the lower mantle structure for 17th and 18th sources, respectively, as a 3-D surface, separating the zone of higher and lower velocities. Trajectories of the sources are embedded in the respective volumes.

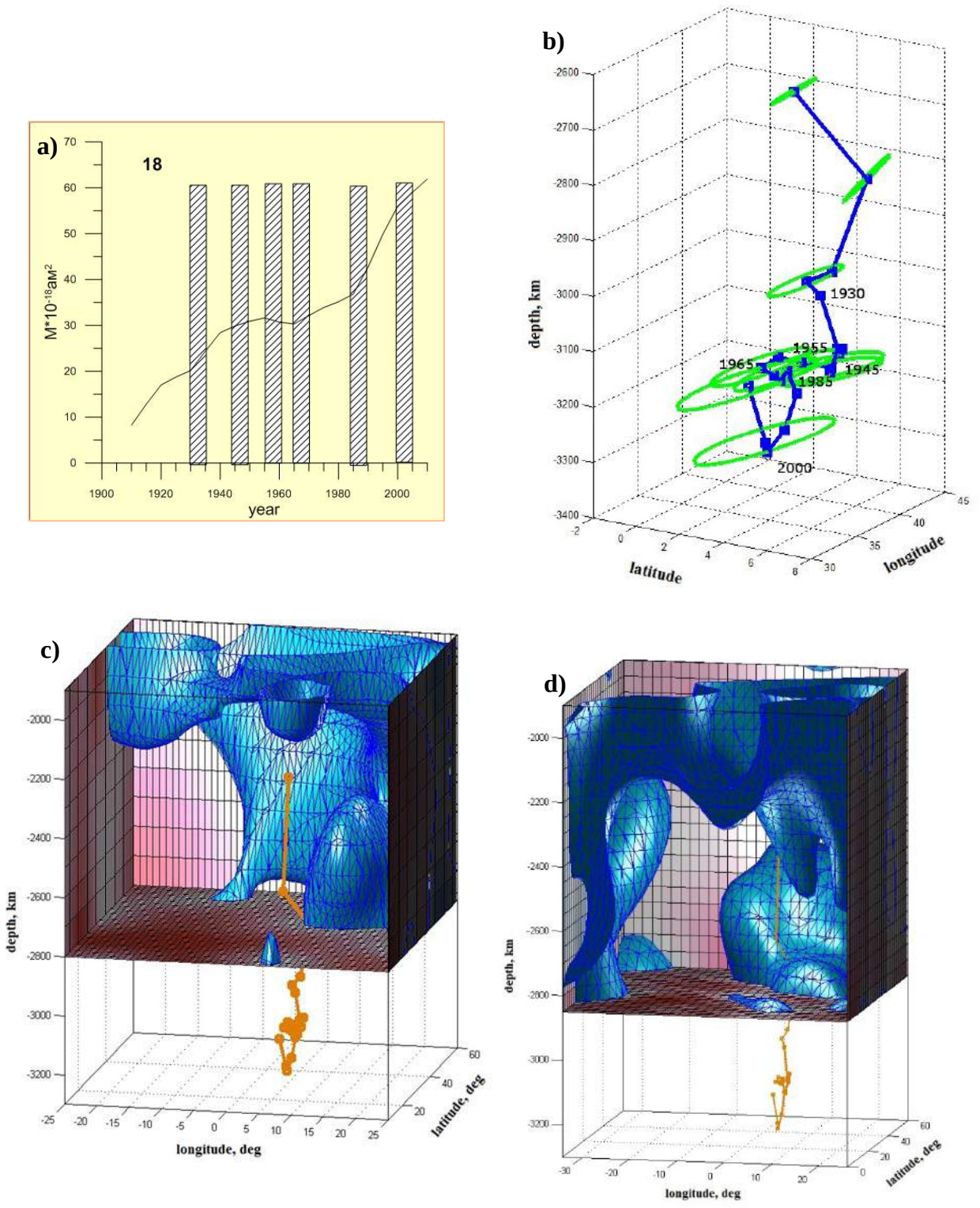

Fig. 3 Change of the 18th source parameters and a comparison with the lower mantle structure. The notation is as in Fig. 2.

Discussion

One can see that the contribution to SV from the two selected sources is determined either by change in the magnitude of the source magnetic moment, which is usually accompanied by a change in depth, or by changing the shape of its trajectory. The trajectory of the 17th source lies entirely in the lower mantle. Its

shape is in a good agreement with models of the lower mantle structure, based on seismic tomography. The trajectory of the 18th source already in the beginning of the considered period crosses the core-mantle boundary, but it's most complex part lies just below the latter, as observed also for the Caribbean region [Demina, 2014]. However, it is clear that this trajectory connects the regions with higher velocities, as if they continue below the deepest level of seismic models. Since in the area traversed by the 18th source trajectory so-called cemeteries of lithospheric plates are believed to exist [Engebretson et al., 1992], it can be assumed that in these areas the topography of the core-mantle boundary is characterized by significant depth heterogeneities that may have a considerable effect on the structure of currents in the liquid core.

Conclusions

In this work, we examined the trajectories of the two possible secular variation sources in comparison with different models of the lower mantle structure, based on seismic tomography. As a result, we obtain that the velocity heterogeneities (heterogeneities of the density) in the lower mantle have a strong influence on the change of the parameters of the small-scale MGMF sources located close to the core-mantle boundary. This result coincides with that obtained previously for the Caribbean.

References

Demina, I. M., Nikitina L. V. and Farafonova Yu. G. (2008a) Secular Variations in the Main Geomagnetic Field in the Scope of the Dynamic Model of Field Sources, *Geomagn. Aeron.*, 48(4), 567–575.

Demina, I. M., Koroleva, T. Yu., and Farafonova, Yu G. (2008b) Anomalies of the secular variations of the main geomagnetic field in the context of the hierarchic dipole model, 2008, *Geomagn. Aeron.,* 48(6), 812–821.

Demina I., Soldatov V. (2012) Structure of the lowermost mantle and secular variation of the main geomagnetic field. *Proceedings of the International Conference "Problem of Geocosmos"*, St.-Petersburg, 2012.

Demina, I. M. (2014) Topographic heterogeneity of the core–mantle boundary in subduction zones and its effect on kinematics of main geomagnetic field sources, *Geomagn. Aeron.*, 54(2), 253–262.

Demina I., Bricheva S. (2014) Correlation properties of the secular variation forecast, In this proceedings.

Engebretson, D. C., Kelley, K. P., Cashman, H. J. and Richards, M. A. (1992) 180 million years of subduction, *GSA Today*, 2, 93–100.

Megnin, C., and Romanowicz, B. (2000) The three-dimensional shear velocity structure of the mantle from the inversion of body, surface and higher modes waveforms, *Geophys. J. Int*, 143, 709-728.

Ritsema, J., van Heijst, H. J. and Woodhouse J. H. (2004) Global transition zone tomography, *J. Geophys. Res*., 109, B02302.

GEODYNAMO-LIKE SCALING LAWS IN PLANETS, GEOMAGNETIC AND PALEOMAGNETIC PERIODICITIES

S.V. Starchenko

IZMIRAN, Kaluzhskoe hwy 4, Troitsk, Moscow, 142190, Russia; e-mail: sstarchenko@mail.ru

Abstract. Scaling laws for hydromagnetic dynamo in planets express the characteristic strength of the magnetic field through the primary quantities, such as size of the conductive core of a planet, angular rotation rate, electrical conductivity and energy flows. Most of the scaling laws proposed earlier are based only on observations and assumptions about force balances. Recent approaches, including mine, to fully take into account the energy and induction balance aim to express such important dynamo characteristics as forces, magnitudes, energies, scales and orientations of hydromagnetic fields in terms of primary quantities. Direct numerical simulations of the hydromagnetic dynamo in a fairly wide range of parameters allowed a direct test of such laws for the first time. The obtained numerical geodynamo-like results for the Earth, Jupiter and partially Saturn postulated not identified previously, analytically simplest law which predicts that the field strength depends only on the specific convection energy density and on the size of the dynamo area. This simplest and already widely used law is analytically justified here along with other previously known and some new laws. This analysis identifies the physical mechanisms determining geomagnetic periodicities for jerks, secular variation and inversions. Average interval between the inversions is found to be roughly proportional to the intensity of the geomagnetic field as suggested by some paleomagnetic studies. Possible dynamos in Mercury, Ganymede, Uranus and Neptune are also discussed.

1. Introduction

The aim of this work is to identify scaling laws associating the magnetic field strength and, as incidentally detected, other key features of planetary hydrodynamic dynamos to fundamental properties of a planet and the region where the dynamo operates. It is not immediately obvious which fundamental quantities play a key role, and, to identify the most suitable candidates, I analyze known characteristics of the observed planetary magnetic fields and dimensionless quantities characterizing the initial similarity criteria. So, the basic fundamental quantites considered here to determine the operation of the dynamo are as follows: a radius R of an electrically conductive liquid core of the planet, an electrical conductivity σ, a density ρ of the planetary core, an angular rotation rate of the planet Ω, and the specific (measured in watts per kilogram) energy density of convective transport F. It is worth noting however, that the same scaling law would hardly be applicable to all planets with an active dynamo, because there are significant differences between the observed magnetic fields in different groups of planets and accordingly we should expect significant differences in the work of their dynamos.

Table 1. Known scaling laws for planetary magnetism

№	Scaling law	Reference	Comment
1	$B_p R_p^3 \propto (\rho\Omega R_p^5)^a$	see [Russell, 1978]	Phenomenological law of Bode
2	$B \propto \sqrt{\rho} R\Omega$	[Busse, 1976]	Proportional to velocity of rotation
3	$B \propto \sqrt{\rho\Omega/\sigma}$	[Stewenson, 1979]	Elsasser number from formula (3) is of the order 1
4	$B \propto R\sqrt{\rho\sigma F}$	[Stewenson, 1984]	For relatively small F
5	$B \propto \sqrt{\rho\Omega}(R^4 F)^{1/6}$	[Curtis and Ness, 1986]	The mixing-length theory of stars
6	$B \propto \sqrt{\rho R}(\Omega^3/\sigma)^{1/4}$	[Mizutani et al. 1992]	Combination of No 2 and 3 laws
7	$B \propto \sqrt{\rho R}\Omega$	[Sano, 1993]	As 2, but with a different "turbulent" scale.

Table 1 (*continuation*)

№	Scaling law	Reference	Comment
8	$B \propto \sqrt{\rho R}(\Omega F)^{1/4}$	[Starchenko and Jones, 2002]	Energy accounting convective transport and MAC balance of forces
9	$B \propto \sqrt{\rho}(RF)^{1/3}$	Christensen and Aubert [2006] gave their own justification.	See the other analytical justifications here.

Here the magnetic field B_p at the surface of the planet (with radius R_p) roughly defines the dipole moment

$$M \approx B_p R_p^3 \ . \qquad (1)$$

2. Observable magnetic fields and dynamo-parameters in planets

Table 2 further shows the observed and reliably measured hydromagnetic parameters in the deep planetary interiors, which are then discussed for each planet.

Table 2. Observed and reliably estimated hydromagnetic parameters in planets

	Earth	Jupiter	Saturn	Uranus	Neptune	Mercury	Ganymede
Ω [1/Ms]	72.9	176	164	101	109	1.24	99.9
***R* [Mm]**	3.48	56	30	17	16	1.7	0.7
ρ [Mg/m^3]	11	1.8	1.8	2	2	10	8
***D* [μT]**	262	1150	250	100	70	1	70
***B* [μT]**	800	3500	750	1000	700	10	200
□ [MS/m]	1-2	0.06-0.2	0.06-0.2	0.002-0.02	0.002-0.02	1-2	1-2
Λ	0.8-1.6	2.3-7	0.1-0.3	0.01-0.1	0.004-0.04	0.006-0.012	0.06-0.12
***F* [πW/kg]**	**0.1**-1	**20**-200	**10**-100	**1**-10	**4**-40	~0.1	~0.06
$\delta = \frac{F}{R^2\Omega^3}$	$\frac{\mathbf{2.1}-21}{10^{14}}$	$\frac{\mathbf{0.1}-1}{10^{14}}$	$\frac{\mathbf{0.3}-3}{10^{14}}$	$\frac{\mathbf{0.3}-3}{10^{14}}$	$\frac{\mathbf{1.3}-13}{10^{14}}$	$\sim\frac{2}{10^8}$	$\sim\frac{1}{10^{13}}$

The main geomagnetic field generated in the Earth's liquid core is the only available to us planetary magnetic field investigated in time and space in sufficient detail. The Earth's core itself is in turn an area of active current dynamo action, which properties can be objectively evaluated on the basis of thermal, seismic and other geodynamic studies. Therefore it is natural to choose the key parameters of a hydromagnetic planetary dynamo based on the characteristics of the geodynamo. The first option is the angular rotation rate Ω, which is most reliably measured for all the planets in Table 2 and appears in the seven (out of 9) scaling laws in Table 1. Generally, as will be shown later, Ω always has a significant impact on the hydromagnetism. The second and third parameters are radius R of the liquid conductive core and its average density ρ as determined reliably enough from astronomical observations and models of the internal structure of the planet. For the Earth, they are determined with high accuracy from seismic data, see, e.g., [Anderson, 1989; Braginsky and Roberts, 1995].

The observed geomagnetic field is dominated by the dipole component. At the core radius R RMS intensity of dipole magnetic field D is expressed in terms of the observed dipole moment M

$$D = \sqrt{2}\mu_0 M / 4\pi R^3 . \qquad (2)$$

Corresponding numerical value of D is shown in Table 2. For use in scaling laws this must be converted to the RMS value of the magnetic field B averaged over the entire volume of the core. Since we are interested only in order of magnitude estimates, the dominant dipole further reduces to $B = 3D$ [Olson and Christensen, 2006]. Also, it must be noted that such important parameter as the electrical conductivity is determined only with an accuracy of tens of percent. Moreover, it has only recently been estimated for the Earth with such

precision from first principles and experiments [Pozzo et al., 2012; Gomi et al., 2013], and before that for decades several times lower value was used.

The above parameters can be combined to produce the Elsasser number

$$\Lambda = \sigma B^2 / \rho\Omega, \quad (3)$$

which characterizes the ratio of the magnetic Lorentz force to the dominant, rotation defined Coriolis force. For the Earth, this number is close to unity, which corresponds to the scaling law number 3 of Table 1, but does not necessarily confirm it.

Last, and perhaps the most important parameter in Table 2 is the specific power density of convective energy transport *F*, which characterizes the energy available for the dynamo. It can be estimated from the outgoing heat flux of the planet and out of the available models of the internal structure. It is necessary to take into account the efficiency of the dynamo and the possibility of not only heat, but also the composition as the excitation mechanism of convection, which drives a dynamo. As a result, even for known estimates for the Earth, *F* varies by up to factor of ten, cf. [Starchenko and Jones, 2002] and [Olson and Christensen, 2006]. The lower range, highlighted in bold, is generally preferred [Christensen, 2010].

We now formulate the most important criterion of similarity, the rotational Rayleigh number

$$\delta = F / R^2\Omega^3, \quad (4)$$

which is very small for all the planets and appears naturally in three most reliable scaling laws in Table 1. Accordingly, we can further assume that all the planets rotate quickly and the impact of the transport coefficients on the typical values is negligibly small.

The powerful magnetic field of Jupiter is similar to the geomagnetic field by the dominance of the dipole component and the axial symmetry. The magnetic field of Saturn is nearly symmetric with respect to the rotation axis, but in other aspects quite similar to those of the Earth and Jupiter. Therefore, for Jupiter and Saturn the internal magnetic field *B* in the dynamo action can be estimated like for the Earth. The values of other dynamo parameters for these planets are taken from [Nellis, 2000; Starchenko and Jones, 2002; Fortney and Hubbard, 2003; Dougherty et al., 2005].

The magnetic moment of Uranus is tilted from the rotation axis by 60 degrees, and that of Neptune by 45 degrees as observed by the Voyager spacecraft (see an explanation of this phenomenon on the basis of successful predictions for Neptune [Ruzmaikin and Starchenko, 1991]). Besides, in these planets the dipole component of the magnetic field is not dominant even at the surface. Accordingly, in the approximation of the average magnetic field in the dynamo action I have used the relation B=10D following [Olson and Christensen, 2006; Christensen, 2010], and the other parameters are taken from [Podolak et al., 1991; Hubbard et al., 1995]. Obviously, in the first place, because of their low "ice" conductivity these planets are so substantially different from the Earth, Jupiter and Saturn in the structure of their magnetic field. Accordingly, based on the low Elsasser number, a different dynamo mechanism in Uranus and Neptune should be expected.

The weakest magnetic field generated in the planetary interior was recorded for Mercury. Its highly uncertain estimated dynamo parameters are taken from [Christensen, 2006, 2010]. This planet is significantly different from all the other planets in both similarity criteria, which should indicate a special mechanism of its dynamo.

Quite substantial magnetic field, generated in the deep interior was recorded by a spacecraft in one of the moons of Jupiter, Ganymede. Its very roughly estimated dynamo parameters are taken from [Kivelson et al., 2002].

3. Tests and scaling laws from numerical simulations

Christensen [2010] presents the results of testing scaling laws in Table 1 on the set of geodynamo-like numerical models for all possible parameters. Geodynamo similarity implies the presence of a dominant dipole component and the possibility of obtaining numerical approximations to the observed value of the magnetic field. Thus the Elsasser number Λ (3) was varied in a wide range, including the values typical for the geodynamo (Table 2). The rotational Rayleigh number δ (4), though quite small (less than 10^{-3}), even in the most extreme numerical models was four or more orders of magnitude larger than values shown in Table 2. Nevertheless, even such a numerical verification explicitly rejected scaling laws 1-4, 6-7 of Table 1. Common to all the remaining laws is the energy estimate [Starchenko and Jones, 2002] for convection power sources:

$$VA=F. \quad (5)$$

Here V is a typical convection velocity, and A is a typical acceleration due to buoyancy force. Equation (5) can be derived from dimensional considerations. Namely, it is obtained by neglecting the effects of diffusion

in the heat and mass transfer equations within the general system of planetary dynamo equations [Braginsky and Roberts, 1995; Starchenko and Jones, 2002]. The derivation of the scaling law further neglects other effects related to the viscosity of the transport and magnetic diffusion.

In the derivation of the law 5 of Table 1, the acceleration of inertia $(\mathbf{V}\cdot\nabla)\mathbf{V}$ is considered comparable to the Archimedes acceleration **A** at the full scale *R* of the planet's core, leading to $V^2/R = A$, which, together with equation (5) completely determines the typical velocity and acceleration as

$$V = (RF)^{1/3} = \delta^{1/3} R\Omega,\ A = (F^2/R)^{1/3} = \delta^{2/3} R\Omega^2. \quad (6)$$

Assuming that everywhere in the core the Coriolis force $\propto \rho V\Omega$ is comparable to the magnetic Lorentz force $\propto B^2/\mu_0 R$, we obtain the law 5 of Table 1, which can be written for the magnetic energy

$$B^2/\mu_0 = \rho\Omega R^{4/3} F^{1/3} = \delta^{1/3}\rho R^2\Omega^2. \quad (7)$$

This result is confirmed numerically in [Christensen, 2010], but the author, in my opinion, is not correct using the velocity value from (6) in the analytical justification of his most significant law 9 in Table 1.

In the derivation of the law 8 of [Starchenko and Jones, 2002], the characteristic scale of the magnetic field was fixed at a quantity ~*d*=*R*/20, justified by considerations about the nature of the dynamo threshold and the majority of numerical studies at that time. Also the MAC balance was taken the in its simplest form $B^2/\mu_0 d = \rho A = \rho\Omega V$. All this, together with (5) gave

$$V = \sqrt{F/\Omega} = \delta^{1/2} R\Omega,\ A = \sqrt{F\Omega} = \delta^{1/2} R\Omega^3,\ B^2/\mu_0 = \rho\sqrt{F\Omega}R/20 = \delta^{1/2}\rho R^2\Omega^2/20. \quad (8)$$

Exponent 1/2 in the last expression for the magnetic energy density (8) represents the best exponent 0.677 obtained from numerical models [Christensen, 2010] slightly better than the 1/3 value from (7),. Ideal correspondence occurs when the exponent is 2/3, which makes it independent of the angular velocity of rotation of the similarity law 9 of Table 1, for which the magnetic energy density is written as:

$$B^2/\mu_0 = \rho(RF)^{2/3} = \delta^{2/3}\rho R^2\Omega^2. \quad (9)$$

The geomagnetic field and the magnetic field of Jupiter from Table 2 are very well interpreted by this law. Slightly worse, but within the margin of error (9), the magnetic field of Saturn is described. For other planets some further assumptions are required to convincingly satisfy (9). Only typical velocity *V* has been investigated numerically among those values. For it, the best exponent of δ was 0.411.

4. Analytic justification of the main scaling laws

To estimate the impact of the Coriolis force, let us apply the rotor operation to the standard equation of motion. The resulting equation establishes the equality of rotor of the dominant Coriolis acceleration $\Omega\partial\mathbf{V}/\partial z$ and rotor of the acceleration caused by Archimedes, Lorentz, inertia and viscosity forces (height *z* is measured from the equatorial plane along the axis of rotation). Equating by the order of magnitude $\Omega\partial\mathbf{V}/\partial z$ to $\nabla\times\mathbf{A}$, we obtain

$$\Omega V/R = A/h. \quad (10)$$

Estimate (10) is obtained assuming the dominance of rotation, that is, for nearly two-dimensional convection [Braginsky and Roberts, 1995; Starchenko, 1999]. The effect of the height *z* is extremely weak so that in the left-hand side of (10) the derivative can be evaluated using the planet's core radius *R*, and in the right-hand side the rotor is evaluated using the smallness of the convection scale $h << R$.

Considering now that the inertia acceleration $(\mathbf{V}\cdot\nabla)\mathbf{V}$ is comparable with the Archimedes acceleration **A** on scale *h*, we obtain $V^2/h = A$, and together with (5) and (10) this gives [Rhines, 1975] a solution:

$$h = \delta^{1/5} R,\ A = \delta^{3/5} R\Omega^2,\ V = \delta^{2/5} R\Omega. \quad (11)$$

Testing numerical models [Christensen, 2010] confirms the scaling law (11) for the velocity *V* with high accuracy (numerically obtained exponent is 0.411, which is very close to 2/5 in formula (11)). Similar 2/5-exponent dependence is confirmed by [Glatzmaier and Roberts, 1997; Takahashi et al., 2008]. Thus we need new numerical experiments to verify laws for a typical hydrodynamic scale *h* and acceleration *A* from (11).

Consider the radial component of the rotor from the equations of motion without the viscous terms:

$$\Omega\frac{\partial V_r}{\partial z} = \hat{\mathbf{r}}\cdot\nabla\times\left(\rho\frac{D\mathbf{V}}{Dt} + \frac{\mathbf{B}\times\nabla\times\mathbf{B}}{\mu_0}\right)/\rho. \quad (12)$$

This equation relates the velocity vector **V** and the magnetic field **B**, but the buoyancy acceleration **A** is absent, because it is parallel to $\hat{\mathbf{r}}$. The dominant term ~Ω in (12) can be removed via integration along the

axis of rotation (z-coordinate) from one boundary to another, because V_r=0 there. Thus, there are only two terms under the rotor on the right side of (12). Balancing these terms in order of magnitude, we obtain

$$B^2 / \mu_0 \rho d^2 = V^2 / h^2 \ . \quad (13)$$

This means that the ratio of magnetic energy to kinetic energy equals to the ratio of the squares of their corresponding scales $B^2 / \mu_0 \rho V^2 = (d/h)^2$, that can be verified by future numerical experiments.

We now use the electric field vector **E** in the Ohm's law

$$\nabla \times \mathbf{B} / \mu_0 \sigma = \mathbf{E} + \mathbf{V} \times \mathbf{B} . \quad (14)$$

Neglecting the magnetic diffusivity ~$1/\mu_0\sigma$ for $r_m=\mu\sigma Vd >>1$ (confirmed further), we obtain

$$E = sVB . \quad (15)$$

In this consideration, s is typically small (to be confirmed below) sine of the angle between the velocity **V** and magnetic field **B**. Therefore to make **E** in the Faraday's law small

$$\partial \mathbf{B} / \partial t = -\nabla \times \mathbf{E} \quad (16)$$

the correspondent typical 'slow' time should be as large as possible, that is, of the order R/V, leading to

$$VB / R = E / d \ . \quad (17)$$

Now relying on the fact that the magnetic scale far exceeds the hydrodynamic scale $d>>h$ (to be confirmed below) let us use the induction equation without magnetic diffusion

$$\partial \mathbf{B} / \partial t \cong \nabla \times (\mathbf{V} \times \mathbf{B}) \quad (18)$$

to estimate a 'faster' typical time as h/sV. It is natural to use this time in assessing the 'fast' balance between the work of the Archimedes buoyancy force and the work of generating a magnetic field:

$$sVB^2 / \mu_0 h = \rho A V \ . \quad (19)$$

Solving the equations (13), (15), (17) and (19) we obtain not only an analytic justification of the numerical law (9), but also three other previously not studied laws:

$$d = F^{2/15} R^{11/15} / \Omega^{2/5} = \delta^{2/15} R \ , \ s = F^{2/15} / R^{4/15} \Omega^{2/5} = \delta^{2/15} \ , \ E = \delta^{13/15} \sqrt{\mu_0 \rho} R^2 \Omega^2 . \quad (20)$$

In conclusion, we calculate on the basis of the data in Table 2 and analytically justified laws (9), (11) and (20) the numerical values of previously known and new parameters for the geodynamo:

B = 820 μT, V = 0.9 mm/s, h = 6.4 km, d = 52 km, s = 0.015, r_m = 54; (21)

Jupiter: B = 4800 μT, V = 10 mm/s, h = 58 km, d = 570 km, s = 0.01, r_m = 430; (22)

and Saturn: B = 3100 μT, V = 7 mm/s, h = 36 km, d = 340 km, s = 0.011, r_m = 170. (23)

Calculations are made for the bold values in Table 2 and it is evident that all statements made (see above before each of the brackets) in the assumptions of this section are satisfied with a good margin, which indicates the reliability of the present study.

5. Energetically determined geomagnetic periods

Energetically determined geomagnetic periods contain, in fact, only one not so well known parameter F (Table 2), and correspondent scaling laws are discussed in the previous section. Numerically, these periods follow from magnetic, velocity and scale estimations in (21), completed with the known parameters range in accordance with Table 2 as

$$B = (800\text{-}1800)\ \mu\text{T} \Rightarrow V_B = \frac{B}{\sqrt{\mu_0 \rho}} = (7\text{-}15)\ \text{mm/s},\ V = (1\text{-}2)\ \text{mm/s},\ h = (6\text{-}10)\ \text{km},\ d = (50\text{-}70)\ \text{km}. \quad (24)$$

Therefore the turbulent transport coefficient and various periods obtained from typical velocity and scales are:

$\kappa_V = hV/9 = (0.7\text{-}2)\ \text{m}^2/\text{s}$, $h/V = (1\text{-}4)$ months, $d/V = (1\text{-}2)$ yrs, $R/V = (50\text{-}100)$ yrs. (25)

Those turbulent periods could be naturally related to short-time phenomena as jerks etc (2nd and 3rd) and sufficiently longer secular variations (the last), while the Alfven velocity V_B (substituted instead of V) determines a few times smaller values to fill all the observable range.

The turbulent coefficient κ_V from (25) is very close to the magnetic diffusion coefficient $1/\mu_0\sigma = (0.5\text{-}1)\ \text{m}^2/\text{s}$ obtained from the electrical conductivity σ of [Pozzo et al., 2012; Gomi et al., 2013] summarized in Table 2. So both coefficients determine similar long-time periods:

$\mu_0\sigma h^2 = (1\text{-}7)$ yrs, $\mu_0\sigma d^2 = (100\text{-}300)$ yrs, $\mu_0\sigma R^2 = (0.4\text{-}0.8)$ Ma. (26)

The first two periods merge with previously discussed jerks and secular variations, while the latter corresponds very well to known ~ 0.5 Ma average interval between geomagnetic reversals [Ogg et al., 2008]. However this estimated is independent of any physical quantities changing with time, and so should itself

depend on time only weakly. This however contradicts to paleomagnetic record demonstrating wide variations in the average interval between reversals [Shcherbakov, Fabian, 2012].

Thermal diffusion coefficient $\kappa = (10\text{-}20)$ m^2/Ms [Pozzo et al., 2012; Gomi et al., 2013] adds

$$h^2/\kappa = (0.06\text{-}0.3) \text{ Ma}, \quad d^2/\kappa = (4\text{-}20) \text{ Ma}. \qquad (27)$$

The first period ($\sim h^2$) corresponds to the shortest intervals between reversals or excursions, while the second ($\sim d^2$) could be related with the longest intervals [Ogg et al., 2008; Shcherbakov, Fabian, 2012]. Thus, both periods could increase with growing magnetic intensity $B \sim F^{1/3}$ as $h^2 \sim B^{6/5}$ and $d^2 \sim B^{4/5}$ in accordance with (9), (11) and (20). This is confirmed in [Shcherbakov and Sycheva, 2013].

The author is grateful to Andrei Kosterov for careful editing of this paper, which led to a much improved presentation. This work was partly supported by the program number 22 of the RAS Presidium and RFBR grant 13-05-00893-a.

References

Anderson Don L. (1989) *Theory of the Earth.* Blackwell Scientific Publications. 366 p.

Busse F.H. (1976) Generation of planetary magnetism by convection. *Phys. Earth Planet. Inter.* V. 12. P. 350-358.

Braginsky S.I., Roberts P.H. (1995) Equations governing convection in the Earth's core and the geodynamo / *Geophys. Astrophys. Fluid Dynamics.* V. 79. P. 1–97.

Christensen U.R. (2006) A deep dynamo generating Mercury's magnetic field. *Nature*. V. 444. P. 1056–1058.

Christensen U.R., Aubert J. (2006) Scaling properties of convection-driven dynamos in rotating spherical shells and application to planetary magnetic fields. *Geophys. J. Int.* V. 166. P. 97–114.

Christensen U.R., Holzwarth V., Reiners A. (2009) Energy flux determines magnetic field strength of planets and stars. *Nature*. V. 457. P. 167-169.

Christensen U.R. (2010) Dynamo Scaling Laws and Applications to the Planets. *Space Sci Rev.* V. 152. P. 565-590.

Curtis, S.A. Ness, N.F. (1986) Magnetostrophic balance in planetary dynamos: Predictions for Neptune's magnetosphere. *J. Geophys. Res.* V. 91. P. 11003-11008.

Dougherty M.K., Achilleos N., Andre N., et al. (2005) Cassini magnetometer observations during Saturn orbit insertion. *Science*. V. 307. P. 1266–1270.

Fortney J.J., Hubbard W.B. (2003) Phase separation in giant planets: inhomogeneous evolution of Saturn. *Icarus*. V. 164. P. 228–243.

Glatzmaier G.A., Roberts P.H. (1997) Simulating the geodynamo. *Contemporary Physics*. V. 38(4). P. 269–288.

Gomi H., Ohta K., Hirosea K. et al. (2013) The high conductivity of iron and thermal evolution of the Earth's core. *Phys. Earth Planet. Int.* V. 224. P. 88-103.

Hubbard W.B., Podolak M., Stevenson D.J. (1995) The interior of Neptune, Neptune and Triton. *University of Arizona Space Science Series*. P. 109–138.

Kivelson M.G., Khurana K.K., Volwerk M. (2002) The permanent and inductive magnetic moments of Ganymede. Icarus. V. 157. P. 507.

Mizutani, H., Yamamoto, T., Fujimura, A. (1992) A new scaling law of the planetary magnetic fields. *Adv. Space Res.* V. 12. P. 265-279.

Nellis W.J. (2000) Metallization of fluid hydrogen at 140 GPa (1.4Mbar): implications for Jupiter. *Planet. Space Sci.* V. 48. P. 671–766.

Ogg J.G., Ogg G., Gradstein F.M. (2008) *The Concise Geologic Time scale.* Cambridge University Press. 150 pp.

Olson P. (2007) Gravitational dynamos and the low-frequency geomagnetic secular variation. *PANS.* V. 104. P. 2159-20166.

Olson P., Christensen U.R. (2006) Dipole moment scaling for convection-driven planetary dynamos. *Earth Planet. Sci. Lett.* V. 250. P. 561–571.

Podolak M., Hubbard W.B., Stevenson D.J. (1991) *Uranus* (Eds.: J.T. Bergstralh, E.D. Miner, M.S. Matthews) Univ. Arizona Press, Tuscon.

Pozzo M., Davies C., Gubbins D., Alfe D. (2012) Thermal and electrical conductivity of iron at Earth's core conditions. *Nature*. V. 485. P. 355–358.

Ruzmaikin A.A., Starchenko S.V. (1991) On the origin of Uranus and Neptune magnetic fields. *Icarus*. V.93. P. 82–87.

Rhines P.B. (1975) Waves and turbulence on a beta plane. *J. Fluid Mech.* V. 69. P. 417–433.

Russell C.T. (1978) Re-evaluating Bode's law of planetary magnetism. *Nature*. V. 272. P. 147-148.

Sano, Y. (1993) The magnetic fields of the planets: A new scaling law of the dipole moments of the planetary magnetism. *J. Geomag. Geoelectr.* V. 45. P. 65-77.

Shcherbakov V., Fabian K. The geodynamo as a random walker: A view on reversal statistics. *J. Geophys. Res.* 2012. V. 117. B03101. doi:10.1029/2011JB008931.

Starchenko S.V. Supercritical convection with superfast MHD-rotation. *JETP*. V. 115. P. 1708–1720. 1999.

Shcherbakov V.P., Sycheva N.K. About intensity of geomagnetic dipole in geological past. *Izvestiya, Physics of the Solid Earth.* No 5. P. 105–124. 2013.

Starchenko S.V., Jones C.A. Typical velocities and magnetic field strengths in planetary interiors. *Icarus*. V. 157. P. 426–435. 2002.

Starchenko S.V., Pushkarev Y.D. Magnetohydrodynamic scaling of geodynamo and a planetary protocore concept. *Magnetohydrodynamics*. V. 49. No. 1. P. 35-42. 2013.

Stevenson D.J. Turbulent thermal convection in the presence of rotation and a magnetic field: a heuristic theory. *Geophys. Astrophys. Fluid Dyn*. V. 12. P. 139-169. 1979.

Stevenson D.J. The energy flux number and three types of planetary dynamo. *Astronom. Nachr.* V. 305. 257-264. 1984.

Takahashi F., Matsushima M., Honkura Y. Scale variability in convection-driven MHD dynamos at low Ekman number. *Phys. Earth Planet. Inter.* V. 167. P. 168-178. 2008.

Thorne L., Hernlund J., Buffett B.A. Core-mantle boundary heat flow. *Nature Geoscience*. V. 1. P. 25–32. 2008.

UNCONVENTIONAL METHOD OF CREATING THE MODEL OF THE MAIN MAGNETIC FIELD OF THE EARTH

T.I. Zvereva

Pushkov institute of Terrestrial Magnetism, ionosphere and Radio wave Propagation (IZMIRAN), Moscow, Troitsk, 142190, Russia, e-mail: zvereva@izmiran.ru

Abstract. The spatial–time model of the geomagnetic field has been constructed using the data of the high accuracy survey of the CHAMP German satellite, obtained during its operation from May 2001 to September 2007. Daily average spherical harmonic models calculated at an interval of four days are used as initial data in order to expand these models by the method of natural orthogonal components (NOCs). It has been indicated that the obtained NOC series rapidly converges. The secular variations, secular acceleration, and *Dst* variation are distinguished as individual NOC components, which makes it possible to construct the spatial–time field model. In addition, the models predictions have been constructed for the year 2008 based on the candidate models of the main field and the secular variation for the year 2005, which were used to obtain the IGRF2005 international model. Comparison of the models predictions with the model constructed for the year 2008 using our method indicates that the accuracy of our model is not lower than that of the models obtained by other scientific groups using the conventional method.

Introduction

Before the appearance of satellite surveys, models of the main geomagnetic field were usually obtained by expanding the average annual field values at the observatories of the global network using the method of spherical harmonic analysis (SHA) and (if possible) the data obtained at the secular variation points and during aeromagnetic and marine magnetic surveys. The appearance of the long-term low orbiting satellite magnetic survey in the last decade resulted in a qualitative and quantitative change in the initial data, which made it possible to use a slightly different method for obtaining the main geomagnetic field and its secular variations. It is known that the field instantaneously measured at a certain point is the sum of the fields of the intraterrestrial and extraterrestrial origin and different spectral composition. Thus, the problem of modeling changed into the problem of separating fields of different origin, some of which could be qualified as errors in measuring the main field.

The conventional and simple method for eliminating these errors during the construction of main field models is the selection of data based on different criteria taking into account the magnetic activity indices, solar zenith angle, and IMF parameters [Olsen, 2002; Olsen et al., 2005; Lesur et al., 2005; Maus et al., 2005]. Only quiet days with $Kp < 1+$, $|Dst| < 10$ nT, and $|dDst/dt| < 3$ nT h–1 are taken in order to eliminate the fields caused by external sources. Only middle and low latitude and the nighttime data (from 2300 to 0500 LT) are taken in order to decrease the contribution of the ionospheric currents. The vector data are used only for the latitudes $|\varphi| < 50°–55°$; scalar data are used for the remaining latitudes. As a result, a latitudinal nonuniformity appears. Only data during the periods when the IMF *Bx* and *By* components satisfy the condition $|Bx|$, $|By| < 3–10$ nT and $0 < Bz < 6$ nT are taken in order to decrease the contribution of the ionospheric currents in the polar caps. The solar wind restrictions are introduced (<450–550 km s–1). At such a selection, most data are rejected, and the advantage of satellite data (homogeneity in space and time) disappears. If the number of measurements is large, the appearance of gaps in data distorts a model much stronger than an artificial decrease in the number of data (e.g., data rarefaction). The degree of data spatial inhomogeneity is substantial in this case. It is evident that the data inhomogeneity originated this way will substantially affect the accuracy of created models. However, the character and degree of this effect are still unclear.

In the present work, we use all satellite daily data, including the data for high latitudes [Golovkov et al., 2005]. Certain filtering takes place naturally: all processes with the period shorter than a day are averaged. In addition, we use the assumption that the fields caused by different processes acting in different media should have different time and spatial characteristics. In other words, the spatial structures of the fields caused by different sources and the time variations in these structures should not correlate with each other. Consequently, the method of expansion into orthogonal components can be applied to data without any selection, and only the components that have intraterrestrial sources will be used as the main field model

[Langel, 1987]. This assumption formed the basis for creating our method for constructing the main geomagnetic field model and secular variations [Golovkov et al., 2007].

Data

In the work we used the vector data of the CHAMP satellite (the ISDC database, level 2) [http://isdc.gfz-potsdam.de/champ] for the period from May 2001 to September 2007 with a resolution of 1 s. The data of another satellite (OERSTED) [http://space center.dk/data/] were only used to confirm the CHAMP data. The data of the global magnetic net work of observatories were also used to independently estimate the accuracy of the model constructed from the CHAMP data. The data of the observatories were taken from the Japan Global Data Center [http://swdcdb.kugi.kyoto-u.ac.jp]. The CHAMP German satellite was launched in 2000, but its data could be used only beginning from May 2001. This satellite has an almost polar orbit with an inclination of 87.3 degrees.

Construction of the model

The method for constructing the model was described in detail in [Golovkov et al., 2007]. We briefly remind here its main aspects. The combination of the NOC and SHA methods is used. The essence of the NOC method considered in detail in Langel [1987] and it was applied to geomagnetic data in many works, e.g. [Golovkov et al., 1989]. The NOC method uses the basis system of functions, which is constructed based on the statistical structure of the studied object. The experimental data are formed as a two-dimensional matrix. For example, when the time series of observatory data are analyzed, a given matrix row is a time variation in any geomagnetic field component in one of the observatories. Other rows correspond to other observatories. Assume that a certain function $H(x,t)$ is specified in a finite number of points in space $x_1, x_2,\ldots, x_j,\ldots,x_n$ at instants $t_1, t_2,\ldots, t_i,\ldots, t_m$. This function can be represented as an expansion

$$H_{ij} = \sum_{k=1}^{K} T_{ki} \cdot S_{kj} \qquad (1)$$

where K is the number of expansion terms or NOCs in other words. The Skj and Tki values can be considered as the n- and m-dimensional vectors $Sk(j)$ and $Tk(i)$, the components of which are the values of the $S_k(x_j)$ and $T_k(t_i)$ functions. Thus, $S_k(x_j)$ and $T_k(t_i)$ are certain numerical functions independent of i and j, respectively.We should note that the NOC method operates in such a way that the component with the maximal variance becomes the first one, and the next NOCs are arranged in the decreasing order according to their variance. The variance of the kth NOC is defined as

$$\lambda_k = \frac{1}{m} \sum_{i=1}^{m} (T_{ki})^2 \sum_{j=1}^{n} (S_{kj})^2$$

The relative contribution of each component (in percent) to the measured field is defined as

$$\frac{\sum_{i=1}^{m} (T_{ki})^2 \sum_{j=1}^{n} (S_{kj})^2}{\sum_{ij} H_{ij}^2} \times 100 \qquad (2)$$

Previously, we performed NOC analyses for different time intervals (as new data appeared). During these analyses, the same magnetic field sources were sometimes identified as differently numbered components; i.e., the NOC numbers varied. We should note that the component number can increase with increasing interval of studies (i.e., with increasing statistics) if the process is random. On the contrary, a systematic process tends to shift toward a component with a smaller number. In our studies the secular acceleration was identified as the second component only for the longest interval (from May 2001 to September 2007). For the shorter intervals, this variation was present in the form of a trend in the components with the larger numbers. Therefore, we are confident that the variation, identified as the second component for the long period, is the secular acceleration rather than a random process.

However, the NOC method cannot be directly applied to satellite data. Therefore, the modeling algorithm included two stages. The first stage consisted in obtaining daily average spherical harmonic models (DSHMs) by expanding the field components of all CHAMP vector data obtained during a day, based on Eqs. (3) and (4) [Yanovskiy, 1978]:

$$U(r,\theta,\lambda) = a \cdot \sum_{n=1}^{N} \sum_{m=0}^{n} \left(\frac{a}{r}\right)^{n+1} (g_n^m \cos m\lambda + h_n^m \sin m\lambda) \times P_n^m(\cos\theta) \qquad (3)$$

$$X = -\frac{1}{r}\frac{dU}{d\theta} \qquad Y = \frac{-1}{r\sin\theta}\frac{dU}{d\lambda} \qquad Z = -\frac{dU}{dr}, \qquad (4)$$

where *U* is the geomagnetic potential at a point with geographic coordinates *r*, θ, λ (radius, colatitude, and longitude); *X*, *Y*, and *Z* are the northern, eastern, and vertical (downward) field components; *a* is the average Earth's radius; $P_n^m(\cos\theta)$ is a Legendre associated function of power *n* and order *m* in the Schmidt normalization; g_n^m and h_n^m are constant coefficients.

The second stage consisted in the expansion of the obtained time series of the DSHM coefficients into NOCs. The NOC method divided DSHM into several models, which have different spatial structures and vary in time independently. As a result the time variation in the potential can be written as:

$$U(r,\theta,\lambda) = a \cdot \sum_{n=1}^{N} \sum_{m=0}^{n} \left(\frac{a}{r}\right)^{n+1} (g_n^m(t) \cos m\lambda + h_n^m(t) \sin m\lambda) \times P_n^m(\cos\theta),$$

where $g_n^m(t)$ and $h_n^m(t)$ are the functions depending on time. These functions are as a rule represented as the first terms of the Taylor series expansion. H independently ere, the functions are described by the numerical functions, which are the result of their expansion (using the NOC method) according to (1) in the form

$$g_n^m(t_i) = \sum_{k=1}^{K} g_{nk}^m T_{ki}$$

where g_{nk}^m are independent of time, and *Tki* reflect time variations $g_n^m(t)$. A similar derivation is true for $(h_n^m(t)$. The requirements to these numerically specified functions are the same as the requirements to any analytical functions. These functions should be mutually orthogonal on the entire time interval, approximate the observed series to the required accuracy, and generate rapidly converging expansion series.

Discussion of results

At the first stage, we constructed DSHMs of the geomagnetic field for the period from May 2001 to September 2007. To decrease laboriousness, we constructed DSHMs at an interval of four days, which was substantiated in [Golovkov and Zvereva, 1998, 2000]. At the second stage, the time series of the $g_n^m(t)$ and $h_n^m(t)$ coefficients were used as initial data for the NOC method. Having performed a NOC analysis, we obtained the numerical functions characterizing the time and spatial variations in coefficients $g_n^m(t)$ and $h_n^m(t)$, which are hereafter denoted as *Tk* and *Sk*. *Tk* are the time variations in the *k*th NOC (NOC_k), and *Sk* represent the set of spherical coefficients for this component.

Fig.1 presents the variations in the first six time orthogonal components of the NOC expansion *T*1–*T*6. It is clear that *T*1 is a slightly disturbed straight line on the entire time interval, and we interpret this component as a secular variation. Disturbances are related to variations in the external field, which is illustrated by tests in [Golovkov et al., 2007]. *T*2 is the field secular acceleration. The remaining curves (*T*3–*T*6) are rather high_frequency and do not show any trend that could be considered as a secular variation. Relative contributions of the NOC1–NOC6 components to the measured total field (according to (2)) are also presented in Fig. 1 and are 97.2, 0.4, 0.3, 0.2, 0.2, and 0.2%, respectively. It is clear that the secular variation mainly contributes to the DSHM time variations, and the contribution of the remaining possible sources is small. In spite of a small relative contribution of NOC2–NOC6 to the measured field, we consider these components in more detail. An additional advantage of the NOC method, as applied to the satellite data according to the technique outlined in this study, is that, besides time characteristics of the sources into which the measured field was divided, it gives spherical harmonic models of each source that can be used to construct the field spatial structure. A map of the field *Z* component of the first spatial NOCs is presented in Fig. 2.

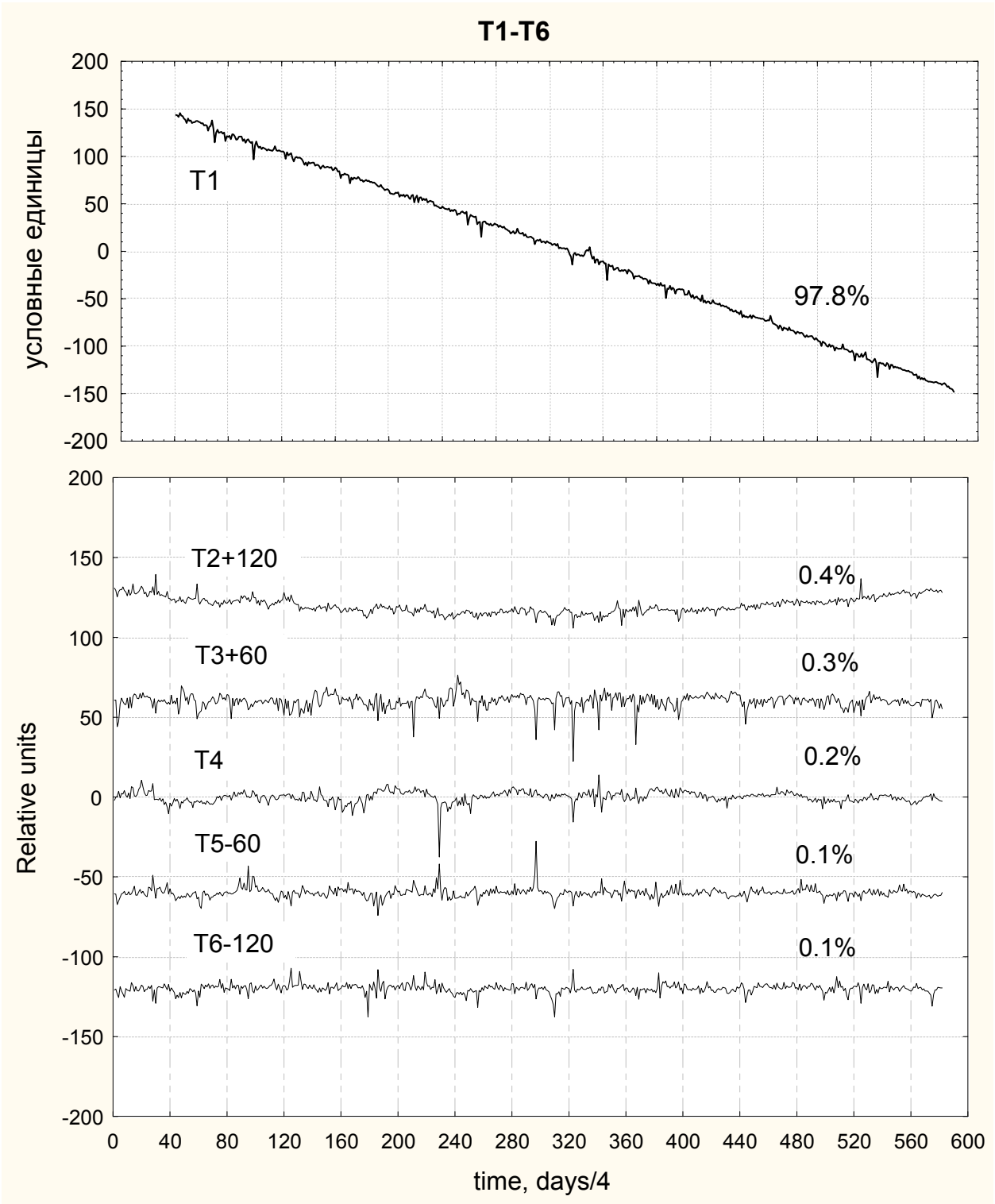

Fig. 1. Six time orthogonal components (*T*1–*T*6), obtained using the NOC method applied to the set of the DSHM coefficients for the time interval from May 2001 to September 2007. The relative contribution of each component to the complete field is indicated near the curves. For clarity, the *T*2, *T*3, *T*5, and *T*6 curves are shifted by 120, 60, –60, and –120 units, respectively.
Time (days/4) and relative units are plotted on the horizontal and vertical axes, respectively.

A map presented in Fig. 2 evidently resembles a conventional map of the secular variation. The map of the second NOC (T2) illustrates the secular acceleration of the *Z* component. The third component (*T*3) reflects the contribution of the *Dst*-variation to the field, which is confirmed by the correlation coefficients between time component *T3* and the *Dst* curve. Maps of the *Z*-component for NOCs 4-6 reflect only the fact that all

distinguished sources are located at high latitudes, they are random and approximately equally contribute to the field (Fig.2).

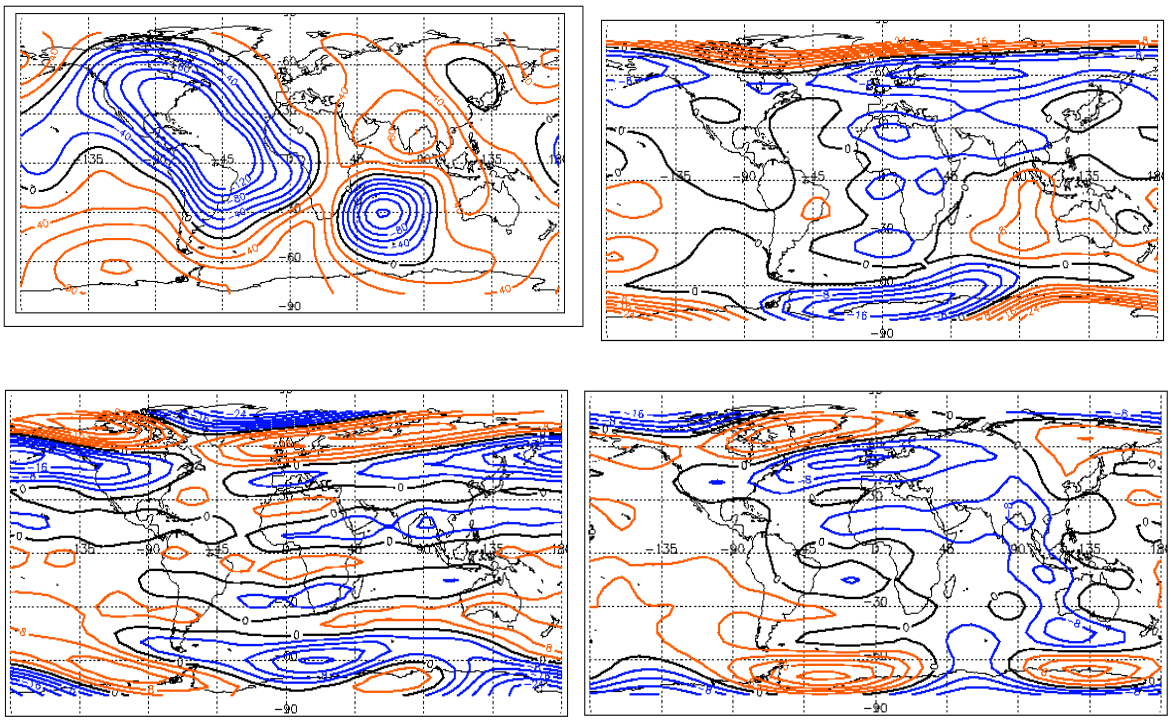

Fig. 2. A map of the *Z* component of the secular variation identified as the first NOC1 (top left). The maps of the field Z-components described by the spatial NOC4 (top right), NOC5 (bottom left) and NOC6 (bottom right) components.

The fact that these sources were included in different components only means that they are distributed in longitude. All sources are at the noise level. The annual variation is observed in the NOC6 component. We anticipated that the results of the expansion by the NOC method would be similar to the results obtained using the observatory data [Golovkov and Zvereva, 1998]. Recall that the secular variation, *Dst*, and annual variations were identified as the first, second, and third components in that work, respectively. The relative contribution of these components to the measured field was 70–90, 7–30, and 0.6–1.5%, respectively, and varied depending on the solar cycle period that fell on the interval of these measurements. Applying the presented method to the satellite data allowed to construct the models of the main geomagnetic field and secular variation (*SV*) on the time interval longer than six years. The above also implies that we can synthesize the field as the sum of the fields, described by their own spherical harmonic models, at an arbitrary instant within the presented time interval at any point on the Earth's surface. For example, the magnetic field value at an arbitrary instant *t*0 within the studied interval at an arbitrary spatial point with coordinates r_0, φ_0, λ_0 will be defined as

$$X = X_{av}(r_0, \varphi_0, \lambda_0) + \sum_{k=1}^{6} X_{k,\sin t}(r_0, \varphi_0, \lambda_0) \cdot T_k(t_0)$$

where r_0 is the distance from the point to the Earth's center; φ_0 and λ_0 are the point geographic latitude and longitude, respectively; X_{av} is the value of the field *X* component synthesized according to the average field spherical harmonic model for the considered period, obtained during processing using the NOC method; $X_{k,\text{synt}}$ is the field of the *k*th component synthesized using the g_{nk}^{m} and h_{nk}^{m} coefficients; and $T_k(t_0)$ is the value of the *k*th component (T_k) at instant t_0. Similar derivations are also true for the *Y* and *Z* field components. We should note that the model was constructed at an interval of four days; therefore, the last formula holds true for the days entering into the studied data series.

The model of the main geomagnetic field constructed for the year 2005 and the *SV* model for the year 2007.5 were presented as the candidate models for constructing the IGRF_MF_2005 and IGRF_SV_2007.5

international models. The IGRF models are accepted at an interval of five years using the candidate models presented by different groups of researchers (from Germany, Denmark, England, and USA) and by Russia IZMIRAN. The method for calculating our model differs from the methods used by other groups of researchers, which was considered in detail in the previous section.

Use of the space-time model

The space–time model of the main geomagnetic field, constructed by us on the six-year time interval, has been used in practice. In [Zvereva et al., 2005; Abramova et al., 2005], this model was used as the normal level in the calculation of the anomalous field. The model can also be very useful in magnetic survey. Specifically, this model makes it possible to increase the number of days with increased geomagnetic activity, when a high-quality geomagnetic survey can be performed [Zvereva et al., 2005]. As an example, we can present the processing of the data of the balloon flight with magnetometers in October 2003 a day after a strong magnetic storm. In this case, only our model made possible to reconstruct the geomagnetic field level, relative to which an anomalous geomagnetic field was detected.

Conclusion

We constructed the space–time model of the geomagnetic field for the time interval from May 2001 to September 2007, jointly using the SHA and NOC methods.
We presented the method for constructing models of the main geomagnetic field and its secular variation using the satellite data. The accuracy of this model is not less than that of the models constructed using pre-selected selected data. The advantage of our method consists in its simplicity and absence of subjectivism, which is unavoidable during pre-selection.

Acknowledgments
This work was supported by the Russian Foundation for Basic Research, project No 13_05_00893.

References

Abramova, D., S. Filippov, T. Zvereva, and A. Frunze (2005), Use One_Day Reference Field Models on CHAMP Data over Kursk Region, in: *Proceedings of the IAGA2005 Scientific Assembly, Toulouse*.

Finlay, C. C., S. Maus, C. D. Beggan, T. N. Bondar, A. Chambodut, T. A. Chernova, A. Chulliat, V. P. Golovkov, B. Hamilton, M. Hamoudi, R. Holme, G. Hulot, W. Kuang, B. Langlais, V. Lesur, F. J. Lowes, H. L¨uhr, S. Macmillan, M. Mandea, S. McLean, C. Manoj, M. Menvielle, I. Michaelis, N. Olsen, J. Rauberg, M. Rother, T. J. Sabaka, A. Tangborn, L. Tøffner-Clausen, E. Th´ebault, A. W. P. Thomson, I. Wardinski, Z. Wei and T. I. Zvereva (2010) International Geomagnetic Reference Field: The Eleventh Generation, *Geophys. J. Int.* V.183. No 3. P.1216–1230, doi: 10.1111/j.1365-246X.2010.04804.x.

Golovkov, V. P., and T. I. Zvereva (2000), The Space–Time Pattern of Midlatitude Geomagnetic Variations, *Geomagn. Aeron.* 40 (1), 84–92.

Golovkov, V. P., and T. I. Zvereva (1998), Expansion of Geomagnetic Variations within a Year in Natural Orthogonal Components, *Geomagn. Aeron.* 38 (3), 140–145.

Golovkov, V. P., T. I. Zvereva, and T. A. Chernova (2005), The IZMIRAN Main Magnetic Field Candidate Model for IGRF_10, Produced by a Spherical Harmonic_Natural Orthogonal Component Method, *Earth Planet. Space,* 57, 1165–1171.

Golovkov, V. P., T. I. Zvereva, and T. A. Chernova (2007), Space–Time Modeling of the Main Magnetic Field by Combined Methods of Spherical Harmonic Analysis and Natural Orthogonal Components," *Geomagn. Aeron*. 147 (2), 272–278.

Langel, R. A. (1987), *Main Field in Geomagnetism*, Ed. By J. A. Jacobs, Academic, London, pp. 249–512.

Yanovskiy, B. M. (1978), *Terrestrial Magnetism,* Leningr. Gos. Univ., Leningrad, [in Russian].

Zvereva, T., V. Golovkov, S. Filippov, and Y. Tsvetkov (2005), Model of the Reference Field on the Satellite Data for Balloon Geomagnetic Researches, in: *Proceedings of the 17th ESA Symposium on European Rocket and Balloon Programmes and Related Researchers, Norway,* p. 205.

ELECTRIC CURRENT PENETRATION FROM A THUNDERSTORM CLOUD INTO THE MIDDLE-LATITUDE IONOSPHERE

V.V. Denisenko

Institute of Computational Modelling RAS, 660036, Krasnoyarsk, Russia, e-mail: denisen@icm.krasn.ru

Abstract A quasi-stationary two-dimensional model of electric fields and currents in the conductor that includes a thunderstorm cloud as well as the Earth's ground, atmosphere and ionosphere is created. A cloud is simulated as a long cylinder with elliptical cross-section in a meridian plane with vertical and horizontal axes 10 km and 40 km respectively. Hall conductivity of the ionosphere is not included into the model that is possible only for a cloud which parameters are independent of longitude. Vertical external current about $10^{-10} A/m^2$ is used in the model as a generator that creates voltage 10 MV between low and upper boundaries of the cloud. The height distribution of the components of the conductivity tensor above the altitude of 90 km is calculated by the empirical models IRI, MSISE, IGRF. We use an empirical model by Rycroft and Odzimek below 50 km where the electric conductivity is isotropic and smooth interface between these regions. In accordance with the used empirical model conductivity inside a cloud is ten times decreased. The steady state electroconductivity problem is solved numerically. Electric fields and currents below 60 km do not depend on the geomagnetic field inclination. At the heights $80 - 100$ km current goes almost along magnetic field lines because of that the field-aligned conductivity is much larger than Pedersen one there. Conductivity current closes about a half and a quarter of the total external current inside and outside the cloud respectively in the atmosphere below 50 km. The rest current goes to the ionosphere where it is distributed all over the globe, goes down to the ground through the whole atmosphere and returns under the cloud by ground. The last current loop is the income of the cloud into the global electric circuit.

Introduction

A thunderstorm cloud is the brightest object in the atmosphere. These clouds also generate voltage between ground and ionosphere. Currents go back to ground as fair-weather ones all over the globe. Modern state of knowledge on this global electric circuit can be found in the review [3].

In this paper we analyze a cloud as a current generator. We study what part of the extrinsic current that exists inside a cloud is closed through the ionosphere.

The electric conductivity equation

We use a steady state model for a conductor with the conductivity tensor $\hat{\sigma}$ since the typical time of the process is much larger than the charge relaxation time $\tau = \varepsilon_0/\sigma$, $\tau < 15$ min. The basic equations for the steady state electric field $\mathbf{E}$ are Faraday's law, the charge conservation law, and Ohm's law,

$$\operatorname{curl} \mathbf{E} = 0, \tag{1}$$

$$\operatorname{div} \mathbf{j} = Q, \tag{2}$$

$$\mathbf{j} = \hat{\sigma}\mathbf{E}, \tag{3}$$

where $\mathbf{j}$ - the current density, $-Q$ - the divergence of the external electric current, that can be calculated by external current density, that is a given vector-function in our model.

In view of (1) the electric potential V can be introduced so that

$$\mathbf{E} = -\operatorname{grad} V.$$

Then the system of the equations (1-3) is reduced to the electric conductivity equation

$$-\operatorname{div}(\hat{\sigma}\operatorname{grad} V) = Q. \tag{4}$$

Conductivity in the Earth's atmosphere and ionosphere

We mark parallel and normal to the direction of magnetic induction **B** components of vectors with $\parallel$ and $\perp$. Then Ohm's law (3) in a gyrotropic medium can be written as

$$j_{\parallel} = \sigma_{\parallel} E_{\parallel}, \qquad \mathbf{j}_{\perp} = \sigma_P \mathbf{E}_{\perp} - \sigma_H \left[\mathbf{E}_{\perp} \times \mathbf{B}\right]/B,$$

with Hall σ_H Pedersen σ_P and field-aligned $\sigma_{\parallel}$ conductivities.

Above $z = 90$ km we use the model [2] for σ_P, σ_H, $\sigma_{\parallel}$, that is based on the empirical models IRI, MSISE, IGRF. The empirical model [4] is used below 50 km and smooth interpolation of these models at $50 - 90$ km. The model [4] presents about ten times conductivity decrease inside thunderclouds.

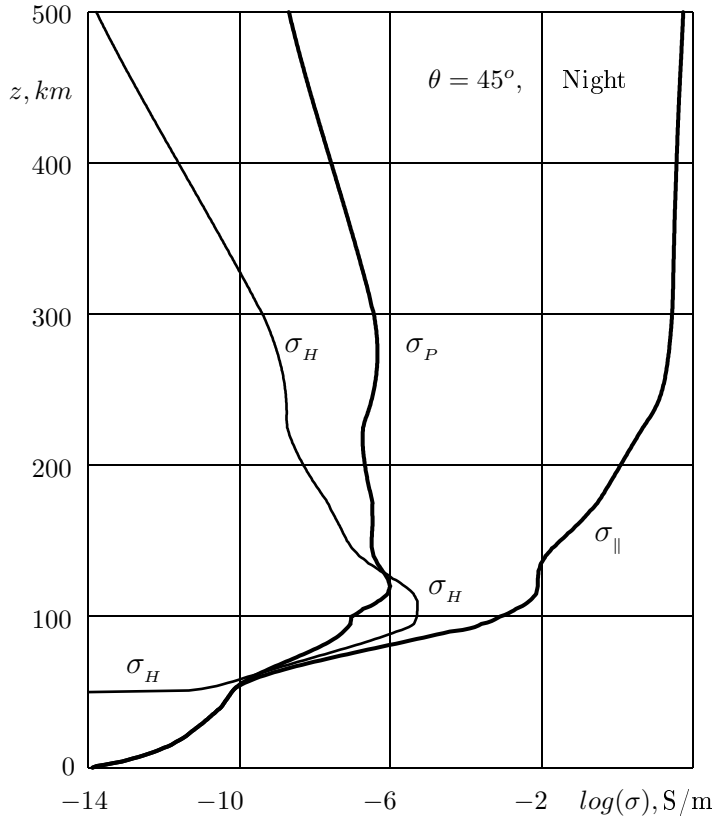

Figure 1: Profiles of the components of the electric conductivity tensor for a mid-latitude night–time ionosphere. Field-aligned conductivity $\sigma_{\parallel}$, Pedersen conductivity σ_P, Hall conductivity σ_H.

We analyze only a 2-D problem in a magnetic meridional plane. It is possible if all parameters are independent of longitude. Then Hall conductivity is not involved into the equations and for magnetic inclination I tensor

$$\hat{\sigma} = \begin{pmatrix} \sigma_{xx} & \sigma_{xz} \\ \sigma_{zx} & \sigma_{zz} \end{pmatrix} = \begin{pmatrix} \cos I & -\sin I \\ \sin I & \cos I \end{pmatrix} \begin{pmatrix} \sigma_{\parallel} & 0 \\ 0 & \sigma_P \end{pmatrix} \begin{pmatrix} \cos I & \sin I \\ -\sin I & \cos I \end{pmatrix}.$$

We simulate the Earth as an ideal conductor since conductivity of ground and especially of sea water is many orders of magnitude larger than conductivity of air. So at the Earth's surface, that we regard as a plane because of small latitudinal size of the clouds, potential is constant

$$V|_{z=0} = V_0. \tag{5}$$

The constant V_0 is defined to fit fair weather vertical electric field strength $E_z(0) = 130\,\mathrm{V/m}$.

External current inside a thundercloud

The cloud is a long horizontal cylinder oriented along geomagnetic parallel in our 2-D model. The cross section of the cloud is the ellipse $5\,\mathrm{km} < z < 15\,\mathrm{km}$, $|x| < 20\,\mathrm{km}$. We take as given some vertical external current. Its density $j_{ext} = const$ inside the cloud and goes to zero in a layer near boundary. Its value is chosen to be $j_{ext} = 110\,\mathrm{pA/m^2}$ to make the potential difference in the cloud equal to 10 MV.

Separation of ionospheric and atmospheric conductors

The electric conductivity equation (4) ought be solved in the conductor that includes ground, atmosphere, ionosphere and even magnetosphere. We already have separate ground by the boundary condition (5). The ionosphere is a good conductor in comparison with atmosphere. In such a case it is usual to do domain decomposition. At the first step the good conductor is approximately regarded as an ideal one. It means the following boundary condition for atmospheric field

$$V|_{z=h_I} = 0, \tag{6}$$

where h_I is some height. Test calculation show that $h_I \geq 90\,\mathrm{km}$ is enough.

The result current density through this boundary is included to the boundary condition of Neumann type for the subdomain that is occupied with good conductor. This second step gives some potential distribution at the same boundary and it ought be used as the right-hand side in the boundary condition (6) and so on. In fact these iterations are not necessary since the ionosphere is a very good conductor and electric field about 1 mkV/m is enough to close this current. Corresponding voltage in the domain of interest is less then 1 V. It can be neglected.

Far from the cloud all parameters become independent of horizontal coordinates. It means that the problem (4, 5, 6) is reduced to 1-D one. This model has some solutio $V_1(z)$ that corresponds vertical current which density is independent of the height. This solution describes fait-weather electric field. For usual fair-weather $E_z(0) = 130\,\mathrm{V/m}$ we obtain this current density $j_0 = \sigma_P(0)E_z(0) = 1.7\,\mathrm{pA/m^2}$ and the voltage between ground and ionosphere $V_0 = 345\,\mathrm{KV}$.

This 1-D solution is an asymptotic at infinity for the atmospheric conductor. We approximately use it as the boundary condition at finite distance

$$V|_{x=\pm x_\infty} = V_1(z), \tag{7}$$

and it is shown by test calculations that $x_\infty \geq 300\,\mathrm{km}$ is enough.

Now we have got Dirichlet boundary value problem (4, 5, 6, 7) for the atmosphere. It has a unique solution.

Numerical method

Our finite element method [1] is based on minimization of the energy functional

$$W(V) = \frac{1}{2}\int \mathrm{grad}\, V \cdot \hat{\sigma}\, \mathrm{grad}\, V\, dxdz - \int QV\, dxdz.$$

Finite element method means minimization of this functional at some set of approximation functions. They are piece-wise ones in our method. We use multigrid method to solve the equations for the nodal values of the approximate solution which are the conditions of minimum.

Results

The results of calculation are presented in Fig. 2 and 3 for the described cloud in hight and middle latitudes. Current lines are presented for the sum of conductivity and external currents, since just

this sum has zero divergence. Fig. 2c presents electric field near ground that is independents of magnetic field inclination. It is equal to the fair-weather value outside the region under cloud with 20 km extension and has opposite direction and twenty times larger strength under the cloud. The last value would be 10 times increased till $E_z(0,0) = 40\,\mathrm{KV/m}$ if external current is 10 times increased, that means the potential difference in the cloud 100 MV instead of 10 MV in actual model.

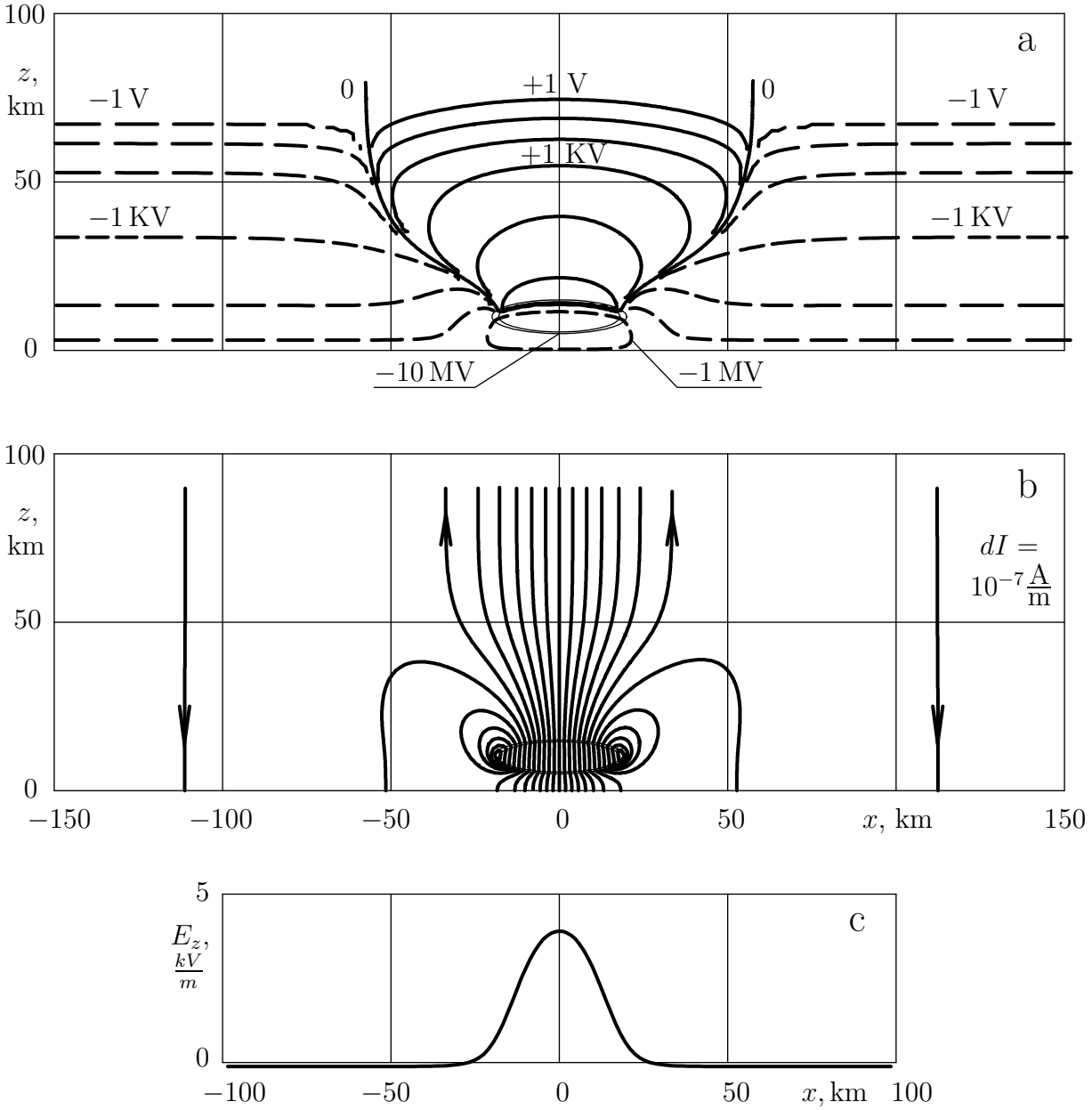

Figure 2: Results for vertical magnetic field. a - electric potential in logarithmic scale. b - current lines for the sum of conductivity and external currents. c - vertical electric field near ground.

Comparison of Fig. 2 and 3 shows that nothing below 60 km is varied with magnetic inclination.

Since the input parameter of the model $j_{ext} = 110\,\mathrm{pA/m^2}$ and the cloud has 50 km width, the total $I_{ext} = 4.4\,\mathrm{mkA/m}$. Fig. 2b, 3b show that 30% of this I_{ext} go to the ionosphere. It is pure conductivity current outside cloud. Naturally, the same current goes from ground to the cloud. Conductivity current closes about a quarter of the total external current outside the cloud in the atmosphere below 50 km.

For a twice wider cloud presented in Fig. 4 the total current to the ionosphere increases till 50% of I_{ext}, for very wide cloud the percentage $\to 60\%$. The rest part is closed inside cloud and through atmosphere in its vicinity as is is seen in Fig. 2b, 3b, 4b.

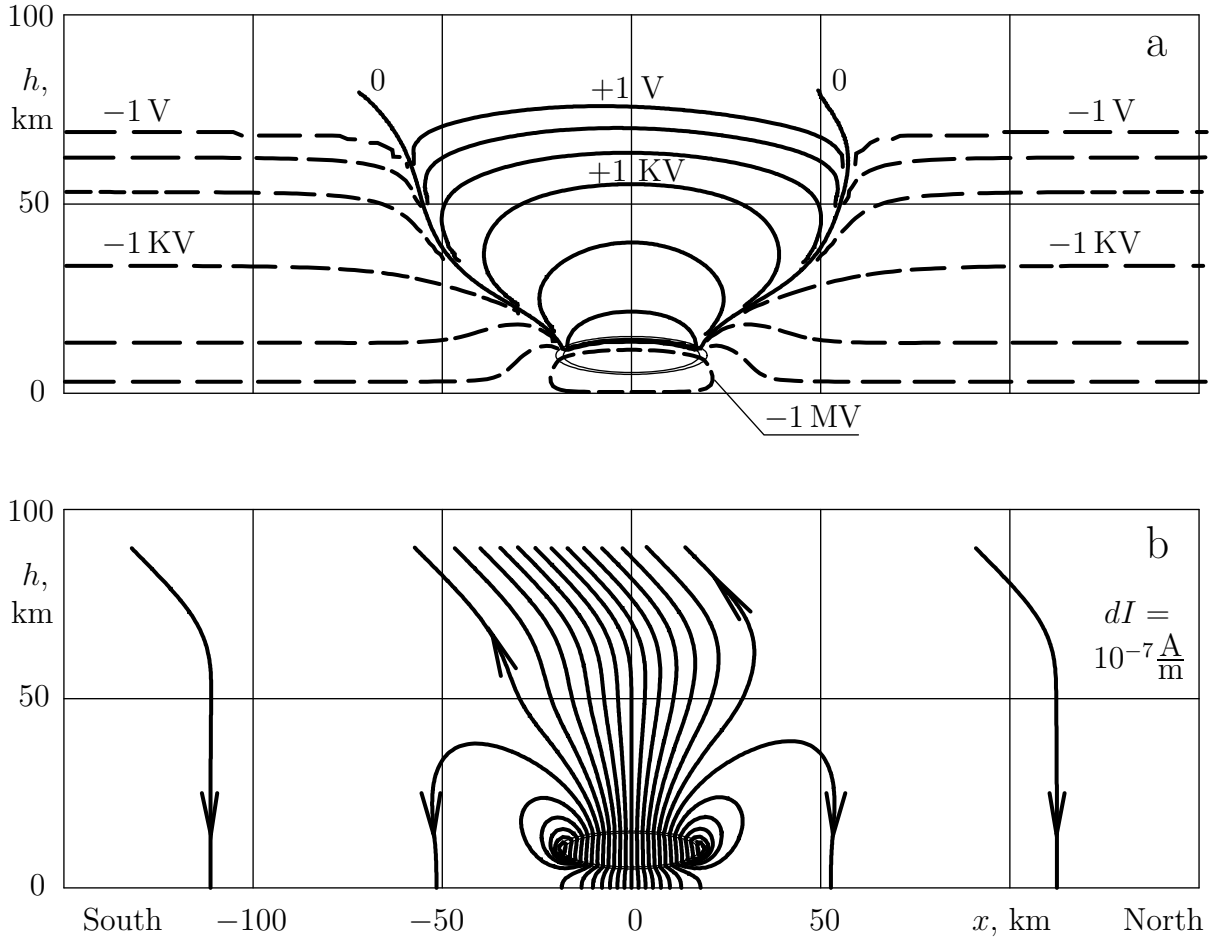

Figure 3: Results for inclined magnetic field. a - electric potential. b - current lines for the sum of conductivity and external currents.

Conclusions

A model of electric current penetration from a thunderstorm cloud into high- and middle-latitude ionosphere is created. It is based on the empirical models of atmospheric and ionospheric conductivities.

In the main part of the atmosphere below 60 km electric fields and currents are almost independent of the magnetic inclination. Above 75 km currents are almost parallel to magnetic field lines.

The potential difference in the cloud 10 MV can be generated with vertical external current $j_{ext} = 110\,\mathrm{pA/m^2}$.

Total current to the ionosphere is of about 30% of the total I_{ext} in the cloud with 40 km horizontal size. For twice wider cloud percentage increase to 50%, for a very wide cloud it $\to$ 60%. These values would be different if another model of conductivity is used. Conductivity inside a cloud is not a well known parameter.

Acknowledgments. This work is supported by grant 12-05-00152 from the Russian Foundation for Basic Research.

References

[1] Denisenko, V.V. (1995), *Energy methods for elliptic equations with asymmetric coefficients*, 204 pp., Publ. house of the Russian Academy of Sciences Siberian Branch, Novosibirsk, [in Russian].

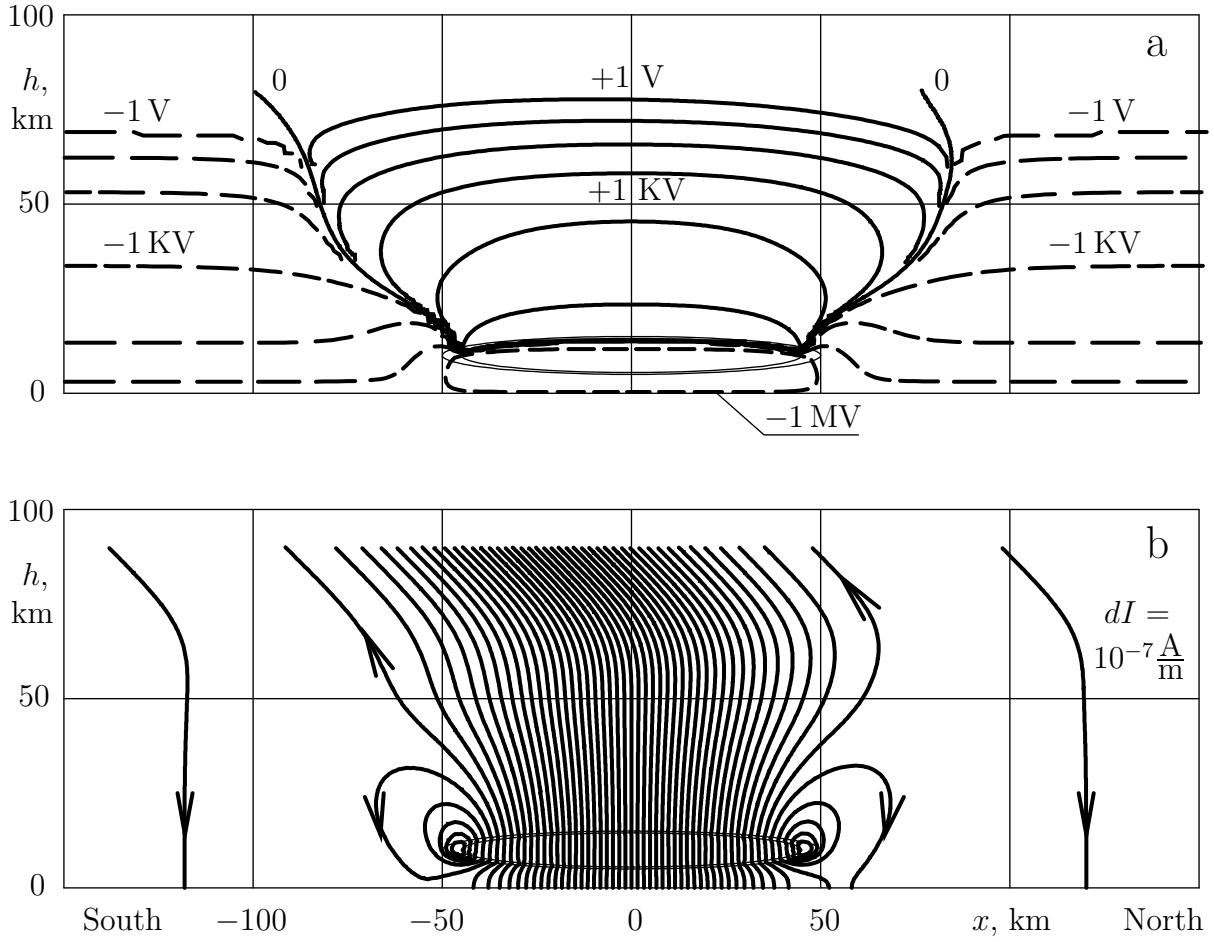

Figure 4: Results for a twice wider cloud in inclined magnetic field. a - electric potential. b - current function.

[2] Denisenko, V.V., H.K. Biernat, A.V. Mezentsev, V.A. Shaidurov, and S.S., Zamay (2008), Modification of conductivity due to acceleration of the ionospheric medium, *Ann. Geophys.* 26, 2111-2130.

[3] Mareev, E.A. (2010), Achievments and prospects of research of the global electric circuit, *Achievments in Physical Sciences*, 180(5), 527534.

[4] Rycroft, M.J., A. Odzimek (2010), Effects of lightning and sprites on the ionospheric potential, and threshold effects on sprite initiation, obtained using an analog model of the global atmospheric electric circuit, *J. Geophys. Res.* 115(A00E37), doi:10.1029/2009JA014758.

ELECTRIC CURRENT PENETRATION FROM A THUNDERSTORM CLOUD INTO THE IONOSPHERE AT THE GEOMAGNETIC EQUATOR

V.V. Denisenko

Institute of Computational Modelling RAS, 660036, Krasnoyarsk, Russia, e-mail: denisen@icm.krasn.ru

Abstract A quasi-stationary two-dimensional model of electric fields and currents in the conductor that includes a thunderstorm cloud as well as the Earth's ground, atmosphere and ionosphere with specific features of equatorial ionosphere is created. A cloud is simulated as a long cylinder with elliptical cross-section with vertical and horizontal axes 10 km and 40 km respectively. The two-dimensional model is applied for two cases when such a long cloud is parallel or normal to the geomagnetic equator. Vertical external current about $10^{-10} A/m^2$ is used in the model as a generator that creates voltage 10 MV between low and upper boundaries of the cloud. The height distribution of the components of the conductivity tensor above the altitude of 90 km is calculated by the empirical models IRI, MSISE, IGRF. We use an empirical model by Rycroft and Odzimek below 50 km where the electric conductivity is isotropic and smooth interface between these regions. Conductivity inside a cloud is ten times decreased in accordance with the used empirical model. The steady state electroconductivity problem is solved numerically. The problem with Hall conductivity is harder from mathematical point of view. We use new statement of the problem that has a symmetrical positive definite operator in contrast with traditional problems for electric potential or current function. Electric fields and currents below 60 km do not depend on the geomagnetic field inclination. The main difference from high-latitude models appears when the cloud is parallel to the geomagnetic field lines. Then the field and current distributions are not symmetrical because of Hall conductivity. The incomes of these type clouds into the global electric net are analyzed.

Introduction

This report is the continuation of the report [1]. We analyze what part of the extrinsic current of a cloud is closed through the ionosphere. Here we study clouds at geomagnetic equator.

For a long cloud 2-D model can be used such as it is described in [1]. The electric conductivity equation takes shape

$$-\operatorname{div}(\hat{\sigma}\operatorname{grad} V) = Q, \tag{1}$$

where $\hat{\sigma}$ is the conductivity tensor, $-Q$ is the divergence of the external electric current, that can be calculated by external current density, that is a given vector-function in our model.

The strength of the steady state electric field $\mathbf{E}$ can be expressed by the electric potential V

$$\mathbf{E} = -\operatorname{grad} V,$$

and Ohm's law gives the current density

$$\mathbf{j} = \hat{\sigma}\mathbf{E}. \tag{2}$$

The model of ideal conductor is used for round and ionosphere. It means the following boundary condition for atmospheric field

$$V|_{z=0} = V_0, \tag{3}$$

$$V|_{z=h_I} = 0, \tag{4}$$

where h_I is some height that separates atmosphere from ionosphere in our method of domain decomposition [1]. Test calculations show that $h_I \geq 90\,\mathrm{km}$ is enough.

If a long cloud is parallel to the geomagnetic equator, it is a particular case of the cloud studied in [1] with specific magnetic inclination $I = 0^o$. Then Hall conductivity is not involved into the equations and conductivity tensor

$$\hat{\sigma} = \begin{pmatrix} \sigma_{xx} & \sigma_{xz} \\ \sigma_{zx} & \sigma_{zz} \end{pmatrix} = \begin{pmatrix} \sigma_{\parallel} & 0 \\ 0 & \sigma_P \end{pmatrix}, \tag{5}$$

where z is the vertical axe of Cartesian coordinates and x is along meridian, σ_P and $\sigma_{\parallel}$ are Pedersen and field-aligned conductivities.

If a long cloud is normal to the geomagnetic equator, then Hall conductivity σ_H is involved into the equations and tensor

$$\hat{\sigma} = \begin{pmatrix} \sigma_{xx} & \sigma_{xz} \\ \sigma_{zx} & \sigma_{zz} \end{pmatrix} = \begin{pmatrix} \sigma_P & \sigma_H \\ -\sigma_H & \sigma_P \end{pmatrix}. \tag{6}$$

Hall conductivity makes tensor $\hat{\sigma}$ and hence the operator of the boundary value problem non symmetrical. Such a problem needs more complicated numerical method [2] which is designed in frame of the energy method [4].

2-D problem in a gyrotropic conductor

Conductivity tensor has shape (6) for the problem in a magnetic equatorial plane, when magnetic field is normal to the plane of interest. Such a tensor is invariant in respect to rotation around axis z and so it presents a gyrotropic conductor. This nonsymmetrical tensor makes difficulties from mathematical point of view in comparison with symmetrical tensor like (5). For solving the problem we use the original energy method [2].

First we return from the second-order equation (1) to the original first-order problem for electric field and current density, that includes the equations

$$\operatorname{curl} \mathbf{E} = 0, \tag{7}$$

$$\operatorname{div} \mathbf{j} = Q, \tag{8}$$

and Ohm's law (2).

The boundary conditions at horizontal lines (3, 4) takes shape

$$E_x|_{z=0} = 0, \tag{9}$$

$$E_x|_{z=h_I} = 0. \tag{10}$$

The boundary conditions at vertical far lines takes shape

$$E_z|_{x=\pm x_\infty} = g(z), \tag{11}$$

where we denote $g(z) = -dV_1(z)/dz$, and $V_1(z)$ is 1-D solution for the atmospheric conductor that corresponds to the vertical current density independent of the height. It is a given function in 2-D problem. This solution describes fait-weather electric field. For usual fair-weather $E_z(0) = 130\,\mathrm{V/m}$ we obtain this current density $j_0 = \sigma_P(0)E_z(0) = 1.7\,\mathrm{pA/m^2}$ and the voltage between ground and ionosphere $V_0 = 345\,\mathrm{KV}$. Strictly speaking, the condition (11) is an asymptotic at infinity, but our test calculations show that $x_\infty \geq 300\,\mathrm{km}$ is enough to avoid any disturbance of the solution in the domain of interest.

Second step of our approach is the symmetrization of the operator by introducing the potentials F, P, so that

$$\mathbf{E} = -\frac{1}{\sigma_0} S\sigma^* \operatorname{grad} F + S \operatorname{rot}_{x,z} P,$$

where P is $z-$ component of $(0,0,P)$.

This potentials satisfy the following boundary conditions, which are referred to as the main ones:

$$F|_\Gamma = 0,$$
$$\int P\, d\Omega = 0, \tag{12}$$

where Ω is our domain and Γ is its boundary. Strictly speaking the second condition is not a boundary one, since it contains integral over the domain. It can be substituted with equivalent zero average over the boundary, that is boundary condition indeed, but the form (12) is convenient in the proofs and so is a traditional one.

The constant σ_0 improves condition number in numerical method as well as an arbitrary symmetrical positive definite matrix S. We choose

$$S = \left(\frac{\sigma + \sigma^*}{2\sigma_0}\right)^{-1}.$$

The following energy scalar product is defined in the space of pairs F, P

$$[\begin{pmatrix} F \\ P \end{pmatrix}, \begin{pmatrix} u \\ v \end{pmatrix}] = \frac{1}{\sigma_0}\int\int \begin{pmatrix} \text{grad } F \\ \text{rot } P \end{pmatrix}^* \begin{pmatrix} \frac{1}{\sigma_0}\sigma S \sigma^* & -\sigma S \\ -S\sigma^* & \sigma_0 S \end{pmatrix} \begin{pmatrix} \text{grad } u \\ \text{rot } v \end{pmatrix} dxdy.$$

The energy functional is constructed as

$$W(F,P) = \frac{1}{2}[\begin{pmatrix} F \\ P \end{pmatrix}, \begin{pmatrix} F \\ P \end{pmatrix}] - \frac{1}{\sigma_0}\int\int FQ\ dxdz + \frac{1}{\sigma_0}\oint Pg(l)\, dl, \tag{13}$$

where $g(l)$ is given tangential component of the electric field. It equals 0, $g(z)$, 0, $-g(z)$ at four sides of our rectangle Ω starting with ground part.

It is proved that minimization of the energy functional gives the solution for the boundary value problem (7, 8, 2, 9, 10, 11). Our finite element method [1] is based on minimization of the energy functional. Finite element method means minimization of this functional at some set of approximation functions. They are piece-wise ones in our method. We use multigrid method to solve the equations for the nodal values of the approximate solution which are the conditions of minimum.

Conductivity and external current

Above $z = 90\,\text{km}$ we use the model [2] for σ_P, σ_H, $\sigma_\parallel$, that is based on the empirical models IRI, MSISE, IGRF. The empirical model [5] is used below 50 km and smooth interpolation of these models at $50 - 90\,\text{km}$. The model [5] presents an order of magnitude conductivity decrease inside thunderclouds.

Height distributions of the components of conductivity tensor are presented in Fig. 1. One more parameter is important in the equatorial ionosphere. It is Cowling conductivity $\sigma_C = (\sigma_P^2 + \sigma_H^2)/\sigma_P$, that is concentrated in a thin layer at heights $90-110\,\text{km}$ and defines horizontal current in equatorial jet. It is shown with dashed line in Fig. 1. It approximately equals to $\sigma_\parallel$ below and σ_P above this layer. The second property is due to $\sigma_H << \sigma_P$. The first one is typical to conductors with one main type of charged particles which define conductivity. Then

$$\sigma_P = \sigma_\parallel/(1+\beta^2), \qquad \sigma_H = \beta\sigma_P,$$

where β equals to the ratio of gyrofrequency and collision rate. One can deduce $\sigma_C = \sigma_\parallel$ from these formulae. Fig. 1 demonstrates this property below 100 km.

The cloud is a long horizontal cylinder in our 2-D model. It can be normal or parallel to the geomagnetic equator. The cross section of the cloud is the ellipse $5\,\text{km} < z < 15\,\text{km}$, $|x| < 20\,\text{km}$. We take as given some vertical external current. Its density $j_{ext} = const$ inside the cloud and goes to zero in a layer near boundary. Its value is chosen to be $j_{ext} = 110\,\text{pA/m}^2$ to make the potential difference in the cloud equal to 10 MV.

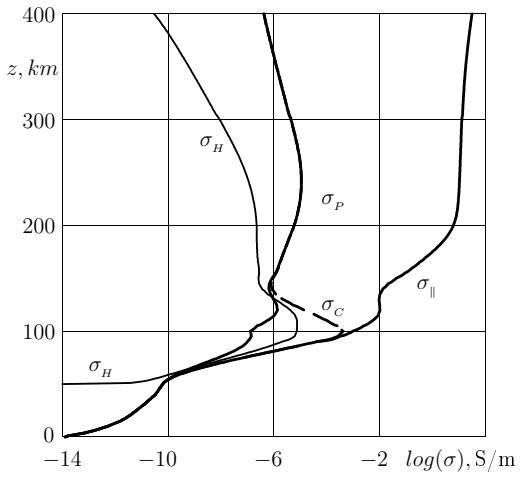

Figure 1: Profiles of the components of the electric conductivity tensor for equatorial night–time ionosphere during minimum of Solar activity. Field-aligned conductivity $\sigma_{\parallel}$, Pedersen conductivity σ_P, Hall conductivity σ_H. Dashed line - Cowling conductivity σ_C.

Results

The results of calculation for a long cloud that is normal to the geomagnetic equator are presented in Fig. 2. Current lines are plotted for the sum of conductivity and external currents, since just this sum has zero divergence. Fig. 3 presents electric field near ground that is independents of magnetic field inclination. It is equal to the fair-weather value outside the region under cloud with 20 km extension and has opposite direction and twenty times larger strength under the cloud.

The pictures can be interpreted as natural ones, since the equation for the electric potential V in a gyrotropic medium (conductivity tensor (6) with Hall and Pedersen conductivities) is the same as the equation of heat transfer in moving medium for temperature T. It is enough to take heat conductance $\lambda = \sigma_P$, and velocity

$$v_x = \frac{1}{\rho C}\,\frac{\partial\,\sigma_H}{\partial z},$$

where ρ is density of the fluid, C is heat capacity per unit mass at constant pressure. So increase of σ_H looks like a wind to the right. Of cause it is not real wind, just mathematical equivalence to the solution of the problem, that is simple for our imagination.

If a long cloud is parallel to the geomagnetic equator, conductivity tensor is a symmetric one and has shape (5). It is a particular case of the cloud studied in [1] with specific magnetic inclination $I = 0^o$. Then the energy functional (13) becomes the sum of the energy functional for Dirichlet and Neumann boundary value problems for the functions F and P. The result $P = 0$ and F is equal to the electric potential V. The results of calculation for such a case are presented in Fig. 4.

Comparison of Fig. 2 and 4 shows that nothing below 60 km is varied with magnetic inclination. These region does not differ from high and middle latitudes studied in [1]. Since the input parameter of the model $j_{ext} = 110\,\mathrm{pA/m^2}$ and the cloud has 40 km width, the total $I_{ext} = 4.4\,\mathrm{mkA/m}$. Fig. 2b, 4b show that 30% of this I_{ext} go to the ionosphere. It is pure conductivity current outside the cloud. Naturally, the same current goes from ground to the cloud.

We see long distance shift to the East due to Hall conductivity in Fig. 1 that does not exist when the cloud is is elongated in the East–West direction. One more difference from high and middle latitudes is closure of the currents about 10 km lower in the ionosphere. It is due to large field-aligned or Cowling conductivities in comparison with σ_P which define horizontal currents near the equator instead of σ_P in high and middle latitudes.

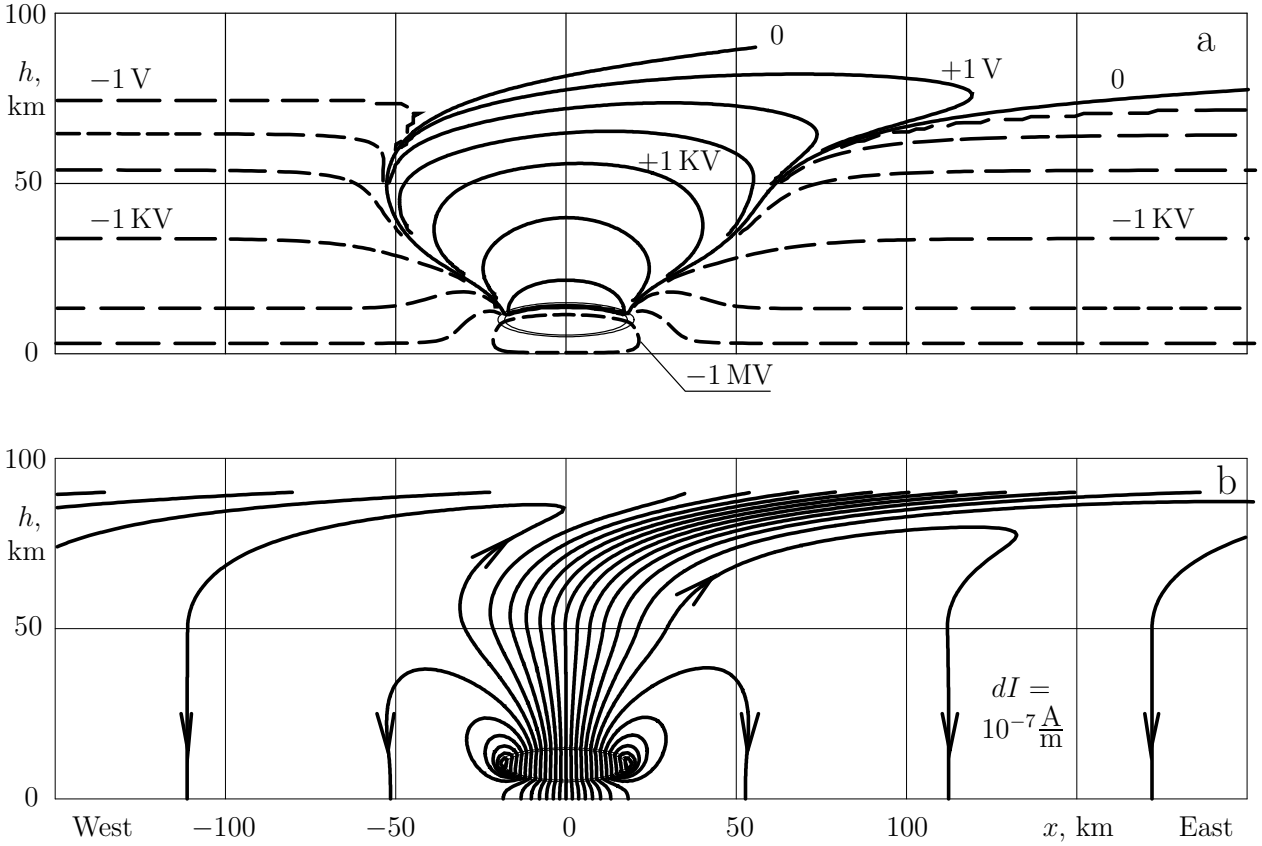

Figure 2: Results for horizontal magnetic field, equatorial plane. a - electric potential. b - current lines for the sum of conductivity and external currents, $dI = 10^{-7}$A/m.

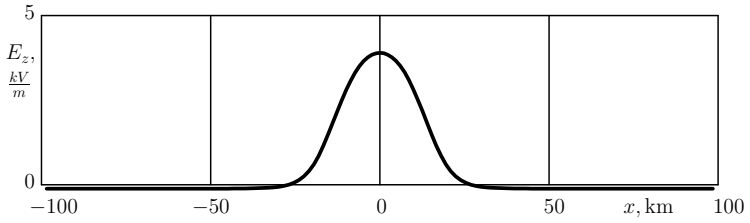

Figure 3: Vertical electric field near ground .

Conclusions

A model of electric current penetration from a thunderstorm cloud into equatorial ionosphere is created. It is based on the empirical models of atmospheric and ionospheric conductivities.

In the main part of the atmosphere that is below 60 km the electric fields and currents are independent of the magnetic inclination.

The potential difference in the cloud 10 MV can be generated with vertical external current $j_{ext} = 110\,\mathrm{pA/m^2}$. Total current to the ionosphere is of about 30% of the total I_{ext} in the cloud with 40 km horizontal size. These numbers are sensitive to the model of conductivity. Conductivity inside a cloud is not a well known parameter.

Atmospheric currents are closed in equatorial ionosphere lower then in middle latitudes. Above 80 km currents turns to horizontal direction, if cloud is elongated along the magnetic equator. The current entry area in the ionosphere is about 100 km shifted to the East from the cloud by Hall conductivity, if cloud is normal to the magnetic equator.

Acknowledgments. This work is supported by grant 12-05-00152 from the Russian Foundation for Basic Research.

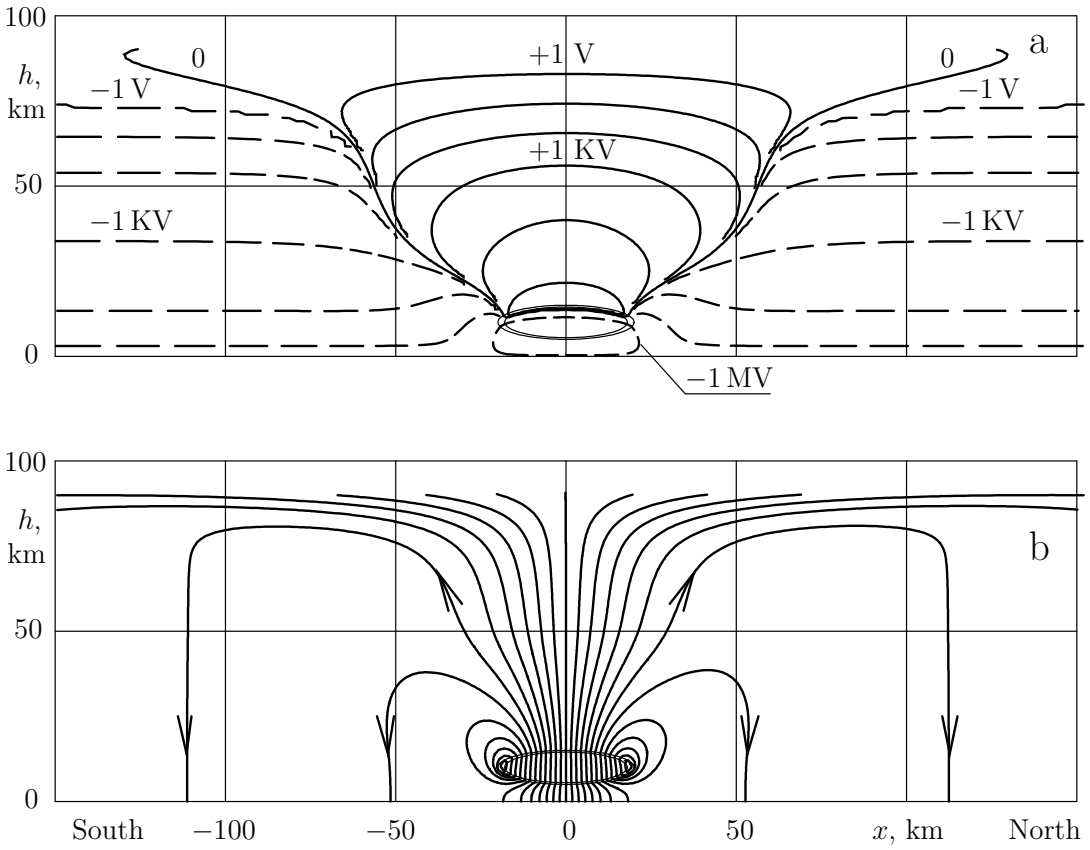

Figure 4: Results for horizontal magnetic field, meridional plane. a - electric potential in logarithmic scale. b - current function, $dI = 10^{-7} A/m$.

References

[1] Denisenko, V.V. (2014), Electric current penetration from a thunderstorm cloud into the middle-latitude ionosphere, *Proceedings of the 10-th International Conference "PROBLEMS OF GEOCOSMOS". St. Petersburg, Petrodvorets, October 4-10, 2014. (This issue)*

[2] Denisenko, V.V. (1995), *Energy methods for elliptic equations with asymmetric coefficients*, 204 pp., Publ. house of the Russian Academy of Sciences Siberian Branch, Novosibirsk, [in Russian].

[3] Denisenko, V.V., H.K. Biernat, A.V. Mezentsev, V.A. Shaidurov, and S.S., Zamay (2008), Modification of conductivity due to acceleration of the ionospheric medium, *Ann. Geophys.* 26, 2111-2130.

[4] Mareev, E.A. (2010), Achievments and prospects of research of the global electric circuit, *Achievments in Physical Sciences*, 180(5), 527534.

[5] Mikhlin, S.G. (1957), *Variational Methods in Mathematical Physics*, 378 pp., Gostekhizdat, Moscow. [in Russian]

[6] Rycroft, M.J., A. Odzimek (2010), Effects of lightning and sprites on the ionospheric potential, and threshold effects on sprite initiation, obtained using an analog model of the global atmospheric electric circuit, *J. Geophys. Res.* 115(A00E37), doi:10.1029/2009JA014758.

CUMULATIVE AND MODULATIONAL EFFECTS OF THE STRONG EARTHQUAKES IN CALIFORNIA

A. V. Guglielmi[1], O. D. Zotov[2]

[1]Institute of Physics of the Earth, RAS, Moscow, Russia, e-mail: guglielmi@mail.ru

[2]Geophysical Observatory Borok, IPE, RAS, Borok, Russia, e-mail: ozotov@inbox.ru

Abstract. In this work we study the earthquakes in California. The aim is to search for the impact of converging seismic waves and free oscillations of the Earth on the earthquake source. Both effects have been discovered previously by statistical analysis of the global seismicity. In this work we have attempted to observe the effects by using the data of regional seismicity. As a result, we succeeded in finding some non-trivial properties of the source of strong earthquake that manifest both before and after the formation of the main discontinuity of rocks at the mainshock. In the course of analysis of the foreshocks and aftershocks we found confirmation of the ideas of round-the-world seismic echo, cumulative effect of converging surface waves, and modulational effect of the free Earth's oscillations. Further research in this direction seems interesting and promising.

INTRODUCTION

The aim of this work is to search for the impacts of converging seismic waves and free oscillations of the Earth on the earthquakes. These effects were discovered earlier in the course of statistical analysis of the global seismicity [1-4]. In the present work we have attempted to observe the effects by using the data of regional seismicity. For this purpose, we have considered the strong earthquakes in California.

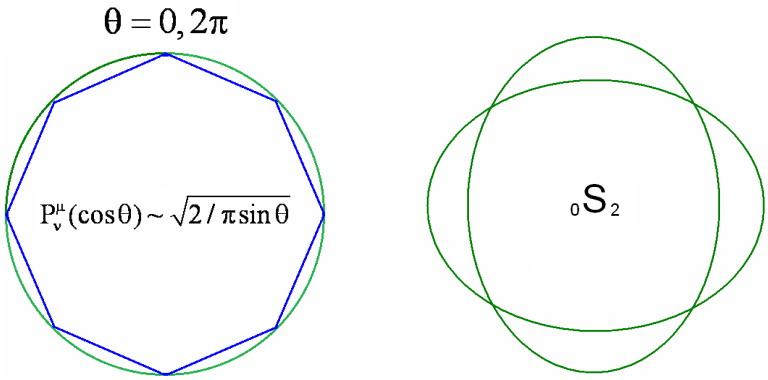

Fig.1. Schematic pictures of the round-the-world seismic echo (left panel) and the spheroidal oscillations of the Earth (right panel). The resonant rays of the round-the-world echo formed by the surface and body waves (the smooth and broken lines, respectively). The angular dependence of the short-wave asymptotics of the associated Legendre polynomials, which are proportional to the amplitude of the oscillations, is shown in the central part of the image.

The idea is that the main shock excites two nontrivial trigger, namely, the round-the world seismic echo and the free oscillations of the Earth, which may affect the dynamics of the "cooling" earthquake source. Figure 1 illustrates schematically the round-the-world seismic echo and the free spheroidal oscillations of the Earth. The time delay of round-the world echo due to the surface Rayleigh wave is 3 h approximately. The frequency of spheroidal oscillations $_0S_2$ equals 0.309 mHz (see [1-4] for the details).

DATA AND METHOD

We used the following data catalogs:

1. The world catalog of earthquakes by U.S. Geological Survey (USGS/NEIC), 1973-2010 http://neic.usgs.gov/neis/epic/epic_global.html
2. The regional catalog of earthquakes in Northern California, 1968-2007 http://www.ncedc.org
3. The regional catalog of earthquakes in Southern California, 1983-2008 http://www.data.scec.org

We used the superposed epoch analysis method for study the cumulative effect. The modulational effect we studied by using the method of spectral analysis.

CUMULATIVE EFFECT

The idea of the round-the-world echo is physically quite transparent. In highly simplified form, just look at the Earth as a specific lens, in which the source and the focus are in one place. The surface seismic waves are excited by the mainshock, and are returned to the epicenter. The amplitude of the waves increases with the approach to the epicenter, because the epicenter is the focus (caustic). We believe that the round-the-world echo is capable of inducing a strong aftershock, since the crust in the vicinity of the epicenter is in the stress-strain state for a long time after the main shock.

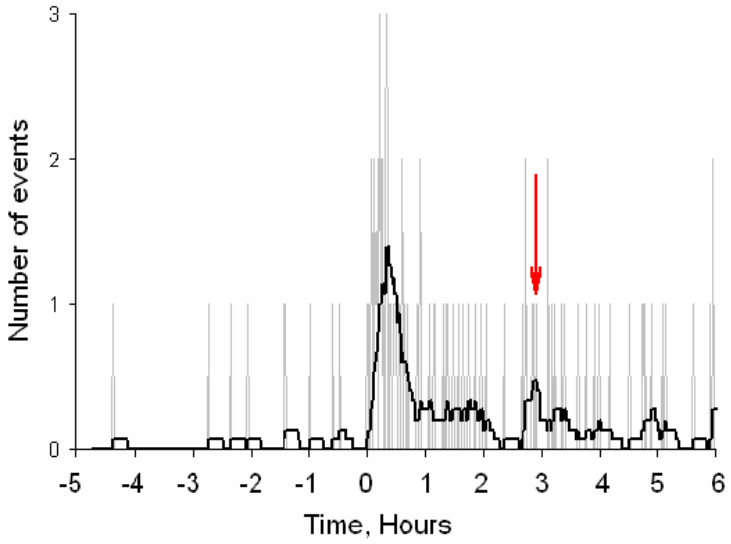

Fig.2. The dynamics of aftershocks with the magnitudes $6 \le M < 7.5$ inside 2° epicentral zones of mainshocks with magnitudes $M \ge 7.5$, according to the USGS catalog for 1973–2010. The thick line is obtained by averaging the initial distribution over 20 points. The arrow marks the expected delay time of the around-the-world surface-wave echo [4].

Figure 2 illustrates the dynamics of the aftershocks after 167 strong earthquakes. Here, we used the superposed epoch analysis. The occurrence times for the earthquakes with $M \ge 7.5$ are used as the references for synchronizing the aftershocks. We see the peak of the global aftershock activity at about three hours later. This observation provides an argument in favor of our idea that the surface elastic waves excited by the main

shock make a full rotation around the world and, having returned to the epicenter, can generate a strong aftershock there.

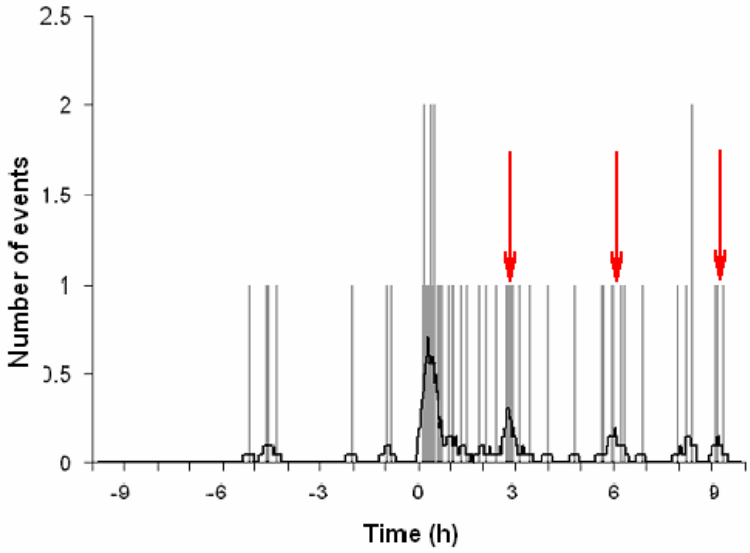

Fig.3. Dynamics of aftershocks with the magnitudes $6.0 \le M < 8.0$ inside 10° epicentral zones of mainshocks with magnitudes $M \ge 8.0$ (USGS, 1973-2010).

We slightly changed the conditions of selection main shocks and aftershocks. We see three maxima in the aftershock activity about three, six and nine hours after mainshocks. It is not excluded that we observe the effect of triple round-the-world echo.

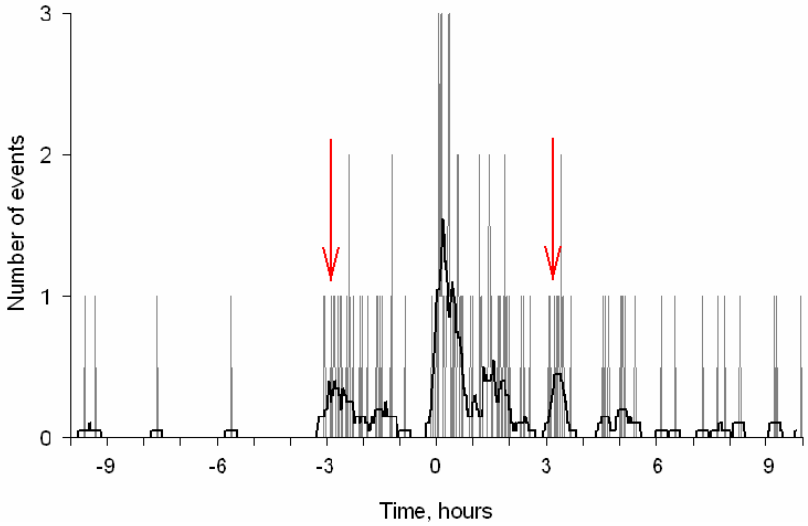

Fig.4. Dynamics of foreshocks and aftershocks with the magnitudes $4.5 \le M < 5.5$ inside 3° epicentral zones of mainshocks with magnitudes $M \ge 5.5$, according to the regional catalog of earthquakes in Southern California (1983-2008).

The analysis of regional catalog testified that round-the-world seismic echo not only generate aftershock but may be the trigger of mainshock also. Figure 4 shows intensification of the foreshocks approximately 3 hours before the main attack.

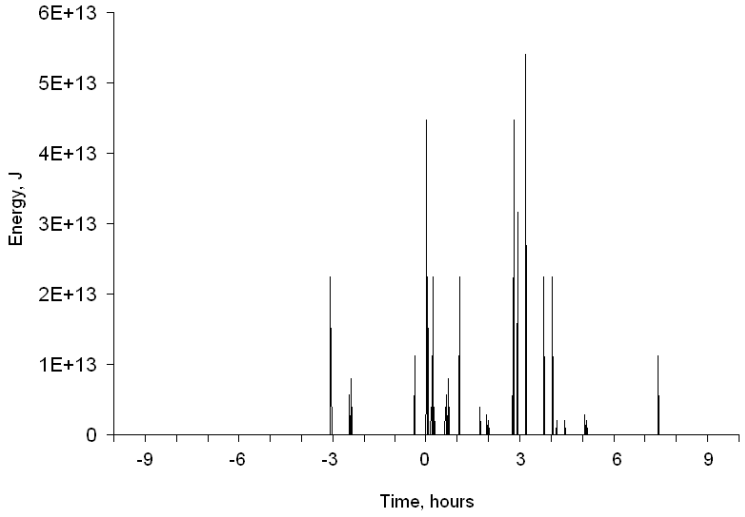

Fig.5. Dynamics of foreshocks and aftershocks with the magnitudes 5≤ M <6 inside 3° epicentral zones of mainshocks with magnitudes M ≥ 6 according to the regional catalogs of earthquakes in Southern (1983-2008) and Northern (1968-2007) California.

Figure 5 shows the joint processing of Northern and Southern California earthquakes catalogs. Here we used the energy as a measure of foreshocks and aftershocks activity. (Of course, we did not consider here the energy of the mainshocks.) We see that the most strong foreshocks and aftershocks are observed respectively for about 3 hours before and 3 hours after the mainshock. This observation is an argument in favor of the idea is that the surface waves propagating outwards from the strong foreshock (mainshock) return back to the vicinity of the epicenter after having made a complete revolution around the Earth and induce there the mainshock (strong aftershock).

MODULATIONAL EFFECT

It is well known that the earthquakes excite the free oscillations of the Earth as a whole at the resonant frequencies of toroidal and spheroidal eigenmodes. We would like to present the arguments in favor of the idea that the Earth's free oscillations induce an earthquake activity. We focused our attention on the spheroidal oscillations ${}_0S_2$, whose period is 54 min. Let us consider the evidences that the seismic activity is really modulated with this period.

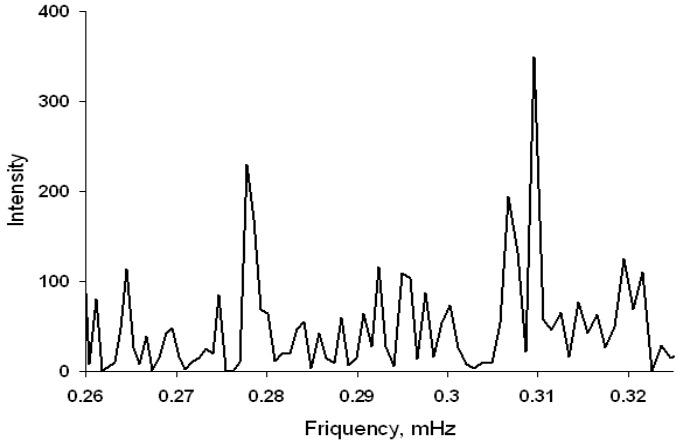

Fig.6. The spectrum of global seismicity (USGS, 1973–2010) [1].

The modulational effect has been discovered earlier by the spectral analysis of the global seismicity [1, 4]. In Figure 6 we observe a sharp peak at a frequency of 0.277 mHz (at a period of 60 min). In our opinion,

this peak has a clear anthropogenic origin and reflects the so-called hour-mark effect [5]. Another peak with a higher amplitude is seen at a frequency of 0.309 mHz, which corresponds to the period of 54 min. The period of 54 minutes coincides with the period of the Earth's fundamental oscillations. This is an indication that the Earth's free oscillations modulate the global seismic activity.

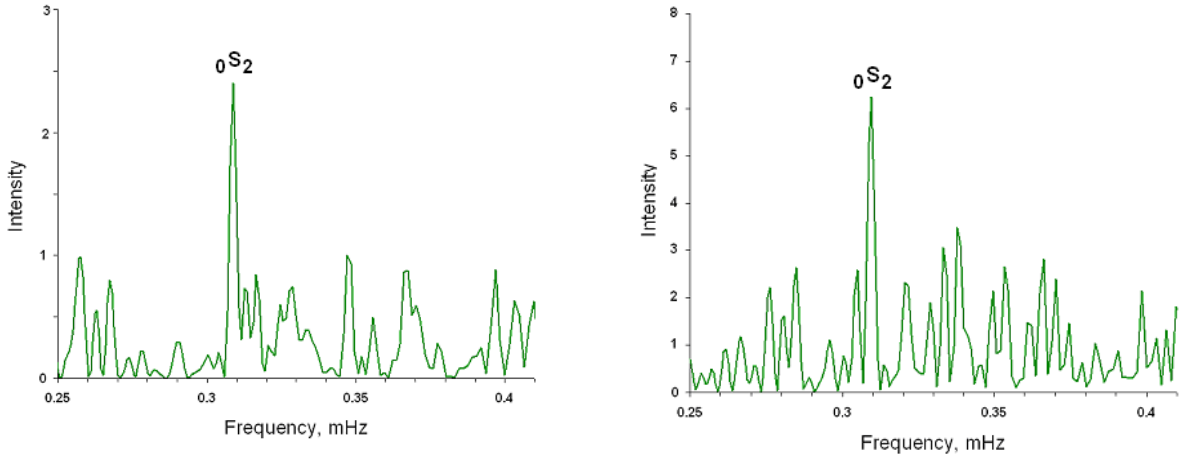

Fig.7. Spectra of aftershocks of two strong earthquakes in California (see the text).

We checked this idea by analyzing the aftershocks in epicentral zones of two strong earthquakes in California. The left panel in Figure 7 shows the spectrum of aftershocks after the mainshock with magnitude M = 5.9 occurred 1994.09.12, 12h 23m 43s in Northern California. The right panel shows the spectrum of aftershocks after the mainshock with magnitude M = 6.0 occurred 1987.10.01, 14h 42m 20s in Southern California. The aftershocks are analyzed in epicentral zones with radius of 3° during the 80 hours after the mainshocks. We see quite clearly the oscillations of the aftershock activity with the period of $_0S_2$ oscillations of the Earth.

SUMMARY

1. The mainshock produces round-the-world seismic echo which may be a trigger of strong aftershock.
2. The strong foreshock produces round-the-world seismic echo which may be a trigger of mainshock.
3. The Earth's free spheroidal oscillations $_0S_2$ modulate the aftershock activity.

Acknowledgments. The work was supported by the Program № 4 of the Presidium of RAS, and RFBR (grant no. 13-05-00066).

REFERENCES

1. Guglielmi A., and O. Zotov (2012), Impact of the earth's oscillations on the earthquakes, *arXiv*:1207.0365v1 [physics.geo_ph].

2. Guglielmi, A.V., and O.D. Zotov (2013), On the nonlinear antipode effect of the earthquakes, *Geophysical research*, 14(1), 54-60. (in Russian).

3. Guglielmi, A. V., and Zotov, O. D. (2013), On the near hourly hidden periodicity of earthquakes, *Izv., Phys. Solid Earth*, 49(1), 1–8.

4. Guglielmi, A. V., O. D. Zotov, and A. D. Zavyalov (2014), The aftershock dynamics of the Sumatra-Andaman earthquake, *Izv, Phys. Solid Earth,* 50(1), 250–258.

5. Zotov O.D., and A.V. Guglielmi (2010), The problems of synchronism of the electromagnetic and seismic events in the dynamical system magnetosphere-technosphere-lithosphere, *Solar-Terrestrial Phys.*, 16, 19-25.

ON THE WAVE FIELD MODELING AND INTERPRETATION IN HIERARCHIC MEDIUM WITH FRACTAL INCLUSIONS

Hachay O.A.[1], Khachay A.Y.[2]

[1]Institute of Geophysics UB RAS, Ekaterinburg, Russia, olgakhachay@yandex.ru;
[2]Ural Federal University, Institute of mathematics and computer sciences, Ekaterinburg, Russia

Abstract. For research of hierarchic medium we had developed an iterative algorithm for electromagnetic and seismic fields in the problem setting similar to analyzed higher for layered-block models with homogeneous inclusions. We had developed an iterative algorithm of inverse problem solution for the same models, using the approach of three stage interpretation. For that we had developed a new integral differential equation for the theoretical inverse problem of 2-D electromagnetic field in a hierarchic inclusion, embedded in the N-layered medium.

Introduction

The last decades are characterized by active development of Earth's sciences. We shall use the materials, published in the book (Dmitrievsky, 2009) by Russian academician Dmitrievsky A.N., who suggested the conception about the development of oil-gas geology in Russian Federation. The modern research methods and technologies give the opportunity to obtain new data about the Earth's structure and processes, which occur in its interior. The conception development about the nonlinear geodynamics practically coincides with research of nonlinear processes in different parts of physics. In geology soliton and auto wave conceptions are developed, principles of synergetic and self organization become be used, and in geodynamics the macro quantum behavior of large mass matter, which are in critical state, in geophysics the auto wave nature of geophysical fields is researched. A new of direction quantum geodynamics appeared. In contrary from traditional approaches in geodynamics, which are based on classical models of continuum, quantum geodynamics allows analyzing the Earth's energetic structure, which evolutes in time and penetrates in all natural phenomena and possesses macro quantum time features. The development of possible methods and approaches must be based on the considering energy of dynamical processes.

For understanding and analyzing the state of the geological medium it is needed to compare the key ideas of geophysics, which give the main ideas to research different dynamical events into the Earth.

"Geophysics of XX century" is the understanding of such features:

- geophysical fields are indicators of the processes, which occur in lithosphere; geophysical parameters, which are registered distantly can have functional or correlation relation with the matter-structural characteristics of geological medium (on macro- and micro levels);
- analysis of space-time and energetic distribution of geophysical field can give information about space-time distribution of geological medium properties;
- registration and analysis of geophysical field in the monitoring regime can give information about the geodynamical processes in near borehole space, in Earth's crust and lithosphere in more deep Earth's layers.

Practical problems of geophysics of XX century had been vigorous stimulus of evolution of theoretical and experimental physics of thin layered, porous and crack media. As a result it had been derived new classes of mathematical models fluid saturated of heterogeneous media, it had been researched anisotropicc effects of geological media, and it had been revealed different physical and physical-chemical effects which occur on the boundaries "solid skeleton-fluid". Geophysics for the first time set a question about possibility of construction physical-geological and mathematical models of geological objects and processes. Applied geophysics of XX century had realized the possibility of research one and the same geological objects on micro level (nuclear geophysics), meso level (electrical, heat, magnetic, acoustic fields) and macro level (fields of elastic waves and low frequency electromagnetic fields).

Geophysics allowed answering on some principal for geological questions:

- what is the value of the depth down and the geometry (sometimes morphology) of researched object;
- what is the matter-structure content of the geological object;
- where and how sub vertical and sub horizontal heterogeneities are located and first of all the zones of micro cracks;

- how are the conditions of filtration in fluid porous aggregate;
- what are the thermal dynamical conditions of researched object location.

We can approve that the modern geophysicists, depending from geological-geophysical conditions, complex of using methods and the level of soft ware can solve these problems."

Key ideas in XXI century in geophysics:

Geophysics of the XXI century is the understanding of that: the Earth is a self evolutionary, self conditioned geo cybernetic system for which the role of a driving mechanism fulfils gradients of geophysical fields. Use in geophysics principles of hierarchic and quantum features of geophysical space, nonlinear effects, effects of re-emission of geophysical fields allow us to create a new geophysics.

New aspects in the methods:

A wide use of interaction and transformation geophysical field's effects.

A wide use of joined measuring systems with use of control influence (type "borehole logging-influence-borehole logging".

Realization by use new investigation methods the recently discovered principles of organization of geological and geophysical space (quantum and hierarchic features).

New aspects in theory and mathematical modeling of geophysical fields and new systems of data interpretation:

Development of new equation classes, which describe the distribution of elastic and electromagnetic fields in heterogeneous media, with account of various effects of nonlinearity of geological media and irreversibility of geophysical processes. It will developed new theories of inverse problems solution with account of the hierarchic structure of inclusions imbedded into the layered medium.

Now we shall investigate and study some results which are into the key direction of geophysics of XXI century, noted by Dmitrievsky, 2009.

New paradigm of mesomechanics

In present day for more adequate understanding of the dynamics of processes, which occur in the geological medium on deep levels by the action of natural and man caused factors Academician V.E. Panin using the results, which had been derived by his colleagues (Panin, 2005) had introduced a new paradigm on the junction between physics and mechanics of deformed solid body, which is the base of physical mesomechanics.

1. Identification of mechanisms of plastic flow on different structural deformation levels, which lead to a fundamental change of the initial inner structure of the solid body and forming into it dissipative substructures as mesoscopic plastic deformation support.

2. Fixing a relation between the outer action, changing of the initial inner structure, forming a hierarchy of mesoscopic self matched structural levels of deformation and occurring as a result of it mechanical fields.
3. Synergetic approach in the methodology of describing the deformed solid body as a non equilibrium many leveled medium, which in the points of bifurcation losses its shift stability on different structural levels and becomes to be destroyed in the conditions of global losses of its shift stability on macro scale level.

For experimental research of deformation mechanisms of specimens on meso level it had been developed new methods with use of speckle interferometer and optical television devices of technical vision, measuring of fractal dimension of deformed solid body. It turns out, that on the meso level 3-D structural elements (meso volumes) move as a whole. In that case it is sufficient to consider a representative volume, which consists on some tens meso volumes, for writing the equations of mesomechanics, taking into account the inner structure of the deforming solid body

For realizing the second point of the new paradigm Panin with his colleagues had written a system of equations, which describes the mechanical field in the deforming solid body on one level (Panin, 2005). It turned out, that it is similarly the Maxwell system of equations for alternating electromagnetic fields. Similarly electromagnetic field, where alternating electric and magnetic fields are mutually linked, the common mechanical field occurs in the deforming solid body, which contains organic mutual linked the translational and rotating modes (Panin, 2005) .

That result was very significant for choice of geophysical methods, using for monitoring of structure and state of rock massif, which is under strong man based action, which is a component of the geological medium in seismic-tectonically areas.

Mathematical modeling, comparison of seismic and electromagnetic response for a block model

It is very significant to define the time of reaction lagging, in spite of the influence on the massive can be assumed as elastic. The unique model which can explain that effect is a model of the massive with a hierarchic structure. We developed a mathematical algorithm using integral and integral-differential equations for 2-D model for two problems in a frequency domain: diffraction a sound wave and linear polarized transverse wave through an arbitrary hierarchy rank inclusion plunged in an N-layered medium. That algorithm differs from the fractal model approach by a freer selecting of heterogeneities position of each rank. And the second the problem is solved in the dynamical approach. The higher the amount of the hierarchic ranks the more is the degree of nonlinearity of the massive response and the longer can be the time of massive reaction lag of the influence. In that paper are derived integral equations and integral differential equations of 2-D direct problem for the seismic field in the dynamical variant and had been provided the joint analysis of the integral equations for 2-D problems for electromagnetic and seismic fields. The received results can be used for definition of the complex criterions of achievement the research of high complicated medium both with seismic and electromagnetic methods. For the problem of sound diffraction on the 2-D elastic heterogeneity, located in the j-th layer of the n-layered medium, using the approach from V.I. Dmitriev and V.D. Kupradze, we can derive the integral differential equation for the distribution of the potential for the vector of elastic displacements inside the heterogeneity.

$$\frac{(k_{1\tilde{n}}^2 - k_{1j}^2)}{2\pi}\iint_{S_\xi}\varphi(M)G_{\tilde{n}j}(M,M^0)d\tau_M + \frac{\sigma_{j\tilde{a}}}{\sigma_{j\tilde{n}}}\varphi^0(M^0) -$$
$$-\frac{(\sigma_{j\tilde{a}} - \sigma_{j\tilde{n}})}{\sigma_{j\tilde{n}}\,2\pi}\oint_C G_{\tilde{n}j}\frac{\partial\varphi}{\partial n}dc = \varphi(M^0) \quad by\, M^0 \in S_C$$
$$\frac{\sigma_{j\tilde{n}}(k_{1\tilde{n}}^2 - k_{1j}^2)}{\sigma(M^0)2\pi}\iint_{S_\xi}\varphi(M)G_{\tilde{n}j}(M,M^0)d\tau_M + \varphi^0(M^0) -$$
$$-\frac{(\sigma_{j\tilde{a}} - \sigma_{j\tilde{n}})}{\sigma(M^0)2\pi}\oint_C G_{\tilde{n}j}\frac{\partial\varphi}{\partial n}dc = \varphi(M^0) \quad by\, M^0 \notin S_C \qquad (1)$$

Using the second integral-differential presentation we can define the potential of the elastic displacements in the arbitrary layer, and then we can calculate the distribution of the vector of elastic displacements in the arbitrary layer. Let us compare the derived expressions with the solution of the diffraction problem for electromagnetic field in the frame of the same geometrical model. That case corresponds to the problem of exciting by a plane wave H -polarization, the solution of which is done in the paper (Hachay et al., 2008a,b). Let us transform it to the form similarly to (1) and let us compare the derived equations for the solution of the inner 2-D seismic and electromagnetic problem: $k^2(M^0) = i\omega\mu_0\sigma(M^0), \mu_0 = 4\pi 10^{-7}\frac{\partial H}{M}, \sigma\ (M^0)$ - conductivity in the point M0., i-the imaginary unit, $H_x(M^0)$ - the summarized component of magnetic field, $H_x^0(M^0)$ - the component of magnetic field in the layered medium without heterogeneity, $k_{ji}^2 = i\omega\mu_0\sigma_{ji}, k_i^2 = i\omega\mu_0\sigma_i$, σ_{ji} -conductivity into the heterogeneity, located into the j-the layer, σ_i - conductivity of the i-th layer of the n-layered medium, $G_m(M,M^0)$ - the Green function of the 2-D problem for the case of H-polarization (Hachay, 2007).The difference in the boundary conditions for the seismic and electromagnetic problems lead to different types of equations: in the seismic case- to the integral-differential equation, in the electromagnetic case to the load integral equation of Fredholm of the second type. If for the solutions of the direct electromagnetic and seismic in dynamical variant problems we can establish the similarity in the explicit expressions for the components of electromagnetic and seismic fields by definite types of excitation then with complicating of the medium structure as can we see from the obtained result by the case of the seismic field linked with longitudinal waves the similarity vanishes. That means that the seismic information is additional to the electromagnetic information about the structure and

state of the medium.

$$\begin{aligned}
&\varphi(M^0) = \frac{(k_{1ji}^2 - k_{1j}^2)}{2\pi} \iint_{S_C} \varphi(M) G_{Sp,j}(M, M^0) d\tau_M + \\
&+ \frac{(\sigma_{ji} - \sigma_{ja})}{\sigma_{ji} 2\pi} \oint_C G_{Sp,j} \frac{\partial \varphi}{\partial n} dc + \frac{\sigma_{ja}}{\sigma_{ji}} \varphi^0(M^0) \; by \; M^0 \in S_C \\
&H_x(M^0) = \frac{k_{ji}^2 - k_j^2}{2\pi} \iint_{S_C} H_x(M) G_m(M, M^0) d\tau_M + \\
&+ \frac{k_{ji}^2 - k_j^2}{k_j^2 2\pi} \oint_C H_x(M) \frac{\partial G_m}{\partial n} dc + \frac{k_{ji}^2}{k_j^2} H_x^0(M^0) \; by \; M^0 \in S_C
\end{aligned} \tag{2}$$

For the problem of diffraction of a linearly polarized elastic transverse wave on the 2-D heterogeneity located in the j-th layer of the n-layered medium, using the approach described in the paper (Hachay et al., 2008a,b) for the electromagnetic wave 2-D problem (case H-polarization), (the geometric model is similar to a that described higher in the previous problem) we obtain the expressions as follows for the components of the displacement vector:

$$\begin{aligned}
&\frac{(k_{2ji}^2 - k_{2j}^2)}{2\pi} \iint_{S_C} u_x(M) G_{Ss,j}(M, M^0) d\tau_M + \frac{\mu_{ja}}{\mu_{ji}} u_x^0(M^0) + \\
&+ \frac{(\mu_{ja} - \mu_{ji})}{\mu_{ji} 2\pi} \oint_C u_x(M) \frac{\partial G_{Ss,j}}{\partial n} dc = u_x(M^0) \quad by \; M^0 \in S_C \\
&\frac{\mu_{ji}(k_{2ji}^2 - k_{2j}^2)}{\mu(M^0) 2\pi} \iint_{S_C} u_x M) G_{Ss,j}(M, M^0) d\tau_M + u_x^0(M^0) + \\
&+ \frac{(\mu_{ja} - \mu_{ji})}{\mu(M^0) 2\pi} \oint_C u_x(M) \frac{\partial G_{Ss,j}}{\partial n} dc = u_x(M^0) \quad by \; M^0 \notin S_C
\end{aligned} \tag{3}$$

The expressions (3) content the algorithm of seismic field simulation for distribution of transversal waves in the n-layered medium, which contain a 2-D heterogeneity. The first expression is a Fredholm load integral equation of the second type the solution of which gives the distribution of the components of the elastic displacements vector inside the heterogeneity. The second of them is an integral expression for calculation of the elastic displacements vector in the arbitrary layer of the n-layered medium. Comparing the expressions (3) with correspondingly for the electromagnetic field (H-polarization) (2) we see that there is a similarity of the integral structure of these expressions. The difference is only for the coefficients of corresponding terms in the expressions (2) and (3).That we can account by choosing the system of observation with one or another field. We must also account the difference of the medium response frequency dependence from seismic or electromagnetic excitation. But keeping within the similarity of the coefficients the seismic field, excited by transversal waves, and the electromagnetic field will contain the similar information about the structure of the heterogeneous medium and state, linked with it. Those results are confirmed by the natural experiments described in the paper (Hachay, 2007). Thus, it is showed that for more complicated, than horizontal-layered structures of the geological medium the similarity between the electromagnetic and seismic problems for longitudinal waves get broken. Therefore, these observations with two fields allow getting reciprocally additional information about the structure and especially about the state of the medium. These fields will differently reflect the peculiarities of the heterogeneous structures and response on the changing their state. If we can arrange seismic observations only with the transversal waves together with the magnetic component of electromagnetic one (H-polarization) in the 2-D medium, it will be establish the similarity, which can be used by construction of mutual systems of observation for magneto-telluric soundings and deep seismic soundings on exchanged waves.

Mathematical modeling of seismic response for a hierarchic model

From the point of view of the paradigm of physical mesomechanics, which includes the synergetic approach to the change of rock massif state of different matter content, that problem can be solved with use of monitoring methods, which are settled on the research of hierarchic structured media (Panin,1995). For description of these effects it is needed to consider the wave process in the hierarchic blocked medium. Let us consider an algorithm of sound diffraction on 2-D elastic heterogeneity with hierarchic structure, located in the j-th layer of n-layered medium (Hachay et al., 2008a,b). If by transition on the next hierarchic level the axis of two-dimensionality does not change and only the geometry of the section of embedded structures change, then we can write the iteration process of modeling of the seismic field (case generation only longitudinal wave). The iteration process covers to modeling of the response of transition from the previous hierarchic level on the next level. Inside each hierarchic level the integral-differential equation and the integral-differential representation are calculated as it is written in the papers (Hachay et al., 2008a,b).

$$\begin{aligned}
&\frac{(k_{1jil}^2-k_{1j}^2)}{2\pi}\iint\limits_{S_{Cl}}\varphi_l(M)G_{Sp,j}(M,M^0)d\tau_M+\frac{\sigma_{ja}}{\sigma_{jil}}\varphi_{l-1}^0(M^0)-\\
&-\frac{(\sigma_{ja}-\sigma_{jil})}{\sigma_{jil}2\pi}\oint\limits_{Cl}G_{Sp,j}\frac{\partial\varphi_l}{\partial n}dc=\varphi_l(M^0)\quad by\,M^0\in S_{Cl}\\
&\frac{\sigma_{jil}(k_{1jil}^2-k_{1j}^2)}{\sigma(M^0)2\pi}\iint\limits_{S_{Cl}}\varphi_l(M)G_{Sp,j}(M,M^0)d\tau_M+\varphi_{l-1}^0(M^0)-\\
&-\frac{(\sigma_{ja}-\sigma_{jil})}{\sigma(M^0)2\pi}\oint\limits_{Cl}G_{Sp,j}\frac{\partial\varphi_l}{\partial n}dc=\varphi_l(M^0)\quad by\,M^0\notin S_C
\end{aligned}\tag{4}$$

$$\begin{aligned}
&\frac{(k_{2jil}^2-k_{2j}^2)}{2\pi}\iint\limits_{S_{Cl}}u_{xl}(M)G_{Ss,j}(M,M^0)d\tau_M+\frac{\mu_{ja}}{\mu_{jil}}u_{x(l-1)}^0(M^0)+\\
&+\frac{(\mu_{ja}-\mu_{jil})}{\mu_{jil}2\pi}\oint\limits_{Cl}u_{xl}(M)\frac{\partial G_{Ss,j}}{\partial n}dc=u_{xl}(M^0)\quad by\,M^0\in S_{Cl}\\
&\frac{\mu_{jil}(k_{2jil}^2-k_{2j}^2)}{\mu(M^0)2\pi}\iint\limits_{S_{Cl}}u_{xl}M)G_{Ss,j}(M,M^0)d\tau_M+u_{x(l-1)}^0(M^0)+\\
&+\frac{(\mu_{ja}-\mu_{jil})}{\mu(M^0)2\pi}\oint\limits_{Cl}u_{xl}(M)\frac{\partial G_{Ss,j}}{\partial n}dc=u_{xl}(M^0)\quad by\,M^0\notin S_{Cl}
\end{aligned}\tag{5}$$

Inverse problem for electromagnetic field propagation through a layered conductive medium with hierarchic inclusions

In the paper (Hachay, 1994) it had been considered a conception of a staged interpretation of the alternating electromagnetic field. On the first stage the parameters of the normal section or the parameters of the one dimensional non magnetic medium in which are embedded anomalous conductive or magnetic inclusions are defined. On the second stage it is developed a procedure of anomalous alternating field fitting by a system of singular sources, which are embedded into the horizontal layered medium with geoelectrical parameters, which had been defined on the first stage. On the third stage it is solved the theoretical inverse problem, that is for the given geoelectrical parameters for the embedded medium for the set of anomalous parameters, defined on the second stage, we define the contours of the inclusions. We had derived explicit integral-differential equations of the theoretical inverse problem for 2-D and 3-D alternating and 3-D stationary electromagnetic fields in a frame of the models: conductive or magnetic body in the J-th layer of the conductive layered half space. Here, using the approach, which was written in the papers (Hachay (1989, 1990), we had derived the equation of the theoretical inverse problem for the 2-D alternating electromagnetic field (scalar case) for the model: a conductive hierarchic inclusion of the k rank, located in the J-th layer of the conductive N-layered half space.

$U^{+(k-1)}(M_k)$ - anomaly component $E_x^{+(k-1)}$ or $H_x^{+(k-1)}$ for the inclusion of k-th rank by $M_k \in \partial D_k$, *U(M)*-sum field E_x or H_x, $U^{i(k-1)}(M)$ -normal field of the layered section E_x or H_x for k=1, for k>1- the field E_x or H_x, must be calculated, using the direct problem solution with use the algorithm (Hachay et al., 2013). $G^{ak}(M_k, M_o)$ - Green function for the inner area of the heterogeneity of the k-th rank, $G(M_k, M_o)$ - Green function of the N-layered medium (Hachay (1989,1990), b_ν, b_i, b_{ak} - complex coefficients for the J-th layer and for the inner area of the heterogeneity of the k-th rank, which are introduced in (6).

$$
\begin{aligned}
&2\pi U^{+(k-1)}(M_0) = \int_{\partial Dk}((U_\nu^{+(k-1)}(M_k) + \\
&U_\nu^{i(k-1)}(M_k))(\frac{\partial G^{ak}(M_k, M_0)}{\partial n} - (\frac{b_\nu}{b_i})\frac{\partial G(M_k, M_0)}{\partial n}) \\
&-b_\nu(\frac{\partial U_\nu^{+(k-1)}(M_k)}{\partial n} + \frac{\partial U_\nu^{i(k-1)}(M_k)}{\partial n}) \times \\
&\times((\frac{1}{b_{ak}})G^{ak}(M_k, M_0) - (\frac{1}{b_i})G(M_k, M_0)))dl_k
\end{aligned}
\tag{6}
$$

The hierarchic heterogeneities are approximated by embedded non axial conductive σ_{ak} cylinders, located along the axes OX. As a result of solution of the equation (1) for the function $r(\varphi)$, which describe the contour of the sought heterogeneity of the k-th rank.

Conclusion

Thus, it is showed that for more complicated, than horizontal-layered structures of the geological medium the similarity between the electromagnetic and seismic problems for longitudinal waves get broken. These fields will differently reflect the peculiarities of the heterogeneous structures and response on the changing their state. If we can arrange seismic observations only with the transversal waves together with the magnetic component of electromagnetic one (H-polarization) in the 2-D medium, it will be established the similarity, which can be used by construction of mutual systems of observation for magneto-telluric soundings and deep seismic soundings on exchanged waves. For research of hierarchic medium we had developed an iterative algorithm for electromagnetic and seismic fields in the problem setting similar to analyzed higher for layered-block models with homogeneous inclusions. These algorithms differ from the fractal model approach by a more free selecting of heterogeneities position of each rank. If the boundaries of the inclusion of the k rank are fractals (Mandelbrot (1982)) the surface and contour integrals in the integral equations must be changed to repeated fractional integrals of Riman-Liuvill (Simko et al., 1987).

We had derived the equation of the theoretical inverse problem for the 2-D alternating electromagnetic field (scalar case) for the model: a conductive hierarchic inclusion of the k rank, located in the J-th layer of the conductive N-layered half space.

References

Dmitrievsky A.N. (2009), *Selected works*. Moscow, Nauka. V.2. 435 p.

Panin V.E. (1995) *Physical mesomechanics and computer construction of materials*. Novosibirsk, Nauka, SB RAS.

Hachay O.A. (2007), Geophysical monitoring of the state of rock massif with use of paradigm of physical mesomechanics. *Physics of the Earth*, 4, 58−64.

Hachay O.A. et al. (2008a) Modeling of seismic and electromagnetic field in the hierarchic heterogeneous media. *Proceedings of International conference. Ekaterinburg*: IGF UB RAS

Hachay O.A. et al. (2008b), Complex electromagnetic and seismic method of research of the crust and Earth's mantle structure. *Proceedings of International conference. Ekaterinburg*: IGF UB RAS

Hachay O.A. et al. (2013), Modeling of electromagnetic and seismic fields in hierarchic heterogeneous media. *Bull. South Ural State Univ. Ser.: "Computational mathematics and Software Engineering"*, 2, 48−55.

Hachay O.A. (1994), *Mathematical modeling and interpretation of alternating electromagnetic field in heterogeneous crust and upper mantle of the earth*. Professor Dissertation. Sverdlovsk: IGF UB RAS.

Hachay O.A. (1989), About interpretation 2-D alternative and 3-D stationary anomalies of electromagnetic field. *Physics of the Earth*, 10, 50−58.

Hachay O.A. (1990), About the solution of inverse problem of 3-D alternating electromagnetic fields. *Physics of the Earth*, 2, 55−59.

Mandelbrot B.B. (1982), *The Fractal Geometry of Nature*. San Francisko. Freeman.

Simko S.G., A.A. Kilbas, O.I. Marichev (1987), *Integrals and derivatives of partial rank and some it's applications*. Minsk, Technique.

SOUNDING OF THE EARTH'S CRUST USING ULF PHASE-GRADIENT METHOD

V.S. Ismaguilov, Yu.A. Kopytenko, Petrishchev M.S.

St. Petersburg Branch of IZMIRAN, St. Petersburg, Russia, e-mail: office@izmiran.spb.ru

Abstract. New method of the phase-gradient sounding (PGS) is proposed for investigation of geoelectric characteristics of the earth's crust. In this method, magnetic gradientometers are used for construction of gradient and phase velocity vectors along the Earth's surface. The magnetic gradientometer consists of three three-component synchronized magnetic stations located in tops of a triangle at small distances (3-5 km) each from the other. The gradient vectors are directed to a local source of the ULF EM waves, and the phase velocity vectors - from the source. The vector directions give an opportunity to determine a location of geoelectric anomalies. Values of the phase velocities allow to calculate apparent resistivity of the earth's crust for different frequencies in ULF range (F=0.001- 10 Hz). The gradient and phase velocity vectors allow detecting epicenters of forthcoming strong earthquakes. Comparisons of the PGS method with the widespread magneto-telluric sounding (MTS) method display a good coincidence.

Phase-gradient method was earlier used for investigations of an anomalous behavior and directions of gradients and phase velocities of ULF geomagnetic disturbances (F=0.001- 10 Hz) arising before a forthcoming strong EQ [Kopytenko et al., 2000, 2001; Ismaguilov et al., 2001, 2002]. In this work, we use gradients for determination of geoelectric anomaly location and phase velocities of ULF geomagnetic variations for determination of the Earth's crust apparent resistivity.

For a harmonic source (~ $e^{i\omega t}$) the diffusion equation in one-dimensional case (plane waves) has a partial solution for magnetic field variations [Semenov, 1968]:

$$B=B_0 e^{-kx} e^{i(\omega t-kx)} \quad (1)$$

In (1) ω - cyclic frequency, wave number $k = 2\pi/\lambda = \sqrt{\omega\mu_0/2\rho}$, where λ - wavelength, ρ – electric resistivity of the Earth's media and μ_0 – the absolute magnetic constant. For the plane waves in the Earth's media, a partial solution of the wave equation with a big accuracy has the same solution.

Using synchronous observations of the magnetic field variations in two points at the Earth's surface, we can find the phase velocity and gradient values between these points:

$$V_{21} = \omega/k = \tau/d_{21}$$
$$G_{21} = (B_2(t) - B_1(t+\tau))/d_{12} \quad (2)$$

In (2) τ is the phase delay and d_{21} is a distance between two points at the Earth's surface, $B_1(t)$ and $B_2(t+\tau)$ – magnetic field amplitudes in two points taking into account the phase delay τ.

If we have three points of observation, it is possible to construct the phase velocity and gradient vectors (directions α and values |V| and |G|) along the Earth's surface.

For the phase velocity vector:

$$\alpha = \mathrm{Arctg}\frac{V_{12}\cos(a_1) - V_{13}\cos(a_2)}{V_{12}\sin(a_1) + V_{13}\sin(a_2)}$$
$$|V| = V_{21}\cos(\alpha) = V_{31}\sin(\alpha+a_1) \quad (3)$$

For the gradient vector:

$$\alpha = \mathrm{Arctg}\frac{G_{13}\cos(a_1) - G_{12}\cos(a_2)}{G_{12}\sin(a_1) + G_{13}\sin(a_2)}$$
$$|G| = G_{21}/\cos(\alpha) = G_{31}/\sin(\alpha+a_1) \quad (4)$$

The angles a_1 и a_2 can be determined through coordinates of magnetic stations 2 and 3 (base station 1 is situated in the origin of coordinates - Fig.1): $a_1 = \mathrm{arctg}(x_2/y_2)$, $a_2 = \mathrm{arctg}(x_3/y_3)$.

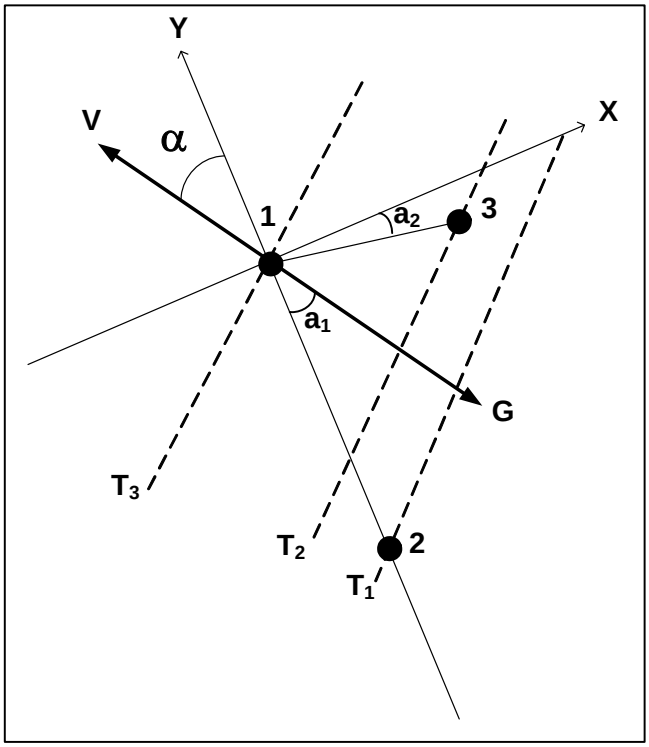

Fig.1. Location of magnetic stations (1, 2, 3), electromagnetic wave front (dashed lines in moments T1, T2, T3) and directions of phase velocity and gradient vectors (**V** and **G**).

The phase velocity along the earth's surface of the primary EM wave falling down from the atmosphere is ≥c (the light velocity) and a phase delay between two points at the earth's surface is very close to zero. Therefore the phase delays of the EM waves observed at the earth's surface are completely determined by the secondary EM waves reflected or generated by the lithosphere sources (geoelectric anomalies of conductivity situated in the earth's crust or sources connected with the EQ preparation region).

From (1) it is possible to determine a velocity of moving plane of a constant phase (the phase velocity V_{ph}) and the apparent resistivity ρ_a of the earth media (integrated value along the EM wave track):

$$V_{ph} = w/k = (2\rho_a/w\mu_0)^{1/2} = (10^7\rho_a/T)^{1/2} \qquad (5)$$

$$\rho_a = 10^{-7}\, V^2_{ph} T$$

Here $T = 1/f = 2\pi/w$ - period of oscillations, $\mu_0 = 4\pi \cdot 10^{-7} N/A^2$- absolute magnetic constant (we suppose that relative magnetic constant $\mu = 1$ in the earth's crust). Therefore, if the phase velocity of the wave propagation in the earth's crust is known, we can find the apparent resistivity of the earth's crust along the way of the EM wave from a lithosphere source to the earth's surface. We apply a statistical study and use mean values of the phase velocities calculated for some time interval.

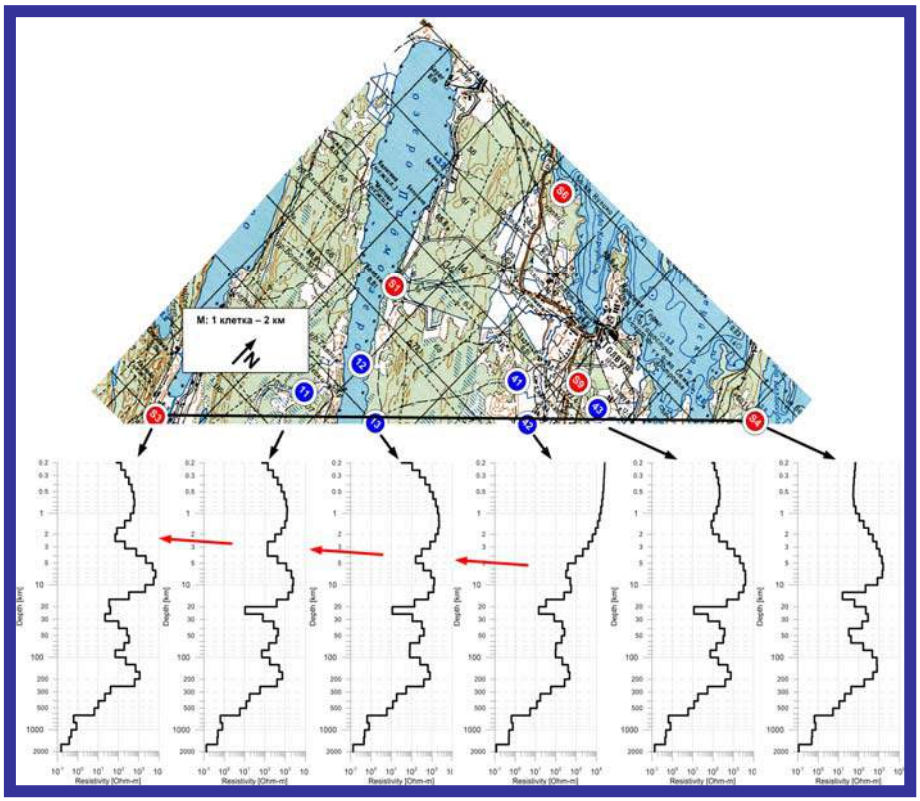

Fig.2. Comparison of results of Earth's crust sounding by MTS and PGS methods.
Red and blue circles – magnetic stations.
Curves presents depth's dependence of apparent resistivity.

Using experimental data in two points and model representations (1) momentary values of the phase velocity in direction between two points is can be determined in the next way [Ismaguilov et al., 2006]:

$$V_{21}(t) = 2\omega d_{21} / \ln[\frac{B_1(t)}{B_2(t+\tau)}] \qquad (6)$$

In (5) $B_1(t)$ and $B_2(t+\tau)$ – magnetic field amplitudes in two points taking into account the phase delay τ, d_{21} is a distance between two points at the Earth's surface, $\omega = 2\pi f$ - cyclic frequency. In the same way the phase velocity $V_{31}(t)$ can be determined. The direction along the Earth's surface (azimuth angle α) and value |V| of the phase velocity can be found too.

Results of experiment in Karelia in 2013 year are presented in Fig.2. The figure represents comparison of magneto-telluric sounding (MTS) and phase-gradient sounding (PGS) methods. Depth dependences of the apparent resistivity at extreme s3 and s4 points at the profile were calculated by the MTS method. The same dependences at inner points of the profile s3-s4 (Fig.2) were calculated by the PGS method. to centers of the magnetic gradientometers attach to these points. The curves in the Fig.2 were supplemented at big depths with a regional curve from the closest geophysical observatory.

For apparent resistivity calculations Z component of magnetic field variations was used because just Z component variations is closely connected with geoelectric structure of the Earth's crust. As it is seen from the Fig.2, comparison of results of the both methods displays a good correspondence.

Fig.3 presents example of the apparent resistivity 2D distribution of the earth's crust at different depths combined by the MTS and PGS methods. Data of experiment in Karelia in 2014 year were used. Preliminary results show presence of high-conducted layers in the Earth's crust.

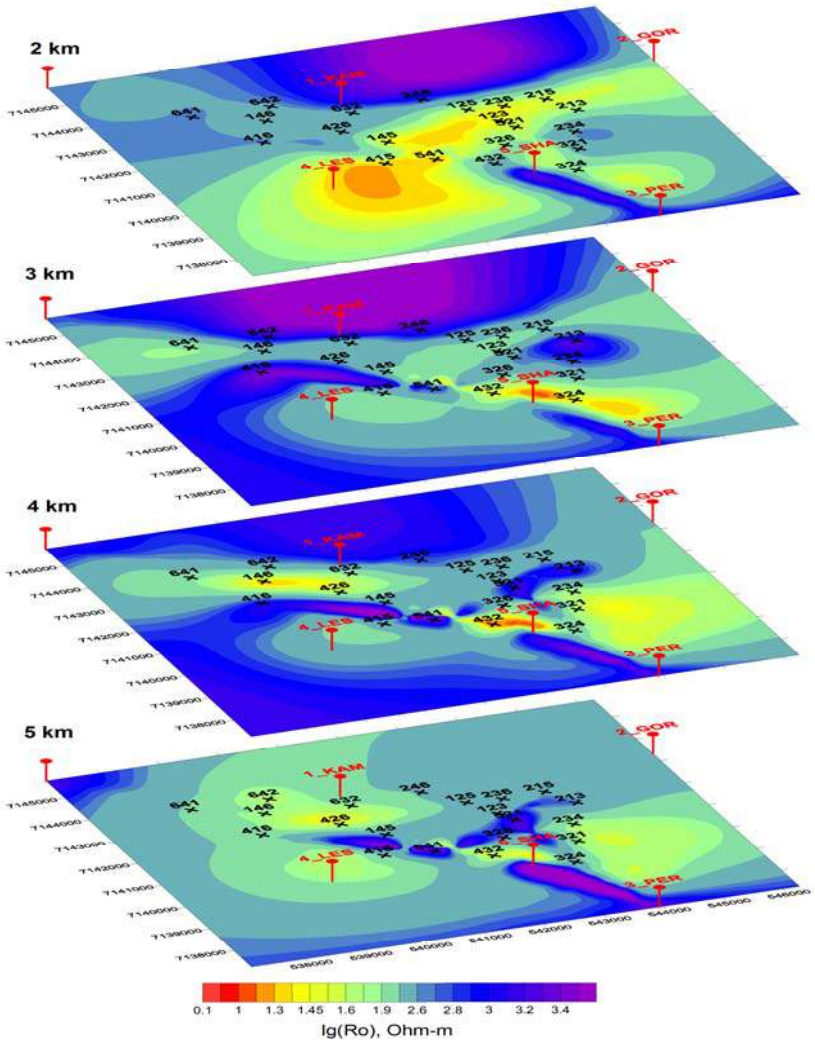

Fig.3. 2D distribution of the apparent resistivity of the earth's crust at different depths by the MTS and PGS methods. Red marks – magnetic stations.

Conclusions

For investigation of geoelectric characteristics of the earth's crust new method of the phase-gradient sounding (PGS) method is proposed. In this method, data from three three-component synchronized magnetic stations (located in tops of a triangle at small distances each from the other - magnetic gradientometer) are used for construction of gradient and phase velocity vectors along the Earth's surface.
The gradient vectors are directed to a local source of the ULF EM waves, and the phase velocity vectors - from the source. The vector directions give an opportunity to determine a location of geoelectric anomalies. Values of the phase velocities allow to calculate apparent resistivity of the earth's crust for different frequencies in ULF range (F=0.001- 10 Hz) or to detect an epicenter of forthcoming strong earthquake.
Comparisons of the PGS method with the widespread magneto-telluric sounding (MTS) method display a good coincidence.
Joint investigation of the earth's crust geoelectric characteristics by MTS and PGS methods gives an opportunity to accelerate geophysical works.
PGS method can be used at difficult regions (mountains, volcanoes, deserts, jungles, at sea bottom and so on).

References

Semenov A.A. (1968) *Theory of electromagnetic waves*. Moscow Univ. Press (in Russian), Moscow, 316 p.

Ismaguilov V.S., Kopytenko Yu.A., Hattori K., Voronov P.M., Molchanov O.A., Hayakawa M. (2001) ULF Magnetic Emissions Connected with Under Sea Bottom Earthquakes. *Natural Hazards and Earth Sys. Sci*., v. 1, p. 1-9.

Ismaguilov V.S., Kopytenko Yu.A., Hattori K., Hayakawa M. (2002) Variations of phase velocity and gradient values of ULF geomagnetic disturbances connected with the Izu strong earthquakes. *Natural Hazards and Earth Sys. Sci*. v.20, p. 1-5.

Ismaguilov V.S., Kopytenko Yu.A., Hattori K., Hayakawa M. (2006) Using of gradients and phase velocities of ULF geomagnetic disturbances for determination of strong forthcoming earthquake hearth. *Geomagnetism and Aeronomy*, v.46, N 3, p. 423-430.

Kopytenko Y., Ismagilov V., Hayakawa M., Smirnova N., Troyan V., Peterson T. (2001) Investigation of the ULF electromagnetic phenomena related to earthquakes: contemporary achievements and the perspectives. *Annali di Geofisika*, v. 44, N 2, p. 325-334.

Kopytenko Yu.A., Ismaguilov V.S., Kopytenko E.A., Voronov P.M., Zaitsev D.B. (2000) Magnetic location of geomagnetic disturbance sources. *DAN, series "Geophysics"*, v.371, N 5, p. 685-687.

INVESTIGATION OF ULF MAGNETIC FIELD VARIATIONS INDUCED BY TSUNAMI IN A COASTAL ZONE

Yu.A. Kopytenko[1], V.S. Ismaguilov[1], M. Hayakawa[2]

[1]St. Petersburg Branch of IZMIRAN, St. Petersburg, Russia, e-mail: office@izmiran.spb.ru
[2]University of Electro-Communications, 1-5-1, Chofugaoka, Chofu, Tokyo, Japan

Abstract. Strongest earthquake with magnitude M=9 had happened 11.03.2011 at 05:46:24 UT near the eastern coast of Japan. EQ epicenter was located 373 km to the northeast from Tokyo. We investigated magnetic field variations induced by tsunami. Data of six three-component magnetic stations and one seismic station situated in the coastal zone of Japan were used. Values of magnetic field variations induced by the tsunami amounted to 6–12 nT in the every magnetic field component at a distance ~30 km from the coast. Extreme values of the magnetic field variations induced by the tsunami at the closest to the EQ epicenter magnetic station Esashi (~130 km from the epicenter) are observed in Z component in ~9 minutes after the EQ moment, in H and D components in ~10 and 12 minutes. Study of the magnetic field variations induced by tsunami in different frequency ranges shows a quite complicated spectrum. Comparing magnetic and seismic variations, we found that the seismic signal arrived in ~1 minute earlier at the observation point Esashi than at the seismic st. Iwato situated very close to the Esashi. We observe magnetic field variations with period T=30–40 s in contrast to seismic field variations. It is possible that these magnetic field variations are closely connected with a process of the tsunami origination. Decreasing of Z component value (~2 nT) just after the main seismic shock can arise from a vertical displacement of a part of the ocean crust as a result of the EQ. These peculiarities of the magnetic field variations arising ~8 minutes before of the tsunami wave arrival to a coastline could be used for tsunami warning.

Introduction

Strongest in the known Japan history earthquake with magnitude M=9 had happened 11.03.2011 at 05:46:24 UT near the eastern coast of Japan. EQ epicenter was located 373 km to the northeast from Tokyo. This EQ stimulated huge tsunami that destroyed APS Fukushima.

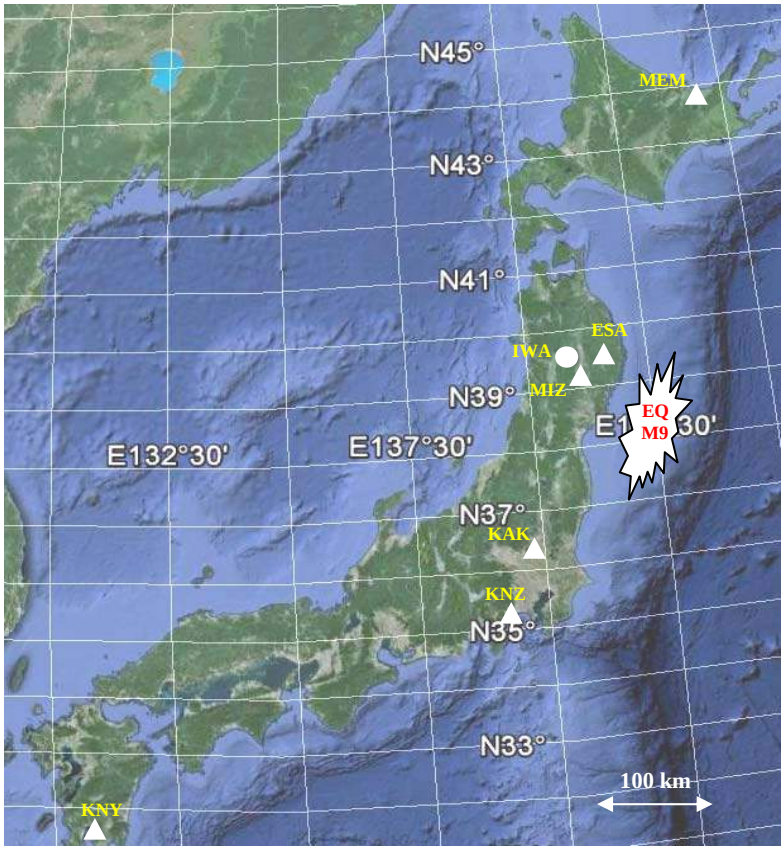

Fig.1. Location of magnetic stations (white triangles), seismic station (white circle) and EQ epicenter (star) in coastal zone of Japan.

In this work, we investigated magnetic field variations induced by tsunami movement. Data of six three-component magnetic stations and one seismic station situated in the coastal zone of Japan were used (Fig.1). Magnetic stations Esashi (ESA), Mizusawa (MIZ) and seismic station Iwato (IWA) were situated at ~30 km from the coast and at ~160 km from the EQ epicenter.

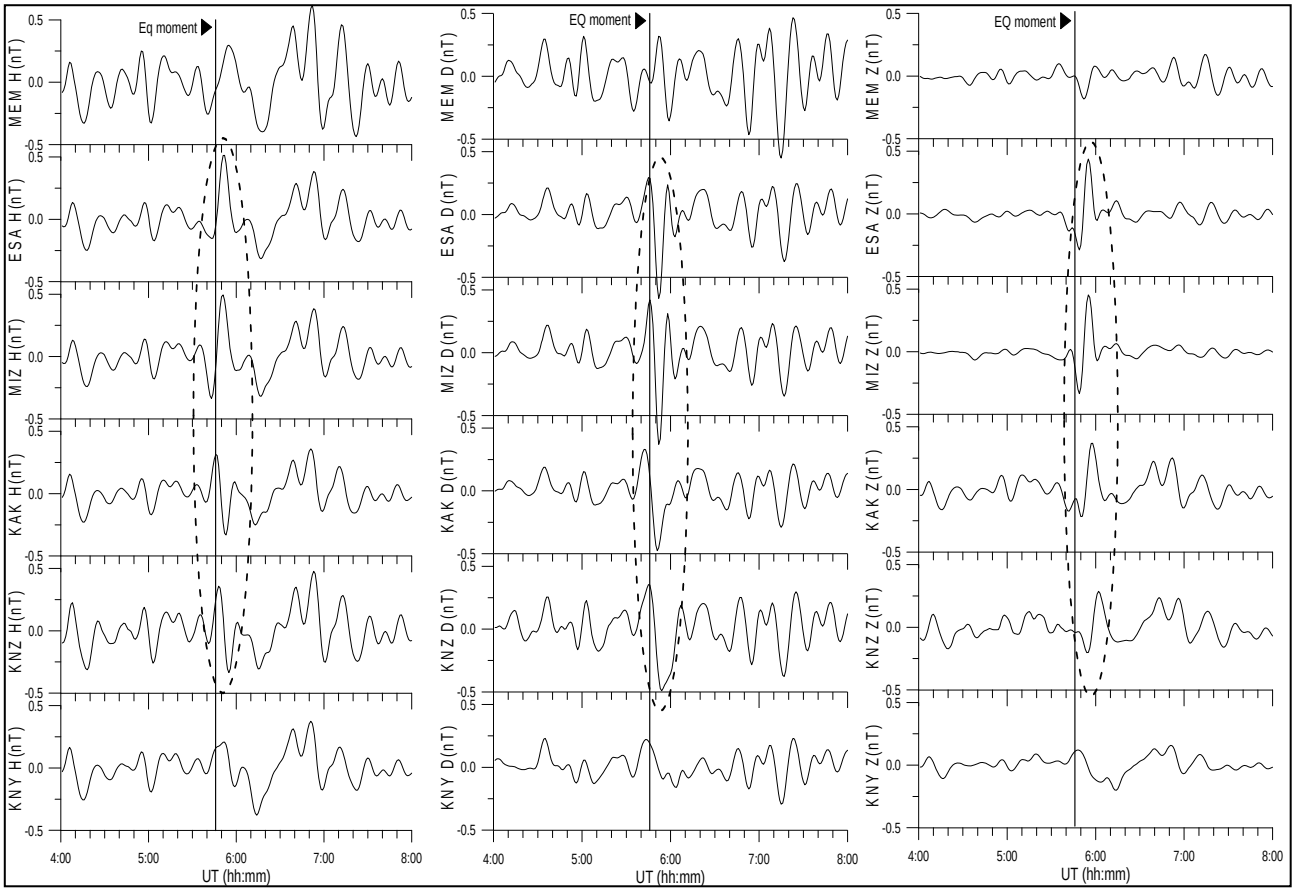

Fig.2. Variations of three magnetic field components along the magnetic station chain before and after the EQ 11.03.2011 (04-08 UT). Vertical lines show the EQ moment

Results and discussion

Variations of three magnetic field components (H, D and Z) along the magnetic station chain before and after the EQ 11.03.2011 (04-08 UT) presented at the Fig.2. The data were preliminary filtered (T=120-1000 s). Vertical lines show the EQ moment.

Dotted rounds in the Fig.2 mark the variations of magnetic field induced by the tsunami at four stations. The variations are more distinctly seen in Z magnetic component at four magnetic stations (Esashi, Mizusawa, Kakioka and Kanozan) closest situated to the EQ epicenter. Very weak magnetic field variations induced by the tsunami were observed at magnetic stations Memambetsu and Kanoya located at distances more than 500 km from the EQ epicenter. The tsunami wave propagates along deep ocean surface with velocity ~ 200 m/s [Sanford, 1971; Tyler at al., 2005]. This wave must arrive to the coast line of Japan in 11-12 minutes. Maximum value of the magnetic field variations induced by the tsunami in Z component coincides with the arrival moment (Fig.2).

Variations of magnetic field components at st. Esashi during 5:00-7:00 UT 11.03.2011 are presented in the Fig.3 in different frequency ranges. The upper curves submit unfiltered data in three magnetic field components. The data filtered in frequency ranges F=0.5 -0.001 Hz, F=0.5-0.005 Hz and F=0.5-0.17 Hz presented by lower curves. Vertical red dotted lines in the Fig.3 mark the EQ moment. In the figure, we observe high frequency variations just after the EQ moment and near the moment of arriving of the tsunami wave to a coast. The magnetic field variations induced by tsunami in different frequency ranges shows a quite complicated spectrum.

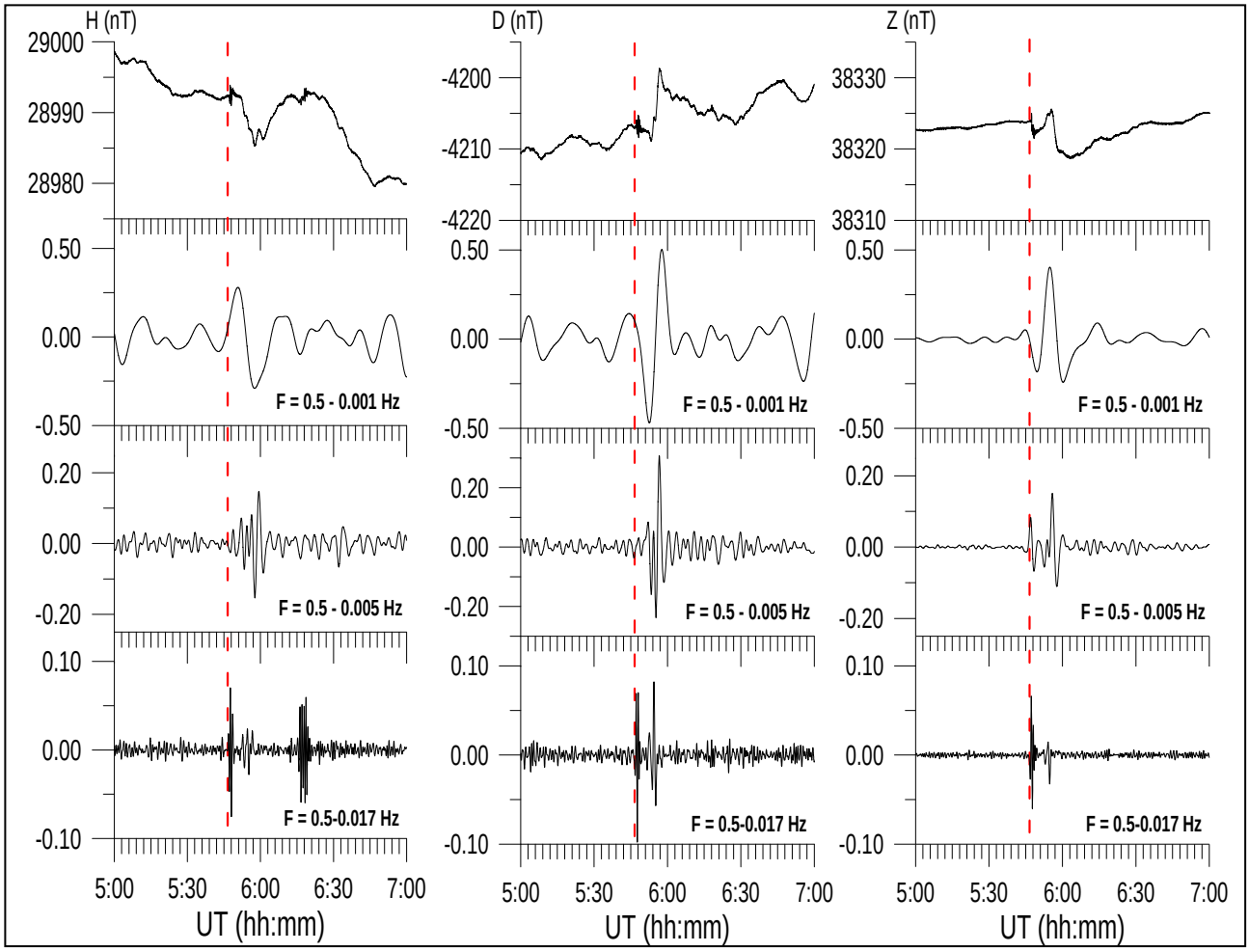

Fig.3. Variations of magnetic field components at st. Esashi during 5:00-7:00 UT 11.03.2011 in different frequency ranges

Magnetic data from st. Esashi and seismic data from st. Iwato were used to construct Fig.4. The st. Iwato is located close to the st. Esashi. Upper part of the Fig.4 presents three components of unfiltered magnetic field variations. Central part presents unfiltered magnetic variations during the time interval 05:46:00 - 05:50:30 UT just after the EQ moment (marked at left lower corner of the upper part by a red segment). Bottom part – three components of seismic variations at st. Iwato during the same time interval. Seismic st. Iwato is located very close to the Esashi. Vertical red lines mark the EQ moment.

In the Fig.4 we observe that the seismic signal arrived ~1 min earlier to st. Esashi (seismic st. Iwato situated very close to the Esashi) than magnetic field variations. These variations have 30 – 40 s period and they are probably connected with a process of the tsunami origination in the ocean.

Extreme values of the magnetic field variations induced by the tsunami at the closest to the EQ epicenter magnetic station Esashi (~130 km from the epicenter) are observed in Z component in ~9 minutes after the EQ moment, in H and D components in ~10 and 12 minutes.

Decreasing in Z component value (~2 nT, Fig.4) just after the main seismic shock can arise from a vertical displacement of a part of the ocean crust as a result of the EQ. These peculiarities of the magnetic field variations arising ~ 6 minutes before the tsunami wave arriving at the coastline could be used for tsunami early warning.

Magnetic fields are induced by tsunami propagation were earlier measured from satellites [Tyler at al., 2003; Glazman and Golubev, 2005], at ocean surface [Sanford, 1971; Chave and Luther, 1990; Manoj and Maus, 2011] and at seafloor observatoty [Toh at al., 2011]. Large number of the works devoted to modeling of tsunami magnetic fields [Tyler, 2005; Sugioka et al., 2014; Moskovchenko and Belocon, 2005]. Presented paper devoted to the magnetic field variations induced by the tsunami at a coast and it can be useful for the tsunami magnetic field modeling.

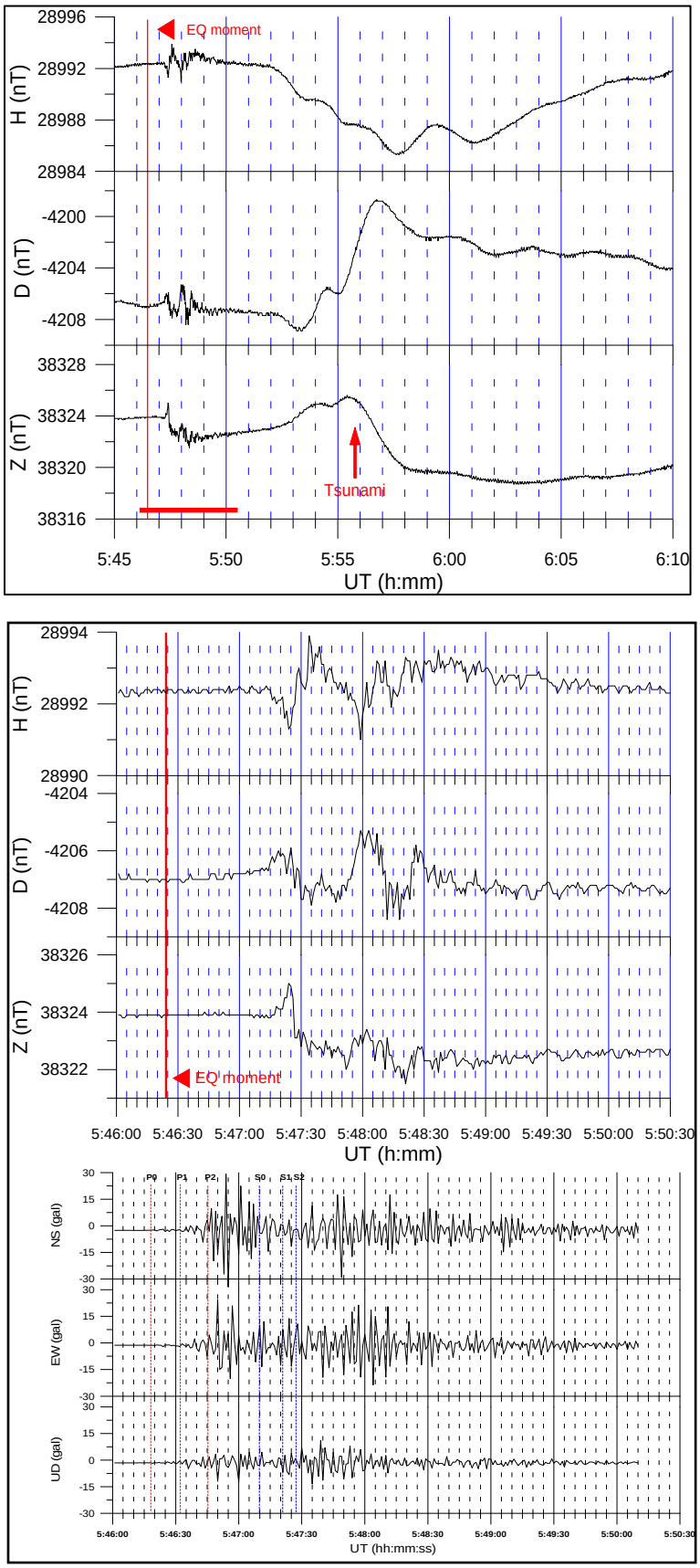

Conclusions

1. Magnetic fields are induced by tsunami near a coast are investigated in this work.
2. The seismic signal arrived ~1 min earlier to st. Esashi (seismic st. Iwato situated very close to the Esashi) than magnetic field variations.
3. Just after the EQ moment we observe magnetic field variations with period T=30-40 s. In seismic field such variations are absent. It is possible that these magnetic field variations are closely connected with process of the tsunami origination in the ocean.
4. Decreasing in Z component value (~2 nT) just after the main seismic shock can arise from a vertical displacement of a part of the ocean crust as a result of the EQ. These peculiarities of the magnetic field variations arising ~ 8 minutes before the tsunami wave arriving at the coastline could be used for tsunami early warning.
5. Values of magnetic field variations induced by the tsunami propagation amounted to 6–12 nT in the every magnetic field component at a distance ~30 km from the coast.
6. The magnetic field variations induced by tsunami in different frequency ranges show a quite complicated spectrum.

Fig.4. Variations of magnetic and seismic field components at st. Esashi 11.03.2011

References

Sanford, T.B. (1971), Motionally induced electric and magnetic fields in the sea. *J. Geophys. Res.*76, 3476–3492.

Tyler, R.H., Maus, S. & Luhr, H. (2003), Satellite observations of magnetic fields due to ocean tidal flow. *Science* 299, 239–241, doi:10.1126/science.1078074.

Tyler, R.H. (2005), A simple formula for estimating the magnetic fields generated by tsunami flow. *Geophys. Res. Lett.* 32, L09608, doi:10.1029/2005GL022429.

Larsen, J.C. (1971), The electromagnetic fields of long and intermediate water waves. *J. Marine Res.* 29, 28–45.

Chave, A. D. & Luther, D. S. (1990), Low-frequency, motionally induced electromagnetic fields in the ocean 1. Theory. *J. Geophys. Res.* 95, 7185–7200.

Glazman, R. E. & Golubev, Y. N. (2005), Variability of the ocean-induced magnetic field predicted at sea surface and at satellite altitudes. *J. Geophys. Res.* 110, C12011, doi:10.1029/2005JC002926.

Toh, H., Satake, K., Hamano, Y., Fujii, Y. & Goto, T. (2011), Tsunami signals from the 2006 and 2007 Kuril earthquakes detected at a seafloor geomagnetic observatory. *J. Geophys. Res.* 116, B02104, doi:10.1029/2010JB007873.

Manoj, C. & Maus, S. (2011), Observation of magnetic fields generated by tsunamis. *EOS Trans. Am. Geophys. Union* 92, 13–14.

Hiroko Sugioka, Yozo Hamano, Kiyoshi Baba, Takafumi Kasaya, Noriko Tada, & Daisuke Suetsugu (2014), *Tsunami: Ocean dynamo generator.* Scientifuc reports 4, Article number: 3596, doi:10.1038/srep03596.

Moskovchenko L.G. and Belocon V.I. (2005), *Electromagnetic signals from tsunamicaused by eartquake*, proc. IWSE-2005, Tokyo.

BEHAVIOR OF ATMOSPHERIC ELECTRIC FIELD DURING ACUSTO-DEFORMATION DISTURBANCES IN KAMCHATKA

M.A. Mishchenko, I.A. Larionov, Yu.V. Marapulets, O.P. Rulenko

Institute of Cosmophysical Research and Radio Wave Propagation of the Far Eastern Branch of Russian Academy of Science, Paratunka, 684034, Russia,e-mail: micle@ikir.ru

Abstract. Near-surface rock deformation effect on the behavior of atmospheric electric field is considered. The investigations are carried out in a seismically active region where the active seismotectonic process affects the most the atmosphere as a whole and particularly its near-ground layer. Within such lithospheric-atmospheric impact, high frequency geoacoustic emission disturbances are considered as an indicator of intensification of deformation processes. Simultaneous disturbances of the electric field vertical potential gradient in the near-ground air and of high frequency geoacoustic emission of rocks were determined. Non-parametric methods of correlation analysis were used. Joint atmospheric-electric, geoacoustic and deformation measurements showed that different in sign anomalous disturbances of emission and of electric field occur when deformation rate of the near-surface sedimentary rocks increases during their tension.

In seismically active regions anomalous disturbances of atmospheric electric field are registered before earthquakes [Gokhberg et al., 1988; Sidorin, 1992]. They occur within the period from the first tens of hours to the first hours before earthquakes in the zone of preparation and are associated with near-surface rock deformations [Rulenko, 2000]. Investigations carried out in Kamchatka showed that during intensification of near-surface sedimentary rock deformations, anomalous disturbances of geoacoustic emission appear. They are observed at the frequencies of a unit of kilohertz within the interval of a day and a half before an earthquake at the distance of the first hundreds of kilometers from an epicenter [Kuptsov et al., 2005]. The common deformation nature of disturbances and the same time of appearance before earthquakes are the basis for the joint investigation of these geophysical fields.

In August-October, 2005 at Mikizha site (52.990 N, 158.230 E), Kamchatka, joint measurements of atmospheric electric field, acoustic emission and meteorological parameters were carried out for the first time [Kuptsov et al., 2007]. Field potential gradient V' measurements were performed by "Pole-2M" sensor at the height of 7 cm from the ground surface. A piezoceramic hydrophone installed at the bottom of a lake at the depth of 4 m was used as a sensor for acoustic signals. The distance between the hydrophone and "Pole-2M" sensor was 130 m. Acoustic pressure P_s accumulated during 4 s in 7 frequency ranges (0.1-10, 10-50, 50-200, 200-700, 700-1500, 1500-6000, 6000-10000 Hz) was considered. In the conditions of fair weather and absence of rain, the relation between anomalous disturbances of electric field and acoustic pressure in kilohertz frequency range was determined. It becomes apparent during seismically calm periods and at the final stage of earthquake preparation [Kuptsov et al., 2007].

The measurements were continued in July-October 2006 and 2007. Acoustic pressure P_s was measured in the frequency range of 2.0-6.5 kHz, since in the result of long observations it was determined that anomalous acoustic signals at Mikizha site occur the most intensive at these frequencies [Kuptsov et al., 2005]. During fine weather conditions (absence of rain, strong and moderate wind, low atmospheric pressure), anomalous bay-like decreases of potential gradient V' up to the sign change were sometimes observed in the experiments. They occurred during sharp and significant increase of acoustic pressure P_s (Fig. 1). We should note that anomalous disturbances of V' and P_s usually last from the first tens of minutes to the first hours filling, as a rule, a part of an hour, two neighbor hours or the initial and the final hour when they continue for several hours. Appearance of such disturbances should manifest itself in the changeability of hourly mean values of potential gradient and of acoustic pressure. Thus, their hourly mean values, which are the average from 900 measurements, were analyzed. Hourly mean values of meteorological parameters are the average from 6 measurements.

To choose an adequate method for data analysis, normalcy of distribution of hourly mean values of all the values was checked. Asymmetry and excess coefficient estimates and their standard errors as well as the Shapiro–Wilk test, which is the most powerful and a universal test among similar ones, were applied.

Distributions of these values differ from the normal one. That is why Spearman rank correlation was used. It is less sensitive to outliers and errors in observation results and is more stable and reliable estimate of the relation between the variables in comparison to Pearson linear correlation coefficient. It also allows one to estimate monotonous nonlinear relations.

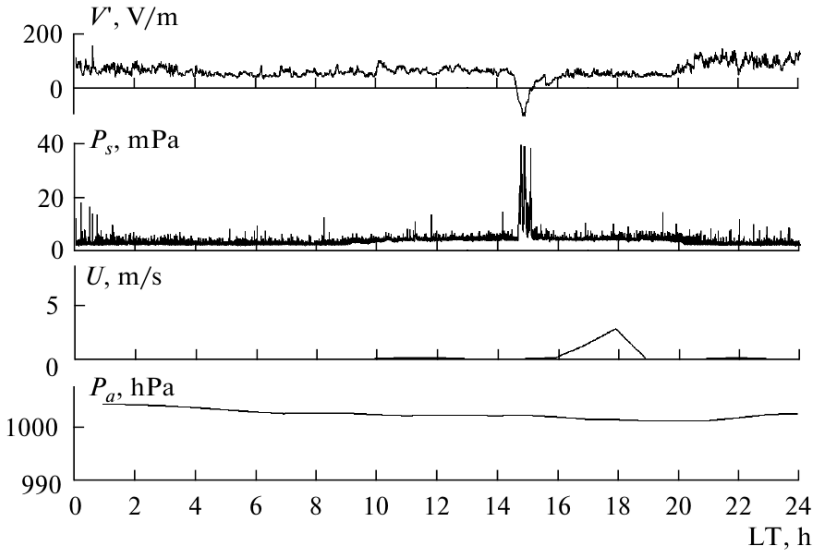

Fig. 1. An example of potential gradient V' decrease during acoustic pressure P_s decrease. U is the wind velocity, P_a is atmospheric pressure

Fig. 2 shows the cross correlation functions (CCF) for hourly mean value series of potential gradient and acoustic pressure. It is clear that the maximal values of CCF are observed for zero shift. Hence, negative disturbances of V' occurred simultaneously with the disturbances of P_s with the accuracy up to one hour. So, their paired hourly mean values $\overline{V'}$ and $\overline{P_s}$ were further considered.

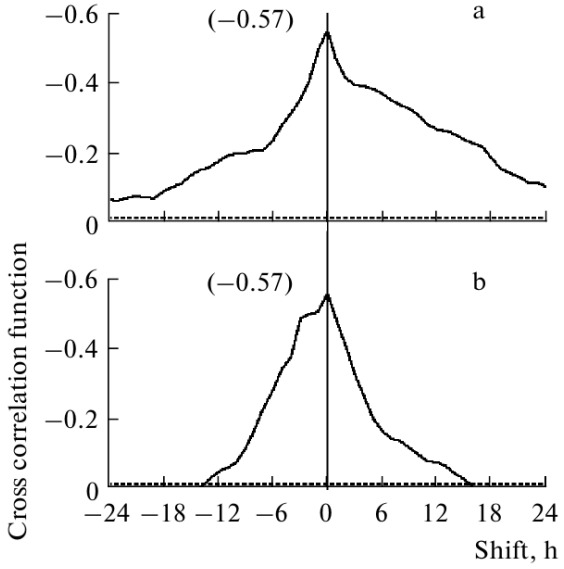

Fig. 2. Cross correlation functions for hourly mean value series of $\overline{V'}$ and $\overline{P_s}$, maximal function values are in brackets

According to the results of correlation analysis, electric field and acoustic pressure correlate the most with wind and, especially, with rain [Marapulets et al., 2010]. Thus, further we considered the relation between the pairs of $\overline{V'}$ and $\overline{P_s}$, when there was no rain and wind velocity was less than 1.5 m/s, and atmospheric pressure was more than 995 hPa. The last condition was accepted to decrease cyclone effect on the behavior of the considered fields. Fig. 3 shows the diagrams of scattering between hourly mean values of electric field and acoustic pressure during such fair weather conditions.

We think [Marapulets et al., 2010] that the relation, illustrated in Fig. 3, contains two components: the background component determined by weak effect of unaccounted meteorological and other factors on

electric field and geoacoustic emission and the component of tectonic origin. The latter is formed by electric field and geoacoustic emission disturbances different in sign occurring during intensification of near-surface rock deformation at the observation site. Such intensification must occur repeatedly during intensive seismotectonic process by the Eastern Kamchatka. Background component is suggested to appear for $\overline{P_s}$ less than $\overline{P_s}*$ value, and the tectonic component arises when $\overline{P_s}$ is more than $\overline{P_s}*$, which occurs during intensification of rock deformation. Different mechanisms for the formation of background and tectonic components of the relation between the electric field and geoacoustic emission, determined by different location of sources of these geophysical field (atmosphere, lithosphere) disturbances, must result in the complicated dependence between $\overline{V'}$ and $\overline{P_s}$. A piecewise-linear regression was applied to distinguish the relation components. Quasi-Newton method was used to estimate regression parameters. Acoustic pressure break point which corresponds to $\overline{P_s}*$ in the first approximation was determined by computational procedure.

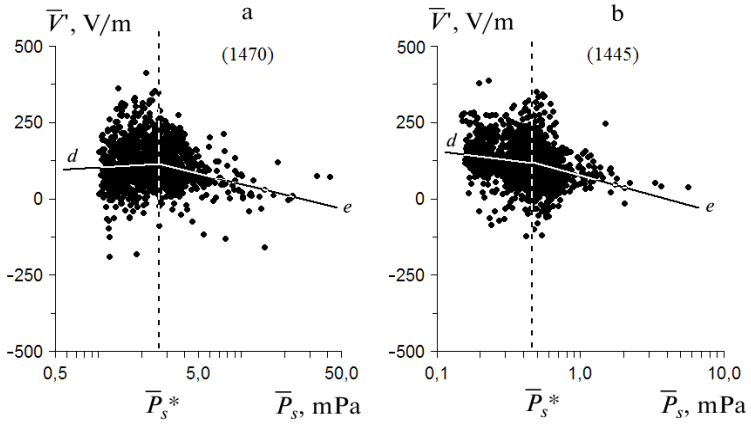

Fig. 3. Diagram of scattering between the hourly mean values of $\overline{V'}$ and $\overline{P_s}$. The number of pairs of hourly mean values is in brackets. Vertical dashed lines are acoustic pressure values $\overline{P_s}*$, which corresponds to the break points of piecewise-linear regression on acoustic pressure; c, d are the lines, illustrating regression for relation background and tectonic components

Spearman correlation coefficients rs were estimated for background and tectonic components of the relation between electric field and geoacoustic emission. In the both experiments, highly significant correlation relation between $\overline{V'}$ and $\overline{P_s}$ in the tectonic component (rs = –0.27 и –0.23, p < 0.001) was statistically determined. Correlation coefficient is negative which corresponds to a different sign of anomalous disturbances of electric field and geoacoustic emission (Fig. 1).

Anomalous disturbances of high frequency geoacoustic emission have deformation nature which was confirmed by joint measurements with near-surface rock deformations at Karymshina site [Dolgikh et al., 2007], located 20 km to the south-west of Mikizha site. At the both sites the near-surface rocks are sedimentary with about 50 m thickness of the layer. It is a sand-clay mixture containing crushed and large stones. Simultaneous atmospheric-electric, geoacoustic and deformation measurements carried out at Karymshina site [Marapulets et al., 2011] showed that different in sign anomalous disturbances of potential gradient V' and acoustic pressure P_s appear during near-surface sedimentary rock tension. During their compression only acoustic emission disturbances are observed. All the disturbances were registered in the conditions of absence of rain and strong wind, weakly changing air pressure and rock deformations two orders higher than those of tidal ones which indicates it tectonic nature.

Simultaneous occurrence of the disturbances of atmospheric electric field and geoacoustic emission may be explained considering the near-surface sedimentary rocks as a polydisperse porous structure of low strength. During tension or compression of such structure, relative micro-shifts of fragments generating acoustic signals take place. Electric field disturbances only during rock tension are the most likely associated with radon and thoron emanations from the ground. Tension is accompanied by pore opening and fracture extension which increases the emission of these radioactive gases, and compression is accompanied by pore closure and fracture bridging which decreases gas emission. Radon and thoron inflowing into the atmosphere will cause the increase of ion formation intensity by the ground surface. In the result, as it was theoretically

shown by Hoppel [Hoppel, 1967], during fair weather conditions the negative charge will appear in some air layer, which will cause a reverse of the usual electrode effect. It is observed by many researchers. The negative volume charge determined by increased air ionization will remain during low wind [Kupovykh et al., 1998]. Formation, existence and destruction of this charge, generating an opposite in sign local electric field, will cause a bay-like decrease of potential gradient V' by the ground surface.

References

Dolgikh, G.I., Kuptsov, A.V., Larionov, I.A., et al. (2007), Strain-caused and acoustic earthquake precursors, *Doklady Akad. Nauk*, vol. 413, no. 1, pp. 96–100.

Gokhberg, M.B., Morgunov, V.A., and Pokhotelov, O.A. (1988), *Seismoelektromagnitnye yavleniya* (Earthquake-Related Electromagnetic Phenomena), Moscow: Nauka.

Hoppel, W.A. (1967), Theory of the electrode effect, *J. Atm. and Terr. Phys.*, vol. 29. pp. 709–721.

Kupovykh, G.V., Morozov, V.N., and Shvarts, Yu.M. (1998), Theory of electrode effect in the atmosphere, Taganrog:TRTU Pub.

Kuptsov, A.V., Larionov, I.A., and Shevtsov, B.M. (2005), Features of geoacoustic emissions during earthquake precursory periods, *Vulkanol. Seismol.*, no. 5, pp. 45–59.

Kuptsov, A.V., Marapulets, Yu.V., Mishchenko, M.A., Rulenko, O.P., Shevtsov, B.M., and Shcherbina, A.O. (2007), On the relation between high frequency acoustic emissions in near-surface rocks and the electric field in the near-ground atmosphere, *J. Vulkanol. Seismol.*, vol. 1, no. 5, pp. 349–353.

Marapulets, Yu.V., Rulenko, O.P., Mishchenko, M.A., and Shevtsov, B.M. (2010), The relationship between high frequency geoacoustic emissions and the electrical field in the atmosphere during a seismotectonic process, *Doklady Akad. Nauk*, vol. 431, no. 2, pp. 242–245.

Marapulets, Yu.V., Rulenko, O.P., Larionov, I.A., and Mishchenko, M.A. (2011), Simultaneous response of high frequency geoacoustic emissions and atmospheric electrical field to deformation in near-surface sedimentary rocks, *Doklady Akad. Nauk*, vol. 440, no. 3, pp. 403–406.

Rulenko, O.P. (2000), Immediate-term precursors of earthquakes in near-ground electricity, *Vulkanol. Seismol.*, no. 4, pp. 57–68.

Sidorin, A.Yu. (1992), *Predvestniki zemletryasenii* (Earthquake Precursors), Moscow: Nauka.

CORRELATION SPECTRA OF THE MAGNETIC FIELD FOR MONITORING OF SEISMICALLY ACTIVE ZONES

L. F. Moskovskaya

SPbF IZMIRAN, St. Petersburg, 199034, Russia, e-mail: lf_mosc@mail.ru

Abstract. The method of correlation spectra for processing of the magnetic field is developed to monitor seismically active zones. Analysis of the effective parameters of the power correlation spectra showed characteristic variations that can be caused by geodynamic processes in the environment of seismic activation.

Motivation for the analysis of magnetic field records in an image of correlation spectra

Electromagnetic monitoring of seismically active regions is one of the basic geophysical methods. A wide range of standard techniques for processing of the measured signals is known. Our task is to study directly the magnetic field components and the possible changes of the signals associated with earthquakes. We can assume that the propagation of electromagnetic waves occurs in the resonator, having a certain frequency response. Change of the waveguide parameters accompanying tectonic processes can affect the effective frequency response of the magnetic field variations. To analyze the frequency characteristics of the electromagnetic field, we have developed the method of correlation spectra. This method has the best resolution on the frequency composition, and it is less dependent on the amplitude of spectral components in comparison with the Fourier spectrum method. The analysis has been performed for multiple frequency bands.

The data

We have analyzed time series of the magnetic field of the two Japan's observatories: Kanoya and Kakioka (http://wdc.kugi.kyoto-u.ac.jp/) and seismic data catalog (http://www.ncedc.org/anss/catalog-search.html). The time resolution of the magnetic field measurements is 1 second, and the accuracy is 0.01 nT. We have analyzed only three hours of the night interval from 1:30 to 4:30 local time.

Mathematical ideas for the processing algorithm

Correlation spectra were calculated for the components of the field daily time series.

1. The source field under study (time series) was split into a set of time series with different degrees of functional smoothness. The division of the field was carried out by using the smoothing operation signal in a sliding window of fixed width. The source signal was divided into a smooth low-frequency and high-frequency components. To the high-frequency component can be applied the similar operation of division with a smoothing window of less width. For splitting the source field into components, we used the original algorithm robust filtering [Moskovskaya, 2000, 2003]. The reduction of the sliding window corresponds to a decrease in the degree of smoothness of the function, i.e. to higher frequency signals. As a result, the original signal f_0 is represented as a sum of fields: $f_0 = {}^1f_{>T_1} + {}^2f_{>T_2}^{<T_1} + \ldots + {}^{(j-1)}f_{>T_{j-1}}^{<T_{j-2}} + {}^jf^{<T_{j-1}}$. We can assume that the component of the i-th level of the frequency division ${}^i f_{>T_i}^{<T_{i-1}} \equiv {}^if$ contains the part of the signal source field, which is approximately in the band periods $T_i \leq\approx T({}^if_i) <\approx T_{i\text{-}1}$. For the first and last components is one-sided inequality.

We conducted a statistical analysis of the separated field's components. For each day of monitoring, the averages and the average variations of the signals were calculated.

2. The cluster correlation spectral analysis was performed for all frequency-separated fields. The time series was divided into a set of realizations of the same length n. A pair of orthonormal discrete etalon-functions $\mathbf{1}_{si}(n), \mathbf{1}_{co}(n)$ was calculated. The correlation spectrum of the i-th realization was defined as the projection of orthonormal vectors f_i on the basis formed by the etalon-functions

$s_i = \sqrt{(f_i, l_{si}(n))^2 + (f_i, l_{co}(n))^2}$. This evaluation shows the energy share of oscillations with period T=n in function of realization. The set of realizations corresponds to the set estimates of the correlation spectra $\{s_i\}$. We used the cluster-robust weighting estimation for the averaging over the ensemble of local spectra [Moskovskaya, 2010,2012]. The number of clusters (K) is fixed. The correlation spectrum of the k-th cluster is defined as a weighted average: $\bar{s}_k = \sum_j s_j w_j^k / \sum_j w_j^k$. The weights are alternative; each local estimate of the correlation spectrum can belong to only one cluster. The power of the cluster is determined as the product

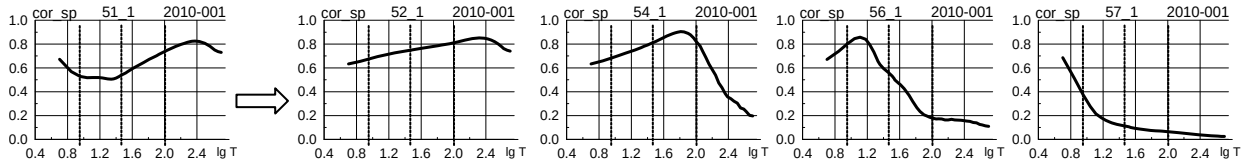

Fig.1 Correlation spectra of the signal in different frequency bands. One cluster. The module of the magnetic field (Fs), calculated from measurements of the three components at 1 January 2010 at Kakioka.

of average on carrier: $M_k = \bar{s}_k \sum_j w_j^k$. Cluster estimations for a sequence of periods form a correlation spectrum. This procedure is compared with the Fourier spectrum reduces the dependence of the result from the influence of the amplitude of the harmonics, and the effect of multiple frequencies. An example of the correlation spectra for frequency-separated fields is shown in Fig.1 and 2. Border strips of the separate fields are marked with vertical dashed lines: T=9, 29,101 s. Comparison of the correlation spectra and Fourier spectra divided by the period (Fig.3) shows that the main energy cluster correlation spectrum is functionally comparable to the Fourier image signal. However, the shape of the curve of the correlation spectrum is more stable, largely reflects the frequency distribution and less dependent on the amplitude of the signal. The power of the second cluster is higher on the flanks of the interval due to the increasing weight of the carrier.

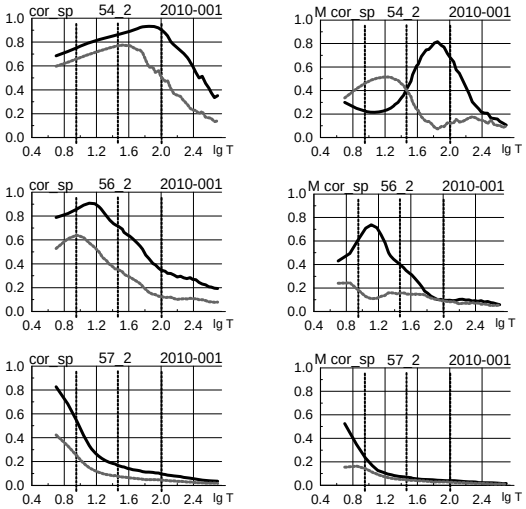

Fig.2 Correlation spectra and power correlation spectra of the signal in different frequency bands. Two clusters. The black line is the first cluster, gray – second.

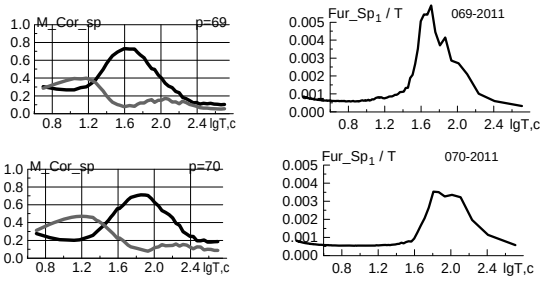

Fig.3. Power correlation spectra of H-component and Fourier spectra, divided by the period, for the bands of 29 c < T< 101 s. Kakioka.

The top pictures relate to the day before the catastrophic earthquake. The bottom corresponds to the day of the earthquake on 11 March 2011. The black line is the first cluster, the gray – second.

3. The point of maximum correlation spectrum characterizes the position of the main effective frequency of the signal in this frequency band. The extent of the fluctuations can be measured by the maximum height and the curvature of the function at this point. The curvature is inversely proportional to the radius of the circle determined by the points function in the region of maximum. Parameters of maximums

are convenient characteristics of the signal to create formalized procedures monitoring of possible variations of the correlation spectra due to seismic activity in the region. Changes in the geodynamic system, initiated the preparation of earthquakes, accompanied by changes in the electromagnetic environment parameters. And can affect change parameters of the electromagnetic field in waveguide earth-ionosphere. Discharging the accumulated tectonic energy occurs in earthquakes. Therefore, large seismic events (M>5) may be temporary rappers of tectonic activity and its accompanying variations of geoelectric parameters of the environment.

We conducted correlation analysis between time series of the parameters of the correlation spectra maximum and a line of seismic events.

4. The results of processing. An interesting feature of the correlation spectra is a high functional similarity of the curves, calculated in the same day in the same frequency band for different components and components of different stations (Fig.4a). This means that there is a uniform, frequency structure of the effective mode of the field. The decrease in the correlation may be due to different causes, including changes in the parameters of the waveguide associated with the preparation of earthquakes. Examples (Fig. 4b,c) show a decrease of the correlation functions before seismic events for different pairs of component of a power correlation spectra. According to monitoring data (H, Z, F) components of the magnetic field, the time

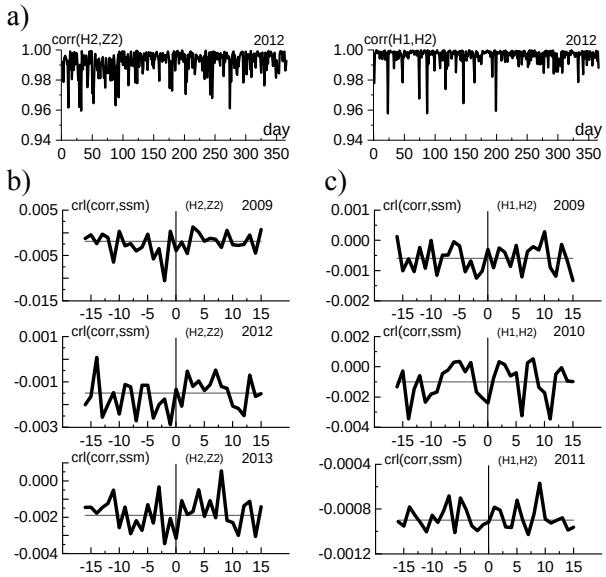

Fig.4. Correlation of the power correlation spectra.

a) Correlations for the (H,Z) components of the station Kakioka (left) and for the (H,H) components of the stations Kakioka and Kanoya (right).

Correlations between the correlations of the pairwise power correlation spectra and the sequence of the earthquakes activations:

b) for the (H,Z) components of the station Kakioka;

c) for the (H,H) and (H,H) components of the stations Kakioka and Kanoya.

In all figures, the first cluster of the two-cluster evaluation is presented. The band of the signals is 9 s < T< 29s.

series of the generalized parameters of the energy correlation spectra of frequency-separated fields (daily) were calculated. Those parameters of the maximum of the correlation spectrum are the following: the period (abscissa), the highs and the curvature of the function at the maximum.

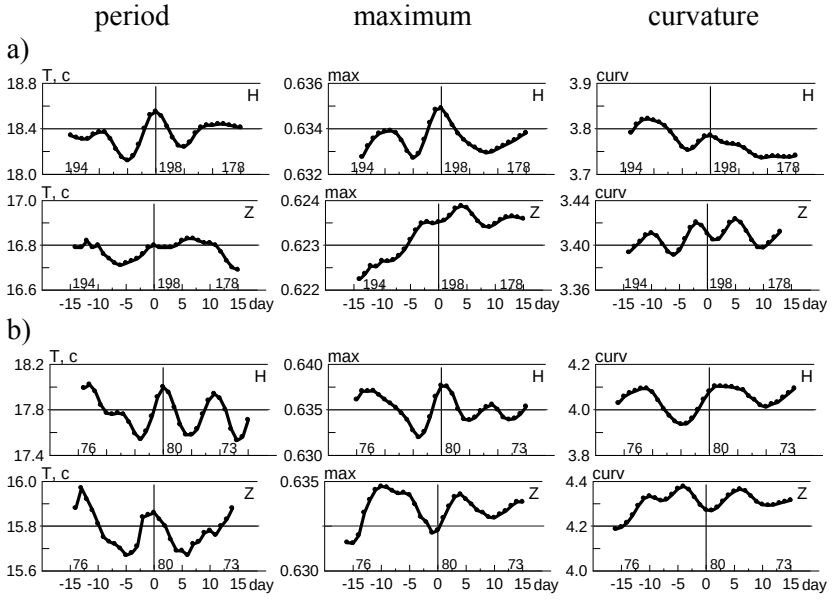

Fig. 5. The correlations between the parameters of maxima of the power correlation spectra and the earthquakes series in the vicinity of the station Kakioka.

The active phase of the seismic zone is considered.

The components of the field lie in the band of periods T= [9-29] s. The first cluster is examined.

a) 11 March 2011 - December 31, 2011, the interval of 296 days; b) 2012, the interval [1-366].

Above the x-axes, the numbers of earthquakes included in the calculation are shown at the edges and in the center of correlation intervals.

We conducted an investigation of the relationship of variations of these parameters with the time series of the earthquake activations in the vicinity of the observatory. The frequency-separated signals in the range of periods T= [9,29], [29,101] s were analyzed. The algorithm of correlation analysis included double filtering of time series parameters of characteristic points. As a result we obtained the separation of the functions: 1) impulses, 2) variations in the band 5-31 days, 3) background component with window w ≥ 31 days. Pulse functions may contain random variations of the magnetic field, the background part of the signal is largely reflects seasonal variations. We assumed that local variations can be associated with the variations of the waveguide earth-ionosphere due to geodynamic cause. It is this component, which was subjected to correlation analysis with the time series of the earthquake activations. In our calculations we used the effective energy (magnitude) of seismic events per day in a radius of 300 km around the station Kakioka [Moskovskaya, 2010, 2012].

Correlation diagrams for the parameters capacity of correlation spectra and earthquakes during the active phase (2011: [70-365] & 2012: [1-366]) revealed a tendency of the increase of the period on the day of the earthquake (Fig.5). It was particularly strong (up to 10%) for the H component and Z component in 2012. Power correlation spectrum and the curvature at the point of maximum increase for the H-components and decrease for the Z-component on the day of the earthquake. Note that in a neighborhood of the earthquake rapper the components of magnetic field in the band periods of [29-101] s have a weak minimum. This shift of the power correlation spectra to the right correspond to the reduction of all components (H,Z, Fs) highs (the extremes are in the neighborhood of T(max) ≈70 s) and curvature fields.

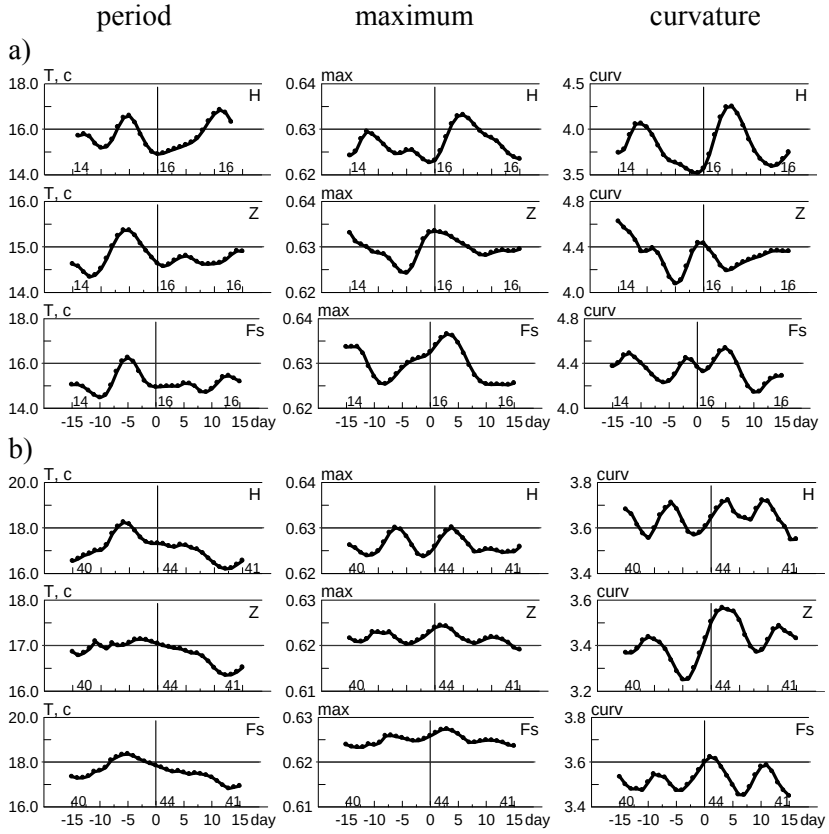

Fig. 6. Correlations between the parameters of the maximum of the power correlation spectra and the earthquakes series in the vicinity of station Kakioka.

The data corresponds to the period before the activation of the seismic zones and during their reduction.

Components of the field lie in the band of periods T= [9-29] s. The first cluster is considered.

a) 2010-2011 interval [1-434] days. Before Eq M(435)=9.1;

b) 2013, the interval [1-365].

Above the x-axes on the edges and in the center of the correlation interval, the numbers of earthquakes included in the calculation are shown.

Thus seismic excitation of the geodynamic system is reflected in the changing of the frequency of effective parameters of the waveguide. The reason of that may be the change of geoelectric parameters of the waveguide, and the appearance of additional active current systems that accompany earthquakes.

Fig. 6 presents similar estimates for time intervals per year + 69 days before the famous earthquake of 11 March 2011 (M=9.1), and for the time of reduction activity in 2013. One can see a significant increase in the frequency of at least 5 days before the rapper earthquake. The maxima of the H-components are increased; of the Z-components are reduced. So we observe the electromagnetic response of the system is similar to the stress state of the system in the active phase.

5. Conclusions

In this paper we propose a new method of analysis of the magnetic field. Correlation spectra are energy characteristic of the field. They display the frequency components of the field much better than in the case of Fourier spectra. In addition, the correlation spectra depend to a lesser extent on the amplitudes of the spectral components, and they are free from the effect of multiple frequencies. A more stable form of the curves of the correlation spectra allows us to implement a simple numerical scheme of analysis of the variations of the effective energy field during monitoring. The high similarity of the shape of the correlation spectra of the different components on different stations shows significant frequency homogeneity of the field in the waveguide for stations Kakioka and Kanoya. We have revealed changes in the correlation spectra of magnetic fields depending on the seismic activity of geodynamic systems.

References

Moskovskaya, L.F. (2000), Filtering of transient fields based on the robust estimation. *Russian geophysical journal*, No. 19-20, 71-78.

Moskovskaya, L.F. (2003), Preprocessing of measurements of transient electromagnetic fields with high spatial and temporal density on the example of sea electric sounding. *Geofizika*, No 4, 25-29.

Moskovskaya, L.F. (2010), Method of cluster directional analysis by monitoring the magnetic field on the Boso Peninsula in 2000, *Geofizika*, No. 6, 39-46.

Moskovskaya, L.F. (2012) Directional and correlation analysis from the geomagnetic monitoring and seismic data on the Boso Peninsula in 2000. *Izvestiya, Physics of the Solid Earth*, 48, 532-546.

EFFECTS IN THE VARIATIONS OF THE AMPLITUDE OF LOW-FREQUENCY RADIO SIGNALS AND ATMOSPHERICS PASSING OVER THE EPICENTER OF DEEP EARTHQUAKES

V.A. Mullayarov, V.V. Argunov, L.M. Abzaletdinova

Yu.G. Shafer Institute of Cosmophysical Research and Aeronomy SB of RAS, Yakutsk, 677980, Russia, e-mail: mullayarov@ikfia.sbras.ru

Abstract. The search for possible earthquake precursors is one of the urgent problems of geophysics. One of the possible tools for detecting the seismic activity is observations of disturbances in the lower ionosphere caused by the effect of lithospheric processes with the help of low-frequency radio signal observations. In a sufficiently large number of studies, it is shown that phase variation of signals of low-frequency radio stations observed a few days before the earthquake can be considered as precursors. The monitoring measurements of characteristics of the electromagnetic radiation of lightning – atmospherics, are also proposed as a variant of this method. It is shown that the earthquakes with the magnitude greater than 5 and the depth not exceeding 50 km are manifested in the form of increasing hourly average amplitude of atmospherics on the day of the event or within three days thereafter. Effects of the amplitude increase in the previous earthquake during the days preceding the earthquake are considered as precursors. At the same time, it has been found that the deep-focus earthquakes also apparently cause disturbances in the ionosphere. In this work examples of manifestations of deep-focus earthquakes in the amplitude variations of the low-frequency radio signal and atmospherics are considered.

Introduction. One of the possible tools for detecting the seismic activity is observations of disturbances in the lower ionosphere caused by the effect of lithospheric processes with the help of low-frequency radio signal observations. In a sufficiently large number of studies, it is shown that phase variation of signals of low-frequency radio stations observed a few days before the earthquake can be considered as precursors [see, for example: Biagi et al., 2001]. The monitoring measurements of characteristics of the electromagnetic radiation of lightning – atmospherics, are also proposed as a variant of this method [Mullayarov et al., 2007]. From observations of atmospherics passing within the first Fresnel zone over earthquake epicenters it is shown that the earthquakes with the magnitude greater than 5 and the depth not exceeding 50 km are manifested in the form of increasing hourly average amplitude of atmospherics on the day of the event or within three days thereafter. Effects of the amplitude increasing in the previous earthquake during the days preceding the earthquake are considered as precursors. It can be assumed that conditions of not deep and strong magnitude are necessary to transfer sufficient energy of the seismic processes to ionospheric heights that can cause detectable perturbation. At the same time, it has been found that the deep-focus earthquakes also apparently cause disturbances in the ionosphere [Mullayarov et al., 2014]. In this work examples of manifestations of deep-focus earthquakes in the amplitude variations of the low-frequency radio signal and atmospherics are considered.

Methods. The measurement procedure is sufficiently described in [Mullayarov et al., 2007]. The signals are received at Yakutsk (φ = 62.1° N, λ = 129.7° E) with three antennae: vertical electrical one (monopole) and two orthogonal magnetic antennae (loops). The error in measuring the azimuth of incoming signals does not exceed 2°. The distance up to the source of atmospherics (lightning) is roughly estimated by the four parameters of the signal waveform. The data are regularly compared with those of the world wide lightning location network WWLLN [fttp://wwlln.net]. The comparison with the data of WWLLN shows that although the distance estimation accuracy is very low (no better than 25 % of the distance), this method allows rather confident detection of the amplitude variations of the atmospherics, which can be associated with the manifestation of lithospheric processes.

The effects of seismic activity have been analyzed on the variations of the hourly averaged amplitude of the signals. The atmospherics with the paths lying within the first Fresnel zones over the epicenter centered in azimuth towards the earthquake epicenter are selected for the analysis.

When we had a weak thunderstorm activity in the areas that lie farther off the epicenter of the earthquake, we used the results of measurements at additional stations. One of these stations is located southwest of Yakutsk in the distance of 660 km (Neryungri). Additionally, analysis of seismic disturbances in the lower ionosphere has been made by measuring the signal amplitude of VLF radio transmitter. Usually

the amplitude variations of the signals of the transmitter in Japan (Ebino, 22200 Hz), in Australia (North West Cape, 19800 Hz) and in Hawaii (Lualualei, frequency 21400 Hz) were analyzed.

Results. The earthquake that took place on June 26, 2014 in Philippines was examined at first. The value of the magnitude was 5.6 and the focus depth was 76.6 km (the earthquake was not clearly "deep" but had the focus at the depth more than usually considered - more than 50 km). The earthquake was registered at 11:52:03 UT for the epicenter at φ=13.58°N, λ=120.69°E. The azimuth from the north of Yakutsk to the seismic epicenter was 191°, and the distance was 5400 km. Before that event, one earthquake had occurred approximately at that direction on June 22, 2014 but at the distance more than the fifth Fresnel zone from the main path of the atmospherics to Yakutsk.

Fig. 1a shows the paths of the signals of atmospherics from the direction to epicenter of the referred earthquake and the signal of the Australian radio station (North West Cap, 19800 kHz). In fig.1b the amplitude variations of the average amplitude of atmospherics at all hours of the day before and during the earthquake are shown (unfortunately, there are no data before 16.06.2014). There was a significant increase in the amplitude of the atmospherics signal 21-22.06.2014 with a maximum at 05 UT which can be considered as a precursor of the earthquake. In the signal of the south transmitters in Australia an additional significant increase in the amplitude was observed from 09 to 14.06.14 (fig.1c).

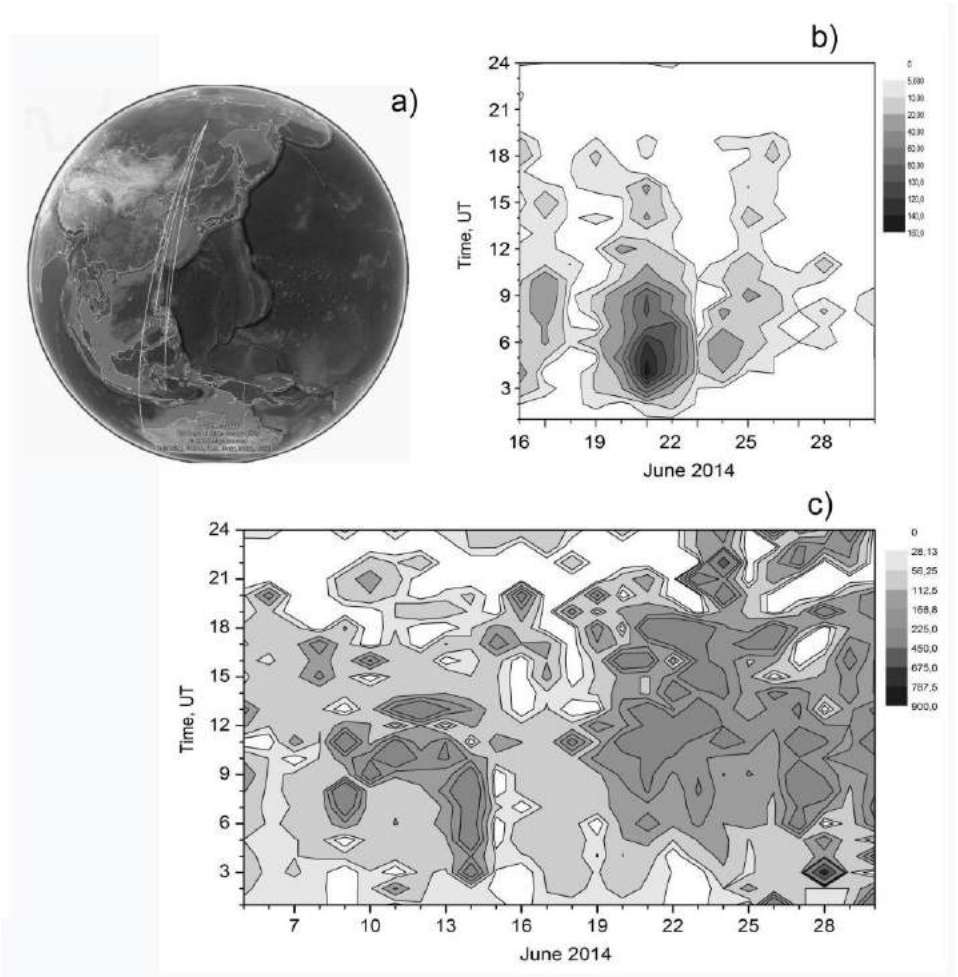

Fig. 1. Paths of the signals of atmospherics from the direction to epicenter of the earthquake of 16.06.2014 and the signal of the Australian radio station (a), the amplitude variations of the average amplitude of atmospherics at all hours of the day before and during the earthquake (b) and the variations of signal of the transmitters in Australia (c).

As it is known, one of the main causes of disturbances in the ionosphere is geomagnetic disturbances. In this connection, consideration of the geomagnetic situation has shown that the increase in the signal amplitude of the south transmitter observed from 09 to 11.06.14 can be connected also with geomagnetic disturbances, because the increase in the amplitude in this interval corresponds to the recovery phase of a weak magnetic storm (Dst-index was up to -40 nT). Thus, there are two increases in the amplitude of the signal which can be considered as precursors: one of them –2 days before the earthquake.

Variations of the average amplitude of atmospherics before and during the next two cases of a deep earthquake are shown in fig. 2. The first earthquake with a magnitude 6.3 occurred on 24.12.2009 in Primor'e, Russia has a very deep focus – 362 km. One day before the earthquake the average amplitude increased more than twice (fig. 2a). In the second earthquake that took place on 26.02.2010 at the depth of 95 km a clear increase of the average amplitude of atmospherics (precursor) was observed during 2 days before the earthquake (fig. 2b).

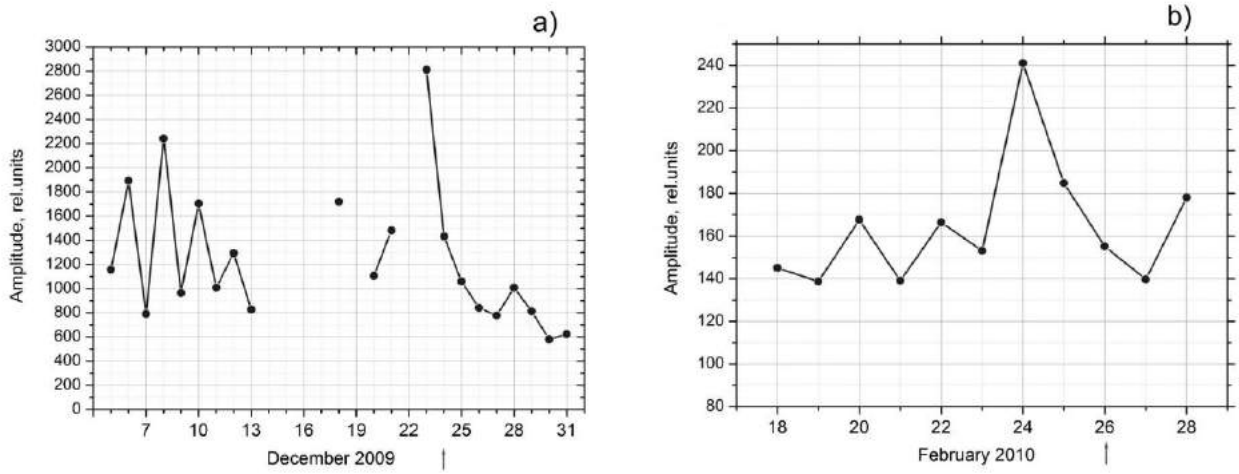

Fig. 2. Amplitude variations of the average amplitude of atmospherics before and during a very deep earthquake (depth 362 km) with a magnitude 6.3 occurred on 24.12.2009 in Primor'e, Russia (a), and earthquake with a magnitude 5.4 occurred on 26.02.2010 near Japan (b).

The behaviour of the average amplitude of atmospherics before and during the earthquake of 27.12.2011 near Japan on the same depth (95 km) is shown in fig. 3. The amplitude began to increase 2 days before the earthquake and reached the maximum on the day of the earthquake.

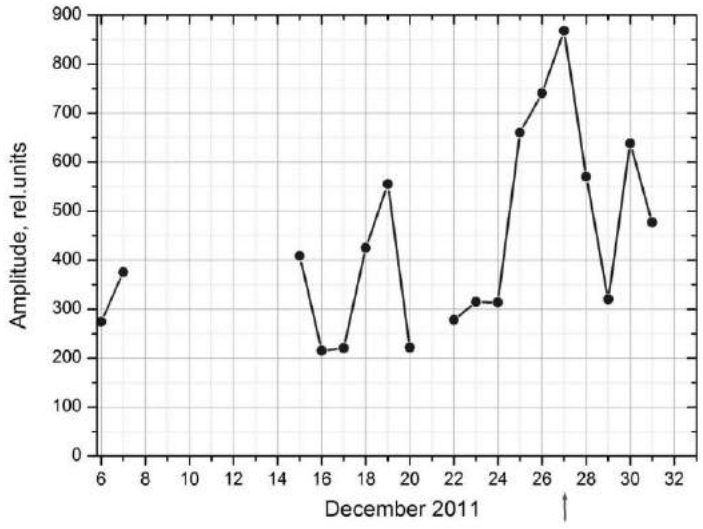

Fig. 3. The behaviour of the average amplitude of atmospherics before and during the earthquake of 27.12.2011 near Japan on the depth 95 km.

In this case, it can be assumed that a precursor passes on the earthquake effect without a gap.

Finally, we considered the earthquake which took place on 05.05.2011 in Indonesia with a magnitude 5.1 and a focus depth of 230 km. This earthquake differs from other analyzed cases because it has no precursor. The behaviour of the average amplitude of atmospherics before and during the earthquake of 05.05.2011 is shown in fig. 4. The very obvious effect of the earthquake started on the 2-nd day after the earthquake (usually the effect in the average amplitude of atmospherics was observed on the 1-3 day after the event).

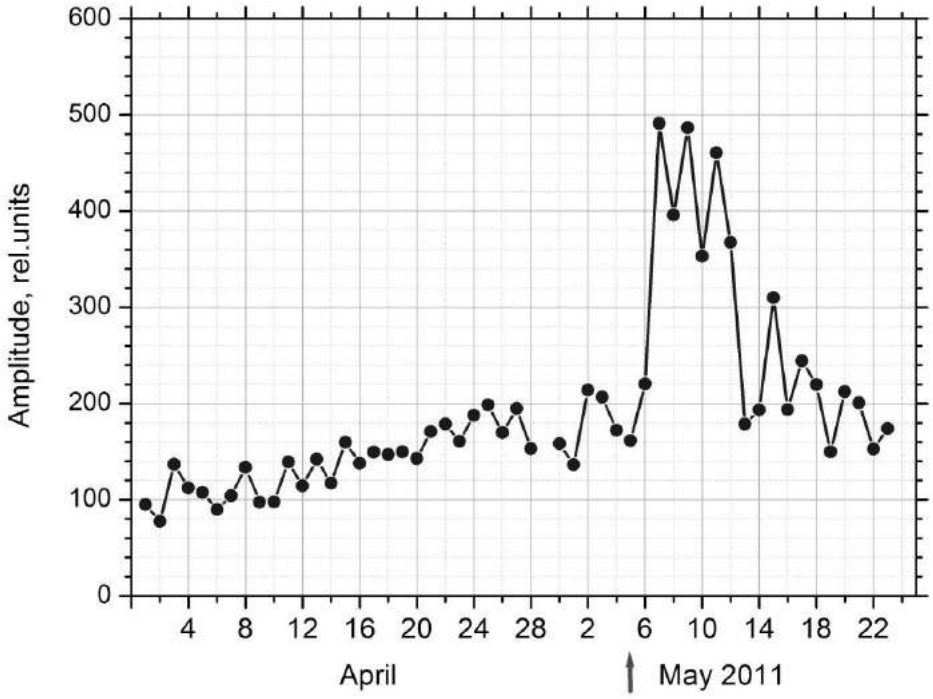

Fig. 4. The behaviour of the average amplitude of atmospherics before and during the earthquake of 05.05.2011 with a magnitude 5.1 in Indonesia on the depth 230 km.

Discussion. According to the observations of atmospherics passing within the first Fresnel zone over earthquake epicenters in Yakutsk [Mullayarov et al., 2007, 2011], it is found that earthquake effects were expressed as an increase of hourly average amplitude of atmospherics on the same day or within 3 days after the event. Possible precursors of earthquake also appeared in one-day increases in the amplitude of atmospherics mainly 5 - 12 days before the event. The analysis shows that the seismic effects in the amplitude of atmospherics are observed in the case of sufficiently strong (magnitude $M \geq 5$) and not very deep earthquake (usually no deeper than 50 km). Conditions of not deep and strong magnitude are necessary to transfer sufficient energy of the seismic processes to ionospheric heights that can cause detectable perturbation. At the same time, in [Mullayarov et al., 2014] the effects of the earthquake with magnitude of 8.2 occurring in the Sea of Okhotsk on 24.05.13 not far from the Kamchatka Peninsula at a depth of 609 km have shown that even deep earthquakes may have precursors in the form of disturbances in the lower ionosphere. In the above-mentioned event of 26.06.2014 in Philippines the earthquake of 24.05.13 has two precursors. One of them was observed 2 days before the event. In the second precursor there probably was also an effect of geomagnetic disturbances. Note that the event of 24.05.13 has been thoroughly considered,– using simultaneous observations at two points (opposite sited relative to the epicenter of the earthquake) and both atmospherics from different directions and signals of some radio stations). The geomagnetic condition was also taken into account.

Thus in the present work we confirm that a deep earthquake, unlike earthquakes at depths less than 50 km, may have two precursors, wherein the second precursor is observed within1-3 days before the event.

Conclusions. In this work examples of manifestations of deep-focus earthquakes in the amplitude variations of the low-frequency radio signal and atmospherics are considered. It is shown that deep-focus earthquakes have a different character of the precursor in comparison with a not very deep earthquake

(usually no deeper than 50 km). The deep-focus earthquakes may have two precursors, the second of them is observed within 1-3 days before the event, while a not very deep earthquake has usually one precursor 5 - 12 days before the event.

Acknowledgements

Some part of this research was conducted in the framework of Project 106 of SB of RAS and NOFMU RS(Y) grant № 2014-01-006.

References

Biagi, P.F., Piccolo R., Ermini, A., Martelucci, S., Belecci, C., Hayakawa, M., Capozzi, V., and S.P. Kingsley (2001), Possible earth-quake precursors revealed by LF radio signals. *Nat. Haz. Earth Sys. Sci.*, 1, 99-104.

Mullayarov, V.A., Karimov, R.R., and V.I. Kozlov (2007), Variations in thunderstorm VLF emissions propagating over the epicenters of earthquakes. *Journal of Atmospheric and Solar-Terrestrial Physics,* 69/13, 1513-1523.

Mullayarov, V.A., Abzaletdinova, L.M., Argunov, V.V., and A.A. Korsakov (2001), Variations in the parameters of thunderstorm electromagnetic signals on paths over earthquake regions. *Geomagnetism and Aeronomy*. 51, 825-834.

Mullayarov, V.A., Druzhin, G.I., Argunov, V.V., Abzaletdinova, L.M., and A.N. Mel'nikov (2014), Variations of VLF radio signals and atmospherics during the deep earthquake with M=8.2 occurred on 24 May 2013 near Kamchatka peninsula. *Natural Science*. 6 (3), 144-149.

SEISMO-IONOSPHERE COUPLING: CURRENT STATUS OF THE PROBLEM

A.A. Namgaladze, M.I. Karpov, O.V. Zolotov

Murmansk State Technical University, Murmansk, Russia, e-mail: namgaladzeaa@mstu.edu.ru

Abstract. Key moments of the seismogenic electricity generation are discussed. Atmosphere conductivity is changed due to enhanced air ionization by radon emanating from the tectonic faults, but these changes are not enough to cause significant increase of the conductivity electric current, which would be able to generate electric fields such as observed over the seismic active regions. It is shown that atmosphere conditions over the faults and the action of the non-electric forces have the largest influence on the generation of the vertical electric current between the Earth and ionosphere and corresponding ionospheric electric field during earthquake preparation processes. This vertical electric current may be very intensive due to the following reasons. Free electrons produced as result of air ionization attach to heavy particles and create heavy negative ions which are divided and carried by the gravity force and pressure gradients. These negative ions act as a potential nucleus of water vapor condensation, then coagulate into bigger water drops and sink down, while the light positive ions go up with warm air fluxes. Thus, the opposite charges separation occurs, and external electric current is generated. The higher number density of the big heavy particles the higher intensity of the external electric current, because the recombination rate of the charged aerosols is several orders less than the recombination rate of the primary charges. The warm humid air over the fault also affects intensity of the external electric current. Corresponding ionosphere effects (electron density and total electron content variations) of the global electric circuit disturbances are discussed, and results of the numerical modeling of the seismo-ionosphere effects are summarized.

Introduction

The problem of seismo-ionosphere coupling has been intensively studied for the last couple of decades (e.g., *Harrison et al*., 2010; *Liu*, 2009; *Pulinets and Boyarchuk, 2004*; *Pulinets and Davydenko*, 2014). Both ground-based and satellite observations revealed modifications of the global electric circuit (GEC) before, during and after strong seismic events in the form of the ionosphere disturbances. Modern satellite data obtained by DEMETER satellite shows the quasi-static electric field disturbances up to 15 mV/m over seismic active regions several days before the main shock *(Ryu et al*., 2014; *Zhang et al*., 2014;). The pre-earthquake GPS derived total electron content (TEC) anomalies represent disturbed areas of thousands kilometers and the magnitude from several tens of percents to hundred and more percents relative to the background values. Important features of observed disturbances are stable position and form as well as magnetic conjugation, modification of the equatorial anomaly and solar luminescence effects (*Zolotov et al*., 2012). These features point to the electromagnetic physical mechanism, namely the electromagnetic [$\boldsymbol{E} \times \boldsymbol{B}$] plasma drift, as a main cause of the ionosphere pre-earthquake anomalies (*Namgaladze et al*., 2009).

Despite numerous papers concerning the seismo-ionosphere coupling, it is a poorly investigated area. Here we highlight the challenges of physical interpretation of the global electric circuit modifications occurring during earthquake preparation processes due to the tectonic plates movements and summarize the results of the numerical modeling of corresponding ionosphere effects on the basis of modern observational data and global physical models.

Pre-earthquake global electric circuit variations

The global electric circuit is a closed system of electric currents flowing in the ionosphere, the Earth and between them. Sources of the air ionization are the galactic cosmic rays and natural radioactivity. The total current in the circuit is about 1.2 kA (*Rycroft et al*., 2012). It is believed that formation of the thunderstorm and shower clouds is the electromotive force in the circuit, which charges the ionosphere positively relative to the Earth with the electric potential difference of about 250 kV between them. The system is closed by the electric current flowing through a low conductive atmosphere in the areas with dry air. This electric current is called the fair-weather current. It is directed from the ionosphere to the Earth and tends to "remove" the electric potential difference between them. The density of this fair-weather current is about 2-3 pA/m^2 (*Rycroft et al*., 2012).

Unlike the fair-weather current produced by the action of the background electric field between the ionosphere and the Earth and depending on the electrical conductivity of the atmosphere, thunderstorm electric current is driven by non-electric forces: the pressure gradients and gravity force. Due to the strong variability of local weather conditions (air humidity and temperature, appearance of different gas mixtures, etc.) electric current charging the ionosphere is also a subject of significant variability which consequently leads to the local variations of the electric potential difference between the Earth and ionosphere. These variations creates disturbances of the electric fields in the ionosphere and corresponding disturbances of the ionospheric parameters, such as electron number density, temperature and TEC. Similar processes take place during earthquake preparation processes related with the tectonic plates movements.

During preparation of the strong earthquakes additional ionization of the air by radioactive gases emanating from the earthquake faults increases electric charges number density and, accordingly, atmospheric electric conductivity. On the other hand, enhanced density of the soil gases' heavy molecules and aerosols lead to the higher collision frequencies of the charged and neutral particles, and the influence of friction forces grows. Aggregated result, i.e. increase or decrease of the air electric conductivity current, depends on which of the processes dominates over another.

Denisenko et al., 2013 showed that the air conductivity changes in the periods of earthquakes preparation do not lead to dramatic changes of the conductivity electric current and resulting electric field in the ionosphere. According to their mathematical simulations, electric field in the ionosphere would not exceed 1 μV/m, i.e. three orders less than seismogenic electric fields observed by DEMETER and Intercosmos Bulgaria 1300 satellites (*Gousheva et al*., 2009; *Zhang et al*., 2014, *Ryu et al*., 2014).

In order to adequately simulate the ionosphere effects of the seismogenic electric current, one should take into consideration the action of the non-electric forces in the resulting generation of the electric current between the tectonic fault and ionosphere, the so called external electric current.

Electrons produced as a result of air ionization by radon near the Earth surface and galactic cosmic rays at higher altitudes attach to the neutral molecules. Newly formed negatively charged particles may act as a nucleus of water vapor condensation, then coagulate into big heavy water drops and mainly sink down due to their bigger mass than positively charges particles. The latter mainly float upward, if the rising warm air fluxes present. Thus, opposite charged particles are divided and transported in the opposite directions by the gravity force and pressure gradients, and external electric current is generated. It is directed towards the ionosphere and delivers additional positive charges to it, thus, creating additional electric potential difference between the Earth and ionosphere.

The process of the external electric current formation is very effective under conditions of the warm humid air with increased number density of heavy neutral molecules and aerosols. Heavy charged particles produced as a result of electrons attachment recombine with each other much slower than primary charges (*Harrison and Carslaw*, 2003), and the bigger the particles the higher electric charge density in the atmosphere. Presence of the warm humid air favors the division and transportation of the oppositely charged particles having different masses (*Ermakov and Stozhkov*, 2004; *Ivlev and Dovgalyuk*, 1999; *Svensmark et al*., 2007).

Such conditions are observed over seismic active regions. Aerosol density increases from several times to several orders (*King et al*., 1997; *Pulinets et al*., 1999; *Omori et al*., 2009) in comparison with background values as a result of emission of soil gases from the Earth crust. The process of earthquake preparation also leads to the appearance of thermal anomalies with horizontal scale from hundreds to thousand kilometers (*Akhoondzadeh*, 2013; *Ouzhounov et al*., 2007) and formation of clouds linearly aligned along the faults (*Guangmeng and Jie*, 2013; *Harrison et al.*, 2014; *Morozova*, 2012).

Resulting seismogenic electric current flowing over the fault is a superposition of the conductivity and external electric current, i.e. the action of both electric and non-electric forces. All processes of charges formation, losses, division and transportation should be taken into account in order to adequately describe electric current generation and its corresponding seismogenic effects in the ionosphere. Full equations system must include not only the Ohm's law but also continuity, momentum and heat balance equations for

all sorts of the neutral and charged particles taking into consideration the processes of ionization, recombination, interaction of the neutral and charged particles, gravity force, pressure gradients as well as action of friction forces and background electric field between the Earth and ionosphere.

Observation and numerical modeling of the seismo-ionosphere effects

Thus, the Global Electric Circuit disturbances before strong earthquakes create additional vertical electric currents flowing between the Earth and ionosphere over the tectonic faults. These vertical electric currents bring up charges through the ionosphere lower boundary into the E layer. Appearance of additional charges triggers their redistribution in the current-caring layer and generates ionosphere electric fields disturbances. According to the quasi-static electric field measurements by Intercosmos Bulgaria 1300 and DEMETER satellites the intensity of the seismic related electric fields is about from several to 10-15 mV/m and the horizontal scale up to thousand kilometers (*Gousheva et al*., 2009; *Zhang et al*., 2013). Measured values show the vertical electric current has to be not less than the magnetospheric electric currents, i.e. several orders higher than the fair-weather currents.

Penetration of additional (disturbed) electric field along ideally conductive geomagnetic field lines from E-region into F-region causes F2-layer plasma electromagnetic drift pattern changes (*Namgaladze et al*., 2009). The eastward (westward) electric fields produce uplift (sinking) of ionosphere plasma to regions with low (high) loss rates in reactions with neutral gas, mainly N_2 and O_2, i.e. vertical plasma transport triggers enhancement (decrease) of the electron number density and, accordingly, the total electron content. Vertical electric fields drive horizontal redistribution of ionosphere plasma. (*Karpov et al*., 2013). F2-region seismo-disturbed electric fields drive modification of the Appleton anomaly at low latitudes as well *(Ryu et al*., 2014).

The GPS derived TEC data obtained for the earthquake preparation periods reveal formation of the strong long-living anomalies with the magnitude of 30-90 % and more relative to the quiet conditions. The disturbed areas extend up to 2000-4500 km over the epicenter, and no noticeable movements are registered (*Romanovskaya et al*., 2014; *Liu*, 2009; *Pulinets and Davydenko*, 2014).

Very important features of observed TEC relative disturbances is that they are also often observed over the point which is magneticaly conjugated to the epicenter. Anomalies start to depress before the sunrise, disappear at daytime and reappear at night. Such characteristics strongly support the electromagnetic mechanism of the TEC pre-earthquake anomalies. The additional electric field formed over the epicenter passes to the opposite hemisphere along infinite conductive geomagnetic field lines, but disappear at daytime due to the high conductive of the sunlit ionosphere (*Namgaladze et al*., 2013).

These effects were reproduced with Upper Atmosphere Model (UAM) (*Karpov et al.*, 2013; *Zolotov et al*., 2012). The vertical electric currents were used as model input at the lower boundary (80 km) of the electric potential equation of the Upper Atmosphere Model. The equation was solved jointly with the continuity, momentum and heat balance equations for all sorts of neutral and charged components. It was shown that the zonal fields of about 1-4 mV/m and 4-10 mV/m are required to generate TEC disturbances at low and middle latitudes, respectively. Corresponding vertical electric currents amplitudes at the ionosphere lower boundary should be ~10 nA/m^2. The results of the UAM modeling agree well with the GPS TEC observations; namely, they reveal all basic signatures of earthquake precursors in the TEC variations: (1) amplitude of the TEC modifications, (2) their spatial scale, (3) lifetime, (4) magnetic conjugation of the effects, and (4) night-time domination of the TEC anomalies.

Resulting ionosphere number density distribution changes also affect the ELF/VLF/ULF signals propagation and may cause effects like reported by *Smirnova et al*., 2001, 2004; *Smirnova and Hayakawa*, 2007. Ionosphere electron density disturbances may result in *foF2* and *hmF2* pre-earthquake anomalies. Moreover, vertical electric current itself generates internal gravity waves in the ionosphere as shown by *Namgaladze et al*., 2015.

Conclusion

The physical mechanism of the generation of the vertical electric current between the Earth and ionosphere during earthquake preparation processes has been discussed. Atmospheric conditions over tectonic faults lead to significant increase of the external electric current due to the appearance of heavy charged particles

with slow recombination rate and due to the presence of humidity warm air. Unlike the conductivity electric current driven by background electric field between the Earth and ionosphere, the external electric current is created by non-electric forces. Oppositely charged particles with different masses are divided and transported due to gravitational sedimentation and convectional transport. Water vapor condensation and coagulation of water drops occurs at the heavy negative ions which move mainly down, while positive ions move mainly up with rising warm air. The process leads to the additional electric potential difference between the Earth and ionosphere and, consequently to formation of additional electric fields in the ionosphere, such as observed by DEMETER, Intercosmos Bulgaria 1300 satellites. These electric fields create the disturbances of the ionosphere GPS TEC variations via electromagnetic plasma drifts. Both seimogemic electric fields and TEC disturbances were successfully modeled using global self-consistent three-dimensional Upper Atmosphere Model.

Acknowledgements

The work is partially supported by project 298 "Multi-instrument Space-Borne Observations and Validation of the Physical Model of the Lithosphere-Atmosphere-Ionosphere-Magnetosphere Coupling" of the International Space Science Institute, Bern, Switzerland.

References

Akhoondzadeh, M. (2013), An Adaptive Network-based Fuzzy Inference System for the detection of thermal and TEC anomalies around the time of the Varzeghan, Iran, (M_w=6.4) earthquake of 11 August 2012, *Adv. Space Res*., 52(5), 837-852.

Ermakov V.I., and Yu. I. Stozhkov (2004), Preprint N 2, LPI RAS, St. Petersburg, (in Russian).

Denisenko, V.V., M. Ampferer, E.V. Pomozov, A.V. Kitaev, W. Hausleitner, G. Stangl, H.K. Biernat (2013), On electric field penetration from ground into the ionosphere, *J. Atm. Sol.-Terr. Phys*., 102, 341-353.

Gousheva, M., D. Danov, P. Hristov, M. Matova (2009), Ionospheric quasi-static electric field anomalies during seismic activity in August–September 1981, *Nat. Haz. Earth Sys. Sci*., 9(1), 3-15.

Guangmeng, G. and Y. Jie (2013), Three attempts of earthquake prediction with satellite cloud images, *Nat. Haz. Earth System Sci*., 13(1), 91-95.

Harrison, R.G., K.L. Aplin, M.J. Rycroft (2010), Atmospheric electricity coupling between earthquake regions and the ionosphere, *J. Atm. Sol.-Terr. Phys*., 72, 376-381.

Harrison, R.G., K.L. Aplin, M.J. Rycroft (2014), Brief Communication: Earthquake–cloud coupling through the global atmospheric electric circuit, *Nat. Haz. Earth Sys. Sci*., 14(4), 774-777.

Harrison R.G., and K.S. Carslaw (2003), Ion-aerosol-cloud processes in the lower atmosphere, *Rev. Geophys.*, 41(3), 1-26.

Ivliev, L.S., and Yu.A. Dovgalyuk (1999), *Fizika atmosfernyih aerozolnyih system*, 94 pp., SPSU, St. Petersburg (in Russian).

Karpov, M.I., A.A. Namgaladze, and O.V. Zolotov (2013), Modeling of Total Electron Content Disturbances Caused by Electric Currents between the Earth and the Ionosphere, *Russ. J. Phys. Chem. B*, 7(5), 594-598.

King, Ch-Yu, Wei Zhang, Bi-Shia King (1993), Radon anomalies on three kinds of faults in California, *Pure Appl. Geophys. PAGEOPH*, 141(1), 111-124.

Liu, J.Y. (2009), Earthquake precursors observed in the ionospheric F-region, in: *Electromagnetic Phenomena Associated with Earthquakes, ed. by M. Hayakawa*, Transworld, Trivandrum, India, 187-204.

Morozova, L.I. (2012), Crustal geodynamic activity: manifestations in cloud fields, *Russ. Geol. Geophys*., 53(4), 416-423.

Namgaladze, A.A., M.I. Karpov, O.V. Zolotov (2015) Ionospheric earthquakes precursors in the total electron content variations: observations and modeling, in: *The Atmosphere and Ionosphere Elementary Processes, Discharges and Plasmoids, ed. by V. Bychkobv et al.*, Springer, Berlin (in press).

Namgaladze, A.A., M.V. Klimenko, V.V. Klimenko, I.E. Zakharenkova, I. E. (2009), Physical mechanism and mathematical modeling of earthquake ionospheric precursors registered in total electron content, *Geom. Aeron*., 49(2), 252-262.

Namgaladze, A.A., O.V. zolotov and B.E. Prokhorov (2013), Numerical simulation of the variations in the total electron content of the ionosphere observed before the Haiti earthquake of January 12, 2010, *Geom. Aeron*., 53(4), 522-528.

Omori, Y., H. Nagahama, Y. Kawada, Y. Yasuoka, T. Ishikawa, S. Tokonami, M. Shinogi (2009), Preseismic alteration of atmospheric electrical conditions due to anomalous radon emanation, *Phys. Chem. Earth*, 34(6-7), 435-440.

Ouzounov, D., D. Liu, K. Chunli, G. Cervone, M. Kafatos, P. Taylor (2007), Outgoing long wave radiation variability from IR satellite data prior to major earthquakes, *Tectonophysics*, 431, 211–220.

Pulinets, S.A., V.A. Alekseev, A.D. Legen'ka, V.V. Khegai (1997), Radon and metallic aerosols emanation before strong earthquakes and their role in atmosphere and ionosphere modification, *Adv. Space Res*., 20(11), 2173-2176.

Pulinets, S. A., and K. Boyarchuk (2004), *Ionospheric Precursors of Earthquakes*, 315 pp., Springer, Berlin.

Pulinets, S., and D. Davidenko (2014), Ionospheric precursors of earthquakes and Global Electric Circuit, *Adv. Space Res*., 53(5) 709-723.

Romanovskaya, Yu.V., and A.A. Namgaladze (2014), Ionospheric earthquake precursors: analysis of the total electron content observation before the strong earthquakes in 2005, *Proc. MSTU*, 17(2), 403-410 (in Russian).

Rycroft, M.J., and R.G. Harrison (2012), Electromagnetic Atmosphere-Plasma Coupling: The Global Atmospheric Electric Circuit. *Space Sci. Rev.*, 168, 363-384.

Ryu, K., E. Lee, J.S. Chae, M. Parrot Ryu, K. (2014), Seismo-ionospheric coupling appearing as equatorial electron density enhancements observed via DEMETER electron density measurements, *J. Geoph. Res.*, DOI: 10.1002/2014JA020284.

Smirnova, N., M. Hayakawa, K. Gotoh, D. Volobuev (2001), Scaling characteristics of the ULF geomagnetic fields at the Guam seismoactive area and their dynamics in relation to the earthquake, *Natural Hazards and Earth System Sciences*, 1, 119–126.

Smirnova, N., M. Hayakawa, K. Gotoh (2004), Precursory behavior of fractal characteristics of the ULF electromagnetic fields in seismic active zones before strong earthquakes, *Physics and Chemistry of the Earth*, 29(4-9), 445-451.

Smirnova, N., M. Hayakawa (2007), Fractal characteristics of the ground-observed ULF emissions in relation to geomagnetic and seismic activities, *Journal of Atmospheric and Solar-Terrestrial Physics*, 69(15), 1833-1841.

Sorokin, V., and M. Hayakawa (2013), Generation of Seismic-Related DC Electric Fields and Lithosphere-Atmosphere-Ionosphere Coupling, *Mod. Appl. Sci.*, 7(6), 1-25.

Svensmark, H., J.O.P. Pedersen, N.D. Marsh et al. (2007), Experimental evidence for the role of ions in particle nucleation under atmospheric conditions, *Proc. Royal Soc. A: Math., Phys. Eng. Sci*., 463 (2078), 385-397.

Zhang, X., X. Shen, S. Zhao, Lu Yao, X. Ouyang, J. Qian (2014), The characteristics of quasi-static electric field perturbations observed by DEMETER satellite before large earthquakes, *J. Asian Earth Sci*., 79, 42-52.

Zolotov, O.V., A.A. Namgaladze, O.V. Martynenko, I.E Zakharenkova and I.I. Shagimuratov (2012), Physical interpretation and mathematical simulation of ionospheric precursors of earthquakes at midllatitudes, *Geom. Aeron.*, 53(3), 390-397.

CURRENT CHALLENGES IN THE RESEARCH OF THE FRACTURE-INDUCED PRE-SEISMIC ELECTROMAGNETIC EMISSIONS IN THE MHZ AND KHZ BANDS

S. M. Potirakis[1], K. Eftaxias[2]

[1]Department of Electronics Engineering, Technological Education Institute (TEI) of Piraeus, 250 Thivon & P. Ralli, GR-12244, Aigaleo, Athens, Greece, e-mail: spoti@teipir.gr; [2]Department of Physics, Section of Solid State Physics, University of Athens, Panepistimiopolis, GR-15784, Zografos, Athens, Greece, e-mail: ceftax@phys.uoa.gr

Abstract. A remote observation stations' network has been developed in Greece for the recording of the pre-seismic electromagnetic (EM) variations at the MHz and kHz bands. The hypothesis that the fracture-induced electromagnetic emissions (EME), which emerge from a few days up to a few hours before the main seismic shock occurrence, permit a real time monitoring of the damage process during the last stages of earthquake (EQ) preparation, as it happens at the laboratory scale, has been formulated based on the analysis of EME recordings in terms of a wide variety of time-series methods. This hypothesis is critically examined through a shift in thinking towards the basic science findings of fracture and faulting processes. The resolution of different puzzling features observed in the recorded pre-seismic EME and the negative views that have been expressed concerning their credibility has been attempted. A three-stage model for EQ generation by means of pre-seismic fracture-induced EME is finally proposed.

1. Introduction

Earthquake (EQ) is a large scale fracture phenomenon happening in the Earth's heterogeneous crust, which occurrence is perceived in the form of a sudden violent shaking of the Earth's surface. However, the processes involved in the preparation of an EQ are complex while it is not easy to be directly monitored. Therefore, the view that "understanding how earthquakes occur is one of the most challenging questions in fault and earthquake mechanics" (Shimamoto and Togo, 2012) is not an overstatement. In the direction of understanding the underlying complex nonlinear processes involved in the preparation of an EQ two research fields have attracted the interest of the scientists; one of them, on which a large effort has been devoted, is the study of fracture phenomena on the laboratory scale (e.g., Lockner et al., 1991; Ben-David et al., 2010; Hadjicontis et al., 2011; Carpinteri et al., 2012; Chang et al., 2012), while the other is the study of different phenomena which are observed in the field prior to the occurrence of significant EQs.

It has been found that opening cracks are accompanied with electromagnetic emission (EME) ranging in a wide frequency spectrum, from the kHz band to the MHz band, while these signals are detectable both at the laboratory scale prior to global failure in fracture experiments (e.g., Hadjicontis et al., 2011; Carpinteri et al., 2012), and at the geophysical scale prior to significant EQs (e.g., Warwick et al., 1982; Hayakawa and Fujinawa, 1994; Qian et al., 1994; Gokhberg et al., 1995; .Kapiris et al., 2004; Contoyiannis et al., 2005, 2014; Uyeda et al., 2009; Cicerone et al., 2009; Potirakis et al., 2012, 2013, 2015; Eftaxias et al., 2013; Eftaxias and Potirakis, 2013). It is practically impossible to install an experimental network to measure stress and strain at the location where an EQ is generated (focus area) using the same instrumentation as in laboratory experiments. It is therefore impossible to investigate the corresponding states of stress and strain and their time variation in order to understand the laws that govern the last stages of EQ generation, or to monitor (much less to control) the principal characteristics of a fracture process. In principle, this disadvantage does not accompany the tool of the fracture-induced EME in the case of significant shallow EQs that occur on land, keeping in mind that laboratory experiments are man controlled while field observations are measurements of events over which researchers have no control. On the contrary, the EME method is expected to reveal more information when it is used at the geophysical scale. Indeed, a major difference between the laboratory and natural processes is the order-of-magnitude differences in scale (in space and time), allowing the possibility of experimental observation at the geophysical scale for a range of physical processes which are not observable at the laboratory scale (Main and Naylor, 2012). At the laboratory scale the fault growth process normally occurs violently in a fraction of a second (Lockner et al., 1991). Thus, the idea that field observations at the geophysical scale by means of EME will probably reveal

features of the last stages of failure process which are not clearly observable at the laboratory scale, allowing the monitoring in real-time and step-by-step of the gradual damage of stressed materials during EQ preparation process, cannot, in principle, be excluded.

Two important features of the EME are observed both at the laboratory and the field: (i) the MHz radiation consistently precedes the kHz one, indicating that these two emissions correspond to different characteristic stages of the fracture / EQ preparation, while (ii) after the emission of the kHz EME an EM silence systematically emerges before the time of the global failure / EQ occurrence (e.g., Kumar and Misra, 2007; Qian et al., 1994; Baddari et al., 2011, Hayakawa and Fujinawa, 1994; Gokhberg et al., 1995; Matsumoto et al., 1998; Hayakawa, 1999; Eftaxias et al., 2013; Eftaxias and Potirakis, 2013; and references therein). Based on these features, and the results obtained through the analysis of the field observed MHz-kHz EME by multidisciplinary time-series analysis tools, we have introduced a three-stage model of EQ preparation process by means of fracture-induced EME (Eftaxias and Potirakis, 2013, and references therein; Contoyiannis et al., 2014, and references therein) as described in Section 3.

2. Telemetric Stations Network

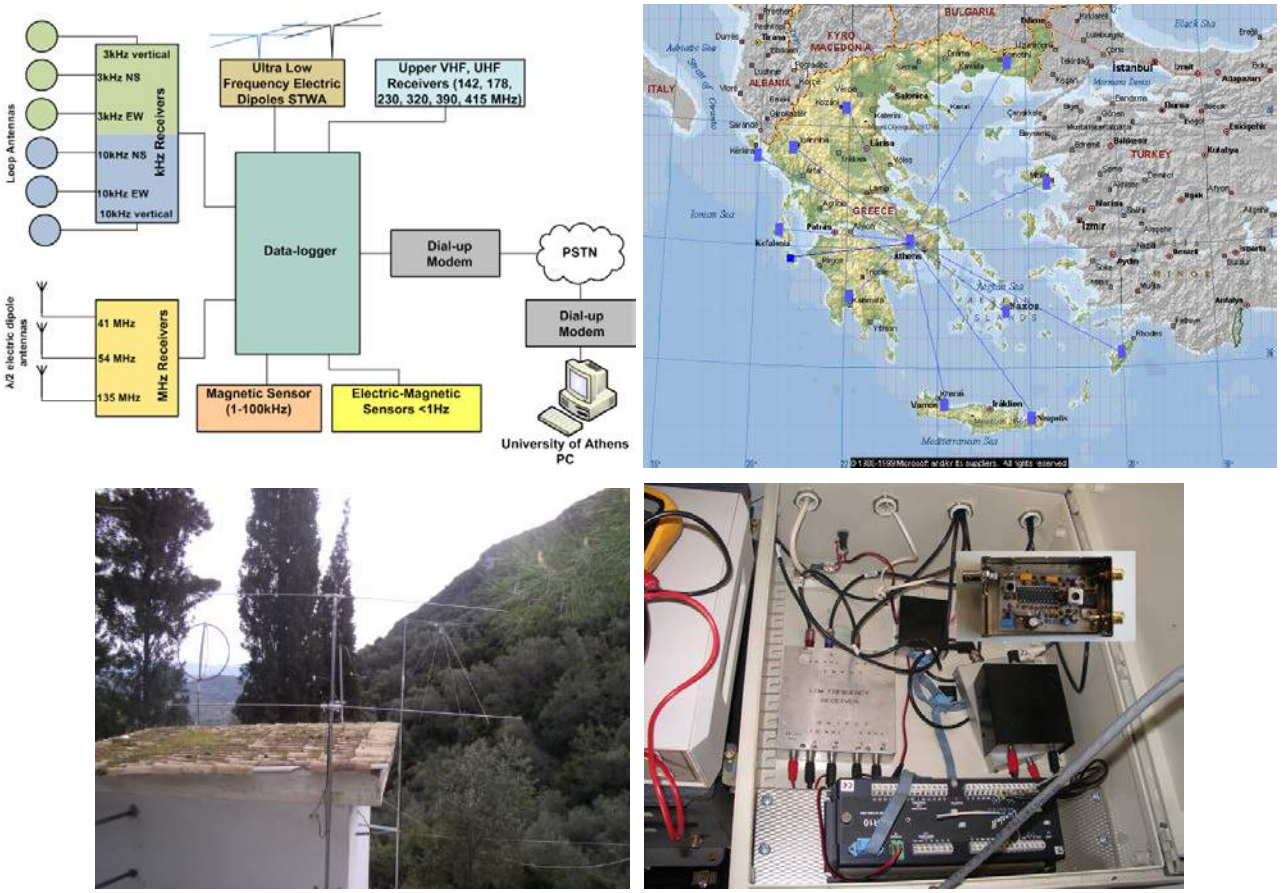

Fig. 1. (Top-Left): Block diagram of the exemplary telemetric measurement station installed at Zakynthos (Zante) Island. (Top-Right): The currently active telemetric stations network of Greece. (Bottom-Left): Typical example of antennas installation at the remote telemetric station of Kerkyra (Corfu) island (39.7127° N, 19.7962°E) for the measurement of geo-electromagnetic field variations. The two $\lambda/2$ dipole antennas can be seen in the foreground, while a pair of loop antennas is also mounted on the hovel hosting the receivers. (Bottom-Right): A typical installation of the receivers along with one of the employed data loggers from the remote telemetric station at Rhodes island (36.2135° N, 28.1212° E). The insert photo depicts the PCB of the MHz receivers unit.

A field measurement network using the same instrumentation as in laboratory experiments for the recording of fracture-induced kHz and MHz magnetic and electric fields, respectively, has been developed in collaboration with Prof. Nomicos. Since 1994, a telemetric remote station has been installed in a carefully selected mountainous site of Zakynthos (Zante) island at the south-west of the island (37.76^o N–20.76^o E) providing low EM background noise. The complete measurement system comprises of (i) six loop antennas

detecting the three components (EW, NS, and vertical) of the variations of the magnetic field at 3 kHz and 10 kHz respectively; (ii) three vertical electric dipole antennas detecting the electric field variations at 41, 54 and 135 MHz respectively; (iii) other magnetic and electromagnetic sensors. All the time-series are sampled once per second, i.e., with a sampling frequency of 1 Hz. The block diagram of the measurement configuration is shown in Fig. 1(top-left). Note that the main focus is on the recorded MHz and kHz EME. The measured frequencies (3 kHz, 10 kHz, 41 MHz, 54 MHz and 135 MHz) were selected in order to minimize the effects of the man-made noise. A reduced configuration is installed at 11 more stations spread all over Greece, Fig. 1(top-right). The recorded data are acquired and regularly forwarded to the central telemetric station in Athens through PSTN. We note that the installed experimental setup helps us not only to specify whether or not a single MHz or kHz EM anomaly is possibly EQ-related in itself, but also whether a sequence of MHz and kHz EM disturbances which emerge one after the other in a short time period, could be characterized as possibly EQ-related one (Eftaxias, 2009; Eftaxias et al., 2001, 2002; Karamanos et al., 2005; Contoyiannis et al., 2005, 2014; Contoyiannis and Eftaxias, 2008; Potirakis et al., 2012, 2013, 2015).

3. Research Objectives - Challenges

Our main research motivation is based on the view that understanding of EM precursors in terms of basic science can lead to more sufficient knowledge of the last stages of the EQ preparation process and strict definitions of EM precursors. In this direction, we try to contribute to the establishment of strict criteria for the definition of an emerged EM anomaly as a possibly EQ-related one, by focusing on the answer of the questions:

(i) How can we recognize a MHz or kHz EME as a pre-seismic one?

(ii) How can we link the MHz and kHz EM precursors and the following EM silence with distinctive last stages of the earthquake preparation?

(iii) How can we identify precursory symptoms in EM observations which signify that the occurrence of the prepared EQ is unavoidable?

(iv) How can we explain the considered as paradoxes features?

(v) How can we link the observed EM precursors with other complex extreme events?

(vi) How can we link the observed EM precursors with other precursors?

As already mentioned in Section 1 (Introduction), (i) the MHz radiation consistently precedes the kHz one, indicating that these two emissions correspond to different characteristic stages of the fracture / EQ preparation, while (ii) after the emission of the kHz EME an EM silence systematically emerges before the time of the global failure / EQ occurrence. Based on these features, and the results obtained through the analysis of the field observed MHz-kHz EME by multidisciplinary time-series analysis tools, we have introduced the following three-stage model of EQ preparation process by means of fracture-induced EME (Eftaxias and Potirakis, 2013, and references therein; Contoyiannis et al., 2014, and references therein):

(1) The initially emerging MHz EM field is attributed to the cracking in the highly disordered material that surrounds the backbone of strong entities (asperities) distributed around the stressed fault sustaining the system (Fig. 2). It has been shown in terms of the Method of Critical Fluctuations (MCF) that this emission shows antipersistency and would be described in analogy to a thermal second order phase transition in equilibrium (Contoyiannis et al., 2005, and references therein), while an analysis by means truncated Lévy statistics, nonextensive Tsallis statistical mechanics, and criticality suggests that a truncated Lévy-walk-type mechanism can organize the heterogeneous system to criticality (Contoyiannis and Eftaxias, 2008). Importantly, based on the recently introduced method of Natural Time, it has been shown that the seismic activity that occurs in the region around the epicenter of the oncoming significant shock a few days up to approximately one week before the main shock occurrence, and the observed MHz EM precursor which emerges during the same period, both behave as critical phenomena (Potirakis et al., 2013, 2015).

(2) Our understanding of different rupture modes is still very much in its infancy; however, laboratory experiments of rock fracture and frictional sliding have shown that the relative slip of two fault surfaces takes place in two phases: a slow stick-slip like fracture-sliding precedes dynamical fast global slip (Ben-David et al., 2010; Chang et al., 2012). It has been suggested that the abrupt emergence of strong avalanche-like kHz EM field is due to the fracture of the family of the asperities themselves (Fig. 2), namely to the slow

stick-slip like stage of rupture mode. This emission shows: high information content and organization, preferred direction in the underlying fracto-EM mechanism, and persistency, namely it includes the key features of an extreme event (Eftaxias et al., 2013; Eftaxias and Potirakis, 2013; and references therein). The observed kHz EME precursor is characterized by the absence of any footprint of a second order transition in equilibrium or truncated- Lévy-walk-type mechanism, on the contrary shows footprints of a first order phase transition (Contoyiannis et al., 2014). The kHz EM time series includes well established universal structural patterns of fracture-faulting process, namely: (i) the activation of a single fault by means of kHz EM activity behaves as a reduced / magnified image of the regional / laboratory seismicity; (ii) its time profile is in consistency with the universal fractional Brownian motion spatial profile of natural rock surfaces; (iii) the roughness of its time profile coincides with the universal spatial roughness of fracture surfaces. Finally, the kHz EM emission is consistent with the fault modeling of the occurred earthquake which has been resulted by studies from different disciplines, e.g., satellite radar interferometry and seismology (Eftaxias et al., 2013; Eftaxias and Potirakis, 2013; and references therein).

(3) The systematically observed EM silence in all frequency bands is sourced in the stage of preparation of dynamical slip which results to the fast, even super-shear, mode that surpasses the shear wave speed. Recent laboratory experiments also reveal this feature (Eftaxias et al., 2013; Eftaxias and Potirakis, 2013; and references therein).

(*4) Recently, we have shown in terms of the MCF that between the first two stages of the fracture process, an intermediate stage exists which reflects the tricritical behavior (Contoyiannis et al., 2014). This stage appears in the kHz EME just before the emergence of the strong avalanche-like kHz emission. The results obtained for the kHz time-series are compatible with the results obtained for an introduced model map which describes the tricritical crossover. The tricritical crossover indicates the boundary of an antipersistence dynamics, namely the existence of a negative feedback mechanism that kicks the system away from extreme behavior.

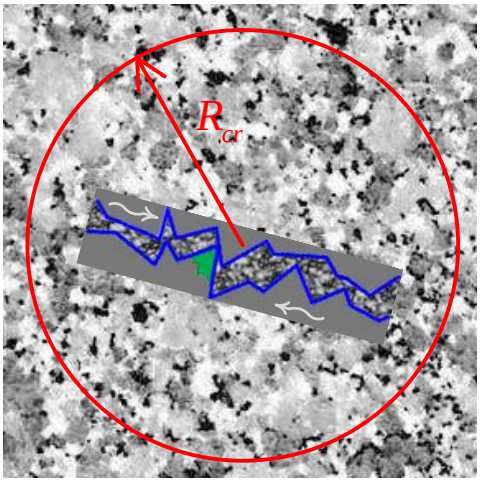

Fig. 2. A significant EQ is what happens when two surfaces of a major fault (blue lines) slip against one another under the stresses rooted in the motion of tectonic plates. A fault is embedded in a heterogeneous environment. The EQ preparation process at the first stage concerns the fracture of a disorder medium surrounding over a critical circle the major fault emitting the MHz EME which can be described by means of a phase transition of second order. The symmetry breaking signalizes the transition from the phase of non-directional, almost symmetrical, cracking distribution to a directional localized cracking zone along the direction of the fault. The EQ is inevitable if and only if the asperities break (green highlighted area), emitting the kHz EME during the second stage, and then an EME silence follows.

We clarify that an EME recording has to satisfy specific criteria (Fig. 3) before it can be considered a valid precursory signal; note that a valid MHz precursor indicates the preparation of a significant EQ, however the EQ is inevitable if and only if a valid kHz precursor is identified after a valid MHz precursor and then an EME silence follows. The above suggested three-stage model of EQ preparation process by means of fracture-induced EME, is a hypothesis that remains to be further verified; however, it should be noted that, up to now, it seems to be in agreement with both experimental (laboratory and geophysical) data, as well as theoretic and simulation studies of fracture phenomena, while no rebuttal has been published yet.

We note that the study of EME possibly related with an oncoming significant seismic event is associated with the existence of "paradox features" that accompany their observation; namely: Why an EM silence observed at the time of the EQ occurrence? Why the emerged EM signals are not accompanied by large precursory strain changes, much larger from co-seismic ones? Why EM emissions are not observed during the aftershock period? How the traceability of EM potential precursors is achieved on the grounds that they should normally be absorbed by the Earth's crust. An attempt to the answer to these questions has been recently presented (Eftaxias et al., 2013; Eftaxias and Potirakis, 2013; and references therein).

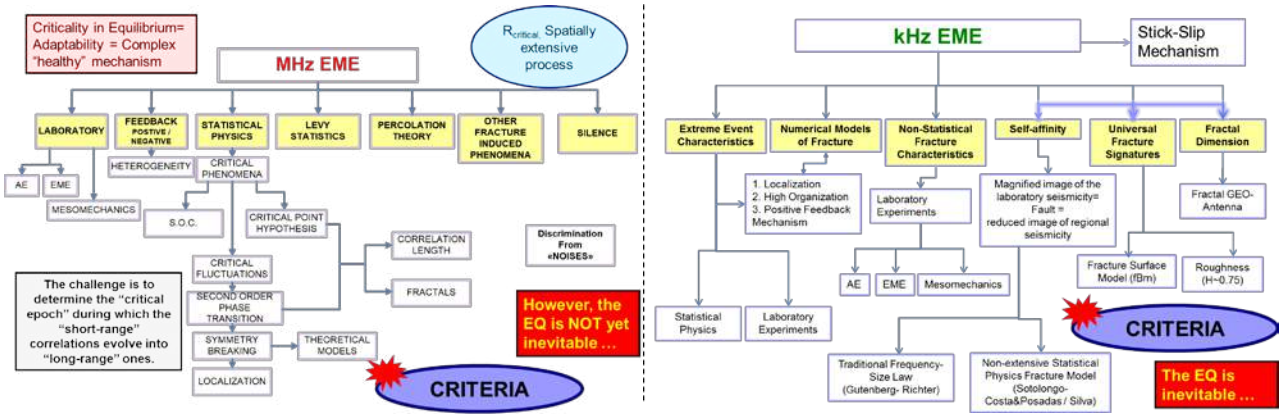

Fig. 3. The identification of a valid EME recording is performed by means of multidisciplinary time-series analysis. An EME recording has to satisfy specific criteria (MHz: left; kHz: right) before it can be considered a valid precursory signal. A valid MHz precursor indicates the preparation of a significant EQ, however the EQ is inevitable if and only if a valid kHz precursor is identified after the emergence of a valid MHz precursor and then an EME silence follows.

4. Conclusion

Fracture-induced EME in a wide range of frequency bands are sensitive to the micro-structural chances. Thus, their study constitutes a nondestructive method for the monitoring of the evolution of damage process at the laboratory scale. It has been suggested that fracture induced MHz-kHz EME, which emerge from a few days up to a few hours before the main seismic shock occurrence permit a real time monitoring of the damage process during the last stages of earthquake preparation, as it happens at the laboratory scale. Importantly, it is noted that when studying the fracture process by means of laboratory experiments, the fault growth process normally occurs violently in a fraction of a second. However, a major difference between the laboratory and natural processes is the order-of-magnitude differences in scale (in space and time), allowing the possibility of experimental observation at the geophysical scale for a range of physical processes which are not observable at the laboratory scale. Therefore, the study of fracture-induced EME is expected to reveal more information, especially for the last stages of the fracture process, when it is conducted at the geophysical scale. In this frame, we have installed a network of remote telemetric stations for the recording of fracture-induced EME and based on the results obtained through the analysis of the field observed MHz-kHz EME by multidisciplinary time-series analysis tools, we have introduced a three-stage model of EQ preparation process by means of fracture-induced EME. Since this is a short overview article, one should refer to our previously published articles in order to get more details on specific recorded MHz-kHz EME signals, their analysis, and the different aspects of the developed model.

5. References

Baddari, K., Frolov, A., Tourtchine, V., and Rahmoune, F. (2011), An integrated study of the dynamics of electromagnetic and acoustic regimes during failure of complex macrosystems using rock blocks, *Rock Mech. Rock Eng*., 44, 269–280.

Ben-David, O., Cohen, G., and Fineberg, J. (2010), The dynamic of the onset of frictional slip, *Science*, 330, 211-214.

Carpinteri, A., Lacidogna, G., Manuello, A., Niccolini, G., Schiavi, A., and Agosto, A. (2012), Mechanical and electromagnetic emissions related to stress-induced cracks, *SEM Exp. Techniq.*, 36, 53-64.

Chang, J., Lockner, D., and Reches, Z. (2012), Rapid acceleration leads to rapid weakening in earthquake-like laboratory experiments, *Science*, 338, 101-105.

Cicerone, R. D., Ebel, J. E., Britton, J. (2009) A systematic compilation of earthquake precursors, *Tectonophysics*, 476, 371-396.

Contoyiannis, Y. F., Kapiris, P. G., and Eftaxias, K. A. (2005), A Monitoring of a pre-seismic phase from its electromagnetic precursors, *Phys. Rev. E*, 71(6), 66123/1–14, doi: 10.1103/PhysRevE.71.066123.

Contoyiannis, Y., Eftaxias, K. (2008), Tsallis and Levy statistics in the preparation of an earthquake, *Nonlin. Processes Geophys*., 15, 379-388.

Contoyiannis, Y., Potirakis, S.M., Eftaxias, K., Contoyianni, L. (2014), Tricritical crossover in earthquake preparation by analyzing preseismic electromagnetic emissions, *J. Geodynamics*, doi: 10.1016/j.jog.2014.09.015.

Eftaxias, K. (2009), Footprints of nonextensive Tsallis statistics, selfaffinity and universality in the preparation of the L'Aquila earthquake hidden in a pre-seismic EM emission. *Physica A*, 389, 133-140.

Eftaxias, K., Kapiris, P., Polygiannakis, J., Bogris, N., Kopanas, J., Antonopoulos, G., Peratzakis, A., Hadjicontis, V. (2001), Signature of pending earthquake from electromagnetic anomalies. *Geophys. Res. Let.*, 28, 3321-3324.

Eftaxias, K., Kapiris, P., Dologlou, E., Kopanas, J., Bogris, N., Antonopoulos, G., Peratzakis, A., Hadjicontis (2002), EM anomalies before the Kozani earthquake: A study of their behavior through laboratory experiments, *Geophys. Res. Lett*., 29(8), 1228(1-4), doi:10.1029/2001GL013786.

Eftaxias, K., and Potirakis, S. M. (2013), Current challenges for pre-earthquake electromagnetic emissions: shedding light from micro-scale plastic flow, granular packings, phase transitions and self-affinity notion of fracture process, *Nonlin. Processes Geophys*., 20, 771-792, doi:10.5194/npg-20-771-2013.

Eftaxias, K., Potirakis, S. M., and Chelidze, T. (2013), On the puzzling feature of the silence of precursory electromagnetic emissions, *Nat. Hazards Earth Syst. Sci.*, 13, 2381-2397, doi: 10.5194/nhess-13-2381-2013.

Gokhberg, M. K., Morgounov, V. A., Pokhotelov, O. A. (1995), *Earthquake Prediction: Seismo-Electromagnetic Phenomena*, Singapore, Gordon and Breach Publishers.

Hadjicontis, V., Mavromatou, C., Mastrogiannis, D., Antsygina, T. N., and Chishko, K. A. (2011), Relationship between electromagnetic and acoustic emissions during plastic deformation of gamma-irradiated LiF monocrystals, *J. Appl. Phys*., 110, 024907.

Hayakawa, M., and Fujinawa, Y. (1994), *Electromagnetic Phenomena Related to Earthquake Prediction*, Tokyo, Japan, Terrapub.

Hayakawa, M. (1999), *Atmospheric and Ionospheric Electromagnetic Phenomena Associated with Earthquakes*, Terrapub, Tokyo.

Kapiris, P., Eftaxias, K., and Chelidze, T. (2004), Electromagnetic signature of prefracture criticality in heterogeneous media, *Phys. Rev. Lett.*, 92(6), 065702/1-4, doi: 10.1103/PhysRevLett.92.065702.

Karamanos, K., Dakopoulos, D., Aloupis, K., Peratzakis, A., Athanasopoulou, L., Nikolopoulos, S., Kapiris, P., Eftaxias, K. (2006), Pre-seismic electromagnetic signals in terms of complexity. *Phys. Rev. E*., 74, 016104.

Kumar, R., Misra, A. (2007), Some basic aspects of electromagnetic radiation emission during plastic deformation and crack propagation in Cu-Zn alloys, *Materials Sci. Eng. A*, 454, 203-210.

Lockner, D., Byerlee, J., Kuksenko, V., Ponomarev, A., and Sidorin, A. (1991), Quasi-static fault growth and shear fracture energy in granite, *Nature*, 350, 39-42.

Main, I., and Naylor, M. (2012), Extreme events and predictability of catastrophic failure in composite materials and in the earth, *Eur. Phys. J. Special Topics*, 205, 183-197, doi:10.1140/epjst/e2012-01570-x.

Matsumoto, H., Ikeya, M., and Yamanaka, C. (1998), Analysis of barberpole color and speckle noises recorded 6 and half hours before the Kobe earthquake, *Jpn. J. App. Phys*., 37, 1409–1411.

Potirakis, S. M., Minadakis, G., Eftaxias, K. (2012), Relation between seismicity and pre-earthquake electromagnetic emissions in terms of energy, information and entropy content, *Nat. Hazards Earth Syst. Sci.*, 12, 1179-1183, doi:10.5194/nhess-12-1179-2012.

Potirakis, S.M., Karadimitrakis, A., Eftaxias, K. (2013), Natural time analysis of critical phenomena: the case of pre-fracture electromagnetic emissions, *Chaos* 23 (2), 023117, doi: 10.1063/1.4807908.

Potirakis, S. M., Contoyiannis, Y., Eftaxias, K., Koulouras, G., and Nomicos, C. (2015), Recent field observations indicating an Earth system in critical condition before the occurrence of a significant earthquake, *IEEE Geosc. Remote Sens. Lett.*, 12(3), 631-635, doi: 10.1109/LGRS.2014.2354374.

Qian, S., Yian, J., Cao, H., Shi, S., Lu, Z., Li, J., Ren, K. (1994), Results of the observations on seismo-electromagnetic waves at two earthquake areas in China, in: *Electromagnetic Phenomena related to Earthquake prediction*, Hayakawa, M., and Fujinawa, Y., (Eds), Tokyo, Japan, Terrapub, 205-211.

Shimamoto, T., Togo, T. (2012), Earthquakes in the Lab, *Science*, 338 (6103), 54-55, doi: 10.1126/science.1227085.

Uyeda, S., Nagao, T., Kamogawa, M. (2009), Short-term earthquake prediction: Current status of seismo-electromagnetics, *Tectonophysics*, 470(3-4), 205-213.

Warwick, J. W., Stoker, C., and Meyer, T. R. (1982), Radio emission associated with rock fracture: Possible application to the great Chilean earthquake of May 22 1960, *J. Geophys. Res.*, 87(B4), 2851-2859.

SEISMO-IONOSPHERIC PRECURSORS OF STRONG EARTHQUAKES: ANALYSIS OF TOTAL ELECTRON CONTENT OBSERVATIONS

Yu.V.Romanovskaya[1], A.A. Namgaladze[1]

[1]Murmansk State Technical University, Murmansk, 183010, Russia, e-mail: romanovskayayuv@mstu.edu.ru, y-romanovskaya@yandex.ru

Abstract. We continue investigating Global Positioning System (GPS) observations of Total Electron Content (TEC) of ionosphere in order to reveal TEC anomalies which can be consider as earthquakes precursors. We have analyzed regional maps of TEC relative disturbances calculated for eight days before each strong seismic event of the years 2005–2006 with a magnitude not less than 6 and a hypocenter depth up to 80 km. On the hypothesis of the electromagnetic mechanism of the pre-earthquakes TEC anomalies formation, TEC positive (or negative) disturbance regions have to satisfy the following main criteria to be accepted as precursors. They are: (1) relative TEC disturbance regions appear near the epicenter and/or in the magnetically conjugated point; (2) such regions exist mainly during the night-time hours; (3) lifetime of such anomalies is 6 hours at least. We have selected 43 seismic events (27 for year 2005 and 16 for year 2006) with required values of a magnitude and a hypocenter depth. Analysis of TEC disturbance maps shows anomalies which can be characterized as precursors revealing before 32 events out of 43 selected earthquakes.

Introduction

Numerous ground and satellite observations reveal ionospheric disturbances over the near epicenter areas during the periods of the strong earthquakes preparation. Nowadays NASA provides the global Total Electron Content (TEC) measurements. The data allow investigating not only the ionospheric TEC variations behavior over the near epicenter areas but also globally. The Global Positioning System (GPS) TEC data analysis showed that during 1-15 days before earthquakes anomalous TEC variations are observed over the near epicenter area and/or at the magnetically conjugated point [Zakharenkova et al., 2007; Lin, 2011 and others].

The vertical electromagnetic F2-layer plasma [**E**×**B**] drift induced by a seismogenic electric field was proposed as the most probable physical mechanism of such anomalies formation [Namgaladze et al., 2007]. The hypotheses was later verified by results of numerical experiments using the global first-principle Upper Atmosphere Model [Karpov et al., 2012; Zolotov et al., 2012; Karpov et al., 2013; Namgaladze et al., 2013].

In order to detect earthquakes precursors we analyzed the TEC disturbances derived from GPS data before strong seismic events of 2005-2006. The investigation was aimed at the formulation of distinct and deterministic criteria for identification of anomalous TEC variations as ionospheric earthquakes precursors. The present paper continues the study described in [Namgaladze et al., 2012; Romanovskaya et al., 2012; Romanovskaya and Namgaladze, 2014].

Method

The TEC data used in this investigation were downloaded from the NASA website (ftp://cddis.gsfc.nasa.gov/pub/gps/products/ionex). This website contains the directory with global ionospheric TEC maps with the spatial resolution of 5 degrees for longitude and 2.5 degrees for latitude and the time interval equal to 2 hours. For each time interval of each day we have calculated the maps of relative (%) TEC deviations over the undisturbed background variations. As background values for the investigated LT moment we apply moving 7-days average TEC data.

Using such maps we investigate TEC disturbances before the earthquakes of 2005-2006 that are of M=6 by magnitude, D≤80 km by hypocenter depth and <50 degrees by the epicenter geomagnetic latitude. We have selected 43 seismic events (27 for year 2005 and 16 for year 2006) with required values of a magnitude and a hypocenter depth. The most part of events belongs to the Oceania region and the Japan Islands region. We have analyzed the TEC disturbances maps calculated for 1-8 days before earthquakes.

Discussion

According to the hypothesis of the electromagnetic mechanism of the pre-earthquakes TEC anomalies formation, to be accepted as precursors positive or negative TEC disturbances areas have to satisfy the following criteria:

(1) relative TEC disturbance areas appear over the near epicenter regions and/or the magnetically conjugated ones;

(2) such TEC anomalies exist mainly during the night-time hours in the conditions of solar radiation deficiency;

(3) their lifetime is of 6 hours at least.

In our investigation20 earthquakes among 27 selected events of the year 2005 were forestalled by TEC anomalies which could be characterized as precursors. The amplitude of TEC disturbances did not exceed 30% over the background level for 5 cases. Among the considered16 strong earthquakes of the year 200612 events have TEC precursors.

Usually TEC precursors are the positive TEC disturbances areas over the near epicenter regions and at the magnetically conjugated point. They exist for more than 6 hours after evening terminator coming. If the epicenter is located near the magnetic equator we can see only one disturbed TEC area- over the equator. The TEC anomalies areas are aligned with geomagnetic parallels of the epicenter and the magnetically conjugated point. Usually earthquake precursor areas extend for 30 degrees in longitude and for 10-15 degrees in latitude.

There are some examples of TEC disturbances dominated in one hemisphere over the near epicenter region or magnetically conjugated one. Probably such asymmetry is related to seasons because positive TEC disturbances are detected just in the winter hemisphere where electron density values are lower.

The main feature of variations related to the geomagnetic activity is their moving from high to low latitudes. In contrast to them the TEC precursor areas caused by electromagnetic plasma drift induced by a seismogenic electric field are practically static.

Figure 1 presents TEC relative deviations (%) from the quiet background variations 2 days before Indonesia, May19, 2005, M6.9 earthquake. The earthquake epicenter position is marked by the star; the magnetically conjugated point is marked by the diamond. Orange circle shows the position of the subsolar point. Black curve is the terminator line. LT labels (above the panels) correspond to the earthquake epicenter position. As typical examples of the TEC precursors we consider the positive TEC disturbances areas which can be seen in Figure 1 after evening terminator coming.

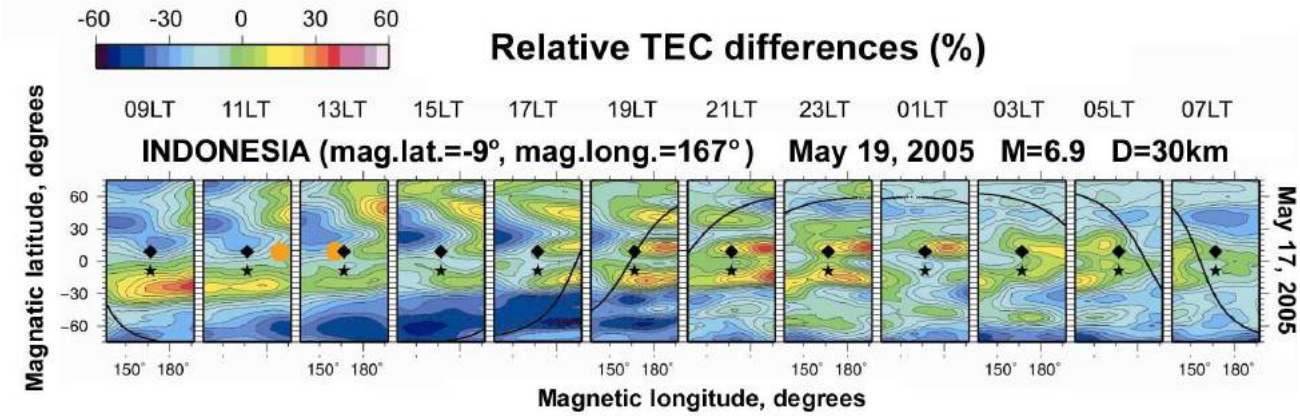

Figure 1. TEC relative deviations (%) from the quiet background variations 2 days before Indonesia, May 19, 2005, M6.9 earthquake. Co-ordinates are magnetic latitude and magnetic longitude.

Conclusion

The analysis of TEC relative deviations maps has shown that TEC disturbances are revealed before 32 events out of 43 selected earthquakes of the years 2005-2006. Additionally to the mentioned criteria the TEC precursors areas have the following features:

1) they are aligned with the geomagnetic latitudes of the near epicenter region and the magnetically conjugated point and extend for 30 degrees in longitude and for 10-15 degrees in latitude;

2) they do not move noticeably in comparison with ionospheric disturbances related to the geomagnetic activity.

Acknowledgments. The author (A.N.) acknowledges International Space Science Institute, Bern, Switzerland for the partial support, project 298 "Multi-instrument Space-Borne Observations and Validation of the Physical Model of the Lithosphere-Atmosphere-Ionosphere-Magnetosphere Coupling". The authors are grateful to Boris E. Prokhorov (Helmholtz Centre Potsdam, GFZ German Research Centre for Geosciences; University Potsdam, Applied Mathematics) for the help in GIM TEC maps processing.

References

Karpov, M.I., O.V. Zolotov, and A.A. Namgaladze (2012), Modeling of the ionosphere response on the earthquake preparation. *Proceedings of the MSTU*, 15(2), 471-476.

Karpov, M.I., A.A. Namgaladze, and O.V. Zolotov (2013), Modeling of Total Electron Content Disturbances Caused by Electric Currents between the Earth and the Ionosphere. *Russian Journal of Physical Chemistry*, 7(5), 594–598.

Lin, J. (2011), Ionospheric total electron content anomalies due to Typhoon Nakri on 29 May 2008: A nonlinear principal component analysis. *Computers & Geosciences*, doi:10.1016/j.cageo.2011.12.007.

Namgaladze, A.A., I.I. Shagimuratov, I.E. Zakharenkova, O.V. Zolotov, and O.V. Martynenko (2007), Possible mechanism of the TEC enhancements observed before earthquakes. *XXIV IUGG General Assembly*, Perugia, Italy, 02-13 July, 2007.

Namgaladze, A.A., O.V. Zolotov, and B.E. Prokhorov (2013), Numerical simulation of the variations in the total electron content of the ionosphere observed before the Haiti earthquake of January 12, 2010. *Geomagnetism and Aeronomy*, 53(4), 522-528.

Namgaladze, A.A., O.V. Zolotov, M.I. Karpov, and Yu.V. Romanovskaya (2012), Manifestations of the Earthquake Preparations in the Ionosphere Total Electron Content Variations. *Natural Science*, 04 (11), 848–855.

Romanovskaya, Yu.V., and A.A. Namgaladze (2014), Ionospheric earthquake precursors: Analysis of total electron content measurements before strong seismic events of the year 2005. *Proceedings of the MSTU*, 17(2), 403-410.

Romanovskaya, Yu.V., A.A. Namgaladze, O.V. Zolotov, N.A. Starikova, and V.Z. Lopatiy (2012), Searching for seismo-ionospheric earthquakes precursors: Total electron content disturbances before 2005-2006 seismic events. *Proceedings of the MSTU*, 15(2), 477-481.

Zakharenkova, I.E., I.I. Shagimuratov, A. Krankowski , and A.F. Lagovsky (2007), Precursory phenomena observed in the total electron content measur ements before great Hokkaido earthquake of September 25, 2003 (M=8.3). *Studia Geophysica et Geodaetica*, 51(2), 267-278.

Zolotov, O.V., A.A. Namgaladze, I.E. Zakharenkova, O.V. Martynenko, and I.I. Shagimuratov (2012), Physical interpretation and mathematical simulation of ionospheric precursors of earthquakes at midlatitudes. *Geomagnetism and Aeronomy*, 52(3), 390-397.

INVERSION OF RELATIVE CHANGES IN MAGNETIC RATIO INTO RELATIVE CHANGES IN THE RESISTIVITIES OF THE ELEMENTS OF A GEOELECTRICAL STRUCTURE (NUMERICAL MODELING)

M.E. Sholpo

St. Petersburg Filial of IZMIRAN, St. Petersburg, 199034, Russia, e-mail: msholpo@mail.ru

Abstract. Sensitivity of the magnetic ratio *h* (ratio of the vertical component of the geomagnetic field to its horizontal component) to changes in resistivity of *i*th element of the 2D geoelectric structure and its temporal and spatial dependences studied. Necessity of similar researches for definition of an effective regime of monitoring of *h* as prognostic parameter is shown. The formula connecting relative changes of *h* with relative changes in the resistivities of elements of geoelectric structure ρ_i is built. On the basis of this formula the method of inversion of relative changes in the magnetic ratio into relative changes in resistivities of structure elements can be developed.

Monitoring the electromagnetic precursors is part of complex prognostic measurements conducted in many geodynamical testing sites in the world. However, the efficiency of the monitoring is controlled by many factors, which were considered in the previous publications (Sholpo, 2006, 2010, 2013). In particular, it was shown that, in order to efficiently apply the magnetotelluric monitoring for prognostic purposes, it is necessary, besides adequately choosing the optimal regime of observations, to have a means for separating the source that generates the seismoelectric effect of the first kind from the other factors that can cause variations in the observed parameter. With this aim in view, the method was developed for inversion of relative variations in the apparent resistivities into the relative variations in the electrical resistivities ρ_i of the elements of the geoelectrical medium. (*i* is number of the element, which coincide with value of their lectrical resistivity in Ω m.) This method allows the researcher to focus on the variations in the electrical resistivity of the particular geoelectric element that is of interest for the particular study. During the work on geodynamic research area is often more convenient and more economic to perform measurements not a electric component, but a vertical magnetic component of a goelectromagnetic field and to observe changes of the values of the magnetic relation – the relations vertical components of a magnetic field to horizontal $h = H_z/H_{hor}$. From there is a question, whether it is impossible to carry out the inversion of changes in the magnetic relation into the changes in the resistivities of the elements of the geoelectric structure which caused them. In this regard researches of sensitivity of *h* to changes in ρ_i for south-western part of the Kamchatka geodynamic research area (in the simplified option – fig 1) were conducted. The used model represents horizontally layered medium which contains three highly conducting inclusions: surface with the resistivity ρ_{30} and two crustal with resistivities ρ_8 and ρ_{10}. The sensitivity of the magnetic relation to the variations in the electrical resistivity of the *i*th element of the geoelectrical model is the logarithmic derivative of *h* on ρ_i: $\varepsilon_i = - d \lg h / d \lg \rho_i$.

Fig.1a

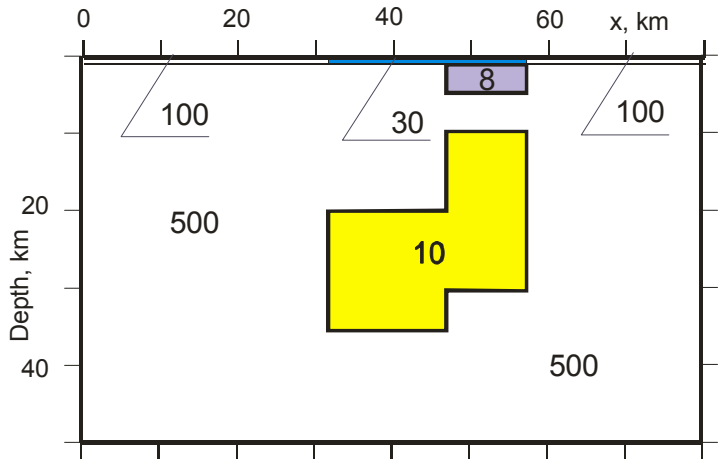

Fig.1b

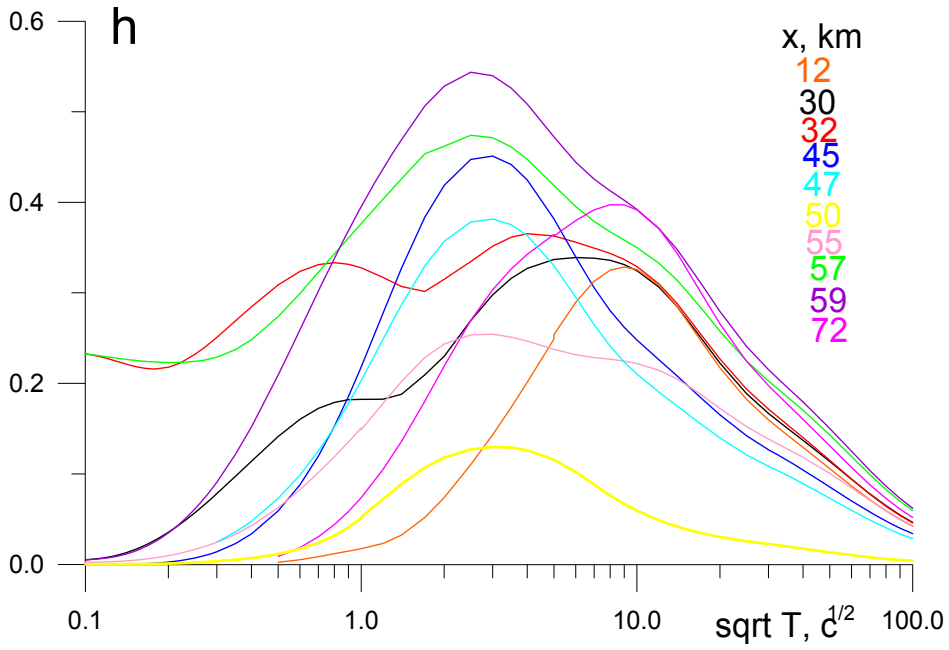

Fig.1c

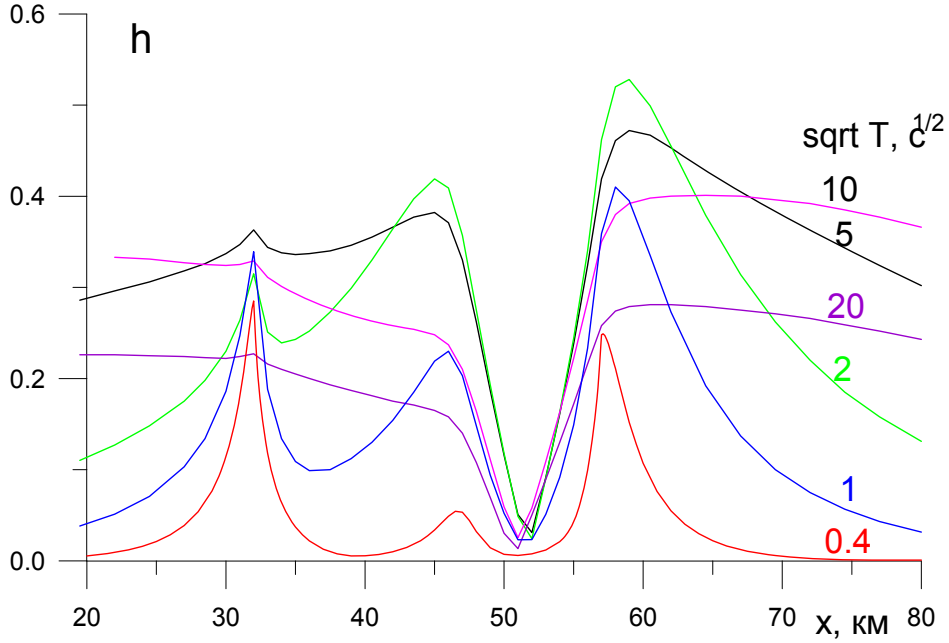

Fig. 1. The (a) simplified option of the south-western part of the Petropavlovsk geodynamic research area. The numerals inside the model denote the electrical resistivities of its elements in Ω m. The (b) temporal dependences for $h(\sqrt{T})$ for different x (km) and the (c) spatial dependences $h(x)$ for different $\sqrt{T}$ (shown by the indices of the curves).

The purpose of this research - to show possibility and need (1) of definition the optimum conditions for the effective monitoring of h and (2) of inversion of the variations in h into a variation in ρ_i. For this purpose it is necessary to study the spatial and temporal dependences of both the most magnetic relation, and its sensitivity to changes in the resistivities of elements of geoelectric structure.

In fig. 1b,c temporal and spatial dependences of the magnetic relation h for model of the geoelectric structure represented in fig. 1a are presented. Fig. 2a,b shows similar dependences for sensitivity of h to change in the resistivity ρ_{10} of the structural element with $i = 10 - \varepsilon_{10}$ ($\sqrt{T}$) and ε_{10} (x).

a

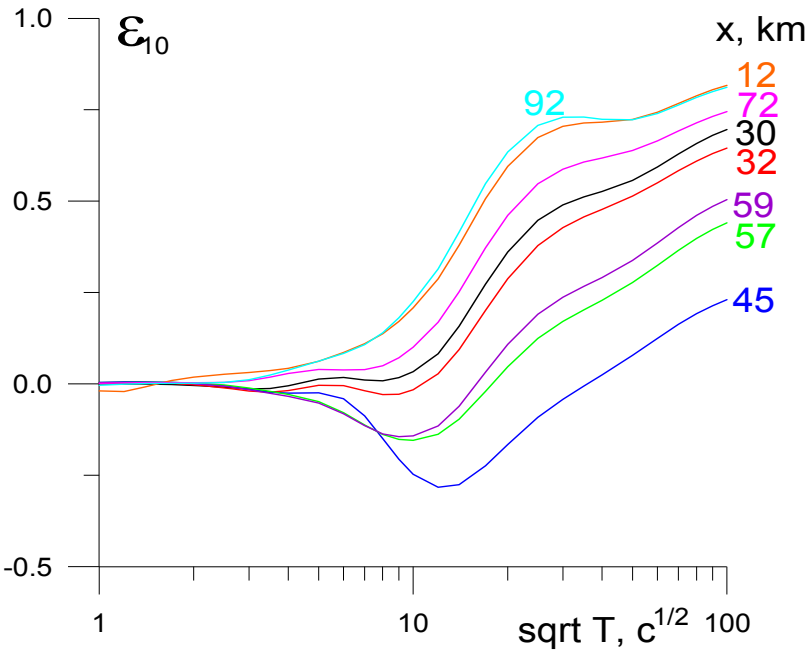

b

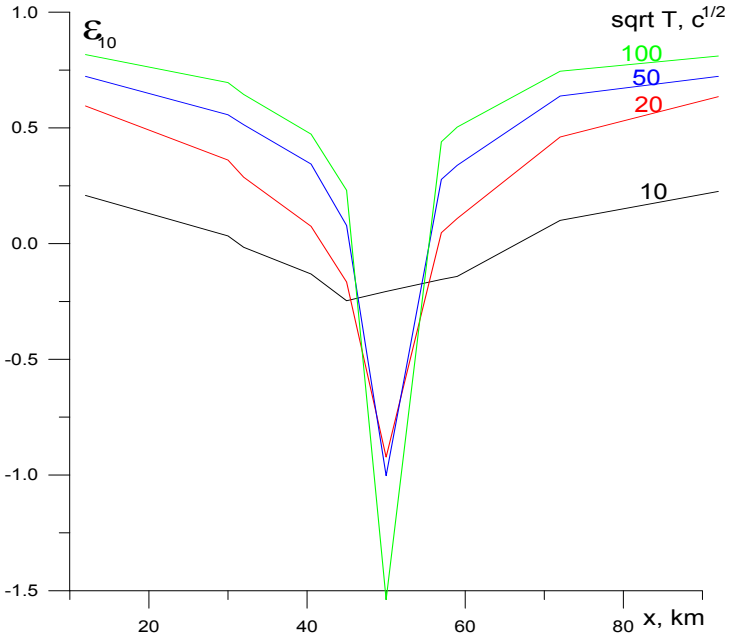

Fig. 2. The (a) temporal dependences for $\varepsilon_{10}(\sqrt{T})$ for different x (km) and the (b) spatial dependences $\varepsilon_{h10}(x)$ for different $\sqrt{T}$ (shown by the indices of the curves).

The analysis of the figures shows that areas of the maximum values of functions h (x, T) and ε(x, T) don't coincide. So for example, maxima of curves of h ($\sqrt{T}$) for different points of a profile settle down in the range of $2 < \sqrt{T} < 10$, and function ε_{10} ($\sqrt{T}$) reaches the maximum values at $\sqrt{T} > 100$. Similarly spatial dependences of sizes h and ε correspond. Maxima of h (x) are dated for edges of the conductive blocks, and its sensitivity to variations in ρ_{10} increases in process of removal from them. It is clear, that for definition of optimum conditions of monitoring ρ_{10} it is necessary to consider these facts. And we should be satisfied not with the maximum values of functions h (x, T) and ε (x, T), but with their acceptable sizes, taking into account opportunities of our measuring equipment. Let's say that the size h = 0.1, minimum possible for measurement, and the satisfactory size ε is 0.2 (At such value ε 60% change ρ_{10} will cause a 10% response in

h). Then for monitoring ρ_{10} accepted will be, apparently, following conditions. First of all for all points of a profile should exclude the range of T < 100 as at such T the changes in ρ_{10} practically don't cause a response in *h* (fig. 2*a*). Range of the periods where *h* reaches the sizes accepted for measurements, doesn't exceed $\sqrt{T} \geq 60$. Besides, it is impossible to make observations ρ_{10} in central area of a profile: 50-5 < *x* (km) < 50+5, in view of a trifle as ε_{10}, and *h* (fig. 2*b*, 1*c*). For other points of a profile reliable is a range $10 < \sqrt{T} < 40$ which for remote points (for example, *x* =12 or 72 km) extends to T=60 (fig. 1*b*).

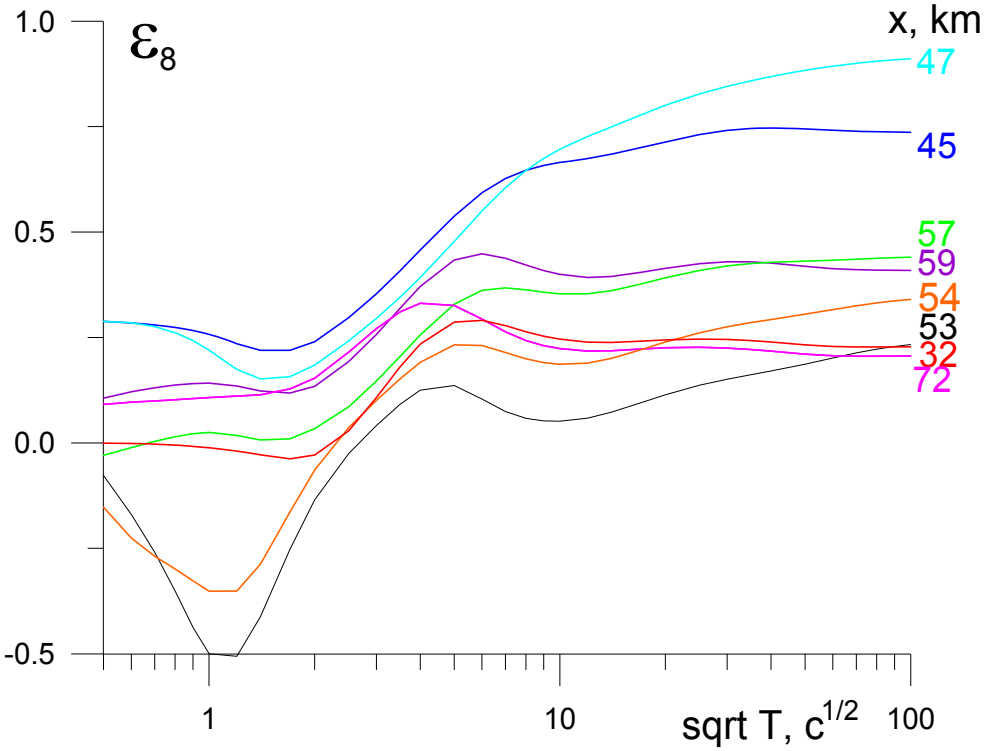

Fig.3. Dependences $\varepsilon_8(\sqrt{T})$ for different *x* (km) (shown by the indices of the curves).

The element with *i* = 8 is located at 47 < *x* (km) < 57. Its depth makes from 1 to 5 km, and the resistivity ρ_8 = 8 Ω m. Fig. 3 shows the temporal dependences for sensitivity of *h* to changes in the resistivity ρ_8 - $\varepsilon_8(\sqrt{T})$ - for a number of characteristic points. Analyzing behavior of functions $\varepsilon_8(x, \sqrt{T})$ and $h(x, \sqrt{T})$ (fig. 1b, c) we come to a conclusion that optimum conditions for the ρ_8 monitoring are: the profile site near the projection of the left edge of this element x ≈ 45 - 47 km and the periods interval 0.5 c < T < 1600 c ($0.7 < \sqrt{T} < 40$). In the range of 16 c < T < 5000 c ($4 < \sqrt{T} < 70$) also the area corresponding to other edge of the conductive inclusion x ≈ 57 - 59 km is acceptable, but here function $\varepsilon_8(x, \sqrt{T})$ has considerably smaller values, that is the *h* response to variations in ρ_8 is less that is connected with the influence of the element with *i* = 10.

The surface element i = 30 stretches from h=32 km to h=57km. Its thickness is 1 km, and resistivity ρ_{30} = 30 Ω m. As shows fig. 4 the *h* response to the change in the resistivity of this element can be very essential. For example, in a point *x* = 30 km in the range of the periods from T ≈ 0.5 s to T ≈ 2.2 s $\varepsilon_{30} > 1$, that is in this point the relative changes in *h* surpass the relative changes in ρ_{30} which caused them. The maximum values of functions as $h(x)$, and $\varepsilon_{30}(x)$ are dated for edges of the conductive inclusion. Coordinates of maxima of functions $\varepsilon_{30}(\sqrt{T})$ and $h(\sqrt{T})$, on the contrary, strongly differ. So in the point *x* = 30 km the function $h(\sqrt{T})$ maximum is at $\sqrt{T} = 6$, thus $\varepsilon_{30} = 0.12$. The maximum of $\varepsilon_{30}(\sqrt{T})$ is in this point at $\sqrt{T} \approx 1.1$, and the value *h* = 0.19. In the point *x* = 32 km the maximum of $\varepsilon_{30}(\sqrt{T}) = 1.1$ is located at $\sqrt{T} = 1.3$, thus the size *h* = 0.32. At other edge of the *i* = 30 element in points *x* = 57, 59 km it is possible to observe the greatest values of *h* = 0.46 and *h* = 0.54 respectively, but here the values ε_{30} less than 0.2. At the same time in the point *x* = 59 km the coordinate of the maximum $\varepsilon_{30}(\sqrt{T})$ corresponds to *h* ≈ 0. However, in the point *x* = 57 km supervision of the changes in *h* are possible as in the range of $0.1 < \sqrt{T} < 1$ its size accepts values from 0.2 to 0.4 thus that its sensitivity to variations in ρ_{30}: $0.2 < \varepsilon_{30} < 0.8$. As a result of similar comparisons, and

also simple calculations for a formula $h_2/h_1 = (\rho_{i1}/\rho_{i2})^{\varepsilon^i}$ we come to the conclusion that optimum conditions for the monitoring ρ_{30} are the points near the left edge of the surface element on the T < 40 s. Less favorable conditions for monitoring at its opposite edge have a talk proximity of other well conductive elements, in particular not deeply lying element with number 8.

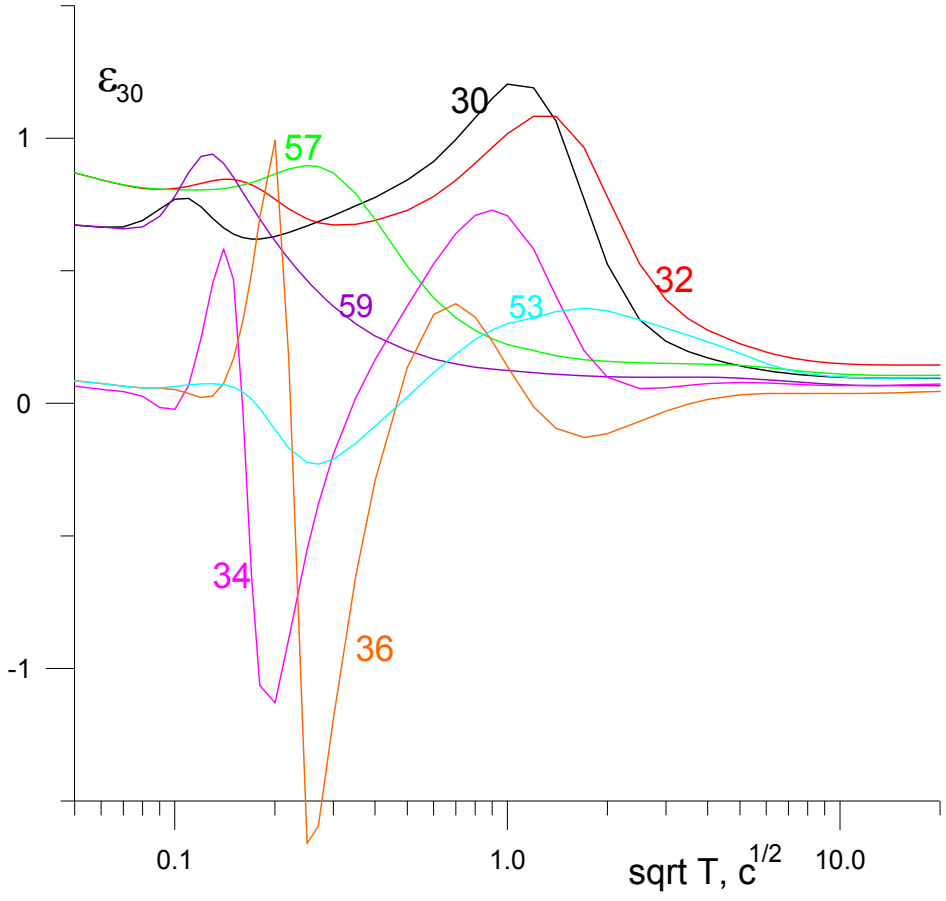

Fig.4. Dependences $\varepsilon_{30}(\sqrt{T})$ for different *x* (km) (shown by the indices of the curves).

The formula connecting relative changes of *h* with relative changes in the resistivities of elements of geoelectric structure ρ_i (similar to the offered earlier for MT apparent resistivity) is built:

$$h_{j2}/h_{j1} \approx \prod_i (\rho_{i1}/\rho_{i2})^{\varepsilon_{ijav}}. \qquad (1)$$

Here, indices 1 and 2 mark the boundaries of the intervals of variations in ρ_i and the changes induced in *h* by these variations; ε_{ijav} is the average in this interval sensitivity of *h* to the variations in ρ_i at the *j*th period.

Research of accuracy of this formula led to the results shown by table 1. Relative change of *h* was calculated in two ways: using the program of calculation of electromagnetic fields over models of two-dimensional structures - $(h_2/h_1)_M$ and on the formula (1) – $(h_2/h_1)_F$. To the index 1 there corresponds the set of values of the resistivities of structure elements: ρ_{30} = 35 Ω m, ρ_8 = 6 Ω m, ρ_{10} = 12 Ω m. To the index 2: ρ_{30} = 25 Ω m, ρ_8 = 10 Ω m, ρ_{10} = 8 Ω m. Calculations are executed for three characteristic points of a profile *x* = 32, 45, 59 km and a number of √T values in the investigated interval of the periods. As show size δ % - a relative error of the values $(h_2/h_1)_F$ - the formula (1) is carried out with high precision. Therefore, the error of recalculation of the observed values h_2/h_1 в ρ_{i1}/ρ_{i2} will be defined by the accuracy of measurements a

component of a geomagnetic field and reliability of geoelectrical model of the geodynamical testing site for which calculations of function $\varepsilon_i(\sqrt{T}, x)$ have to be made.

Table 1. Research of accuracy of the formula (1).

$(\rho_2/\rho_1)_{30}$ =.714 $(\rho_2/\rho_1)_8$ = 1.667 $(\rho_2/\rho_1)_{10}$ = .667						
$\sqrt{T}$, $c^{1/2}$	ε_{30}	ε_8	ε_{10}	$(h_1/ h_2)_F$	$(h_1/ h_2)_M$	δ%
x = 32, km						
0.5	0.728	- 0.00043	0.	0.7824	0.7815	0.1
1.	1.018	- 0.0119	- 0.00117	0.7054	0.7073	0.3
5.	.224	0.285	- 0.00419	1.0749	1.0724	0.2
10.	.150	0.245	- 0.0163	1.0845	1.0891	0.4
50.	.138	0.231	0.514	0.8723	0.8782	0.7
100.	.130	0.226	0.645	0.8272	0.8314	0.6
x = 45 km						
0.5	- 1.280	0.288	0.00020	1.785	1.799	1.0
1.	- 1.007	0.257	0.0040	1.437	1.431	0.5
5.	- 0.0757	0.536	- 0.0246	1.362	1.355	0.5
10.	- 0.0382	0.662	- 0.247	1.570	1.560	0.6
50.	- 0.0114	0.739	0.0779	1.419	1.417	0.2
100.	- 0.00430	0.731	0.230	1.326	1.324	0.1
x = 59 km						
0.5	0.1987	0.1058	0.00026	0.987	0.995	1.
1.	0.1239	0.1415	0.00288	1.030	1.026	0.1
5.	0.0947	0.4329	- 0.05271	1.235	1.227	0.6
10.	0.0701	0.3978	- 0.1424	1.268	1.267	0.1
50.	0.0615	0.4156	0.3377	1.057	1.061	0.4
100.	0.0581	0.4060	0.5041	0.984	0.989	0.4

Our analysis suggests the following conclusions. If the structure of the geodynamical testing site is studied so well that it is possible to construct its geoelectric model, to calculate (with the aid of numerical modeling) the sensitivity of the magnetic ratio *h* to the changes in resistivities of the elements of this structure and to define the optimum conditions for the *h* monitoring, then the observed variations in the *h* can be promptly inverted into relative variations in resistivities of these structural elements; i.e. it is possible to monitor directly variations in the resistivity of rocks, which are a more effective prognostic indicator compared to variations in *h*. Without having sufficient data of a geoelectric structure of the area of researches, it is impossible to interpret behavior of the magnetic relation correctly.

References

Sholpo M.E. (2006), Monitoring of relative changes in the electrical conductivity of rocks from observations of the magnetotelluric apparent resistivity (Numerical modeling), *Izvestiya, Physics of the Solid Earth*, 42, 4, 323–329.

Sholpo M.E. (2010), Inversion of relative changes in the magnetotelluric apparent resistivity into the relative changes in the resistivity of the elements of a geoelectric structure, *Izvestiya, Physics of the Solid Earth*, 46, 9, 780–787.

Sholpo M.E. (2013), Sensitivity of transversal apparent resistivity to the variations in electrical resistivities of the elements of a 2D geoelectrical structure, *Izvestiya, Physics of the Solid Earth*, 46, 9, 113–119.

SELF-ORGANIZED CRITICAL (SOC) DYNAMICS OF THE FAULT SYSTEMS: SOC-BASED MODELING OF SEISMIC-ELECTROMAGNETIC PROCESSES

N.A. Smirnova[1], V.M. Uritsky[2], M. Hayakawa[3]

[1]St. Petersburg University, St. Petersburg, 198504, Russia, e-mail: nsmir@geo.phys.spbu.ru;
[2]CUA at NASA Goddard Space Flight Center, Greenbelt, USA
[3]Institute of Seismo Electromagnetics, UEC Incubation Center, Chofu Tokyo, Japan

Abstract. In our previous presentations at the "Geocosmos 2010 and 2012" conferences, fractal and multifractal properties of geophysical fields related to earthquakes were considered and analyzed both in space and time domains. Since one of the most reasonable mechanisms underlying fractal properties of geophysical parameters in spatiotemporal domains is self-organized critical (SOC) dynamics of the source system, it is essential to develop the SOC modeling of the earthquake processes. Here we describe the basis SOC model, which is the BTW (Bak, Tang, and Wiesenfeld) "sandpile", and introduce the novel approach to SOC dynamics based on the so-called HP (Hughes and Paczuski) model. We advance the HP model with particular application to seismic-electromagnetic processes. We show that only non-Abelian SOC approach is able to explain the critical spatiotemporal dynamics of fractal tectonic systems exhibiting power-law earthquake statistics. Using a definite rule of the conductivity distribution upon a two-dimensional matrix, we calculate both the bulk and the percolation conductivities and demonstrate conformity between the fluctuations of conductivity obtained in our model and the real-observed preseismic ULF emissions. That proves the adequacy of the developing SOC model.

1. Introduction

It is now recognized that seismic activity exhibit properties of a spatiotemporal fractal, which is executed in the power-law distribution of the earthquake characteristics. Among such patterns we can indicate the following findings: the power-law distribution of earthquake magnitudes (Gutenberg-Richter statistics), fractal clustering of seismic hypocenters in space, temporal clustering of the earthquake onset times, power-law decay of aftershock activity (the Omori law), fractal matrix of faults etc (see Smirnova et al., 2005 and references therein). Also in our previous presentations at the "Geocosmos 2010 and 2012" conferences (Smirnova et al., 2010, 2012), fractal and multifractal properties of geophysical fields related to earthquakes were considered and analyzed both in space and time domains. Since one of the most reasonable mechanisms underlying fractal properties of geophysical parameters in spatiotemporal domains is self-organized critical (SOC) dynamics of the source system, it is essential to develop the SOC modeling of the earthquake processes. The first consideration of the SOC dynamics attributed to the systems with spatial degrees of freedom is contained in the seminal papers by Bak, Tang, and Wiesenfeld, 1987, 1988 (the BTW model),. The authors have introduced the concept of SOC (Self-Organized Criticality) providing a universal framework for studying scale-invariant spatiotemporal fluctuations in complex disordered systems.

In the "canonical" SP (sandpile) BTW model, a square grid of n boxes is considered, as it is shown in Fig.1. A particle is randomly added to one of the boxes. Each box on the grid is assigned a number, and a random- number generator is used to determine the box to which a particle is added. When a box has zc=4 particles it goes unstable and the four particles are redistributed to the four adjacent boxes (see Fig.1b). Redistribution from edge boxes results in loosing of one particle from the grid. Redistribution from the corner boxes leads to the dissipation of two particles. If after a redistribution of particles from an unstable box any of the adjacent boxes accumulates four or more particles, it is also considered unstable, and one or more further redistributions are carried out. Multiple events can occur on large grids (see Fig.1c).

The SOC theory is widely used for investigation of the dynamics of natural hazard systems, including the hazard system of earthquakes. Here we introduce the novel approach to SOC dynamics based on the so-called HP (Hughes and Paczuski) model. And we'll advance the HP model with particular application to seismic-electromagnetic processes.

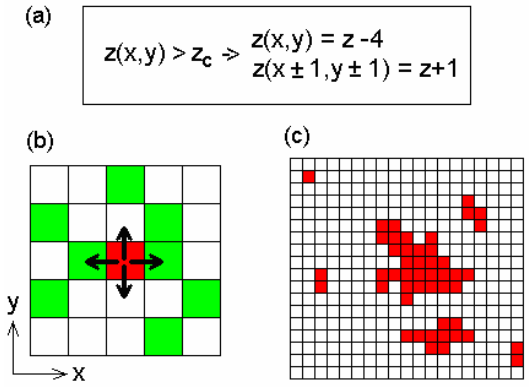

Fig. 1. Sketch of the BTW sandpile (a) Redistribution rule of the model (1); (b) Active element (shown in red) interacting with its four nearest neighbors. The green elements are sub-critical and will become unstable after the interaction; (c) Examples of scale-free avalanches (connected regions of unstable elements).

2. The HP SOC model by Hughes and Paczuski

The considered BTW SP model is able to explain some signatures of the scale-free dynamics of tectonic systems: the Gutenberg-Richter statistics, the Omori law etc. But this model is unable to explain fractal clustering of earthquake hypocenters and their relation to the evolution of fault systems, which seem to play an important part in real seismic systems. The first SOC model that successfully incorporated scale-free avalanche activity with a fault matrix dynamics has been proposed by Hughes and Paczuski, 2002 (HP model). Here we consider the SOC model based on a 2-dimensional HP sandpile algorithm. A sketch in Fig.2 gives its illustration. The HP model is defined on a two-dimensional rhombic grid. Each grid site is prescribed the integer-valued coordinates $x=0...Nx$-1 and $y=0...Ny$-1, as well as the state variable $z(x,y)$ arbitrarily called energy. The amount of energy stored in a given element determines its ability to interact with other elements. When at any site the variable z exceeds constant instability threshold ($z > zc$) it "topples" transferring certain amount of its energy to downstream neighbors in accordance with the interaction rules:

$$\begin{aligned} z_{t+1}(x,y) &= z_t(x,y) - dz \\ z_{t+1}(x+1,y+1) &= z_t(x+1,y+1) + p\,dz \\ z_{t+1}(x,y+1) &= z_t(x,y+1) + (1-p)\,dz \end{aligned} \qquad (2)$$

Here p is a random variable distributed uniformly within the interval 0…1, and dz is the parameter controlling the Abelian property of the model: $dz = d = 2$ - *Abelian;* $dz = z_t$ - *non-Abelian* (see section 3).

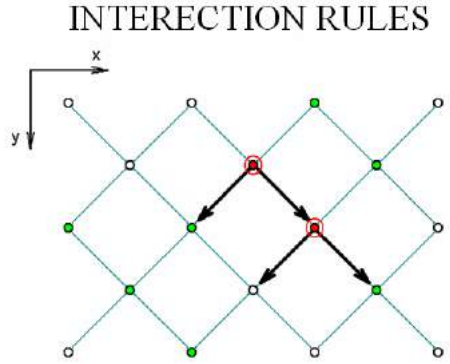

Fig. 2. A sketch illustrating the interaction rules in 2-D HP sandpile model. Active grid sites ($z > z_c$) marked with large open red circles interact with downstream nearest neighbors which can produce further activity provided their energy before the interaction exceeds the level z_c - dz (green circles).

After receiving a portion of energy from the excited element, one or two of its downstream nearest neighbors can also go unstable producing a growing avalanche of activity that propagates along the y direction. The avalanche stops when its front reaches "cold" grid sites whose z values is low enough to absorb the energy from the unstable elements without producing new activity, or when it reaches the open bottom boundary at $y=N_y$-1. The left and right edges of the grid are subject to the periodic boundary condition $z(0,y) \equiv z(N_x\text{-}1,y)$.

The model is driven randomly at y=0 until the condition $z > z_c$ is fulfilled and an instability is initiated in some site. During the subsequent avalanche propagation, the driving is suspended which provides infinite separation between the driving and the avalanche time scales necessary for SOC in sandpile-type models. After a transient period, the model reaches the SOC state at which the probability distributions of avalanches over size s and lifetime t are given by

$$\begin{aligned} p(s) &\sim s^{-\tau_s} f(s/s_c) \\ p(t) &\sim t^{-\tau_t} g(t/t_c) \end{aligned} \qquad (3)$$

where f and g are appropriate scaling functions controlling the cutoff behavior of the distributions; s_c and t_c are finite-size scaling parameters; and τ_s and τ_t are the avalanche scaling exponents.

In general, the scale-free avalanche statistics (3) does not necessarily imply any significant correlations between spatially separated grid sites over time scales exceeding avalanche lifetimes. Most of the known sandpile models do not exhibit any spatial correlations which means that spatial distribution of grid site energy $z(x,y)$ between the avalanches is effectively random. In this context, the HP model presents a new opportunity to study the emergence of nontrivial large-scale structures appearing self-consistently in the SOC state. We consider this HP algorithm as a generalized toy model of nonlinear interactions in the Earth crust in seismic active regions. In particular, one can think of a qualitative analogy with cracking processes:
$z \leftrightarrow$ stress field; "occupied" grid sites with $z > 0 \leftrightarrow$ locally stable state (no cracks); "empty" sites with $z = 0 \leftrightarrow$ developed cracks. An example of generated avalanches in the 2D HP model is shown in Fig.3.

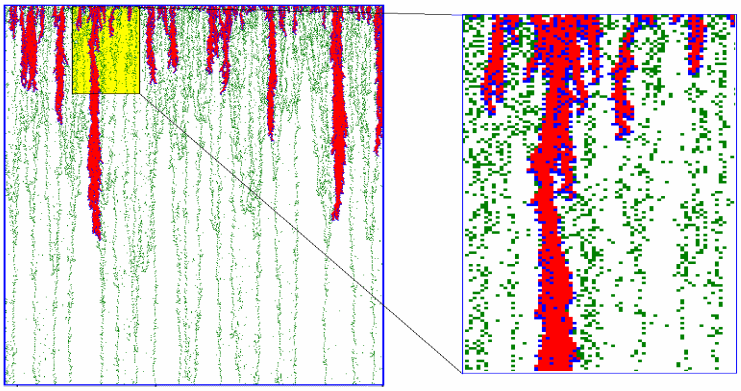

. Generation of sample avalanches
HP model:
anel: sample avalanches in the model
Abelian interaction rules); right panel:
arged portion of the same image.
coding: red – unstable grid sites;
– stable grid sites; blue – nearest
ors of unstable sites.

3. Abelian versus non-Abelian approach

The key parameter in the HP model that controls large-scale correlations in $z(x,y)$ is dz, the fraction of energy involved in local interactions. Keeping the value of dz constant and independent of z makes the sandpile algorithm Abelian and eliminates any spatial structures. On the contrary, setting dz to the current value of energy $z_t(x,y)$ at each point makes the algorithm non-Abelian and, as shown by Hughes and Paczuski, 2002, leads to the emergence of complex spatial patterns.

Fig.4 illustrates topological differences between the behavior of the HP model in the Abelian and non-Abelian regime. As one can see from Fig.4, spatial distribution of energy stored by subcritical grid sites with $z \le z_c$ differs dramatically in these regimes. In the Abelian case, the model has effectively no correlations in space (see Fig. 4 right); in the non-Abelian case, it shows distinct multiscale structures constituting complex branching network of interconnected subcritical elements (Fig. 4 left). However, avalanche size probability

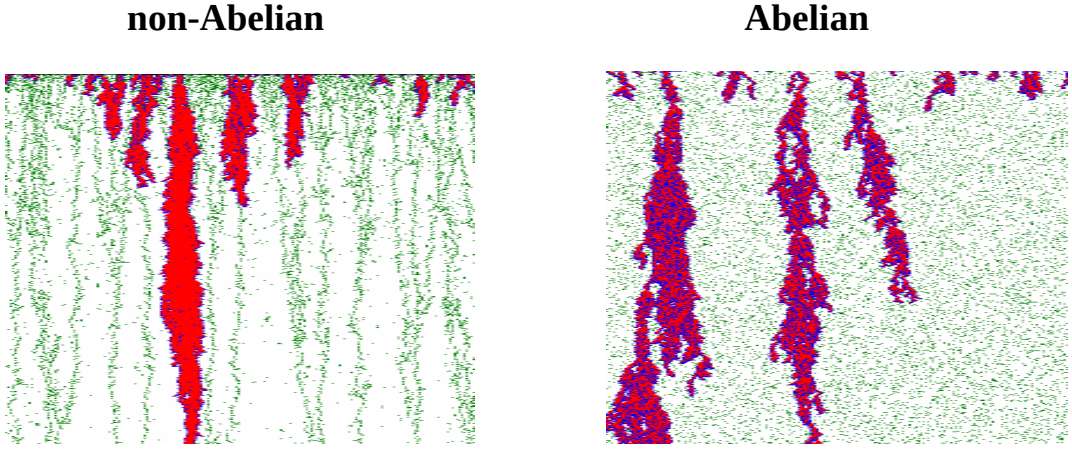

Fig. 4. Enlarged portions of HP model simulation grid showing avalanche traces in Abelian and non-Abelian cases

distributions are nearly identical and follow power-law relations, signaling that the model reaches the SOC state in both regimes, and that the dynamics of excited grid elements on the time scale of individual instability propagation are strongly correlated in both regimes. So the Abelian symmetry does not affect avalanche statistics but does affect their interaction with the background field. In the non-Abelian case, avalanches leave traces of "empty" grid regions with $z = 0$, which leads to the appearance of a large-scale spatial structure of occupied sites (see Fig. 4 left)..

To visualize the emergence of non-trivial large-scale correlations in the non-Abelian PH model, we have evaluated the entropy characterizing spatial disorder of subcritical grid sites as a function of spatial scale. The simulation grid was divided into square boxes of linear size l, for which mean values z of energy were calculated at every time step (i.e. after every avalanche). The degree of disorder (the information capacity) associated with non-uniform energy distribution can then be characterized by the information entropy

$$S(l) = -\int_0^\infty p_l(\bar{z}) \log_2 p_l(\bar{z}) d\bar{z} \quad (bits) \qquad (4)$$

where $p_l(\bar{z})$ is the probability distribution of $\bar{z}$ at the spatial scale l.
The comparison between the scaling of entropy in the discussed regimes is shown in Fig.5. As one can see, S decreases with the box size l much faster in the Abelian case. In the non-Abelian case, the entropy decays considerably slower, so that for large l it exceeds the entropy of the Abelian model by several orders of magnitude revealing the spatial complexity of the non-Abelian SOC regime.

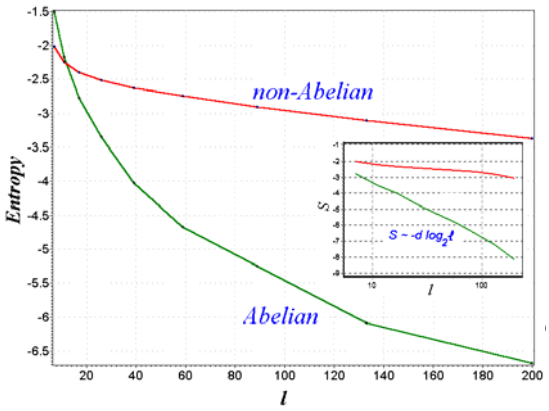

Dependence of the information entropy S on the spatial scale l in Abelian and non-Abelian cases.

4. Modeling the critical dynamics of fractal fault systems

Regional seismicity is known to demonstrate scale invariant properties in different ways. Some typical examples are fractal spatial distributions of hypocenters, Gutenberg-Richter magnitude statistics, fractal clustering of earthquake onset times, power-law decay of aftershock sequences, as well as scale-invariant geometry of fault systems. In some regions, the observed scale-free effects are likely to be connected to a cooperative behavior of interacting tectonic plates and can be described in terms of the SOC concept. Here we have investigated a new SOC model incorporating short-term fractal dynamics of seismic instabilities and slowly evolving matrix of cracks (faults) reflecting long-term history of preceding events. The model is based on a non-Abelian HP sandpile algorithm described above, and it displays a self-organizing fractal network of occupied grid sites similar to the structure of stress fields in seismic active regions. Depending on the geometry of local stress distribution, some places on the model grid have higher probability of major events compared to the others. This dependence makes it possible to consider a time-dependent structure of the background stress field as a sensitive seismic risk indicator. We have also proposed a simple framework for modeling ultra low frequency (ULF) electromagnetic emissions associated with abrupt changes in the large-scale geometry of the stress distribution before characteristic seismic events, and demonstrate numerically how such emissions can be used for predicting catastrophic earthquakes.
Two complementary approaches to modeling pre-seismic stochastic electromagnetic signals based on SOC algorithms have been proposed. Our simulations suggest that both conductivity and electric field fluctuations associated with local propagation of instability fronts can carry information on coupling effects between the

evolution of fractal fault systems and the statistics of major earthquakes, which makes SOC a possible underlying mechanism of the precursory dynamics of ULF electromagnetic emissions.
In the anisotropic SP model presented in section 3, one can associate different energy levels of grid elements with different values of Earth's crust electric conductivity. Let stable ($z = 0$) and subcritical ($0 < z \le z_c$) grid sites represent two different phases (e.g. rocks and liquids filling up cracks in the rocks) having different conductivity. For the sake of simplicity, the conductivity of occupied sites can be set to zero and the conductivity of empty sites can be set to 1. The conductivity of a finite portion of the grid was estimated using one of the following approaches (see Uritsky et al., 2004 for details):

"Bulk" conductivity: $C = \langle \theta(1-z(x,y)) \rangle_{x,y}$ (5)
Percolation conductivity: $C_p = \rho \langle \theta(1-z(x,y)) \rangle^{P}_{x,y}$ (6)

Here $\langle\rangle_{x,y}$ denotes averaging over all x- and y-positions within a chosen spatial domain and $\langle\rangle^{P}_{x,y}$ is averaging over the elements involved in the percolation cluster. Factor ρ equals to 1 or 0 depending on whether or not the percolation through empty grid sites of the studied domain is possible.
The conductivity C is proportional to the concentration of the conducting phase. In addition to that, C_p takes into account effects of connectivity**,** which play an important role in fractal-disordered materials. We have also considered time series of temporal derivatives of the introduced conductivity measures:

$I = dC/dt$; $Ip = dC_p/dt$ (7)

Time evolution of $C(t)$ signals (Fig.6, left) reflects changes in model configuration due to SOC avalanches, and its dynamics is very similar to dynamics of the time series of earthquake energy release. It has been suggested that fluctuations of the percolation conductivity defined above can be used for short-term prediction of the expected range of avalanche sizes, and represent a simple model of fractal precursor of major fault matrix reconfiguration due to strong earthquakes. Time derivatives of conductivity (Fig.6, right) are reminiscent of pre-seismic ULF electromagnetic emissions displaying characteristic clustering of activity spikes before major events (Fig.7, after Koputenko et al. 1994).

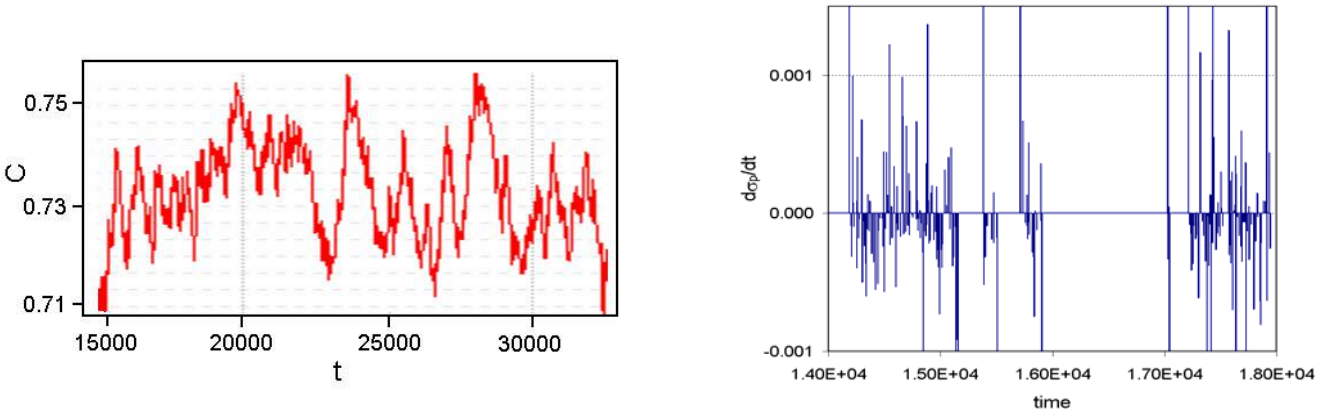

Fig. 6. Examples of fluctuations of conductivity C (5) in the non-Abelian model (left); time evolution of dC_p/dt (7) in the same model (right).

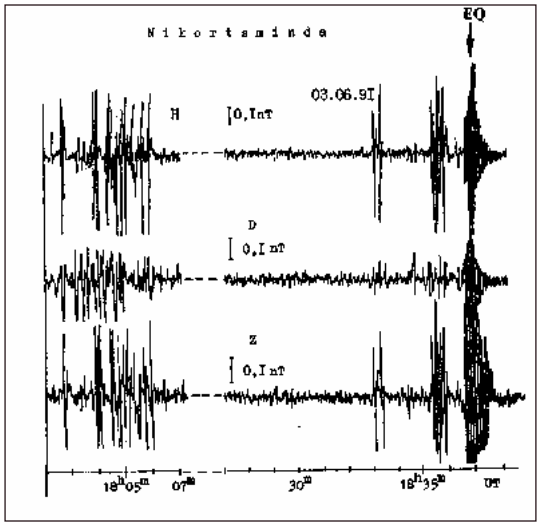

Fig. 7 Ultra-low frequency Lithospheric Emissions registered prior to the moderate (M=4) Racha aftershock of 3 June 1991 (marked as EQ). The observation point (Nikortsminda station) was located about 40 km from the epicenter [after Koputenko et al. 1994].

5. Conclusions

In this work, we investigate the SOC models possessing a non-trivial spatial structure generated self-consistently, and discuss how the dynamics of such structure can reflect processes preceding major quakes. We have introduced the novel SOC models based on the HP (Hughes and Paczuski, 2002). We advance the HP model with particular application to seismic-electromagnetic processes. We show that only non-Abelian SOC approach is able to explain the critical spatiotemporal dynamics of fractal tectonic systems exhibiting power-law earthquake statistics. Using a definite rule of the conductivity distribution upon a two-dimensional matrix, we calculate both the bulk and the percolation conductivities and demonstrate conformity between the fluctuations of conductivity obtained in our model and the real-observed pre-seismic ULF emissions. That proves the adequacy of the developing SOC model. So we conclude that the considered HP SOC model with broken Abelian symmetry seems to be promising for modeling pre-seismic ULF emissions. This model represents basic physical scenarios of self-organization and catastrophes in complex geophysical systems and offer insight into most complicated aspects of the observed seismic and electromagnetic phenomena.

References

Bak P., C. Tang, and K. Wiesenfeld (1987), Self-organized criticality: an explanation of 1/f noise, *Physical Review Letters*, 59, 381-384.

Bak P., C. Tang, and K. Wiesenfeld (1988), Self-organized criticality, *Physical Reviews,* 38, No.1, 364-374.

Hughes D., and M. Paczuski (2002), Large scale structures, symmetry, and universality in sandpiles, *Physical Review Letters*, 88(5), 054302-1 - 054302-4.

Kopytenko Yu.A., T.G. Matiashvili, P.M. Voronov, and E.A. Kopytenko (1994), Observation of Electromagnetic Ultra-Low-Frequency Lithspheric Emissions (ULE) in the Caucasian Seismicallly Active Area and Their Connection with the Earthquakes, in: *Electromagnetic Phenomena Related to Earthquake Prediction, edited by M. Hayakawa and Y. Fujinawa*, Terra Sci. Pub. Co., Tokyo, 175-180.

Smirnova, N. A., V. M. Uritsky, A. Tzanis, and F. Valianatos (2005), Modeling and Visualization of Emergent Behavior in Complex Geophysical Systems for Research and Education, *WSEAS TRANSACTIONS on ADVANCES IN ENGINEERING EDUCATION*, 2(2), 45-54.

Smirnova, N. A., Kiyashchenko, D.A., Troyan, V.N., Hayakawa, M (2010): Fractal approach to search for the earthquake precursory signatures in geophysical time series *in: Editor: V.S. Semenov. Proceedings of the 8th InternationalConference "Problems of Geocosmos"*. – SPb., ISBN 978-5-9651-0504-5, 433-438.

Smirnova, N.A, Kiyashchenko, D.A, Troyan, V.N., and Hayakawa, M. (2012): Multifractal approach to study the earthquake precursory signatures using the ground-based observations*, in: Editors:V.N. Troyan, V.S. Semenov, M.V. Kubyshkina Proceedings of the 9th International Conference "PROBLEMS OF GEOCOSMOS",* St. Petersburg, Petrodvorets, October 8-12, 2012, ISBN 978-5-9651-0685-1, 125-132.

Uritsky V., N. Smirnova, V. Troyan, and .F. Vallianatos (2004): Critical dynamics of fractal fault systems and its role in the generation of electromagnetic emissions before major earthquakes, *Physics and Chemistry of the Earth*, 29, 473-480.

ACOUSTO-ELECTROMAGNETIC EMISSION OF THE EARTH CRUST

V.N. Uvarov, E.I. Malkin, G.I. Druzhin, A.Yu. Isaev, A.N. Melnikov, D.V. Sannikov, V.N. Pukhov

Institute of Cosmophysical Research and Radio Wave Propagation Far-Eastern Branch of the Russian Academy of Sciences Kamchatsky krai, Paratunka, Mirnaya 7,
e-mail: malkinevgeniy@mail.ru

Abstract. To study the relation of acoustic and electromagnetic components of deformation effects of the Earth crust, registration of acoustic and electromagnetic radiation was carried in a well. To eliminate the powerful noise from the world lightning activity and industrial sources, a compensating scheme with independent registration of noise and the mixture of useful signal with noise was applied. Determination of the useful signal was carried out by minimization of the mean square deviation of the mixture from noise.
In the result of analysis of acoustic and electromagnetic signals the following facts were discovered:
1) High degree correlation of acoustic and electromagnetic signals;
2) High peaks of acoustic and electromagnetic signals of 2-4 minutes length.
3) Different kinds of peaks characterized by different composition may be referred to 4 types.
4) A suggestion was made that the tectonic-deformation processes of the crust in the conditions of dry friction are in the basis of the mechanism of this phenomenon.

Introduction

The acoustic and electromagnetic signals of lithospheric origin accompanying earthquakes are usually associated with the processes of tectonic stress [1]. Thus, we may say that acousto-electromagnetic radiation of the lithosphere is the reflection of its geodynamic state.
Fracture of a solid may be referred to the process of relaxation of the preliminary accumulated stress. Acoustic and electromagnetic emission appearing during the solid fracture is quite enough studied [2]. In the material sciences this phenomenon is used in nondestructive testing methods to get the information of the media of radiation propagation and its sources [3,4]. Seismology, investigation of the Earth by super low frequency oscillations of density, is well known among the geophysical applications of this approach. As for the acousto-electromagnetic investigations of the low frequency range, we should note that geophysical aspects of this phenomenon are still almost unstudied due to a number of interfering and masking factors. Electromagnetic radiation of the lithosphere is observed at the background of powerful radiation of atmospheric-magnetospheric origin, investigation of which has a long and rich history. Estimations show that atmospheric-magnetospheric radiation is incomparably stronger than the lithospheric one [5]. Thus, to study this radiation, it is necessary to apply some special methods. Development of such methods [6,7] allowed us to begin the purposeful and the correct investigation of electromagnetic radiation of lithospheric origin. An additional and supremely important circumstance, making the investigation the crust wave processes by the surface instrumentation more complicated, is significant attenuation of both acoustic and electromagnetic radiation in the friable near-surface layer of outwash and eolian origin. The Buger-Lambert-Beer empirical law determines the dependence of the transmission capacity of inhomogeneous medium on distance $\frac{J(r)}{J} = e^{-kr}$,
where k coefficient is the measure of medium inhomogeneity, which does not depend on propagation distance. In the geology, the porosity is such a measure of media inhomogeneity associated with fluid content. This parameter depends on depth and may characterize wave field propagation: $k \sim p$.
Due to the great diversity of geological conditions, one may comment only on the general dependence of porosity on depth. In the result of investigation of the porosity on large missives of homogenous rock, Athy law was established [8]. One of the most frequently used formulas is the following: $p = p_0 e^{-\alpha H}$.

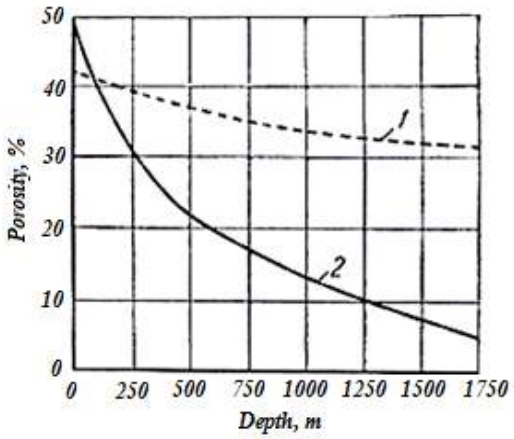

Fig. 1. The effect of natural rock compacting on their porosity: 1 - sandstone, 2 – clay [9].

Therefore, media absorption coefficient also decreases with depth according to exponential law. It follows from this that for the effective investigation of lithosphere wave fields, it is necessary to have an access to the crust deep layers with high permeability providing the possibility of wave propagation at large distance. Such access is possible in mines and wells. Application of wells is preferable since they are numerous and cover wider diversity of geological conditions.

Description of the field experiment

Well investigations of acoustic and electromagnetic radiation have been carried out long enough [10]. A number of interesting data were obtained on the relation of electromagnetic and acoustic radiation with seismic activity, weather and season condition effect and the Earth natural electromagnetic field [11]. In these studies a well is considered as a system for the delivery of a sensor into the interior and its radio physical properties are not taken into the account. The more effective application of the radio physical properties of wells would significantly increase the efficiency of investigations.

From our point of view, the most important acoustic and radio physical properties of a well are waveguide and metamorphic ones. The latter one is the capability of a well to transfer the density waves of different polarization into the corresponding electromagnetic ones. This property is due to the fact that a part of a well is cased in a pipe which is frequently made of steel. Naturally, the case pipe is magnetized by the Earth magnetic field. Since it is cemented in the surrounding rock, rock oscillations cause acoustic oscillations in the case pipe. Elastic stress in the magnetized ferromagnetic pipe results in the breaking of the domain structure and in the changes of its magnetic permeability, Villari effect [Physics encyclopedia]. As the consequence, the magnetic induction in the vicinity of a case pipe changes. Thus, the inductor used as a core, placed on the part of a case pipe sticking out over the ground, is a magnetically-elastic converter of acoustic oscillations of the case pipe body into the inductor current. Due to the ferromagnetism, a case pipe is a quite good magnetic circuit taking the magnetic field of the interior to the surface.

To investigate the relation of acoustic and electromagnetic components of deformation effects of the Earth crust at the 74^{th} well at Korkina brook in the basin of Paratunka river (Kamchatka), a field experiment was carried out. This well was made in 1968 to the depth of 649 m during the investigation of Paratunka hydrothermal deposit of Kamchatka. The casing was made of a steel pipe with the diameter of 168 mm from the surface to the depth of 195 m. The maximum water temperature of 56,8 C^0 was registered at the depth of 620 m. At the beginning, the well spring of thermal water was observed with the flow rate of 0.4 l/s with the temperature of 31 C^0. There is no well spring now. The well is in the zone of a sub-latitudinal left-shearing fault at the intersection with the North-Western transform zone. The zone of central planetary fault NNE 20^0 is also located there, i.e. the area of fault junction ("opening" zone NE 50^0, sub-parallel to the Kuril-Kamchatka trench subduction zone). Analysis of the rock mass structure allows us to suggest that the main sources of radiation may be located at the depth of 120-650 m. The characteristic distance of propagation of acoustic radiation in the range of 10-100 Hz in the rocks at this depth may be within 100-10,000 m.

Acoustic field registration was carried out by an equipped pre-amplifier and a hydrophone, sunk into the well at the depth of about 1 m. To register the magnetic vertical component of the electric field, an inductor, placed on the sticking out part of the casing pipe of the well, was used. To detect weak signals of lithospheric

origin from the powerful noise background of atmospheric-magnetospheric origin, a compensation method was used [7, 8].

Elimination of noise from EMR channel was carried out by subtraction of the noise weighted value from the signal mixture. The weight factor was determined by minimization of the mean square deviation of the mixture from the noise value. In the result of this procedure we succeeded to achieve the significant suppression of noise shown in Fig. 2, which illustrates averaged spectra of the detected electromagnetic signal of the interior and the acoustic signal after elimination of industrial noise. The figure 3 clearly shows the presence of the mode structure of the well acoustic natural oscillations, the pronounced spectral bands in the frequency range less then 70 Hz. The result of measurement of the frequency difference between the neighbor harmonics Δf=3.1 Hz corresponds to the estimation.

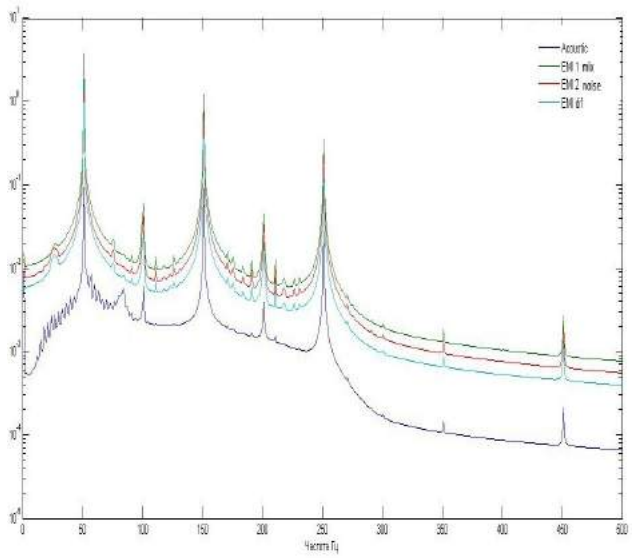

Fig. 2. Averaged spectra of the initial, differential and acoustic signals.

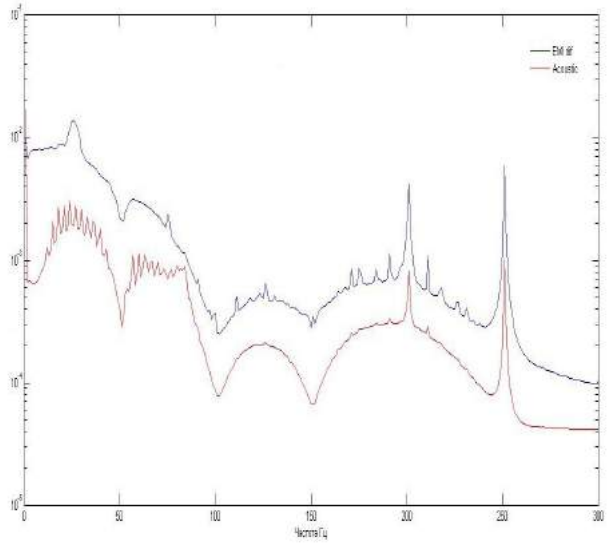

Fig. 3. Spectra of differential, electromagnetic and acoustic signals without noise.

The major analysis of signals was carried out by Fourier transform with Haar window with the length of 44100 points, the number of signal sampling counts per 1 second. The obtained spectrum has the frequency scale in hertz.

Analysis of measurement results

In the result of the analysis of the obtained data, sharp deviations of the background signal from the average level were discovered. The peculiar feature of the anomalies is their duration which is within the interval of 2-5 seconds and the intensity exceeding the background value by more than one order. The anomalous deviations are observed both in electromagnetic and in acoustic channels. These anomalies were classified into four types:

1) Narrow-band signal, the frequency of which decreases with time (dynamic specter shown in Fig.4). The duration of anomalies of this type is 3-4 minutes. The frequency range is 70 ÷ 100 Hz. In the wave forms the signal appears as a weakly distorted sinusoidal one. The peculiarity of such anomalies is the similarity of spectra with the spectral dependence describing Doppler effect. The absence of external sound sources at the time of signal registration, confirmed by experiment journal records, indicates the relation with some process within the rock mass causing acoustic emission. This type of anomalies was also recorded by the magnetic antenna at the well. The stability of phase relations between acoustic and electromagnetic signals (Fig. 5) allows us to indicate the coherence of acoustic and electromagnetic oscillations, which, in its turn, allow us to state the community of a source for acoustic and electromagnetic radiation of this type. The most probable reason of high correlation is the magnetoelastic transformation of acoustic radiation in the case pipe (Villari effect). We should also note that there is not sequence of anomalies of this type.

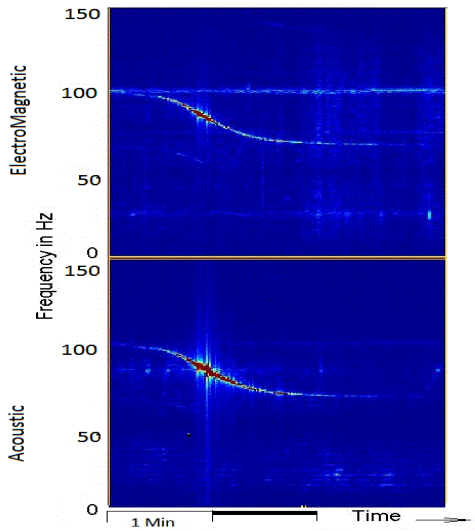

Fig. 4. An example of the dynamic spectrum of the first type anomalous signal.

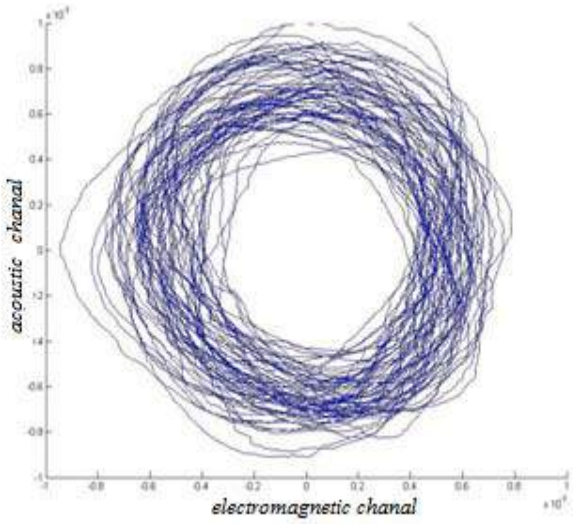

Fig. 5. Phase relations of acoustic and electromagnetic channels. Horizontal axis is electromagnetic channel amplitude, vertical axis is acoustic channel amplitude.

2) Narrow-band signal with line spectrum (dynamic specter shown in Fig.6). The duration of these anomalies is 3-4 minutes. The frequency range is mainly less than 100 Hz. This type of anomalies is a set of spectral components in the form of synchronous anomalies of the first type, shifted by 29 Hz. The form of spectrograms is a set of lines with continuously changing frequency. The final change of spectrum line frequencies is proportional to the average frequency of spectral component. Phase relations of electromagnetic and acoustic signals do not have a clear pattern. According to the structure of the anomalies of this type it is evident, that they are nothing but a sequence of pulses, the period of which changes with time. Logically to suppose, that a self-oscillating process is in the basis of nature of this phenomenon. The closest model, according to the parameters, i.e. band sequence, relative intensity and oscillation phase, is the one of self-oscillatory system on the basis of dry friction forces.

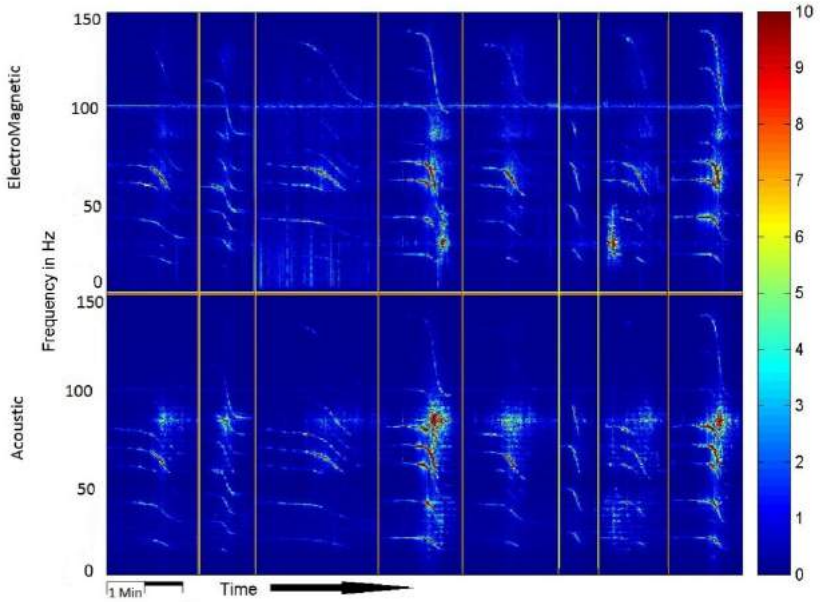

Fig. 6. Examples of dynamic spectrum of the second type anomalous signal.

3) Narrow-band signal with chaotically changing frequency (dynamic specter shown in Fig.7). This type of anomalies has one narrowband component with randomly changing frequency. The duration is 1-2 minutes. The frequency range is 50-80 Hz. This type of anomalies does not almost appear in the wave forms.

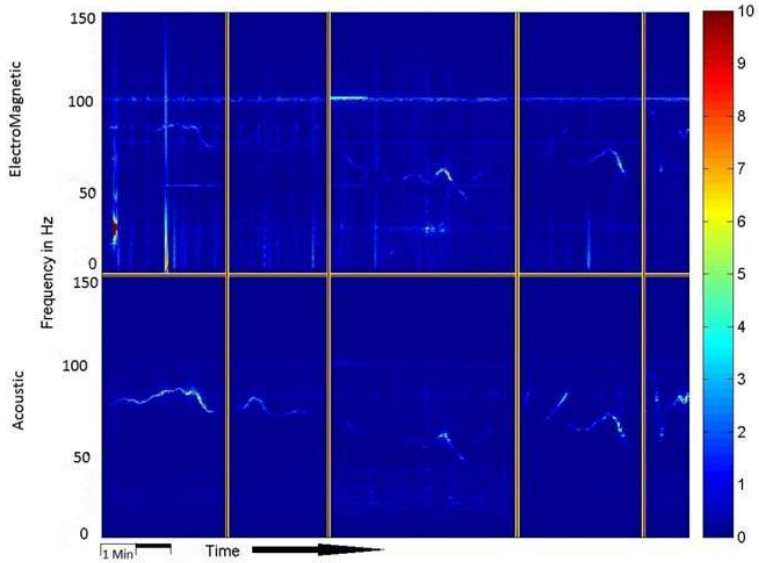

Fig. 7. An example of the dynamic spectrum of the third type anomalous signal.

4) Broadband signal (dynamic specter shown in Fig.8). This type of signals is powerful broadband noise which 6-10 times exceeds the background value in the range of 20-40 Hz with the duration of about one minute and a continuous spectrum. A series of such anomalies following each other is frequently observed.

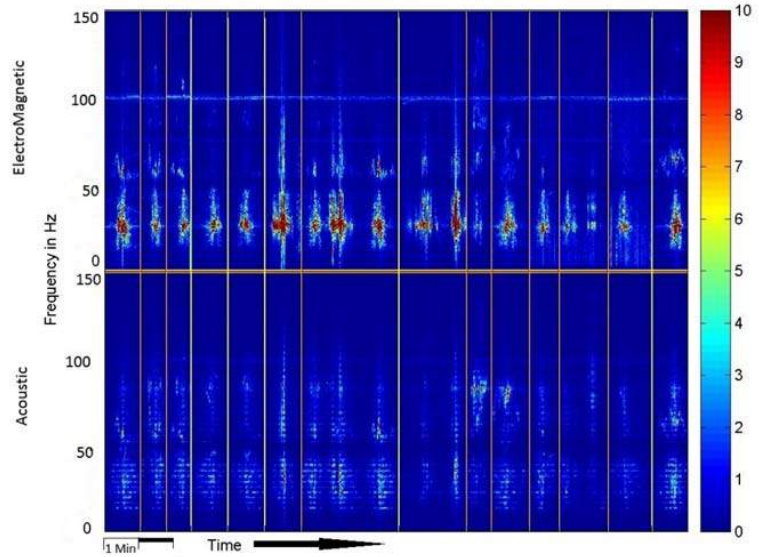

Fig. 8. An example of the dynamic spectrum of the fourth type anomalous signal.

Conclusions

High degree of correlation between acoustic and electromagnetic signals was determined in the area of anomalous deviation from the average background radiation.

Four main types of anomalies of acousto-electromagnetic radiation were distinguished. The stability of phase relations for some types of acoustic and electromagnetic signal anomalies indicates their coherence. Acoustic signal advances the electromagnetic signal showing the primary nature of the acoustic signal. The most probabilistic reason of acoustic signal transformation into the electromagnetic one is the magnetoelasticity effect of the case pipe (Villary effect).

The observed anomalies of both acoustic and electromagnetic origin have lithospheric nature and are associated with relaxation of tectonic stress.

The assumption was made that the second type of anomalies is the result of the self-oscillating process in the interior in the conditions of dry friction.

References

1. Sobolev G.A., Ponomarev A.V. (2003), *Earthquake physics and precursors*, Nauka, ISNB 5-02-002832-0, 270 pp.
2. Hadjicontis V., Mavromatou C., Antsygina T.N., Chishko K.A. (2007), Mechanism of electromagnetic emission in plastically deformed ionic crystals. *Phys. Rev.* B 76, 024106.
3. Sikula J., Y. Mori, T. Lokajicek, P. Koktavy, J. Majzner and P. Sedlak (2008), Crack creation kinetics characterization by electromagnetic and acoustic emission. *Proc.28th European Conf. AE Testing*, Kracov, Poland, 118-123.
4. Mori Y., Y. Obata, J. Sikula (2009), Acoustic and electromagnetic emission from crack created in rock sample under deformation, *J. Acoustic Emission*, 27, 157-166.
5. Uvarov V.N. (2012), Electromagnetic effect of the lithosphere in SLF-VLF range. *Geophysical Journal*, V.34, N6, 133-146.
6. Uvarov V.N., Druzhin G.I., Sannikov D.V. (2010), Electromagnetic radiation of lithospheric origin. Detection method and first results., *PTE,*N6, 131-137
7. Uvarov V.N. et al. (2011), *Method of passive location of closely located sources of electromagnetic radiation at the background of powerful radiation from remote sources*. Patent of the Russian Federation N 2473101, 30.06.2011.
8. Athy L.F. (1930), Density, porosity and compaction of sedimentary rocks, *Bull. Amer. Assoc. Petrol. Geol*. v. 14, 1-24.
9. Engelgardt V. (1961), Pore space of sediments, translated from German, M., 1964; *Investigations of physical-mechanical properties of rocks*, M.
10. Gavrilov V.A., I.A. Panteleev, G.V. Ryabinin, and Yu.V. Morozova (2013), Modulating impact of electromagnetic radiation on geoacoustic emission of rocks. *Russian Journal of Earth Science*, v. 13, ES1002, doi:10.2205/2013ES000527.
11. Gavrilov V.A., Morozova Yu.V. (2003), Main properties of geoacoustic emission according to the results of observations in a deep well G-1, *Modern volcanism and processes associated with it,* Petropavlovsk-Kamchatsky, 44-47.

ON QUASI-STATIC IONOSPHERE ELECTRIC FIELDS OBSERVATIONS OVER EARTHQUAKE PREPARATION REGIONS

O.V. Zolotov

Physics Department, Murmansk State Technical University, Murmansk, 183010, Russia,
e-mail: ZolotovO@gmail.com

Abstract. Quasi-electrostatic ionosphere electric field disturbances observed over seismically active regions on board of INTERCOSMOS-BULGARIA-1300 and DEMETER satellites are summarized. The disturbances (1) take place for all (E_x, E_y, E_z) electric field components and (2) happen at the near-epicenter as well as magnetically conjugated to it areas (3) from a few minutes to tenth of hours before and after strong earthquakes. (4) Their amplitudes are in range 1-26 *mV/m* and spatial sizes are >1-20◦. (5) Quasi-electrostatic disturbances dominate mostly at night-time, their amplitudes depend on the earthquake's magnitude and depth of the hypocenter location.

Ionosphere Total Electron Content (TEC) is known to have features associated with earthquakes' preparation processes [Pulinets and Boyarchuk, 2004; Namgaladze et al., 2011, 2013; Namgaladze and Zolotov, 2012]. We explain those features in terms of the ionosphere *F2*-region vertical plasma [$\boldsymbol{E}\times\boldsymbol{B}$]-drift under action of zonal electric fields of seismic origin and support this hypothesis with numerical simulations [Namgaladze and Zolotov, 2011; Karpov et al., 2012, 2013]. Model results show that zonal electric fields of 1-4 *mV/m* and 4-10 *mV/m* are required to generate TEC disturbances, similar to the observed ones, at low and middle latitudes respectively [Zolotov et al., 2012; Namgaladze et al., 2013]. However, a few researchers strongly doubt that mechanism. The objection is the ionosphere electric fields of seismic origin do not exist in nature (or orders less than *mV/m*) and the numerical studies we performed are nothing but some kind of casual exercises without any physical basis. Therefore, the observational evidences of such electric fields' existence are strongly required. Table 1 of this paper presents explicit summary on quasi-static ionosphere electric fields observed over seismically active regions on board of satellites; for more details see [Zolotov, 2015].

A set of case studies and large series of events, summarized in Table 1, show that ionosphere quasi-static electric field disturbances:

(1) happen for all (E_x, E_y, E_z) components,

(2) are located at the near-epicenter as well as magnetically conjugated to it areas,

(3) from a few minutes to tenth of hours before and after strong earthquakes,

(4) have amplitudes in range 1-26 *mV/m* and spatial sizes of about 1-20°,

(5) dominate at night-time,

(6) and their amplitude depends on the earthquake's magnitude and depth of the hypocenter' location.

Table 1

Ionosphere quasi-electrostatic fields disturbances, observed on INTERCOSMOS-BULGARIA-1300 (IC-B-1300) and DEMETER satellites. Symbol ↕ denotes disturbances, ***E*** – electric field vector amplitude.

Satellite [publication]	Reported quasi-static electric field disturbances
IC-B – 1300; [Chmyrev et al., 1989]	↕ E_z ~ 3-7 *mV/m* for M 4.8 earthquake (EQ) over the epicenter and magnetically conjugated regions; disturbed areas size - 1°-1.5° along the meridian.
IC-B – 1300; [Gousheva et al., 2006a]	↕ E_x, E_y up to ~7 *mV/m* at low and middle latitudes for 10 M 5.6 – 5.9 EQs during 12.08.1981 – 30.12.1981.
IC-B – 1300; [Gousheva et al., 2006b, 2008a]	↕ ***E*** ~2-25 *mV/m* for 30 min – 4 h before and after mid-latitudinal EQs. E_x, E_y, E_z disturbances were up to 10, 14 and 25 *mV/m*, respectively. Disturbed areas were shifted from the epicenter, their sizes were >5°-20°. The results were derived for 6 M5.1 -5.9 EQs, 16.09.1981 – 01.10.1981 period.
IC-B – 1300; [Gousheva et al., 2007a, 2007b, 2008b]	Polar latidudes: ↕ E_z (1) ~26 *mV/m* 33 h before EQ, the disturbed region was shifted Northward; (2) 15 *mV/m* 31 min before EQ over the epicenter region. Mid-latitudes: ↕ E_z ~15 *mV/m* 89 h before the EQ; the disturbed region was shifted Northward. Low latitudes: ↕ E_z (1) 5-10 *mV/m* 12 h before EQ, the disturbed region was shifted Southward; (2) ~10 *mV/m* 32-33 h before EQ, the disturbed region was shifted Northward. The results were obtained for 12 M5.0 -6.9 EQs, 22.08.1981 –27.11.1981 period.
IC-B – 1300; [Gousheva et al., 2009]	↕ E_z ~18 *mV/m* over the near-epicenter and magnetically conjugated regions for 14.08.1981 – 20.09.1981 period. Night-time domination and dependence of E_z disturbances both on the EQ magnitude and hypocenter depth were reported.
IC-B – 1300; [Gousheva et al., 2012]	↕ E_z for 106 EQs during 17.08.1981-19.12.1981 (at night-hours). ↕ E_z 2-18 *mV/m* were reported for sources located at mobile structures of the plates.
DEMETER, [Zhang et al., 2012]	↕ ***E*** 3-5 *mV/m* for M8.0, May 12, 2008, Wenchuan EQ, China. Only night-time data were analyzed.
DEMETER, [Zhang et al., 2014]	↕ ***E*** 1.5-16 *mV/m*. 27 earthquakes were selected and analyzed in regions of Indonesia and Chile at equatorial and middle latitude area respectively.

References

Chmyrev, V.M., N.V. Isaev, S.V. Bilichenko, G.A. Stanev (1989), Observation by space-borne detectors of electric fields and hydromagnetic waves in the ionosphere over on earthquake center. *Phys. Earth Planet. Inter.*, 57, 110-114, doi: 10.1016/0031-9201(89)90220-3

Gousheva, M., R. Glavcheva, D. Danov, et al. (2006a), Satellite monitoring of anomalous effects in the ionosphere probably related to strong earthquakes. *Adv. Space Res.*, 37(4), 660-665, doi:10.1016/j.asr.2004.12.050

Gousheva, M., R. Glavcheva, D. Danov, I. Boshnakov (2006b), Satellite observations of ionospheric disturbances associated with seismic activity. *Comptes rendus de l'Académie bulgare des Sciences.*, 59(8), 821-826, URL: http://goo.gl/5KmPnj

Gousheva, M., R. Glavcheva, D. Danov, et al. (2007a), Possible pre and post-earthquake effects in the ionosphere. *3rd International Conference on Recent Advances in Space Technologies. IEEE.*, 754–759, doi:10.1109/RAST.2007.4284094

Gousheva, M., D. Danov, P. Hristov (2007b), Ionospheric pre- and post-effects of earthquakes at polar, middle, low and near-equatorial latitudes. *Comptes rendus de l 'Académie bulgare des Sciences .*, 60(9), 939-946, URL: http://goo.gl/TrHIwI

Gousheva, M.N., R.P. Glavcheva, D.L. Danov, et al. (2008a), Electric field and ion density anomalies in the mid latitude ionosphere: Possible connection with earthquakes? *Adv. Space Res.,* 42(1), 206-212, doi:10.1016/j.asr.2008.01.015

Gousheva, M., D. Danov, P. Hristov, M. Matova (2008b), Quasi-static electric fields phenomena in the ionosphere associated with pre- and post earthquake effects, *Nat. Haz. Earth Syst. Sci.,* 8(1), 101-107, doi:10.5194/nhess-8-101-2008

Gousheva, M., D. Danov, P. Hristov, M. Matova (2009), Ionospheric quasi-static electric field anomalies during seismic activity in August–September 1981, *Nat. Haz. Earth Syst. Sci.,* 9(1), 3-15, doi:10.5194/nhess-9-3-2009

Gousheva, M., D. Danov, P. Hristov (2012), Statistical study of the quasi-static electric field anomalies in the upper ionosphere related to seismic activity above different tectonic structures of the Earth, *Comptes rendus de l'Académie bulgare des Sciences.,* 65(9), 1249-1260, URL: http://goo.gl/g6pgwB

Karpov, M.I., A.A. Namgaladze, O.V. Zolotov (2012), Three-dimensional structure of the seismo-electromagnetic ionospheric electron density disturbances. *Proc. MSTU,* 15(3), 595–603

Karpov, M.I., A.A. Namgaladze, O.V. Zolotov (2013), Modeling of Total Electron Content disturbances caused by electric currents between the Earth and the ionosphere. *Russian Journal of Physical Chemistry B,* 7(5), 594–598, doi:10.1134/S1990793113050187

Namgaladze, A.A., O.V. Zolotov (2011), Ionospheric effects from different seismogenic electric field sources. *XXX URSI General Assembly and Scientific Symposium,* Istanbul, Turkey. IEEE, doi:10.1109/URSIGASS.2011.6051040

Namgaladze, A.A., O.V. Zolotov, B.E. Prokhorov (2011), The TEC signatures as strong seismic event precursors. *XXX URSI General Assembly and Scientific Symposium.* Istanbul, Turkey. IEEE, doi:10.1109/URSIGASS.2011.6051048

Namgaladze, A.A., O.V. Zolotov (2012) Ionospheric effects of seismogenic disturbances of the global electric circuit seismogenic disturbances, *In: "Earthquakes: Triggers, Environmental Impact and Potential Hazards",* Nova Publishers, 233-266.

Namgaladze, A.A., O.V. Zolotov, B.E. Prokhorov (2013), Numerical simulation of the variations in the Total Electron Content of the ionosphere observed before the Haiti earthquake of January 12, 2010. *Geomagnetism and Aeronomy,* 53(4), 522–528, doi:10.1134/S0016793213030122

Namgaladze, A.A., M. Förster, B.E. Prokhorov, O.V. Zolotov (2013) Electromagnetic Drivers in the Upper Atmosphere: Observations and Modeling, *In: "The Atmosphere and Ionosphere Elementary Processes Discharges and Plasmoids Physics of Earth and Space Environments",* Springer, 55 p. doi: 10.1007/978-94-007-2914-8_4

Pulinets, S.A., K. Boyarchuk (2004) Ionospheric Precursors of Earthquakes. *Springer:Berlin,* 315p.

Zhang, X., H. Chen, J. Liu, et al. (2012) Ground-based and satellite DC-ULF electric field anomalies around Wenchuan M8.0 earthquake, *Adv. Space Res.,* 50(1), 85-95, doi: 10.1016/j.asr.2012.03.018

Zhang, X., X. Shen, S. Zhao, et al. (2014), The characteristics of quasistatic electric field perturbations observed by DEMETER satellite before large earthquakes, *J. Asian Earth Sci.,* 79, 42–52, doi: 10.1016/j.jseaes.2013.08.026

Zolotov, O.V., A.A. Namgaladze, I.E. Zakharenkova, et al. (2012), Physical interpretation and mathematical simulation of ionospheric precursors of earthquakes at midlatitudes. *Geomagnetism and Aeronomy,* 52(3), 390–397, doi:10.1134/S0016793212030152

Zolotov, O.V. (2015), Ionosphere quasi-static electric fields over seismically active regions: A review, *Russian Journal of Physical Chemistry B* (in Press)

THE POSSIBLE TECHNOSPHERE IMPACT ON THE EARTHQUAKE FOCAL MECHANISMS IN JAPAN

O.D. Zotov[1], I. P. Lavrov[1]

[1]Geophysical Observatory Borok, IPE, RAS, Borok, Russia, e-mail: ozotov@inbox.ru

This paper is devoted to the problem of technosphere-lithosphere interaction. The so-called weekend effect in the global seismic activity has been discovered earlier. The essence of the effect is that the seismicity (number of earthquakes) is experiencing a strict seven-day modulation, with the maximum of activity in weekends. This definitely indicates the effects of industrial activity on the lithospheric processes. The question arises whether it is possible to detect the weekend effect in variations of the earthquake focal mechanisms? To answer the question we examined the earthquake catalogue of Kanto-Tokai observation network (http://www.bosai.go.jp/kotai/kanto/kanto-tokai/index_e.html) of National Research Institute for Earth Science and Disaster Prevention (NIED, Japan). The weekend effect in variation of the earthquake focal mechanisms has been detected for the relatively shallow (less than 10 km) earthquakes and was not found for the more deep earthquakes.

Introduction

This research addresses to the effects of synchronism in geospheres under the influences of technosphere. Earlier, this effect which manifests itself in the form of so-called ***Big Ben*** and ***Weekend*** effects was observed by statistical analysis of the electromagnetic and seismic events [Guglielmi, Zotov, 2012].

Weekend effect, or, more generally, a specific weekly cycle (septan variation) were found in the magnetosphere [Guglielmi and Zotov, 2007] (Pc1 wave activity) and lithosphere [Zotov, 2007] (global seismic activity). Fig. 1 shows these periodicities. The period of synchronous detection (epoch duration) is 7 days. The number of events means the number of Pc1 series (left) and number of earthquakes (right).

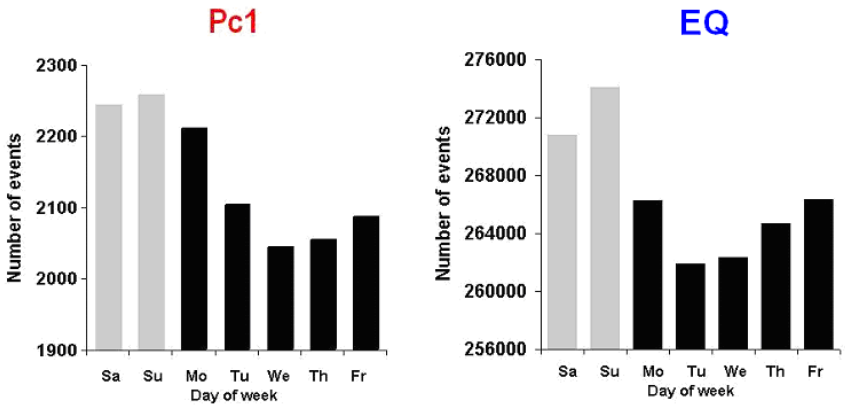

Fig.1. Weekend effect in the magnetospheric Pc1 wave (obs. Borok 1958-1992, http://www.wdcb.ru/stp/data/catal_pc) and seismic activity (EQ, catalog ISC, 1964-2003, http://www.isc.ac.uk, M ≤ 5.5). Days of week are plotted on the horizontal axis. The signs **Sa** and **Su** denote Saturday and Sunday and the vertical gray columns indicate the weekend. Number of one week intervals (number of epochs) is ~1800 for Pc1 and ~2000 for EQ.

It is supposed that weekend effect has anthropogenic origin because natural variations with a period of strictly equal to 7 days are not known. The phenomenon indicates that the technosphere has a nontrivial impact on the magnetosphere and lithosphere.

Fig. 2 shows weekend effect in the chemical (a, left) and nuclear (b, left) explosions (catalog ISC) [Zotov, 2007], in the power consumption (bottom right, catalog NYISO,

http://www.nyiso.com/public/market_data/load_data/rt_actual_load.jsp) [Guglielmi, Zotov, 2012] and in the launch of spacecraft (top right, catalog LSC, http://www.zabor.com/launch).

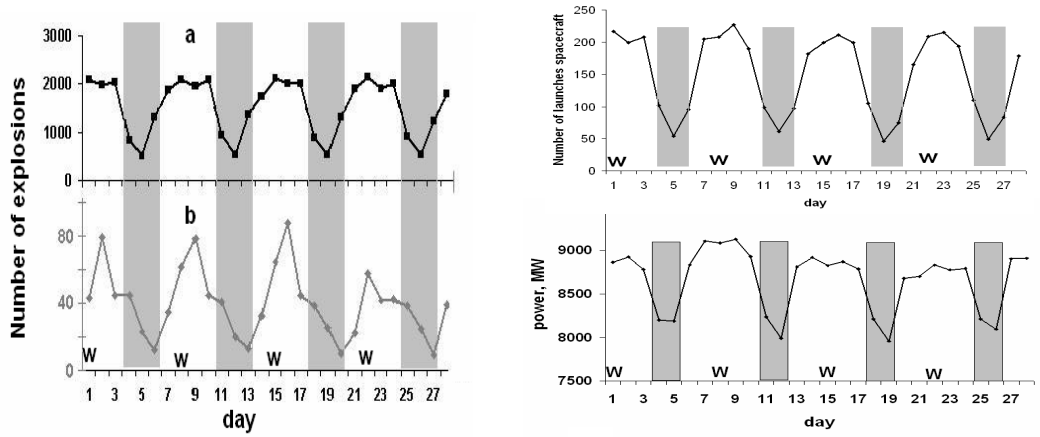

Fig.2. Weekend effect in anthropogenic seismic events (left), namely, chemical explosion (a, the black line, 40 000 events, catalog ISC) and the nuclear explosions (b, the gray line, 1100 events, catalog ISC), the number of events is plotted on the vertical axis; weekend effect in power consumption (bottom right, catalog NYISO); weekend effect in the launch of spacecraft (top right, catalog LSC). The synchronous detection interval (epochs duration) of 28 days plotted on the horizontal axis (**W** denotes the first day Wednesday).The gray vertical columns indicate the weekends.

The seven-day modulation of anthropogenic activity is clearly seen for all groups of events.

A large number of studies are devoted to the presentation of experimental results related to the influence of different sources of natural and artificial origin on seismic and magnetospheric activities. The different so-called active experiments (MGD-generator, mechanical vibration, explosion etc) demonstrate the influence on seismic activity of the physical fields of different nature. But a distinctive feature of active experimentation is their episodic. It is logical to assume that the response of the geosphere to external influence depends on it physical condition. Active experiments are short and pre-planned. In this cases it is difficult take into account the conditions in the geosphere during the experiment. Unfocused but regular impact may be more effective. Continuous impact covers the entire spectrum of conditions of the geosphere including the most favorable conditions for the occurrence of the effect of influence. The source of such a continuous influence on the geosphere is the technosphere.

The industrial activity characterized by variety of types of generated physical fields which have the same periodicities which we find in the lithosphere and magnetosphere.

So, there is an experimental foundation for phenomenon of synchronism of the electromagnetic and seismic events which manifests itself in the form weekend effects.

Thus we have many reasons for the search of similar effects in other characteristics of the geospheres. We will study the earthquakes (EQ) in Japan.

Is it possible to detect the weekend effect in variations of the earthquakes mechanisms?

Method and data

The synchronous detection method (in form the superposed epoch analysis) has been used. Method is effective way to detect a weak periodic signal on a background of noise.

In this work we have attempted to observe the effect by using the regional seismicity data. For the present statistical study we have used data from the earthquake catalogue of Kanto-Tokai observation network (http://www.bosai.go.jp/kotai/kanto/kanto-tokai/index_e.html) of National Research Institute for Earth Science and Disaster Prevention (NIED, Japan). Catalogue contains 55000 earthquakes with fault plane solution data from 1980 to 2002.

General characteristics of earthquakes are given in Fig. 3a, b.

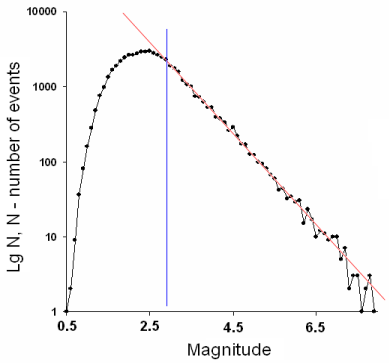

Fig.3a. The distribution of magnitude.

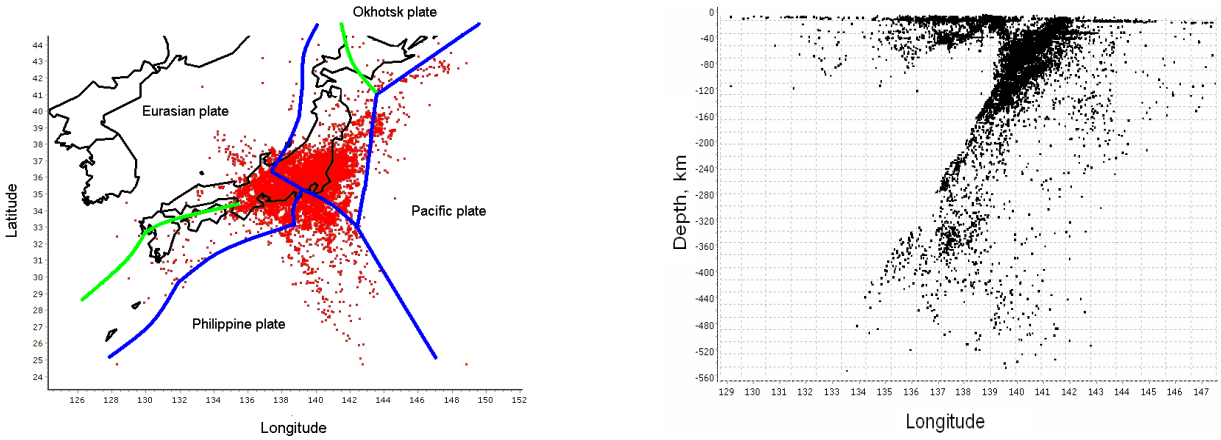

Fig.3b. The distribution of epicenters (on the left, red dots) and the distribution of hypocenters (on the right, black dots, shown one of projection) earthquakes. Dark blue line marks the boundaries of tectonic plates.

Catalogue contains focal mechanism solution for each earthquake, in particularly, angles STRIKE, DIP and SLIP. Fig. 4 schematically shows these angles and the three main types of focal mechanisms earthquakes.

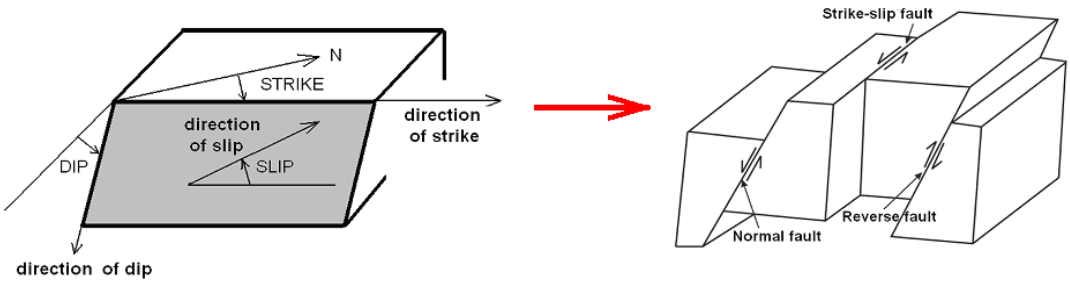

Fig.4. Type of focal mechanism = function (STRIKE, DIP, SLIP).

Consider the weekend effect. Null hypothesis: the ratio of types of focal mechanisms does not depend on the day of the week (weekday - weekend) and alternative hypothesis - there is dependence (exist the real impact of industrial activities on the seismic activity).

For each day of the week was calculated ratio of types of mechanisms in percentage. The ratio calculated in order to avoid dependence on the number of earthquakes.

Results

Japanese islands region is an interesting seismic region, since there are four tectonic plates - two continental (Eurasian Plate and Okhotsk Plate) and two oceanic (Philippine and Pacific plate). The oceanic plate subducts below the edge of the continental plate when continental and oceanic plates converge (see Fig.3a, b).

We hypothesized that the impact of the technosphere will be more effective firstly on shallow earthquakes and secondly, on the earthquakes which belong to the continental plates. And it was so (see Fig. 5, 6).

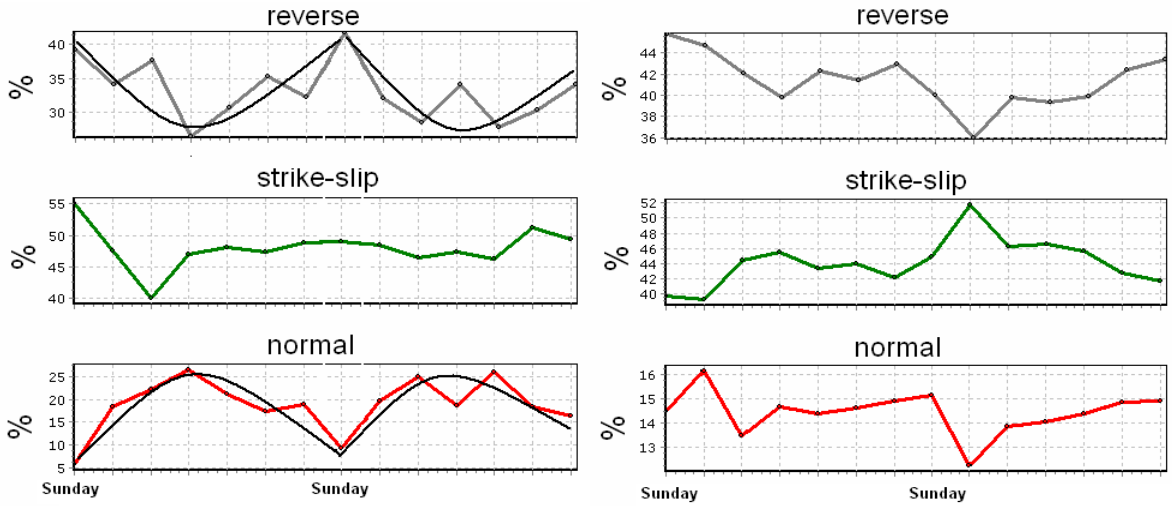

Fig.5. The dependence of ratio of types of focal mechanisms from the day of the week. On the left - continental plates, on the right - oceanic plates. Black line - approximation of initial curves.

For continental plates were selected earthquakes with longitude from 125 to 142 , latitude from 35.5 to 44 , magnitude from 0 to 10 and depth from 0 to 7 km, total 3158 events. For oceanic plates were selected 46600 earthquakes (Long 130.5 - 148 , Lat 24.7 - 43.5 , M 0-10, depth 7 500 km.

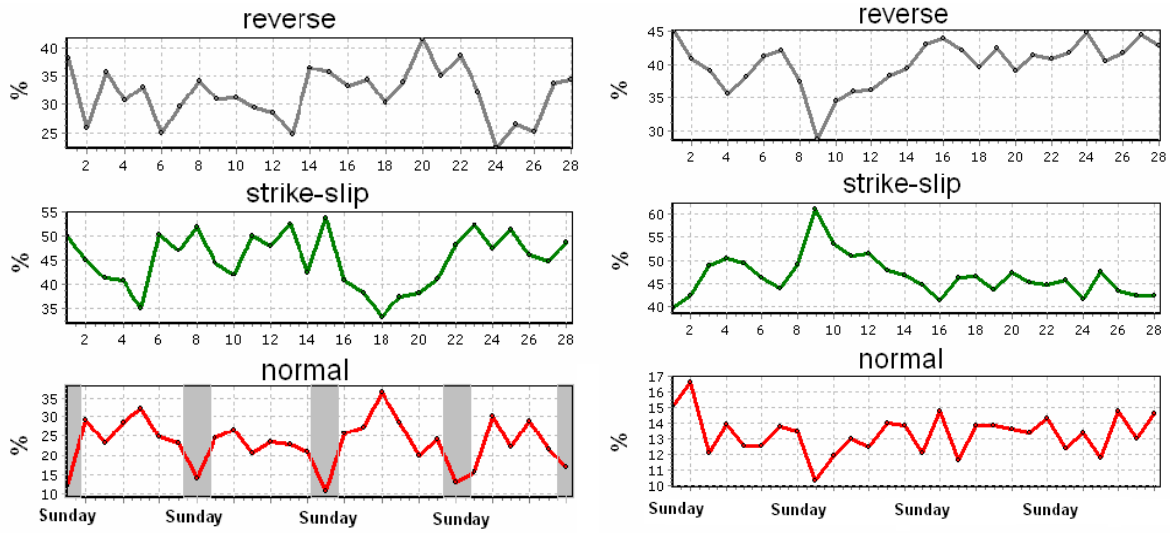

Fig.6. The dependence of ratio of types of focal mechanisms from the day of the week. Left panel - shallow earthquakes, and right panel - deep earthquakes. The gray vertical columns indicate the weekends.

For shallow earthquakes were selected events regardless of latitude and longitude with M 0-3 and depth 0 6 km, total 3569 events. For deep earthquakes were selected 33740 events regardless of latitude and longitude with M 0-3 and depth 7-500 km.

Fig. 5 shows that for continental earthquakes reverse and normal types of focal mechanisms have a weekly cycle with minimum in Sunday. For oceanic plates no mechanisms has septan variation.

Fig. 6 shows that for shallow earthquakes normal types of focal mechanisms have a weekly cycle with minimum in Sunday. For deep earthquakes no mechanisms has septan variation.

So, probably shallow earthquakes with small magnitudes that have occurred in continental plates have a best weekly cycle with minimum in Sunday. These earthquakes, more exactly their mechanisms are the most sensitive to the effects of the technosphere.

Fig. 7 shows one more preliminary result. Catalogue contains for each earthquake the angles AZP (azimuth of P-axes) and AZT (azimuth of T-axes). P - the axis of maximum compression (P - pressure) and T – the axis of minimum compression (T - tension) in earthquake source. For each day of the week, we calculated the average value of these angles.

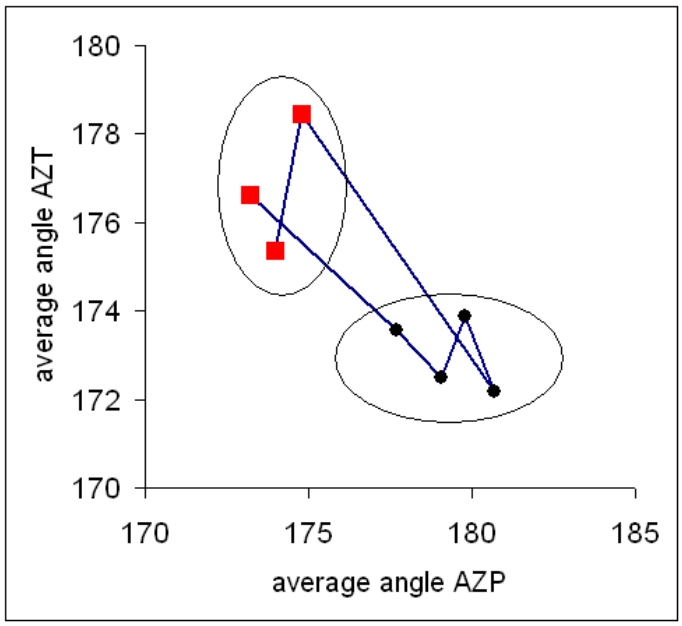

Fig.7. Dependence average value AZT from AZP (**rad** square – day of week Friday, Saturday, Sunday; **black** dots – Monday, Tuesday, Wednesday, Thursday).

Ellipses mark the two groups of points (days), one group - the weekend, the second group – weekdays. Such clustering also indicates the seven-day cycle in the dynamics of types of focal mechanisms.

Summary

The main conclusion is that the weekend effect is the real geophysical phenomena, and evidently human in origin. This effect indicates that there is some nontrivial impact caused by industrial activity on the natural processes in the lithosphere.

Weekly cycle in the earthquake focal mechanisms is an interesting and strange and unusual result.
Why only the normal and reverse mechanism has weekly variation?
What physical mechanism of the influence of the technosphere on earthquake focal mechanisms?
To these questions yet to be answered.

Acknowledgements

We appreciate the National Research Institute for Earth Science and Disaster Prevention (NIED, Japan). We are grateful to Prof. A.V. Guglielmi for his interest to this work and for some valuable remarks, A.O. Mostryukov and V.A. Petrov for help in working with earthquake catalog and discussion, and B.I. Klain for useful comments. The work was supported by the Program № 4 of the Presidium RAS and RFBR (grant no. 13-05-00066).

References

1. Guglielmi, A.V., and O.D. Zotov (2012), The phenomenon of synchronism in the magnetosphere–technosphere–lithosphere dynamical system, *Physics of the Solid Earth*, 48(6), 486–495.
2. Guglielmi, A., and O. Zotov (2007), The human impact on the Pc1 wave activity, *Journal of Atmospheric and Solar-Terrestrial Physics,* 69, 1753–1758.
3. Zotov, O.D. (2007), Weekend Effect in Seismic Activity, *Izvestiya, Physics of the Solid Earth,* 43(12), 1005–1011.

STUDY OF POLE TIDE TRIGGERING OF SEISMICITY

V. L. Gorshkov

Central (Pulkovo's) astronomical observatory of RAS, St. Petersburg, 196140, Russia
e-mail: vigor@gao.spb.ru

Abstract. The pole tide (PT) is generated by the centrifugal effect of polar motion on the chandler (f_{cw} = 0.84 cpy) and annual (f_a = 1.0 cpy) frequencies. These frequencies, their beat frequency (0.16 cpy) and doubled frequency of chandler wobble (1.66 cpy) were revealed in seismic intensity spectrum of weak (M < 5) earthquake. The failure time for the weak earthquakes with magnitudes $3 < M_W < 5$ averages 1-10 years for various regions that is in a good agreement with the periodicity of stress oscillations excited by PT. The CMT global seismic databases (1976 – 2014) were used for search of the pole tide influence on the intensity of seismic process. For 32.2 thousand seismic events from CMT were calculated normal and shear stresses excited by PT using strike, dip and rake angles of the earthquake fault plane from this catalogue. The phases of the PT stresses for each earthquake were assessed and subsequently were used for statistical estimation of pole tide influence on seismicity. The PT stress oscillations excite the weak earthquakes of thrust-slip fault type on 95% significance level by χ^2 and Schuster's statistical tests.

MOTIVATION

The triggering of seismicity by the lunisolar tide (LST) is widely discussed last decades. But there is some confirmation of the PT influence on seismic process also, i.e. it can be found in the papers (Levin, Sasorova, 2002; Gamburtsev et al., 2004). The direct exciting of slow slip seismic events by PT was revealed in the work (Shen et al., 2007). The influence of PT on seismicity was revealed by test research in our previous work (Gorshkov, Vorotkov 2012). There was searched the seismic reaction on PT induced variations of vertical displacement in earthquake location.

There is periodicity of intensity of seismic process in pole tide (PT) frequency band (0.6, 1.2 and 6 – 7 years) as it can be seen at fig.1 where were used seismic events for 1973-2009 from data base NEIC (http://earthquake.usgs.gov/regional/ neic).

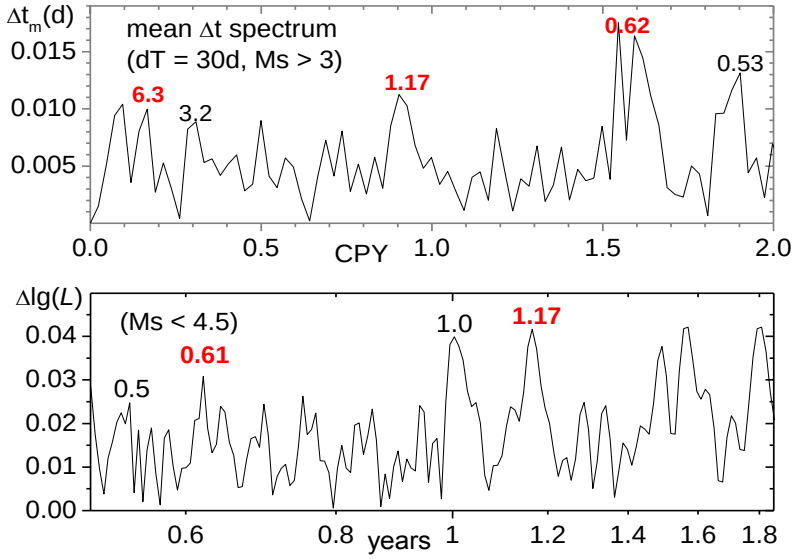

Figure 1. Amplitude FFT spectrum of seismic intensity (mean interval between earthquakes averaged in dT = 0.05 year) (*up*). Increments of maximum logarithmic likelihood function (Δlg(*L*)) for periodic point seismic process by method of Lyubushin (1998) for detecting of hidden periodicities within flow of events (*below*).

The most obvious excitation factor of these seismic intensity variations is PT. But excited stress variations in the crust by PT are less 1kPa while LST stress variations achieve 5 kPa. Why PT can trigger seismicity but it is almost impossible to reveal earthquake triggering by more powerful LST? First of all PT is significantly powerful than LST in above-mentioned frequency band while LST is the most powerful near

0.5 – 1 day periodicity. Secondly the failure time t_n is depend on energy of seismic event and t_n = 1 – 10 years for magnitude 3 < M < 5 (Sadovsky, Pisarenko, 1985).

Thus preparation time t_n for weak earthquakes coincides with frequency band of PT induced stress variations. So it is intuitively obvious that LST are added to stress accumulation process in fault zone as powerful high-frequency noise while PT acts as systematic, nearly synchronous component for preparation of weak earthquakes.

The objective of this work is to estimate PT triggering of seismicity by using of earthquake focal mechanism from CMT catalogue (http://www.globalcmt.org/CMTfiles.html).

STRAIN AND STRESS EXCITED BY POLE TIDE

Centrifugal polar motion perturbation in the potential ΔU (Wahr, 1985) is equal:

$$\Delta U(r,\lambda,\theta) = -0.5(\Omega r)^2 \sin 2\theta (X\cos\lambda - Y\sin\lambda),$$

where Ω = 7 292 115×10^{-11} rad s^{-1} – the mean angular velocity of rotation of the Earth, r – geocentric distance to the station, λ, θ – longitude and colatitude (90º – φ) of the station, $X(t)$ и $Y(t)$ – polarr motion coordinates (EOP C04, http://hpiers.obspm.fr/eop-pc/) after removing of mean polar motion.Corresponding displacement of any point on the Earth's surface is equal (IERS conventions, 2003):

$$S_r = \frac{h}{g}\Delta U = -\frac{h}{2g}(\Omega r)^2[\sin 2\theta (X\cos\lambda - Y\sin\lambda)]$$

$$S_\theta = \frac{l}{g}\partial_\theta \Delta U = -\frac{l}{g}(\Omega r)^2[\cos 2\theta (X\cos\lambda - Y\sin\lambda)]$$

$$S_\lambda = \frac{l}{g\sin\theta}\partial_\lambda \Delta U = \frac{l}{g}(\Omega r)^2[\cos\theta (X\sin\lambda + Y\cos\lambda)],$$

where h = 0.60267, l = 0.0836 – Love numbers for PT frequency band. Positive displacement is upwards, south and east and don't exceed 25 and 7 mm for vertical and horizontal displacement, respectively.

The strain tensor elements are the partial derivatives of displacements:

$$\varepsilon_{rr} = \partial_r S_r = -h\frac{\Omega^2 r}{g}[\sin 2\theta (X\cos\lambda - Y\sin\lambda)]$$

$$\varepsilon_{\theta\theta} = (\partial_\theta S_\theta + S_r)/r = (2l - h/2)\frac{\Omega^2 r}{g}[\sin 2\theta (X\cos\lambda - Y\sin\lambda)]$$

$$\varepsilon_{\lambda\lambda} = (\partial_\lambda S_\lambda/\sin\theta + S_\theta ctg\theta + S_r)/r = (l - h/2)\frac{\Omega^2 r}{g}[\sin 2\theta (X\cos\lambda - Y\sin\lambda)]$$

$$\varepsilon_{\theta\lambda} = (\partial_\lambda S_\theta/\sin\theta - S_\lambda ctg\theta + \partial_\theta S_\lambda)/2r = -l\frac{\Omega^2 r}{g}[\sin\theta (X\sin\lambda + Y\cos\lambda)].$$

Positive ε_{ii} are tension, positive $\varepsilon_{\theta\lambda}$ – right-hand shift. In view of free surface boundary condition (Melchior, 1978) $\tau_{rr} = \tau_{r\theta} = \tau_{r\lambda} = 0$, therefore stress tensor elements are:

$$\tau_{\theta\theta} = 2\mu\varepsilon_{\theta\theta} + \Lambda\Sigma$$

$$\tau_{\lambda\lambda} = 2\mu\varepsilon_{\lambda\lambda} + \Lambda\Sigma$$

$$\tau_{\theta\lambda} = \mu\varepsilon_{\theta\lambda},$$

where $\Sigma = \varepsilon_{rr} + \varepsilon_{\theta\theta} + \varepsilon_{\lambda\lambda}$ – dilatation, $\mu(d)$ - shear modulus, $\Lambda(d)$ – elastic modulus of the Earth according PREM (Dziewonski, Anderson, 1981), d – depth of Earth's layer. Taking into account the displacement value restrictions, limitations for stress tensor elements are the next: $|\tau_{\theta\theta}| < 0.9$, $|\tau_{\lambda\lambda}| \le 0.9$, $|\tau_{\theta\lambda}| \le 0.1$ kPa.

Hence normal and shear stresses are (Zhu P., 2013):

$$\sigma_n^0 = \tau_{\theta\theta}\cos^2\alpha + \tau_{\lambda\lambda}\sin^2\alpha + \tau_{\theta\lambda}\sin 2\alpha$$

$$\tau_s^0 = 0.5(\tau_{\lambda\lambda} - \tau_{\theta\theta})\sin 2\alpha + \tau_{\theta\lambda}\cos 2\alpha.$$

At last for free oriented fault these stresses are:

$$\sigma_n = \sigma_n^0 \sin^2 \delta$$
$$\tau_s = \tau_s^0 \sin\delta\cos\psi + 0.5\sigma_n^0 \sin 2\delta \sin\psi, \qquad (*)$$

where α, δ, ψ – strike, dip and rake angles of earthquake fault plane. Fig. 2 demonstrates the common view of coordinate and time dependences of PT induced stresses.

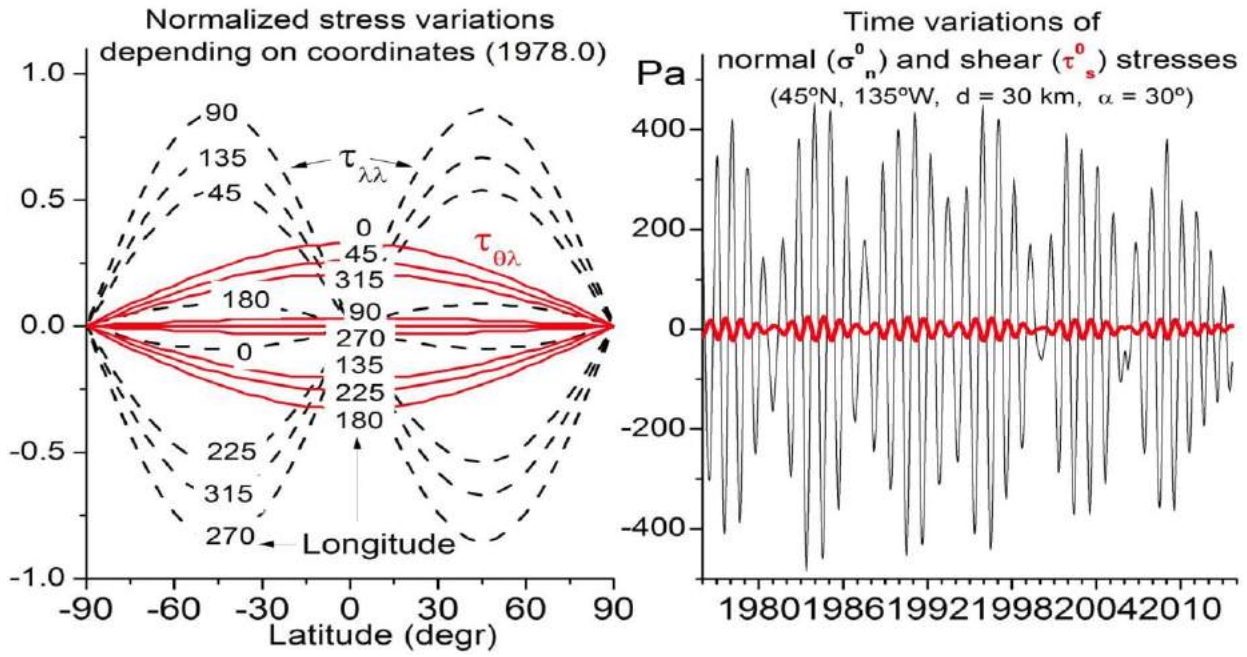

Figure 2. Coordinate ((left) and time (right) dependences of PT induced stresses.

DATA AND METHOD

There were used 32264 seismic events from CMT (1976-2014) to search the trace of PT in seismicity after declustering for strong earthquakes with Mw > 7.2 as CMT is full only for M > 5.2. The modified window algorithm of (Uhrhammer, 1986) was used for declustering: $\Delta L(km) = 1.2exp(0.8M_W - 1.0)$ for spatial distribution of aftershocks and $\Delta t(days) = 1.2\exp(0.8M_W - 2.9)$ for temporal one with 1.2 year Δt limitation. The fig.3 shows the PT generated shear τ_s and normal σ_n stresses for CMT (points) against background of pole variations (X, Y).

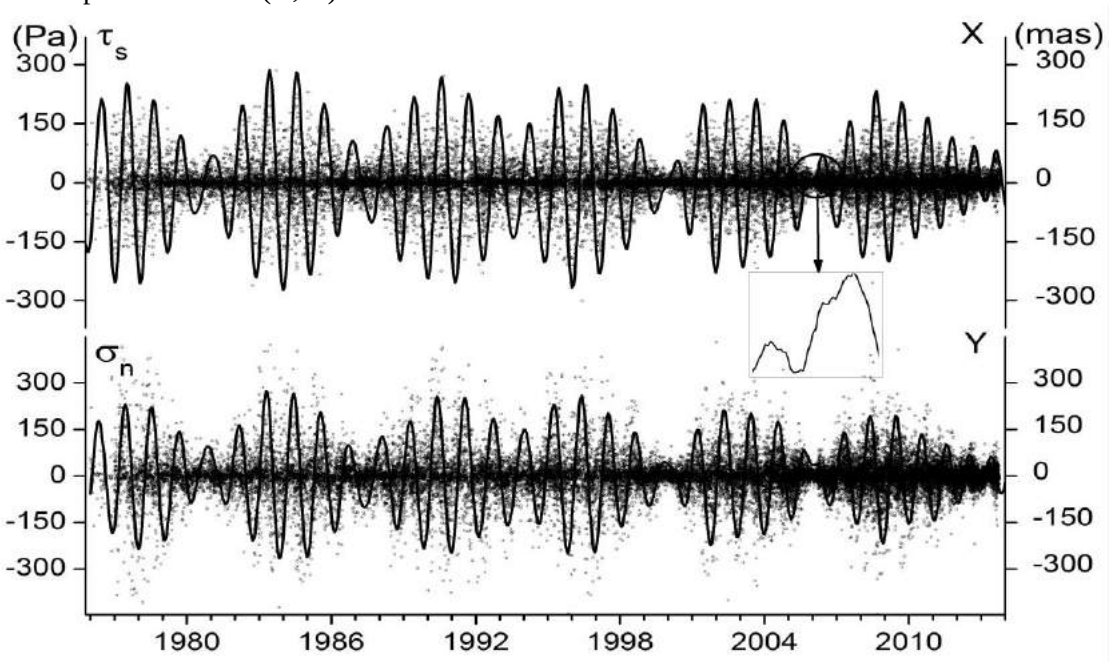

Figure 3. PT induced shear τ_s (up) and normal σ_n (bottom) stresses (points, in Pa) are shown against a background of coordinate variations of polar motion (X, Y in millisecond of arc, mas).

It is obvious that approximately 90% of seismic events are indifferent to the coordinate variations of the Pole and hence to the corresponding stress variations. The rest of events (~10%) repeat time variations of the Pole. It is remarkable that ~ 10% events in CMT have magnitude $M_w < 5.1$. What are these earthquakes? This question is resolved by study of shear stress distribution for various kind of earthquake fault plane.

Phases β_i of σ_n and τ_s stresses were estimated for each earthquake as a part between its previous and following max/min values in each earthquake coordinate point. Time span between these extrema is considered as period of PT. There were used period estimations as between max-to-max (max) as between min-to-min (min) values.

The coordinates of the Pole (X,Y) are the real-time monitoring values and so they have some noise variations especially in time of its amplitude damping (less 100 mas). This leads to additional extrema as it can be seen in the fig.3 inset. In this connection coordinates (X,Y) were high-frequency filtered and then were interpolated with 0.02 year interval. That ensures the 5º – 6º measurement accuracy for β_i. The reduced data without damping time span (r) were used separately for more precise estimation of β_i.

The number of earthquakes n_k was counted in 30º phase boxes for next faulting type of earthquakes: normal-slip (-120º < ψ < -60º), thrust-slip (60º < ψ < 120º), strike-slip (0º < |ψ| < 30º, 150º < |ψ| < 180º) and the rest – oblique strike-slip. The total number of earthquakes for these samples is $N_\psi = \sum_{k=1}^{12} n_k$. Schuster (1897) and χ^2 statistic tests were used for assessment of significance of phase concentration near some particular phase. Null hypothesis on random distribution of phase is rejected if probability $p_S = \exp(-R^2 / N) \le 0.05$ for Schuster and $\chi^2 > \chi^2_{0.95} = 18.307$ for χ^2 statistic tests, where $C = \sum_{i=1}^{N_\psi} \cos\beta_i$, $S = \sum_{i=1}^{N_\psi} \sin\beta_i$ and $R^2 = C^2 + S^2$. The values $\cos\bar{\beta} = C/R$, $\sin\bar{\beta} = S/R$ allows to assess the most reliable mean $\bar{\beta}$.

RESULTS AND CONCLUSIONS

As it can be seen from tabl. 1 PT induced stresses has an influence on seismic intensity with 95% confidence level only for thrust-slip earthquakes with magnitude $M_w < 5.5$. Other fault types of earthquakes are indifferent to PT influence according to used statistic. The study of depth distribution is complicated for insufficient data of weak earthquakes in CMT.

Tabl. 1. Reliability assessment of PT induced shear stress on exciting of earthquake with d < 70 km

Magnitude	4.0 – 5.0				5.0 – 5.5			5.5 – 6.0		
Fault type	N_ψ	p_s(%)	χ^2	$\bar{\beta}^\circ$	N_ψ	p_s(%)	χ^2	N_ψ	p_s(%)	χ^2
Normal	586	42.4	9.4	359	1457	60.3	10.5	440	22.3	9.3
(r)	317	86.3	10.8	14	1006	37.6	14.8	341	23.8	11.9
Thrust	535	**2.9**	**18.2**	152	2890	**2.6**	16.6	1472	68.1	6.3
(r)	282	**1.5**	**20.0**	154	1976	**2.2**	15.8	1025	55.3	10.1
Strike-slip	816	78.2	12.5	90	3502	68.6	9.1	1666	17.7	14.0
(r)	434	53.1	11.9	109	2307	92.3	7.1	1329	21.8	16.6
Oblique strike	488	31.1	17.1	172	2222	90.8	13.8	769	54.0	10.0
(r)	251	13.6	11.4	89	1580	61.1	10.5	616	17.5	12.0
Total	2425	17.8	11.4	349	10071	13.3	13.4	4347	95.9	11.3

The frequency distribution of phases β_i are shown in fig.4. It is evident that there are two but not equal maxima of PT influence on the thrust type of earthquakes. This result could explain 0.6-year periodicity in seismic intensity.

The PT influence on seismicity when Pole variation damping (less 100 mas) becomes actually noise as it was checked by independent estimations of Schuster and χ^2 statistics. Therefore the PT is the most probable reason of 6 – 7 years periodicity in seismic intensity.

So we may conclude:

- Pole tide influence on seismic intensity is revealed only for thrust-slip type of earthquake with 95% reliability.

- This influence falls with rise of magnitude and vanishes for $M_W > 5.5$.
- There are two maxima of this influence approximately coinciding with both extreme of shear stresses. This result can explain 0.6-year periodicity in seismic intensity.
- Pole tide influence on seismic intensity for time of Pole wobble damping (less 100 mas) is actually noise. This could explains 6 – 7-year periodicity in seismic process.
- Synphasing of shear and normal stresses for thrust-slip earthquakes (see equation (*) by ψ = 90º) could explain the exciting of these earthquakes by weak PT induced stress variations.

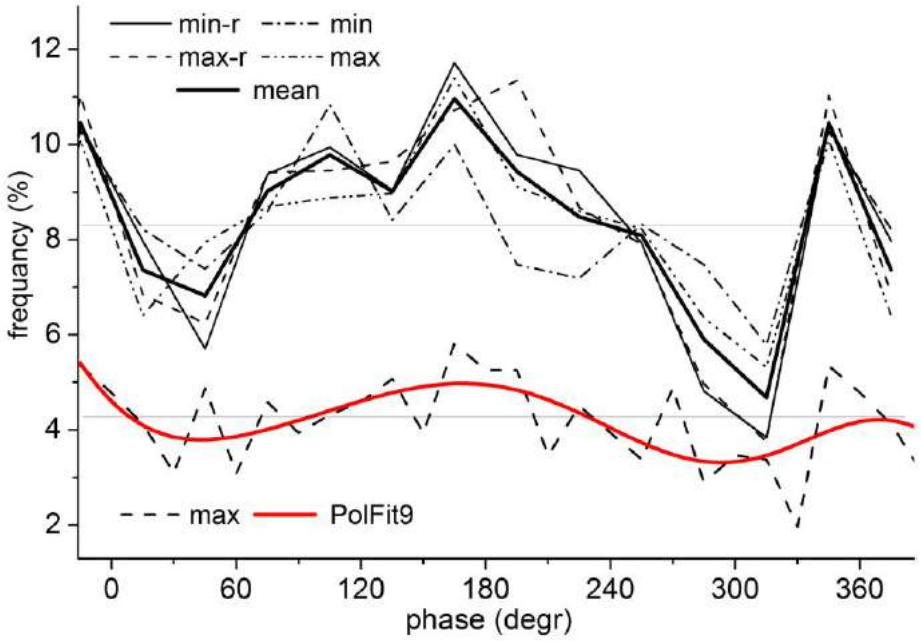

Fig. 4. (Up) - Frequency distribution of shear stress phases of thrust earthquakes for 30º phase boxes (k=12). Straight line corresponds to even distribution of phase (8.3%). The convergence of these plots gives view on the level of phase determination error. (Bottom) – The same for 15º phase boxes (k=24). Line of even distribution of phase is equal 4.15%.

REFERENCES

Dziewonski, A. M., D. L. Anderson (1981), Preliminary reference Earth model, *Phys. Earth Planet. Inter*. 25, pp. 297-356.

Gamburtsev, A.G., Kondorskaya N.V., Oleinik O.V., Khrometskaya E.A., Frantsuzova V.I., Yudakhin F.N. (2004), Seismicity rhythms of the Earth, *Izvestiya. Physics of the Solid Earth*, 5, pp. 441–453.

Gorshkov, V., M. Vorotkov (2012), On the pole tide excitation of seismicity, *Proceedings of the 9-th International Conference "Problems of Geocosmos"*, Editors: Troyan V. N., V. S. Semenov, M. V. Kubyshkina, SPb, pp.142-145.

IERS conventions (2003), *IERS Technical Note*, № 32. 2004. Denis D. McCarthy, Gerard Petit (eds), Frankfurt am Main. 127 p.

Levin, B., E. Sasorova (2002), On the 6-Year Tsunami Periodicity in the Pacific. *Izvestiya, Physics of the Solid Earth*, 38, 12, pp. 1030-1040.

Lyubushin, A.A., V.F. Pisarenko, V.V. Ruzich, V.Yu. Buddo (1998), A new method for identifying seismicity periodicities, *Volcanology and Seismology*, 20, pp. 73-89.

Mardia, K.V. (1972), *Statistics of directional data.* Academic press. London and NY, 240 p.

Melchior, P. (1978), *The tides of the planet Earth*. Pergamon press. NY, 608 p.

Sadovsky, M.A., V.F. Pisarenko (1991), *Seismic process and the block medium*, 96 pp., Nauka, Moscow.

Schuster, A. (1897), On lunar and solar periodicities of earthquake, *Proc. R. Soc. London*, 61, pp. 455--465.

Uhrhammer, R. (1986), Characteristic of Northern and Central California seismicity, 57(1), 21.9.

Wahr, J.M, (1985), Deformation Induced by Polar Motion, *J. Geophys.Res.*, 90, pp. 9363-9368.

Shen Zheng-Kang, Qingliang Wang, Roland Bürgmann, Yongge Wan and Jieyuan Ning (2007), Pole-Tide Modulation of Slow Slip Events at Circum-Pacific Subduction Zones, *Geoph. J. Int.*, 53, 3, pp. 617-621.

Zhu, P.P. (2013), Normal and shear stresses acting on arbitrarily oriented faults, earthquake energy, crustal GPE change and the coefficient of friction, *J. Seismol*., 17:985-1000, doi: 10.1007/s10950-013-9367-2.

WAVELET TRANSFORM AS A TOOL FOR PROCESSING AND ANALYSIS OF SEISMOGRAMS

V.V. Gravirov[1], K.V. Kislov[2], F.E. Vinberg[2]

[1]Institute of Earthquake Prediction Theory and Mathematical Geophysics, Russian Academy of Science (IEPT RAS), Moscow, 117997, Russia, e-mail: gravirov@rambler.ru;

[2]Institute of Earthquake Prediction Theory and Mathematical Geophysics, Russian Academy of Science (IEPT RAS), Moscow, Russia.

Abstract. One of the current tasks of seismology is the improvement of the automated processing of seismic records on a time scale as close to reality. Along with the traditional methods of filtration and processing, using wavelet transform allows to simultaneously conduct any necessary filtering, and easily select a different phase of the input signal. The entire process of filtering and analysis can be represented as three-dimensional graphic images, which greatly simplifies the process of interpretation of seismograms. Since this method does not require large computational effort there is a possibility of its realization in the form of real-time algorithms.

Currently one of the seismology urgent tasks is the automated processing of seismic records in a real time scale. Specific requirements for these systems are presented in the registration and processing of poor and very noisy seismic signals. Obviously, in this case, that pre-filtering is indispensable. Unfortunately, widely used methods for filtration and allocation of seismic signals as the STA / LTA, LPF, HPF, etc. do not lead to satisfactory results. During the research it was determined that the wavelet transform, in most cases to provide the necessary filtering.

The wavelet transform method has advantages that it is well frequency-time localized, the results can easily be visualized, added to the fact that it is possible to investigate not only stationary signals but also irregular, fractal series having a hierarchical structure. In contrast to the filtering technique using the Fourier transform, the wavelet transform provides better representations of seismic wave onsets (which can be considered as a problem in the analysis of transient signals) and, secondly, requires a computation time for signal processing smaller by a factor of a few times.

With regard to the Wavelet decomposition problem of signal filtering can be implemented directly by removing detailing coefficients of the corresponding levels. However, it should be noted that wavelets have in this respect more opportunities.

Noise components, and especially large accidental peaks of signal values can also be seen as a set of local features of the signal. By setting a threshold level for them, and thereon by cutting the detail coefficients can not only reduce the noise level, but also to set threshold limits at multiple levels of decomposition according to the specific characteristics of noise and signals for various types of wavelets.

This allows to realize the adaptive system of noise reduction signals, depending on their characteristics. Also the choice of analyzing wavelet is largely determined by the type of information to be extracted from the signal. Taking into account the characteristics of different wavelets in the time and frequency domain can be detected in the analyzed signals certain properties and features that are imperceptible on the seismograms, especially in the presence of strong noise (see Fig. 1).

The choice of the wavelet decomposition and depth depends on the properties of a specific signal. Smoother wavelets provide a smooth approximation of the signal, and vice versa, "short" wavelets better track the peaks of the approximated function. Depth decomposition affects the scale of screening details. By increasing the depth of the decomposition model will subtract the noise level increasing. In this case it can be smoothed not only noise, but also some local features of the signal. In addition to the use of wavelet

processing allows to track and highlight critical points of change the spectral structure of the signal (see Fig. 2).

Let us consider the use of wavelet transformation in the example of low-frequency component separation from nonstationary signal.

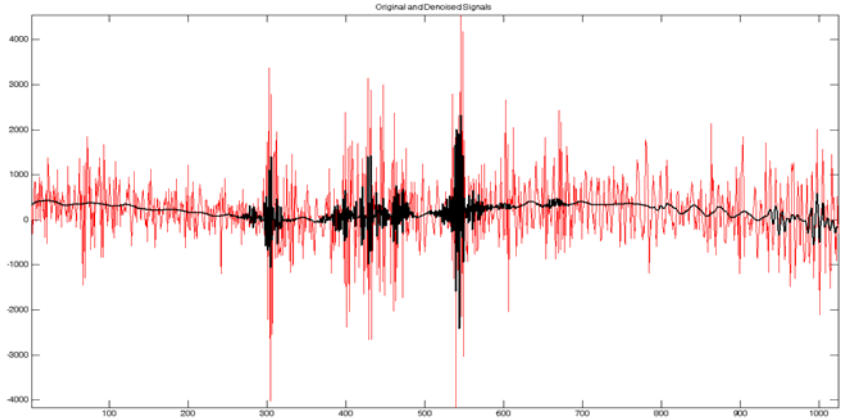

Fig.1.The original process (red) and that with noise eliminated (black).

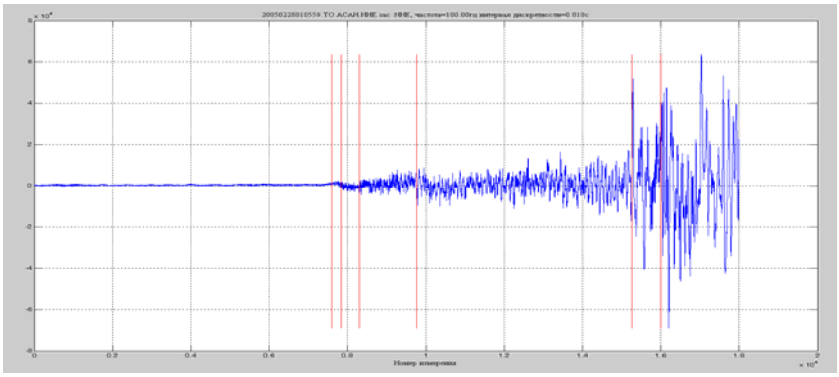

Fig.2. Labeling (red) characteristic places changes the spectral structure of the signal.

The model of a noise-contaminated signal is usually assumed to be additive: $s(n) = f(n)+\eta(n)$ with a constant step over the argument n, where $f(n)$ is the useful information-rich component and $\eta(n)$ the noise signal. The noise signal is usually assumed to be white noise at a prescribed level with zero mean. The procedure of identifying the low frequency component is done using orthogonal wavelets and involves the following steps:

- Wavelet decomposition of the signal $s(n)$ down to level N. The value N is determined by the frequency-dependent spectrum of the information part $f(n)$, which it is desired to leave in the series of fitting coefficients. The type and order of the wavelet can significantly affect the thoroughness with which the noise will be removed from the signal, depending both on the shape of $f(n)$ and on the correlation characteristics of the noise.
- Specifying the type and threshold levels of noise removal based on known prior information on noise or judging by certain criteria of the noise in the input signal. The threshold levels of noise removal may be flexible (depending on the number of decomposition level) or rigid (global).
- Modifying the coefficients which specify the detail available in the wavelet decomposition in accordance with the removal conditions specified.
- Reconstruction of $f(n)$ from the fitting coefficients and the modified detailing coefficients.

A continuous wavelet transform is described by the following relation:

$$CWT_X^{\psi}(t,s) = \psi(t,s) = \frac{1}{\sqrt{s}} \int x(t) * \psi\left(\frac{t-t'}{s}\right) dt',$$

where $x(t)$ being the signal and $\psi(t)$ the window function.

The wavelet decomposition of a signal must, by analogy with the Fourier transformation, be such as to ensure complete informational equivalence of the new signal representation (the wavelet spectrum) and the temporal (dynamic, coordinate) representation, accordingly, to ensure uniqueness for signal decomposition and for signal reconstruction from wavelet spectra. This is however possible only by using orthogonal basis functions, which include among others also a rather limited number of orthogonal and biorthogonal wavelets. Unlike the Fourier transform, the wavelet transform ensures a two-dimensional imaging of the signal under study, the frequency and the time being treated as independent variables. As a result, we are enabled to examine the properties of a signal both in a physical (time) and a scale (frequency) spaces.

The noise component of a signal is mostly reflected in the detailing coefficients, consequently, it is these coefficients which are being affected by the processing.

The standard method for noise suppression is the elimination of noise components from the spectrum of the signal. In application to wavelet decomposition this can be realized in a straightforward manner by removing the detailing coefficients of high frequency levels (see Fig. 3).

This task was solved in the MATLAB programming shell. We used the entropy-log-energy criterion to choose the optimal wavelet decomposition.

The entropy of the original signal is at the maximum because of noise contamination. As the level of wavelet decomposition increases, the entropy diminishes down to the minimum value corresponding to the optimal level of wavelet decomposition of the original signal. Noise was eliminated by the Birge-Massart method: a threshold value was determined for the ***K*** criterion to be applied to the detailing coefficients. The coefficient values below the threshold were set equal to zero and the value of ***K*** was subtracted from the values of the remaining coefficients. The optimal value of the ***K*** test was selected by the minimum entropy-log-energy principle. The choice of the optimal wavelet which produced the best level of wavelet elimination of noise was by the criterion of the ratio between the entropy of the original signal and that with noise eliminated.

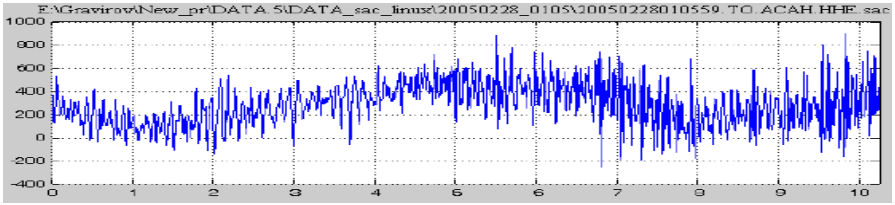

Fig.3.1. The original signal.

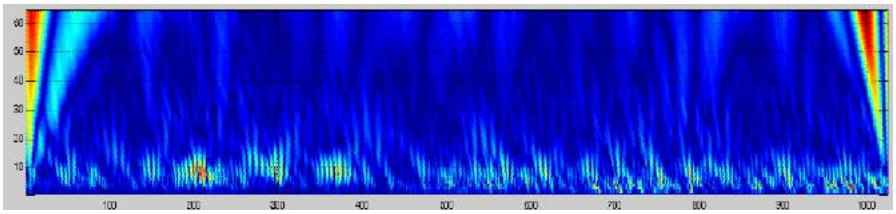

Fig.3.2. The wavelet representation (db4 of) the original signal.

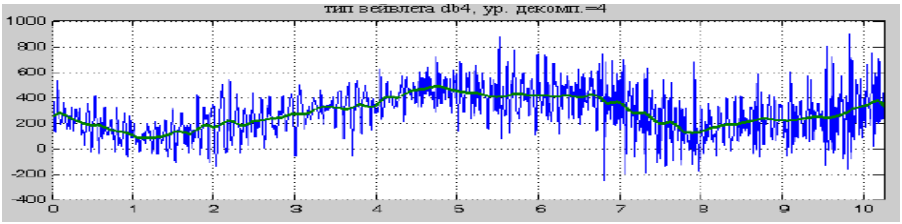

Fig.3.3. The original signal with identified low frequency component.

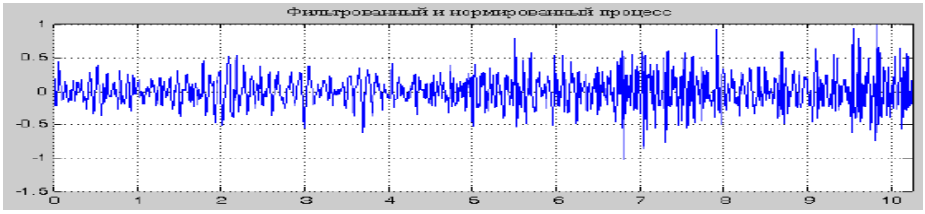

Fig.3.4. Signal with removed low frequency component.

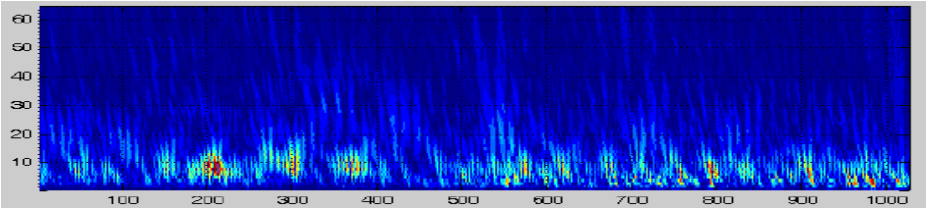

Fig.3.5. The wavelet representation (db4) signal with removed low frequency component.

CONCLUSION

On the basis of given example of seismic signal low-pass filtering using wavelet transform technology is shown that this technology can be successfully used for automated processing and analysis in seismology. Necessary to note that the advantages of this method are relatively small (in comparison with the technology based on the Fourier transform) the computational computer time, so it takes advantage to use widespread computing systems. Also it essentially allows to realize adaptive noise reduction systems, depending on signal and noise characteristics. And taking into account the characteristics of used wavelets in the time and frequency domain can be detected in the analyzed signals certain properties and features that are not visible on the original seismograms, especially in the presence of strong noise.

REFERENCES

Baranov, S.V. (2007) The uses of the wavelet transform for automatic detection of seismic signals. *Fizika Zemli*. No.2. pp. 83-94.

Dunaeva K.A. and Sagaidachnaya O.M. (2008) A technique of using the discrete wavelet transform to suppress unwanted waves on seismic records, in: *The Tenth Intern. Sci. Conf., GEOMODEL-2008, 21-26 September 2008*, Gelendzhik, Russia.

D'yakonov V. and Abramenkova I. (2002) *The MATLAB Processing of Signals and Images.* A special handbook, St. Petersburg.

Gravirov V.V., Kislov K.V. (2009) The First Results of Testing Methods and Algorithms for Automatic Real Time Identification of Waveforms Introduction from Local Earthquakes in Increased Level of Man-induced Noises for the Purposes of Ultra-short-term Warning about an Occurred Earthquake, *Eos Trans. AGU, 90(52), Fall Meet. Suppl.*, Abstract S13A-1731.

Horiuchi S., Negishi H., Kamimura A., Iwata T. &Yamamoto S. (2003) An Automatic Processing System of Hi-net Wave-form Data for the Earthquake Alarm Information. *New Technologies for Urban Safety of Mega Cities in Asia; Proc. of 2-nd intern. symp.*, Tokyo, 30-31 October 2003.: Univ. Tokyo.

Kulesh M.A. (2008) *Developing Methods for Time-Frequency Analysis of Polarization and Dispersion in Wave Processes*, Extended abstract, Dissert. Doct. Phys.-Math. Sci., Perm'.

Kushnir A.F., Nikiforov I.V., and Savin I.V. (1983) Statistical adaptive algorithms for automatic detection of seismic signals, I. The one-dimensional case, in Earthquake Prediction and Studies in the Earth's Structure (*Computational Seismology 15*), Moscow: Nauka, pp. 134-143.

Stolnits E., De Rose T., and Salezin D. (2002) *Wavelets in Computer Graphics. Theory and Applications*, Izhevsk.

Vityazev V.V. (2001) *Wavelet Analysis of Time Series*, St. Petersburg University.

Yakovlev A.N. (2002) Applications of the wavelet transform for the processing of hydroacoustic signals, in: *Proc. Sixth Intern. Sci. Tech. Conf. Urgent Problems in Electronic Design-2002*, Novosibirsk, Vol. 4.

NUMERICAL SIMULATION OF THE RESTORATION OF THE LOCAL INHOMOGENEITIES BY THE APPROACHES BASED ON THE DIFFRACTION TOMOGRAPHY METHOD

Yurii Kiselev[1], Vladimir Troyan[2]

[1]St.Petersburg University, St.Petersburg, 198504, Russia, e-mail: kiselev@jk6907.spb.edu;
[2]St.Petersburg University, St.Petersburg, 198504, Russia, email: vtroyan@hq.pu.ru

Abstract. Geophysical diffraction tomography is an imaging technique that makes use of a large volume of the input data (recorded traces) to produce the image of underground medium parameters with a high spatial resolution. Diffraction tomography with a sounding by elastic waves and with the help of the first-order Born approximation leads to the satisfactory images for not too weak inhomogeneities with the sizes comparable with the wavelength. In this case the relative error of restoration can be approximately equal to a ratio of the desired parameter perturbation relatively to a value of such parameter for the reference medium (a contrast of inhomogeneity). We consider the results of numerical simulation on restoration of local inhomogeneities with the sizes smaller or approximately equal to the wavelength of the sounding signal and with the contrast of shear modulus not greater than 0.5 relatively to the reference medium. The results of restoration by the diffraction tomography method are considered together with two approaches based on the diffraction tomography method and also with restoration using the reverse time migration with the imaging principle.

Introduction

Geophysical diffraction tomography is an imaging technique [2] that makes use of a large volume of the input data (recorded traces) to produce the image of underground medium parameters with a high spatial resolution. The seismic waves as a sounding signal may bring an information about the seismic parameters of underground medium. The inverse problem on restoration of such parameters with the help of seismic sounding signals is nonlinear one. Linearization of the inverse problem, for example, with the use of the first-order Born approximation allows to obtain the solution at enough small computational burden, but it brings the limitations in restoration of the medium parameters. We consider the restoration of medium parameters by the two approaches based on the diffraction tomography method with the help of the first-order Born approximation [4], [5] and also with the use of the reverse time migration based on the Claerbout imaging principle [1]. The image restoration is implemented in a time domain with a finite shape of the sounding signal. The desired parameters are found by the algebraic method with an appropriate regularization, which is based on a priori information about smoothness of the desired parameter as a spatial function and on a priori information about possible location and sizes of the target object [3].

We consider the results of numerical simulation on restoration of local inhomogeneities with the sizes approximately equal to the wavelength of sounding signal and with the contrast of shear modulus not greater than 0.5.

The restoration using diffraction tomography method is implemented with the help of the iteration procedures with two steps. At the each step of the iterative procedure the direct problem (2-D SH problem) is solved by the finite difference method to calculate the difference field between the "experimental" data and the model data.

Basic formulas and algorithms

The source $\hat{\boldsymbol{f}} \equiv \hat{\boldsymbol{f}}(\boldsymbol{x},t) \equiv \hat{f}(\boldsymbol{x},t)\boldsymbol{e}_2$, located in the point ($x = x_s$, $z = z_s$) of Cartesian system of coordinates $(x,y,z;\boldsymbol{e}_1,\boldsymbol{e}_2,\boldsymbol{e}_3)$, produces the wave field $\boldsymbol{u} \equiv \boldsymbol{u}(x,z,t) \equiv u(\boldsymbol{x},t)\boldsymbol{e}_2$ which satisfies the equation

$$\mu\Delta u + (\nabla\mu\cdot\nabla u) + \hat{f} = \rho\frac{\partial^2 u}{\partial t^2} \tag{1}$$

where μ is the Lame parameter, ρ is mass density.
The velocity of the shear (v_s) waves, expressed through the quantities μ and ρ, read as

$$v_s = \sqrt{\mu/\rho}. \tag{2}$$

We introduce the differences $\delta\mu = \mu - \mu_{\rm rf}$ and $\delta\rho = \rho - \rho_{\rm rf}$ of the values μ, ρ for the unknown medium which are connected with the wave field $u(\boldsymbol{x}, t)$

$$Lu = -\hat{f}, \quad \left(Lu \equiv \mu\Delta u + (\nabla\mu \cdot \nabla u) - \rho\frac{\partial^2 u}{\partial t^2} \right) \tag{3}$$

and the values $\mu_{\rm rf}(\boldsymbol{x})$, $\rho_{\rm rf}(\boldsymbol{x})$ for the known, reference (rf) medium for which the wave field is $u_{\rm rf}(\boldsymbol{x}, t)$

$$L_{\rm rf}u_{\rm rf} = -\hat{f}, \quad \left(L_{\rm rf}u_{\rm rf} \equiv \mu_{\rm rf}\Delta u_{\rm rf} + (\nabla\mu_{\rm rf} \cdot \nabla u_{\rm rf}) - \rho_{\rm rf}\frac{\partial^2 u_{\rm rf}}{\partial t^2} \right) \tag{4}$$

Assuming $\delta\mu$ and $\delta\rho$ small, we can write

$$L_{\rm rf}\delta u \approx -\delta L u_{\rm rf}, \tag{5}$$

where $\delta u = u - u_{\rm rf}$ is the difference field. The right hand side of (5)

$$\delta L u_{\rm rf} = (\nabla \cdot \delta\mu\nabla u_{\rm rf}) - \delta\rho\frac{\partial^2 u_{\rm rf}}{\partial t^2} \tag{6}$$

can be considered as a source of that field.

We shall represent the components of the difference field δu from (5) at the observation point of $\boldsymbol{x} = \boldsymbol{x}_r$ as following

$$\delta u(\boldsymbol{x}_s, \boldsymbol{x}_r, t) = \int_S \int_0^\infty u_{out}(\boldsymbol{x}, \boldsymbol{x}_r, t-\tau) \cdot \delta L u_{\rm in}(\boldsymbol{x}, \boldsymbol{x}_s, \tau) d\tau d\boldsymbol{x}, \tag{7}$$

where S is the region of restoration; $u_{\rm in} \equiv u_{in}(\boldsymbol{x}, \boldsymbol{x}_s, t)$ and $u_{out} \equiv u_{\rm out}(\boldsymbol{x}, \boldsymbol{x}_r, t)$ are the wave fields for the appropriate sources [4].

After introducing the tomography functionals $p_\rho(\boldsymbol{x}, \boldsymbol{x_r}, \boldsymbol{x}_s, t)$, $p_\mu(\boldsymbol{x}, \boldsymbol{x_s}, \boldsymbol{x}_r, t)$ [4]

$$p_\rho(\boldsymbol{x},\, \boldsymbol{x}_r,\, \boldsymbol{x}_s, t) = -\int_0^\infty u_{out}(\boldsymbol{x},\, \boldsymbol{x}_r, t-\tau)\frac{\partial^2}{\partial\tau^2}u_{\rm in}(\boldsymbol{x},\, \boldsymbol{x}_s, \tau)d\tau \tag{8}$$

$$p_\mu(\boldsymbol{x},\, \boldsymbol{x}_s,\, \boldsymbol{x}_r, t) = -\int_0^\infty (\nabla\varphi_{out}(\boldsymbol{x},\, \boldsymbol{x}_r, t-\tau) \cdot \nabla\varphi_{in}(\boldsymbol{x},\, \boldsymbol{x}_s, \tau))\, d\tau, \tag{9}$$

the components of the difference field δu (7) can be written down as

$$\delta u(\boldsymbol{x}_s, \boldsymbol{x}_r, t) = \int_S [\delta\mu(\boldsymbol{x}) p_\mu(\boldsymbol{x}, \boldsymbol{x}_s, \boldsymbol{x}_r, t) + \delta\rho(\boldsymbol{x}) p_\rho(\boldsymbol{x}, \boldsymbol{x}_s, \boldsymbol{x}_r, t)] d\boldsymbol{x}. \tag{10}$$

Using the linear relations between $\delta\rho(\boldsymbol{x})$ and $\delta\mu(\boldsymbol{x})$

$$\delta\rho(\boldsymbol{x}) = c_\rho\delta\mu(\boldsymbol{x}), \quad (c_\rho = const), \tag{11}$$

the equation (10) can be rewritten as

$$\delta u(\boldsymbol{x}_s, \boldsymbol{x}_r, t) \approx \int_S [p_\mu(\boldsymbol{x}, \boldsymbol{x}_s, \boldsymbol{x}_r, t) + c_\rho p_\rho(\boldsymbol{x}, \boldsymbol{x}_s, \boldsymbol{x}_r, t)]\delta\mu(\boldsymbol{x}) d\boldsymbol{x}. \tag{12}$$

After digitization of the equation (12) the system of equations for determination of $\delta\mu$ (vector $\mathbf{d}_\mu$), c_λ and c_ρ can be written as

$$P(c_\rho)\mathbf{d}_\mu = \mathbf{d}_u, \tag{13}$$

where $\mathbf{d}_u$ are the samples of the scattered field. The final version of this system after introducing regularizing terms reads as

$$[P^T(c_\rho)P(c_\rho) + \alpha_1(B_x^T B_x + B_z^T B_z) + +\alpha_2 C^T C + \alpha_3 D^T D]\mathbf{d}_\mu = P^T(c_\rho)\mathbf{d}_u, \tag{14}$$

where α_1, α_2, α_3 are the regularizing coefficients; matrices B_x and B_z are the finite difference images of second partial derivatives with respect to x and z correspondingly; C and D are penalty matrices for non-zero values of $\mathbf{d}_\mu$ correspondingly at boundary and near boundary points of restored region S.

We implement restoration by the solution of the equation (14) with the help of iterative procedure. The next two approaches are based on the equation (14). In the first case the matrix

$$P^T(c_\rho)P(c_\rho) + \alpha_1(B_x^T B_x + B_z^T B_z) + \alpha_2 C^T C + \alpha_3 D^T D \tag{15}$$

is considered as a diagonal one and in the second case this matrix is considered as identity one. Restoration using the reverse time migration is implemented with the help of the Claerbout imaging principle [1]

$$d(\boldsymbol{x}) = \sum_{i=1}^{k} \int_0^T u_{in}^i(\boldsymbol{x}, \boldsymbol{x}_s, t) u_{rt}^i(\boldsymbol{x}, t) dt, \tag{16}$$

where $u_{rt}^i(\boldsymbol{x}, t)$ is the wavefield obtained by the reverse time migration from the free surface and $u_{in}^i(\boldsymbol{x}, t)$ is the source field in the reference medium, k is the number of the sources.

Restoration of inhomogeneities

Numerical simulation is implemented in 2-D case. The direct (SH) problem is solved by the finite difference method. Let us consider the results of numerical simulation on restoration of the local inhomogeneities by the four approaches. The models of inhomogeneities are represented on Fig. 1. The results of restoration of shear modulus μ are represented in Fig. 2–5. The main frequency of the sounding signal is 25 Hz and, consequently, the wavelength in the reference medium with $v_s = \sqrt{(}\mu/\rho) = 1km/s$ is equal to 0.04 km. The restoration of inhomogeneities with the contrast 0.44 Fig. 1ac and -0.44 Fig. 1bd of shear modulus μ (0.2 and -0.25 of v_s) and the sizes 0.25 of the wavelength Fig. 1ab and 0.25 and 1.0 of wavelength Fig. 1cd is implemented using the back scattering data, when the sources and the receivers are located at the observation line which coincides with the Cartesian x-axis and belongs to the free surface. The sources and receivers are located in the points 0.5, 0.7 and 0.9 km. Eight source-receiver pairs are used for the restoration. For the restoration by the reverse time migration six sources are used.

Conclusions

The results of the numerical simulation on restoration of elastic small inhomogeneities or comparable in size with the wavelength inhomogeneities are considered. The restoration is implemented by the four methods: diffraction tomography method, two methods based on the diffraction tomography method, method using reverse time migration with the imaging principle.

The restoration by the diffraction tomography method and approximate method with diagonal matrix from the left hand side of equation (14) give an estimation of the value of the μ perturbation. The restoration using reverse time migration and the approximate method with identity matrix from the left hand side of equation (14) give the location of the inhomogeneity. The accuracy of restoration by the diffraction tomography method can be increased by the additional steps of the iteration procedure.

References

[1] Claervout, J. F., Toward the a unified theory of reflector mapping, *Geophysics*, **36**, 467-481, 1971.

[2] Devaney, A. J., Geophysical diffraction tomography, *IEEE Trans. Geosci. Remote Sensing*, **GE-22**, 3, 1984.

[3] Kiselev, Yu.V., V.N. Troyan, Restoration of Elastic and Velocity Parameters in Diffraction Tomography, *Proc of the International Seminar "Day on Diffraction-99"*, St. Petersburg, Russia, June 1–3, 1999, Faculty of Physics, SPbU,97–97,1999.

[4] Ryzhikov, G.A., V.N. Troyan, *Tomography and inverse sounding problems*, St.Petersburg, St.Petersburg University, 1994.

[5] Kiselev, Yu.V., V.N. Troyan, Statistical Methods of Geophysical Data Processing. World Scientific Publishing Company, 2010.

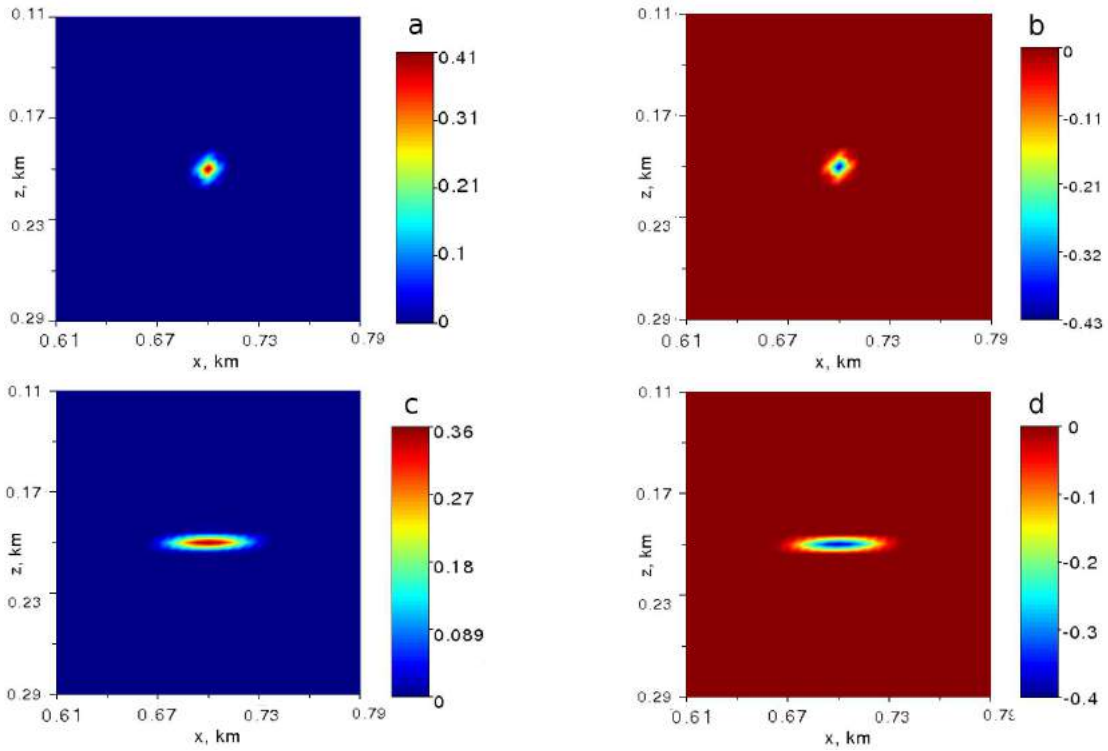

Figure 1: The models with high and low velocity local inhomogeneities with contrast 0.44 of μ relatively to the uniform reference medium.

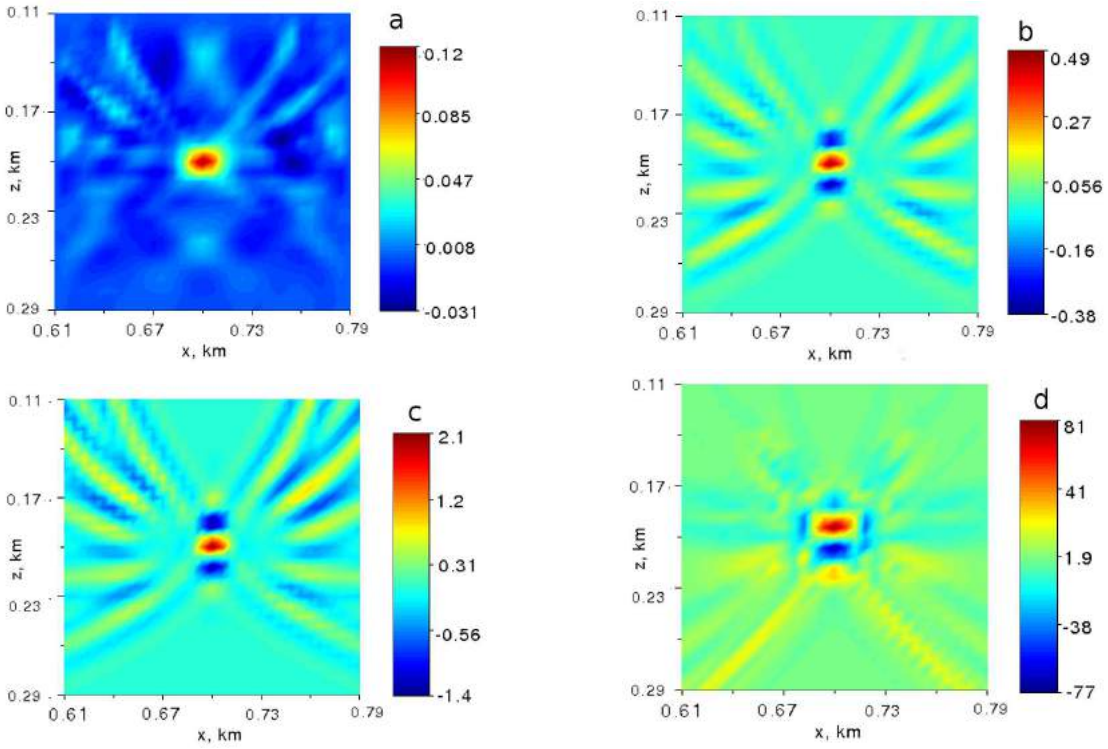

Figure 2: Restoration of high velocity inhomogeneity – Fig. 1a. Restoration by the diffraction tomography method (solution of the system of the linear equations (14)) (a); restoration by the solution of the system of the linear equations (14), if the matrix from the left hand side considered as diagonal one (b) and as identity one (c); restoration by the reverse time migration with the imaging principle (formula (16)).

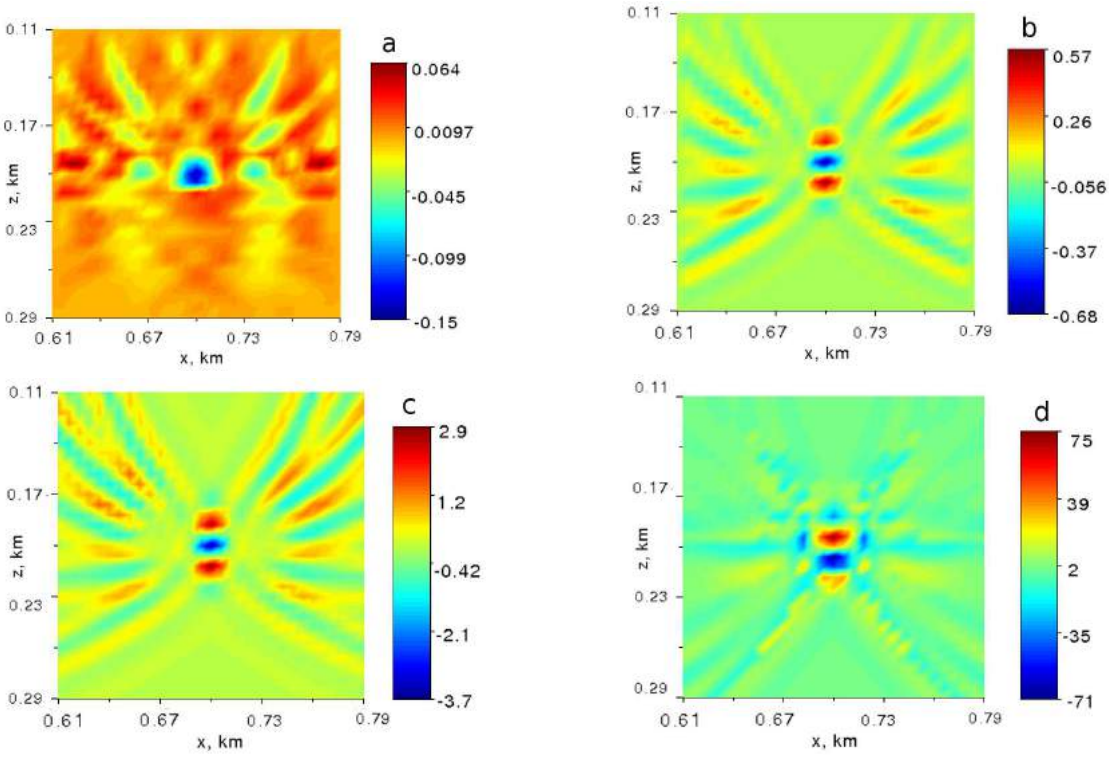

Figure 3: Restoration of high velocity inhomogeneity – Fig. 1b. Notations are the same as in the Fig.2.

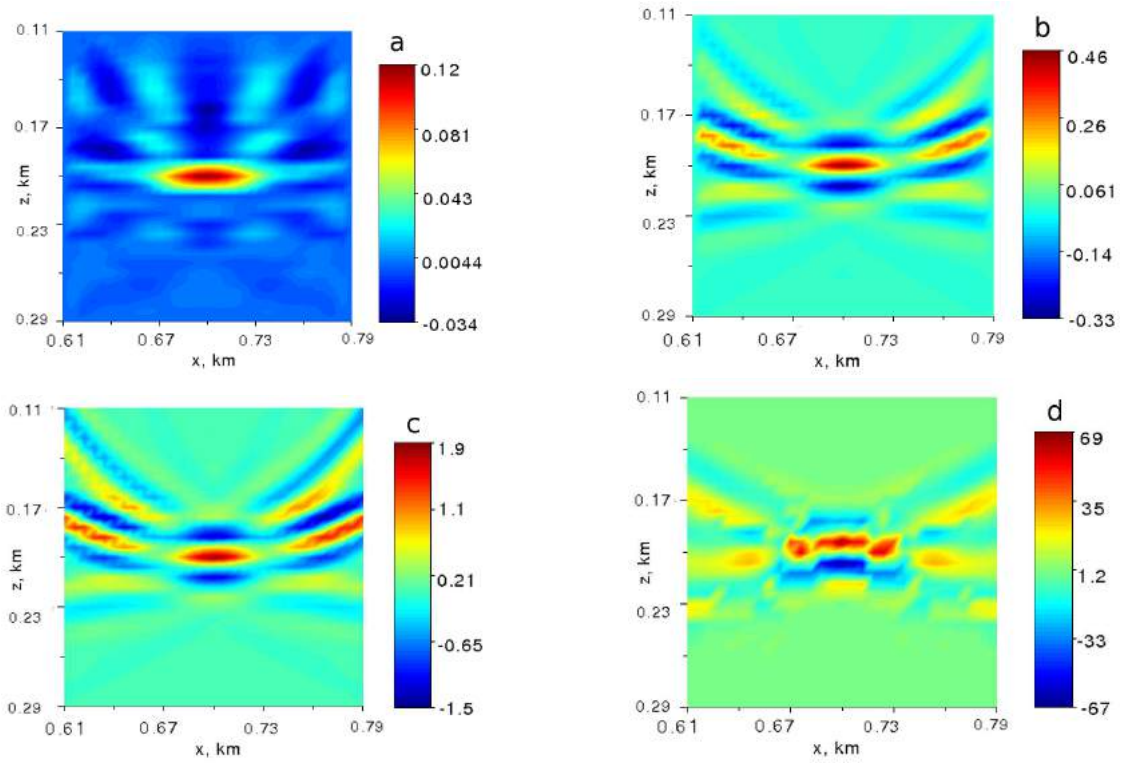

Figure 4: Restoration of high velocity inhomogeneity – Fig. 1c. Notations are the same as in the Fig.2.

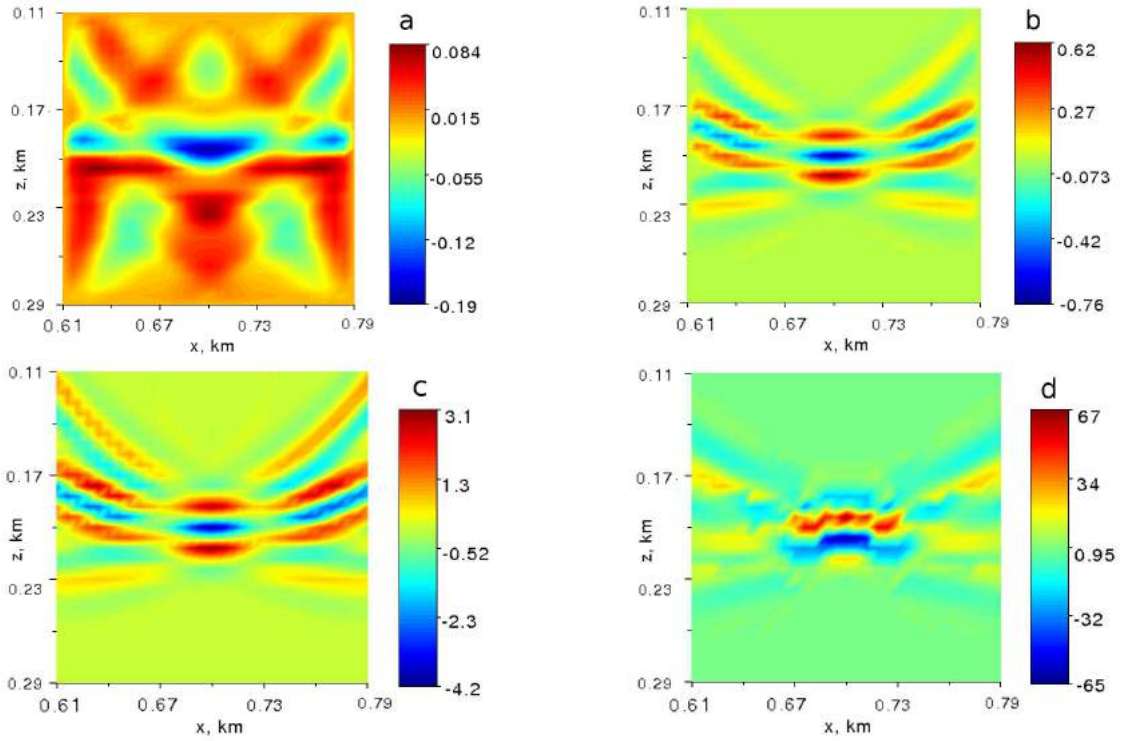

Figure 5: Restoration of high velocity inhomogeneity – Fig. 1d. Notations are the same as in the Fig.2.

MAGNITUDE THRESHOLD REDUCING FOR A NETWORK OF CLOSE LOCATED MOBILE STATIONS

K.V. Kislov, V.V. Gravirov
Institute of Earthquake Prediction Theory and Mathematical Geophysics, Russian Academy of Science (IEPT RAS), Profsoyuznaya str. 84/32 Moscow 117997 Russia, e-mail: kvkislov@yandex.ru

Abstract. It is known that earthquakes of smaller magnitude occur more often. If the magnitude is decreased by 1 unit, the number of earthquakes grows about eight times. Reducing an amplitude threshold of the of registered kinematic components of Earth movements, first, is equivalent to decrease in the density of a network of observation and, secondly, allows to study of oscillations of small amplitudes, to determine their nature and common relations with other seismic and geophysical phenomena, interrelations.

Each seismic sensor is characterized by the radius of events detection of a certain magnitude. Stations of the mobile group have to be in close proximity so that the radii of event detection minimum magnitude intersect. If records of adjacent stations contain appropriate signal (amplitude, spectrum and arrival time), the seismic event is detected. However, the signal can be invisible at a high noise level. In addition, bursts of the noise may take place on neighboring stations simultaneously. We are feeling around for an answer to our difficulty by using an artificial neural network as a signal detector. What is more the artificial neural network will allow classifying seismic events by source type (earthquakes, landslides, nuclear or chemical explosions, collapsing caverns, etc.).

INTRODUCTION

Group of mobile seismic stations (GMSS) are a powerful tool for seismological research. They are essential when you are using non-standard methods of mineral exploration, to search for hydrocarbons, to seismic monitoring, as well as to earthquake prediction and solving engineering-geological problems. Mobile stations provide an opportunity to explore the regions of weak seismicity which usually don't have high density seismic networks. The lowest detection threshold of seismic networks is desirable when monitoring the natural seismic activity aimed to imaging the fault structures in 3D and to understanding the ongoing processes in the crust. Lowering the GMSS threshold allows to investigate in short terms the correspondence between microearthquakes and geological structures, to keep watch advancement of natural (slope phenomena, karst, and so on) and technogenic (frac propagation, deformation pit and so on) geomechanical processes. Similarly, it becomes of increased importance for monitoring induced seismicity due to underground operations. Achieving the maximum possible sensitivity of industrial seismic monitoring is a precondition for successful control of technological procedures. The monitoring system should be able to record the seismic events with $M < -1$ for grade control of acreage.

Sharing of network data can improve the detectability of seismic events in noise. However, the low-noise immunity of the mobile stations and the diversity of noise necessitate continuous updating and enhancement of the digital processing, allowing to work with seismic signals that are visually unapparent [1].

Operating conditions of stand-alone mobile station can be very adverse: on unprepared sites in the field, in the engineering constructions, in inaccessible places. Installing the sensor registration can be made by unskilled staff. To obtain high signal to noise ratio of data, significant effort is required to achieve noise attenuation in seismic data processing, which is costly in materials, and human and financial resources [2].

To increase the sensitivity of seismic observation it is possible make a network dense well and to optimize the station configuration. [3, 4] It requires an increase in the amount of sensors. Another method is resolution of the individual stations and the network as a whole - the selection of weak signals in noise.

GMSS has some similarity to the small aperture seismic array, which is also used to study weak seismicity [5]. However, there is a difference. If small aperture seismic array acts as a single station and serves a large area around it, a main object of GMSS is seismic monitoring within a network. Thus seismic event can be registered by one or two sensors only. In this case, it is important to separate the events from noise burst, but do not miss the event. It is necessary to have an estimate of the network, i.e. to know which the magnitude of seismic events are reliably detected by the network [6].

The station is usually equipped with short-period seismic sensors and geophones [7], the GPS/GLONASS receiver, the system of preprocessing, storage and/or data transmission.

Capacity of the existing seismic networks on the East European platform allows the monitoring of events with M> 2.5 for the most part of the platform, and M> 3 for a large part. The Mikhnevo small aperture seismic array can independently monitor (registration and location) all events with M> 1.0 at distance to 80 km [8].

Without appropriate precautions, the useful signals, which carry information from inside the Earth, would be hidden by noise signals from various sources. These noise signals must be kept below the level of the smallest wanted signal to be observed. In any case great care has to be taken to protect instruments from pressure, temperature, humidity and other environmental factors. Noise, which is emitted by changes in temperature and atmospheric pressure, is very powerful. At the same time, they are easy enough to filter (fig.1).

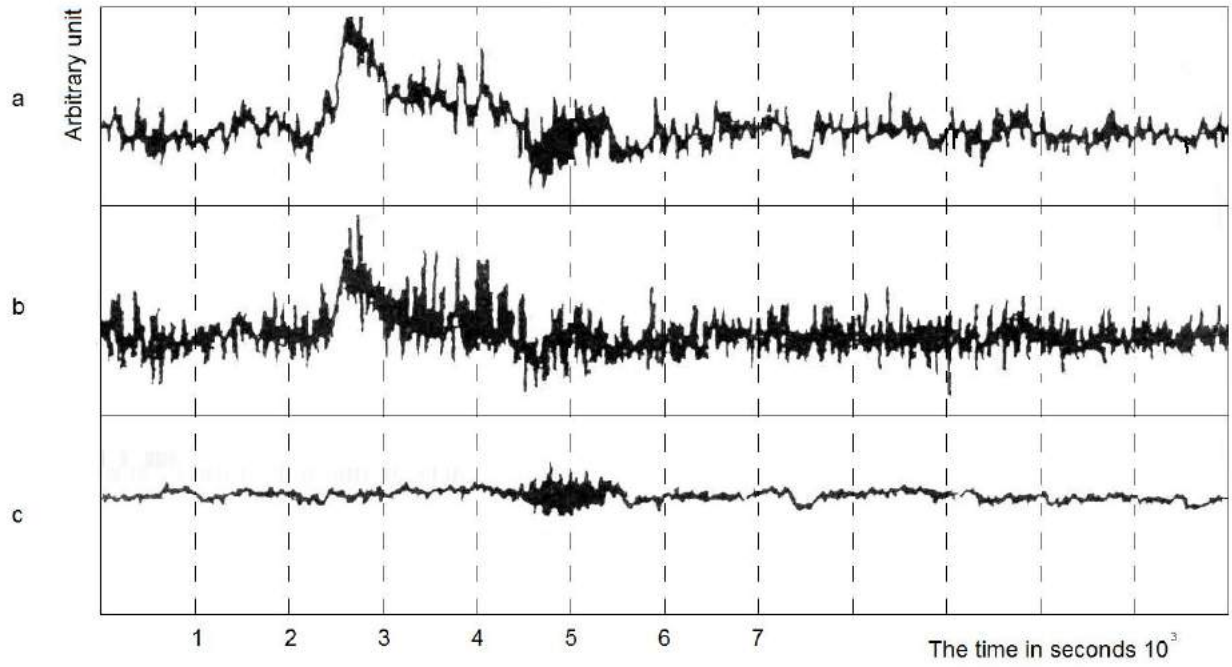

Fig. 1. Data noise clearing from pressure signal [9]:

a - signal from the seismic sensor;

b - atmospheric pressure;

c - extracted seismic signal.

Even minimal passive temperature protection - foam cap - significantly reduces the seismic noise level. The most effective tool for reduction of influence of temperature and pressure is the optimal filtering [10]. This signal processing can be performed directly at the station in automatic mode. It allows you to not save the data of temperature and pressure. Application of pressure and temperature sensors at the station does not lead to a large increase in the cost of network.

DATA PROCESSING

Data processing is performed, firstly, to detect useful signals in background noise, to exclude noise splashes from consideration and, secondly, to determine the parameters of the recorded seismic events (hypocenter location and depth, magnitude). Detection of signal in noise in our opinion is not given enough attention.

The majority of algorithms is based on the concept of STA/LTA ratio and is designed for strong events registered at many stations. Unfortunately, they usually fail in the case of detecting weak events in the presence of seismic noise and a large number of disturbances, which are treated by typical detection

algorithms as seismic signals. The presence of high noise requires an alternate method of seismic detection capable of recognizing small seismic events [11].

The first stage is the processing of each station data. The application of neural network technology allows selecting a signal even if the noise amplitude exceeds the useful signal [12]. We have used several types of neural networks. Each of the neural networks was used to analyze the initial two seconds of the sensed earthquake accelerogram.

The second stage - a comparison of records of neighboring stations [13]. After the detection on single stations had been calculated, some methods of comparing them were applied. It was chosen to simply check whether the detection on one station coincides with detection on other stations. Then a voting process was used. An event is detected when it is detected two stations at least.

If at one station the signal is registered, and the accurate signal isn't present at next, it means that, either the signal of an earthquake is detected incorrectly, or at the neighboring stations the signal is hidden by noise.

Let the signal was recorded at station «Lutowiska» (Fig. 2), but the characteristics of the seismic events was difficult to determine.

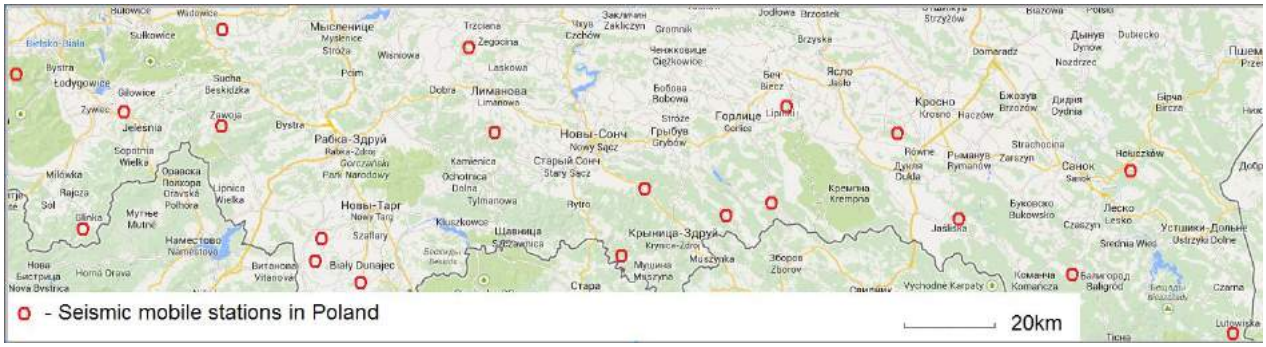

Fig. 2 Example GMSS location in the south of Poland.

Assume that the station is the closest to the epicenter. Then time shift of a signal at the nearest (40 km) station «Hołuczków» will be from zero (if the earthquake occurred directly between stations), to such time interval, for which the seismic wave travels distance between stations. In this interval it is necessary to look for a record of the event. It is necessary to add to this interval the time during which the signal changes from the first arrival up to a maximum value. First, you need to spend clipping. If the amplitude of the signal in this interval is below than required (note: amplitude attenuation depends on the progressive increasing distance from the epicenter), the registered signal at station «Lutowiska» is false.

It is convenient to use the neural network again as the detector of the signal. [14]. The neural networks learning capabilities, which differ them from other mathematically formulated methods, are provided by the unique structure of neural networks and allow the development of neural network based methods for certain mathematically intractable problems. The training set was prepared on the basis of period from 06 to 10 October 2008. We used the recordings of Belgian network of mobile stations. They were precisely studied and 167 seismic events were found. Among them were regional events, teleseismic earthquakes, as well as a few technological explosions. We used noise records too. This gave a reasonable number of detections and quite good sensitivity, with the lowest detected magnitude M_L = 0.4. The problem discovered at the early stage caused a lot of false detections.

CONCLUSION

Records from GMSS are usually of worse quality than from permanent networks, because less time and effort is spent on site selection and deployment. Signals of weak seismic events are difficult to identify in noisy and disturbed data.

It is necessary to efficiently recognize local events and automatically locate them. Developed software further should be a kernel of system of monitoring. The detection from at least two stations is a useful tool, although some events are then missed.

Software should provide:

(1) Decrease the quantity of seismic sensors in the network, necessary for confident detection and a location of micro-earthquakes in comparison with a technique that in use now;

(2) Exception seismic sensor embedding under a layer of distribution of technogenic superficial waves from the man-made sources;

(3) Exception signals from meteorological sources on seismic records;

(4) Improvement of characteristics definition quality of the centers of micro-earthquakes at the expense of detection phases of micro-earthquakes in noise,

(5) Inclusion of other methods of the analysis of microseismicity, such, as a method of a seismic issue tomography at use more robustness schemes of data processing expanding possibilities of the microseismic data analysis.

The developed software will raise localization resolution of the centers of micro-earthquakes.

Application of this technique will provide:

- decrease in magnitude of detected events,
- increase of earthquakes detection reliability,
- increase in the radius of low-amplitude signals location,
- decrease in density of GMSS.

A detection algorithm has to reduce a number of false detections in order to make it possible to manually check all detections.

This method of seismic event detection proved its efficiency and eventually it was used as a convenient tool for small local event detection.

The authors presented the development of technology networks of mobile stations using several different methodology including neural networks.

REFERENCES

1. Xi-Qiang Liu, Yin Cai, Rui Zhao, Bao-An Qu, Zhi-Jun Feng, Hong Li (2014), An automatic seismic signal detection method based on forth-order statistics and applications. *Applied Geophysics*, 11(2), 128-138.
2. Hui-Qun Xu, Zhi-Xian Gui (2014), Signal-to-noise ratio application to seismic marker analysis and fracture detection. *Applied Geophysics*, 11(1), 73-79.
3. Nguyen Van Phong (2000), Planning optimal network of seismological observations numerically. *Extended Abstract of a dissertation for the degree of Candidate in Physics and mathematics,* Moscow.
4. Kraft, T., A. Mignan and D. Giardini (2013), Optimization of a large-scale microseismic monitoring network in northern Switzerland. *Geophys. J. Int*, 195, 474-490.
5. Kushnir A.F., Lapshin V.M. et al. (1989), Statistically optimal selection of seismic signals using a group of stations. *Vychislitelnaya seismologiya* 22, Moscow: Nauka, 193-210.
6. Tomáš Fischer, Martin Bachura (2014), Detection capability of seismic network based on noise analysis and magnitude of completeness. *Journal of Seismology,* 18(1), 137-150.
7. Besedina A.N. (2014), Scientific methods justification of waveform correction during seismic observations. *Dissertation for Cand. Phys.-Math. Sci.*, Moscow,
8. Chernyh O.A. (2011), Seismic monitoring of East European platform with application the Mikhnevo small aperture seismic array. *Extended Abstract of a dissertation for the degree of Candidate in Physics and mathematics*, Moscow.
9. Kislov K.V., Kolesnikov Yu.A., Marchenkov A.Yu., and Starovoit Yu.O. (1991), A seismic microbarograph. *Vychislitelnaya seismologiya* 24, Moscow: Nauka, 292 – 299.
10. Kislov K.V., Gravirov V.V. (2013), Investigation of the environment influence on the noise of broadband seismic equipment *Vychislitelnaya seismologiya* 42, Moscow: KRASAND, 240 pp.
11. Jan Wiszniowski, Beata M. Plesiewicz, Jacek Trojanowski (2014), Application of real time recurrent neural network for detection of small natural earthquakes in Poland. *Acta Geophysica*, 62(3), 469-485.

12. Gravirov V.V., Kislov K.V. and Vinberg F.E. (2012), The Informative Signal Separation from the High Noise Level Non-stationary seismic Data with the Use of the Neural Network Classifiers. *Industrial Automatic Control Systems and Controllers*, 12, «Nauchtechlitizdat», Moscow, 55-59.
13. David P. Schaff and Felix Waldhauser (2010), One Magnitude Unit Reduction in Detection Threshold by Cross Correlation Applied to Parkfield (California) and China Seismicity. BSSA, 100(6), 3224–3238.
14. Kislov K.V., Gravirov V.V. (2011), Earthquake Arrival Identification in a Record with Technogenic Noise. *Seismic Instruments*, 47(1), 66-79.

ON THE METROLOGICAL SUPPORT OF THE LONG-PERIOD SEISMOLOGY

K.V. Kislov, V.V. Gravirov
Institute of Earthquake Prediction Theory and Mathematical Geophysics, Russian Academy of Science (IEPT RAS), Profsoyuznaya str. 84/32 Moscow 117997 Russia, e-mail: kvkislov@yandex.ru

Abstract. Modern seismological analyses require well-calibrated instruments. What is the quality of the seismic station? What is the data precision? Procedures obtaining the answers to these questions are half-finished.

Seismic stations and their long-period sensors are not measuring instruments. Standard procedures of in-use testing aren't applicable to them. Nor their accuracy cannot be determined.

Some Russian stations are part of the Global Seismographic Network (GSN) and International Monitoring System (IMS). These stations should use appropriate methods of verification. These methods presuppose three basic approaches.

- There are two sets of long-period sensors installed at the same station and the data are compared.
- They produce original calibration. They bring the reference instrument, which is considered as good, to the station and set it next to compare data.
- They compare how earthquakes records of other stations correspond to records of this station.

These techniques have already been partially applied.

The first two approaches appear to be too expensive and time consuming for the Russian stations, which are not in the GSN and the IMS.

In our opinion, in-depth development of the third approach, bringing it to a routine maintenance process stations, i.e. the creation of user-friendly programs and algorithms, is the most promising way out of this situation.

INTRODUCTION

The records of ground motion, measured by broadband seismometers, serve for a wide range of scientific research activities. Accordingly, the knowledge of key parameters of seismometers is important for providing reliable results [1].

It is known [2] that from the standpoint of Federal Agency on Technical Regulation and Metrology (Rosstandart) seismic station can't be considered as a means of measurement. It is device for the qualitative analysis of seismic processes. Metrological problems are shifted to shoulders of users. If you place confidence in data, use them, if the answer is no... You have no other data.

Application of various methods of calibration and validation of metrological characteristics of seismometers breaks traceability of measurements [3]. Some Russian stations are part of the Global Seismographic Network (GSN) and International Monitoring System (IMS). These stations should use appropriate methods of verification [4]. And, above all, globality of the studied processes demands the uniformity of measurements worldwide.

Let's consider how the metrological procedures are carried out in world practice.

Global Seismographic Network (GSN)

Test of seismic GSN stations regarding compliance to the metrological norms is made as follows:

- Validation of orientation and polarities of the sensors.
- Calibration using coils of the seismometer.
- Comparison of installed instrument signals to known reference sensor.
- Installation of the second (auxiliary) constantly operating sensor.
- Noise analysis.
- Data analysis.

Let us examine these procedures in more detail.

1. Orientation and polarities of the sensors.

The uncertainty of true North may be the single greatest source of error in orientation metadata.

The procedure to orient a sensor involves the following three steps:

a). Determining True North

b). Translating True North to a fiducial line

c). Orienting sensor to fiducial line

For cases in which a sensor of unknown orientation is down a borehole or in an underground vault with no accurate fiducial line available, a second broadband sensor may be emplaced at the surface. Data from both sensors are then analyzed to determine their relative orientation.

It was decided to check the orientation and polarity of the pendulum at all stations GSN. Although modern methods allow to orient pendulum with an accuracy of 20 ', it was decided not to reinstall the sensors when they deviate from the north to 3 °. At the same time the sensors will be considered orthogonal if their relative orientation is within 1.5 degrees of 90.

2. Calibration using coils of the seismometer.

A calibration is the analyses of instrument response to signals injected through the calibration coils of the seismometer [5]. The calibration shall be conducted at least once annually at all stations.

There are methods to calibrate the instrument by the tides [6, 7]. For broadband seismographs at quiet sites, the tides of the solid Earth are a reliable and predictable test signal (fig.1). They have a predominant period of slightly less than 12 hours and an amplitude in the order of 10^{-6} m/s2 [12]. [8]. They may be extracted by low-pass filtration with a corner frequency of 1 mHz. By comparison with the predicted tides, the gain and polarity of the seismograph may be checked. However so useful method isn't mentioned in long-term plans of GSN [10].

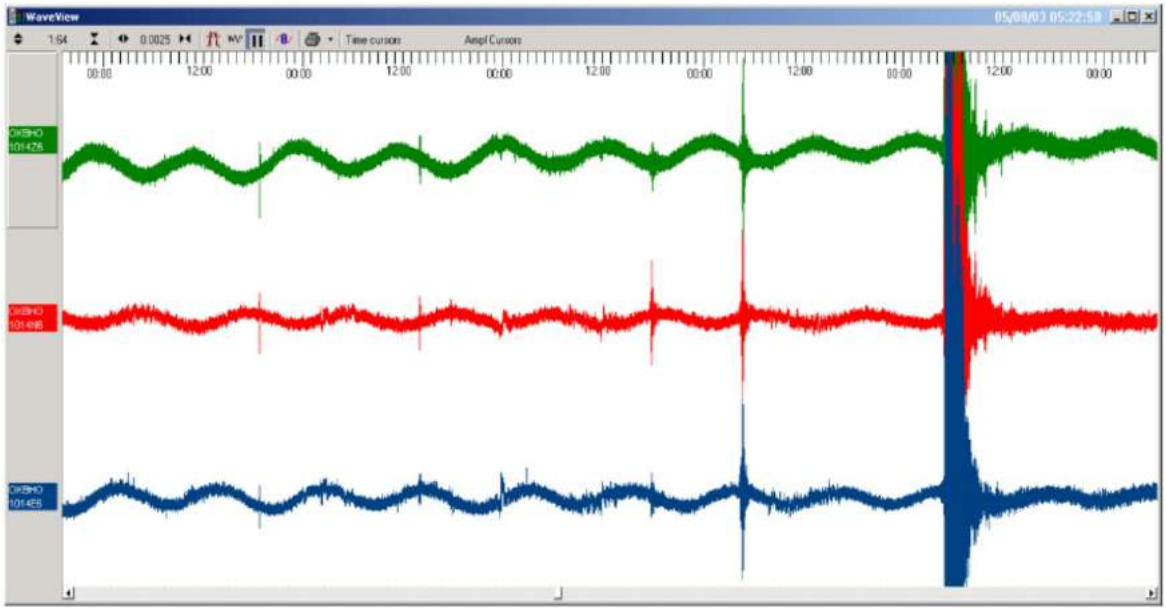

Fig.1. Recording of tides and natural oscillations of the Earth by seismometer CMG-3TB with the built-in digitizer CMG-DM24 [9].

The relative transfer function of the channel can be calculated on a first approximation on base of impulsive excitation, and, based on amplitudes of the tidal waves it is possible to estimate absolute transfer function of system roughly.

3. Comparison of installed instrument signals to known reference sensor (singular intercomparison).

It is assumed network operators will measure the absolute calibration and orientation of deployed sensors by installing a temporary sensor whose absolute orientation and sensitivity is known, and comparing that seismometer's output with that from the permanent GSN seismometers.

The reference seismometer must be installed (to within 20') side by side with the tested one. The temperature mode in the seismic vault has to be restored. It will take the time needed for noise at sites to stabilize after deployment of the sensor. Finally, parallel records of two sensors have to contain multiple earthquakes with a magnitude more, than 6.5. The temporary instrument will then be returned to the network operations center and its response verified after each use [11].

Naturally such verification is ineffective and can be done at the stations only every few years.

4. Installation of the second (auxiliary) constantly operating sensor with similar parameters (mutual control).

This gives you the opportunity to make absolute comparisons between different models of seismic sensors. This also provides a method of identifying quality variations between two or more of the same model sensor [12, 13].

It is necessary to calculate the coherence of the deconvolved vertical, N–S, and E–W components of main and auxiliary sensors. The coherence is calculated for ~ 2-hour-long time windows containing the signals for earthquakes with $M_W \geq 6.5$. For each pair of seismograms, the coherence is calculated in narrow frequency bands around 32 s, 64 s, 128 s and 256 s. If the coherence is greater than 0.95, the value is stored together with the complex scaling factor (represented here as a scaling factor and phase shift) that should be applied to the secondary-sensor data to bring the two time series into the best agreement. In the following, the discussion is based on the assumption that the secondary sensor is properly calibrated and that deviations from a scaling factor of 1.0 and a phase shift of 0° should be attributed to differences between the true and reported response functions of the primary sensor.

Duplication of the long-period instruments at all stations is a very expensive method.

5. Noise analysis

A next method for investigating the overall performance of the sensors is to monitor background noise levels for all seismic channels, after conversion of the data to ground acceleration. For this purpose it is necessary to calculate hourly rms values of the time-domain seismic signal in narrow frequency bands, and convert the rms values to a power spectral density (PSD) at that frequency using Parseval's theorem. For each month, we will calculate the low-noise value at each frequency by determining the PSD amplitude not exceeded 10% of the time.

The PSD data provide a wealth of information about the station and the sensors (fig.2.). Results from this noise analysis are useful for characterizing the performance of existing broadband stations, for detecting operational problems, and for learning about sources of seismic noise within a data set.

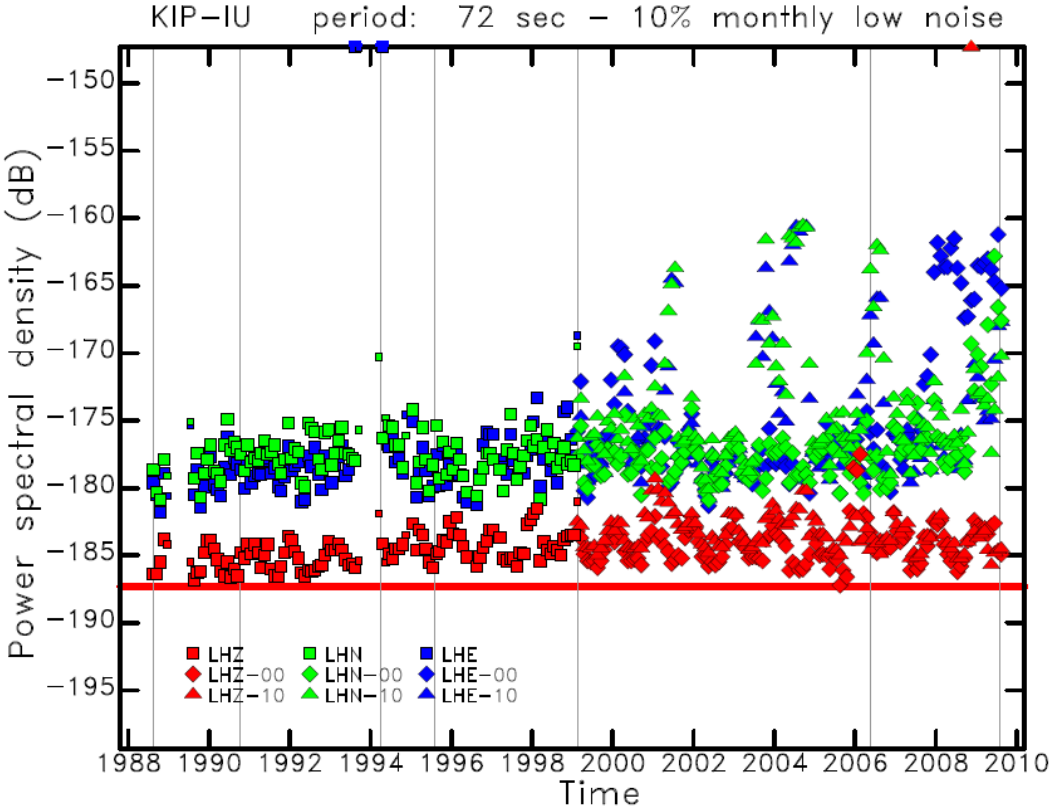

Fig.2. Monthly PSD of ground acceleration at 72-s period for all long-period (LH) channels at station KIP for the period 1988–2009. Smaller symbols are used for months with fewer available hourly measurements. Each component and sensor is represented by a distinct symbol and color. The red horizontal line indicates the level of Peterson's (1993) Low Noise Model (LNM) at 72 s.

The thin vertical lines show the times of epoch boundaries in the station metadata [14].

6. Data analysis.

This method for assessing the quality of the data is the systematic comparison of recorded long-period waveforms with synthetic seismograms calculated for known seismic events [15].

Seismic data for the long-period and very-long-period channels of station are collected. Corresponding synthetic waveforms for all earthquakes in the Global CMT catalog (Global Centroid Moment Tensor database) with MW $\geq$ 6.5 are calculated. Correlation coefficients and optimal scaling factors between observed and synthetic waveforms are calculated for the three types of data used in the standard CMT analysis: body waves, with periods in the range 50–150 sec, mantle waves, with periods in the range 125–350 sec, and surface waves, with periods in the range 50–150 sec.

When confronted with the seismograms for an individual earthquake, it is often difficult to assess whether a poor fit is due to incorrect source parameters, inadequate modeling of wave propagation through an Earth model, or some problem with the recorded seismograms. Therefore the scaling factor is only calculated for waveforms with a correlation of 0.75 or greater. The scaling factor is the number by which the synthetic seismogram should be multiplied to maximize the agreement with the observed seismogram. Annual averages of the scaling factors are calculated when four or more individual event scaling estimates are available for the year.

From the above procedures only calibration using coils of the seismometer is done under any schedules basis.

Management of effective metrological support

Amplitude variations of 10% and smaller are interpreted as signals in modern studies that seek to map the attenuating properties of the Earth's interior. Phase anomalies of a few seconds at long periods are similarly interpreted in terms of Earth's elastic structure by numerous authors. Therefore it is important to ensure station instrumentation is functioning as expected and that the response of the system is well characterized by the metadata.

When there is confidence that a calibration has provided an accurate estimate of the instrument response at a station, the appropriate Data Collection Center then should update the station's metadata. Sustaining our fleet of equipment and infrastructure with its spectrum of ages requires a continuous engagement in monitoring the state of the network.

It is clear that the most important and effective metrology procedure is data analysis. This method doesn't answer a question of a measurement error of the ground motion. However, it is the best approximation of the transfer functions of the channels for seismic events. This is the best of what scientists were able to come up. We should add the remote calibration of instruments (including calibration using the tides), the noise analysis and the validation of orientation and polarities of the sensors using Web access. The exact geographical (latitude and longitude) for each site is also being confirmed with GPS techniques for comparison with early map based determinations. All procedures should be determined for long term Web access.

The method could and should be developed. The data analysis has to take place in the center of information processing, by means of completely automated procedure. The synthetic seismograms for all stations must be prepared after each earthquake with a big magnitude (more than 6.5). Results of comparing with real data should be embodied in metadata. Thus the metadata must be available to users on an equal basis (together) with the seismic data.

So, in the processing centers for each station must be taken measures:

- The remote calibration of instruments (including calibration using the tides) – annually.
- Noise analysis (deviations from long-term noise characteristics of data streams) – annually for each month.
- Data analysis (comparison of recorded long-period waveforms with synthetic seismograms) – after each earthquake with a big magnitude (more than 6.5).
- Validation of orientation and polarities of the sensors based on comparison between observed and synthetic seismograms (the azimuth residuals show polarization anomalies).
- Documentation of the current waveform quality problems.
- Review and correct current metadata for all stations, as necessary.

- Finding sources of waveform quality problems and development timetable for correction.

This will require additional resources and personnel, to fully implement these methods, to develop standards, procedures, programs for routine data processing.

If a station produces anomalous calibration results, or appears to be providing rapidly changing response information, we will calibrate stations more frequently until a resolution of the problem can be found.

Web-published metrics not only offer a clear status and history of sensor data quality for the scientist using the data, but also better enable network operators to monitor quality, to bring engineering expertise to problems identified, and for making decisions on the allocation of resources for field trips.

This metrological scheme in the long-period seismology will allow to have a constant confidence in the reliability of seismic data.

CONCLUSION

There is an urgent need to solve the problem of metrological assurance in long-period seismometry, because the quality of seismic measurements has a decisive influence on a number of the most important indicators in various branches: the economic efficiency of prospecting for useful minerals, the confidence in the operation of the system for predicting earthquakes etc.

In order to verify that seismic instruments meet the above demands and other user requirements it is important from a testing standpoint, that one be able to measure the self-noise of seismic sensors.

The lack of systematic calibrations, and inspection of calibration results, makes it difficult to identify instrument problems.

Metrological assurance of Russian long-period seismology should be brought into line with international standards. Assurance of measurements' uniformity and accuracy is necessary owing to globality of studied processes. However procedures which are applied for GSN stations are far from perfect (sites not visited often enough for good calibration, sensors operating out of specification, metadata not updated). It is necessary to adopt the principles and, at the same time reduce the cost and simplify the procedure, and to make them more efficient by using the automatic data analysis. This will require additional staff and special seismological metrological service. It is necessary to develop an industry-specific standards, programs, and procedures.

The capability of remote automatic calibration via the telemetry link is essential for routine monitoring of sensor state-of-health, documenting the sensor response, and tracking data quality. Along with other methods of inspection stations, it'll allow to stay abreast of the quality of data for each station and of the seismic network as a whole.

The special attention should be paid to metadata, i.e. their availability and possible errors descriptions of station parameters: orientation of the sensors, response functions, polarities. Regardless of the cause, it is necessary to document and publicize the lack of accurate and reliable station characteristics, especially when it is not obvious from simple inspection of the data that a problem exists. Information about the state of GSN data—quality metrics—must be on a par with the data themselves. This information must be as routinely, easily available to the user community as it is for the network operators themselves.

Confidence in data requires knowledge of their quality.

REFERENCES

1. Krivtsov E.P., Sinel'nikov A.E., Yankovskii A.A. (1993), Supporting unified seismometry measurements. *Measurement Techniques*, 36(8), 895-898.
2. Zakharchenko N. Z. (2007), Scientific and legal aspects of seismometry metrology, *in: Proc. Ist regional technical conf. "Problems of Integrated Geophysical Monitoring of the Russian Far East*" (Petropavlovsk-Kamchatsky, 11-17 November 2007), GS RAS, 122-126.
3. Sargsyan V.K., Sargsyan R.E. (2009), On some metrological problems in seismometry, *Proceedings of NAS RA & ESUA - Series of Technical Sciences*,. T. LXII, N3, 330-336.
4. Mishatkin V. N., Zakharchenko N. Z. (2009), The problem of the seismic stations certification, *in: Proc. IInd regional technical conf. "Problems of Integrated Geophysical Monitoring of the Russian Far East*" (Petropavlovsk-Kamchatsky, 11-17 October 2009), GS RAS, 278-282.
5. Wielandt E. (2003), Seismometry, *in IASPEI International Handbook of Earthquake and Engineering Seismology edited by W. H. K. Lee, H. Kanamori and P. C. Jennings,* 44pp.

6. Osipov K.S. (1992), Adaptive analysis of non-stationary time series in the study of seismic waves in the period range 0.5 - 5 hours. *Extended Abstract of a dissertation for the degree of Candidate in Physics and mathematics*, S-t Petersburg.
7. Davis, P and Berger, J. (2007), Calibration of the Global Seismographic Network Using Tides. *Seismological Research Letters*; 78(4), 454-459.
8. Wielandt E. (2012), Seismic sensors and their calibration. Chapter 5, *in: New Manual of Seismological Observatory Practice (NMSOP-2),* IASPEI, ed. By Bormann, P., GFZ German Research Centre for Geosciences, Potsdam, 46 pp.
9. http://www.vulcan-seismicsystems.com/images_guralp/L_Guralp_CMG-3T_portable_rus.pdf
10. GSN Calibration Policy (2010), http://www.iris.edu/hq/files/programs/gsn/gsnqual/GSN_Calibration_Policy_rev1.pdf
11. Tasič I., Runovc F. (2014), The development and analysis of 3D transformation matrices for two seismometers. *Journal of Seismology*, 18(3), 575-586.
12. Ringler A.T. and Hutt C.R. (2010), Self-Noise Models of Seismic Instruments. *Seismological Research Letters*, 81(6), 972-983.
13. Hutt R.C., Evans R.J., Followill F., Nigbor L.R., Wielandt E. (2009), Guidelines for standardized testing of broadband seismometers and accelerometers. *USGS Open-File Report 2009–1295,* U. S. Geological Survey, 66 pp.
14. Ekström G., Nettles M. (2010), Performance of the GSN station KIP-IU, 1988-2009. *A report in a series documenting the status of the Global Seismographic Network*, 15pp.
15. Pavlov V. (2002), A convenient technique for calculating synthetic seismograms in a layered half-space, *in: Proc. 4th International Conference «Problems of Geocosmos»* (St. Petersburg, 3-8 June 2002), P.320-323.

SEISMIC MONITORING AND PROTECTION OF EXTENDED OBJECTS

K.V. Kislov, V.V. Gravirov
Institute of Earthquake Prediction Theory and Mathematical Geophysics, Russian Academy of Science (IEPT RAS), Profsoyuznaya str. 84/32 Moscow 117997 Russia, e-mail: kvkislov@yandex.ru

Abstract. The extended objects are construction objects and technological devices that make with them a single unit or a complete functional unit, which designed for transporting liquids, gases and other objects, or for transmitting power and signals. Thus, roads, power lines, communication lines, oil and gas and other pipelines, railway lines, network hardware and other similar structures here were meant. The Early Warning System allows getting current information on natural hazards (primarily talking about earthquakes) and in such a manner protects objects. If such information is received before the event, it is possible to considerably reduce material and human losses by automatic shutdowns (to stop of trains, set up the red signals of traffic lights, kill power, reduce the pressure in the oil and gas pipelines, etc.). After the event such information will allow to estimate the volume of destructions, to define necessary measures of a rescue and restoring of extended object to working condition. We, sometimes, pay a very high price for absence something similar, including in human lives.

Ensuring of the object seismic monitoring can demand additional seismic stations. Sites for them have to be chosen after mapping of the medium-term earthquake prediction. Well known that for approximate determination of the earthquake characteristics can be used for cheap short-period sensors, it does not cause great difficulties. More serious technical problem is a creation of warning data-transmission system.

We elaborate on these and some other tasks arising at development of the protection system of extended objects.

INTRODUCTION

An earthquake warning system (EWS) is a system of several seismic stations, communication, computers, and alarms that is devised for notification of a substantial earthquake while it is in progress. Seismic monitoring by the system allows getting short-term data about the seismic events. Thus information can be received before strong concussion. During this time, it is possible take preventive steps to reduce the human and material losses. Another purpose of EWS is the help in a preliminary estimate of possible destructions for taking measures to assistance and restoration (fig.1). In addition, EWS can and should be involved in the system of seismic monitoring.

The first seismic arrival from an earthquake is the P wave, which is usually relatively low-amplitude and causes no damage. It is followed by the S wave, which usually has larger amplitude, causing most of the damage in an earthquake. The warning time can be increased by use of the P-wave arrival to estimate the magnitude and location of an earthquake. EWS initially determines the location, origin time, and magnitude of an event using the first detected P-wave arrivals. Finally, the warning time is estimated based on the origin time and travel time curves for S waves.

EWS applications in operation focuses on the special requirements of extended objects (EO) are in Japan (for safety on the railways, so-called UrEDAS – Urgent Earthquake Detection and Alarm System [1]), California (Metro San Francisco and Los Angeles) and some other places. Protection of other EO is under development [2].

In addition the protection of some segments of EO can be carried out by means of regional EWS. For example, in Japan, bus drivers receive a signal to put on the emergency brake after recognizing the regional EWS alarm.

The Russian systems of seismic monitoring designed to protect EO are underdeveloped. After the 7.3 magnitude earthquake that occurred on August 14, 2012 in the Okhotsk Sea, it is decided to organize a system of seismic monitoring on Berkakit-Tommot-Yakutsk railroad [3]. The 1995 Neftegorsk earthquake with a magnitude of 7.6 led to the rupture of the pipeline in 33 sites. After it the 13 sensors network of seismic monitoring will be organized at oil pumping stations of the oil pipeline Eastern Siberia-Pacific Ocean [4]. However, such systems can be called early warning systems only conditionally. Stopping fast

moving train and the pressure relief in the pipeline, both require about 1 minute. Such systems the most frequently can not ensure a sufficient time. They are becoming more and more relevant in Russia [5, 6, 7].

The earthquake and tsunami, on January 6, 2013, Indonesia. The magnitude 5.1, depth 147 km.

The earthquake, on September 4, 2010, New Zealand. The magnitude 7.1, depth 10 km (http://railgo.ru).

The Northridge earthquake, on January 17, 1994, in Sylmar, California. The magnitude 6.7 (Jonathan Nourok/AFP/Getty Images)

The earthquake, on November 10, 2008, Sichuan (China). The magnitude 8, depth of 19 km (http://mirvkartinkah.ru/posledstviya-zemletryaseniya-gorode-bejchuan-kitaj-shest-mesyacev-spustya.html#ixzz3DViUYYUU).

Fig.1. The aftermath of the earthquake for the EO.

Arranging of EWS EO network

Game Plan

If we could rapidly estimate the earthquake magnitude and epicenter location with depth, the area to be alerted is clearly shown. We will review the example of Japanese seismic networks (fig.2). Earthquake detectors for the railway system were developed and spread from the second half of 1950s in Japan. It was started by the strong motion observation in 1964. The EWS was developed to slow down or stop trains before seismic shaking affected trains running at high speed [8]. They used a single-station approach, where seismic signals are processed locally and an earthquake warning is issued when ground motion exceeds the trigger threshold.

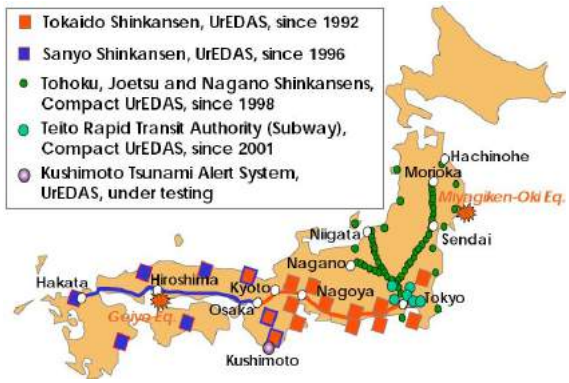

Fig.2. Seismic network for EO protection (railways). The distribution of UrEDAS and Compact UrEDAS in Japan [8].

There are two strategies organizations of EWS EO. According to the first, seismic stations are installed along the EO with a certain step. In Japan alarm seismometers were installed every 20 to 25 km along the railway lines adjusted to issue alarms if preset levels of horizontal ground acceleration (40 cm/s2) were exceeded. This strategy, first, controls all parts of the object equally and, second, monitors not only earthquakes, but also other natural and manmade disasters. In addition, installation of the data communication is easier along the EO. Diagnostics of damages and amount of works on disaster recovery of object it is easier too. However, this approach does not provide the most rapid estimate of earthquake parameters.

The second strategy is designed primarily for protection against earthquakes. In this case, the seismic stations are located near the earthquake epicenters. When the earthquake source region is some distance from the EO, seismometers can be deployed between the source and it to detect any earthquake and transmit a warning electronically, ahead of the more slowly moving ground motion. Application of this strategy leads to a significant reduction in the number of seismic stations. Moreover if station is distant from the object, this provides additional time to respond to an alarm.

The best mode is an integration of these strategies. Currently the second strategy is digestible option for Russia. It is cheaper and easily workable. Thus functions of the first strategy (determination of a source of fluctuations and of intensity of fluctuations on various sites of object and, therefore, the scale of destructions) are partially carried out also. There is more time for protective actions before arrival of destructive waves of the earthquake. It is very important. There is emergency shutdown system in power systems. It takes a split second. There is the emergency decompression of gas and oil pipelines too. Connection of these systems to EWS comes easy. Additional time to protection is particularly topical for EO such as railways and highways, especially highways. The railways system usually involves automatic braking and constant communication with train crews. For example, there is an Integrated Train Protection System (KLUB). There aren't automatic braking systems on roads. The lighting up of red signals and the organization of additional information displays, announcements on radio and a radio communication with bus drivers is possible only.

The spacing of seismic sensors

Ideally, the EWS network should provide seismic monitoring of the entire object and provide the maximum possible time for action. As noted above, for this purpose it is necessary to unite the first and second strategy. At the first stage EWS should include the minimum possible number of stations installed by the second strategy. To do this, it is necessary to draw up a refined map of possible earthquake epicenters [9]. Then you define the potentially dangerous areas of the EO, which can be affected by relatively small earthquake (bridges, tunnels, high embankments, avalanche places, etc.). It is necessary to define, what intensity of an earthquake is dangerous to these objects (foreign colleagues use the PGA (peak ground acceleration) in this case). The EWS network is calculated based on these data.

There are the natural cataclysms (abrasion of coast, collapse of karst cavities, etc.), able to damage of objects, which also can be identified by seismic monitoring system. If such phenomena are taking place in this region, the network should be organized by the first strategy.

It happens that various EO are situated in parallel at a short distance from each other. In this case, the EWS can serve them simultaneously.

If the EWS is based on sparse seismic network, it is very sensitive to the seismic noise [2]. Seismic stations are generally located in remote areas, as far as possible away from any human activity. Nevertheless, road and railway traffic, heavy industry, mining and quarry activities, extensively exploited agricultural areas, and many other sources of manmade seismic noise around the seismic stations, along with natural sources can be strong noise sources. If a seismic signal is noisy and the loss of information content even at one station only, it can decrease the effectiveness of the system. There is a special technique for detecting the useful signal (P-wave) in a noisy signal. It is based on the use of wavelet transforms and artificial neural networks [10]. If the seismic station site is noisy, it is necessary to apply this technique.

Alarming scenarios can be run from the signals of other services, such as the Pacific Tsunami Warning Center, Hydrometeorological Centre of Russia.

Functions

The accuracy and reliability of earthquake information is of the utmost importance and is of immense benefit in the mitigation of earthquake hazards. Main EWS EO functions are estimation of magnitude and location, vulnerability assessment and warning within a few seconds of initial P wave motion at a single station. It has to calculate parameters such as back azimuth, predominant frequency and vertical to horizontal

ratio in real time and then estimates earthquake parameters such as magnitude, epicentral and hypocentral distance. The earthquake parameters are extracted from the sensor network via artificial neural net technology. After that the intensity maps are calculated (including PGA for responsible objects and the time until the S-wave arrival).

Modern systems of monitoring of objects have to allow:

a) implementation of the intellectual analysis of obtained data;

b) identification of the facts of destructive processes which are at intensive advancement;

c) the efficiency and reliability of information;

d) automatic generation of warning signals;

e) the possibility of timely management decisions;

f) stability of work after strong ground shaking.

Communication of early warning information

An effective early warning system needs an effective communication system. Early warning communication systems have two main components:

• communication infrastructure hardware that must be reliable and robust, especially during the disaster;

• appropriate and effective interactions among the main actors of the early warning process, such as the EWS seismic network, alarm breaking systems, decision makers, the public, and the media.

Redundancy of communication systems is essential for disaster management. Frequencies and channels must be reserved to ensure the communication systems operate reliably and effectively during and after a disaster occurs, and to avoid network congestion. In Japan, public access communication is used for alerting EWS. After the catastrophic earthquake on March 11, 2011 networks of three largest Japanese communications operators (NTT DoCoMo, KDDI, and Softbank) have suffered damage, especially in coastal areas. EWS has to lean on own communication system and use the public access communications only for duplication of alerting.

The datacom can be a wireless system based on special devices which allow Ethernet traffic in the frequency bands 2.4-2.7 GHz and 4.9-6.0 GHz and provide traffic capacity of up to 48 Mbit/s. In such systems, data transmission can be over a distance to 80 km, and the controllers must communicate with each other by means of the special synchronizer to eliminate overlapping-channel interference. So it is possible to provide a lower cost compared to alternative solutions with leased or fiber optic lines.

All information must be stored as a basis for further actions.

Autonomous power supply

Emergency power supplies and back-up systems are critical in order to avoid the collapse of communication systems after disasters occur. Sites, where you want to place the seismic stations, are not always electrified. Implementation of the power supply system for each stand-alone station or a permanent replacement and recharging the batteries involve significant financial costs. Therefore use of renewable, such as a wind, the sun will be relevant. Autonomous power supply is especially important for EO outside the densely populated regions of Russia.

Action level

The short-term warnings include automated systems that can use a few seconds to slow and stop trains, prevent additional cars from entering the freeway, shut down power plants, close gas valves, alert wide segments of the population, etc.

The system calculates the intensity of an earthquake in each point of EO. The possible damage is determined by intensity then rescue and recovery work will be organized.

The use of neural network classifier allows us to identify such processes as landslides, collapses, mudflows, sags, a collapse of karst cavities, abrasion of sea coast, avalanches. Each of these influences can disrupt the EO.

CONCLUSION

Early warning systems help to reduce economic losses and mitigate the number of injuries or deaths from a disaster, by providing information. The worldwide trend is that populated areas of the Earth will be covered with the EWS networks. Sooner or later it will happen in Russia [11]. The first step in this work will

be the development of EWS for the protection of critical facilities, for earthquake-prone areas and for EO. There are areas of high seismicity in Russia. Large part of the territory of Russia has seismicity, which, however, from a global viewpoint is low but not negligible. It is important that systems were developed as an initial stage of the general program that they had possibility of modernization and integration into the general system. The EWS needs appropriate standardized solutions.

The system doesn't start working as if touched with a wand. It takes some years to train, adjust and test the system. It is very important to start as soon as possible the data accumulation and testing of methods. There is a method of training the system using synthetic seismograms. But training and testing of system by using real data always yields better results.

The alarm in the expected damage area is of prime importance. Another purpose of EWS is the preliminary estimate of destructions for taking measures to assistance and disaster recovery of object. It is important to have a clear picture of potential damages shortly after the event. Finally, the permanent infrastructure monitoring use case addresses the continuous monitoring of infrastructure elements. A permanent and continuous infrastructure monitoring network may help in avoiding extensive repairs by detecting deviations in an early stage. A sufficiently dense sensor network may be used for permanent infrastructure monitoring and thus be helpful for the identification of critical EO irregularities.

The system should be applicable to other types of natural disasters or to the protection of other types of infrastructure systems. But the possibility of false alarm and information error is recognized. Since there is always a possibility of issuing a false alarm, organizations that use the alarm system should understand taking risk.

It is necessary that the measuring and processing functions of an earthquake disaster prevention information system will be constructed in fully automated fashion and operated quick and reliable.

The motivations for our work are based on the knowledge gained from major advances in the fields of sensor, computer and information and communication technologies. The purpose of our work is development of a scientific and technical potential for emerging technologies in the field of EWS EO, design of "standard" intellectual monitoring systems of EO, which help to analyze object condition and make timely decisions on safety. Nevertheless many gaps still exist in early warning technologies and capacities and a lot more has to be done to develop this system.

REFERENCES

1. Nakamura Y. & Saita J. (2007), UrEDAS, the Earthquake Warning System: Today and Tomorrow, *in* Earthquake Early Warning Systems. *ed. by* P. Gaspsrini, G. Manfredi, J. Zschau. Berlin Heidelberg: Springer,249–281.
2. Hilbring D., Titzschkau T., Buchmann A., Bonn G., Wenzel F., Hohnecker E. (2010), Earthquake early warning for transport lines. *Nat Hazards*., Springer Science+Business Media B.V. 31p.
3. Scientific session of the Ministry of Transport of the Republic of Sakha (Yakutia) http://sakha.gov.ru/node/84468
4. Kolomeytsev S. (2014), Earth shake. *Amur Pravda*, June 13,.
5. The national program of modernization and development of roads of the Russian Federation until 2025.
6. The Strategy of Railway Transport Development of the Russian Federation until 2030.
7. The control system of seismic effects // *ZETLAB, ZAO "Digital technology and metrology systems"*, http://www.zetlab.ru/support/articles/seismo/pipe.php
8. Nakamura Y. (2004), UrEDAS, Urgent Earthquake Detection and Alarm System, Now and Future, *in 13th World Conference on Earthquake Engineering* (Vancouver, B.C., Canada, 1-6 August 2004) , Paper No. 908, 9pp.
9. Kislov K.V., Gravirov V.V., Novikova O.V. (2014), Early warning of earthquakes and other natural and man-made disasters for Russia, *in Proc. XIII Scientific-Practical Conference "Problems of emergencies forecasting "* (Moscow, 14-15 May 2014), 61-63.
10. Gravirov V., Kislov K., Gravirova L., Vinberg F. (2013), The Use of Wavelet Transformation Techniques in Structure of an Artificial Neural Network for Recognition of Early Arrival of Earthquakes on Strongly Noisy Seismic Records, *in Book of Abstracts CTBT: Science and Technology*, T3-P132, p.139.
11. Kislov K.V., Gravirov V.V., Novikova O.V. (2014), Seismic early warning for Russia. *This conference,* poster.

SEISMIC EARLY WARNING FOR RUSSIA

K.V. Kislov, V.V. Gravirov, O.V. Novikova
Institute of Earthquake Prediction Theory and Mathematical Geophysics, Russian Academy of Science (IEPT RAS), Profsoyuznaya str. 84/32 Moscow 117997 Russia, e-mail: kvkislov@yandex.ru

Abstract. Earthquakes are a serious threat for many regions of Russia. Early warning systems, based on real time, automated analysis of ground motion measurements, can play an important role in reducing material and human losses. Russia is covered by numerous seismic networks. However seismic stations are located at considerable distances from each other and unevenly spaced. The early warning system should be geared at fully exploiting the possibilities offered by a real time analysis of the signals coming from seismic networks for a wide range of actions. These actions range from the shut down of critical systems of lifelines, industries, highways, railways, etc. and the activation of control systems for the protection of crucial structures, to decision support for rapid response of the emergency management (ground shaking maps, continuously expected damage scenarios, aftershocks hazard etc.).

Working is structured into the following blocks:

1. Mapping of the medium-term earthquake prediction/
2. Choosing sites for additional stations.
3. Installing at stations hardware-software complexes of automatic picking p and s waves of large earthquakes.
4. Making data communication systems and data processing centers.
5. Developing of disturbing scenarios.

INTRODUCTION

The number of annually recorded earthquakes exceeds 100,000; of these, more than 1000 are large events. The earthquake usually caused tremendous damages to human beings and these irreversible damages include loss of human lives, as well as huge adverse economic impacts. Losses of insurers from earthquakes and accompanying industrial disasters, according to the reinsurance company Swiss Re, exceed $ 250 billion per year. The greatest danger posed by earthquakes consists in their suddenness. However, if people can receive the warning for the coming of the earthquake even by only a few seconds, the damages can be reduced due to possible appropriate reaction.

Among the most important strategies for earthquake risk reduction is the development of the earthquake early warning system (EWS). Such systems make it possible to issue warning alarm before the arrival of severe shaking to provide sufficient time for quick response to prevent or reduce casualty and damages [1].

An earthquake produces four types of waves that emanate from its hypocenter; P or primary waves, S or shear waves and surface waves (L and P). A P-wave is weak and travels faster and can be sensed much earlier, depending upon distance from epicenter, than other destructive waves. The typical speed for the P-wave is around 5 km/sec and the speed for the S-wave is around 3 km/sec.

One of the technical limits is applicability to the near-source earthquakes. The warning is only useful for the area located outside about 50 km radius from the earthquake epicenter. If you're right next to the epicenter, you might get no warning at all. The shaking at the epicenter occurs about a second after the P-waves [2]. If the area is far from the epicenter, say for example 200 kilometer, then we will have about 30 seconds before the S-wave arrives if the sensor at the observation station was able to pick up P-wave right away.

What can you do with a few seconds of warning? [3]

Rescue Services:

- Warn personnel.
- Cut-in backup power in hospitals.
- Opening fire station doors so rescue trucks can get out.

Transport:

- Set up all-red signals.

- Automatic braking of the trains.
- Abort airplane landings

Industry:

- Shut off gas main valves to prevent fire damage.
- Isolate chemicals, gases, and fuel tanks.
- Shut down industrial processes.
- Data retention of computer center.

Population protection:

- Arrest elevators, open doors, and lock in place.
- Automatic bulk SMS emails and faxes to users.
- Activate emergency power generation.

Earthquake is a serious threat for many regions of Russia [4, 5]. Earthquake endangered areas contain about 20% of Russian territory where there are more than 20 million people.

Russia is covered by numerous seismic networks, but the stations are rare and irregularly. Another feature is that fortunately large seismic events in Russia do not occur often. However, from the standpoint of learning the warning system by real data, it is a negative factor.

Development of early warning system

How can we plan the EWS, if seismic network is not dense? At the first stage it is necessary to draw up a refined map of possible earthquake epicenters. In our Institute it was developed a method for determining the possible locations of the epicenters, based on the method of pattern recognition, which determines the position of seismic hazardous and non-hazardous lineaments [6] (fig.1).

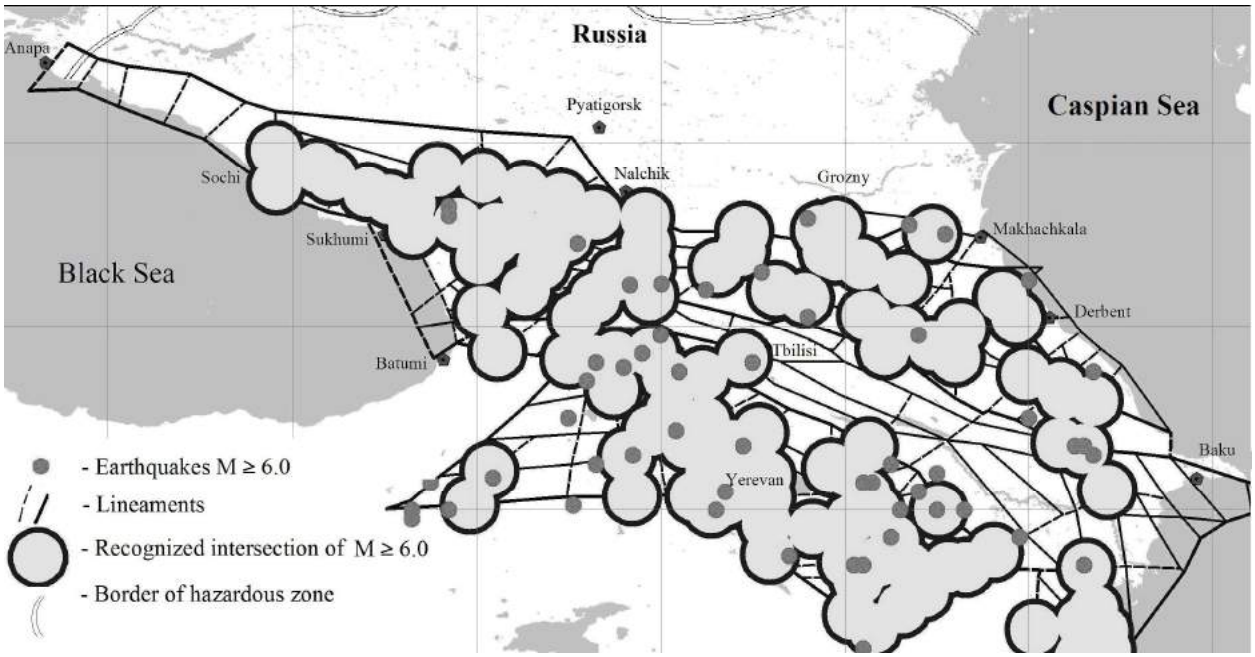

Fig. 1. Results of recognition of earthquake-prone crossings of morphologic lineaments on the example of the Caucasus.

Naturally enough, an earthquake of magnitude M5 may also pose some threat. However, the damaged zone will correspond to the "blind zone" of EWS.

The second step is to map the protected objects in near-term economic perspective (fig.2). Early warning can be used to protect certain areas (large cities, industrial areas), extended objects (railways, roads, oil and gas pipelines), point-like objects (industrial plants, cities, tunnels, etc.).

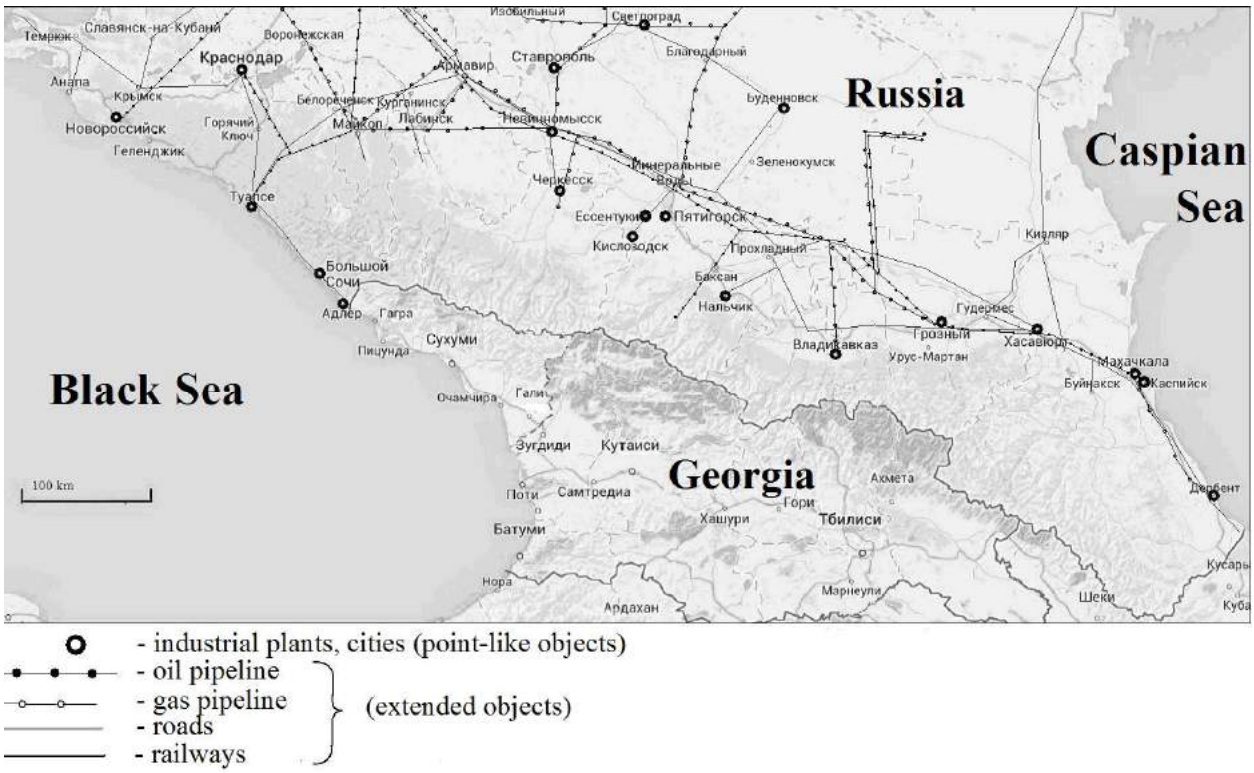

Fig. 2. The model of the map of protected objects on the example of the Russian Caucasus.

The third step is to define sites for additional seismic stations. It may be necessary to provide sufficient warning time for protected objects (fig.3).

The algorithm for determining of additional stations locations, taking into account degree of importance of protected objects, is developed at our Institute.

Fig. 3. Preliminary map of additional stations on the example of the Russian Caucasus.

All stations must be provided with a permanent link. To share data of individual stations, the data processing centers must be created. According to recent studies, early warning systems can use cheap short-period sensors that do not require complicated installation. The system which is based on MEMS technology is tested on Taiwan.

If the early warning system based on sparse seismic network, it is very sensitive to the seismic noise. The loss of data even from one seismic station can lead to integrating system failure. We have developed a special technique for detecting the useful signal (P-wave) in a noisy signal. It is based on the use of wavelet

transforms and artificial neural networks [7]. If the seismic station site is noisy, it is necessary to apply this technique.

The neural network provides additional opportunities [8]. Such qualifier allows to determine the source of ground shaking, whether earthquake, explosion, landslide movement of glaciers or other natural or man-made disasters (fig.4).

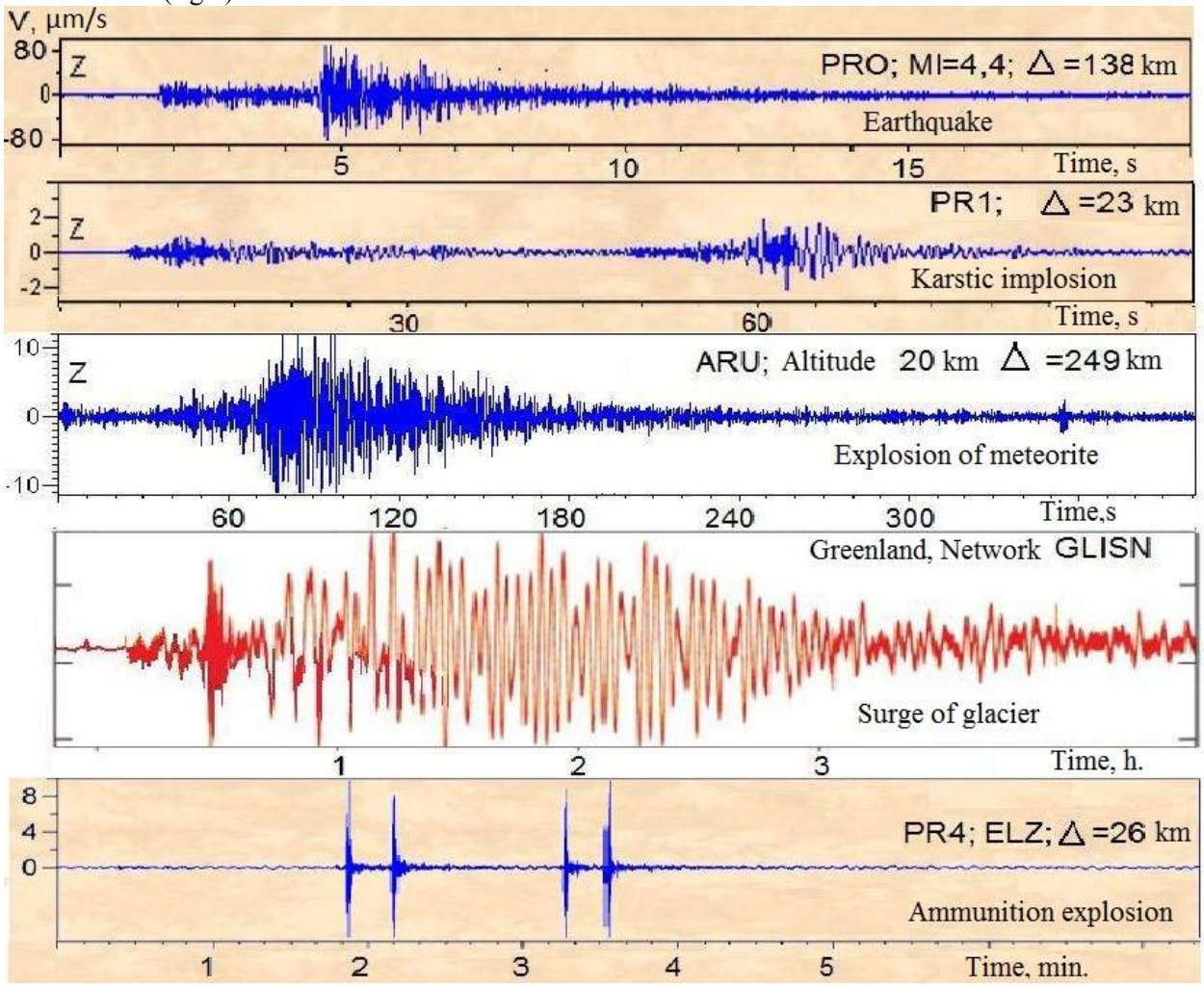

Fig. 4. Seismic signals of different sources (from [9], surge of glacier from [10]).

CONCLUSION

Create EWS is a very big and complex task. We did not discuss many of the technical, organizational, financial and political aspects of its decision. However, it is a feasible task. Sooner or later, such system will be established in Russia. The sooner it will start creating the more accumulated data for training the neural network, the more effective the system will be. You can start by regions of high seismic activity, and especially important objects. By producing accurate and informative warnings, the system has the potential to significantly minimize the hazards of catastrophe ground motion.

REFERENCES

1. Gravirov V.V., Kislov K.V. (2012), Development of a hybrid earthquake early warning system based on single sensor technique. *NED University Journal of Research, Thematic Issue on Earthquakes*, Karachi, Pakistan, 1-20, http://www.neduet.edu.pk/NED-Journal/pdf/12 earthquakespaper1.pdf
2. Chu-Chieh J. Lin, Pei-Yang Lin, Tao-Ming Chang, Tzu-Kun Lin, Yuan-Tao Weng, Kuo-Chen Chang and Keh-Chyuan Tsai (2012), Development of On-Site Earthquake Early Warning System for Taiwan, *in Earthquake Research and Analysis – New Frontiers in Seismology, ed. by S.D'Amico,* In Tech, , 329-358.

3. J.Saita, T.Sato, Y.Nakamura (2008), What is the useful application of the earthquake early warning system? , *in: Proc. 14-th World Conference on Earthquake Engineering*, Beijing, China, 7pp., http://www.iitk.ac.in/nicee/wcee/article/14_S05-03-008.PDF
4. Natural hazards of Russia (2000), *ed. byV.I. Osipov, S.K. Shoigu. Volume 2: Seismic hazard.* - M. Crook,. – 295pp.
5. Kislov K.V., Gravirov V.V., Novikova O.V. (2014), Early warning of earthquakes and other natural and man-made disasters for Russia, *in Proc. XIII Scientific-Practical Conference "Problems of emergencies forecasting "* (Moscow, 14-15 May 2014), 61-63.
6. Soloviev A.A., Novikova O.V., Gorshkov A.I., Piotrovskaya E.P. (2013), Recognition of the potential epicenters of strong earthquakes in the Caucasus region using GIStechnik. *"REPORTS ACADEMY OF SCIENCES,* 450(5), 1-3.
7. Gravirov V., Kislov K.V., Gravirova L., Vinberg F. (2013), The Use of Wavelet Transformation Techniques in Structure of an Artificial Neural Network for Recognition of Early Arrival of Earthquakes on Strongly Noisy Seismic Records, *in Book of Abstracts CTBT: Science and Technology*, T3-P132, 139.
8. Gravirov V.V., Kislov K.V., Winberg F.E. (2012), Acquisition of intelligence signal from nonstationary noisy seismic data using neural network classifiers. *Industrial Automatic Control Systems, and Controllers*, 12, 45-49.
9. Seismological monitoring of the Western Ural http://pts.mi-perm.ru/region/types.htm
10. J.F. Clinton, M.Nettles, F.Walter, K.Anderson, T.Dahl-Jensen, D.Giardini, A.Govoni, W.Hanka, S.Lasocki, W.S.Lee, D.McCormack, S.Mykkeltveit, E.Stutzmann and S.Tsuboi (2014), Seismic Network in Greenland Monitors Earth and Ice System. *Eos Trans. AGU*, 95(2), 13–14.

HIGH LATITUDE CONTINUATION OF THE ORDINARY RING CURRENT AND AURORAL STRUCTURES

E.E. Antonova[1,2], V.G. Vorobjev[3], I.P. Kirpichev[2], O.I. Yagodkina[3], V.V. Vovchenko[2], M.O. Riazantseva[1,2], I.A. Kornilov[3], T.A. Kornilova[3], O.V. Kozyreva[4], S.S. Znatkova[1], M.S. Pulinets[1], M.V. Stepanova[5]

[1] Skobeltsyn Institute of Nuclear Physics Lomonosov Moscow State University, Moscow, 119991, Russia, e-mail: antonova@orearm.msk.ru

[2]Space Research Institute RAS, Moscow, Russia

[3]Polar Geophysical Institute, Apatity, Murmansk Region, Russia

[4] Institute of the Physics of the Earth, Moscow, Russia

[5]Universidad de Santiago de Chile, Chile

Abstract. We summarize the results demonstrating the existence of surrounding the Earth plasma population having the form of plasma ring at geocentric distances from 6-7R_E till magnetopause near noon and till ~10-12R_E near midnight. Plasma characteristics of the ring are near to plasma sheet proper. However in difference with plasma sheet proper, where the magnetic field lines are stretched in the antisolar direction, magnetic field lines in the ring have dipole like characteristics during quite time. Plasma pressure in the ring is larger than in the plasma sheet proper. Transverse currents in the surrounding the Earth plasma ring are closed inside the magnetosphere. Nightside part of the ring was previously selected as near the Earth plasma sheet. Magnetic field lines of the plasma sheet proper are stretched and its transverse currents are closed by magnetopause currents. It is a rather turbulent region with large fluctuations of plasma velocity and magnetic field filled by bursty bulk flows (BBF), thin current sheets, beams etc.

Plasma pressure at geocentric distances >6-7Re is near to isotropic. Such feature gives the possibility to use plasma pressure as the natural marker of the magnetic field line as in the condition of the magnetostatic equilibrium plasma pressure has the constant value along the field line. We compare values of plasma pressure measured at low latitudes by DMSP satellites and plasma pressure measured at the equatorial plane. We show that the main part of the discrete auroral oval is mapped to the surrounding the Earth plasma ring. Such feature explains the existence of quite comparatively stable auroral arcs inside the oval. Mechanism of arc formation is discussed. We show that the obtained picture of auroral domain mapping is rather useful for the explanation of different events including appearance of electrons-"killers".

Introduction

The development of the technique of experimental observations and computer modeling of the magnetospheric processes leads to the real reexamination of the number of the main approaches in the physics of the magnetosphere. This reexamination is mainly connected with the analysis of the plasma sheet as the turbulent wake under the magnetic field of the Earth which is the obstacle for solar wind flow. Formation of the turbulent wake is the natural consequence of the flows with high values of Reynolds numbers. Plasma sheet turbulence began to be examined by using a global MHD simulation [El-Alaoui et al., 2010, 2012] only recently. Properties of plasma sheet turbulence are experimentally analyzed now in many papers. However such studies are much more difficult than widely developed studies of solar wind turbulence in spite of the realization of multi-satellite missions. Only well selected elements of the plasma sheet turbulence such as bursty bulk flows (BBF), thin current sheets, beams etc. are proper analyzed. The existence of such well developed elements can be the consequence of the intermittency of the plasma sheet turbulence. However this problem was not proper analyzed.

The existence of the high level of plasma sheet turbulence has an obvious disagreement with the traditional statement of the discrete auroral oval mapping to the plasma sheet as it is well known that nearly stable systems of auroral arcs can be observed during many hours. However from the beginning of auroral observations it is known that polar boundary of the oval is ordinarily very dynamic. Such feature leads to the natural question: is the plasma sheet proper (the region with magnetic field lines stretched in the antisolar direction) is mapped to the auroral oval? Such question is especially interesting as electron precipitations from the plasma sheet without field-aligned acceleration can not produce visible aurora [Korniliv et al.,

2008; Antonova et al., 2011]). However, Stepanova et al. [2009, 2011], Pinto et al. [2011] show that the level of velocity fluctuations at geocentric distances X>-10R_E is greatly decreased during quite conditions. This can mean that stable auroral arcs can be mapped to smaller geocentric distances.

In this paper we summarize the results of data analysis (mainly of authors of the paper due to limits of paper volume) and modeling giving the possibility to show that main part of discrete auroral oval does not map to the plasma sheet proper. We also briefly discuss the contribution of different sources in the Dst variation and the problem of the formation of the outer electron radiation belt.

Surrounding the Earth plasma ring and transverse currents in the ring

From the very beginning of the space explorations [Vasyliunas, 1970] it has been known that the region between the plasmapause and daytime magnetopause is filled with plasma whose characteristics are similar to those observed in the plasma sheet (see also [Antonova et al., 2011] and references therein). The nightside part of the surrounding the Earth plasma population at geocentric distances up to ~10R_E was identified as the near Earth part of central plasma sheet by Galperin and Feldstein [1991]. However the topological characteristics of both dayside and nightside populations are quite different from the conventional plasma sheet where the magnetic field points predominantly parallel or antiparallel to the solar wind direction. In addition the region spaced from the geostationary orbit up to ~13–16R_E was selected as a region of quasitrapping at the first stages of space study [Vernov et al., 1969] where the drift trajectories of the most part of the energetic particles are closed inside the magnetosphere (Shabansky-type orbits).

Analysis produced by Kirpichev and Antonova [2011], Antonova et al. [2013, 2014a] using data of particle and magnetic field measurements of THEMIS mission [http://themis.ssl.berkeley.edu/data; Angelopoulos, 2008] show that the plasma structure surrounding the Earth at geocentric distances from ~6R_E to ~10–12R_E has the form of a ring. The particle spectra measured by ESA (an electrostatic analyzer of ions with energies from 1.6 eV to 25 keV and electrons with energies from 2 eV to 32 keV) and SST (solid state telescope which measures ions with energies from 25 keV to 6 MeV and electrons with energies from 25 keV to ~900 keV) instruments of THEMIS mission were used to calculate plasma pressure including ion and electron contributions. Periods when ESA and SST measurements are inconsistent in the overlapped energy intervals and the inconsistency is larger than 20% have been excluded from the analysis. Fig. 1 shows the averaged distribution of the plasma pressure and magnetic field (black lines) at the equatorial plane and pressure anisotropy from the paper [Antonova et al., 2014a]. The averaged solar wind for the analyzed period from the April 2007 to September 2012 were: P_{din}=1.8 nPa, IMF B_z=0.2 nT, B_y=0 nT; and the averaged geomagnetic parameters were: Dst>-20 nT, AE<100 nT. It is possible to see that plasma pressure in the quite time plasma ring is nearly isotropic and azimuthally symmetric. Obtained distributions of plasma pressure are in a very good coincidence with the plasma pressure distributions obtained by DeMichelis et al. [1997], Lui [1994] using data of AMPTE/CCE observations and by Tsyganenko and Mukai [2003] using data of Geotail observations for X<-10R_E in overlapped intervals.

Plasma pressure gradients in the ring are mainly directed to the Earth till geocentric distance ~3R_E which means the existence of westward transverse currents. Calculating the current it is necessary to take into account that a surface of minimal values of the magnetic field does not coincide with the equatorial plane near noon. Antonova et al. [2009a, b] show that dayside transverse currents in contrast to nighttime currents do not concentrate at the equatorial plane and are smoothed along the field lines. Antonova and Ganushkina [2000] named the surrounding the Earth current system the cut ring current (CRC) because the transverse current lines in this current system have a form of distorted rings. This current system is not included in magnetic field models with determined current systems. However it appears (A.Y. Ukhorskiy, private communication) in the model [Sitnov et al., 2008] in which magnetic field modeling was realized without using definite current systems. The MHD modeling of Liemon et al. [2011] also show the formation of such oblique to the equatorial plane current loops (see figure 1 of their paper).

Knowledge about the plasma pressure and magnetic field distribution makes it possible to calculate the current density in plasma in magnetostatic equilibrium. Antonova et al. [2009a,b] estimated the value of transverse current at the dayside field lines using data of AMPTE/CCE and THEMIS-B satellites taking into account compression of dayside field lines and shift of minimal values of magnetic field B_{min} from the equatorial plane. It was shown that the integral transverse current at the daytime field line is comparable with integral transverse current near midnight at the same geocentric distances. Kirpichev and Antonova [2014] obtain the value of integral currents in RC and CRC regions during quite geomagnetic conditions using distribution of plasma pressure gradients and magnetic field at the equatorial plane. Tsyganenko-2001 model was used for the calculation of magnetic field on the magnetic field lines near noon where minimal values of magnetic field are shifted from the equatorial plane. Kirpichev and Antonova [2014] demonstrate the

possibility of closing of nighttime transverse currents at geocentric distances of up to ~12R_E inside the magnetosphere.

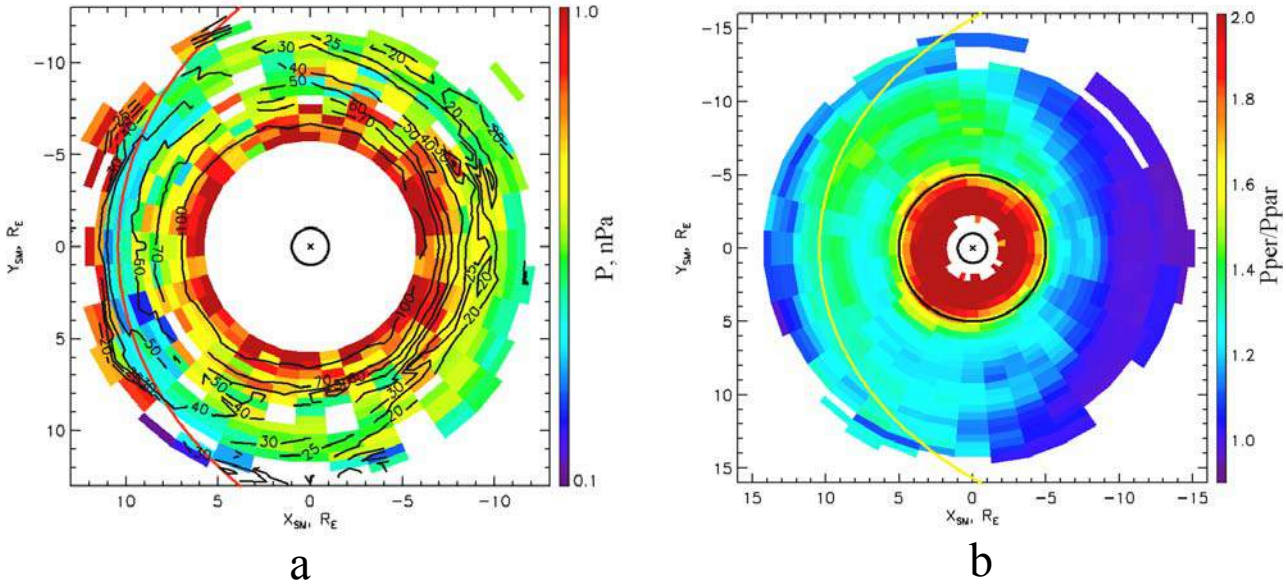

Fig. 1. The averaged distribution of the plasma pressure and magnetic field (black lines) (a) and pressure anisotropy (b) at the equatorial plane. Orange line shows the magnetopause position in accordance with Shue et al.'s [1998] model.

Introduction of CRC leads to reanalysis of the problem of the nature of Dst variation during magnetic storm. The problem appears due to the statement in the paper [Hamilton et al., 1988] that the measured energy content of the ring current (RC) ions was typically less than the value predicted by the Dessler-Parker-Sckopke relation. However the contribution of induction currents in Dst [Feldstein, 1992; Grenspan and Hamilton, 2000] was not taken into account. Vovhenko and Antonova [2010, 2011], Antonova et al. [2013] analyze the distortion of the magnetic field of dipole by experimentally measured radial plasma pressure profile, take into account the nonlinear effects and show that it is possible to obtain the correct values of Dst variation during magnetic storms. This means that it is possible to restore the traditional interpretation of the nature of Dst variation as mainly the ring current effect including RC and CRC.

Auroral oval mapping

The existence of the CRC, which is not included in already developed models of the magnetic field with fixed magnetic field geometry, poses the problem of mapping the auroral region to the equatorial plane since the traditional mapping procedure based on magnetic field models can lead to significant errors. However, having the picture of pressure distribution at the equatorial plane and at low altitudes it is possible to obtain the information about mapping under conditions of the magnetostatic equilibrium [**jB**] = □*P* (where **j** is the current density and **B** is the magnetic field) and assuming *P*=const along the field line. This means that *P* can be considered as a "natural tracer" or landmark of field lines [Dubyagin et al., 2002]. Such kind of comparison was used for example by Dubyagin et al. [2003] as the evidence of near-Earth breakup location of substorm on January 28, 2000 (21:22 UT).

The distribution of plasma pressure at low altitudes was obtained by [Wing and Newell, 1998; Wing et al., 2013] using results of DMSP observations. It was mapped to the equatorial plane using the Tsyganenko-1989 model by Wing and Newell [1998]. However Tsyganenko and Mukai [2003] stressed that the overstretched model fields leads to the discrepancy of Wing and Newell [1998] and their results. The distribution of plasma pressure at the DMSP altitudes during different phases of a magnetospheric substorm was obtained in the paper [Wing et al., 2013]. Fig. 2a shows such distribution 60 min before the substorm onset. However, the electron precipitations were not compared with the pressure distribution. It is possible to see that shown values of plasma pressure are much larger than corresponding values in the plasma sheet where the magnetic pressure balance in the tail lobes and at the center of the plasma sheet [Baumjohann et al., 1990; Petrukovich et al., 1999] is observed. The plasma pressure is 0.16 nPa at the center of the plasma sheet when the typical magnetic field in the tail lobes is 20 nT. The averaged plasma pressure in the tail is 0.229 nPa, according to [Tsyganenko and Mukai, 2003]. This averaged estimation include not only the plasma sheet proper but also part of plasma ring analyzed in [Antonova et al., 2013, 2014a].

Fig. 2b shows the distribution of the ion pressure at low altitudes obtained using data of DMSP observations and boundaries of the electron precipitations according to the AMP model of [Vorobjev et al., 2013] for quite geomagnetic conditions. Field-aligned potential drops leading to pressure decrease at low altitudes was not taken into account. Electron contribution to pressure was not determined. The obtained values set a lower bound of the whole pressure. Green lines show the polar and equatorial boundaries of auroral oval. It is possible to see that values of plasma pressure at the latitudes of the auroral oval are much larger than in the plasma sheet proper. Fig. 2c shows the distribution of the plasma pressure in the surrounding the Earth plasma ring according to the data of the THEMIS mission in magnetically quiet conditions. Comparison of Fig. 2b and 2c shows [Antonova et al., 2014b] that the most part of auroral oval should map to the surrounding the Earth plasma ring. It is necessary to stress that such mapping explains the ring like form of the auroral oval.

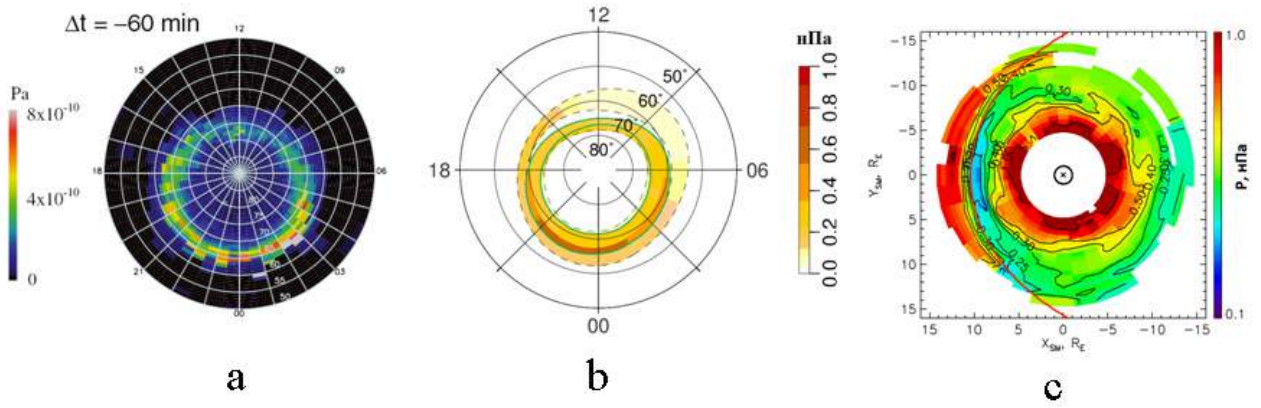

Fig. 2. The distribution of the ion pressure at low altitudes obtained by Wing et al. [2013] 60 min before the substorm onset (a), the distribution of the ion pressure at low altitudes and boundaries of the electron precipitations according to the AMP model (green lines show the polar and equatorial boundaries of auroral oval) in [Vorobjev et al., 2013] (b) and the distribution of the plasma pressure at the equatorial plane according to the data of the THEMIS mission for magnetically quiet conditions.

Traditional interpretation of the auroral oval as the region of plasma sheet mapping leads to the real misunderstandings in the solution of the problem of the outer electron radiation belt formation and appearance of large fluxes of relativistic electrons (electrons-"killers") during the recovery phases of geomagnetic storms. The auroral oval moves to low latitudes during magnetic storms and its thickness increases. Such motion is accompanied by changes of the magnetic field at the equatorial plane and great fluctuations inside the oval. Position of the region of the formation of new belt of relativistic electrons coincides with the position of storm time electrojet and the equatorial boundary of penetration of solar cosmic rays (see the review [Tverskaya, 2011] and latest results of Kozyreva and Antonova [2014]). This means the deep connection of the processes of acceleration of electrons-"killers" with auroral dynamics which is not proper analyzed till now. Considering the auroral oval as the region of mapping of the external part of the ring current greatly simplifies the solution of the problem.

Discussion and conclusions

Obtained results give the possibility to remove in many cases contradictions in the description of magnetospheric processes. It was very difficult until now to understand why the discrete auroral oval has well developed ring-like form suggesting that the oval is the region of plasma sheet mapping. It was also difficult to understand why constantly observed plasma sheet fluctuations do not influence on the stable slow moving auroral arcs in the auroral oval. The auroral oval moves to low latitudes during magnetic storm. Such motion becomes quite natural considering the auroral oval as the mapping of the external part of the developing ring current instead of the mapping of plasma sheet (considering the last as a nearly two-dimensional structure with antisunward directed field lines) and suggesting its shift to the Earth. Multiple results of the observations of plasma sheet disturbances 1-3 min before the isolated substorm onset become rather natural as in accordance with Borovsky et al. [1997] the correlation time of magnetic field fluctuations in the plasma sheet is ~8 min and velocity fluctuations ~2 min. This is why it is possible to find comparatively large plasma sheet disturbances before any substorm onset. Even the probability to observe BBF before the first auroral arc brightening is very high as BBFs are observed comparatively frequently ~10-15% of the time in the midnight plasma sheet [Angelopoulos et al., 1994]. Nakamura et al. [2004] show that

the full width of the flow channel producing BBF is 2–3 R_E in the "dawn-dusk" direction. This can mean that BBF leading to auroral streamer can be observed in the plasma sheet with very high probability before the onset which creates the real difficulty to the neutral line model of substorm. Considering BBF as the result of the development of ballooning/interchange instability [Panov et al., 2012] only complicates the situation. It is possible to mention also that in accordance with the substorm scenario of Stepanova et al. [2002] and the mechanism of bright auroral arc formation due to ionospheric plasma penetration in the region of preexisting field-aligned potential drop the auroral brightening can be only the result of the change of convection at the auroral field lines.

Acknowledgements
This work was partially supported by the grants of Russian Foundation for Basic Research 12-02-00217, 13-05-00233 and FONDECYT grant 1110729.

References

Angelopoulos, V. (2008), The THEMIS mission. *Space Sci. Rev.* 141, 5-34, http://dx.doi.org/10.1007/s11214-008-9336-1.

Angelopoulos, V., C. F. Kennel, F. V. Coroniti, R. Pellat, M. G. Kivelson, R. J. Walker, C. T. Russell, W. Baumjohann, W. C. Feldman, and J. T. Gosling (1994), Statistical characteristics of bursty bulk flow events, *J. Geophys. Res.,* 99, 21257-21280, doi:10.1029/94JA01263.

Antonova, E.E., I.P. Kirpichev, M.V. Stepanova, K.G. Orlova, and I.L. Ovchinnikov (2009a), Topology of the high latitude magnetosphere during large magnetic storms and the main mechanisms of relativistic electron acceleration. *Adv. Space Res.* 43, 628–633, http://dx.doi.org/10.1016/j.asr.2008.09.011.

Antonova, E.E., I.P. Kirpichev, I.L. Ovchinnikov, K.G. Orlova, and M.V. Stepanova (2009b), High latitude magnetospheric topology and magnetospheric substorm. *Ann. Geophys.* 27(10), 4069-4073, http://dx.doi.org/10.5194/angeo-27-4069-2009.

Antonova, E.E., I.P. Kirpichev, I.L. Ovchinnikov, M.S. Pulinets, S.S. Znatkova, K.G. Orlova, and M.V. Stepanova (2011), Topology of high-latitude magnetospheric currents. *IAGA special Sopron book series*. In: Liu, William, Fujimoto, Masaki (Eds.), The Dynamic Magnetosphere, vol. 3. Springer, pp. 201–210.

Antonova, E. E., and N. Yu. Ganushkina (2000), Inner magnetospheric currents and their role in the magnetosphere dynamics, *Phys. Chem. Earth (C)*, 25(1–2), 23–26, doi:10.1016/S1464-1917(99)00028-8.

Antonova E.E., I.P. Kirpichev, V.V. Vovchenko M.V. Stepanova, M.O. Riazantseva, M.S. Pulinets, I.L.Ovchinnikov, and S.S. Znatkova (2013), Characteristics of plasma ring, surrounding the Earth at geocentric distances ~7–10R_E, and magnetospheric current systems. *J. Atmos. Sol. Terr. Phys.*, 99, 85-91, doi:10.1016/j.jastp.2012.08.013.

Antonova E.E., I.P. Kirpichev, and M.V. Stepanova (2014a), Plasma pressure distribution in the surrounding the Earth plasma ring and its role in the magnetospheric dynamics. *J. Atmos. Sol. Terr. Phys.*, 115-116, 32-40, http://dx.doi.org/10.1016/j.jastp.2013.12.005.

Antonova, E. E., V. G. Vorobjev, I. P. Kirpichev, and O. I. Yagodkina (2014b), Comparison of the plasma pressure distributions over the equatorial plane and at low altitudes under magnetically quiet conditions, *Geomag. Aeron.*, 54(3), 278–281, doi:10.1134/S0016793214030025.

Baumjohann, W., Puscmann, G., and Luhr, H., Pressure balance between lobe and plasma sheet, *Geophys. Res. Lett.*, 1990, 17(1), 45–48, doi:10.1029/GL017i001p00045.

Borovsky, J.E., R.C. Elphic, H.O. Funsten, and M.F. Thomsen (1997), The Earth's plasma sheet as a laboratory for turbulence in high-β MHD, *J. Plasma Phys.*, 57 (1), 1–34, http://dx.doi.org/ 10.1017/S0022377896005259.

Galperin, Y.I., and Y.I. Feldstein (1991), Auroral luminosity and its relationship to magnetospheric plasma domains, in *Auroral physics,* edited by C.-I. Meng, M.J. Rycroft, and L.A. Frank, Cambridge Univ. Press, New York, 207-222.

DeMichelis, P., I.A. Daglis, and G. Consolini (1997), Average terrestrial ring current derived from AMPTE/CCE-CHEM measurements. *J. Geophys. Res.* 102 (A7), 14103–14111, http://dx.doi.org/ 10.1029/96JA03743.

Dubyagin, S. V., M. V. Kubyshkina, and V. A. Sergeev (2002), On the remote sensing of plasma sheet from low altitude spacecraft, *J. Atmos. Solar Terr. Phys*., 64(5-6), 567-573, doi: 10.1016/S1364-6826(02)00014-7.

Dubyagin, S.V., V.A. Sergeev, C.W. Carlson, S.R. Marple, T.I. Pulkkinen, and A.G. Yahnin (2003), Evidence of near-Earth breakup location. *Geophys. Res. Lett.,* 30(6), 1282, doi:10.1029/2002GL016569, 2003.

El-Alaoui, M., M. Ashour-Abdalla, R.L. Richard, M.L. Goldstein, J.M. Weygand, and R.J. Walker (2010), Global magnetohydrodynamic simulation of reconnection and turbulence in the plasma sheet, *J. Geophys. Res.*, 115, A12236, doi:10.1029/2010JA015653.

El-Alaoui, M., R. L. Richard, M. Ashour-Abdalla, R. J. Walker, and M. L. Goldstein (2012), Turbulence in a global magnetohydrodynamic simulation of the Earth's magnetosphere during northward and southward interplanetary magnetic field, *Nonlin. Processes Geophys*., 19, 165-175, doi:10.5194/npg-19-165-2012.

Feldstein, Ya. I. (1992), Modelling of the magnetic field of magnetospheric ring current as a function of interplanetary medium parameters, *Space Sci. Rev*., 59(1/2), 83-166.

Greenspan, M.E., D.C. Hamilton, (2000), A test of the Dessler–Parker–Sckopke relation during magnetic storms. J. Geophys. Res., 105 (3), 5419–5430, doi:10.1029/1999JA000284.

Hamilton D.C., G. Gloeckler, F.M. Ipavich, W. Studemann, B. Wilken, and G. Kremser (1988), Ring current development during the great geomagnetic storm of February 1986. *J. Geophys. Res.* 93(A12), 14343-14355, doi:10.1029/JA093iA12p14343.

Kirpichev, I.P., and E.E. Antonova (2011), Plasma pressure distribution in the equatorial plane of the Earth's magnetosphere at geocentric distances of 6–10R_E according to the international THEMIS mission data. *Geomag. Aeron.* 51(4), 450-455, http://dx.doi.org/10.1134/S0016793211040049.

Kirpichev, I. P., and E. E. Antonova (2014), Estimation of the current density and analysis of the geometry of the current system surrounding the Earth. *Cosmic Research*, 52(1), 52-60, doi:10.1134/S0010952514010043.

Kornilov, I. A. E. E. Antonova, T. A. Kornilova, and O. I. Kornilov (2008), Fine structure of auroras during auroral breakup according to the ground-based and satellite observations, *Geomag. Aeron.,* 48(1), 7-19. doi:10.1134/S0016793208010027.

Kozyreva, O.V., and E.E, Antonova (2014), The storm time position of the auroral electrojet and the acceleration of the outer belt relativistic electrons, Abstracts of 40th COSPAR Scientific Assembly, Moscow, Russia, August 2-10, PRBEM.1-0008-14.

Liemohn, M.W., D. L. De Zeeuw, R. Ilie, and N. Y. Ganushkina (2011), Deciphering magnetospheric cross-field currents. *Geophys. Res. Lett*, 38, L20106, doi:10.1029/2011GL049611.

Lui, A. T. Y., Inner magnetospheric plasma pressure distribution and its local time asymmetry. *Geophys. Res. Lett*., 30(16), 1846, doi:10.1029/2003GL017596, 2003.

Nakamura, R., et al. (2004), Spatial scale of high-speed flows in the plasma sheet observed by Cluster, *Geophys. Res. Lett., 31*, L09804, doi:10.1029/2004GL019558.

Panov, E. V., et al. (2012). Kinetic ballooning/interchange instability in a bent plasma sheet. *J. Geophys. Res.*, 117(A6), 6228, doi:10.1029/2011JA017496.

Pinto, V., M. Stepanova, E.E. Antonova, and J.A. Valdivia (2011), Estimation of the eddy diffusion coefficients in the plasma sheet using THEMIS satellite data. *J. Atmos. Sol. Terr. Phys*. 73 (11-12), 1472–1477, http://dx.doi.org/10.1016/j.jastp.2011.05.007.

Petrukovich, A.A., Mukai, T., Kokubun, S., et al., (1999), Substorm associated pressure variations in the magnetotail plasma sheet and lobe, *J. Geophys. Res.*, 104(A3), 4501–4513. doi: 10.1029/98JA02418.

Shue, J.-H., P. Song, C.T. Russell, J.T. Steinberg, et al. (1998), Magnetopause location under extreme solar wind conditions. *J. Geophys. Res.,* 103 (A8), http://dx.doi.org/10.1029/98JA01103.

Sitnov, M. I., N. A. Tsyganenko, A. Y. Ukhorskiy, and P. C. Brandt (2008), Dynamical data-based modeling of the stormtime geomagnetic field with enhanced spatial resolution, J. Geophys. Res., 113, A07218, doi:10.1029/2007JA013003.

Stepanova, M.V., E.E. Antonova, J.M. Bosqued, R.A. Kovrazhkin, and K.R. Aubel (2002), Asymmetry of auroral electron precipitations and its relationship to the substorm expansion phase onset, *J. Geophys. Res.,* 107(A7), 10.1029/2001JA003503.

Stepanova, M., E.E. Antonova, D. Paredes-Davis, I.L. Ovchinnikov, Y.I. Yermolaev (2009), Spatial variation of eddy-diffusion coefficients in the turbulent plasma sheet during substorms. *Ann. Geophys.* 27 (4), 1407–1411, http://dx.doi.org/10.5194/angeo-27-1407-2009.

Stepanova, M., V. Pinto, J.A. Valdivia, E.E. Antonova (2011), Spatial distribution of the eddy diffusion coefficients in the plasma sheet during quiet time and substorms from THEMIS satellite data. *J. Geophys. Res.*, 116, A00I24, http://dx.doi.org/10.1029/2010JA015887.

Tsyganenko, N.A., and T. Mukai (2003), Tail plasma sheet models derived from Geotail data, *J. Geophys. Res.,* 108(A3), 10.1029/2002JA009707.

Tverskaya, L. V. (2011), Diagnostics of the magnetosphere based on the outer belt relativistic electrons and penetration of solar protons: A Review. *Geomag. Aeron,* 51(1), 6–22, doi:10.1134/S0016793211010142.

Vasyliunas, V. M., Mathematical models of magnetospheric convection and its coupling to the ionosphere, *Particles and Fields in the Magnetosphere*, ed. B.M. McCormac, Higham, Mass., Holland, 60-71, 1970.

Vernov, S.N., E.V. Gorchakov, S.N. Kuznetsov, Yu.I. Logachev, E.N. Sosnovets, and V.G. Stolpovsky (1969), Particle fluxes in the outer geomagnetic field. *Rev. Geophys. Space Phys*., 7 (1-2), 258–279, doi:10.1029/RG007i001p00257.

Vorobjev, V.G., O.I. Yagodkina, and Yu.V. Katkalov, Auroral Precipitation Model and its applications to ionospheric and magnetospheric studies, *J. Atmos. Sol. Terr. Phys.*, 2013, vol. 102, pp. 157–171, doi:10.1016/j.jastp.2013.05.007.

Vovchenko, V. V., and E. E. Antonova (2010), Nonlinear disturbance of the dipole field by an axisymmetric plasma distribution, Geomag. Aeron., 50(6), 739-748, doi 10.1134/S0016793210060058.

Vovchenko, V. V., and E. E. Antonova (2012), Dependence of volumes of magnetic flux tubes on plasma pressure and disturbance in the magnetic field in the axially symmetric case, *Geomag. Aeron.,* 52(1), 49-59, doi:10.1134/S0016793212010161.

Wing, S., and P.T. Newell (1998), Central plasma sheet ion properties as inferred from ionospheric observations. *J. Geophys. Res.,* 103 (A4), 6785–6800, http://dx.doi.org/10.1029/97JA02994.

Wing, S., M. Gkioulidou, J.R. Johnson, P.T. Newell, and C.-P. Wang (2013), Auroral particle precipitation characterized by the substorm cycle. *J. Geophys. Res. Space Phys.* 118, 1022–1039, http://dx.doi.org/10.1002/jgra.50160.

ON THE MID-LONG TERM WEATHER AND CLIMATE FORECAST BASED ON THE SOLAR-GEOMAGNETIC SIGNAL

S.V. Avakyan [1, 2, 3], L.A. Baranova [4]

[1] All-Russia Science Center "S.I. Vavilov State Optical Institute",
St. Petersburg, 199034, Russia; e-mail: avak2@mail.ru;
[2] St. Petersburg State Polytechnic University, St. Petersburg, Russia;
[3] The Central (Pulkovo) astronomical observatory of RAS, St. Petersburg, Russia;
[4] A.F. Ioffe Physico-technical Institute of RAS, St. Petersburg, Russia

Abstract. We suggest that factors of solar and geomagnetic activity should be taken into account in forecasting weather and climatic variations (i.e., cloudiness, temperature and precipitation). The "solar signal" may be taken into account in medium-to-long-term forecasts in two possible ways. The first of them is related to the detected quasi-cyclicity in the occurrence of large solar flares and worldwide magnetic storms within the basic 11-year solar cycle. Generally, in each solar cycle, both flares and storms display from two to three maxima with intervals from 2 to 6 years between them. The temperature of the ground-level air and the precipitation also display from 2 to 5.5-year periodicity, which makes it possible to use flares and storms for long-term forecasts of cloudiness and anomalies in temperature and precipitation. The other possibility is based on the correlation (found by us) between the global occurrence of the total and especially upper cloudiness (on the month scale), on one hand, and the flux of solar radiation (the solar constant and the facular activity), and also the number of solar spots, on the other hand. Using the statistics of the lifetime of these formations in the solar atmosphere (between a week and three months), it is possible to forecast the magnitude of the cloudiness and hence the anomalies of the ground air temperature on the week-to-season scale.

1. Introduction

The observed dependence of weather and climatic effects on the cycles of solar activity is to be explained, and thereby the importance of the mechanism of this dependence is to be confirmed. Meteorologists (and sometimes geophysicists) study correlations between weather and climatic parameters, on the one hand, and the general characteristics of solar activity: Wolf numbers (related to formation of solar spots) and the solar constant (which describes the total flux of electromagnetic solar radiation and its variations), on the other. The result of these studies was generally negative: neither Wolf numbers nor the variability of the solar constant displayed any significant correlation with meteorological parameters. This fact cast doubt on the very possibility of the effect of solar-geomagnetic activity on the weather and climate on the Earth [Kolesnikova, Monin, 1968; Monin, 1969; Pittock, 2009].

In our works, from the analysis of trends in the variation of cloudiness and radiative balance of the Earth for the latest decades (in the time of a secular maximum of solar-geomagnetic activity) we have proven the combined influence of solar flares and geomagnetic storms on the global degree of total cloudiness. In these studies, we have revealed the contribution of the flares (the increases in the flux of ionizing radiation of the Sun) and magnetic storms (the electrons precipitating in the ionosphere from radiation belts) to the contemporary global warming. According to our radio-optical three-stage trigger mechanism of the relation between solar magnetosphere and the Earth weather and climate, the evolution of cloudiness is controlled by the microwave radiation of the ionosphere, which is sporadically enhanced in the time of solar flares and worldwide magnetic storms [Avakyan, Voronin, 2011; Avakyan, 2012].

This radiation is formed by spontaneous fine-structure transitions from relatively low Rydberg levels (with principal quantum numbers n~10) excited in the upper-atmosphere gas by the shocks of high-energy ionosphere electrons: photo-electrons and Auger-electrons in a solar flare, secondary and Auger-electrons in corpuscle precipitations in the time of worldwide geomagnetic storms. Since the microwave radiation (with millimeter to decimeter wavelengths) penetrates into the troposphere virtually freely, it promotes the

formation of condensation-cluster haze, and further on, of optically thin cloudiness, which heats the ground-level air [Avakyan, 2008].

2. On possible manifestations of the solar activity in weather characteristics within 11-year cycle

The study of correlation between the temperature of the ground-level air (measured in Moscow - Leningrad and in Oslo) and Wolf numbers revealed that the temperature does not oscillate with the 11-year period (the basic period of the solar activity). Instead, steady variations within the interval of 2 to 5.5 years are observed [Kolesnikova, Monin, 1968; Monin, 1969; Benestad, 2002]. This result is totally consistent with the radio-optical three-stage trigger mechanism: the heating (optically thin) cloudiness grows due to the increased microwave flux from the ionosphere, both under the action of solar flares, and in the time of magnetic storms [Avakyan, 2013a,b]. The 11-year cycle displays two-to-three maxima of probability of the occurrence of these flares and storms, which, as a rule, do not coincide [Avakyan et al., 1994]; time intervals between them span from 2 (for flares) to 5-6 (for large magnetic storms) years, fig. 1 and 2.

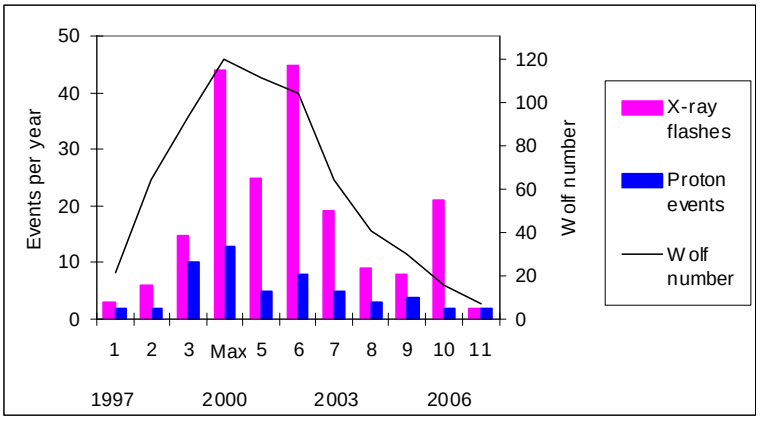

Fig. 1. There are two - three maxima of SOLAR X-rays FLARES during 23-th cycle.

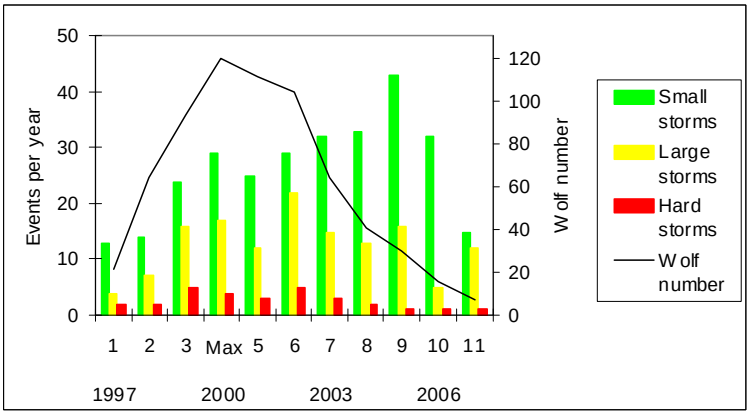

Fig. 2. There are two - three maxima of geomagnetic storms during 23-th solar cycle.

As a result, within 11 years, two most powerful microwave impacts on the abundance of water vapor in the troposphere occur (with the coagulation of clusters) – one in the times of magnetic storms and the other, generally less intense, in the times of solar flares, as a rule, in the intervals between the maxima of geomagnetic storms. This explains the scatter from 2 to 5.5 years in the periods of the temperature maxima observed in Leningrad and Moscow, and later in Oslo. In the study [Benestad, 2002] in Oslo, periods of 2 to 6 years for precipitation were also manifested. Within the framework of the radio-optical mechanism, the influence of the cyclicity of the solar-geomagnetic activity on hydrological processes should be traced taking into account stimulation of the precipitation from low cloudiness in the case of formation of optically thin cloudiness after flares and magnetic storms. As it was stated in [Borisenkov et al., 1981], cirrus clouds, which are analogous to the above kind of cloudiness, may "seed" the lower clouds with crystals and thereby cause precipitation.

Then we should state that the statistics of the distribution of major solar flares and worldwide magnetic storms within the 11-year solar cycle makes it possible to reveal variations in the ground-level air temperature and the intensity of precipitation in the interval of quasi-periods of 2 to 5.5 years.

In the study [Bogdanov, 2006] it was obtained that the atmospheric pressure on a given altitude above the sea level decreases after a solar flare. Previously, however, it had already been noted in [Borisenkov et al., 1989] that the occurrence of cirrus clouds (which, according to our radio-optical mechanism are generated after solar flares and geomagnetic storms, and are heating) is accompanied with a decrease in the pressure by 5 to 6 hPa, with simultaneous minor increase in the air temperature. In [Starkov, Roldugin, 1994], a decrease in the transparency of the atmosphere was detected both after a solar flare (by 5 %) and 6 to 7 hours after an intense aurora (IBC-III).

It was noted in [Eigenson, 1963] that in the day of the beginning of a magnetic storm, the atmosphere above the observing station is usually dominated by anti-cyclone, which changes to cyclone one or two days later. According to our analysis of numerous studies of the incidence of cloudiness (primarily, of cirrus clouds), firstly, in the case of both solar flares and magnetic storms, the cloudiness generally increases (while the atmospheric pressure decreases), and secondly, these variations are not monotonous (for example, see [Dmitriev, Govorov, 1972; Dmitriev, Lomakina, 1977]). More precisely, the cloudiness reaches its absolute maximum at the end of the first - the beginning of the third day after the appearance of the flare. Later on (with the start of a worldwide magnetic storm), it decreases for a day, to the beginning of the fourth day, when it grows again during the fourth day; only from the beginning of the fifth day after the appearance of the flare on the Sun, the cloudiness begins to decrease again. In total, these variations are also accompanied with those in the transparency of the Earth atmosphere in the zone of the absence of clouds: in the time of the flare and the magnetic storm, the transparency decreases to 5%, while in the first day and four days after the beginning of the storm the transparency reaches its maximum. The above time limits may shift for a day, depending primarily on the intensity of the flares and storms.

The result of the impact of cosmic factors on weather and climatic events depends more on the correspondence of phases of the space-physical and meteorological phenomena than on the power and duration of the solar flare or magnetic storm. Here, the primary factor is the initial conditions, i.e. the state of the lower atmosphere by the time of the event of the solar-geomagnetic activity in each given region of the planet [Mustel, 1974; Avakyan, 2010]. One initial condition, namely, the presence of optically thick cloudiness (which is very common for high and medium latitudes, especially taking into account that the density only slightly exceeds unity) strongly levels the effect of solar flares and geomagnetic storms on the weather in a given region, since in this case the genesis of new thin cloudiness is indistinguishable: for ground-level air, the thermo-radiation balance is determined by the thick cloud cover. At night, naturally, flares yield no contribution, while in winter the night optically thick cloudiness decelerates the cooling of the ground-level air. On the night side of the Earth, all types of cloudiness, both optically thick (strongly connected with variations in the flux of cosmic rays) and optically thin (newly formed under the influence of a geomagnetic storm) eventually result in the deceleration of the cooling of ground-level air in winter [Avakyan, 2010; 2012].

3. Taking into account solar activity in medium-term forecasts of weather characteristics

The studies [Avakyan, 2012; 2013a,b], using the example of the 23-rd 11-year cycle of the solar activity, revealed the correlation of the area of cloudiness with bursts in the value of the solar constant (positive) and with the number of solar spots (negative) on the timescale of several months. It was stated that the number of spots that appear on the solar disc and the facular regions in the solar photosphere may be used to forecast variations in the area of the cloud cover (magnitude of the cloudiness), and consequently the thermo-radiation balance of the Earth by several months ahead (based on the known statistics of the lifetime of these formations in the photosphere of the Sun).

The connection between bursts in the value of the solar constant and facular regions (TSI bursts are related with facular UV radiation of the solar atmosphere), as well as the role of spot activity in the photosphere of the Sun, was discussed in [Makarova et al., 1991]. Note especially a dual manifestation of the spot activity in TSI variations. Long-term TSI variations within a solar cycle are of the same sign as those in the number of spots: the fewer spots, the smaller TSI. On the contrary, the well-understood short-term correlation between TSI and the spots is of the opposite sign: the more numbers, the smaller TSI. Individual large spots (groups) reduce instantaneous values of TSI, especially in the time of the emergence of the groups. In spite of the fact that the lifetime of facular component exceeds two revolutions of the Sun, while spots on average exist for one revolution (and thereby, the facular component is generated by structures with

substantially larger lifetime than that of spots), the study [Makarova et al., 1991] presents approximate faculae-to-spots balance between the excess and lack of radiation of the objects. In total, spots do not block UV radiation of faculae to the extent in which they block optical and IR radiation of the solar disc.

Statistical data on the duration of spot and facular activities of the Sun are presented in [Allen, 1977]. The lifetime of an average group of spots is 6 days; for larger groups, which specify variations of solar activity, it reaches 1.5 months. For a large spot, the time of a decrease in the area by the factor of *e* is roughly equal to 11 days. The lifetime of an average facula is 15 days; that of a large facula, which determines variations of solar activity, reaches 2.7 months. Indeed, the facular component is generated by structures with lifetime greatly exceeding a typical lifetime of a spot. Within the framework of our method of taking into account the activity of the Sun in medium-term forecasts of weather and climatic characteristics, the presented times of relaxation of spot and facular structures on the Sun determine the shortest (a week) and the longest (up to 2.7 months) intervals of forecasting of variations of the area of the total cloud cover. This part of forecasts is based on manifestations of the spot activity (which results in the decrease in the area of cloudiness equivalent to that in the cloudiness magnitude) and facular activity (which results in the increase in the magnitude of the cloud cover).

From the database of temperature anomalies collected in the World Data Center of the Institute of hydro-meteorological information, Obninsk, using the total volume of measurements obtained by all meteorological stations of the Russian Federation since 1966, it was obtained [Sherstyukov, 2008] that in the cold half-year the warming effect of cloudiness determines about 50 % of the total temperature variability. In the warm half-year, the cooling effect of cloudiness determines about 25 % of the total variability. In April and October (the months of the change of half-years) the proportion of temperature variation explained by cloudiness accounts for only about 5 %. The same study presents relations between variations in the total (general) cloudiness (in the form of cloudiness magnitudes) and the absolute temperature for anomalies, based on the generalization over all meteorological stations of Russia within the latitude zone 50 – 70^{o} NL, from eight-term (i.e., after each three hours) daily observations since 1966. As the norms, the average values for 1966-1990 were taken; anomalies in temperature and cloudiness for five-day stretches were calculated for 1991-2004. On average, in all cases, a 0.1 magnitude variation of cloudiness was accompanied with that of ground-level air temperature approximately by 0.4-0.5°C.

In some months and five-day stretches, temperature variations (in degrees of Celsius) related to those of the area of cloud cover (in magnitudes of cloudiness) appeared to be several times higher; corresponding conversion factors may be obtained from the graphs of the World Data Center of the Institute of hydro-meteorological information, Obninsk,, Fig. 3 and 4 [Sherstyukov, 2008]. (These graphs make it possible to determine temperature anomalies from variations of the magnitude of the total (general) cloudiness, with the increase in intermittence factor to five days). In January – February, 1991 – 2004, a relatively large increase in cloudiness (by the magnitude 0.5-1.0) was accompanied with that in the air temperature over Russia by 3-5°C, while in October – early November and in the second half of December the cloudiness increased by the magnitude 0.3-0,4 with the growth of the temperature by 1-2°C. The decrease in cloudiness in the second half of November and in the early December by 0,4 magnitude was accompanied with that in decrease in the air temperature over Russia by 2°C.

In the warm half-year (21st to 59th five-day stretch), negative anomalies of cloudiness are accompanied with increase in temperature, while positive with decrease. For negative anomalies of cloudiness from –0.21 to –0.26 magnitudes, positive temperature anomalies are observed, +1.1 to +1.4°C; a negative temperature anomaly (–0.2°C) is observed only in the 52nd five-day stretch (September), with the largest positive anomaly of cloudiness (0.51 magnitude).

4. Conclusion

1. We early [Avakyan, Voronin, 2011; Avakyan, 2012, 2013 a,b] present evidences for possible contribution of radio-optical three-stage trigger mechanism to solar-troposphere relations. Some poorly understood phenomena were explained that accompany the global warming in the latest decades: perennial variations of cloud cover, including redistribution of the types of cloudiness and observed variations of the flux of long- and short-wavelength radiation escaping from the Earth.

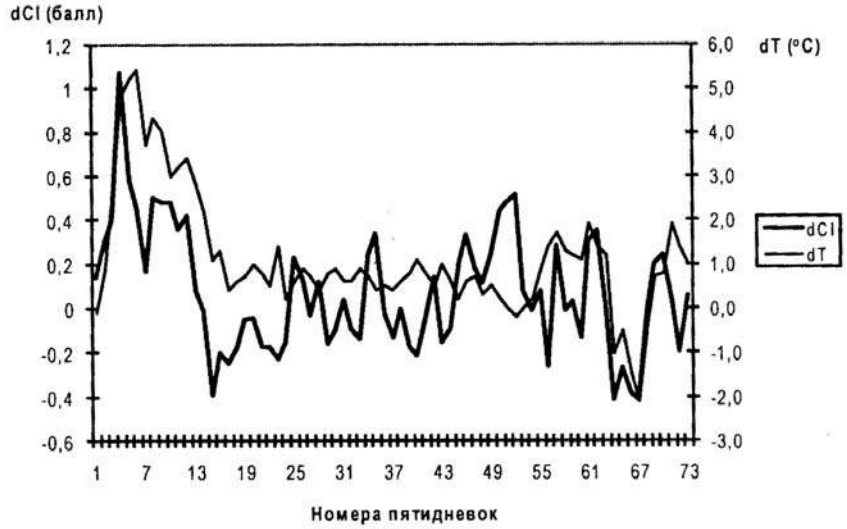

Fig. 3. Annual cycle (for five-day stretches) of air temperature anomalies (dT) and the total (general) cloudiness (dCl) for 1991 – 2004, relative to averages for 1966 - 1990. [Sherstyukov, 2008].

Fig. 4. Variations in the warm half-year (for five-day stretches) of air temperature anomalies (dT) and the total (general) cloudiness (dCl), in magnitudes for 1991 – 2004, relative to averages for 1966 – 1990, for stations of Russia in the latitude zone 50 - 70° [Sherstyukov, 2008].

2. We analyze the known spectral results for the air temperature and precipitation and suggest possible application of the data on solar-geomagnetic activity to medium- and long-term forecasts of such basic weather characteristics as cloudiness, temperature anomalies, and, possibly, precipitation.

In the suggested method of medium-term (week-to-month) forecasts of weather characteristics, we use as predictors the best known and reliably determined parameters of current solar activity: the number of solar spots and bursts of the solar constant.

In long-term forecasts (2 to 5 - 6 years), the solar activity is taken into account in the form of the statistics of distribution (within 11-year solar cycles) of both the number of appearance of powerful solar flares and that of the principal (worldwide) geomagnetic storms. This approach also makes it possible to determine variations of magnitudes (occurrence) of the cloud cover and anomalies of the ground-level air temperature [Avakyan, Baranova, 2014].

References

Allen, C.W. (1973), *Astrophysical quantities*, Un. L., The Athlone Press, 2nd edition, 446 pp.

Avakyan, S.V (2008), Physics of the Solar–Terrestrial Coupling: Results, Problems, and New Approaches. *Geomagn. Aeron.*, 48(4), 417–424.

Avakyan, S.V. (2010), Channels of Influence of Cosmophysical Factors on the Weather and Climate Characteristics, *in: Proc. All_Russia. Conf. on the Physics of the Sun: Solar and Solar_Terrestrial Physics 2010, October 3–9, 2010,* GAO, St. Petersburg, 19-22.

Avakyan, S.V. (2012), Problems of climate as a problem of solar-terrestrial physics, *Report Delivered at the First Plenary Session of the All-Russia Conference on Solar Activity and the Weather of Global and Regional Climate Changes, Institute of Solar-Terrestrial Physics, SO RAN, June 19, 2012, Irkutsk,* in: Collection of Scientific Works on Solar-Terrestrial Physics, No. 21, 18–27.

Avakyan, S.V. (2013a), The Role of Solar Activity in Global Warming. *Herald of the Russian Academy of Sciences,* 83(3), 275-285.

Avakyan, S.V. (2013b), Problems of climate as a problem of optics. *Journal of Optical Technology, Optical Society of America*, 80(11), 717-721.

Avakyan, S.V. and L.A. Baranova (2014), *Patent of Russian Federation* on the "Method of taking into account solar activity for middle-term forecasting of weather-climate characteristics", (No. 052242 from 19 November 2014), with the priority from 24 July 2013.

Avakyan, S.V. and N.A. Voronin (2011), The role of space and ionospheric disturbances in the global climate change and pipeline corrosion. *Izvestija, Atmosferic and Oceanic Physics*, *Springer*, 47(9), 1143-1158.

Avakyan, S.V., A.I. Vdovin, and V.F. Pustarnakov (1994), *Ionizing and Penetrating Radiation in the Near-Earth Space: A Reference Book*, Gidrometeoizdat, St. Petersburg, 501 pp.

Benestad, R.E. (2002), *Solar Activity and Earth's Climate,* Springer-Praxis, Chichester, 288 pp.

Bogdanov, M.B., A.N. Surkov, and A.V. Fedorenko (2006), Effect of cosmic rays on atmospheric pressure at high altitudes. *Geomagn. Aeron.*, 46 (2), 268-274.

Borisenkov, E.P., T.A. Bazlova and L.N. Efimova (1989), *Cirrus Cover and Its Influence on Atmospheric Processes*, Gidrometeoizdat, Leningrad, 119 pp.

Borisenkov, E.P., V.P. Meleshko, and A.P. Sokolov (1981), The influence of high level clouds on the thermodynamic regime and circulation of the atmosphere. *Meteorology and Hydrology,* №11, 15-17.

Dmitriev, A.A. and D.V. Govorov (1972), Interrelation between the Physical and Heliophysical Experiments. *Rep. Arct. Antarct. Res. Inst.*, 311, 132-137.

Dmitriev, A.A. and T.Yu. Lomakina (1977), Clouds and X_Ray Emission of Space, *in: The Effects of Solar Activity in the Lower Atmosphere,* ed by L.R. Rakipova, Gidrometeoizdat, Leningrad, 70-77.

Eigenson M.S. (1963) *Sun, weather and climate.* Gidrometeoizdat, Leningrad, 274 pp.

Kolesnikova, V.N. and A.S. Monin (1968), About the spectra micrometeorological, sinoptical and climate oscillation of meteorological fields. Meteorological Research, No 16, Nauka, Moscow, p. 30-56.

Makarova, A.V. Kharitonov, and T.V. Kazachevskaya (1991), *Solar Radiation Flux*, Nauka Publ., Moscow, 397 pp.

Monin, A.S. (1969), *Prognoz of weather as task of physics,* Nauka, Moscow, 184 pp.

Mustel, E.P. (1974), The role of initial conditions in the formation of the pressure field. In: *Solar-atmospheric links in the theory of climate and weather forecasting.* Gidrometeoizdat, Leningrad, p.143-148.

Pittock, A.B. (2009), Can solar variations explain variations in the Earth's climate? *Clim. Change,* 96, 483-487, doi:10.1007/s10584-009-9645-8.

Sherstyukov, B.G. (2008) *Regional and seasonal regularities of modern climate change*. "VNIIGMI-WCD" Publ., Obninsk, 246 pp.

Starkov, G.V. and Roldugin V.K. (1994), About the link of variation in transparency of the atmosphere with the geomagnetic activity. *Geomagn. Aeron.*, 34(4), 156-159.

CORRELATION OF GLOBAL CLOUDINESS WITH BURSTS IN TOTAL SOLAR IRRADIANCE

S.V. Avakyan[1,2,3], N.A.Voronin[1], S.S. Kavtrev[3]

[1]All-Russian Scientific Center "S.I. Vavilov State Optical Institute",
St. Petersburg, Russia, e-mail: avak2@mail.ru;
[2]St. Petersburg State Polytechnical University, St. Petersburg, Russia;
[3]Russian State Scientific Center for Robotics and Technical Cybernetics, St. Petersburg, Russia

Abstract. Studies of the response of the global cloudiness to solar forcing are essential for meteorological forecasting. From ISCCP data we found positive reaction of two types of cloudiness to bursts in the total solar irradiance on the month scale. The best correlation with TSI is displayed by upper cloudiness (in 93% cases against 81% for the total cloudiness). This result is consistent with our idea that in the times of solar forcing the upper cloudiness is generated basically as a result of acceleration of water vapour clusterization due to the increase in microwave fluxes from ionosphere (this mechanism was suggested by us previously). Another manifestation of the response of parameters of global cloudiness to solar forcing was revealed in trends observed in the total and upper cloudiness. Within 1983-2004, i.e. for about 80% of the total time of the measurements, these trends displayed the same direction, and were consistent with the hypothesis of the prevalence of secular variations in solar-geomagnetic activity at the present stage of global warming. Corresponding parameters of solar-geomagnetic activity are the number of large solar flares and principal geomagnetic storms accompanied with the increase in fluxes of ionizing solar radiation and corpuscles resulting in supplementary microwave emission from the terrestrial ionosphere.

1. Studies of the response of characteristics of global cloudiness to variations of solar activity present considerable scientific and practical interest. Given the revealed influence of rapid variations in the solar constant (TSI) on the formation of clouds in the global scale, data on the solar geomagnetic activity can be used in weather and climatic forecasting, in particular, for middle- and long-term weather forecasts.
Here, we describe the stable positive reaction to TSI bursts for two types of cloudiness (total and high), derived from ISCCP global data for the years 1984-2009 averaged over months. The highest positive correlation is obtained for the upper cloudiness (UC) averaged over months (93% of the cases), while for the total cloudiness (TC) the correlation is lower (81% -- Fig. 1). Within the interval 1983-2009, 32 cases of coincidence of all three parameters (TSI, TC and UC) were found, 8 cases for TSI and UC, and 3 cases for TSI and TC. No significant correlation with the lower cloudiness was detected (Fig. 3), and only 50% coincidence was seen in the case of middle cloudiness (Fig. 2).

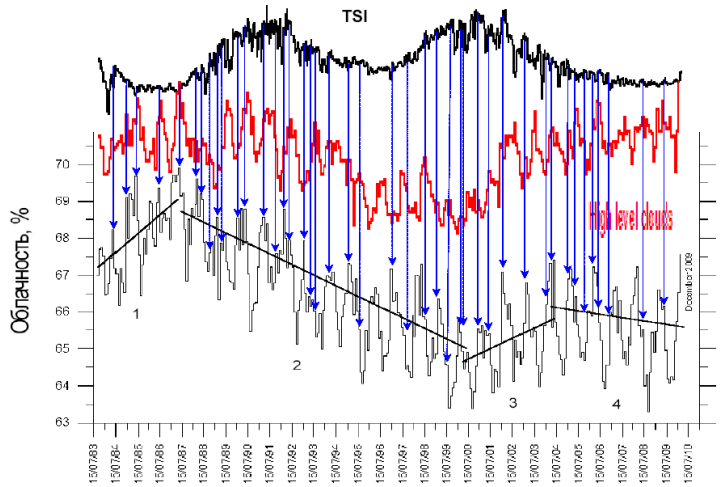

Fig. 1. Comparison between variations of the global total and upper cloudiness (ISCCP/GISS/NASA data) and those of the solar constant (Total Solar Irradiance - TSI).

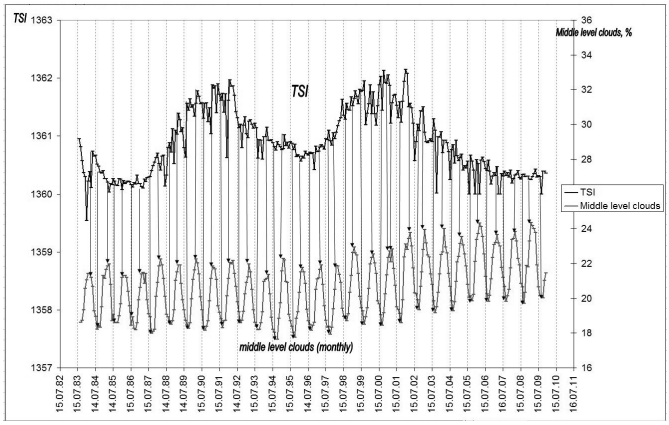

Fig. 2. Comparison between variations of the global middle cloudiness (ISCCP/GISS/NASA data) and those of the solar constant (TSI).

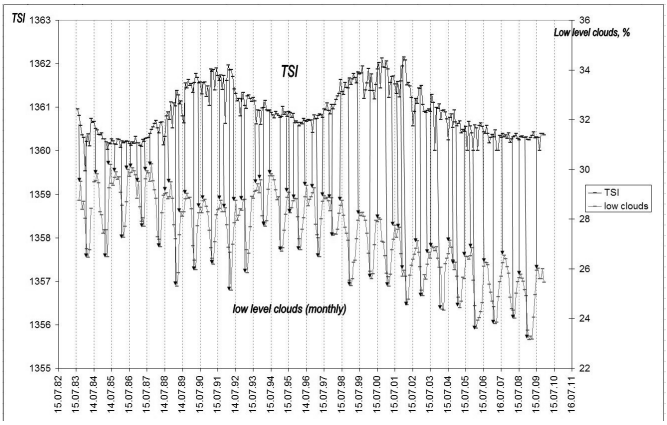

Fig. 3. Comparison between variations of the global lower cloudiness (ISCCP/GISS/NASA data) and those of the solar constant (TSI).

These results indicate the decisive contribution of microwave radiation from the ionosphere to the formation of primarily upper (as a rule, cirrus) optically thin cloudiness. Thereby, it is indeed UC that contributes mostly into the correlation between TSI and TC; this is consistent with the radio-optical mechanism of solar-to-atmosphere correlations previously suggested by The S.I. Vavilov Optical Institute. It determines the speed is increased clustering of water vapor due to increasing ionospheric microwave radiation during periods of solar forcing in the formation of condensation-cluster haze in the troposphere, which develops later in optically thin, usually the upper (cirrus) cloudiness [Avakyan, 2013].

2. The detected effect of coincidence of TSI bursts and peaks of the total cloudiness (averaged over months) may be applied to forecasting regional anomalies in the air temperature.
We are planning to use statistical data of:

- evolution of the faculae activity in the solar spectrum;
- correlation between the average long-term variability of cloudiness and temperature anomalies (known for 5-day intervals through a total year) in a given region.

3. We also compared the type and magnitude of trends in TC and UC, and noted that:

- for about 80% of the time, they are of the same direction;
- variations in the rate of this direction is consistent with the hypothesis of the domination of secular variations of solar-geomagnetic activity at the current stage of the global warming.

The above is seen in Fig.1, which presents the trends for TC and UC:

(1) the interval until the years 1985/87, when both the solar and geomagnetic activity grew in the secular cycle;

(2) the interval 1987 to 2000, when the solar electromagnetic (since 1985) and corpuscular activity was falling;

(3) the interval 2000 to 2003, when the geomagnetic activity kept growing; this growth lasted from the 19-th century to the absolute maximum in 2003;

(4) a new decrease since early 2004, related to the total decline of the solar-geomagnetic activity in the current secular cycle.

For the upper cloudiness, the first three trends are the same; from the beginning of 2004, instead of the decline, a growth is detected, which we relate to previously registered increase in the flux of the cosmic rays, up to the maximum reached in September, 2009.

The presented evidences of the dependence of the global cloudiness on the level of solar-geomagnetic activity in the decades of the observed maximum of the current secular cycle confirm the conclusion [Avakyan, 2013] that the solar activity is a natural driving force of the current stage of the global warming.

4. Besides, we analyzed the comparison between time variations of the total column atmospheric water vapor (TCAWV) and the occurrence of cloudiness in different layers, as well as the column atmospheric water vapor in two altitude zones with the pressure 1000-680 mb and 680-310 mb.

For TCAWV, we found coincidence in more than 92 % of the cases, i.e. the total synchronicity of the variations (derived from overlapping of the maxima and minima – see Fig. 4, 5) of all three parameters, and also good similarity of their trends.

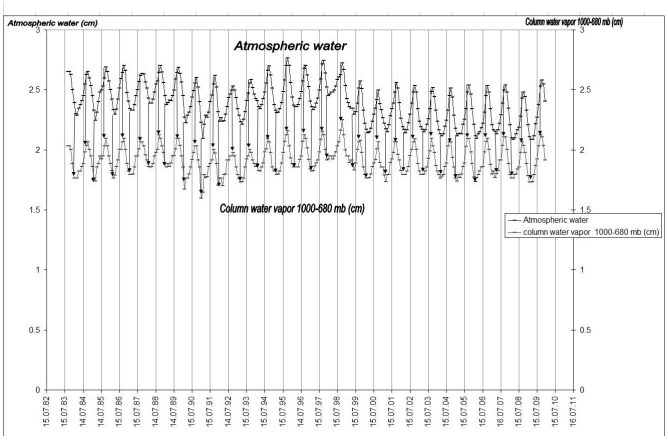

Fig. 4. Comparison between TCAWV time variations and column atmospheric water vapor in the altitude zone with the pressure 1000-680 mb

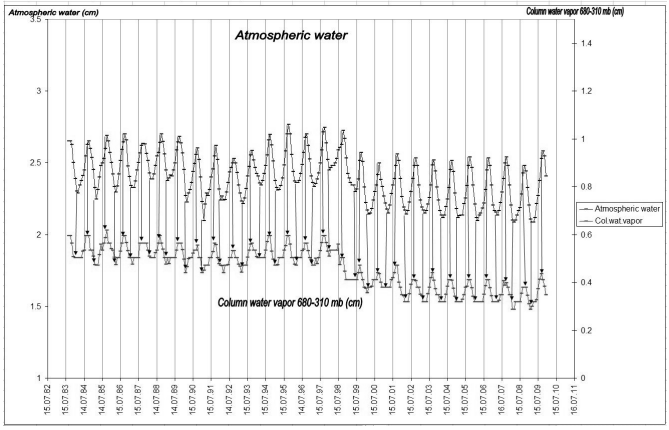

Fig. 5. Comparison between TCAWV time variations and column atmospheric water vapor in the alttiude zone with the pressure 680-310 mb

From the comparison of TCAWV variations with the lower cloudiness (LC), we derived that, despite the fact that their minima coincide in 86 % cases, the maximum of LC usually precedes that of TCAWV. This is apparently a manifestation of the effect known from model calculations, when along with the increase in the upper level cloudiness, LC decreases due to decay of descending vertical flows [Borisenkov et al., 1989]. This is what results in earlier appearance of LC maxima in 88% cases. Consequently, this process is not related directly to water vapor clusterization, and it cannot be considered directly controlled by the level of the solar activity, either. Clearly, this process is not determined by solar forcing in a direct way.

The values of TCAWV and middle-level cloudiness (MC) virtually totally anti-correlate, i.e. the MC is generated through water vapor clusterization.

For high cloudiness (UC), the correlation is seen in 62 % cases; it is obvious that the water vapor clusterization also occurs here. The contribution of ion formation under the action of galactic cosmic rays is substantial, since it is from this altitude zone that the ionization rate becomes appreciable.

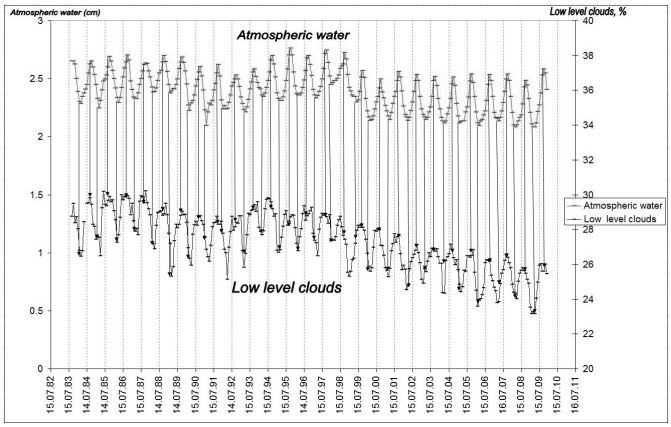

Fig. 6. Comparison between TCAWV time variations and lower cloudiness (LC).

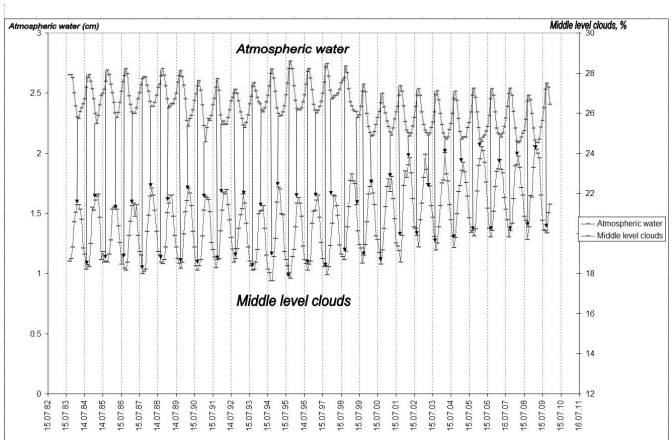

Fig. 7. Comparison between TCAWV time variations and middle cloudiness (MC).

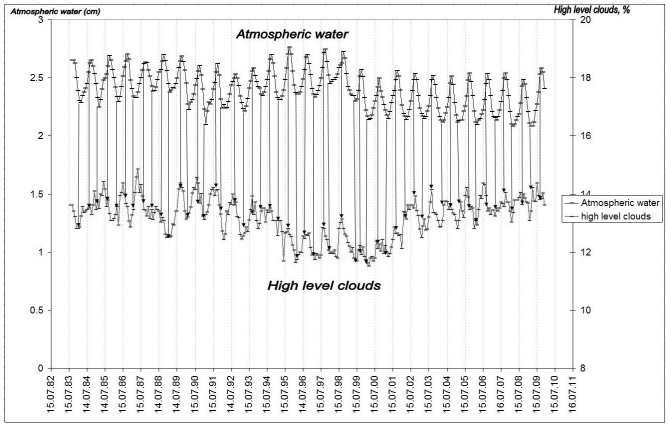

Fig. 8. Comparison between TCAWV time variations and upper cloudiness (UC).

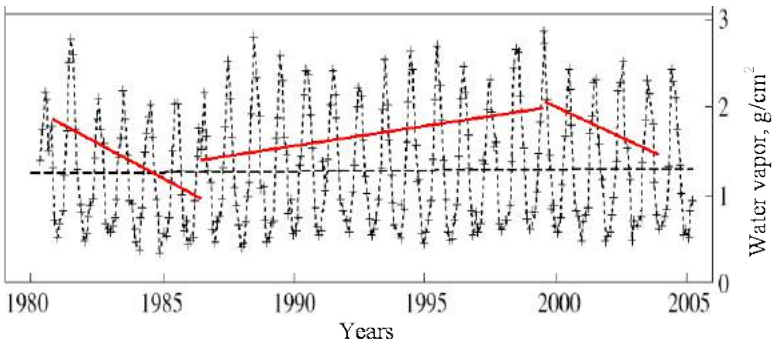

Fig. 9. TCAWV time variation at the altitude 1600 m, Tien-Shan (Kyrghyzia).

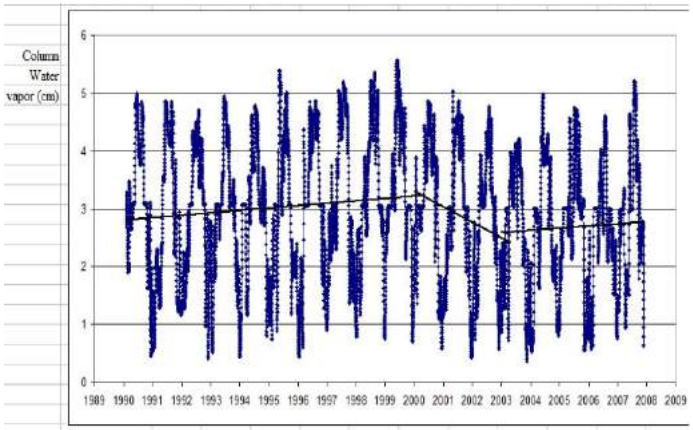

Fig. 10. TCAWV time variation in Texas (USA).

5. The comparison between time variations of TCAWV at the heights of 1600 m (Tien-Shan, Kyrghyzia, [Aref'ev et al., 2006]) and 500 m (Texas, USA, [Mims et al., 2011]), with the correlation 0,765 within the interval of synchronous measurements 1990 to 2005, presented in Figs 9 and 10, taking into account the anti-correlation between trends in cloudiness and in TCAWV, confirm the global spread of their (TCAWV) reaction to variations of solar-geomagnetic activity.

6. In the study [Pokrovskii, 2012], a striking inconsistency is noted between the decrease in the global cloudiness with the simultaneous increase in the temperature of the ocean surface (apparently accompanied with the increase in vaporization from the surface of water) and the existing mechanisms of cloud formation. This effect was detected in ISCCP experiment and observed up to the interval 2005/9.
Our results indicate that the evolution of the global cloudiness is basically driven by the variations of the solar-geomagnetic activity, while TCAWV remains a second-order factor in the formation of clouds. In fact, TCAWV does not specify the formation of cloudiness in the global scale, since the abundance of water vapor is, as a rule, sufficient for that. Within the framework of the radio-optical mechanism of solar-terrestrial links, which we previously developed in The S.I. Vavilov Optical Institute, the microwave flux from the ionosphere is another important controlling factor of the cluster condensation in the troposphere. Therefore, the phenomenon presented in [Pokpovskii, 2012] also confirms the idea of domination of solar-geomagnetic activity in the condensation-cluster mechanism of the formation of cloudiness, and subsequently in the control over weather and climatic parameters [Avakyan, 2013].

References

Aref'ev, V.N., F.V. Kashin, V.K. Semenov, R.M. Akimenko, N.E. Kamenogradskii, N.I. Sizov, V.P. Sinyakov, L.B. Upenek, V.P. Ustinov (2006), Water vapor in the atmosphere over the northern Tien Shan. *Izvestiya, Atmospheric and Oceanic Physics*, 42 (6), 739-751.

Avakyan, S.V. (2013), The role of solar activity in global warming. *Herald of the Russian Academy of Sciences*, 83 (3), 275-285.

Borisenkov, E.P., T.A. Bazlova, and L.N. Efimova (1989), *Cirrus and its influence at the atmospheric processes*, Gidrometeoizdat, Leningrad, 119 pp.

Mims, F.M. III, L.H. Chambers, and D.R. Brooks (2011), Measuring Total Column Water Vapor by Pointing an Infrared Thermometer at the Sky. *Bull. Amer. Meteor. Soc.*, 92, 1311-1320.

Pokrovskii, O.M. (2012), Climatology of clouds on the results of the international satellite project. *Trudy A.I. Voeikov GGO*, 565, 115-131 (In Russian).

THE RESPONSE OF ATMOSPHERIC PRESSURE AND AIR TEMPERATURE TO SOLAR EVENTS IN OCTOBER, 2003

S.V. Avakyan[1,2], N.A. Voronin[1], G.A. Nikol'skii[3]

[1]All-Russian Scientific Center "S.I. Vavilov State Optical Institute",
St. Petersburg, Russia, e-mail: avak2@mail.ru;
[2]St. Petertsburg State Politechnical University, St. Petersburg, Russia;
[3]St. Petersburg State University, St. Petersburg, Russia

Abstract. We set the problem of search for effects of solar flares and magnetic storms in variations of basic weather parameters: air temperature T and pressure P. We compare the data obtained at the mountain solar observatory near Kislovodsk (2100 m above sea level) and by the solar patrol of powerful solar-geomagnetic perturbations (bursts in the X-ray flux of solar radiation and indices of solar magnetic activity K_P), within one of the spells of most active space-physical perturbations, in October, 2003.
Thereby, we have proven direct manifestation of flares and magnetic storms in variations of meteorological parameters (T and P) at the height of 2100 meters.

We present the results of our analysis of correlations between tropospheric meteorological parameters, solar flares, and principal magnetic storms.

Fig. 1 presents variations of surface pressure P and air temperature T according to three-hour data obtained at Shatzhatmas synoptic station (near Kislovodsk, Russia) in October, 2003, along with variations of the solar constant (SC). A "quiet" behavior of synoptic variations observed in the first half of the month (when solar-geo-magnetic perturbations, including solar flares and principal magnetic storms, were virtually absent) was violated in subsequent weeks. On average, at the Northern Caucasus in the second half of October a deep anticyclone is settled, with the pressure roughly indicated with the straight line marked as «Trend of P». The analysis of the current synoptic process showed that since October, 16 the natural thermobaric relation in the air mass above the station started to deteriorate, first under the influence of geo-magnetic activity, and, after October, 19, also due to the flare activity of the Sun.

Our analysis of surface pressure variations in October, 2003, which takes into account the variations of the most important parameters of solar-geomagnetic activity (the soft X-ray flux from the Sun and the magnetic activity index K_p; see the bottom part of Fig. 1) confirms the impact of solar flares and magnetic storms, the basic manifestations of this activity, on the pressure P.

We will consider this effect in more detail. The pressure variations at the height of 2100 m under the influence of solar flares (or groups of flares) are totally consistent with experimentally measured data [Bogdanov et al., 2006], according to which a flare resulted in a decrease in atmospheric pressure at the high-mountain station Jungfraujoch (3475 m), while the Forbush decrease in the intensity of omnidirectional flux of galactic cosmic rays (GCR) in the vicinity of the Earth resulted in an increase in P. In the considered time interval, Forbush effect, being anomalously strong, was observed once, early on October, 29, with the maximum at 14 to 16 UT, and the value exceeding 20 % (from neutron monitor data at Apatity station). The pronounced minimum at this level ended by October, 30, and this ending was indeed accompanied with a dramatic outburst of the atmospheric pressure P (see Fig. 1). Such a pronounced pressure peak was possibly due to contribution from two powerful events of solar cosmic rays (SCR), which arrived at the surface of the Earth on October, 28, at 12.20 UT and October, 29, at 00.03 UT. SCR events can affect the troposphere in the same way as solar short-wave (X-ray) flares do [Veretenenko and Pudovkin 1996], increasing the total cloudiness, and consequently, as a rule, resulting in a decrease in the pressure P. The two events were indeed accompanied with dramatic decreases in P late of October, 28 and on October, 29. According to [Veretenenko and Pudovkin 1994], Forbush effect is related to a decrease in the number of cirrus clouds; in the study [Borisenkov et al., 1989] it was shown that when such clouds appear (they are generated after solar flares and geo-magnetic storms and are, as a rule, heating), the pressure decreases by 5 – 6 GPa, and at the same time the air temperature slightly increases. Thereby, when Forbush effect is observed, the air temperature should be expected to decrease, which was actually seen (up to the moment when the absolute temperature minimum in October, 2003 was reached) – see Fig. 1.

We compare the pattern of X-ray solar flares (GOES data, the lower curve in Fig. 1) with the variations of pressure P, taking into consideration only flares of medium and high intensity (of the type M4

and higher). In October, 2003, there were 11 such flares, all of which occurred after October, 19; 4 of them were of X type. As a rule, the most intense flares were preceded by several M1 to X1 type flares, which occurred 10 hours or more earlier. Recall that, according to radio-optical mechanism, the efficiency of manifestations of X-ray flares in the troposphere depends on the solar illumination of the higher ionosphere, at heights exceeding 100 km, i.e., of the regions of generation of microwave radiation between Rydberg (highly excited) states.

For almost all the intense flares, a decrease in the pressure P was observed (9 cases), and only two cases indicated an increase, following (X17.2) and (X10.0) type flares. However, as we showed before, these exceptions were likely to be caused by the dominating contribution of the most intense SCR events in 2003.

Let us now consider the cases of strong geo-magnetic perturbations (principal magnetic storms with the planetary index of geo-magnetic activity K_p = 5 and more). According to radio-optical mechanism, a storm affects the troposphere in the same way as a flare does: by strengthening of ionosphere microwave flux. Respectively, the storm is accompanied with an increase in cloudiness, which initially is mostly cirrus (heating). This effect was clearly manifested in the increases in the air temperature in 16 out of 19 storm events (Fig. 1). The difficulty of this juxtaposition is that, as it was noted in [Dmitriev and Govorov 1972], parameters of the troposphere, primarily the cloudiness, react to storm effects of particle precipitation with a delay of 1 to 3 days. Generally, a storm results in a decrease in pressure; two of these decreases followed the simultaneous impact of solar flares, which almost always lead to pressure decline.

In total, from the second half of October the anticyclone started to disintegrate under the influence of strong solar-geo-magnetic activity. Initially, this disintegration was caused by singular geo-magnetic perturbations (magnetic storms), though the absolute minimum of pressure and temperature was reached against the background of the strongest (X17.2) solar flare of October, 28. It was largely due to imposition of events, which were unique in the total scale of the year: two SCR events (the flux of solar protons was detected on the Earth's surface) and the most powerful for the year Forbush-type decrease in the flux of galactic cosmic rays (which in ordinary cases result only in a pressure increase [Sherstyukov 2008]). Thereby, the destruction of the standard (for this time of the year in Kislovodsk) anticyclone in October, 2003 was promoted by the chain of solar-terrestrial events: a series of solar flares and geo-magnetic storms. Two uniquely powerful SCR events and most intense (exceeding 20 %) Forbush-type reduction of GCR contributed additionally. It follows from the radio-physical mechanism that flares and storms, first, form optically thin (heating) cloudiness, usually in the upper layer (cirrus), and second, are followed with a decrease in atmospheric pressure. As a result, the anticyclone type of the weather is substituted with the cyclone. Note that M.V. Lomonosov described aurorae, which he had observed as a child in Kholmogory, as follows: "The aurorae were more often seen when it was windy, through discontinuous clouds". This directly corresponds to the hypothesis of the connection between the cyclone type of the weather (wind and clouds) and particle precipitations (which excite the aurora) [Alekseeva 1985].

For analysis of climate changes during last decades we bring about data on global cloudiness ISCCP, fig. 2, and for the first time we make comparison with events of arrival of extraordinary fluxes of solar cosmic rays (Ground Level Events - GLE). Solar cosmic rays also substantially affect the behavior of cloudiness. Fig. 2 shows solar proton events detected by neutron monitors on the Earth's surface – GLE [Miroshnichenko and Perez-Peraza, 2008]; as a rule, these events are followed by an increase in the total amount of cloudiness. It is straight shown that in this case the previously well known hypothesis of Resonance structure of Solar System is confirmed [Molchanov 1968]. Testing of this theory carried out previously in experiments on Rio metric registration of solar cosmic ray splashes during more than thousand flares [Kozelov, 1971] have shown that the most strong solar flares occur in March, June-July and September-October each year. And our results confirm that arrival of most powerful Solar Cosmic Rays (of GLE–type) takes place mostly in these periods: when expected mean probability of the event for two months is 16.7 % (in case of equally probable distribution during the year) in September-October there were 30 %, and in June-July – 25 % events. This effect requires further analysis taking into account the time delay after the penetration of SCR through the polar cap, and also the relations between SCR and the parameters of the solar flare: its grade in the optical wavelengths and type in X-rays.

Also these results, fig. 2, allow data of present helio-geophysical monitoring to be used for developing new approaches to solving forecasting problems in meteorology and climatology.

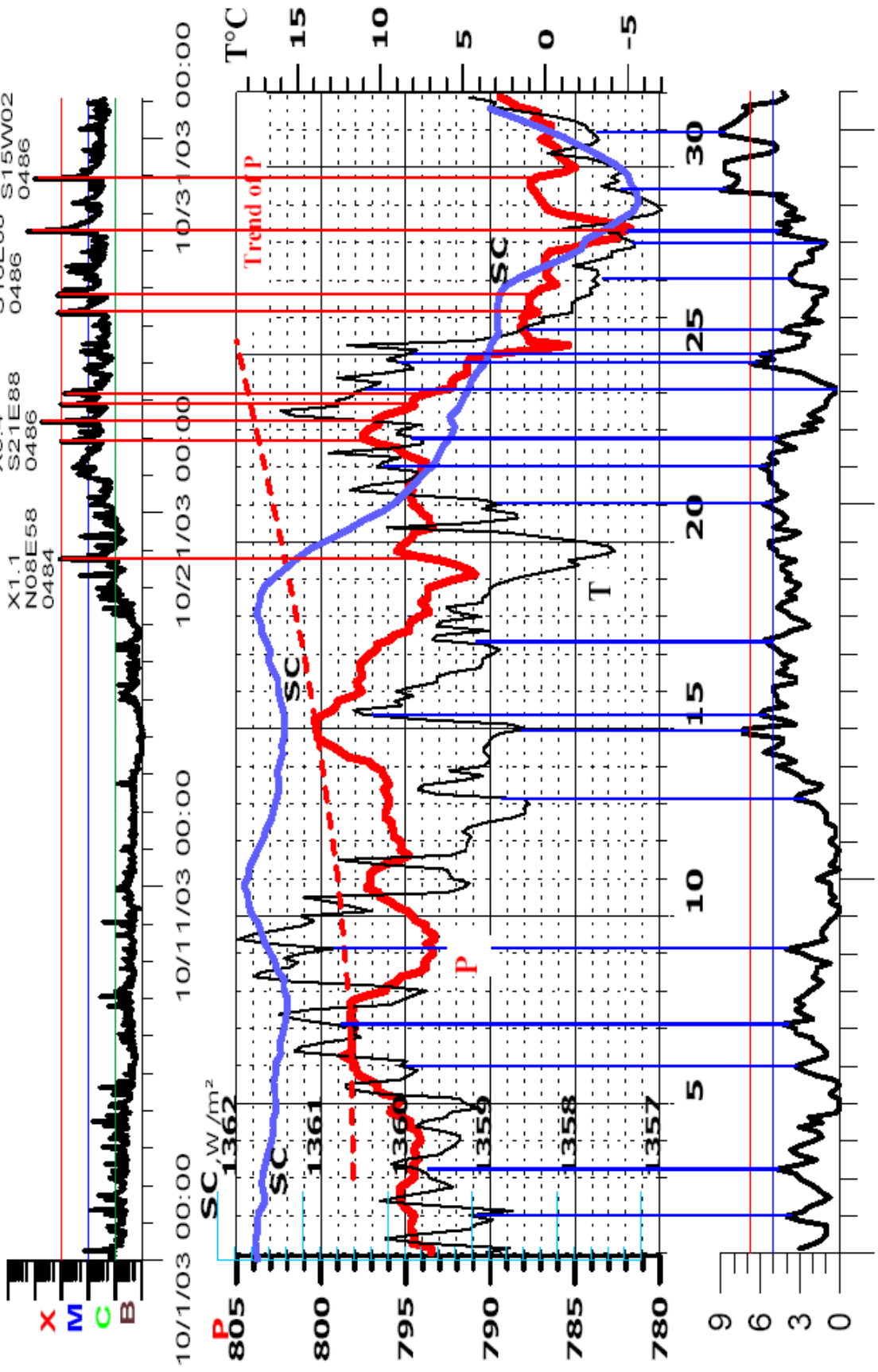

Fig. 1. Changes of the SC, ground atmospheric pressure P and air temperature T are given according to three-hour data of weather station Shadgatmas for October 2003. Upper curve corresponds to X-ray flare (classes X, M, C and B) and lower curve corresponds to magnetic storms (K^p is three-hour index of magnetic activity).

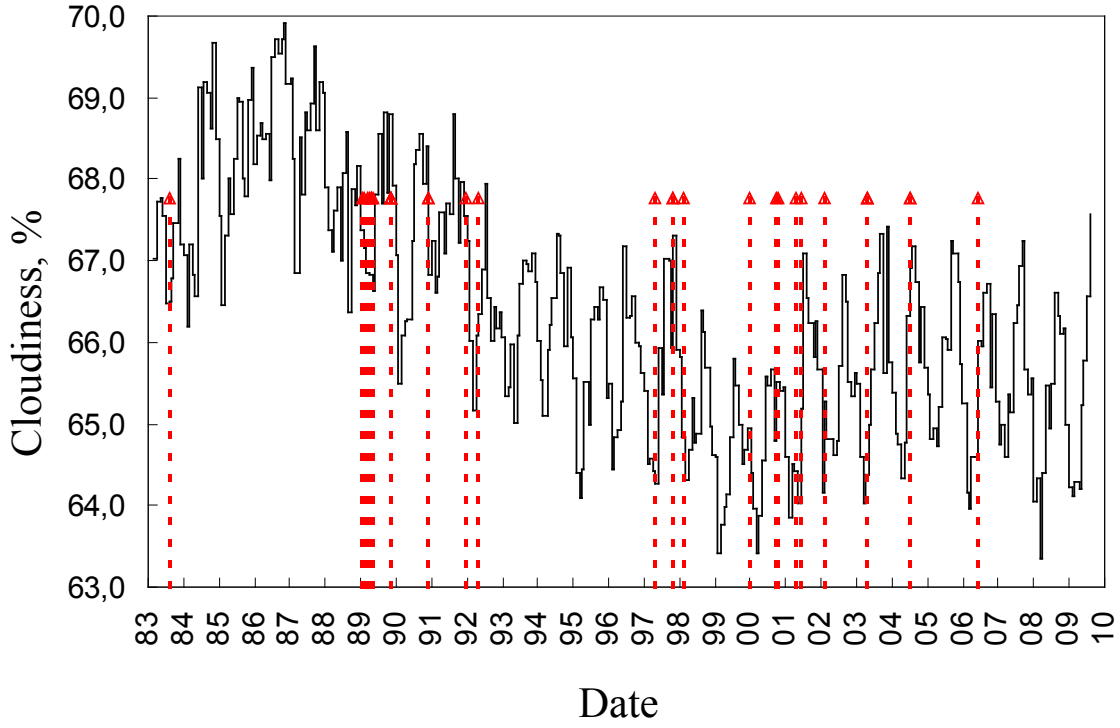

Fig. 2. Changes of global cloudiness obtained from satellite data. Vertical arrows indicate solar proton events (Ground Level Events).

Conclusion

We present the results of the comparison of meteorological parameters at the high-mountain station near Kislovodsk (at the height of 2100 m) with patrol data for intense effects of solar-geo-magnetic perturbations in October, 2003. The contribution of radiooptical three-step trigger mechanism of solar-weather relations [Avakyan and Voronin 2011; Avakyan 2013] was qualitatively confirmed.

References

Alekseeva, L.M. (1985), *Heavenly and earthly concerns flashes*. M. Znaniye. 160 p.

Avakyan, S.V. (2013), The Role of Solar Activity in Global Warming. *Herald of the Russian Academy of Sciences*, 83 (3), 275-285.

Avakyan, S.V. and N.A. Voronin (2011), The role of space and ionospheric disturbances in the global climate change and pipeline corrosion. *Izvestija, Atmosferic and Oceanic Physics*. Springer, 47 (9), 1143-1158.

Bogdanov, M.B., A.N. Surkov, A.V. Fedorenko (2006), Effect of cosmic rays on atmospheric pressure at high altitudes. *Geomagn. Aeron.*, 46 (2), 268-274.

Borisenkov, E.P., T.A. Bazlova and L.N. Efimova (1989), *Cirrus Cover and Its Influence on Atmospheric Processes*. Gidrometeoizdat, Leningrad, 1989.

Dmitriev, A.A. and D.V. Govorov (1972) Interrelation between the Physical and Heliophysical Experiments. *Rep. Arct. Antarct. Res. Inst.*, 311, 132-137.

Kozelov, V.P. (1971), On the gravitational influence of the planets on the solar activity. *Program and abstract for the XV IUGG General Assembly*, Moscow, 398 p.

Miroshnichenko, L.I. and J.A. Perez-Peraza (2008), Astrophysical aspects in the studies of solar cosmic rays. International Journal of Modern Physics A., 23 (1). 1-141.

Molchanov, A.M. (1968), The resonant strucnure of the solar system. The law of planetary distances. *Icarus*, 8 (2), 203-215.

Sherstyukov, B.G. (2008) *Regional and seasonal regularities of modern climate change*. "VNIIGMI-MZD" Publ., Obninsk, 246 p.

Veretenenko, S.V. and M.I. Pudovkin (1994), Forbush-decreases of galactic cosmic rays and the variation of cloudiness. *Geomagn. Aeron.*, 34, (4), 38-44.

Veretenenko, S.V. and M.I. Pudovkin (1996), Variations of Total Cloudiness during Solar Cosmic Ray Events. *Geomagn. Aeron.*, 36 (1), 108-111.

ULF EXCITATION AND ABSORPTION REVEALED BY THE DOPPLER RADAR DATA

V.I. Badin and M.G. Deminov

Institute of Terrestrial Magnetism, Ionosphere and Radio Wave Propagation, IZMIRAN, Troitsk, Moscow, 142190, Russia, e-mail: badin@izmiran.ru

Abstract. The Doppler radar data on the electron drift velocities detected in the E layer of the high-latitude ionosphere at moderate disturbances are analyzed for studying the ultra-low-frequency (ULF) oscillations. The narrowband filtering of the data reveals spatial distributions of the intensity of ULF signals. These spatial distributions show the geometry and scales of the ULF excitations that enables us to make some conclusions on the origin of the signals revealed. Low-pass filtering of the Doppler data shows that the ULF half-shadows extend equatorwards as far as the low-pass filter broadens, i.e. as far as the filtered frequencies increase. We expect this frequency-dependent behavior to be an indication of the resonant ULF absorption. For each event analyzed, discrete Fourier transforms of the Doppler data reveal stepwise decreases in the spectral power density above a certain frequency, which can be regarded as the minimum frequency of the magnetospheric continuum of the field line resonance (FLR). Using both the geometry and the frequency of the excitations revealed by the narrowband filtering, the non-resonant ULF signals can be firmly distinguished from the FLR excitations.

Introduction

When we speak on the origin of ULF signals, we first recall the magnetic field line resonances (FLRs). The MHD theory of long-period magnetic pulsations has been proposed by L. Chen and A. Hasegawa [1974] and by D.J. Southwood [1974]. There are numerical computations of magnetospheric eigenfrequencies calculated for both dipole [e.g. Lee and Lysak, 1999] and more realistic Tsyganenko [1995] models of the geomagnetic field [Cheng and Zaharia, 2003]. The numerical calculations yield the lowermost eigenfrequencies about 5 or 3 mHz at quiet conditions for dipole and non-dipole models, respectively.

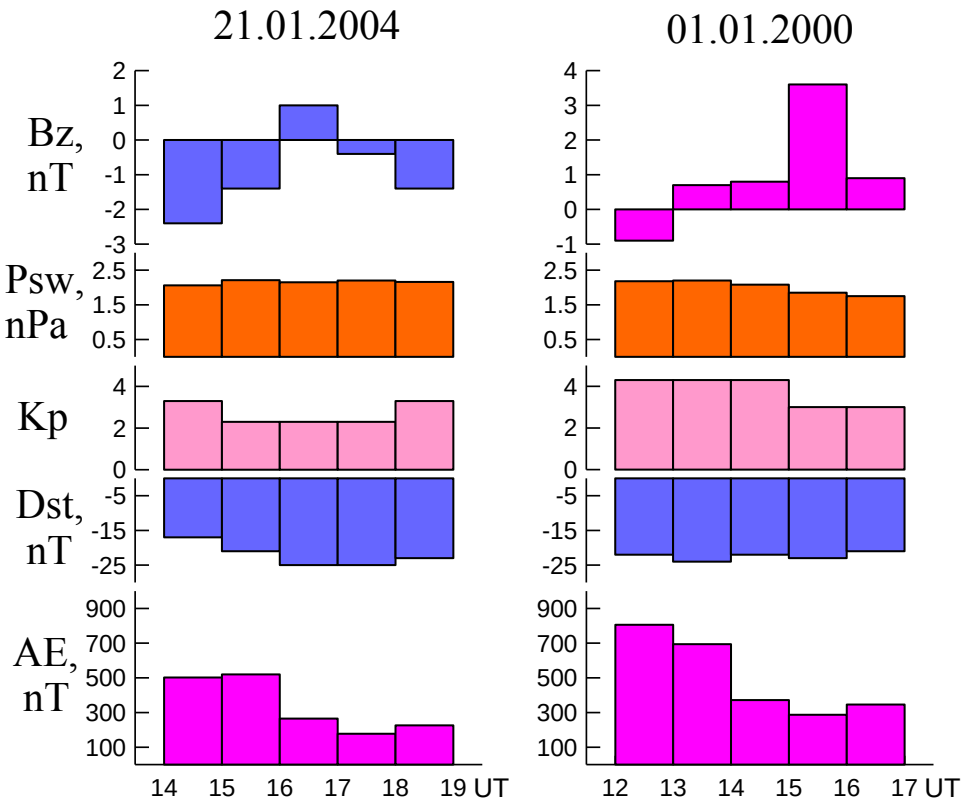

Fig. 1. Heliogeophysical description of two high-latitude events analyzed.

There is a great number of experimental observations of long-period pulsations detected by both spacecraft and ground facilities. There are numerous papers reviewing observational data accumulated over long-term activities, [e.g. Anderson et al., 1990; Baker et al., 2003]. Experimenters indicate both resonant and non-resonant origins of Pc5 pulsations. Discussing probable non-resonant sources of pulsations, we reference the paradigm of splitting the magnetospheric convection into vortices of various scales [Trakhtengerts and Feldstein, 1982] including some small-scale with comparatively high angular frequencies of rotation.

We use the Doppler data of the Norwegian STARE radar presenting the experimental information on the ionospheric E layer observed by eight angular channels/beams [Greenwald et al., 1978]. When plasma drift velocities exceed the ion-acoustic speed while the ionospheric irregularities are generated by the Farley-Buneman instability, the Doppler radar measurements suffer from the so-called ion-sound saturation that is the velocity of irregularities can be retained near 400 m/s regardless of the real velocity of the plasma drift [Nielsen and Schlegel, 1985; Koustov et al., 2005].

Depending on the direction of the interplanetary magnetic field (IMF) and the dynamic pressure of the solar wind (SW), the magnetopause position determines the maximum length of closed magnetic field lines and the minimum frequency of the MHD resonant continuum. For a single moderate dynamic SW pressure, the noon magnetopause approaches the Earth for southward IMFs compared with northward while the evening magnetopause moves away from the Earth when the IMF direction is switched to southward [Roelof and Sibeck, 1993; Fairfield, 1995].

We have analyzed two high-latitude events observed by the STARE radars. Figure 1 presents the helio-geophysical description of these events that includes (from top to bottom) the Bz IMF component, dynamic pressure of the solar wind Psw, and the geophysical indices Kp, Dst, and AE. The main difference between the two events analyzed is in the IMF Bz polarity.

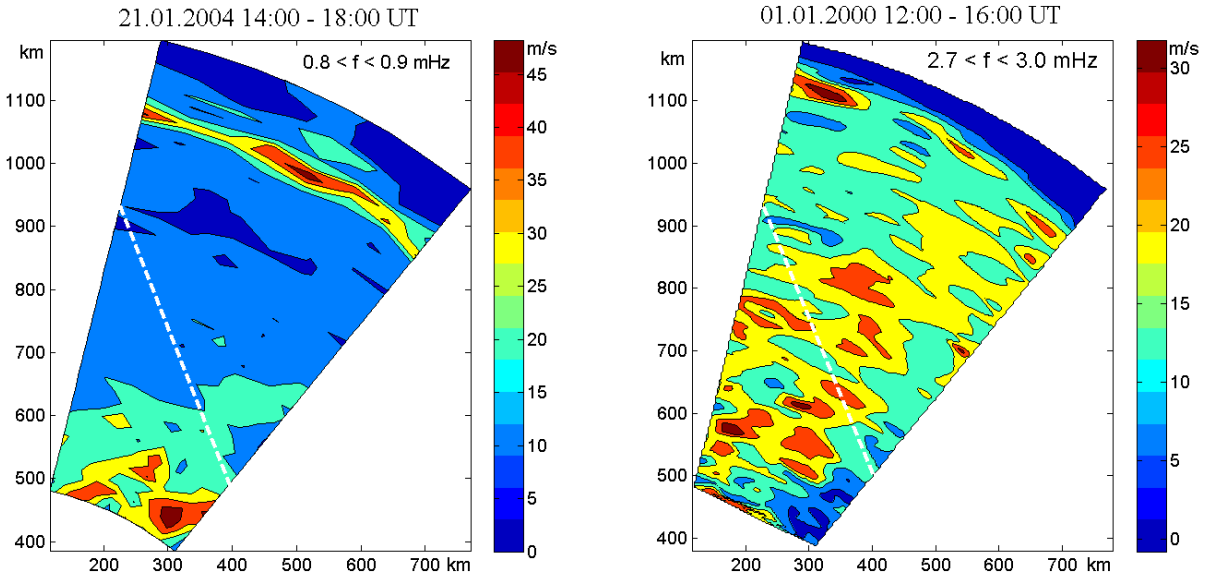

Fig. 2. Standard deviations of the Doppler data processed by the narrowband filtering.

Results

Figure 2 presents standard deviations of the plasma drifts upon the narrowband filtering. The left-hand panel shows the results for the event observed 21.01.2004 and the right-hand panel for 01.01.2000. Here and below, in all maps constructed for the radar field of vision, the vertical axis is parallel to the geographic meridian and the geomagnetic meridian is shown white dashed. The frequencies for the narrowband filtering were found earlier by the comparative spectral analysis of the magnetic and radar observations [Badin, 2013]. In the left-hand panel, we can see the quasi-monochromatic excitation of a nearly circular geometry with a comparatively large curvature radius that probably traces a vortex of the convection split into local motions. It must be noted that the geometry of this excitation may have been distorted by the ion-sound saturation (see Fig. 3). In either case, such an excitation is definitely non-resonant, since its outline nearly

parallel to the geomagnetic meridian is inconsistent with the monochromatic MHD eigenmodes. In the right-hand panel, we can see the excitations of the form of rings or semirings. These excitations probably result from the turbulent vortices generated by the magnetospheric convection.

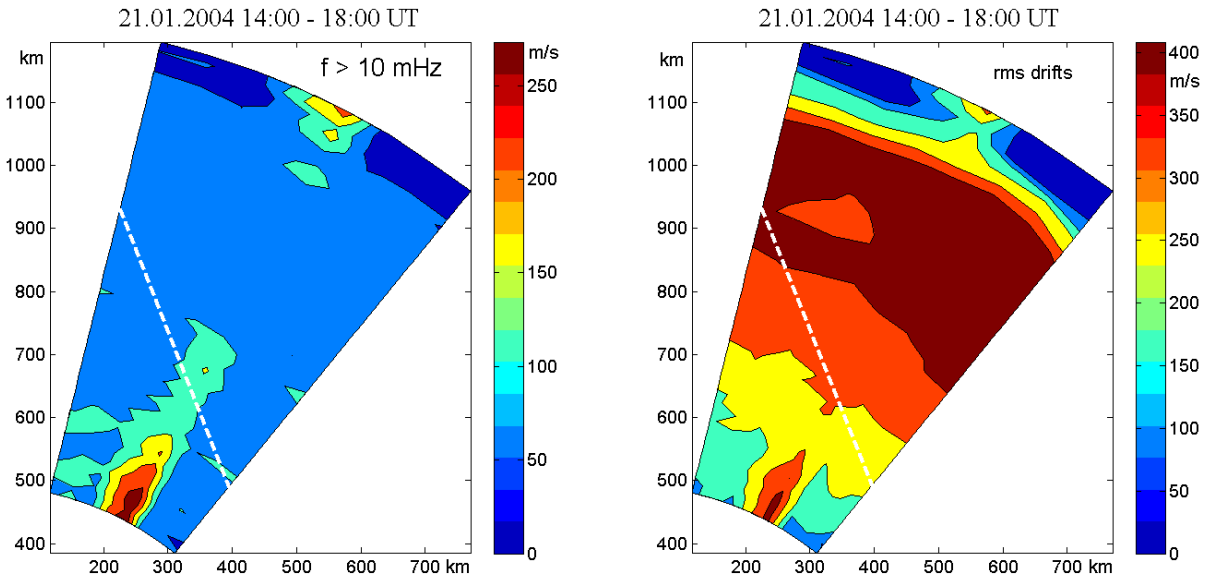

Fig. 3. Highpass-filtered standard deviations compared with rms drifts.

The left-hand panel in Fig. 3 presents the standard deviations of the highpass-filtered Doppler data. We can see an excitation of the straight form (except a gap in the middle). By geometry, this excitation can be considered as resonant, if we attribute the gap in the middle to the ion-sound saturation. The right-hand panel shows that the gap nearly matches the area of drifts being about 400 m/s that is the threshold of saturation. On the other hand, the excitation is broadband and takes a sharp angle with the geomagnetic meridian. An alternative explanation associates this excitation with the auroral electrojet.

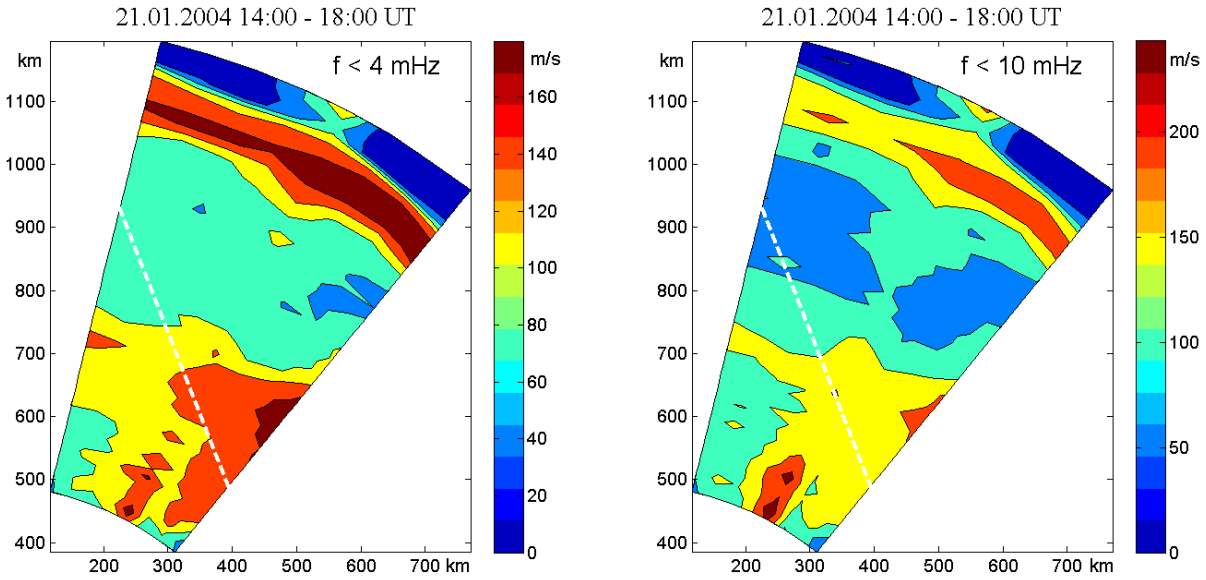

Fig. 4. Standard deviations of the lowpass-filtered Doppler data.

Figure 4 presents the standard deviations of the Doppler data upon the lowpass filtering. In both left and right panels, yellow and green areas correspond to nearly one-half relative intensities, although the maximum intensity increases when the lowpass filter is broadened. Thus, yellow and green areas indicate relative half-shadows of the lowpass excitations. We can see that the half-shadow extends equatorwards as far as the lowpass filter is broadened. Such a behavior indicates an observation of the resonant ULF absorption. The

physics of the phenomenon is that the energy of the oscillations occurring in the transverse electric field is FLR transformed (dynamic damping) into the energy of field-aligned currents. The latter energy is absorbed in the ionosphere. Higher frequencies passed by the broadened filter involve the resonance on shorter field lines located equatorward of longer field lines. Therefore, the half-shadow extends equatorwards when the filter is broadened. Note that shorter field lines cannot resonate at lower frequencies.

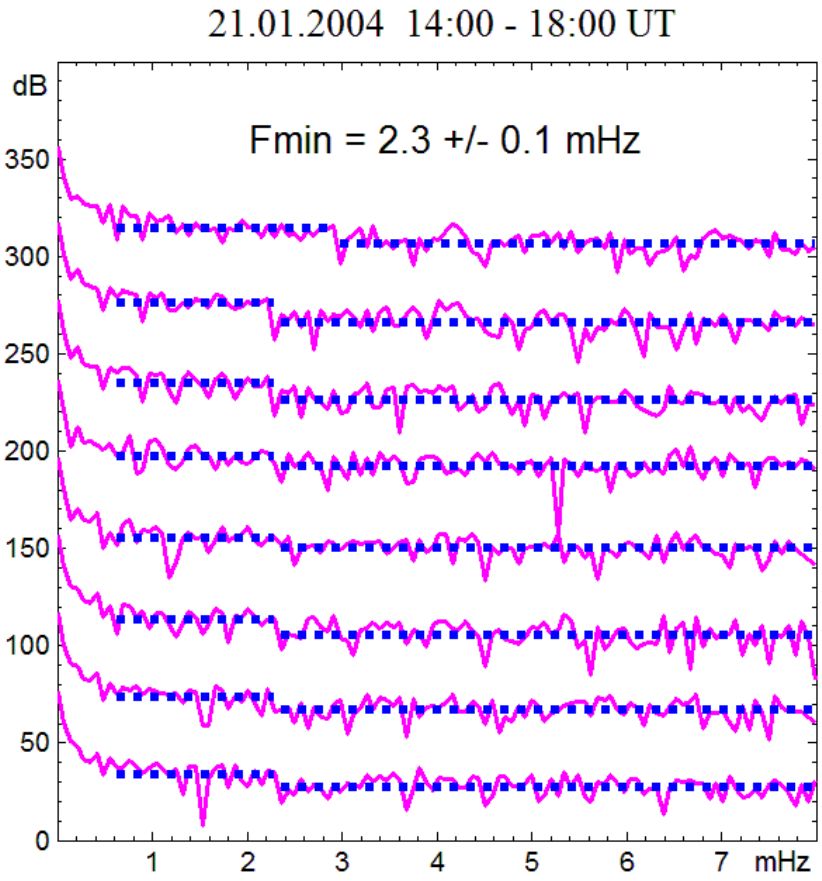

Fig. 5. Spectral power density averaged over each radar beam.

Figure 5 presents the discrete Fourier transforms (magenta curves) of the Doppler data averaged over each radar beam. Polar beams are shown at the bottom and equatorial at the top. For convenience, 40 dB are added to every overlying curve with respect to underlying. Blue dots (squares) show the arithmetic mean of the spectral power corresponding to each frequency interval used. These frequency intervals are determined by least squares minimizing the total squared distance between the particular and mean spectral powers. Thus, the blue dots show the best fitting of spectral powers with the one-step profile. Here the one-step profiles model the effect of the resonant ULF absorption within the magnetospheric FLR continuum. We can see that the effect (the height of the step) is on the order of 10 dB that is an order of magnitude in the spectral power density. The frequency boundary between two intervals found for each beam indicates the minimum (cutoff) frequency of the resonant absorption observed on this beam. Figure 5 shows that seven beams (among eight used) yield the cutoff frequencies coinciding about 2.3 mHz within the 5% error. This finding well corresponds to the configuration where the magnetopause projection crosses all beams except the most equatorial eighth beam.

Figure 6 shows the standard deviations of the lowpass Doppler data for the event observed 01.01.2000. Again, the relative half-shadow (yellow-green areas) extends equatorwards as far as the lowpass filter is broadened. This behavior indicates the resonant ULF absorption by magnetic field lines.

Figure 7 presents the beam-averaged spectral power densities for the event observed 01.01.2000. Seven beams of eight used yield the cutoff frequencies coinciding about 3.9 mHz within the 5% error. This again corresponds to the configuration where the magnetopause projection crosses seven beams on the polar side

of the radar field of vision. The minimum FLR frequency found for this event is significantly higher than that found for the event observed 21.01.2004. We can see in Fig. 1 that the southward interplanetary magnetic field dominates in the 21.01.2004 event whereas the northward IMF dominates in the event observed 01.01.2000. Thus, the minimum FLR frequencies found satisfy the general rule established for the evening magnetopause position depending on the IMF polarity [Roelof and Sibeck, 1993].

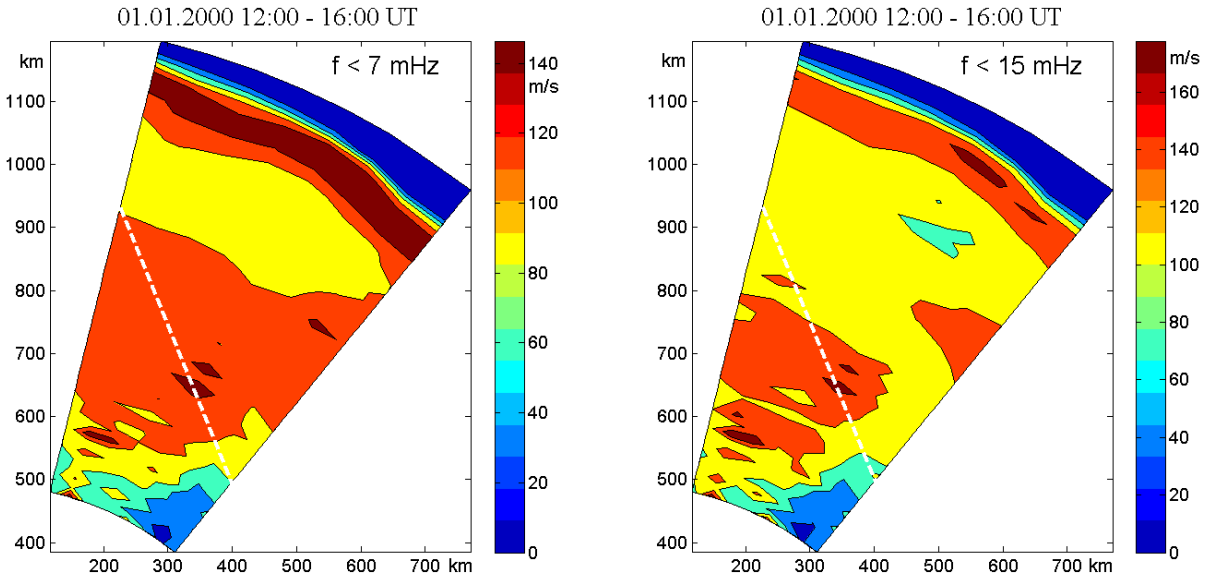

Fig. 6. The same as that shown in Fig. 4 but for the event observed 01.01.2000.

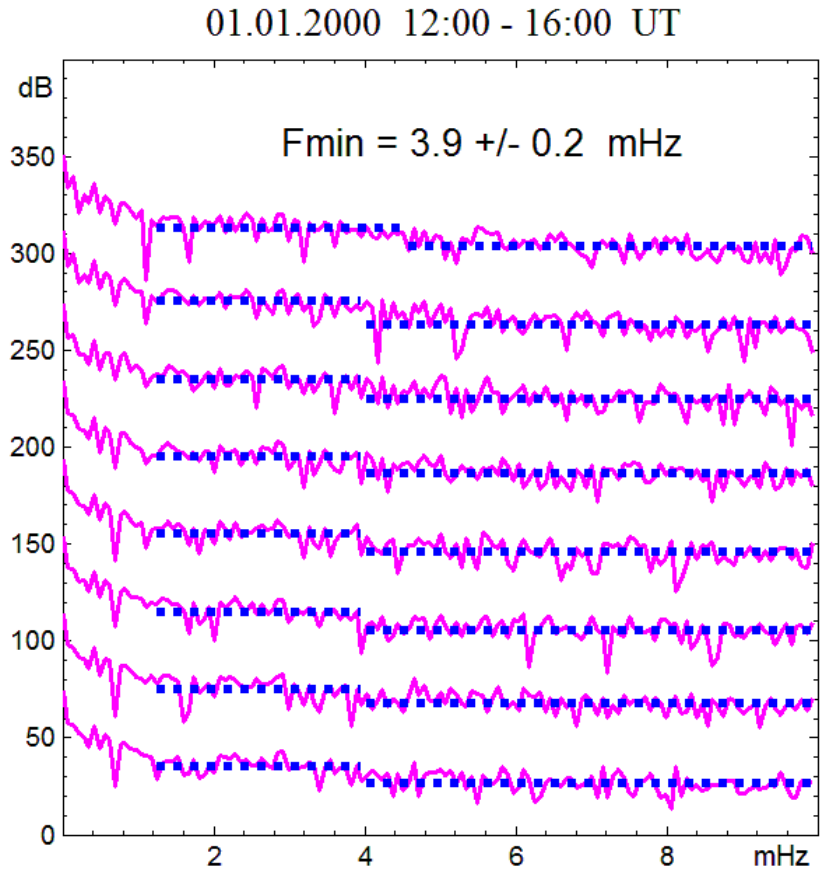

Fig. 7. The same as that shown in Fig. 5 but for the event observed 01.01.2000.

Conclusions

1. Minimum frequencies of the FLR continuum are estimated by fitting a simple one-step profile to the spectral power density calculated for the Doppler data of each radar beam.
2. Non-resonant ULF excitations are firmly identified by the Doppler radar data using both the geometry of excitations and the frequencies compared with those of the resonant continuum.

Acknowledgments

The STARE system was operated jointly by the Max Planck Institute for Aeronomie, Germany, and by the Finnish Meteorological Institute, Finland, in cooperation with SINTEF, University of Trondheim, Norway.

This work was supported by the Russian Foundation for Basic Research (project code 14-05-00179) and by the Russian Academy of Sciences Presidium Program no. 22.

References

Anderson, B.J., M.J. Engebretson, S.P. Rounds, L.J. Zanetti, and T.A. Potemra (1990), A statistical study of Pc3-5 pulsations observed by the AMPTE/CCE magnetic field experiment: 1. Occurrence distributions, *J. Geophys. Res.*, 95(A7), 10495-10523.

Badin, V.I. (2013), Spectral studies of oscillations observed by the high-latitude radar and magnetometers, *J. Phys. Sci. App., ISSN 2159-5348*, 3(4), 244-248.

Baker, G.J., E. F. Donovan, and B. J. Jackel (2003), A comprehensive survey of auroral latitude Pc5 pulsation characteristics, *J. Geophys. Res.*, 108(A10), 1384, doi:10.1029/2002JA009801,.

Chen, L., and A. Hasegawa (1974), A theory of long-period magnetic pulsations:1. Steady state excitation of field line resonance, *J. Geophys.Res.*, 79(7), 1024-1032.

Cheng, C.Z. and S. Zaharia (2003), Field line resonances in quiet and disturbed time three-dimensional magnetospheres, *J. Geophys. Res.*, 108(A1), 1001, doi:10.1029/2002JA009471

Fairfield, D.H. (1995), Observations of the shape and location of the magnetopause: a review, *Physics of the Magnetopause, ed. by P. Song, B.U.O. Sonnerup, and M.F. Thomsen*, AGU, 53-60.

Greenwald, R.A., W. Weiss, E. Nielsen, and N.R. Thomson (1978), STARE: A new radar auroral backscatter experiment in northern Scandinavia, *Radio Science*, 13, 1021-1039.

Koustov, A. V., D.W. Danskin, R. A. Makarevitch, and J. D. Gorin (2005), On the relationship between the velocity of E-region HF echoes and E×B plasma drift, *Ann. Geophys.*, 23, 371-378.

Lee, D.-H. and R.L. Lysak (1999), MHD waves in a three-dimensional dipolar magnetic field: a search for Pi2 pulsations, *J. Geophys. Res.*, 104(A12), 28691-28699.

Nielsen, E. and K. Schlegel (1985), Coherent radar Doppler measurements and their relationship to the ionospheric electron drift velocity, *J. Geophys. Res.*, 90, 3498-3504.

Roelof, E. C. and D. G. Sibeck (1993), Magnetopause shape as a bivariate function of interplanetary magnetic field Bz and solar wind dynamic pressure, *J. Geophys. Res.*, *98*, 21421-21450.

Southwood, D. J. (1974), Some features of field line resonances in the magnetosphere, *Planet. Space Sci.*, 22, 483-491.

Trakhtengerts, V.Yu. and A.Ya. Feldstein (1982), O rassloenii magnitosfernoi konvektsii (Stratification of the magnetospheric convection), *Fiz. Plasmy*, 8**(**1), 140-147.

Tsyganenko, N. A. (1995), Modeling the Earth's magnetospheric magnetic field confined within a realistic magnetopause, *J. Geophys. Res.*, 100(A4), 5599-5612.

ON THE RELATION BETWEEN SOLAR WIND AND EVENINGSIDE UNDULATIONS DURING LOW PLANETARY MAGNETIC ACTIVITY (Kp<3)

D.G. Baishev[1], E.S. Barkova[1], K.Yumoto[2]

[1]Yu.G.Shafer Institute of Cosmophysical Research and Aeronomy SB RAS, Yakutsk, 677980, Russia, Russia, e-mail: baishev@ikfia.sbras.ru; [2]International Center for Space Weather Science and Education, Kyushu University, Fukuoka, Japan

Abstract. A statistical study of eveningside undulations during low planetary magnetic activity (Kp<3) is performed using optical observations at Tixie (71.6º N, 128.9º E) in the interval of 1994-2008. Based on 1-min data from OMNI database (http://omniweb.gsfc.nasa.gov/) the solar wind and geomagnetic activity conditions for 14 undulation events are examined. It is found that undulations occurred when the interplanetary magnetic field was southward and the solar wind energy flux was high for a durable (up to 4 hours) time before undulation event. A significant smooth growth in values of AE index and H component of the magnetic field at Tixie due to increased solar wind energy transfer into the Earth's magnetosphere is recorded. It is suggested that a generation of eveningside undulations under Kp<3 is associated to a physical processes in the inner magnetosphere, which captures midlatitude variations of plasma drift on the duskside and is enhanced during subauroral polarization stream events as revealed by Cousins et al. (JGR, 2013).

INTRODUCTION

Large-scale undulations on the equatorward boundary of the diffuse aurora in the evening sector near a maximum development of the ring current were first discovered by Lui et al. (1982) in DMSP photographs. A number of the results testifying to a relationship of undulations to geomagnetic storms was obtained (Lui et al, 1982; Kelley, 1986; Baishev et al., 1997; Baishev et al., 2000; Zhang et al., 2005; Baishev and Rich, 2006; Henderson et al., 2010). However, Baishev et al. (2010b, 2012) on the statistical data of optical observations during 1994-2008 have been shown that eveningside undulations were occurred both during and in the absence of magnetic storms. Full list of undulation events registered by all-sky TV camera at Tixie and Zhigansk has been published in the work (Baishev et al., 2012).

In the present paper we determine a spatial parameters of eveningside undulations by using a TV observations at Tixie and examine the solar wind and geomagnetic activity conditions based on 1-min data from OMNI database for undulation events under Kp<3.

OBSERVATIONS

For the analysis, 14 events of undulations observed by all-sky TV camera at Tixie (71.6º N, 128.9º E) in the interval of 1994-2008 are used. To determine a spatial parameters of undulations a TV frame was mapped in the orthogonal coordinate system taking into account the height of aurora on ~110 km. To calculate a velocity of the diffuse tongue structures a keogram in the east-west direction was built. Calculated parameters for undulation events under Kp<3 are listed in Table 1.

The main results from Table 1 may be summarized as following:
1) a duration of undulation event ranges from ~8 minutes to about 3 hours;
2) a number of diffuse tongues ranges from 1 to 23;
3) a velocity of undulation propagation to the west is V~0.6-0.8 km/s, with an exception of the event of V~0.3 km/s observed in the interval of 12.41-13.33 UT on 20 February 2001;
4) an amplitude and wavelength of undulations varies within 50-200 km and from 50 to 300 km, respectively. It is noted that a smallest wavelength was observed at a lowest velocity of undulations;
5) a position of the equatorward boundary of diffuse aurora (EBDA) during the undulation events remain on latitude of ~71.5-72.5º.

Table 1. Parameters of large-scale undulations observed at TIX under *Kp*<3

№	Date	Observational interval (UT)	*N*	*V* (km/s)	*A* (km)	λ (km)	Position of EBDA* (deg)
1	01.03.1997	10.55-11.26	7	0.7	100	150	72
2	02.03.1997	12.14-12.40	6	1.0-0.7	100	250	72
3	22.02.1998	11.27-12.21	14	0.8-0.6	200	50-250	72
4	20.03.1998	13.34-13.48	6	0.6	100	<50	71.5
5	20.02.2001	10.25-10.39	3	0.9	50	200	72.5
6	20.02.2001	12.08-12.16	1	0.8	100	300	72.5
7	20.02.2001	12.41-13.33	12	0.3	50	50	72.5
8	21.02.2001	10.56-11.12	2	0.8	50	190	72
9	21.02.2001	12.00-12.22	3	0.7	50	190	72
10	23.01.2002	12.21-13.37	12	0.6-0.3	80	180	72
11	03.03.2003	10.53-11.48	11	0.6	60	100	72
12	25.12.2005	09.48-12.05	23	0.8-0.6	90	160	72
13	28.10.2006	10.23-10.38	5	0.8	70	150	72
14	10.12.2007	12.20-13.49	14	0.6	50-100	290	72.5

Position of EBDA* - position of the equatorward boundary of diffuse aurora in the geographical coordinates

The distribution of different solar wind (SW) parameters and geomagnetic indices (*AE, AU, AL, PCN*) from OMNI database are examined for 14 events of undulations. Variations of the magnetic field *H*-component at auroral station Barrow (71.3° N, 203.4° E; *H*brw) in the midnight sector and Tixie (*H*tix) in the evening sector are additionally used. The superposed epoch analysis was performed for data in interval of 5 hours before and after the undulation events. The 1-min values of analyzed parameters were averaged over 1-hour intervals and their standard deviations were calculated (see Tables 2 and 3). A high value of standard deviations may be caused by low number of undulation events.

Table 2 shows that a value of the SW velocity of ~380 km/s during the analyzed interval corresponds to a calm conditions in the interplanetary medium, while a values of the SW density of ~8.8 particles/cm^3, and the magnitude of interplanetary magnetic field (IMF) *B* equal to ~7 nT before (~7.8 nT after) the undulation events were a higher values than ones for quiet conditions.

In the IMF variations a positive values in the IMF *Bx* (~1 nT before and 2.5 nT after the events), and negative values in the IMF *By* (-2 nT before and -2.5 after the events) and a change of sign from negative to positive in the IMF *Bz* (-1.5 nT before and ~1 nT after the events) are observed.

Sign distributions of 1-min values for IMF *Bx*, *By* and *Bz* components during 1-hour intervals, illustrated in Figure 1, show approximately a same results. Fig.1a (Fig.1b) demonstrates that a positive (negative) sign is

Table 2. Hourly averaged values of IMF and solar wind parameters

Interval	*B*, nT	*Bx*, nT	*By*, nT	*Bz*, nT	*V*sw, km/s	*N*sw, cm^{-3}	*ε*, GW
[-5;-4]	6.4±2.1	0.9±3.3	-2.3±4.4	-1.0±2.9	356±63	9.0±4.6	139±124
[-4;-3]	6.0±2.0	0.6±2.6	-1.7±3.7	-1.6±3.5	359±61	9.7±5.6	150±169
[-3;-2]	6.3±1.9	0.8±2.6	-1.5±3.7	-2.5±3.7	364±60	8.7±3.9	185±166
[-2;-1]	6.7±2.0	0.6±2.9	-2.1±4.3	-2.2±3.5	366±61	8.4±3.7	190±170
[-1;0]	7.3±2.0	0.4±3.0	-1.8±4.7	-1.0±4.5	369±61	8.8±3.9	171±150
[0;1]	**7.4±2.3**	**0.4±3.2**	**-1.4±5.4**	**0.4±4.2**	**372±65**	**8.8±3.6**	**121±133**
[1;2]	7.9±2.4	1.7±3.4	-2.6±4.5	1.2±4.8	374±65	9.2±3.6	135±178
[2;3]	8.1±2.7	2.3±3.9	-0.8±4.4	2.3±5.1	369±64	8.7±3.3	107±163
[3;4]	7.9±2.8	2.9±3.7	-3.2±3.7	1.1±4.7	374±67	8.7±3.8	119±125
[4;5]	7.9±3.5	2.8±3.9	-2.5±4.3	1.3±5.0	376±62	9.0±4.5	123±195

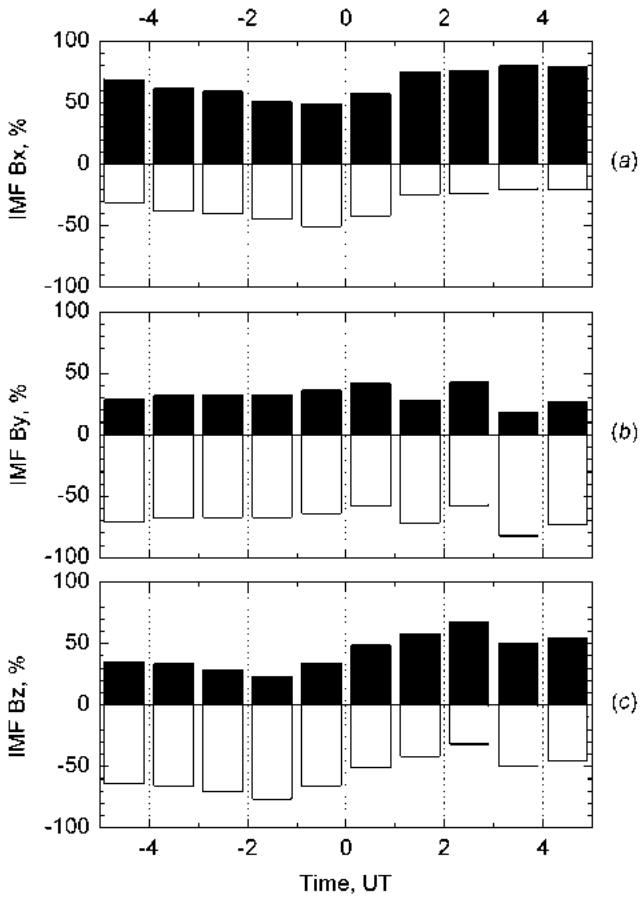

Fig.1. The distribution for the hourly averaged IMF component signs up to 5 hours before and after the undulation event as percentages

dominated in the distribution of IMF *Bx* (*By*) component. Fig.1c shows that in the distribution of IMF *Bz* component a predominance of negative signs (~70%) before and a equality with positive signs after the undulation events are marked.

Averaged over a 1-hour interval values of the Akasofu-Perreault epsilon parameter **ε** exceeded the threshold of 100 GW required for a development of magnetospheric substorms when the SW energy transfer into the Earth's magnetosphere (Akasofu, 1981). There is a gradual growth before the undulation events in variations of the *AE*, *AU* and *PCN* indices, as well as in *H*tix (see Table 3), but low hourly averaged values (259 nT, 127 nT, 1.4, 98 nT) corresponded to a periods of weakly disturbed geomagnetic activity. It may be noted almost same averaged values of the *AU* index (127 and 111 nT) and *H*tix (98 and 94 nT) in the intervals of 1 hour before and during the undulation events that indicate a location of center of eastward electrojet near Tixie in the evening sector.

A gradual decrease in hourly averaged values of *H*brw from -8 to -96 nT was observed (see Table 3). Contribution of values of *H*brw to a variation of the *AL* index characterizing the westward electrojet intensity before the undulation events is negligible and becomes a crucial during and after the undulation events.

Figure 2 presents a variations of the superposed average of IMF *Bz* (Fig.2a), the epsilon parameter **ε** (Fig.2b), *AE* (magenta curve) and *AL* (dashed blue curve) indices, as well as *H*brw (black curve) (Fig.2c), and *H*tix (black curve) and *AU* index (dashed green curve) (Fig.2d) for analyzed events.

Fig.2a shows that a durable (about 4 hours before the undulation events) southward IMF orientation is observed. In this time interval the superposed average of IMF *Bz* was almost constant at -2 nT. However, it should be emphasized that in the events of 23 January 2002, 03 March 2003, 28 October 2006 and 10 December 2007 a short-term (~10-30 min) and intense (up to ~4-8 nT) IMF *Bz* excursions to the north were observed. Synchronously with the IMF *Bz* a variation of the parameter **ε** is changed, whose the superposed average is in the range of 160-220 GW (see Fig.2b) before the undulation events.

Table 3. Hourly averaged values of geomagnetic indices and H-components at BRW (midnight), TIX (evening)

Interval	*AE*, nT	*AL*, nT	*H*brw,nT	*AU*, nT	*H*tix, nT	*PCN*
[-5;-4]	127±95	-52±72	22±36	75±41	14±21	1.0±0.5
[-4;-3]	137±122	-61±102	-1±93	76±39	26±27	1.0±0.4
[-3;-2]	172±118	-81±77	-8±75	90±53	40±43	1.2±0.6
[-2;-1]	203±124	-106±89	-39±83	96±57	59±46	1.3±0.6
[-1;0]	259±112	-133±78	-59±72	127±55	98±55	1.4±0.6
[0;1]	**244±143**	**-133±122**	**-96±124**	**111±56**	**94±51**	**1.1±0.6**
[1;2]	198±152	-118±114	-69±107	81±54	53±55	1.0±0.7
[2;3]	161±154	-107±127	-60±84	54±39	9±72	0.7±0.6
[3;4]	182±218	-121±163	-95±149	61±66	-26±109	0.9±0.8
[4;5]	186±179	-131±144	-116±134	55±50	-56±108	0.9±0.7

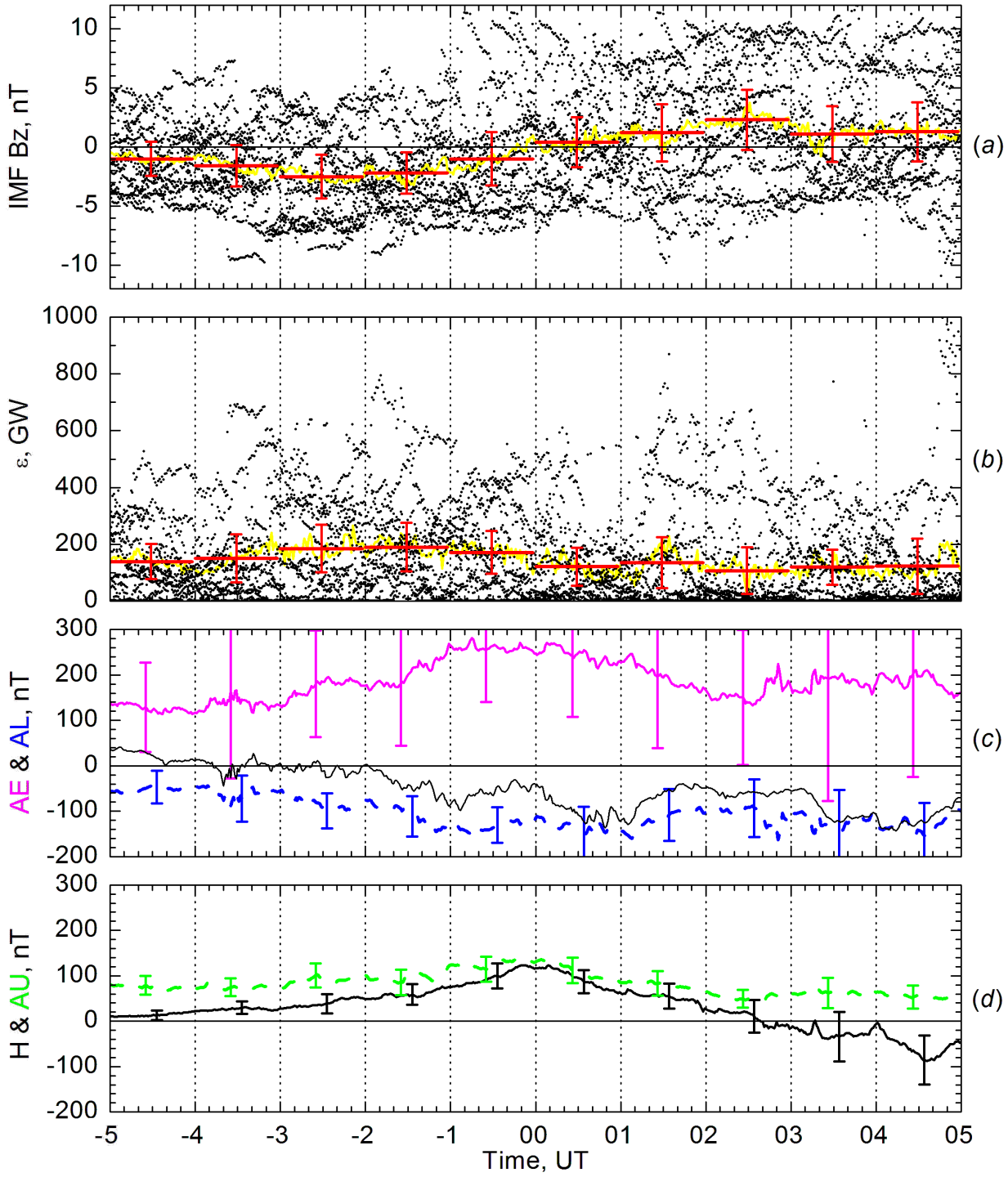

Fig.2. Variations of the superposed average: IMF *Bz* (a), **ε** (b), *AE* (magenta), *AL* (dashed blue) and *H*brw (black) (c), *H*tix (black) and *AU* (dashed green) (d). The red horizontal lines represent hourly averaged values of IMF *Bz* and **ε**. The vertical (red and others) lines represent the data variations, ±0.5σ (standard deviation). The zero epoch is the beginning of undulation registration.

A significant smooth growth in the variation of the *AE* index and *H*tix recorded synchronously for about 1.5 hours before the undulation events. The superposed average of AE index increased from ~180 to ~260 nT for half an hour and remained at the same level in the 1-hour interval (see Fig.2c), while in the variation of *H*tix observed a gradual growth from ~60 to ~120 nT with a peak near the beginning of undulation registration (see Fig.2d). In variations of *AL* (see Fig.2c) and *AU* (see Fig.2d) indices a changes of the superposed average are less pronounced, but their behaviors are similar to the variations of *H* component at Barrow and Tixie, respectively. In the variation of *H*brw (Fig.2c) two negative bays are clearly seen in the time intervals of from -2 to 0 hours and 0 to 2 hours, associated to a local magnetic activations in the midnight sector.

DISCUSSION AND SUMMARY

Classification of magnetic disturbance events in the midnight sector have been performed by Kullen and Karlsson (2004) and Janzhura et al. (2007) using the interplanetary medium parameters and geomagnetic indices *AE* and *PCN*, respectively. Our findings on a prevalence of negative signs of the IMF *Bz* with a mean value of -2 nT and a mean value of the energy parameter **ε**~200 GW provide a conditions for substorm development (Akasofu, 1981) and are typical for the "medium oval substorm" (Kullen and Karlsson, 2004). However, taking into a consideration of the results in the work (Janzhura et al., 2007), a mean values of *AE*~260 nT and *PCN*~1.4 before the undulation events are closer to a values observed in periods of pseudobreakups or "weak magnetic bays".

Kelley (1986) has been supposed the Kelvin-Helmholtz instability as a mechanism explaining a generation of large-scale undulation during magnetic storms. This instability occurs when a strong shear plasma flow near the equatorward boundary of the auroral oval is occurred as a result of formation of the intense poleward electric field or subauroral polarization stream - SAPS (Foster and Burke, 2002; Foster and Vo, 2002).

Zhang et al. (2005), Baishev et al. (2010a) and Henderson et al. (2010) have been noted that a generation of both undulations and SAPS are caused by strong subauroral electric field. Zhang et al. (2005) have been defined a necessary conditions for a generation of large-scale undulations, namely, high westward velocity of diffuse tongues (> 1000 m/s) and their strong latitudinal gradient (> 0.1 s^{-1}). This result is confirmed by Baishev et al. (2010a) and Henderson et al. (2010).

Baishev et al. (2010b) on the basis of comparisons of SAPS events recorded by DMSP satellites (Wang et al., 2008), and undulation events (Baishev et al., 2012) have been suggested that a phenomenon of SAPS and generation of eveningside undulations are causally related.

It is known that an important role in the plasma convection configuration in the ionosphere are caused by an external factors, mainly, IMF *Bz* and *By* components (Heppner and Maynard, 1987). When *Bz* <0 in the morning and evening sectors twin-vortex magnetospheric convection is developed, and when *By* <0 in the northern hemisphere the morning vortex expands to the afternoon hours. Therefore, an observed growth in the magnetic field *H* component at Tixie in the evening sector can be explained by increased large-scale magnetospheric convection at IMF *Bz* <0, and a location of the equatorward boundary of the diffuse aurora near Tixie can be determined by a location of the evening vortex at IMF *By* <0.

Cousins et al. (2013) performed a detailed analysis of plasma drift observations by SuperDARN radars. Using the data decomposition on the empirical orthogonal functions (EOF) it is revealed that the first two modes responsible for strengthening/weakening of the large-scale magnetospheric convection and change of shape of the vortices are correlated with the IMF *Bz* and *By* components, respectively. Authors found the notable exception of random behavior of the higher-order functions for EOF 11, which captures midlatitude variations on the duskside and is enhanced during subauroral polarization stream events.

Thus, we can assume that a generation of eveningside undulation under Kp<3 depends on a physical processes in the inner magnetosphere associated with a change of the magnetospheric convection configuration and a formation of narrow (~1-2º on latitude) subauroral polarization stream due to increased transfer of the solar wind energy into the Earth's magnetosphere under a durable (up to 4 hours) southward IMF orientation.

ACKNOWLEDGMENTS

The OMNI data were obtained from the GSFC/SPDF OMNIWeb interface at http://omniweb.gsfc.nasa.gov and magnetic data at Barrow were obtained from the SPIDR interface at http://spidr.ngdc.noaa.gov/spidr/. This work was partially supported by program "JSPS Core-to-Core Program, B. Asia-Africa Science Platforms".

REFERENCES

Akasofu, S.-I. (1981) Energy coupling between the solar wind and the magnetosphere, *Space Sci. Rev.*, 28, 121-190.

Baishev, D.G., and F.J. Rich (2006), Undulations observed by the DMSP satellites during magnetic superstorms of November 2004, *in Proc. of the Second Intern. Symp. "Solar Extreme Events". Fundamental Science and Applied Aspects (Nor-Amberd, Armenia, 26-30 Sept. 2005)*, Yerevan: Alikhanyan Physics Institute, 100-103.

Baishev, D.G., E.S. Barkova, S.I. Solovyev, K. Yumoto, M.J. Engebretson, and A.V. Koustov (2000), Formation of large-scale, "giant" undulations at the equatorial boundary of diffuse aurora and Pc5 magnetic pulsations during the January 14, 1999 magnetic storm, *in Proc. of Fifth Intern. Conf. on Substorm (St.Petersburg, Russia. 16-20 May 2000)*, Netherlands, Noordwijk: ESA, 427-430.

Baishev, D.G., E.S. Barkova, A.E. Stepanov, and K. Yumoto (2010a), Electric fields and large-scale undulations in the eveningside diffuse auroral zone, *Geomag. Aeron*., 50(1), 41-47.

Baishev, D.G., E.S. Barkova, A.A. Fedorov, and K. Yumoto (2010b), Optical observations of the eveningside undulations during solar cycle 23, in *Proc. 8th International Conference "Problems of Geocosmos", (St. Petersburg, September 20-24, 2010)*, ed. by V.S. Semenov, St. Petersburg, P. 31-35.

Baishev, D.G., E.S. Barkova, and K. Yumoto (2012), Optical observations of large-scale undulations in the 23rd cycle of solar activity, *Geomag. Aeron*., 52(2), 197-203.

Baishev, D.G., K. Yumoto, S.I. Solov'ev, N.E. Molochushkin, and E.S. Barkova (1997), Magnetic storm time variations of the geomagnetic field during large scale undulations of the evening diffuse and aurora, *Geomag. Aeron*., 37(6), 706-711.

Cousins, E.D.P., T. Matsuo, and A.D. Richmond (2013), Mesoscale and large-scale variability in high-latitude ionospheric convection: Dominant modes and spatial/temporal coherence, *J. Geophys. Res*., 118, doi:10.1002/2013JA019319.

Foster, J. C., and W. J. Burke (2002), SAPS: A new characterization for sub-auroral electric fields, *EOS Trans. AGU*, 83(36), 293-294.

Foster, J.C., and H.B. Vo (2002), Average characteristics and activity dependence of the subauroral polarization stream, *J. Geophys. Res*., 107(A12), 1475, doi:10.1029/2002JA009409.

Henderson, M.G., E.F. Donovan, J.C. Foster, I.R. Mann, T.J. Immel, S.B. Mende, J.B. Sigwarth (2010), Start-to-end global imaging of a sunward propagating, SAPS-associated giant undulation event, *J. Geophys. Res*., 115, doi:10.1029/2009JA014106.

Heppner, J.P., and N.C. Maynard (1987), Empirical high-latitude electric field models, *J. Geophys. Res*., 92, 4467-4489.

Janzhura, A., O. Troshichev, and P. Stauning (2007), Unified PC indices: Relation to the isolated substorms, *J. Geophys. Res*., 112, A09207, doi:10.1029/2006JA012132.

Kelley, M.C. (1986), Intense sheared flow as the origin of large-scale undulations of the edge of the diffuse aurora, *J. Geophys. Res.*, 91, 3225-3230.

Kullen, A., and T. Karlsson (2004), On the relation between solar wind, pseudobreakups, and substorms, *J. Geophys. Res*., 109, A12218, doi:10.1029/2004JA010488.

Lui, A.T.Y., C.-I. Meng, and S. Ismail (1982), Large amplitude undulations on the equatorward boundary of the diffuse aurora, *J. Geophys. Res.*, 87, 2385-2400.

Nishitani, N., G. Hough, and M.W.J. Scourfield (1994), Spatial and temporal characteristics of giant undulations, *Geophys. Res. Lett*., 21(24). 2673-2676.

Zhang, Y., L.J. Paxton, D. Morrison, A.T.Y. Lui, H. Kil, B. Wolven, C.-I. Meng, and A.B. Christensen (2005), Undulations on the equatorward edge of the diffuse proton aurora: TIMED/GUVI observations, *J. Geophys. Res*., 110, A08211, doi:10.1029/2004JA010668.

Wang, H., A. J. Ridley, H. Luhr, M. W. Liemohn, and S. Y. Ma (2008), Statistical study of the subauroral polarization stream: Its dependence on the cross-polar cap potential and subauroral conductance, *J. Geophys. Res*., 113, A12311, doi:10.1029/2008JA013529.

A COMPARISON OF THE ELECTRON DENSITY HEIGHT PROFILES CALCULATED BY THE THEORETICAL UAM AND EMPIRICAL IRI MODELS

M.G. Botova, Y.V. Romanovskaya, A.A. Namgaladze

Murmansk State Technical University, Murmansk, 183010, Russia, e-mail: botovamg@gmail.com

Abstract. We have performed simulations of the ionosphere behavior for two solar activity levels and different seasons using the Upper Atmosphere Model (UAM). The model results are presented as electron density height profiles. The numerically calculated parameters are compared with the empirical IRI-2012 values. It is shown that the UAM results agree with empirical the IRI-2012 values calculated for the middle and low latitudes and daytime hours at both low and high solar activity levels. The maximum difference between the UAM electron density and the IRI-2012 values belongs to results for high latitudes. Besides, large discrepancies of the electron density height profiles by UAM and IRI-2012 are detected in calculation results for plasmasphere heights and low solar activity conditions.

1. Introduction

Testing and verifying of numerical models is a significant problem for all modelers. A great part of papers are devoted to the description of so-called "case-studies" and "event-studies" by which the ionosphere behavior is investigated using observation data from separate stations or for the particular ionospheric events [Namgaladze et al., 2006; Burns et al., 2008; Klimenko et al., 2011; Codrescu et al., 2012; Solomon et al., 2013].

Global patterns of investigated parameters can be simulated using empirical models. Constructed by observation data averaging the IRI family models [Bilitza et al., 2008, 2014] have been widely accepted as the international standard for ionosphere parameters predictions. The IRI models are used both in the ionosphere behavior investigations [Ünal et al., 2011; Han et al., 2011 and others] and in the statistical models validations [Souza et al., 2010; Lin et al., 2014 and others].It is significant that the empirical IRI models themselves are subject of validations [Potula et al., 2011; Okoh et al., 2012; Yu et al., 2013].

In our previous papers we compared the UAM results with data of seven incoherent scatter radars and the IRI-2001 [Namgaladze et al., 2006] with the thermospheric wind data provided by the CHAMP satellite [Forster et al., 2011]. In this work we continue the investigation which previous results are described in [Botova et al., 2014].

2. Model calculations

The Upper Atmosphere Model is a global three-dimensional time-dependent mathematical model of the Earth's upper atmosphere [Namgaladze et al., 1988, 1991, 1998a-c]. It calculates physical parameters of the Earth's upper atmosphere at the altitude range from 60-80 km to 15RE of geocentric distance (RE– the Earth radius) depending on latitude, longitude, altitude and time for different helio-geophysical conditions (time, season, levels of solar and magnetic activity, etc.).

Model simulations were performed using two different UAM versions: 1) with neutral densities and temperature calculated by the empirical NRLMSISE-00 model (marked as UAM-TM) and 2) the fully self-consistent version with theoretically calculated thermospheric parameters (marked as UAM-TT).

Input parameters were set for both versions identically: 1) solar UV and EUV spectra are taken from the model by [Nusinov, 1984]; 2) the potential drop across the polar cap is calculated by the empirical AE-index relation of [Weimer at al., 1990]; 3) precipitating fluxes are calculated by the empirical model of [Hardy et el., 1985].

The model spatial grid had variable latitudinal step (from 2° near the equator to 2.5° near the pole for ionospheric parameter calculation and from 4° near the pole to 4° near the equator for thermospheric parameters calculation) and the variable altitude step (from 3 km on the lower boundary to 20 km in the F2-region). The constant longitudinal step equal to 15° was used.

The calculations were executed for two solar activity levels and different seasons. For the low solar activity (F10,7~90) the modeled dates were the December solstice of 2004 and the April equinox of 2005. For the

high solar activity (F10,7~180) the modeled dates were the December solstice of 2000 and the April equinox of 2002.
Initial conditions were prepared for the each date using the following procedure: 1) firstly, model data was calculated according to the empirical NRLMSISE-00 and the IRI-2007 models for the ionosphere and thermosphere respectively; 2) to obtain the stationary state of the ionosphere and thermosphere two consequent runs were performed; 3) then five model days were calculated as usual. The paper presents the results for the 24:00 UT of the fifth model day (00:00 UT, next day).

3. Simulation results

The simulation results are also presented as electron density height profiles for the following coordinates: the geomagnetic latitudes of 60°, 45°, 30°, 15° and 0° of the northern hemisphere and the geomagnetic longitudes of 115° and 295° corresponding to 03:00 MLT and 15:00 MLT. The model electron density profiles are compared with the empirical IRI-2012 values. The Figure 1 and Figure 2 show the height profiles of the electron density common logarithm calculated by the UAM and the IRI for low and high levels of solar activity correspondingly for different seasons. The UAM profiles are presented by circles, the IRI-2012 profiles – by the solid lines.
Figures 1-2 show that both UAM versions give electron density altitudinal variations with a similar shape and reproduce:
1) the electron density maximum at ~ 250 km in daytime and at ~ 300 km in nighttime under the low solar activity conditions;
2) the electron density maximum at ~ 300 km in daytime and at ~ 350 km in nighttime under the high solar activity conditions.
Figure 1 shows that for the low solar activity both UAM versions give practically the same height variations of the parameter. For the altitudinal range up to ~ 500-750 km at least one of the UAM versions reproduces the IRI-2012 values with the discrepancy up to 10% in the larger half of the demonstrated cases.
Figure 2 shows for the high solar activity the UAM versions disagreement increases correspospondingly both variations shapes and parameter values. In the most cases for the height range up to ~ 750 km at least one of the UAM versions gives electron deisity variation practically the same as the IRI-2012 one.
The maximal quantitive disagreement with the empirical model electron density in the height range up to 750 km belonges to the numerical results for nighttime hours and the geomagnetic latitude of 60° underestimating the IRI-2012 values up to factor 10.
Let consider the height range above 750 km. For the low solar activity the empirical IRI-2012 reproduces faster electron density decreasing with increase in the altitude. At the same time the numerically calculated electron density does not change or decreases very slowly than the IRI-2012 values. But the behaviour of the UAM results for the high solar activity is overwise. In most cases the theoretical model gives tha same angle of electron density incidence as the IRI-2012. This fact can be explained by the following. The electron density variations at the F2-region upper boundary and in the plasmasphere are determined including processes of plasma tubes filling and depletion.
Figure 2 demonstrates the small inclination angle in the top parts of the UAM electron density profiles. This might be due to the initial conditions features, in particular, plasma tubes electron densities obtained from previous 5 days model run for exceptionally quiet conditions.
The rate of the electron number density decreases with altitude is nearly the same for the IRI-2012 and the UAM models results obtained for equinox and solstice conditions and high solar activity level.

4. Conclusion

This paper analyzes the height profile of electron densities obtained using two versions of the global three-dimensional time-dependent mathematical model of the Earth's upper atmosphere (UAM) for two solar activity levels and different seasons. The numerically calculated parameters are compared with the empirical IRI-2012 values.
It is shown that the UAM results agree with the empirical IRI-2012 values calculated for the middle and low latitudes and daytime hours at both low and high solar activity levels. The maximum difference between the UAM electron density and IRI-2012 values belongs to results for high latitudes. Besides, large discrepancies take place in the electron density profiles at the plasmasphere heights for low solar activity level. The UAM profiles demonstrate significantly less decrease rate over the IRI-2012 ones. We expect the latter is due to initial conditions used in UAM simulations, in particular, plasma tubes electron densities.

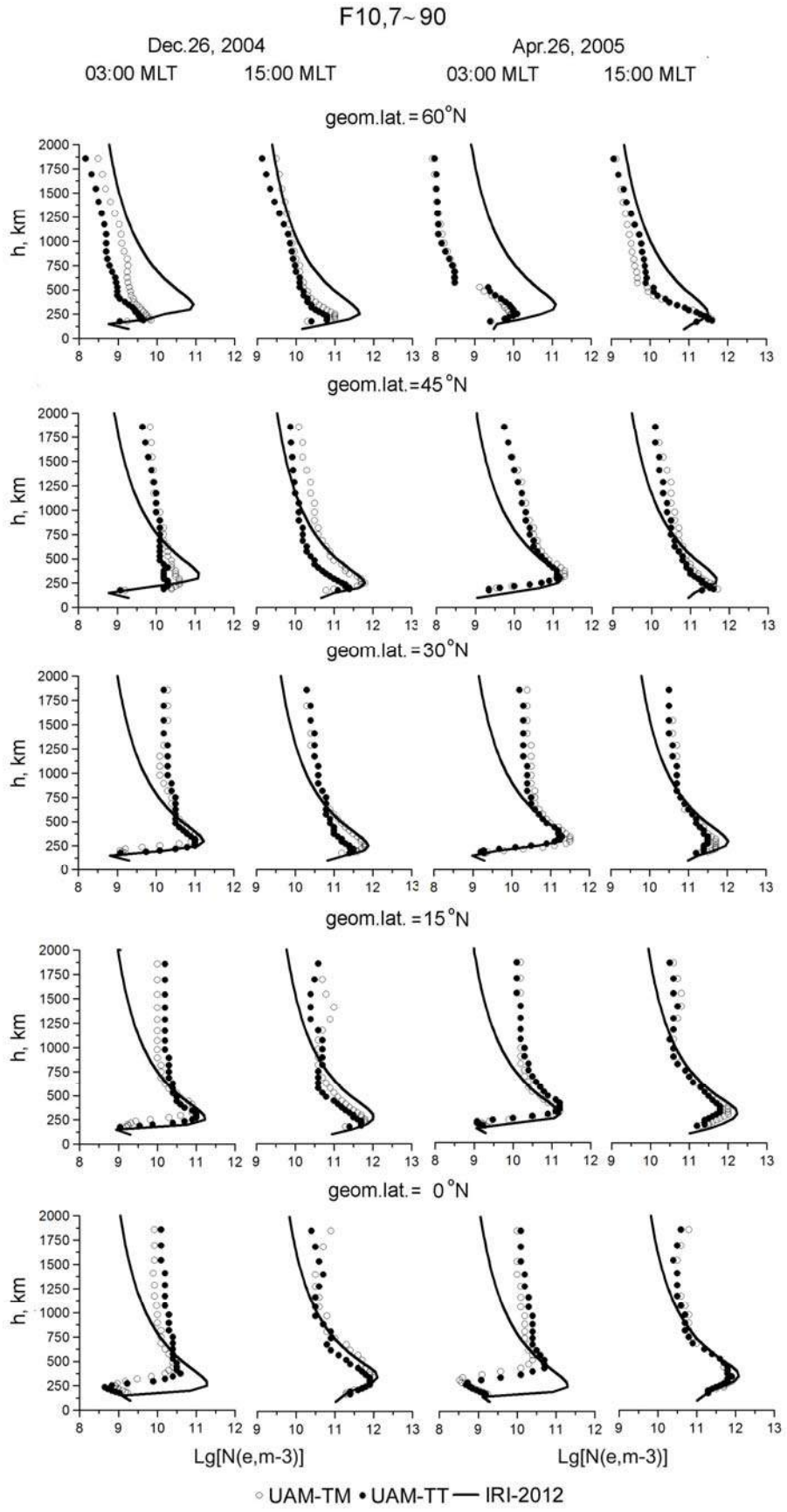

Figure 1. Height profiles of electron density common logarithm calculated by the UAM-TM (white circles), the UAM-TT (black circles) and the IRI-2012 (solid lines) for the solstice of December 26, 2004 and the equinox of April 26, 2005 (low solar activity).

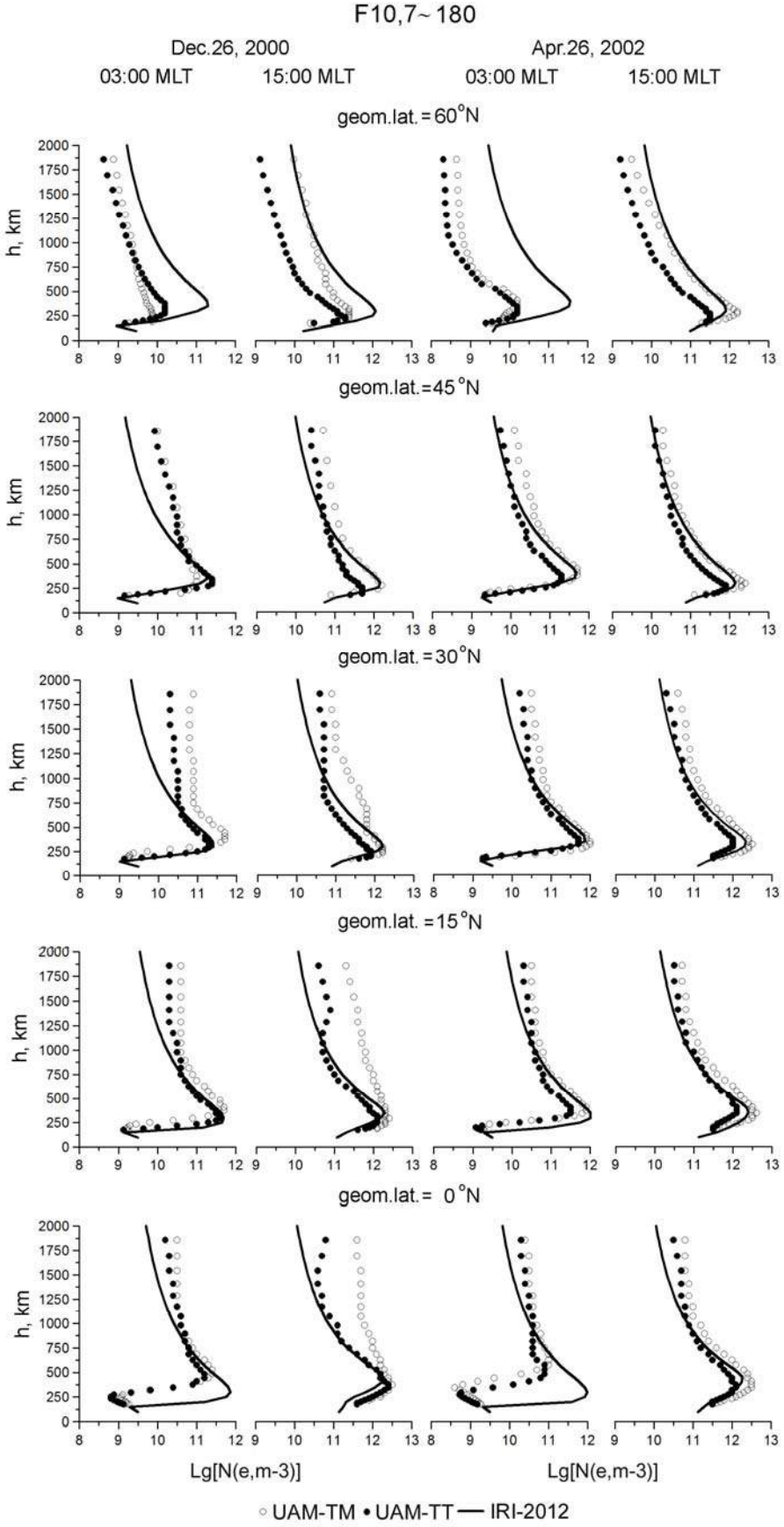

Figure 2. Height profiles of electron density common logarithm calculated by the UAM-TM (white circles), the UAM-TT (black circles) and the IRI-2012 (solid lines) for the solstice of December 26, 2000 and the equinox of April 26, 2002 (high solar activity).

References

Bilitza, D., B.W. Reinisch (2008), International reference ionosphere 2007: improvements and new parameters. *Adv. Space Res.*, 42, 599-609.

Bilitza, D., D. Altadill, Y. Zhang, C. Mertens, V. Truhlik, P. Richards, L.-A. McKinnell, B. Reinisch (2014), The International Reference Ionosphere 2012 - a model of international collaboration. *J. Space Weather Space Clim.*, 4, A07.

Botova, M.G., Y.V. Romanovskaya, A.A. Namgaladze (2014), Ionosphere variations in model calculations and observation data. *Proceedings of the MSTU*, 17(2), 385–393 (in Russian).

Burns, A. G., W. Wang, M. Wiltberger, S. C. Solomon, H. Spence, T. L. Killeen, R. E. Lopez, J. E. Landivar (2008), An event study to provide validation of TING and CMIT geomagnetic middle-latitude electron densities at the F2 peak. *J. Geophys. Res.*, 113, A0531.

Codrescu, M.V., C. Fedrizzi, T. J. Fuller-Rowell, A. Dobin, N. Jakowsky, H. Khalsa, T. Matsuo, N. Maruyama (2012), A real-time run of the Coupled Thermosphere Ionosphere Plasmasphere Electrodynamics (CTIPe) model. *Space Weather*, 10, S02001.

Forster, M., A. A. Namgaladze, E. N. Doronina, B. E. Prokhorov (2011), High-latitude thermospheric winds: Satellite data and model calculations. *Russian Journal of Physical Chemistry B, Focus on Physics*, 5(3), 439-446.

Han, F., S. A. Cummer, J. Li, G. Lu (2011), Daytime ionospheric D region sharpness derived from VLF radio atmospherics. *J. Geophys. Res.: Space Physics (1978-2012)*, 116(A5).

Hardy, D.A., M.S. Gussenhoven, E.A.Holeman (1985), A statistical model of auroral electron precipitation. *J. Geophys. Res.*, 90, 4229-4248.

Klimenko, M. V., V. V. Klimenko, K. G. Ratovsky, L. P. Goncharenko, R. R. Fagundes, R. de Jesus, A. J. de Abreu, A. M. Vesnin (2011), Numerical modeling of ionospheric effects in the middle- and low-latitude F region during geomagnetic storm sequence of 9–14 September 2005, *Radio Science*, 46(3).

Lin J., X. Y. Zhen Zeng, Y. Lou, X. Shen, Y. Wu, W.S. Schreiner, Y.-H. Kuo (2014), Empirical orthogonal function analysis and modeling of the ionospheric peak height during the years 2002-2011. *J. Geophys. Res.: Space Physics*, 119(5), 3915-3929.

Namgaladze, A.A., Yu.N. Korenkov, V.V. Klimenko, I.V. Karpov, F.S. Bessarab, V.A. Surotkin, T.A. Glushchenko, N.M. Naumova (1988), Global model of the thermosphere-ionosphere-protonosphere system. *PAGEOPH*, 127(2/3), 219-254.

Namgaladze, A.A. Korenkov, Yu.N. Klimenko, V.V. Karpov, I.V. Surotkin, V.A. Naumova, N.M. (1991), Numerical modelling of the thermosphere-ionosphere-protonosphere system *J. Atmos. Terr. Phys.*53(11/12),1113-1124.

Namgaladze, A.A., O.V. Martynenko, A.N. Namgaladze (1998a), Global model of the upper atmosphere with variable latitudinal integration step. *Geomagn. Aeronomy Int.*, 1(1), 53-58.

Namgaladze, A.A., O.V. Martynenko, M.A. Volkov, A.N. Namgaladze, R.Yu. Yurik (1998b), High-latitude version of the global numerical model of the Earth's upper atmosphere. *Proc. of the MSTU*, 1(2), 23-84.

Namgaladze, A.A., A.N. Namgaladze, M.A. Volkov (1998c), Seasonal effects in the ionosphere-thermosphere response to the precipitation and field-aligned current variations in the cusp region. *Ann. Geophys.*, 16(10), 1283-1298.

Namgaladze, A.A., Yu.V. Zubova, A.N. Namgaladze, O.V. Martynenko, E.N. Doronina, L.P. Goncharenko, A. Van Eyken, V. Howells, J. P. Thayer, V. I. Taran, B. Shpynev, Q. Zhou (2006), Modelling of the ionosphere/thermosphere behavior during the April 2002 magnetic storms: A comparison of the UAM results with the ISR and NRLMSISE-00 data. *Adv. Space Res.*, 37 (2), 380-391.

Nusinov, A.A.(1984) Dependence of the short-wave solar radiation intensity on the activity level. *J. Geomagnetism and Aeronomy*, 24(4), 529–536 (in Russian).

Okoh, D., A. Eze, O. Adedoja, B. Okere, P. N. Okeke (2012), A comparison of IRI-TEC predictions with GPS-TEC measurements over Nsukka, Nigeria. *Space Weather*, 10, S10002.

Potula, B. S., Y.-H. Chu, G. Uma, H.-P. Hsia, K.-H. Wu (2011), A global comparative study on the ionospheric measurements between COSMIC radio occultation technique and IRI model. *J. Geophys. Res.*, 116, A02310.

Solomon, S.C., L. Qian, A. G. Burns (2013), The anomalous ionosphere between solar cycles 23 and 24. *J. Geophys. Res.*, 118 (10), 6524-6535.

Souza, J.R., C.G.M. Brum, M.A. Abdu, I.S. Batista, W.D. Asevedo Jr., G.J. Bailey, J.A. Bittencourt (2010), Parameterized Regional Ionospheric Model and a comparison of its results with experimental data and IRI representations. *Adv. Space Res.*, 46(8), 1032-1038.

Ünal, İ., E. T. Şenalp, A. Yeşil, E. Tulunay, Y. Tulunay (2011), Performance of IRI-based ionospheric critical frequency calculations with reference to forecasting. *Radio Science*, 46(1).

Weimer, D.R., N.C. Maynard, W.J. Burke, C. Liebrecht (1990), Polar cap potentials and the auroral electrojet indices. *Planetary and Space Science*, 38(9), 1207-1222.

Yu, Y., W. Wan, B. Zhao, Y. Chen, B. Xiong, L. Liu, J. Liu, Z. Ren, M. Li (2013), Modeling the global NmF2 from the GNSS-derived TEC-GIMs. *Space Weather*, 11(5), 272-283.

STRUCTURE OF WEATHER SYSTEM OVER THE NORTH-WESTERN PART OF THE PACIFIC OCEAN IN CONNECTION WITH LIGHTNING ACTIVITY OF THE FAR-EASTERN REGION

N.V. Cherneva[1], B.M Shevtsov[1], M.S. Permyakov[2], E.Yu. Potalova[2], R.H. Holzworth[3], D.V. Sannikov[1]

[1]Institute of Cosmophysical Research and Radio Wave Propagation (IKIR) FEB RAS, 684034, Russia, e-mail: nina@ikir.ru; [2]Pacific Oceonological Institute FEB RAS, Vladivostok, Russia; [3]University of Washington, Seattle, USA

Abstract. Applying the data of VLF direction finder receiving station of IKIR FEB RAS, included in the World Wide Lightning Location Network (WWLLN), the paper investigates the relations of field characteristics of recorded lightning discharges in the north-western part of the Pacific ocean with field characteristics of weather formation meteorological elements, evaluated according to the data of Earth remote sounding from satellites. On the example of separate tropical cyclones (TC) for 2012-2013, the relation of lightning discharge frequency and density with spatial distribution of driving wind vortex is shown. TC structure evolution is traced in cloudiness fields, driving wind vortex, and lightning discharge distribution. This publication is based on work supported by a grant from the U.S. Civilian Research and Development Foundation (RUG1-7084-PA-13) with funding from the United States Department of State.

Introduction. During the last decay a relatively new passive method for investigation of weather systems has developed. This method is associated with registration of lightning activity by lightning discharge direction-finder network applying a very low frequency (VLF) range of electromagnetic waves (Druzhin G.I., Cherneva N.V., 2011, Abarca S.F., K. L. Corbosiero and D. Vollaro, 2011, Leary L.A., Ritchie E.A., 2009, Squires K., S. Businger, 2008, Virts K.S., J. M. Wallace, M. L. Hutchins, and R. H. Holzworth, 2013). Investigations of lightning activity, its spatial-temporal changeability is very significant in the area of investigation of atmospheric electricity, radio wave propagation. In synoptic and mesoscale weather systems over the ocean and seas, lightning activity, its intensity and spatial distribution via cloud scale processes are modulated by dynamic structure of these weather systems. Thus, on the data of weather system structural elements obtained by meteorological systems or remote sounding systems in space, it is possible to study the relation of lightning activity with these structural elements and their characteristics. The paper presents some preliminary results of such investigations on the example of separate **tropical cyclones** (**TC**) in the North-Western part of the Pacific Ocean.

Data and methods

Distribution of the influence range for lightning activity is presented by lightning discharge density per a square unit. In order to do that we used the data of the World Wide Lightning Location Network (WWLLN) (http://wwlln.net), distribution of this network VLF stations is shown in (Virts K.S., J. M. Wallace, M. L. Hutchins, and R. H. Holzworth, 2013). These data give coordinates and time for recorded lightning discharges in the atmosphere. Applying TC center coordinates, specifying the range of its influence (a ~10×10^{o} square) and sampling the WWLLN data in a certain interval, lightning discharge density is calculated in the regular rectangular grid nodes with 25 km coordinate step, which is close to the grid step according to scatterometer driving wind (0.25×0.25^{o}), to discharge point number falling within the given radius with a center in the current node. All the charges falling within the circle are summed up with the weight depending on the magnitude difference of a given time moment (usually it is the time with wind fields) and a separate discharge time in WWLLN data. Gaussian weighting function with 1.5 hour width (for small discharge density this width increase to 3 hours). In the result we obtain discharge density field, which may be called lightning activity field.

To determine the structural elements in TC region the data on driving wind velocity and direction were used. This data were obtained by QuikSCAT scatterometer and they are available on the site of Remote Sensing Systems, morning and evening satellite circles. Wind vectors are reduced to 10 m level above the surface in the suggestion of driving wind neutral stratification and interpolated into nodes of geographical grid with the

resolution 0.25º×0.25º. Wind estimation error is ~1.7 m/s, its directions are ~14º. The data of a passive polarimetric microwave WindSat radiometer were also applied (http://www.remss.com).

Data sampling was carried out in the regions of initiation and evolution of tropical cyclones in the North-Western part of the Pacific Ocean in 2005-2013. Only cyclones which generation and development was occurring over open ocean areas away from mainland were chosen. TC must also be covered by scatterometer scan line. TC characteristics, date/time and coordinates of center location, minimum near ground pressure and wind maximum velocity, were obtained from the archive of Japanese Meteorological Agency (JMA), RSMC Tropical Cyclone Best Track (http://www.usno.navy.mil/JTWC). TC coordinates and characteristics are given on the time grid in standard time with 6 hour interval. Fig. 1 shows trajectories of three TC, Haitang (TY0505), Sonca 2005, Lekima (2013); the results of processing of their data are presented in the report. All the chosen cyclones during their evolution reached typhoon intensity (wind velocity more than 33 m/s). TC structure was analyzed by driving wind vortex field (Permyakov M.S., Potalova E.Yu.., 2013, Potalova E.Yu., Permyakov M.S., Kleshcheva T.I., 2013). Wind velocity vortex was calculated on a 5-point scale. Vortex fields were smoothed by a smoothing function with Gaussian kernel with 75 km scale. Coordinates and intensity of separate meso-vortexes were calculated by location and amplitude of extremums in vortex fields, which were estimated by vortex local (on 3×3 pattern) approximation by second order surface. For the further analysis only cyclonic vortexes with the intensity higher than estimation errors (~$5 \cdot 10^{-5}$ s^{-1}) were used.

TC mesostructure main parameters are determined by the stage of its development and intensity. To trace such changeability of the mesostructure and lightning activity, we chose wind data and WWLLN data on characteristic moment of TC evolution. These moments (exact dates and standard time) are determined mainly according to Tropical Cyclone Best Track archive (http://www.usno.navy.mil/JTWC). There the information on every TC is given from a certain moment when a TC, as a rule, has tropical depression intensity. But before this moment, a cyclone may exist for several days as weak, formless tropical disturbance (or a usual cluster) and this period will be further called an *initiation period* and its beginning is the appearance of significant disturbances in the vortex field (or mesovortex clusters). During this period the data were chosen in ~10×10º latitude region with the center which is determined by time reverse (from the first message) extrapolation by TC motion velocity. TC initiation period is changed by a *formation period*, the beginning of which is the time of the first message on TC. This period is terminated at the moment of TC *development initiation*, which is the time of pressure decrease maximal rate in the center of a TC. Then, a TC reaches the moment of *maximum development* when pressure in the center of TC is minimum.

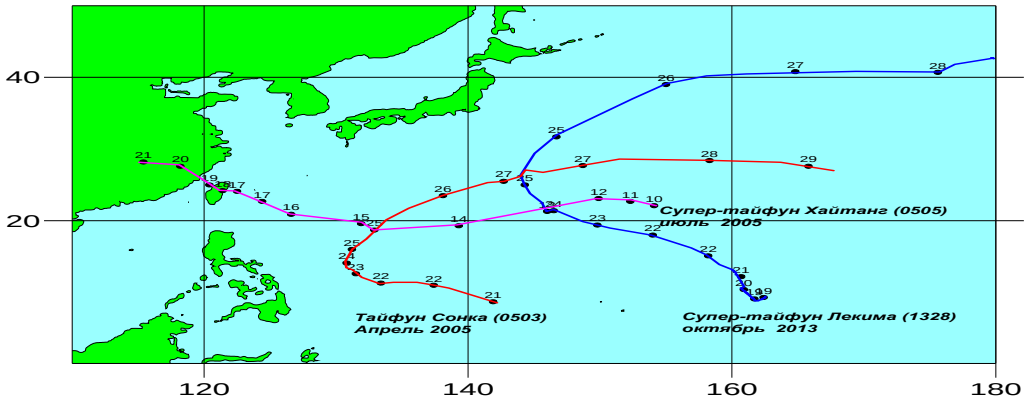

Fig.1. Trajectories of Sonca (0503), Haitang (0505) u Lekima(1328) tropical cyclones according to the data of Japanese Meteorological Agency.

Results and discussion

During WWLLN data analysis and interpretation it should be noted, that due to different reasons only a part of lightning discharges are registered by it. As it is shown in (Virts K.S., J. M. Wallace, M. L. Hutchins, and R. H. Holzworth, 2013), the efficiency of discharge registration may be from 10% to 90%. Thus, during some periods of TC development discharge point distribution reflects poorly (or does not reflect at all) its structure. We also note a significant diurnal variation of discharge frequency in the TC range of influence.

Fig. 2 and 3 illustrate the results of comparison of QuikSCAT scatterometer driving wind fields, the vortex, discharge distribution for the current day and calculated discharge density, as a lightning activity coefficient, for Sonka TC (2005). Density fields are calculated for the given time moments with Gaussian time

window width of 3 hours. Fig. 3 illustrates a histogram for discharge diurnal distribution on hour intervals, showing lightning activity significant changeability within a day. It may be associated with the known factor of diurnal variation in humidity convection intensity in tropics.

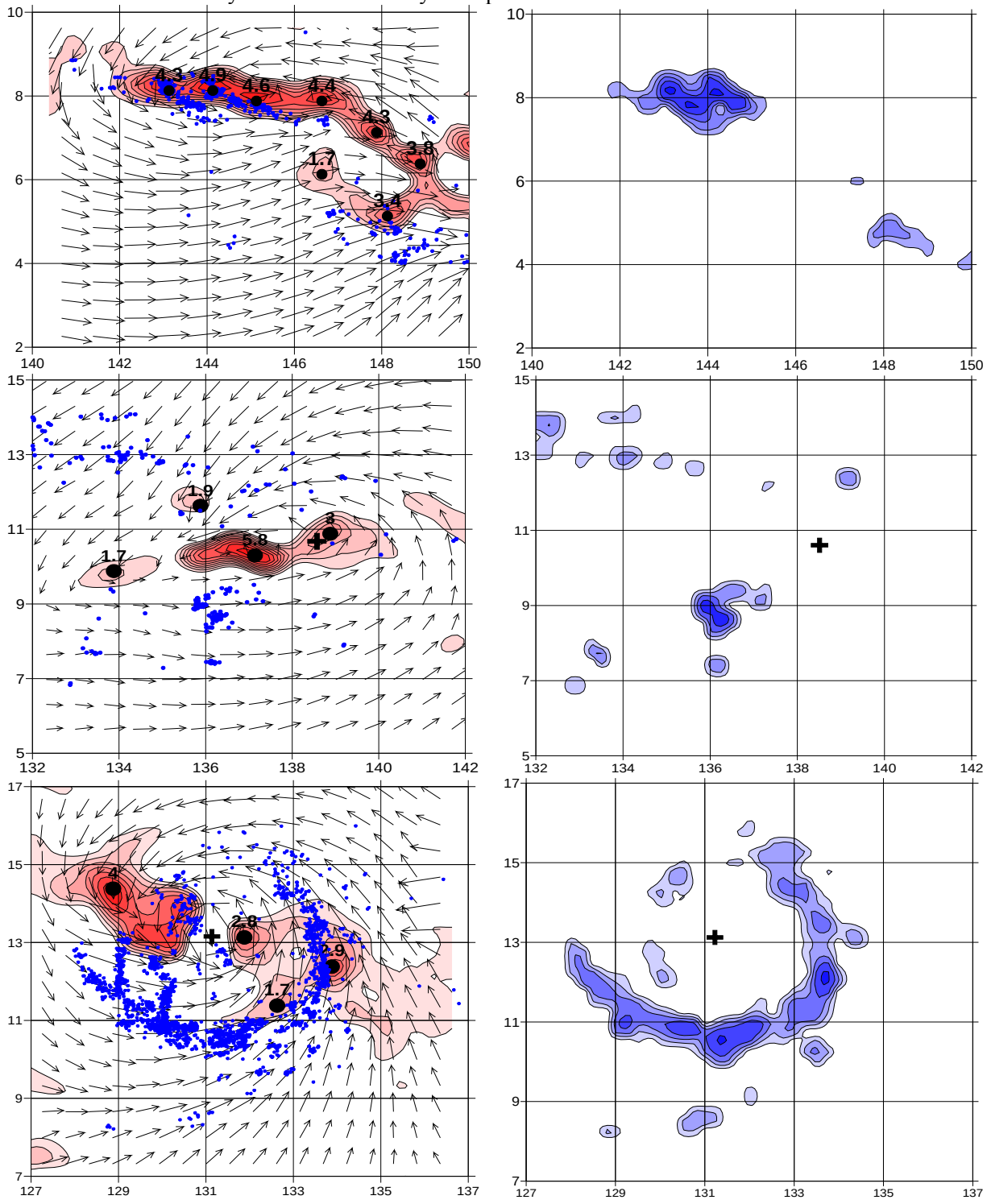

Fig. 2. Sonca TC (2005) during the stages of (from the top) initiation (April 20, 8:18), formation (April 21, 20:24) and development initiation (April 23, 21:12). To the left are driving wind and vortex fields, blue dots are WWLLN lightning discharges for the current day. To the right are discharge density fields for QuikSCAT data time.

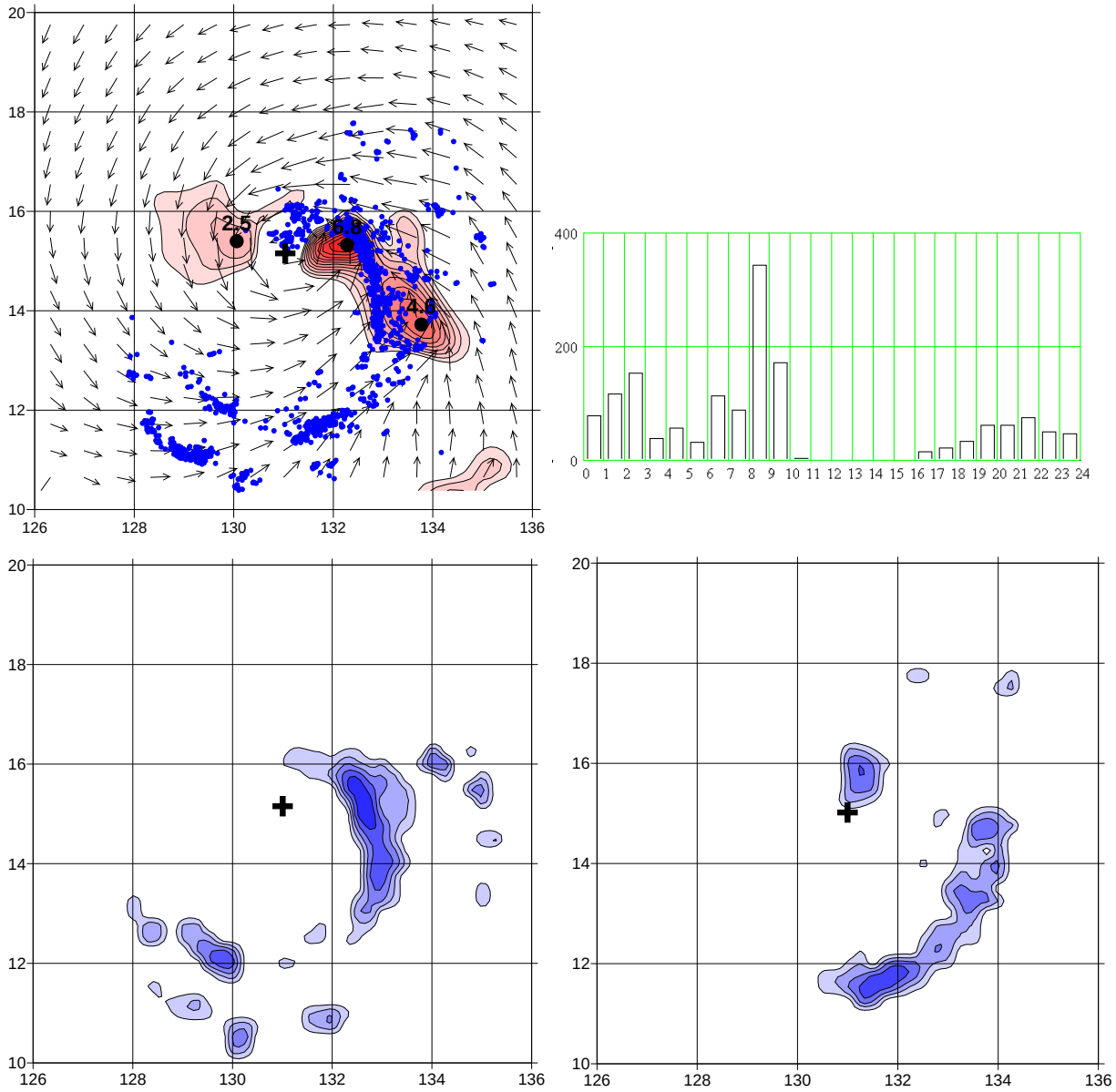

Fig.3. In the top is the same as for the previous figure for the stage of maximum development on April 24, at 20:48. To the right is the histogram of discharges. In the bottom are discharge density fields for two moments at 8:30 (left) and 21:00 (right).

Fig. 4 shows the results for Lekima TC (2013) for the stages (from the top) of initiation (October 19, at 4:15), formation (October 20, at 22:15) and development initiation (October 23, 23:00). In this case the driving wind fields were obtained by passive polarimetric microwave WindSat radiometer (http://www.remss.com).

In the both TC in charge distribution and in lightning activity field, we can see typical structures for convective cloudiness in TC; these structures are the parts of circular and spiral formations of mesometeorological scale. It should be marked that these structures are slightly similar to the mesostructures in driving wind vortex fields.

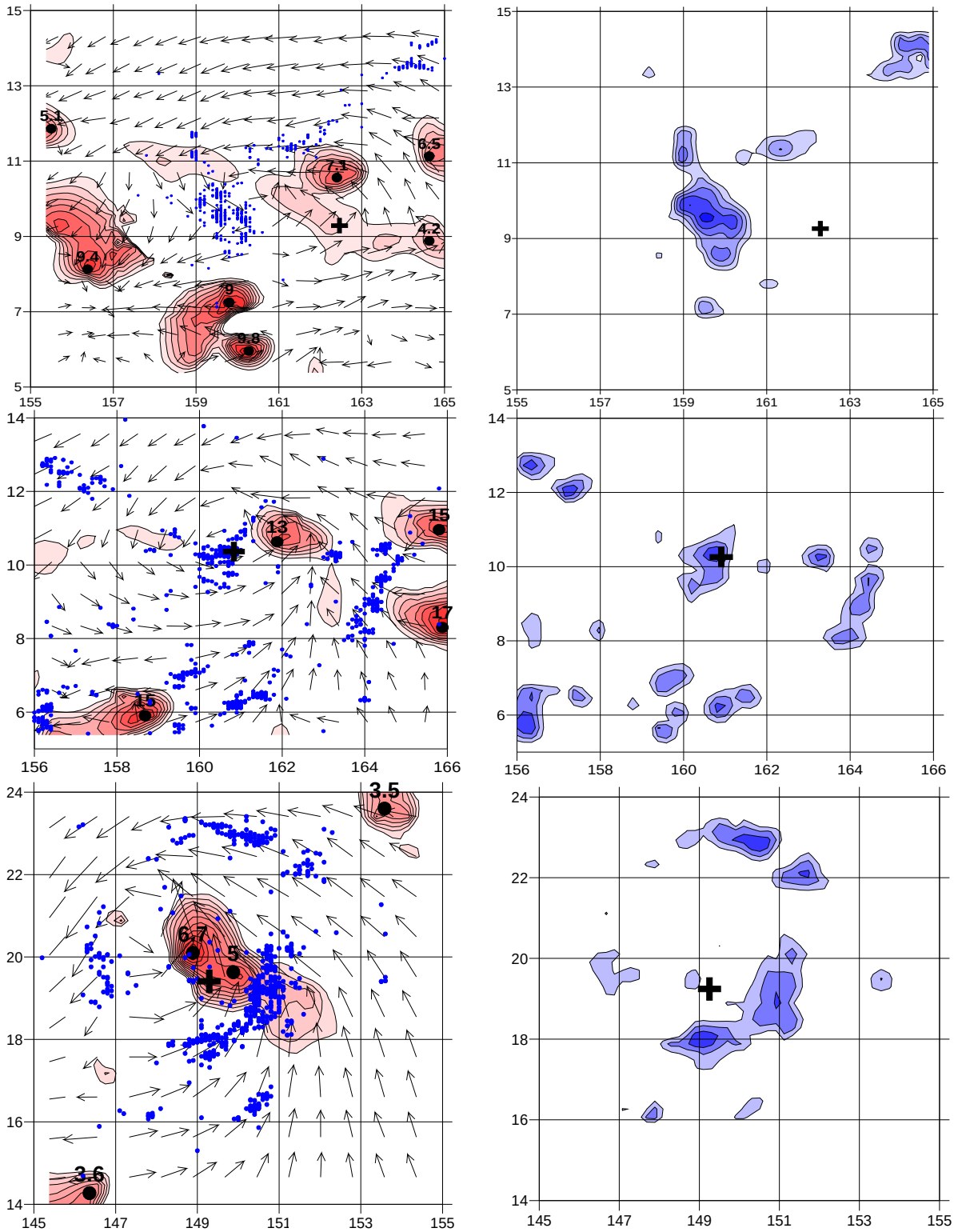

Fig.4. Lekima TC (2013) during the stages of (from the top) initiation (October 19 4:15), formation (October 20, 22:15) and development initiation (October 23, 23:00). To the left are wind and vortex fields, dots are lightning discharges on the current day. To the right are discharge density fields.

According to the data for Haitang TC (2005), Fig. 5 shows a histogram for discharge distribution in hour intervals for 8 days of its evolution from initiation to the date of maximum development (July 16). On the days

of deepening (the 6-th and the 7-th) and maximum development (the 8-th), lightning activity significantly increases in TC region. On the day of maximum intensity, when TC reaches typhoon intensity, discharge number (and density) is more than two times higher than that on the preceding two days of TC deepening. Diurnal variation with the maximum in the evening (local time) was observed during all three days. The discharge density field at 6:00 (Greenwich time) may be compared with cloudiness field on a satellite image at the same time (http://agora.ex.nii.ac.jp/). Thin enough elements are seen in discharge density fields which may be also found in typhoon cloudiness field.

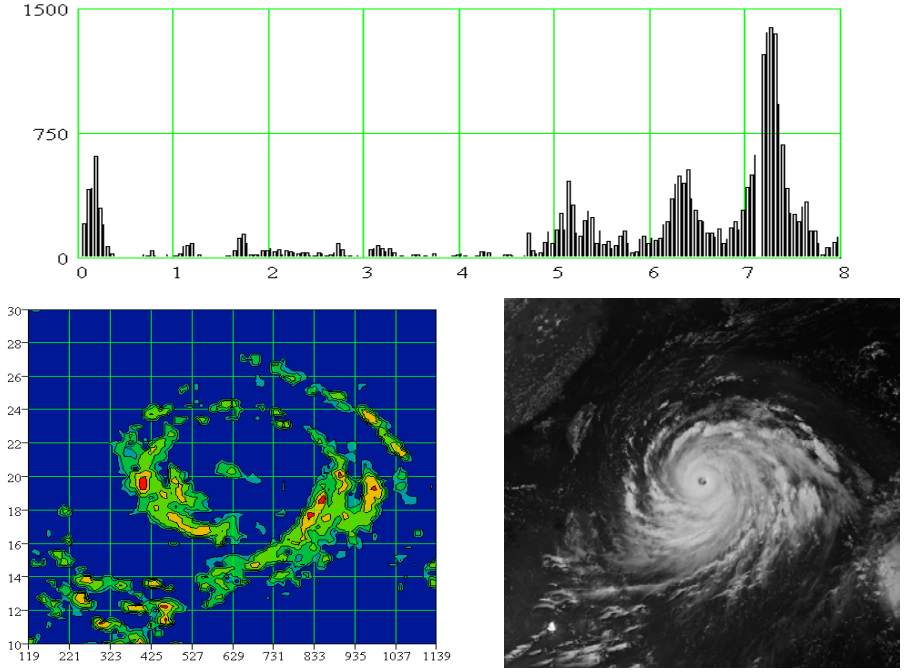

Fig.5. Haitang TC (2005). In the top is the histogram of discharge distribution in hour intervals for 8 days from initiation to the date of maximum development (July, 16). In the bottom is discharge density field at 6:00, to the right are satellite images at 6:00 UTC (http://agora.ex.nii.ac.jp/).

Conclusion

On the example of tropical cyclones in the North-Western part of the Pacific Ocean the relation of lightning discharge density fields with cyclone structure and intensity is shown at different stages of their development. The preliminary results show the possibility of WWLLN to monitor weather systems with intensive enough humid convection with lightning cloudiness. Extending of the WWLLN station network in the North-Western part of the Pacific Ocean may make it an important additional passive remote instrument to trace tropical cyclones, storms and typhoons, and the basis for a new method of their investigation.

References

Druzhin G.I., Cherneva N.V. (2011), Lightning in the region of Kamchatka Peninsula according to the data of VLF radiation observations. *Meteorology and Hydrology,* 7, 32-38.

Permyakov M.S., Potalova E.Yu. (2013), Mezoscale structure of tropical cyclones. *Current problems in remote sensing of the Earth from Space,* 10(1), 72-80.

Potalova E.Yu., Permyakov M.S., Kleshcheva T.I. (2013), Mesoscale structure of tropical cyclones in driving wind field. *Meteorology and Hydrology,* 11, 22-29.

Abarca S.F., K. L. Corbosiero and D. Vollaro (2011), The World Wide Lightning Location Network and Convective Activity in Tropical Cyclones. *Mon. Wea. Rev*., 139, 175-191.

Leary L.A., Ritchie E.A. (2009), Lightning Flash Rates as an Indicator of Tropical Cyclone Genesis in the Eastern North Pacific. *Mon. Wea. Rev.*, 137, 3456-3470.

Squires K., S. Businger (2008), The Morphology of Eyewall Lightning Outbreaks in Two Category 5 Hurricanes. *Mon. Wea. Rev*., 136, 1706-1726.

Virts K.S., J. M. Wallace, M. L. Hutchins, and R. H. Holzworth (2013), Highlights of a New Ground -Based, Hourly Global Lightning Climatology, *Bulletin American Meteorological Society,* D-12-00082, 1381-1391.

THE TENDENCY OF CLIMATE CHANGE OVER THE PAST SEVERAL MILLIONS OF YEARS AND THE CURRENT INTERGLACIAL DURATION

V.A. Dergachev

Ioffe Physical-Technical Institute, St. Petersburg, 194021, Russia, e-mail: v.dergachev@mail.ioffe.ru

Abstract. The Earth's climate, from regional to global, varies on all time scales. Large-scale climate variations in the past can be related to changes in geological processes (plate tectonic) and orbital cycles upon the Earth's climate. Astronomical theories of paleoclimate attribute climate cycles to changes in the Earth's orbital parameters: eccentricity (~100 kyr), obliquity (~41 kyr), precession (~22 kyr). It has been established from the paleoclimate and paleo-oceanographic data that during last more than 50 millions of years planetary temperatures were several degrees warmer than today, but there has been a progressive decrease in the average surface temperature on this time interval. Substantial glacial and interglacial temperature fluctuations are imposed on this decrease since about 2.8 million years ago. The last interglacial peak (at ~130 kyr ago) was a period with significantly higher temperatures in many parts of the Northern Hemisphere compared to the currant interglacial period, which started ~ 11,000 years ago. A detailed analysis of the recent oscillations in temperature shows a clear 100,000 year correlation with the interglacial periods coinciding with the maxima of the elipticity of the Earth's orbit. To understand better our current interglacial period (the Holocene, MIS-1 [Marine Isotope Stage]) and its future, it is necessary to investigate the response of the climate system to the peaks of interglacials in the past. Start of the last interglacial period occured at ~130 kyr ago (MIS-5). Similar to the Holocene, the latitudinal and seasonal distributions of the incoming solar radiation show two interglacials: MIS 11 (start - 427 kyr ago) and MIS 19 (start - 790 kyr ago). However, it is difficult to find in the available climate data a complete analogue to the current interglacial climate. The available data on climatic changes and the cyclic influence of solar radiation on the climate change are analyzed and the problem of current interglacial duration is discussed.

Introduction

The climate of the distant past (the first billion years of the Earth existence), where geological records are almost non-existent or sparse, is very poorly understood. During the evolution of our planet its climate was characterized by a large variety of climate stages. There were periods of increased variability or regular oscillations or almost quiet phases. Over the entire time coverage of the Earth's history the main external and internal natural mechanisms of climate variability are related to changes in plate tectonics, orbital changes with different periodicities, the sun's output on different time scales, and volcanism. Natural climate variability in the past was the *rule* and not the exception and the evolution of life on Earth was closely linked to climate and its change. The usual definition of climate is that it includes the slowly varying aspects of the atmosphere–hydrosphere–surface system. Let's look at the climate change over longer (millions and thousands of years) time scales.

It has been established from the paleoclimate and paleo-oceanographic data (Zachos et al., 2001) that during the past 100 million of years in the Cretaceous epoch, which ended 65 Myr BP (Figure 1), surface air temperatures were higher than they are at present. Since about 65 million years ago, Earth's climate has undergone a significant cooling and complex evolution. About 55 million years ago, at the end of the Paleocene, there was a sudden warming event in which temperatures rose by about 6ºC globally and by 10-20ºC at the poles (Zachos et al., 2008). Hansen et al. (2011) showed that the deep-sea temperature is closely related to the global average temperature and they roughly estimated that the change in global average temperature was perhaps ~ 12 ^{o}C over the past 50 million years. The Earth's climate has cooled over the last 5 million years. Today, mankind is living in an interglacial period that began about 11 ky ago. In the light of discussion about global warming observed in recent decades, which advocates an anthropogenic impact associated with the emission of greenhouse gases due to combustion of fossil fuel, the question concerning the duration of the current interglacial arises. The available data on climate change and solar radiation on a time scale of the last millions of years are critically analyzed and the problem of the length of the current interglacial is discussed.

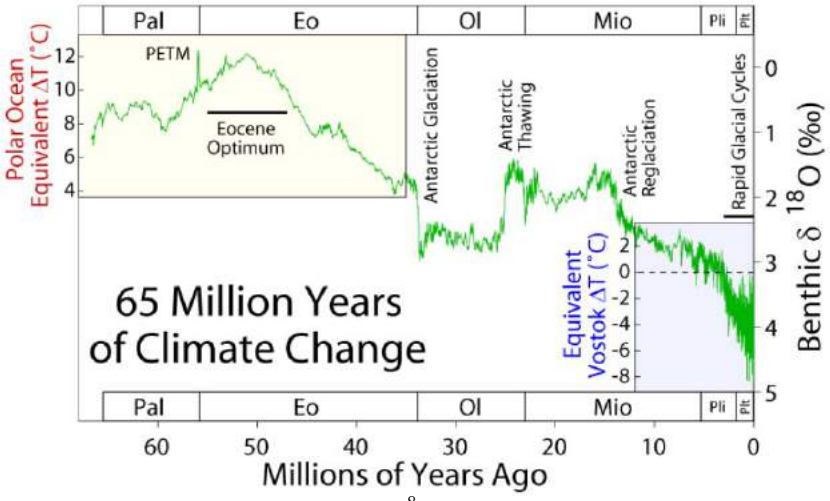

Figure 1. Climate during the Cenozoic Era (~10^8 years). Oxygen isotope measurements of benthic foraminifers (Zachos et al., 2001).

Climate changes over the past and orbital cycles

One of the highest resolution records of global proxy temperature data over the last 5.3 million years was published by Lisiecki and Raymo [2005] (Figure 2a). This set consists of a stack of 57 globally distributed benthic $\delta^{18}O$ records. The data are based on samples of deep sea sediments consisting of calcium carbonate from plankton. As one can see from Figure 2, the Earth's climate has cooled down over the last 5 million years. The data provide overwhelming evidence for a major cooling trend. The cooling culminated in the Pleistocene glaciation, which began about 2.5 Myr ago. As a result, the Earth's climate has been marked by temperature swings between extended glacial periods, leading to a series of major glaciations over the last 900,000 years, which were characterized by thick ice sheets covering large parts of North America, Northern Europe and Siberia, and interglacial times characterized by the ice coverage only in Antarctica and sometimes Greenland, as at the present time.

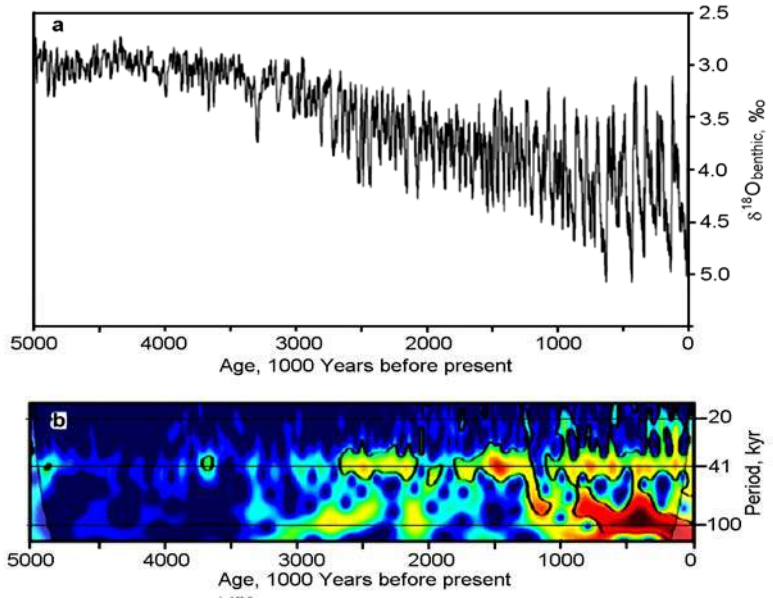

Figure 2. a - $\delta^{18}O$ benthic stack over the past 5 Myr [Lisiecki and Raymo, 2005]. **b** - Local wavelet power spectra of $\delta^{18}O$ data derived using a modified version of the WTC-16 code [Grinsted et al., 2004]. Shaded areas show the cone-of-interference, within which edge effects become significant. The data were smoothed to 5 kyr resolution before wavelet decomposition [Russon et al., 2011], which limits the capacity of the method to resolved periodicities <20 kyr.

The causes of glacial–interglacial climate changes can be linked to solar activity or to processes occurring on earth. Since major climate changes have a cyclic character, the astronomical theory, proposed by

Milankovitch [1948], relates glacial–interglacial changes to changes in the Earth's orbit and its rotation axis in time. Theory suggests that a primary driver of ice ages is the total summer radiation received in northern latitude zones where major ice sheets have being formed in the past, near 65 degrees of Northern latitudes.

A spectral analysis (Figure 2b) of the data supports this relationship up to a certain degree. These climatic data clearly show a certain kind of periodic variability. The main orbital periodicities are the precession (~20 kyr), eccentricity (~100 kyr and ~400 kyr) and obliquity (~40 kyr) cycles (Laskar et al., 2004). The combined effect of these orbital cycles causes long term changes in the amount of sunlight hitting the Earth in different seasons, particularly at high latitudes. The data of $\delta^{18}O$ exhibit the cycles 20, 41 and 100 kyr (Figure 2b), which coincide with the orbital periodicities mentioned above. Climate variability during the last three million years, on the basis of Lisiecki and Raymo data, was investigated by Dergachev and Dmitriev (2014) to reveal the hidden periodicities. The authors have found in this sample five periodicities of about 19, 22.4, 23.7, 41 and 98 kyrs which are similar to the Earth' orbital cycles. It is clear that the climatic system does not respond linearly to the insolation variations though astronomical frequencies corresponding to orbital cycles are found in almost all paleoclimatic records.

Ice cores from Greenland and Antarctica provide at present the most detailed information about climate change in the past. Figure 3 shows a comparison of changes in climate parameters in the ice core from the Antarctic Dome 2 station (concentration D) (Jouzel et al., 2007) and from ocean sediments (concentration ^{18}O) (Lisiecki and Raymo, 2005) during the last 800-900 kyr. It is seen that the curves reflecting alteration of warm and cold periods nicely match each other. Over the last 800 kyr, the orbital cycles were the dominant causes and pace-makers for climate variability. Global temperatures cooled at irregular rates during the extended glacial epochs and rose much faster at the beginning of the interglacials (MIS-1 – MIS-19). These interglacials recurred during the recorded period at intervals of roughly 100,000 years and had durations typically of about 12,000 years. Documenting natural interglacial climate variability in the past provides a deeper understanding of the physical climate responses to orbital forcing.

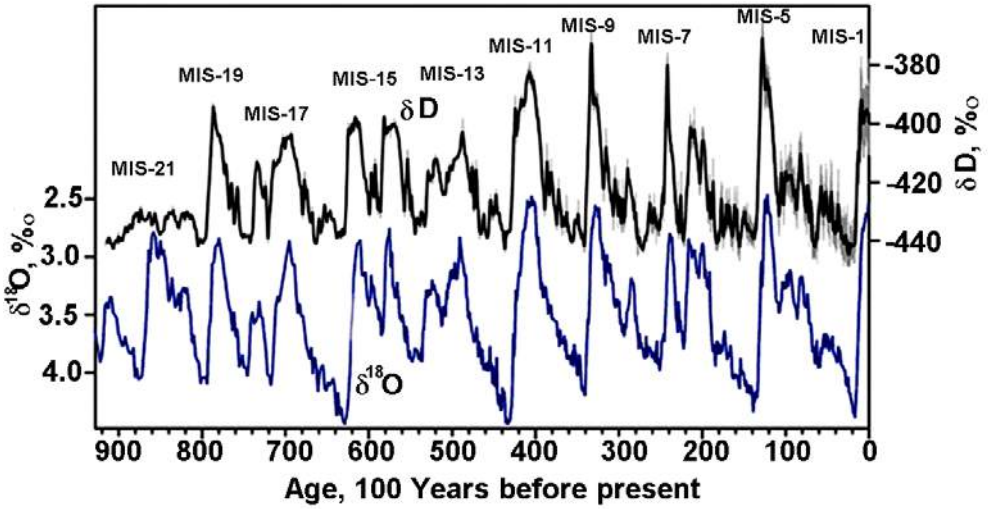

Figure 3. Comparison between climate changes reconstructed from Antarctic ice cores for various glacial–interglacial intervals (δD) (Jouzel et al., 2007) and $\delta^{18}O$ in ocean sediment cores (Lisiecki and Raymo, 2005) during the last 900 kyr. Interglacials are indicated MIS (Marine Isotope Stage). MIS-1 is the current interglacial.

Detailed records from ice cores show that three previous interglacials (Figure 3) differ from the fourth which, as well as Holocene, coincides with the period when orbital eccentricity approaches to the minimum of a 400-thousand-year orbital cycle. The duration of the interglacial which took place ~ 400 kyr ago, is estimated to be much longer, than of the subsequent interglacial. New data with the updated age models, have provided an expanded view on temperature patterns during interglacials since 800 kyr (e.g., Rohling et al., 2012). However, there is currently no consensus on whether the interglacial periods have changed their intensity after ~430 kyr.

Interglacials

Interglacials can be defined as time intervals, during which the global climate was incompatible with the wide extent of glacier conditions. In the context of future global warming induced by human activities, it is essential to assess the role of natural climatic variations. Precise knowledge of the duration of past interglacial periods is fundamental to the understanding of the potential future evolution of the Holocene. Past interglacials are characterized by different combinations of orbital forcing, atmospheric composition and climate responses. Palaeorecords from ice, land and oceans extend over the last 800 kyr, revealing eight glacial-interglacial cycles, with a range of insolation and greenhouse gas influences. To understand better our current interglacial (the Holocene, MIS-1 [Marine Isotope Stage]) and its future, it is necessary to investigate the response of the climate system to the peaks of interglacials in the past.

Yin and Beger (2010) used the Earth system model of intermediate complexity to assess the contributions of insolation and greenhouse-gas concentrations to the climate associated with the peaks of all the interglacials over the past 800,000 years. The effect of boreal winters and of the Southern Hemisphere, which is also warmer during austral winters, on the carbon cycle should be assessed when investigating the underlying causes of the higher CO_2 concentrations during the later interglacials. The interglacials are compared in terms of their forcings and responses of surface air temperature, vegetation and sea ice. The results show that the relative magnitude of the simulated interglacials is in reasonable agreement with proxy data.

The interglacials (Figure 4) display a correspondingly large variety of intensity and duration, thus providing an opportunity for major insights into the mechanisms involved in the behaviour of interglacial climates. A comparison of the duration of these interglacials, however, is often difficult, as the definition of the interglacial depends on the archive that is considered. Therefore, to compare interglacial length and climate conditions from different archives, a consistent definition of the interglacial conditions is required. The phasing and strengths of the precessional parameter and obliquity varied over past interglacials, influencing their timing, duration, and intensity (Tzedakis et al., 2012; Yin and Berger, 2012).

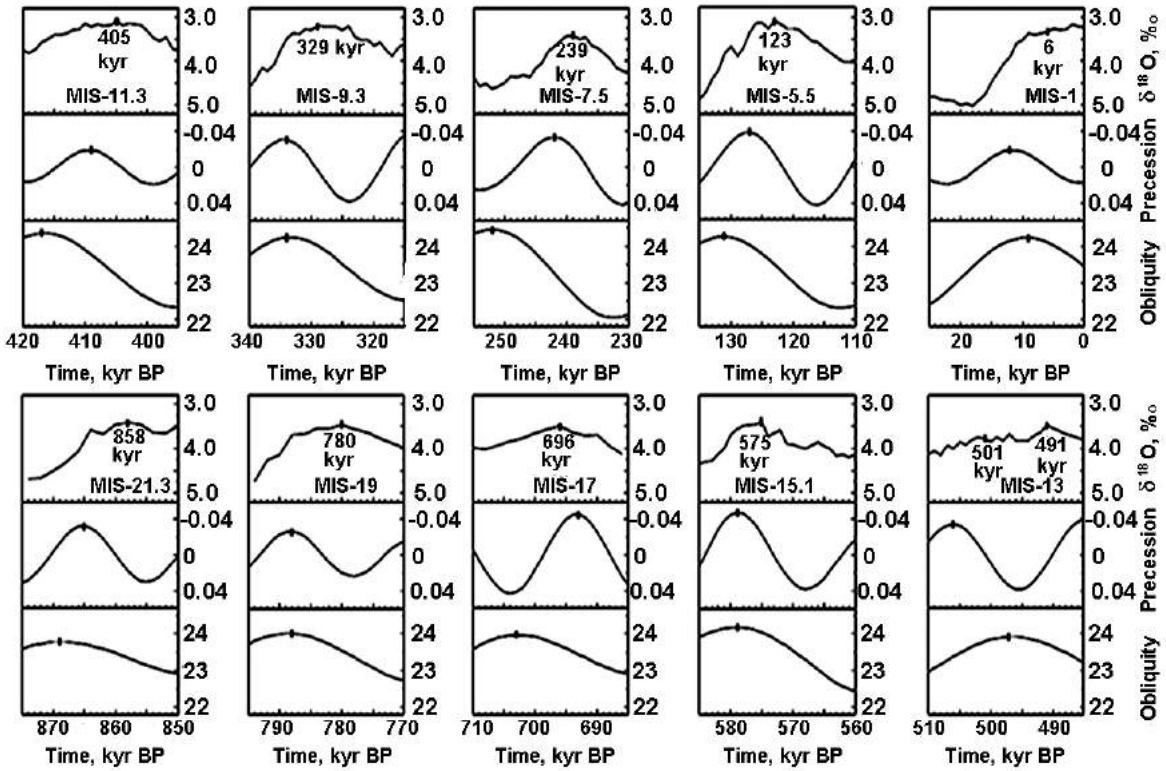

Figure 4. Marine $\delta^{18}O$ (Lisiecki and Raymo, 2005), precession and obliquity around the past 10 interglacial peaks ((Laskar et al., 2004)). The black bars localize $\delta^{18}O$ minima, precession minima and obliquity maxima. The dates of $\delta^{18}O$ minima and corresponding MISs (Tzedakis et al., 2012) are indicated.

Lang, and Wolff (2011) have compiled the data from 37 glacial, terrestrial and marine archives to obtain a data set covering 800 000 years and allowing to study the features of glacial and interglacial periods. The comparison of interglacials concentrates on the peaks immediately before and after the terminations; particularly strong and weak interglacials have been identified. This confirms the idea that strong interglacials are limited to the last 450 kyr, and that this is a globally robust pattern.

Orbital parameters as an analogue for the future current interglacial duration

In order to understand better our current interglacial and its future, it is necessary to investigate the response of the climate system to insolation at the peaks of the interglacials with similar latitudinal and seasonal distribution of the incoming solar radiation over the past 800,000 years, which can lead to the similar climate response to insolation in the Holocene. Figure 5 shows three astronomical analogs of our Holocene interglacial in the vicinity of MIS-1, MIS-11 and MIS-19 (red arrows). The previous (in respect to the current one) interglacial period is marked by the green curve.

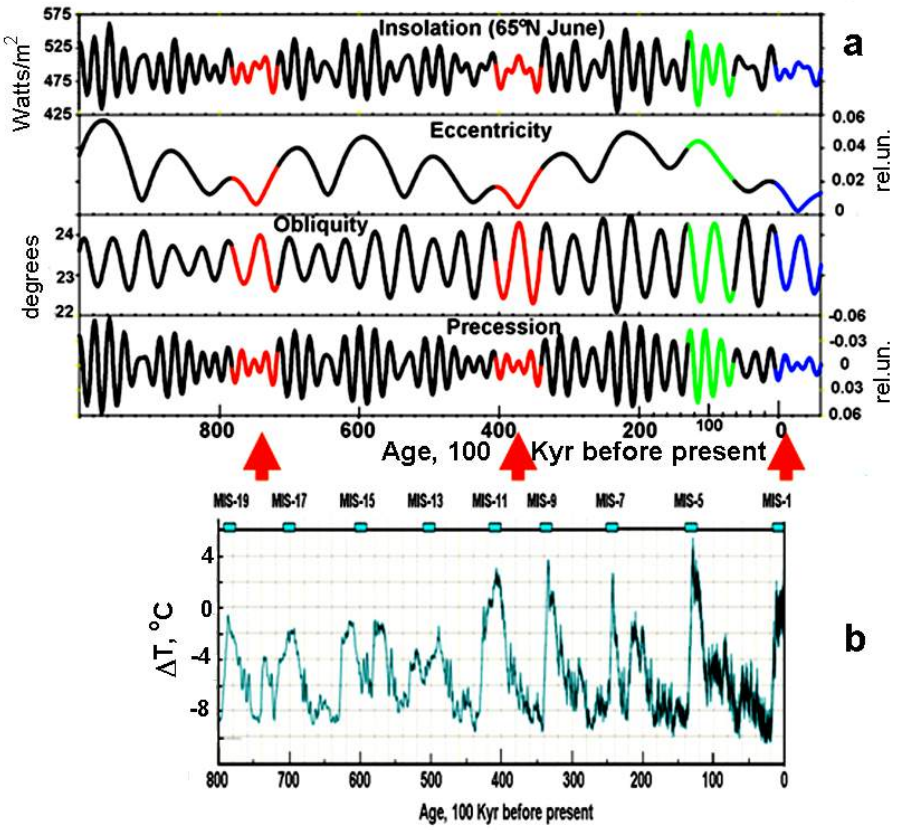

Figure 5. Comparison of the orbital parameters (a) and various interglacial intervals (b). The red arrows show the analogs of the future current duration (Yin and Berger, 2012) of the current interglacial (blue). The green curve shows the last interglacial.

Figure 6 compares similar latitudinal and seasonal distribution of the incoming solar radiation (precession and obliquity) and marine $\delta^{18}O$, around the past 3 interglacial peaks (MIS-1, MIS-11, MIS-19).

MIS-1, MIS-11 and MIS-19 show as well similar latitudinal and seasonal distributions of the incoming solar radiation, which lead to similar climate response to insolation, however, differences exist. Recent research has focused on MIS 11 as a possible analog for the current interglacial, but the estimated length of MIS-11 seems to vary from 20 to 33 kyrs. Besides of this, it has been shown that MIS-11 consists of at least two insolation peaks. At the same time, MIS19 exhibits a very similar insolation minimum in the Holocene as MIS11, but it lasts for only 10.5-12.5 kyr, similar to the current interglacial. Berger and Yin (2014) have shown that the equivalent of CO2 concentration is basically the same for MIS-1 and MIS-19 but larger for MIS-11. The evidences from MIS19 help to confine the debates about the real length of the current interglacial.

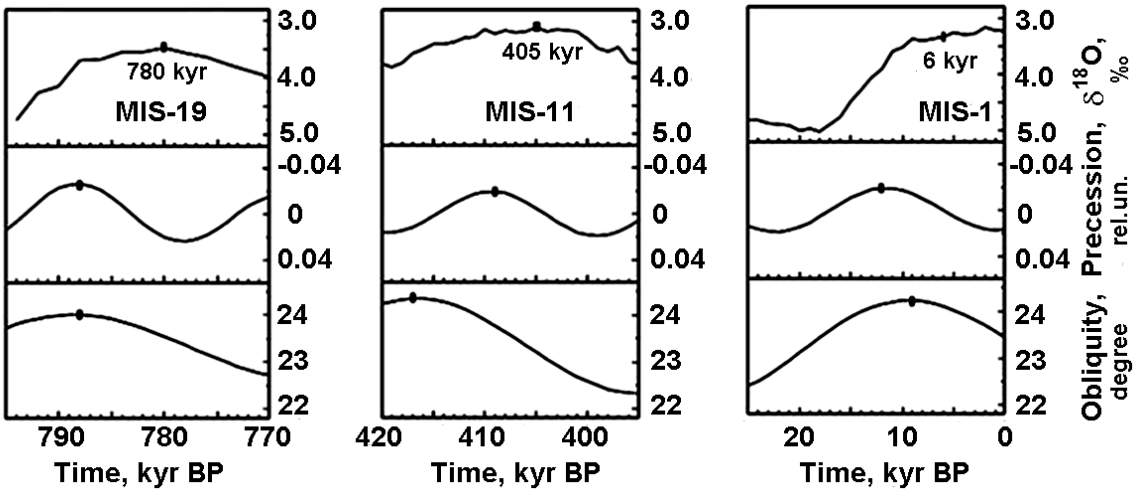

Figure 6. Marine $\delta^{18}O$, precession and obliquity around the past 3 interglacial peaks (MIS-1, MIS-11, MIS-19). The black bars localize $\delta^{18}O$ minima, precession minima and obliquity maxima (see Figure 4). The dates of $\delta^{18}O$ minima and corresponding MISs are indicated.

Conclusion

The most recent researches have focused on MIS 11 as a possible analog for the current interglacial. However, MIS 11 spans two precession cycles, when the Holocene contains one insolation peak so far. Besides, the warm period around 400 kyr ago remains a contradiction. MIS-19 appears to be the best analogue for MIS-1.

MIS19 represent a very similar insolation minimum to the Holocene and MIS11, but lasted for only 10.5-12.5 kyr. It is interesting that CO2 concentration at that time were approximately 240 ppm. Thus with respect to the Holocene, MIS19 may act as a good analogue for climatic change under "natural" conditions, i.e. CO_2 levels are not influenced by mankind. Assuming the Holocene followed the pattern seen during MIS19, we would have expected that the inception of the next glacial period will start soon, if it is not already underway.

References

Berger, A. and Q. Yin (2014), About past interglacials as analogues to the Holocene and Anthropocene. *Geophysical Research Abstracts* Vol. 16, EGU2014-3326, 2014.

Dergachev, V.A., P.B. Dmitriev (2014), The orbital cycles of climate variability during the last three million years. *XVIII Russian annual international conference "Solar and Sun-Earth physics-2014»* (20-24 October 2014, St. Petersburg, Pulkovo Observatory RAS).

Grinsted, A., J.C. Moore, and S. Jevrejeva (2004), Application of the cross wavelet transform and wavelet coherence to geophysical time series. *Nonlin. Processes Geophys*., 11, 561-566.

Jouzel, J., V. Masson-Delmotte, O. Cattani, et al. (2007), Orbital and millennial Antarctic climate variability over the past 800000 Years, *Science*, 2007, 317, 793–796.

Lang, N.and E. W. Wolff (2011), Interglacial and glacial variability from the last 800 ka in marine, ice and terrestrial archives. *Clim. Past*, 7, 361–380, doi:10.5194/cp-7-361-2011.

Laskar, J., P. Robutel, F. Joutel, M. Gastineau, A. C. M. Correia, and B. Levrard (2004), A long-term numerical solution for the insolation quantities of the Earth. *Astron. Astrophys.,* 428(1), 261–285, doi:10.1051/0004-6361:20041335.

Milankovitch, M. (1948), *Ausbau und gegenwartiger Stand der astronomischen Theorie der erdgeschichtlichen Klimate, Experientia*, 4(11), 413–418, doi:10.1007/BF02144986.

Rohling, E.J., A. Sluijs, H.A. Dijkstra, P. Köhler, R.S.W. van de Wal, et al. (2012), Making sense of palaeoclimate sensitivity. *Nature*, 491, 683-691, doi:10.1038/nature11574.

Russon, T., M. Elliot, A. Sadekov, G. Cabioch, T. Corrège and P. De Deckker (2011), The mid-Pleistocene transition in the subtropical southwest Pacific. *Paleoceanography*, 26 (1), March 2011.

Tzedakis P.C., J. E. T. Channell, D. A. Hodell, H. F. Kleiven and L. C. Skinner (2012), Determining the natural length of the current interglacial. *Nature Geoscience*: 8 January 2012, doi:10.1038/ngeo1358.

Yin, Q. Z. and A. Berger (2010), Insolation and CO_2 contribution to the interglacial climate before and after the Mid-Brunhes Event. Nature Geoscience, 3, 243-246, doi:10.1038/ngeo771.

Yin, Q. Z. and A. Berger (2012), Individual contribution of insolation and CO2 to the interglacial climates of the past 800,000 years. *Clim. Dynam.,* 38 (3-4), 709-724.

Zachos, J., M. Pagani, L. Sloan, E. Thomas, and K. Billups (2001), Trends, rhythms, and aberrations in global climate 65 Ma to present. *Science,* 292, 686-693.

Zachos, J.C., G.R. Dickens, and R.E. Zeebe (2008), An early Cenozoic perspective on greenhouse warming and carbon-cycle dynamics. *Nature*, 451, 279-283.

STUDY OF SOLAR CYCLICITY STABILITY ON TIME SCALE OF HUNDREDS OF MILLIONS OF YEARS

V.A. Dergachev[1], O.M. Raspopov[2], M.I. Tyasto[2], P.B. Dmitriev[1], V.S. Ismagilov[2], E.E. Blagoveschenskaya[2]

[1]Ioffe Physical-Technical Institute, St. Petersburg, 194021, Russia,

[2]SPb IZMIRAN St.-Petersburg, Russia

e-mail: v.dergachev@mail.ioffe.ru

Abstract. Palaeoclimatic data with a high temporal resolution, i.e., fossil tree ring widths and varve thicknesses, have been analyzed for time scales of several hundreds of millions of years with the aim of revealing periodicities in climatic processes. The climatic periodicities thus found are compared with the solar and climatic periodicities observed at present. The periodicities revealed in the climatic parameters prove to be similar in many cases to the modern solar activity cyclicities. This can indicate that the solar activity effectively affects climate change.

Introduction

The climate change of the last decades stimulates the interest of researchers to studies of palaeoclimate. The palaeoclimatic information which can be obtained from the data on annual variations in ring widths of fossil trees or varve thicknesses is extremely important for the understanding of not only the climate in the past but also solar variability, which was confirmed by a number of researchers. It has been shown that the palaeoclimatic data exhibit in many cases the periodicities similar to the modern cyclicity of solar activity [**1-5**].

Our goal was to study periodicities in variations of the radial growth of fossil trees that grew ~100-150 million years ago. The fossil trees studied were found in the Antarctic in the region of the Antarctic Peninsula and Alexander Island near the western coast of the Antarctic. The time of growth of these trees is the middle Cretaceous and early Tertiary period [**6, 7**]. The Cretaceous period, according to **IUGS (2013**), is the interval from 146 million to 65 million years ago.

Climate change in the Antarctic 100 million years ago

The fossil trees and shrubs were found on Alexander Island in sediments of the middle Cretaceous period (Triton Point Formation, Fossil Bluff Group). Some trees were in the original growth position in which they were during the growth period [**6**].

Alexander Island lies at latitude ~ 70° S and longitude ~ 70° W near the western coast of the Antarctic peninsula. The climate of the middle Cretaceous period was much warmer than the modern climate [**6,7**]. For example, the mean annual temperature in the Albian age of the Cretaceous period (~100 million years ago) is estimated to be from 10 to 20 °C [**6]**. At that time the forests in the Antarctic grew under the conditions of global warming at palaeolatitudes 69-75°S [**6**]. The forests consisted of different vegetation types, such as conifers, ferns, angiosperms shrubs and herbs. The conditions under which trees can grow at polar latitudes include a photoperiodic ecotype, a higher rate of cambial activity during the summer season and the structure of the tree crown tailored to optimal "catching" of solar radiation when the Sun is low above the horizon. The fact that the fossil trees preserved a pronounced ring structure indicated that the climate was seasonal, rather wet and warm.

It should be noted that the conditions in polar regions play a key role in the global processes in the atmosphere and ocean, i.e., in the entire global climate system.

We studied variations in the ring widths of the samples of fossil trees collected from sediments in the region of peaks of the south-eastern part of Alexander Island and in the region of the Antarctic peninsula. To reveal periodicities in the ring width variations, we employed a modified method of spectral analysis which was earlier used to find hidden periodicities [**8, 9**]. A sample spectral density for the initial time series is calculated depending on the sampling period which is chosen from the conditions of the task of revealing a hidden periodicity in the initial data. It is assumed that the initial time series consists of a polyharmonic

series with a finite number of harmonics having different amplitudes and periods and "interferences" having random and determinated signals, but not having harmonics of the first polyharmonic part. The number of harmonics and their values are determined by using the so-called sampling period, the values of which are chosen from the range of possible values dictated by physical conditions of the event studied. Then the initial series are subjected to a preliminary high-frequency filtering with a specified frequency of the filter "cutoff" at a half of the signal power to which a "separation" period $T_{cut\text{-}off}$ in the time domain corresponds. The set of values of parameter $T_{cut\text{-}of}$ is chosen from physical conditions of the task under the assumption of possibility of existence of one or another periodicity in the initial data. The normalized spectral density for each series filtered with its own $T_{cut\text{-}off}$ and all the obtained estimates are superimposed on each other in one graph field, thus forming a combined spectral periodogram. The advantage of the modified spectral analysis method is that it allows one to study the stability of position of the period revealed in the periodogram by eliminating from the initial series the trend and more powerful long-period constituents which make a major contribution into the signal dispersion.

Let us first of all see what periods are revealed by the modified spectral analysis method in the data on variations in the ring widths of the trees from the Antarctic. To this end, we calculated the periodograms of variations in the radial growth of the fossil trees from the south-eastern part of Alexander Island: samples KG 4937.1 (Nunatack Titan, Bed 526, Log 8) and KG 4940.19 (Nunatack Titan) [**6**].

Fig. 1 shows variations in ring widths of fossil trees from Alexander Island: A) sample KG.4937.1 and B) sample KG.4940.19.

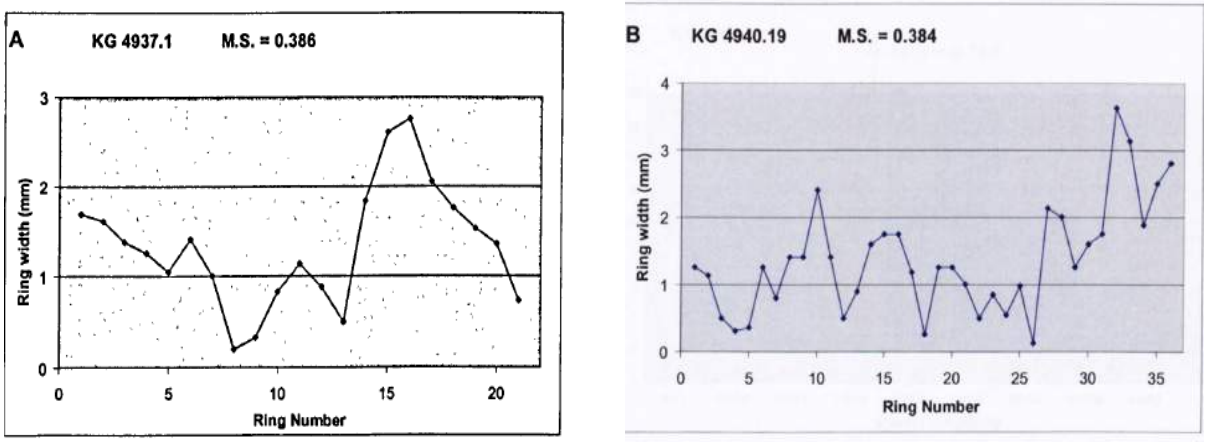

Figure 1. Variations in radial growth of fossil trees from the region of south-eastern peaks of Alexander Island: A) KG. 4937.1 (West Titan, Bed 526, Log 8), and B) KG. 4940.19 (West Titan).

The periodograms of variations in ring widths of fossil trees KG.4937.1 and KG 4940.19 are presented in Fig.2 and Fig.3.

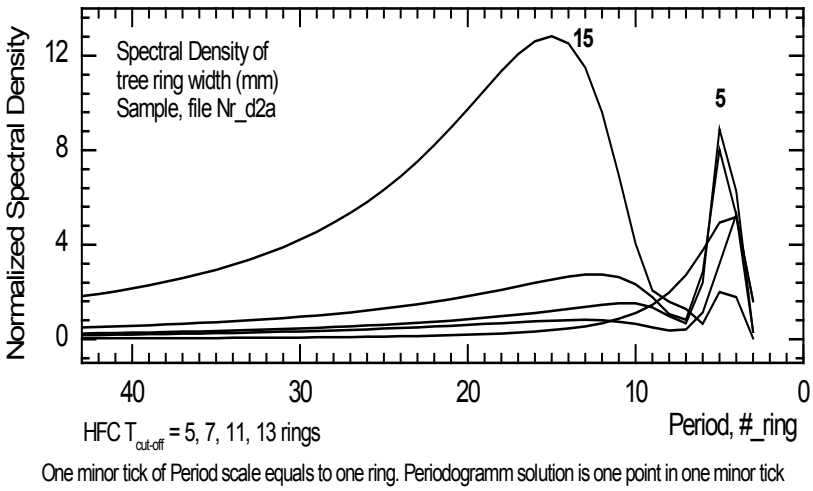

Figure 2. Periodogram of variations in ring widths of fossil tree KG.4937.1 (Alexander Island) obtained by the modified spectral analysis method used to reveal hidden periodicities, graphs for initial data and filtered components with $T_{cut\text{-}of}$ = 5,7, 11, 13 years are given.

As follows from the periodogram of Fig.2, the variations in ring widths of fossil tree KG 4937.1 are characterized by periods of ~15 and ~5 years, while the periodogram of Fig.3 shows that the variations in ring widths of fossil tree KG.4940.19 have pronounced periods close to 20 and 6 years. Thus, it can be concluded that the short-period changes in the ring widths of both samples are close.

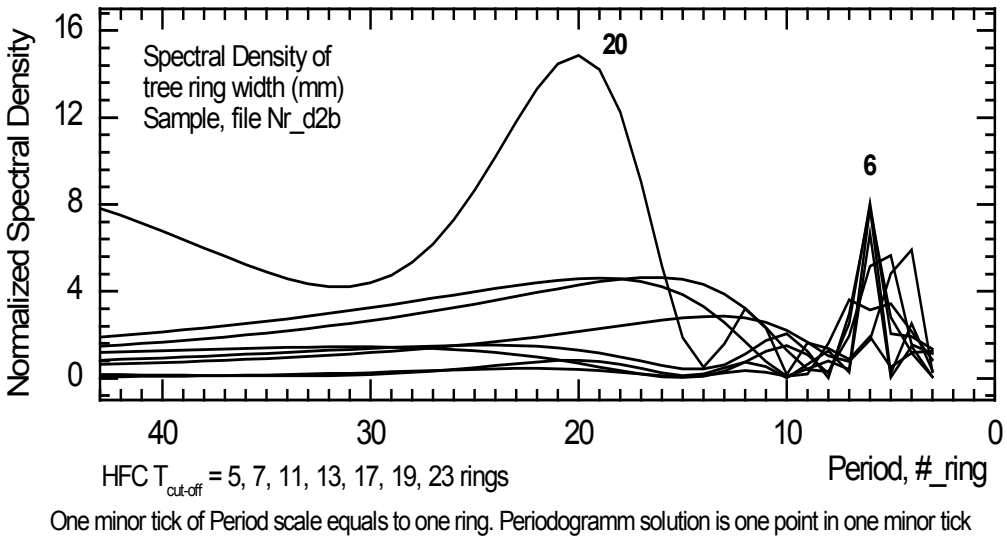

Figure 3. Periodogram of variations in annual growth of fossil tree KG.4940.19 (Alexander Island) obtained by the modified spectral analysis method. A graph for initial data and filtered curves with T_{cut-of} = 5, 7, 11, 13, 17, 19 and 23 years are given.

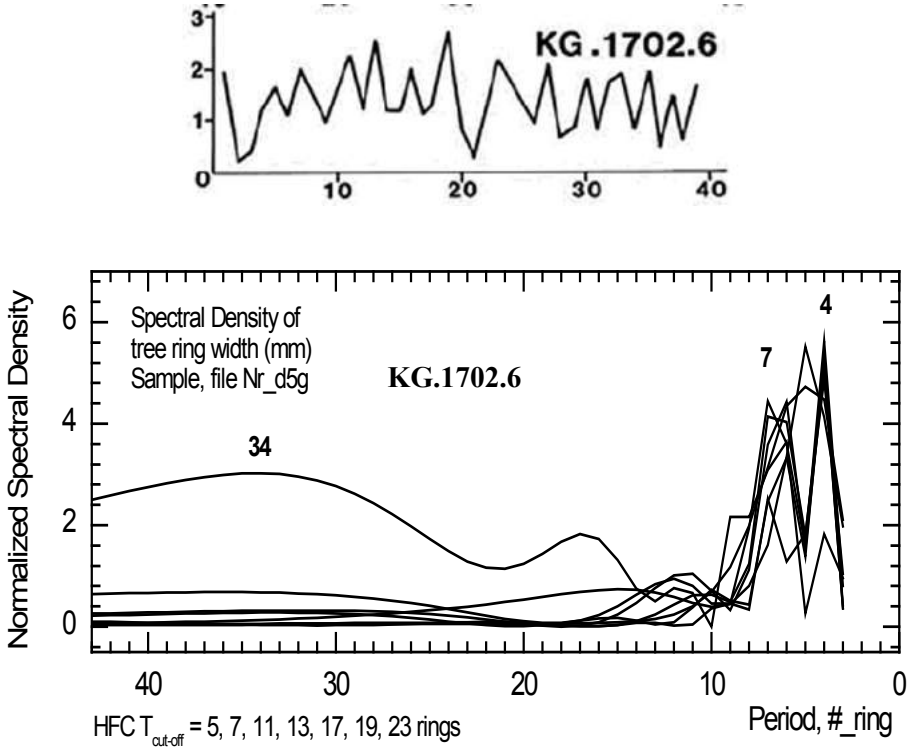

Figure 4. Variations in ring widths of fossil tree KG.1702.6 (upper) from the south-eastern part of Alexander Island (Hybperion Nunataks, Fossil Bluff Formation) and periodogram of these ring width variations and periodogram of the filtered curves with T_{cut-of} =5, 7, 11, 13, !7, 19 and 23 years.

Fig.4 presents initial variations in ring widths of fossil tree KG.1702.6 from the south-eastern part of Alexander Island (Hyperion Nunataks, Fossil Bluff Formation) and a periodogram of the initial series obtained by the modified spectral analysis method. The tree belongs to the early Cretaceous period [**7,1**0].
As one can see from the periodogram shown in Fig.4, the most pronounced periodicities are 4-7 years in the high-frequency part and ~ 34 years in the low-frequency one. In addition, the spectrum exhibits a periodicity of ~15 years.
In another part of the Antarctic, in the region of the Antarctic Peninsula, fossil trees of the Cretaceous and Early Tertiary period (~100 million years ago) were found [**7,10**]. Palaeoclimatologists revealed a well preserved structure of rings in the trees, which indicates that the climate had a seasonal character and was rather warm **[7].**
Fig.5 presents changes in the ring widths for two fossil trees from the region of the Antarctic Peninsula: 4774 (Lachman Cregs, James Ross Island) and D.20.16 (Mount Flora Formation, Hope Bay, Trinity Peninsula).

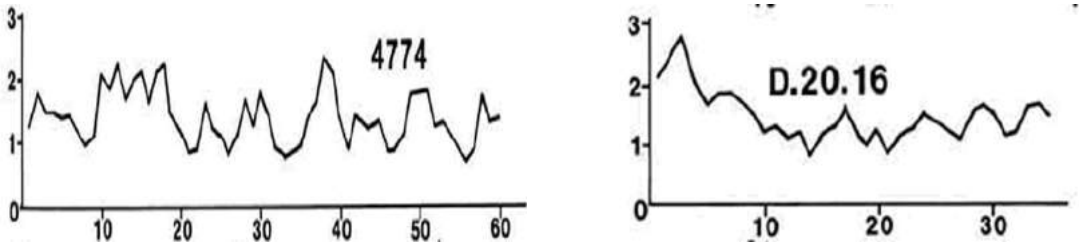

Figure 5. Variations in ring widths of fossil tree samples 4774 (Lachman Cregs, James Ross Island) and D.2016 (Mount Flora Formation, Hope Bay, Trinity Peninsula) from the region of the Antarctic Peninsula.

The periodograms of ring width variations of fossil tree samples 4774 and D.20.16 (Antarctic) are presented in Fig.6 and Fig.7.

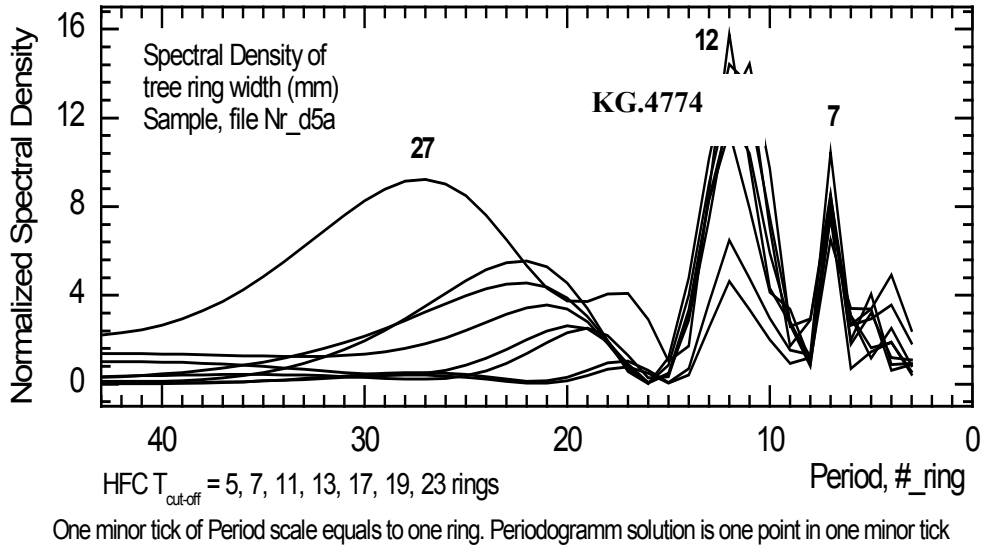

Figure 6. Periodogram of variations in ring widths of fossil tree 4774 (the Antarctic Peninsula) obtained by the modified spectral analysis method. Graphs are for initial data and filtered curves with $T_{cut\text{-}of}$ =5, 7, 11, 13, 17, 19 and 23 years.

The peaks of increased spectral density in Fig.6 (sample 4774) are at periods of 7, 12, ~21-22 and 27 years. Most pronounced pick is at the perid 12 years.
As one can see from the periodogram of Fig. 7 (sample D.20.16), the ring width variations exhibit periods of 8 and 36 years.

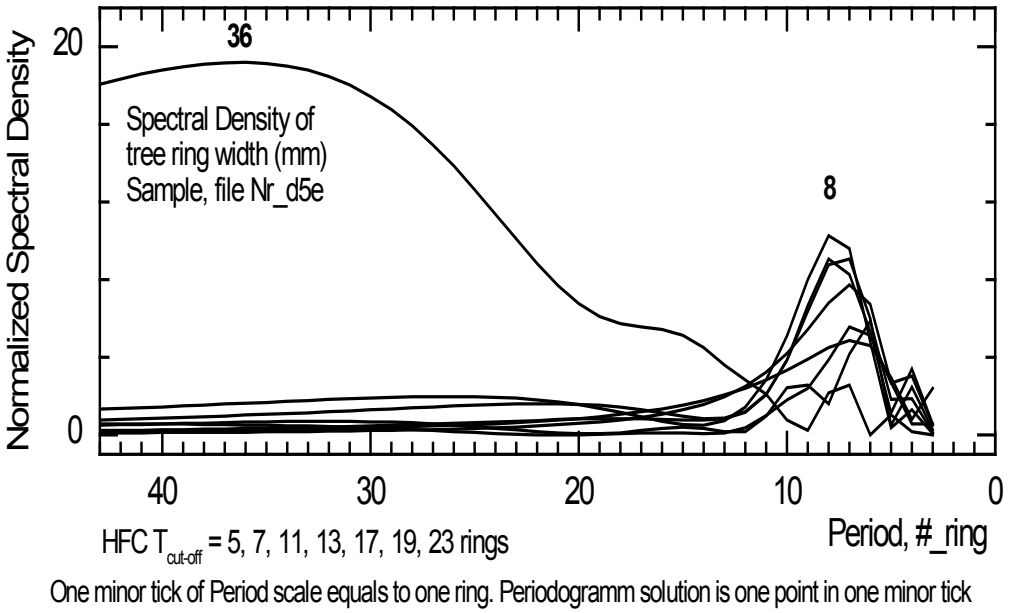

Figure 7. Periodogram of variations in ring widths of fossil tree D.20.16 (the Antarctic Peninsula) obtained by the modified spectral analysis method for initial data and filtered curves with $T_{cut\text{-}of}$ =5, 7, 11, 13, 17, 19 and 23 years.

Table summarizes the periodicities revealed in the ring width variations of the fossil trees from the Antarctic. In addition, Table presents results of spectral analysis of changes in varve thicknesses of Upper Jurassic Todilto limestone, New Mexico (samples 105 U and 101U) and Upper Devonian Ireton, Alberta, Canada 470U [**11**].

Table

Periodicities in variations of ring widths of fossil trees (Antarctic) and in variations of varve thicknesses (Ireton, Alberta, Canada, and Todilto, New Mexico [**11**]).

Sample	T4-6	T7-9	T10-12	T14-16	T17-18	T20-22	T25-27	T32-38	N
KG-4937,1 Ant	5			15					21
KG-4940.19 Ant	6					20			36
KG-1702, Ant	4	7		16				34	39
4774 Ant		7	12			22	27		60
D-2016 Ant		8						36	35
105U, Todilto	4	8		16		22			100
101U,Todilto	4	8		16		22		32	40
470U , Ireton		8		16		22		32	40

N – number of rings.

As one can see from Table, the periods of T~4-6 and T~7-9 years and T~30 years are observed in both the ring width variations of fossil trees and the power spectra of varve thickness of the Devonian and Upper Jurassic period. The periodicities of ~10-12 years and 20-22 years correspond with the 11-year solar cycle Schwabe cycle and 22-year Hale cycle. At present a spectral analysis of characteristics of annual flows of a number of rivers of the north-western region of Russia and solar activity revealed peaks at the frequencies corresponding to the periods of 10-12 and 30-31 years (Bruckner cycle), which points to the influence of solar activity on hydrologic processes [**12**]. The periodicity of 16-18 years and that close to 30 years are possibly due to the effect of cosmic ray fluxes on climatic processes: the spectral wavelet analysis revealed

periodicities of ~30 years and ~16 years from the data on ^{10}Be and ^{14}C for the Northern and Southern poles [**13**].

Conclusion

Analysis of the data on ring width variations in the fossil trees that grew in the Antarctic ~ 100 million years ago and the data on variations in varve thicknesses of Devonian Ireton, Alberta, Canada (~400 million years ago) and Jurassic Todilto limestone, New Mexico (~150 million years ago) has revealed the periodicities that are similar to basic modern solar activity cycles, i.e., Schwabe and Hale cycles (about 11 and 22 years), and Bruckner cycle (~30 years). This suggests that solar forcing of climate has a stable global nature.

The conclusion made in [**4**] that analysis of climatic periodicities in the time interval of 100-150 million years ago gives information on solar activity which cannot be obtained at present by other methods is confirmed.

References

1. Dergachev, V.A., Kartavykh, Yu.Yu., Ogurtsov M.G., and Raspopov O.M. (2007), Dendroindication of solar forcing of climate in last millenium. *Bull of Russian Academy of Sciences*, *Geography*, No 3, 107-114.
2. Dergachev, V.A. (2006), Solar forcing of climate. *Bull. of Russian Academy of Sciences. Physics*,70 (10), 1544-1548.
3. Raspopov, O.M., V.A. Dergachev, M.G. Ogurtsov, and O.V. Kozyreva (2010), Climate periodicities millions of years ago and its relation with solar activity, *http://geo.phys.spbu.ru/materials of a conference 2010/Raspopov et al 2010*
4. Raspopov, O.M., V.A. Dergachev, M.G. Ogurtsov, T. Kolstrom, H. Jungner, and P.B. Dmitriev (2011), Variations in climate parameters at time intervals from hundreds to tens of millions of years in the past and its relation to solar activity. *J. Atmosph. and Solar-Terrestrial Phys.,*2011, 73, 380-399.
5. Raspopov, O.M., V.A. Dergachev, and P.B. Dmitriev P.B. (2013), Manifestation of solar activity variations 70-45 million years ago. *Geophysical processes and biosphere*, 2013, 12, 3, 33-65.
6. Howe, J. (2003), Mid Cretaceous fossil forests of Alexander Island, Antarctica. *The University of Leeds. The School of Earth Sciences*. 2003.
7. Francis, J. E. (1986), Growth rings in Cretaceous and Tertiary wood from Antarctica and their Palaeclimatic Implications. *Paleontology*, 1986, 29 (5), 665-684.
8. Dmitriev, P.B., I.V. Kudryavtsev, V.P. Lazukov, G.A. Matveev, M.I. Savchenko, D.V. Skorodumov, and Yu.E. Charikov (2006), Solar flares registered by the ''IRIS'' spectrometer onboard the Coronas-F satellite: peculiarities of the X-ray emission. *Solar System Research* 40 (2), 142–152.
9. Raspopov, O.M., E.V. Lopatin, T. Kolstrom, V.A. Dergachev, P.B. Dmitriev, X.-P. Kale, and X. Spiecker (2013), Spatial structure of periodicity in radial growth of conifers at the territory of Komi Republic. *Geophysical processes and biosphere*, 12, 1, 44–61.
10. Jefferson, T. H. (1982), Fossil forests from the Lower Cretaceous of Alexander Island, Antarctica. *Palaeontology,* 25, 681-708.
11. Anderson, R.Y. (1961), Solar-terrestrial climatic Patterns in varved sediments, University of New Mexico, Albuquerque, N. Mex.
12. Zaretskaya, I. P., G.V. Lobasenko, and V.A. Roumyantsev (1992), Variability of the river flows in the solar activity cycles. *Biophysics,* 1992, 37, 3, 517-523.
13. Perez-Peraza, J., V. Velasco, I. Libin I. et al (2012), Thirty-Year Periodicity of Cosmic Rays. *Advances in Astronomy,* 2012 doi10.1155/2012/691408.

STUDY OF SUBSTORMS OCCURRENCES AT HIGH LATITUDES DEPENDING ON THE SOLAR WIND CONDITIONS

I.V. Despirak[1], A.A. Lubchich[1], N.G. Kleimenova[2]

[1]Polar Geophysical Institute RAS, Apatity, 184209, Russia, e-mail: despirak@gmail.com
[2]Schmidt Institute of the Earth Physics RAS, Moscow, Russia

Abstract. All substorm disturbances observed in polar latitudes can be divided into two types: polar, which are observed at geomagnetic latitudes higher than 70° in the absence of substorms below 70°, and high latitude substorms, which travel from auroral (<70°) to polar (>70°) geomagnetic latitudes. The aim of this study is to compare conditions in the IMF and solar wind, under which these two types of substorms are observed on the basis of data from meridional chain of magnetometers IMAGE and OMNI database for 1995, 2000, and 2006–2011. In total, 105 polar and 55 high latitude substorms were studied. It is shown that the main factor on which the difference between these two types of substorms is clearly expressed is the solar wind velocity. The polar substorms are observed at low velocity and high latitude ones - at the higher values of velocity. In addition, high-latitude substorms are observed under increased temperature and pressure of the solar wind; polar substorms are observed mainly under positive values of B_Y component of IMF. It is shown also that high latitude substorms are observed during high speed recurrent stream (HSS) in the solar wind. Polar substorms, in contrast, are observed at the end of HSS or after propagation of HSS, during the late recovery phase of a magnetic storm.

Introduction

It is well known that auroras and the westward electrojet move poleward during the expansion phase of a substorm [Akasofu, 1964; Kisabeth and Rostoker, 1974]. Substorm disturbances propagate sometimes to extremely high geomagnetic latitudes. Substorms observed at high geomagnetic latitudes can be divided into two different types: "polar" and "high latitude" substorms. In the first type, a disturbance starts at geomagnetic latitudes higher 71° and then propagates poleward; geomagnetic disturbances are absent at latitudes below 70°. These substorm disturbances were called "polar" substorms [Kleimenova et al., 2012]. Substorms of the second type starts at auroral latitudes, then propagate poleward, and the westward electrojet (or the westward electrojet center) moves to extremely high geomagnetic latitudes (>75°) in the substorm development maximum. These substorm disturbances were called "high latitude" substorms [Sergeev et al., 1979; Yahnin et al. 2004; Despirak et al., 2008].

Substorms of the first type, i.e., "polar" substorms, where all disturbances are concentrated in a narrow latitude region near the polar cap, usually occur under a low geomagnetic activity, when the auroral oval is contracted and poleward shifted [Feldstein and Starkov, 1967]. Such substorm disturbances are often called "substorms on the contracted oval." Studies have shown that "substorms on the contracted oval" do not differ from usually substorms in the parameters, both in the ionosphere and the magnetospheric tail, and usually occur when the B_Z IMF component is northward directed (B_Z>0) [Akasofu et al., 1971; Lui et al, 1976].

Substorms of the second type, i.e., "high latitude" substorms, start in the auroral zone and then propagate to high latitudes [Akasofu, 2004; Loomer and Gupta, 1980; Doolitle et al., 1998; Kuznetsov et al., 2001; Mende et al., 1999; Weatherwax et al., 1997; Gussenhoven 1982]]. No differences in parameters were revealed between "high latitude'and ordinary substorms; however, it was shown that the solar wind velocity is a determining factor for occurrence of "high latitude" substorms. "High latitude" substorms are mainly observed during the period of a solar activity minimum, where recurrent high speed streams from coronal holes prevail [Sergeev et al.,1979; Dmitrieva and Sergeev, 1984]. During a solar activity maximum, where streams related to coronal mass ejections (CMEs) prevail, "high latitude" substorms are observed seldom [Despirak et al., 2008, 2009]. "High latitude" substorms are also identified during compressed plasma propagation at fronts of solar wind streams, the so called Sheath and CIR regions [Despirak et al., 2011]. However, these substorms contribute a little in the observation statistics of substorms at high latitudes, since the duration of Sheath and CIR regions is small as compared to the duration of recurrent high speed solar wind streams.

The aim of this work is the comparison of the interplanetary conditions under which "polar" and "high latitude" substorms are observed.

Data

We used the magnetic data of the IMAGE meridional chain Nurmijarvi - Ny Alesund, from 57º to 75º of geomagnetic latitudes. To construct the latitudinal profile of the westward electrojet, we used the MIRACLE model of the corresponding electrojet currents development (http://www.space.fmi.fi/MIRACLE/). The solar wind and Interplanetary Magnetic Field parameters measured by Wind spacecraft were taken from OMNI database. The 1995 and 2006-2011 time intervals, close to the minimum of the solar activity, and 2000 year close to the solar activity maximum are used. There were selected and analyzed the 160 events of different types of substorms observed at high geomagnetic latitudes (105 cases of polar substorms and 55 cases of high-latitude substorms). Figure 1 shows the examples of the "polar" and high-latitude" substorms observed at the IMAGE magnetometer chain.

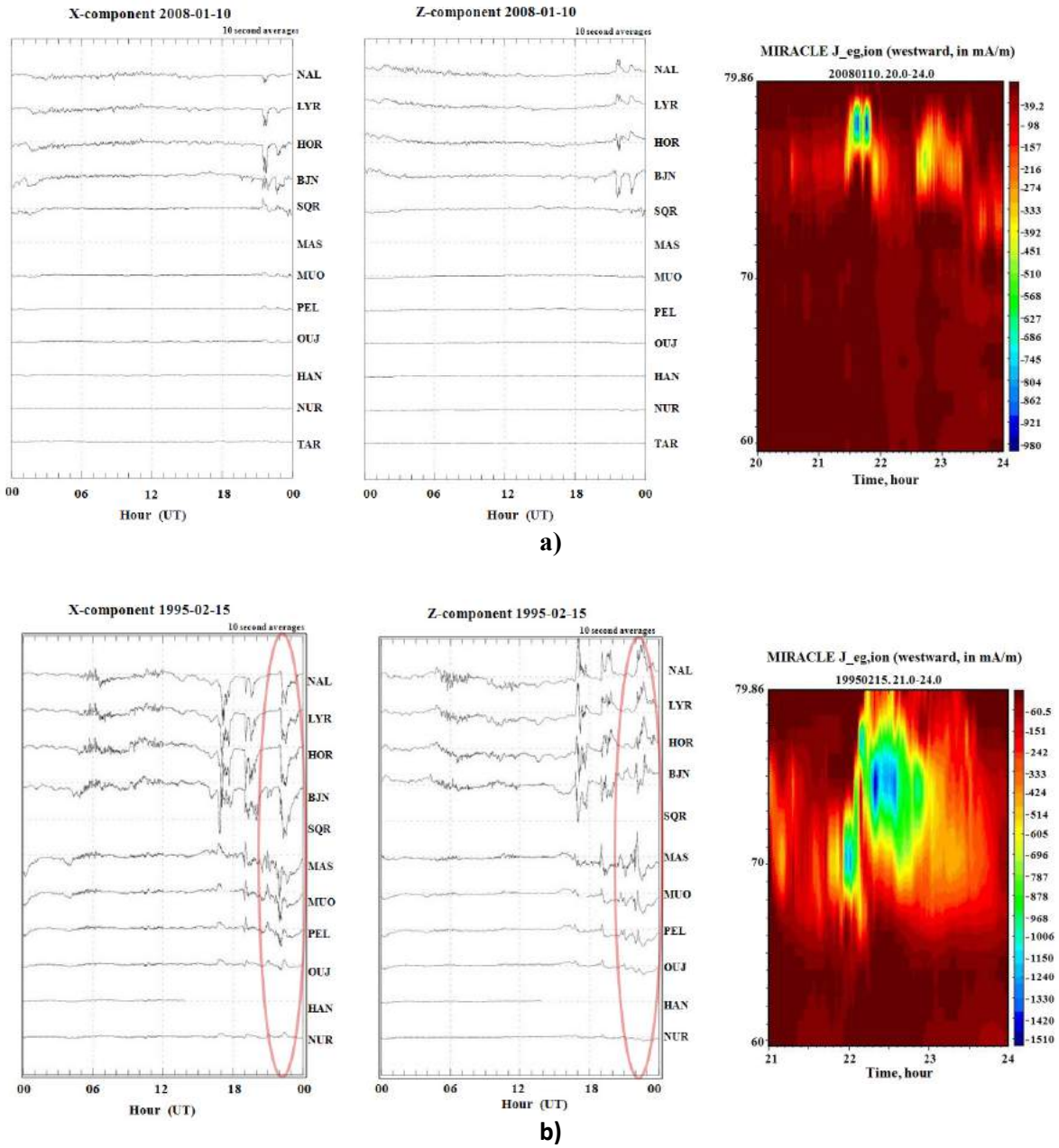

Fig.1. Examples of the "polar" and "high-latitude" substorms observed at the IMAGE magnetometers: magnetograms (X and Z components) of the IMAGE TAR–NAL station chain (left and middle panels); position of the westward electrojet in geographic coordinated according to the MIRACLE data (right panel).

The concept of the westward electrojet "center" (the region of the highest currents) is often used for latitudinal positioning of the westward electrojet, since it occupies a large spatial area during the substorm expansion phase and can be inhomogeneous [Pudovkin et al. 1995]. The method for electrojet "center"positioning is described in detail in [Despirak et al., 2008]. Let us note that we consider a "high-latitude" substorm if it starts at the auroral zone and the westward electrojet "center" is observed at LYR or NAL stations during the maximal substorm phase, i.e., at 75.12° (78.9°) or 75.25° (78.2°) geomagnetic (geographic) latitude.

Results

Both types of substorms -"polar" and "high-latitude"—were compared with the interplanetary conditions, i.e., the presence/absence of high speed solar wind streams, the presence of a geomagnetic storm, etc. The examples of considered events are presented in Figure 2.

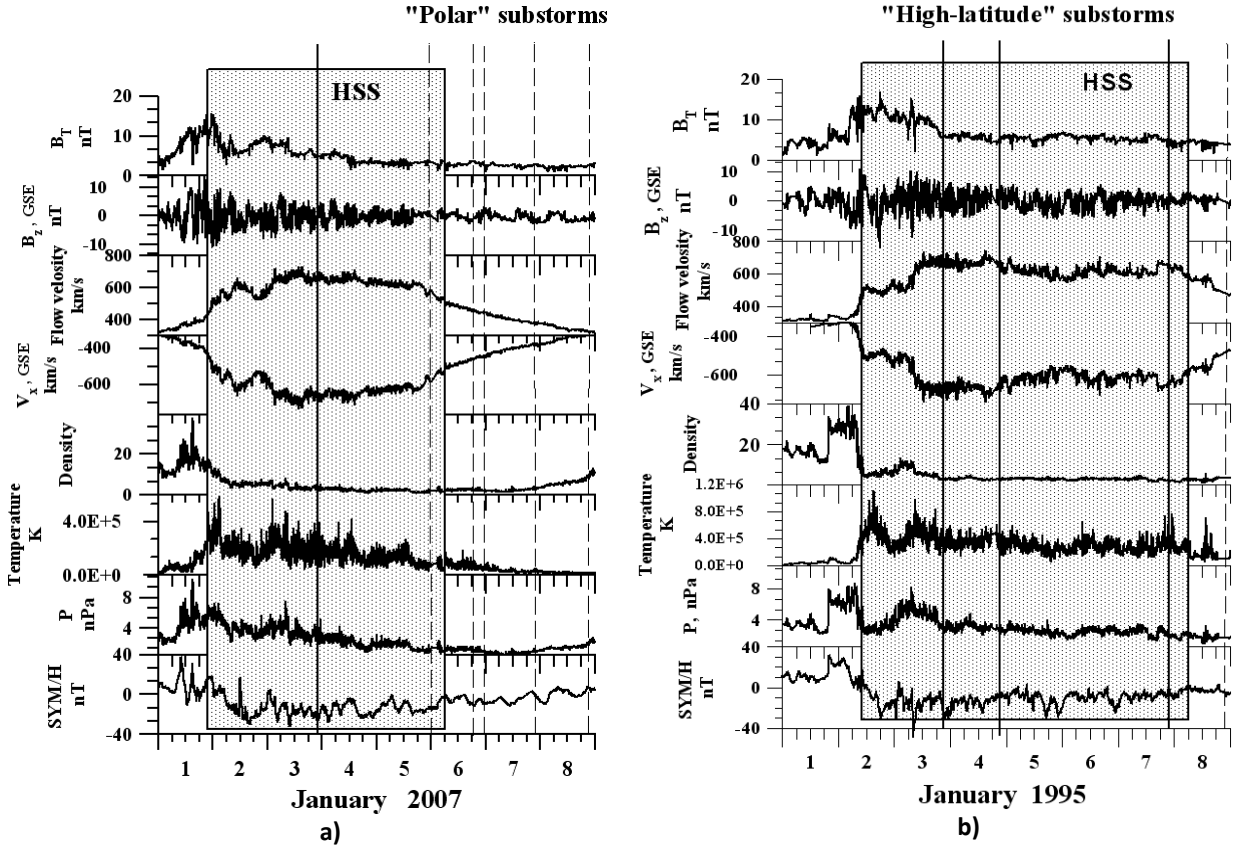

Fig. 2. Solar wind and IMF parameters (B_T, B_Z, V, V_X, N, T, P) and the SYMN/H index for two high speed streams on January 1–6, 2007 and January 2–8, 1995. Boundaries of the high speed stream (HSS) are shown by gray rectangles. The onset times of "polar" and "high-latitude" substorms according to the IMAGE data are marked by the vertical solid and dashed lines, respectively.

Figure 2 shows the solar wind and IMF parameters for two high speed streams, on January 1–6, 2007 and January 2–8, 1995. High speed streams are shown in the both cases by gray rectangles. The onset times of "high latitude" and "polar" substorms are superimposed on these data according to the IMAGE data; they are shown by the solid and dashed lines, respectively. Figure 2a presents the solar wind conditions during the observation of a "polar" substorm, and Fig. 2b shows them during the observation of "high-latitude" substorms. In the first case (January 1–6, 2007), "polar" substorms occurred on January 5, 6, 7, and 8, i.e., at the end of a high speed stream and after it, when the solar wind velocity decreased from the high values to low ones. The solid curve shows a "high-latitude" substorm that was observed on January 3, 2007. Figure 2b presents solar wind conditions during "high-latitude" substorms; they occurred on January 2, 3, and 7, i.e., during the high speed stream on January 2–8, 1995; after the stream passed, during the solar wind velocity drop, a "polar" substorm was observed. According to the SYMN\H index, no geomagnetic storm was observed during January 1–6, 2007. There was a geomagnetic storm January 2–8, 1995, and the"polar" substorm was observed during its recovery phase.

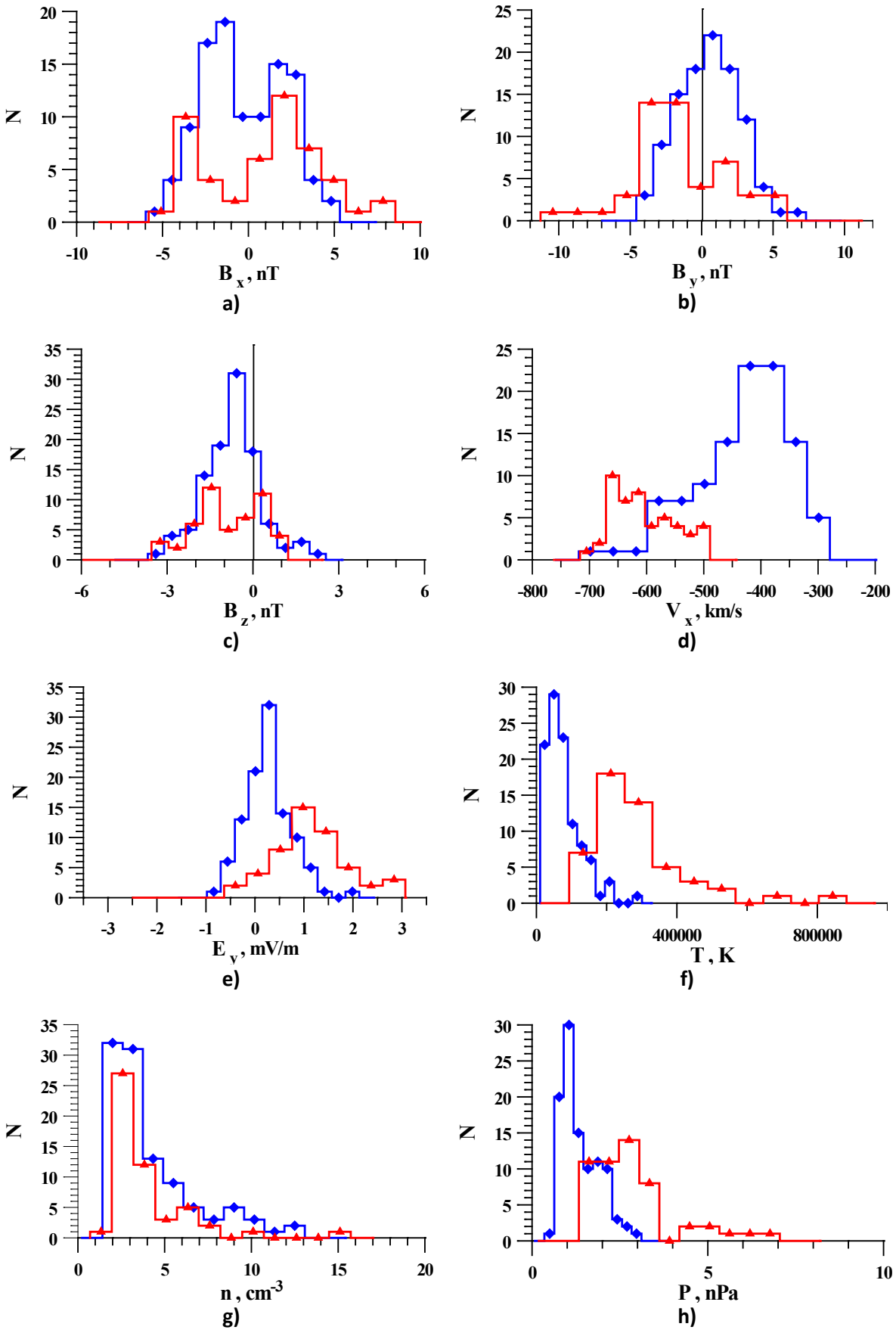

Fig. 3 Histograms of the solar wind and IMF parameters (B_X, B_Y, B_Z, V_X, E_Y, T, N, P) averaged over one and a half hours before the maximal phase of the "polar"(blue diamonds) and "high-latitude" (red triangles) substorms.

Figure 3 shows the histograms of the solar wind and IMF parameters (B_X, B_Y, B_Z, V_X, E_Y, T, N, P) observed before the onset of the "polar"and "high-latitude" substorms. It can be seen that the main factor on which the difference between these two types of substorms is clearly expressed is the solar wind velocity. The "polar" substorms are observed at low velocity (generally ~ 300-400 km/s) and "high-latitude" ones - at higher values of the solar wind velocity (larger than 500 km/s). It is seen also that "polar" substorms are observed mainly under positive values of B_Y component of IMF, while "high-latitude" ones – under negative values of B_Y component. It should be noted that there were no differences in the distributions of B_Z and B_X component of the magnetic field and solar wind density before observations of both types of substorms. In addition, the "high-latitude" substorms are observed under the higher values of the temperature and pressure of the solar wind than "polar" substorms.

The standard deviation was calculated for all considered solar wind parameters (V_X, B_Z, E_Y, T, P) before the onsets of these two substorm types. It is shown that disturbances (the standard deviations) of the parameters are higher before the occurrence of "high latitude" substorms than "polar" substorms. (The picture is not presented here).

Discussion

We have carried out a comparative analysis of the conditions for occurrence of substorms at high geomagnetic latitudes on the basis of IMAGE geomagnetic stations data. It should be noted that in this work we compare only two types of substorms at high latitudes - polar and high latitude ones. Comparison of these types with typical substorms was carried out earlier [e.g., Dmitrieva and Sergeev, 1984; Despirak et al., 2008; Kleimenova et al., 2012].

The following pattern can be imaged from the results of this and previous works. Polar substorms occur under positive and small negative values of the B_Z component of the IMF and a low solar wind velocity ($V < 500$ km/s). A high solar wind velocity ($V > 500$ km/s) and relatively small negative values of the B_Z component of IMF (approximately from 0 to –4 nT) are required for the occurrence of high latitude substorms [Despirak et al., 2008]. Note that a substorm remains in low latitudes and does not propagate poleward at a very high velocity but at large negative values of the B_Z component of IMF [Despirak et al., 2009, 2011].

We can suggest the following quite simplified scheme of substorm at high latitude appearance. The onset of a high latitude substorm, as classical substorms, is connected with dipolization (or current disruption) in the nearest magnetotail. Then under small negative values of IMF B_Z component and high values of solar wind velocity or dynamic pressure continued receipt of solar wind energy to the magnetosphere. This leads to movement of the substorm source region in the more distant (from the Earth) magnetotail. And so-called high-latitude substorm is observed. The situation is different in the case of polar substorms. They usually are observed mainly during the late recovery phase of a magnetic storm and at the ends of high speed solar wind streams, under small values of solar wind parameters. Accumulated by this time energy is small, and the current disruption (or dipolization) can develop only in the removed area in the magnetotail. That results in substorm emerging at very high latitudes.

Thus, the question about the geoefficiency of the solar wind velocity and substorm sources at high latitudes remains unsolved. It is not clear at what distances into the magnetospheric tail can be projected the positions of the sources of the substorms under study, or with which processes in the magnetospheric tail they are connected.

In this work, we also analyze the occurrence of polar and high latitude substorms depending on different solar wind streams. It is shown that high latitude substorms are observed during a recurrent high speed stream, while polar substorms are observed after the high-speed stream during the phase of solar wind velocity decrease. It should be noted that it is important to consider the interplanetary parameters that are characteristic for different solar wind streams and structures in combination but not the solar wind effect separately. Studies of the effect of different solar wind streams on the polar expansion of substorms have shown that high latitude substorms are observed during the passage of recurrent high-speed streams and stream fronts (CIR and Sheath regions of compressed plasma) [Despirak et al., 2011]. High latitude substorms are observed very seldom during the passage of solar wind magnetic clouds. This result explains the fact that high latitude substorms are very seldom observed during periods of solar activity maximum, where magnetic clouds prevail in the solar wind.

Thus, in our opinion, when studying the solar wind effect on the poleward expansion of a substorm, it is important to consider combinations of interplanetary parameters in different solar wind streams and structures, since the magnetosphere probably "remembers" which solar wind stream affected it.

Conclusion

Polar substorms, i.e. substorms recorded at latitudes > 70º, are observed after the passage of a high-speed recurrent stream of the solar wind (when the velocity is reduced from high to low values), on late recovery phase of a geomagnetic storm. High-latitude substorms, on the contrary, are observed during the passage of a recurrent high-speed stream of the solar wind.

The main factor on which the difference between these two types of substorms is clearly expressed is the solar wind velocity. The polar substorms are observed at low velocity and high latitude ones – at higher values of the solar wind velocity. In addition, high-latitude substorms observed under increased temperature and pressure of the solar wind. Polar substorms are observed mainly under positive values of B_Y component of IMF, while high-latitude ones – under negative values of B_Y component.

The variability of solar wind parameters for the high-latitude substorms is stronger than for polar substorms.

Acknowledgment. This study was supported by RFBR grants N 13-05-00233 and N 12-05-01030 and by Program No 22 of the Presidium of the RAS "Fundamental problems of the Study and Exploration of the Solar system". The study is part of a joint Russian - Bulgarian Project 1.2.10 of PGI RAS and IKIT-BAS under the Fundamental Space Research Program between RAS and BAS.

References

Akasofu, S.I. (1964), The development of the auroral substorm. *Planet.Space Sci*., 12, 273–282.

Akasofu, S.-l., C.R. Wilson, A.L. Snyder, P.D. Perreault (1971), Results from a meridian chain of observations in the Alaskan sector, 1. *Planet. Space Sci*., 19, 477-482.

Akasofu, S.I. (2004), Several "controversial" issues on substorms. *Space Sci. Rev.*, 113, 1– 40.

Despirak, I.V., A.A. Lyubchich, Kh.K. Birnat, A.G. Yakhnin (2008), Poleward expansion of the westward electrojet depending on the solar wind and IMF parameters. *Geomagn. Aeron.*, 48, no. 3, 284-292.

Despirak, I.V., A.A. Lubchich, A.G. Yahnin, B.V. Kozelov, H.K. Biernat (2009), Development of substorm bulges during different solar wind structures. *Ann. Geophys*., 27, 1951–1960.

Despirak, I.V., A.A. Lubchich, V. Guineva (2011), Development of substorm bulges during storms of different interplanetary origins. *J. Atmos. Sol.-Terr. Phys*., 73, 1460–1464.

Dmitrieva, N.P., and V.A. Sergeev (1984), Occurrence of an auroral electrojet at polar cap latitudes: Characteristics of the phenomenon and possibilities of its use for diagnostics of large-scale high speed solar wind streams. *Magnitos. Issled.*, 3, 58–66.

Doolittle J.H., S.B. Mende, H.U. Frey, T.J. Rosenberg, A.T. Weatherwax, L.J. Lanzerotti, C.G. Maclennan, R.L. Arnoldy, M.J. Engebretson, H. Fukunishi, U.S. Inan (1998), Substorm auroral expansion to high latitudes and the dawn/dusk flanks, *in: Proc. 4th Int. Conf. on Substorms, (Japan, March 9–13, 1998),* Japan, 47–50.

Feldstein, Y.L., and G.V. Starkov (1967), Dynamics of auroral belt and geomagnetic disturbances. *Planet. Space Sci*., 15, 209-229.

Gussenhoven, M.S. (1982), Extremely high latitude auroras. *J. Geophys. Res*., 87, 2401–2412.

Kisabeth, J.L., and G. Rostoker (1974), The expansive phase of magnetospheric substorms. Development of the auroral electrojets and auroral arcs configuration during substorm. *J. Geophys. Res.*, 79, 972 –984.

Kuznetsov, S., L.L. Lazutin, T. Rosenberg, L. Borovkov, Yu. Gotselyuk, A. Weatherwax (2001), Energetic electron and ion dynamics and polar aurora during magnetospheric substorm of March 10, 1994, *in: Proc. 5th Int. Conf. on Substorms, (St. Petersburg, Russia, May 16–20, 2000),* Russia, 511–514.

Loomer, E.I., and J.C., Gupta (1980), Some characteristics of high latitude substorms. *J. Atmos. Terr. Phys*., 42, 645 - 652.

Lui, A. T. Y., S.-I. Akasofu, E.W., JR., Hones, S.J. Bame, C.E. McIwan (1976), Observation of the plasma sheet during a contracted oval substorm in a prolonged quiet period. *J. Geophys. Res*., 81, 1415-1419.

Mende, S.B., H.U. Frey, S.P. Geller, J.H. Doolittle (1999), Multistation observations of auroras: Polar cap substorms. *J. Geophys. Res.* 104, 2333–2342.

Pudovkin, M.I., V.S. Semenov, A.L. Kotikov, E.M. Shishkina (1995), Dynamics of auroral electrojets and energetics of substorm. *J. Atmos. Terr. Phys.,* 57, 187–192.

Sergeev, V.A., A.G. Yakhnin, N.P. Dmitrieva (1979), Substorms in the polar cap - effect of high_speed solar wind streams. *Geomagn. Aeron.*, 19, 1121–1122.

Weatherwax, A.T., T.J. Rosenberg, C.G. Maclennan, J.H. Doolittle (1997), Substorm precipitation in the polar cap and associated Pc5 modulation. *Geophys.Res.Lett.*, 24, 579–582.

Yahnin, A.G., I.V. Despirak, A.A. Lubchich, B.V. Kozelov (2004), Solar wind control of the auroral bulge expansion, *in: Proceedings of the 7th International Conference on Substorms*, Helsinki, 31–33.

MAGNETOTAIL SUBSTORMS OBSERVATIONS DURING SOLAR WIND MAGNETIC CLOUDS AND HIGH SPEED STREAMS

I.V. Despirak[1], A.A. Lubchich[1], R. Koleva[2]

[1] Polar Geophysical Institute, RAS, Apatity, Murmansk region, 184200, Russia, e-mail: despirak@gmail.com;
[2] Space Research & Technologies Institute, BAS, Sofia, Bulgaria

Abstract. In this work we discuss the problem of the magnetic reconnection site location in the magnetotail during substorms associated with different solar wind streams. It was shown recently that solar cycle variations of the solar wind control the location of magnetic reconnection in the tail. A well-known fact is that solar wind high-speed streams have different nature during different phases of solar activity. During the declining phase and minima of the solar cycle predominate the high speed recurrent streams (HSS) originating from coronal magnetic holes. During solar cycle maxima the flare streams connected with coronal mass ejections prevail. We analyze the relationship between the locations of the tail magnetic reconnection site during substorms connected with solar wind magnetic clouds (MC) and recurrent streams. We use data from Geotail spacecraft in the magnetotail and solar wind parameters from Wind spacecraft observations; the auroral bulge parameters were obtained by the Ultra Violet Imager onboard Polar. We show that magnetic reconnection in the magnetotail takes place closer to Earth when substorm is observed during MC, and further in radial distance for substorms during solar wind high speed recurrent streams.

Introduction

Recently the authors in [Nagai et al., 2005] showed that the location of the reconnection site in the magnetotail depends on the phase of the solar activity cycle. They found out that during solar cycle maximum magnetic reconnection is observed nearer to Earth than during the minimum of solar activity.

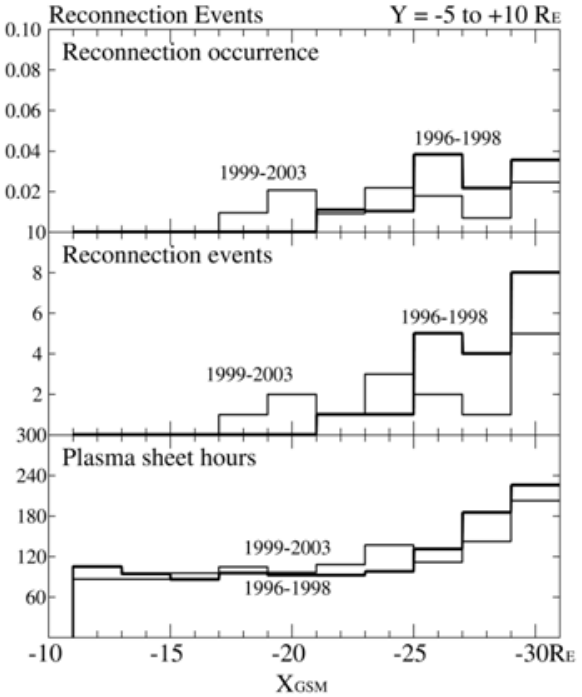

Fig.1 The occurrence of reconnection events as a function of X_{GSM} for the two periods. Thick lines present values for solar minimum (1996- 1998), thin lines present values for solar maximum (1999-2003). (Figure taken from [Nagai et al., 2005]).

Figure 1 shows the occurrence of reconnection events as a function of X_{GSM} for the two periods [Nagai et al., 2005]). There are 19 solar minimum events (1996–1998) and 15 solar maximum events (1999–2003). In the solar minimum (1996–1998), reconnection events are observed only beyond 21 R_E, and occurrence is high beyond 25 R_E. In the solar maximum (1999–2003), reconnection events can be found inside 21 R_E, and occurrence is relatively constant at X_{GSM} = 17 to 31 R_E.

It is well known that solar wind is not a uniform flow; various large-scale structures and streams exist within it [e.g. Pudovkin, 1996; Yermolaev et al., 2009]. Besides during different solar activity phases prevail different solar wind flows [Krieger et al., 1973; Burlaga et al., 1982; Richardson et al., 2001]. During the declining phase and at the minimum of solar activity high speed recurrent solar wind streams (HSS) originating in coronal holes prevail while in solar activity maximum prevail flows from coronal mass ejecta which are observed as magnetic clouds (MC) near Earth. In this work we will investigate the reconnection site location in the magnetotail during substorms observed under different solar wind structures. When a reconnection site passes through a satellite in the night plasma sheet first a fast earthward plasma flow is registered and then – a fast tailward flow. In one of the main substorm models – NENL, the observation of a fast flow reversal is interpreted as a tailward motion of the reconnection site past the satellite [Hones, 1979; Angelopoulos et al., 1996; Petrukovich et al.; 1998; Yahnin et al., 2006]. In another substorm model, the Current Disruption model, the observation of a fast flow reversal is interpreted as a passage along the satellite the current disruption region [e.g. Lui et al., 2008].

The goal of this work is to determine the reconnection site location in the magnetotail associated with substorms developed under different solar wind streams – high-speed recurrent streams (HSS), magnetic clouds (MC), and the region of compressed plasma in front of these streams (Sheaths and CIRs). For this purpose we used Geotail position at the moment of observation of an X-line moving tailward (observation of a fast flow reversal) for cases related to different solar wind streams.

Data

We combine the data of the UV Imager onboard the Polar satellite [Torr et al., 1995] with Geotail plasma measurements by LEP instrument [Mukai et al., 1994], and magnetic field measurements by MGF instrument [Kokubun et al., 1994].

The auroral disturbances are studied by Polar UVI data. It is known that auroral disturbances in the ionosphere is investigated by means of the device UVI, registering glow in the ultraviolet region of the spectrum. The main source of radiation in the UV range is the system of Lyman Birdge Hopfield Spectral bands - LBH), we used data from the emission band in LBHL (1600-1800Å). The method of determining the auroral bulge parameters was described in detail in [Despirak et al., 2009, 2011].

The solar wind and interplanetary magnetic field parameters measured by Wind spacecraft were taken from OMNI database. Sheath and CIR regions were detected by their typical showings – as regions in front of recurrent streams or magnetic clouds, which are characterized by an increase of solar wind pressure, temperature and density. For high speed recurrent streams (HSS) high velocities and low values of the negative B_Z component of the IMF are typical characteristic [see e.g., Tsurutani et al., 2006]. The magnetic clouds (MCs) have high magnetic field values with long interval of negative B_Z component of the IMF and also increased values of plasma velocity [e.g. Burlaga et al., 1982].

The events were selected using the following criteria:

1) The auroral disturbances should be observed by the UVI onboard Polar;
2) The auroral disturbances should be observed during MC, HSS, Sheath, CIR solar wind structures;
3) The meridian of the Geotail footprint should cross the auroral bulge;
4) Geotail should be in the night plasma sheet. The criterion $\beta > 0.1$ (β is the ratio of kinetic plasma pressure to magnetic pressure) and eye inspection of ion and electron spectra are applied for the plasma sheet identification.

All auroral disturbances observed by Polar during MC, HSS, Sheath, CIR for the periods 1997-1998; 2000; October 2001 and December 1996 were studied. The MC, Sheath, CIR solar wind regions discussed by us are events with small duration [see for example Yermolaev et al., 2009] and hence observations of substorms during MC, Sheaths and CIRs are quite rare cases. Coincidence of Polar observations of such substorms with Geotail measurements in the plasma sheet is yet a much rarer event. During the whole period that we have analyzed (1997-1998; 2000; October 2001 and December 1996) we have found only 6 events when Geotail was in the plasma sheet during auroral bulge formation related to Sheath regions in the solar wind; 3 events- to CIR regions; 3 events- to MC and 7 events – to HSS.

Below we present one example connected to solar wind magnetic cloud (MC).

Results

Auroral disturbances during MC event on 13 November 1998

A magnetic cloud (MC) arrived at ~ 05:00 UT on 13 November and passed away at ~ 07 UT on 14 November 1998 (as deduced from Wind data). The Sheath was registered from ~01 UT to ~05 UT. A substorm was observed at 21:47 during the MC passage. The blue line on Fig. (2a) delimits the intervals of Sheath and MC, the interval of MC is red-crosshatched. In front of the magnetic cloud there is a region of interaction with slower streams (Sheath). This is a region with magnetic field and plasma compression. Vertical blue lines and blue crosshatched regions show the times of Sheath (Fig.2a) The black solid line shows the onset time of the substorm registered by the Polar satellite.

On the top panel of Fig. (2b), the auroral bulge development from 21:47 to 22:11 UT according to Polar UVI data is shown. The onset latitude L_0 of the bulge was 53.3º CGLAT; the maximum latitude L_m – 72.6º CGLAT; the latitudinal size L_{lat} ~16.7º CGLAT, the longitudinal size L_{long} ~ 162º CGLAT, the ratio between the longitudinal and the latitudinal sizes L_{lat}/Ll_{ong} was equal to ~ 9.7. Keograms on the bottom panel of Fig. (2b) demonstrate the clear poleward expansion of the bulge.

Geotail data for the period 20 – 24 UT on 13 November 1998 are presented in Fig. (2c). The satellite started registering fast tailward plasma flows about 21:59 UT, a flow reversal took place at ~ 22:00 UT and a maximum of earthward flow is observed at 22:07 UT. The flow reversal is associated with a decrease of the total (magnetic plus plasma) pressure, which followed a period of a pressure increase.

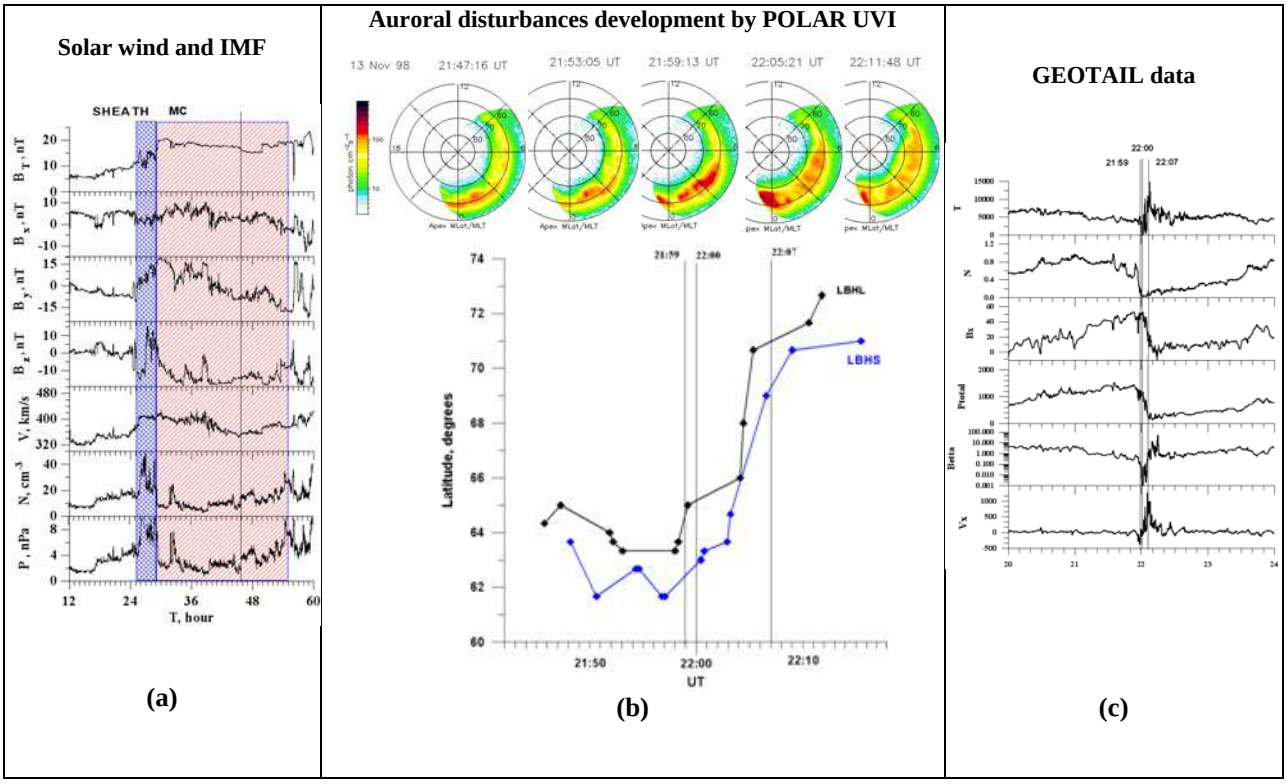

Figure 2. Auroral disturbances during MC event - 13 November 1998.

(a) From top to bottom: total magnetic field B, three magnetic field components, SW flow velocity, density, dynamic pressure;

(b) Top: auroral bulge development from onset to maximal phase. Bottom: keograms in the LBHL emission (black line) and LBHS emission (blue line) at the meridian of Geotail footprint. Vertical lines indicate the times of plasma flows in magnetotail by Geotail data;

(c) From top to bottom: temperature, density, MF component Bx, total pressure, plasma β, GSM X component of the velocity.

Relationship between the latitude of the poleward edge of the auroral bulge and the distance of the reconnection site from the Earth

For all 19 selected cases we determined the latitude of the poleward edge of the auroral bulge at Geotail footprints meridian at the moment when Geotail registered a fast flow reversal in the magnetotail. Then we related this latitude with Geotail position in the magnetotail. The results are shown in Fig. 3, where the distance between Geotail and the Earth is evaluated by Geotail X-coordinate in earth radii. On the right panel cases observed during MCs are depicted in red, cases during HSS – in blue, those observed during Sheath – in green, and cases during CIRs – in black. On the left panel cases are grouped according their origin: cases connected with MCs and Sheaths are depicted in red, cases of HSS and CIRs – in blue.

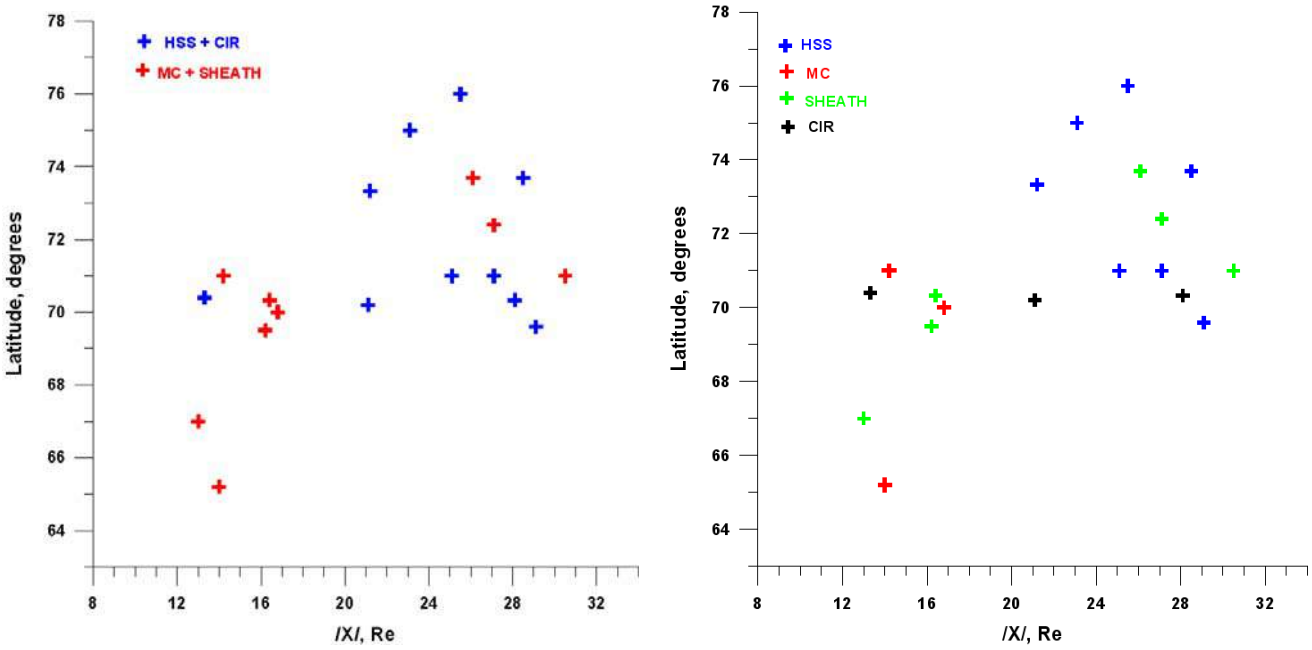

Figure 3. Latitude of the poleward edge of the aurora (seen by Polar UVI at the meridian of Geotail) as a function of the distance between Geotail and Earth at the moment of the flow reversal registration

From Fig.3 it is clearly seen that the reconnection site during substorms associated with high speed recurrent solar wind streams is observed on the average at larger distances from earth $|X|=25.7\pm2.8$ R_E than during substorms associated with magnetic clouds, the latter being at $15.\pm1.5$ R_E.

Discussion

In all cases considered here, during the auroral disturbances in the ionosphere fast plasma flows in the magnetotail are observed. In the literature there is enough evidence that in the course of substorm fast plasma flows in the magnetotail are observed and satellites in the near or middle tail can register a reversal of a tailward plasma flow to an earthward plasma flow. In the midtail initiation model or alternatively referred to as the near-Earth neutral line model (NENL), the flows are ordered by the magnetic field – tailward flows accompanied by negative Bz, earthward flows under positive Bz, the region where these flows are generated is associated with the formation of a near-Earth X-line. The observation of oppositely directed flows is interpreted as tailward movement of the reconnection site [Hones, 1979; Angelopoulos et al., 1996; Runov et al., 2003], the tailward flow being inside a plasmoid. At the moment, when a maximum of tailward flows is observed, the satellite is situated inside the plasmoid; when a maximum of earthward flows is observed, the spacecraft is within the dipolarized region earthward of the X-line. In the near-Earth initiation scenario oppositely directed flows are also observed, but not organized by the magnetic field; their generation evoked by current disruption (CD), the region of current disruption and dipolarization proceeds progressively down the magnetotail [e.g. Lui et al., 2008]. The earthward flow is observed in the depolarized region, the tailward – tailward of the CD region. The observation of fast flow reversal by a spacecraft in the plasma sheet

indicates passage of the reconnection site around the spacecraft in the NENL model [e.g. Yahnin et al. 2006] or passage of the current disruption region in the CD model.

The latitudinal profiles in Figure 2b show that the oppositely directed flows and the flow reversals are observed during poleward aurora expansion. The relation of fast flows observation in the plasma sheet with the poleward expansion of the aurora is reported in many works [e.g. Fairfield et al. (1999); Borodkova et al. (2002); Perraut et al., 2003; Yanin et al. 2006]. In particular authors in Borodkova et al. (2002) and Yanin et al. (2006) demonstrated that the flows were directed tailward when the auroral bulge developed equatorward of the spacecraft ionospheric footprint. Earthward fast flow bursts were observed when active auroras moved poleward of the spacecraft ionospheric footprint.

As seen in Figure 2c, in the magnetotail at Geotail location a sharp decrease of the total pressure following the interval of pressure increase was observed. The total pressure decrease (TPD) is associated with the time of plasma flow direction change. From the pressure balance condition, which is suggested to held across the plasma sheet and tail lobe boundary, the total pressure ($P = nkT + B^2/8\pi$) in the plasma sheet must be equal to the lobe magnetic pressure. The decrease below the lobe magnetic pressure characterizes that part of the magnetic energy stored in the tail, which dissipates during the substorm. As is well known during substorm growth phese, as a result of reconnection at the magnetopause magnetic flux is stored in the magnetotail lobes, the volume of the flux stored depending on solar wind parameters and interplanetary magnetic field [e.g. Shukhtina et al., 2005]. However it is possible that during the substorm not all the stored flux but only a part of it is dissipated in the ionosphere. The area of the auroral bulge could be a measure of the dissipated magnetic flux [e.g. Miyashita et al., 2003]. So the total pressure increase followed by a decrease observed during the substorm-related fast flows is one of the signatures of substorm development in the magnetotail.

Thus, in all 19 cases we have analyzed, in the course of auroral disturbances development in the ionosphere, in the magnetotail typical substorm signatures - fast plasma flows (tailward/earthward flows) and a sharp decrease of the total pressure following the interval of pressure increase are observed.

Conclusions

In this work we discuss the problem of the magnetic reconnection site location in the magnetotail during substorms associated with different solar wind streams. It is shown that magnetic reconnection in the magnetotail takes place closer to Earth when substorm is observed during MC, and further in the tail for substorms during solar wind high speed recurrent streams (HSS). In this way our results confirm the results of Nagai et al. (2005).

However using one-point data it is difficult to separate space and time variations. We plan to continue the investigations on reconnection site location for substorms driven by different solar wind structures using CLUSTER and THEMIS data.

Acknowledgements

WIND data used in this study were taken from OMNI through http://cdaweb.gsfc.nasa.gov/cdaweb/istp_public/; Polar UVI data were downloaded from UVI official site http://uvisun.msfc.nasa.gov/UVI/brwseimages.html). We are grateful to K. Ogilvie and R. Lepping, PIs of the experiments conducted with these instruments. We thank G. Parks and other members of the Polar UVI team who made the data of the UV Imager available to the community. Data from the MFI and LEP instruments onboard Geotail were retrieved from the DARTS database. We are thankful to S. Kokubun and T. Mukai for providing the data.

The paper was supported by the RFBR Grants 12-05-01030 and Program No 22 of the Presidium of the Russian Academy of Sciences (RAS) "Fundamental problems of the Solar system exploration".

The study is part of a joint Russian - Bulgarian Project 1.2.10 "The influence of solar activity and solar wind streams on the magnetospheric disturbances, particle precipitations and auroral emissions" of PGI RAS and IKIT-BAS under the Fundamental Space Research Program between RAS and BAS.

References

Angelopoulos, V., D.G. Mitchell, R.W. McEntire, D.J. Williams, A.T.Y. Lui, S.M. Krimigis, R.B. Decker, S.P. Christon, S. Kokubun, T. Yamamoto, Y. Saito, T. Mukai, F.S. Mozer, K. Tsuruda, G.D. Reeves, W.J. Hughes, E. Friis-Christensen, O. Troshichev (1996), Tailward progression of the magnetotail acceleration center: Relationship to substorm current wedge. *J. Geophys. Res.,* 101, 24 599–24 619.

Borodkova N.L., A.G. Yahnin, K. Liou, J.-A. Sauvaud , A.O. Fedorov, V.N. Lutsenko, M. N. Nozdrachev, A.A. Lyubchich (2002), Plasma sheet fast flows and auroral dynamics during substorm: a case study. *Ann. Geophys*, 20, 341–347.

Burlaga, L.F., L. Klein, Jr., Sheeley, D.J. Michels, R.A. Howard, M.J. Koomen, R. Schwenn, H. Rosenbauer (1982), A magnetic cloud and a coronal mass ejection. *Geophys. Res. Lett.* 9, 1317-1320.

Despirak, I.V., A.A. Lubchich, A.G. Yahnin, B.V. Kozelov, H.K. Biernat (2009), Development of substorm bulges during different solar wind structures. *Ann. Geophys*., 27, 1951 –1960.

Despirak, I.V., A.A. Lubchich, V. Guineva (2011), Development of substorm bulges during storms of different interplanetary origins. *J. Atmos. Sol.-Terr. Phys*., 73, 1460–1464.

Fairfield D. H., T. Mukai, M. Brittnacher, G.D. Reeves, S. Kokubun , G.K. Parks, T. Nagai, H. Matsumoto, K. Hashimoto, D.A. Gurnett, T. Yamamoto (1999), Earthward flow bursts in the inner magnetotail and their relation to auroral brightenings, AKR intensifications, geosynchronous particle injections and magnetic activity, *J. Geophys. Res*. 104, 355-370.

Hones, Jr., E. W. (1979), Transient phenomena in the magnetotail and their relation to substorms. *Space Science Reviews* 16, 617–410.

Kokubun, S., T. Yamamoto, M.H. Acuna, K. Hayashi, K. Shiokawa, H. Kawano (1994), The Geotail Magnetic Field Experiment. *J. Geomag. Geoelect*. 46, 7-21.

Krieger, A.S., A.F. Timothy, E.C. Roelof (1973), A coronal hole and its identification as the source of a high velocity solar wind stream. *Sol. Phys*. 23, 123-128.

Lui, A. T. Y., A. Zheng, H. Reme, , M.W. Dunlop, G. Gustafsson (2008), Evaluation of substorm models with Cluster observations of plasma flow reversal in the magnetotail. *Adv. Space Res*. 41, 1611–1618.

Miyashita Y., S. Machida, K. Liou, T. Mukai, Y. Saito, C.-I. Meng, G.K. Parks (2003), Relationship between magnetotail variations and auroral activities during substorms. *J. Geophys. Res.* 108, 1022, doi:10.1029/2001JA009175.

Mukai, T., S. Machida, Y. Saito, M. Hirahara, T. Terasawa, N. Kaya, T. Obara, M. Ejiri, A. Nishida (1994), The low energy particle (LEP) experiment onboard the Geotail satellite. *J. Geomag. Geoelectr.* 46, 669-692.

Nagai, T., M. Fujumoto, R. Nakamura, W. Baumjohann, A. Ieda, I. Shinohara, S. Mashida, Y. Saito, T. Mukai (2005), Solar wind control of the radial distance of the magnetic reconnection site in the magnetotail. *J. Geophys. Res.*, 110, A09208, doi: 10.1029/2005JA011207.

Perraut S., O. Le Contel, A. Roux, G. Parks, D. Chua, M. Hoshino, T. Mukai, T. Nagai (2003), Substorm expansion phase: Observations from Geotail, Polar and IMAGE network. *J. Geophys. Res.* 108, 1159, doi:10.1029/2002JA009376.

Petrukovich, A.A., V.A. Sergeev, L.M. Zelenyi, T. Mukai, T. Yamamoto, S. Kokubun, K. Shiokawa, C.S. Deehr, E.Y. Budnick, J. Büchner, A.O. Fedorov, V.P. Grigorieva, T.J. Hughes, N.F. Pissarenko, S.A. Romanov, I. Sandahl (1998), Two spacecraft observations of a reconnection pulse during an auroral breakup. *J. Geophys. Res.,* 103, 47–59.

Pudovkin, M.I. (1996), Solar wind. *Soros Educational Journal* 12, 87-94.

Richardson, I. G., H. V. Cane, E. W. Cliver (2001), Sources of geo-magnetic storms for solar minimum and maximum conditions during 1972– 2000. *Geophys. Res. Lett.,* 28, 2569.

Runov A., R. Nakamura, W. Baumjohann, R.A. Treumann , T.L. Zhang, M. Volwerk, Z. Vörös, A. Balogh, K.-H. Glaßmeier, B. Klecker, H. Rème, L. Kistler (2003), Current sheet structure near magnetic X-line observed by Cluster. *Geophys. Res. Lett.* 30, 1579, doi: 10.1029/2002GL016730.

Shukhtina M.A., N.P. Dmitrieva, N.G. Popova, V.A. Sergeev, A.G. Yahnin, I.V. Despirak (2005), Observational evidence of the loading-unloading substorm scheme. *Geophys. Res. Lett*. 32, LI7107, doi:10.1029/2005GL023779.

Torr, M. R., D. G. Torr, M. Zukic, R. B. Johnson, J. Ajello, P. Banks, K. Clark, K. Cole, C. Keffer, G. Parks, B.Tsurutani, J. Spann (1995), A Far Ultraviolet Imager for the International Solar Terrestrial Physics Mission. *Space Sci. Rev.* 71, 329-383.

Tsurutani B.T., W.D. Gonzalez, A.L.C. Gonzalez et al. (2006), Corotating solar wind streams and recurrent geomagnetic activity: A review, *J. Geophys. Res.* 111. doi: 10.1029/2005JA011273.

Yahnin, A.G., I.V. Despirak , A.A. Lubchich, B.V. Kozelov, N.P. Dmitrieva, M.A. Shukhtina, H.K. Biernat (2006), Indirect mapping of the source of the oppositely directed fast plasma flows in the plasma sheet onto the auroral display. *Ann. Geophys*., 24, 679–687.

Yermolaev, Yu.I., N.S. Nikolaeva, I.G. Lodkina, M.Yu. Yermolaev (2009), Catalog of Large-Scale Solar Wind Phenomena during 1976– 2000. *Kosmicheskie Issledovaniya* 47, 99–113.

OBJECTIVE DISCRIMINATION OF GEOMAGNETIC DISTURBANCES AND PREDICTION OF DST INDEX BY ARTIFICIAL NEURAL NETWORKS*

S.A. Dolenko, I.N. Myagkova, V.R. Shiroky, I.G. Persiantsev

D.V. Skobeltsyn Institute of Nuclear Physics, M.V. Lomonosov Moscow State University, Moscow, Russia; e-mail: shiroky@srd.sinp.msu.ru

Abstract. Strong disturbances of the Earth's magnetic field (geomagnetic storms) may have significant effect upon operation of engineering devices and well-being of people. Therefore, prediction of the state of magnetosphere is a very important problem. Geomagnetic disturbances (or magnetic storms) are one of important factors of space weather. In this study, we suggest an algorithm for objective discrimination of boundaries and different phases of magnetic storms based on the time series of hourly values of Dst-index. Two or three phases were marked for each storm: initial phase (optional), main phase, and recovery phase. With the help of the suggested algorithm, the boundaries of magnetic storms and their phases for the period from November 1997 till March 2014 have been marked automatically in an objective way. Then, neural network prediction of the value of Dst index by the parameters of solar wind and interplanetary magnetic field in L1 point and by preceding values of Dst index itself, has been performed. In this study, we perform detailed analysis of the results obtained for storm data, and suggest ways of improving existing approaches to neural network prediction of Dst-index.

INTRODUCTION

Space weather effects upon the near-Earth environment are due to dynamic changes in "Sun – solar wind – Earth" chain. The Earth's magnetosphere is one of the key space environment domains affected by space weather. Developing successful prediction of the occurrence of geomagnetic disturbances (storms) is one of the important aims of solar-terrestrial physics research, since geomagnetic storms may have significant effect upon operation of engineering systems both in space and on Earth, and upon well-being of people.

The Dst index is one of the most important solar-terrestrial indices. It is used in numerous studies as a measure of intensity and temporal development of magnetic storms. The Dst index has been calculated at the World Data Center WDC-C2 at Kyoto, Japan (Geomagnetic Equatorial Dst index Home Page, http://wdc.kugi.kyoto-u.ac.jp/dstdir/index.html) since the International Geophysical Year, 1957, using data from four observatories at low to mid-latitudes; its hourly values are available online.

The main reason causing disturbances of the Earth's magnetosphere are the fluxes of ionized particles from the Sun – the so-called solar wind (SW) (e.g. Akasofu and Chapman, 1972). For short-term prediction it is especially important to have operative information about the values of SW parameters. The input data usually used for Dst index prediction are the parameters of SW plasma and of interplanetary magnetic field (IMF), measured at Earth's orbit. The data used in this work were obtained onboard ACE (Advanced Composition Explorer) spacecraft (http://www.srl.caltech.edu/ACE).

There are several different methods used to predict Dst index. For example, Space Research Institute (Russia) provides an advance warning about the future geomagnetic storm magnitude: real-time predictions of the geomagnetic storm magnitude are updated every hour and published at http://spaceweather.ru (Podladchikova and Petrukovich, 2012). The project of University of California, Berkeley (http://sprg.ssl.berkeley.edu/dst_index/welcome.html) produces a prediction of Dst index one hour ahead using data from spacecraft ACE, based on the modification of the empirical formula of Burton (Burton et al., 1975), the same way as it is done in the above-mentioned group at Space Research Institute. The Swedish Space Weather Center (http://src.irf.se/en/forecasts/) predicts the next hourly mean value of the Dst index (one hour forward in relation to the last entered data) using a recurrent Elman neural network. The project WINDMI Real-Time Dst and AL indices at the CCMC (http://ccmc.gsfc.nasa.gov/cgi-bin/WINDMIpred.cgi) provides a Dst prediction, which is performed using a physical model based on the calculation of ring currents in the magnetosphere-ionosphere system, and which also receives as input the data from the spacecraft ACE (Patra et al., 2011). A modern model used to predict the Dst index 1 hour ahead proposed in (Revallo et

* This study was supported by the Russian Foundation for Basic Research (RFBR), project no. 14-01-00293.

al., 2014) is based on artificial neural networks (ANN) combined with an analytical model of the SW–magnetosphere interaction.

The authors of this paper have their own experience of the Dst index prediction using scientific models based on ANN technology (see e.g. Dolenko et al., 2005). The website of the Space Weather Analysis Center at SINP MSU provides online prediction of Dst index 0.5-1.5 hour ahead by the parameters of SW and IMF measured by the ACE satellite using ANN (http://swx.sinp.msu.ru/models/dst.php).

The main goal of this study is improving existing approaches to ANN prediction of Dst index.

OBJECTIVE DISCRIMINATION OF GEOMAGNETIC DISTURBANCES

Correct prediction of Dst index is most valuable during geomagnetic disturbances (GMD), especially during strong magnetic storms. Since such events are relatively rare, it is necessary to have an opportunity to extract data sets with samples corresponding only to the disturbed state of magnetosphere. Such data sets may be used for adequate assessment of prediction quality, and also in ANN training – to make the ANN perform better during GMD.

A geomagnetic disturbance consists of three phases. The main phase is characterized by a rapid fall of Dst index from background values (-15…-20 nT to 3…5 nT) down to large negative values (lower than -30 nT for weak GMD, -50 nT for moderate GMD, -100 for strong GMD etc.). The main phase is followed by the recovery phase, during which the value of the Dst index gradually returns to the background level; the duration of this phase may reach several days. The main phase is preceded by the initial phase, which often starts with the so-called sudden storm commencement (SSC). We suppose, that in this case during the initial phase the Dst index takes on positive values greater than 3…5 nT, and here we shall consider that detecting such positive values corresponds to detecting initial phase with SSC.

While the point of the minimum value of Dst index is considered to separate the main phase from the recovery phase, there are no commonly accepted criteria to determine the exact hour of GMD start, GMD end, or the border between the initial and the main phases. To mark such points, a human expert usually analyses not only the time series (TS) of the Dst index, but also the behavior of SW and IMF parameters. Therefore, discrimination of GMD requires much human effort, and it is subjective, as different experts may come to different conclusions.

So there is a demand for an algorithm for objective discrimination of GMD and their phases, which would require no human expertize. Here we report for the first time the results of such an algorithm created by the authors. Note that this version of the algorithm analyses only the TS of the Dst index itself and it does not analyze the behavior of SW and IMF parameters, thus having natural limits in its efficiency. However, the algorithm uses several passes over the data, and its parameters were developed and fine-tuned in such a way that our human expert agrees with most of the results of GMD marking by the algorithm.

This version of the algorithm has seven parameters:

- A_{min} is the maximum negative value of Dst index in nT required for the GMD to be detected (a negative integer) – minimal amplitude of detected GMD.
- t_+ is the upper boundary of background Dst values in nT (an integer).
- t_- is the lower boundary of background Dst values in nT (an integer).
- s is the TS smoothing parameter in hours (a non-negative integer). If s=0, smoothing is turned off.
- B_{short} is the short merging parameter in hours (a non-negative integer).
- B_{long} is the long merging parameter in hours (a non-negative integer).
- ***maxRewind*** is the starting point search parameter in hours (a non-negative integer).

The main stages of the algorithm are the following.

1) Time series smoothing. A working TS is created, each point of which assumes a value equal to the average value of the initial Dst TS over a window $2*s+1$ points wide centered at this point in time.

2) Preliminary marking. Each point of the working TS with amplitude d is marked as belonging to one of the four types:

- Type **A** ($d \geq t^+$) – possible initial phase point;
- Type **B** ($t_+ > d > t_-$) – possible background point;
- Type **C** ($t_- \geq d > A_{min}$) – possible main phase or relaxation phase point;
- Type **D** ($d \leq A_{min}$) – definite main phase or relaxation phase point.

3) Interval creation. All adjacent points of the same type (except type **B**) are joined into intervals of this type.

4) Interval joining. Intervals separated with number of type **B** points less or equal to B_{short} (or B_{long}, depending on types of these intervals), are merged into joint intervals.

5) Event determination. Each of the joint intervals containing at least one type **D** point is considered to be a separate event (GMD). All the other joint intervals are disregarded.

6) Initial phase refinement. If a joint interval includes at least one type A point, the corresponding GMD is considered to have the initial phase with SSC. A special iterative search procedure to the left of the current beginning of the joint interval with the ***maxRewind*** parameter is used to locate the first point of GMD as a local minimum or a first positive value point in the working TS.

7) Starting point refinement. For joint intervals considered having no initial phase with SSC, a special iterative search procedure to the left of the current beginning of the joint interval with the ***maxRewind*** parameter is used to locate the first point of GMD as a local maximum or a first negative value point in the working TS. If type **A** points are found during this search, then the GMD is considered to have the initial phase with SSC, and the algorithm goes back to Stage 6.

8) Output of the results. Each of the finally obtained joint intervals is treated as a separate GMD. The algorithm outputs the list of found GMDs, specifying for each GMD: minimum Dst index value, hours of GMD start, of Dst minimum, of GMD end, and presence of the initial phase with SSC. In a separate log file, each point is marked with the ID of GMD it belongs to and with the GMD phase it belongs to.

A detailed description of the algorithm and the results of its work will be published separately.

The optimal parameter values were fine-tuned to be the following: $t_+ = 5$ nT, $t_- = -20$ nT, $s = 1$ hour, $B_{short} = 2$ hours, $B_{long} = 4$ hours, ***maxRewind*** = 24 hours. For this study, A_{min} was set to -30 nT (weak and stronger GMD), but this value can be changed if it is necessary to mark only strong or only extreme GMD.

For the total period from October 22, 1997 till March 31, 2014, the algorithm has marked 867 GMDs, 300 of them having the initial phase with SSC.

As an example, the Table displays the list of GMD marked by the algorithm for the period from 0-1h UT March 1, 2012 till 23-24h UT April 30, 2012. To avoid confusion, each hour is specified by both its beginning and its end. The time in the Table is UT. Fig. 1 displays the Dst index TS for the same period.

Table. Geomagnetic disturbances marked by the algorithm from March 1 to April 30, 2012.

№	Min of Dst, nT	Start of GMD at: yyyy-mm-dd_hh$_b$-hh$_e$	Dst minimum at: yyyy-mm-dd_hh$_b$-hh$_e$	End of GMD at: yyyy-mm-dd_hh$_b$-hh$_e$	Init.phase with SSC?
1	-34	2012-02-29_23-24	2012-03-02_01-02	2012-03-02_05-06	yes
2	-32	2012-03-03_18-19	2012-03-04_02-03	2012-03-04_05-06	no
3	-74	2012-03-07_02-03	2012-03-07_09-10	2012-03-08_08-09	no
4	**-131**	**2012-03-08_10-11**	**2012-03-09_08-09**	**2012-03-11_11-12**	**yes**
5	-50	2012-03-12_09-10	2012-03-12_16-17	2012-03-14_09-10	yes
6	-33	2012-03-14_11-12	2012-03-15_02-03	2012-03-15_07-08	no
7	-74	2012-03-15_13-14	2012-03-15_20-21	2012-03-17_11-12	no
8	-43	2012-03-17_13-14	2012-03-18_02-03	2012-03-18_23-24	no
9	-55	2012-03-27_06-07	2012-03-28_04-05	2012-03-28_19-20	yes
10	-30	2012-04-02_14-15	2012-04-02_19-20	2012-04-03_03-04	no
11	-54	2012-04-04_21-22	2012-04-05_07-08	2012-04-05_17-18	no
12	-31	2012-04-07_02-03	2012-04-07_10-11	2012-04-07_12-13	no
13	-49	2012-04-12_11-12	2012-04-13_04-05	2012-04-13_12-13	yes
14	**-108**	**2012-04-23_02-03**	**2012-04-24_04-05**	**2012-04-26_04-05**	**yes**

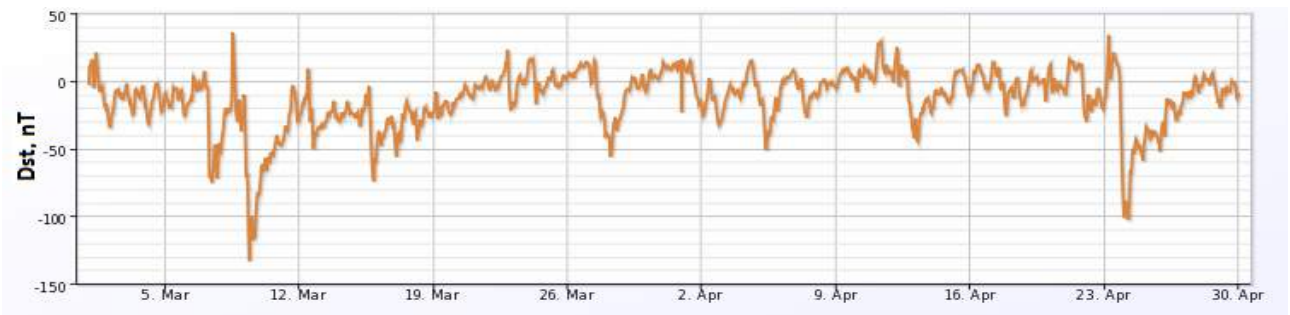

Fig. 1. Dst index time series from March 1 to April 30, 2012.

INPUT DATA FOR PREDICTION

As input data, TS of hourly values of the following physical quantities were used:

1) SW parameters in Lagrange point L1 between the Earth and the Sun:

- Speed v (in km/s); protons density n_P (in cm^{-3}); temperature T_{rr} (in K).

The data used was from ACE spacecraft, measured by SWEPAM device.

2) IMF vector parameters in Lagrange point L1 (in nT) in GSM system:

- *Bx*, *By*, *Bz* (IMF x-, y-, and z-components), *B* magnitude (IMF modulus).

The data used here was also from ACE spacecraft, MAG device.

3) Geomagnetic indexes:

- Equatorial geomagnetic index Dst (measured in nT).

The data used was from World Data Centre for Geomagnetism in Kyoto.

4) Earth movement phase parameters (two phases of harmonic function for each movement):

- With the period equal to that of the Earth's revolution round the Sun;
- With the period equal to that of the Earth's rotation around its axis.

The considered data period was from November 1997 to the end of March 2014.

Due to specifics of data obtained from measurements onboard spacecraft, there were some missing values in SW and IMF parameters. If the duration of the gap did not exceed 10 hours, the missing values were replaced by linear interpolation between the last known data value before the gap and the first known data value after the gap, separately for each TS.

After interpolation, delay embedding of all TS (except Earth movement phase parameters) for 24 hour depth was used, to account for the previous history of input features. Thus, each data pattern was a point in 204-dimensional feature space (8 TS × 25 hours + 4 TS), assigned to the latest point of the 25-hour window.

NEURAL NETWORK MODELS

In this study, we used perceptron type ANN with one hidden layer, 204 neurons in the input layer, 32 neurons in the hidden layer, and 1 output neuron. For each model, 5 ANN were trained that were identical except for various initialization of weights. The answers of these 5 ANN were averaged, and the obtained value was considered to be the output value of the model. Prediction horizon for all models was one hour.

All the available samples were divided into training, test and examination data sets. The training set was used to determine the error for weights adjustment, the test set was used for recurrent testing during network training to provide timely termination of the training (to prevent overtraining), and the examination set was used to test the trained network on out-of-sample data to assess the network quality. The data from 1997 to 2009 (105187 samples), which approximately correspond to one full solar activity cycle, were randomly divided into training and test sets with 3:1 ratio respectively. All the remaining samples (from 2010 to 2014) were used as the examination set (37178 samples).

Most interesting is the quality of prediction for the samples corresponding to the disturbed state of magnetosphere. So, a separate "disturbed" data set has been extracted, which included all the samples marked as belonging to GMD by the above-described algorithm. Intersection of the disturbed set with training, test, and examination data sets gave the three more special disturbed sets that provided the possibility to assess network quality for GMD samples only.

The statistical indicators used to assess model quality on various data sets were root mean squared error (RMSE) and coefficient of multiple determination R squared (R^2).

The following five models were compared.

1) *Full model* trained on full data sets, including samples corresponding to as disturbed, as non-disturbed state of the Earth's magnetosphere. Delay embedding depth was *24 hours* as described above (204 input features), the number of samples in the training set for this model was 78890.

2) *Disturbed model* trained using the special disturbed data sets as described above. Delay embedding was also to the depth of 24 hours (204 input features). The number of samples in the training set was 24157.

3) *Full model* completely similar to the first one except for delay embedding depth that was set to *8 hours*. So, the number of input features was 8 TS × 9 hours + 4 TS = 76, the number of training samples was 78890. Note that maximum of correlation between Dst value and delayed values of some input time series is achieved at delays greater than 8 hours, so this means some reduction in the amount of information.

4) *Intermediate model* completely similar to the first one except for the fact that it had as many samples in all the sets as the second model; however, these samples were randomly selected from full data sets,

therefore they contained both GMD and non-GMD samples. So this model also had 204 input features and 24157 training samples, just like the second one.

5) *Trivial model* used as a reference point in model assessment. For the trivial model, the predicted value of the Dst index is set to its current value. Therefore, it is completely useless, but its statistical indicators are often quite good, so comparison with this model is necessary for real estimation of the prediction quality of any more sophisticated model.

RESULTS AND DISCUSSION

In this study, we compare the performance of the five described models on the special disturbed datasets. Fig. 2 compares values of RMSE in nT, and Fig. 3 compares values of R^2.

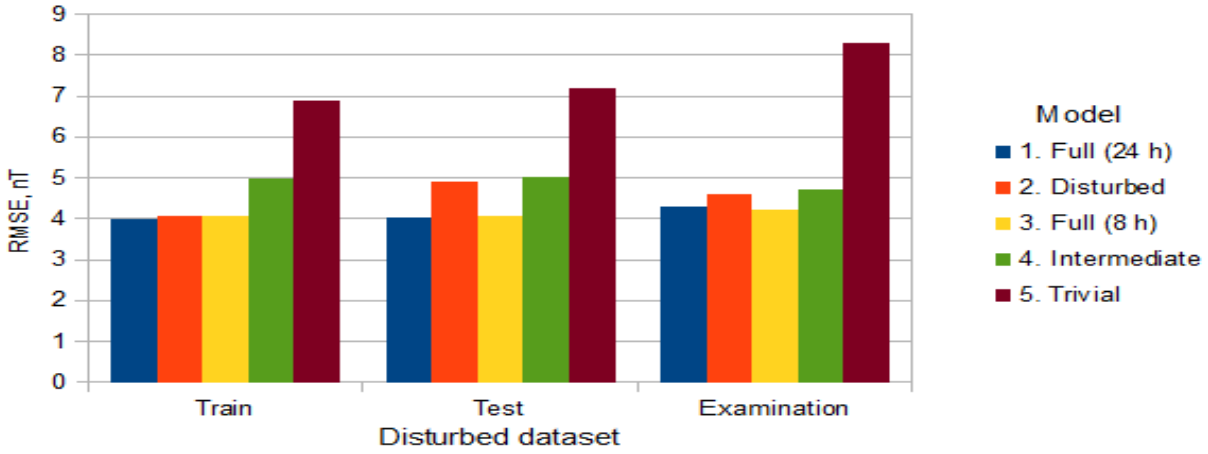

Fig. 2. RMSE of the models on the special disturbed datasets.

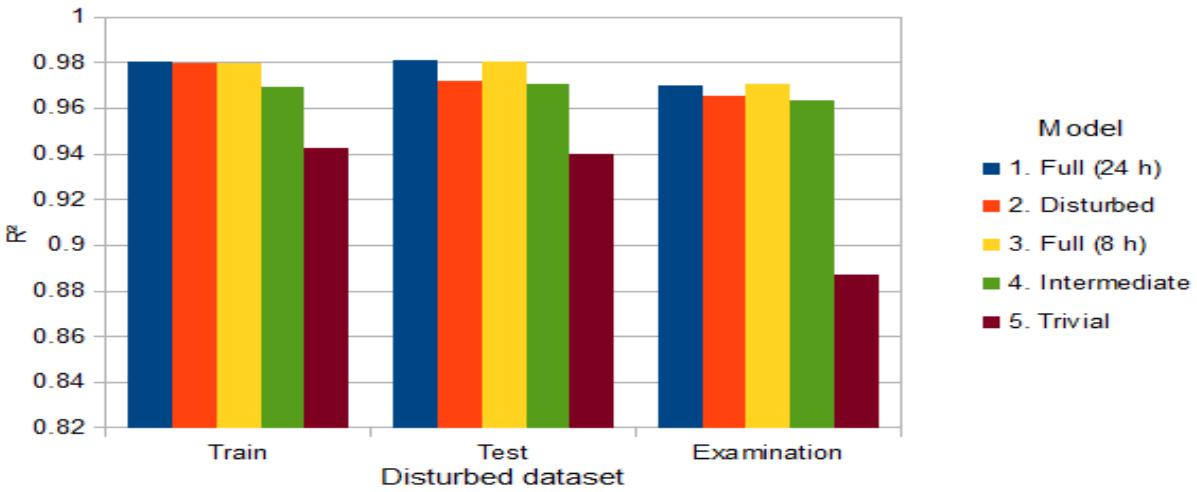

Fig. 3. R^2 of the models on the special disturbed datasets.

From Fig. 2, 3, one can draw the following conclusions.

1) The results on training and test sets are in general alike, for all models except the disturbed one. This means that for the non-GMD data that was used to train these models, the test set was representative enough, and training termination at minimum error on test set succeeded in preventing ANN overtraining. This is not the case with the disturbed model, which gets somewhat overtrained; this may mean that the disturbed data set is not large enough to provide due representativity even for random choice of the test set.

2) The examination set displays worse results for all the models including the trivial one. This may mean that the present solar cycle starting from 2010 is somewhat different from the preceding one – at least, the storms are much more volatile.

3) Comparing full model (24 h) with intermediate model, one can see that in spite of the relatively large number of training samples (24157) even in respect to the number of input features, they are not

enough to fully describe the extremely complex object that is studied. 3+ fold decrease in the number of samples (even with random selection of these samples) the ANN is trained on results in noticeable degradation of its performance, in particular, on the disturbed data sets.

4) Comparison of the intermediate and the disturbed models, both of which were trained on equal number of samples, shows that the model trained on GMD data performs on disturbed data sets better, than the model trained on all kinds of data. This is not surprising – more interesting is small difference of these two models on test and examination data sets. This may mean that the non-GMD data bears a significant amount of information about the dynamics of the magnetosphere in the whole, and this information can be acquired by the ANN.

5) Comparison of the two versions of the full model with different time series embedding depth shows that the reduction in network performance for smaller embedding depth is insignificant. However, this does not necessarily mean that 8 hours are enough. In fact, what we see is the result of two concurring processes – a) ANN performance degradation due to lack of information brought by the features corresponding to time delays larger than 8 hours, and b) improvement of ANN performance due to a significant reduction in the number of input features. Proper selection of the most significant input features from the whole range of delays from 0 to 24 hours may result in a configuration having as little input features as the 8-hour model, but performing better. Elaboration of an algorithm of such selection should be the aim of future studies.

It should be also noted that all the considered models much outperform the trivial model.

CONCLUSION

An algorithm for objective discrimination of boundaries and different phases of geomagnetic disturbances, based on the time series of hourly values of Dst geomagnetic index, has been elaborated. With the help of the suggested algorithm, the boundaries of GMD and their phases for the period from November 1997 till March 2014 have been marked automatically in an objective way.

A neural network prediction of the value of Dst index by the parameters of solar wind and interplanetary magnetic field in L1 point and by preceding values of Dst index itself, has been performed. The networks were trained on data of the complete cycle of solar activity from 1997 till 2009, and examined on samples from 2010 till March 2014 belonging to GMD, marked by the above algorithm.

It has been demonstrated that the best results on the GMD samples are provided by the ANN model trained on the whole data array disregarding presence or absence of GMD. The situation may change with time, when the representativity of the disturbed set will increase together with total number of samples, as an ANN trained only on GMD samples outperforms an ANN trained on the same amount of general data.

The prediction may be also improved with proper selection of significant input features, as even a simple reduction in delay embedding depth equilibrates decrease in the amount of information with the decrease of the number of input features.

ACKNOWLEDGEMENT

The authors thank the teams of ACE project and WDCC2 Kyoto for the possibility to access and use the data of their experiments.

REFERENCES

Akasofu, S.-I. and S. Chapman (1972), *Solar-Terrestrial Physics*, 889 pp., Clarendon Press, Oxford.

Burton, R.K., R.L. McPherron, and C.T. Russell (1975), An empirical relationship between interplanetary conditions and Dst, *J. Geophys. Res.*, 80, 4204–4214.

Dolenko, S.A., Yu.V. Orlov, I.G. Persiantsev, and Ju.S. Shugai (2005), Neural network algorithm for events forecasting and its application to space physics data, *Lecture Notes in Computer Science*, 3697, 527-532.

Patra, S., E. Spencer, W. Horton, and J. Sojka (2011), Study of Dst/ring current recovery times using the WINDMI model, *J. Geophys. Res.*, 116, A02212, doi:10.1029/2010JA015824.

Podladchikova, T.V. and A.A. Petrukovich (2012), Extended geomagnetic storm forecast ahead of available solar wind measurements, *Space Weather: The International Journal of Research and Applications*, 10, CiteID S07001.

Revallo, M., F. Valach, P. Hejda, and J. Bochníček (2014), A neural network Dst index model driven by input time histories of the solar wind-magnetosphere interaction, *Journal of Atmospheric and Solar-Terrestrial Physics*, 110, 9-14.

X-RAY EFFECT IN VLF RADIATION DIURNAL VARIATIONS

G.I. Druzhin, N.V. Cherneva, A.N. Mel'nikov

Institute of Cosmophysical Research and Radio Wave Propagation (IKIR) FEB RAS, 684034, Russia,
e-mail: nina@ikir.ru

Abstract. According to the results of observations in Kamchatka, spectral analyses of VLF radiation noise component at the frequencies of 0,7, 1,2, 5,3 kHz for 1997 — 2006 and of pulse component in the frequency range of 3 — 60 kHz for 2002 — 2006 has been carried out. The analysis has shown that there are diurnal maxima in the spectra of VLF noise envelope and in the pulse component, which coincide with the Earth rotation relative to the Sun (1440 min) and relative to stars (1436 min). The highest intensity in spectral components coincides with the period of the Earth rotation relative to the Sun, and it is observed in radiation arriving from the south-western direction of Kamchatka. The cause of appearance of the maxima in spectral components with the periods of 1440 min and 1436 min may be the Sun X-radiation and the galactic X-radiation.

Introduction

The major factor affecting the ionosphere D-region and the conditions for radio wave propagation in the very low frequency range is the Sun X-radiation (Murzaeva, 1977, Mullayarov, Karimov, Kozlov, Murzaeva, 1998). Weak sources of ionization, such as meteorites burning at the heights of 60-100 km, cosmic rays, magnetosphere energetic particles brought into this layer during magnetic storms, also have small impact. Sun diurnal rotation (~ 27 days), Moon rotation (29,5 days) and man industrial activity (week cycle) may also affect the spectral characteristics of the received VLF-radiation (Kozlov V.I., Mullayarov V.A., 2004). Nevertheless, spectral characteristics of VLF-radiation close to the diurnal period at long time intervals (more than a year) have not been considered in detail.

The aim of the paper

Investigation of noise and pulse characteristics of VLF signals at long time intervals in the period range close to the Earth diurnal rotation and detection of their possible relation with X-radiation sources.

Tasks

Spectral analysis of the natural VLF-radiation envelope according to the data of noise and pulse signals registered in Kamchatka in the period range close to the Earth diurnal rotation. Estimation of the intensity of X-radiation sources.

Spectral characteristics

Registration of noise radiation was carried out by a multi-channel VLF-recorder located in Kamchatka at Karymshina river observation point ($j=52^0 49'$ N, $l=158^0 07'$ E), which records signals at fixed frequencies in narrow frequency bands. The VLF-recorder consists of a frame antenna, a pre-amplifier located at the basis of the antenna, cable communication line, a signal filtration device, and an output device. The frame antenna has the size of 7,5 x 15 m and its plane is oriented in the East-West direction.

The time interval of T=10 years was chosen for spectral analysis of VLF-noises and periodograms in the period range close to the diurnal one were plotted for the tree registered frequencies (Fig. 1).

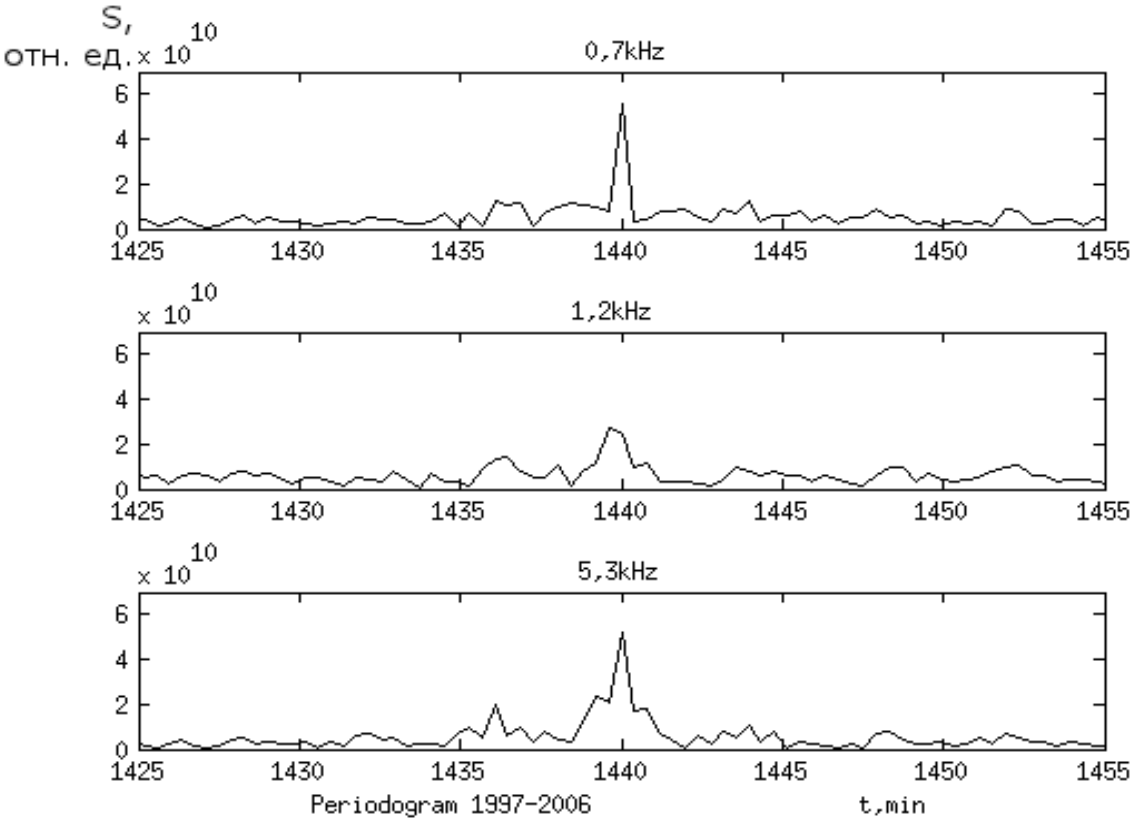

Fig.1. Periodograms of VLF-noise envelope (1997-2006) at three frequency bands.

It is clear from Fig. 1 that two main maxima with the period of 1440 min (24 hours) and 1436 min (23 hours and 56 min) are clearly seen at all the frequencies. It is also clear that the spectral components of 1440 and 1436 min are confidently distinguished (period resolution is 0.4 min). The highest maximum coincide with the Earth diurnal rotation (1440 min) relative to the Sun, and the second maximum of less magnitude coincide with the Earth diurnal rotation relative to stars, 23 hours and 56 minutes (1436 min).

In order to register electromagnetic radiation from lightning discharges, a VLF direction-finder was developed at IKIR FEB RAS which is able to receive signals in the frequency range from 3 kHz to 60 kHz arriving from different azimuthal directions. The VLF direction-finder is located in Kamchatka at Paratunka (j=$52^0 58'$ N, l=$158^0 15'$ E), on the territory of IKIR. It consists of antenna system, pre-amplifiers, signal analogue and digital processing units. The antenna system includes two mutually-perpendicular frame antennas and a rod antenna.

Lightning discharges were registered when the threshold level of 1 V/m was exceeded. Hour number of atmospherics arriving from azimuthal directions (0^0 — 90^0; 90^0 — 180^0; 180^0 — 270^0; 270^0 — 360^0) was counted for the five-year period, then, spectral analysis was carried out. Its results are shown in Fig. 2.

It is clear from Fig. 2 that the highest amplitude of oscillations with the periods of 1436 and 1440 min was observed from the azimuthal sector of 180^0 — 270^0, i.e. from the south-western direction; the least amplitude is in the north-eastern (0^0 — 90^0) and north-western directions. The resolution in this case was 0.8 min.

We should note that on the periodograms shown in Fig. 1 and 2 the component associated with the radiation of galactic origin (1436 min) is confidently distinguished. The reason of appearance of this component may be X-radiation sources affecting the ionosphere D-region.

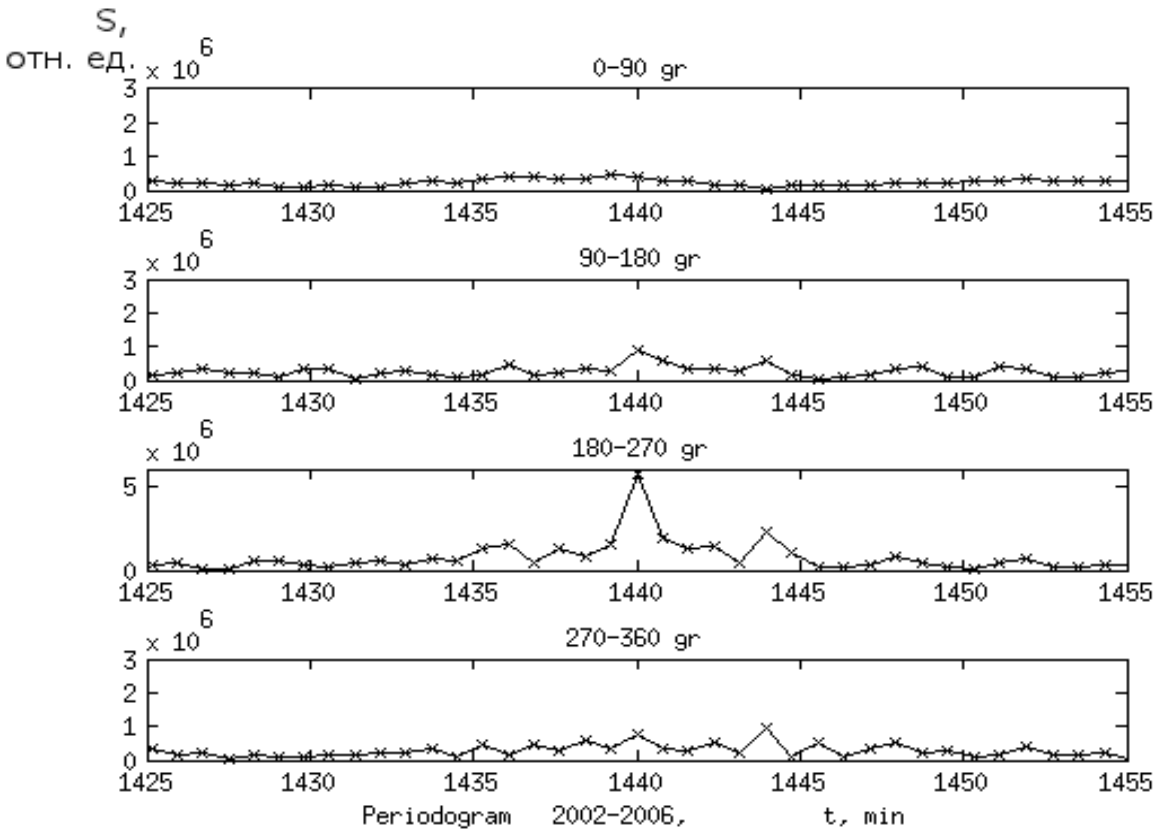

Fig.2. Periodograms (2002-2006), received from different azimuthal directions by VLF direction-finder.

X-radiation sources

The Sun X-radiation effect on the ionosphere D-region and on the characteristics of VLV radiation was studied in detail (Murzaeva N.N. (1977), *http://w-rabbit.narod.ru/raznoe/rentgen.htm*), but similar estimations of galactic X-radiation source effect on VLF radiation are not known.

S.L. Mandelshtam (*http://w-rabbit.narod.ru/raznoe/rentgen.htm*) wrote that by the boundary of the Earth atmosphere the Sun X-radiation flux in the region of 1-10 angstrom is 10^{-4} erg/(cm^{2}s), and the most powerful source of the Galaxy is in Scorpio constellation and Sco X-1, the flux from which is $5 \cdot 10^{-7}$erg/(cm^{2}s). There is about a hundred of discrete X-radiation sources. X-radiation is also observed from the Galactic ridge of X-radiation. It is long radiation of low surface brightness which extends along the Galaxy plane as a band of about 1-2 degrees wide [http://ru.wikipedia.org/wiki]. Hereof, the Galaxy X-radiation may affect the level of ionosphere D layer ionization and, as it is clear from Fig. 1 and 2, this effect results in the maximum of amplitude at the period of 1436 min.

We should also note that by the boundary of the Earth atmosphere, only ~10^{-10} from the Sun electromagnetic radiation total flux (total flux is — 1,5•10^6 erg/(cm^{2}s)) fall on the X-ray range and 10^{-3} — 10^{-4} of the luminosity from the Galaxy relatively the optical range.

Conclusion

Analysis of registration data of natural electromagnetic radiation at the frequencies of 0.7, 1.2 and 5.3 kHz for 1997 — 2006 showed that there are maxima in VLV noise envelope spectra which coincide with diurnal periods of the

Earth rotation relatively the Sun (1440 min) and relatively the stars (1436 min). On the basis of the data of direction-finding observations in 2002-2006, it was also shown, that in the frequency range of 3-60 kHz these maxima (at the periods of 1440 min and 1436 min) are also observed in the spectra of atmospheric pulse signals. The highest intensity of spectral components fall on the period coinciding with the period of the Earth rotation relatively the Sun and it is observed from the south-western direction of Kamchatka. In the north-western and north-eastern directions the radiation intensities at the periods of 1440 min and 1436 min are comparable in value.

The most probable reason for the appearance of the maxima in VLF-radiation at the periods of 1440 min and 1436 min is the Sun X-radiation and the galactic X-radiation.

References

Murzaeva N.N. (1977), *The relation of VLF radiation of the upper atmosphere with other geophysical phenomena*. Yakutsk. Pub.: Ya.B SO AN USSR. P. 21-24.

Mullayarov V.A., Karimov R.R., Kozlov V.I., Murzaeva N.N. (1998). *Meteoroglogy and Hydrology.* N 8. P.48-56.

Kozlov V.I., Mullayarov V.A. (2004), *Lightning activity in Yakuriya*. Yakutsk. Pub.: Ya.B SO AN USSR. 104 p.

Mitra A. (1977). *Solar flare effect on the Earth ionosphere*. Moscow, Mir. 370 p.

EVOLUTION OF THE SPECTRAL STRUCTURE AND SPECTRAL WIDTH OF THE Pc1 PULSATIONS

F.Z. Feygin[1], Yu.G. Khabazin[1], N.G. Kleimenova[1], L.M. Malysheva[1], N.E. Vasilieva[1], T. Raita[2]

[1]Schmidt Institute of the Earth Physics RAS, Moscow, 123995, Russia, e-mail: feygin@ifz.ru;
[2] Sodankylä Geophysical Observatory, Sodankylä, Finland

Abstract. The analysis of the polarization properties of the Pc1 geomagnetic pulsations, recorded at the latitude network of several Finnish ground stations, has been performed. It was found that typically in the morning (i.e. before noon) the Pc1 polarization was left-handed. That fact may suggest that the given ground-based station is located in vicinity of the projection of the field line of the Pc1 generation region. After noon the Pc1 wave polarization changes and becomes right-handed one. It could be a result that our stations occur far from Pc1 source meridian due to the Earth rotation, but the Pc1 generation still continues at the same magnetosphere area**.** The right-hand polarization could be a result of the horizontal propagation of the magnetosonic waves in the ionosphere waveguide. These waves can carry energy across the magnetic field lines. The performed theoretical calculations showed that the evolution of the frequency width of the dynamic spectrum of the Pc 1 wave packets depends on the magnetosphere plasma parameters. It was found that the Pc1 spectral width increases with decreasing of the proton thermal anisotropy. We suppose that under quiet conditions, the Pc1 generation takes place near the plasmapause located at higher L-shells with small V_A values. This results in a narrow width of the wave spectra.

Introduction

The Pc1 geomagnetic pulsations known as "pearls" have been the subject of extensive study since many years ago [Troitskaya, 1964, Jacobs and Watanabe, 1964; Obayashi, 1965]. Their theory of generation and the morphological properties are widely discussed in the literature list time, e.g. in several books and revues [e.g., Troitskaya and Guglielmi, 1967; Jacobs, 1970; Bespalov and Trakhtengerts, 1986]. The results of the last 10-years satellites (THEMIS, CHAMP, Cluster space crafts) measurements are presented in some papers, e.g. [Min et al., 2012; Park et al., 2013; Lin et al., 2014].

The Pc1 pulsations are repeated wave packets of Alfven waves in the frequency range of 0.2–5.0 Hz travelling between the conjugated hemispheres. Their theory of generation and the morphological properties are widely discussed in the literature list time, e.g. in several revues [Guglielmi and Pokhotelov, 1994; Kangas et al., 1998; Demekhov, 2007]. The results of the last 10-years satellites (THEMIS, CHAMP, Cluster spacecrafts) measurements are presented in some papers, e.g. [Min et al., 2012; Park et al., 2013; Lin et al., 2014]. It is no doubt that Pc1 pulsations ("pearls") are generated via the cyclotron instability of radiation belt protons with anisotropic velocity distribution [Cornwell, 1965; Kennel and Petchek, 1966; Feygin and Yakimenko, 1971; and many others].

The ground-based data demonstrated the maximum of the mid-latitude (Borok observatory) Pc1 activity in the anti-phase with the solar activity [Matveeva, 1987], and the Pc1 activity in California, USA was strongest during the declining phase of a solar cycle [Fraser-Smith, 1970]. The rather similar results was obtained in the auroral latitudes (Sodankylä, Finland), where the Pc1 occurrence rate appeared inversely correlated with solar activity with the phase delay of about two or one year (Mursula et al., 1991), which was explained in terms of magnetospheric ion composition [Guglielmi and Kangas, 2007).

This phenomenon still attracts the attention of many authors and our understanding about its nature is far from complete. The main goal of this paper is to continue the studies of Pc1 properties such as the polarization and the wave spectral width.

The theoretical consideration

We consider electromagnetic wave, with electric and magnetic components $\mathbf{E_1}$, $\mathbf{B}_1$ perpendicular to the constant magnetic field $\mathbf{B}_0$. The wave vector **k** is assumed parallel to the **z** axis, which is directed along $\mathbf{B}_0$. The wave amplification is due to a cyclotron interaction between the wave and hot particles. The amplification coefficient (growth rate) γ is a function of the wave number k. It reaches its maximum at value of k, namely k_0, which corresponds to a pulsation frequency ω_0 (central frequency of the wave packet on the sonagrams). The frequency of the pulsations ω and k for the EMIC waves, as it is known, are connected by the relation

$$\omega^2 = k^2 V_A^2 (1 - \omega / \Omega_i) \tag{1}$$

If the concentration of the hot protons in the plasma n_1 is low as compared with the cold plasma number density N ($n_1 \ll N$), the distribution function of the hot protons is presented by the Maxwell function with different temperatures $T_\perp$ and $T_{||}$ relative to the magnetic field $\mathbf{B}_0$, then the growth rate of the EMIC waves, with the wave vector k||$\mathbf{B}_0$ is given by the formula [Feygin, Yakimenko, 1969, 1970; Gendrin at al., 1971]

$$\gamma = \frac{\pi^{1/2}\left(n_1 / N\right)(1-x)\left[A - (A+1)x\right]}{x(2-x)}\sqrt{y}\exp(-y), \tag{2}$$

$$y = \frac{V_A^2}{U_{||}^2}\frac{(1-x)^3}{x^2}, \tag{3}$$

where $\Omega_i = eB_0/m_i c$ is ion gyrofrequency, $x = \omega/\Omega_i$, $U_{||} = (2T_{||}/m_i)^{1/2}$ is the mean parallel velocity of the particles, $V_A = B_0(4\pi N m_i)^{1/2}$ is the Alfven velocity, and $A = (T_\perp/T_{||} - 1)$.

The growth rate $\gamma = \gamma_{\max}$ for the wave with frequency $\omega = \omega_{\text{opt}} = (V_A/U_{||})\Omega_i \ll \Omega_i$. Over time, the form of the wave packet is determined predominantly by the Fourier components with frequencies close to ω_{opt}. If the initial disturbance, for example, a magnetic field at time $t = 0$ has the form of $B_1(z,0) = B_1^0 \exp(-z^2/b^2)$, then the value $B_1(z,t)$ in the presence of the cyclotron instability during the time defined by the formula [Feygin, Yakimenko, 1969,1970; Gendrin at al., 1971]

$$B_1(z,t) = B_1^0 \exp[(\gamma_0 - \gamma_{\text{eff}})t]\exp\left\{i\left[k_0 z - \omega_{\text{opt}}(t_n + \tau) + \frac{\beta V_{g0}^2\tau^2 + \alpha k_0 b^2 V_{g0}\tau}{2(\alpha^2+\beta^2)t} - \right.\right.$$
$$\left.\left. - \frac{\beta k_0^2 b^4}{8(\alpha^2+\beta^2)t}\right]\right\}\exp\left\{\frac{-\alpha V_{g0}^2\tau^2 + k_0\beta b^2 V_{g0}\tau}{2(\alpha^2+\beta^2)t}\right\}\exp\left(-\frac{k_0^2 b^2}{4}\right)(pt)^{-1/2}, \tag{4}$$

where $t_n = z_n / V_{g0}$, $\tau = t - t_n$, $\alpha = -d^2\gamma/dk^2\big|_{k=k_0}$, $\beta = d^2\omega/dk^2\big|_{k=k_0}$, and $V_{g0} = \partial\omega/\partial k\big|_{k=k}$ are terms of the expansion of the growth rate γ and frequency ω on the wave number k ($\gamma_{\max}$ corresponds $k = k_0$), γ_{eff} is the effective decrement, taking into account the attenuation in the ionosphere, $p = 2(\alpha + i\beta)b^{-2}$. We assume that the wave packet is reflected from both ends of the field line, and it comes back to the equator, where it is amplified, after distance z_n and travel time t_n (corresponding to the central frequency of the wave packet ω_{opt}), n being the number of passes through the amplifying region, τ describes the time inside the wave packet. Wave packet propagates with the group velocity V_{g0}, and the rate of the amplification is determined by γ_0. The specific form of the initial disturbance $B_1(z,0)$ does not have a crucial matter. Summands in the exponents of the formula (4), proportional b^2 and b^4, give only some additions to the oscillation phase, frequency ω_{opt} and position of the signal maximum. These

modifications do not change a lot over time of the signal passes through a given point (assuming that this time is $t^* \sim [(\alpha^2+\beta^2)t\alpha^{-1}]V_{g0} \ll t$, and $\tau \ll t_n$). We do not stop here on the analysis of these modifications. The width of the frequency spectrum of the wave packet during its duration (τ) is derived from the expression (4) and has the form

$$\Delta\omega \propto 2\beta V_{g0}\, \alpha^{-1/2} (\alpha^2+\beta^2)^{-1/2}\, t_n^{-1/2}. \tag{5}$$

Using expressions (1) and (2) we obtain the formula for evaluating α, β and V_{g0}:

$$\alpha \simeq \frac{8\pi^{1/2}(n_1/N)V_A^2(1-x)^2[A-(A+1)x]}{x^3(2-x)^3\Omega_i}\Psi\sqrt{y}\exp(-y), \tag{6}$$

$$\beta = -\frac{V_A^2}{\Omega_i}\frac{(1-x)^2(1-x/4)}{(1-x/2)^3}, \tag{7}$$

$$V_{g0} = V_A(1-x)^{3/2}(1-x)^{-1}, \tag{8}$$

$$\Psi = 1+\frac{x(1-7x^2/16)}{(1+x/2)(1-x/2)^2}+\frac{3x(1+x/3+x^2/6)}{4(1+x/2)[A-(A+1)x]}+\frac{Ax^2(1-x)}{4[A-(A+1)x]^2}. \tag{9}$$

The formula for the growth rate (2, 3) includes an important magnetospheric parameter ($V_A/U_{||}$). Numerical calculations (Fig.1) show that for small value of this parameter the amplification of Pc1 wave packets with narrow frequency spectrum is possible. When the parameter ($V_A/U_{||}$) increases, Pc1 wave packets with wider frequency spectra could generate.

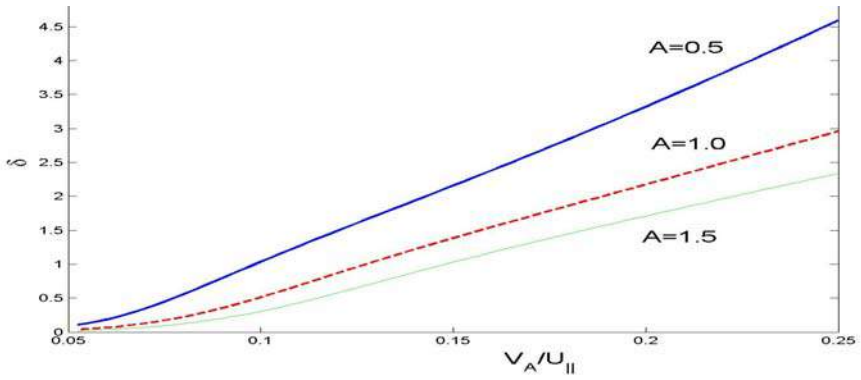

Fig.1. The dependence of the normalized width of the frequency spectrum $\delta = [\Delta\omega / (\Omega_i / t_n)^{1/2}]$ on the parameter ($V_A/U_{||}$) for different value of anisotropy A.

The optimal frequency of the signal ω_{opt} (corresponding to the central frequency of the wave packet on the sonograms) connected with this parameter as $\omega = \omega_{opt} = (V_A/U_{||})\Omega_i << \Omega_i$. Figure1 shows that with increasing of the anisotropy coefficient A, the frequency spectrum width is reduced. Furthermore, according to the relation $\omega_{opt} = (V_A/U_{||})\Omega_i$, the decreasing in the normalized frequency also leads to the decrease in the width of the frequency spectrum.

Numerical results show that the frequency width of the spectrum (at $L \approx 5$) has a minimum density of the background plasma 50–300 cm^{-3}. Moreover, at the same frequency widths smaller density values correspond to smaller values of the anisotropy coefficient.

The Pc1 wave packet frequency band $\Delta\omega$ is determined by the expression (5). The growth rate γ given by the expression (2) depends on the parameter $V_A/U_{\|}$, where V_A is the Alfven speed in the top of the magnetic field line, and $U_{\|}$ is the average field-along speed of the anisotropic protons. The numeric calculations showed that at the small values of $V_A/U_{\|}$, the frequency Pc1 band could be small as well as the width of the wave spectra. However, when values of this parameter are large, the Pc1 pulsation frequency band becomes wide.

The shape of the dynamic spectra of Pc1 pulsations was different under the quiet and disturbed conditions (see Fig. 2). The 178 selected pulsation events under Kp < 2 and 193 events under Kp > 2 have been studied. We found that the Pc1 events, being under low Kp very monochromatic, last not more than 3–5 hours as a narrow frequency band (0.2–0.4 Hz) with the central frequency ~ 0.5–0.7 Hz. Under the disturbed conditions (Kp ~ 2–3), the bandwidth and central frequency of emissions became two times higher, i.e. 0.5–0.7 Hz and 1.0–1.2 Hz, respectively.

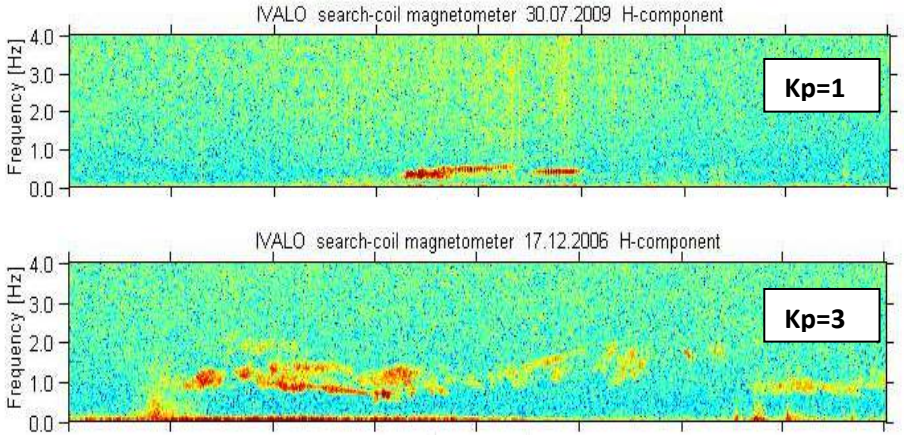

Fig.2. The spectra of Pc1 pulsations under quiet (Kp = 1) and disturbed (Kp = 3) conditions.

Results of the Pc1 polarization observations and discussion

The Pc1 polarization properties have been studied based on the data of the Finnish pulsation magnetometer chain, available via (http://sgo.fi/Data/Pulsation/pulArchive.php). Here we present the data from 4 stations; Ivalo (IVA), Sodankylä (SOD), Rovaniemi (ROV), Nurmijarvi (NUR), located between 66° and 56° geomagnetic latitude.

We found that the most events demonstrate the same direction of the wave polarization rotation. The typical observation (Fig. 3) showed the relative regular signature with the left-handed polarized waves before the magnetic noon and the right-handed ones in the afternoon. The observations of the left-hand polarized Pc1 pulsations may suggest that the given ground-based station is located near the projection of the field line of Pc1 wave generation region. The observations of the right-hand polarized Pc1 pulsations at higher and lower latitudes could be a result of the horizontal propagation of magnetosonic waves in the ionosphere waveguide.

We assume that the morning (before magnetic noon) left-handed Pc1 polarization may indicate the location of the Pc1 source in vicinity of this meridian. After magnetic noon, the polarization changes and becomes right-handed. It could be a result that our stations occur far from Pc1 source due to the Earth rotation, but the Pc1 generation still continues at the same magnetospheric area.

However, sometimes one can see (e.g. Fig. 3) an opposite Pc1 wave signature. In Fig. 3, before noon, the Pc1 pulsations at NUR demonstrated the presence of the right-hand polarization instead the typical left-hand one. We suggest that in that time the Pc1 source was located at higher latitude then NUR.

The similar uncommon Pc1 event is shown in Fig. 4. We expect that in this event, in the morning the Pc1 source was located far from Sodankylä and approached to this observatory near noon.

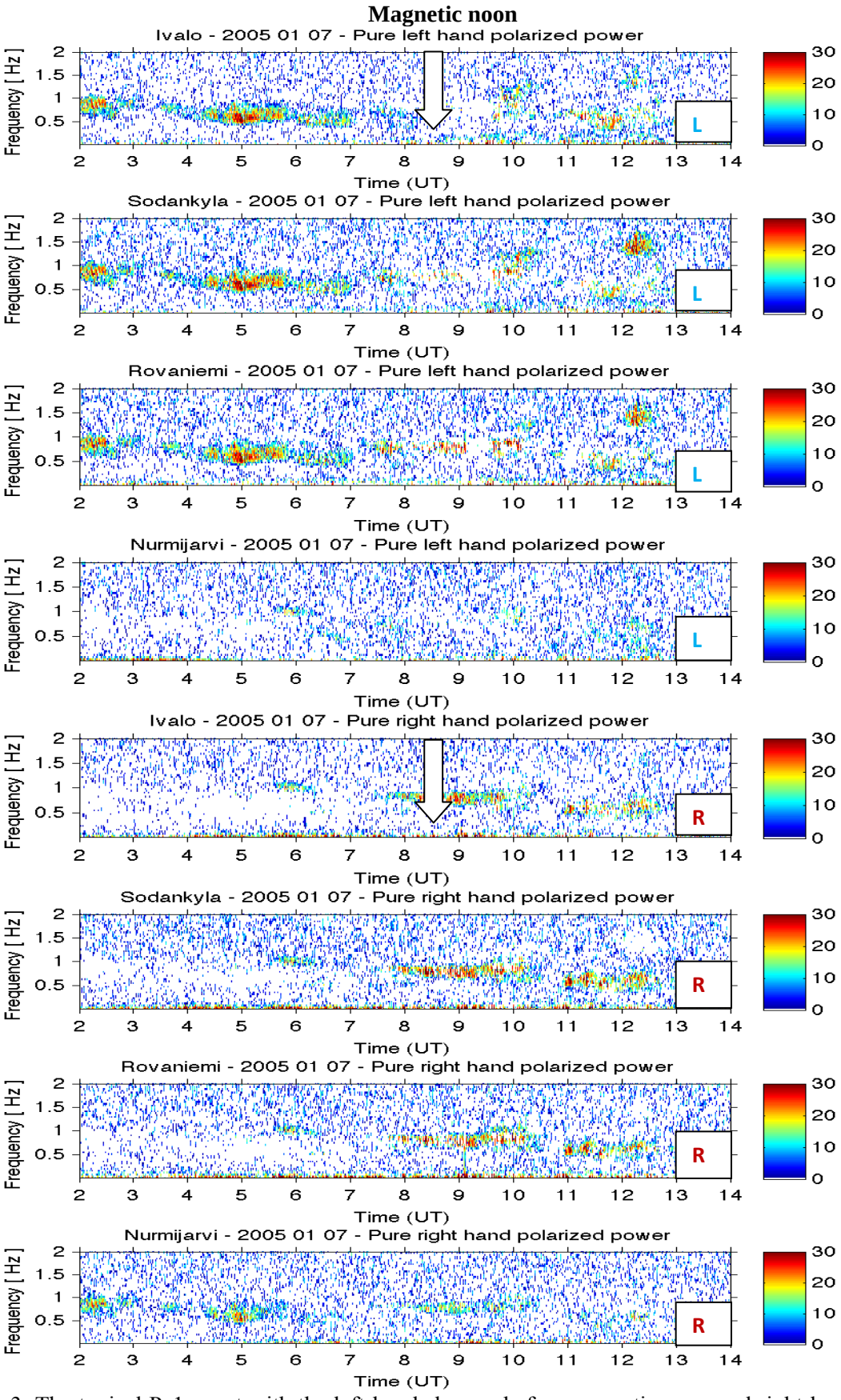

Fig. 3. The typical Pc1 event with the left-handed wave before magnetic noon and right-handed wave in the afternoon.

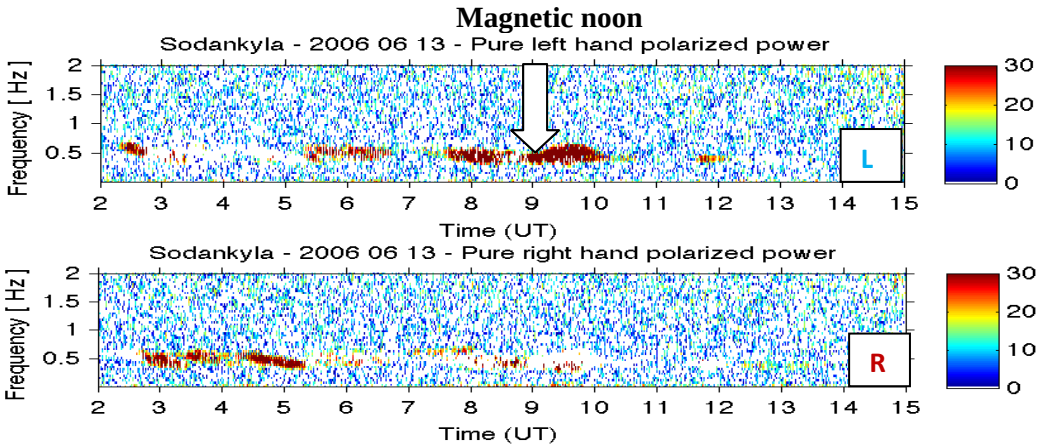

Fig.4. An example of the Pc1 event with the right-handed waves in the morning and left-handed ones around magnetic noon.

Conclusion

1. We suppose that under quiet conditions, the Pc1 generation takes place near the plasmapause located at higher *L*-shells with smaller V_A values. This results in a narrow width of the Pc1 wave spectra. Under disturbed conditions, the plasmapause is located at lower *L*-shells with higher V_A values increasing the width of the wave spectra.

2. In the most of selected events, the Pc1 polarization was the same at all stations located at different latitudes along the given meridian demonstrating the left-handed polarized waves before magnetic noon and the right-handed ones after magnetic noon. The observations of the left-hand polarized Pc1 pulsations may suggest that the given ground-based station is located near the projection of the field line of Pc1 wave generation region.

Acknowledgements. The paper was partly supported by the Program No 4 of the Presidium of the Russian Academy of Sciences (RAS) and partly supported by the RFBR Grant No 14-05-00850.

References

Bespalov, P.A., Trakhtengerts, V.Y. (1986), The cyclotron instability in the Earth radiation belts. *Rev. Plasma Physics*, vol. 10. Plenum, New York, Leontovich, M.A. (Ed.), 155–192.

Cornwall, J. M. (1965), Cyclotron instabilities and electromagnetic emission in the ultra low frequency and very low frequency ranges. *J. Geophys. Res*., 70(1), 61–69.

Demekhov, A.G. (2007), Recent progress in understanding Pc1 pearl formation. *J. Atm. Solar-Terr. Phys*., 69, 1609-1622.

Feygin, F.Z, Yakimenko, V.L. (1971), Appearance and development of geomagnetic Pc1 type micropulsations ('pearls') due to cyclotron instability of proton belt. *Ann. Geophys*., 27, 49–55.

Fraser-Smith, A.C. (1970), Some statistics on Pc 1 geomagnetic micropulsation occurrence at middle latitudes: Inverse relation with sunspot cycle and semi-annual period. *J. Geophys. Res*., 75, 4735–4745.

Gendrin, R., Lacourly, S., Roux, A., Solomon, J., Feygin, F.Z., Gokhberg, M.B., Troitskaya, V.A., Yakimenko, V.L. (1971), Wave packet propagation in an amplifying medium and its application to the dispersion characteristics and to the generation mechanism of Pc1 events. *Planet. Space Sci*., 19, 165–194.

Guglielmi, Kangas, J. (2007), Pc1 waves in the system of solar–terrestrial relations: New reflections. *J. Atmos. Solar-Terr. Phys*., 69, 1635–1643.

Guglielmi, A., Pokhotelov, O. (1994), Nonlinear problems of physics of the geomagnetic pulsations. *Space Sci. Rev*., 65, 5-57.

Jacobs, J.A., Watanabe, T. (1964), Micropulsation whistlers. *J. Atmos. Terr. Phys,* 26, 825–829.

Jacobs, J.A., (1970). *Geomagnetic micropulsations*. Springer-Verlag, Berlin-Heidelberg-New-York, 179 p.

Kangas, J., Guglielmi, A., Pokhotelov, O. (1998), Morphology and physics of short-period magnetic pulsations. *Space Sci. Rev*., 83, 435–512.

Kennel, C.F., Petschek, H.E. (1966), Limit on stably trapped particle fluxes. *J. Geophys. Res*., 71(1), 1–28.

Lin, R.-L., Zhang, J.-C., Allen, R.C., Kistler, L.M., Mouikis, C.G., Gong, J.-C., Liu, S.-Q., Shi, L.-Q., Klecker, B., Sauvaud, J.-A., Dunlop, M.W. (2014),Testing linear theory of EMIC waves in the inner magnetosphere: Cluster observations. *J. Geophys. Res*., 119, 1004–1027.

Matveeva, E.T. (1987), Cyclic variation of geomagnetic Pc1 activity. *Geomagnetism and Aeronomy*, 27, 3, 392-395.

Min, K., Lee, J., Keika, K., Li, W. (2012), Global distribution of EMIC waves derived from THEMIS observations. *J. Geophys. Res*., 117, A05219. doi:10.1029/2012JA017515.

Mursula, K., Kangas, J., Pikkarainen, T., Kivinen, M. (1991), Pc1 micropulsations at a high-latitude station: A study over nearly four solar cycles. *J. Geophys. Res*., 96, 17651–17661.

Obayashi, T. (1965), Hydromagnetic whistlers. *J. Geophys. Res.*, 70, 1069–1078.

Park, J., Lühr, H., Rauberg, J., (2013). Global characteristics of Pc1 magnetic pulsations during solar cycle 23 deduced from CHAMP data. *Ann. Geophys*., 31, 1507–1520.

Troitskaya, V.A. (1964), Rapid variations of the electromagnetic field of the Earth. *Res. Geophys*., 1, 485–532.

Troitskaya, V.A., Guglielmi, A.V. (1967), Geomagnetic micropulsations and diagnostics of the magnetosphere. *Space Sci. Rev*., 7, 5/6, 689–768.

IONOSPHERIC DISTURBANCES AS A MANIFESTATION OF CLOUDY IMF STRUCTURE

L.D. Filippov[1], A.E. Stepanov[1,2], I.Ya. Plotnikov[1]

[1]Institute of Cosmophysical Research and Aeronomy, Yakutsk, 677980**,** Russia, e-mail: a_e_stepanov@ikfia.sbras.ru;
[2]Technological Institute of North-Eastern Federal University, Yakutsk, Russia, 677000

Abstract. Variations of the foF2 critical frequency and the height of the ionospheric F2 layer with events result of coronal mass ejections in the near-Earth space are compared. Dayside measurements (06-18 LT) of DPS-4 digisonde at the Yakutsk ionospheric station were analyzed. We discuss the statistical relationship between the characteristics of the regular course of the semi-diurnal foF2 with the parameters of the magnetic cloud associated with a coronal mass ejection. There were considered short-period components of the semi-diurnal course of foF2 and their dependence on the possible dynamics of the geometric parameters of the magnetosphere under the influence of magnetic clouds on it.

Introduction

Effect of travelling ionospheric disturbances (TIDs) on ionospheric parameters, in particular, variations in the spectral characteristics foF2 was shown in [*Gershman and Grigoriev*, 1978]. The authors identified a large-scale TIDs (characteristic size of >1000 km, the velocity of 250 - 1000 m/s, the period > 1 hour) and medium (characteristic size of 10 - 1000 km, the velocity of 100 - 250 m/s, the period of 10-60 min). Experimental measurements provide exactly this wavelength range [*Solodovnikov et al., 1979; Fedorenko et al., 2011; Paznukhov et al., 2012; Stepanov and Filippov, 2013*].

Experimental results

It is interesting to consider the frequency spectra of the observed temporal variation in the diurnal and semidiurnal courses of the critical frequency (foF2) in Yakutsk and Zhigansk using DPS-4 ionospheric data (Fig.1).

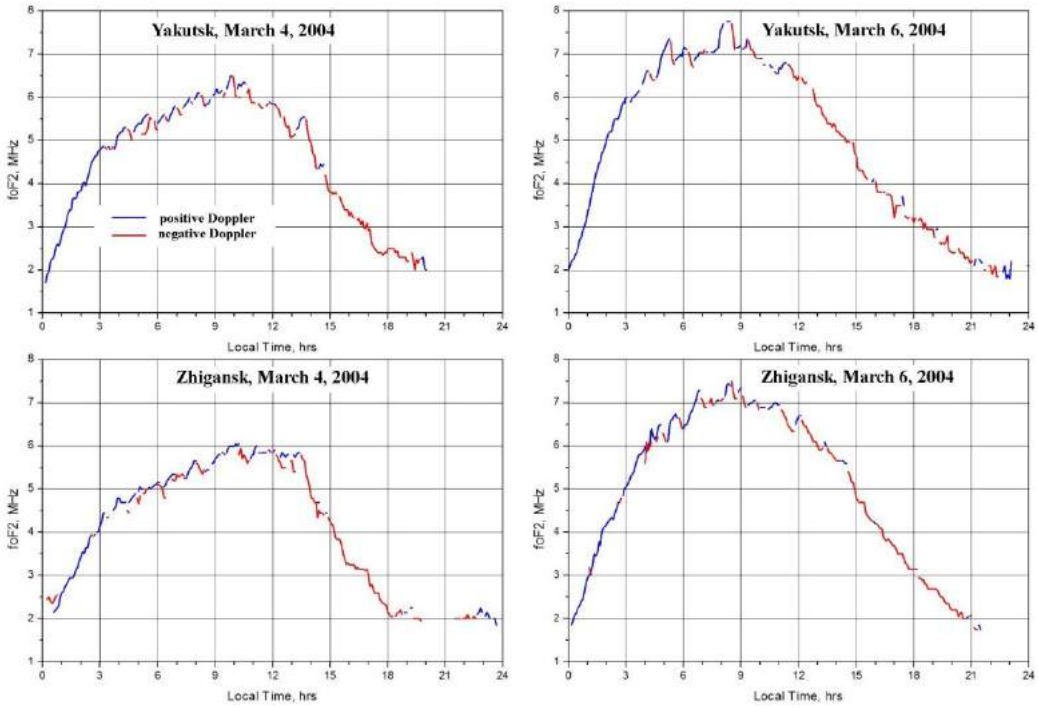

Fig.1. Variations of daily courses of the critical frequency in Yakutsk and Zhigansk.

Increasing and decreasing of the foF2 accompanied by positive and negativeDoppler frequency shift. The general increase in foF2 in the forenoon - with positive Doppler shift and afternoon - with negative Doppler shift can be explained with influence of magnetospheric dawn-dusk electric field. Small-scale positive and negative variations of foF2 are causes by effect of TIDs.

Spectral components that form the diurnal course of the foF2 in Yakutsk and Zhigansk are identical. Differences in the spectra begin with periods less than 300 minutes, i.e. in the spectral range of TIDs. TIDs range in Yakutsk spectrum is shifted to long-period part of the spectrum concerning a range in Zhigansk (Fig.2).

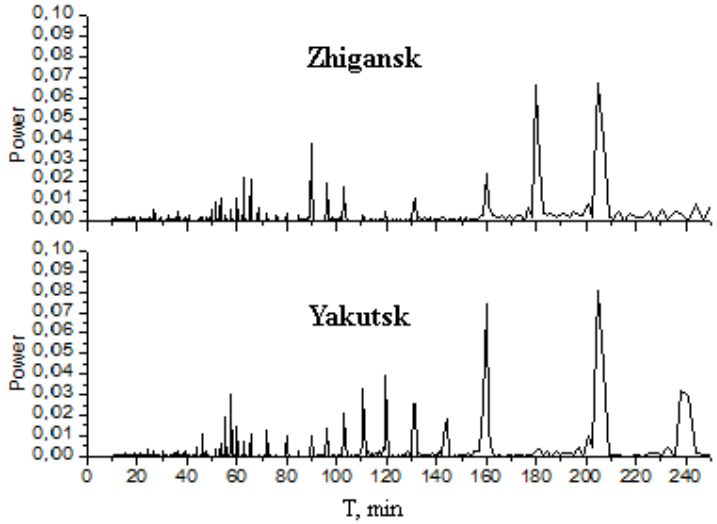

Fig.2. The spectra of the critical frequencies in Yakutsk and Zhigansk.

Consideration of variations foF2 spectra depending on the Kp-index sum during TIDs observation shows that with Kp-index increasing the spectra are shifting to the more long-period part of spectra (Fig.3).

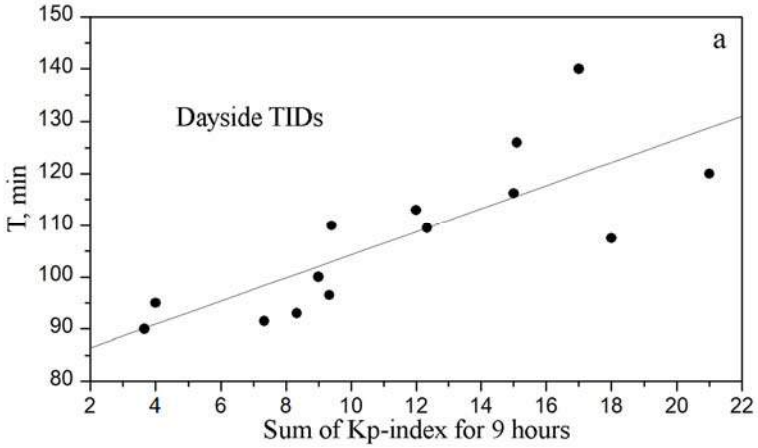

Fig.3. Expanding the spectra to the longer periods.

Problem definition, model calculations and discussion

It is known that TIDs moves to the south [*Gershman and Grigoriev*, 1978, *Maltsev,* 1995] that is a basis to look for TIDs sources on polar edge of a plasmasphere as there are zones with strong field-aligned currents, the shift currents which capable to excite TIDs. Flutter mode or interchanging instability can be one of TIDs mechanisms [*Maltsev,* 1995]. It occurs when the motion of the magnetic flux tube with a polarized ionization, in condition of non-compatible isolines of the plasma volume V and pressure P inside the tube (Fig.4a [*Maltsev,* 1995]). Such instabilities form a dynamic outer shell around the radiation belts (Fig.4b).

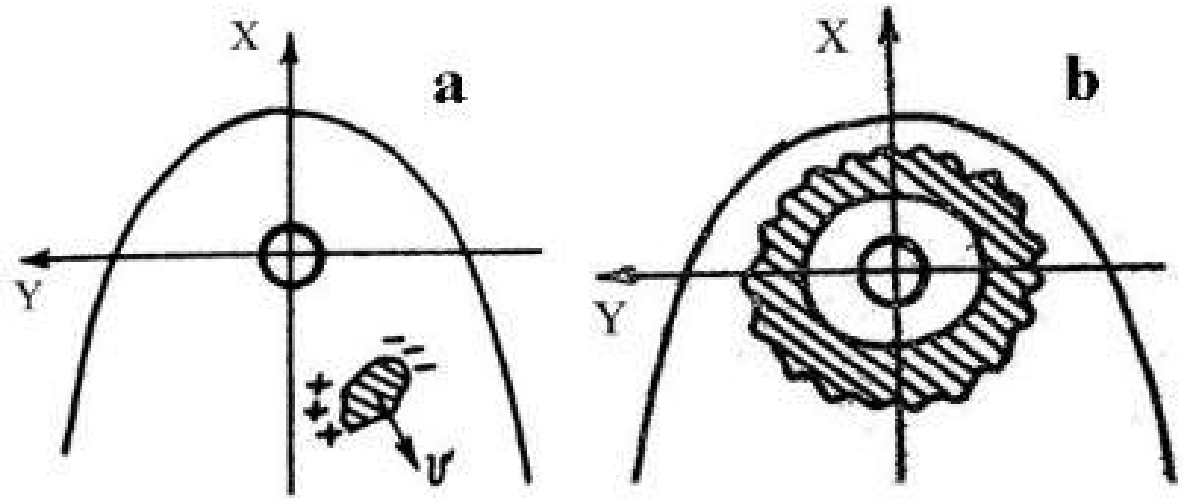

Fig.4. Polarization of a hot plasma cloud in a non-uniform magnetic field (a) and radiation belt with an interchange instability(b).

The purpose of this work - model calculations of the mechanism of formation of TIDs at ionospheric heights as a result of influence of interchange instability.The problem of processing of a signal is solves. For this purpose the day semidiurnal temporary of foF2 and h'F2 courses are presented by superposition's of smoothed trends and short-period harmonicas. The decision is reduces to allocation of the correlated fluctuations of critical frequency and height of F2 layer which correlate with each other and fast magnetospheric fluctuations.

Dependence the frequency spectra of the foF2 variations from Kp-index (Fig.3) provides a basis to analyze the dispersion relation of the interchanging instability by

$$\omega^2 = \pm \left| \mathbf{k} \right| \, g_e,$$

where

$$g_e = 2 \, c^2_S \, \mathbf{R} \, / \, \gamma \, R^2$$

is the equivalent of gravity acceleration is inversely proportional to scale of irregularity of a magnetospheric field R. Taking into account the effect of magnetopause currents(DCF currents), further in calculations is accepted R ~ 1/Rbow to distance to a front point of a near-Earth shock bow. Respectively, period $T = 2\pi/\omega \sim 1/\sqrt{Rbow}$, and Rbow changes it is controlled according to 5-min data from the OMNI database (http://cdaweb.gsfc.nasa.gov).

The selected short-period harmonica is described by model of an analytical signal with the period of T(t)/b and three free parameters

$$S(t) = S_0(t) + a \sin[2 \pi b \, t/T(t) + c],$$

where $S_0(t)$ – smoothed trend, a – amplitude of the oscillations, b – multiplicity coefficient of period, c – phase of the oscillation.

Fig.5 presents a test which shows the manifestation in the oscillations depending on the control signal Rbow(t) at b = 1. It is possible to see that the variant **A** better than **B** for modeling of the temporary courses of ionospheric parameters.Therefore, we consider justified the accounting of the experimental size Rbow in all the range of its values.

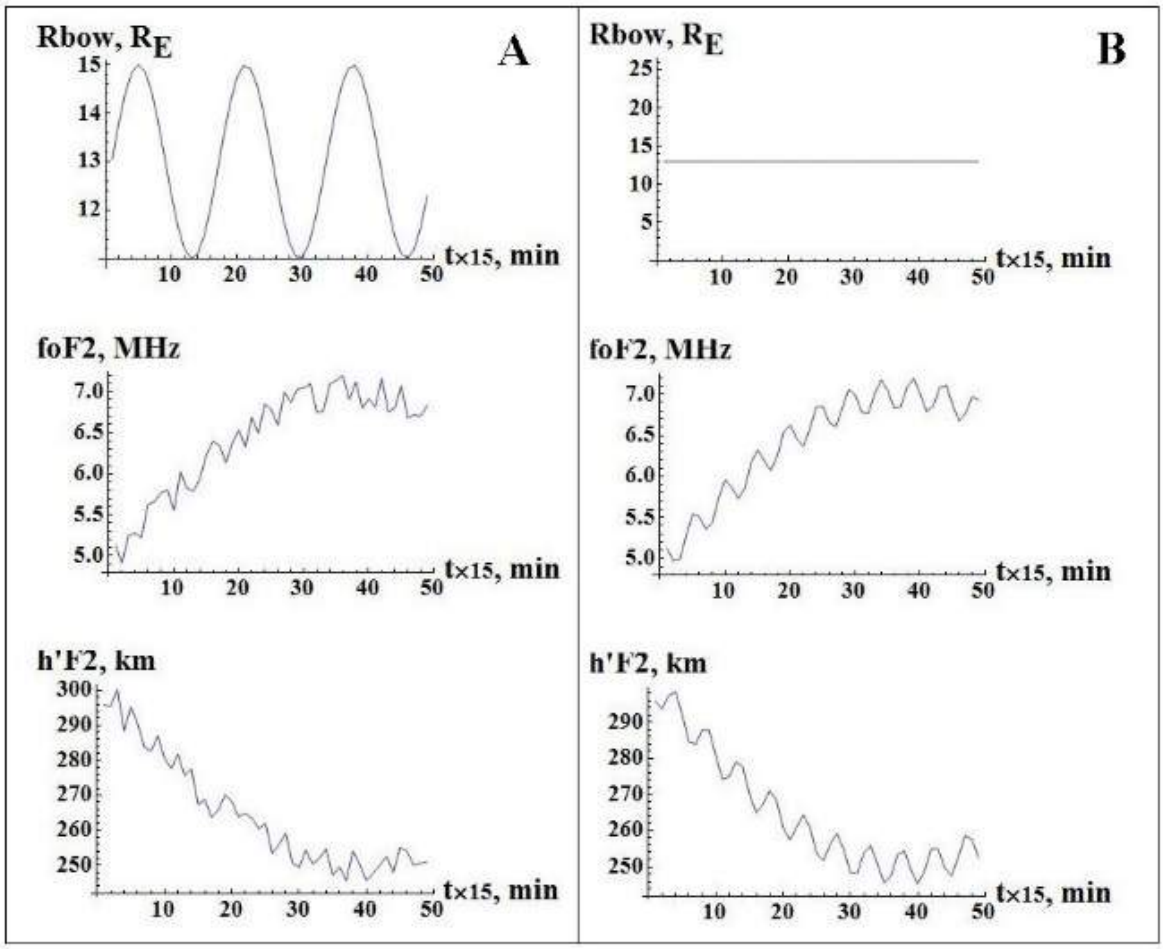

Fig.5. Test calculations of a model signal with the variable and constant period.

At the first stage in Fig.6 and Fig.7 the periods of the allocated fluctuations of the temporary semidiurnal courses at ionospheric stations of Yakutsk and Zhigansk are compared under various conditions in near-Earth space.

Regular long-period changes are removed from the time interval of courses by subtraction of values of optimal $S_0(t)$ of a polynomial of degree three. On a difference of an irregular short-period component and values of a model signal by means of method of least squares are calculated the optimal free parameters. Model fluctuations, settlement in these parameters, have in Fourier's range on the periods one allocated line. At this stage the corresponding periods give the solution of a signal processing.

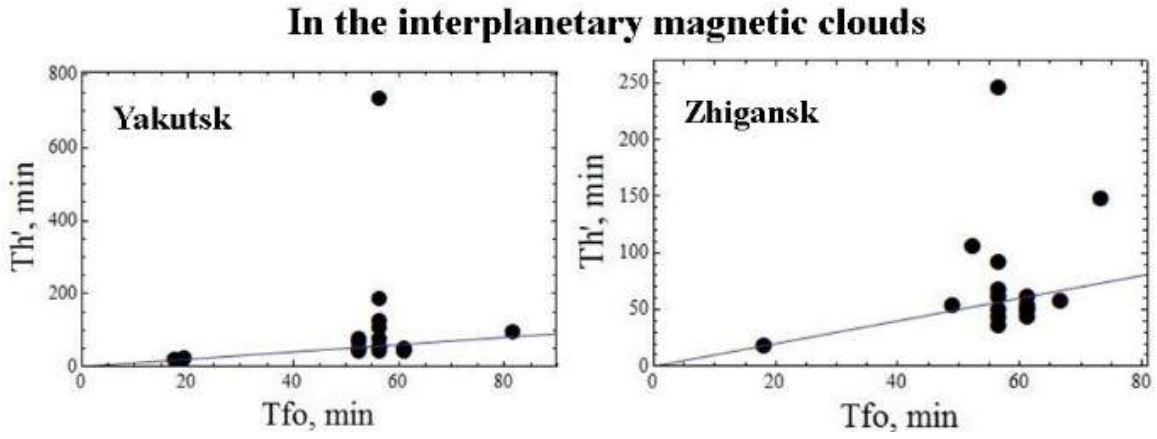

Fig.6. A ratio of the periods of the allocated fluctuations at various ionospheric stations during interaction of interplanetary magnetic clouds with Earth magnetosphere.

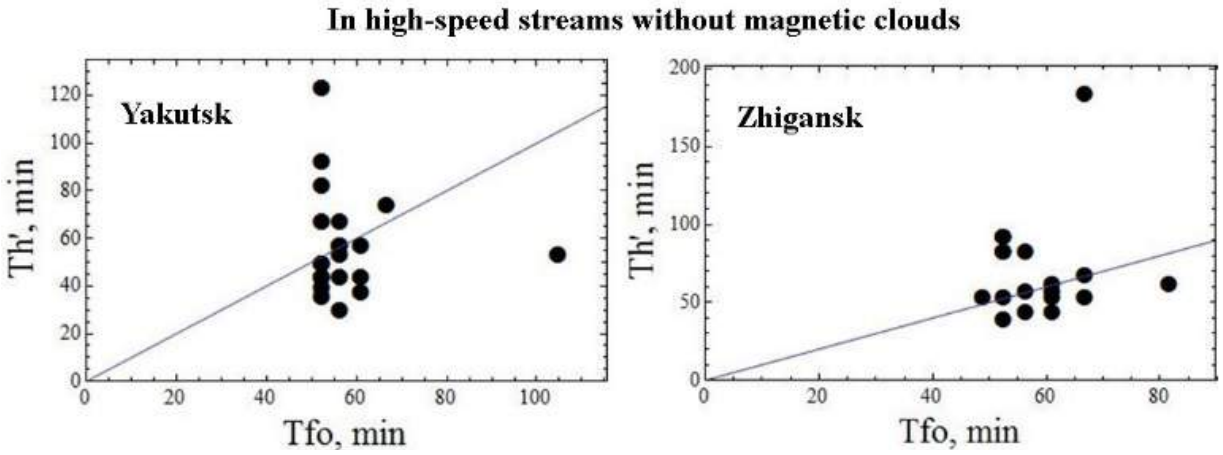

Fig.7. The same as in Fig.6 - during interaction of the Earth magnetosphere with high-speed streams of the solar wind without magnetic clouds.

It's seen from Fig.6 and Fig.7 that related with magnetospheric nonstabilities the **fo** and **h** parameter's fluctuations have the periods near 60 min at both stations and as a first approximation don't depend on types of disturbances in a solar wind. Despite casual dispersion of points concerning the line of the equal periods, in general, results in figures correspond to the correlated fluctuations in both parameters of an ionosphere.

Calculation of periods were made for 20 semi-diurnal courses for Yakutsk and 17 – for Zhigansk which were associated with the events of occurrences near-Earth interplanetary of magnetic clouds (MO). As an example, in Fig.8 were selected intervals 1 and 2, where the parameter characterizing the MOβ <1 (β is the ratio of the gas and magnetic pressure). For comparison the calculation of periods of ionospheric data of 21 alternative events for Yakutsk and 18 –for Zhigansk that occur in similar conditions, but on time are not associated with the appearance of MO in near-Earth space. In Fig.8 selected interval 3 where the parameter β>1.

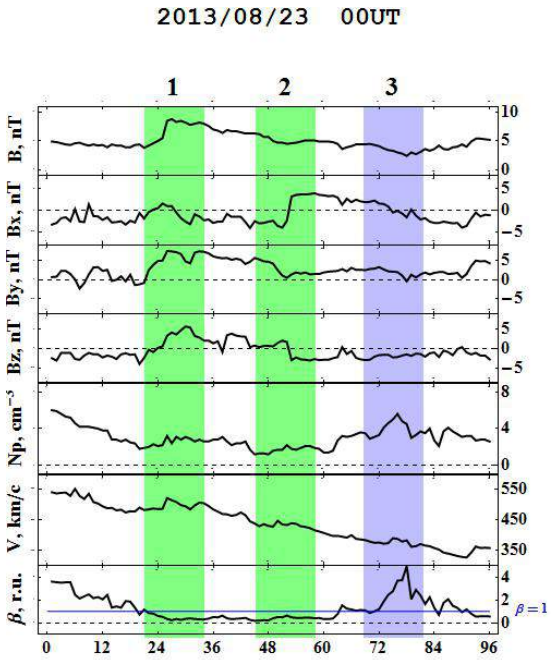

Fig.8. Variations of component B, B_x, B_y and B_z of the magnetic field, density N_p and the velocity V of the plasma, and parameter β in the near-Earth space according to the OMNI database.

Summary

1. In magnetosphere-ionosphere interaction the type of fluctuations with the ~1-hour period is steadily formed whatever type of disturbances.
2. It is confirmed that the large-scale TIDs at ionospheric heights are formed by interchanging instability at the edge of plasmapause.

The work was supported by the Russian Foundation for Basic Research (grant N 12-05-98523).

References

Gershman, B.N., and G.I. Grigoriev(1978), Traveling ionospheric disturbances and their relationship with internal gravity waves. *Ionospheric Res*., 25, 5-15.

Fedorenko,Yu.P.,V.N. Fedorenko, and V.N. Lysenko (2011), Experimental parameters of the model of midlatitude traveling ionospheric disturbances. *Geomagn. and Aeron*., 1, 91-106.

Maltsev,Yu.P. (1995), *Lectures on the magnetosphere-ionosphere physics*, 124 pp., Apatity, KSC RAS.

Paznukhov, V.V., V.G.Galushko, and B.W. Reinisch (2012), Digisonde observations of TIDs with frequency and angular sounding technique*, Adv. Space Res*. 49, 700–710.

Solodovnikov, G.K., A.S. Bakai, and V.M. Russkin (1979), Statistics of irregular structures in the ionosphere, *in: High-latitude manifestations of magnetospheric processes*, Nauka, Leningrad, 118-122.

Stepanov, A.E., and L.D. Filippov (2013), Spectral characteristics of the TIDs by ionospheric data, *in: Proc. Conf."Physics of the Sun and near-Earth space" (Irkutsk, Russia, 16-21 September 2013), ed. by V.M. Grigoriev*, ISZF SO RAN, Irkutsk, 215-216.

RELATIONSHIP OF GROUND GEOMAGNETIC ACTIVITY WITH THE INTERPLANETARY MAGNETIC FIELD AND SOLAR WIND PARAMETERS

S.V. Gromov, A.E. Levitin, L.A. Dremukhina, L.I. Gromova

Pushkov Institute of Terrestrial Magnetism, Ionosphere and Radio Wave Propagation RAS, Moscow, 142190, Russia, e-mail: dremukh@izmiran.ru

Abstract. The correlations between a ground-based geomagnetic activity and the different functions of the state near-earth interplanetary environment are investigated. To determine a quantitative assessment of the local and planetary geomagnetic activity we use the method, proposed earlier as a method of IZMIRAN. Quantitative assessment of a geomagnetic activity is determined on the basis of the data of 26 stations of the Northern Hemisphere as the difference between the observed value of the geomagnetic field at each observatory and field level 2009, the most quiet year for the whole period of the quality observatory measurements. Correlation analysis is performed for the data of 1995-2009 because there is the most comprehensive set of data on the parameters of the interplanetary medium after.

Introduction

The relationship of indices of geomagnetic activity with plasma parameters and the magnetic field of the solar wind near the earth's orbit were studied in numerous works from the time of occurrence data from the spacecrafts. Most often for research were selected average hourly planetary index *Dst*, *Kp*, *ap* and auroral indices *AL*, *AU* and *AE* . All of the above indices were introduced more than half a century ago and have drawbacks. They reflect the increasing of one or another of equivalent current system associated with the calculation of each index. Some researchers have attempted to present the magnetic activity as a number proportional to the change of the magnetic energy in a given period of time. In this case the potential energy of a uniform magnetic field in one cubic centimeter is represented by the expression: $(H^2 + Z^2)/8\pi$, where H and Z are the magnetic field vector horizontal and vertical components, respectively. We consider that the present day approach to the quantitative determination of ground geomagnetic activity should be based on a similar method. Therefore in this work we used quantitative characteristics of the ground-based geomagnetic activity introduced in [Levitin, A. E. et al., 2014].

Methods

Method of estimate of ground geomagnetic activity is based on the data average hourly values of *H*-component measured at 102 observatories of the northern hemisphere as it was described in [Levitin, A. E. et al., 2014]. We selected the geomagnetic field *H*-component registered at observatories since this component most intensely responds to a change in a variable geomagnetic field generated by magnetospheric and ionospheric current systems. As a reference level we selected observations performed in 2009, when extremely low solar and geomagnetic activity was registered. From the observations performed in 2009 we count off geomagnetic activity variations for all previous and subsequent years when the geomagnetic field was registered at each observatory. The method includes processing the hourly average geomagnetic data from the observatories for 1958–2009. It was tested using the data obtained at IZMIRAN observatory and we call this value H_{izm}. Processing includes three steps: selection of the quiet level for each month of year; calculation of the correction for secular variations; calculation of H_{izm}. At the first stage for each month of 2009, we select the day (24 hourly values) when geomagnetic activity was the lowest and the *H*-component amplitude variations (the difference between the maximal and minimal amplitudes) were the smallest. At the second stage a correction for the geomagnetic field secular variations is found from the difference between the quietest days in January for two adjacent years since the geomagnetic field at the observatories in the Northern Hemisphere is most quiet precisely in January. Finally, in the third, the hourly average amplitudes of the *H*- component on a geomagnetically quiet day corrected for the secular variations are then subtracted from the hourly average amplitudes for the same month in all previous and subsequent years. Thus, we obtain the H_{izm} hourly average amplitudes (nT) for each hour on every day of each observatory operation in all years, i.e., the numerical characteristic of local geomagnetic activity. The method described above was

used to process the data of 102 observatories in the Northern Hemisphere and 27 observatories in the Southern Hemisphere, for which the global data centers present rather long data series, including the data for 2009. For further studies from all observatories were selected 26 observatories most evenly distributed on the earth surface. Next the Northern Hemisphere is spatially divided into seven latitudinal belts (from the equator to the pole): 0°–20°, 20°–40°, 40°–55°, 55°–62°, 62°–69°, 69°–80°, and 80°–90°.These belts correspond to the generally accepted regions for determining geomagnetic activity indices. The correspondence of each belt in the Northern Hemisphere to the regions for determining the classical geomagnetic activity indices is presented in the Table 1.

Table 1.
Correspondence of the selected belts in the Northern Hemisphere to the regions where the classical indices of geomagnetic activity are determined

Belt number	Region boundaries (dipole coordinates)	Region characterization
I	00° – 20°	Equatorial region;
II	20° – 40°	*Dst* index determination region;
III	40° – 55°	*Kp* index
IV	55° – 62°	determination region;
V	62° – 69°	Region for determining *AU, AE* and *AL* indices*;*
VI	69° – 80°	Zone of transition from the high latitude current system region to the polar cap
VII	80° – 90°	*PC* index determination region

Each belt includes four observatories, locating possibly longitudinal evenly that is in each of four 90° longitudinal segments, by analogy with the technology for calculating the *Dst* index.

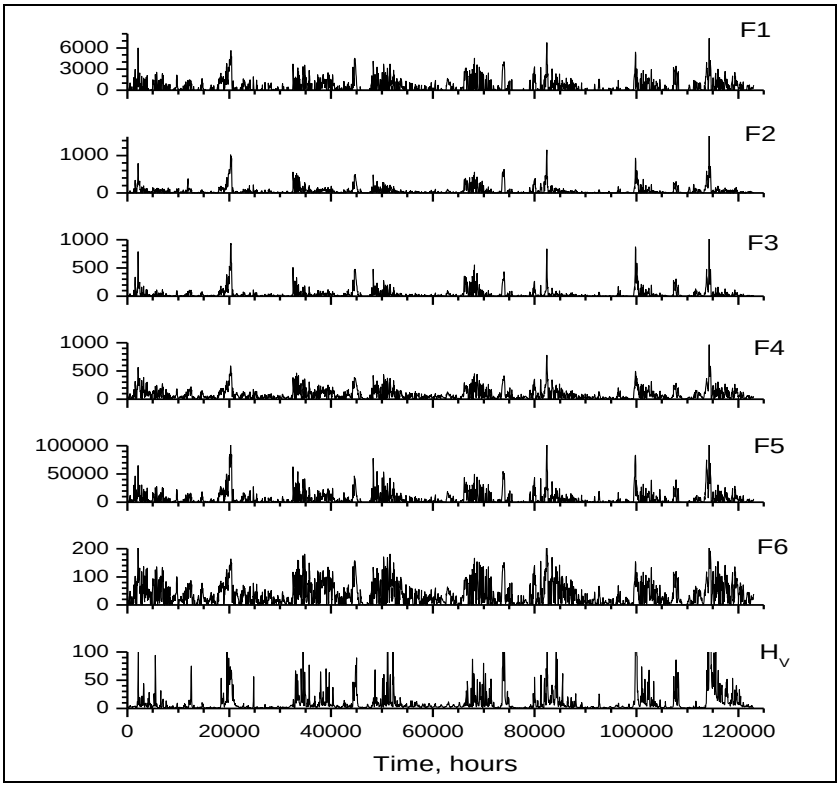

Figure 1. Top six panels – the time variations of the solar wind-magnetosphere coupling functions (F1-F6 from the Table 2) used for correlation analysis for the period 1995-2009. Bottom panel - hourly values of energy estimate of geomagnetic activity H_V*(total)* integrated over the surface of the Northern hemisphere. The abscissa axis represents time in hours.

Using the H_{izm} values obtained by us, we calculate the $(H_{izm})^2$ values for each observatory in each belt. The arithmetic mean for the observatories in each belt is calculated similarly to the *Dst* index. Thus, we obtain the average values of the H_{izm} amplitudes squared for the belts (called H_V by us). The values of the H_V normalized by the area of corresponding belts H_V *(zonal)* characterize the hourly average energy density of a variable geomagnetic field in the selected belts (H_V(I) - H_v(VII)), and their sum corresponds to geomagnetic activity over the entire hemisphere $H_V(total)$ in our opinion.

The obtained values $H_V(zonal)$ and $H_V(total)$ for the period 1995-2009, was used in this work to analyze their relationship with the parameters of the interplanetary medium, taken on the website http//omniweb.gsfc.nasa.gov. The selected period is characterized by the complete data. To perform correlation analysis solar wind-magnetosphere coupling functions of solar wind parameters, the most frequently cited in the scientific literature as geoeffective, were selected . For example, such function were analyzed in [Newell et al., 2007]. Selected for analyze six coupling functions as well their origins are presented in the Table 2.

Table 2.
Solar wind-magnetosphere coupling functions and their origins

Number	Name	Functional form	Origin (reference)
F1	Half-wave rectifier	$V \times B_s$	Burton et al. 1975
F2	ε	$V \times B^2 \times sin^4(\theta/2)$	Perrault and Akasofu, 1978
F3	ε_2	$V \times B_T^2 \times sin^4(\theta/2)$	Variant on ε
F4	E_{KLV}	$V^{4/3} \times B_T \times sin^4(\theta/2) \times p^{1/6}$	Vasyliunas et al., 1982
F5	E_{TL}	$n^{1/2} \times V^2 \times B_T \times sin^6(\theta/2)$	Temerin and Li, 2006
F6	$d\Phi_{MP}/dt$	$V^{4/3} \times B_T^{2/3} \times sin^{8/6}(\theta/2)$	Newell et al., 2007

Functions F1-F5 from the Table 2 are various combinations of the basic solar wind parameters: flow speed *V*, proton density *n*, IMF south component B_S magnetic field magnitude *B*, vertical component $B=(B_Z^2+B_Y^2)$, IMF clock angle $\theta=arctan(B_Y/B_Z)$, and F6 represents the rate magnetic flux opened at the magnetopause [Newell et al., 2007]. Figure 1 shows the time variations of solar wind-magnetosphere coupling functions used for the analysis over the period 1995-2009 years. On the bottom panel of Figure 1 the time variations of $H_V(total)$ for the 1995-2009 are presented.

Results

Correlations between all six solar wind-magnetosphere coupling functions (from the Table 2) and the values of the energy assessment of geomagnetic activity of each latitudinal belt separately and integrated over all latitudes were calculated.

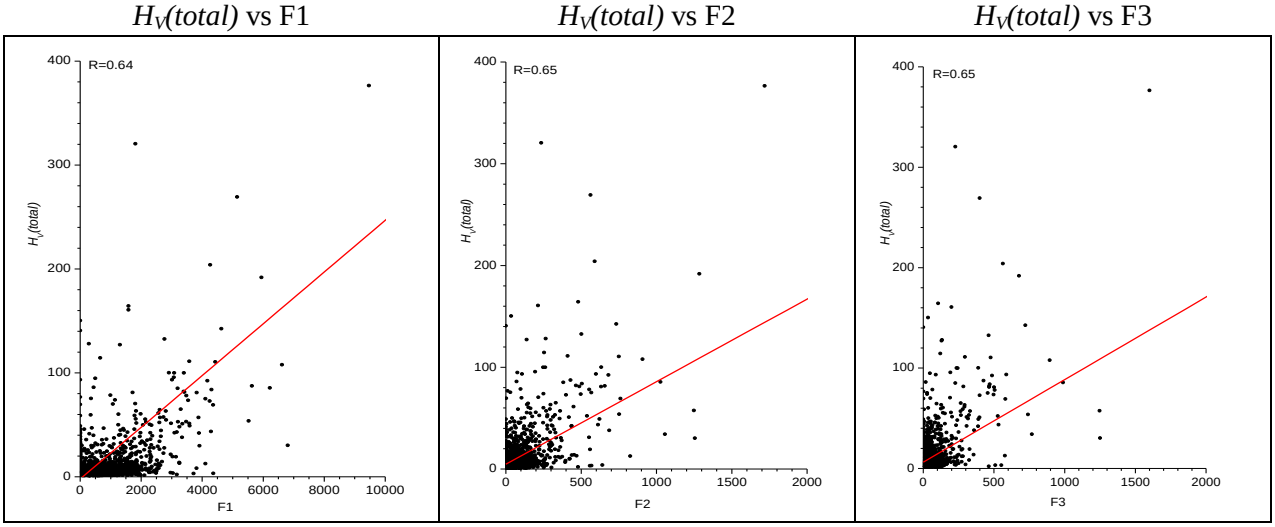

Figure 2. Scatterplots (left to right) of: $H_V(total)$ versus $V \times B_s$, $H_V(total)$ versus ε and $H_V(total)$ versus ε_2

Figure 2 illustrates scatterplots of $H_V(total)$ versus $V \times B_s$ (left), $H_V(total)$ versus ε (in the center) and $H_V(total)$ versus ε_2 (right), producing R=0.64, R=0.65 and R=0.65, respectively. The same but for the E_{KLV}, E_{TL} and $d\Phi_{MP}/dt$ is shown in Figure 3. Correlation coefficients are, respectively, R=0.60, R=0.65 and R=0.61. Thus, the best coupling function is ε Akasofu and its variant. Examples of scatterplots of zonal H_V(V) versus ε and H_V(V) versus ε_2 are presented in Figure 4. Correlations between zonal H_V(V) are the best with all coupling functions.

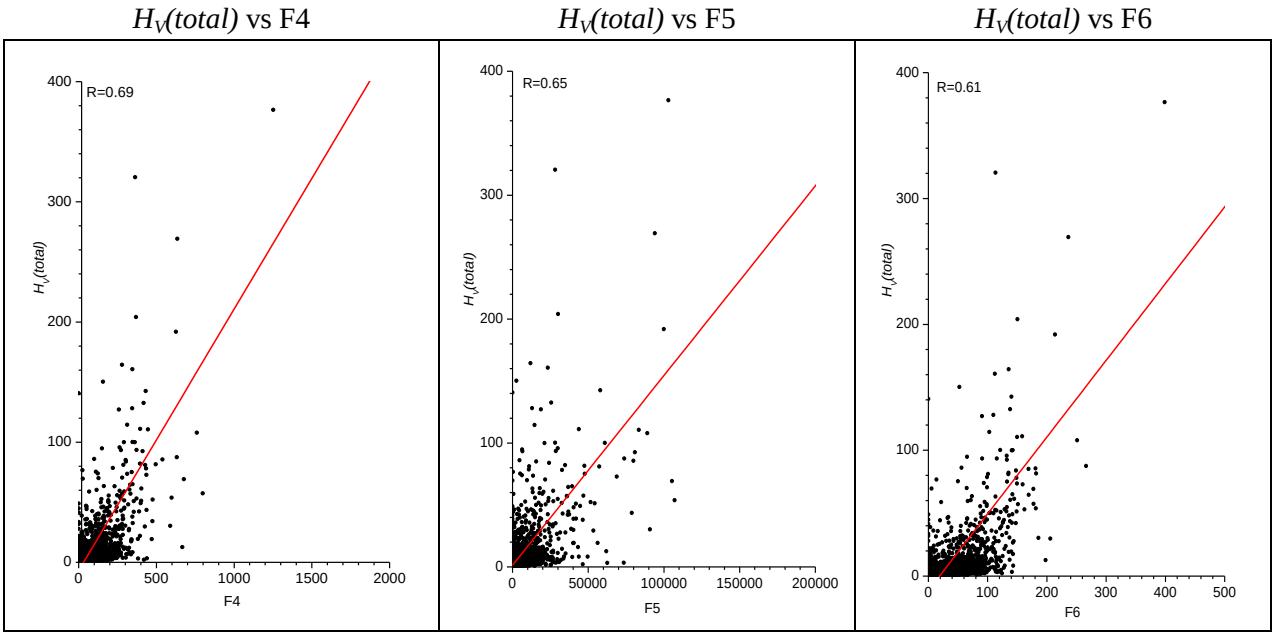

Figure 3. Scatterplots (left to right) of: $H_V(total)$ versus E_{KLV}, $H_V(total)$ versus E_{TL}) and $H_V(total)$ versus $d\Phi_{MP}/dt$.

Numerical results of made correlation analysis are presented in the Table 3. From the Table 3 it can be seen that the correlation between the analyzed parameters is very weak (the correlation coefficients do not exceed the value 0.50) for two high-latitudinal belts, and increases for mid-latitudinal regions, reaching maximum

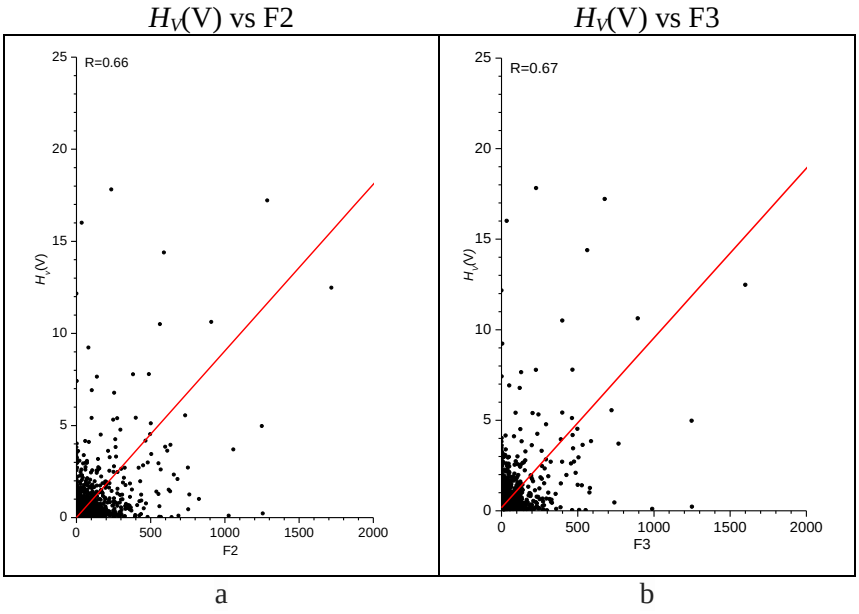

Figure 4. Scatterplots of H_V(V) versus E_{KLV} (a) and H_V(V) versus ε_2 (b).

values in the belt V. The maximum relationship between parameters within the belt V was received for functions F2 and F3 (Akasofu parameter and its modification). The integral over the Northern Hemisphere geomagnetic activity is correlated considerably better with all solar wind-magnetosphere coupling functions. The correlation coefficients for all functions F1-F6 exceed the value 0.60 at a maximum value of 0.69 for the function F4, which includes magnitude of the solar wind dynamic pressure.

Table 3**.**
Correlation coefficients between solar wind - magnetosphere coupling functions F1-F6 and H_V*(zonal)* for belts I-VII and H_V*(total)*

F/H	$H_V(I)$	$H_V(II)$	$H_V(III)$	$H_V(IV)$	$H_V(V)$	$H_V(VI)$	$H_V(VII)$	$H_V(total)$
F1	0.39	0.39	0.60	0.52	0.51	0.46	0.44	0.64
F2	0.31	0.31	0.49	0.62	0.66	0.54	0.54	0.65
F3	0.29	0.29	0.47	0.63	0.67	0.54	0.53	0.65
F4	0.42	0.42	0.60	0.56	0.60	0.52	0.50	0.69
F5	0.36	0.36	0.55	0.58	0.59	0.48	0.47	0.65
F6	0.43	0.43	0.59	0.44	0.45	0.42	0.39	0.61

It is interesting how the relationship between solar wind - magnetosphere coupling functions and geomagnetic activity changes during disturbed periods. The next step was the correlation analysis for periods with *Dst* <- 30 nT that is a week magnetic storm. The results such correlation analysis are presented in the Table 4. One can see from the Table 4 that correlations change differently depending on a latitude of belts. Correlations deteriorate for three high-latitude belts except function F4 in the belt I and function F6 in the belt VI. But in all belts with latitudes below 55° correlations improved, and the correlation coefficients between H_V*(total)* and all coupling functions exceed value 0.65.

Table 4**.**
Correlation coefficients between solar wind - magnetosphere coupling functions F1-F6 and H_V*(zonal)* for belts I-VII and H_V*(Total)* for periods with *Dst* < -30 nT

F/H	$H_V(I)$	$H_V(II)$	$H_V(III)$	$H_V(IV)$	$H_V(V)$	$H_V(VI)$	$H_V(VII)$	$H_V(total)$
F1	0.29	0.29	0.46	0.62	0.66	0.53	0.54	0.65
F2	0.29	0.29	0.47	0.63	0.67	0.54	0.53	0.65
F3	0.29	0.29	0.46	0.64	0.68	0.53	0.54	0.65
F4	0.38	0.38	0.58	0.63	0.65	0.55	0.54	0.72
F5	0.32	0.32	0.53	0.62	0.62	0.49	0.49	0.65
F6	0.39	0.39	0.63	0.55	0.55	0.46	0.45	0.67

Our study is of a pioneering nature. The introduction of a new parameter to characterize geomagnetic activity requires a careful approach. It is likely that low values of the correlation coefficients, received for high-latitudinal belts, indicate that one of the horizontal *H*-component of observed geomagnetic field is not enough to describe an energy estimate of ground geomagnetic activity at high latitudes. A significant contribution can be provided by a vertical *Z*-component, and it needs to be taken into account in such studies.

Conclusions

The results of correlation analysis confirm the existence of a good relationship between the ground geomagnetic activity obtained from the data of observatories in the Northern Hemisphere according to the method of IZMIRAN, and the plasma and the magnetic field parameters of the solar wind near the earth's orbit in the form of functions, reflecting the magnitude of the electric field of the solar wind and the magnetic flux penetrating in the magnetopause (solar wind-magnetosphere coupling functions). It was not found suffice relationship between the coupling functions and values of the zonal geomagnetic activity for high-latitudinal belts with latitudes greater than 55°. It is probably, that correlations between the ground geomagnetic activity in high-latitudinal regions can be improve taking into account in the calculations the vertical *Z*-component of geomagnetic field in the calculation of the energy estimate of ground geomagnetic activity.

It was shown a slight increase in correlation coefficients for periods of increased geomagnetic activity (index *Dst* < -30 nT).

Acknowledgements

This work was supported by the Russian Foundation for Basic Research, project nos. 13_05_00233.

References

Levitin, A. E., L. I. Gromova, S. V. Gromov, and L. A. Dremukhina (2014), Quantitative Estimation of Local Geomagnetic Activity Relative to the Level of the Magnetically Quiet Period in 2009. *Geomagnetism and Aeronomy*, 54, No. 3, 315–323.

Newell, P. T., T. Sotirelis, K. Liou, C.-I. Meng, and F. J. Rich (2007), A nearly universal solar wind-magnetosphere coupling function inferred from 10 magnetospheric state variables. *J. Geophys. Res.*,112, A01206, doi:10.1029/2006JA012015.

SPATIAL DISTRIBUTION OF QUANTITATIVE ASSESSMENT OF GEOMAGNETIC ACTIVITY DURING STORMS OF DIFFERENT INTENSITY

S.V. Gromov, A.E. Levitin, L.I. Gromova, L.A. Dremukhina

Pushkov Institute of Terrestrial Magnetism, Ionosphere and Radio Wave Propagation , Troitsk, 142090, Russia, e-mail : sgromov@izmiran.ru

Abstract. To estimate local geomagnetic activity during storms of different intensity we used our method of quantitative assessment of geomagnetic activity. It is based on measurements of *H*-component of the geomagnetic field of observatories located in the Northern hemisphere. Hourly data of 1958 -2009 from more than 100 magnetic observatories were processing. Extremely quiet 2009 state of the geomagnetic field was assumed as a reference level of the geomagnetic activity magnetic observations. Local geomagnetic activity is estimated in the latitudinal belts close to the geomagnetic activity indices domains. Our estimation of local geomagnetic activity differs from that presented by *Dst* index. We demonstrate our results for moderate, intensive, large and major storms selected during 1958 - 2009 in different seasons of a year and propose a method to estimate intensity of magnetic storms based on our quantitative assessment of geomagnetic activity.

Quantitative assessment of geomagnetic activity *Hizm*

To quantitatively describe local geomagnetic activity, we selected the geomagnetic field *H* component registered at observatories since this component most intensely responds to a change in a variable geomagnetic field generated by the magnetospheric and magnetospheric_ionospheric current systems. As a reference level we selected 2009, when solar and geomagnetic activity was the lowest when magnetic stations registered mainly variation of the internal field of the Earth. The method for determining the geomagnetic activity value (this value is named *Hizm*) includes processing the hourly average geomagnetic data from the observatories for 1958–2009. For each month of 2009, we select the day when geomagnetic activity was the lowest and the *H* component amplitude variations (the difference between the maximal and minimal amplitudes) were the smallest. A correction for the geomagnetic field secular variations is found from the difference between the quietest days in January for two adjacent years since the geomagnetic field at the observatories in the Northern hemisphere is most quiet precisely in January in our opinion. The hourly average amplitudes of the *H* component on a geomagnetically quiet day corrected for the secular variations are then subtracted from the hourly average amplitudes for the same month in all previous and subsequent years. Thus, we obtain the *Hizm* hourly average amplitudes (nT) for each hour on every day of each observatory operation in all years, i.e., the numerical characteristic of local geomagnetic activity reflected mainly the impact of an external sources on variation of the geomagnetic field. [Levitin et al., 2014**].** We measure geomagnetic activity is measured as an hourly amplitude squared (i.e., $Hizm^{2)}$, calculated using the *H* component method described above. This assessment provides an opportunity to compare the geomagnetic activity at different stations, not only qualitatively but also quantitatively.

The method described above was used to process the data of 102 observatories in the Northern hemisphere for which the global data centers present rather long data series, including the data for 2009 (http://http://www.wdc.bgs.ac.uk).

Assessment of geomagnetic activity during storms of different intensity in dirrefent seasons

To estimate spatial distribution of geomagnetic activity the Northern hemisphere was divided into belts with widths 15°–20°, so that each belt includes four observatories, possibly locating symmetrically in each of four 90° longitudinal segments, by analogy with the technology for calculating the *Dst* index. The Northern hemisphere is spatially divided into seven latitudinal belts (from the equator to the pole): 0°–20°, 20°–40°, 40°–55°, 55°–62°, 62°–69°, 69°–80°, and 80°–90° (Fig.1). These belts correspond to the generally accepted regions for determining geomagnetic activity indices. Three lower belts coincide with the belts in the Northern Hemisphere, and a higher belt (from –55° to –69°) forcedly combines part of the region where the *Kp* index is determined with the region for determining the *AU*, *AE*, and *AL* indices. One polar region also

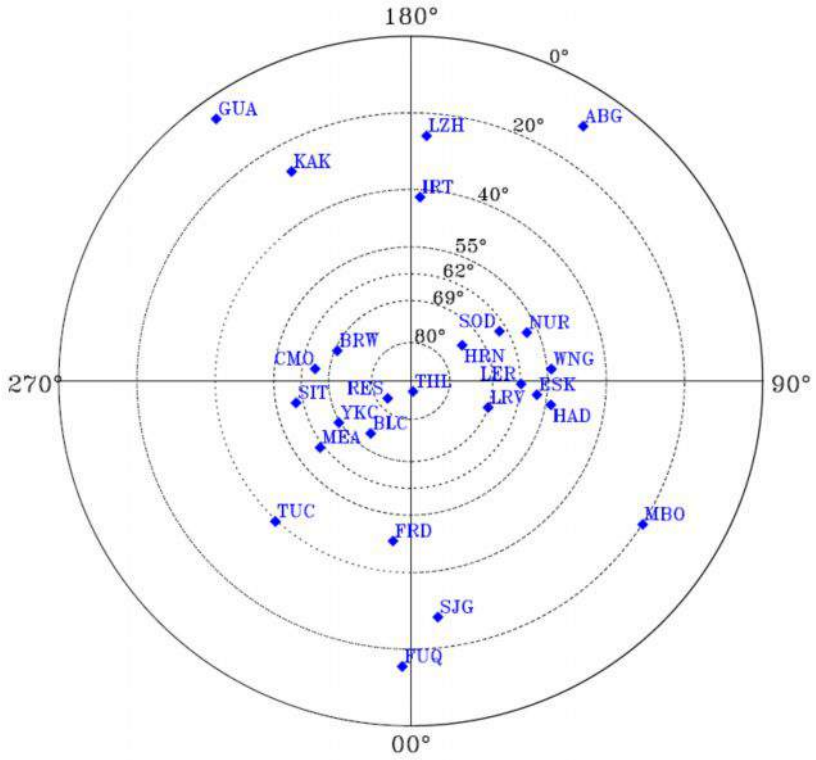

Fig.1 Division of the Northern hemisphere into belts and the location of the geomagnetic observatories selected in order to analyze *Hv* in different latitudinal belts during magnetic storms. Dipole coordinates.

combines the zone of transition from the area of high_latitude current systems to the polar cap and the polar cap. The location of the observatories selected for processing are presented in Fig. 1.

Using obtained *Hizm* values, $Hizm^2$ values were calculated for each observatory in each belt. The arithmetic mean for the observatories in each belt is calculated similarly to the *Dst* index. Thus, we obtain *Hv* value as the average values of the *Hizm* amplitudes squared for the belts which characterize the hourly average energy density of a variable magnetic field in the selected belt in our opinion.

Geomagnetic activity was examined during some storms of different intensity occurred in the different seasons of 2000 -2009 years. Major storms are identified with Dstmin < -300 nT; large ones are identified with 300 nT < Dstmin < -200 nT; intense ones are identified with -200 nT < Dstmin < -100 nT; moderate storms are identified with -100 nT < Dstmin < -50 nT.

Figures 2, 3, 4, and 5 show the *Hv* values (a solid line) in comparison with the *Dst* index (a dotted line) in the belts in the Northern hemisphere for major, large, intensive, and moderate magnetic storms. The boundaries of the selected belts (from top to bottom) from the polar belt to the equatorial belt in dipole coordinates are shown on the left. Roman numerals correspond to regions in the Northern hemisphere taken for determining the classical geomagnetic activity indices. Vertical dashed lines mark the beginning of the storm initial phase and the end of the recovery phase. Each figure presents comparison of spatial distribution of geomagnetic activity in the Northern hemisphere during major/ large/intensive/ moderate storms in Winter, Equinox, and Summer.

Conclusion

Method of quantitative assessment of local geomagnetic activity was used to describe spatial distribution of geomagnetic activity during storms of different intensity in different seasons of year. Analyze allows to assume that total planetary geomagnetic activity is created in the high_latitude regions. This is part of the high_latitude activity that is formed from the compression of the dayside magnetosphere caused by solar wind (a change in the geomagnetic field topology) and is shifted to subauroral latitudes: in winter up to 55°-80° during major and large storms and up to 62° - 69°during intensive one, in equinox and summer distributions shift up to 55°- 62°. During moderate storms perturbation don't shift up to 55°-62°**.** Geomagnetic activity in the polar region (80° - 90°) generally weaker than in the auroral latitudes in winter and equinox, and during major and large storms perturbations shift up to the polar cap only.

Acknowledgment. This study was supported by RFBR grant № 13-05-00233

References

A.E. Levitin, L. I. Gromova, S. V. Gromov, and L. A. Dremukhina (2014) Quantitative Estimation of Local Geomagnetic Activity Relative to the Level of the Magnetically Quiet Period in 2009, *Geomagnetism and Aeronomy,* 54, No. 3, 292–299

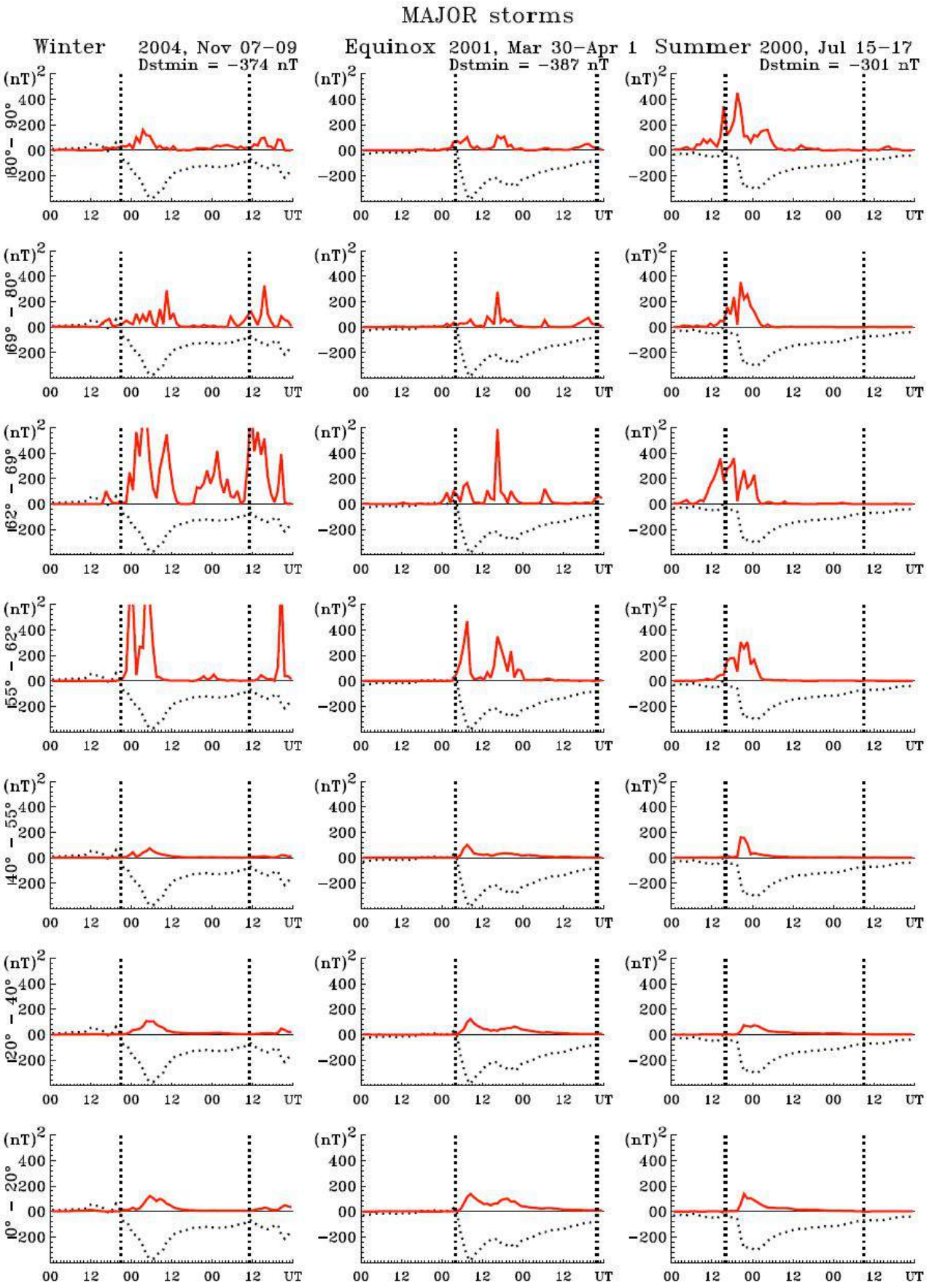

Fig. 2. Variation of energy estimation *Hv*, in selected latitudinal belts of the Northern hemisphere in comparison with *Dst*-index during major magnetic storms occurred in the different seasons of a year. Solid line marks *Hv* variation, dotted one marks variation of *Dst* module. The moments of the beginning of the preliminary phase and the end of the recovery phase of each storm are shown by vertical dotted lines.

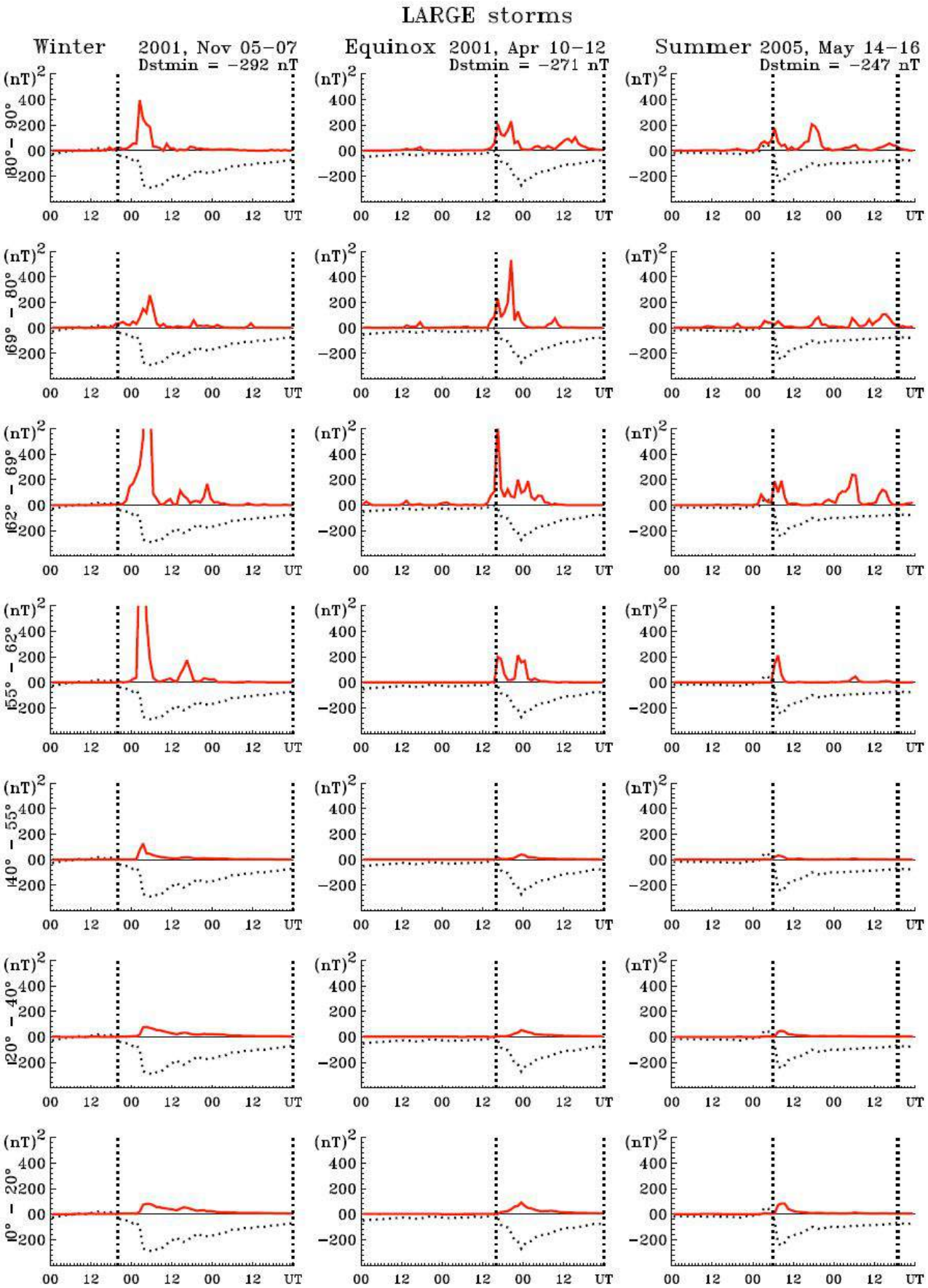

Fig. 3. The same as Fig. 2 but during large storms.

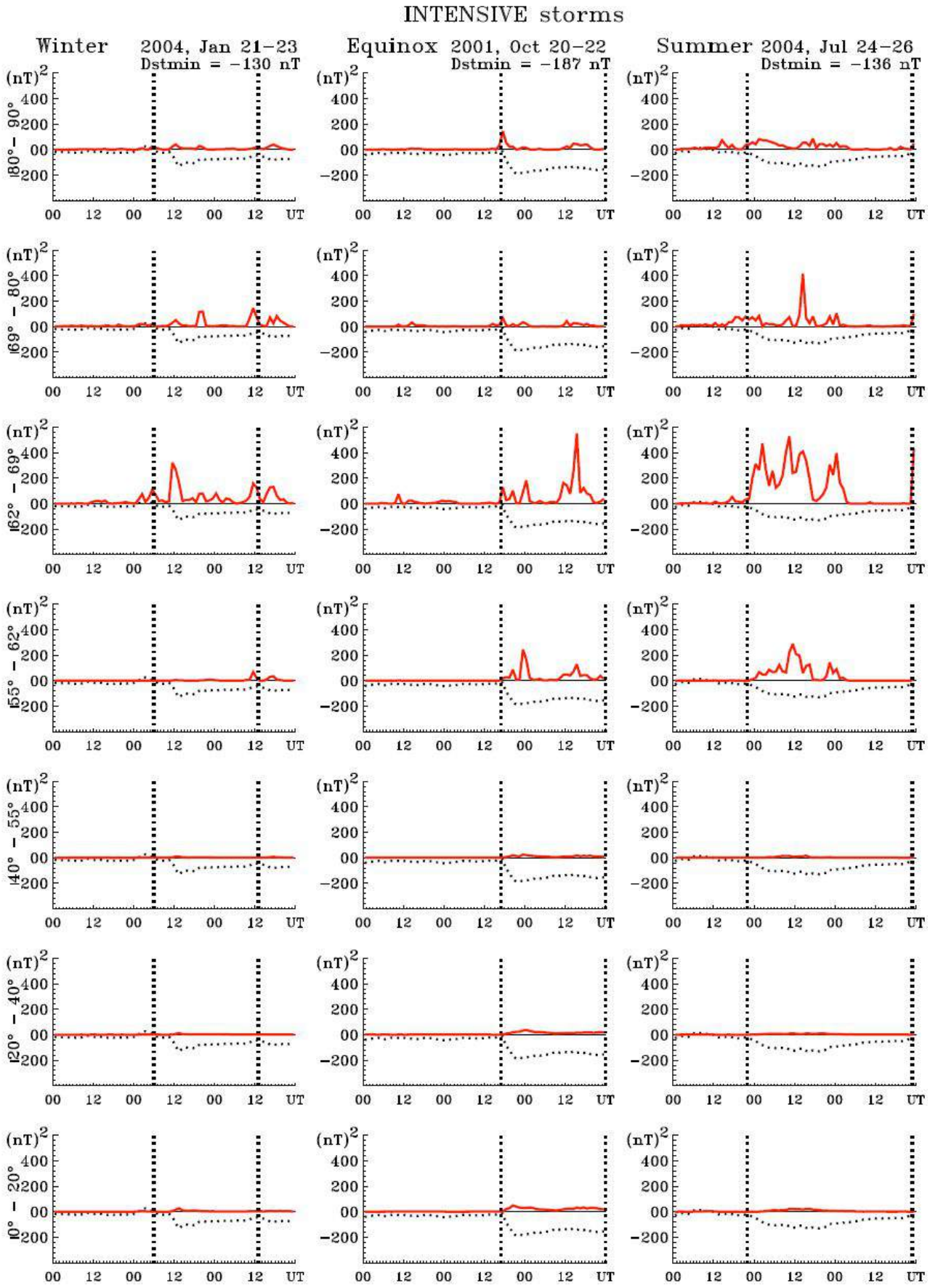

Fig. 4. The same as Fig. 2 but during intensive storms.

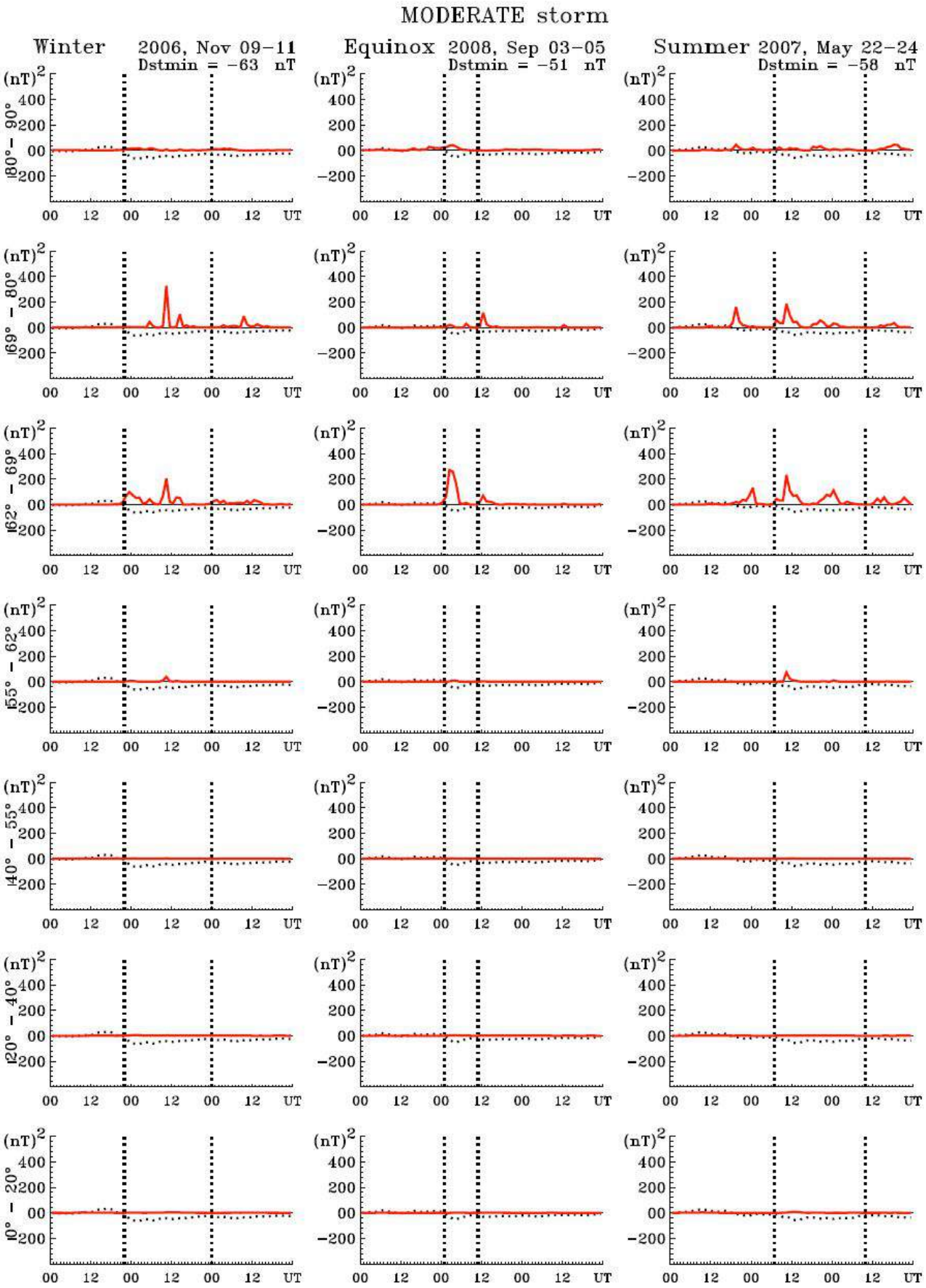

Fig. 5. The same as Fig. 2 but during moderate storms.

SUBSTORM OBSERVATIONS IN APATITY DURING DIFFERENT SOLAR WIND CONDITIONS

V. Guineva[1], I.V. Despirak[2], B.V. Kozelov[2]

[1]Space Research and Technology Institute, BAS, Stara Zagora, Bulgaria, e-mail: v_guineva@yahoo.com;
[2]Polar Geophysical Institute, RAS, Apatity, Russia

Abstract. All-sky camera data obtained at Apatity (Kola Peninsula) during 2012/2013 winter season have been used to study the variation of substorm development during different conditions of the interplanetary medium. Solar wind and interplanetary magnetic field parameters were taken from CDAWeb. Using WIND satellite data for the examined periods, the different solar wind streams were revealed: high speed streams from coronal magnetic holes (HSS) and magnetic clouds (MC) connected with non-stationary processes at the Sun. It is known that these solar wind structures are the sources of geomagnetic storms. Furthermore, the storms originating from these sources differ in intensity, recovery phase duration, etc. We investigated substorm development during storms and during quiet conditions. Substorm onset time and further development were verified by ground-based data of IMAGE magnetometers network and Apatity all-sky camera. The particularities in the behavior of substorms observed during storms and during quiet conditions are discussed.

Introduction

It is known, that the substorm appearance and development depend on the conditions in the solar wind [e.g., Yahnin et al., 2004]. Studies were carried out on the influence of different geoeffective parameters of the solar wind and IMF (IMF B_z component, solar wind flow speed etc.) on the position of the auroras boundaries during substorms [e.g., Vorobev and Zverev, 1982], on the latitude of the substorm onset [e.g., Gerard et al., 2004], on the substorm appearance at high geomagnetic latitudes [e.g., Sergeev, Yakhnin and Dmitrieva, 1979; Despirak et al., 2008; Despirak, Lyubchich and Kleimenova, 2014]. It should be noted that it is important to consider the interplanetary parameters that are characteristic for different solar wind streams and structures in combination but not the solar wind effect separately. It is known that different combinations of geoeffective parameters (velocity, density, the B_z component of the IMF, etc.) are typical for solar wind streams different in nature [e.g. Yermolaev et al., 2009]. So, for high speed recurrent solar wind streams high velocities and low values of the negative B_Z component of the IMF are typical characteristic [see e.g., Tsurutani et al., 2006]. The magnetic clouds (MCs) have high magnetic field values with long interval of negative B_Z component of the IMF and also increased values of plasma velocity [Klein and Burlaga, 1982; Burlaga et al., 1982]. The compressed plasma regions in front of these streams (the CIR and Sheath regions) are characterized by high solar wind density and a high magnitude of magnetic field [Balong et al., 1999]. It is known also that these three types of solar wind structures (MC, CIR and Sheath) are usually reasons of geomagnetic storms that differ by their main characteristics depending on the generating structure [e.g. Yermolaev and Yermolaev, 2006; Tsurutani et al., 2006]. Therefore, substorms could be observed under different interplanetary conditions: during the passage of different solar wind streams and structures by the Earth, during development of different geomagnetic storms, as well as in quiet conditions.

In our paper we are presenting substorm observations in Apatity under different interplanetary conditions. Apatity is settled at auroral latitudes. Its geographic coordinates are: 67.58ºN, 33.31ºE, and the corrected geomagnetic ones – 63.86ºN, 112.9ºE. This location is expedient to examine the variety of substorms.

Data

All-sky camera data observed at Apatity during the 2012/2013 winter season have been used. The all-sky camera has being installed in Apatity since 2008 as a part of the observational system MAIN (Multiscale Aurora Imaging Network). It comprises 4 auroral cameras with different fields of view providing simultaneous observations from spatially separated points. The cameras characteristics, their mutual situation and the measurement process are described in detail by [Kozelov et al., 2011] and [Kozelov et al., 2012].

Solar wind and interplanetary magnetic field parameters were taken from CDAWeb (http://sdaweb.gsfc.nasa.gov/cdaweb/istp_public/). OMNI data base revealed different solar wind streams: high speed recurrent streams from coronal magnetic holes (HSS) and magnetic clouds (MC) or quiet conditions for the examined periods.

Substorm onset time and further development were verified by data of Apatity all-sky camera and by ground-based data of IMAGE magnetometers network (using meridional chain Nurmijarvi (NUR) - Ny Alesund (NAL)), Lovozero and Loparskaya magnetometers.

The measurements during 2012/2013 season were examined together with the interplanetary conditions during the measuring periods. During the winter observational season, from October 2012 to March 2013, 4 magnetic clouds (MC) and 6 high speed recurrent streams (HSS) were detected. Some of them provoked geomagnetic storms. During the storm development and under quiet conditions the Apatity all-sky camera registered 37 substorm disturbances (substorms and their intensifications).

Below we are going to present 3 typical examples of substorm observations in Apatity: during a magnetic cloud under highly disturbed conditions, during a high speed recurrent stream under disturbed conditions and in non-storm time, under quiet conditions.

Observations

Case 1: 17.03.2013.

On 17.03.2013 a magnetic cloud passed by the Earth, and a geomagnetic storm with Dst ~ -140 nT developed. We considered substorms observations during the highly disturbed period, 17-18 March 2013, in Apatity. Figure 1 presents some solar wind and IMF parameters and observations of substorm westward electrojet development by IMAGE magnetometers chain on 17 March 2013.

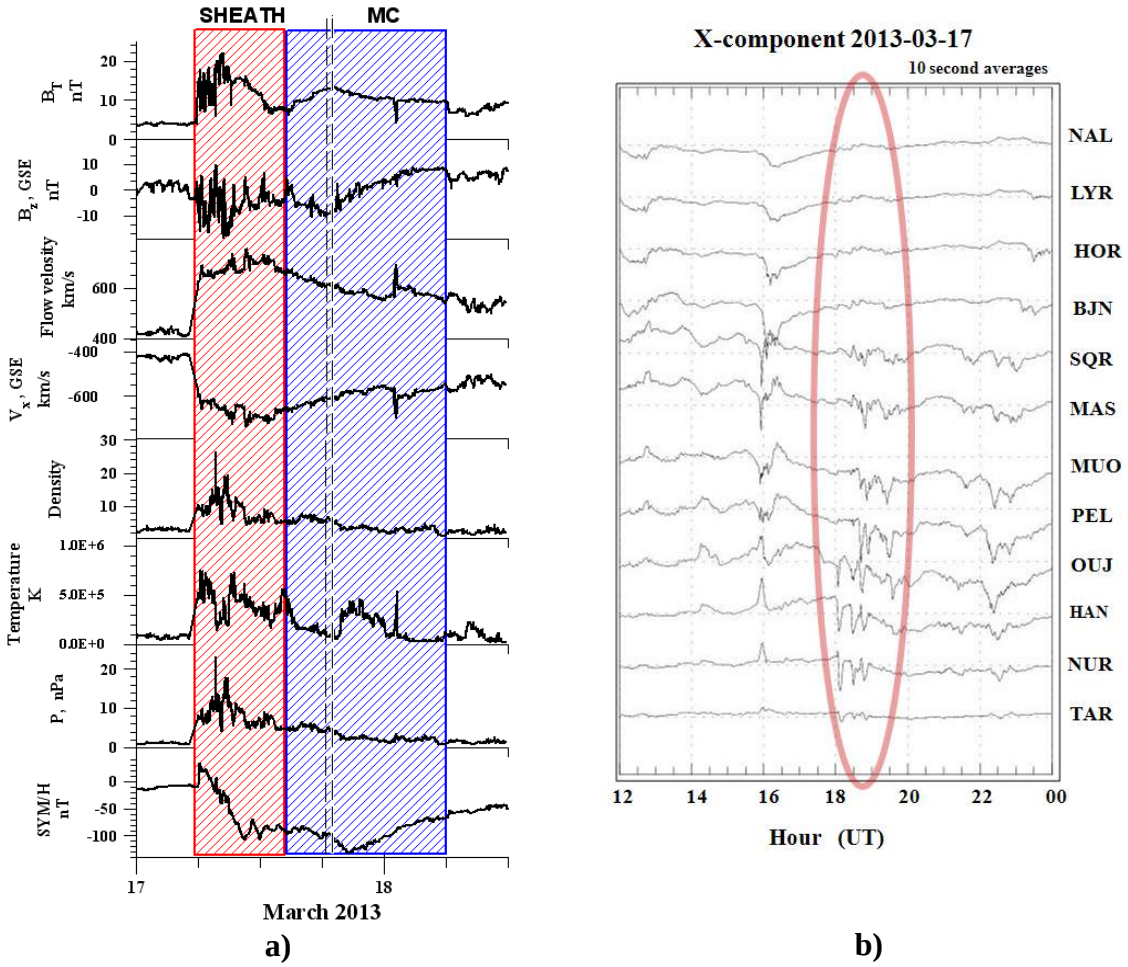

Fig.1. Event on 17 March 2013 – Magnetic cloud. (a) - parameters of the solar wind and the IMF and index SYMN \ H. The boundaries of the magnetic cloud (MC) and Sheath regions are shown by shaded blue and red rectangles, respectively. The onset of the substorms according IMAGE and all-sky camera are marked by dashed vertical lines; (b) - magnetograms (X- components) of the IMAGE TAR–NAL station chain in the 12–24 UT interval (right panel); the oval shows substorms at 18:26 UT and 18:39 UT under study.

The all-sky camera data on 17 March 2013 are presented in Figure 2. The all-sky camera in Apatity registered the substorm onset in 18:26:40 UT and the second substorm intensification in 18:39:40 UT. In Figure 2, chosen images of the substorm developments are shown, the world directions are marked in the first image, the universal time is written above each image. The substorm beginning to the South from the station, the arcs movement to the North, reaching the station zenith (18:32 UT) and surpassing it are seen. The second intensification at Apatity begins with an equatorial arc burst in 18:39:40 UT. After that, auroras move toward zenith, reach it at 18:41:40, and continue moving northward.

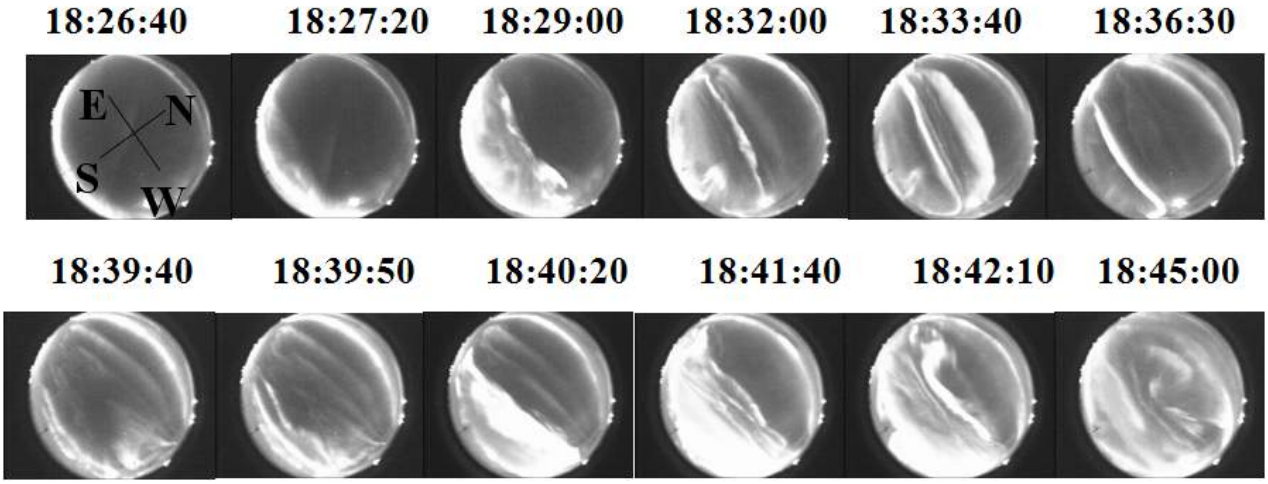

Fig. 2. Dynamics of auroras according to the all-sky camera data during two substorms of March 17, 2013. The top panel shows some all-sky camera images for first substorm (from 18:26 to 18:36 UT), the bottom panel shows ones – for second substorm (from 18:39 to 18:45 UT). The world directions are marked in the first image, the universal time is written above each image

Case 2: 29-30 March 2013.

On 29-31 March 2013, a high speed recurrent stream (HSS) passed by the Earth, and a geomagnetic storm with minimal D_{st} ~ -65 nT developed. The conditions can be considered as disturbed.

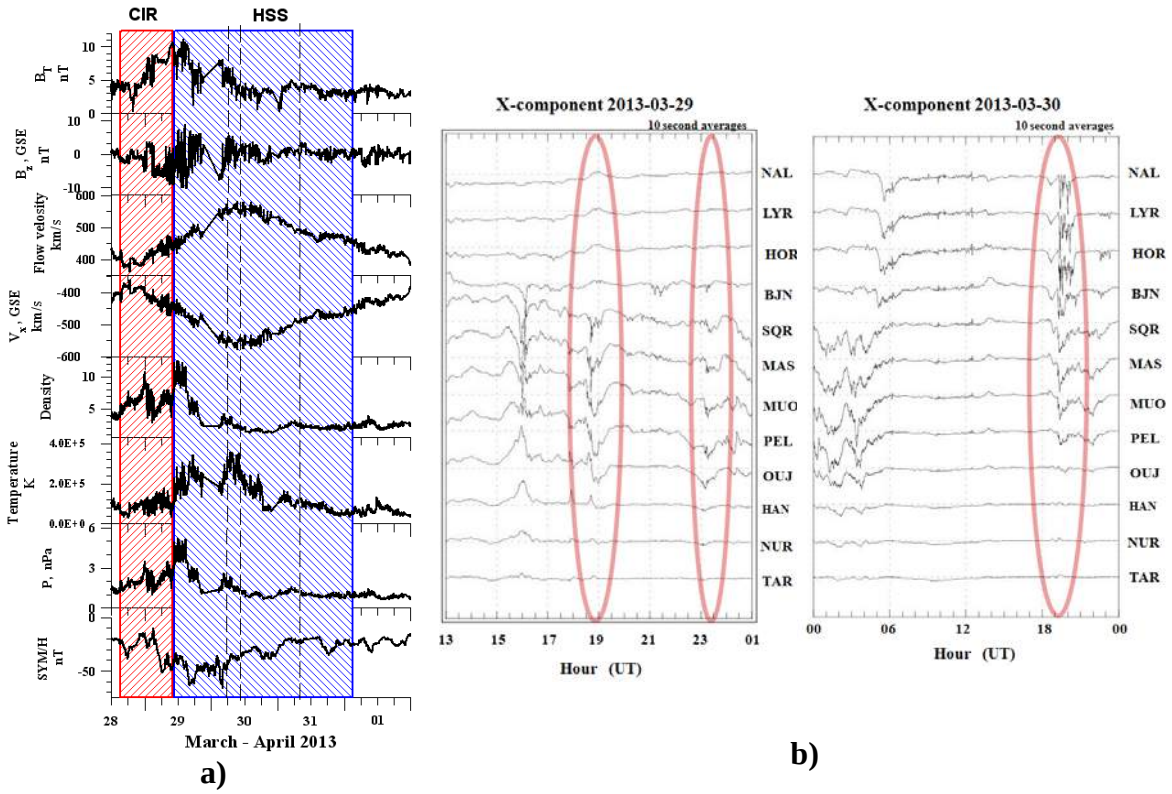

Fig. 3. Event on 29 March 2013 – High speed recurrent stream. The format of Figure 3 is the same as that of Figure 1. However in Figure 3b are presented two days of observations: on 29 March (top panel) and on 30 March (bottom panel), 2013.

In Fugure 4 the auroras dynamics according to the all-sky camera data during these 3 substorms of March 29 and 30 March, 2013 is presented. The format of Figure 4 is the same as the one of Figure 2. On 29 March the all-sky camera in Apatity registered two substorms: in 18:26:00 UT and in 23:07:20 UT. In Figure 4a and 4b, chosen images of the substorms developments are shown. These two substorms develop by a similar scheme: substorm beginning to the South from the station, arcs movement to the North, reaching the station zenith and surpassing it. On 30 March, 2013 the all-sky camera in Apatity registered one substorm, beginning in 19:11:20 UT. In Figure 4c, chosen images of this substorm development are shown. This substorm behavior follows another scheme: substorm beginning to the North from the station, arcs movement to the South, reaching the station zenith and surpassing it. This substorm is observed during the recovery phase of the geomagnetic storm associated with CIR as shown in Figure.3a. The substorm onset was to the North of Apatity and only the South part of the substorm is observed from the station.

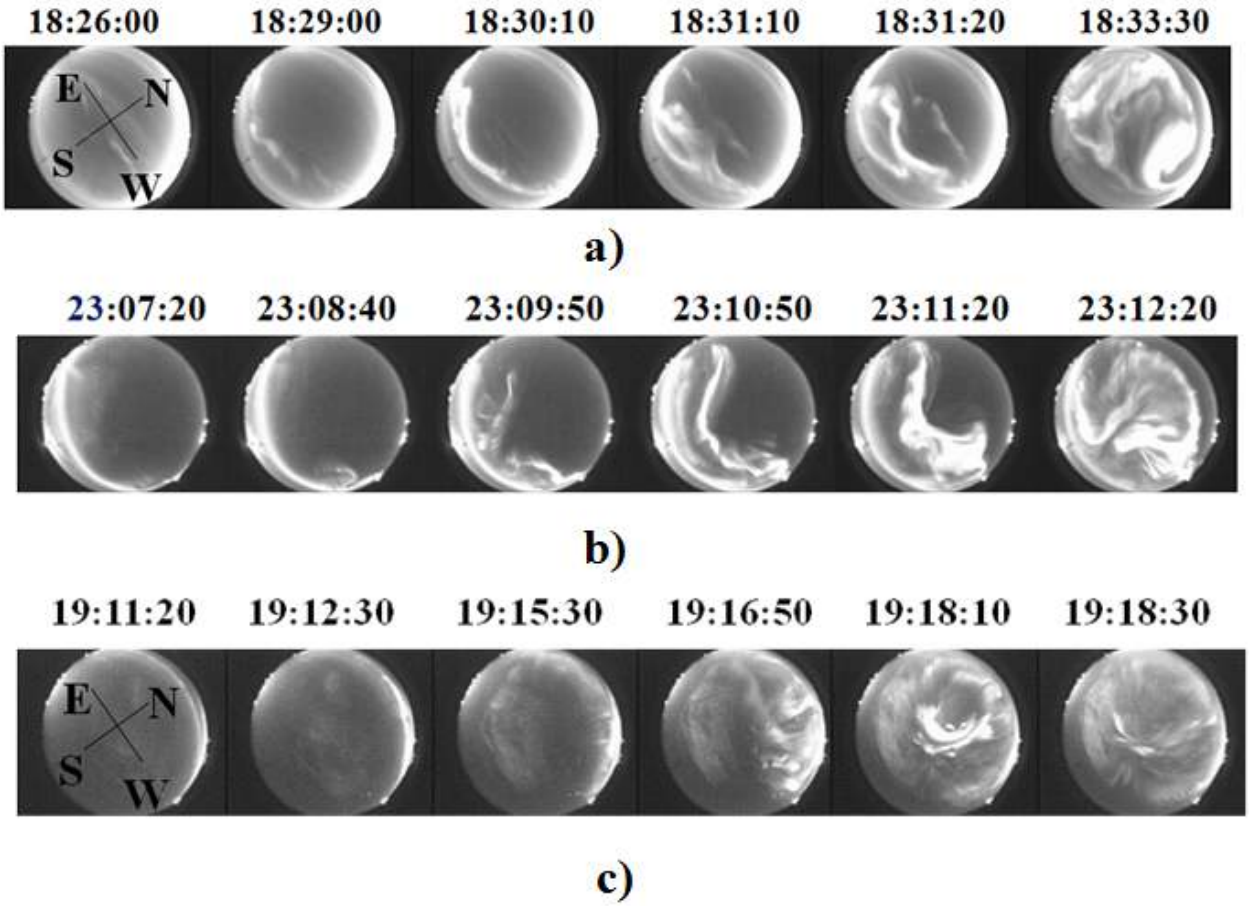

Fig. 4. Dynamics of auroras according to the all-sky camera data during 3 substorms of March 29 -30, 2013. 3(a) - some all-sky camera images for first substorm (from 18:26 to 18:33 UT), 3(b) - for second substorm (from 23:07:20 to 23:12:20 UT), 3(c) – for third substorm (from 19:11:20 to 19:18:30 UT).

Case 3: 10.04.2013.

On 10 April 2013 non-storm, quiet conditions were observed in the solar wind.

Figure 5 presents solar wind and IMF parameters and observations of substorm westward electrojet development by IMAGE magnetometers chain on 10 April, 2013.

In Fugure 6 the auroras dynamics according to the all-sky camera data during this substorm on April 10, 2013 is presented. The all-sky camera in Apatity registered one substorm in 21:28:00 UT. In Figure 6, chosen images of the substorm development are shown. It is seen that the substorm begins to the North from the station, then the auroras move to the South, reaching the station zenith and surpassing it. It should be noted that this substorm develops by a scheme similar to the event on 30 March 2013 when the substorm onset was also to the North from Apatity and only the development of the South part of the substorm was observed from the station.

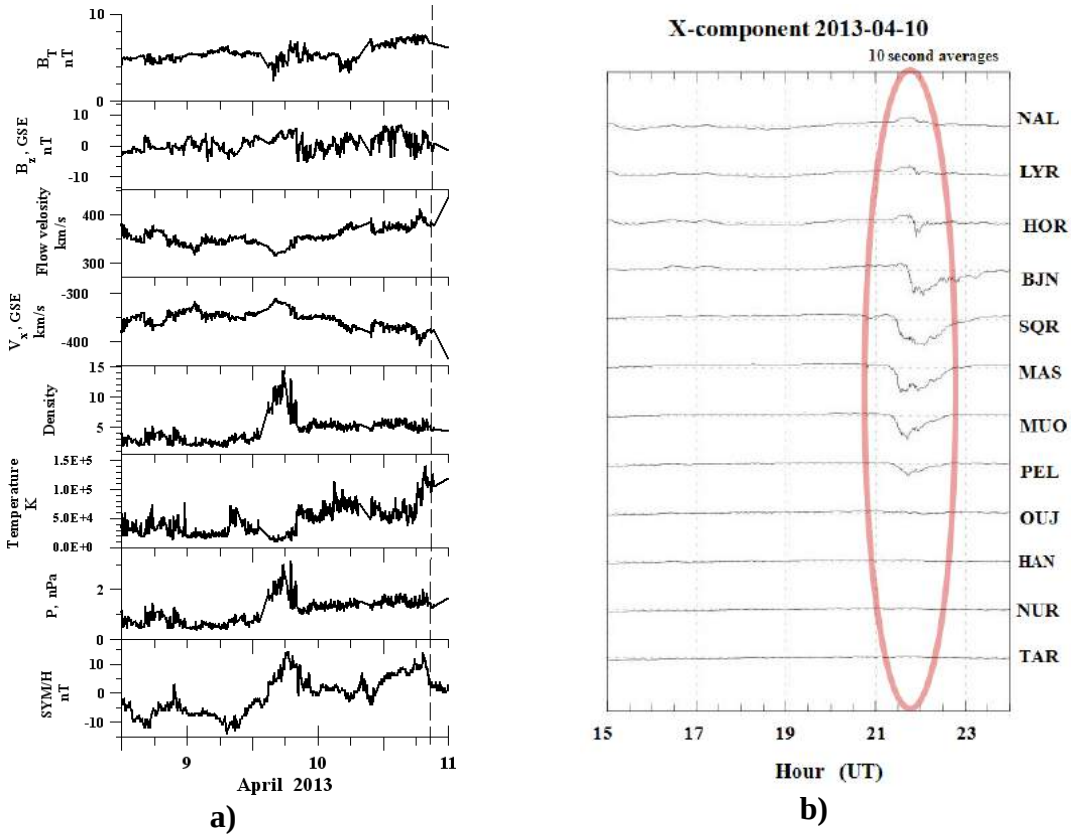

Fig. 5. Event on 10 April 2013 – Quit solar wind conditions. Simultaneously observations solar wind and IMF parameters (a), magnetic field disturbances by IMAGE magnetometer chain (b) are presented.

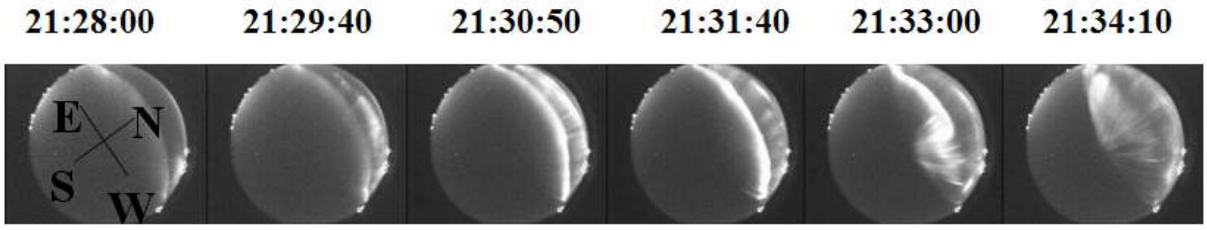

Fig. 6. Event Dynamics of auroras according to the all-sky camera data during one substorm of April 10, 2013. The format of Figure 6 is the same as that of Figure 2. Some all-sky camera images for the substorm from 21:28:00 to 21:34:10 UT are presented.

Discussion

We investigated substorm developments during storms caused by different sources in the solar wind and during quiet conditions using observations of auroras in Apatity during 2012/2013 winter season. The observations of substorm developments by the all-sky camera in Apatity confirm the typical morphology: in disturbed geomagnetic conditions, when storms are generated, the auroral oval lies at lower latitudes. Thus the substorm onset is located to the South of Apatity and the motion of the polar edge of the substorm bulge can be seen moving in South-North direction over Apatity. This situation was observed mainly for |Dst|>40nT. And vice versa, under quiet conditions or during the recovery phase of a geomagnetic storm, the auroral oval is located at higher latitudes, to the North of Apatity. The substorms arise to the North and during the bulge expansion the movement of the equatorial edge of the auroral bulge in North-South direction can be observed. This situation was observed mainly for |Dst|<40nT.

It should be noted that such research of geomagnetic disturbance development and ionospheric currents associated with them is important for understanding of the regional space weather problems which can be scaled to lower latitudes for higher disturbance levels.

Conclusion

It is shown that 2 types of substorm development occur over Apatity. First type: substorm onset is to the South of Apatity, and the "usual" development of the substorm bulge is seen – from South to North; the polar edge of the bulge is observed to pass over zenith. Second type: the auroral oval is situated at higher latitudes, substorm generates to the North from Apatity, and the movement of the auroral bulge to the South is seen from Apatity, i.e. the equatorial edge of the auroral bulge is observed. It is shown that the first type of substorm development over Apatity happens during geomagnetic storms (|Dst|>40nT), associated with both magnetic clouds and high speed recurrent streams of the solar wind. The second type of substorm development is observed under quiet (non-storm) conditions or during the storm recovery phase (|Dst|<40nT).

Acknowledgments. This study was supported by RFBR grants № №13-05-00233 and 12-05-01030 and by Program No 22 of the Presidium of the RAS "Fundamental problems of the Study and Exploration of the Solar system". The study is part of a joint Russian - Bulgarian Project 1.2.10 "The influence of solar activity and solar wind streams on the magnetospheric disturbances, particle precipitations and auroral emissions" of PGI RAS and IKIT-BAS under the Fundamental Space Research Program between RAS and BAS.

References

Balogh A., J.T. Gosling, J.R. Jokipii, R. Kallenbach, H. Kunow (1999), Corotating interaction region. *Space Sci. Rev.* 89, 141-411.

Burlaga, L.F., L. Klein, N.R. Sheeley, Jr. Michels, D.J. Howard, R.A. Koomen, M.J. Schwenn, H. Rosenbauer (1982), A magnetic cloud and a coronal mass ejection. *Geophys. Res. Lett.*, 9, 1317-1320.

Despirak, I.V., A.A. Lubchich, H.K. Biernat, A.G. Yahnin (2008), Poleward expansion of the westward electrojet depending on the solar wind and IMF parameters. *Geomagn. Aeron*., 48 (3), 284-292.

Despirak, I.V., A.A. Lubchich, A.G. Yahnin, B.V. Kozelov, H.K. Biernat (2009). Development of substorm bulges during different solar wind structures. *Ann. Geophys*., 27, 1951-1960.

Despirak I.V., A.A. Lyubchich, N.G. Kleimenova (2014). Polar and high-latitude substorms and solar wind conditions. *Geomagn. Aeron*., 54(5), 575-582.

Gerard J.-C., B. Hubert, A. Grard, M. Meurant (2004), Solar wind control of auroral substorm onset locations observed with the IMAGE-FUV imagers. *J. Geophys. Res.,* 109, A03208, doi: 10.1029/2003JA010129

Klein L.W. and L.F. Burlaga (1982), Interplanetary magnetic clouds at 1 au. *J. Geophys. Res.* 87, 972–984.

Kozelov, B.V., S.V. Pilgaev, L.P. Borovkov, V.E. Yurov (2011), Multi-scale auroral observations in Apatity: winter 2010-2011,. *in: Proc. XXXIV Annual Seminar, Apatity, "Physics of auroral phenomena"*. 129-132.

Kozelov, B.V., S.V. Pilgaev, L.P. Borovkov, V.E. Yurov (2012), Multi-scale auroral observations in Apatity: winter 2010-2011. *Geosci. Insrum. Method. Data Syst*., 1, 1-6.

Sergeev, V.A., A.G. Yakhnin, N.P. Dmitrieva (1979), Substorm in the polar cap – the effect of high-velocity streams of the solar wind. *Geomagn. Aeron*., 19, 1121-1122.

Tsurutani B.T., W.D. Gonzalez, A.L.C. Gonzalez A.L.C., et al. (2006), Corotating solar wind streams and recurrent geomagnetic activity: A review. *J. Geophys. Res.* 111. doi: 10.1029/2005JA011273.

Vorobjev V.G. and V.L. Zverev (1982), The influence of the solar wind velocity on the position and structure of auroras in the midnight sector. *Geomagn. Aeron*., 22(1), 81-84.

Yahnin, A.G., I.V. Despirak, A.A. Lyubchich, B.V. Kozelov (2004), Solar wind control of the auroral bulge expansion. *in Proceedings of the 7h International Conference on Substorms*, *(Levi, Finland, 2004),* Ganushkina N. and T. Pulkkinen (Ed.), (Helsinki: Finnish Meteorological Institute), 31-34.

Yermolaev Yu.I., and M.Yu. Yermolaev (2006), Statistic study on the geomagnetic storm effectiveness of solar and interplanetary events. *Adv. Space Res.* 37, 1175–1181.

IMAGING THE ENERGETIC PARTICLE PENETRATION FROM THE SUBSTORM INJECTION REGION UP TO THE PLASMAPAUSE

I.B. Ievenko, S.G. Parnikov
Yu. G. Shafer Institute of Cosmophysical Research and Aeronomy, Yakutsk, 677980 Russia,
e-mail: ievenko@ikfia.ysn.ru

Abstract. The analysis results of dynamics of diffuse aurora and mid-latitude red arc in the 557.7 and 630.0 nm emissions at the Yakutsk meridian (CGM: 58ºN, 200ºE) during the isolated substorm on February 13, 2013 are presented. The Van Allen Probe (A) satellite has detected the onset of dispersionless substorm injection near the center of the substorm activization at the magnetic meridian at 0059 MLT in the orbit apogee at L = 6.4. The ground all-sky imager has registered the equatorward and eastward extension of DA and the occurrence of SAR arc in the 0200-0425 MLT sector. We believe that the dynamics of DA and SAR arc maps the overlap of hot plasma with the outer plasmasphere as a result of electric drift from the substorm injection region.

1. Introduction

The stable auroral red (SAR) arcs are the consequence of interaction of the outer plasmasphere (plasmapause) with energetic ions of the ring current during the magnetic storms (Cole, 1965, 1970; Kozyra et al, 1997). The diffuse aurora (DA) is caused by the low-energy electron precipitation from the near-earth plasma sheet. According to the mechanism of SAR arc generation proposed by Cole (1965, 1970), red arcs appear during the main phase of a magnetic storm in the development process of auroral disturbance. Cole supposed that energy transfer from the ring current to the thermal plasma in the outer plasmasphere takes place at all times of a storm. The Cole generalization was in a good agreement with the results of SAR arc observations available at that time. Subsequently, after the theoretical work of Cornwall et al. (1971), it were established that SAR arcs are formed during the storm recovery phase.

The photometric observations of the DA and SAR arc dynamics in the 557.7 and 630.0 nm emissions at the Yakutsk meridian (199° E geomagnetic longitude) during substorms have been presented in details by Ievenko (1994, 1999). These studies indicate that the SAR arc appears and/or brightening during the substorm expansion phase. The SAR arc formation begins in the equatorward boundary region of DA. In the case of prolonged substorm activity, a SAR arc separates from DA and moves equatorward (Ievenko et al, 2004; Ievenko et al, 2008). In this work we analyze the observation of DA and SAR arc dynamics at the Yakutsk meridian during the isolated substorm injection on February 13, 2013 detected with the Van Allen Probe (A) satellite near the orbit apogee with L = 6.4.

2. Methods of Observation

The observation of DA and SAR arcs in the 630.0 and 557.7 nm [OI] emissions was carried out using the digital meridian-scanning photometer (MSP) and the all-sky imager (ASI). The registration of the 427.8 nm and 630.0 nm emissions intensity in the magnetic zenith was registered with the four channel photometer. In order to analyze, the MSP and ASI data are presented in this work as isophots of the surface brightness of the 557,7 and 630,0 nm emissions in Rayleighs (R) in a projection to the Earth's surface for the luminosity heights of 110 (DA) and 450 (SAR arc) km, respectively (keograms and images). To determine time intervals when the magnetospheric convection is enhanced, the measurement data of the interplanetary magnetic field (IMF) and the solar wind (SW) speed from the ACE spacecraft were used. The location of center of the substorm expansion onset was identified using magnetograms at the low-latitude stations.

3. Results of Observation

Fig.1 shows the dynamics of the DA and occurrence of SAR arc during the isolated substorm on February 13, 2013. The simultaneous increase of the density and Ey dawn-dusk of solar wind was manifested in the brightening of DA on the northern horizon. After the onset of substorm expansion at 1849 UT the equatorward extension of DA occurs and the SAR arc in the 630 nm emission appears. The red arc is separated from the DA and moves equatorward through the observation station zenith in the morning MLT sector. During the negative Ey a rapid decay of DA and SAR arc is observed.

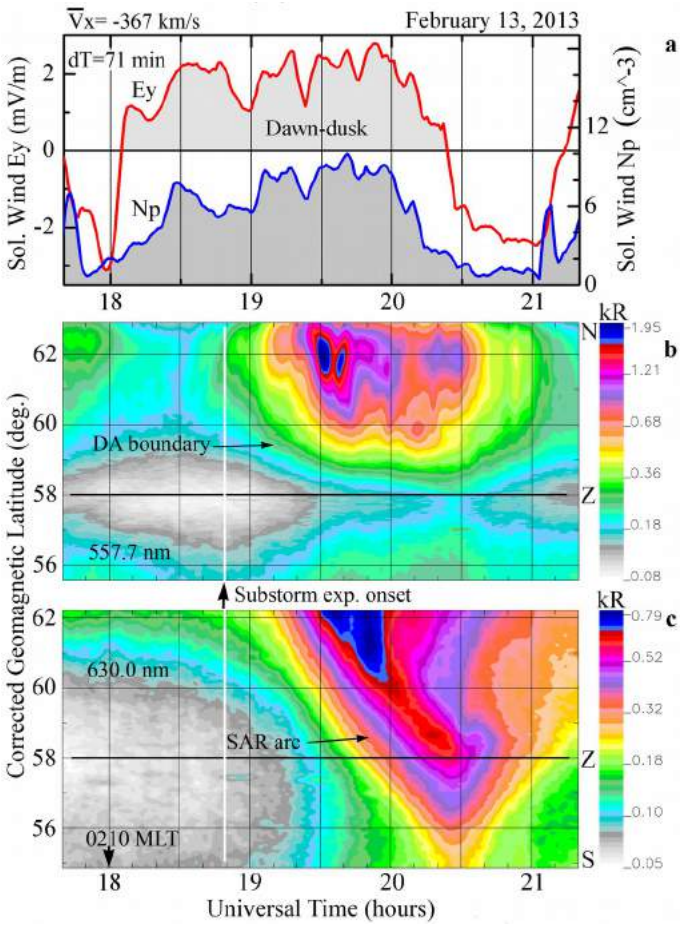

Fig. 1 Changes in the solar wind and the subauroral luminosity dynamics on February 13, 2013
(**a**)- the electric field (E_Y) and density (Np) of the solar wind with the dT shift time; (**b**) and (**c**) meridian-scanning photometer data as keograms in the 557.7 and 630.0 nm emissions for the luminosity heights of 110 and 450 km, respectively. **Z** is a zenith of observation station.

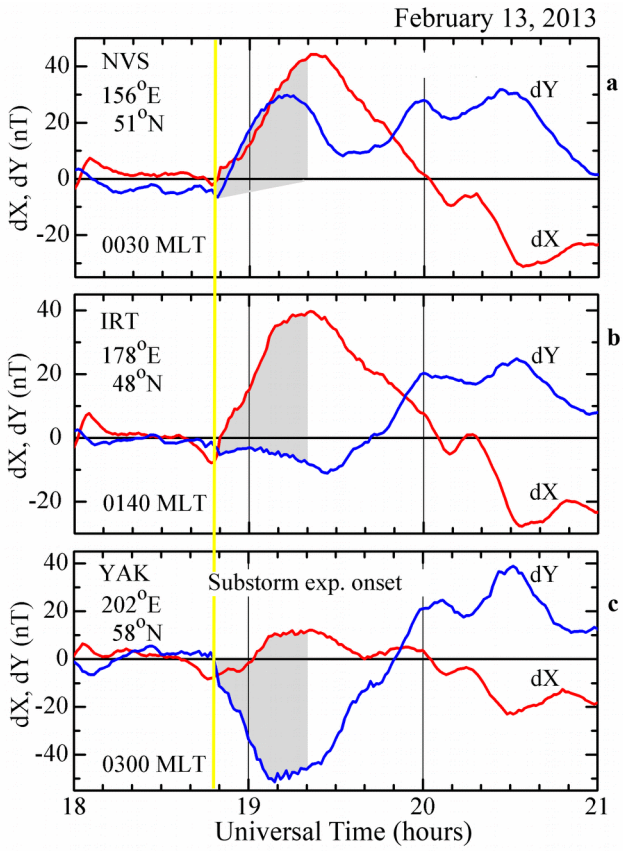

Fig. 2 Mid-latitude magnetic disturbances during the substorm expansion phase on February 13, 2013
Magnetograms of mid-latitude stations at magnetic meridians of 156ºE (**a**), 178ºE (**b**) and 202ºE (**c**). On the magnetograms MLT of the substorm expansion onset is indicated.

Fig.2 shows the longitudinal distribution of magnetic field disturbances during the substorm on February 13, 2013 at the magnetic meridians of 156ºE, 178ºE and 202ºE. The isolated substorm with the onset of expansion phase at 1849 UT was clearly revealed in the variations of magnetic field after the MLT midnight. The sign and amplitude of the X and Y component variations indicate to the position of the activization center in the vicinity the magnetic Irkutsk meridian with the onset of substorm expansion at 0140 MLT.

Fig. 3 shows the energetic electron flux measured with the ECT HOPE instrument aboard Van Allen Probe (A) satellite during the isolated substorm on February 13, 2013. At the onset of substorm expansion the satellite was located near the apogee with the GSM X = -5.1, Y = -1.8, Z = -1.9 R_E at the magnetic meridian at 0059 MLT. The dispersionless injection of electrons with the energies 10-51 keV started at ~ 1846 UT. The front duration of injection was ~ 4 min. The injection was registered near the center of the substorm activization onset. For the indicated five-minute 1 and 2 intervals the average spectra of fluxes of electrons, ions H^+ and O^+ before and after the substorm injection have been calculated.

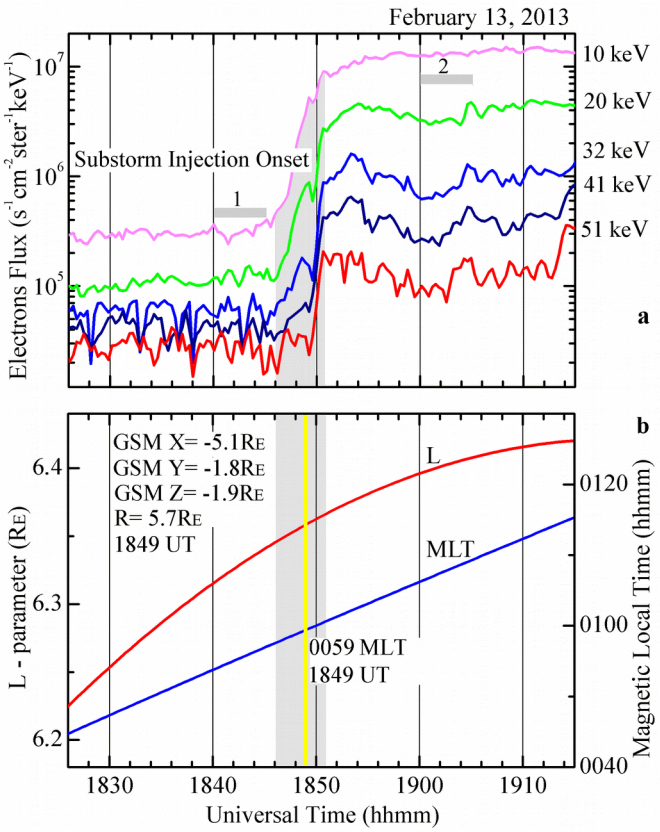

Fig. 3 Observation of the substorm injection with Van Allen Probe (A) satellite on February 13, 2013
a-the energetic electron flux measured with ECT HOPE instrument; **b**- calculated L-parameter and MLT of the satellite.

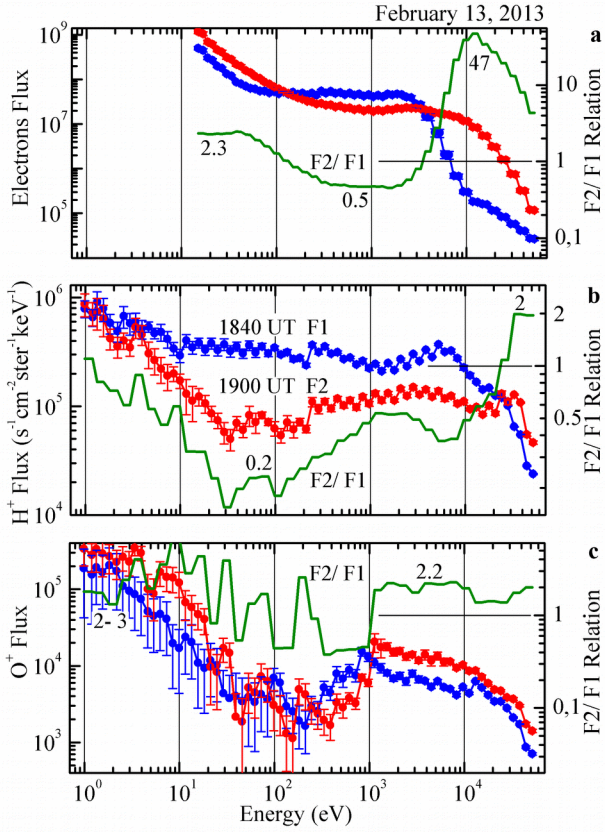

Fig. 4 Particle spectra measured aboard Van Allen Probe A satellite on February 13, 2013
The dependences of average fluxes on the energy before (F1) and after (F2) the onset of substorm injection and the ratio F2 / F1 for the electrons (**a**), ions H^+ (**b**) and O^+ (**c**). The standard error of mean are indicated on the spectra.

Fig. 4 shows the dependences of the average fluxes on the energy before (F1) and after (F2) the onset of substorm injection and the ratio F2 / F1 for the electrons, ions H^+ and O^+. During the injection there was a significant increase of electron fluxes with energies of 6-51 keV with a maximum at 12 keV (in 47 times) as well as the growth of fluxes of the over thermal electrons (in 2.3 times). In the spectrum of protons the injection was manifested both in the increase of fluxes in 2 times in the energy range 30-50 keV and in the decrease of fluxes for the low-energy particles (in 2-5 times). During the injection the fluxes of O^+ ions were increased by a factor of 2.2 in the energy range of 1-10 keV. The thermal ion flux was also increased in 2-3 times.

The set of all-sky images in the 630.0 nm emission during the SAR arc formation on February 13, 2013 is presented in Fig. 5. The all-sky imager registered the manifestation of substorm injection in the 630.0 nm emission at the Yakutsk meridian in the interval of 0200-0425 MLT At first, the equatorward and eastward extension of DA took place. The maximum intensity of 1.6 kR was observed in the spots of weak DA. Further, the formation of broad SAR arc at the geomagnetic latitude of ~ 60ºN on the equatorial boundary of DA began. The red arc moved up to the station zenith. The width and intensity of arc are significantly greater in the eastern part of the sky up to the horizon.

Fig. 6 shows the set of all-sky images in the 557.7 nm emission with the frame time as in Fig. 5. In this emission only the weak DA dynamics with the maximum of intensity of 2.8 kR is mapped. As a result of the equatorward and eastward extension the boundary of DA reached the latitude of 60-59ºN. On the basis of observations the radial and azimuthal movement velocities of energetic plasma in the inner magnetosphere have been determined.

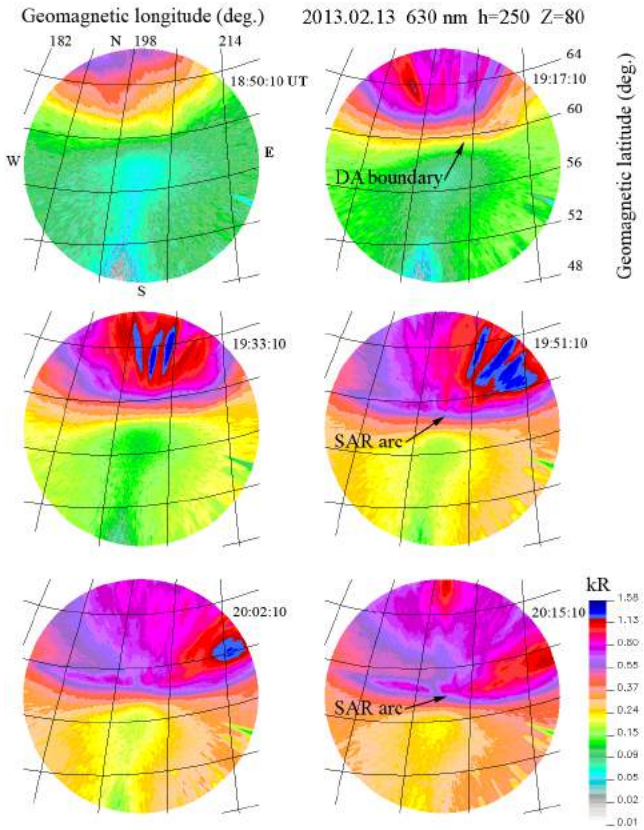

Fig. 5 All-sky images in the 630.0 nm emission during the SAR arc formation on February 13, 2013
Geomagnetic coordinate are shown for h=250 km

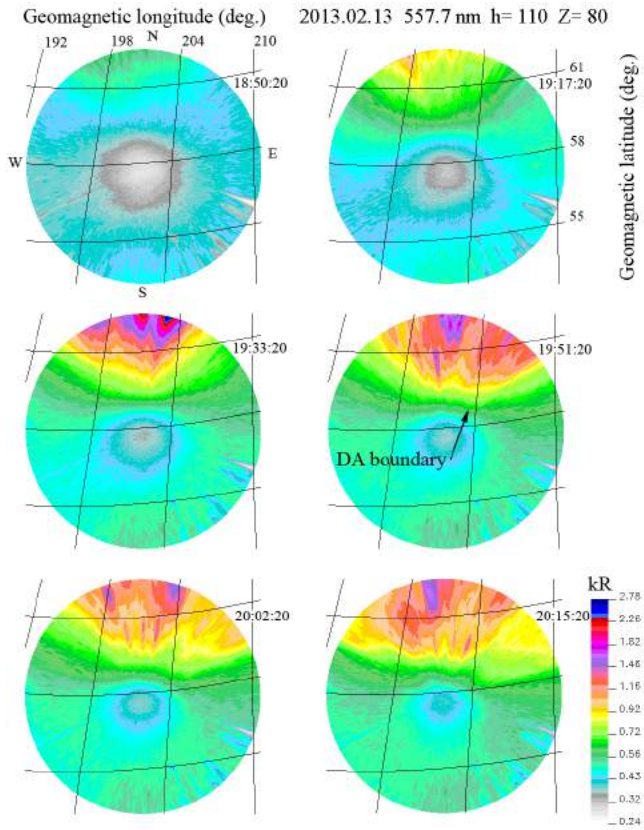

Fig. 6 All-sky images in the 557.7 nm emission during the SAR arc formation on February 13, 2013
Geomagnetic coordinate are shown for h=110 km.

Conclusion

As a result of complex analysis of the event of 13 February 2013 has been obtained the following:

- The center of region of the substorm expansion onset was located at the meridian about MLT midnight.
- Van Allen Probe (A) registered the dispersionless injection of energetic electrons and ions near the center of active region on the GSM X = -5.1 R_E.
- At the Yakutsk meridian ASI registered the equatorward and eastward extension of DA and the occurrence of inhomogeneous SAR arc in longitude.
- We believe that the dynamics of DA and SAR arc maps the overlap of hot plasma with the outer plasmasphere as a result of the electric drift from the substorm injection region.
- The observed DA extension velocities can be explained by a drift of hot plasma in the substorm electric field with $E_{Azimuth}$ = 1.76 and E_{Radial} = 0.98- 1.73 mV / m.

Acknowledgments. This work was supported by Program of Russian Foundation for Basic Research (project no. 12-05-98523_p_vostok_a). The data on solar wind and IMF were obtained in the ACE Science Center (*http://www.srl.caltech.edu/ACE/ASC/level2/index.html*). Spin averaged ECT-HOPE science data with Van Allen Probe (A) spacecraft were obtained in CDAWeb (http://cdaweb.gsfc.nasa.gov/istp_public/). The geomagnetic data were provided by INTERMAGNET (www.intermagnet.org).

References

Cole, K.D. (1965), Stable auroral red arcs, sinks for energy of Dst Main phase. *J.Geophys.Res.* 70, 7, 1689-1706.

Cole, K.D. (1970), Magnetospheric processes leading to mid-latitude auroras. *Annales de Geophysique.* 26, 1, 187-193.

Cornwall, J.M., Coroniti, F.V., Thorne, R.M. (1971), Unified theory of SAR arc formation at the plasmapause. *J.Geophys.Res.* 76, 19*,* 4428-4445.

Ievenko, I.B. (1994), Dynamics of diffuse aurora and SAR arc during substorm. *Geomagnetism and Aeronomy.* 33, 5, 599-611, (In Russian, English translation).

Ievenko, I.B. (1999), Effects of magnetospheric activity on the plasmasphere as inferred from observations of diffuse aurora and SAR arc. *Geomagnetism and Aeronomy.*. 39, 6, 697-703, (In Russian, English translation).

Ievenko, I.B., Alexeyev, V.N., (2004), Effect of the Substorm and Storm on the SAR Arc Dynamics: A Statistical Analysis. *Geomagnetism and Aeronomy.* 44(5), 592-602 (In Russian, English translation).

Ievenko I.B., S.G. Parnikov, V.N. Alexeyev (2008), Relationship of the diffuse aurora and SAR arc dynamics to substorms and storms. *Adv. Space Res.*, Vol. 41/8, 1252-1260, DOI: 10.1016/j.asr.2007.07.030.

Kozyra, J.U., A.F. Nagy, D.W. Slater (1997), High-altitude energy source(s) for stable auroral red arcs. *Reviews of Geophysics,* 35, 2, 155-190.

POLAR GEOMAGNETIC EFFECTS OF MAGNETIC STORM OF 24 NOV 2001 UNDER STRONG POSITIVE Bz IMF

N.G. Kleimenova[1], N.R. Zelinsky[1], L.I. Gromova[2], L.A. Dremukhina[2], A.E. Levitin[2], S.V. Gromov[2]

[1]Schmidt Institute of the Earth Physics RAS, Moscow, 123995, Russia, e-mail: kleimen@ifz.ru;
[2] Pushkov Institute of Terrestrial Magnetism, Ionosphere and Radio Wave Propagation, RAS, Moscow, Troitsk, Russia

Abstract. The huge positive Bz IMF values (up to ~+60 nT) were observed during the main phase of the strong magnetic storm on 24 Nov 2011 (Dst~-220 nT) under the very high solar wind speed (~ 900 km/s) and several sharp bursts of the solar wind dynamic pressure (at ~7.30, 09.30, 12.00 and 14.00 UT). About 30 min after SC, the Bz IMF value reached ~-40 nT and the strong substorm with the highest amplitudes at the morning sector occurred. Later on, at ~07 UT, the Bz IMF turned to the very high positive values reaching more than +60 nT. The most unusual phenomenon during this storm was the bay-like magnetic disturbance at 08-11 UT with the amplitude of ~1500 nT which was observed near local magnetic noon only at the polar latitudes (> 70º) at the Scandinavian IMAGE magnetometer profile. At that time, AE-index was < 300 nT. This event occurred after very strong burst of the solar wind dynamic pressure (up to ~60 nPa). We suppose that the polar magnetic bay was caused by the enhanced high-latitude NBZ system of the field aligned currents (FAC). The IZMEM model distribution of the high-latitude FAC confirmed this suggestion and demonstrated strong FAC at the polar magnetic bay location. The irregular bursts of 2-7 mHz geomagnetic pulsations (ULF waves) represented the fine wave structure of this daytime magnetic bay. However, the ULF bursts were not coincided with the similar frequency range bursts of the fluctuations in the solar wind density and IMF. We suppose the polar ULF pulsations represented the fluctuations of the intensity of the corresponding field aligned currents associated with processes of nonlinear interactions of solar wind irregularities at the magnetopause.

Introduction

The last time, there are very many papers denoted to discussions of non-typical geomagnetic effects of extreme events of the space weather such as very strong magnetic storms, e.g. [Du et al., 2008; Dandouras et al., 2009; Baker et al., 2013; Dmitriev et al., 2014; and etc].

One of the strong magnetic storms was the event on 24 November 2001 with Dst ~220 nT. There were unusually strong variations in the solar wind and in Interplanetary Magnetic Field (IMF). After the SC near 06 UT, during the storm main phase beginning, the IMF Bz suddenly turned from very strong negative vales (- 42 nT at 07 UT) to very strong positive values (~+20 nT), which quickly increased up to +64 nT at ~10 UT. The solar wind speed was as high as ~850 km/s, and some peaks of the solar wind dynamic pressure sometimes reached ~50-70 nPa. The positive IMF Bz occurrence at 08-11 UT leads to slow the typical storm main phase Dst (SymH) decreasing. The UT time variations of the Dst (SymH) as well as some IMF and solar wind parameters are shown in the upper part of Fig. 1. The aim of this paper is to study the untypical geomagnetic effects of the strong positive IMF Bz lasting about 4 hours in the storm main phase.

Observation data analysis and Discussion

1. We studied high-latitude geomagnetic disturbances by applying the new method proposed by Levitin et al. [2014] for determining geomagnetic activity based on calculation of the hourly amplitudes of magnetic field variations at ground-based observatories. Observations, performed in 2009, when extremely low solar and geomagnetic activity was registered, were used as a reference level. According to this method, the observation data are counted off from the reference level 2009.

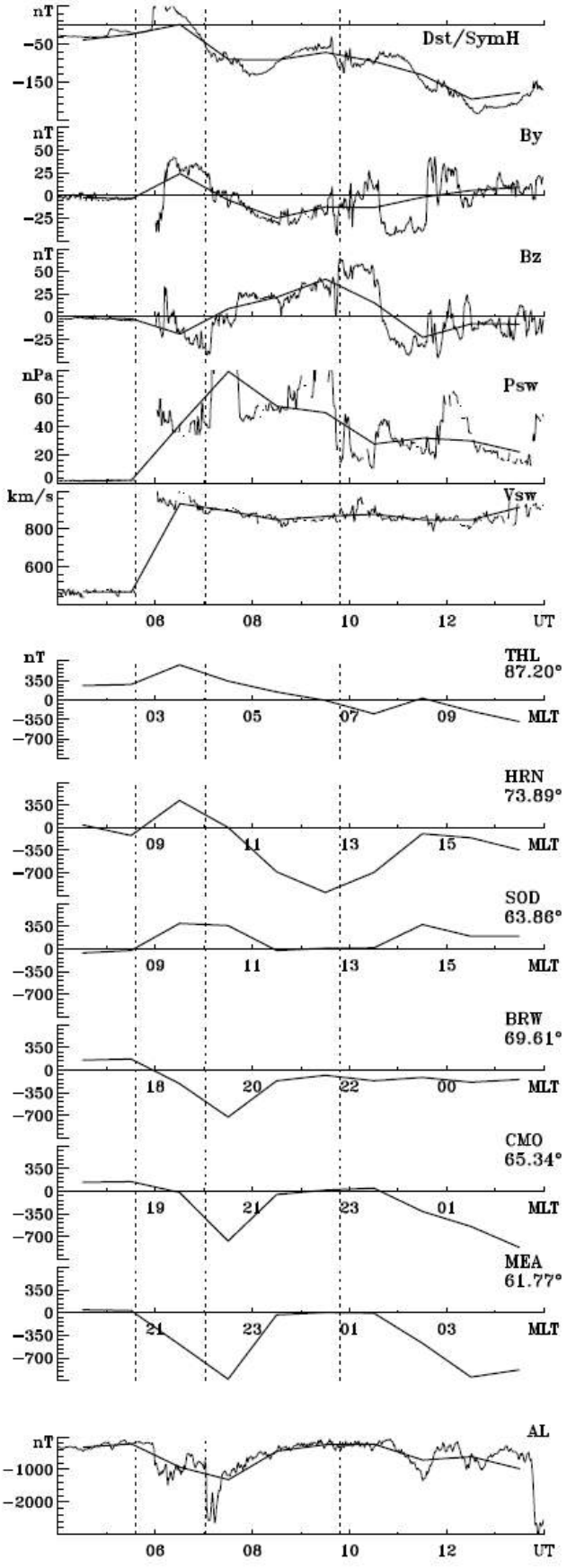

Fig.1. IMF and solar wind parameters during this storm and geomagnetic data from some high latitude stations. The solid lines are the hourly values and the thin lines – the minutes ones.

We assume that the ground-based magnetic measurements performed on the quietest days in this year register only the main geomagnetic field and the deviations from this level represent the amplitude of a variable magnetic field.

This assumption forms the basis for the characterization of geomagnetic activity based on the energy of a variable magnetic field.

To quantitatively describe local magnetic activity, we selected the geomagnetic field *H* component registered at observatories since this component most intensely responds to a change in a variable geomagnetic field generated by the magnetospheric and magnetospheric-ionospheric current systems.

We used the following calculation method for the ground-based data of the Northern Hemisphere:

For each month of 2009, we select the day when geomagnetic activity was the lowest and the *H* component amplitude variations (the difference between the maximal and minimal amplitudes) were the smallest. A correction for the geomagnetic field secular variations is found from the difference between the quietest days in January for two adjacent years since the geomagnetic field at the observatories in the Northern hemisphere is most quiet precisely in January in our opinion.

The hourly average amplitudes of the *H* component on a geomagnetically quiet day corrected for the secular variations are then subtracted from the hourly average amplitudes for the same month in all previous and subsequent years.

The middle part of Fig. 1 demonstrates the calculated the hourly magnetograms from several high latitude ground stations located at different longitudes by the described above method. The MLT hours have been indicated on the horizontal axis for each given stations, thus, we may compare the simultaneous geomagnetic disturbances at different local magnetic time. It is seen that after SC under negative IMF Bz there was a strong substorm at the night side of the Earth (obs. BRW, CMO, MEA). It is typical for magnetic storms.

With the positive IMF Bz turning (at ~07 UT), the night substorm activity dropped, and AL index, shown in the bottom part of Fig.1, became very small (~ -300 nT).

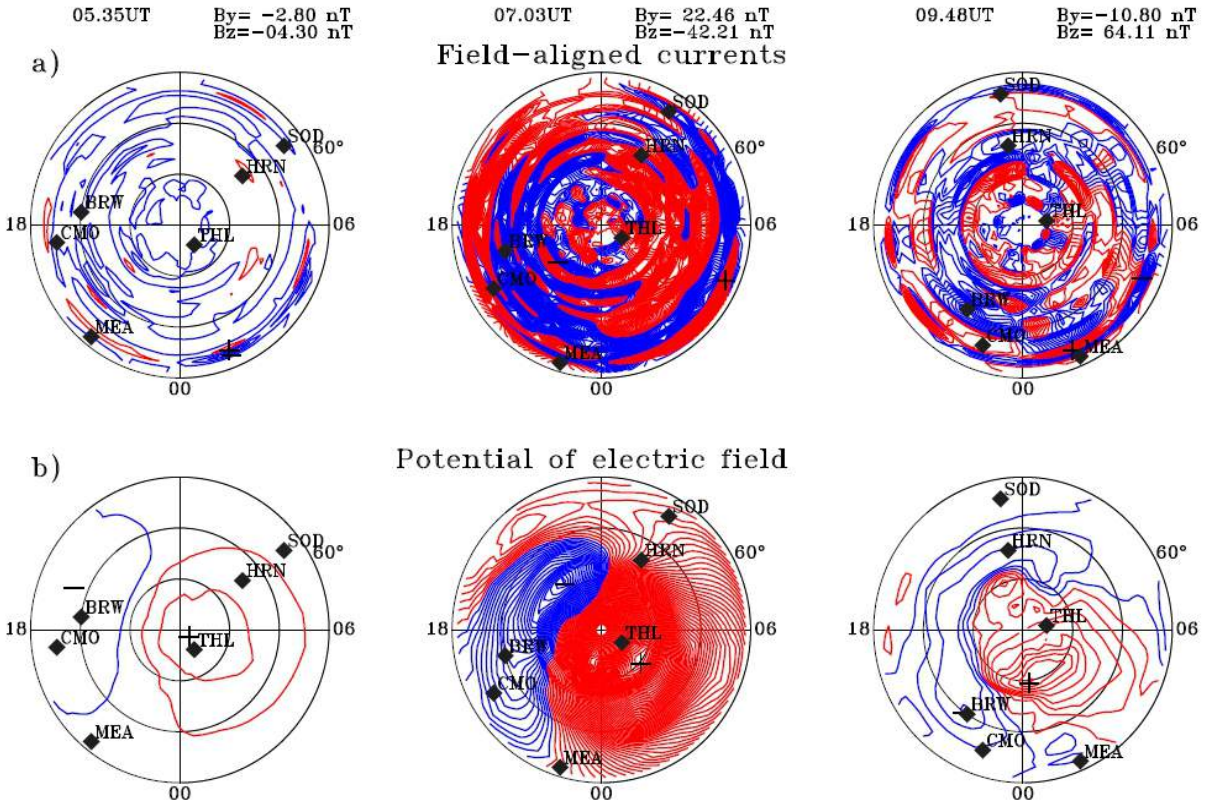

Fig.2. The maps of the field aligned currents (a) and polar convection (b)

However, an unusual strong negative magnetic bay occurred in the dayside sector of the Earth at polar geomagnetic latitudes (obs.HRN, Φ~74°, ~11-14 MLT), where the dayside polar cusp could be located. This bay disappeared with negative values of IMF Bz occurred.

2. We applied the IZMIRAN model of the field aligned currents and convection distribution in the North hemisphere based on the correlation of the X and Y geomagnetic field at high-latitude ground stations with the solar wind density and velocity and the IMF Bz and By components [Feldstein and Levitin, 1986; Dremukhina et al., 1998]. The calculated maps are presented in Fig.2 for 3 selected intervals marked by the vertical dotted lines in Fig. 1: before SC (leftward), under high negative IMF Bz (in the middle) and under huge positive IMF Bz (rightward). The middle plots shows typically strong enhancement of FAC intensity and convection under high negative IMF Bz values.

Under the very strong positive IMF Bz, the auroral latitude FAC intensity significantly dropped as it is seen in the rightward maps of Fig. 2. However, in the dayside polar cusp area (near HRN station), the upward and downward FACs were intense. The station HRN was located in the area of negative convection sell. These FAC could be attributed to the special NBZ current system under positive IMF Bz [Iijima et al., 1984; Zanetti et al., 1990]. Some authors, e.g. [Wilhjelm et al., 1976] showed that in the northern dayside polar cusp under negative IMF By, the westward electrojet is dominated as it is seen in Fig.1 at HRN station at 08-11 UT (11-14 MLT).

3. The magnetograms from the selected stations of the IMAGE magnetometer chain are presented in Fig. 3 for the discussed time interval (04-14 UT). One can see that a strong negative magnetic bay with the amplitude about 1500 nT was observed at 08-11 UT only at polar geomagnetic latitudes higher 71° (obs. NAL-HOP), at lower latitudes there were no magnetic disturbances. We call this magnetic bay "*dayside polar magnetic substorm*" by parity of reasoning with the magnetic substorm. However, there were no a Pi2 geomagnetic pulsation burst which is typical for classical substorm onset.

It is known that a source of a night substorm is the energy accumulated in the magnetosphere tail under previous negative IMF Bz, and the substorm onset (breakup) if a result of dipolization and current disruption exiting Pi2 pulsation generation. However, at the dayside of the magnetosphere, there is no such energy

reservoir. So, it is logical to assume that a source of the daytime polar substorm could be associated with the solar wind and IMF interaction with the Earth magnetosphere at the sunlit magnetopause.

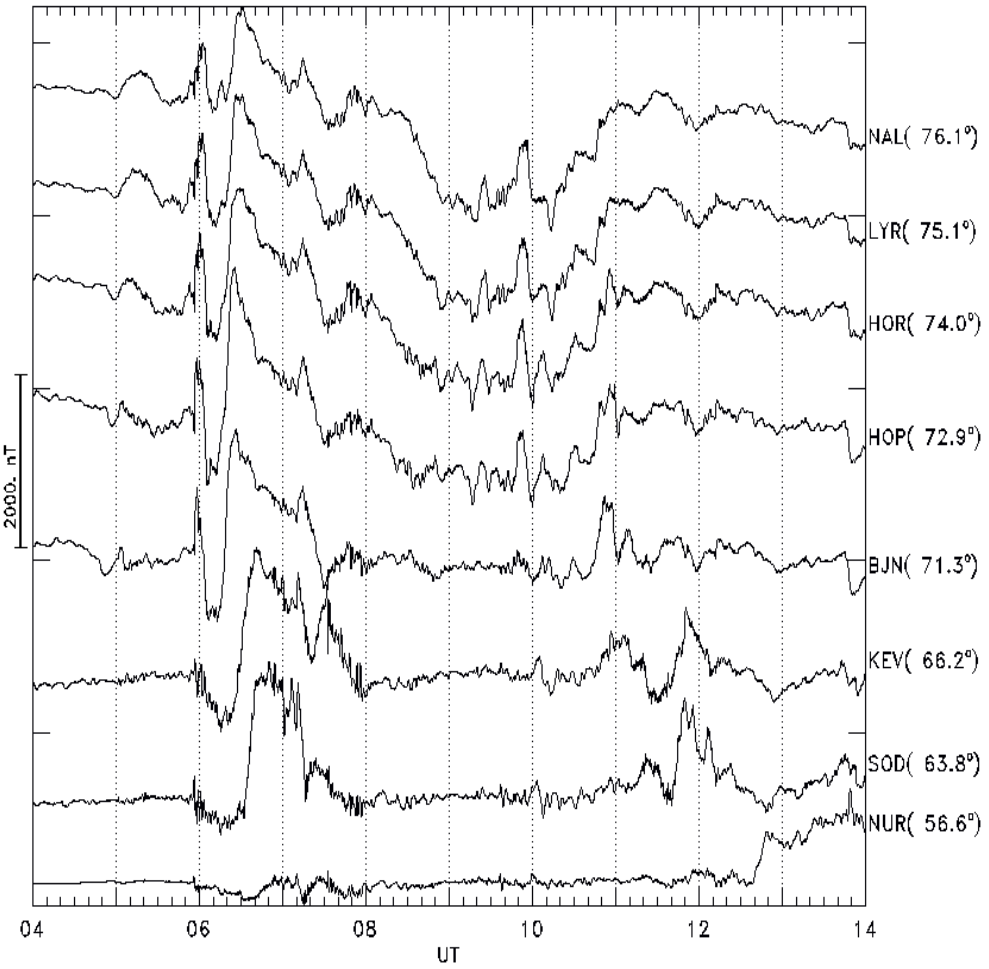

Fig. 3. The magnetograms (X-component) from selected IMAGE magnetometer chain.

4. The ULF (2-7 mHz) geomagnetic pulsation accompanied the dayside polar magnetic substorm (08-11 UT) have been studied by applying of fuzzy logic methods of the Discrete Mathematical Analysis –DMA [e.g., Agayan et al., 2005; Zlotnicki et al., 2005; Gvishiani et al., 2008].

The first step of observation processing included data filtration within the 2–7 mHz range using a band-pass Butterworth filter with a zero-phase shift [Kanasevich, 1985], the amplitude-response curve of which is maximally smooth in the frequency bandwidth. In this work for investigation of geomagnetic pulsations, we used a DMA "survey fragment energy" rectifying functional (Agayan et al., 2005). The applying of this rectification allows us to identify sections of the initial time series that are anomalous in a certain vicinity of a given point, i.e., the "energy" rectification carries information about the signal amplitude *relative to* the neighboring points of the time series and does not correspond to the *absolute* signal amplitude.

The obtained results of these calculations are demonstrated in Fig. 6 for fluctuations of the IMF components and solar wind dynamic pressure as well as for geomagnetic pulsations from some stations at polar, auroral and equatorial latitudes (auroral obs CMO and equatorial obs. PPT are located at the night side). It is seen that the strongest high-latitude ULF wave were observed during SC (near 06 UT) and strong negative IMF Bz (near 07 UT). During the discussed above *dayside polar magnetic substorm,* there were irregular pulsations at polar latitudes not correlated with fluctuations in the interplanetary medium. Despite the fact that the time interval of the polar irregular geomagnetic pulsations and interplanetary fluctuations was the same, it was unlikely a direct wave penetration from the solar wind to the ground.

At this time, there were observed three strong ULF bursts at dayside equator (obs. AAE) in association with similar bursts in the solar wind dynamic pressure fluctuations as it was found previously by Pathan et al. [1999].

We suppose that the polar irregular geomagnetic pulsations accompanied the dayside polar magnetic substorm are associated with processes of the solar wind – magnetosphere interaction which leads to

fluctuating NBZ field aligned current generation or nonlinear wave penetration (or generation) in the turbulent boundary layer over polar cusps. Some of such phenomena have been discussed by Savin et al. [2002].

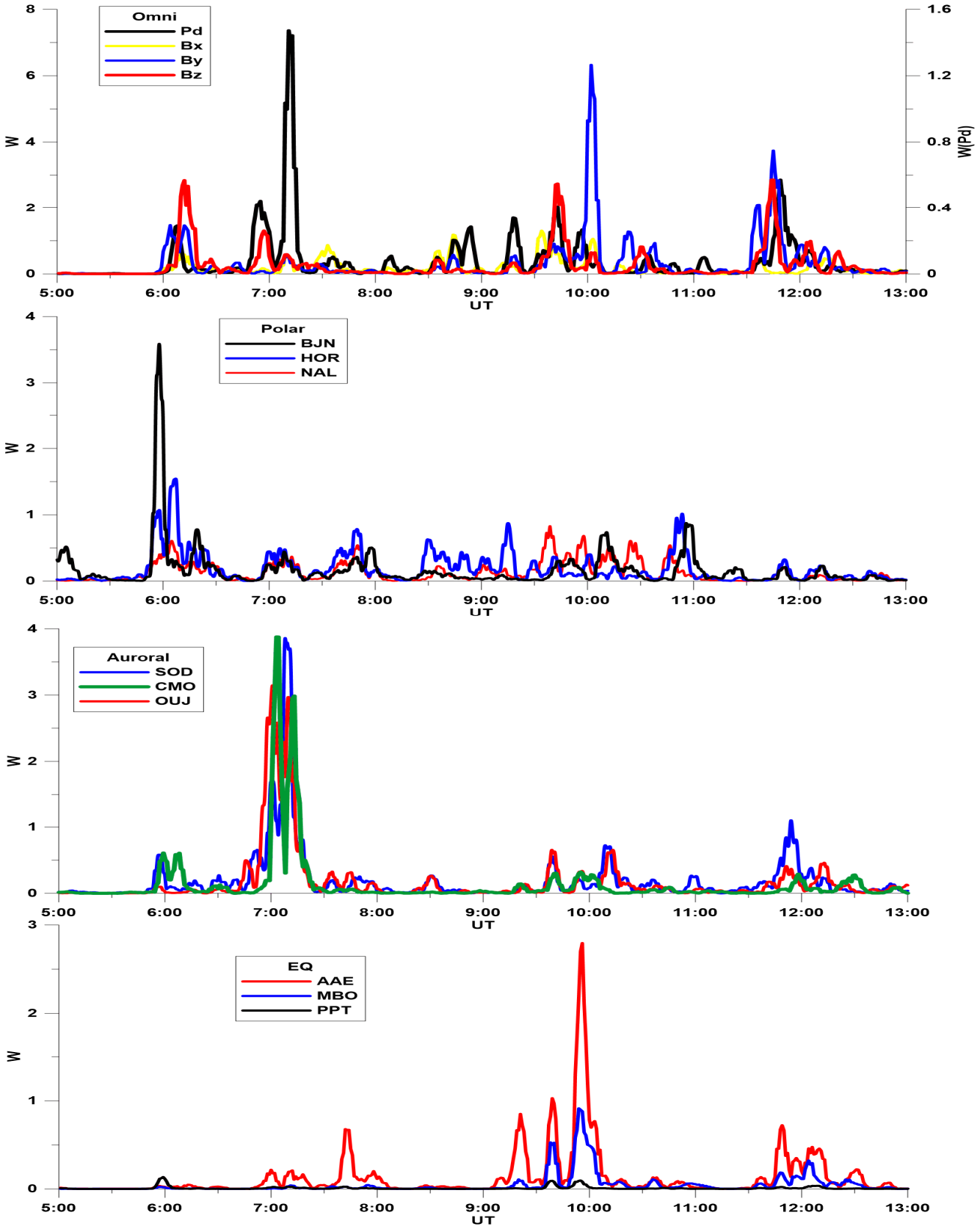

Fig. 6. The results of applying the calculations of DMA "survey fragment energy" rectifying functional to the analysis of interplanetary fluctuations and ground-based geomagnetic pulsations at different latitudes.

Conclusion

The key non-typical phenomena of the magnetic storm main phase of Nov 24, 2001 was a negative magnetic bay-like disturbance in the day side polar cusp area as a result of the huge positive Bz IMF values reaching more than +60 nT occurrence. We call this disturbance *dayside polar magnetic substorm.*

The substorm was accompanied by irregular pulsations at polar latitudes not correlated with fluctuations in the interplanetary medium. Despite the fact that the time interval of the polar irregular geomagnetic pulsations and interplanetary fluctuations was the same, it was unlikely a direct wave penetration from the solar wind to the ground. We suppose that the polar geomagnetic pulsations accompanied the dayside polar magnetic substorm are associated with processes of the solar wind – magnetosphere interaction which leads to fluctuating NBZ field aligned current generation or nonlinear wave penetration (or generation) in the turbulent boundary layer over polar cusps.

Acknowledgment. This study was supported by RFBR grant № 13-05-00233 and partly by the Program № 7 of the Earth Science Department RAS.

References

Agayan, S.M., Bogoutdinov, Sh.R., Gvishiani, A.D.,Graeva, E.M., Diament, M., Zlotnicki, J., and M.V. Rodkin, (2005), Issledovanie morfologii signala na osnove algoritmov nechetkoi logiki (Signal morphology analysis based on fuzzy logic algorithms), *Geofiz. Issled.,* 1, 143–155. (in Russian).

Gvishiani, A.D., Agayan, S.M., and Sh.R. Bogoutdinov (2008), Fuzzy recognition of anomalies in time series, *Dokl. Earth Sci.,* 421, 1, 838–842.

Akasofu, S.I. (1975), The roles of the north-south component of the interplanetary magnetic field on large-scale auroral dynamics observed by the DMSP satellite, *Planet. Space Sci*., 23 (10), 1349–1354.

Baker, D.N., Li, X., Pulkkinen, A., Ngwira, C.M., Mays, M.L., Galvin, A.B., and K.D.C. Simunac (2013), A major solar eruptive event in July 2012: Defining extreme space weather scenarios, *Space Weather,* 11, 585–591, doi:10.1002/swe.20097.

Dandouras, I. S., Rème, H., Cao, J., and P. Escoubet (2009), Magnetosphere response to the 2005 and 2006 extreme solar events as observed by the Cluster and Double Star spacecraft. *Adv. Space Res*., 43, 618–623, doi:10.1016/j.asr.2008.10.015

Dmitriev A.V., Suvorova A.V., Chao J.-K. et al. (2014),Anomalous dynamics of the extremely compressed magnetosphere during 21 January 2005 magnetic storm, *J. Geophys. Res. Space Physics*, 119. 877–896, doi:10.1002/ 2013JA019534, 2014.

Dremukhina, L.A., Levitin, A.E., and V.O. Papitashvili (1998), Analytical representation of IZMEM model for near-real time prediction of electromagnetic weather, *J. Atmos. Sol. Terr. Phys*., 60 (15), 1517-1529.

Du, A.M., Tsurutani, B.T., and W. Sun (2008), Anomalous geomagnetic storm of 21–22 January 2005: A storm main phase during northward IMFs. *J. Geophys. Res*., 113, A10214, doi:10.1029/2008JA013284.

Feldstein, Ya.I. and A.E. Levitin (1986), Solar wind control of electric fields and currents in the ionosphere, *J. Geomag. Geoelectr*., 38, 1143-1182.

Iijima T., Potemra T.A., Zanetti L.J., and P.F Bythrow (1984), Large-scale Birkeland currents in the dayside polar region during strongly northward IMF: A new Birkeland current system, *J. Geophys. Res.,* 89, 7441-7452.

Kanasevich, E.R., (1985), Analiz vremennykh posledovatel'nostei v geofizike (Time Sequence Analysis in Geophysics), Moscow: Nedra.

Pathan, B.M., Kleimenova, N.G., Kozyreva, O.V., Rao, D.R.K., and R.L. Asinkai (1999), Equatorial enhancement of Pc5-6 magnetic storm time geomagnetic pulsations. *Earth, Planets Space*, 51, 959-964.

Savin, S. et al. (2002), On the properties of turbulent boundary layer over polar cusps, *Nonlinear Nonlinear Processes in Geophysics*. 9, 443-451.

Wilhjelm, J., Friis-Christensen, E., and T.A. Potemra (1978), The relationship between ionospheric and field-aligned currents in the dayside cusp, *J. Geophys. Res*., 83, A12, 5586-5594.

Zanetti, L.J., Potemra, T.A, Erlandson, R.E., Bythrow, P.F., Anderson, B.J., Murphree, J.S.,and G.T. Marklund (1990), Polar region Birkeland current, convection, and aurora for Northward Interplanetary Magnetic Field, *J. Geophys. Res*., 95, 5825-5833.

Zlotnicki, J., LeMouel, J.-L., Gvishiani, A., Agayan, S., Mikhailov, V., and Sh. Bogoutdinov (2005), Automatic fuzzy logic recognition of anomalous activity on long geophysical records. Application to electric signals associated with the volcanic activity of la Fournaise volcano (Reunion Island), *Earth Planet. Sci. Lett.*, 234, 261–278.

ON THE UNEXPLORED BIOPHYSICAL PROBLEM OF MANNED FLIGHT TO MARS

V.V. Kovalenok[1], S.V. Avakyan[2, 3, 4], N.A. Voronin[2], A. Trchounian[5], I.V. Sterlikova[6]

[1] Federation of Cosmonautics of Russia, Moscow, Russia;
[2] All-Russian Scientific Center "S.I. Vavilov State Optical Institute", St. Petersburg, Russia, 199034, avak2@mail.ru;
[3] Central (at Pulkovo) Astronomical observatory RAS, St. Petersburg, Russia;
[4] St. Petersburg State Politechnical University, St. Petersburg, Russia;
[5] Yerevan State University, 0025, Yerevan, Armenia;
[6] Moscow Psychological and Social University, Murom branch, Russia

Abstract. The paper discusses so far unexplored biophysical problem of manned flight to Mars, scheduled for the next decade. In long-term manned space flights on the orbital stations "Salyut" Soviet cosmonaut crews under the command of one of the co-authors (cosmonaut V.V. Kovalenok) had repeatedly observed effect of certain geophysical conditions on the psychological state of each crew. These effects are coinciding with the increased intensity of global illumination in the upper ionosphere space on flight altitudes (300-360 km). It is important that, during all these periods, most of geomagnetic pulsation's were completely absent. Possible ways to study synergy effects of simultaneous absence of the geomagnetic field, magnetic pulsation's and microwave radiation of terrestrial ionosphere are considered for flight to Mars.

1. Introduction

Since the beginning of XXI century the focus of the manned space flight is forwarded towards important issues related to the preparation of the flight to the Moon and most importantly, to Mars [Systems, 2003].

Among these concerns the most attention bears investigations of the approaches relating to the problem of life-support of cosmonaut crew that consists of six people, based on current assumptions. For the most of the duration of the flight from Earth to Mars and landing study plans on Mars module assume the crew to be separated for periods exceeding one month. While the issues of radiation safety of the crew are traditionally considered as the primary part of the flight, the presence of the radiation zones as well as the destructive role of fluxes of solar energetic protons in interplanetary space flight require taking into account. These protons are known to appear in the form of solar proton events (SPE) after strong solar flares.

Previously a new, but very important for long interplanetary expeditions problem of psychophysical state of the crew in the absence of alternating electromagnetic fields and radiation, including the ionosphere one, was first raised for evolutionarily adapted humanity [Kovalenok et al., 2005]. However, up to date, this subject, in particular, during the long simulation experiments such as "Mars 500", which eliminates much of their value and contribution to the Mars mission, has almost no attention. Indeed, the results have clearly shown that the cosmonaut crews in orbital flight, even deep within geomagnetic sphere, may experience severe psychological discomfort, the nature of which is fully defined [Kovalenok et al., 2005]. This was the appearance of such rather unusual geophysical periods of different durations (ranging from minutes to days) those were in the form of an almost complete lack of geomagnetic pulsations on Earth.

Geomagnetic pulsation's (P) are the ultra-low frequency electromagnetic waves with a period of 0.2 to 600 seconds or more, and are divided into stable continuous (periodic) pulsation's (Pc) and irregular ones (Pi). The effect of such waves is known by geo-biological correlation study and has strong biophysical arguments [Bingi 2002; Sterlikova 2012]. It is obvious to assume that due to permanent effects of natural rhythms of the external synchronizer, those are geomagnetic pulsation's, these rhythms are the own ones of certain brain structures electrical activity. Indeed, the super slow fluctuations of potentials (SSFP) in the brain cerebral cortex were discovered, described and studied by [Aladjalova 1962, 1969, 1979]. In this case, the field of subsonic frequencies from 10^{-5} to 0.5 Hz, e.g. oscillations with a period of a few seconds to tens of minutes or hours, is coupled with the regulatory activities at different levels of the central nervous system (CNS). SSFP are the result of redistribution of electric charges on the cell membrane of an excited formation,

changing its membrane potential. These processes occur on the surfaces of opposing glial and neuronal cell membranes.

The aim of this paper is to confirm the need to consider possible pathological effects of the complete lack of rhythm forming, inherent for terrestrial environment geomagnetic pulsation's on the psychological and physical state of the cosmonaut crew for the preparation and conduct the manned flights beyond the Earth's magnetosphere, particularly to Mars.

Recently [Sterlikova, 2012] has presented new experimental data on the relationship of periods of extreme tension irritability and inappropriate behaviour of patients with neurological diseases to the absence of high-frequency types of geomagnetic pulsation's. The author has investigated the influence of the presence of different types of geomagnetic pulsation's recorded by Geophysical Observatory "Borok" of the Joint Institute of Physics of the Earth after O.Yu. Schmidt, Russian Academy of Sciences, on the statistics manifestations of various diseases for Murom City, located in the same region at a distance of about 50 km. It has been observed that period of the absence of pulsation's is typical for the maximum number of events in the manifestation of the diseases, especially nervous ones. High-frequency pulsation's, similar to frequency in the basic human biorhythms, were absent in 60 - 100 % for neurasthenia, 100 % - for neurosis and psychosis.

In [Sterlikova, 2012] represents data on number of attacks of cardiovascular and nervous illnesses in connection with absence and presence of geomagnetic pulsations of a range of biorhythms of the person for separate versions of cardiovascular and nervous illnesses. The subject and object of research are townsmen of Murom of Vladimir region. Control over geomagnetic conditions is conducted by geophysical observatory of Borok of Yaroslavl region (geomagnetic latitude Φ=53). Geomagnetic pulsations of types Pc1, Pi1C, Pi1B, IPDP are considered both at the moment of a first aid call, and in preceding 6 hours. The six-hour time interval is time of reaction of plasmapause on which the natural resonator (plasmasphere) changes the configuration and the sizes. We will carry out the analysis of the tabular data. Registration of calls of first aid concerning sudden attacks of cardiovascular and nervous illnesses was carried out both at the moment of absence, and at the moment of presence of geomagnetic pulsations of the specified types. However the number of patients needing medical aid sharply increased in process of increase in duration of absence of geomagnetic pulsations in region of inhabitancy of the person. One person has addressed for the help concerning chronic ischemic heart illness in a time interval corresponding to a recurrent storm by duration of 12 hours at Kpmax = 7, and to pulsations of type Pc1 by duration above 6 hours.

At short-term generation of Pc1 which have stopped at the moment of a call of first aid, the number of references has reached 5. 16 persons have addressed for the help in total absence of generation of geomagnetic pulsations of all specified types more than 6 hours in connection with aggravation of chronic ischemic heart illness. The similar picture in medical statistics of cardiovascular and nervous illnesses is traced at magnetic storms of character of flash. Even more considerable growth of attacks of cardiovascular and nervous illnesses with the same law is observed in absence of magnetic storms at low geomagnetic activity in the spring of 4.03-22.03.86.

The attacks of the cardiovascular and nervous illnesses is not observed practically during the moments of generation of geomagnetic pulsations Pi1B, Pi1C and IPDP, accompanying phases of development and restoration of a magnetic substorm. Besides, the table represents data on change of a sign of a direction of an interplanetary magnetic field. A sign of the interplanetary magnetic field changed from plus on a minus (25.02.85 - 01.03.85) in a recurrent storm with high geomagnetic activity (Kp =7). The Same character of change of sign of MMF is observed in absence of storms (04.03.86-22.03.86) at moderate geomagnetic activity (Kp =0-4). A sign of the interplanetary magnetic field is positive basically during magnetic storm of character of flash (5.02.86-14.02.86) with high geomagnetic activity (Kp =9) and only 09.02.86 has change of sign of MMF from minus on plus. However, negative sign of MMF was observed during rather short time (some hours).

2. Lack of geomagnetic pulsation's during observation periods of the planetary glow of the ionosphere

One of the co-authors (cosmonaut V.V. Kovalenok) during his 140-day mission from June to November, 1978, had recorded increased nervous irritability and conflict relationships between cosmonauts through the visual and instrumental observations of night emissions of the upper atmosphere of the Earth at mid-latitudes (on a planetary scale) [Avakyan et al., 1981; Kovalenok and Avakyan 1987].

It should be emphasized that the visual and instrumental studies of Soviet cosmonauts conducted during most flights on manned space crafts and orbital research stations had given many new data on various large-scale events and objects in the Earth's atmosphere and ionosphere, on the surface and in the depths (up to

several hundreds of meters) of the oceans [Kovalenok and Avakyan 1987; Avakyan et al., 1981, 1984, 1991; Avakyan et al., 1994; Lazarev et al., 1981, 1987]. Particularly important were the results on the impact of the factors of increased solar-geomagnetic activity on atmospheric optical and meteorological phenomena. Registration of variations in the upper atmosphere (ionosphere) glow and changes in cloud characteristics globally after such solar events as flares and following geomagnetic storms allowed to give a new interpretation of the causes of the current phase of global warming and its relation to solar activity [Avakyan and Voronin 2010, 2011].

Interpretation of the results concerning observations of optical radiation pattern in the upper atmosphere of the Earth on the board of orbital manned space station "Salyut-6" has shown [Avakyan et al., 1984; Avakyan 1997] that one of the unusual facts in geophysical weather, relevant to *all* these cases, was the absence of geomagnetic pulsations, always 1-2 days before a change of sign of the sectors of the interplanetary magnetic field (IMF) occurred. Discovered planetary glow was interpreted as a new geophysical phenomenon - the reaction of the night upper atmosphere to ultraviolet solar flares [Avakyan et al., 1984, 1985, 1991].

In a personal diary Kovalenok noted that in the period of registration of the planetary night glow of the upper atmosphere crew was experiencing increased excitability, which was expressed in the conflicts in radio communication with the Mission Control Center. It is certainly surprising that the sensitivity to very low levels of the amplitude of geomagnetic field variations persists even within the metal shell space station, although there are windows. Perhaps this is due to the lack of effect for the absorption of this type of pulsation's in the ionosphere, as orbital station was located in the upper part of the main peak of the ionization of the ionosphere [Avakyan et al., 1984]. Therefore, the presence of pulsation's is usually perceived by cosmonaut's body as stable, granted, ordinary factor, but the disappearance - creates the crew discomfort. It should be emphasized that these results are consistent with a serious analysis of the notorious problem of "*unfavourable days*" [Avdyushin and Danilov 1993] and confirmed to be promoted to the impact of "space weather" on the human state through study of the reaction to geomagnetic pulsation's.

Information on the observation periods of the psychophysical instability and the presence or, more typically, a lack of geomagnetic pulsations is shown in Table 1 [Kovalenok et al., 2005]. It also presents the main characteristics of the pulses [Pudovkin et al., 1976]: the period (frequency) and amplitude. The information about the manifestation of geomagnetic pulsation's in the Table 1 was obtained by measurements of the Geophysical Observatory "Borok". In the first six dates (see Table 1) cosmonauts Kovalenok, Ivanchenkov and Savinykh recorded usual in such cases "planetary glow of the second emissive layer," i.e. emissive radiation of the night F-region of the Earth-bound ionosphere at the time - in the mentioned periods. The four events are tied to time on the basis of data on the strong emission light of the night F-region (the red *emission* of the oxygen atom - 630 nm), according to the Abastumani Astrophysical Observatory, Georgian Academy of Sciences (Georgia) [Avakyan et al., 1985], cosmonauts in the period from 6th to 9th July, 1978, observed "planetary glow" almost every turn (for its dark side.)

Then, Table 1 summarizes information about the four types of geomagnetic pulsations of the following considerations. Ripple Pi1C, like all irregular pulses, usually characterize periods of geomagnetic disturbance. However, in times of global emission monitoring by cosmonauts its visual pattern was radically different from the pictures of auroras, which could also be observed on the middle and lower latitudes, but this was done during strong geomagnetic storms [Avakyan et al., 1984, 1991; Lazarev et al., 1981, 1987]. But Avakyan and colleagues [Avakyan et al., 1984] have examined in detail the ability, according to (ref. [Borovkova et al., 1983]), of observed glow of red emission of 630 nm with the appearance of class Pi1C oscillations. This does not observed for the dates covered in Table 1. Therefore, the phenomenon of "planetary glow of the second emissive layer" is different from the nature of auroras. The remaining ripple Pc2 - Pc4 are stable type and usually regularly recorded.

It is followed from Table 1 that in all the time (as periods of "planetary glow" time and time periods of increased conflict), there were no recorded geomagnetic fluctuations of stable type and of irregular ones.

An important factor to ensure adequate results for allocated special periods in geophysical weather (just without pulsation of Pi1C type, according to the Geophysical observatory "Borok") is that the observations of planetary glow of the upper ionosphere (i.e. it describes the pattern of reaction night-time ionosphere to solar flares [Avakyan et al., 1984, 1985, 1991]) by the station "Salyut-6" are usually performed at night by the Bork time zone (Table 1). And so the observed lack of Pi1C is really unusual phenomenon, because this type of daily maximum ripple falls exactly on 23.00-1.00 UT.

Table 1. Geomagnetic pulsation's during the observation periods for the phenomenon of the reaction the night, upper ionosphere to solar flares [Kovalenok et al., 2005].

		Irregular	Continuous (periodic)		
		Pi1C	Pc2	Pc3	Pc4
Frequency, Hz		More than 1	2x10–1 ÷ 6x10–2	6 ÷ 2x10–2	2x10–2 ÷ 6x10–3
Period, sec		1 ÷ 40	5 ÷ 15	15 ÷ 45	45 ÷ 150
Amplitude, 10–5 E		0.02	0.6	0.6	up 10
Date	Time, UT	Pulsation's recorded by Geophysical observatory "Borok"			
14.08.78	00.45-00.50	Very weak Pi1C	no	yes	no
16.09.78	20.00-03.00	no	no	From 00.40 - yes	no
28.10.78	20.30-21.16	no	no	no	no
28.10.78	22.44	no	no	no	no
03.05.81	00.38	no	no	no	no
03.05.81	15.52-15.56	no	no	no	no
06.07.78	23.30-01.00	no	no	yes	no
07.07.78	18.00-20.30	no	no	no	no
08.07.78	20.00-22.30	no	no	no	no
09.07.78	18.20-20.10	no	no	no	no

Earlier [Nikolaev et al., 1982] have pushed hypothesis about the decisive role of the disappearance of geomagnetic pulsations (short-period variations of the geomagnetic field), especially Pc2 - Pc4 with periods ranging from 5 to 150 seconds, in disorders of human CNS. It could be emphasized that another fact - special influence of polarity changes in IMF sectors (most of all – under the change from negative polarity to positive one) was marked experimentally. To explain this phenomenon it is proposed to take into account that the patient's (and in our opinion, in the case of space flight – cosmonaut subjected to stress, gravity and other factors) body needs almost constant exposure to the electromagnetic field quasi sinusoidal oscillations of a certain frequency from external sources to synchronize the operation of its various systems [Nikolaev et al., 1982]. Therefore, it is noted that such external factors may ripple geomagnetic field, sometimes disappearing all over the Earth simultaneously [Nikolaev et al., 1982].

In general, the natural electromagnetic field of the Earth is a whole spectrum of electromagnetic "noise" in a wide frequency range from 10^{-3} Hz to 10^{9} Hz [Pudovkin et al., 1976]. Recently attention to the higher frequency range - microwave radiation of the ionosphere was drawn [Avakyan 2005, 2006]. Because of the existence of wave motions in the upper atmosphere in the form of acoustic-gravity and infrasound waves, this radiation of the ionosphere is modulated in amplitude just in subsonic frequencies - from 10^{-5} Hz to a few Hz, in the area of the SSFP in the brain cerebral cortex [Aladjalova 1962, 1969, 1979]. So background of electromagnetic waves always existed on the surface of the Earth is generated by several sources. Among them – micro-pulsations of geomagnetic field, very low frequency (VLF) radiation of the magnetosphere and ionosphere, and atmospherics (low-frequency part of the spectrum of lightning charges). The oscillation amplitude (field intensity) is maximal in the VLF range (less than 5 Hz), where the magnetic component is usually recorded - short-period variations of the geomagnetic field (micro-pulsation's). These micro-pulsation's as well as fluctuations in the high frequencies (kHz) are generated in the magnetosphere, or on its border.

Different types of pulses appear mainly at certain times of day. In times of disturbances (magnetic storms) global micro-pulsation's excitement are observed and then they can be recorded during dozens of hours in a row around the Earth. Top-of-the storm is preceded by the appearance of oscillations in the band Pc1-called pearl. The main frequency of 3±0.3 Hz for these oscillations is amplitude-modulated with a period of 2-5 min.

All these electromagnetic waves are usually the background for the earthling to disappear with the release of the interplanetary spacecraft beyond the magnetosphere, and after a few days of flight the cosmonauts will be out of the usual electromagnetic "noise", as well as outside the geomagnetic field. As shown in (ref. [Kholodov and Lebedeva 1992]), hypo-geomagnetic field also affects humans. The person may feel (pain as the impact) of 1000 weakened field, as well as increased one at about the same time in 1000. It is unknown,

however if the simultaneous absence and the geomagnetic field, and electromagnetic waves in a wide range of frequencies - from low (including in the field of brain rhythms, heart, etc.), to the highest, the extremely high frequencies affect the human organism upon the resonance effects on the body cells [Avakyan 2005, 2006]. Therefore, in the coming years, in the preparatory stages of the first interplanetary flight, it is required to study synergistic effects of exposure to the fields on human - under expected absence of the usual, "sets" oscillations of electromagnetic fields, especially geomagnetic pulsations, when real background of hypo-magnetic field exists.

It should be emphasized that the flights and landings on the Moon cannot be analogous to discuss the situation, as the flights continued outside the magnetosphere of the Earth less than a week. Perhaps it is most importantly, the Moon during each lunar month (29 days) for several days is trailing geomagnetosphere.

Summary

This paper discusses the new priority tasks that are necessary to ensure the safety of manned flight to Mars and more in detail considers the issues raised earlier by Kovalenok et al. [Kovalenok et al., 2005].

The core of the study is the situation in the psychological state of the crew of cosmonauts when there is completely no natural electromagnetic "noise" which accompanies the whole evolution of mankind. A part of the study can be realized on the international space station by the same scenario as in the observation made by the orbital manned space station "Salyut-6" [Kovalenok et al., 2005]. This can be done, for example in the framework of European Space Agency – "Roscosmos" Agency Joint Program, as the detection and study of potential hazards for interplanetary flight. It should use just the technique of visual detection of an elevated emission of the upper atmosphere on a global scale [Avakyan et al., 1984]. The rest of the program will require a special experimental study with the construction of chamber with hypo-magnetic field while shielding microwave radiation generated in the Earth's ionosphere [Avakyan 2005, 2006].

References

Aladjalova, N.A. (1962), *Slow Electrical Processes in the Brain*, Moscow, Acad. Sci. USSR.

Aladjalova, N.A. (1969), *Super slow rhythmic processes in the nervous system in: Continuous Potentials of the Nervous System*, Tbilisi.

Aladjalova, N.A. (1979), *Psychophysiological aspects of brain super slow rhythmical activity*, Moscow: Nauka.

Avakyan, S.V. (1997), Investigations of heliogeophysical disturbances under nocturnal conditions from manned spacecraft, *J. Opt. Technol*. 64, 940-945.

Avakyan, S.V. (2005), Microwave radiation of the ionosphere as a factor in the way solar flares and geomagnetic storms act on biosystems, *J. Opt. Technol*. 72, 608-614.

Avakyan, S.V. (2006), Microwave ionospheric emission as a new factor of Solar-biosphere relations, *Proc. 4th Int. Workshop "Biol, Effects of Electromagn, Fields",* Crete, 2, 1513-1522.

Avakyan, S.V. and N.A. Voronin (2010), On the radiooptical and optical mechanisms of influence of cosmic factors on the global warming, *J. Opt. Technol*. 77, 141-144.

Avakyan, S.V. and N.A. Voronin (2011), The role of space and ionospheric disturbances in the global climate change and pipeline corrosion, *Proc. Atmospher. & Ocean. Physics* 47, 1143-1158.

Avakyan, S.V., G.S. Kudryashev, L.M. Fishkova (1985), Concerning the amplification of the O I 630-nm emission of luminescence of the sky during solar flares, *Geomagnetism i Ae´ronomiya*, 25, 415-419.

Avakyan, S.V., L.S. Evlashin, V.V. Kovalenok, A.I. Lazarev, V.G. Titov (1991), *Observations of the Auroras from Space*, Leningrad: Gidrometeoizdat.

Avakyan, S.V., V.I. Drobzev, V.M. Krasnov, G.S. Kudrjashev, A.I. Lazarev, A.G. Nikolaev, V.I. Sevastjanov, A.F. Yakovets (1981), *Waves and Emissions of the Upper Atmosphere*, (Eds. S.V. Avakyan, V.M. Krasnov, A.I. Lazarev) Alma-Ata: Nauka.

Avakyan, S.V., V.V. Kovalenok, N.F. Solonitsyna (1984), *The nighttime F region of the Ionosphere in the Period of Flares on the Sun*, Nauka: Alma-Ata.

Avdyushin, S.I. and A.D. Danilov (1993), *An Account of Space Weather*, Leningrad: Gidrometeoizdat.

Bingi, V.N. (2002), *Magnetobiology. Experiments and Models*, Moscow, IOF RAN.

Borovkova, O.K., Yu.E. Borovkov, V.A. Troitskaya (1983), On the connection of the amplification of the 6300 Å emission in middle latitudes with geomagnetic pulsations, *Geomagnetizm i Ae´ronomiya*, 23, 494-496.

Kholodov, Yu.A., and N.N. Lebedeva (1992), Electromagnetic Biology (ed. Ayrapetyants, M.G.) Moscow: Nauka.

Kovalenok, V.V., and S.V. Avakyan (1987), *The colours of space, in: Space*, Leningrad: FTI.

Kovalenok, V.V., S.V. Avakyan, O.K. Borovkova, N.A. Voronin (2005), Space solar patrols and some problems of manned flight to Mars, *J. Opt. Technol.* 72, 8 615-619.

Lazarev, A.I., V.V. Kovalenok, A.S. Ivanchenkov, S.V. Avakyan (1981), *The Earth's Atmosphere from Salyut-6*, Leningrad: Gidrometeoizdat.

Lazarev, A.I., V.V. Kovalenok, S.V. Avakyan (1987), Investigation of Earth from Manned Spacecrafts, Leningrad: Gidrometeoizdat.

Nikolaev, Yu.S., J.J. Rudakov, S.M. Mansurov, L.G. Mansurova(1982), Interplanetary magnetic field sector structure and disturbances of central nervous system activity, *Probl. Space Biol*. 43, 51-59.

Pudovkinm M.I., O.M. Raspopov, N.G. Kleimenova (1976), *Perturbations of the Earth's Magnetic Field. Chap. 4*, Leningrad: Leningr. State Univ. Press.

Sterlikova, I.V. (2012), Research of influence of the corpuscular agent of solar activity on the human organism, Fundament. *Res. Phys. & Math. Sci.* 11, 715-721.

Systems and technologies for future exploration and development of space – Intern. Conference, Abstracts (Moscow: ISTC, 2003).

MAIN (MULTISCALE AURORA IMAGING NETWORK) AURORAL CAMERAS: OVERVIEW OF EVENTS OBSERVED DURING LAST WINTER SEASONS

Boris V. Kozelov

Polar Geophysical Institute, Apatity, Murmansk region, 184209; e-mail: boris.kozelov@gmail.com

Abstract. The report presents an overview of aurora events observed by MAIN (Multiscale Aurora Imaging Network) camera system during last three winter seasons 2011-2014. The MAIN camera system consists of 4 auroral cameras installed at Kola Peninsula in Apatity for observations of auroral structures at different scales: from fine structures near magnetic zenith to all-sky luminosity. The MAIN cameras and all-sky camera in Lovozero observatory give possibilities to triangulate auroral structures. Two pairs of cameras can be employed i) narrow (18 degrees) field-of-view cameras with 4 km distance between them and ii) two all-sky cameras which were 86 km spaced. Typically there are more than 200 hours of aurora observations by the MAIN cameras during each winter season. The most part of the observations contains of slow aurora which is located near the north horizon and which is always seen near the local midnight in cloudless sky even in quiet geomagnetic conditions. The disturbed magnetospheric conditions lead to active aurora near the zenith of the camera system. There are a few events (magnetic storms) then the bright aurora moves to south horizon of the field of view. The report presents a statistics of observed auroral events and some interesting examples. All the data are available through INTERNET and the description of the access to the data is given. The work is supported by Presidium of Russian Academy of Sciences through Program 22.

Introduction

Aurora is the most impressive manifestation of the Earth's magnetosphere dynamics. Optical observations of the aurora display give unique spatial-temporal information about individual processes in the natural plasma machine - magnetosphere-ionosphere system. Systematic permanent observations are needed to fill by measurements the possible phase space of the system under study.

Recently, the Multiscale Aurora Imaging Network (MAIN) camera system has been installed in the Apatity. The MAIN camera system consists of 4 auroral cameras installed at Kola Peninsula in Apatity for observations of auroral structures at different scales: from fine structures near magnetic zenith to all-sky luminosity. Then MAIN system and some results have been described in papers [Kozelov et al., 2011, 2012a, 2012b, 2013].

The data of the MAIN auroral cameras located in Apatity and all-sky camera in Lovozero observatory have been used to triangulate auroral structures. Two pairs of cameras are possible to employ: i) narrow (18^o) field-of-view cameras with ~4 km distance between them and ii) two all-sky cameras which are ~86 km spaced. Triangulation abilities and discrepancies are tested by events of satellite flashes and meteor tracks [Kozelov et al., 2012b]. The results are compared with previous findings and theoretical estimations [Störmer, 1910; 1911; Stenbaek-Nielsen et al., 1976].

The report presents statistics of auroral events observed by MAIN cameras during three winter seasons (2011-2014), describes the data products and the data availability.

Equipment

A schema of the MAIN observational system is shown in Fig. 1. Four cameras were operated automatically during dark time, independently of weather conditions. The cameras were installed on the main building of the Apatity division of the Polar Geophysical Institute (PGI) and at Apatity stratospheric range. The system is described in details in paper [Kozelov et al., 2012a].

Two identical cameras AVT Guppy F-044B NIR with narrow (18^o) field of view are aimed to be used for triangulation. The cameras contain the most sensitive non-intensified interlaced Sony CCD sensors of TV format. Each camera is placed in an individual housing box with a heater located near the input glass window. Both cameras are additionally equipped by blue-green glass filter (C3C21) to decrease influence of long-lived excited states of atomic oxygen. The cameras were mounted on industrial pan-tilt motorized

mounts to fit the direction of observation. Usually the cameras are directed to a region near magnetic zenith. The distance between the points of observation is 4120 m, so identical monochromatic cameras can be used as a stereoscopic system to resolve auroral structures at altitudes of 90-300 km. A special module was developed for precise synchronization of image capture by the cameras. The estimated precision of time synchronization for simultaneous images is better than a few milliseconds, which is a good precision for auroral observations.

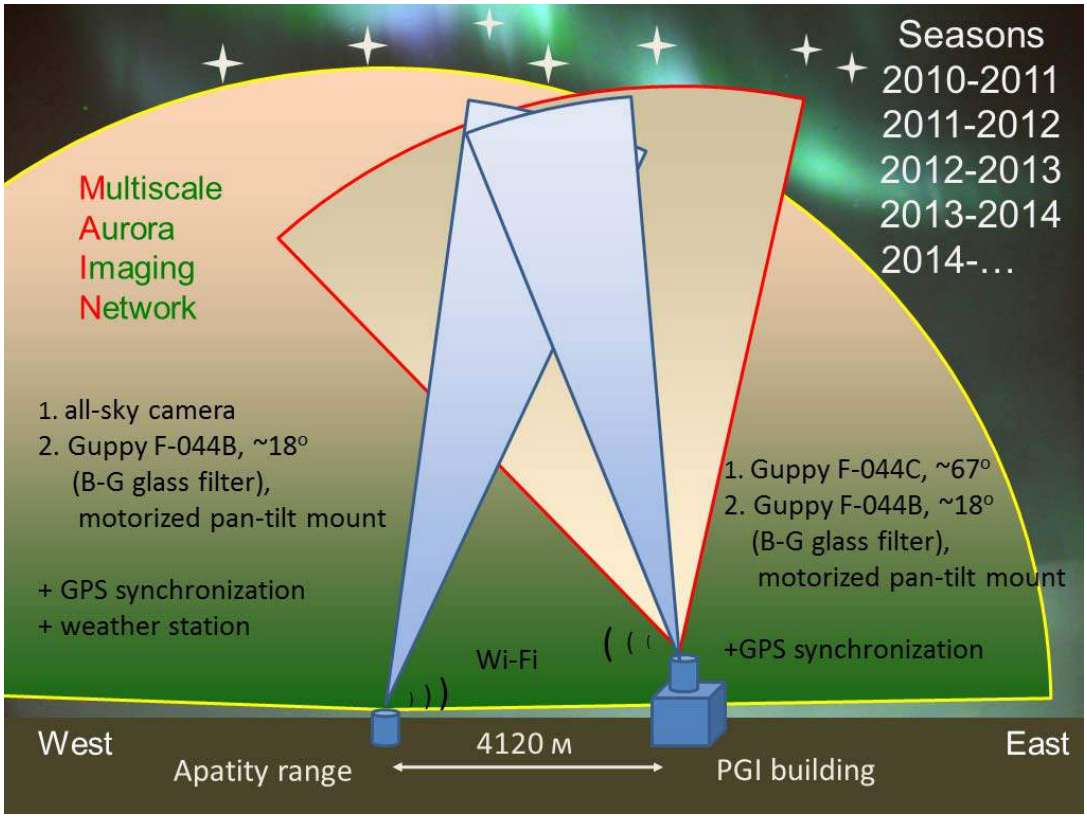

Figure 1. Schema of the MAIN camera system in Apatity.

Table 1. Parameters of the MAIN cameras.

Name	Camera	Interface	Lens	Field of view	Position	Resolution
AS	LCL-902K or LCL-811K	Analog video with frame grabber	Fujinon YV2.2x1.4A-SA2	180°	67°34' N, 33°18' E	232x232 (290x288), 12 bits, 1s (sum of 24 frames)
G1	AVT Guppy F-044B NIR	IEEE 1394a	Fujinon HF25HA-1B + BG filter	15°x10° 18° diag.	67°34' N, 33°18' E	376x288 8(12) bits, 1s
G2	AVT Guppy F-044B NIR	IEEE 1394a	Fujinon HF25HA-1B + BG filter	15°x10° 18° diag.	67°34' N, 33°24' E	376x288 8(12) bits, 1s
GC	AVT Guppy F-044C NIR	IEEE 1394a	Fujinon DF6HA-1B	56°x44° 67° diag.	67°34' N, 33°24' E	376x290 4 colors CMY+G, 8(12) bits, 1s

Scientific problems

The main scientific problems aimed by the MAIN camera system are:

i) Scaling in small-scale structures of aurora. This is one of the key questions in studying of the magnetosphere-ionosphere plasma turbulence.

ii) Spatial and temporal structure of pulsating aurora. This information is needed for next step in investigation of the wave-particle interactions in the magnetosphere-ionosphere system.

iii) Vertical distribution in rayed structures. This specific case is important to understand a structure of electric fields and particle sources in the region of auroral acceleration.

The all-sky camera included in the MAIN system can also be used in traditional studies of the magnetosphere substorm dynamics, see Fig.2.

Two examples of multiscale observations of different auroral structures are shown in Fig.3 and Fig.4.

Data products and access

There are three levels of data produced by the MAIN camera system.

"Level 0" consists of raw image arrays with resolution 1 frame per second. The data are available by request to author, but it should be taken into account the data volume. Estimated size for cameras G1 and G2 is ~370 Mb/hour, for allsky camera (AS) is ~ 740 Mb/hour and for color camera GC is ~ 1.5 Gb/hour.

"Level 1" data contains of hourly keograms and separated frames with 10 s intervals. This data produced automatically for time then the cameras were operated and it assumed be used to search events. This data are available on-line here: http://aurora.pgia.ru/archive.html.

"Level 2" data is a table which summarizes all visually selected hourly intervals with aurora in the field of view of the cameras. The table has links to pre-generated avi-movi, keograms, some additional information about geophysical conditions (Dst, AE, AL, magnetograms), and other simultaneous observations (Lovozero, Barentsburg). This information is available on-line here: http://aurora.pgia.ru/events/.

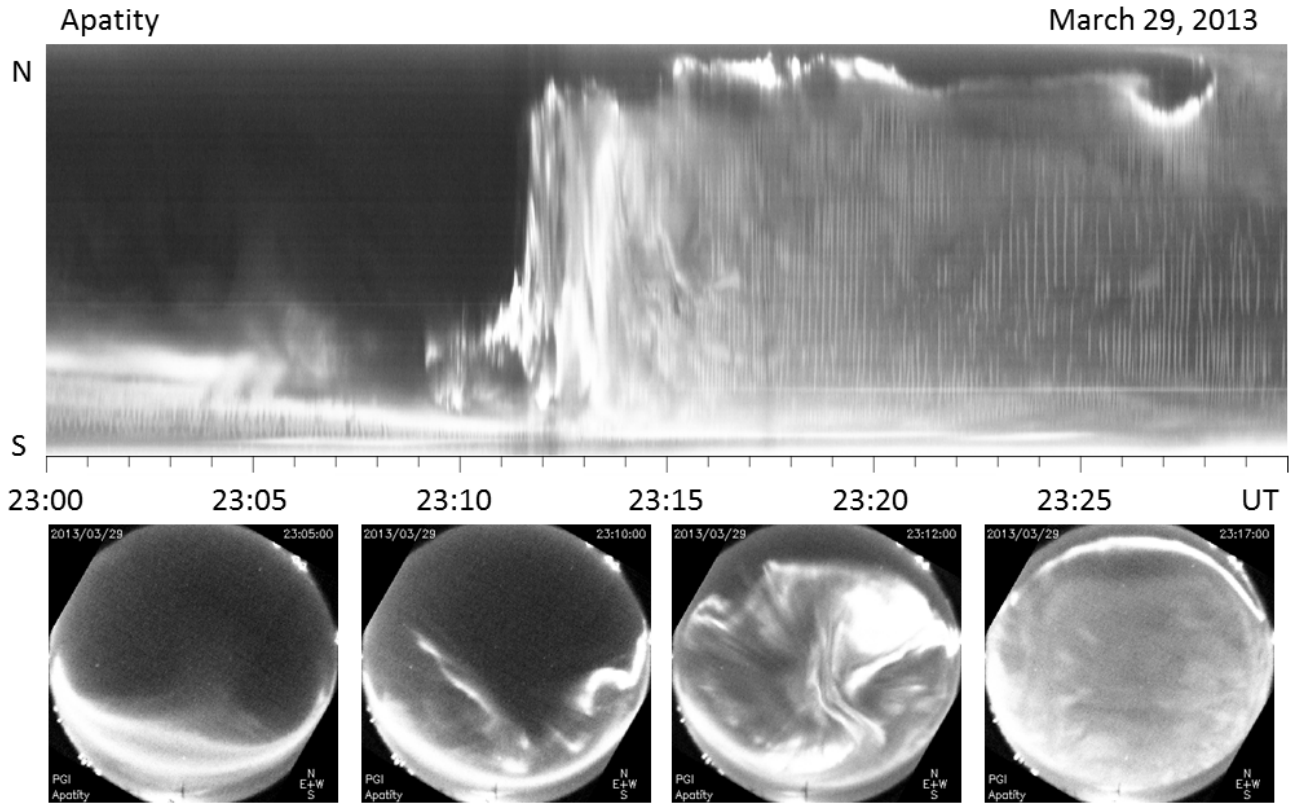

Figure 2. Typical auroral substorm onset and following pulsing aurora observed by Apatity all-sky (AS) camera: top panel – keogram, bottom panel – several frames.

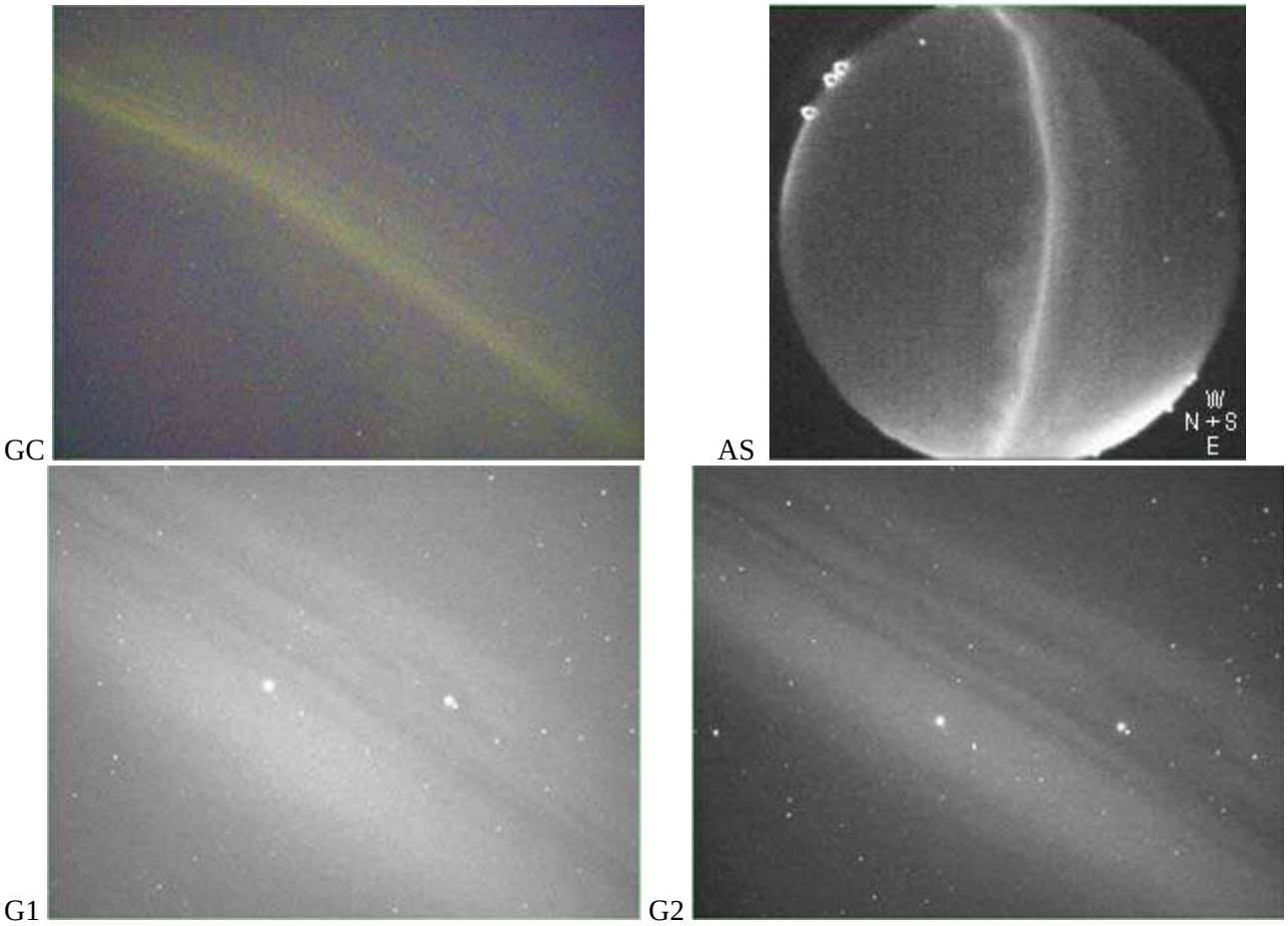

Figure 3. MAIN observation of multiple auroral arc, 25 March 2014, 22:56:50 UT.

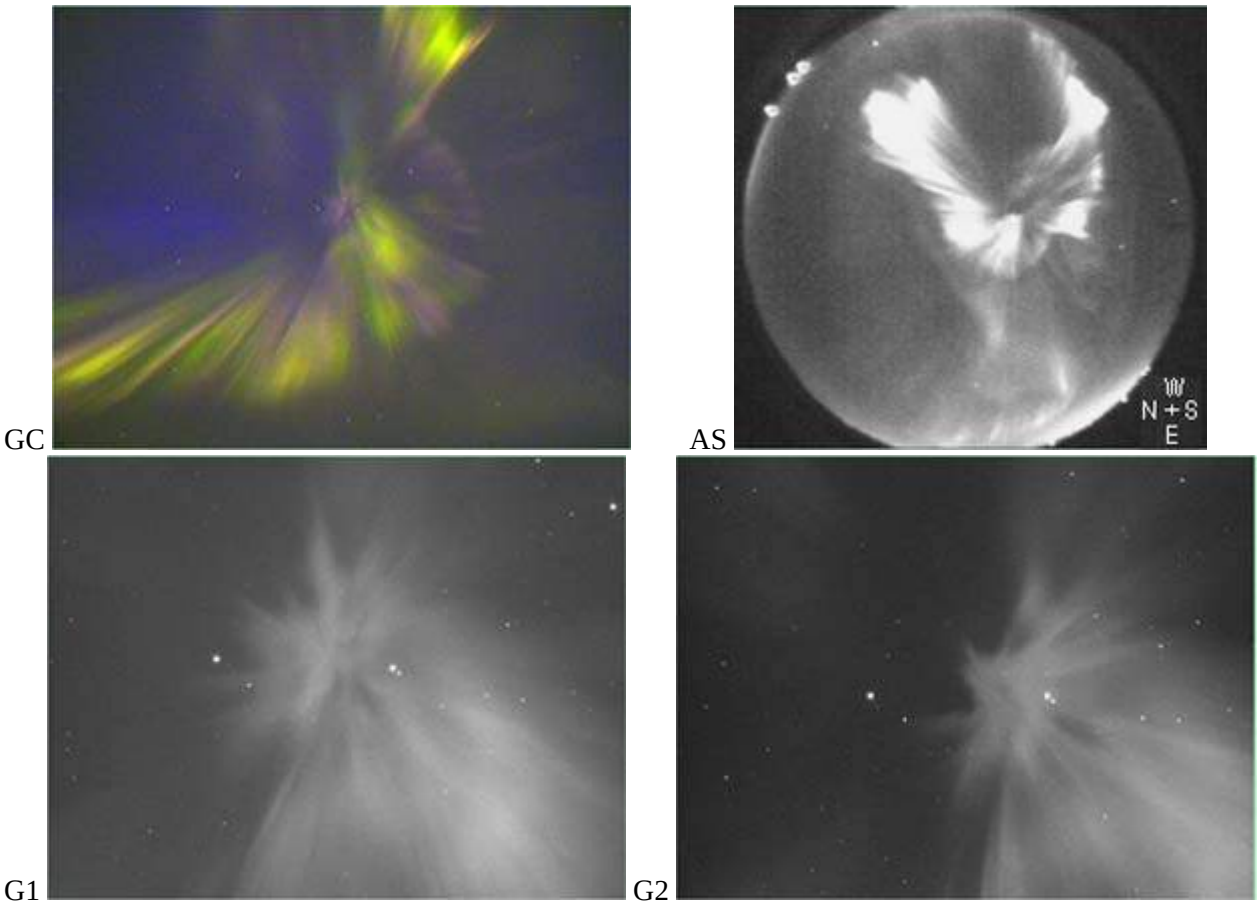

Figure 4. MAIN observation of auroral corona (system of rays), 25 March 2014, 23:05:20 UT.

Statistics of observed events

Some preliminary statistic of events observed by the MAIN cameras during three winter seasons is presented in Table 2. As a unit we use an hourly interval when aurora was observed by given camera (possible not whole hour, but during this hour). During each season we had above 220 such individual hours. Most of them were obtained by allsky (AS) camera. The main limitation factor is cloudiness. The hardware and software problems are less important, but also influence mainly on AS and G2 cameras. The city-light pollution decrease number of observed events by G1 and GC cameras.

Statistic of intervals of possible triangulation by G1 and G2 cameras is also presented in separated column "G1+G2" of Table 2. Another triangulation pair is possible with all-sky camera in Lovozero observatory. As one can see in the last column of the Table 2, the simultaneous observation with Lovozero all-sky camera was only in ~50% of all intervals. So, the observations in Apatity give additional original information to observation in Lovozero.

Table 2. Number of hourly intervals when aurora was observed by the MAIN cameras.

Season	Total	AS	GC	G1	G2	G1+G2	+LOZ AS
2013 – 2014	222	222	58	54	34	29	110
2012 -2013	225	225	70	82	95	78	128
2011 -2012	210	178	110	85	86	64	95

Figure 5 presents statistical information about geomagnetic conditions during the events observed in 2011-2014 winter seasons: distributions of hourly *Dst* and *AE* indexes.

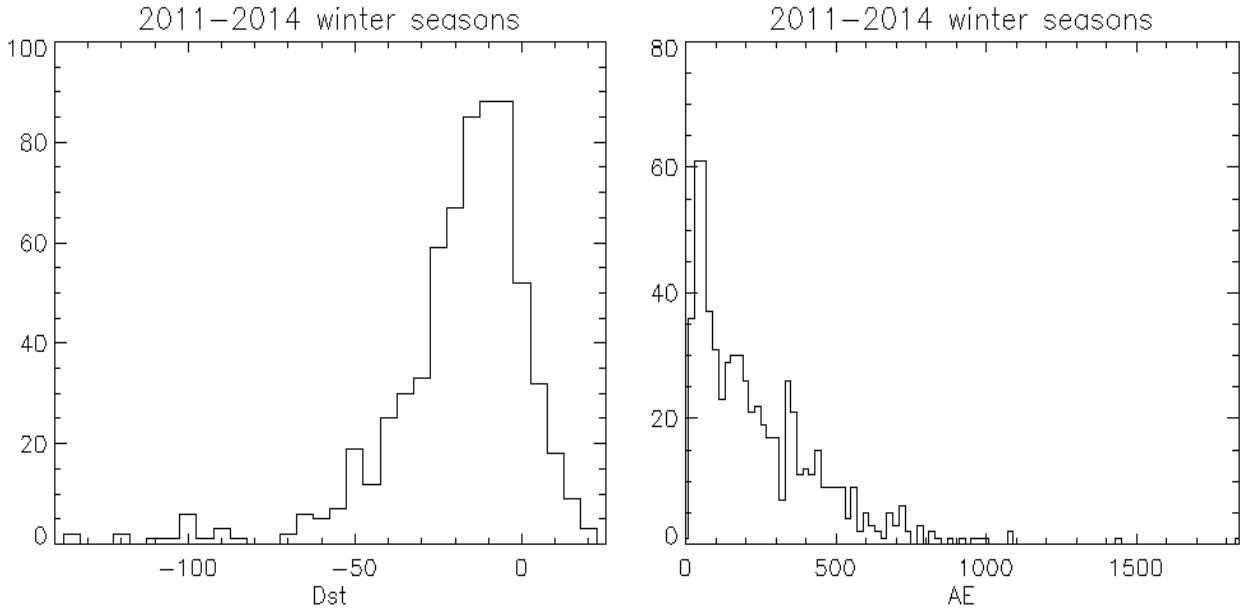

Figure 5. Distributions of hourly *Dst* and *AE* indexes for intervals of observed aurora events.

Morphological classification of observed event for last two seasons is presented of Table 3. One can see that the most observable events are pulsations near the North horizon. Really we can see there the quite auroral oval. Aurora in the zenith of Apatity occurs much rare, in more disturbed conditions. The camera positions are separated in E-W direction, so to use the data in triangulation algorithm we need an intensity gradient in this direction. Therefore the N-S structures in the aurora are the most preference events for this type of analysis.

Table 3. Types of observed events.

Season	**2012-2013**	**2013-2014**
Pulsations near the North horizon	120	122
Arcs in zenith of GC	24	31
Possible triangulation G1-G2, where:	78	29
- rays	17	8
- pulsations	28	14
- N-S structures	20	8

Conclusions

The MAIN (Multiscale Aurora Imaging Network) camera system is successfully operated during more than three years. The data produced by the cameras are useful as well for traditional geophysical studies of substorm dynamics as for multiscale analysis. In average for ~50% cases the MAIN all-sky camera observed aurora then the Lovozero had no observations. Small separation the cameras G1 and G2 location gives possibility for simple estimation of altitude by triangulation. The report presents statistics of auroral events observed by MAIN cameras during three winter seasons (2011-2014): statistics of the geomagnetic conditions and morphology of the auroral structure observed. Description of the data products and the data availability are also given.

Acknowledgements.
The work is supported by Presidium of Russian Academy of Sciences through Program 22.

References

Kozelov B.V., Golovchanskaya, I.V. (2010), Derivation of aurora scaling parameters from ground-based imaging observations: Numerical tests. *J. Geophys. Res.*, 115, A02204, doi:10.1029/ 2009JA014484.

Kozelov B.V., Pilgaev S.V., Borovkov L.P., Yurov V.E. (2011), Multi-scale auroral observations in Apatity: winter 2010-2011. *Proceedings of XXXIV Apatity seminar "Physics of auroral phenomena"*. - Apatity: Kola Science Center RAS, 129-132.

Kozelov B.V., Pilgaev S.V., Borovkov L.P., Yurov V.E. (2012a), Multi-scale auroral observations in Apatity: winter 2010-2011, *Geosci. Instrum. Method. Data Syst*., 1, 1-6, www.geosci-instrum-method-data-syst.net/1/1/2012/doi:10.5194/ gi-1-1-2012a.

Kozelov B.V., Pilgaev S.V., Borovkov L.P., Yurov V.E. (2012b), On triangulation by auroral cameras. *Proceedings of XXXV Apatity seminar "Physics of auroral phenomena"*. - Apatity: Kola Science Center RAS, 41-44.

Kozelov B.V., Brandstrom B.U.E., Sigernes F., Roldugin A.V., Chernouss S.A. (2013), Practice of CCD cameras' calibration by LED low-light source. *Proc. of 36th Annual Seminar "Physics of auroral phenomena"*, 26 February-1 March 2013. Apatity, 151-154.

Stenbaek-Nielsen H.C., T.J.Hallinan, and T.N.Davis (1978), Stereo-TV Observations of Pulsating aurora, *J. Geomag. Geoelectr*., 30, 343-344.

Störmer, C. Photographies des aurores boreales et nouvelle methode pour mesurer leur altitude (1910). *Comptes Rendus de l'Academie des Sciences*, 150, 1631–1634.

Störmer, C. (1911) Resultats des mesures photogrammetriques de l'altitude de l'aurore boreale a Bosekop aux mois de fevrier et de mars 1910. *Comptes Rendus de l'Academie des Sciences*, 152, 1194–1196.

VARIATIONS OF TOPSIDE N(h)-PROFILES OF THE IONOSPHERE DURING SPACE WEATHER EVENTS

O.A. Maltseva, G.A. Zhbankov, N.S. Mozhaeva

Institute for Physics, Southern Federal University, Rostov-on-Don, 344090, Russia, e-mail: mal@ip.rsu.ru

Abstract. The article is devoted to the possibility of the electron density Ne determination in the plasmasphere using experimental values of the total electron content TEC. It is shown that in the conditions of Space Weather event on April 21, 2001 only the global map JPL showed response to disturbance. The latitude distribution of density at plasmaspheric heights has been tested by means of the RPI model using radio plasma imager measurements on NASA's IMAGE satellite. The conclusion was made that for the unambiguous determination of Ne in the plasmasphere it is necessary to have both more exact values of TEC, and a more perfect model of the ionosphere.

Introduction

Knowledge of Space Weather effects is important both for geophysical investigations, and for applications. As it is noted in the report of authors on the previous symposium, Space Weather effects are studied in behavior of such ionospheric parameters, as the critical frequency foF2, the maximum height hmF2, the total electron content TEC, but not in behavior of electron density N(h)-profiles (Maltseva et al., 2012b). In our previous paper, the behavior of topside parts of a N(h)-profile is explored during disturbances. The IRI-Plas (Gulyaeva, 2003; 2011) model and the following data were used: 1) foF2 of a chain of ionosondes (Loparsk, Leningrad, Moscow, Rostov), 2) TEC of the JPL global map, 3) plasma frequencies fne measured on satellites CHAMP and DMSP on an example of April 2001 including two strong disturbances (1-2.04, minimum Dst =-228 nT, 11-12.04, minimum Dst =-271 nT) and two weak disturbances (18 and 22-23.04) with minimum Dst ~-100 nT. 9 cases of flights of satellites over all stations have been selected. It allows for estimation of latitudinal variations. These flights were near to midday and midnight and captured both the positive (1-6.04) and negative (all the other days) disturbances. Quantitative estimation of variations is given for an electron density Ne in the topside ionosphere for each station, and gradients in a chain. It was indicated on redistribution of ionization in the topside ionosphere and sign change of latitudinal gradients. The presented report is development of the previous paper with reference to density in the plasmasphere. The plasmasphere plays an important role in space weather. It is very important to have an empirical model of electron density Ne in the plasmasphere as it can be used for investigation of propagation of waves (whistler, chorus, hiss), dynamics of radiation belts, an estimation of velocity of filling of a plasmasphere after disturbances, for forecast of Space Weather. It is necessary to estimate whether the IRI-Plas model can serve as such a model. Development and addition was fulfilled in following directions: (1) maps CODE, UPC, ESA are used, (2) coefficient K(PL) for updating plasmaspheric parts of N(h)-profile is introduced and dependence of its behavior on UT and latitude is investigated, 3) behavior of Ne in the plasmasphere is explored during disturbances of April 2001, 4) distribution of Neq(L) is obtained in an equatorial plane with use of data of measurements from the radio plasma imager (RPI) on NASA's IMAGE satellite.

Usage of TEC to obtain plasmaspheric part of Nh-profiles

Parameter TEC (the total electron content) possesses a number of advantages: continuing global monitoring, availability of values on the Internet, information about a N(h)-profile. Usage of TEC for determination of electron density in a plasmasphere is attractive. One of possibilities is given by the IRI-Plas model which includes a plasmaspheric part of a profile, and also allows a model to be adapted for current value of TEC (Gulyaeva, 2003; 2011). However comparison of the adapted profiles with density measurements on low-altitude satellites shows that values of TEC calculated for the model differ from the experimental ones. The experimental values of TEC are designated as TEC(obs) below. One of the reasons is the mismatch of shape of a N(h)-profile from real dependence. For the clearing up, what part of a profile is more responsible for discrepancies, we divided it into 3 parts: (1) bottom side from the beginning of the ionosphere up to the

maximum height hmF2, (2) topside from hmF2 up to 2,000 km, (3) plasmaspheric higher 2,000 km. In the present paper some types of profiles settle up and are compared. Following designations are used. Profiles for the initial IRI-Plas model (without adaptation) have designation IRI. Appropriate value of TEC is equal TEC(IRI). At adaptation of a model to various parameters, we obtained various profiles and values of TEC corresponding to them. Profiles for the model adapted for the experimental values foF2(obs) and TEC(obs) have designation All. Profiles for the model adapted for the experimental values of plasma frequency fne(sat) of one satellite have a designation s1. Value of TEC(s1) corresponding to them is not equal TEC(obs) in most cases. For correspondence with TEC(obs) the coefficient K(PL) modifying a plasmaspheric part of a profile is introduced. The corresponding profile has a designation s1+PL that means the result of adaptation to a plasma frequency fne(sat) and modification by means of the coefficient K(PL). In most cases value TEC is equal TEC(obs) after this procedure.

Results

Observational data of TEC values were used from the global maps of JPL, CODE, UPC, ESA, which were calculated from IONEX files (ftp://cddis.gsfc.nasa.gov/pub/gps/products/ionex/) for given coordinates and epoch. Values of ionospheric parameters were taken from the SPIDR database (http://spidr.ngdc.nasa.gov/spidr/index.jsp). Results are given on an example of the latitudinal chain of points for a longitude 30° and the April 2001 including two strong disturbances (1-2.04, minimum Dst =-228 nT, 11-12.04, minimum Dst =-271 nT) and two weak disturbances (18 and 22-23.04) with minimum Dst ~-100 nT. In Fig. 1 behavior of Dst index within a month and behavior of plasma frequency fne(CHAMP) of the CHAMP satellite is shown. Altitude of CHAMP was ~420-440 km.

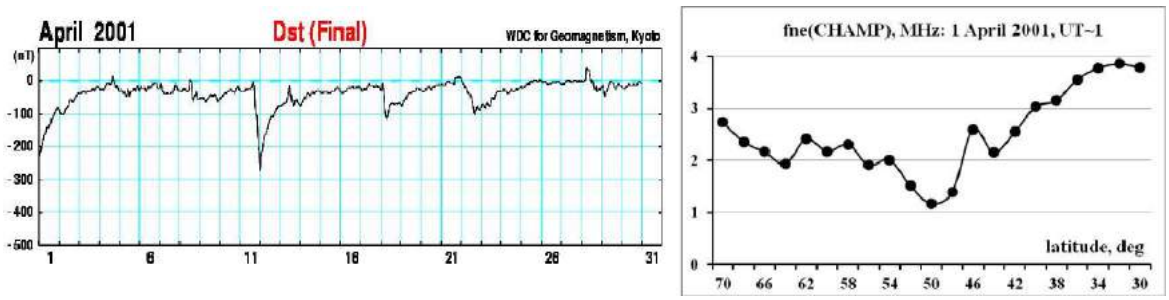

Fig. 1. Behavior of parameters Dst and fne (CHAMP) during disturbances considered

It is seen that one of the strongest disturbances corresponds to April, 1st. Flight of the CHAMP satellite was in this day on UT~1. The trough was drifted to latitude ~50°. In Fig. 2 profiles for the initial model IRI-Plas which are considered as profiles for a quiet (non disturbed) state, and profiles of the model adapted to TEC(JPL) are shown. The profile is divided into 2 parts: from the beginning of an ionosphere to height of 1,000 km and from height of 1,000 km to 20,000 km, appropriate height of TEC measurement.

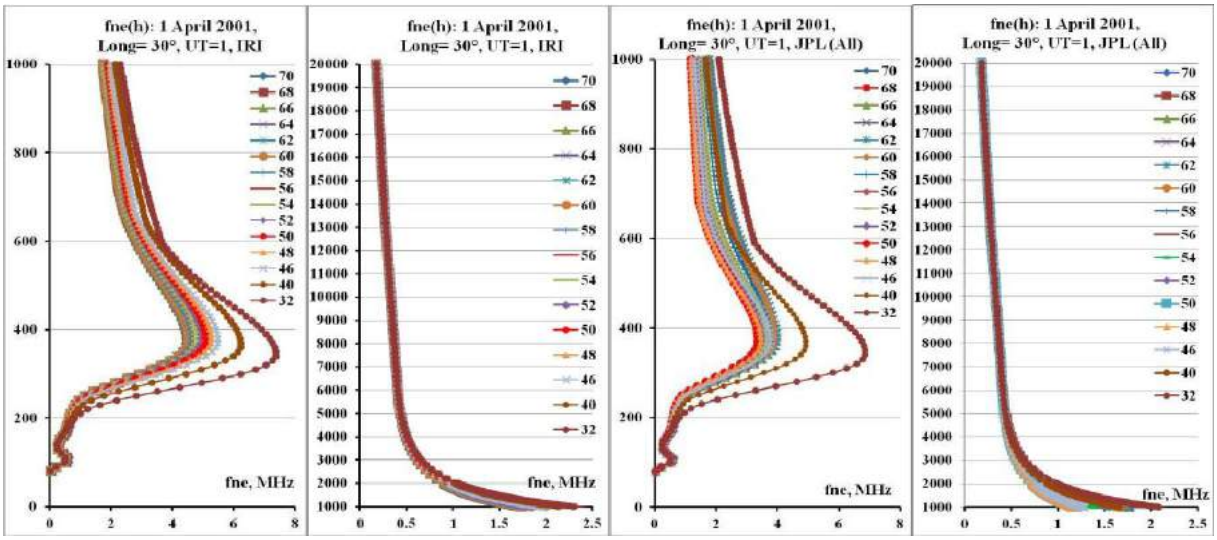

Fig. 2. Profiles for the initial IRI-Plas model and the model adapted to foF2(obs) and TEC(JPL).

The range of latitudes in this Figure corresponds to the European part of Russia with a longitude 30°, a latitudinal step was 2°. Critical frequencies for each point were calculated according to the following procedure (Maltseva et al., 2012a). For stations Loparsk, Leningrad, Moscow, Rostov, Athens values of a median of an equivalent slab thickness τ(med) have been calculated with use of corresponding global maps. Latitudinal dependences τ(med) were under construction from them and these dependences were used for obtaining τ(med) in each point. Then these τ(med) were used for calculation critical frequences.

It is seen that critical frequencies for all profiles were decreased, profiles with the minimum density for the initial IRI-Plas model concern latitudes 60-64°, and for adapted model - to the trough latitude on 50° as a result of response of foF2(obs) on disturbance. Profiles of plasmaspheric parts coincide at the large heights. Profiles for the model adapted for plasma frequency fne(CHAMP), and also for the model modified by K(PL), are shown in Fig. 3.

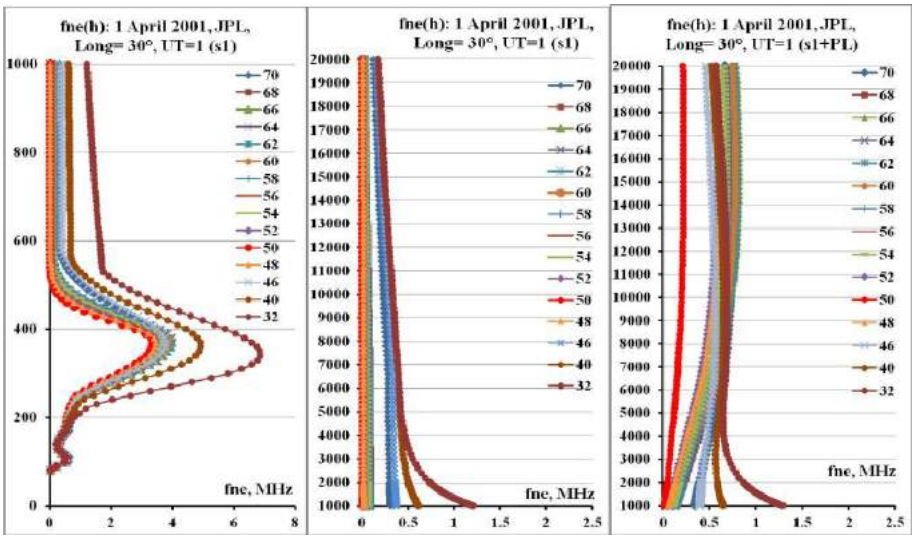

Fig. 3. Profiles for the model adapted to fne(CHAMP), and also for the model modified by K(PL)

Essential decrease of density as in the topside, and also plasmaspheric parts of profiles for all latitudes is seen. Profiles for TEC(JPL) in plasmaspheric parts have an atypical view. It is quite reasonable to assume that values TEC(JPL) may be overestimated. As it is known, other maps give various values. Values of TEC for other maps (CODE, ESA), and also for the initial IRI-Plas model and the model adapted to fne(CHAMP), are shown in the left part of Fig. 4. Values of the UPC map are very close to TEC(JPL) in this case. In the right part appropriate coefficients K(PL) are presented.

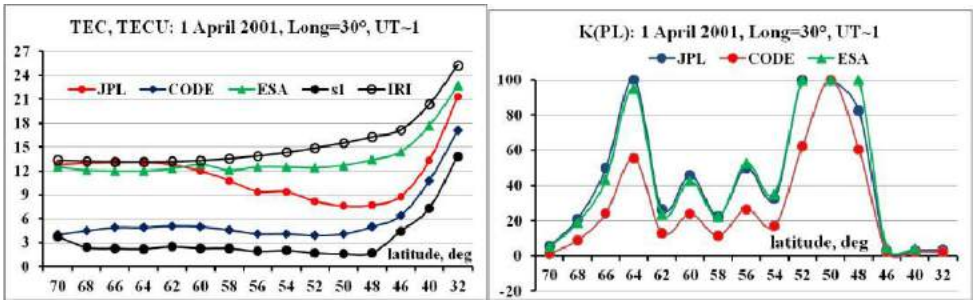

Fig. 4. Behavior of TEC for various maps and model options (the left panel) and coefficients K(PL) (the right panel)

It is seen that the JPL map reacts to disturbance most strongly. TEC for initial model and for the ESA map show an increase with latitude decrease. From maps, TEC(CODE) values are the lowest ones, however values of TEC for the model adapted to fne (CHAMP) appeared even less. The majority of values K(PL) exceeds 1 that speaks about overestimation of TEC. What profiles correspond to maps CODE and ESA, it is possible to see in Fig. 5 and 6.

The greatest interest represents behavior of plasma frequencies at certain heights. Such behavior for heights 450, 600 and 2,000 km in the topside part is shown in Fig. 7.

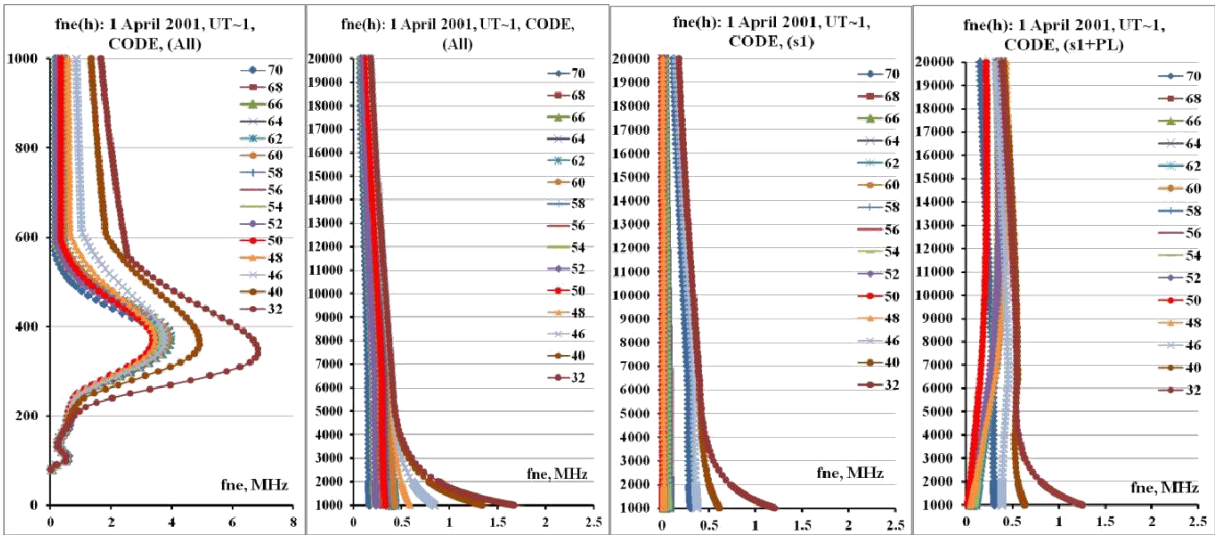

Fig. 5. The profiles calculated with usage of TEC(CODE)

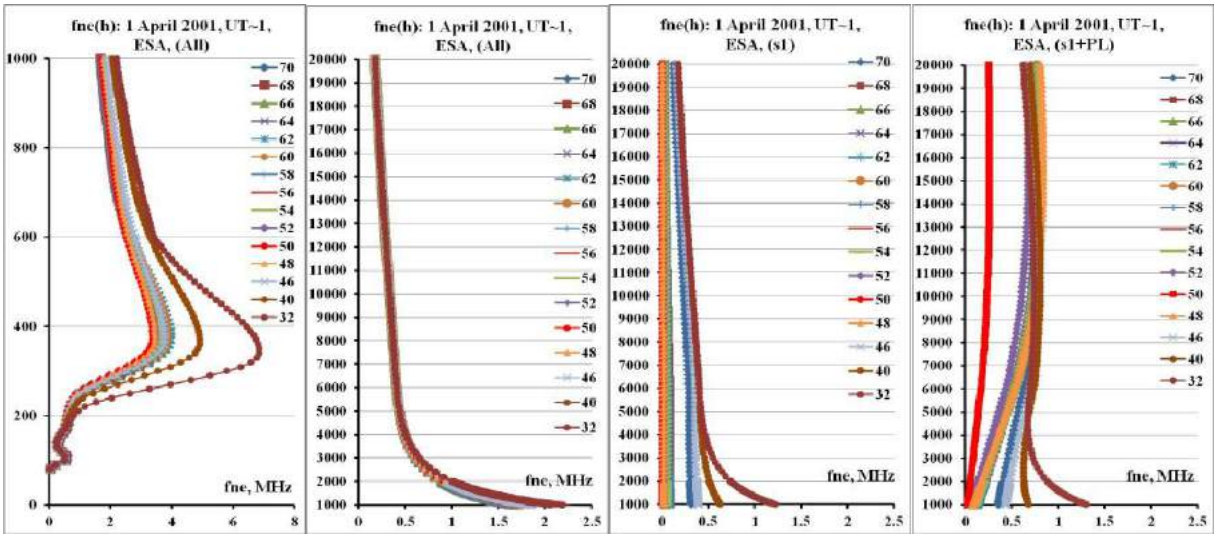

Fig. 6. The profiles calculated with usage of TEC(ESA)

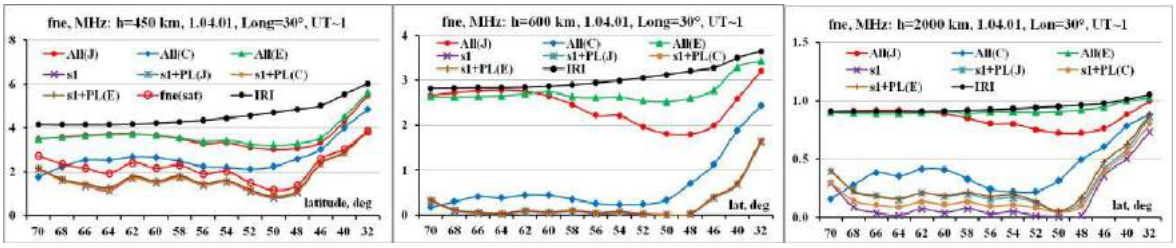

Fig. 7. The latitudinal course of fne at heights 450, 600 and 2,000 km

It is seen that in behavior at various heights frequency fne(CHAMP) influences only near to a satellite height, then this influence can be blurred because of the various area importing the contribution to value of TEC: the lower the latitude, the more is contribution. There was an influence for TEC(CODE). Distinctions for various maps are big, i.e. uncertainty of TEC is the important factor of distinction of profiles.

Distribution of fne at plasmasphere heights can be tested by means of the model constructed with data of measurements from the radio plasma imager (RPI) on NASA's IMAGE satellite. Model Ne(RPI) was constructed for L=1.6-4 (Ozhogin et al., 2012), therefore we could use profiles only for stations in a restricted range. Results in Fig. 8 are presented for heights of 3,000 and 5,000 km. Values of the RPI model are shown by red full circles.

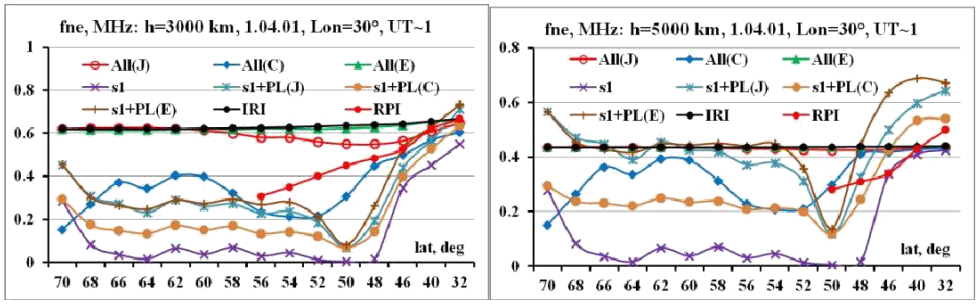

Fig. 8. Comparison of the latitudinal distributions at the various heights obtained with usage of TEC and the plasmaspheric model RPI

It is necessary to note that the RPI model is statistical, i.e. it is close to a model of a quiet state therefore in some range of latitudes even the initial model may give values, close to the RPI model. Nevertheless, at height of 3,000 km at low latitudes correspondence is rather well. At height of 5,000 km, values are close, but gradients are strongly differed. Generally, for the initial IRI-Plas model, there is no latitudinal dependence of Ne in a plasmasphere. It testifies that for uniquely identifying Ne in a plasmasphere it is necessary to have both more exact values of TEC, and more perfect model of the ionosphere.

Conclusion

Possibility of the electron concentration Ne determination in a plasmasphere is useful to the decision of many tasks of ionosphere and magnetosphere research. In the present paper for such determination the experimental values of the total electron content TEC and model IRI-Plas are used owing to the advantages marked in introduction. It is shown that Nh-profiles in a plasmasphere strongly differ for various global maps. The reason may be both overestimated values of TEC and underestimated values of Ne in the topside ionosphere. Knowledge of more exact values of TEC and plasma frequencies in the topside ionosphere would allow us to investigate behavior of electronic density in a plasmasphere during Space Weather events.

Acknowledgements

The authors thank the scientists who provided the data of SPIDR, satellites CHAMP, global maps of TEC, operation and modification of the IRI model, Dr. A. Karpachev (IZMIRAN, karp@izmiran.ru) for CHAMP data, Southern Federal University for financial support (project N 213.01-11/2014-22).

References

Gulyaeva, T.L. (2003), International standard model of the Earth's ionosphere and plasmasphere, *Astron. and Astrophys. Transactions,* 22(4), 639-643.

Gulyaeva, T.L. (2011), Storm time behavior of topside scale height inferred from the ionosphere-plasmasphere model driven by the F2 layer peak and GPS-TEC observations, *Adv. Space Res*., 47, 913-920.

Maltseva, O.A., N.S. Mozhaeva, O.S. Poltavsky, and G.A. Zhbankov (2012a), Use of TEC global maps to study ionospheric response to geomagnetic disturbances, *Adv. Space Res*., 49, 1076-1087.

Maltseva, O.A., N.S. Mozhaeva, G.A.Zhbankov, and T.V.Nikitenko (2012b) Variations of topside N(h)-profiles of the ionosphere during Space Weather events, in: *Proceedings of the 9th International Conference "Problems of Geocosmos".* Editors: V.N. Troyan, V.S. Semenov, M.V.Kubyshkina. – SPb., 311-316.

Ozhogin, P., J. Tu, P. Song, and B.W. Reinisch (2012), Field-aligned distribution of the plasmaspheric electron density: An empirical model derived from the IMAGE RPI measurements, *J. Geophys. Res.*, 117, A06225, doi:10.1029/2011JA017330.

FEATURES OF WAVE ACTIVITY EXCITATION IN THE MAGNETOSPHERE DURING ABRUPT VARIATIONS OF THE SOLAR WIND DYNAMIC PRESSURE

A.V.Moiseyev[1], D.G. Baishev[1], V.V. Mishin[2]

[1]Yu.G. Shafer Institute of Cosmophysical research and Aeronomy SB RAS, Yakutsk, Russia,
e-mail: moiseyev@ikfia.ysn.ru
[2]Institute of Solar-Terrestrial Physics SB RAS, Irkutsk, Russia

Abstract. The spatio-temporal characteristics of geomagnetic pulsations in the Pc4-Pc5 range at high-latitudes in a few events during interaction of sharp solar wind inhomogeneities with the Earth's magnetosphere are considered. It has been found that simultaneous excitations of different types of geomagnetic pulsations occur: first type, pulsations with a fixed frequency at different latitudes can be caused by surface waves on the magnetopause or directly penetrate from the solar wind; second type, Alfvenic resonant oscillations are caused by magnetosphere compression. Asymmetric appearance of pulsations relative to the noon meridian can be driven in general by IMF orientation in the azimuthal plane.

1. Introduction

Geomagnetic sudden impulses (SI), caused by an interaction of inhomogeneities in the solar wind (SW) with the Earth's magnetosphere, often accompanied by a generation of geomagnetic pulsations in the range of 1-1000 mHz, noted as Psi [Saito and Matsushita, 1967]. In most events, the Psi frequency depends on the geomagnetic latitude, reflecting the resonant nature of the interaction of the solar wind with the magnetosphere. Geomagnetic pulsations can be generated not only at the boundary and inside the magnetosphere, but also penetrate into the magnetosphere from the SW. In the study Gogatishvili [1976] of relation of Pc5 pulsations occurrence at mid-latitudes with the IMF magnitude and orientation, it was suggested that Pc5 could be formed outside the magnetosphere. Kepko and Spence [2003] have been analyzed a number of events of the geomagnetic pulsations caused by the variations of SW dynamic pressure and founded that the discrete frequencies of the magnetospheric field line resonances were observed in the variations of SW density.

Thus, the mechanisms of Psi excitation remain controversial. Based on analysis of three events in which the maxima of intensity of pulsations was distributed asymmetrically relative to the noon meridian and different types of pulsation simultaneously excited we have tried to determine a source of these pulsations in the interplanetary medium.

2. Results

Psi event of June 25, 2008 Fig. 1a presents variations of a geomagnetic field H-component by data of high-latitude stations distributed on longitude within two latitude ranges on June 25, 2008. It is clear from Figure that pulsations with a period of 7.5-9 min lasted for forty minutes at auroral latitudes in all MLT sectors and at stations of L~2, L~9 (not shown). The maximum of pulsation amplitude of 30-40 nT was observed in the 15 MLT sector (shown by red). Phase delays of oscillations at stations in different MLT sectors testify to an azimuth propagation of pulsations (it is shown by arrows) in the anti-sunward direction. Fig. 1b illustrates the spectra of the geomagnetic pulsations. It is obvious from this figure that pulsations were registered in two spectral bands about 2 mHz (main maximum) and about 3 mHz (poorly expressed maximum). The pulsation amplitude decreased when geomagnetic latitude were decreased. From the spectra, an asymmetric distribution of pulsation amplitude relative to the noon meridian is also obvious with a maximum in the sector of 15.00-15.30 MLT.

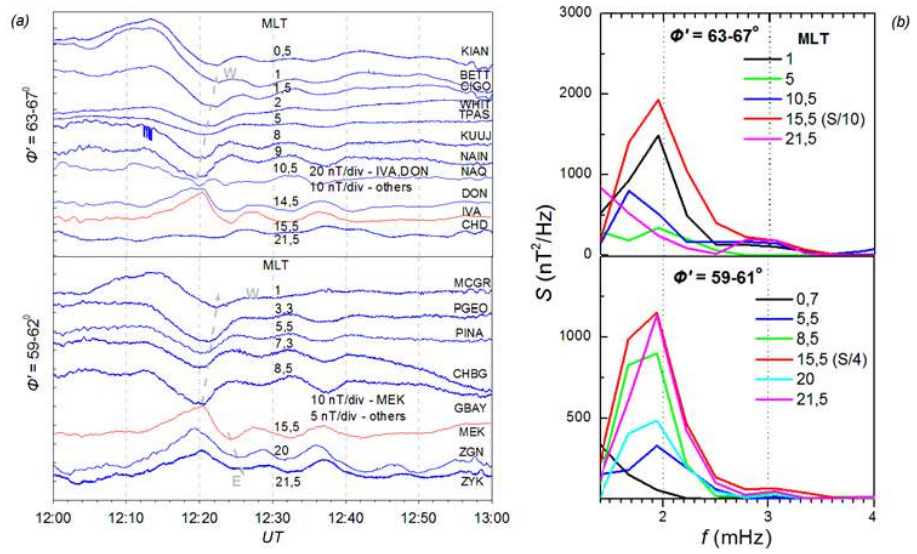

Fig. 1. Variations of a geomagnetic field H-component at stations distributed on longitude within two latitude ranges of 63-67° and 59-62° *(a)* and their spectra *(b)* for the 25.06.2008 event. The station's MLT are given at 12.30 UT. Arrow marks the direction of propagation of pulsations to the west (W) and to the east (E).

Fig. 2 presents the solar wind parameters data aboard the *WIND* (blue lines, left scale) and *THEMIS C* (*ThC*) (red lines, right scale) satellites. The *WIND* (X_{GSM} ~260 R_E) satellite was in the solar wind (SW), and the *ThC* (X_{GSM} ~11 R_E) satellite - near the bow shock. The data of the *WIND* is presented with a ~71 min shift.

From top to bottom the IMF magnitude, the SW density, SW dynamic pressure, plasma beta, cone angle and azimuth angle are shown.

It is seen, that in the interval of registration of geomagnetic pulsations aboard both satellites the decrease of IMF magnitude (Fig. 2a) was observed. The $\Delta B/B$ ratio was ~0.4. The SW density N (Fig. 2b) changed in the antiphase relative to the IMF B, i.e. increased. Small variations of SW dynamic pressure ($\Delta Pd/Pd$~0.1, Fig. 2c) were noted. The decrease of B was accompanied by a growth of plasma beta (Fig. 2d). Low values of the cone angle (Fig. 2e) corresponds to nearly radial IMF. At values of cone angle ≤ 45° near the bow shock the foreshock region is formed. In the intervals 1207-1211 UT and 1247-1251 UT, the high-frequency wave activity typical for the foreshock region was registered. The negligible change of electron fluxes in comparison with the ion (not shown) is indicative of the fact that the *ThC* was on the boundary of ion foreshock region.

The azimuth angle values are in two ranges: about 10 deg and 270 deg, at these values IMF has (unusual) ortospiral orientation.

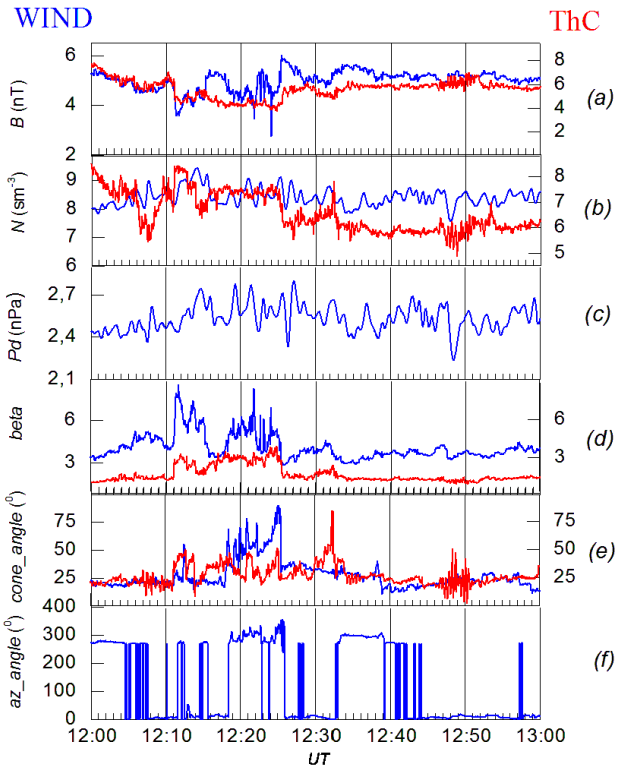

Fig. 2 Variations of interplanetary medium parameters by satellites observations: WIND (blue line, scale at the left) and THEMIS C (ThC, red line, scale on the right). IMF magnitude B (a), ion density (b), SW dynamic pressure (c), plasma beta (d), cone and azimuth angles (e, f) in 12.00-13.00 UT are shown. The data of the WIND satellite shifted on ~71 min.

Psi event of August 4, 2010

Fig. 3a,b illustrates variations of a geomagnetic field H-component at high latitudes and their spectra for the August 4, 2010 event. The pulsation in this event was excited just after the SI. The duration of this event was about 20 min as it follows from the magnetic field variations at stations distributed by the longitude. Similar to the previous event considered two maxima in the spectra of pulsations are registered about 4.5 mHz and in the band of 7-8 mHz. First maxima registered in the all MLT sectors but with the peak amplitude in 18.00-18.30 MLT

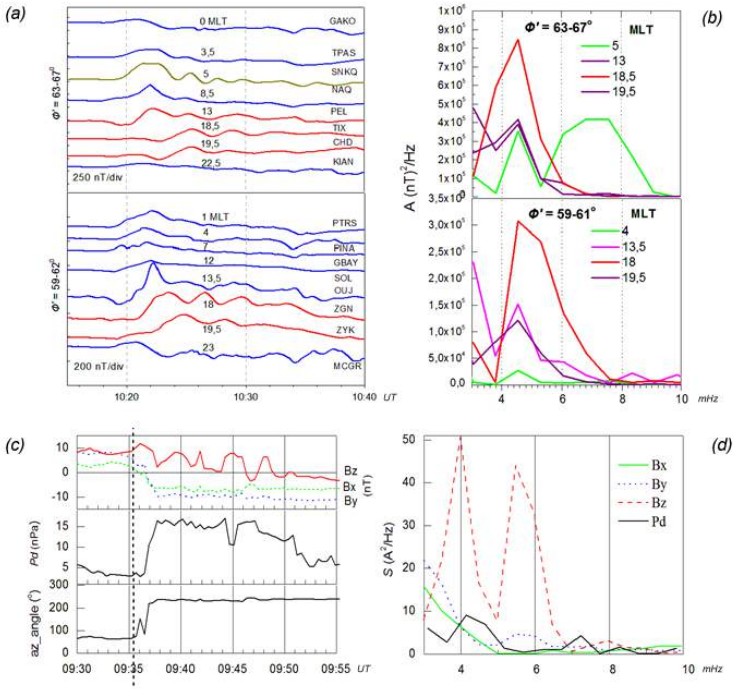

Fig. 3. Variations of a geomagnetic field H-component at latitudes 63-67°, 59-62° at stations distributed by the longitude and their spectra *(a, b)*. Variations of interplanetary medium parameters aboard WIND: IMF Bx, By, Bz-components, SW dynamic pressure, azimuth angle and their spectra *(c, d)* for the 04.08.2010 event.

sector. Second maximum at higher frequency registered in the morning sector ~5 MLT. The asymmetric distribution of the pulsations of different types relative to the noon was observed. Fig. 3c,d presents the SW parameters data aboard the *WIND* satellite. From top to bottom Bx-, By-, Bz-components of IMF, SW dynamic pressure and azimuth angle are shown.

It is seen from the figure that positive IMF Bz variations close by duration and frequency of oscillation to the first type pulsations (first maximum) is observed. Solar wind Pd variations is typical for interplanetary shock, which interacted with the magnetosphere and caused SI. The azimuth angle values was about ~ 70° before and increase up 240° after the interplanetary shock front, at these values the IMF also has (unusual) ortospiral orientation.

The IMF Bz spectra has two peaks 4 and 5.5 mHz which are very close to low-frequency maximum of geomagnetic field pulsations spectra. There are two spectral maxima 4.2 and 7.3 mHz in Pd, which very similar to maxima in geomagnetic pulsations spectra.

Fig.4 illustrates the development of pulsations in the evening (first type pulsations, Fig.4a) and in the morning sectors (second type pulsations, Fig.4b). Observations data aboard the Cluster satellites located also in the morning sector are shown. Fixed frequency of first type pulsations at different latitudes give an evidence that these pulsations are forced oscillations. Second type pulsations likely to be resonance Alfven oscillations because they frequency depend from the latitude both by the ground and satellite observations (see the Cluster 2, 3, 4 magnetic field measurements – red curves superposed on ground magnetograms, Fig.4b).

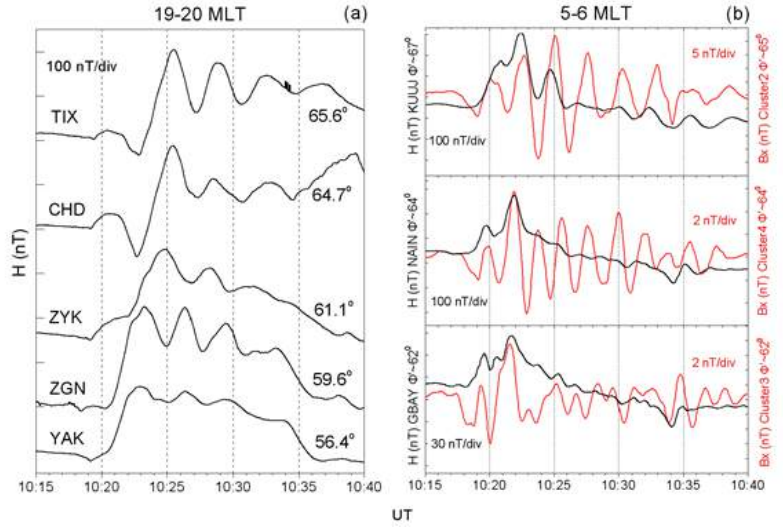

Fig. 4. Geomagnetic field H-component variations in the sector of 19-20 MLT (a) and in the sector of 5-6 MLT by data of the ground and satellite (Bx-component aboard Cluster 2, 3, 4 satellites is shown by red, the scale on the right) observations (b). The data of Cluster satellites have been filtered in the range of 30-300 sec.

Psi event of April 24, 2009 Fig. 5a,b illustrates variations of the geomagnetic field H-component at high latitudes and their spectra for the April 24, 2009 event. In this event pulsation was excited in the limited sector of 10-11 MLT just after the SI at 00.50 UT (they shown by the red curves on Fig. 5a). Spectra of the geomagnetic variations shows the maximum at ~2 mHz in the morning sector (Fig. 5b). Parameters of interplanetary medium are shown below aboard the ACE (Fig. 5c) and WIND (Fig. 5d) satellites: variations of IMF Bx, By, Bz-component, the SW dynamic pressure and the azimuth angle. Dashed lines mark the moment of registration of interplanetary shock responsible for the observed geomagnetic variations.

At the WIND satellite (X_{GSM} = 230.14 Re; Y_{GSM} = 79.81 Re; Z_{GSM} = 55.84 Re), located closer to the magnetosphere, shock front was recorded at about 17 minutes earlier than at the ACE satellite (X_{GSM} = 238.94 Re; Y_{GSM} = -23.10 Re ; Z_{GSM} = -34.59 Re). Consequently, the shock front was inclined relative to the Earth-Sun line. Taking into account the front inclination, the first contact of the shock with magnetopause should be in the dusk sector. Obviously, it takes place: the point from which the disturbance propagates in the antisunward direction located in the postnoon sector ~16 MLT (shown by arrows on the Fig. 5a). The azimuth angle values lies in the range ~100-150° (Fig. 5c,d) that correspond to spiral IMF unlike the events considered earlier.

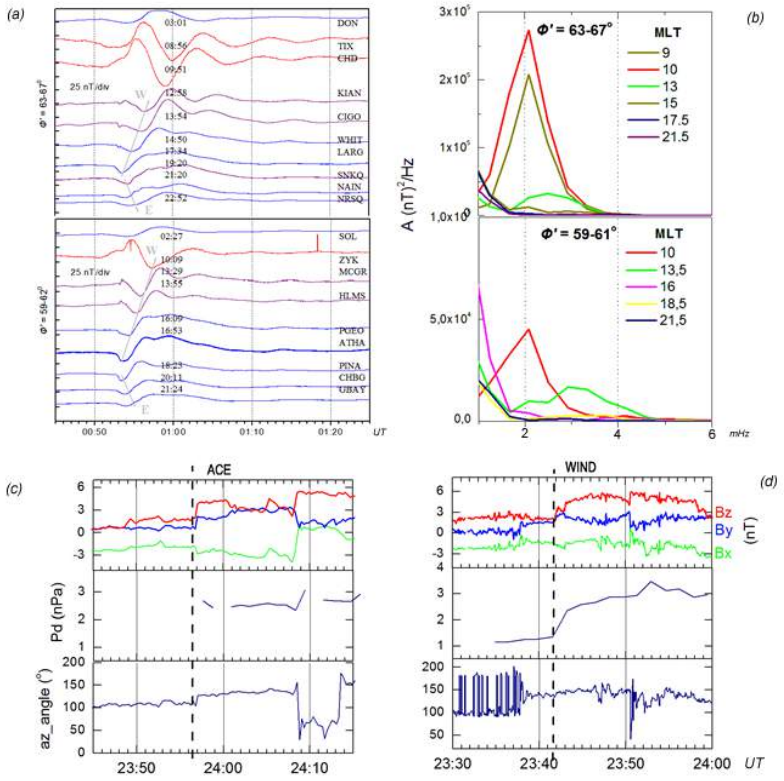

Fig. 5. Variations of a geomagnetic field H-component at latitudes 63-67°, 59-62° at stations separated by longitude and their spectra *(a, b)*. Variations of interplanetary medium parameters aboard ACE and WIND satellites: IMF Bx, By, Bz-components, SW dynamic pressure, azimuth angle *(c, d)* for the 24.04.2009 event. Arrow marks the direction of propagation of pulsations to the west (W) and to the east (E).

3. Discussion

3.1 Pulsation sources.

3.1.1 SW dynamic pressure pulses

Psi pulsations in our events similar to the geomagnetic pulsations considered in the works [Parkhomov et al.,1998; Han et al., 2007]. Parkhomov et al. [1998] founded that a sharp decrease of SW dynamic pressure was manifested in a generation of two types of pulsations at frequencies of 2.3 мHz and 4-6 мHz. The authors supposed that the first type of oscillations with a period independent of a latitude was related to the oscillations of magnetopause, and the second type of oscillations whose period depends on latitude was caused by field line resonances in the magnetosphere. Han et al., [2007] studied the geomagnetic pulsations with the frequency of 3.4 mHz caused by the variations of SW plasma density. The authors termed them as "global Pi3 pulsations" and explained it by oscillations of three-dimensional current system, which was modulated by the variations of SW density. Probably in the June 25, 2008 Psi pulsations with the frequency ~2 mHz was also caused by SW density or Pd variations. There are two maxima in the spectra of oscillation (not shown) in the interplanetary medium, and in the magnetosphere as well as in the ground oscillations. Perhaps, that low-frequency and high-frequency oscillations reflect different modes.

The changes of Pd in the June 25, 2008 Psi event are connected with the IMF variations. The character of change of the IMF magnitude in the interval of the ground pulsations observation is similar to the behavior of magnetic field in a "magnetic hole" [Turner et al., 1976], but unlike their work the duration of event analyzed by us is by an order greater. The antiphase changes of IMF magnitude and plasma density and high plasma beta (see Fig. 2 a-d) testify to the development of mirror instability in this event [Hasegawa, 1969]. We suppose that the generation of ground oscillations occurred when contacting a magnetic hole with the ion foreshock.

Dependence of oscillations frequency from the latitude in the morning sector in August 04, 2010 Psi event allows to suggest that high-frequency pulsations are Alfvenic resonance oscillations excited during the magnetosphere compression as suggested in the work [Parkhomov et al., 1998].

3.1.2 Direct penetration from the interplanetary medium

Fixed period of low-frequency pulsations at different latitudes allows to suggests that they are forced oscillations. Source of forced oscillations can be the IMF Bz oscillations (see Fig. 3, 4a), coincident by the

period and duration with the geomagnetic pulsations. Thus, the most likely source of the oscillations the IMF Bz variations should be considered.

As the mechanism of penetration of IMF Bz fluctuations in the Earth's magnetosphere it can be assumed that geomagnetic pulsations at the frequency of ~4.5 mHz is the result of amplification and oscillation of three-dimensional current system that occurs during periods of northward IMF Bz direction: the NBz current system [Zanetti et al., 1984; Kozyreva and Kleimenova, 2007]. It is known that Pc5 pulsations recorded mainly under the northward IMF Bz due to the generation of surface wave due to reconnection [Belakhovsky and Roldugin, 2008]. Perhaps, in this case, the IMF Bz oscillations modulate the reconnection rate.

3.2 Reasons of asymmetric distribution of pulsations relative to the noon

It is suggested in [Sibeck, 1990] that a necessary requirement for a generation of compression wave in the magnetosphere is the $\Delta Pd/Pd \sim 1$ ratio. It was shown in [Han et al., 2007] that pulsations were observed at $\Delta Pd/Pd \sim 0.6$ when the SW speed was higher than 500 km/s. In the event of June 25, 2008 the value of $\Delta Pd/Pd$ was ~0.1, and the SW speed did not exceed 400 km/s (not shown). One can suppose that in the ion foreshock region the plasma pressure increases at the expense of its dynamics caused by IMF variations. In [Hartinger et al., 2013] it is shown that the variations of plasma pressure in the foreshock region increased by the order in comparison with *Pd* in the SW. The comparison of variations of SW density aboard *WIND* ($\Delta N \sim 0.8$ sm^{-3}) and *ThC* ($\Delta N \sim 1.8$ sm^{-3}) at 12.11 UT (Fig. 2b) shows that the change of ion density in the foreshock region is greater by a factor of 2.2 than in the SW. The same changes of density are noted in [Hartinger et al., 2013]. In June 25, 2008 event, the oscillation amplitude maximum was observed in the afternoon sector, which coincides with the position of ion foreshock. Perhaps that the ion foreshock region served as the resonator of long-period oscillations. This resonator can be excited by variations of *Pd*.

In [Zolotukhina and Parkhomov, 1992] it was studied the resonant long-period pulsations Psi3-5, the properties of which are asymmetric with respect to the noon meridian, which is probably related to the asymmetry of the magnetosphere compression. Not excluding this possible reason we can suggest that pulsations localization asymmetry is due to orientation of the IMF in the azimuthal plane (spiral/ortospiral). Spiral (ortospiral) IMF orientation correspond to the values of the azimuthal angle 90-180° and 270-360° (0-90° and 180-270°). Relation of IMF orientation with the high-latitude impulsive events occurrence studied in [Korotova et al., 2002]. It was found, that the magnetic impulsive events observed in the morning sector at spiral IMF and in the evening sector at ortospiral.

It is known that the intensity of the field-aligned currents that produce the ground events is proportional to the azimuthal pressure gradient applied to the magnetosphere. During periods of orthospiral IMF orientation the greater pressure variations to be applied to the postnoon magnetopause and to the prenoon magnetopause in the opposite case. The first and second events examined, recorded at ortospiral IMF, while the third one was observed at spiral IMF. The maximum of amplitude of the pulsations in the first two events were recorded in the afternoon sector, when in the third event was observed in the prenoon sector.

Conclusion

1. The simultaneous excitation of different type of geomagnetic pulsations occurs. First type: pulsations with a fixed frequency at different latitudes can be caused by surface waves on the magnetopause or directly penetrate from the solar wind. Second type: Alfvenic resonant oscillations are caused by magnetospheric compression.
2. Asymmetric appearance of pulsation relative to the noon meridian can be driven in general by IMF orientation in the azimuthal plane (IMF By/Bx ratio).

Acknowledgements

The authors are grateful for the opportunity to use THEMIS data: V. Angelopous, U. Auster, K.H. Glassmeier, V. Baumjohann, as well as data from CDAWEB site – D.J. McComas, R. Lepping, K. Ogilvie, G. Paschmann (MPE).

This work was supported by RFBR grants N 13-05-00363, 14-05-91165-GFEN_a, and 13-05-92219-Mong_a.

References

Belakhovsky V.B. and Roldugin V.K. (2008), Excitation of Pc5 pulsations at the change of IMF Bz sign, *Geomagnetism and aeronomy*. V.48. N2. P. 188-194.

Gogatishvili Ya. M. (1976), Interplanetary magnetic field and long-period geomagnetic pulsations at the middle latitudes, *Geomagnetism and aeronomy*. V.16. N 2. P. 382-384.

Han D.-S., Yang H.-G., Chen Z.-T., Araki T., Dunlop M. W., Nose M., Iyemori T., Li Q., Gao Y.-F. and Yumoto K. (2007), Coupling of perturbations in the solar wind density to global Pi3 pulsations: A case study, *J. Geophys. Res.* V.112. doi:10.1029/2006JA011675.

Hartinger M. D., Turner D. L., Plaschke F., Angelopoulos V., Singer H. J. (2013), The role of transient ion foreshock phenomena in driving Pc5 ULF wave activity, *J. Geophys. Res.*, doi:10.1029/2012JA018349.

Hasegawa A. (1969), Drift mirror instability in the magnetosphere, *Phys. Fluids.* V.12. P. 2642–2650.

Kepko, L. and Spence H. E. (2003), Observations of discrete, global magnetospheric oscillations directly driven by solar wind density variations, *J. Geophys. Res.* V.108. P.1257. doi:10.1029/2002JA009676.

Korotova G. I., Sibeck D. G., Singer H. J. and Rosenberg T. J. (2002), Tracking transient events through geosynchronous orbit and in the high-latitude ionosphere, *J. Geophys. Res.* V. 107. P. 1345-1363.

Kozyreva O.V. and Kleimenova N.G. (2007), Geomagnetic pulsations and magnetic disturbances in the beginning phase of the strong magnetic storm of May 15, 2005, *Geomagnetism and aeronomy*. V.47. N4. P. 501-511.

Parkhomov V.A., Mishin V.V. and Borovik L.V. (1998), Long-period geomagnetic pulsations caused by the solar wind negative pressure impulse on March 22, 1979 (CDAW-6), *Ann. Geophys.* V. 16. P. 134–139.

Saito T. and Matsushita S. (1967), Geomagnetic pulsations associated with sudden commencements and sudden impulses, *Planet. Space Sci*. V.15. P.573-587.

Sibeck D. G. (1990), A model for the transient magnetospheric response to sudden solar wind dynamic pressure variations, *J. Geophys. Res.*, V.95. P.3755 – 3771.

Turner J.M., Burlaga L.F., Ness N.F. and Lemaire J.F. (1976), *Magnetic holes in the solar wind*, NASA Preprint TM-X-71109.

Zanetti L. J., Potemra T. A., Iijima T., Baumjohann W. and Bythrow P. F. (1984), Ionospheric and Birkeland Current Distributions for Northward Interplanetary Magnetic Field: Inferred Polar Convection, *J. Geophys. Res.* V. 89. P. 7453–7458.

Zolotukhina N.A. and Parkhomov V.A. (1992), Longitude asymmetry of geomagnetic phenomena sudden storm commencement of Mar. 22, 1979 (CDAW-6) as an example, I*ssledovania po geomagnetizmu, aeronomii i fizike Solntsa*. M.: Nauka, Iss. 97, P. 55-67 (in Russian)

STUDY OF THE OUTER RADIATION BELT OF THE EARTH BY SEGMENTATION OF MULTI-DIMENSIONAL TIME SERIES*

Myagkova I.N., Dolenko S.A., Persiantsev I.G.

D.V.Skobeltsyn Institute of Nuclear Physics, M.V.Lomonosov Moscow State University, Moscow, Russia, e-mail: irina@srd.sinp.msu.ru

Abstract. Study and prediction of the relativistic electron flux in the outer ERB is a complicated problem. This is due to the fact that Earth's magnetosphere is a complex dynamical system. The state of this system can be described by a multi-dimensional time series, including various physical features - parameters of interplanetary magnetic field, solar wind, geomagnetic indexes, relativistic electron flux at geostationary orbit etc. Here we consider the approach to investigation of time series characterizing the dynamics of the outer ERB with the help of machine learning algorithms. To separate out such regions, in this study we used segmentation of multi-dimensional time series with the help of k-means clusterization algorithm and Kohonen neural networks. The initial data which are a multi-dimensional time series with delay embedding were split into three, four, and five clusters (segments) with Kohonen self-organizing map and k-means algorithm. The obtained variants of segmentation of the time series were compared to each other and correlated with various possible states of the outer ERB.

INTRODUCTION

The outer radiation belt of the Earth (OERB) is a part of inner Earth's magnetosphere. It is well known that strong (more than two orders of magnitude) and abrupt changes of relativistic and sub-relativistic electron flux intensity in the OERB occur during magnetic disturbances due to arrival of both coronal ejections and high-speed solar wind streams to the Earth's orbit (e.g. Tu et al., 2009). The intensity of the flux of relativistic electrons in the outer ERB is subject to the influence of solar wind (SW) and interplanetary magnetic field (IMF) parameters (e.g. Reeves et al., 2011), that are difficult to take into account (refer to Fig. 1 as an example).

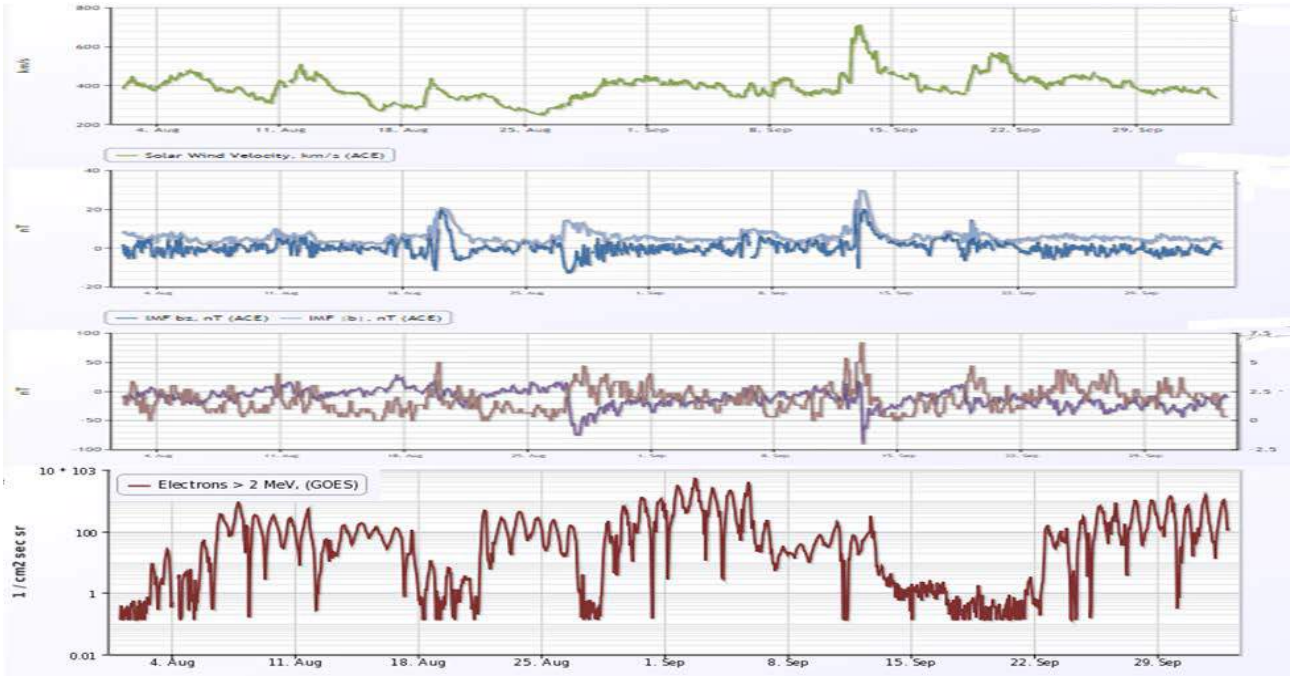

Fig. 1. Time variations of solar wind speed, IMF (|B| and Bz), Dst and Kp indexes, relativistic electron flux (E>2 MeV) during August – September 2014.

* This study was supported by the Russian Foundation for Basic Research (RFBR), project no. 14-01-00293. Myagkova I.N. thanks RFBR project no 12-05-01030.

There is every reason to believe that there may exist several different basic states of the magnetosphere – significantly diverse regions in the phase space of the states of this dynamical system, for which the most efficient prediction models may be different. To separate out such regions, in this study we used segmentation of multi-dimensional time series with the help of Kohonen artificial neural networks (ANN), self-organizing maps (SOM), and with the help of k-means clusterization algorithm.

Acceleration and losses of relativistic electrons of ERB in the Earth's magnetosphere is an important fundamental problem in space physics (e.g. Friedel et al., 2002), so the main goal of our research is to improve understanding of the Earth's magnetosphere dynamics. From the other hand, relativistic electrons may cause dangerous malfunction of the electronics onboard spacecraft and therefore they are often called killer electrons (Iucci et al., 2005, Pilipenko et al., 2006). So forecast of relativistic electron flux in OERB is an important practical task, and the second goal of this study is to improve our forecast.

METHOD AND INPUT DATA

In this study, we used the implementation of Kohonen ANN and SOM in the software package Deductor 5.3 – the Russian version of Loginom software (Loginom – analytical platform. http://loginom.basegroup.ru). The following network parameters were used: the network consisted of 16×12 hexagonal cells with Euclidean distance function; the initial learning rate was 0.5, the finishing learning rate was 0.1; training continued for 500 epochs. The number of obtained clusters varied from 2 to 5.

As input data, time series (TS) of hourly values of the following physical quantities were used:

1) Solar wind (SW) parameters in Lagrange point L1 between the Earth and the Sun:

- SW speed v (measured in km/s)
- SW protons density n_P (measured in cm^{-3})
- SW temperature T_{rr} (measured in K)

The data used was from ACE (Advanced Composition Explorer) spacecraft, measured by SWEPAM (Solar Wind Electron Proton Alpha Monitor) device.

2) Interplanetary magnetic field (IMF) vector parameters in Lagrange point L1 (measured in nT) in GSM system:

- Bx, By, Bz (IMF x-, y-, and z-components)
- B magnitude (IMF modulus)

The data used here was also from ACE spacecraft, MAG device.

3) Geomagnetic indexes

- Equatorial geomagnetic index Dst (measured in nT)
- Planetary index Kp (dimensionless)

The data used was from World Data Centre for Geomagnetism in Kyoto (Japan).

4) Relativistic electrons (>2 MeV) flux measured at geostationary orbit by GOES satellite.

The considered data period was from November 1997 to March 2014.

To account for the previous history of input features, delay embedding of all TS for 24 hour depth was used. Thus, each data pattern was a point in 200-dimensional feature space (8 TS × 25 hours), assigned to the latest point of the 25-hour window.

KOHONEN MAPS

Fig.2 displays the SOM obtained with the listed parameters for 5 clusters. Cell colors represent average value of the corresponding parameter for this cell. Brighter color corresponds to higher parameter value (please refer to the legend bar at the bottom of each map).

The obtained clusters were interpreted in the following way:

a) Cluster 0 (dark blue): minimum of electron flux, Kp and SW speed are also low; such a state was mainly observed during the extreme minimum in 2009;

b) Cluster 1 (light blue): electron flux is low but higher than in cluster 0; SW speed, Kp are similar to cluster 0; this cluster can correspond to low geomagnetic disturbance;

c) Cluster 2 (medium blue): here, the highest values of Kp index, Dst amplitude, SW speed, and B are observed, so this is possibly the main phase of magnetic storms;

d) Cluster 3 (green): higher values of electron flux, Kp and Dst than in cluster 2; this can be the beginning of the recovery phase;

e) Cluster 4 (red): maximal values of electron flux; Dst amplitude and Kp are low again; this cluster corresponds to the end of the recovery phase.

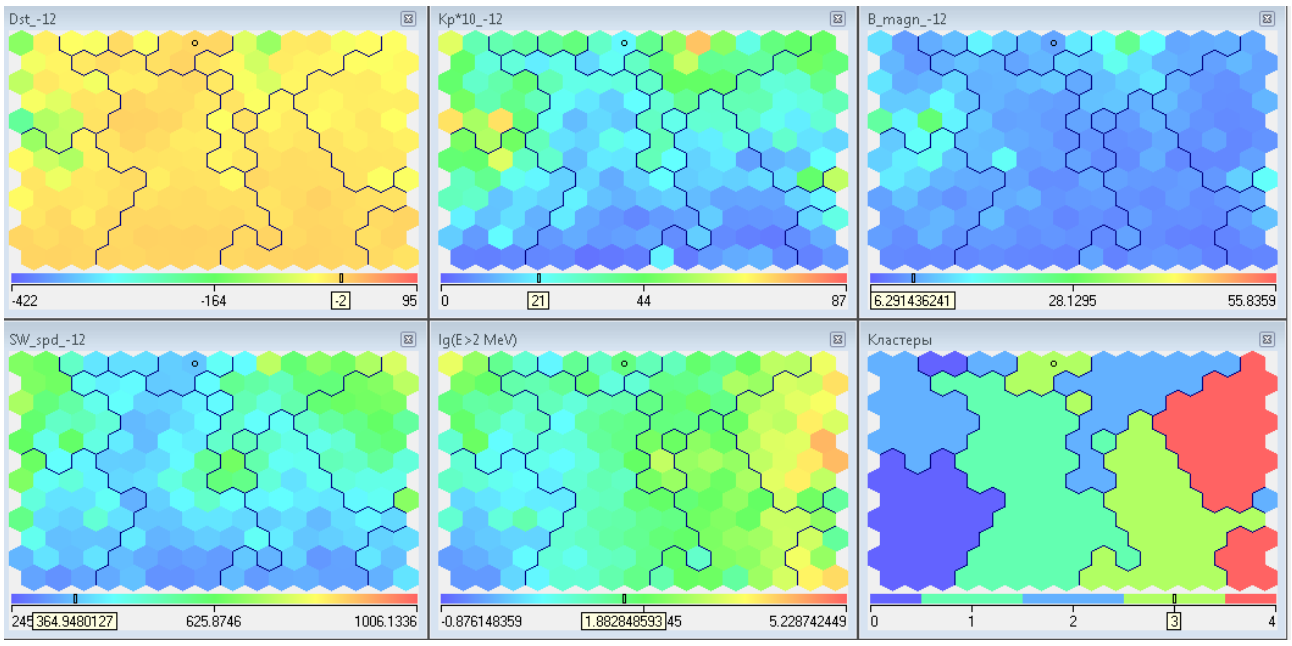

Fig. 2. Kohonen maps for Dst, Kp, B, SW speed, logarithm of electron flux and clusters.

In order to test this interpretation, we calculated the number of samples (measurement hours) assigned to each cluster, and compared it to the number of magnetic storms with an amplitude greater than -30 nT and -40 nT. The result of the comparison is presented in Fig. 3.

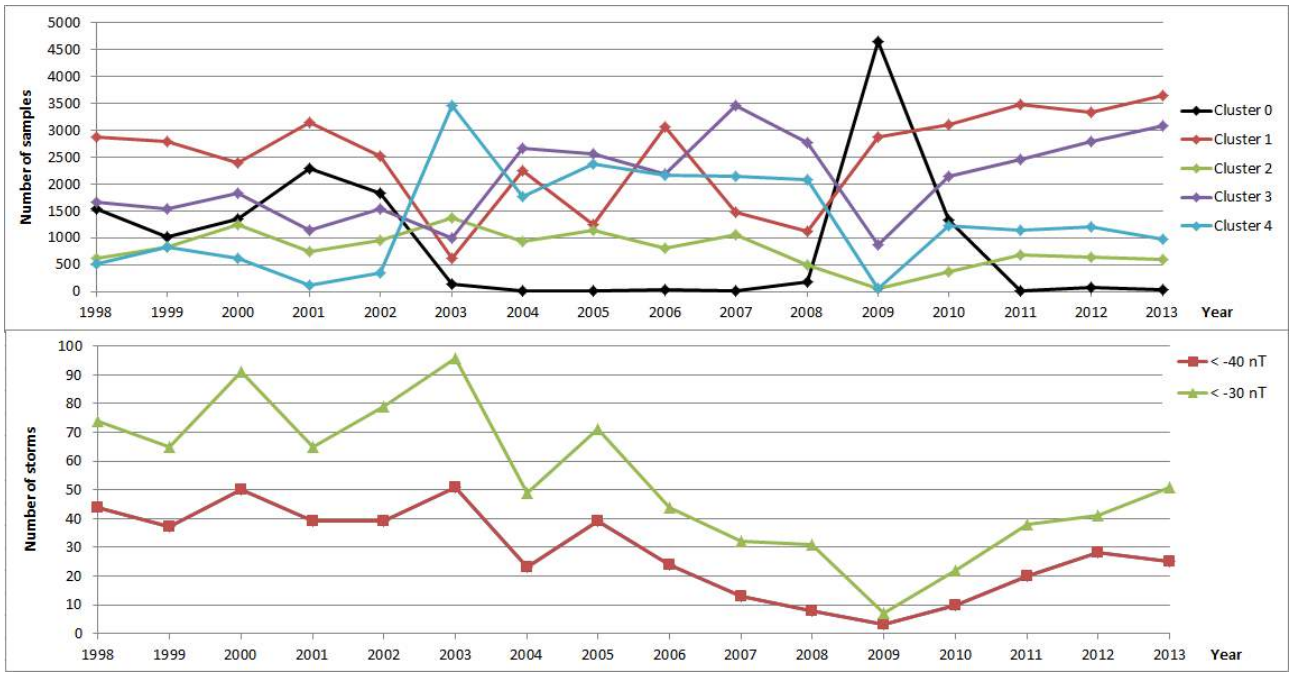

Fig. 3. The yearly number of samples assigned to each cluster (top panel) and the yearly number of magnetic storms with an amplitude greater than -30 nT and -40 nT (bottom panel) from 1998 to 2013.

Figure 3 shows that this interpretation is consistent with our physical picture of the phenomenon under study. Thus, the maximal number of samples with minimum of electron flux (cluster 0, black line) was really in 2009, when the number of magnetic storms was minimal. The fraction of background low fluxes of electrons (cluster 1, red line) is maximal, and the number of samples related to the cluster 4 (blue line), which corresponds to the maximal flux of electrons, by contrast, has its maximum in 2003, when there was a period of extremely high solar activity. Cluster 2 (green line) that we interpreted as events relevant to the main phase of storms is in good agreement with the time dependence of the number of storms in the bottom panel.

RESULTS AND DISCUSSION

Examples of the obtained results are presented in Figs.4-6. Three time intervals with different solar and geomagnetic activity were selected – decay phase of solar activity (SA) cycle 23: February 1, 2006 – July 31, 2006 (Fig.4); anomalous minimum of SA in 2009 and the beginning of SA cycle 24: November 20, 2009 – June 30, 2010 (Fig. 5); maximum of SA cycle 24: September 1, 2013 – January 31, 2014 (Fig.6).

In all figures, the three upper diagrams present TS of logarithm of relativistic electrons (>2 MeV) flux measured at geostationary orbit by GOES satellite (blue, left axis) and the results of TS segmentation into 5,4 and 3 clusters (cluster numbers from 0 to 4) with Kohonen SOM (red) and k-means algorithm (green), right axis. The fourth diagram presents TS of Kp-index multiplied by 10 (blue, left axis) and Dst-index in nT (black), right axis. The bottom diagram presents TS of SW speed (blue, left axis), B magnitude (red) and Bz (green), right axis.

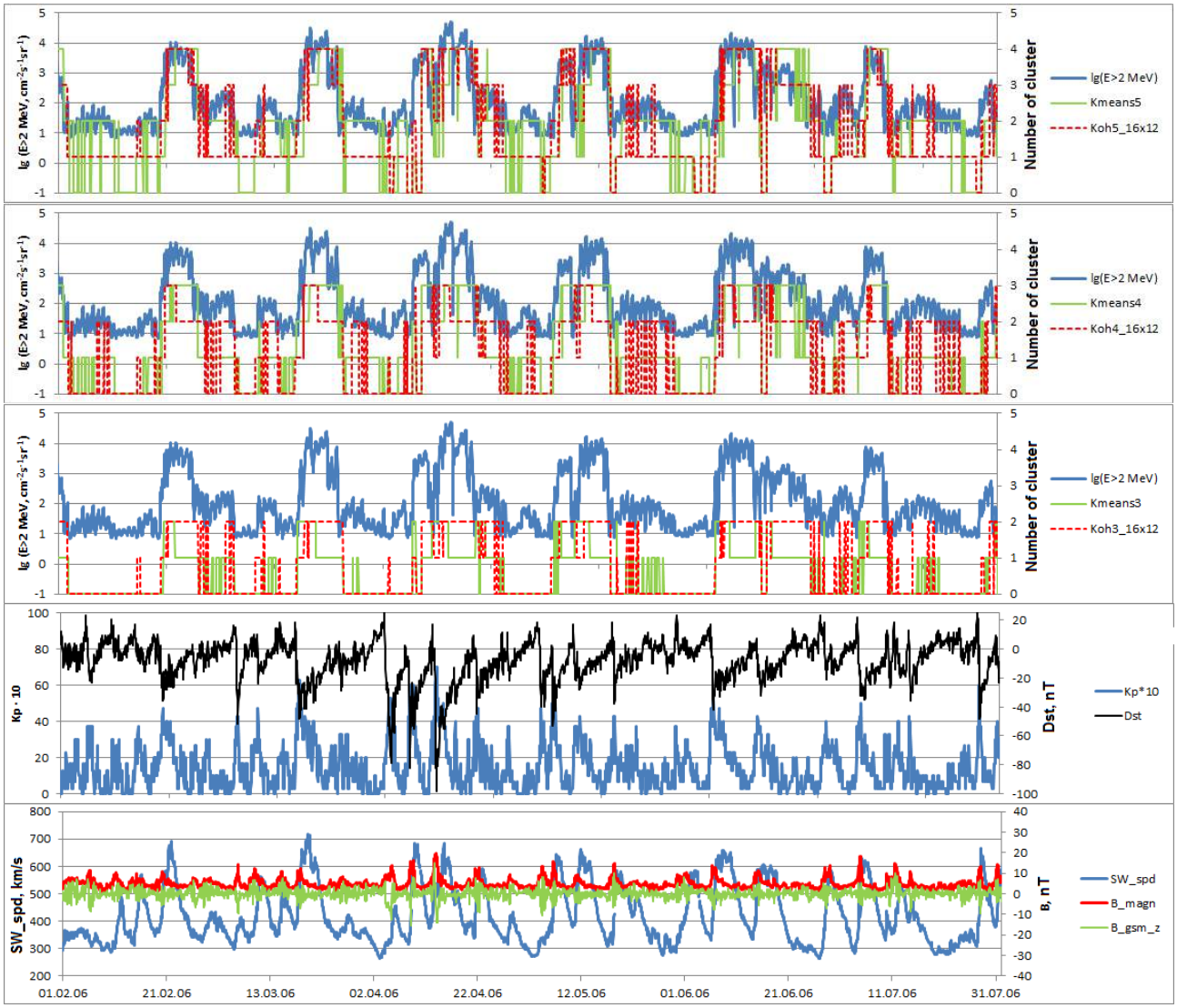

Fig. 4. The results of clustering obtained for time range from February 1, 2008 till July 31, 2006.

Figure 4 corresponds to the decay period of solar activity cycle 23, when the average flux of electrons in the outer belt was high, and during the analyzed time period, ten significant electron flux enhancements were observed. One can see that when dividing into five clusters, clustering works satisfactorily both when K-means and Kohonen SOM are used, although the second clusterization looks more stable. When the number of clusters is reduced to 4, stability of clusterization with Kohonen SOM method also decreases, although the increase in the flux of electrons is still pointed out quite reliably. For three clusters, SOM method clusterization for the given period also looks adequately.

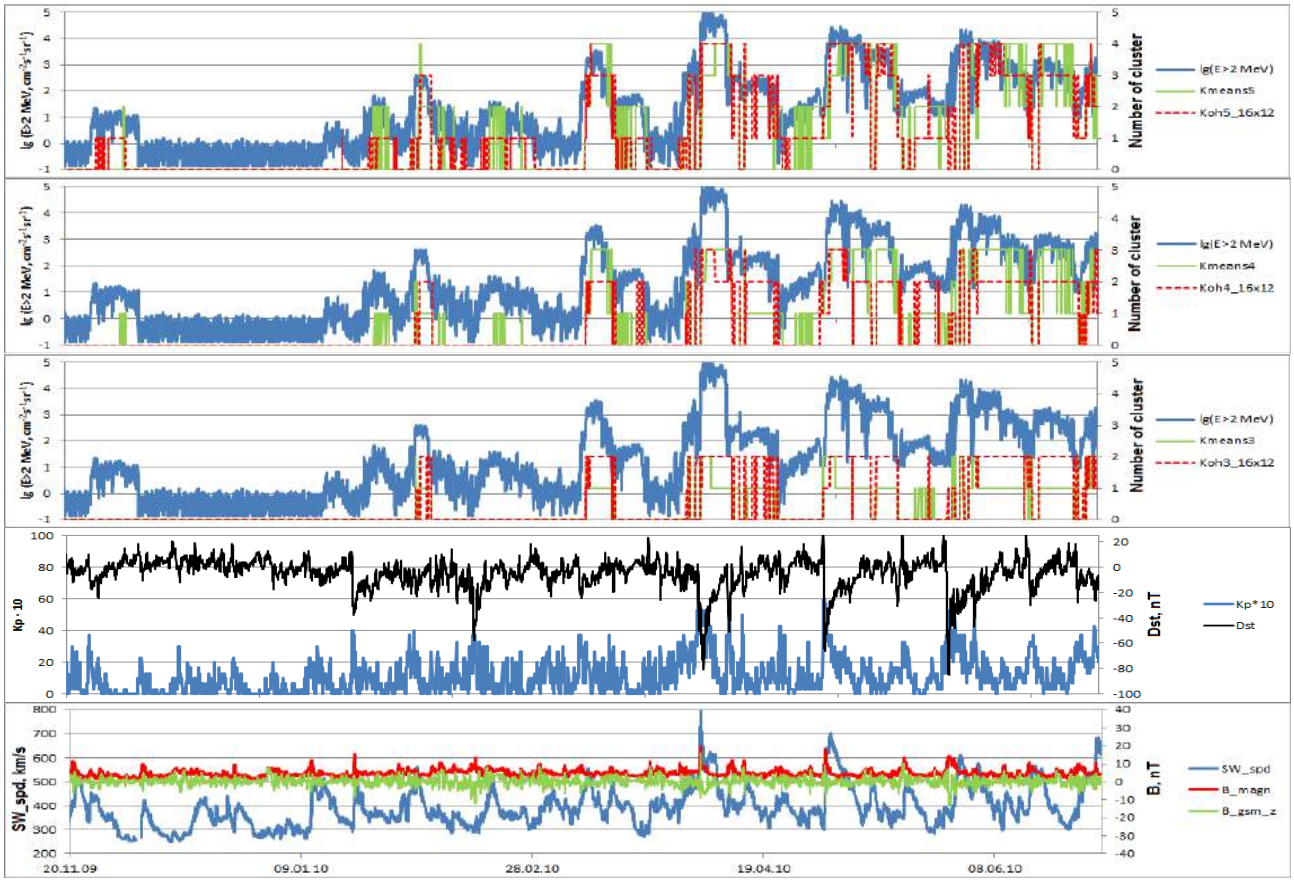

Fig. 5. The results of clustering obtained for time range from November 20, 2009 till June 30, 2010.

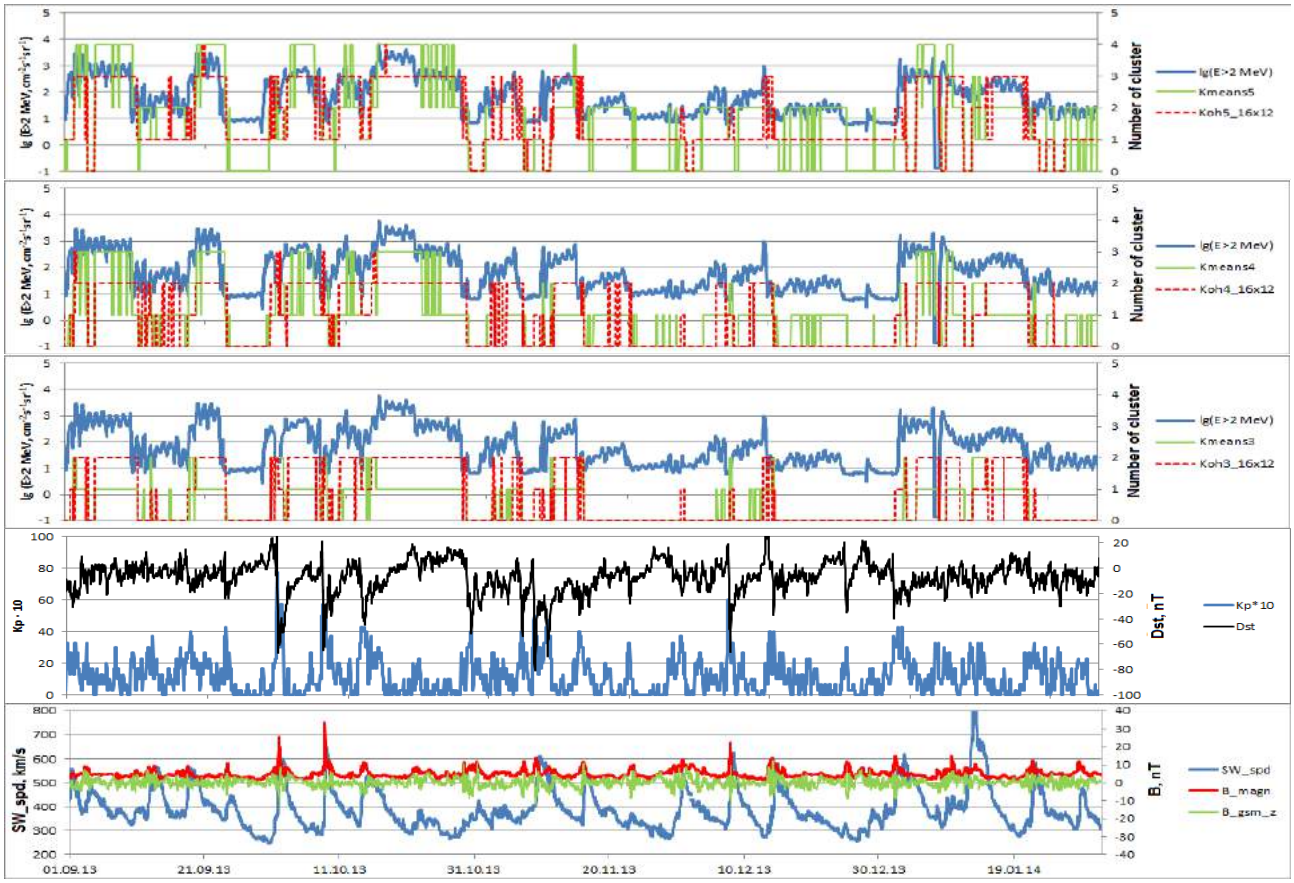

Fig. 6. The results of clustering obtained for time range from September 1, 2013 till January 31, 2014.

Figure 5 shows the results of clustering for the period of the abnormal minimum of SA (2009 year, when the electron flux in OERB was abnormally low) and the beginning of the current growth phase of 24 SA cycle. As can be seen from the figure, during this time period, the main conclusions regarding the quality of clusterization are the same – Kohonen SOM method works better than K-means, and five clusters show the situation in the Earth's magnetosphere more clearly. As figure 5 shows, the segmentation obtained by k-means algorithm is more sensitive in case of very low values of the electron flux. The main result of the study of this period is that clustering works also during the SA minimum at low OERB electron fluxes.

In Figure 6, one can see the results of clustering for the period of maximum of SA cycle 24 – the current cycle of solar activity. Figure 6 shows that compared to the two time periods discussed above, during SA maximum clusterization using SOM algorithm becomes less stable and less explicable from the physical point of view. We assume that this is connected with the significant fraction of sporadic increases in the solar wind, and therefore with strong magnetic storms and variations of electron fluxes in OERB. This may require separating out a special type of dynamics (a special cluster). During SA decline and in the minimum of SA, the main contribution to geomagnetic activity and electron fluxes is given by recurrent solar wind streams from coronal holes.

CONCLUSION

The multi-dimensional time series consisting of the values of logarithm of electron flux in OERB, parameters of SW, IMF and geomagnetic indexes, with delay embedding to the depth of 24 hours, was split into three, four, and five clusters (types of segments) with Kohonen self-organizing map and with k-means algorithm.

The obtained results were analyzed for different time intervals – for decay, minimum and maximum of solar activity cycle. The following conclusions can be made:

1. The segmentation that was best corresponding to physically different states of the OERB, was obtained by the Kohonen self-organizing map with 5 clusters, 16×12 cells.
2. Clustering methods, if properly used, can give adequate results for different periods of solar and geomagnetic activity.
3. Segmentation obtained by k-means algorithm is usually more sensitive at low values of the electron flux, but less stable in respect to high-frequency switching from one cluster to another and back.
4. The quality of clusterization might possibly depend on the contribution of recurrent SW fluxes to geomagnetic storms and partly on the level of the electron flux.

Summarizing, segmentation of multi-dimensional time series with clustering algorithms is able to separate physically different situations. This may help scientists to understand outer ERB dynamics. This may also help to improve forecasts of geomagnetic activity and electron flux, if the forecasts are made separately for each type of dynamics (cluster).

ACKNOWLEDGEMENT

The authors thank the teams of ACE and GOES projects and WDCC2 Kyoto for the possibility to access and use the data of their experiments.

REFERENCES

Friedel, R.H., W.G.P. Reeves, and T. Obara, (2002), Relativistic electron dynamics in the inner magnetosphere –A review, *J. Atmos. Solar. Terr. Phys.*, 64, 265–283.

Iucci, N., A.E. Levitin, A.V. Belov et al. (2005), Space weather conditions and spacecraft anomalies in different orbits, *Space Weather*, 3(1), S01001.

Pilipenko, V., N. Yagova, N. Romanova, and J. Allen, (2006), Statistical relationships between the satellite anomalies at geostationary orbits and high-energy particles, *Advances in Space Research*, 37(6), 1192–1205.

Reeves, G.D., S.K. Morley, R.H.W. Friedel et al. (2011), On the relationship between relativistic electron flux and solar wind velocity: Paulikas and Blake revisited, *J. Geophys. Res.*, 116, A02213.

Tu, W., X. Li, Y. Chen, G.D. Reeves, and M. Temerin (2009), Storm-dependent radiation belt electron dynamics, *J. of Geophys. Res.*, 114(A2), A0221.

CORONAL MASS EJECTION, GEOMAGNETIC STORMS AND GROUND-BASED COSMIC RAY INTENSITY DECREASES

I.Ya. Plotnikov [1], L.P. Shadrina [2], S.A. Starodubtsev [1], G.F. Krimsky [1]

[1] Yu.G. Shafer Institute of Cosmophysical Research and Aeronomy of SB RAS, 677980 Yakutsk, Russia, plotnikov@ikfia.sbras.ru
[2] Academy of Sciences of Republic of Sakha (Yakutia), 677007 Yakutsk, Russia

Events of geomagnetic storms and cosmic ray intensity Forbush-decreases are compared with coronal mass ejections. On the basis of catalogue of interplanetary shocks the predictors of ground manifestations of various types of the events are extracted: (a) geomagnetic storms with a Forbush decreases; (b) geomagnetic storms without Forbush-decreases; (c) Forbush-decreases without a magnetic storms; (d) events without geomagnetic storms and Forbush-decreases. The dependence of four helio- and geoeffects (a-d) on a compression ratio σ and interplanetary shock velocity Vsh is considered. There were revealed the features of these parameters which show a central or peripheral location of the heliogeoeffective structures in the body of coronal mass ejection. The results of the ground diagnostics of their location are in a qualitative agreement with the normal **n** orientation of the registered interplanetary shocks.

Introduction

The moved solar wind disturbances caused by coronal mass ejections (CME) of the solar substance are source of some dynamic helioeffects on the Earth's orbit [1]. One of them is a sudden geomagnetic field change connected with the ejection entering into the near-Earth space. It causes the observed geomagnetic disturbance and forms geomagnetic storms of various intensity [2]. Another cosmophysical phenomenon is decrease of galactic cosmic ray (GCRs) intensity caused by plasma flux ejection from the solar surface into the heliosphere which modulates the peculiar distribution of high-energetic particles in the space [3]. The non stationary transport of GCRs is namely connected with the evolution of modulation region i.e. helioeffect of the ejection. In the ground experiment the effect of Forbush decrease which is often registered simultaneously with a geomagnetic storm is connected with the modulation region. Furthermore, CMEs also initiate the considerable number of events which occur separately [3, 4].

In this study the events of geomagnetic storm and Forbush decrease registered simultaneously with the penetration of the ejection into the near-Earth space are considered. In the framework of representations of geophysics the compatibility conditions of these effects have been analyzed. The events connected with the interplanetary shocks (IPS) which are generated by explosions in the lower corona of the Sun and supersonic distribution of CME in the solar wind [5] have been selected.

The aim of this paper is to reveal relationships between helio- and geoeffects of CME and dynamic IPS parameters as a predictor of moved solar wind disturbances and magnetosphere interaction.

Data and results

The data of ground observations of four typical events are the following: geomagnetic storm with Forbush-decrease (a - 2001/10/21 17 UT); geomagnetic storm without Forbush-decrease (b - 1999/09/22 12 UT); Forbush-decrease without geomagnetic storm (c - 2002/07/17 16 UT); both without geomagnetic storm and Forbush-decrease (d - 2000/07/28 07 UT). Those data are compared with the registration of IPS in the near-Earth space.

The results are shown in Fig. 1 and Fig. 2. Vertical lines indicate the moments of IPS registration on the SC WIND (catalogue http://www.cfa.harvard.edu/shocks/wi_data/00021/wi_00021.html). These shocks are the isolated event predictors since disturbances in the first third of time intervals are absent. Fig. 1 shows Dst-indices of geomagnetic field variations have been obtained from the OMNI database (http://cdaweb.gsfc.nasa.gov/), and changes of the isotropic component of GCR intensity (δI/I) have been

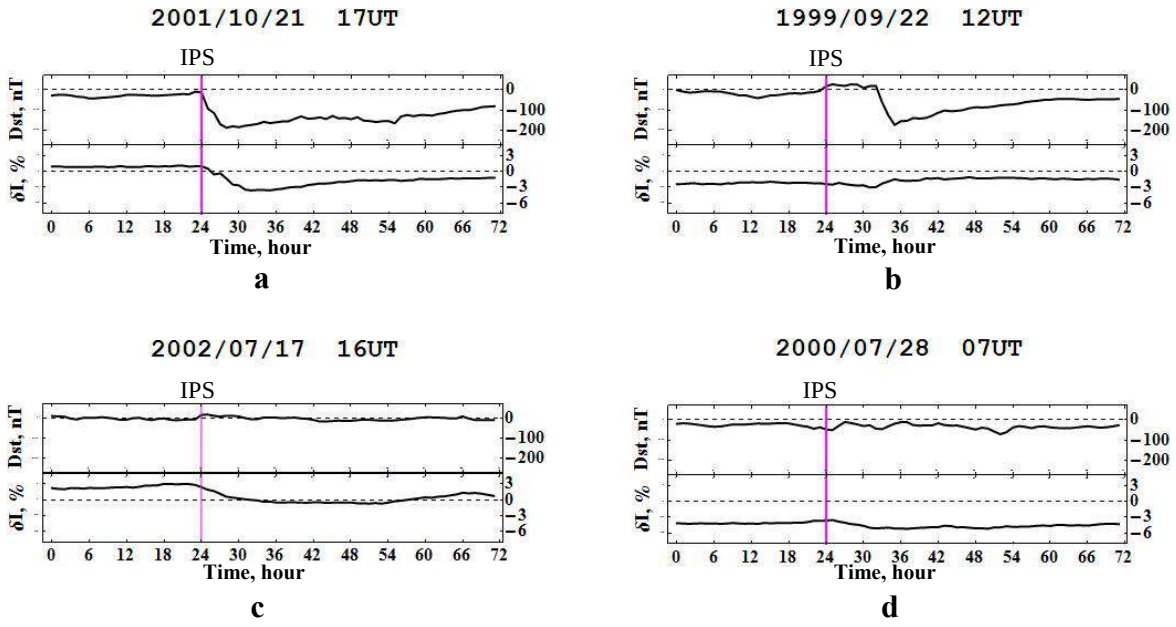

Fig. 1. Time dependence the geomagnetic activity Dst-index and GCR intensity δI/I for 4 types of the events. Color vertical lines indicate the moments of IPS registration.

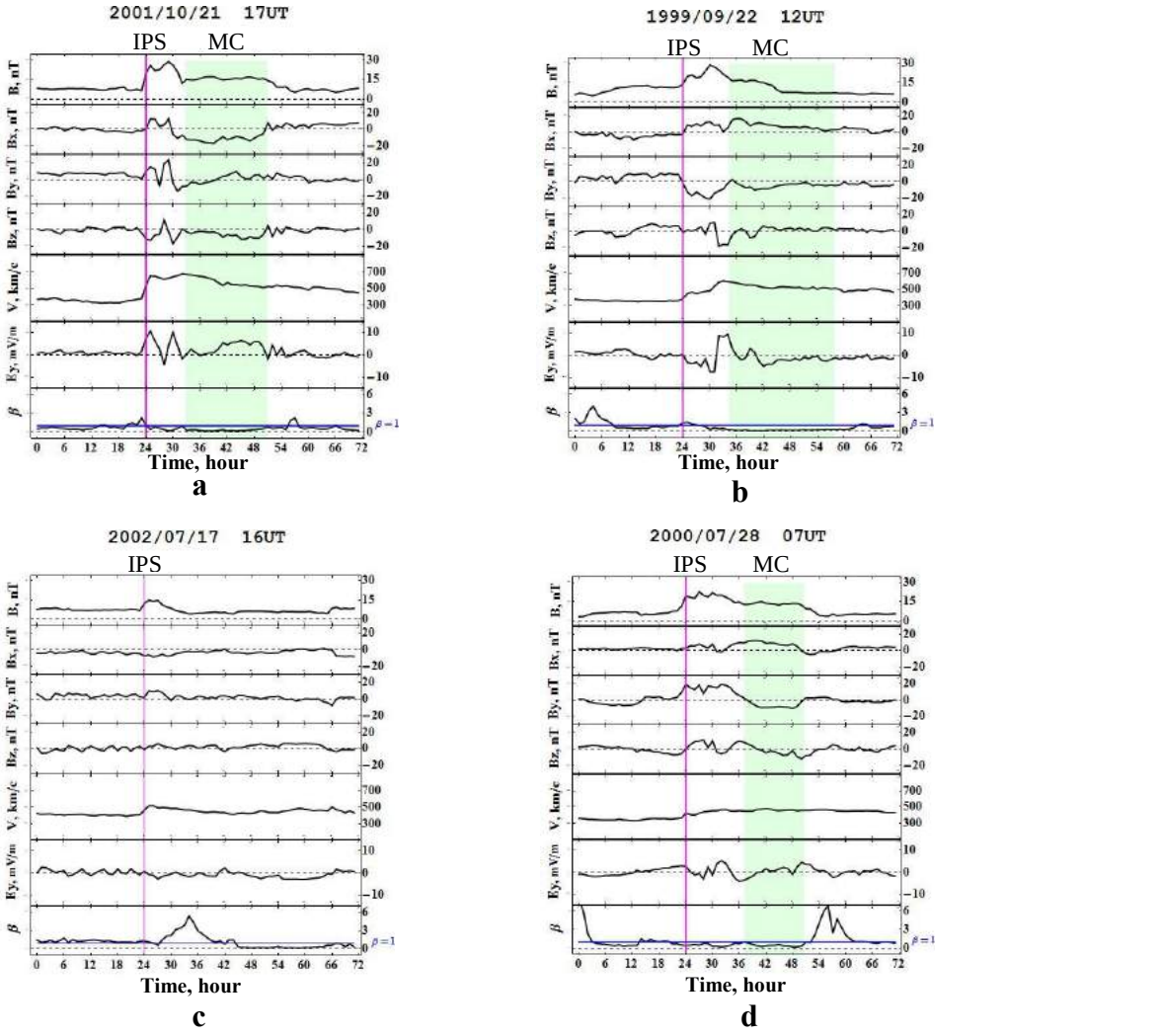

Fig. 2. Time dependence of solar wind parameters characterizing a degree of interplanetary disturbances for the same 4 types of the events

calculated at ShICRA of SB RAS using a method of global survey by data of the world-wide neutron monitor network. Fig 2 shows solar wind parameters: interplanetary magnetic field module B and components of Bx, By, Bz (GSE system of coordinates), plasma velocity Vs, interplanetary electric field Ey and parameter β (the ratio of gas pressure to the magnetic).

Discussion

Fig. 2 shows that each events in Fig. 1 is associated with the increase of the solar wind velocity typical for the CME in the area behind IPS front and on three cases (**a, b** and **d**) there are magnetic clouds (MC). It should be noted feature: at all events in a single case in Fig. 2c MC behind the front is missing. Such feature is due to the value β>1 and possibly corresponds to explosive IPS from the Sun. In contrast, the other three shocks can be attributed to the piston IPS. Further it is interesting the compare explosive and piston IPS and also the heliogeoeffects followed them.

The magnitude of the positive electric field directly determines the geomagnetic storm generation – decreasing fields in its main phase. Actually, only one from three MCs (Fig. 2a) is related to changes of the GCR intensity (Fig 1a). The comparison of IPS and MC orientation parameters as possible 3-D structures connected with the body of CME is considered below. Apparently, only with involving of 3-D model of GCR particle modulation [5] it is possible to find the answer to a problem: is the Forbush-decrease a response to IPS, ICME or MC [6]? In this case it is necessary to pay attention to the peculiarities of explosive CME (Fig. 2c).

Information on IPS and MC parameters are presented in the Table and in Fig. 3.

Table. The IPS parameters and markers of MC for four types of heliogeoeffects

Type	Date	V_{sh}	σ	**n**	MC
a	2001/10/21 17 UT	562	4.31	−0.84, −0.04, −0.54	WSE
b	1999/09/22 12 UT	428	2.64	−0.89, 0.46, 0.03	SWN
c	2002/07/17 16 UT	483	3.14	−0.84, −0.51, −0.2	
d	2000/07/28 07 UT	399	2.82	−0.83, 0.01, 0.56	NWS

Data from the Table shows that piston-type IPS of **a, b** and **d** type correspond to different markers: WSE, SWN and NWS. Taking into account their axial field MC have various orientations. In the first case the axis is directed almost vertically, and in two other cases – at an angle of < 45° to a horizontal plane in the GSE system. The negative sign of the IPS normal $\mathbf{n_z}$ of **a** type allows to think that there was an interaction of the Earth's magnetosphere with the southern sector of MO which is above defined as a vertically oriented one.

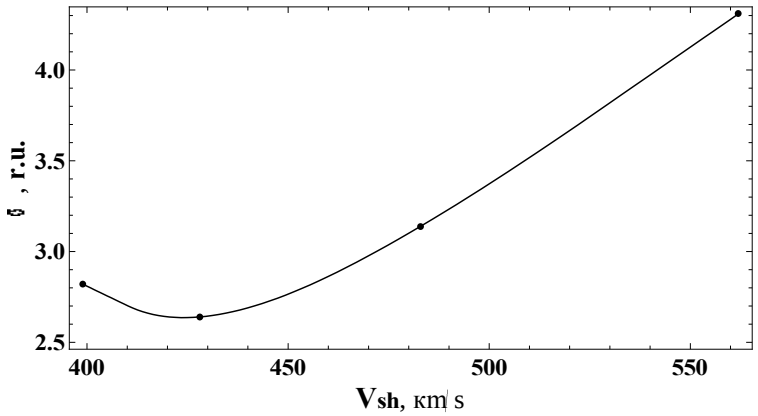

Fig. 3. Dependence of compression degree of IPS σ on their velocity V_{sh} for various types of heliogeoeffects.

The positive sign of IPS normal $\mathbf{n_y}$ allows to think that there was a contact of the Earth with a eastern sector of MC with a horizontal orientation. According to the experimental data [7], the probability of Forbush-decrease registration in this sector is small. It is probably to explain such fact only after studying of 3-D model of GCR modulation region.

The positive sign of the IPS normal $\mathbf{n_z}$ of **d** type allows regarding that the geomagnetosphere contacts with a northern zone of MC oriented horizontally too. The value of $\mathbf{n_z}$ allows to consider the contact region near the boundary of MC and located more far from its axis relative to the other cases. Probably the helioeffects are absent because of such remoteness and proximity to the boundary.

The negative sign of the explosive IPS normal $\mathbf{n_y}$ of **c** type, probably not having the extracted orientation, is connected with the western sector of CME. According to [8], in this sector there are more probable helioeffects in the absence of geoeffects.

Fig.3 shows the dependence s of IPS on its velocity V_{sh} and contains the information on a source location of CME on the Sun. Apparently, the event of **a** type with great values σ and V_{sh} is connected with CME which is propagated near to a central meridian in the heliosphere. Other three events are initiated by sources which are substantially displaced relative a central meridian.

Conclusions

1. The geomagnetic storms and Forbush-decreases of GCR intensity registered simultaneously are generated by the central region of CME.

2. The absence and non-simultaneous development of storms and Forbush-effects after the registration of IPS take place if Earth's magnetosphere interacts with periphery part of the CME.

The obtained results are preliminary. Their legitimacy of due to the fact that they are based on actual physical 3-D representation of the generation of geomagnetic storms and GCR modulation in the inner heliosphere.

The work has been supported by the RFBR grant 12-02-98507-r_vostok_a, programme of RAS Presidium № 10 and grant of the RF President for a support of leading scientific school № НШ-3269.2014.2.

References

1. *Plasma heliogeophysics* (2008), 672 pp / Ed.by L.M.Zeleny, I.S.Veselovsky, Moscow, Vol. I-II (in Russian).

2. Yermolaev Yu.I. (2002), *Experimental study of the solar wind large-scale structure*, Manuscript. Moscow.

3. Cane H V. (2000), Coronal mass ejections and Forbush decreases. *Space Sci. Rev.*, 93, 1-2, 55-77.

4. Krymsky G.F. et al. (2009) Piston shock and Forbush effect. *Astronomy Letters*, 35, 10, 696-700.

5. Alania M., Modzelewska R., Wawrzynczak-Szaban A. (2012) 3-D models of the Forbush decrease and 27-day variation of galactic cosmic rays with three dimensional divergence-free interplanetary magnetic field, in: *Abstr. 39th COSPAR Scientific Assembly. 14-22 July 2012*, in Mysore, India. D1.2-15-12, 35.

6. Babu A. et al. (2013), High rigidity Forbush decreases: due to CMEs or shocks? *arXiv:* 1304.5343v1.

7. Shadrina L.P., V.P. Mamrukova, I.Ya. Plotnikov (1996) Complex analysis of solar wind disturbances cosmic ray depressions and geomagnetic storms. G*eomagnetism and Aeronomy*, 36 (3), 169-173.

8. Shadrina L.P., I.Ya. Plotnikov, and S.A. Starodubtsev (2002) Geomagnetic storms and Forbush decreases during the passage of the Earth through the flanks of large-scale solar wind disturbances, *Int. J. Geomagn. Aeron*., 2(3), P.45.

IAR EMISSION CHARACTERISTICS AND PARAMETERS OF THE IONOSPHERE

A.S. Potapov[1], T.N. Polyushkina[1], B.V. Dovbnya[2], B. Tsegmed[1,3], R.A. Rakhmatulin[1]

[1]Institute of Solar-Terrestrial Physics SB RAS, Irkutsk, Russia, e-mail: potapov@iszf.irk.ru; [2]Borok Geophysical Observatory of Institute of Physics of the Earth RAS, Borok of Yaroslavl region, Russia; [3]Research Center for Astronomy and Geophysics MAS, Ulaan-Baator, Mongolia

Abstract. Continuous magnetic observations of IAR emission at the mid-latitude observatory Mondy performed by search coil magnetometer LEMI-30 in the period from March 2010 to May 2011 are analyzed and compared with results of the simultaneous ionosphere sounding. We show good correlation of diurnal and seasonal IAR frequency variations with changes in the critical frequency f_0F_2 of the ionosphere. An attempt is made to model diurnal variation of IAR frequency calculating expected frequency scale of emission with use of IRI-2012 model. The results show good agreement with measurements, but contain a systematic error. Its source is discussed.

1. Introduction. Ionospheric Alfvén resonator (IAR) is an interesting subject of research. Its multiband electromagnetic emission in the frequency range between 0.5 and 10 Hz was first discovered in mid-eighties of the last century [1]. IAR emission is a manifestation of Alfvén waves captured between the lower part of ionosphere and a bend of plasma density in the region of transition from the ionosphere to magnetosphere at the height of about 3000 km [2]. Frequency of discrete spectral bands (DSB) and spacing between them are determined by the geometry of the resonator and the Alfvén speed in its cavity; the change in band frequency during the day with a minimum around noon and a maximum after midnight or in the early morning hours is due to diurnal variation of ionospheric parameters. Close connection of DSB mode and features with state of the ionosphere motivates many authors to study the details of this connection, and make suggestions about how to use observations of the spectral structure of the electromagnetic background in the range of 0.5–10 Hz for sounding ionospheric parameters and clarifying ionospheric models [3, 4].Low noise level at the observatory, high sensitivity of the magnetic sensors and the proximity of observation period to the minimum of solar activity have helped us to acquire a large enough sample of distinct DSB occurrences (350 events). Fig. 1 shows a typical example of winter event.

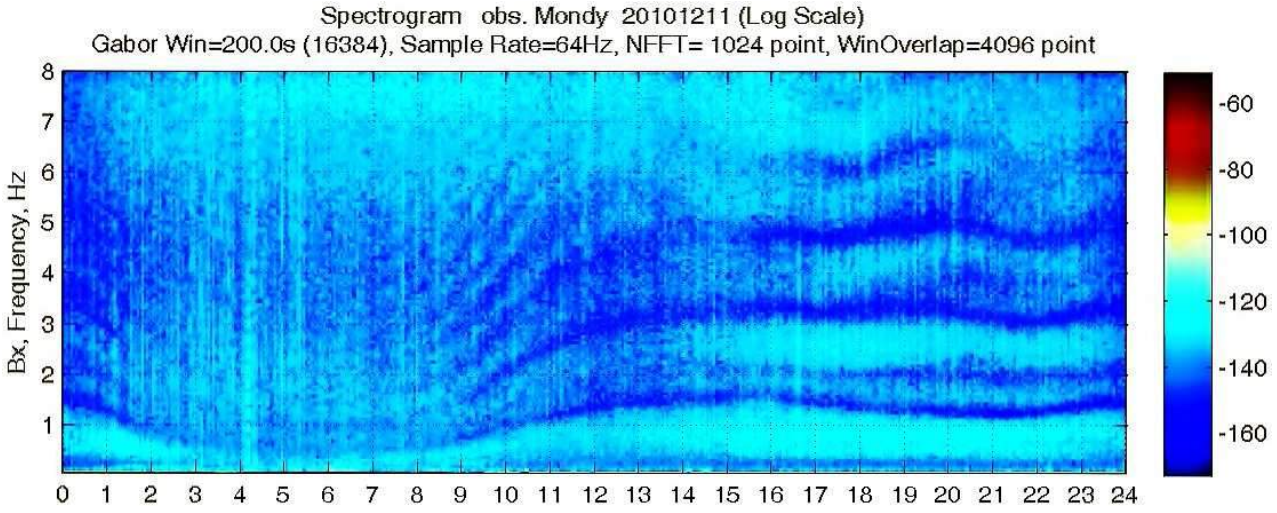

Fig. 1. An example of spectrogram demonstrating discrete spectral bands of IAR emission.

2. Equipment and Processing Technique. Sayan Solar Observatory Mondy (geographic coordinates φ = 51.6°, λ = 100.9°; McIlwain parameter L = 2.1) is situated near the border between Russia and Mongolia. Induction magnetometer LEMI-30 measures signals within 0.001–30 Hz frequency range. Noise level does not exceed 0.2 pT/Hz$^{1/2}$ at 1 Hz and 0.2 pT/Hz$^{1/2}$ at 10 Hz frequency. ADC has 24 digits. Sampling rate is

60 Hz. To compare magnetic data with ionospheric data we used 15-min values of critical frequency f_0F_2 from DPS-4 digital ionosounder installed in Irkutsk, about 260 km from the observatory.

Digital magnetic records in the range of 1-10 Hz were processed using specifically developed MATLAB code. The program calculates dynamic spectrum of the signal in two components and builds daily spectrogram in coordinates "frequency-time". The intensity of the signal at a given frequency in a given time is displayed in color. Spectrograms obtained were analyzed visually. Usually we managed to make measurements of 5–6 harmonics (bands), but more often three or four. These data we used for detailed comparison with changes in ionospheric parameters and to calculate the correlation coefficients and regression line between harmonics and critical frequency variations of the ionosphere F2 layer.

3. Morphology of DSB. Intensity of IAR emission is rather weak and usually it is difficult to find it against noisy background. But in our case, a set of favorable conditions for ULF measurements stipulated high quality of observations. Experience of visual processing of spectrograms obtained showed that the most suitable for digitizing is the second harmonic frequency of the signal; the first harmonic is often noisy owing to lower-frequency irregular emission, and the higher harmonics are not always distinct due to the natural decay of the IAR signal amplitude with frequency. The observation period (March 2010 – May 2011) coincides in time with beginning of ascending branch of solar cycle 24 and is characterized by low solar and magnetic activity. Mean occurrence rate of DSB was almost 90% that is much higher comparing with occurrence of these structures reported in earlier papers [4, 5]. We found that duration of DSB observation within a day strongly depends on season. Fig. 2 is a comparison between time interval of IAR emission and duration of nighttime. It is clear from the figure that the emission is a nighttime event: DSB are mainly observed during shadowing of the lower ionosphere.

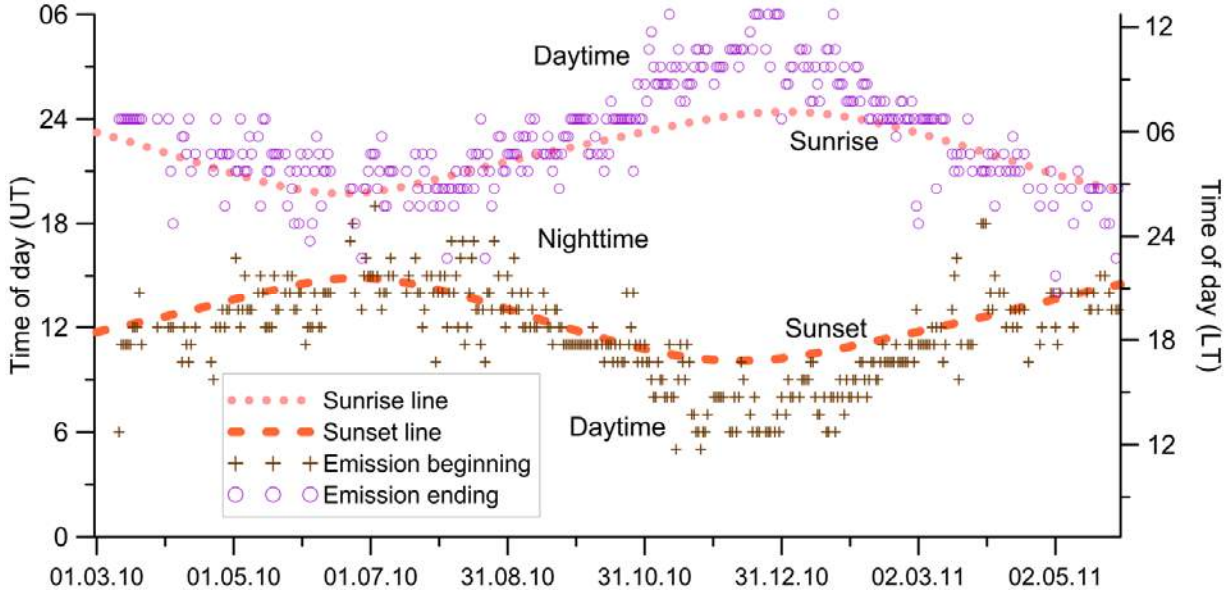

Fig. 2. Time of beginning (crosses) and ending (circles) of DSB in different seasons. Dashed lines show time of sunrise and sunset.

4. DSB Frequency and f_0F_2. Since the observed discrete spectral bands are formed by capturing low-frequency emission in the ionospheric Alfvén resonator being ionospheric structure, the behavior of the main characteristics of DSB should closely correlate to variations of ionospheric parameters, primarily to changes in the electron concentration. In turn, the electron number density in the F2 layer is uniquely linked to the critical frequency f_0F_2, measured by ionosonde: $f_0F_2 = 8.98*10^{-3}N_e^{1/2}$, where number density is measured in cm^{-3}, and critical frequency in MHz.

We compared behavior of DSB frequency and f_0F_2 depending on the season. To do that, we calculated a reverse value of $1/f_0F_2$ for 15 monthly median values of critical frequency and plotted them in Fig. 3 along with mean values of frequency scale Δf IAR, that is, the spacing between neighbor bands of the IAR emission. Overall progress of the averaged monthly ionospheric characteristics and DSB matches well, although there is a discrepancy at the transition from summer to autumn months of 2010.

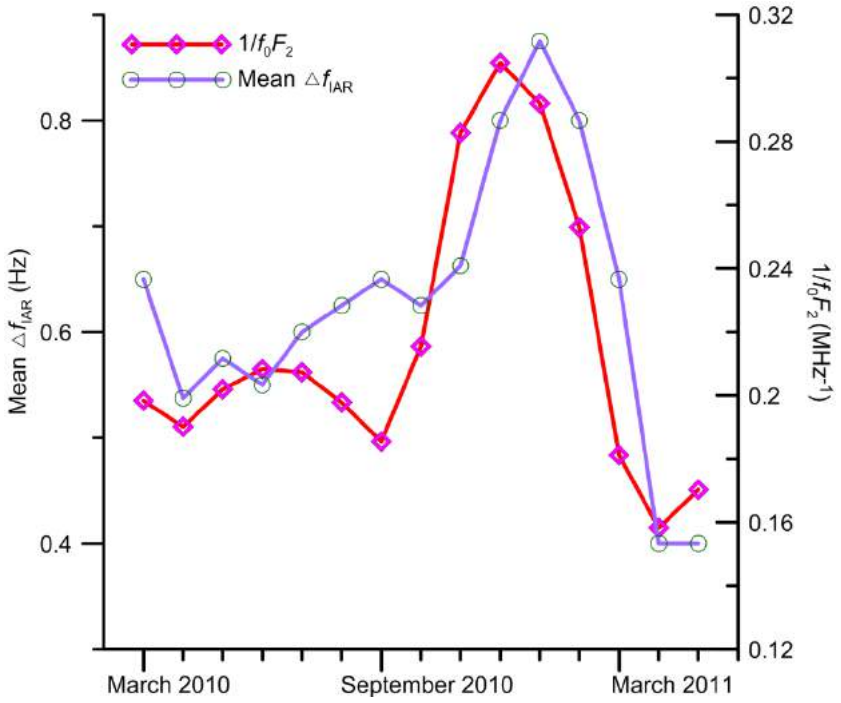

Fig. 3. Comparison between seasonal dependence of $1/f_0F_2$ and variations in DSB frequency gap Δf IAR.

5. Model of the IAR spectrum formation. The literature offers different versions of the model of the ionospheric Alfvén resonator [6, 3, 7]. The models are based on the resonance conditions of Alfvén wave reflection from the lower and upper ionosphere and capture analysis of Alfvén waves in the cavity being formed along the magnetic field lines between the local maxima of the Alfvén speed ("walls" of the resonator) in the F_2 layer and at altitude of 2,000-6,000 km. All authors agree that for resonance of waves with wave speed A in a uniform cavity of length L, the frequency f of harmonic number n is given by $f = (n + \Phi)/(2L/A)$. In reality, the cavity is not uniform, and the phase factor Φ is complicated function of conditions on the walls of the resonator. To exclude phase factor Φ we can measure not frequency f, but frequency scale $\Delta f = f_n - f_{n-1} = A/(2L)$. For non-uniform cavity, the latter relation can be rewritten as $\Delta f = 1/(2T_0)$, where

$$T_0 = \frac{1}{2}\int_{l_{bottom}}^{l_{top}} \frac{dl}{A(l)}. \qquad (1)$$

Here l_{bottom} and l_{top} are positions of the lower and upper walls of the resonator, respectively; Alfvén speed $A(l) = B(l)\Big/\sqrt{4\pi m_{eff}(l) N_e(l)}$, magnetic field B, electron number density N_e, and effective ion mass m_{eff}, all vary with l. Using formula (1) we calculated transit time T_0 for some hours of 13 events, taking one event per month. D layer height of 100 km was taken as a lower wall of the resonator. The height of maximum Alfvén speed above the F_2 layer was taken as the upper wall. Altitude profile of the magnetic field $B(l)$ was calculated by DGRF/IGRF model. Altitude profiles of the electron density $N_e(l)$, the effective mass m_{eff}, and the Alfven speed $A(l)$ were calculated to the height $l^* = 2{,}000$ km based on the International Reference Ionosphere model IRI-2012, and above 2,000 km based on extrapolation formula similar to that used in [8].

Fig. 4 shows the altitude profiles of N_e, m_{eff}, B, and A for one of the runs (1300UT January 15, 2011). Time $2T_0$ in this case was found to be 0.57 sec, which corresponds to the frequency scale $\Delta f = 1.75$ Hz. This exceeds spacing between the harmonics measured on the spectrogram by 0.25 Hz. In total, for 13 selected days of observations we have performed 99 calculations of the frequency scale Δf_{calc} and compared them with the measured values Δf_{meas}. The result is shown in Fig. 5, which shows that the correlation between the calculated and measured values is quite high (correlation coefficient $r = 0.9$), but the regression line does not pass through zero, although it has the slope of nearly 45 degrees. Calculated frequency scale Δf_{calc} exceeds measured value Δf_{meas} on average by 0.35 Hz. This means that there is some systematic error in the determination of Δf_{calc}.

6. Discussion. Both systematic and random errors in modeling frequency structure of IAR can be explained by different reasons. One of them is that we considered vertical alignment of resonance cavity, not along the geomagnetic field line. Other causes may be a mismatch between DSB measurement site and the point of ionospheric sounding, inaccurate reflection of ionospheric conditions model IRI-2012, etc. Search for possible ways of a method refinement is a task for future work (see [9]). Whatever it was, we can conclude

that, as far as we know, this is the first attempt to directly compare the measurements of variations in IAR emission frequency with more or less realistic description of the resonance structure on the basis of the available models of the ionospheric plasma and magnetic field. It seems to us, in the future this way can be utilized to develop methods for verifying ionospheric models and diagnostic parameters of the upper ionosphere on the basis of magnetic measurements in the ultralow-frequency range.

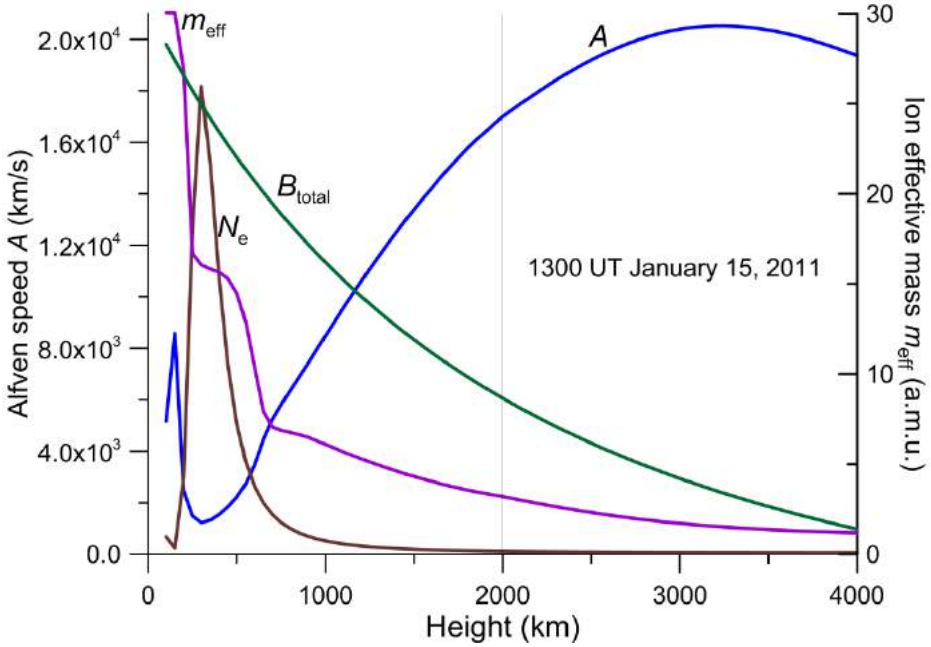

Fig. 4. Altitude profiles of N_e, m_{eff}, B, and A for one of the runs.

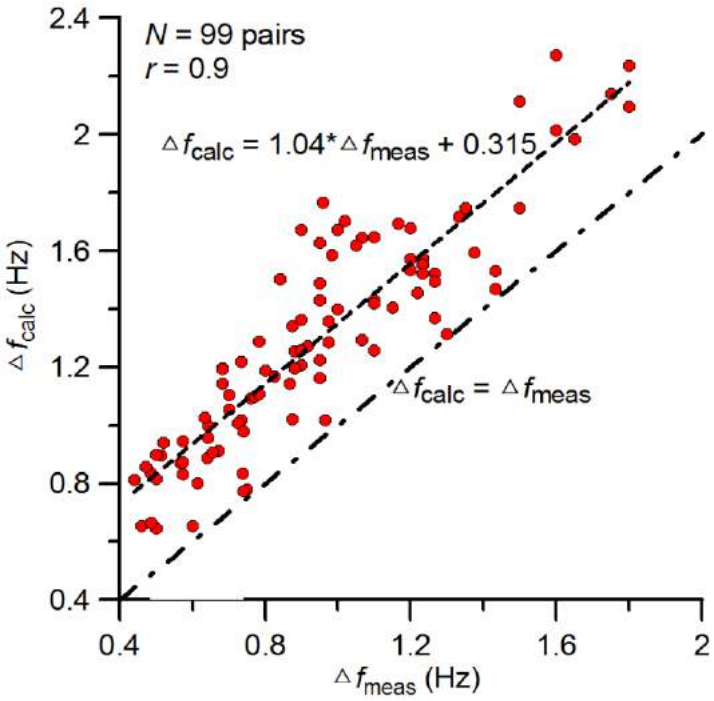

Fig. 5. Correlation between the calculated and measured values of Δf.

Acknowledgements. The part of work done by A.S.P. (development of the IAR spectrum formation model) was supported by the Russian Science Foundation, grant 14-37-00027; the part of work done by T.N.P, B.V.D., B.T., and R.A.R. (observations and morphological studies) was supported by the Russian Foundation for Basic Research, grant 13-05-00529.

References

1. Belyaev, P.P., S.V. Polyakov, V.O. Rapoport, and V.Yu. Trakhtengerts (1987), Detection of the resonance structure of spectrum of the atmospheric electromagnetic background noise in the range of short-period geomagnetic pulsations, *Doklady AN SSSR*, 297, 840–843.
2. Belyaev, P.P., S.V. Polyakov, V.O. Rapoport, and V.Yu. Trakhtengerts (1990), The ionospheric Alfvén resonator, *J. Atmos. Solar-Terr. Phys.*, 52(9), 781–788.
3. Demekhov, A.G., P.P. Belyaev, S.V. Isaev et al. (2000), Modeling the diurnal evolution of the resonance spectral structure of the atmospheric noise background in the Pc1 frequency range, *J. Atmos. Sol. Terr. Phys.* 62, 2000, 257–265.
4. Yahnin, A.G. , N.V. Semenova, A.A. Ostapenko et al. (2003), Morphology of the spectral resonance structure of the electromagnetic background noise in the range of 0.1–4 Hz at L = 5.2, *Ann. Geophys.*, 21, 779–786.
5. Molchanov, O.A., A.Yu. Schekotov, E. Fedorov, and M. Hayakawa (2004), Ionospheric Alfvén resonance at middle latitudes: Results of observations at Kamchatka, *Phys. Chem. Earth*, 29, 649–655.
6. Polyakov, S.V. and V.O. Rapoport (1981), Ionospheric Alfvén resonator, *Geomagnetism and Aeronomy*, 21 (5), 816–822.
7. Hebden, S.R., T.R. Robinson, D.M. Wright et al. (2005), A quantitative analysis of the diurnal evolution of Ionospheric Alfvén resonator magnetic resonance features and calculation of changing IAR parameters, *Ann. Geophys*., 23, 1711–1721.
8. Lysak, R.L. (2004), Magnetosphere-ionosphere coupling by Alfvén waves at midlatitudes, *J. Geophys. Res*., 109, A07201.
9. Potapov, A.S., T.N. Polyushkina, B.V. Dovbnya et al. (2014), Emissions of ionospheric Alfvén resonator and ionospheric conditions, *J. Atmos. Sol. Terr. Phys.* 119, 91–101.

CATALOGUE OF AURORA BOREALIS OBSERVED IN THE 19th CENTURY IN RUSSIA

N.G. Ptitsyna, M.I.Tyasto, B.A. Khrapov

St. Petersburg Institute of Terrestrial Magnetism and Radiowave Propagation, 199034, Russia, e-mail nataliaptitsyna@ya.ru; mtyasto@mail.ru

Abstract. We have compiled a catalogue of aurora borealis registered in 1837 - 1900 by the Russian network of meteorological observatories. We collected and analyzed data from 128 stations localized in a very wide geographical zone in Europe, Asia and Alaska (geographical coordinates:φ =39 °57′N ÷ 72°30′N; λ = 21º26′÷224º35′). It was found that mid-latitude (geomagnetic $\varphi_m < 56º$) and high-latitude ($\varphi_m \geq 56º$) segments of our data show different long-term and cyclic behavior. Number of auroral occurrence N in the mid-latitude segment declines toward the end of the 19th c. with a minimum around 1900. The high latitude segment demonstrates an upward trend over the century that was not found in other works. The longest data series of aurora borealis observed in observatory St. Petersburg (φ_m=56º14′) also shows this upward trend. The 11-year variations are superimposed on this trend, and a minimum in vicinity of 1900 is also traced. Aurora occurrence N at mid-latitudes show clear 11-year variations which are in correlation with solar and geomagnetic activity. In the mid-latitude segment the most pronounced peaks are closely related to solar maxima; the second peak that is in a declining solar activity phase is less significant. Aurora occurrence N at high latitudes also show 11-year variations. However here the first aurora peaks close to solar maxima are almost absent. The aurora maxima at declining phase of solar cycles are dominant ones in this case. The 22-year periodicity could be traced in some parameters of auroral activity.

INTRODUCTION

In the middle of the 19th century the relation between the processes on the Sun and magnetic field variations on the Earth was detected, when it was found the same 11-year cyclicity in the geomagnetic field variations and in the sunspot numbers (see [Sabine, 1852; Schwabe, 1844]). By that time, it was recognized that periods of geomagnetic field disturbances cause auroras [von Humboldt, 1808].

At present it is established that variable magnetic fields on the Earth derive from unstable processes on the Sun, move through interplanetary space to the Earth. This constantly changing electromagnetic environment in vicinity of the Earth is named "space weather", their long-term variations can be considered "space climate". Intense solar events can lead to storms in space and to magnetic storms on the Earth. This "bad" space weather may have adverse effects on the human technology and could be a threat to our civilization. Due to this, studies on space climate variations and extreme events are important not only from the theoretical, but also from the practical point of view.

For studies of solar-terrestrial periodicities and their behavior it is usually used aa index of geomagnetic activity because the time series spans further back than any of the other planetary index time series. It goes back to 1868. In determining variability of solar -terrestrial activity ptior to 1868 it is necessary to involve other sources. Such additional source is auroral activity which was registered throughout human history. Systematic and careful observations of aurora borealis were performed in 19 c. At that time several catalogues of aurora borealis were compiled. The most polular are [Angot, 1896; Křivský L., Pejm, l985]. On the basis of such catalogues and other records several number of studies were performed for determining solar – terrestrial activity in various time periods [see e.g. Feynman J. and Silverman, 1980; Silverman, 1992; Vázquez, Vaquero, Gallego, 2014].

However, there was a lack of available data on aurora borealis registered in vast European and Asian territories of Russia. Our aim has been to support and extent the existing databases on aurora borealis by collecting data that were registered by the Russian network of meteorological observatories in the 19 c.[for yearly books of observations see Ptitsyna et al., 2013]. The additional purpose was to investigate long-term trends and variations that could be present in aurora occurrence in relation to solar and geomagnetic activity.

DATA

We have compiled a catalogue of aurora borealis registered in 1837 - 1900 by the Russian network of meteorological and geomagnetic observatories. The catalogue also comprises data from those stations

which does not belong to Russian, but where Russian scientists were able to do observations as Chinese Beiging or Norvegian Hammerferst. Our catalogue comprises 2170 auroral events registered by 128 stations located in a wide geographical zone (geographical latitude φ from 39 °57′N till 72°30′N and longitude λ from 21°1′E до 2°35′E; geomagnetic latitude φ_m from 28°25′ N till 67°08′ N and λ_m from 104°2′ E till 275°23′ E).

Table 1 lists number of frequency registered in 1837-1900. N was calculated as a cumulative number summarized over a year of days (nights) when aurora was visible.

Табл.1. Frequency of aurora N reguistered by the Russian meteorological network in 1837-1900.

Year	N	Year	N	Year	N	Year	N
1837	16	1853	21	1869	37	1885	19
1838	23	1854	15	1870	76	1886	29
1839	27	1855	10	1871	56	1887	39
1840	16	1856	13	1872	60	1888	59
1841	7	1857	9	1873	64	1889	52
1842	16	1858	31	1874	28	1890	30
1843	7	1859	35	1875	42	1891	58
1844	8	1860	30	1876	22	1892	53
1845	7	1861	10	1877	19	1893	94
1846	10	1862	10	1878	31	1894	60
1847	21	1863	8	1879	37	1895	74
1848	20	1864	5	1880	30	1896	94
1849	7	1865	9	1881	44	1897	82
1850	14	1866	36	1882	60	1898	83
1851	22	1867	13	1883	58	1899	76
1852	40	1868	15	1884	46	1900	35

In Fig. 1 and Fig. 2 we present frequency of occurenee N together with sunspots W and index of geomagnetic activity CP9 and data series from catalogues Angot [1896] and Křivský and Pejml [1985]. CP9 is Bartels index of geomagnetic activity C9 computed for St Petersburg magnetic observatory.

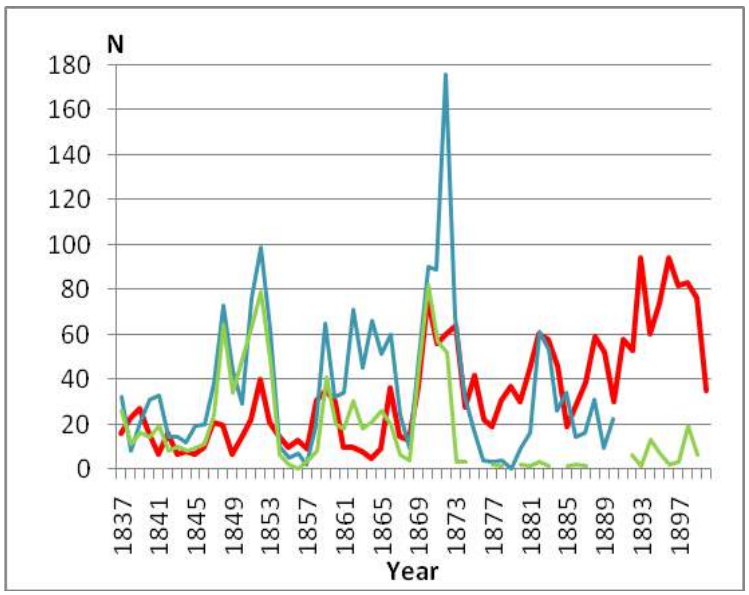

Figure 1. Frequency of aurora occurrence N observed in Russia (red) and N according to Angot [1896] (blue), Křivský and Pejml [1985] (green).

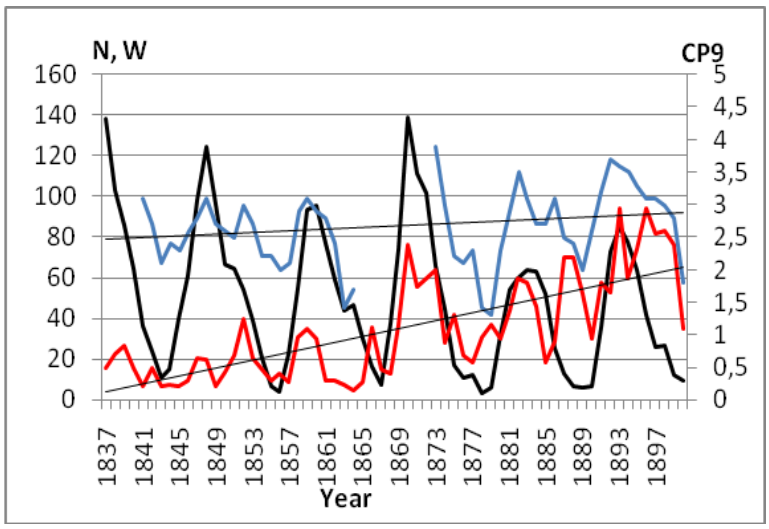

Figure 2. Frequency of aurora occurence N, according to our data (red), CP9 index of geomagnetic activity (blue) and Wolf numbers (black). Linear trends are also shown.

It is known that auroral events are controlled by solar and geomagnetic activity. Auroras from our list demonstrate good relationships with solar and geomagnetic activity. Auroras number of occurrence N is in correlation with W and CP9. In Fig 2 it is seen that auroras show 11-year variations which are related to solar cycles № 8-13. Peaks of auroral activity are one year ahead of the solar activity in cycles 9, 10 and 12 and they coinsides with it in odd-numbered cycles 11 and 13.

In this period geomagnetic activity is 1 year ahead of the solar activity in cycles 10, 12 and 13 and coincides with it in odd-numbered cycles 9 and 13. Note, that such relation between solar and geomagnetic maxima differs from the pattern which was observed in the 20th c. starting from solar cycle14: geomagnetic activity delay by 2-3 years [see e.g., Stamper et al., 1999].

In Fig. 1 and 2 there are two peaks in geomagnetic and auroral activity during a solar cycle. This well-known double peaks are due to two different sources of geomagnetic activity on the Sun: coronal mass ejections (CME) connected to the Sun's closed magnetic fields and corotating solar wind streams from open magnetic fields [see e.g. Vázquez et al., 2014]. The first auroral peaks are closely related to solar maxima. These peaks in N are generated by CME. The second peak is in a declining phase which is related to corotating streams. Tsurutani et al., 2006; Vázquez et al., 2014].

Our data is in general agreement with data presented in catalogues Angot [1896], Křivský and Pejml [1985]. However there are some discrepancies, mainly in the second part of the century, and they will be discussed later.

LONG-TERM TRENDS IN AURORA ACTIVITY OBSERVED IN RUSSIA IN 1837-1900

Aurora borealis observed in Russia show continuing upward trend during the century (Fig. 1 and Fig. 2). This trend is not seen in data of Angot [1896] and Křivský and Pejml [1985] catalogues. The main difference between these catalogues is that Angot [1896] and Křivský and Pejml [1985] aurora borealis were registered by stations at mid latitudes (geographical latitude $\varphi<55^{o}$) while our data base contains mid-latitude observations as well as high latitude ones. Thus it could be considered that the upward trend was defined by high-latitude auroras. For checking this assumption the data were divided in two segments according to their geomagnetic latitudes. In this paper high-latitudes stations are supposed to lay at geomagnetic latitudes $\varphi_m \geq 56^{o}$ and mid-latitude stations lay at $\varphi_m < 56^{o}$.

In Fig. 3 we show frequency of aurora occurrences N in both segments in comparison with solar activity index W.

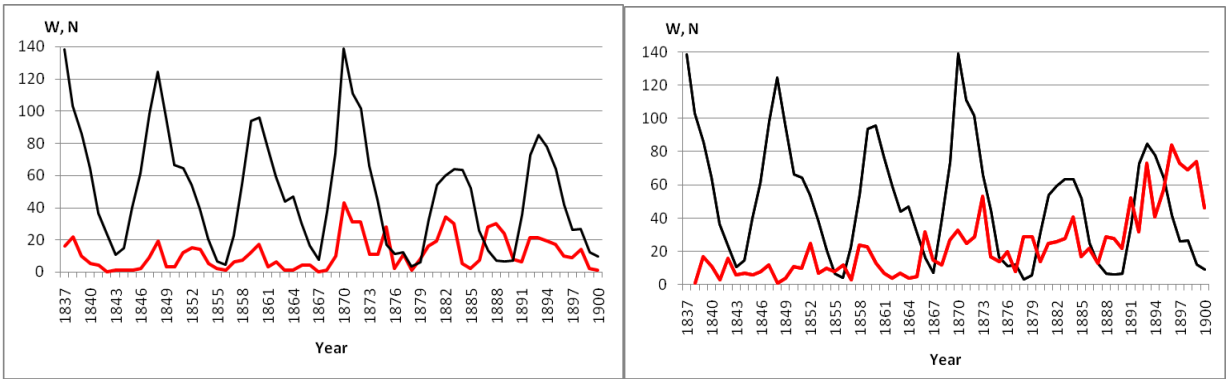

Fig. 3.Variations of aurora occurrence N registered in Russia at mid and high latitudes in 1837-1900. Left: mid-latitude segment (geographical latitude $\varphi \lessapprox 60^{\circ}$; $\varphi_m < 56^{\circ}$). Right: high-latitude segment ($\varphi_m \geq 56^{\circ}$).

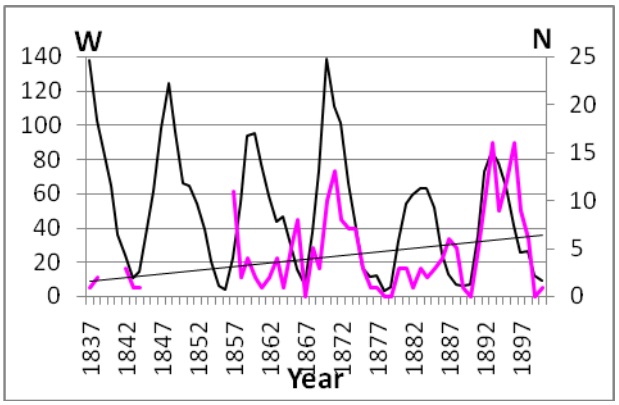

Fig. 4. Auroral occurence N (pink) in St. Petersburg/Pavlovsk and Wolf numbers. Geomagnetic latitude of the observatory ($\varphi_m = 56^{\circ}14'$; from 1878 $\varphi_m = 55^{\circ}58'$) is inbetween mid and high-latitude segments of our database.

We see that number of auroras in the mid-latitude segment does not show the upward trend, instead they show decline toward the end of the 19th c. The minimum in vicinity of 1900 coincides with one of the minima around turns of the centuries in 1700, 1800, and 1900 that were pointed out by Silverman [ ].

Polar auroras of the high-latitude segment show continuing increase over the century. 11-year variations are superimposed on this trend, and a inimum in vicinity of 1900 is also traced.

Aurora occurrence N in the mid-latitude segment show clear 11-year variations which are in correlation with solar activity. The most pronounced peaks are closely related to solar maxima. These peaks in N are generated by CME. The second peak in a declining phase which is related to corotating solar wind streams is less pronounced in the mid-latitude segment. Aurora occurrence N in the high-latitude segment also show an 11-year variations. However, this variation is not so clear because here the first aurora peaks at solar maxima are more or less absent. The second aurora maxima at declining phase of solar cycles are dominant ones in this case.

An insight of the upward trend and solar cycle variations are provided by Fig. 4, where we show auroras registered in an individual station St. Petersburg at geomagnetic latitude $\varphi_m = 56^{\circ}14'$ (in 1878 because of industrial pollution and city lights it was moved to Pavlovsk at $\varphi_m = 55^{\circ}58'$).

It is seen in Fig. 4 that N systematically increases in 1837-1900. However, following the declining phase of the solar cycle 13, N decreases to values 0 and 1 in 1899 and 1900.

Thus the upward trend in our data apparently is provided by input of auroras registered by stations at latitudes $\varphi_M > 56^{\circ}$ (geographical $\varphi > 59^{\circ}$).

22-YEAR CYCLE

In this paragraph we consider behavior of some features of auroral activity in odd- and even-numbered solar cycles. Different polarity of sunspots in odd and even solar cycles determines 22-year

periodicity. The Gnevyshev-Ohl rule is an empirical rule according to which the sum of sunspot numbers over an odd-numbered cycle exceeds that of the preceding even-numbered cycle [Gnevishev and Ohl, 1848].

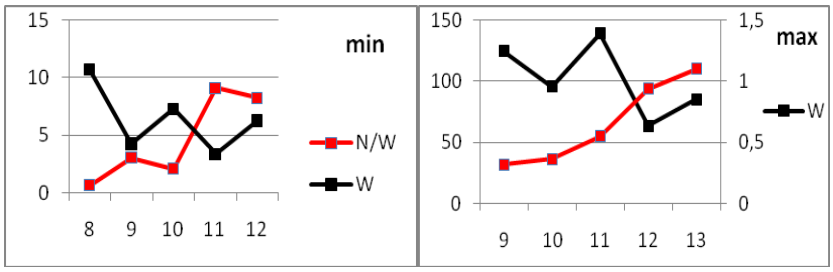

Fig, 5. Number of auroral occurrence normalized by W (N/W) at solar minima (left) and maxima within 8-13 solar cycles.

In Fig. 5 we show number of auroral occurrence normalized by W (N/W as well as sunspot numbers W at solar minima and maxima within 8-13 solar cycles. Minima are numbered by a previous solar cycle number. We see that the maximal sunspot numbers W in the odd cycles are higher than in the preceding even cycles (Fig. 5, right) and *vice versa* for W in minima of solar activity (Fig. 5, left). Polar aurora occurrence N/W follows the Gnevyshev-Ohl rule in minima of solar cycles showing 22-year variation. Maximal values of auroral N show the upward trend.

Possibly another indications of the 22-year periodicity we can find in unusual solar cycle behavior of auroras in St. Petersburg (Fig. 4). Polar activity in odd cycles 11 and 13 demonstrate clear correlation with solar activity with classical two peaks: one close to solar maxima and another one after 2-3 years on declining phases. However in odd cycles 10 and 12 clear dependence of N from W breaks: the auroral curve does not show clear maximum around solar maximum, it rather goes in antiphase.

Thus the 22-year variation is traced also in St. Petersburg number of aurora occurrence.

SUMMARY OF RESULTS AND CONCLUSION

We have compiled a catalogue of aurora borealis registered in 1837 -1900 by the Russian network of meteorological and geomagnetic observatories. Our database combines mid and high latitude auroras observed by the Russian network of meteorological observatories. The catalogue comprises 2170 auroral events registered by 128 stations located in a wide geographical zone (geographical latitude φ from 39 °57′N till 72°30′N). Analysis of trends and cyclic variations among aurora borealis shows the following:

- The feature which was not recognized in previous works is an upward trend of auroral activity since the first part of 19th c. This trend is supported by moderate but stable trend in the geomagnetic activity index CP9. Our data on aurora occurence show different behavior in mid- and high- latitude segments. Auroras in the mid-latitude segment (geomagnetic latitudes φ_m <56º) does not show the upward trend, instead they show decline toward the end of the 19th c. The high latitude segment of our data (geomagnetic latitudes $\varphi_m \geq 56º$) demonstrates the upward trend over the century. The longest data series of aurora borealis observed in observatory St. Petersburg (φ_m =56º14′) also show this upward trend. The 11-year variations are superimposed on this trend, and a minimum in vicinity of 1900 is also traced.

- Annual frequency of aurora occurrence show appearance of 11-year solar cycle which is in general agreement with results found by other authors. **A**urora occurrence N in the mid-latitude segment show clear 11-year variations which are in correlation with solar and geomagnetic activity. The most pronounced peaks are closely related to solar maxima. These peaks in N are believed to be generated by transient coronal mass ejections related to closed magnetic fields in the Sun [Vázquez et al., 2041]. The peak in a declining solar activity phase is less pronounced in the mid-latitude segment. Aurora occurrence N in the high-latitude segment also show 11-year variations. However, this variation is not so clearly seen, because here the first aurora peaks at solar maxima are more or less absent. The aurora maxima at declining phase of solar cycles are dominant ones in this case. This peak is produced by corotating solar wind streams that are generated from coronal holes that are characterized by open magnetic fields[Tsurutani et al., 2006; Vázquez et al., 2014].

- Some characteristics of aurora show 22-year variation.

We interpret that the continuing increase of aurora numbers at high magnetic latitudes during 19 c., starting from 1837, is associated with the long-term increase of solar open magnetic [Echer et al., 2004]. This increase has been suggested recently by Echer et al., 2004] and has been obtained by using aa index, i.e. traced from 1868. Our results could testify that dominant increase of open solar MF started earlier than in 1868.

REFERENCES

Angot A. (1896), T*he Aurora Borealis.* London: K. Paul, Trench, Trubner, 318 pp.

Gnevishev M.N., Ohl A.I., (1948), About 22-year cycle of solar activity. *Astronomical Journal*. V.25, 18-20 (in Russian).

Feynman J. and Silverman S.M. (1980), Auroral changes during the 18th and 19th centuries and their implications for the solar wind and the long term variation of sunspot activity, *J. Geophys* Res. V. 85. P. 2991–2997.

Echer E., W. D. Gonzalez, A. L. C. Gonzalez, A. Prestes, L. E. A. Vieira, A. dal Lago, F. L Guarnieri., and N. J. Schuch, Long-term correlation between solar and geomagnetic activity. *J. Atmos. Sol. Terr. Ph*ys. V. 66, P. 1019–1025. 2004.

Křivský L., K. Pejml, (1985), Solar Activity, Aurorae and Climate in Central Europe in the last 1000 Years. *Travaux de l`Institut Geophysique de l`Academie Tchecoslovaque Des sciences, Publications of the Astronomical Institute of the Czechoslovak Academy of Sciences* V. 33. No. 606. P. 77-151.

N. G. Ptitsyna, M. I. Tyasto, and B. A. Khrapov. Secular variations in the Geomagnetic field in St Petersburg and in adjacent area from historic data, 1630-1930. *Geomagnetism and Aeronomy*, 53, 5, 642-649, 2013.

Silverman S.M. (1992), Secular variation of the aurora for the past 500 years, *Rev. of Geophys.* V. 30. Issue 4. P. 333–351. 1992.

Stamper, R., M. Lockwood, M. N. Wild, and T. D. G. Clark, (1999), Solar causes of the long-term increase in geomagnetic activity, *J. Geophys. Res.*, V. 104, 28325–28342.

Tsurutani *B.T., González W.D., Gonzalez A.L.C. et al*. (2006), Corotating solar wind streams and recurrent geomagnetic activity: A review, *J. Geophys. Res.* 111 A07S01. doi:10.1029/2005JA011273

Vázquez M., J.M. Vaquero and M. C. Gallego, (2014), Long-term Spatial and Temporal Variations of Aurora Borealis Events in the Period 1700–1905, *Solar Physics*. V. 289. Issue 5. P. 1843-1861.

Zosimovich I. D. (1981), *Geomagnetic Activity and Stability of the Solar Corpuscular Fi*eld, Nauka, Moscow, 191 pp. [in Russian].

.

CORRELATION ANALYSIS OF SIMULTANEOUS SOLAR WIND AND MAGNETOSHEATH MEASUREMENTS AT DIFFERENT LOCATIONS OF NEAR-EARTH SPACE

Rakhmanova L.[1], Riazantseva M.[1,2], Zastenker G.[1]

[1]Space Research Institute of RAS, Moscow, 117997, 84/32 Profsoyuznaya Str, Russia, e-mail: rakhlud@gmail.com; [2]Skobeltsyn Institute of Nuclear Physics, Lomonosov Moscow State University, Moscow, Russia

Abstract. Magnetosheath modifies solar wind structures during their propagating to the magnetopause. The report is devoted to study of the modification of solar wind plasma and magnetic structures in magnetosheath using correlation analysis of simultaneous measurements in solar wind and magnetosheath. We analyze more than 300 hours of data both in the subsolar region and flank. We use magnetosheath data measured behind bow shock of different geometry (quasiparallel and quasiperpendicular). We find out that though magnetosheath variations with durations exceeding 100 s have solar wind origin predominantly, they may be created also at the bow shock and inside the magnetosheath. We consider dependencies of correlation level on different factors such as: the angle between bow shock normal and interplanetary magnetic field vector, Alfven's Mach number, relative standard deviation in SW and MSH and its ratios, solar wind density and velocity and interplanetary magnetic field magnitude.

Introduction

The interaction of supersonic solar wind (SW) flow with the Earth's magnetosphere results in formation of the bow shock (BS) in front of the magnetopause (MP). The region between BS and MP called magnetosheath (MSH) differs from undisturbed SW. At the BS plasma decelerates, heats, compresses and changes the flow direction. All plasma and magnetic field parameters inside the MSH vary in a wide frequency range, and these variations level is much higher than in the SW.

Number of papers describes MSH fluctuations. *Zastenker et al. [2002]* have suggested that sometimes MSH fluctuations originate in the SW and propagate through the BS, but in the most cases they are produced inside the MSH. *Shevyrev et al., [2003]* have showed that ion flux and magnetic field (MF) magnitude fluctuations profiles are similar both at the dusk and dawn MSH flanks and for high and low frequency ranges. High-frequency fluctuations level is strongly influenced by BS and interplanetary magnetic field (IMF) mutual direction which is characterized by θ_{BN} angle. The amplitude of high-frequency fluctuations behind quasiparallel ($\theta_{BN}<45°$) bow shock is two times larger than behind quasiperpendicular ($\theta_{BN}>45°$) one (*Shevyrev and Zastenker, [2005]*). *Nemecek et al., [2001]* have showed that MSH fluctuation level is higher for fast SW flow versus slow SW flow.

Number of papers is devoted to the interplanetary (IP) shock propagation through the BS and MSH. *Koval et al., [2006]* and *Safrankova et al., [2007]* have showed that IP shock decelerates in the MSH. Moreover, the interaction between BS and IP shock creates several discontinuities of different types that also move through the MSH and affect additionally on the magnetopause.

Other abrupt changes of SW dynamic pressure or ion flux (*Riazantseva et al., [2005, 2007]*) have significant influence on magnetosphere too. *Rakhmanova et al. [2012]* have showed that amplitude and duration of abrupt (by 20% of amplitude or larger during several seconds) changes of ion density and MF magnitude are usually increased in the MSH versus SW.

Thus, interaction between SW structures and BS results in structures' modification. These are the MSH parameters and structures that affect on the magnetopause and magnetosphere. It is important to understand how BS and MSH change SW parameters. Present paper is dedicated to the study of SW plasma and magnetic structures modification during interaction with BS and propagation through the MSH. We use correlation analysis of simultaneous SW and MSH measurements to compare structures in these two regions. We consider the dependencies of correlation level on different parameters and SW conditions to find parameters that have influence on SW structure modification in the MSH.

Methods

For the study we use THEMIS mission (*Angelopoulos, [2008]; Sibeck and Angelopoulos, [2008]*) data during period 1.V.-1.X.2008. During this period spacecraft orbits configuration allows us to find intervals

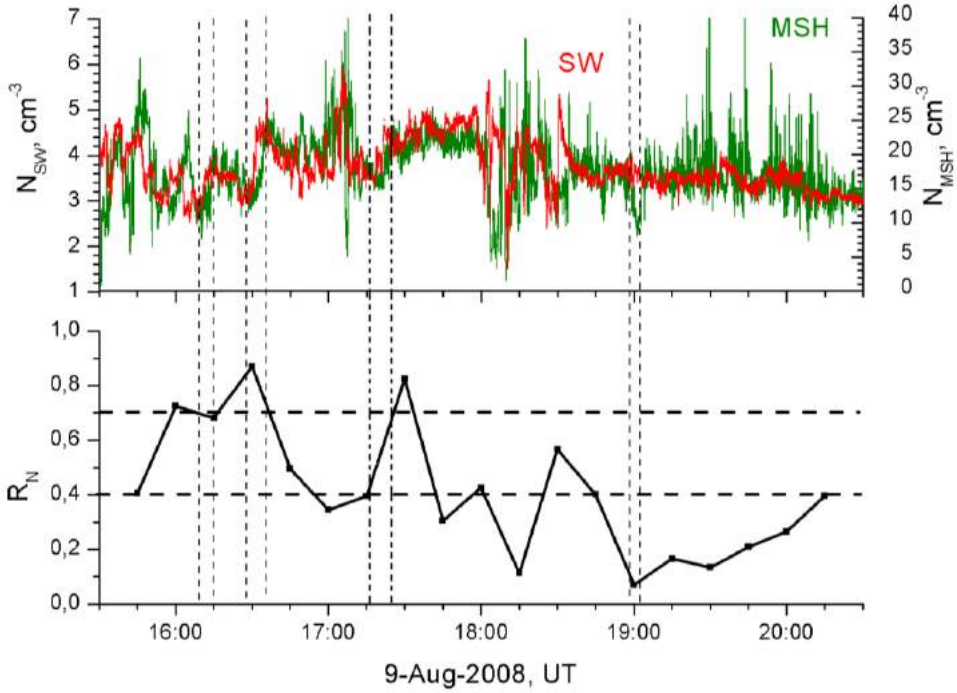

Figure 1. top panel - THEMIS-C (red line) and THEMIS-E (green line) ion density measurements during 15:30-20:30 UT August 9, 2008; bottom panel – correlation coefficient, calculated on 30-min intervals of ion density data.

when one spacecraft is located in the SW and another one is scanning the MSH. We select intervals with durations exceeding 3 hours for the further analysis. We use 3-sec ion number density and MF magnitude measurements. The distance between spacecraft pair usually does not exceed 30 R_E. The example of the interval is presented at figure 1. Top panel shows density measurements in SW (red line, THEMIS-C) and MSH (green line, THEMIS-E) during 5 hours on the August 9, 2008. A lot of plasma structures are observed in SW during this interval. Some of these SW structures are repeated in the MSH.

Firstly we calculate correlation coefficient between SW and MSH parameters on each of the obtained data intervals. Correlation coefficient is calculated for different time lags between SW and MSH measurements. Time lag of maximum correlation value corresponds to the time of plasma propagation between two spacecraft. For the interval presented at Fig.1 correlation coefficient is equal to 0.48 for 135-s lagged SW data. Correlation coefficient is quite low for the whole interval as sometimes SW structures are repeated in the MSH (e.g. at ~16:10, 16:30, 17:20) but sometimes they don't. Sometimes we observe structure in the MSH that does not originate in the SW (e.g. at ~19:00).

We define structure as density/MF magnitude increase or decrease at least by the 20%. Examples of structures are marked at the figure 1 by vertical dashed lines. The main objects of the study are structures of small and middle scales with durations from tens of seconds to several minutes. Therefore we divide continuous intervals into 30-min intervals, overlapped by 15 minutes. We calculate correlation coefficient on each 30-min interval as a function of time lag and obtain time of structures propagation more precisely. Hereafter we use the maximum value of correlation coefficients that correspond to the time of structure propagation. Time evolution of correlation coefficient calculated on 30-min intervals for presented example is shown at bottom panel of figure 1.

We call cases when correlation coefficient is lower than 0.4 the "absence of correlation", whereas the cases when correlation coefficient is higher than 0.7 we call "high correlation" cases. Correlation coefficients from 0.4 to 0.7 we call "sufficient correlation". One can see that correlation level strongly varies during the interval presented at figure 1. When we observe SW structure repetition in the MSH at the 30-min interval, correlation coefficient (related with the center of this interval) is usually high or sufficient (e.g. at 16:15, 16:30, 17:30). When we do not see SW structure in the MSH or observe MSH structure that does not originate in the SW, correlation is absent (e.g. at 19:00). Moreover correlation can disappear in 15 minutes (e.g. at 17:30-17:45) and then appear again. We try to find out reasons of such abrupt changes of correlation level on statistical study.

We have obtained 1360 30-min intervals. The distributions of these intervals by the value of density correlation coefficient, R_N, and MF magnitude correlation coefficient, R_B, are shown by green bars at the top

and bottom panels of figure 2 respectively. Correlation coefficients change in wide range – from -0.5 to 1 - with the maximum at 0.3-0.4 for density and 0.2-0.3 for MF magnitude.

At the previous studies (i.e. *Rakhmanova et al., [2013]*) we have suggested that fluctuations with frequencies exceeding 0.01-0.02 are created mainly at the BS and inside the MSH. Thus for the further study we used data, smoothed at 100-sec subintervals. Smoothing (running averaging) suppresses high-frequency fluctuations and decreases their influence on correlation level. Red bars at the figure 2 show distributions of correlation coefficients, calculated on smoothed data. One can see that smoothing leads to significant correlation increase: the maximum of distribution replaces to 0.6-0.7 both for density and MF magnitude

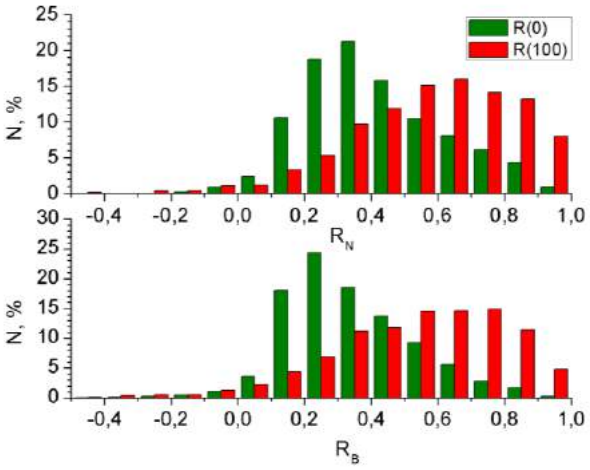

Figure 2. Distributions of 30-min intervals by the value of density correlation coefficient (top panel) and MF magnitude correlation coefficient (bottom panel) for non-smoothed data (green bars) and for 100-sec smoothed data (red bars).

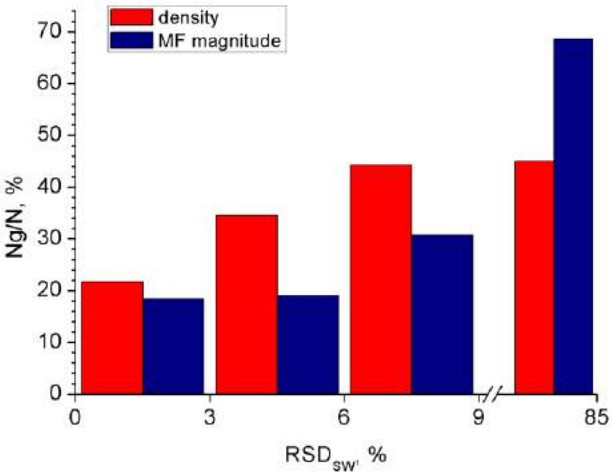

Figure 3. Dependence of relative number of intervals with high correlation on RSD value calculated in the SW for ion density (red bars) and MF magnitude (blue bars).

correlation coefficients. Nevertheless even for smoothed data at 28% (for density) and at 21% (for MF magnitude) of cases correlation is absent (R<0.4).

To find out the way of structures modification in the MSH, we consider the dependencies of relative number of intervals with high correlation – N_g/N – on the set of parameters. N_g is the number of intervals with high correlation value in some parameter's range, N is the full number of intervals in the same range. Firstly we consider the dependence on *RSD* value that is determined as a relative standard deviation of the 100-sec smoothed SW data calculated on 30-min intervals. *RSD* characterizes the variations value on each 30-min interval. As we use 100-sec smoothed data, these variations are mainly plasma or magnetic structures. The dependence of N_g/N on SW *RSD* value is shown at figure 3. In case of density correlation we consider the dependence on density *RSD* value, in case of MF magnitude correlation we consider the dependence on MF magnitude *RSD* value. Red bars represent the dependence for ion density; blue bars represent the dependence for MF magnitude. Events with *RSD*>9% are merged into one bin to enlarge statistics. Clear dependence is observed: number of intervals with high correlation increases with *RSD* value. Thus, we observe better correlation when SW structures are observed during the 30-min interval.

For the further study we exclude intervals with *RSD*<10% from our statistics to avoid intervals of undisturbed SW. The dependencies of N_g/N on the number of parameters are presented at the figure 4.

Figure 4a shows the dependence of correlation level on SW ion density. One can see that high correlation level is usually observed during higher values of SW density. This dependence is true both for density and MF magnitude correlations. Figure 4b shows the dependence of N_g/N on IMF magnitude. Both density and MF magnitude correlation increase with IMF magnitude. Thus high density and MF magnitude correlation level is usually observed for higher values of SW density and IMF magnitude.

The dependence of correlation value on SW bulk velocity is presented at the figure 4c. MF magnitude correlation does not depend on the SW velocity. SW and MSH densities correlate better for intermediate values of velocity: for slow (V<400km/s) and fast (V>550km/s) solar wind flow high correlation value is observed in 40% of cases, whereas for intermediate velocity values N_g/N equals to 60%. At earlier studies (e.g. at *Nemecek et al., [2001]*) authors have showed that MSH fluctuation level increase with SW velocity value, therefore correlation level should decrease. We do not see this effect. That may be caused by

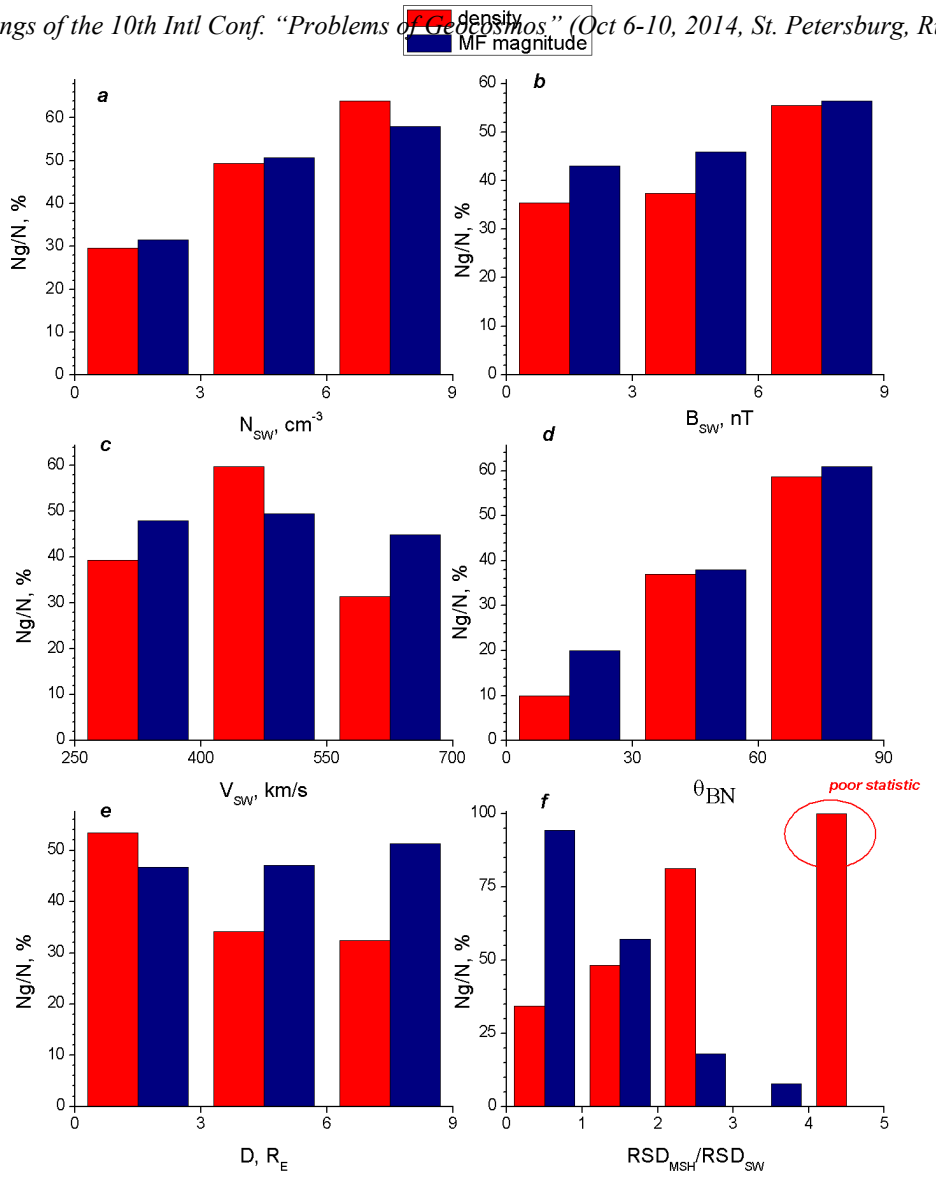

Figure 4. Dependence of relative number of intervals with high correlation value - N_g/N – on (a) SW ion density, (b) IMF magnitude, (c) SW bulk velocity, (d) θ_{BN} angle (e) distance between MSH spacecraft and magnetopause, (e) ratio of MSH *RSD* to the SW *RSD* value.

suppression of high-frequency fluctuations by smoothing. However we can conclude that plasma structures are less modified during intermediate (400-550 km/s) values of SW velocity. Magnetic structures' modification does not depend on SW velocity.

Figure 4d shows the dependence of N_g/N on θ_{BN} angle. We use the angle between bow shock normal and IMF direction, calculated at the point, where plasma enters the MSH. We find this point using streamlines from the MSH model by Spreiter et al., [1966] scaled to the mean upstream dynamic pressure taken from ACE (*Shevyrev and Zastenker, [2005]*). Significant increase of N_g/N for both density and MF magnitude is observed. In the previous studies (e.g. *Rakhmanova et al., [2013]*) we have not seen this dependence because of limited statistics for low θ_{BN} angles. We have not excluded intervals with undisturbed SW also. Thus, structures are less modified during quasiperpendicular bow shock. However even for θ_{BN} angles near 90° high correlation level is observed only at 60% of cases.

Number of studies suggests that magnetopause processes are the one of the source of MSH fluctuations (i.e. *Gutynska et al., [2012]*). One expects correlation level decrease observing MSH near the magnetopause. The dependence of number of intervals with high correlation value on the distance between spacecraft scanning the MSH and the magnetopause – *D* - is shown at figure 4e. The distance is calculated using *Shue et al., [1997]* model. MF magnitude correlation does not depend on the distance to magnetopause. Number of intervals with high density correlation decreases from 53% for spacecraft located near the magnetopause to 32% for its location near the bow shock. Thus we do not see the decrease of correlation at the magnetopause vicinity, as it may be expected from previous studies. On the contrary, we see the increasing of correlation near the magnetopause versus bow shock. This fact may be caused by data smoothing on 100 s subintervals that suppresses high-frequency fluctuations created at the BS and by the

magnetopause processes. However this result requires more accurate analysis. Nevertheless plasma structures are less modified near the magnetopause than near the bow shock. Magnetic structures' modification does not depend on MSH spacecraft position.

At last figure 4f presents the dependence of N_g/N on the ratio of *RSD* value calculated in MSH to the one calculated in the SW. We calculate *RSD* in the MSH taking into account time lag between SW and MSH data. Also we use 100-sec smoothed data for the *RSD* calculations. Thus the ratio $RSD_{MSH}/RSD_{SW}>1$ means that variations with time scales exceeding ~100 s are created or amplifying during plasma propagation between spacecraft The ratio value characterizes the relation between low-frequency variations amplitude in SW and MSH. Number of intervals with high MF magnitude correlation decreases with increase of the ratio. On the opposite number of intervals with high density correlation seems to increase with the ratio. Last bin for density N_g/N contains poor statistics. However this is our first result and it needs further study to make accurate conclusion.

Relation between density and magnetic field correlation

At this section we consider the dependence of density correlation coefficient on MF correlation coefficient, calculated on the same 30-min interval on 100-sec smoothed data. The dependence is shown at the figure 5. One can see that even when we smooth data we obtain high density and MF magnitude correlation values only at 18% of cases. At 31% of cases one of the parameters has high correlation value whereas another one has not. At 8% of cases neither density nor MF magnitude correlation do not exceed 0.4.

We consider separately the same dependence for intervals with *RSD*>10%. The dependence is shown at the figure 5 by red points. The dependence's character is similar to the one without sorting by *RSD* values.

Thus, high correlation of density does not guarantee high value of MF magnitude correlation and vice versa. Usually one expects density and MF magnitude change corresponding to each other. Our result shows

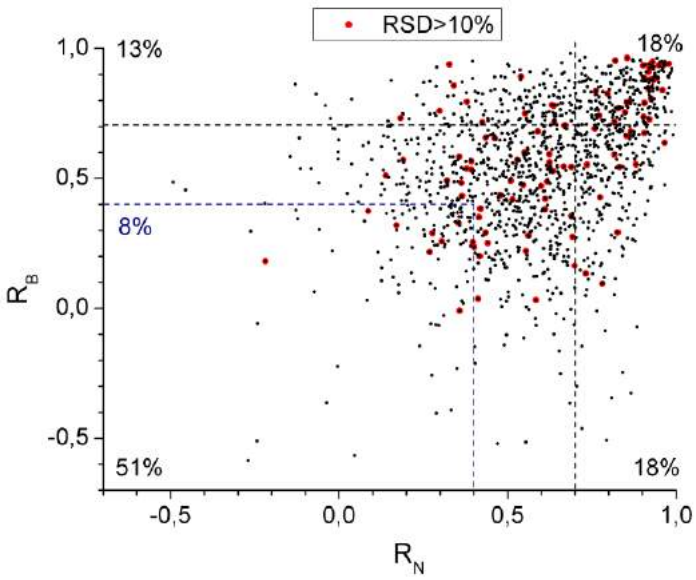

Figure 5. Dependence of density correlation coefficient on MF correlation coefficient, calculated on the same 30-min interval on 100-sec smoothed data. Colored points represent intervals with RSD>10%.

that really situation is much more complicated. During BS crossing and propagation trough the MSH plasma and magnetic field may change inconsistently. This fact should be taking in the account in MSH modeling.

Conclusions

At the present study we make correlation analysis of large set of THEMIS measurements in the SW and MSH during 6 months of 2008 year. We suggest the follows:

Both ion density and MF magnitude correlation coefficient calculated on 30-min intervals of 100-sec smoothed data equals 0.6-0.7 in average. However correlation value varies in a wide range though we suppress high-frequency fluctuations producing by BS and MSH. Only at 18% of cases both density and MF magnitude correlations are high (more than 0.7) whereas at 8% of cases correlation is absent.

High correlation value of plasma parameters does not guarantee high correlation value of magnetic field parameters on the same interval and vice versa. Thus, plasma and magnetic field may change

inconsistently during transfer through the BS and MSH. This fact should be taken into account for MSH modeling.

SW structures are less modified in MSH during quasiperpendicular bow shock and during higher values of SW density and IMF magnitude. Plasma structures are less modified during SW velocity values from 400 to 550 km/s and when the spacecraft in MSH is farther from the bow shock ; magnetic structures' modification does not depend on these parameters.

Thus, presented statistical study shows the main parameters that have influence on solar wind structures' modification at the bow shock and inside the MSH. The results should be used for developing of solar wind-magnetosphere interaction models.

Acknowledgements

The present work was supported by Grants RFBR 12-05-00984-a, 13-02-00819-a and program P-22 of Russian Academy of Science.

References

Angelopoulos V. (2008), The THEMIS Mission, *Space Sci. Rev*., 141, 5–34, doi: 10.1007/s11214-008-9336-1.

Gutynska O., J. Simunek, J. Safrankova, Z. Nemecek, and L. Prech (2012), Multipoint study of magnetosheathmagnetic field fluctuations and their relation to the foreshock, *J. Geophys. Res*., 117, A04214.

Koval A, J. Safrankova, Z. Nemecek and L. Prech (2006), Propagation of interplanetary shocks through the solar wind and magnetosheath*, Adv.Space Res*., 38, 552-558.

Nemecek Z., J. Safrankova, P. Pisoft, and G.N. Zastenker (2001), Statistical Study of ion flux fluctuations in the Magnetosheath, *Czech. J. of Phys.*, 51, 853-862.

Rakhmanova L.S., M.O. Riazantseva, and G.N. Zastenker (2012), Dynamics of the small-scale solar wind structures with sharp boundaries under transfer from the solar wind to magnetosheath, *in WDS'12 Proceedings of Contributed Papers: Part II – Physics of Plasmas and Ionized Media (eds. J. Safrankova and J. Pavlu), Prague, Matfyzpress*, 176–181.

Rakhmanova L., M. Riazantseva, and G. Zastenker (2013), Small- and Middle-scale Solar Wind Structures, Transferring from Solar Wind to the Magnetosheath: Correlation Analysis, *in WDS'13 Proceedings of Contributed Papers: Part II – Physics of Plasmas and Ionized Media (eds. J. Safrankova and J. Pavlu), Prague, Matfyzpress,* 30–36.

Riazantseva, M., G. N. Zastenker, J. D. Richardson, and P. Eiges (2005), Sharp boundaries of small- and middle-scale solar wind structures, *J. Geophys. Res.*, 110, A12110, doi:10.1029/2005JA011307.

Riazantseva M.O., O.V. Khabarova, G.N. Zastenker, and J.D. Richardson (2007), Sharp boundaries of the solar wind plasma structures and their relationship to the solar wind turbulence, Adv. Space Res., V.40, PP.1802-1806.

Safrankova J., Z. Nemecek, L. Prech, A.A. Samsonov, A. Koval and K. Andreeova (2007), Modification of interplanetary shock near the bow shock and through the magnetosheath, *J. Geophys. Res,* 112, A08212.

Shevyrev N., G.N. Zastenker, M.N. Nozdrachev et al. (2003), High and low frequency large amplitude variations of plasma and magnetic field in the magnetosheath: radial profile and some features, *Adv. Space Res*., 31, 1389-1394.

Shevyrev N., and G. Zastenker (2005), Some features of plasma flow in the magnetosheath behind the quasi-parallel and quasi-perpendicular bow shocks*, Planet. Space Sci.,* 53, 95-102.

Shue J.-H., J.K. Chao, H.C. Fu, K.K. Khurana, C.T. Russel, H.J. Singer, and P. Song (1997), A new functional form to study solar wind control of the magnetopause size and shape, *J. Geophys. Res.,* 102, 9497-9511, doi: 10.1029/97JA00196.

Sibeck D.G., and V. Angelopoulos (2008), THEMIS science objectives and mission phases, *Space Sci. Rev.*, 141, 35–59, doi: 10.1007/s11214-008-9393-5.

Zastenker G., M.N. Nozdrachev, Z. Nemecek et al. (2002), Multispacecraft measurements of plasma and magnetic field variations in the magnetosheath: Comparison with Spreiter models and motion of the structures, *Planet. Space Sci.*, 50, 601-612.

SOUTHERN BOUNDARY OF THE ULTRARELATIVISTIC ELECTRON PRECIPITATIONS (FOR SEVERAL CASES IN 1982-1987 YEARS)

G.F. Remenets, A.M. Astafiev

St. Petersburg University, St. Petersburg, 198504, Russia, e-mail: g.remenets@spbu.ru

Abstract. An inverse problem was solved for VLF wave propagation on the base of monitoring of the radio navigation signals for two radio paths: one was purely auroral, another was partly auroral, and both had a mutual point of receiving of the signals. The southern boundaries of the ultrarelativistic electron precipitations were determined for several dates: on September 15, 1982; on December 3, 1982; on April 16, 1984; on April 23, 1986, and on May 13, 1987.

To the memory of Michail Ivanovich Beloglazv

The phenomenon of ultrarelativistic electron precipitation into the polar atmosphere from the near-Earth space was analyzed earlier [1-3]. The analysis was based on the very low frequency (VLF) data in the cases of abnormal disturbances for two radio paths: a shorter $\boldsymbol{S_1}$ one (Aldra (in Norway) - Apatity) and a longer $\boldsymbol{S_2}$ one (Ragby (in England) - Apatity) with the common receiving point in Apatity (Russia), see Figure 1. The experimental data were obtained in the Polar Geophysics Institute of RAS by M. I. Beloglazov [1, 2].

Figure 1. Two radio paths with the common receiving point: $\mathbf{S_1}$ - Aldra -Apatity; $\mathbf{S_2}$ - Ragby -Apatity.

According to the analysis of the $\boldsymbol{S_1}$ radio path [1, 2], the energy of precipitating electrons was such (about 100 MeV) that they could generate X-rays during deceleration, which was capable to create a sporadic D_S-layer of electric conductivity at the altitudes 10-40 km. The effective height h of radio wave reflection was changing during a disturbance at day time from the undisturbed value $h \approx 60$ km to $h \approx 30$ km in the maximum of powerful disturbance.

The same VLF data together with the VLF data for the longer radio path S_2 can be used for the estimation of latitude of the southern boundary of an abnormal disturbance. This report is devoted to the determination of the conductivity parameters and southern boundaries of the disturbances for the following dates: on September 15, 1982; on December 3, 1982; on April 16, 1984; on April 23, 1986, and on May 13, 1987.

The VLF data in the cases of abnormal disturbances are characterized by strong changes of the amplitudes and the phases, their variations being approximately similar; see Figure 2 for the case on December 3, 1982 [1, 2]. The amplitude data on left part of the figure are given in the dimensionless units and normalized to values at the starting time (10:00 UT). The initial values of the phases (on the right part of the figure) do not have any physics sense. The signals represented on this Figure with frequencies (10.2, 12.1 and 13.6 kHz) had been obtained for the shorter radio path, its length being equal to 885 km. This path is completely auroral. The 4-th signal (16 kHz) came to Apatity from the UK (GBR station) along the radio path with its length equal to 2497 km. Only northern part of this path goes through the auroral region. The intensity of this abnormal disturbance for the shorter radio path was not weaker than for a disturbance caused by the proton precipitations [4, 5], but the variations were qualitatively different due to the abnormal attenuation of the ray with two reflections from a sporadic layer above.

The qualitative similarity of the signal variations for $\boldsymbol{S_1}$ and $\boldsymbol{S_2}$ radio paths indicates the same physical cause of the disturbances of the both paths.

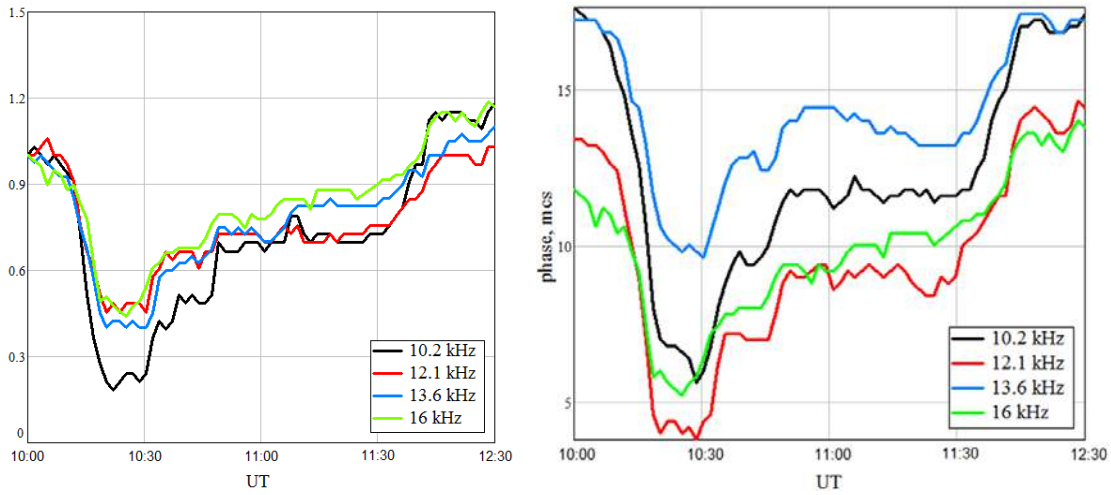

Figure. 2. The amplitude (left) and phase (right) experimental data on December 3, 1982 for both radio paths (strong VLF disturbance under conditions of polar night).

The represented problem was solved in two steps. **First stage:** solution of the VLF inverse problem of first kind by the self-consistent method [6, 2] using the data for the auroral radio path $\boldsymbol{S_1}$. In frames of this VLF inverse problem we found the reflection coefficient $R(t)$ of the first ray from the ionized middle atmosphere and the effective height $h(t)$ of the radio path, the near Earth waveguide being considered homogeneous at every moment of the disturbance. Such kind results for the event on December 3, 1982 are presented on Figure 4. They were obtained by the self-consistent VLF method, in which a diffraction ray W_0 (Watson-Fock wave) and two rays reflecting from the ionized middle atmosphere were used (W_1, W_2) [7], see Figure 3.

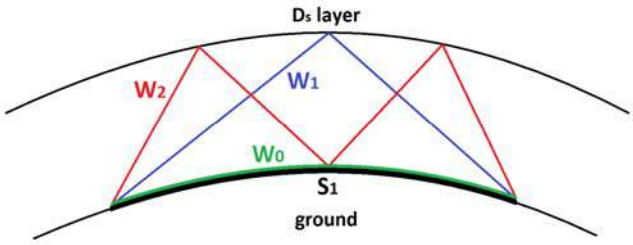

Figure 3. A scheme of 3 mode approximation in a regular spherical waveguide.

In Figure 4, the variations of the effective height $h(t)$ (red curve) and reflection coefficient modular $R(t)$ (blue curve) as functions of time for $\boldsymbol{S_1}$ radio path are represented. The first part of the disturbance (the dot curves) was obtained using the positive direction of time and determination of the initial values $h(t_0)$ and $R(t_0)$, for t_0 = 10:00 UT. The second part (a restoring one) of the disturbance (solid curves) was obtained using the negative direction of time and determination of initial values for analysis $h(t_0)$ and $R(t_0)$, where $t_0 = t_m$ = 12:30 UT is the final time t_m of the disturbance.

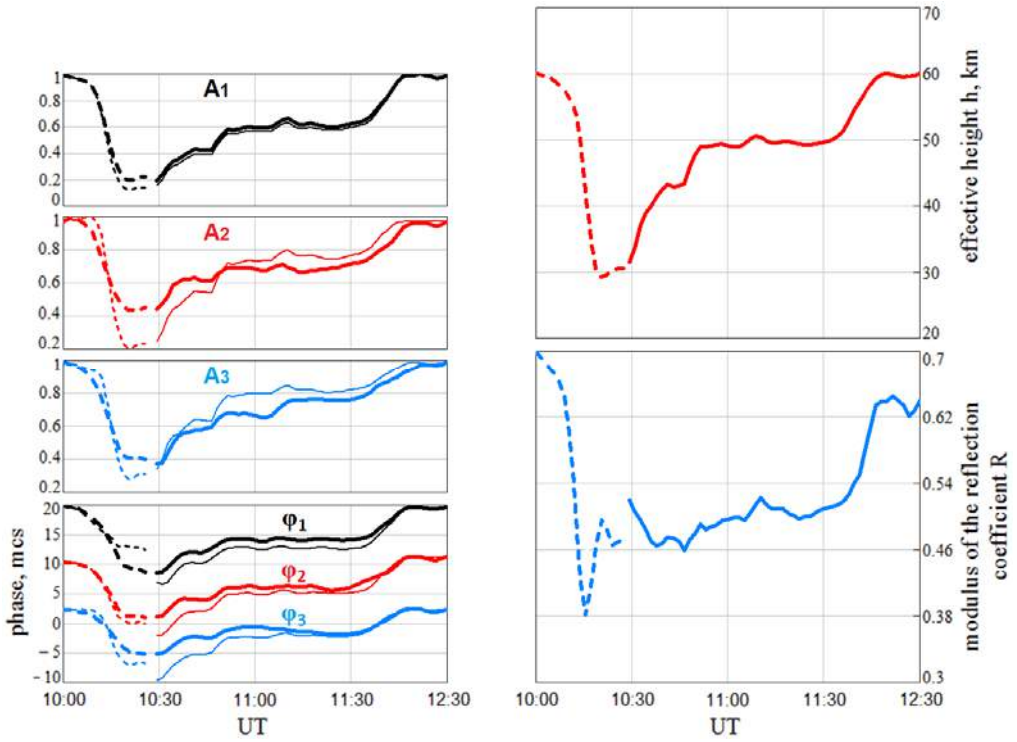

Figure 4. **Left:** Comparison of the curves calculated (light curves) against the experimental data (solid curves) for 3 amplitudes and 3 phases according to the solution of inverse VLF problem of 1-st kind by self-consistent method. **Right:** Effective height of near ground waveguide *h* (red curve) and the model of reflection coefficient *R* (blue curve) from the atmosphere ionized layer (for the first ray).

Second Stage (VLF inverse problem of 2-nd kind). The second kind of the problem is formulated for an inhomogeneous radio path consisting of 3 homogeneous parts: (i) a middle latitude part of the path, having its length equal to $S_2 - D_{avr}$, with a VLF source at the southern terminal of the path, (ii) an auroral undisturbed part of the path, having its length equal to $D_{avr} - D$ and (iii) a disturbed northern part of the radio path with its length D, all lengths being counted from the Apatity receiver. A place of the boundary between (i) and (ii) parts (D_{avr}) was taken at 62°13'N latitude. A value of distance D of the boundary between (ii) and (iii) parts is a clue object of this work and is calculated below.

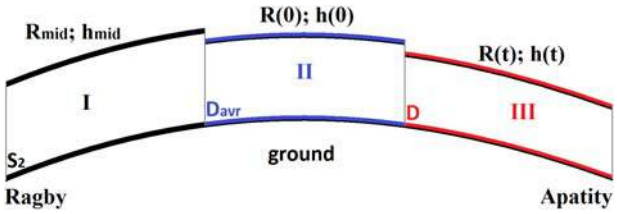

Figure 5. A scheme of irregular spherical waveguide with length S_2 consisting of 3 regular parts: (i) - is a middle latitude part $S_2 - D_{avr}$ which was modeled with the help of the middle latitude ionosphere R_{mid} and h_{mid}; (ii) - is an auroral undisturbed part $D_{avr} - D$ which was modeled with the help of the initial values *R(0)* and *h(0)* of the *R(t)* and *h(t)*; (iii) - is a disturbed northern part which was modeled with the help of the *R(t), h(t)* defined form the VLF problem of first kind.

The discrepancy functions $G_{00}(D)$ and $G_0(D)$ of the distance parameter D, which is the distance between the receiver and the southern boundary of ultrarelativistic electron precipitation (UREP), were postulated as follows:

$$G_0(D) = \sum_{n=1}^{n=m} \frac{[\tilde{E}(t_n) - E_{calc}(t_n)]^2}{\tilde{E}(t_0)^2},$$

$$G_{00}(D) = \sum_{n=1}^{n=m} \frac{[\tilde{E}(t_n) - E_{calc}(t_n)]^2}{\tilde{E}(t_0)^2} + G_0(D)$$

,

where φ and E with "~" are experimental values of amplitudes and phases of the signal with frequency f_4 = 16 kHz (long radio path). E_{calc} and φ_{calc} are the amplitudes and the phases calculated for a moment of disturbance t_n and a fixed distance D:

$$E_{calc}(t_n, D) = E * \exp\left[-\frac{Im(v) * (S_2 - D_{aur})}{R}\right] * \exp\left[-\frac{Im(v_{aur}) * (D_{aur} - D)}{R}\right] * \exp\left[-\frac{Im(v_{dist}(t_n)) * D}{R}\right],$$

$$\varphi_{calc}(t_n, D) = \left[\frac{Re(v) * (S_2 - D_{aur})}{R}\right] + \left[\frac{Re(v_{aur}) * (D_{aur} - D)}{R}\right] + \left[\frac{Re(v_{dist}(t_n)) * D}{R}\right],$$

were v - is an eigenvalue with zero number for a model of undisturbed middle latitude wave-guide; v_{avr} - is analogous one for an undisturbed part of auroral wave-guide; v_{dist} - is an eigenvalue for a disturbed part of the wave-guide at the moment of the disturbance; R = 6370 km -is the Earth radius. The v_{avr} and v_{dist} eigenvalues were calculated according to the generalized Schumann's method [8].

The minimums of the discrepancy functions indicate the positions of the southern boundaries of the UR electron precipitations, as the parameter D being a distance between the receiver and a boundary (Figure 6 and Table 1). Five numbers of the curves correspond to 5 dates. The boundaries of the perturbations in columns 2 and 4 in Table 1 were obtained by minimizing the discrepancy – functions $G_{00}(D)$ and $G_0(D)$ (columns 3 and 5 - the same boundaries converted to degrees north latitude). The uncertainty intervals ΔD (given in brackets) were selected as 10% deviations from the minimum discrepancy – functions $G_{00}(D)$ and $G_0(D)$ for each date.

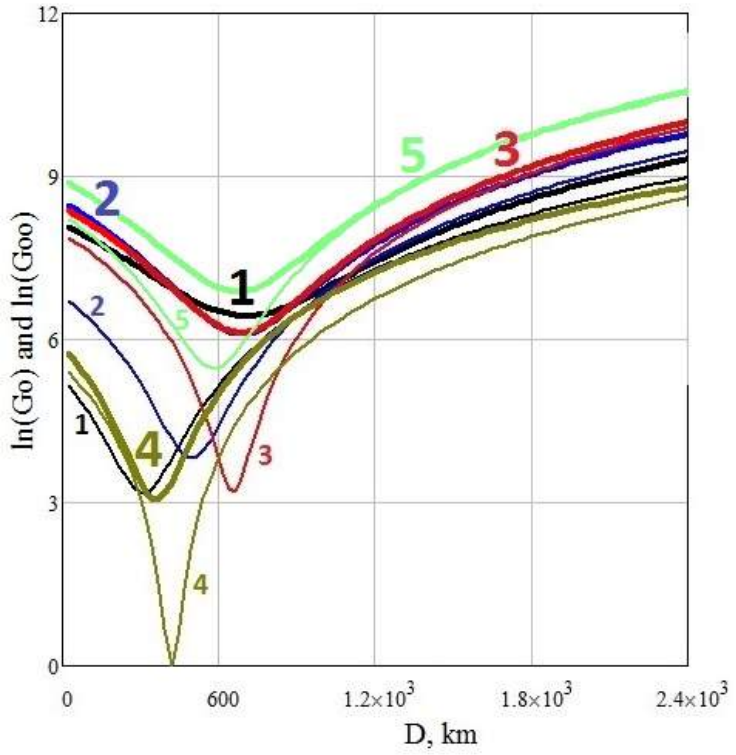

Figure 6. Discrepancy functions G_0 (thin curves) and G_{00} (thick curves) for all 5 dates: 15 September (number 1) and 3 December 1982 (num. 2), 16 April 1984 (num. 3), 23 April 1986 (num. 4), 13 May 1987 (num. 5).

Table 1. Values of the distance D from receiver (located in the auroral zone) to the boundaries of the ultrarelativistic electrons precipitations and corresponding to them uncertainty intervals ΔD (in the brackets) are given in columns 2 and 4 for all dates 1982-1987. Intervals ΔD determined by the level of 1.1 for the discrepancy-functions G_{00} and G_0, normalized to 1 at their minimums. Columns 3 and 5 - the same values of borders converted to the North latitude degrees.

	result of the G_{00} minimization		result of the G_0 minimization	
1	2	3	4	5
Date of disturbance	D and ΔD, km	D and ΔD, degrees	D and ΔD, km	D and ΔD, degrees
15 September 1982	600 (490-710)	64.7^0 (65.4^0-64.2^0)	400 (360-440)	65.8^0 (66^0-65.6^0)
3 December 1982	700 (630-770)	64.2^0 (64.6^0-63.9^0)	500 (460-540)	65.2^0 (65.5^0-65.1^0)
16 April 1984	700 (610-790)	64.2^0 (64.8^0-63.8^0)	670 (640-700)	64.3^0 (64.6^0-64.2^0)
23 April 1986	350 (320-380)	66^0 (66.2^0-65.9^0)	400 (390-410)	65.8^0 (65.8^0-65.7^0)
13 May 1987	650 (560-740)	64.4^0 (65^0-64^0)	570 (530-610)	64.9^0 (65.2^0-64.8^0)

In our calculations of the long radio path, we ignored the effects of reflection and of cross excitation of the main normal wave of a waveguide (at the heterogeneity boundary) into another normal waves. These effects lead to an additional weakening of the signal which is not considered in our calculations. Because of that we prefer the calculation results for the phase data, see Figure 7.

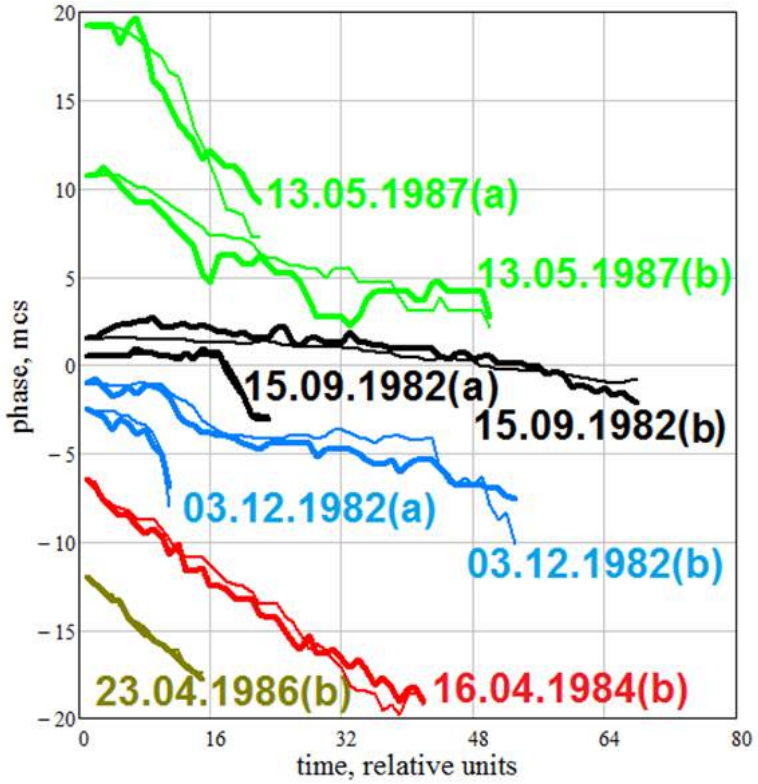

Figure 7. Comparison of the experimental (thick curves) and computed (thin curves) phase data (with D which corresponds to minimum of G_0 function) for all 5 disturbances according to the VLF inverse problem of 2-d kind for long radio path Ragby-Apatity (16 kHz). **(a)** - starting part of a disturbance (before minimum); **(b)** - restoring part of a disturbance (after minimum). Initial values of the phases for different events do not have any physical sense. Relative units of time - is a number of time points (one time step was equal to either 100 s or – 100 s)

Conclusion. According to the analysis of phase experimental data, the southern boundaries of several disturbances in 1982 – 1987 were placed in the auroral zone D = 400–670 km (66^0 – 64.3^0 N). The boundary

of ultrarelativistic electron precipitations did not move below 64^0 N lat, and so these precipitations were not connected with the inner radiation belt. The places of the boundaries represented are effective ones, because we know nothing about movement of the boundaries along the latitude during disturbances.

References:

1. Beloglazov, M. I., and G. F. Remenets (2010) Ultra-relativistic Electron Precipitations as a Main Cause of the Most Powerful Disturbances in the Middle Polar Atmosphere, *in: Proceedings of the 8th International Conference "Problems of Geocosmos" (St. Petersburg, September 20-24, 2010)*, edited by V.S. Semenov, SPb, 51-56. ISBN 978-5-9651-0504-5.

2. Remenets, G. F., and M. I. Beloglazov (2013) Ultrarelativistic electrons in the near cosmos and X-ray aurora in the middle polar atmosphere. *JGR – Space Physics*, 118, 6829-6838, doi: 10.1002/2013JA018822.

3. Remenets, G. F., and A. M. Astafiev (2014) Correction to the report "Southern boundary of the ultrarelativistic electron precipitation on May 13, 1987", in: Proceed. 36 Annual Seminar "Physics of Auroral Phenomena", Apatity, 2013, 163 – 165 (*in print in: Proceed. 37 Annual Seminar "Physics of Auroral Phenomena"*).

4. Remenets, G. F., M. I. Beloglazov, and L. G. Tamkun, (1989) A modified method of analysis of the VLF abnormalities and the dynamics of a low ionosphere fringe at a PCA event. *Geomag. Aeronomy*, 29, 45-50 (in Russian).

5. Remenets, G. F., and M. I. Beloglazov, (1992) Dynamics of an auroral low ionospheric fringe at geophysical disturbances on 29 September 1989, Planet. Space Sci., v. 40, p. 1101--1108.

6. Beloglazov, M. I., and G. F. Remenets, (1982) *Very Long Wave Propagation at High Latitudes,* 240pp, edited by L. L. Lazutin ; "Nauka", Leningrad (in Russian).

7. Gunninen, E. M., and I. N. Zabavina (1966), Propagation of long radio waves above the earth's surface, *in: Problems of the radio wave propagation and diffraction.* Issue 5, Leningrad, 5-30.

8. Remenets, G. F. (1973) About the conditions of quasi-degeneracy of the normal waves in an anisotropic waveguide, *in: Problems of the radio wave propagation and diffraction.* Issue 12, Leningrad, 188-207.

SOME FEATURES OF THE SC ON 24 JANUARY 2012 UPON OPTICAL AND MAGNETIC OBSERVATIONS IN SCANDINAVIAN SECTOR

V. Roldugin[1], F. Sigernes[2], A. Roldugin[1], S. Pilgaev[1]

[1]Polar Geophysical Institute, Apatity, Russia
[2]The University Centre in Svalbard, Norway

Abstract. An intensive sudden commencement (SC) on 24 January 2012 at 1503 UT was observed in good weather conditions in Lovozero, Barentsburg and Longyearbyen that permitted to make optical observations there. In Lovozero three minutes after the SC and two minutes after an electron aurora the hydrogen emission Hα appeared. It lasted 5 minutes and moved poleward. In Barentsburg the Hα appeared eight minutes after the SC at the same time with 1PGN2 band caused by high energy electrons, and it was observed during twenty minutes.
In Lovozero a particle precipitation started at 15:03.30 UT, but a perceptible magnetic disturbance of negative polarity began at 15:04:20, i.e. 50 sec later. The peak of luminosity lagged one and half minute to the positive magnetic peak. In Barentsburg the SC did not induce particle precipitations. In Lovozero the SC gave rise to beginning of Pc2, Pc3 and Pc5 geomagnetic and auroral pulsations, but they were absent in Barentsburg.

The sudden commencement (SC) on the 24th of January 2012 occurred at 15:03 UT during clear sky weather conditions over Lovozero (Kola peninsula), Longyearbyen and Barentsburg (Svalbard). The optical observations from these observatories give us an excellent opportunity to study particle precipitation in detail. The all-sky cameras in Barentsburg and Lovozero were setup with 1 sec time resolution. In addition the meridian scanning photometer in Longyearbyen was scanning with a 16 s period of rotation. The meridional spectro-meters in Lovozero and Barentsburg gave spectral images of the arch of local geomagnetic meridian. Hyper spectral data from the NORUSCA cameras were also available. We also use the Norwegian geomagnetic network with 10 s resolution, and 0.1 second magnetic data from Lovozero. The SC on the 24th of January 2012 was caused by the arrival of a strong shock wave in the solar wind. On the shock wave front the pressure increased from 1 to 10 nPa, the velocity from 400 to 700 km/s, and the positive Bz component of magnetic field from 3 to 15 nT.

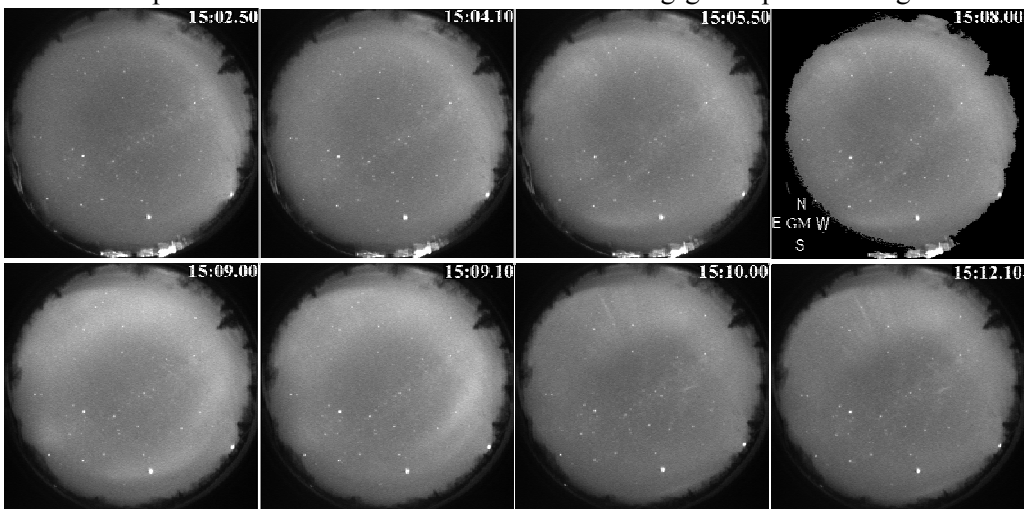

Figure 1. All sky film snapshots during the SC from Lovozero.

Before the SC auroras were absent in Lovozero and Svalbard. In Lovozero after 15:03.50 UT a weak luminescence, having the form of broad diffuse band, spreads from S-W horizon to the zenith. At 15:04.10 UT its forms came to be more allocated. After 15:05.10 UT ray forms appear in NE, that indicates electron precipitation, and then the intensity grew, see Fig.1. At about 15:05.40 UT in the south, an extensive diffuse spot appears, which is morphologically similar to proton aurora. At 15:06.00 UT the luminosity in NE intensified and spreads along the horizon to NW-W. The diffuse glow shifted from south to north, and at 15:07.09 UT it is seen all over the sky. In spite of its low intensity, the aurora is very dynamic, see frames at 15:09.00 and 15:09.10 UT. After 15:10 UT the ray structure of the aurora near the north horizon became more pronounced, and the intensity of the diffusive forms decreased, located near the south horizon. They were not observed after 15:18.

In Svalbard the 557.7 nm channel of the allsky cameras detected no aurora prior to 15:07:40 UT (Fig. 2). After 15:07:40 UT rayed arcs appeared in the zenith, oriented in SE – NW direction, and their intensity increased quickly up to 15:10:30 UT. At 15:11:40 to 15:20 UT they developed into a "tent" structure.

The multi-channel scanning photometer in Longyearbyen, see Fig.3, shows that the flare of auroral intensity in the 557.7 nm emission occurred close to 15:08 UT. After a small decrease in intensity, the auroral forms appear to quickly move poleward.

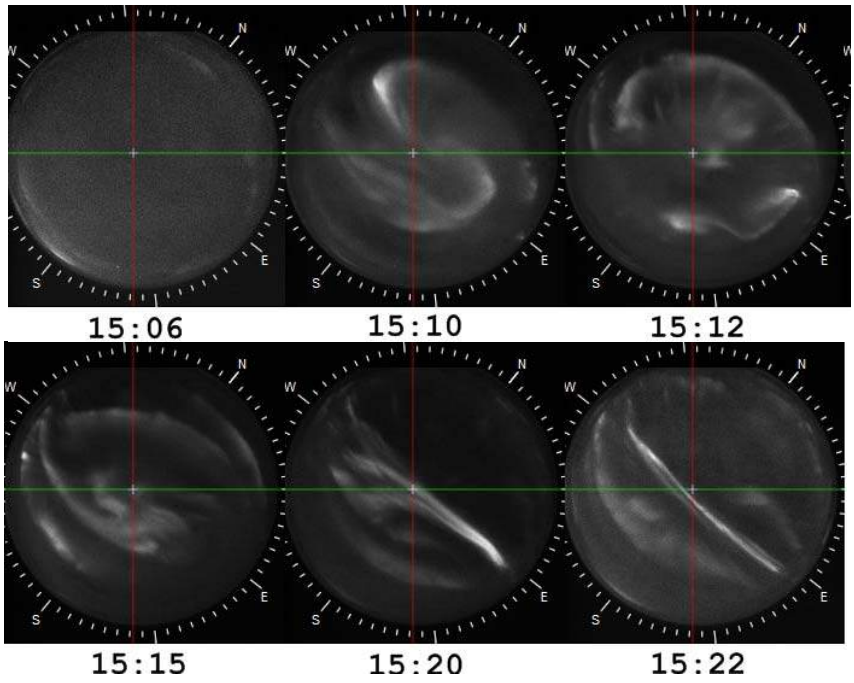

Figure 2. Hyperspectral images from the NORUSCA camera at channel 557.7 nm in Longyearbyen.

Note that on 15:11 UT the hydrogen emission appears, somewhat after the 557.7 emission, localized near the south horizon. The appearance of the *Hα* emission after the SC is clearly identified in the data of the meridian spectrometers in Lovozero and Barentsburg.

Three spectra of the spectrometer in Lovozero are shown in Fig. 4. Geomagnetic North is to the top.Beside auroral emissions, the doublet Na 589.0/589.6 nm and the anthropogenic line of mercury at 546.1 nm with the doublet 577/579 nm are all identified in the spectra.

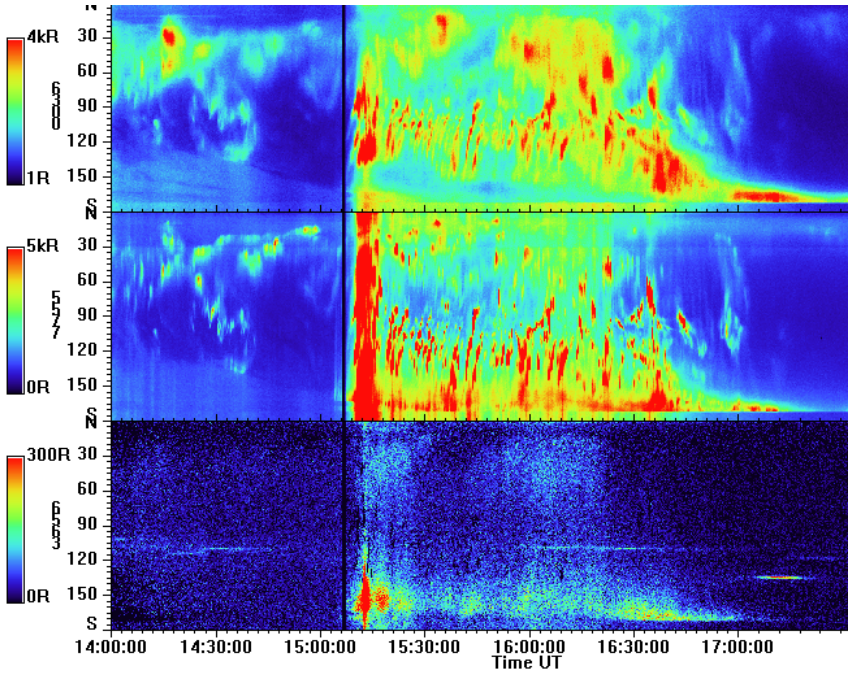

Figure 3. Records of multi-channel scanning photometer in Longyearbyen.

The *Hα* emission (656.3 nm) appears at 15:06 UT to the south from Lovozero observatory. In the next spectrum at 15:07 UT the Hα emission is observed all over the meridian. At 15:08 its peak is situated in the north. The maximum intensity is detected at 15:10 UT. At15:11 UT the Hα emission is not observed.

Hence the hydrogen emissions in Lovozero appear two - three minutes after the SC, and two minutes after the onset of the aurora. It is observed five minutes as the area of proton precipitation moves from south to north.

In Barentsburg the Hα 656.3 nm emission emerges at 15:11 UT simultaneously with the appearance of 1PGN2 band along all vertical arch, what may be partly connected with atmospheric scattering over small transparency and orientation of the auroral forms. The 1PGN2 emission, girdling the hydrogen emission, is evidence of high energy electron precipitation. Both emissions have maximal intensities at 15:12 UT, after that they weakened, but up to 16:25 UT the Hα emission is still seen.

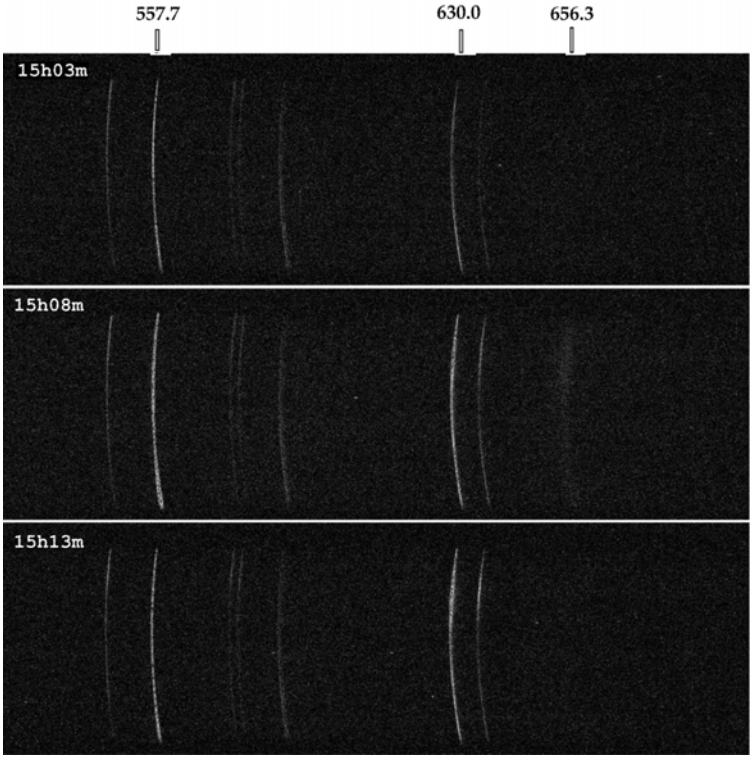

Figure 4. The spectra of meridian spectrometer in Lovozero.

The field of view of the all-sky cameras in Lovozero and Barentsburg have been divided into 11 circles and the averaged intensities in each circle were determined for each 1 sec frame, see Fig.5. These pseudo-photometric curves were compared with magnetic variations at both stations. The plot for Lovozero is shown in Fig. 6. The integral luminosity as a function of time for the zenith circle #1 with 60º radius is plotted in black. The monotonic decrease of the intensity up to 15:03.20 UT is due to decrease of scattered solar light with the Sun sinking. The rise of intensity from 15:03.25 UT and its sharp ascent at 15:04.00 UT marks the beginning of the SC. The maximal integral intensity of the auroral intensity occurs at 15:08 UT followed by a rapid decrease. The magnetic perturbation (red line) begins at 15:04.20 UT. That is 55 sec after the luminosity curve. Polarity of the start impulse is negative, at 15:05 UT. The H-component begins to increase quickly to 350 nT, and the luminous intensity increases simultanesously.

In Lovozero, during the SC interval 15:03.25 - 15:04.20 UT, there is particle precipitation without magnetic disturbances.

The same type of data from Barentsburg is shown in Fig. 7. The rise of sky intensity occurs at 15:09.30 UT. That is 6 min later than in Lovozero. The main SC impulse between 15:05 and 15:10 UT has a negative sign in contrast to positive one in Lovozero. The negative peak 15:03 – 15:09 UT is not accompanied by particle precipitation. The latter one starts simultaneously with the appearance of hydrogen emissions and H-component increase.

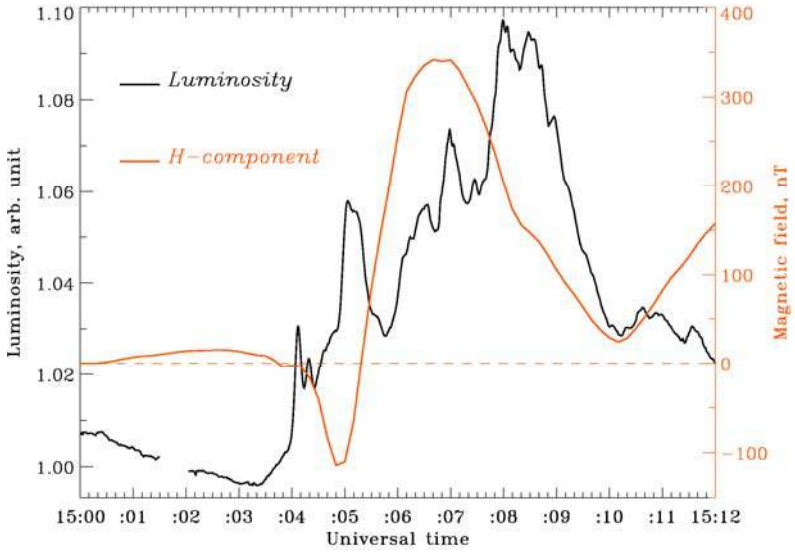

Figure 6. The variations of integral luminous intensity over Lovozero in zenith circle with 60º radius (black line) and of H-component (red line).

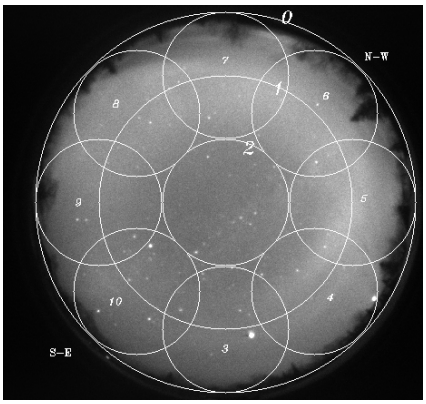

Figure 5. The circles for calculations of luminous intensity variations across parts of the sky.

It is well known that a SC evokes geomagnetic pulsations Pc5. Our SC is not exception. Fig. 8 upper panel shows three components of filtered magnetic records from Lovozero by black lines. The cutoff frequency of the high-frequency filter is equal to 0.005 Hz. The low-frequency Pc5 oscillations are seen as well on account of their high power. One can see that the period of Pc5 is about of 4-5 min, the pulsations starts simultaneously with SC. But it is seen too that simultaneously with Pc5 and SC the Pc3 pulsation appears with the period about of 15-20 s and

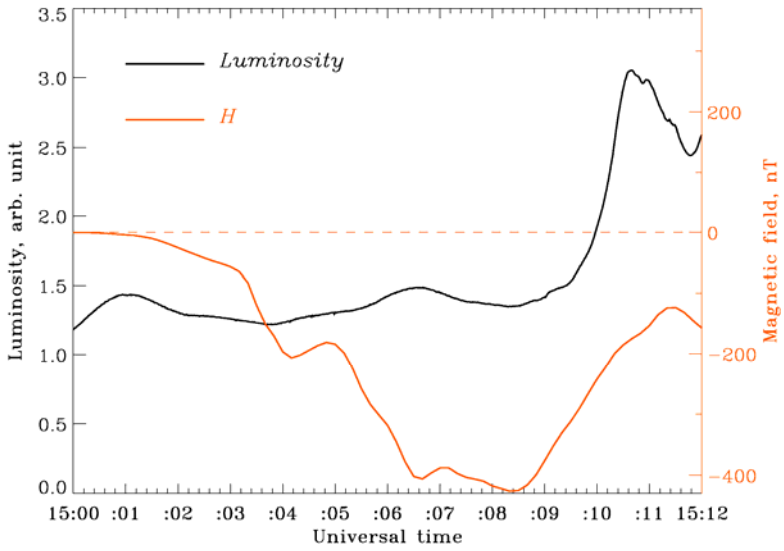

Figure 7. The variations of integral luminous intensity over Barentsburg in zenith circle with 55º radius (black line) and of H-component there (red line).

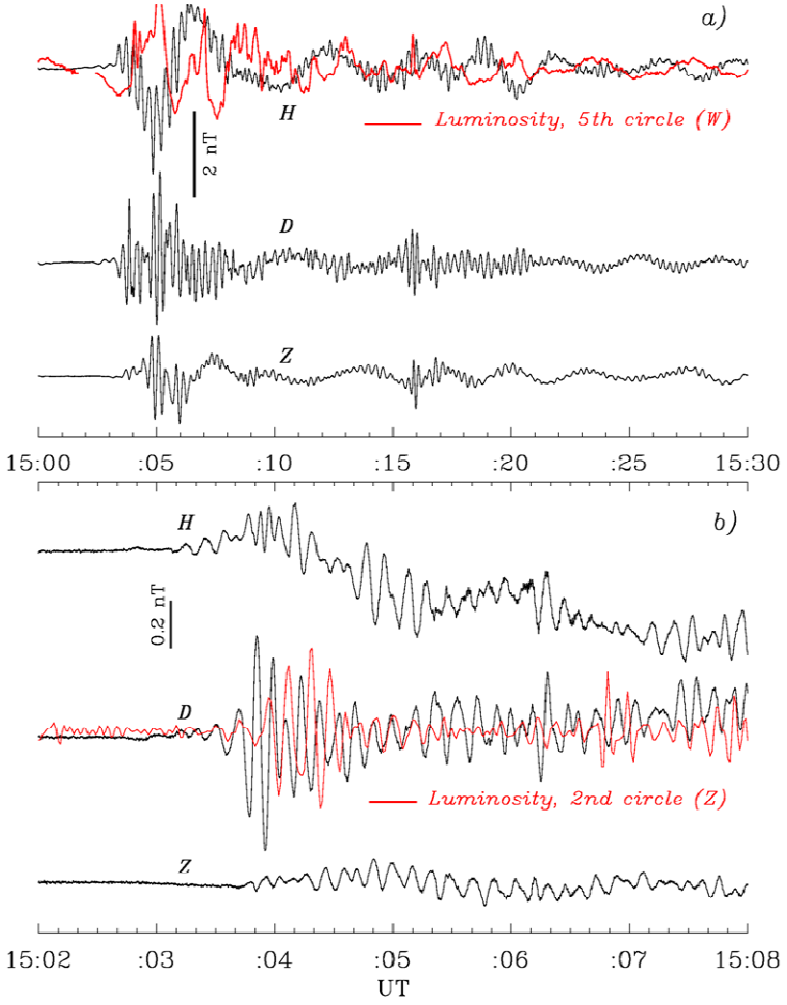

Figure 8. Pulsations of the magnetic field (black) and auroral luminosity (red) in Lovozero after high-frequency filtration with cutoff a) 0.005 Hz; b) 0.1 Hz.

amplitude about of 1 nT. With pulsations of H-component the pulsation of luminosity in the west circle, see Fig. 5, is presented by red curve. In spite of not too good similarity, the auroral pulsations of both types are seen in luminosity also.

The magnetic and luminous data are filtered also with cutoff frequency equal to 0.1 Hz. It is seen that this SC causes pulsation with 9 –10 sec period and amplitude about of 0.1 nT too; it is Pc2 pulsation. In parallel with D-component the luminous pulsation in zenith circle 2 is shown, good correlation with the geomagnetic pulsation is seen.

The auroral Pc5 pulsations are seen well in the variations of 630.0 and 557.7 emissions in Longyearbuen's scanning photometer in Fig. 3.

CONCLUSIONS

Three peculiarities of the SC on the 24th of January 2012 at 15.03 UT in Scandinavian sector have been found:

1) The emergence of proton aurora, which appears on the south of the auroral zone and expands towards the pole.

2) On the equatorial edge of the auroral zone, particle precipitation forestalls magnetic impulse. Near the polar cap strong magnetic impulse is not accompanied by particle precipitation.

3) Pc2, Pc3 and Pc5 pulsations are generated at once after SC.

SOLAR X-RAY FLARES INFLUENCE ON VLF/LF SIGNALS IN DIFFERENT MIDDLE-LATITUDES PATHS

A. Rozhnoi[1], M. Solovieva[1], K. Schwingenschuh[2], V. Fedun[3]

[1]Institute of Physics of the Earth RAS, Moscow, 123995, Russia, e-mail: rozhnoi@ifz.ru;
[2]Institute of Space Research AAS, Graz, Austria; [3]Department of Automatic Control and Systems Engineering, University of Sheffield, Sheffield, UK

Abstract. Sudden Phase Anomalies (SPAs) of VLF/LF signals recorded in Graz (Austria), Sheffield (UK) and Moscow (Russia) stations during two solar flares of intensity class X1.0 and M3.8 in November 2013 are examined. Data from seven transmitters in frequency range from about 20 to 45 kHz are used for the analysis. SPAs were observed in middle-latitudes paths with length from 200 to 7000 km and different orientation. Solar X-ray burst data were taken from the satellite GOES observations in the band of 0.1-0.8 nm. SPA characteristics like types, onset times, growth times, duration of SPA events and their amplitudes are studied. Observed SPAs are positive in 24 cases and they are negative in 2 cases regardless of the length or orientation of paths or signal frequency. The amplitude of SPAs in different paths varies from 10 to 230 degrees and no clear correlation between amplitude of SPAs and intensity of the solar flares or length of the paths are found. The SPAs begin within 3 and 4 minutes after the start of the first and second flare events, respectively. The time of growth for the first event is from 4 to 23 minutes and for the second event it is only 2-5 minutes. The duration is longer for the first event (~1h20 min-2 h) and it is shorter for the weaker flare (~30 min-1h30min).

Introduction

During the most solar X-ray flares the electron density is greatly enhanced and ionization is usually produced below the normal D-region (e.g. Chilton et al., 1963), so this region responds dramatically. To study of the D region behavior the Very Low and Low Frequency (VLF/LF) wave measurements are used because these waves are reflected by the D region, and the received signals inherently contain information of the reflection height of the region and its variability. This is a great advantage, as these heights are too high to study them by using balloons, and too low for in-situ measurements of satellites. Moreover, measurements with the use of rockets are very transient and spatially limited. Since Kreplin et al. (1962) have reported the relationship between flare time X-ray bursts and Sudden Phase Anomalies (SPAs), numerous works have been published on the study of flare characteristics and SPA phenomenology (e.g. Mitra, 1974; Muraoka, 1977; Kamada, 1985; Khan et al., 2005). Thomson et al. (2005) modeled the D region electron densities as functions of X-ray flux up to the level of the great X45 flare. During this great flare, they found that the reflecting height was about 17 km below the normal midday level (about 70 km).

In present work we investigate SPA characteristics from VLF/LF signals recorded in three European middle latitude VLF stations during two solar flares of intensity class X1.0 and M3.8 in November 2013.

Used data

Data from the receiving stations in Graz (Austria), Sheffield (UK) and Moscow (Russia) were used for the analysis. The stations are equipment with UltraMSK receivers which can record simultaneously both the amplitude and phase of MSK (Minimum Shift Key) modulated signals in frequency range 10-50 kHz from several navigational or time service VLF/LF transmitters. MSK signals have fixed frequencies in narrow band 50-100 Hz around the main frequency and adequate phase stability. The receivers provide measurements with time resolutions ranging from 50 msec to 60 sec. For our purpose we used sampling frequency of 20 sec. In every station the amplitude and phase of VLF/LF signals from seven transmitters were considered. The relative locations of the transmitters and our observing stations are plotted in Figure 1. The length of sub-ionosperic wave paths ranged from about 200 to near 7000 km and their orientation was different.

Solar X-ray burst data were taken from the satellite GOES-15 observations in the band of 0.1-0.8 nm (long) with time resolution of 1 min (http://www.swpc.noaa.gov/ftpmenu/lists/xray.html).

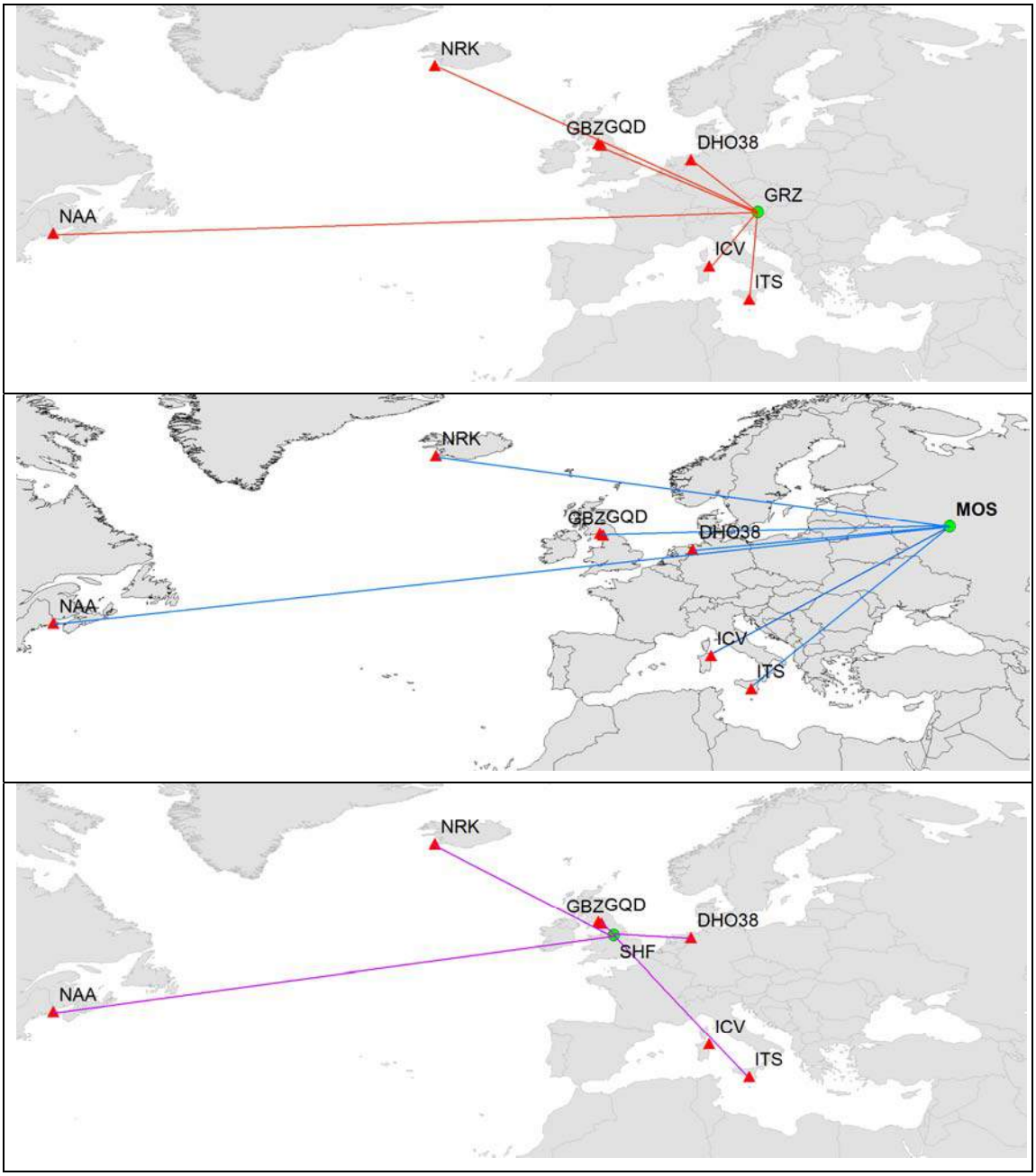

Figure 1. Positions of the receivers (green circles) in Graz (GRZ), Moscow (MOS) and Sheffield (SHF) (from top to bottom) together with the positions of the transmitters (red triangles) NAA (24.0 kHz), NRK (37.5 kHz), DHO (23.4 kHz), ICV (20.29 kHz), ITS (45.9 kHz), GBZ (19.58 kHz) and GQD (22.1 kHz).

Results

We studied SPA's characteristics like types, onset times, growth times, duration of SPA events and their amplitudes during solar X-ray flares – on November 19, 2013 (class X1.0) and November 6, 2013 (class M3.8).

A typical SPA is characterized by a sudden advance of phase followed by a rounded maximum and generally an exponential decay or a recovery phase. Typical SPAs in the NRK signal are shown in Figure 2 during X-ray burst on November 6, 2013. The character of phase and amplitude anomalies is practically identical in the all three stations. Sometimes SPAs have gradual onset (example see in Figure 3). The data from Moscow station are rather noisy because of the station location in the center of megalopolis. Unlike Graz and Sheffield, no noticeable effect is seen in the amplitude of the signal in Moscow.

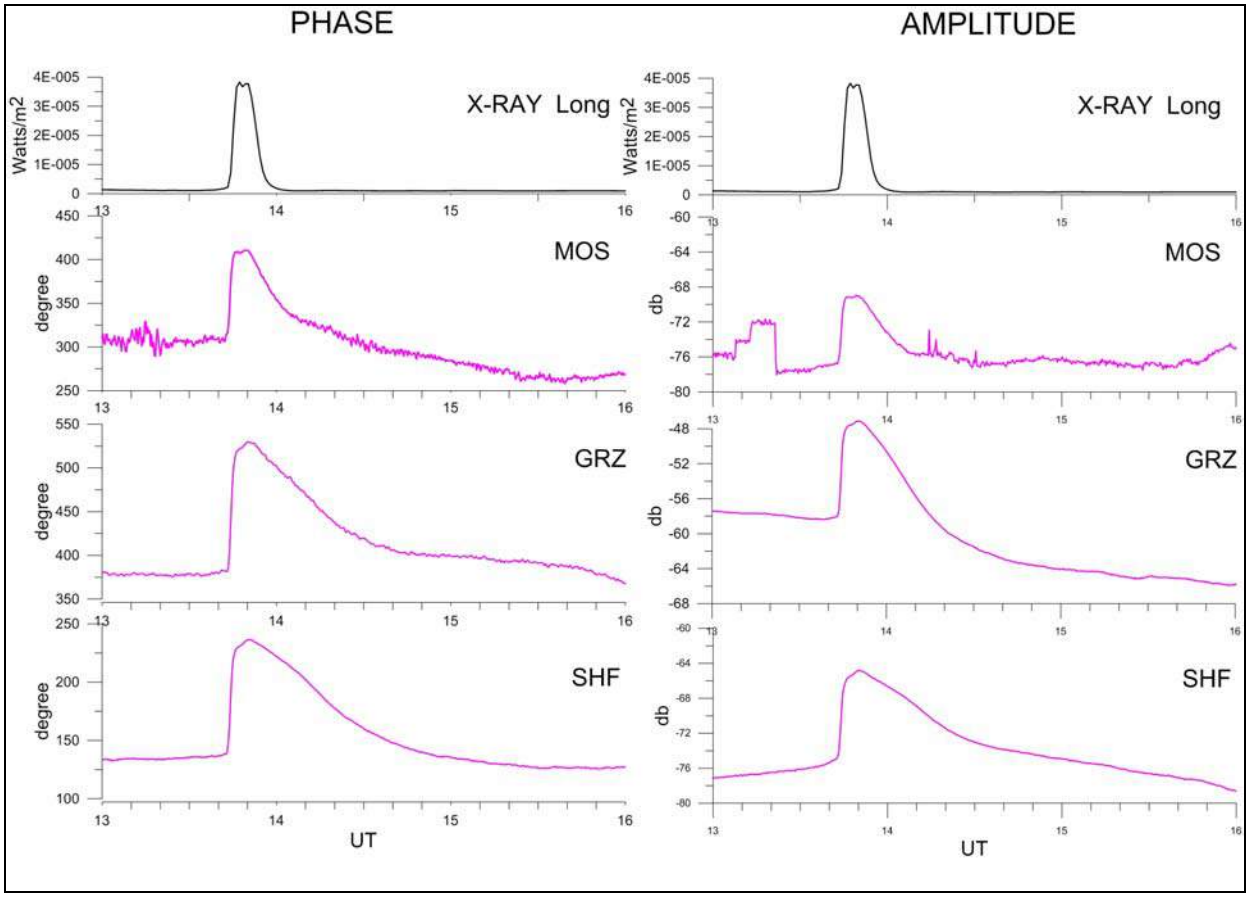

Figure 2. SPAs recorded in the NRK signal at Moscow, Graz and Sheffield receiving stations during X-Ray burst on November 6, 2013. Top panel shows X-ray observed in the GOES satellite.

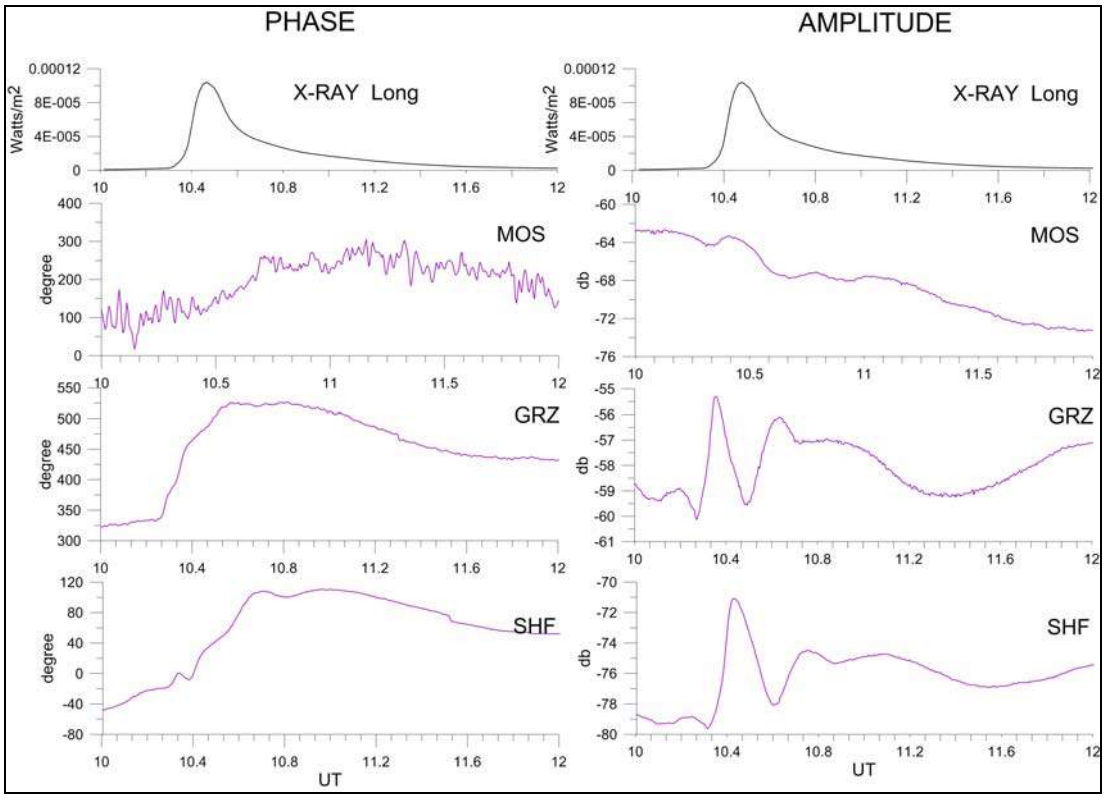

Figure 3. SPAs recorded in the NAA signal at Moscow, Graz and Sheffield receiving stations during X-Ray burst on November 19, 2013.

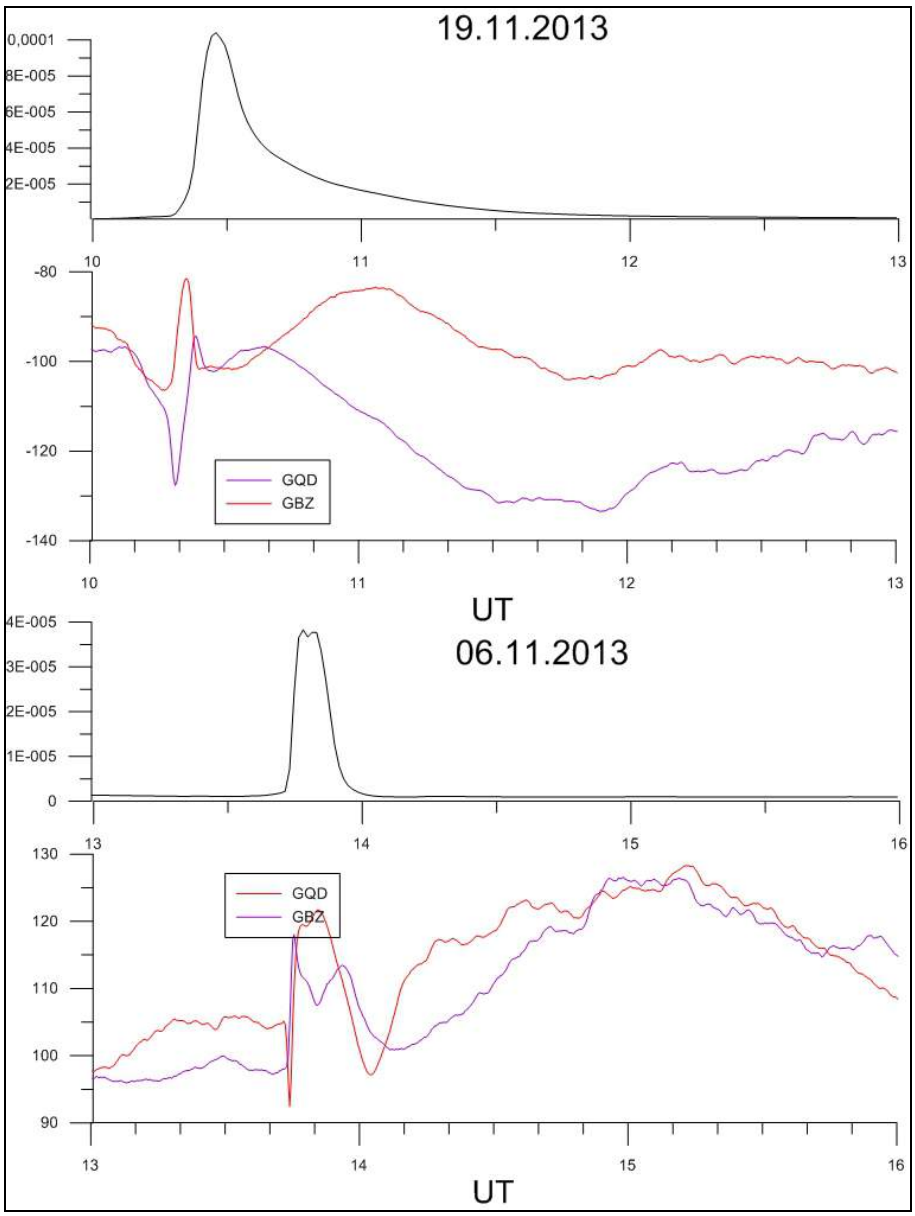

Figure 4. SPAs recorded in the phase of the GQD and CBZ signals at Sheffield receiving stations during X-ray burst on November 19 (top panel) and November 6, 2013 (bottom panel).

Infrequently, events have either a complex onset or complex phase variation (Figure 4). In the Figure the signals from the two nearest transmitters-GBZ and GQD are shown for the two X-ray flares recorded at the Sheffield station. It is the most interesting result. The distance between the transmitters and the receiver is about 200 km and VLF wave's propagation has multi-mode type, unlike all the other paths where the propagation is one-mode. All the previous investigations of SPAs (including mentioned above) were made for very long paths.

The classification of events as simple (S), gradual (G) and complex (C) types of SPAs was made by Kamada (1985). The majority of the SPAs we observed for both flares were of S type. This is in conformity with Khan et al. (2005) while Kamada (1985) reported that he mainly identified G type of anomalies.

The SPAs show varied temporal development. The onset time is generally defined as time difference between beginning of the flare and start of SPA. SPAs in all the paths for the x-ray flare on November 19 (class X1.0) began within three minutes of the start of the flare event, and for the x-ray flare on November 6 (less intensive) the onset time was four minutes. This is in good agreement with Deshpande et al. (1972) who found a delay of 3–4 minutes between beginnings of X-ray and SPA events.

Table 1. SPAs in the VLF/LF signals on November 19, 2013 (class X1.0, active region 1893, X-Ray 0.1-0.8, Amax=0.000104 Watts/m^2, Tstart=10:14, Δt=8 min)

Path	Power, kW	Frequency, kHz	Length, km	Orien-tation	Sign of SPA*	Type**	Amax, degree	Tstart	Growth, min	Dura-tion
NAA-GRZ	1000	24.0	6000	W-E	+	G	200	10:17	23	1:43
NAA-SHF	1000	24.0	4700	W-E	+	G	100	10:17	23	1:43
NRK-GRZ	100	37.5	3000	N-S	+	S	233	10:17	9	1:53
NRK-SHF	100	37.5	1700	N-S	+	S	110	10:17	9	1:53
ITS-GRZ	unknown	45.9	1100	S-N	+	S	75	10:17	9	2:03
ITS-SHF	unknown	45.9	2200	S-N	+	S	73	10:17	9	2:03
GBZ-GRZ-	30	19.58	1500	N-S	+	S	23	10:17	4	1:43
GBZ-SHF	30	19.58	200	N-S	-	C	30	10:17	3	1:43
GQD-SHF	60	22.1	200	N-S	+	C	19	10:17	4	1:43
ICV-GRZ	unknown	20.27	850	S-N	+	S	12	10:17	10	1:13
DHO-GRZ	800	23.4	900	N-S	+	S	100	10:17	4	2:30
DHO-SHF	800	23.4	600	E-W	+	S	125	10:17	20	1:23

* Sign is +, if SPA and X-Ray curves have the same direction, and sign is -, if SPA has downward direction
** S-simple, G-gradual, C-complex

Table 2. SPAs in the VLF/LF signals on November 6, 2013 (class M3.8, active region 1890, X-Ray 0.1-0.8nm, Amax=0.0000383 Watts/m^2, Tstart=13:39, Δt=7 min)

Path	Frequency, kHz	Length, km	Orienta-tion	Sign of SPA*	Type**	Amax, degree	Tstart	Growth, min	Duration, min
NAA-MOS	24.0	7000	W-E	+	S	100	13:43	3	1:30
NAA-GRZ	24.0	6000	W-E	+	S	185	13:43	3	1:30
NAA-SHF	24.0	4700	W-E	+	S	134	13:43	3	1:30
NRK-MOS	37.5	3500	W-E	+	S	125	13:43	3	40
NRK-GRZ	37.5	3000	N-S	+	S	150	13:43	4	40
NRK-SHF	37.5	1700	N-S	+	S	110	13:43	5	40
GBZ-MOS	19.58	2500	W-E	+	S	25	13:43	3	25
GBZ-GRZ-	19.58	1500	N-S	+	S	50	13:43	3	55
GBZ-SHF	19.58	200	N-S	+	C	15	13:43	3	50
DHO-MOS	23.4	2000	W-E	+	S	80	13:43	3	30
DHO-GRZ	23.4	900	N-S	+	S	200	13:43	3	35
DHO-SHF	23.4	600	E-W	+	S	75	13:43	3	40
GQD-MOS	22.1	2500	W-E	-	C	10	13:43	2	30
GQD-SHF	22.1	200	N-S	+	C	20	13:43	2	30

The time taken from the beginning of the event to reach the maximum is normally denoted as the time of growth of SPA. The time of growth for the first event (X1.0) was from 4 to 23 minutes and for the second event (M3.8) it was only 2-5 minutes. This does not contradict to Deshpande et al. (1972) who reported the average times of growth of 10 minutes for SPAs.

The duration of SPA event, i.e., the time from the beginning of the event to recovery normally varies from 30 minutes to 2–3 hours (Chilton et al., 1963). In the present investigation, the duration was found to be longer for the first event (~1h20 min-2 h) and it is shorter for the weaker flare (~30 min-1h30min). As it can be seen in the typical SPA records shown in Figure 2, the recovery part of the phase anomaly is very nearly exponential in conformity with earlier observations (e.g. Chilton et al., 1964).

All SPAs characteristics together with the information about the X-ray flares and wave paths under investigation are presented in Table 1 (for the event on November 19) and Table 2 (for the event on November 6).

Conclusion

In this study we investigated SPAs in VLF/LF signals propagating in the middle latitude paths during two solar flares of intensity class X1.0 and M3.8 in November 2013. On the whole analysis was made for 17 paths with length from 200 to 7000 km and different orientation. We have found that the observed SPAs were positive in 24 cases and they were negative in 2 cases regardless of the length or orientation of paths or signal frequency. The amplitude of SPAs in different paths varies from 10 to 230 degrees and no clear correlation between amplitude of SPAs and intensity of the solar flares, transmitter power or length of the paths were found. The SPAs began within 3 and 4 minutes after the start of the first and second flare events, respectively. The time of growth for the first event was from 4 to 23 minutes and for the second r event it was only 2-5 minutes. The duration was longer for the first event (~1h20 min-2 h) and it was shorter for the weaker flare (~30 min-1h30min).

Acknowledgements

This research is supported by Royal Society International Exchanges Scheme and RFBR under grant 13-05-92602 KOa.

References

Chilton, C. J., F. K. Steele, and R. B. Norton (1963), Very-Low-Frequency phase observations of solar flare ionization in the D region of the ionosphere, *J. Geophys. Res.*, 68, 5421–5435.

Kamada, T. (1985), VLF sudden phase anomalies, *J. Geomag. Geoelectr.*, 37, 667–699.

Muraoka, Y., H. Murata, and T. Sato (1977), The quantitative relationship between VLF phase deviations and 1–8°A solar X-ray fluxes during solar flares, *J. Atmos. Terr. Phys.*, 39, 787–792.

Khan, Ibrahim, M. Indira Devi, T. Arunamani, and D. N. Madhusudhana Rao (2005), A synoptic study of VLF sudden phase anomalies recorded at Visakhapatnam, *Earth Planets Space*, 57, 1073–1081.

Deshpande, S. D., C. V. Subrahmanyam, and A. P. Mitra (1972), Ionospheric effects of solar flares-I. The statistical relationship between X-ray flares and SID's, *J. Atmos. Terr. Phys.*, 34, 211–227.

Thomson, N.R., C.J. Rodger, and M.A. Clilverd (2005), Large solar flares and their ionospheric D region enhancements, *J. Geophys. Res.*, 110, A06306, doi: 10.1029/2005JA011008.

Kreplin, R. W., T. A. Chubb, and H. Friedman (1962), X-ray and Lyman-alpha emission from sun as measured from the NRL SR-I satellite, *J. Geophys. Res.*, 67, 2231–2253.

Mitra, A. P. (1974), Ionospheric Effects of Solar Flares, *D. Reidel Publishing Company*, Dordrecht-Holland, 307 pp.

INTERPLANETARY SHOCK GEOEFFECTIVENESS DURING A GROWTH PHASE OF SOLAR ACTIVITY

L.P. Shadrina[1], G.F. Krimsky[2], I.Ya. Plotnikov[2], S.A. Starodubtsev[2]

[1]Academy of Sciences of Republic of Sakha (Yakutia), Yakutsk, 677007, Russia, e-mail: lushard@mail.ru; [2]Yu.G. Shafer Institute of Cosmophysical Research and Aeronomy of SB RAS, Yakutsk, 677007, Russia

The results of the analysis of interplanetary shocks manifestations on Earth in the cosmic ray intensity and geomagnetic field are presented. There were selected 96 interplanetary shocks during the growth phase of 23-th solar cycle. More than half of the events, 49 of them, were accompanied by cosmic ray intensity and geomagnetic field decreases. Other 40 shocks changed whether the cosmic ray intensity or geomagnetic field, and 7 shocks had none ground effect. The most part of the strong and moderate geomagnetic storms with amplitude more than 60 nT (44 from 60) did not associated with the cosmic ray intensity decreases or these effects were very week. Those results confirm our preliminary conclusions that the regions responsible for the generation of geomagnetic storms and cosmic ray Forbush decreases are spatially separated in the interplanetary disturbances.

Introduction

Problem of the ratio geoeffectiveness of different solar wind structures, despite of the large number of papers on this topic still did not get a solution. On one hand, the statistical analysis of geomagnetic field depressions shows that geomagnetic storms are generated by the passage of interplanetary shocks (IS), magnetic clouds (MC), sheath, coronal mass ejection (CME), compression regions at the boundary of the slow and fast streams (corotating interaction regions CIR) etc. [1-5]. On the other hand, mentioned heliospheric disturbances structure modulates the cosmic rays (CR) distribution, which is manifested on the ground as their intensity depression [6-8].

Geomagnetic storms are the result of some sort of "point of interaction" – their occurrence and intensity mainly depends on the IMF structure (southward Bz component) at the point of interaction of interplanetary disturbance and Earth's magnetosphere. This is one side of the geoefficiency. On the other hand, cosmic rays in addition to the geoefficiency (i.e. CR intensity decreases on the ground), are helioeffective. Since the CR-intensity decrease is due to their interaction with the heliospheric disturbance: CRs change their trajectory, and a region with a reduced CR content appears in interplanetary space. So geomagnetic storms as a manifestation of the geoefficiency have a local character, whereas Forbush effects reflect influence of space and therefore they are helioeffective.

The analysis of interplanetary disturbances geoefficiency on their manifestations in CR and geomagnetic-field was presented in papers Kudela K. and Brenkus R. [9] and Papailiou M. et al. [10] and etc. The authors consider the possibility of a joint consideration of CR and the Dst data in order to find a precursor of heliospheric disturbance arrival to the Earth. The difference of our approach is that we aim to clarify the role of the geometrical factor of moving solar wind structure intersections respect to the Earth by the ratio of their geoeffective manifestations in the geomagnetic field and in the CR.

The purpose of this paper is to estimate the ratio geoeffectiveness of the interplanetary shock manifestations on the Dst index decreases (geomagnetic storms, St) and CR intensity variations at st. Yakutsk (Forbush decreases, F).

Results

A list of interplanetary shocks (IS) related with CME from paper Manoharan P.K. et al. [11] during 6 years (1997-2002) on the growth phase of 23 solar cycle was used as a basis for investigations. Dates geomagnetic storms were determined by Dst-index of geomagnetic field, and CR Forbush decreases by the galactic CR isotropic component at st. Yakutsk.

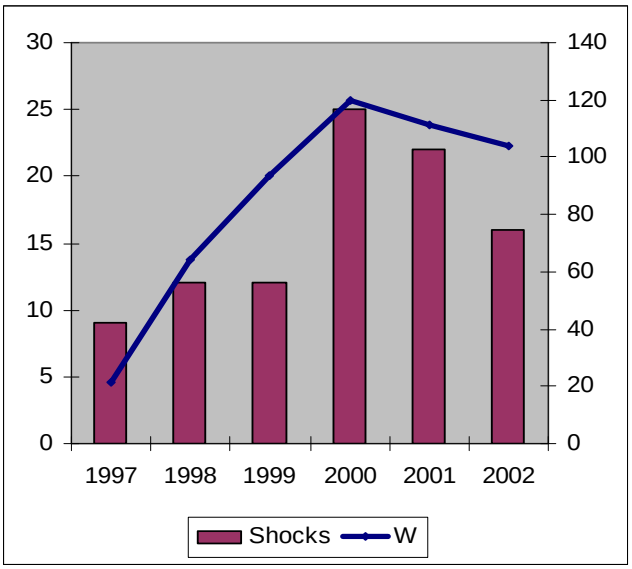

Fig. 1. Solar activity (W – Wolf number, right scale) and number of interplanetary shocks (Shocks – columns, left scale) during growth phase and maximum of 23th solar cycle

Four types of ground events during the IS registration were examined. Firstly, three types of CR intensities and the geomagnetic field decreases – simultaneously (with a scatter not more then 24 hours) (Forbush decrease + storm, F + St), or manifestation only in one of this parameters (storm without Forbush decrease, St – F or Forbush decrease without storm, F – St). Fourth type consist of the events when there are no noticeable decreases nor in the geomagnetic field or in the CR (– St – F).

The investigated time interval occurs in the first half of the 23rd solar cycle. The minimum of the cycle was observed in 1996 (annual average sunspot number W = 8,6), the maximum – in 2000 (W = 119,6). Number of IS varies synchronously with solar activity (Fig. 1): it increases at the growth phase, reaches a maximum at the maximum of the cycle and decreases at the declining phase. 25 of 96 shocks (over a quarter) occurs at the year of solar activity maximum.

The distribution of these 96 IS for the four described above types of geoeffective responses is: 43 events (44,8%) – storms with Forbush decreases (F + St), 38 events (39,6%) – storms without Forbush decreases (St – F), 8 events (8,3%) – Forbush decreases without storms (F – St) and in 7 cases there are no geoeffective events (– St – F) (7,3%) (Fig. 2). Thus, we can write the ratio geoeffectiveness: (F – St) : (F + St) : (St – F) : (– St – F) as **1,1 : 6,1 : 5,4 : 1,0.**

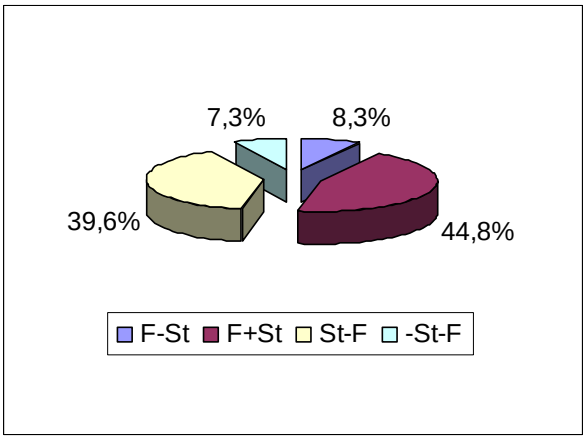

Fig. 2. Ratio geoeffectiveness – relations of four types of geoeffective events: Forbush decreases and geomagnetic storms

Geomagnetic storms and CR Forbush decreases usually are characterized by their intensity. According to the accepted classification [Ермолаев и др., 2010] the storms are big (intensive) for δDst > 100 nT (bSt), are moderate for 50 < δDst < 100 nT (mSt), small for 30 < δDst < 50 nT (sSt) by the value of amplitude of Dst index decrease during main phase. Similarly, Forbush decreases are big for CR intensity declines δI/I > 7% (bF), moderate for 4% < δI/I < 7% (mF) and week for 1,5% < δI/I < 4 % (sF). If there is no response in the geomagnetic field or in the CR intensity the events are denote as nSt or nF. Thus we have 16 types of the vents – from (bSt, bF) to the (nSt, nF). Distribution of 96 events for these 16 types is shown in Table.

One can see in Table that the big geomagnetic storms more frequently accompanied with small CR-intensity decreases: 17 cases (17,7%) of (bSt, sF) events. Quite often there are events of geomagnetic storms without Forbush decreases – 10 big (10,4%) of (bST, nF) events, 13 moderate (13,5%) of (mST, nF) and 15 small (15,6%) of (sST, nF) storms. This statistics and classification agrees with the results of paper [Kudela K. and Brenkus, 2004], where there were found 28% of the events in Dst without significant CR decreases (here 24%) and 19% CR decreases without Dst changes (here 8%) for 20 years from 1982 to 2002.

Number of 16 types of geoeffective events in geomagnetic field (St) and in cosmic rays (F)

δDst, nT δI/I, %	bSt	mSt	sSt	nSt
bF	6	0	0	0
mF	6	4	1	2
sF	17	3	6	6
nF	10	13	15	7

A statistical analysis of the table was fulfilled. The values of the two-dimensional random quantity nij (St, F) compares with a set of matrices Nij, calculated according to the formula of binormal probability density:

$$p(x, y) = \mathrm{Exp}[-\frac{(x - \mu_1)^2 / 2\sigma_1^2 + (y - \mu_2)^2 / 2\sigma_2^2 - (x - \mu_1)(y - \mu_2) / \sigma_1 \sigma_2}{1 - \rho^2}] / 2\pi\sqrt{1 - \rho^2}\,\sigma_1 \sigma_2$$

for xi = {<nSt>, <sSt>, <mSt>, <bSt>} and yj = {<nF>, <sF>, <mF>, <bF>} and for set of the free parameters in the range (0 ÷ ∞): mathematical expectations μ_1 and μ_2, and dispersions σ_1 and σ_2, and the correlation coefficient ρ between the components of two dimensional random variable (x, y) in the range (-1 ÷ 1).

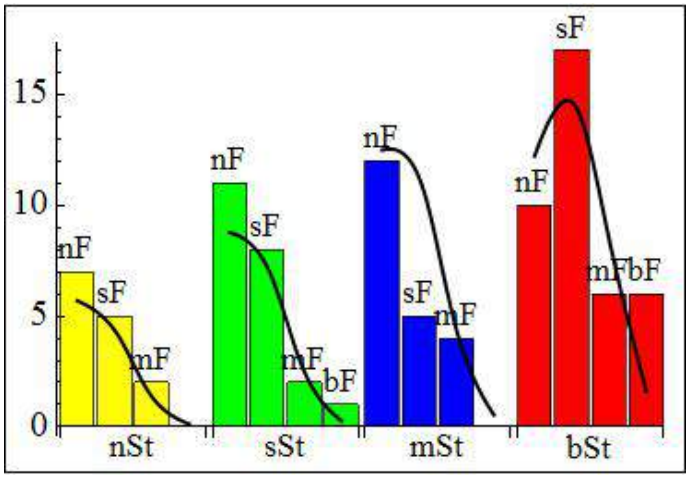

Fig. 3. The frequency distribution of 16 types of the geoeffective events and their best approximation

Figure. 3 shows the frequency distribution of the 16 types of the events and their best approximation calculated by the formula (1), normalized to the setpoint xi = {15; 45; 80; 200} and yj = {0,75; 2,75; 5,5; 10,0}. The values of the five free parameters $\mu_1 = 150\pm15$, $\mu_2 = 2\pm0{,}5$, $\sigma_1 = 91\pm5$, $\sigma_2 = 3\pm0{,}5$ and $\rho = 0{,}3\pm0{,}05$ are defined in accordance to the condition of the discrepancy minimum

$$\Delta(\mu_1, \mu_2, \sigma_1, \sigma_2, \rho) = \sum_{i=1}^{4}\sum_{j=1}^{4}(n_{ij} - k\,N_{ij})^2$$, were ($k = \sum_{i=1}^{4}\sum_{j=1}^{4} n_{ij} / \sum_{i=1}^{4}\sum_{j=1}^{4} N_{ij}$ normalization coefficient).

Hence, the distribution of geoeffective responses on the interplanetary shock passages by 16 types of the events are well described by the binormal distribution. And with the increase of magnetic storm intensity (nSt → sSt → mSt → bSt) share of small CR intensity decreases (sF) grows faster than the share of moderate and big Forbush decreases (mF and bF).

Discussion

The above results shows that the ratio geoeffectiveness of 4 types of the events in geomagnetic field and in CR at the beginning of the 23rd solar cycle is: (F – St) : (F + St) : (St – F) : (– St – F) = 1,1 : 6,1 : 5,4 : 1. This is, in our view, evidence that at the projection of the interplanetary disturbance on the plane perpendicular to the Earth-Sun line, the area responsible for the CR and geomagnetic field decreases does not coincide spatially and displaced from each other in the interplanetary disturbances. Areas with reduced CR located on the flanks of interplanetary disturbances, and the region responsible for the production of magnetic storms - in the central part. Therefore, big geomagnetic storms often accompanied by Forbush effect of low intensity.

This conclusion confirms the earlier results of the authors [12, 13] that the observation of these four types of groundbased responses on the interplanetary disturbances are caused by the geometric factor of the Earth entering to the center or the flanks of the interplanetary disturbance. Also the study are consistent with the results of paper Takeuchi et al. [14] that the IS geoeffectiveness is manifested mainly in the short-term changes of the geomagnetic field and pre-increases or pre-decreases of the CR-intensity, usually but not necessarily followed by Forbush effects. IS produces shock compression of the magnetosphere and generates geomagnetic variations SSC, SC, and I [14], but regular acceleration and scattering of CR particles in the vicinity of the IS generates brief (less than one day) variation of the CR intensity [10].

Conclusions

From analysis presented here we conclude the following.

1. The more is the geomagnetic storm intensity the less is share of small CR intensity decreases versus moderate and large Forbush decreases.

2. The ratio geoeffectiveness of 4 types of the events in geomagnetic field and in CR at the beginning of the 23rd solar cycle is: (F – St) : (F + St) : (St – F) : (– St – F) = 1,1 : 6,1 : 5,4 : 1. So< the frequency of observations of the geomagnetic storms, accompanied by CR intensity decreases is only 10% more than storms without Forbush decreases and 6 times higher than Forbush decreases without storms.

3. Such the ratio geoeffectiveness may be explained by assumption that the areas responsible for the storms and Forbush decreases are displaced in the interplanetary disturbances: the first is located near the central part, and the second is in the flank parts.

References

1. Badruddin (1998), Interplanetary shocks, magnetic clouds, stream interfaces and resulting geomagnetic disturbances. *Planet. Space Sci.,* 35 (7), 1015-1028.

2. Echer E. and W. D. Gonzalez (2004), Geoeffectiveness of interplanetary shocks, magnetic clouds, sector boundary crossings and their combined occurrence. *Geophys. Res. Lett*., 31. L09808, doi:10.1029/2003 GL019199.

3. Chin-Chun Wu and R.P. Lepping (2008), Geomagnetic activity associated with magnetic clouds, magnetic cloud-like structures and interplanetary shocks for the period 1995–2003. *Adv. Space Res.,* 41, 335-338.

4. Xu D., T. Chen, X.X. Zhang, Z. Liu (2009), Statistical relationship between solar wind conditions and geomagnetic storms in 1998–2008. *Planet. Space Sci.,* 57, 1500-1513.

5. Ermolaev Yu.I. et al. (2010), The relative frequency of occurrence and geoeffectiveness of large scale solar wind types. *Cosmic Research,* 48 (1), 1–31.

6. Richardson I.G. and H.V. Cane (2011), Geoeffectiveness (Dst and Kp) of interplanetary coronal mass ejections during 1995–2009 and implications for storm forecasting. *Space Weather,* 9. S07005, doi:10.1029/2011SW000670.

7. Badruddin (2002), Transient modulation of cosmic ray intensity: role of magnetic clouds and turbulent interaction regions. *Astrophys. Space Sci.,* 81, 651-661.

8. Krymsky, G.F. and I.A. Transky (1977), The Forbush-decreases profile and convective shock waves in the interplanetary medium. *in Proc. XV th ICRC,* 3, 181-185.

9. Kudela K. and R. Brenkus (2004), Cosmic ray decreases and geomagnetic activity: list of events 1982–2002. *J. Atmosph. Solar-Terr. Phys.,* 66, 1121-1126.

10. Papailiou M. et. al. (2013), Forbush decreases associated with western solar sources and geomagnetic storms: a study on precursors. *Solar Phys.* doi 10.1007/s11207-013-0231-x.

11. Manoharan P. K. et. al. (2004), Influence of coronal mass ejection interaction on propagation of interplanetary shocks. *J. Geoph. Res.,* 109, A06109. doi:10.1029/2003JA010300.

12. Shadrina L.P., V.P. Mamrukova, I.Ya. Plotnikov (1996) Complex analysis of solar wind disturbances< cosmic ray depressions and geomagnetic storms. G*eomagnetism and aeronomy,* 36 (3), 169-173.

13. Shadrina L.P., S.A. Starodubtsev, I.Ya. Plotnikov (2000), Geophysical manifestations of large-scale solar wind disturbances at intersection of their flanks by the Earth. *in Proc. First S–RAMP, Conf. Sapporo,* 106.

14. Takeuchi T., C.T. Russell and T. Araki (2002), Effect of the orientation of interplanetary shock on the geomagnetic sudden commencement. *J. Geophys. Res.,* 107, 1423-1433.

SPORADIC AND RECURRENT GEOMAGNETIC STORM RESPONSES IN THE HUMAN CARDIOGRAM

L.P.Shadrina[1], S.N. Samsonov[2], V.I. Manykina[2]

[1] Academy of Sciences of Republic of Sakha (Yakutia), Yakutsk, 677007, Russia, e-mail: lushard@mail.ru; [2] Yu.G. Shafer Institute of Cosmophysical Research and Aeronomy of SB RAS, Yakutsk, 677007, Russia

Abstract. The analysis of two types of geomagnetic storms (recurrent and sporadic) responses in human's electrocardiograms was fulfilled. The inhabitants of Yakutsk city and of the geophysical observatory in Tiksi Bay, which are located near the auroral zone, were included in the selection. It was shown that with the beginning of a storm the increase of the parameter characterizing a condition of a human cardiovascular system (a symmetry coefficient of a T-wave of the electrocardiogram) was observed. Maximum values were reached on the first day after the sporadic storms beginning and two days before Dst minimum for a recurrent storms.

Introduction

Despite of the obvious successes of cardiology which revealed a number of risk factors for cardiovascular diseases still remain unclear start reason of a sharp developing coronary insufficiency and the role of external factors in this process.

The aim of our work is to analyze the dependence of the human cardio-vascular system from the geomagnetic conditions (during two types of magnetic storms) by the example of inhabitants of Yakutsk city and of polar village Tiksi. The experiment on registration of electrocardiogram parameter characterizing the state of cardio-vascular system was carried out in October-November 2009 and March-April 2011 with groups of volunteers from Yakutsk (30) and Tiksi (17). The results were compared with the geomagnetic storms.

The parameters of 11 geomagnetic storms during the experiment – date, hour of the storm onset, main phase duration (Δt), low latitude Dst-index amplitude (ΔDst), class of the storm (S – small, M – moderate), sum of the high latitude index AE for the main phase of the storm (ΣAE), parameter β and storm type (sporadic or recurrent) – are shown in the Table.

Table. Dates and geomagnetic storm parameters

№	Date	Begin	Δ t	Δ Dst	Class	Σ AE	β	Type
1	23.10.2009	16	12	48	S	3746	0,0128	spor
2	25.10.2009	18	12	44	S	2594	0,0170	spor
3	30.10.2009	14	20	54	M	3610	0,0150	spor
4	08.11.2009	10	12	39	S	3651	0,0107	rec
5	01.03.2011	10	6	84	M	3358	0,0250	spor
6	11.03.2011	01	31	84	M	15153	0,0055	rec
7	01.04.2011	17	11	52	S	5191	0,0099	rec
8	06.04.2011	10	11	67	M	8022	0,0084	rec
9	08.04.2011	15	13	40	S	4436	0,0090	rec
10	11.04.2011	17	18	79	M	3930	0,0201	spor
11	19.0402011	23	11	42	M	3313	0,0127	spor

Storm class was determined using the Dst index amplitude – the difference among maximum and minimum values of the index in main phase of the storm. According to [2, 3] storms are divided into 5 classes according to their Dst value: those with the amplitude of Dst from 31 to 50 nT are small (S); from 51 to 100 nT, moderate (M); from 101 to 150 nT, big (B); from 151 to 200 nT, very big (Vb); and if the amplitude of Dst is more than 200 nT, the storm is extra- or superstorm (Ex). As one can see from the Table, during two investigated intervals there were 5 moderate (M) and 6 small (S) geomagnetic storms.

The division of storms into sporadic and recurrent types is in some degree associated with the source generating them. Sporadic storms are caused by the flare streams of the solar wind but recurrent ones are generated by long-lived high speed streams. In [4] it was suggested to use parameter β calculated by the formula $\beta = \Delta Dst / \Sigma AE$, where Σ AE is a sum of AE index during storm main phase Δt, and Δ Dst is amplitude of Dst index. The introduction of the parameter was based on the idea that these indices characterize the energy input from the interplanetary medium into the magnetosphere during the storm main phase: ΣAE, into the auroral region; ΔDst, into the equatorial (ring current). It was shown [4] that parameter β is differs significantly for two types of storms. The storms of sporadic (flare) type have $\beta < 0{,}0100$, and recurrent ones have $\beta > 0{,}0120$. Thus the value of β can be used to determine the storm type – sporadic (sp) or recurrent (rec). Calculated values of ΣAE and β and storm types are shown in three last columns of the Table. There were 6 sporadic (3 moderate and 3 small) and 5 recurrent (2 moderate and 3 small) storms during the investigated intervals.

Results and discussion

A symmetry coefficient of T-wave of the electrocardiogram (parameter T of ECG) was selected for this study. The value or amplitude of the waves is one of the main indicators used for the ECG interpretation [5]. View of ECG teeth and spaces between them depends on how the phases of excitation and relaxation of the cardiac muscle alternate. ECG teeth appear and grow in moments when certain areas of myocardium work, while others are at rest. In a normal ECG T wave is positive and asymmetric (it has slightly sloping upward and sharper downward knee). As it was shown in some studies, an increase in the symmetry coefficient of T wave often indicates various violations in the heart muscle state. Detailed description of the method of parameter T measurement procedure used in this experiment was presented in paper [6].

The parameter T varies from 0.2 to more than 3.0. An example of this parameter measurements in a group of volunteers from the institute IKFIA SB RAS (Yakutsk) between March 1 and April 29, 2011 is shown at Fig. 1. One can see that for some individuals the oscillation amplitude of this parameter is high but for the others it is rather small. Preliminary analysis shows that the variation limits of the parameter T mean value significantly depends on the age.

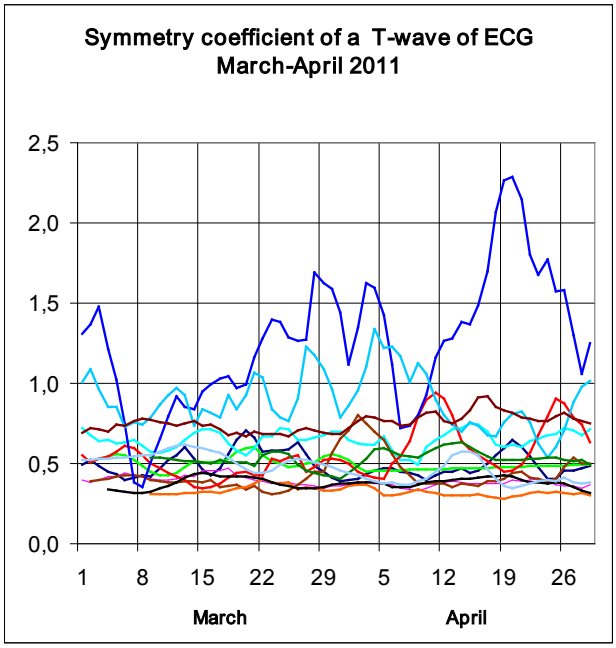

Fig. 1. An example of measurements of symmetry coefficient of T-wave of the ECG for the 13 inhabitance of Yakutsk city in 2011

Fig. 2 shows the diagram of the age of experiment participants (left scale, columns and subscribes) and corresponding mean values of parameter T (right scale, curve). One can see a trend as a linear dependence between those two values.

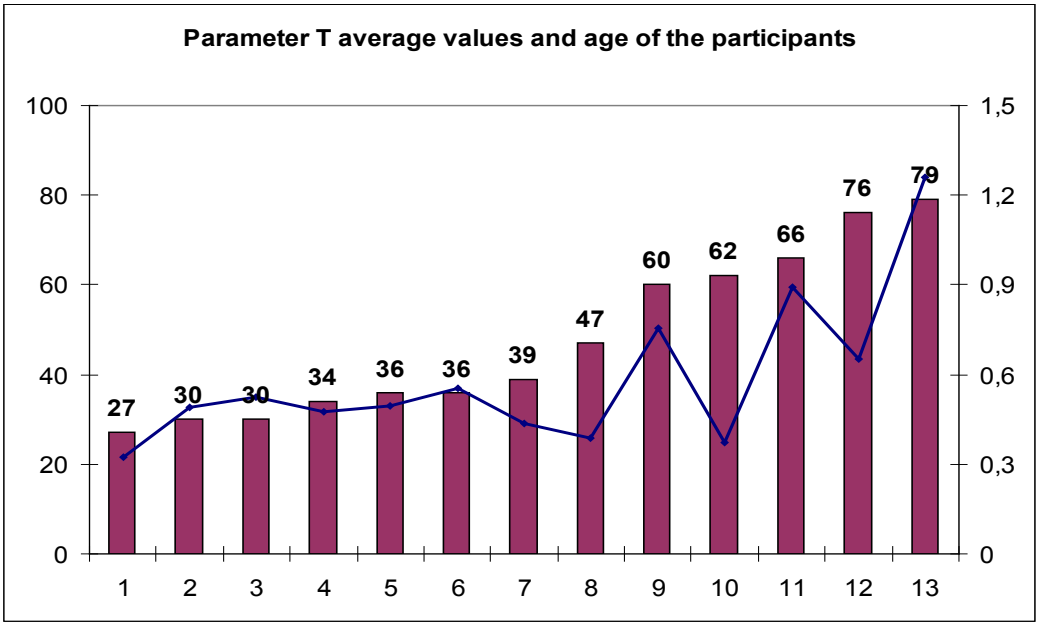

Fig. 2. Mean values of symmetry coefficient of T-wave of the ECG (right scale, broken curve) and the age of experiment participants (left scale, columns and subscribes) for the 13 inhabitance of Yakutsk city in 2011

As it was noted above, the parameter T changes regularly (Fig. 1), and of course not all increases are caused by storm disturbances. To find the connection of it changes with the geomagnetic storms we calculated the amount of maximums of this indicator during two types of storms (sporadic and recurrent) for the time intervals from −2 to +3 days corresponding to the storm onset. Day of Dst minimum is 0-day of the storm. The results are shown on Fig. 3. One can see that for the sporadic storms the greatest number of parameter T maximums appears on the first day after the Dst minimum. For the recurrent storms, the greatest number of parameter T maximums occurs on the second day before the Dst minimum, i.e. people feel the approach of those storm beforehand.

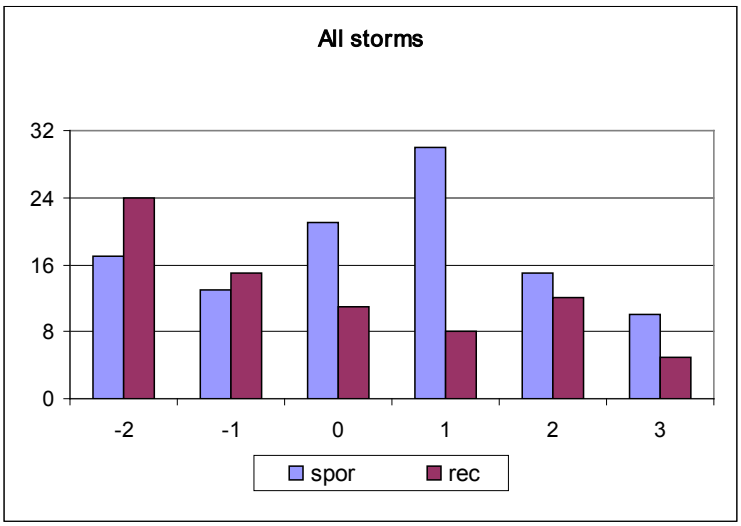

Fig. 3. Amount of parameter T maximums respective to the geomagnetic storm's onsets for the time intervals from −2 to +3 days for the sporadic (spor) and recurrent (rec) storms

To verify what is the relationship of parameter T changes with the storm intensity, similar histograms were made for small and moderate storms (Fig. 4). There is an increase in parameter T maximum amount on −2 day before the storm beginning for sporadic storms too, but it is lower than on the +1 day after the storm beginning both for small and for moderate intensity storms. For recurrent storms there is a pronounced maximum on the −2 day before the storm for small ones, but for moderate storms there is a small increase on the 0-day of the storm.

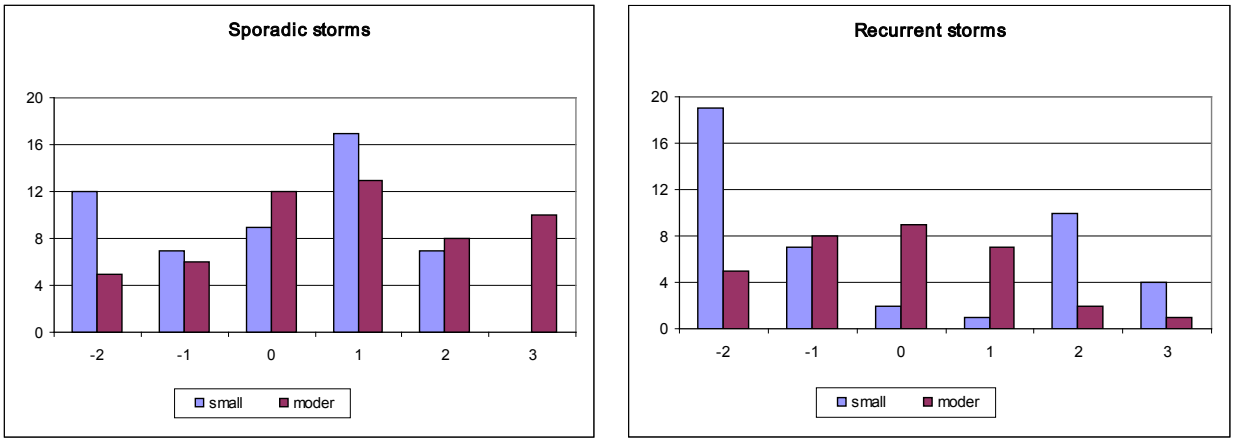

Fig. 4. The number of parameter T maximum for small and moderate sporadic (left) and recurrent (right) storms

It should be noted that geomagnetic storms are not the only factor causing the parameter T change. All people have some maximums of this parameter in geomagnetically quiet time or during the recovery phase of the storm along with the maximums on days, close to the 0-day of a storm. However, associated with storms parameter T growth, on average, make up more than a half of all the peaks, and for older people this relation is manifested more clearly.

Conclusion

Thus, the comparison of the amount of maximums of symmetry coefficient of T-wave of ECG (parameter T maximums) in groups of volunteers with geomagnetic conditions showed:

1. Human cardiac activity indicators, in particular, a symmetry coefficient of T-wave of ECG has a relationship with geomagnetic storms

2. During sporadic storms the greatest number of parameter T maximums appears at the first day after the storm beginning.

3. For recurrent storms the greatest number of parameter T maximums occurs at the second day before the storm beginning. The same but more week increase takes place for the small sporadic storms.

Acknowledgements. The work was financially supported by RFBR grant No. 12-02-98508-p_vostok_a.

References

1. Breus T.K. (2009), Cosmic weather influence to the biological objects. *Earth and Universe,* 3, 53-62.

2. Gonzalez,W.D. et. al. (1994), What is a geomagnetic storm. *J. Geophys. Res.*, 99, 5771-5792.

3. Ermolaev Yu.I., M.Yu. Ermolaev (2002), Statistical relationships among solar, interplanetary and geomagnetic disturbances, 1976–2000, *Cosmic Research,* 40 (1), 3-16.

4. Shadrina L.P., V.G. Vasilieva (2001), Numeric parameter for the geomagnetic storm class determination. *Investigations on geomagnetism, aeronomy and solar physics,* 112, 163-167.

5. Murashko V.V., A.V. Strutinsky (1991), *Electrocardiography,* Moscow, Medicine Publ.Co., 288 pp.

6. Manikina V.I., S.N. Samsonov (2008), Influence of heliogeophysical activity on a functional state of cardiovascular systemof human being, *in: Proc. XXXI Annual Seminar "Physics of Auroral Phenomena",* Apatity, 206-209.

7. Gurfinkel' Yu.I. (2004), *Coronary heart disease and solar activity,* Moscow, Publ. Co. "El'f-3", 170 pp.

EARTH MAGNETIC FIELD DISTURBANCES AND ACTIVE EXPERIMENTS IN THE IONOSPHERE

V.P. Sivokon', N.V. Cherneva, S.Yu. Khomutov, A.S. Serovetnikov

Institute of Cosmophysical Research and Radio Wave Propagation (IKIR) FEB RAS, 684034, Russia,
e-mail: nina@ikir.ru

Abstract. Variations of the ionosphere-magnetosphere energy relation, as one of possible outer climatology factors, may be traced on the basis of analysis of natural geophysical phenomena such as ionosphere artificial radio radiation and magnetic storms. Experiments on active impact on the ionosphere have been carried out during quite a long time in Russia as well. The most modern heating stand is located in Alaska; it has been used in the HAARP Program. The possibility of this stand to affect geophysical fields, in particular, the geomagnetic field is of interest.

Introduction

Ionosphere property changes under the influence of powerful radio wave were first detected in 1933 and it is known as a Luxemburg-Gorkov'skiy effect (Ginzburg, 1960; Gurevich, A.V., 2007). Intensive investigations of ionosphere modification, which were begun in 60-es of the last century, were stopped in 90-es. At present, such investigations in Russia are carried out at Sura test stand (Nizhniy Novgorod, NIRFI). There are several programs within which modification is studied and the effect technology on the ionosphere is developed. The most famous of them is HAARP (High Frequency Active Auroral Research Program). Investigations on this program are carried out in Alaska, not far from Gakona with geographic coordinates 62°23′36″ N, 148°08′03″W. As an instrumentation to affect the ionosphere a powerful electromagnetic radiation in decameter range is used. The radiation effective power is of hundreds of megawatt and the radiation frequency range is 2.8÷10.0 MHz.

Data and methods

Experiments, carried out within the program, also included investigations on possible operation of ionosphere-magnetosphere coupling. In order to do that, electrojet, natural current structure, located in the ionosphere at E layer level, was affected. Current variations in electrojet lead to the Earth magnetic field disturbance. To evaluate the possibility of the stand to affect the Earth magnetic field we used the results described in (Cohen, 2009) in comparison with decameter range spectrograms from HAARP site http://www.haarp.alaska.edu/data/spectrum2/www/hf.html. It follows from the comparison that evident variations of the Earth magnetic field are possible when highest harmonics of a heating wave appear on the spectrogram, i.e. when the effect is quite intensive. Thus, we make a sampling of the experiments according to their intensity and duration. As an initial suggestion we accept that a heating experiment may have an effect in the Earth magnetic field when there are highest harmonics of a heating wave on a spectrogram and its duration is not less than half an hour, i.e. the effect is powerful and long. Processing of spectrograms from HAARP program data base has shown that there are 55 such heating experiments for 2007-2013 from the total number of 24277 which is small enough. The obtained sampling of extreme heating experiments was compared to the level of geomagnetic disturbance which was evaluated by planetary Kp-index data provided by WDC on geomagnetism, Kyoto, http://wdc.kugi.kyoto-u.ac.jp/kp/index.html. Fig. 1 shows Kp values on the days of HAARP intensive sessions (55 days).

It is clear from the graph that on the days of intensive heating session both disturbed and calm magnetic field was registered. Evident disturbances with Kp>20 were registered on 14 out of 55 days. These days will be further considered since significant effects of heating experiments are of interest.

We should note that on separate days during intensive effect on the ionosphere there was no any reaction of the Earth magnetic field. The strongest disturbance of the Earth magnetic field was on April 5, 2010, which

coincided in time with the experiments of active effect on the ionosphere. Fig. 2 shows the comparison of the time of effect with the beginning of the geomagnetic storm. In the first case the disturbance began before the active experiment, in the second case it coincides with the disturbance development.

For the further analysis we apply the data of a magnetic station network in Alaska (the University of Alaska Fairbanks, https://www.asf.alaska.edu/magnetometer). Temporal relations between the beginning of magnetic disturbances and HAARP sessions were considered and the days when sessions preceded or coincided with disturbances were chosen (Fig.3).

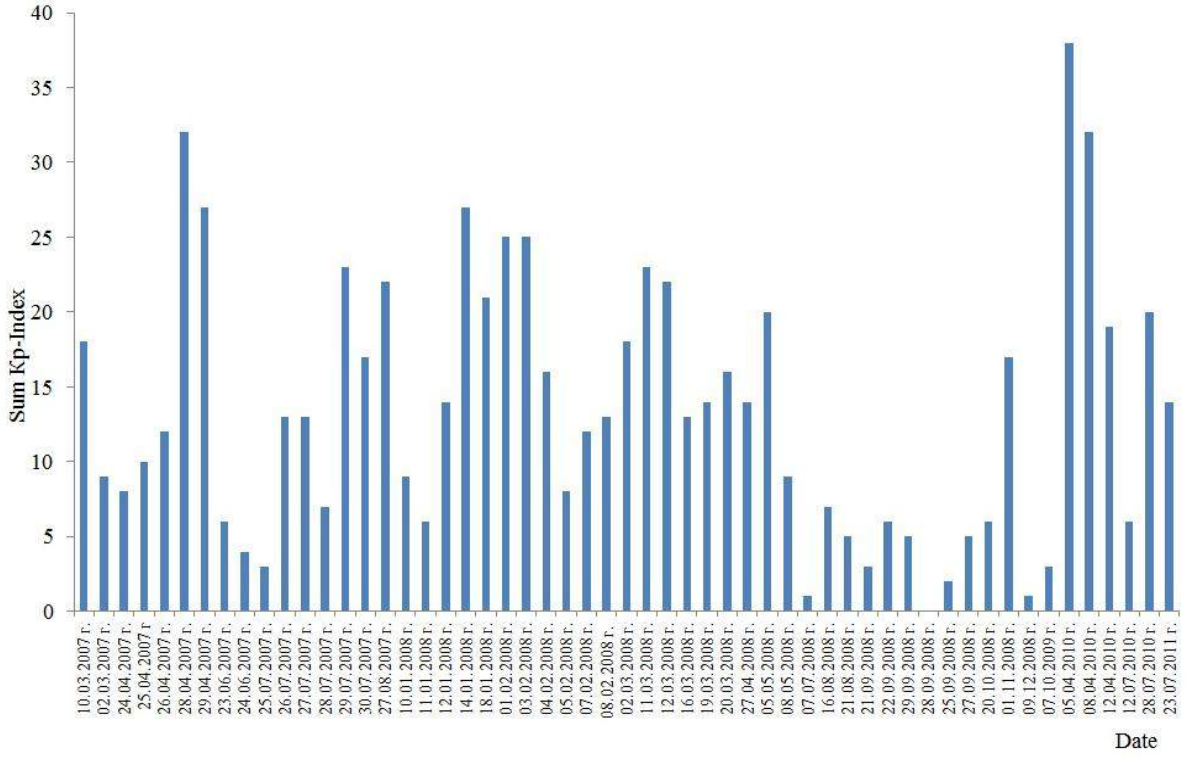

Fig. 1. Planetary magnetic Kp-index on the days of HAARP intensive heating experiments.

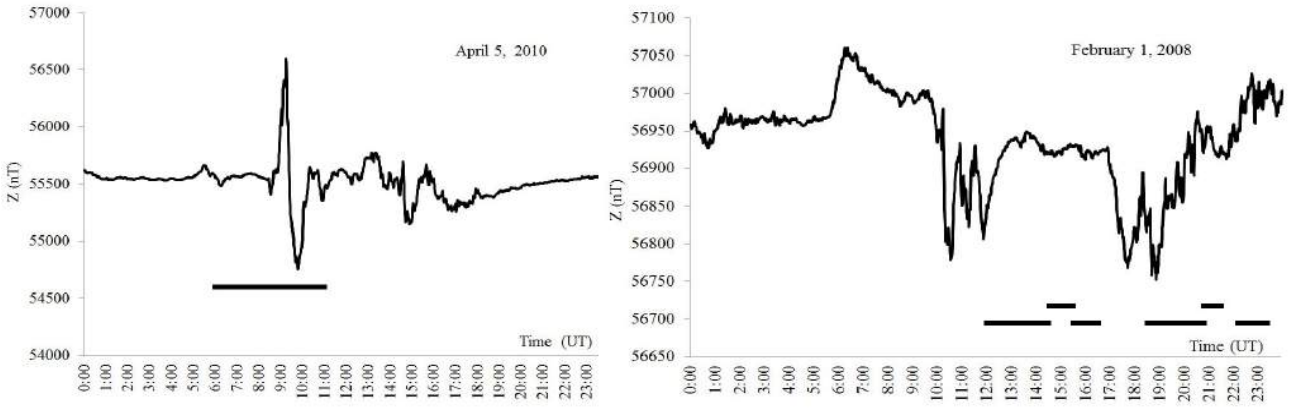

Fig.2. Comparison of effect time with geomagnetic storm beginning. Straight line shows the duration of the effect experiments on the ionosphere, in the right figure is the magnetic disturbance before active effect, in the left figure they coincide.

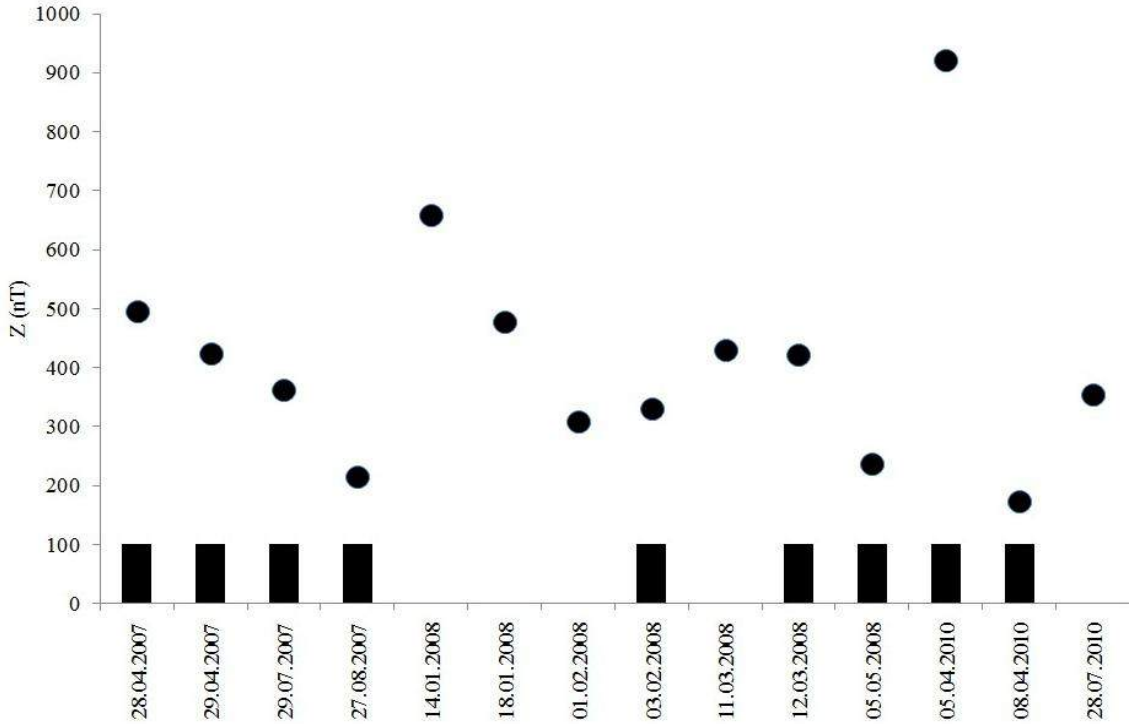

Fig.3. Earth magnetic field variations during disturbances (Kp>20) on the days of intensive heating experiments. Rectangular indicate HAARP operation days, when the beginning of sessions preceded magnetic disturbances, circles show geomagnetic variation amplitudes at the disturbance maximum phases.

Conclusions

The results of Fig. 3 show that:

1. Five out of fourteen magnetic storms are possibly not associated with the experiments on active effect on the ionosphere.
2. The strongest disturbance of the Earth magnetic field was on April 5, 2010, which coincides in time with the experiments of active effect on the ionosphere.
3. The obtained results do not contradict with the suggestion that active effect on the ionosphere may locally modify ionosphere-magnetosphere coupling.
4. Local modification of the ionosphere may be a trigger for energy release from the magnetosphere into the ionosphere which in a number of cases may lead to magnetic storms.
5. Active effect on the ionosphere to regulate energy release via the ionosphere-magnetosphere channel may reduce the risk of destructive effects of magnetic storms on anthropogenic systems.

References

Ginzburg, V.L., Gurevich, A.V. (1960), Nonlinear phenomena in plasma in a variable electromagnetic field, *Physics-Uspekhi*, V. LXX. I.3, 393-428.

Gurevich, A.V. (2007), Nonlinear phenomena in the ionosphere, *Physics-Uspekhi*, V.177, No 11, 1145-1177.

Cohen, J. (2009), *Excitation of forced ion acoustic waves, large plasma sheets, and magnetic field fluctuations over Gakona, Alaska*, Plasma Science and Fusion Center, Massachusetts Institute of Technology, Cambridge, USA, 77.

GENERAL RELATIONS FOR PARTICLE DIFFUSION IN PITCH ANGLE AND ENERGY

S.V. Smolin

Department of Theoretical Physics, Siberian Federal University,
Krasnoyarsk, 660041, Russia, e-mail: smolin@krasu.ru

Abstract. General expressions for particle diffusion coefficients in both pitch angle and energy are obtained. Simple relations between the diffusion coefficients are found. The results illustrate how particle diffusion coefficients vary with pitch angle, energy and other parameters in the Earth's magnetosphere.

1. Introduction

Earlier standard quasi-linear diffusion theory has been used to evaluate dynamic changes of particle fluxes in the radiation belts. Using the quasi-linear diffusion theory to model radiation belt dynamics requires at least two kinds of computations: numerical solution of a diffusion equation, which is a one-dimensional or multi-dimensional Fokker-Planck equation, depending on diffusion processes we are interested in, and calculation of diffusion coefficients. In this work is offered other variant for particle diffusion coefficients in pitch angle and energy. Particle diffusion coefficients in dependence on pitch angle, energy and other parameters in the Earth's magnetosphere will be studied.

2. Diffusion coefficients and numerical results

Using [1], the following equations of motion of particles are received

$$\frac{d\alpha}{dt} = -\frac{\sin\alpha\cos\alpha}{2L}\frac{dL}{dt}, \tag{1}$$

$$\frac{dE}{dt} = -\frac{E(\sin^2\alpha + 2)}{L}\frac{dL}{dt}. \tag{2}$$

Here, t is the time, α is the local pitch angle, E is the energy, L is the McIlwain parameter, $d\alpha/dt$ is the pitch angle rate, dE/dt is the energy rate.

These equations describe the evolution of pitch angle and energy in the velocity space.

Further we use results [2] for definition of diffusion coefficients. Therefore the pitch angle diffusion coefficient is determined so [3]

$$D_{\alpha\alpha} = D_{\perp}\sin^2\alpha = \frac{1}{\gamma_{\perp 0}(\gamma_{\perp 0}+2)T_{wp}}\sin^2\alpha\ , \tag{3}$$

$$T_{wp} = k\frac{2R_E L^4\sqrt{4L-3}\sqrt{m}}{\sqrt{2EL}}(1-0.15Kp)\ , \tag{4}$$

where $\gamma_{\perp 0}$ is the pitch angle anisotropy index for $\alpha = 90°$ and $t = 0$, T_{wp} is the lifetime due to wave-particle interactions, k is the variable parameter, R_E is the average radius of the Earth, m is the mass of a particle, Kp is the index of geomagnetic activity.

The energy diffusion coefficient is determined as follows [4]

$$D_{EE} = \frac{4E^2 D_{\perp}(\sin^2\alpha + 2)^2}{\cos^2\alpha}. \tag{5}$$

Further for an example we shall solve the non-stationary one-dimensional equation of "pure" pitch angle diffusion. This equation is solved numerically using the finite element projection method with initial and boundary conditions [3].
The dynamics of the protons during the magnetic storm, similar to that on 1 - 7 May 1998 [5], is studied. The Kp index changes as a function of the run time RT during the magnetic storm on 5 - 7 May 1998 (00:00 RT = 04:00 UT on 5 May, 68:00 RT = 00:00 UT on 8 May).
Figure 1 summarizes the model evolution of the proton pitch angle distributions and the perpendicular pitch angle diffusion coefficients for E = 20 keV, MLT = 19:30, L = 3.5 (left column); for E = 10.82 keV, MLT = 15:00, L = 4 (right column) during the magnetic storm on 5 - 7 May 1998 (00:00 RT = 04:00 UT on 5 May, 68:00 RT = 00:00 UT on 8 May) for different coefficients k, determining under the formula (4) various lifetime due to wave-particle interactions.

3. Conclusion

General expressions for particle diffusion coefficients in both pitch angle and energy are obtained.
Simple relations between the diffusion coefficients are found.
The dynamics of the protons (E = 20 keV and E = 10.82 keV) in the inner magnetosphere (L = 3.5, MLT = 19:30 and L = 4, MLT = 15:00) during the magnetic storm on 5 - 7 May 1998 is studied.

References

1. Pudovkin, M.I., and S.V. Smolin (1988), Particle pitch angle distribution in the convecting magnetospheric plasma, *Geomagnetism and Aeronomy*, 28(2), 268-271 (in Russian).
2. Lyons, L.R., and D.J. Williams (1984), *Quantitative aspects of magnetospheric physics*, 312 pp., Springer, New York.
3. Smolin, S.V. (2012), Modeling of pitch angle distribution on the dayside of the Earth's magnetosphere, *Journal of Siberian Federal University. Mathematics & Physics*, 5(2), 269-275 (in Russian).
4. Smolin, S.V. (2013), Three-dimensional model of the evolution of the ring current protons during the magnetic storm in the Earth's magnetosphere, *Journal of Siberian Federal University. Mathematics & Physics*, 6(2), 270-276.
5. Jordanova, V.K., L.M. Kistler, J.U. Kozyra, G.V. Khazanov, and A.F. Nagy (1996), Collisional losses of ring current ions, *J. Geophys. Res.*, 101(A1), 111-126.

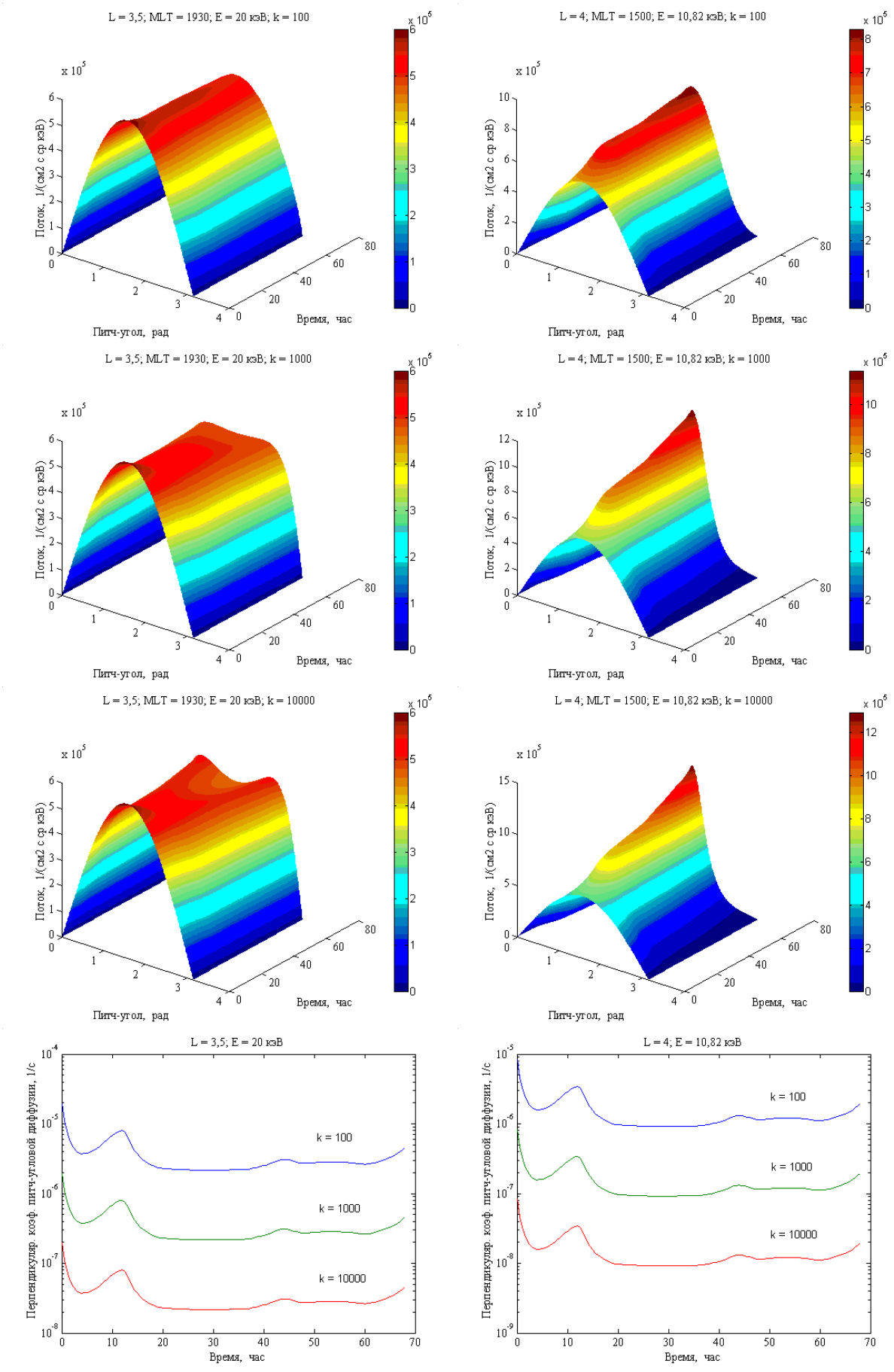

Figure 1. Model evolution of the proton pitch angle distributions and the perpendicular pitch angle diffusion coefficients during the magnetic storm on 5 - 7 May 1998 for different coefficients k (formula (4)).

MODELING OF PROTON RING CURRENT DYNAMICS WITH VARIABLE BOUNDARY CONDITIONS

S.V. Smolin

Department of Theoretical Physics, Siberian Federal University,
Krasnoyarsk, 660041, Russia, e-mail: smolin@krasu.ru

Abstract. The dynamics of the ring current protons with variable boundary conditions in the inner magnetosphere during the magnetic storm is studied. The temporal and spatial evolution of the proton phase space densities in a dipole field is calculated using a two dimensional ring current model, considering radial and pitch angle diffusions. The loss terms are described due to charge exchange and wave-particle interactions. The simulation starts with a quiet time distribution. The model is tested by comparing calculated proton fluxes with Polar/MICS measurement during the magnetic storm on 21 - 22 October 1999.

1. Introduction

During the magnetic storm, energetic plasmas are injected on the nightside from a boundary near the geosynchronous orbit. In response to the convection electric field, these particles drift inward and are trapped by the geomagnetic field and form the storm time ring current. The dynamics of the ring current protons during the main phase of a magnetic storm will be studied.

2. The mathematical model

The 2D Fokker-Planck equation for the phase space density, describing radial and pitch angle diffusions, charge exchange and due to wave-particle interactions losses, can be expressed by [1 - 3]

$$\frac{\partial f}{\partial t} = L^2 \frac{\partial}{\partial L}\left(L^{-2} D_{LL} \frac{\partial f}{\partial L}\right) + \frac{1}{\sin\alpha}\frac{\partial}{\partial \alpha}\left(\sin\alpha \cdot D_{\alpha\alpha} \frac{\partial f}{\partial \alpha} - \sin\alpha \frac{d\alpha}{dt} f \right) - \\ - \lambda \cdot f - \frac{f}{T_{wp}} + S_{\perp} \sin^2 \alpha \cdot f. \qquad (1)$$

Here, f is the phase space density (referred to as distribution function), t is the time, L is the McIlwain parameter, α is the local pitch angle, D_{LL} is the radial diffusion coefficient, $D_{\alpha\alpha}$ is the pitch angle diffusion coefficient, $d\alpha/dt$ is the pitch angle rate, λ is the loss rate for protons against neutralization by charge exchange, T_{wp} is the lifetime due to wave-particle interactions, $S_{\perp}$ is the perpendicular coefficient of the particle source function.

The simulation starts with quiet time conditions [4, 5]. The ion composition compiled by Sheldon and Hamilton [4] during the quietest days in 1985-1987, seen by the AMPTE/CCE/charge-energy-mass (CHEM) instrument in near-equatorial orbit at L = 2 - 9 R_E, is used as initial distribution before storm onset. This data set provides average differential ion fluxes in an energy range 1 - 300 keV.

Variable boundary conditions on the nightside (MLT = 23:00, E = 90 keV, k = 353) for L = 2.26 and L = 6.6 have been certain, solving the non-stationary one-dimensional equation of "pure" pitch angle diffusion [3].

The dynamics of the ring current protons during the magnetic storm, similar to that on 21 - 22 October 1999 [6], is studied. The Kp index is show in Fig. 1 as a function of the run time RT during the magnetic storm on 21 - 22 October 1999 (00:00 RT = 06:13 UT on 21 October 1999, 20:00 RT = 02:13 UT on 22 October 1999).

Further, the equation (1) is solved numerically using the finite element projection method with initial and variable boundary conditions.

3. Calculations

Figure 2 summarizes the model evolution of the proton pitch angle distributions for E = 90 keV, MLT = 23:00, L = 2.26 – 6.6, k = 353 at 00:00 RT = 06:13 UT on 21 October 1999 (prestorm condition), 04:00 RT and 08:00 RT, respectively.
Figure 3 summarizes the model evolution of the proton pitch angle distributions for E = 90 keV, MLT = 23:00, L = 2.26 – 6.6, k = 353 at 12:00 RT, 15:00 RT and 18:00 RT = 00:13 UT on 22 October 1999 (storm main phase), respectively.
Figure 4 compares the proton pitch angle distributions observed by Polar/MICS for E = 80 - 100 keV, L = 5, MLT = 22.9 - 23.2. Lines (circles and squares) indicate the differential flux at 00:00 RT = 06:13 UT on 21 October 1999 (prestorm condition) and 18:02 RT = 00:15 UT on 22 October 1999 (storm main phase), respectively. Dashed and solid lines indicate the model differential flux (L = 5, MLT = 23:00, E = 90 keV, k = 353) at 00:00 RT and 18:00 RT = 00:13 UT on 22 October 1999, respectively. The pitch angle distribution is pancake-like in the prestorm condition, while it becomes butterfly-like in the storm main phase. The same tendency is seen in, for example, [6].

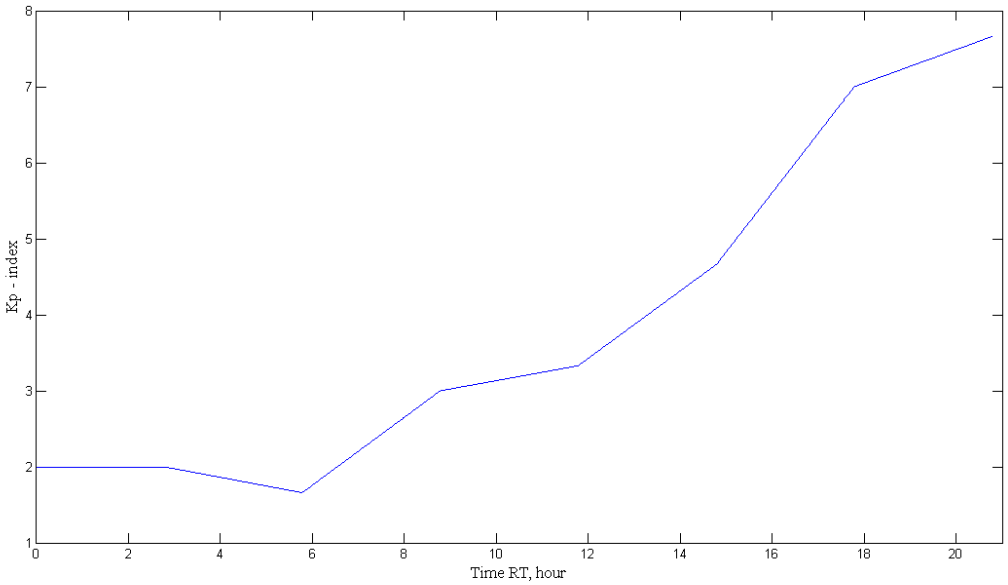

Figure 1. Kp – index as a function of the run time RT during the magnetic storm on 21 - 22 October 1999 (00:00 RT = 06:13 UT on 21 October 1999, 20:00 RT = 02:13 UT on 22 October 1999).

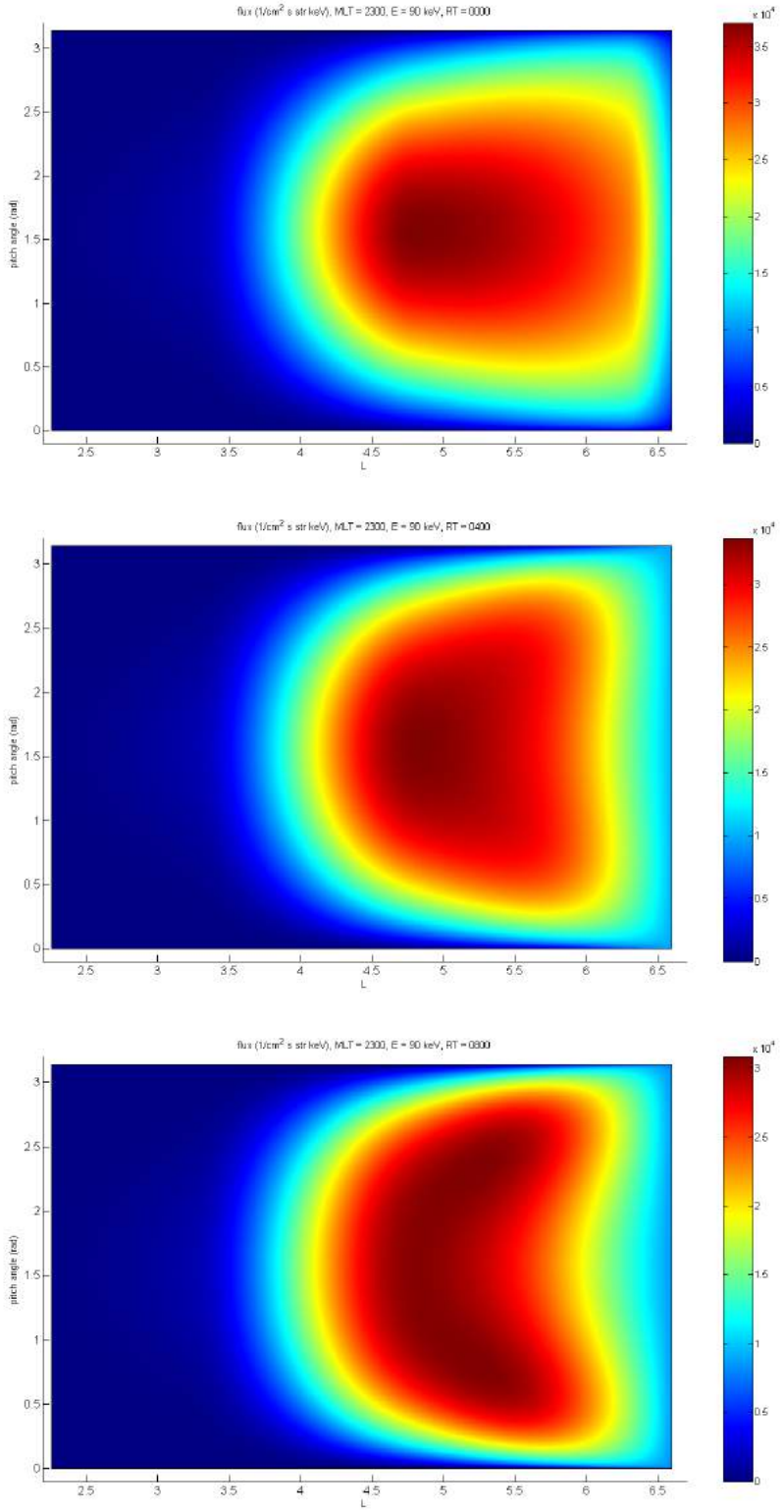

Figure 2. Model evolution of the proton pitch angle distributions for E = 90 keV, MLT = 23:00, L = 2.26 – 6.6, k = 353 at 00:00 RT = 06:13 UT on 21 October 1999 (prestorm condition), 04:00 RT and 08:00 RT, respectively.

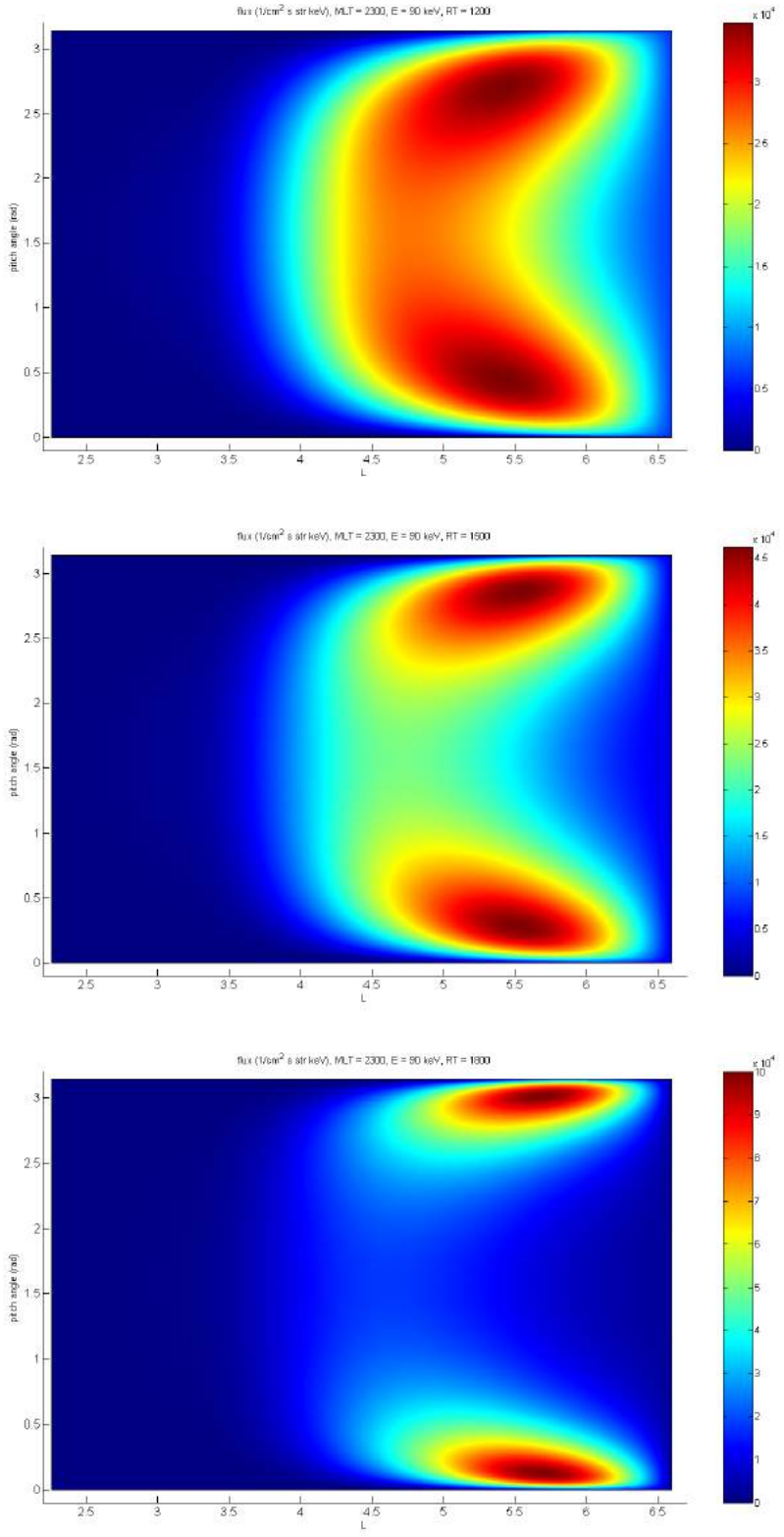

Figure 3. Model evolution of the proton pitch angle distributions for E = 90 keV, MLT = 23:00, L = 2.26 – 6.6, k = 353 at 12:00 RT, 15:00 RT and 18:00 RT = 00:13 UT on 22 October 1999 (storm main phase), respectively.

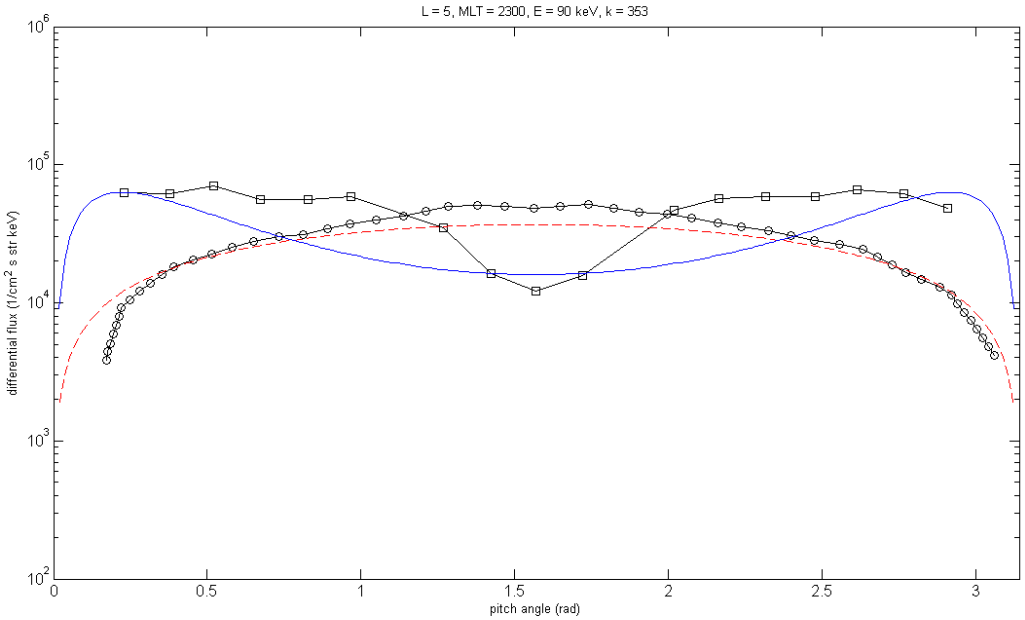

Figure 4. Pitch angle distributions of protons measured by Polar/MICS for E = 80 - 100 keV, L = 5, MLT = 22.9-23.2. Lines (circles and squares) indicate the differential flux at 00:00 RT = 06:13 UT on 21 October 1999 (prestorm condition) and 18:02 RT = 00:15 UT on 22 October 1999 (storm main phase), respectively. Dashed and solid lines indicate the model differential flux (L = 5, MLT = 23:00, E = 90 keV, k = 353) at 00:00 RT and 18:00 RT = 00:13 UT on 22 October 1999, respectively.

4. Conclusion

The development of the ring current protons (E = 90 keV) in the inner magnetosphere (L = 2.26 - 6.6, MLT = 23:00) during the magnetic storm on 21 - 22 October 1999 is studied.
The pitch angle distribution is pancake-like in the prestorm condition, while it becomes butterfly-like in the storm main phase.

References

1. Smolin, S.V. (1996), *Modeling of the pitch angle diffusion in the Earth's magnetosphere*, 205 pp., Publishing Company "Libra", Krasnoyarsk (in Russian).
2. Smolin, S.V. (2010), Effect of magnetospheric convection on the energy distribution of protons from the Earth radiation belts, *Geomagnetism and Aeronomy*, 50(3), 298-302.
3. Smolin, S.V. (2012), Modeling of pitch angle distribution on the dayside of the Earth's magnetosphere, *Journal of Siberian Federal University. Mathematics & Physics*, 5(2), 269-275 (in Russian).
4. Sheldon, R.B., and D.C. Hamilton (1993), Ion transport and loss in the Earth's quiet ring current. 1. Data and standard model, *J. Geophys. Res.*, 98(A12), 13,491-13,508.
5. Fok, M.-C., T.E. Moore, and M.E. Greenspan (1996), Ring current development during storm main phase, *J. Geophys. Res.*, 101(A7), 15,311-15,322.
6. Ebihara, Y., M.-C. Fok, J.B. Blake, and J.F. Fennell (2008), Magnetic coupling of the ring current and the radiation belt, *J. Geophys. Res.*, 113, A07221, doi: 10.1029/2008JA013267.

GEOMAGNETIC OBSERVATIONS AT PAVLOVSK OBSERVATORY IN 1878-1914

S.N. Sokolov, V.A. Soldatov

SPbF IZMIRAN, St.Petersburg, 199034, Russia, e-mail: sergnsokolov@yandex.ru

Abstract. Magnetic and meteorological observations at Pavlovsk observatory were conducted from 1878 to 1941. Most results of observations made before 1914 were scanned at NOAA in 2000 and are now available to the public (http://docs.lib.noaa.gov/rescue/data_rescue_russia.html). These measurements over the years were published in 1879-1916 and are available in a few libraries and archives. Only data on average annual declination (D), horizontal (H) and vertical (Z) components of the geomagnetic field in Pavlovsk is available in World Data Centers (Kyoto and Edinburgh). Hourly values of D, H and Z, as well as inclination, north and west field components in Pavlovsk are given in the original form of monthly tables. We have transferred them to a digital format by hand, visually, as some pages of paper originals are worn-out and contain a significant amount of text fragments, poorly recognizable by OCR software. As an intermediate result, we have produced tables of the geomagnetic field elements for 1878-1911 and 1914 in form similar to the original (useful for comparison with paper version and error checking). The data then has been converted into time series (in netCDF format) which is more suitable for further processing and analysis. This database (http://db.izmiran.nw.ru/geomag) may be useful to study different variations of the geomagnetic field, for example, magnetic storms, and reconstruct the solar wind at 12-14th cycles of solar activity.

Introduction

The task of preserving and putting data of relatively few observations of magnetic observatories, as well as expeditions conducted geomagnetic observations in the 19th - early 20th centuries, into scientific use cannot be solved without the transfer of analog data into digital format.

The body of digitized data from observatories conducted hourly magnetic measurements in the years and collected in the World Data Center, is gradually increasing. However, until now such data is available only since 1883; it includes observations of a single observatory in 1883-1886, 2-3 observatories in 1887-1896, 4-5 in 1897-1901, 8-9 in 1902-1906, 10-11 in 1907-1910 and 12 in 1911-1914 (http://www.wdc.bgs.ac.uk/catalog/master.html). From Russian observatories, the digitized hourly data is available only for the observatory Ekaterinburg (for 1887-1924).

In Russia, a network of stationary observatories performing geomagnetic and meteorological observations on a single program, was established in 1830s. In the 1840-1860s the network included St. Petersburg, Kazan, Tiflis, Ekaterinburg, Barnaul, Nertchinsk, Sitka and Peking [e.g. Raspopov et al., 2009; Nevanlinna, Häkkinen, 2010]. Later in the 1870s-1900s, the number of Russian observatories conducting geomagnetic measurements decreased. In these years, hourly observations were carried out only in St. Petersburg (1873-1877) and its suburb Pavlovsk (since 1878); in Irkutsk the observations (every three hours) were conducted since 1905.

The primary supervising observatory was in St. Petersburg (Pavlovsk). Continuous surveillance last here until August 1941, which gave the opportunity to get one of the longest in the world series of observations of declination (D), horizontal (H) and vertical (Z) components of the field. In 1941, the Pavlovsk observatory was evacuated and 1946 observations resumed in another suburb of Petersburg, Voeikovo.

The program of observations in Pavlovsk was coordinated with the programs of other observatories of the world; correspondence and data exchange was conducted. The program included a weekly determination of absolute D, H and inclination; observing variations of D, H and Z by single-filament and bifilar magnetometers three times a day; continuous photographic paper recording of D, H and Z variations by Adie magnetograph. The results of observations at Pavlovsk in 1878-1911 and 1914 were published in 1879-1916 as yearbooks stored in several Russian and foreign libraries and archives.

86 **Склоненіе.** Павловскъ. — 1911. — Pavlovsk. **Déclinaison.**

Отклоненія отъ мѣсячн. средней въ минутахъ дуги. Знакъ + обозн. отклоненіе къ западу, знакъ — откл. къ востоку. Le signe + désigne l'ecart vers l'ouest, le signe — celui vers l'est. Écarts avec la moyenne mensuelle en minutes d'arc.

Число. Dates.	1	2	3	4	5	6	7	8	9	10	11	Полд. Midi.	1	2	3	4	5	6	7	8	9	10	11	12
Іюль. Среднее мѣсячное склоненіе: — 1° 37.'2 (восточное). Déclinaison moyenne mensuelle: (d'Est). **Juillet.**																								
1	−2.8	−8.8	−4.8	−3.2	−4.4	−4.0	−2.7	1.5	1.7	2.0	3.8	6.3	7.6	−10.4	11.6	10.2	15.4	−0.7	1.1	2.0	2.2	0.6	−5.5	−1.5
2	−1.7	−2.0	−0.9	2.5	−1.6	−3.9	−3.5	−4.1	−4.7	−3.1	−3.8	−0.6	0.8	2.9	4.5	4.1	2.6	2.5	2.5	0.3	−0.9	−1.6	−1.9	−2.8
3	3.0	0.9	−4.2	−4.0	−4.6	−4.7	−4.8	−4.3	−2.8	−1.1	−0.3	2.0	2.5	3.9	3.4	3.3	2.9	2.5	0.8	−1.4	0.9	0.7	1.1	0.0
4	−0.7	−1.1	−2.1	−3.0	−3.8	−5.1	−5.6	−5.1	−4.2	−1.7	0.7	3.1	4.0	4.4	5.0	4.2	3.1	1.6	1.0	−1.5	0.9	1.3	1.1	4.9
5	−0.3	−1.6	0.2	−1.4	−2.8	−5.5	−5.5	−3.0	−3.2	−3.5	−0.6	3.2	5.1	4.8	3.1	2.4	1.0	1.5	2.3	−0.7	1.7	0.8	1.1	0.2
6	−0.9	−1.4	−2.5	−0.8	−2.7	−2.9	−3.2	−3.2	−2.8	−2.6	−1.1	0.9	3.6	5.1	4.1	3.1	2.1	−1.3	1.5	2.5	2.2	2.1	0.9	1.1
7	−2.2	−1.8	−2.7	−3.8	−2.6	−0.8	−0.9	−0.8	−1.4	−0.8	1.2	3.9	6.4	5.0	8.6	6.9	2.6	5.9	5.0	0.9	1.3	2.3	3.1	−0.2
8	−3.7	1.1	1.0	6.6	4.9	−5.7	−5.6	−5.4	−3.1	−1.6	−0.2	5.3	4.4	5.5	5.9	1.1	2.6	4.0	−0.9	2.0	2.3	1.7	0.7	−0.8
9	−0.8	−1.1	−3.3	4.2	−5.1	−6.2	−5.6	−4.1	−3.0	−0.8	1.6	4.0	5.0	6.1	2.3	2.0	1.5	0.2	0.3	0.1	1.1	0.1	0.0	−0.3
10	0.1	−0.9	−1.7	−2.9	−4.4	−5.6	−2.7	−3.6	−3.0	−1.8	−0.7	2.0	4.8	7.1	6.7	5.1	3.0	1.1	1.2	1.0	1.3	1.0	0.3	2.9
11	−0.8	−2.9	−6.6	−6.6	−7.5	−5.7	−4.6	−5.4	−3.0	−2.3	−1.9	1.6	3.5	3.6	3.7	3.1	1.1	−1.0	−2.5	0.1	0.9	−0.8	−3.2	−0.9
12	−1.8	1.6	0.0	−4.6	−4.6	−5.6	−4.6	−4.6	−3.7	−2.3	0.1	2.3	4.0	5.1	4.9	3.2	3.1	2.2	0.9	1.1	0.6	−1.4	−2.7	−3.4
13	−3.9	0.2	−0.1	−2.6	−3.8	−4.4	−5.2	−4.7	−5.3	−4.6	−0.9	2.1	5.1	7.8	7.8	6.0	3.5	2.0	1.0	0.7	−0.5	0.2	−0.3	−0.9
14	−1.3	−1.0	−1.3	−1.9	−3.8	−4.3	−4.6	−4.8	−4.1	−4.1	−0.8	2.1	5.0	7.9	7.7	6.1	3.1	1.2	1.0	−0.8	−0.7	−0.3	−0.7	−0.6
15	−1.1	−1.1	−1.9	−3.0	−3.9	−4.8	−5.6	−6.6	−5.6	−3.0	−0.6	2.9	5.0	6.5	5.5	4.1	1.9	0.2	0.2	0.2	0.2	−0.6	0.0	0.4
16	−0.7	−1.1	−1.5	−2.5	−3.3	−5.6	−5.7	−4.4	−5.5	−3.6	−0.1	3.6	5.9	6.7	6.5	4.0	3.3	2.9	2.1	0.2	1.1	1.2	1.1	0.2
17	0.2	−0.3	−0.8	−2.7	−3.7	−4.7	−5.6	−5.8	−3.5	−0.8	2.0	5.9	8.7	9.8	6.3	4.7	4.6	4.9	2.5	2.1	−1.6	−5.4	−1.7	2.1
18	−12.4	−4.9	−3.9	−3.3	−3.9	−3.2	−2.0	−2.2	−1.0	−1.4	−0.1	1.6	3.8	3.0	3.4	4.6	−0.7	1.1	2.1	1.6	−1.7	0.5	−0.6	−0.8
19	−3.0	−1.7	−2.5	−0.3	7.8	−2.2	−2.2	1.2	−1.6	−1.7	−0.9	0.1	0.3	3.1	5.9	3.7	0.2	3.0	4.0	2.5	1.2	−1.0	2.1	−2.3
20	−3.8	0.4	−2.7	−2.8	−5.6	−4.4	−4.5	−3.9	−4.5	−2.8	−1.7	1.1	2.0	3.5	3.1	2.1	0.7	−0.5	0.2	−0.5	0.4	0.1	0.3	−0.8
21	−1.1	−1.6	−2.6	−2.2	−1.7	−1.7	−1.6	−2.7	−3.4	−1.8	−0.9	0.6	3.4	4.2	4.1	4.2	3.9	3.1	2.1	1.1	0.2	0.0	2.2	−1.7
22	−1.9	−3.5	−4.6	−2.7	−1.9	−1.7	−3.8	−4.5	−4.6	−2.6	−0.9	1.1	3.0	4.9	3.1	2.1	3.1	1.4	1.2	1.2	0.5	1.0	−0.7	−0.3
23	−0.7	−1.1	−1.3	−0.8	−1.7	−1.7	−1.9	−0.9	−0.4	0.2	1.0	2.2	3.1	1.8	1.1	0.3	0.2	1.0	1.0	1.1	0.4	0.5	1.0	0.6
24	0.2	−1.1	−1.5	−2.0	−4.5	−5.4	−4.5	−2.7	−1.0	−1.5	−0.8	1.2	4.1	7.0	4.7	4.6	2.9	2.2	−0.3	−0.1	−0.3	−0.8	−1.5	−1.2
25	−1.3	−0.8	−1.7	−2.6	−3.7	−3.7	−1.8	−1.8	−1.2	0.8	3.0	4.0	3.9	4.5	4.6	2.6	1.2	0.1	0.0	0.7	1.0	0.2	0.9	−0.9
26	−0.8	−0.8	−1.1	−2.7	−3.8	−5.6	−6.1	−6.5	−6.7	−4.6	−1.1	3.1	5.1	6.8	4.5	2.7	1.6	0.7	0.2	−2.2	0.1	0.4	0.2	−0.1
27	−0.7	−1.1	−2.0	−2.1	−3.1	−4.7	−6.7	−7.1	−6.4	−4.1	−1.3	2.1	4.8	5.7	4.1	2.1	0.0	0.2	0.9	0.9	2.8	−0.5	0.2	−0.4
28	−0.6	3.2	−3.7	−4.5	−5.5	−7.6	−5.6	−2.4	−2.3	−0.5	4.0	7.0	8.9	10.2	11.9	6.1	6.0	2.0	−0.8	1.3	−0.7	−6.0	−13.0	−4.4
29	−1.6	6.2	1.2	−2.2	−2.1	−2.1	−7.3	−5.5	−3.8	−1.5	0.1	4.2	5.1	6.4	3.5	4.1	1.0	−0.7	0.5	1.5	0.6	0.8	1.3	−1.4
30	2.2	0.2	0.0	−2.8	−3.9	−7.2	−6.4	−5.3	−4.4	−1.7	−0.4	0.5	2.6	3.4	2.9	2.7	0.3	−3.4	−1.5	−0.1	2.2	0.5	−1.0	0.3
31	0.0	−1.7	−0.5	−1.4	−3.7	−3.8	−5.3	−3.8	−4.4	−1.4	−0.7	1.9	3.7	3.6	3.2	2.6	1.2	−0.4	−2.5	0.0	0.2	−0.6	0.3	0.1
Срд. Moyen.	−1.4	−0.9	−1.9	−2.2	−3.0	−4.3	−4.3	−3.7	−3.5	−1.9	0.0	2.7	4.6	5.6	5.1	3.8	2.6	1.3	0.9	0.6	0.7	−0.1	−0.4	−0.4
Августъ. Среднее мѣсячное склоненіе: — 1° 37.'7 (восточное). Déclinaison moyenne mensuelle: (d'Est). **Août.**																								
1	1.6	0.0	−0.9	−1.9	−3.1	−3.7	−3.8	−2.3	−2.9	−3.1	−0.7	1.8	3.8	3.8	4.7	4.2	2.8	−0.1	0.1	−0.1	−0.1	−0.8	0.1	−0.2
2	0.4	−0.2	−0.6	−1.3	−2.4	−3.3	−2.6	−2.7	−1.5	−1.0	−0.6	0.8	2.6	3.3	3.9	2.8	2.3	1.6	1.4	1.4	2.3	2.7	2.7	0.1
3	−0.1	−0.2	−0.7	−2.0	−2.9	−4.0	−2.0	−1.6	−1.5	−1.7	0.3	4.1	7.0	5.9	6.6	5.8	0.8	1.8	2.0	0.5	−0.8	−2.9	−1.3	−2.0
4	−2.7	−4.0	1.2	1.7	−2.9	−2.9	−0.8	0.2	−1.3	−0.8	−0.2	2.8	3.7	4.0	4.0	3.0	2.1	2.2	1.8	2.2	2.0	1.7	−0.1	0.7
5	−1.1	−4.7	−3.1	0.9	−2.1	−2.1	−4.8	−3.0	−2.0	−0.3	1.7	3.7	6.3	7.7	5.9	3.9	1.3	2.5	1.0	1.5	−1.0	0.0	−0.5	0.8
6	1.8	−3.0	−5.8	−4.7	−5.0	−3.0	−4.0	−4.4	−3.8	−3.0	−0.4	1.7	4.3	3.9	4.6	2.8	0.1	−0.2	−0.1	0.4	0.0	−0.1	−1.0	0.9
7	−0.1	−1.9	−2.1	−3.0	−4.0	−4.0	−3.9	−2.3	−2.0	−1.8	0.9	2.8	3.7	4.7	4.7	3.5	1.8	−0.1	−0.1	0.1	0.8	0.7	0.3	−0.7
8	−0.7	−1.0	−1.2	−1.7	−3.7	−5.1	−5.5	−5.4	−4.9	−2.6	0.9	2.9	4.9	5.2	4.5	2.0	0.9	0.9	1.4	1.6	1.7	−3.2	−0.1	1.7
9	−0.5	−0.8	−1.4	−1.3	−2.9	−4.4	−3.9	−4.4	−3.8	−1.9	1.7	5.0	7.6	8.7	7.6	4.7	2.8	1.8	0.9	1.0	0.4	−0.1	0.1	−0.3
10	0.0	−0.8	−1.0	−2.0	−3.9	−4.9	−5.8	−5.8	−3.9	−1.6	3.8	5.4	7.5	6.7	5.7	4.6	1.8	0.9	0.8	0.9	0.6	−0.1	−0.6	−0.2
11	−0.9	−0.2	0.4	−1.9	−2.1	−3.3	−3.7	−4.9	−4.9	−3.1	0.8	3.9	6.6	7.5	6.6	4.8	2.1	0.8	0.9	1.0	1.0	0.0	−3.0	−2.5
12	−1.3	−1.3	−1.9	−1.9	−2.9	−3.8	−3.7	−4.0	−3.5	−1.6	0.0	1.5	4.0	5.9	5.8	4.7	2.3	1.0	1.0	1.8	1.1	0.8	0.6	0.0
13	0.1	−0.9	−0.9	−1.0	−3.8	−5.0	−3.1	−6.6	−4.0	−1.9	1.7	2.9	5.7	5.3	4.5	1.9	0.6	−1.4	−0.9	−3.8	0.0	0.9	0.5	0.0
14	−0.1	−0.2	−0.8	−0.8	−3.1	−3.6	−3.6	−4.0	−1.9	1.0	3.9	4.8	5.8	6.0	4.8	2.9	0.4	0.0	0.0	0.0	0.2	0.9	1.7	1.0
15	1.0	0.3	−0.9	−1.9	−3.7	−3.7	−2.9	−3.3	−3.8	0.0	1.0	2.3	4.6	6.0	3.9	3.3	2.9	1.0	1.0	0.0	0.9	0.0	−1.7	−1.6
16	−0.9	−2.2	−4.8	−4.9	−5.9	−5.9	−2.4	1.8	4.1	3.9	4.0	4.6	5.3	4.6	3.8	1.7	0.4	0.0	1.1	1.3	1.3	1.7	0.0	−0.8
17	−1.0	−1.6	−0.7	1.9	−0.7	−3.1	−3.8	−3.6	−2.7	−1.7	−0.1	2.0	3.0	4.6	5.7	3.7	2.9	1.7	1.2	0.0	0.0	0.1	0.4	0.4
18	−0.9	−1.9	−2.4	−0.3	−2.9	−5.3	−3.8	−4.1	−2.9	−2.0	−0.3	1.7	4.8	5.3	2.7	1.9	1.5	0.9	0.1	0.7	−0.1	0.9	0.8	0.2
19	−0.1	−0.5	−0.9	−1.2	−2.2	−2.7	−2.9	−3.3	−2.4	−1.1	1.7	4.8	6.5	5.7	6.7	4.8	4.6	3.0	−0.8	2.9	2.6	1.7	0.4	−7.0
20	−7.4	−6.0	−3.0	−3.1	−3.9	−3.0	−3.9	−4.6	−1.9	−0.6	1.4	4.0	4.9	5.9	4.9	2.8	1.1	−0.3	−3.5	−0.8	−0.8	−0.6	−0.8	−0.8
21	−0.8	−1.1	−0.6	−1.0	−2.0	−1.7	−2.4	−3.3	−3.3	−1.8	0.4	3.3	4.8	4.9	3.2	1.8	0.0	−0.5	−0.5	−0.7	−0.8	−0.7	−0.7	−0.8
22	−1.2	−1.1	−1.1	−1.8	−3.5	−3.8	−3.7	−3.0	−2.0	−0.1	2.1	4.9	5.4	4.9	3.6	1.9	1.4	1.1	1.1	0.9	1.1	1.2	0.0	0.1
23	−0.1	−0.8	−1.5	−1.8	−3.2	−3.7	−2.8	−1.8	−0.2	1.2	5.9	9.0	7.8	12.3	7.3	11.5	1.4	−0.6	1.0	−3.5	0.1	−4.7	2.1	6.4
24	−3.0	−3.7	2.0	−1.0	−5.6	−2.5	−1.8	−4.7	−1.8	0.1	0.1	4.2	4.0	4.0	1.1	0.9	−4.5	−6.6	−0.9	−5.5	−1.8	4.9	−1.8	−1.5
25	−1.0	−1.7	1.8	1.0	1.1	−2.8	−5.9	−3.8	−2.8	0.0	2.1	5.2	3.7	4.1	4.5	−3.7	0.1	−0.2	−2.9	−0.6	−1.5	−2.9	−0.1	−1.3
26	−1.7	4.8	0.2	−0.7	−2.6	−4.7	−3.0	−4.7	−1.6	−1.0	3.1	1.8	4.1	4.6	4.0	2.0	−10.2	−2.5	−3.5	−4.7	−4.9	−0.2	0.0	3.3
27	0.2	−2.7	−2.3	1.1	−3.1	−3.7	−4.2	−4.8	−3.7	−3.4	−1.8	1.2	1.9	4.7	4.0	3.0	−0.4	−2.1	−4.7	−1.6	−0.6	0.2	0.0	0.1
28	4.9	−1.6	0.1	−2.1	−2.0	−3.7	−4.7	−3.8	−3.0	−2.1	0.3	4.1	6.2	5.1	4.8	3.0	0.9	−2.6	−0.9	−0.6	−0.6	−2.6	−3.7	−1.3
29	−1.3	−1.7	−1.6	−1.1	−2.3	−2.7	−2.9	−4.7	−4.7	−3.7	−1.5	1.9	3.9	3.7	3.2	2.5	0.1	−2.8	−0.8	−0.4	−0.7	−0.8	−1.0	−0.9
30	−0.7	1.6	−1.3	−0.6	−1.0	−1.9	−2.8	−3.5	−3.9	−1.9	0.1	2.9	3.7	3.5	3.0	1.2	0.6	−1.0	−1.3	−3.7	−2.8	−1.9	−0.8	−1.4
31	−1.0	−1.8	−1.8	−2.1	−2.7	−3.2	−4.4	−2.7	−2.4	−1.0	1.8	3.0	5.1	3.8	5.9	5.7	0.1	2.1	0.4	−1.2	−0.6	−0.8	−6.3	−2.2
Срд. Moyen.	−0.6	−1.3	−1.2	−1.3	−3.0	−3.5	−3.6	−3.5	−2.6	−1.3	1.1	3.4	4.9	5.4	4.7	3.2	0.8	0.0	−0.1	−0.3	0.0	−0.2	−0.5	−0.4

Fig. 1. Monthly table of observatory measurements

Data and Results

In 2000, the data of most Russian meteorological and magnetic observations for 1837-1913 available in the NOAA library, were scanned by its employees under the global program (National Oceanic and Atmospheric Administration Environmental Data Rescue Program) and is now publicly available (http:// docs.lib.noaa.gov/rescue/data_rescue_russia.html). In 2010, employees of the Finnish Meteorological Institute (FMI) for the first time digitized some data of these measurements: D and H for 1850-1862 in St.Petersburg, Ekaterinburg, Barnaul, Nertchinsk. These data as well as data from Helsinki (1844-1909), is available at FMI (http://space.fmi.fi/MAGN/russia_1800/, http://www.geo.fmi.fi/MAGN/magn/).

We first have translated into a digital format the data of hourly measurements of D, H and Z in Pavlovsk (1878-1914), St.Petersburg (1873-77) and Irkutsk (1905, 1906, 1908, 1910, 1912, 1913), as well as monthly tables of all measured or calculated values.

The observatory measurements, as published in yearbooks, are shown in monthly tables (Fig.1). As an intermediate result, we have produced tables of the geomagnetic field elements in form similar to the original (useful for comparison with paper version and error checking). The data then has been converted into time series (in netCDF format) which is more suitable for further processing and analysis. Time series of hourly observations are also given in the form of interactive charts online (http://db.izmiran.nw.ru/geomag).

We first have digitized data of hourly magnetic observations on Novaya Zemlya, conducted by Russian expedition during the first International Polar Year (1882/83).

In addition, we have digitized the catalogs of geomagnetic storms for 19-20 centuries observed in Pavlovsk, Greenwich and Bombay. These catalogs, published in 1941, 1955 and 1910, respectively, cover more than 100-year period of observations.

All this data is accessible (or underway) at the site of SPbF IZMIRAN (databases).

This database (http://db.izmiran.nw.ru/geomag) may be useful to study different variations of the geomagnetic field, for example, geomagnetic activity, magnetic storms, and reconstruct the solar wind at 11-14th cycles of solar activity [e.g., Vokhmyanin et al., 2013; Lockwood et al., 2014].

Acknowledgements

The authors are grateful to A.N. Zaitsev (IZMIRAN), N.G. Ptitsyna (SPbF IZMIRAN), D.I. Ponyavin, M.V. Vokhmyanin (St.Petersburg State University), and M. Lockwood (University of Reading, UK), for their support and useful discussions.

References

Lockwood, M., H. Nevanlinna, M. Vokhmyanin, et al. (2014), Reconstruction of geomagnetic activity and near-Earth interplanetary conditions over the past 167 yr – Part 3: Improved representation of solar cycle 11, Ann. Geophys. 32 (4), 367-381.

Nevanlinna, H., Häkkinen, L. (2010), Results of Russian geomagnetic observatories in the 19th century: magnetic activity, 1841-1862, Ann. Geophys. 28 (4), 917-926.

Raspopov, O.M., Yu.A. Kopytenko, M.A. Efendieva, V.V. Mescheryakov (2009), History of geomagnetic research in Russia: from the earliest observations to 1918, History of Earth Sciences 2(1), 18-43. (in Russian).

Vokhmyanin, M.V., D.I. Ponyavin (2013), Sector structure of the interplanetary magnetic field in the nineteenth century, Geophys. Res. Lett. 40 (14), 3512–3516, doi:10.1002/grl.50749.

MIGRATION OF THE NORTH MAGNETIC POLE OF THE EARTH, INCREASE IN THE CONCENTRATION OF CO_2 AND CLIMATE CHANGE IN THE TWENTIETH CENTURY

S.S. Vasiliev[1], V.A. Dergachev[2]

Ioffe Physical-Technical Institute, Russian Academy of Sciences, Polytekhnicheskaya 26, St. Petersburg, 194021, Russia
E-mail: [1]sergey.vasiliev@mail.ioffe.ru; [2]v.dergachev@mail.ioffe.ru

Abstract. It is now widely discussed increase in the concentration of carbon dioxide in the atmosphere due to changes in the Earth's climate. Is this the only reason for the increase in global warming? Work is devoted to the study of a possible link between the position of the magnetic north pole of the Earth and the change in the average temperature in different latitudinal zones.

INTRODUCTION

It is generally accepted that the cause of global warming – increasing the concentration of greenhouse gases in the atmosphere due to emissions associated with industrial activity [1]. The strongest impact on the environment is carbon dioxide emissions from the burning of fossil fuels [2]. The main contribution to the emission of CO_2 makes carbon dioxide, which is released during the combustion of solid and liquid fuels [3]. Currently, about 9 billion tons of carbon is released during the year [1]. Emission into the atmosphere in 1850 was 4 million tons of carbon. In the second half of the twentieth century, the rate of carbon emissions has increased significantly: from 1,630 million tons in 1950 to 9,170 million tons in 2010. The concentration of carbon dioxide in the atmosphere has increased, respectively, from 311 ppm in 1950 to 390 ppm in 2010. It is estimated Stern (2006), a dramatic change in the environment will occur if the concentration of carbon dioxide in the atmosphere exceed 450 ppm [4]. In this case, the global temperature will increase by more than 2° C compared with an average temperature for the period from 1951 to 1980. Since the concentration of CO_2 in 2010 had reached a value of 390 ppm, and increases by 2-3 ppm per year, the critical concentration will be exceeded in 20-30 years from now.
Obviously, the increase in carbon dioxide concentration in the atmosphere is an important factor when considering changes of the Earth's climate.

CHANGING THE ZONAL TEMPERATURE

Currently, there is evidence of a change in global temperature in the world from 1880 to the present [5]. An important indicator of climate change is the zonal temperature, which is the average temperature within the zone. Often not the temperature is compared, and their deviation from the mean. In what follows, as mean value is taken the time-averaged temperature for the interval 1951 - 1980 years. An essential feature of the temperature deviation is the presence of two components: an oscillating and trend (see Figures 1 and 2).

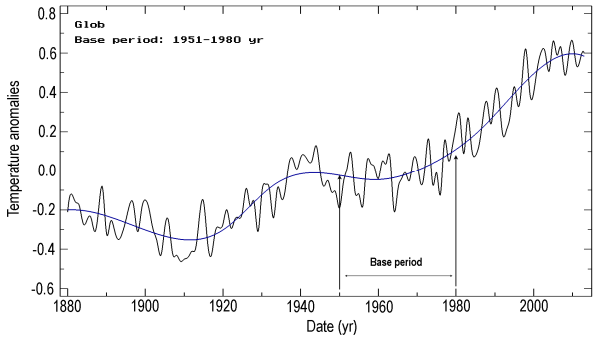

Fig. 1. Global temperature anomalies (deviations) averaged over the geosphere for the 1880-2013 years. The picture shows the averaging period (1951-1980 years). Blue color indicates a trend.

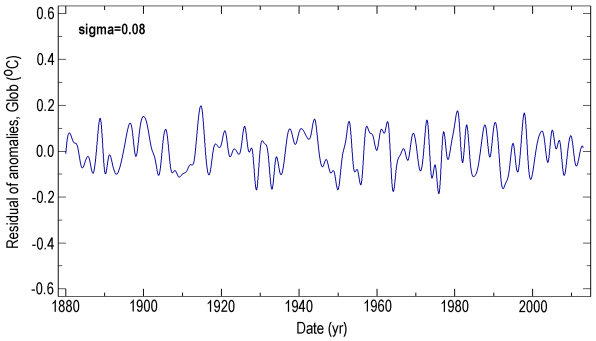

Fig. 2. The oscillating component of the global temperature deviations (anomalies). The standard error σ is 0.08 ° C.

[1] Here annual emission is measured in millions of tons of carbon. To convert to the amount of emissions of carbon dioxide corresponding values should be multiplied by 3.667

Line with a period of about 21 years dominates in oscillatory component (see Figure 3).

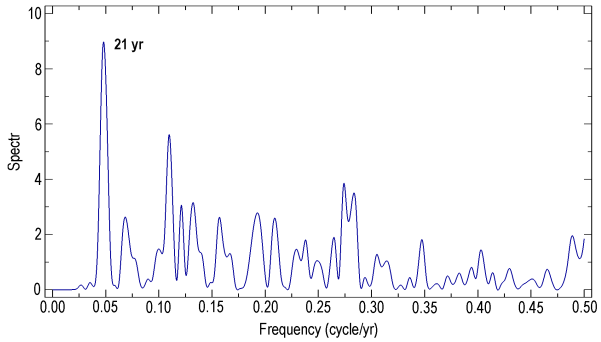

Fig. 3. The spectrum of the oscillating components of global temperature anomalies. Component with a period of about 21 years is the dominant.

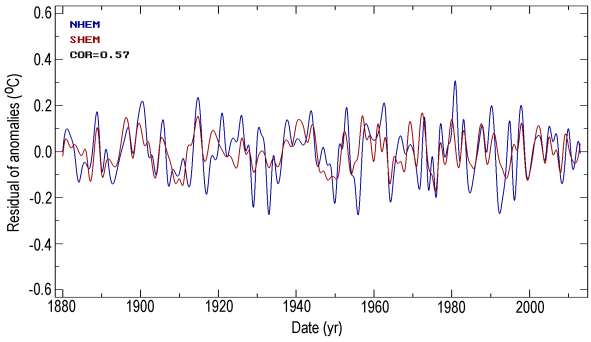

Fig. 4. Comparison of the temperature oscillations of the northern (blue) and southern hemispheres (red). One can observe a significant correlation (r = 0.57, n = 132, p <0.0005) between the two curves.

It points to the possible connection between short-term changes in the Earth's temperature and the 22-year cycle of solar activity. In this case, there should be a significant correlation between the oscillations in both hemispheres. Indeed, short-term changes in temperature in the northern and southern hemispheres are correlated (see Figure 4). The correlation coefficient r = 0.57. For number of degrees of freedom n = 132 the correlation is statistical significant (probability of the null hypothesis p <0.0005). In addition to short-term oscillations in temperature there is a long-term temperature change (trend). The existence of a trend is usually attributed to the greenhouse effect of carbon dioxide. Comparison of temperature trend curve and changes in CO_2 concentration indicates a discrepancy between them at some time intervals, for example, 1880-1910, 1910-1940 and 1940-1960 (see Figure 5). Apparently, there are other factors besides the greenhouse effect influencing long-term temperature change on the Earth.

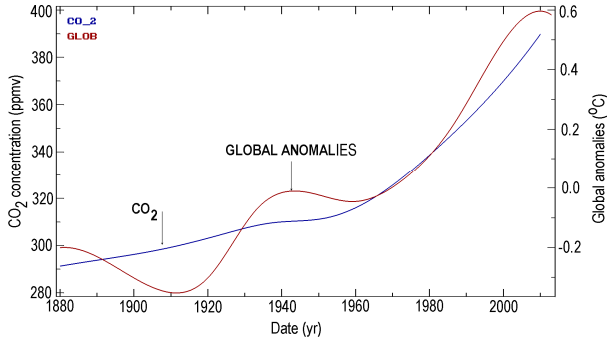

Fig. 5. Comparison of the concentration of CO_2 (blue) and global temperature anomalies (red).

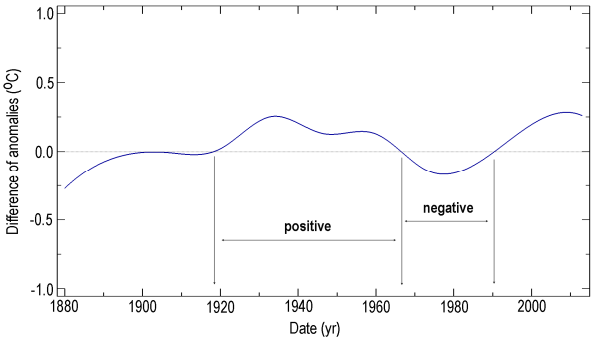

Fig. 6. The difference between the temperature anomalies of the northern and southern hemisphere.

One can see the difference in the change in temperature in the northern and southern hemisphere (see Figure 6). There are long periods during which the average temperature of the hemispheres differs markedly (e.g., 1918-1968, 1968-1980).

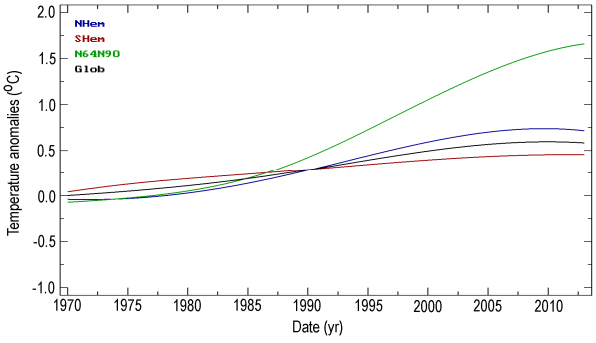

Fig. 7. Comparison of the behavior of the temperature variations in the northern hemisphere (NHem), southern hemisphere (SHem), the northern polar zone (90° N – 64° N) and average geosphere anomalies (**Glob**).

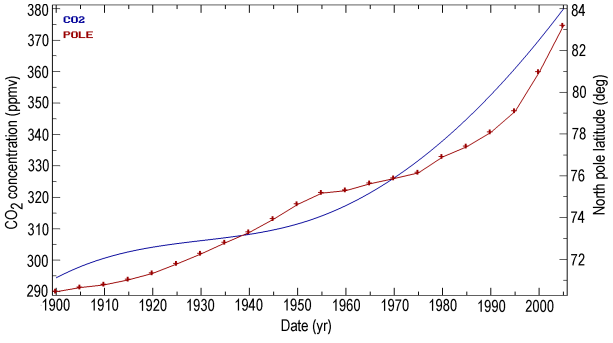

Fig. 8. The concentration of carbon dioxide in the atmosphere (blue) and the latitude of the north magnetic pole (red).

Emissions of carbon dioxide occur mainly in the northern hemisphere. The mixing time in the hemisphere is about 3 months, and between the hemispheres - about 1 year. Therefore, differences in temperature changes in the hemispheres can not be due to the uneven distribution of CO_2. Next, we will analyze only the smoothed component of temperature variations (trends). After 1970, the temperature of both the northern and southern hemisphere, increases monotonically. Now it is important the examination of the behavior of trends in the range of 1970-2013 (see Figure 7). Attention is drawn to the behavior of temperature deviations to the polar zone. For interval of 1970-2013 the temperature rise exceeded the average for geosphere by 1° C.

REGRESSION ANALYSIS

In this section, we discuss the correlation between the temperature variations, the concentration of carbon dioxide in the atmosphere, as well as with the position of the magnetic north pole. [6]. A comparison will be made between the zonal temperature, which we denote by Y, CO_2 concentration, and some other parameters, which we denote by X_1 and X_2.

$$Y = aX_1 + bX_2. \quad (1)$$

We will look for options a and b, such that they will give the maximum correlation between the right and left side of (1). This approach is called multiple regressions [7]. It allows you to determine which parameters of the (X_1, X_2) have significant effect on the change in the right-hand side of (1). Since the changes in CO_2 concentration are not fully explained the change in the zonal temperature anomalies, we will extend the set of parameters $\{X\}$, adding the latitude of the north magnetic pole (NMP) as the second parameter. Basis for the inclusion of latitude north magnetic pole into the parameter set $\{X\}$ is similarity between the two curves:

1. changes in the concentration of CO_2 and
2. changes in latitude of the magnetic pole in the 20th century (see Figure 8).

So we have carried out the regression analysis of data. We examined the dependence of the zonal temperature deviations on two parameters: the concentration of carbon dioxide and latitude of the north magnetic pole for the period 1970-2010 years. The results are shown in Table 1.

Table 1: The dependence of the zonal temperature on the concentration of CO_2 and the latitude of the north magnetic pole

Zone of the northern hemisphere	$\partial T/\partial C$	$\partial T/\partial L$	R
90° N –64° N	0.671	0.726	0.99
90° N –24° N	0.757	0.189	0.97
90° N –0°	0.827	0.0	0.98

In Table 1, the following notation is used.

1. $\partial T/\partial C$ – partial correlation coefficient of zonal temperature by the concentration of CO_2
2. $\partial T/\partial L$ – too, for the zonal temperature and latitude of NMP
3. R – coefficient of determination. The value indicating what proportion of variation of the independent variable (temperature) is explained by the parameters of right-hand side (CO_2 and latitude)

As follows from the Table 1 (see Column 3), the effect of the pole position on the zonal temperature in the northern hemisphere decreases with displacement of the outer boundaries of the zone to the equator (see Column 1). This suggests that the physical factor which determining the impact on the zonal temperature, localized in the polar region. One of these factors, that determine the transport processes in the atmosphere of the polar zones, is Arctic oscillation [8].

ARCTIC OSCILLATION AND THE POSITION OF THE NORTH MAGNETIC POLE

Arctic oscillation or changes in the northern circulation is an index of change of pressure at sea level to the north of 20° N (see Figure 9).

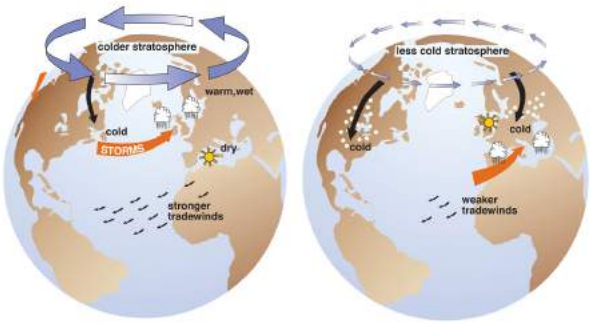

Fig. 9. The two phases of the Arctic oscillation. Left figure shows the negative phase, characterized by increased pressure in the stratosphere of the polar zone and a strong jet stream at the border zones of high and medium pressure. Right figure shows the positive phase, characterized by a lower pressure in the stratosphere of the polar zone and less intense jet stream.

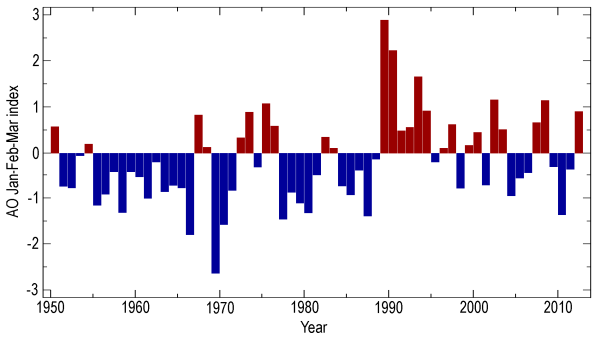

Fig. 10. Winter indices (January-March) of Arctic oscillation for 1950-2013 years. The blue color corresponds to periods when prevailed negative AO phase, the red color indicates to the time intervals when prevailed positive phase AO.

It characterizes the pressure anomalies in the Arctic relative to the pressure in the lower latitudes of the northern hemisphere with the center of the measurement at latitudes 37-45° N. Arctic oscillation is one of the main factors that determine the weather of the northern hemisphere during the winter period. Change in the index over long time intervals has no strict periodicity. There are two phases of Arctic oscillations. Negative phase is characterized by increased pressure in the stratosphere of the polar zone and a strong jet stream at the edge of high and medium pressure. Positive phase is characterized by a lower pressure in the stratosphere of the polar zone and less intense jet stream.

Figure 10 shows that on the considered time interval the years with predominantly positive phase appear after 1970. Approximately in the same time period the temperature in the northern hemisphere begins to increase monotonically, and particularly in the polar zone 90° N – 64° N (see Figures 7 and 11). In the 70s begins a period of rapid increase in temperature in the northern hemisphere, which ends in 2010. During this time, the rate of increase in temperature in the northern hemisphere exceeded the rate changes in the southern hemisphere.

To explain the phenomenon of the rapid increase in temperature in the northern hemisphere, we compare the latitude the north magnetic pole and AO indices (see Figure 13).

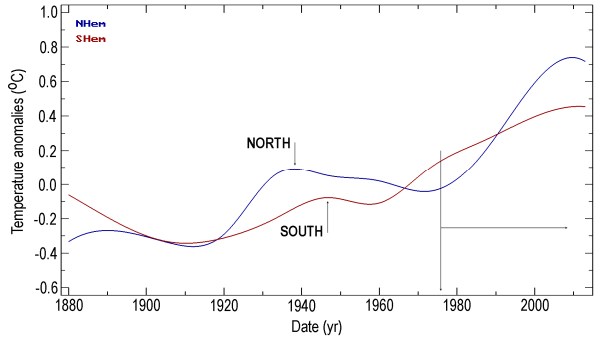

Fig. 11. Temperature deviations for the northern (blue) and southern hemispheres (red). In the 70 years of the twentieth century began a period of rapid increase in temperature in the northern hemisphere, which ends in 2010

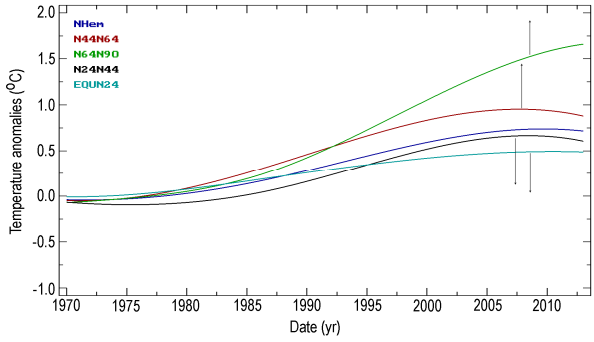

Fig. 12. Comparison of temperature anomalies of several zones of the northern hemisphere. The arrows indicate the positions of the curves relative to the average curve for the northern hemisphere.

It is seen (see. Figure 13) that in the time intervals in which the latitude of pole increases rapidly, AO goes to the positive phase, which is characterized reduced pressure and less cold air in the polar zone. If we compare the changes of temperatures in several areas of the Northern Hemisphere (see Figure 12), it becomes clear that the excessive warming in the polar (90 ° N – 65 ° N) and in the middle zones of the Northern Hemisphere (65 ° N – 44 ° N) was accompanied at the same time with less warming in the subtropical (44 ° N – 24 ° N) and tropical (24 ° N – 0 °) zone. Thus, there is following conception, explaining the effect of a stronger warming of the polar zone at the end of the twentieth century. Due to the rapid movement of the magnetic north pole the arctic oscillation goes in a positive phase. In the Arctic region of the northern hemisphere was formed area of low pressure, which contributed to the transfer of warm air masses from the mid-latitudes in the northern areas. As a result, in the northern hemisphere has been a redistribution of heat.

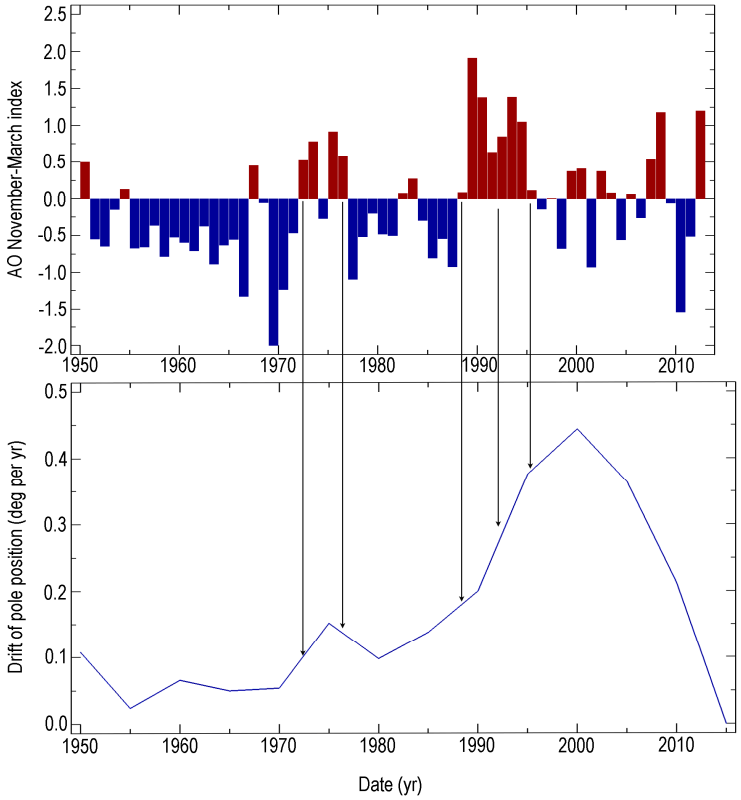

Fig. 13. Top panel: AO index for the cold season (November – March). Bottom panel: change of latitude NMP (degrees / year). Arrows indicate the correspondence between the positive AO phases and periods of rapid movement of NMP.

SUMMARY AND CONCLUSIONS

The direct indicator of the observed global warming is the temperature. The properties of temperature changes were considered at different time scales. It is shown that short-term fluctuations have a time scale of ~21 years and occur simultaneously in the northern and southern hemispheres. It was suggested a connection between these fluctuations and solar activity. Long-term changes in temperature are usually associated with an increase in the concentration of carbon dioxide in the atmosphere. The performed analysis has shown that the increase in temperature not uniquely is associated with increased CO_2 concentration. Currently, works have appeared in which examines the relationship of climate change with the position of the magnetic poles (eg, [9]). We performed a regression analysis of data on temperature, carbon dioxide concentration and latitude of the north magnetic pole for the 1970-2010 years. It is shown that the dependence of zonal temperature on latitude pole increases significantly for the subpolar zone (90° N - 64° N) *compared with zones that include* the middle and subtropical latitude (90° N → 24° N, 90° N → 0°). This allows us to conclude that the processes which additionally affect the change in temperature, localized in the polar zone. We have considered connection of the Arctic oscillation (AO) with the change in the latitude of the north magnetic pole (NMP). It is shown that the phase change AO occurs in the periods of increasing velocity of the NMP.

REFERENCES

1. Houghton, John (2005).Global warming. *Reports on Progress in Physics* 68, 1343-1403. doi: 10.1088/0034-4885/68/6/R02.
2. IPCC Fifth Assessment Synthesis Report. Climate change 2014. 116 pp. URL: http://www.ipcc.ch/
3. Boden, T.A., G. Marland, and R.J. Andres (2013). *Global, Regional, and National Fossil-Fuel CO_2 Emissions.* Carbon Dioxide Information Analysis Center, Oak Ridge National Laboratory, U.S. Department of Energy, Oak Ridge, Tenn., U.S.A. doi 10.3334/CDIAC/00001_V2013.

4. Timilsina, G. R. (2007). Atmospheric Stabilization of CO_2 Emissions: Near-term Reductions and Intensity-based Targets. World Bank, Washington, DC. © World Bank. URL: https://openknowledge.worldbank.org/handle/10986/7300
5. Lawrimore, J. H., J. Menne, B. E. Gleason, C. N. Williams, D. B. Wuertz, R. S. Vose, and J. Rennie (2011). An overview of the Global Historical Climatology Network monthly mean temperature data set, version 3. *J. Geophys. Res.* 116, D19121, doi:10.1029/2011JD016187.
6. WDC for Geomagnetism, Kyoto: Magnetic North, Geomagnetic and Magnetic Poles. URL: http://wdc.kugi.kyoto-u.ac.jp/poles/polesexp.html
7. Afifi, A. A., Azen, P. Statistical analysis: a computer oriented approach. NY, Academic Press, 1979, 442 pp.
8. NOAA NWS Climate Prediction Center: Arctic Oscillation. URL: http://www.cpc.ncep.noaa.gov/products/precip/CWlink/daily_ao_index/ao.shtml
9. Bakhmutov, V. (2006). The connection between geomagnetic secular variation and long-range development of climate changes for the last 13,000 years. *Quaternary International* 149, 4, http://dx.doi.org/10.1016/j.quaint.2005.11.013

POSSIBLE REASONS FOR THE CORRELATION REVERSAL BETWEEN LOW CLOUDS AND GALACTIC COSMIC RAYS

S.V. Veretenenko[1,2], M.G. Ogurtsov[1,3]

[1]Ioffe Physical-Technical Institute, St. Petersburg, 194021, Russia, e-mail: s.veretenenko@mail.ioffe.ru; [2]St. Petersburg State University, St. Petersburg, 198504, Russia; [3]Central (Pulkovo) Astronomical Observatory, St. Petersburg, 196140, Russia

Abstract. The nature of correlation links detected between low cloud anomalies and galactic cosmic ray (GCR) variations in ~1983-2000 was investigated, with possible reasons for the correlation reversal after 2000 being discussed. It was shown that cloud field formation at middle latitudes is closely related to cyclonic activity, so GCR effects on low clouds observed on a decadal time scale are not direct, but they are realized through circulation changes associated with GCR variations. The character of GCR influence on the lower atmosphere dynamics was found to reveal a roughly 60-year periodicity related to the evolution of the stratospheric polar vortex. It was suggested that the reversal of correlation between cloud cover anomalies and GCR intensity detected after 2000 is due to the change of the vortex state which resulted in the sign reversal of GCR effects on the development of extratropical baric systems. The results obtained provide evidence for an important part of the stratospheric polar vortex in solar-atmospheric links.

1. Introduction

One of possible mechanisms of solar activity (SA) influence on the lower atmosphere, weather and climate suggests impact of galactic cosmic ray (GCR) variations on the cloud cover state which, in turn, affects the radiation and heat balance of the atmosphere, e.g. [Dickinson, 1975; Svensmark and Friis-Christensen, 1997]. Experimental data confirming a possibility of this mechanism were reported in a number of works [Pudovkin and Veretenenko, 1995; Todd and Kniveton, 2001, etc.]. On a decadal time scale a strong positive correlation between global cloud cover variations and GCR fluxes was revealed by Svensmark and Friis-Christensen [1997], with the satellite observations ISCCP (International Satellite Cloud Climatology Project) being used. Later it was found that namely low cloud anomalies (LCA) correlate well with changes in GCR flux [Marsh and Svensmark, 2000], the highest correlation being observed in the period 1983-1994. However, since the middle of the 1990s this correlation started decreasing and in the early 2000s its reversal took place [Gray et al., 2010]. This gave rise to doubts in a possible influence of cosmic ray variations on processes in clouds and their role in solar-atmospheric links. So, the aim of this work is to study the nature of LCA-GCR correlation observed in 1983-2000, as well as to consider reasons for the violation of this correlation after 2000.

2. Formation of cloud fields at extratropical latitudes

It is known that the main reason for cloud formation is vertical transport and cooling of water vapor, i.e. formation of cloud field is determined by vertical movement of air. Most large (macro-scale) vertical air movements, horizontal scales being from several hundred to several thousand kilometers, are closely related to extratropical baric systems. Upward movements take place in low pressure areas (cyclones and troughs). On the contrary, in high pressure areas (anticyclones and crests) downward movements are observed.

Upward air movements in an extratropical cyclone are due, first of all, to convergence of air flows near the Earth's surface to the cyclone center. On the other hand, the evolution of these cyclones is closely related to atmospheric fronts which are characterized by regular ascending movements. At warm fronts warm air slides along a frontal surface resulting in the formation of a strong system of stratiform clouds Ns-As-Cs (nimbostratus Ns, altostratus As and cirrostratus Cs), so called 'frontal' cloudiness. In the case of fast moving cold fronts warm air is displaced upward more intensively, so the formation of vertical development clouds (cumulonimbus Cb) also takes place. Cloud field of an atmospheric front represents a long band, its width being from one to several hundred kilometers and its length reaching several thousand kilometers. Fig.1 (left panel) shows cloud systems of an extratropical frontal cyclone at different stages of its evolution. At the first stage it is a wave at a cold front. A characteristic feature of the second stage ('young cyclone') is a warm sector formed between the cold and warm fronts of a cyclone. At the next stage ('maximum development') the cyclone occlusion starts, i.e. the cold and warm fronts start merging. This results to the

formation of so called 'occluded' front and the displacement of a warm sector to the cyclone periphery. At the final stage the occlusion continues accompanied by the cyclone filling. So, cloudiness associated with fronts is observed at all stages of the cyclone evolution. The cloud field of a developed cyclone as seen from the satellite is shown in Fig.1 (right panel). It is a cloud vortex with a spiral structure and horizontal dimensions comparable with the cyclone dimensions, i.e. up to several thousand kilometers.

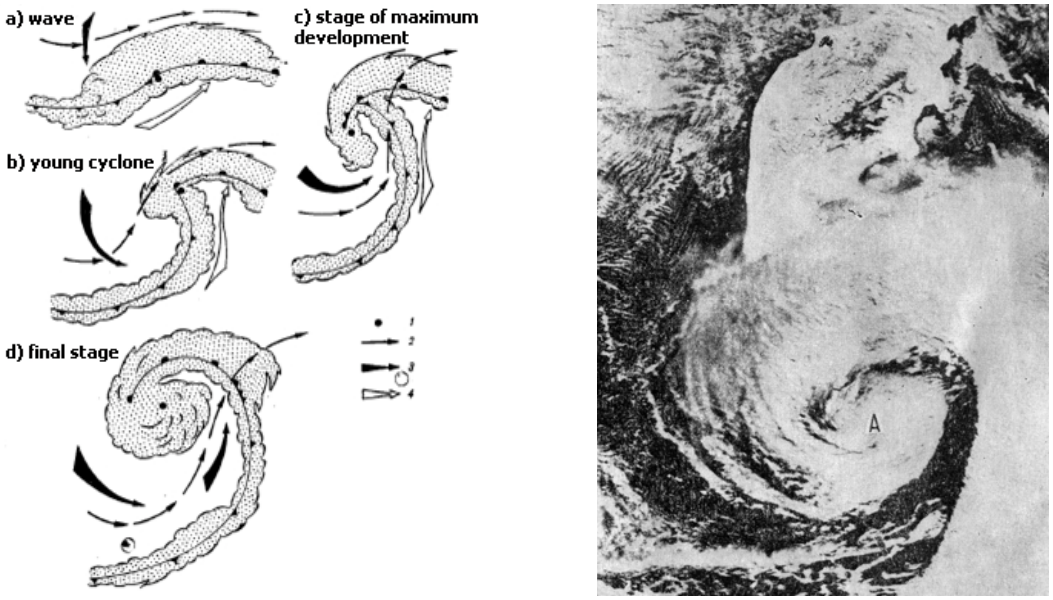

Fig.1. *Left panel*: Cloud systems of a frontal cyclone at different stages of its evolution: *1* – the cyclone center near the Earth's surface; *2* – the axis of a jet stream; *3* and *4* – the direction of the movement of cold and warm air, respectively [Vorobjev, 1991]. *Right panel*: Cloud vortex (A is the vortex center) associated with an extratropical cyclone in the Northern hemisphere [Vorobjev, 1991].

Thus, cloudiness at extratropical latitudes is closely related to dynamic processes in the atmosphere. Upward movements associated with macro-scale systems such as atmospheric fronts and cyclones contribute significantly to the formation of cloud fields. This allows suggesting that correlations observed between cloud cover anomalies and cosmic rays [Svensmark and Friis-Christensen, 1997; March and Svensmark, 2000] are caused by cosmic ray influence on the development of weather systems.

3. ISCCP data and troposphere dynamics

Let us consider variations of low cloudiness and cyclonic processes at middle latitudes 30-60°N which is the region of intensive cyclogenesis. As experimental base we used cloud cover anomalies from ISCCP-D2 archive (http://isccp.giss.nasa.gov/pub/data/D2CLOUDTYPES) available for the period 1983-2009. Low clouds are defined as clouds with pressure on the cloud top CP > 680 hPa. These clouds involve stratus (St), nimbostratus (Ns) and stratocumulus (Sc) and their formation is closely related to atmospheric fronts and frontal cyclones. Low cloud amount (the fraction of the area covered by these clouds) is given as a percentage of the total area. Low cloud anomalies (LCA) are determined as the difference between monthly values and the climatic mean over the whole period of observations. To estimate intensity of cyclonic processes we used monthly values of tropospheric pressure characterized by geopotential (gp) heights of the isobaric level 700 hPa (GPH700) according to NCEP/NCAR reanalysis data [Kalany et al., 1996].

Anomalies of low clouds at mid-latitudes 30-60°N are presented in Fig.2a. We can see a gradual decrease of LCA since the early 1980s. The time variations of pressure (GPH700) values area-averaged over the same belt are shown in Fig.2b. One can see long-term variations in troposphere pressure in this belt, with the minimum taking place in the 1960s. During the period since ~1970 till ~2010 pressure was gradually increasing which indicates a weakening of cyclonic processes on average over the mid-latitudes. Anomalies of GPH700 calculated similarly to LCA anomalies are presented in Fig.2c. One can see a positive linear trend in pressure anomalies for all the period of cloud cover observations, i.e. the trend in pressure variations is opposite to the trend in low cloud anomalies. Detrended values of LCA and GPH700 anomalies (Fig.2d) are also opposite. Thus, low clouds and pressure at middle latitudes, both the trends and the deviations from these trends, vary in opposite ways. This indicates a close connection between cloud cover and atmosphere dynamics, with the increase of pressure (decrease of cyclonic activity) resulting in the decrease of low cloud cover. Dynamical nature of low cloud anomalies is also confirmed by their seasonal variations. Indeed, the

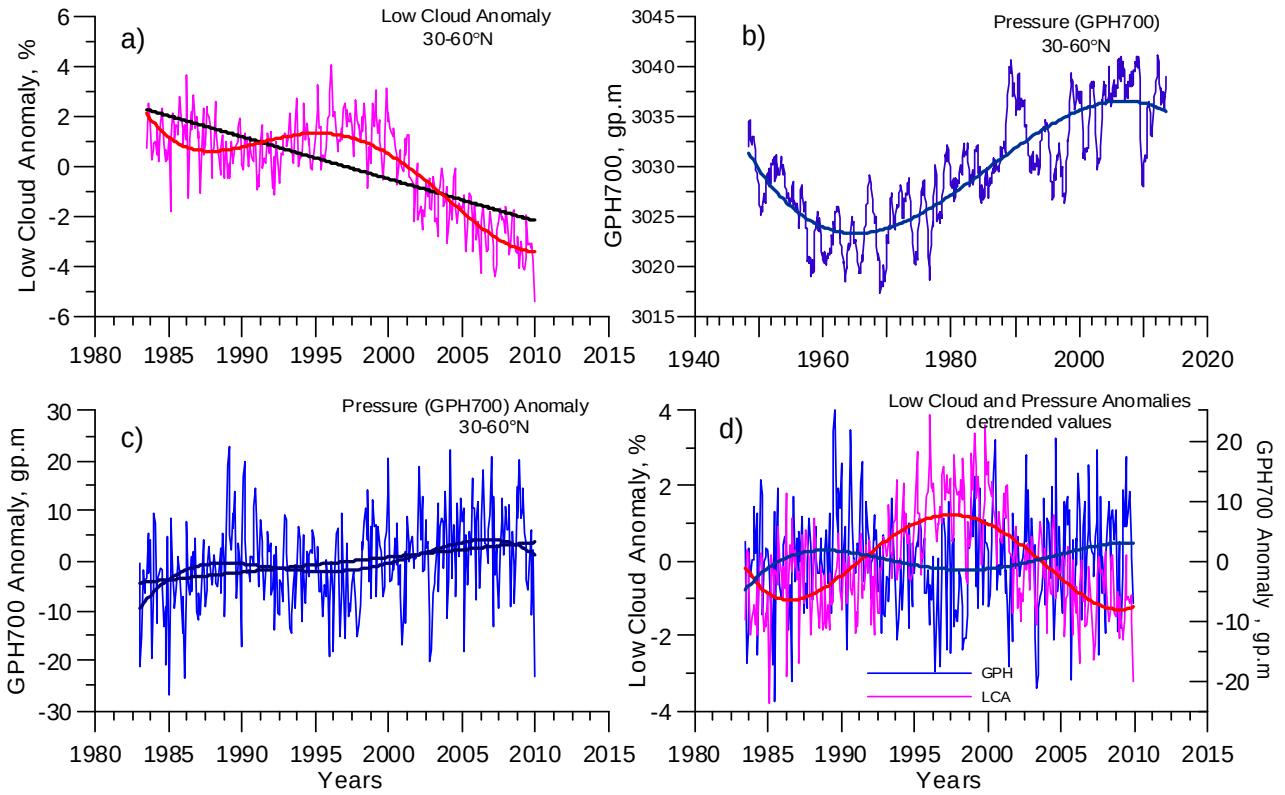

Fig.2. Time variations of low-level cloud and pressure anomalies at middle latitudes: a) monthly values of LCA; b) 12-month running means of pressure (GPH700); c) monthly values of pressure (GPH700) anomalies; d) detrended monthly values of low cloud and pressure anomalies. Thick lines show linear trends and polynomial smoothing of LCA and GPH700.

data in Fig.3a show that highest variations of LCA are observed in cold months (winter and spring) when extratropical cyclogenesis is most intensive due to enhanced temperature contrasts in the troposphere. The link 'low cloud – troposphere dynamics' manifests itself most distinctly in yearly values of LCA and pressure anomalies (Fig.3b), since averaging over a year decreases noises caused by micro- and meso-scale processes. One can see a rather strong negative correlation LCA-GPH700, the correlation coefficient amounts to –0.63 and reaches –0.8 for 3-year running means.

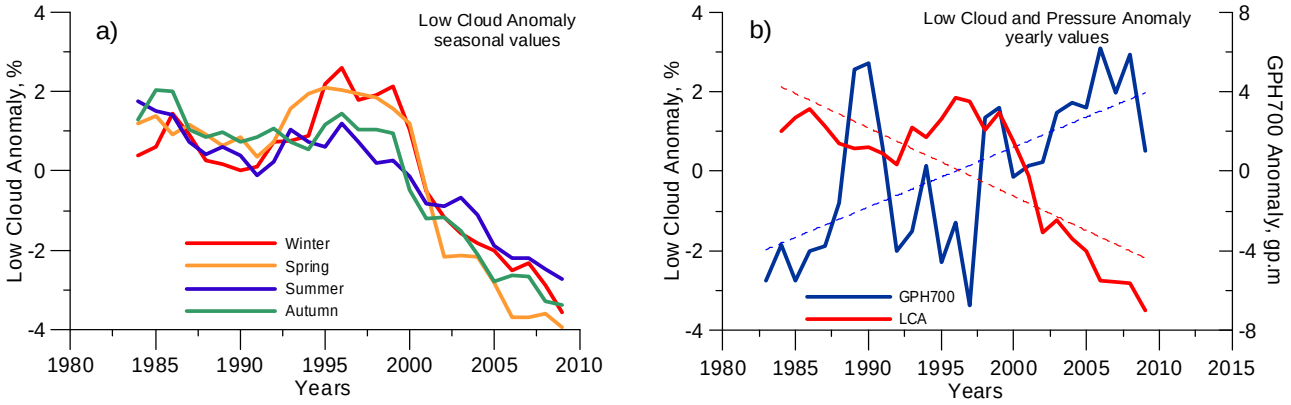

Fig.3. a) Time variations of low cloud anomalies in different seasons; b) time variations of yearly values of low cloud (LCA) and pressure (GPH700) anomalies at middle latitudes.

Thus, the above results show that low cloud anomalies at middle latitudes are closely related to the development of cyclonic processes; the decrease of cyclonic activity is accompanied by the corresponding decrease of cloud cover. The detected pressure growth may be due to cyclone weakening and/or the decrease of their areas on the average over the belt under study, as well as to the shift of cyclone tracks to higher latitudes. Indeed, the intensification of C-type meridional processes according to Vangengeim-Girs classification [Girs, 1974] was observed since the early 1980s till the early 2000s [Veretenenko and Ogurtsov, 2013]. This type of circulation is characterized by the formation of a crest over the eastern part of

the North Atlantic and Europe which blocks the cyclone movement to the Eurasian continent and shifts their tracks to the north. So, pressure changes at latitudes 30-60°N observed in 1983-2009 seem to agree with long-term variations of the large-scale circulation.

4. Cosmic ray effects on troposphere dynamics/cloud cover and their temporal variability

As cloud fields at middle latitudes are influenced significantly by macro-scale weather systems (cyclones and troughs), we should consider, first of all, GCR effects on the development of cyclonic processes. Indeed, a number of studies show correlations between cosmic ray variations and troposphere dynamics on different time scales. In particular, increases of energetic solar cosmic ray fluxes in the Earth's atmosphere were found to contribute to cyclone regeneration near the Greenland coasts [Veretenenko and Thejll, 2004]. On the contrary, Forbush decreases of GCR fluxes contribute to weakening of cyclones and intensification of anticyclones at middle latitudes [Artamonova and Veretenenko, 2011]. It should be noted that a pronounced intensification of cyclones at Polar fronts associated with GCR increases on a decadal time scale was detected for the period 1983-2000 [Veretenenko and Ogurtsov, 2012] which is the period of highest correlation between LCA and GCR intensity [Marsh and Svensmark, 2000]. The above data suggest a possibility of indirect influence of GCR variations on cloud cover, i.e., through changes in the evolution of baric systems which, in turn, influence cloud fields at extratropical latitudes.

However, solar-atmospheric links are often characterized by temporal variability, with correlation changes and reversals being observed. A roughly 60-year periodicity was found in correlation coefficients between troposphere pressure at middle and high latitudes and sunspot numbers [Veretenenko and Ogurtsov, 2012]. This periodicity seems to be caused by the epochs of the large-scale circulation which, in turn, depend on the evolution of the stratospheric polar vortex (a large-scale cyclonic circulation in the polar stratosphere which is an important factor of climate variability).

Let us consider temporal behavior of SA/GCR effects on troposphere dynamics. The data in Fig.4 (left panel) show time variations of sliding correlation coefficients between troposphere pressure at high latitudes and SA/GCR characteristics (a) compared with long-term changes of the vortex intensity (b, c) and the evolution of the main forms of the large-scale circulation according to Vangengeim-Girs classification (d). We can see that since the end of the 19th century several reversals of the correlation sign took place coinciding with the changes in the evolution of the C-type meridional circulation. The vortex strength was estimated using NCEP/NCAR reanalysis data (available since 1948). The data in Fig.4b and 4c indicate that the vortex was weak in the period ~1950-1980. This was manifested in a decrease of pressure gradients between middle and high latitudes and an increase of stratospheric temperature in the vortex area. In ~1980-2000 the vortex was strong, with the pressure gradients being enhanced and stratospheric temperature being low. So, the reversals of correlations between troposphere pressure and SA/GCR characteristics near 1950 and in the early 1980s coincided with the vortex transitions between its different states and the corresponding changes in the evolution of meridional circulation. As the vortex intensity reveals a roughly 60-year variability, one can expect the subsequent change of the vortex state in 2000-2010. This change may result in the reversal of the correlations between lower troposphere dynamics and SA/GCR characteristics which were observed in the period ~1980-2000.

Indeed, the data in Fig.4 (right panel) show that the response of cyclonic activity to GCR variations on a decadal time scale strongly depends on the vortex conditions. Increases of GCR intensity in minima of the 11-year solar cycle contribute noticeably to the strengthening of cyclonic activity (decrease of pressure) at climatic Polar fronts only under the strong vortex conditions. Under the weak vortex conditions there is no cyclone intensification associated with GCR variations. A possible reason for the detected change of the response of cyclonic activity to GCR variations may be changes in the troposphere-stratosphere coupling caused by different conditions for planetary wave propagation in the periods of a strong and weak vortex. According to [Perlwitz and Graf, 2001], the stratosphere may influence the troposphere only under the strong vortex conditions when planetary waves are reflected back to the troposphere. Under the weak vortex conditions planetary waves propagate upward and only the troposphere influences the stratosphere. This may explain why GCR variations contribute to cyclonic processes only under a strong polar vortex.

Now let us consider temporal variability of the links between troposphere pressure in the belt 30-60°N and GCR fluxes and compare them with temporal variability of the LCA-GCR links. To characterize GCR intensity we used fluxes of charged particles F_{CR} in the maximum of the absorption curve (the heights ~15-25 km) at the station Dolgoprudny (geomagnetic cut-off rigidity 2.35 GV) according to balloon measurements [Stozhkov et al., 2009]. In Fig.5a there are presented time variations of yearly values of troposphere pressure (GPH700) anomalies at middle latitudes and cosmic ray fluxes for the period 1983-2013, the linear trends being subtracted. It is seen that before 2000 pressure and GCR fluxes varied in

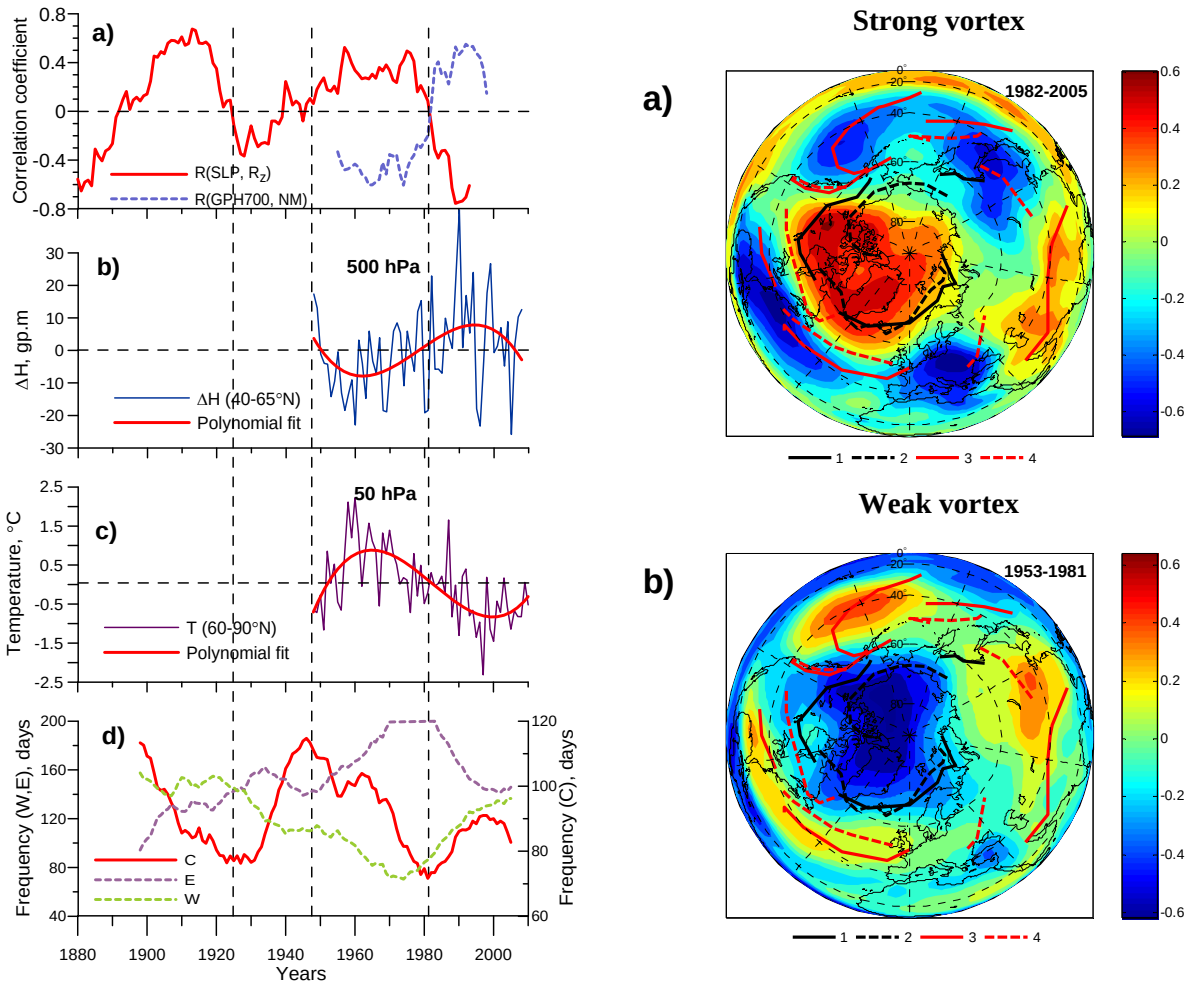

Fig.4. *Left panel:* a) Time variations of correlation coefficients between troposphere pressure at high latitudes (60-85°N) and SA/GCR characteristics for 15-year sliding intervals; b) anomalies of yearly pressure difference between the latitudes 40 and 65°N in the middle troposphere; c) anomalies of yearly stratospheric temperature at high latitudes 60-90°N; d) annual frequencies of occurrence of the large-scale circulation forms according to Vangengeim-Girs classification (15-year running means). The vertical dashed lines show the years of the correlation reversals [Veretenenko and Ogurtsov, 2013].
Right panel: Correlation coefficients between yearly values of troposphere pressure (GPH700) and GCR intensity for the periods of a strong (a) and weak (b) polar vortex. Curves 1 and 2 indicate climatic Arctic fronts in January and July, respectively. Similarly, curves 3 and 4 indicate climatic Polar fronts.

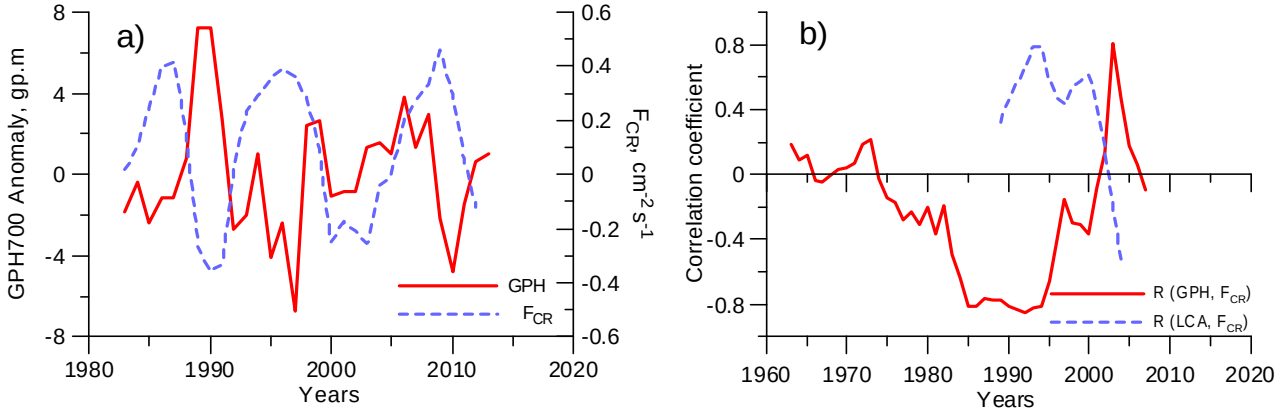

Fig.5. a) Time variations of yearly values of pressure (GPH700) anomalies at middle latitudes and charged particle fluxes (F_{CR}) in the maximum of the absorption curve at the station Dolgoprudny [Stozhkov et al., 2009]; b) time variations of correlation coefficients for sliding 11-year intervals: *solid line* – between pressure anomalies at middle-latitudes and charged particle fluxes; *dashed line* – between low cloud anomalies and charged particle fluxes.

opposite phases indicating the strengthening of cyclonic processes (and, therefore, increase of cloud cover) associated with GCR increases. This agrees well with cyclone intensification at Polar fronts due to GCR increases in the epoch of a strong vortex (Fig.4). However, the character of the correlation GPH700-GCR changed sharply in the early 2000s. The time behavior of sliding correlation coefficients between GPH700 and GCR intensity (Fig.5b, solid line) show that the strongest negative correlation (about −0.8) was observed in ~1985-1995, then it started weakening and its sharp increase took place after 2000. This may indicate the beginning of the polar vortex transition to its weak state after the period of a strong state in ~1980-2000.

Thus, the data in Fig.5b confirm the suggestion that the character of solar-atmospheric links may change in 2000-2010 due to the change of the polar vortex state. Let us consider the evolution of the LCA-GCR link. Sliding correlation coefficients between low cloud anomalies and charged particle fluxes are presented in Fig.5b (dashed line). We can see that the time variations of GPH700-GCR and LCA-GCR correlation coefficients are opposite. The strongest positive correlation between LCA and GCR intensity took place in ~1985-1995, i.e. in the period of the strongest negative correlation between troposphere pressure and GCR intensity. The sign reversals of GPH700-GCR and LCA-GCR correlations occurred simultaneously in the early 2000s. This provides evidence that the violation of a positive correlation between low clouds and GCR fluxes is caused by the reversal of GCR effects on the development of extratropical cyclones.

5. Conclusions

The link between low cloudiness at middle latitudes and GCR fluxes observed on a decadal time scale is not direct, but realized through GCR effects on the development of baric system (cyclones and troughs) which form cloud fields. A high positive correlation between low cloud anomalies and GCR variations in the period 1983-2000 resulted from intensification of cyclonic activity associated with GCR increases under a strong stratospheric polar vortex. The violation of a positive correlation LCA-GCR in the early 2000s is likely to be caused by the beginning of the vortex transition to its weak state which resulted in the reversal of GCR effects on troposphere dynamics at extratropical latitudes.

Acknowledgments. This work was supported by the Presidium of the Russian Academy of Sciences (Program N 22) and Russian Foundation for Basic Research (Grant N 13-02-00783).

References

Artamonova, I., and S. Veretenenko (2011), Galactic cosmic ray variation influence on baric system dynamics at middle latitudes. *J.Atm.Sol.-Terr.Phys*., 73, 366-370.

Dickinson, R.E. (1975), Solar variability and the lower atmosphere. *Bull.Amer.Meteorol.Soc*., 56,1240-1248.

Girs, A.A. (1974), Macro-*Circulation Method of Long-Term Meteorological Forecasts,* 488 pp., Gidrometeoizdat, Leningrad.

Gray, L.J., et al. (2010) Solar influences on climate. *Rev.Geophys*. 48, RG4001.doi:10.1029/2009RG000282.

Kalnay, E., et al. (1996) The NCEP/NCAR 40-year reanalysis project. *Bull.Amer.Meteorol.Soc*., 77,437-472.

Marsh, N., and H. Svensmark (2000), Cosmic rays, clouds and climate. *Space Sci. Rev*., 94, 215-230.

Perlwitz J., and H.-F. Graf (2001), Troposphere-stratosphere dynamic coupling under strong and weak polar vortex conditions? *Geophys. Res. Lett.*, 28, 271-274.

Pudovkin, M.I., and S.V. Veretenenko (1995), Cloudiness decreases associated with Forbush-decreases of galactic cosmic rays. *J.Atm.Sol.-Terr.Phys*., 57, 1349-1355.

Stozhkov, Yu.I., et al. (2009), Long-term (50 years) measurements of cosmic ray fluxes in the atmosphere. *Adv. Space Res*., 44, 1124-1137.

Svensmark, H., and E. Friis-Christensen (1997), Variations of cosmic ray flux and global cloud coverage – a missing link in solar-climate relationships. *J.Atm.Sol.-Terr.Phys*., 59, 1225-1232.

Todd, M., and D. Kniveton (2001), Changes of cloud cover associated with Forbush-decreases of galactic cosmic rays. *J.Geophys. Res*., 106, 32031-32041.

Veretenenko, S., and M. Ogurtsov (2012), Regional and temporal variability of solar activity and galactic cosmic ray effects on the lower atmosphere circulation. *Adv. Space Res*., 49,770-783.

Veretenenko, S., and M. Ogurtsov (2013), Stratospheric polar vortex as a possible reason for temporal variations of solar activity and galactic cosmic ray effects on the lower atmosphere circulation. *Adv.Space Res*., doi:10.1016/j.asr.2013.09.001.

Veretenenko, S., and P. Thejll (2004), Effects of energetic solar proton events on the cyclone development in the North Atlantic. *J. Atmos. Sol.-Terr. Phys*., 66, 393-405.

Vorobjev, V.I. (1991), *Synoptic Meteorology*, 616 pp., Gidrometeoizdat, Leningrad.

EFFECT OF LIGHTNING ACTIVITY OF THE WORLD LIGHTNING CENTERS ON WHISTLER RATE VARIATIONS RECORDED IN KAMCHATKA

G.M. Vodinchar[1,2], N.V. Cherneva[1], B.M. Shevtsov[1], I.V. Agranat[1], J. Lichtenberger[3,4], R. Holzworth[5]

[1]Institute of Cosmophysical Research and Radio Wave Propagation (IKIR) FEB RAS, 684034, Russia, e-mail: nina@ikir.ru;
[2]Vitus Bering Kamchatka State University, Russia;
[3]Eotvos University, Budapest, Hungary;
[4]Geodetic and Geophysical Institute, Research Center for Astronomy and Earth Sciences, Sopron, Hungary,
[5]University of Washington, Seattle, USA

Abstract. Data on March 2013 were used to verify the theory of whistler propagation along a magnetic field tube, from which the recorded whistlers are expected to be associated with lightning discharges in Kamchatka and in magnetically conjugate point in Australia. When comparing the whistler rates recorded at AWDANet station in Kamchatka with lightning discharge rates according to the data of the World Wide Lightning Location Network, it was determined that the intensity highest values are associated with lightning in magnetically conjugate points. At the same time there were some small splashes in the intensity which clearly correlated with the activity of American and African sources. Some splashes may be associated with the activity in all three sources in America, Africa and Indonesia.
This publication is based on work supported by a grant from the U.S. Civilian Research and Development Foundation (RUG1-7084-PA-13) with funding from the United States Department of State.

There is a World Wide Lightning Location Network (WWLLN, R.H. Holzworth) to register atmospherics and an Automatic Whistler Detector and Analyzer systems' network (AWDANet, J. Lichtenberger) to detect whistlers. Receiving stations integrated into the both networks were constructed and installed at the Institute of Cosmophysical Research and Radio Wave Propagation FEB RAS (IKIR). AWDANet (Lichtenberger et al., 2008) together with WWLLN allows us to trace sounding radio signal propagation paths. To detect whistlers automatically considering local peculiarities, a detection algorithm was developed [Cherneva, Vodinchar et al. 2013], in the basis of which is a method of two-dimensional correlation of initial signal spectrum and template signal spectrum of whistler detection suggested by the founder of automatic detection and whistler analysis (Lichtenberger et al., 2008). The system based on this method consists of a detector and an adaptive threshold determining factor. The detector makes two-dimensional correlation of signal fragment spectrum in 4 s time window and a model template spectrum. The adaptive threshold is some average value; if it is exceeded the preliminary conclusion is made that the signal may contain a whistler.

According to the theory of whistler propagation along a magnetic field tube, one may expect that whistlers recorded in Kamchatka should be associated with lightning discharges in Kamchatka and in the magnetically conjugate region in Australia. These are the whistlers generated by discharges in the magnetically conjugate point in Australia and propagating from it via a magnetic field tube and the whistlers generated by Kamchatka lightning and propagating via this tube an even number of times. Whistlers of Australian origin may also propagate via the tube an uneven number of times and then be recorded in Kamchatka. Whistler drift between different tubes is also possible, thus, they may arrive from other sources, first of all, from the greatest world lightning centers in America, Africa and Indonesia. To check the idea if drift whistlers are recorded in Kamchatka, whistler rates registered by AWDANet in Kamchatka were compared with lightning discharge rates according to the data of WWLLN network.

We carried out the analysis for two time intervals, March 1-11, 2013 and September 1-30, 2013. The analysis was performed by different methods for these two periods.

Time interval March 1-11, 2013 and the following lightning source regions were under the analysis: Kamchatka (LAT 43N-63N LON 150E-170E), Australia (LAT 25S-45S LON 140E-160E), American (LAT 0N-45N LON 40W-110W), African (LAT 10S-20N LON 15W-45E), Indonesian (LAT10S-30N LON 100E-130E) lightning centers. Whistler and lightning discharge rates were characterized by a number of events per a sampling interval (15 min). Comparison of rates was made both visually and by calculation of Spearman rank correlation during whistler intensity increase intervals.

The choice of rank correlation for rate relation evaluation was determined by the following factors. The usual correlation coefficient (Pearson) is a linear measure for the relation between random values. In the case of strong but nonlinear relation, correlation coefficient may be small and even equal to zero. Thus, this characteristic is good for Gaussian distributions or close to them. Rank correlation coefficients are arbitrary monotonic relation measures. Moreover, rank correlation value does not change for any growing transformation of a measurement scale, thus, it is less sensitive to large data outliers (Aivazyan et al., 1985). Figs. 1-2 show whistler and lightning discharge intensity rate series normalized to the maximum number of events for the analyzed period for magnetically conjugate points.

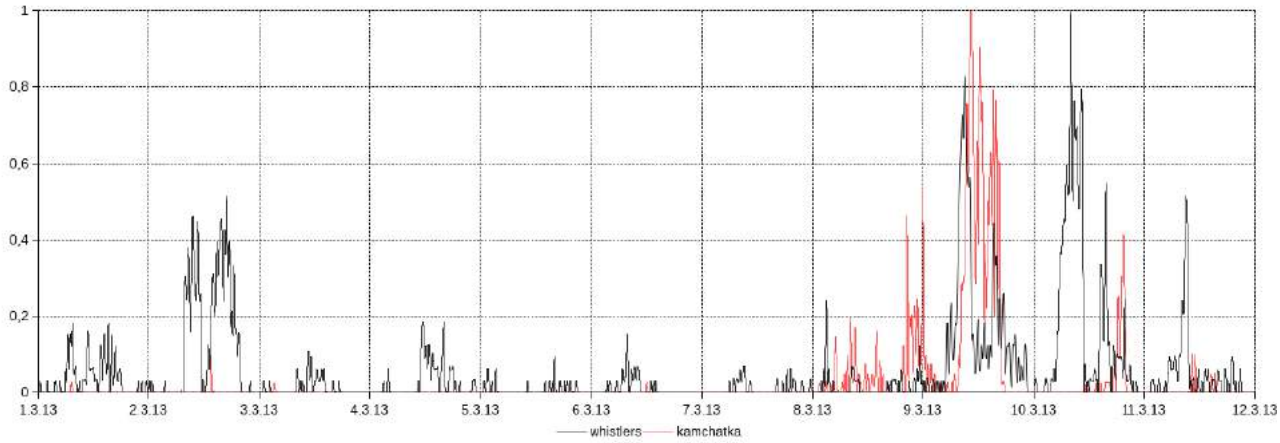

Fig. 1. Whistler rate in Kamchatka and lightning discharge rate in Kamchatka.

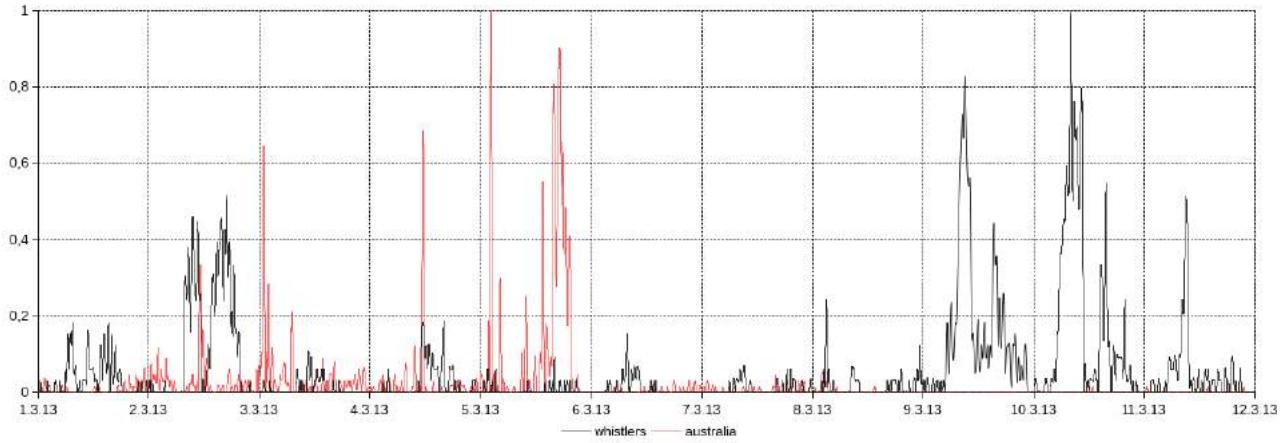

Fig. 2. Whistler rate in Kamchatka and lightning discharge rate in Australia.

Visually, comparison of these series shows a definite relation between these rates. For example, there is a clear relation of the sharp increase of whistler rate on March 9 with Kamchatka lightning. Further correlation analysis determined a splash of whistler rate on March 2 which coincides with the increase of discharge intensity growth in America, Africa and Indonesia. It is difficult to separate them visually. Consider the

results of rank correlation calculation presented in Table 1. The first column contains time intervals of whistler rate increase, and the following ones show correlation coefficient between the whistlers and lightning discharges during these periods. Significant levels of positive correlation are marked by bold, and splashes separate significance levels on which the hypothesis on noncorrelatedness is rejected.

Table 1

Date, time	Kamchatka	America	Africa	Indonesia	Australia
01.03 5:45-9:15	0.25	**0.37/0.2**	-0.44	-0.35	-0.16
01.03 9:45-13:00	-	-0.64	**0.42/0.15**	0.06	-0.19
01.03 13:15-19:00	-	-0.31	-0.23	-0.38	-0.38
02.03 7:30-12:15	-	-0.54	-0.34	-0.34	-0.34
02.03 12:30-21:00	-0.06	0.24	**0.62/0.0001**	0.43/0.01	-0.28
03.03 8:00-15:00	-	0.06	0.06	-0.37	-0.05
04.03 10:45-20:30	-	-0.26	-0.61	0.18	**0.35/0.03**
05.03 14:30-22:00	-	-0.21	-0.05	0.23	**0.34/0.1**
06.03 5:30-14:00	-0.17	**0.2/0.25**	-0.08	-0.26	-0.3
08.03 2:15-5:15	0.05	-0.04	**0.46/0.15**	-0.62	0.11
09.03 4:45-13:45	0.08	-0.57	0.14	-0.65	-
09.03 14:15-23:15	**0.57/0.0005**	0.005	-0.34	0.26	0.06
10.03 4:00-13:00	-0.25	-0.47	0.29	-0.29	-0.17
10.03 13:15-22:15	**0.42/0.01**	0.02	0.14	0.09	-
11.03 5:00-11:30	-0.59	-0.36	**0.56/0.005**	0.09	-

It is clear that there were significant positive correlations of whistler rates in Kamchatka (March 9 and 10), in Australian (March 4 and 5), in American source (March 1 and 6), in African source (March 1 and 2 and 8 and 11). Splashes on March 3, 9 and 10 are difficult to attribute to one of the considered sources; their sources are possibly located in other regions.

The method described in (Collier et al., 2009) was applied to analyze the interval of September 1-31, 2013. The Earth's surface was divided into the regions of 3×3 degrees and a time series L(t) of lightning discharge number per 1 min was composed for each region. A similar time series W(t) was composed for Kamchatka whistlers. Then, correlation coefficient between the series was calculated. To reduce the effect of big outliers, the correlation was estimated for the series coarsened to Boolean values. The scheme of coarsening is the following. If the series element was zero, its value was saved. If it was nonzero, the value was changed to 1. The hypothesis on zero correlation for the considered series and the significance level γ=0.05 is rejected when the correlation sample value is 0.011. Fig. 3 shows the distribution of correlation coefficient value for those elements of the grade grid where its value exceeds the significance bound.

It is clear from this distribution that correlation between Kamchatka whistlers and lightning in the conjugate

point in Australia was not observed for the considered time interval. At the same time, we may see the correlation between the whistlers and the activity of the Indonesian and American lightning sources.

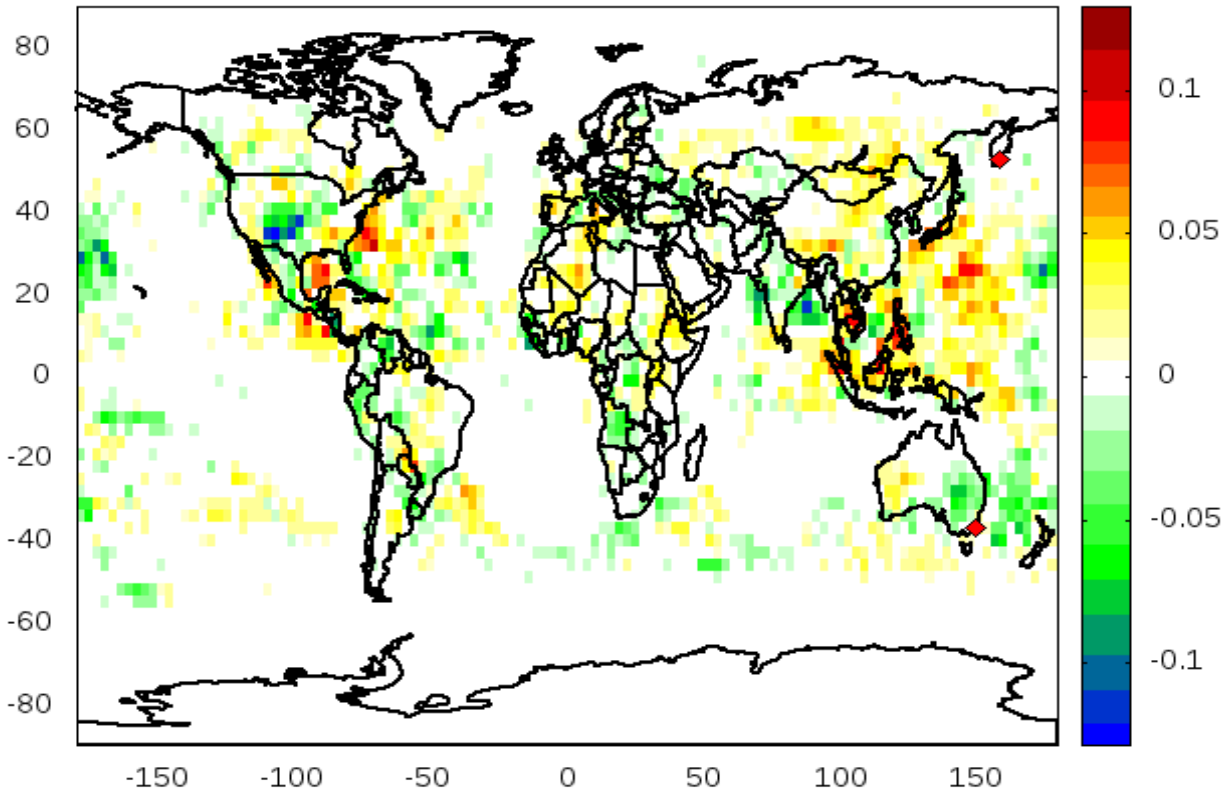

Fig. 3. Distribution of correlation coefficient between Kamchatka whistler series and lightning discharge series on the grade grid of 3×3. Red rhombs indicate the location of Kamchatka observatory (LAT 52.97N LON 158.25E) and the conjugate point in Australia (LAT 36.77S LON 149.40E). Cell color corresponds to correlation coefficient value. Correlation is insignificant in white colored cells.

Conclusion

The analysis of whistler intensity series for March 1-13, 2013 and September 1-30, 2013 recorded in Kamchatka showed that the registered signals may have lightning sources both from "Kamchatka" magnetic field tube and from other regions. Kamchatka and Australian lightning did not dominate as it could be expected. The possible explanation is that during the considered periods, lightning intensity in American, African and Indonesian sources was significantly higher than that in Australia and especially in Kamchatka.

References

Aivazyan, S. A., Enyukov I.S., Meshalkin L.D. (1985), [Applied statistics. Study of dependences], *Finances and statistics*, Moscow, 487.

Cherneva, N.V., Vodinchar, G.M., Sivokon, V.P., Melnikov, A.N., Sannikov, D.V., Agranat, I.V. (2013), Correlation alalysis of whistler and lightning discharge rates, *Vestnik KRAUNTS. Phys.-Math. Sciences*. Petropavlovsk-Kamchatksiy, N 2(7), 59-67.

Lichtenberger, J. (2009), A new whistler inversion method, *J. Geoph. Res., Space Physics*, v. 114, N A7, doi:10.1029/2008JA013799.

Lichtenberger, J., Ferencz, C., Bodnár, L., Hamar, D., Steinbach, P. (2008), Automatic Whistler Detector and Analyzer system: Automatic Whistler Detector, *J. Geoph. Res.: Space Physics*, v. 113, N A12. doi:10.1029/2008JA013467.

Collier, A. B., Delport, B., Hughes, A.R.W., Lichtenberger, J., Steinbach, P., Oster J., Rodger C. J. (2009), Correlation between global lightning and whistlers observed at Tihany, Hungary, *J. Geoph. Res., Space Physics*, v. 114, N A07210, doi:10.1029/2008JA013863.

THE FORMATION OF THE TWO-DIMENSIONAL AURORAL STRUCTURES OF THE IONOSPHERIC CONVECTION

Volkov M.A.

Murmansk State Technical University, 183010 Murmansk, e-mail: volkovma@mstu.edu.ru

Abstact. The formation of the two-dimensional auroral structures in the cold ionospheric-magnetospheric plasma under convection is considered. The convection inhomogeneity leads to the currents across and along the magnetic field lines. The field-aligned currents flowing from the ionosphere into the magnetosphere are creating positive feedback between magnetospheric and ionospheric perturbations. The ionosphere is assumed by a thin conductive layer, but the processes of the ionization and recombination of charged particles are considered. The ionospheric processes were considered as non-linear. In the magnetosphere the linear approximation was used. The linear equation for the Alfven waves propagating along the magnetic field from the ionosphere to the magnetosphere was solved with the realistic change of the velocity along the magnetic field lines. The growth rate of the disturbances with the scale 1 km is ~ 60 c for the enhanced Hall ionosphere conductivity 8*S*. The growth rate of the disturbances depends on the conductivity of the ionosphere. The disturbances at the smaller scale also developed faster. The consideration of the thermal motion of particles in the ionosphere leads to weakening and even suppression the development of ionospheric disturbances.

Introduction

In the works [*Atkinson*, 1970; *Holzer and Sato*, 1973] have been predicted feedback mechanisms between the moving plasma in the magnetosphere and ionosphere. Even in the case of the cold plasma due to collisions with neutral particles in the ionosphere perturbations of the electric and magnetic fields occur. In the cold plasma they propagate along the magnetic field from the ionosphere into the magnetosphere in the form of Alfven waves. The field-aligned currents arise because of the polarization currents at the edges of the field perturbations. These currents may give rise to the field-aligned electric field acceleration and the precipitation of the electrons in the ionosphere. This feedback can be positive and lead to an increase in disturbances. Studies of feedback are usually held in the approximation of small perturbations [*Trakhtengerts and Feldstein,* 1991; *Lysak and Yan Song*, 2002]. But even in this case a more accurate solution for this problem can be obtained using numerical methods because of the non-uniform profile of the Alfven velocity along the magnetic field lines. The field-aligned currents ~ 10^{-5}A/m^2 can significantly modify the ionospheric conductivity at the same time they have small effect on the concentration of the cold magnetospheric plasma. In this work has been considered the development of two-dimensional auroral disturbances which are nonlinear in the ionosphere and linear in the magnetosphere using numerical calculations taking into account realistic changes Alfven velocity along the magnetic field lines.

Model of the ionosphere

We use a rectangular coordinate system, the *y*-axis direct to west, the *x*-axis direct south, axis *z* - down along the magnetic field (Northern Hemisphere). We will consider two-dimensional perturbations depending on *x* and *z*, i.e. $\partial/\partial y = 0$.
The continuity equation for the electrons with the ionization and recombination processes is as follows:

$$\partial n/\partial t + \partial(nv_{ex})/\partial x = -\gamma/e\partial j_z/\partial z - r(n^2 - n_0^2), \quad (1)$$

where n, v_{ex}- the concentration and velocity of electrons; n_0-the undisturbed ionospheric concentration of the charge particles; r - the rate of recombination , j_z-the field-aligned current density, e - the charge of proton, γ-the factor of multiplication pairs of ions during ionization.
We are interested in processes whose duration is much greater than 0.01 s. In this case the ions motion expression is :

$$v_{xi}=(-kT\partial ln(n)/\partial x+eE_x)f(\nu/\omega_i)/m_i\omega_i \quad (2)$$

where v_{xi} – the velocity of the ions, kT - the thermal energy of the ions, m_i is the mass of the ion, n - concentration of ions in the ionosphere, ν - the frequency of collisions between ions and neutrals, ω_i - the ion gyrofrequency, E_x - x component of the electric field intensity, $f(\nu/\omega_i) = (\nu_{in}/\omega_i)/(1+ (\nu_{in}/\omega_i)^2)$.
The continuity equation for the current in the ionosphere is:

$$\partial/\partial x(\sigma_p E_x - \sigma_h E_{0y}) = -\partial j_z/\partial z, \quad (3)$$

where σ_{ph} – the ionospheric Pedersen and Hall conductivity, E_{0y} – intensity electric field of the ionospheric-magnetospheric convection.
Collision frequency of electrons with neutrals is much less than the electron gyrofrequency in the ionosphere, so we can assume that the electrons move at the speed of convection $v_e = E_{0y}/B_0$ (B_0 –magnetic induction in the ionosphere). The ionospheric conductivity depends on the concentration of charged particles and the frequency as follows:

$$\sigma_h = en/B_0, \qquad \sigma_p/\sigma_h \approx f(\nu/\omega_i).$$

We consider the ionosphere as thin conductive layer. Equations (1-3) we integrate over the thickness of the ionosphere h. For this purpose we define the concentration changes with the height s: $n(s) = n_0 \exp(-((s-s_0)/h)^2)$, where s_0- height of the maximum E layer, the distribution f(s) define the same way, where $f(s_0) = 0.5$.
The equation (1,3) integrated over the thickness of the ionosphere can be written then as follows:

$$\partial N/\partial t + E_{0y}/B_0 \partial N/\partial x = -\gamma j_z/e - r(N^2 - N_0^2)/(2^{3/2}h) \quad (4)$$

$$\partial/\partial x(eNE_x/(2^{3/2}B_0) - kT\partial ln(N)/\partial x//(2^{3/2}eB_0) - eNE_{0y}/B_0) = j_z \quad (5)$$

Model of the magnetosphere

Magnetospheric plasma is believed cold, density perturbation is neglected and the field-aligned electric field equal zero. The only component of the perturbed electric field is E_x, magnetic – H_y. From equation of cold plasma motion in a coordinate system moving with the plasma we obtain the expression for the polarization current in the Alfven wave:

$$j_x = 1/(\mu_0 v_a^2)\partial E_x/\partial t, \quad (6)$$

where μ_0- permeability of vacuum, $v_a^2 = \rho\mu_0/B^2$ - square of Alfven velocity, ρ is the plasma density, B- the magnetic field in the magnetosphere.
From Maxwell's equations:

$$\partial E_x/\partial z = -\mu_0 \partial H_y/\partial t, \qquad \partial H_y/\partial z = -j_x, \qquad \partial H_y/\partial x = j_z,$$

and the continuity equation for the current $\partial j_z/\partial z = -\partial j_x/\partial x$ obtain the equations for E_x and j_z:

$$\partial^2 E_x/\partial z^2 = 1/(v_a^2)\partial^2 E_x/\partial t^2, \quad (7)$$

$$\partial j_z/\partial t = -1/(\mu_0)\, \partial^2 E_x/\partial z \partial x \quad (8)$$

The magnetic field lines are considered direct but divergent, the magnetic field varies with the distance r from the center of the earth according to the law: $B = B_0(r_g/r)^3$, r_g - radius of the Earth. The concentration of the magnetospheric plasma (electrons, protons) $n = n_0 \exp(-(r/2r_з)^2)$, n_0 - the concentration in the ionosphere. The profile of the Alfven velocity from the ionosphere $z = 0$ to the equatorial plane of the magnetosphere $z = -(r-r_з)/r_з = -10$ is shown in Figure 1. The z values decrease with increasing distance from the Earth to the upper boundary of the ionosphere. The plasma density in the ionosphere at $z = 0$ was set equal to $n_0 = 0.5 \cdot 10^{11}$ $1/m^3$.

Boundary conditions

To solve the equation (7) is necessary to write the boundary conditions for the E_x on the lower and upper boundaries in the ionosphere and in the equatorial plane of the magnetosphere. In the moving coordinate system the equation (5) does not change and the second term on the left side in equation (4) vanishes. It

obtains the condition on the lower boundary. The equation (5) is differentiated with respect to time, the current j_z is substituted from (8), and then we omit the x derivative. As a result, we obtain at $z = 0$:

$$\partial E_x/\partial t = -(E_x - 2^{3/2}E_{0y})\,\partial(lnN)/\partial t - 2^{3/2}B_0/(e\,\mu_0 N)\,\partial E_x/\partial z + kT/(e^2N)\,\partial^2(lnN)/\partial z\partial t \quad (9)$$

The upper boundary condition at $z = -10$ is:

$$\partial E_x/\partial z = 0 \quad (10)$$

This condition determines the node for the magnetic field in the equatorial plate of the magnetosphere (E_x = 0 - node for electric field).

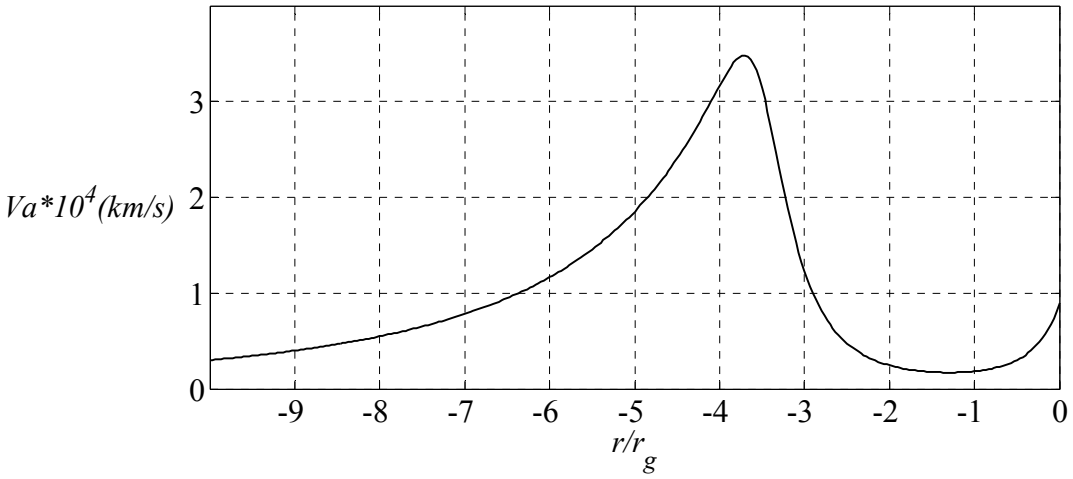

Figure 1. The changes of the Alfven velocity along the magnetic field lines from the ionosphere $z = 0$ to the equatorial plane of the magnetosphere $z = -10$.

Results of numerical simulation

The system of equations (4,7,8) with the boundary conditions (9,10) was solved by numerical integration with a time step dt = 0.005 *s* and with a step on the coordinates x, z , dx = 100 *m* and dz=100 *km*, respectively. The initial perturbation of the E_x component electric field (the field in the incident on the ionosphere Alfven waves) at the ionospheric level was set in the form of gaussoid in x:

$$E_x(x) = E_{x0}exp(-((x - L/2)/dL)^2) \quad (11)$$

The duration of the initial perturbation $\tau = 4$ *s*. The amplitude of the perturbation E_{x0} was set to 5 *mV/m*, L = 100 *km* - the size of the region of integration for x, dL - spatial scale of the initial perturbation in the coordinate x, $dL = v_{x0}\,\tau$, $v_{x0} = E_{0y}/B_0$ - convection velocity, we obtain dL = 2*km* taking the rate of the convection v_{x0} = 500 *m*/*s*. On the right boundary at $x = L$ is satisfied:

$$\partial E_x/\partial t - (dx/dt)\partial E_x/\partial z = 0, \quad (12)$$

this condition means waves transparency of the right boundary.

Figure 2 (a, b, c) shows the results of numerical modeling of the concentration of N, E_x component of the electric field, the field-aligned current j_z by ionospheric level at different time. The calculation was performed for the parameter value $\gamma = 10$, the integral ionospheric Hall conductivity in this calculation was 8 *S*, which corresponds disturbed conditions. The growth rate of the perturbation is ~ 60 *s*, the propagation time of the Alfvén waves to the equatorial plane and back ~ 40 *s*. With the decrease of the conductivity of the ionosphere growth rate of the disturbances reduced. Despite significant field-aligned currents 10 A/km^2 the changing of the ionospheric density is very small. It is connected with a small value of the parameter γ, which determines the number of pairs of ions produced by ionization of a single electron. In the auroral arcs this parameter may be more than 100. The thermal diffusion of the particles inhibits the growth of perturbations. The disturbance propagates in direction opposite to convection with velocity ~ 100 *m*/*s*.

Figure 3 shows the distribution of the electric field component E_x at different times. The magnitude of the electric field intensity increases with time and with distance from the ionosphere.

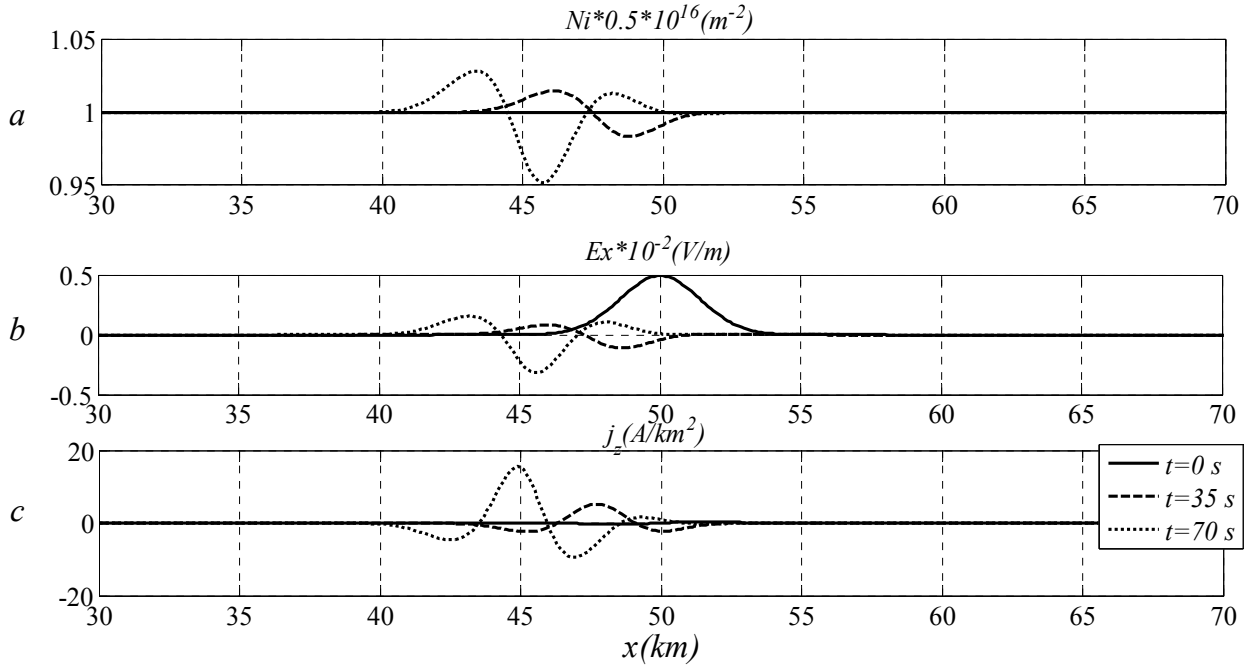

Figure 2. The development of the ionospheric disturbances initiated E_x electric field pulse at time $t = 0$ and duration $\tau = 4s$.

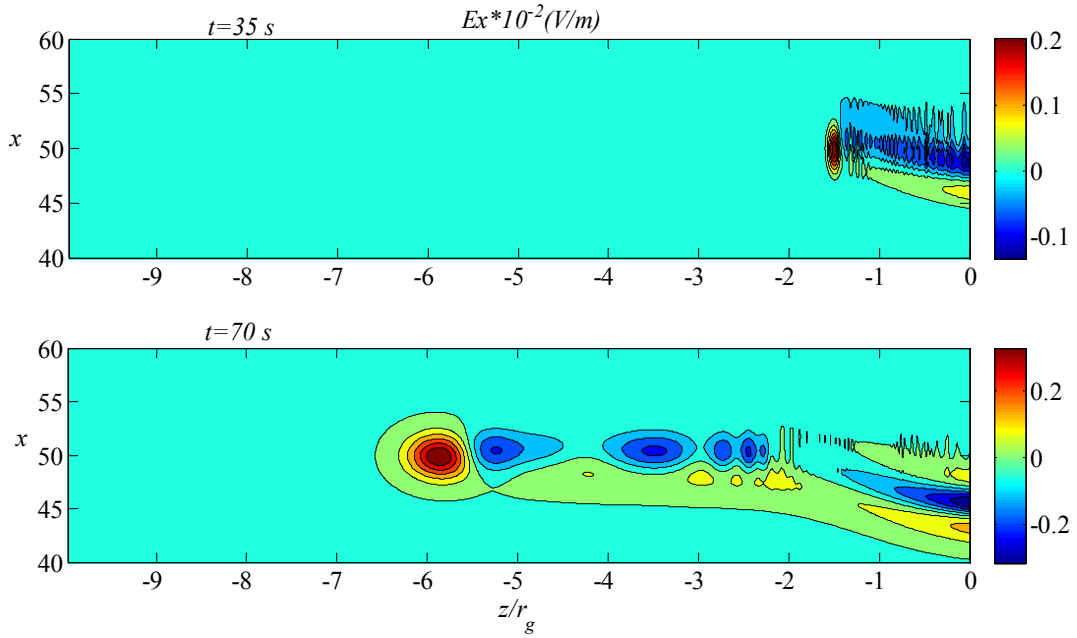

Figure 3. The distribution of E_x perturbations along the magnetic field from ionosphere $z = 0$ to the magnetosphere.

Conclusions

We have been considered the problem of the development perturbations in the moving ionospheric plasma using methods of numerical simulation. The calculations are performed in two-dimensional approximation for the perturbations with scale across the magnetic field ~ 1 *km* and ~ 1000 *km* along magnetic field. In the ionosphere the processes were considered as non-linear, in the magnetosphere we used linear approximation.

The linear equation of the Alfven wave propagation is solved taking into account the change of velocity along the magnetic field. The growth rate of the perturbation is ~ 60 *s* (for the ionospheric Hall conductivity equal 8 *S*). The growth rate of the perturbation depends on the conductivity of the ionosphere, with a decrease in conductivity perturbations develop faster. Perturbations on a smaller scale are also developing rapidly. The consideration of the thermal motion of the particles in the ionosphere leads to the weakening of the ionospheric disturbances. The field-aligned currents up to 10 A/km^2 cause minor changes in the concentration of the ionospheric plasma due to the underestimation of the ionization term in the equations. The velocity of the perturbation across the magnetic field relative the convection is ~ 100 *m*/*s*. The electric field strength of the perturbation increases with distance from the ionosphere and reaches a maximum in the equatorial plane of the magnetosphere.

References

Atkinson, G. (1970), Auroral arcs: Result of the interaction of a dynamic magnetosphere with the ionosphere, *J. Geophys. Res.*, 75, 4746.

Holzer, TE, and T. Sato (1973), Quiet auroral arcs and electrodynamic coupling between the ionosphere and magnetosphere*, J. Geophys. Res*., 78, 7330.

Lysak, RL, Yan Song (2002), Energetics of the ionospheric feedback interaction, *J. Geophys. Res*., 107, A8, 1160, 10.1029/2001JA000308.

Trakhtengerts, V.Yu., Feldstein, A.Ya. (1991), Turbulent Alfven boundary layer in the polar ionosphere, *J. Geophys. Res*., 96, All, 19,363-19,374.

Pi2 GEOMAGNETIC PULSATIONS BEHAVIOR IN "POLAR" AND "HIGH-LATITUDE" SUBSTORMS: CASE STUDY

N.R. Zelinsky[1], N.G. Kleimenova[1], L.M Malysheva[1], I.V. Despirak[2], A.A. Lubchich[2], N.E. Vasilieva[1]

[1]Schmidt Institute of the Earth Physics RAS, Moscow, 123995, Russia, e-mail: kleimen@ifz.ru;
[2]Polar Geophysical Institute RAS, Apatity, Russia

Abstract. In our terminology, the "polar substorms" are isolated substorms, observed at geomagnetic latitudes higher 71° and not accompanied or preceded by substorms at auroral latitudes. The "high-latitude substorms" are the substorms which start at auroral and then drift to the polar latitudes. Here we apply the methods of the discrete mathematical analysis (DMA), namely the calculation of the general dispersion of the two-dimensional covariance matrix of the wave, to study the global latitudinal structure of the Pi2 (f=8-20 mHz) geomagnetic pulsations, which were observed during several "polar" and "high-latitude" substorms. For this analysis, we used the observations of 10-s sampled IMAGE meridian magnetometer profile data and 1-s sampled data from some mid-latitude and equatorial INTERMAGNET stations. We found that generally the Pi2 pulsations bursts associated with both types of substorms occurred simultaneously from polar to equatorial latitudes. However, the wave polarization was different at different latitudes. The Pi2 pulsations exited at auroral latitudes were left-hand polarized and the Pi2 pulsations exited at polar latitudes were right-hand polarized. The strongest Pi2 pulsations were recorded at the electrojet centre location. The examples of Pi2 behaviour during two considered types of substorms are shown.

Introduction

Despite the fact that Pi2 geomagnetic pulsations (f=8-20 mHz) have been widely studied for more than half a century, and several hundred works are devoted to them, the mechanism of their generation and their role in the physics of magnetosphere substorms have not been finally established so far. There are some monographs and reviews in which the morphological characteristics of Pi2 pulsations at different latitudes and possible mechanisms of their generation are discussed, e.g., [Troitskaya and Gul'el'mi, 1969; Saito, 1969; Pudovkin et al., 1976; Baumjohann and Glassmeier, 1984; Yumoto, 1986; Olson, 1999; Kepko et al., 2001; Kleimenova, 2007; Keiling and Takahashi, 2011]. The mechanisms of Pi2 propagation in the magnetosphere from the generation area to the Earth's surface have also not been established. Consequently, the analysis of Pi2 features remains an important task for studying the physical mechanism of the generation of this type of pulsation and its source localization.

One of the most important properties of Pi2 pulsations is their clear link with onset of the explosive phase (breakup) of the magnetospheric substorm [Saito et al., 1976]. The magnetic substorms are observed not only at auroral latitudes but at polar latitudes as well. All substorm disturbances observed in polar latitudes we divided into two types: "high-latitude substorms" [Despirak et al., 2008] (Fig. 1), which expand from auroral (<70°) to polar (>70°) geomagnetic latitudes and "polar substorms" [Kleimenova et al., 2012] (Fig.2), which are observed at geomagnetic latitudes higher than 70° in the absence of disturbances below 70°.

The aim of this paper is to study the Pi2 latitude distribution and wave polarization during these types of substorms. For the analysis, we used the observations of 10-s sampled IMAGE meridian magnetometer profile data and 1-s sampled data from some mid-latitude and equatorial INTERMAGNET stations.

Method of the analysis

The Pi2 pulsations here have been analyzed by applying the fuzzy logic methods of the Discrete Mathematical Analysis – DMA developed in some papers [e.g., Agayan et al., 2005; Gvishiani et al., 2008; Bogoutdinov et al., 2010].

The first step of the observation data processing included the filtration within the 8–20 mHz range using a band-pass Butterworth filter with a zero-phase shift [Kanasevich, 1985], the amplitude-response curve of which is maximally smooth in the frequency bandwidth. The chosen DMA rectification for this analysis was so called the generalized variance, calculated as the Kolmogorov mean [Kolmogorov, 1985] of eigenvectors

of the covariance component data [Means, 1972]. The covariance matrix calculation in the window is the known procedure for polarization analysis.

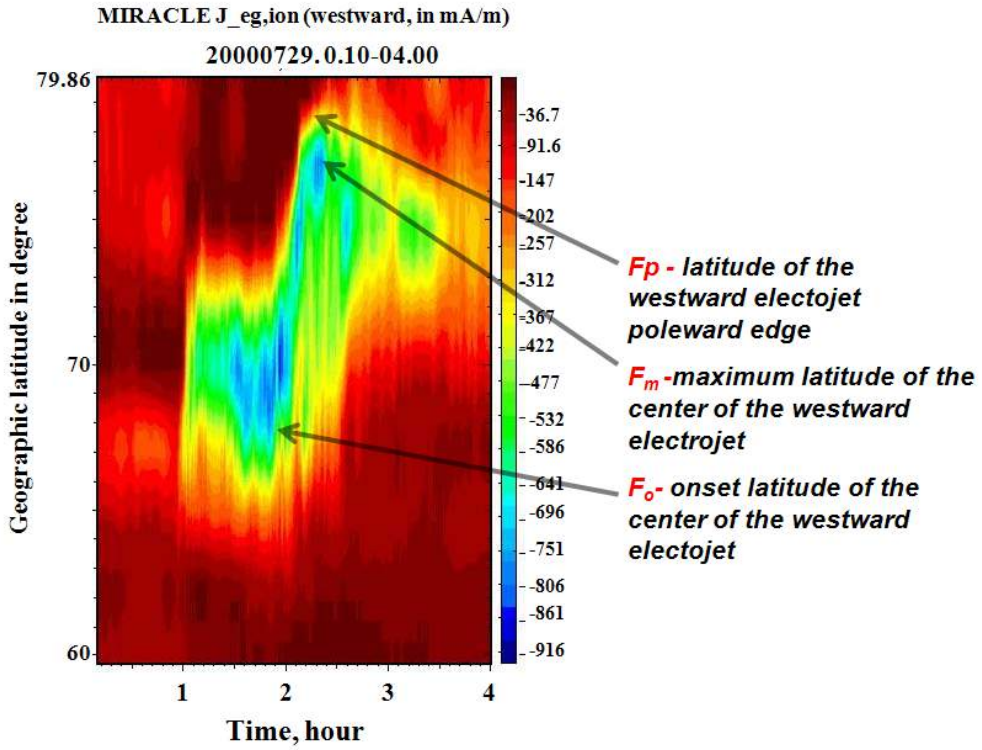

Fig. 1. The example of the westward electrojet development during "high-latitude" substorm in geographic coordinated according to the MIRACLE model which calculated ionospheric equivalent currents.

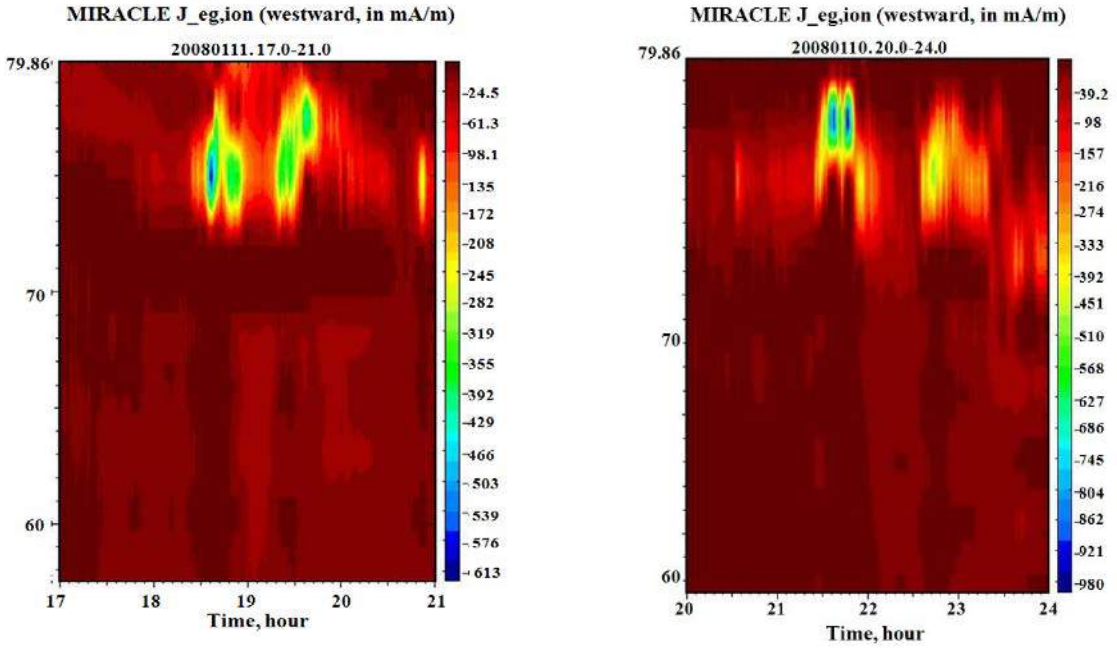

Fig. 2. Two examples of the "polar substorms".

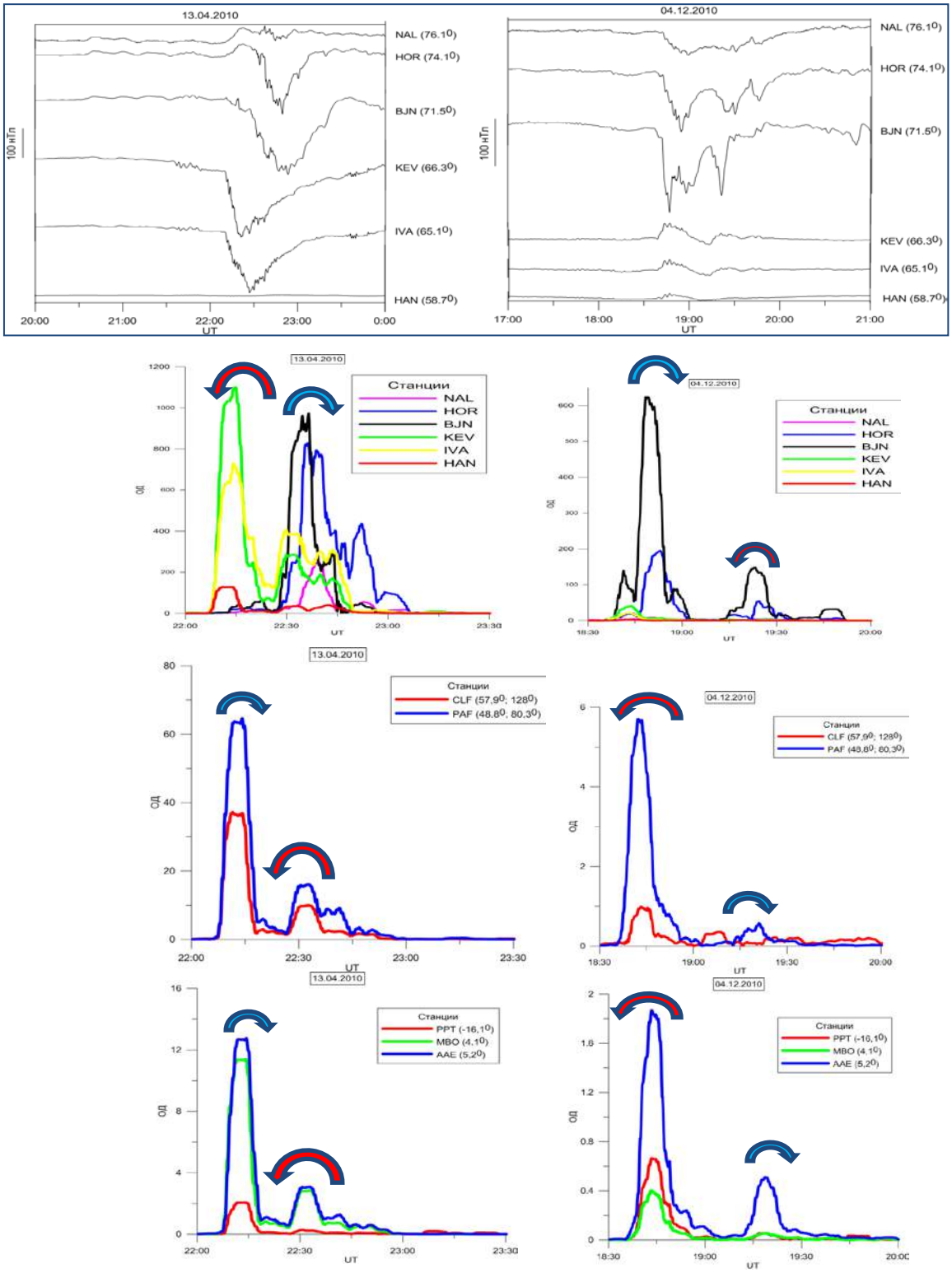

Fig. 3. Magnetograms from some IMAGE stations and plots of the generalized variance of Pi2 pulsations (relative units) at high, middle, and equatorial latitudes during the "high-latitude" (left) and "polar" (right) substorms; the arrows indicate the rotation direction of the wave polarization.

Results and discussion

First at all it was found that each Pi2 bursts in both types of substorms was observed in the global scale of the latitude: the Pi2 bursts were coherent at high, middle and equatorial stations located along the same geomagnetic meridian. It was sharp amplitude decreasing with latitude declining. The Pi2 amplitude at the equator was much stronger at night side than at day side.

The principal axis of the polarization ellipse and the direction of the polarization vector rotation were determined (shown by the arrows in Fig. 3). It can be seen that the auroral burst of Pi2 pulsations in the region of their amplitude maximum was characterized by the left-hand polarization, while the polar Pi2 burst was chartered by the right-hand polarization. We note that the right-hand polarization burst of Pi2 pulsations at polar latitudes was also observed during the "polar substorm" (right side of the Fig. 3). The change of the Pi2 polarization with the substorm shift from auroral to polar latitude is seen in the left part of Fig. 3.

We found that the Pi2 polarization change near the geomagnetic latitude ~70° is the regular fact. One can see it clearly in Fig.4, illustrated that for two more examples.

Another change of the sign of the wave polarization was observed near the plasmapause and then it remains the same to the equator (Fig. 3).

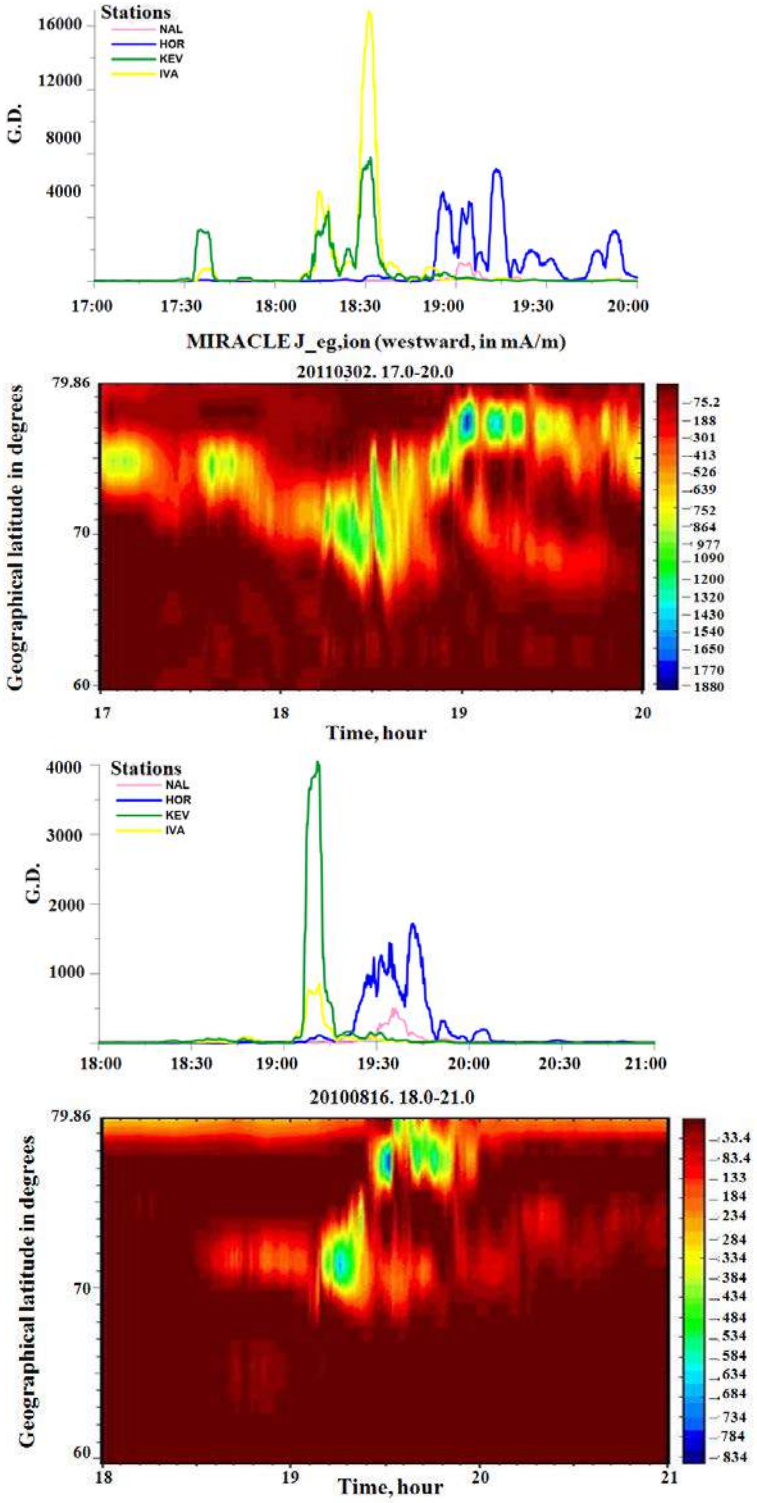

Fig.4. Two more examples of Pi2 pulsations in the "high-latitude" substorms

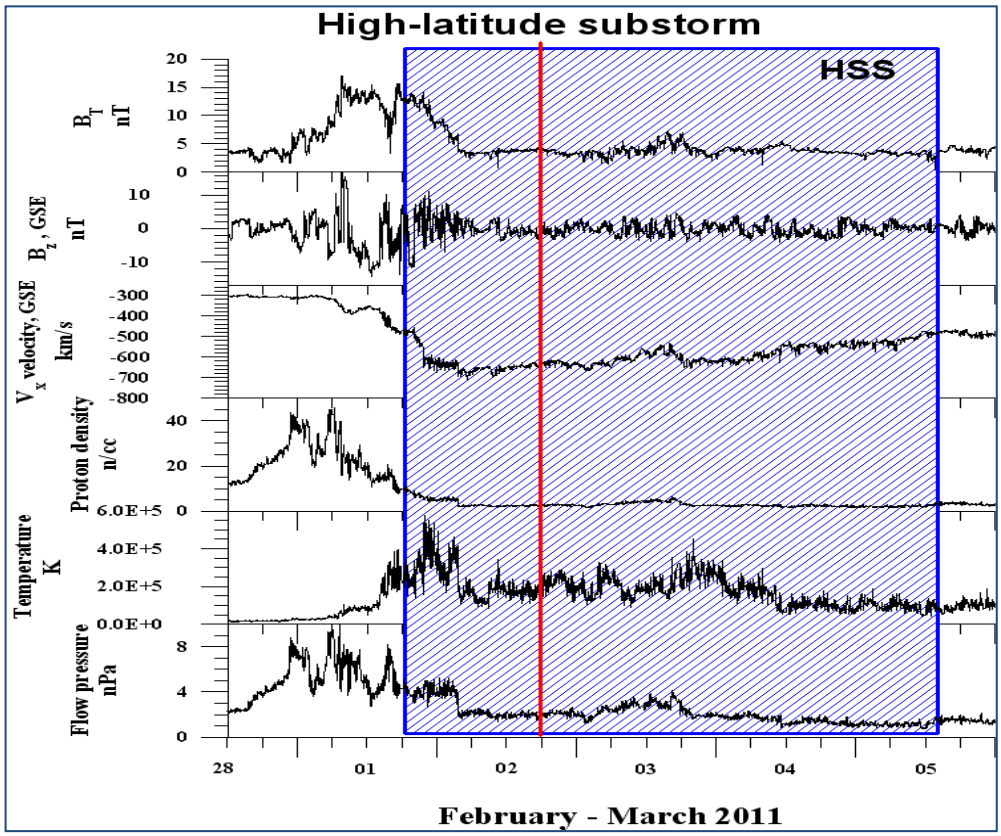

Fig. 5. Solar wind and IMF parameters typical for "high-latitude" magnetic substorm

It was found that the solar wind and IMF parameters are different in the case of the "polar" and "high-latitude" substorms. Typically, the "polar" substorms occur under the low solar wind velocity < 500 km/s in the late recovery phase of a magnetic storm. Contrary to that, the "high-latitude" substorms are observed during high speed solar wind streams (HSS) in the early recovery phase of a magnetic storm under the high solar wind velocity > 500 km/s (Despirak et al., 2009). The typical solar wind and IMF parameters for the "high-latitude" substorms are shown in Fig. 5.

One of the presumable sources of the Pi2 pulsations could be fast plasma flows in the magnetotail (BBFs) that are directed to the Earth. A statistical link of these flows with generation of Pi2 pulsations is shown in a number of works, e.g., (Hsu and McPherron, 2007). A possible scheme of the generation of the BBF-induced Pi2 pulsations is shown by Kepko et al. (2001, Fig. 15). A BBF "impact" on the closed magnetosphere generates a fast mode of wave (compression wave) propagating along the Earth`s radius to the equator, as it was recorded on satellites and at the ground-based low-latitude stations. These Pi2 pulsations are referred by Kepko et al. (2001) to "*directly driven Pi2*". Moreover, the appearance of the fluctuating field aligned electric currents is most likely connected to the auroral and polar bursts of Pi2 pulsations discussed in this work.

Conclusion

1. It was shown that the bursts of Pi2 pulsations in a frequency band of 8–20 mHz accompanied substorm both types ("polar" and "high-latitude") occur simultaneously at a global latitude scale: from polar to equatorial latitudes. The spatial dynamics of the maximum amplitude location of the Pi2 pulsations corresponds to the spatial dynamics of the westward electrojet center location.
2. We revealed a very important fact, namely, the regular change of the polarization rotation direction of the substorm associated Pi2. It was left-handed at the auroral latitudes (< 70°) while right-handed at the polar ones (> 70°). During both types of substorms, the sigh of the polarization vector rotation changed near plasmapause and then remains the same to the equator. Thus, the direction of the Pi2 polarization vector rotation, observed at low and even equatorial latitudes could be used as an indicator where are these Pi2 pulsations were generated low or higher of 70° geomagnetic latitude.
3. The "high latitude" substorms are observed during a recurrent high speed stream (HSS), while the "polar" substorms are observed after HSS then the solar wind velocity decreases.

Acknowledgment. This study was supported by RFBR grants 13-05-00233 and 12-05-01030 and partly by the Program no 7 of the Earth Science Department RAS and by Program No 22 of the Presidium of the RAS "Fundamental problems of the Study and Exploration of the Solar system".

References

Agayan, S.M., Bogoutdinov, Sh.R., Gvishiani, A.D.,Graeva, E.M., Diament, M., Zlotnicki, J., and M.V. Rodkin (2005), Issledovanie morfologii signala na osnove algoritmov nechetkoi logiki (Signal morphology analysis based on fuzzy logic algorithms), *Geofiz. Issled.*, 1, 143–155 (in Russian).

Gvishiani, A.D., Agayan, S.M., and Sh.R. Bogoutdinov (2008), Fuzzy recognition of anomalies in time series, *Dokl. Earth Sci.*, 421, 1, 838–842.

Baumjohann, W. and Glassmeier, K.-H. (1984), The transient response mechanism and *Pi*2 pulsations at substorm onset: Review and outlook, *Planet. Space Sci.*, 1984, 32, 1361–1370.

Bogoutdinov, Sh.R., Gvishiani, A.D., Agayan, S.M., Solovyev, A.A., and Kin, E. (2010), Recognition of disturbanceswith specified morphology in time series. Part 1: Spikes on magnetograms of the worldwide INTERMAGNET network, *Izv., Phys. Solid Earth*, 46, 11, 99-1012.

Despirak I.V., Lyubchich A.A., Biernat H.K., Yakhnin A.G. (2008), Poleward expansion of the westward electrojet depending on the solar wind and IMF parameters, *Geomag. Aeron*., 48, no. 3, 284–292.

Despirak I.V., Lubchich A.A., Yahnin A.G., Kozelov B.V., Biernat H.K. (2009), Development of substorm bulges during different solar wind structures. *Ann. Geophys*. 27, 1951-1960.

Hsu, T.-S. and McPherron, R.L. (2007), A statistical study of the relation of *Pi*2 and plasma flows in the tail, *J. Geophys. Res.*, 112, A05209. doi 10.1029/2006JA011782.

Kanasevich, E.R., (1985), *Analiz vremennykh posledovatel'nostei v geofizike* (Time sequence analysis in geophysics), Moscow: Nedra.

Keiling, A. and Takahashi, K. (2011), Review of *Pi*2 models, *Space Sci. Rev.*, 2011, 161, 63–148.

Kepko, L., Kivelson, M.G., and Yumoto, K. (2001), Flow bursts, braking, and *Pi*2 pulsations, *J. Geophys. Res.*, 106, A02, 1903–1915.

Kleimenova, N.G. (2007), Geomagnetic pulsations, in *Modeli kosmosa* (Models of Space), Panasyuk, M.I., Ed., Moscow: Moscow State Univ., 1, 511–627.

Kleimenova, N.G., Antonova, E.E., Kozyreva, O.V., Malysheva, L.M., Kornilova, T.A., Kornilov, I.A. (2012), Wave structure of magnetic substorms at high latitudes, *Geomag. Aeron*. 52 (6), 746–754.

Kleimenova, N.G., Zelinskii, N.R., Kozyreva, O.V., Malysheva, L.M., Solov'ev, A.A., and Bogoutdinov, Sh.R. (2013), *Pc*3 geomagnetic pulsations at near-equatorial latitudes at the initial phase of the magnetic storm of April 5, 2010, *Geomagn. Aeron.*, 53 (3), 330-336.

Kolmogorov, A.N. (1985), *Matematika i mekhanika. Izbrannye trudy* (Mathematics and Mechanics: Selected Works),Nikol'skii, S.M., Ed., Moscow: Nauka, 1985, v. 1, 136–138.

Means, J.D. (1972), Use of the three-dimension covariance matrix in analyzing the polarization properties of plane waves, *J. Geophys. Res.*, 77 (28), 5551–5559.

Olson, J.V. (1999), *Pi*2 pulsations and substorm onsets: A review, *J. Geophys. Res.*, 104, 17499–17520.

Saito, T. (1969), Geomagnetic pulsations, *Space Sci. Rev.*, 10, 319–412.

Saito, T., Yumoto, K., and Koyama, Y. (1976), Magnetic pulsation *Pi*2 as a sensitive indicator of magnetospheric substorm, *Planet. Space Sci.*, 24, 1025–1029.

Troitskaya, V.A. and Gul'el'mi, A.V. (1969), Geomagnetic pulsations and diagnostics of magnetosphere, *Usp. Fiz.Nauk,* 196997, 453–494.

Yumoto, K. (1986), Generation and propagation mechanisms of low-latitude magnetic pulsation: A review, *J. Geophys.Res.*, 60, 79–105.